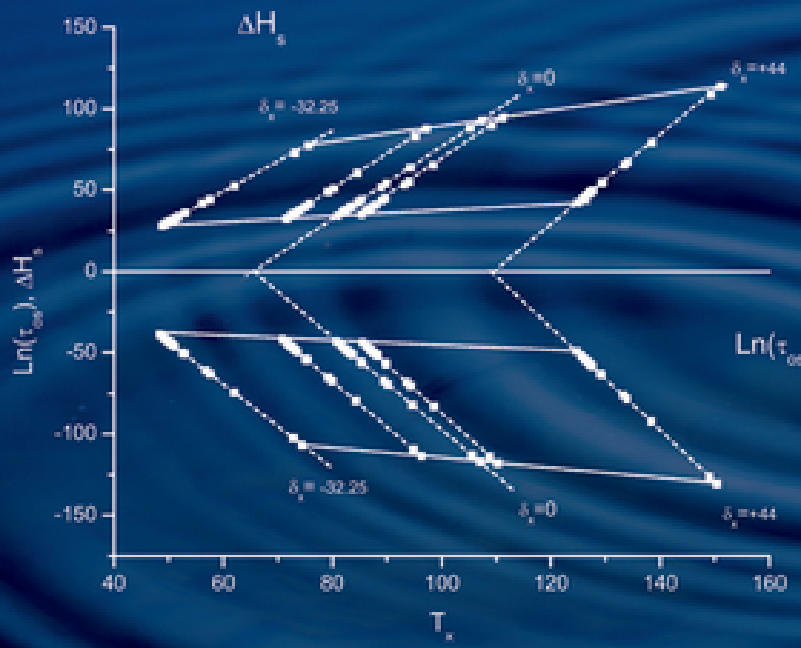
DE GRUYTER REFERENCE

Jean Pierre Ibar

DUAL-PHASE DEPOLARIZATION ANALYSIS

INTERACTIVE COUPLING IN THE AMORPHOUS STATE OF POLYMERS



DUAL-PHASE POLYMER SCIENCE AND TECHNOLOGY

Copyright 2022. De Gruyter. All rights reserved. May not be reproduced in any form without permission from the publisher, except fair uses permitted under U.S. or applicable copyright law.

EBSCO Publishing : eBook Collection (EBSCOhost) - printed on 2/13/2023 12:32 AM via
AN: 3269302 ; Jean Pierre Ibar.; Dual-Phase Depolarization Analysis : Interactive
Coupling in the Amorphous State of Polymers
Account: ns335141

Jean Pierre Ibar

Dual-Phase Depolarization Analysis

EBSCOhost - printed on 2/13/2023 12:32 AM via . All use subject to https://www.ebsco.com/terms-of-use

EBSCOhost - printed on 2/13/2023 12:32 AM via . All use subject to https://www.ebsco.com/terms-of-use

Jean Pierre Ibar

Dual-Phase Depolarization Analysis

Interactive Coupling in the Amorphous State of Polymers

DE GRUYTER

EBSCOhost - printed on 2/13/2023 12:32 AM via . All use subject to https://www.ebsco.com/terms-of-use

Author
Dr. Jean Pierre Ibar
Professeur des Universités
University of the Basque Country
Avenida Tolosa 72
20018 Donostia–San Sebastian
Spain
jpibar@alum.mit.edu

ISBN 978-3-11-075669-2
e-ISBN (PDF) 978-3-11-075674-6
e-ISBN (EPUB) 978-3-11-075684-5

Library of Congress Control Number: 2021949661

Bibliographic information published by the Deutsche Nationalbibliothek
The Deutsche Nationalbibliothek lists this publication in the Deutsche Nationalbibliografie; detailed bibliographic data are available on the Internet at http://dnb.dnb.de.

© 2022 Walter de Gruyter GmbH, Berlin/Boston
Cover image: creation of Pink Flow Technologies Inc.
Typesetting: VTeX UAB, Lithuania
Printing and binding: CPI books GmbH, Leck

www.degruyter.com

EBSCOhost - printed on 2/13/2023 12:32 AM via . All use subject to https://www.ebsco.com/terms-of-use

Abstract

Several techniques exist to analyze the molecular response of materials to physical or chemical inputs, in order to determine their specific performance. Differential scanning calorimetry (DSC) and differential thermal analysis (DTA) are among the most popular in laboratories and on production sites. Other techniques include thermal mechanical analysis (TMA), dynamic mechanical analysis (DMA), stress relaxation or creep analysis, thermal expansion coefficient devices, and dielectric analysis (DEA). The method of Thermal-Stimulated Depolarization (TSD), the subject of this book, consists in putting the specimen rapidly at high temperature (above the transition temperature at which the relaxation phenomenon is expected), orient the dipoles at that temperature, and freeze in the orientation thus produced by quenching at low temperature. The depolarization stage occurs in a second step when the temperature of the polarized sample is increased at a constant rate, thermally triggering the deactivation of the dipoles, producing a microcurrent that is measured.

Originally, thermal-stimulated current depolarization techniques were used to measure charge detrapping in low-molecular-weight organic and inorganic compounds. Ever since 1967 they have been applied to the study of structural transitions in polymers by the use of "Thermal-Windowing Deconvolution" (TWD), a filtering experimental method that allows to decouple the relaxations modes collectively describing the interactive coupling resulting in molecular motions in amorphous matter. The experimental deconvolution of the relaxation modes responsible for internal motion in the amorphous phase of amorphous or semi-crystalline polymers is coupled with a mathematical procedure (relaxation map analysis) that leads to the understanding of their coupling characteristics which often relate to the state of the material itself, for instance its non-equilibrium state.

This book covers the fundamental equations describing the polarization and depolarization stages, the interactions between dipoles and space charges to follow the free volume evolution, and how interactive coupling can be mathematically modeled by compensations and super-compensations of the relaxation map spectral lines in the ΔG plane.

Case studies are provided as examples of application of the TSD and TWD characterization techniques to describe coupled molecular motions in resins, medical tissues, wood, blend interfaces, rubbers, and can coatings, internal stress in molded parts, etc.

The novel approach of the Dual-Phase and Cross-Dual-Phase conformers statistics to explain interactions in polymers is the core of all the research and teaching of the New School Polymer Physics founded to develop and disseminate a new paradigm in polymer physics. This book is the second of a series of six books dedicated to the dissemination of the principles of the new paradigm and of its practical applications to polymer characterization and polymer processing.

https://doi.org/10.1515/9783110756746-201

EBSCOhost - printed on 2/13/2023 12:32 AM via . All use subject to https://www.ebsco.com/terms-of-use

It is anticipated that the results of TSC/TWD will help provide the fundamental parameters of the new statistics between the conformers.

Keywords: polymer characterization, thermal analysis, amorphous phase characterization, Thermal-Stimulated Depolarization (TSD), Thermal-Windowing Deconvolution (TWD), interactive coupling between dipoles, dipole interactions, dipole polarization, dipole depolarization, Debye relaxation, relaxation mode, Arrhenius mode of relaxation, WLF mode of relaxation, relaxation map, Arrhenius plane, Eyring plane, ΔG plane, T_g transition, T_{LL} transition, glass transition, liquid–liquid transition, space charges, free volume, $T_{g\rho}$ peak, compensation, compensation line, supercompensation, compensation point, enthalpy of activation, entropy of activation, degree of disorder (DOD), Dual-Phase model and Cross-Dual-Phase model of polymer interactions, dissipative interactions (temperature and voltage field), interactions, horizontal structuring, vertical structuring, dissipative function, open dissipative systems, polymer physics

EBSCOhost - printed on 2/13/2023 12:32 AM via . All use subject to https://www.ebsco.com/terms-of-use

Preface

This book is a totally revised edition of a manual of instructions I once wrote (in 1993) which had the purpose to second the sales of the TSC/RMA spectrometers, in the Thermal Instrumentation division of Solomat Enterprises Corp. (Stamford, CT, USA). When I left this start-up in 1994, we had sold a few dozen instruments and had approximately twice as many orders of these instruments to deliver. This showed the strong interest in this new technology [141, 142]. I moved on to new polymer horizons, especially in the area of the flow enhancement of melts by processing them under vibration conditions (Rheomolding and rheo-fluidification): this was another particular application requiring the understanding of how the interactive coupling between molecular motions controlled the properties, in particular their processing easiness.

In Chapter 6 of the 1993 manual, I disclosed that the relaxation map of the interactive relaxation modes of the dipoles of a series of Rheomolded PS samples structured as a network of compensation lines, themselves compensating into a supercompensation macrostructure. The pattern of the macrostructure was a function of the Rheomolding thermomechanical history. This was, and still is, an extraordinary and astonishing discovery: how could we explain such a high level of relaxation order across T_g for a pure amorphous polymer?

This discovery, that no current theory can explain, was buried in the middle of a manual of instructions dedicated to the sale of a commercial instrument!

The book that I wrote in 1993 could not benefit from the background knowledge that I have acquired ever since I made a career move to focus and carry on my research in academia. The book had lots of interesting data on dielectric relaxation but needed to be rewritten from a different perspective: not only to remove all the references to the commercial aspect that were part of the first publication, but also, and mainly, because the new physics of polymer interactions appears to be the reason for the manifestation of compensations of the Arrhenius relaxation modes in a relaxation map and of the super-network of compensation structures found for the Rheomolded PS samples mentioned above.

There are two reasons for me to resurrect the subject of thermal-stimulated activation and depolarization of dipoles in polymers: one is theoretical and the other one practical. This presentation of my work on interactive coupling between electric charges in polymers, in particular between dipoles, is composed of two specific parts published in one single book.

Part I deals with the physics of interactions under a voltage field excitation. This part explains the effect of a voltage field coupled with temperature to induce space charges and dipolar activity in dielectric materials that can be measured by very sensitive electrometers. The sophistication of this science of activation and deactivation of dipoles to produce an understanding of the coupling forces of interactions that control molecular motions is fascinating. Part I is dedicated to the fundamentals of this dielectric characterization technique: the origin of the dipole formation, induced or

https://doi.org/10.1515/9783110756746-202

EBSCOhost - printed on 2/13/2023 12:32 AM via . All use subject to https://www.ebsco.com/terms-of-use

permanent dipoles, the origin of the Wagner space charges, of the $T_{g,\rho}$ transition, and of the T_{LL} manifestation, the origin of the Debye elementary relaxations of the relaxation map and of their compensation, and the origin of their super-compensations.

Part II is practical and filled with case studies giving examples on how to apply the characterization techniques of Thermal-Stimulated Depolarization (TSD) and Thermal-Windowing Deconvolution (TWD) described and explained in Part I. In Part II we characterize a multitude of samples given to us because other thermal analysis techniques (DSC, DMA, DEA) have had a hard time to characterize them. This volume is dedicated to help the engineers and researchers of the industry find answers: the characterization of interfaces in blends, two-phase copolymers, coated films, wood samples, paints, etc.

I am currently writing a series of books dedicated to the dissemination of a new understanding of the interactions in polymers using the concepts of "Dual-Phase" and "Cross-Dual-Phase" to describe their rheology, their crystallization kinetics, and the origin and the stability of their entanglement ability. I have designated this research and the teaching of its principles and objectives under the name "New School Polymer Physics." Note that in the title of the book, "*Dual-Phase Depolarization Analysis*," you see the word "Dual-Phase." These are open dissipative statistical phases and should not be confused with the phases that are observed in immiscible blends or block copolymers, for instance. Mind you that I *do* spend half of the book, though, describing how to characterize real phases in polymer blends and block polymers!

With the proliferation of fully automated TSD instruments in the labs of the universities and of the industry for the last 30 years [141], the field of thermal-stimulated current depolarization has advanced a great deal, as evidenced by the large increase of the number of publications in this area of thermal analysis.

This book on thermal-activated depolarization in no way represents a review of the field of thermal-stimulated current depolarization; it is a reflection of my own interpretation of the interactions in polymers, what I call "interactive coupling" [140] applied to Thermal-Stimulated Depolarization (TSD) and Thermal-Windowing Deconvolution (TWD) results. Interactive coupling is presented as a recursive process modulating the local interactions by the system organized by the collective aspect of those interactions. Thus, in a sense, without the reader even realizing it, because the emphasis is not brought onto that aspect, this work – in Chapter 3 of Part I and its Appendix – may be viewed as a new and original attempt to describe the mathematical correlations between the properties of what interacts and the number of units defining the systems of interactions at play. This is a classical field of physics that will be recognized by those scientists working on chaos, fluctuations, and long-range order generated by local disorder, a field now called "complex systems" which assumed other names in the past such as "open dissipative systems." My reference on the subject is, indeed, Prigogine, but his mathematical framework being very sophisticated and mine perhaps more accessible, I intended to remain at a very simple level of presentation and,

EBSCOhost - printed on 2/13/2023 12:32 AM via . All use subject to https://www.ebsco.com/terms-of-use

moreover, I wanted to dedicate this book to the understanding and the characterization of relaxations in polymers, only.

The characterization methods described in this book provide the best way to study local and cooperative relaxations in the amorphous state of matter that are, in my opinion, essential to understand the glass transition, molecular motions in the rubbery and molten states, and even the processes leading to crystallization. Only the last chapter of Part I and its Appendix address the fundamental nature of the local and collective aspects of the interactions, proposing an explanation of compensations and multi-compensations based on the new advances I have made on the understanding of the interplay between the Dual-Phase and Cross-Dual-Phase models. This was my main interest in completing and rewriting the work of 1993. This is why this new book can be part of my "Dual-Phase" collection currently in the works [137, 138, 143, 144].

March 17th 2022 Jean Pierre Ibar

EBSCOhost - printed on 2/13/2023 12:32 AM via . All use subject to https://www.ebsco.com/terms-of-use

EBSCOhost - printed on 2/13/2023 12:32 AM via . All use subject to https://www.ebsco.com/terms-of-use

Contents

Abstract —— V

Preface —— VII

About the author —— XIX

0 Preamble: Introduction —— 1
Introduction to the Thermal-Stimulated Depolarization (TSD) and the Thermal-Windowing Deconvolution (TWD) characterization techniques —— **1**

Part I: **A Dual and Cross-Dual interpretation of interactive coupling of conformers applied to Thermal-Stimulated Depolarization (TSD) and Thermal-Windowing Deconvolution (TWD)**

1 Principle of Thermal-Stimulated Depolarization & Thermal-Windowing Deconvolution —— 15
I.1.1 The different types of polarization —— **15**
I.1.1.1 Deformation polarization —— **17**
I.1.1.2 Dipolar orientation polarization —— **18**
I.1.2 Thermal-Stimulated Polarization and Depolarization —— **19**
I.1.3 Model calculation of the thermal-windowing steps —— **20**
I.1.3.1 General polarization equation —— **21**
I.1.3.2 Polarization stage —— **22**
I.1.3.3 Equations of depolarization —— **23**
I.1.3.4 Expression of the thermally stimulated current of depolarization —— **24**
I.1.3.5 Single Debye relaxation —— **25**
I.1.3.6 Distributed Debye processes —— **25**
I.1.4 Computer simulation —— **26**
I.1.5 Influence of ΔH and τ_o on a Debye relaxation peak —— **29**
I.1.6 Debye curve-fits —— **33**
I.1.6.1 The Bucci–Fieschi–Guidi integral solution —— **34**
I.1.6.2 The Lacabanne (2/3) rule —— **35**
I.1.6.3 Simplex curve-fitting methods —— **41**
I.1.6.4 Curve-fitting methods based on peak half-width —— **42**

EBSCOhost - printed on 2/13/2023 12:32 AM via . All use subject to https://www.ebsco.com/terms-of-use

I.1.7 Deconvolution of thermally windowed peaks — **44**
I.1.8 Properties of Debye peaks. Influence of peak shifting on τ_o and ΔH — **46**
I.1.9 Influence of the thermal-windowing experimental parameters on the characteristics of the depolarization peak — **56**
I.1.9.1 Polarization voltage — **56**
I.1.9.2 Effect of polarization time t_p — **58**
I.1.9.3 Effect of the time of depolarization t_d — **59**
I.1.9.4 Effects of the polarization temperature T_p and the window width — **61**
I.1.10 Acknowledgment — **64**

2 Thermal-Windowing Deconvolution, relaxation map analysis, and compensation phenomena to determine the amorphous state of polymers — 65
I.2.1 Introduction — **65**
I.2.2 Arrhenius transform. Relaxation map. Thermal-Windowing Deconvolution — **66**
I.2.3 Eyring transform. Thermokinetic functions — **69**
I.2.4 Compensation phenomena. Degree of disorder — **72**
I.2.5 Compensation search. Z-structure. Z-line — **73**
I.2.6 Determination of T_g. Activation entropy and enthalpy at T_g — **80**
I.2.7 DOD number — **80**
I.2.8 Duality at T_g — **83**
I.2.9 Compensation in the sub-EE plane — **85**
I.2.10 Normalization of the $\Delta G - T$ curves. Discussion — **92**
I.2.10.1 Expression of the entropy ΔS_p vs. T_p — **94**
I.2.10.2 Expression of the enthalpy ΔH_p vs. T_p — **98**
I.2.10.3 Expression of the free energy ΔG vs. T_p — **99**
I.2.10.4 Discussion — **99**
I.2.10.5 Conclusion — **100**
I.2.11 Characterization of the amorphous phase in semi-crystalline polymers by TWD spectroscopy — **101**
I.2.11.1 PTMG 2035 — **101**
I.2.11.2 Polyamide 12 — **111**
I.2.11.3 Polypropylene (undrawn and drawn) — **120**
I.2.11.3.1 Undrawn polypropylene — **120**
I.2.11.3.2 Drawn polypropylene — **127**
I.2.11.3.3 Comparison between undrawn and drawn polypropylene — **134**
I.2.12 Conclusion — **137**

EBSCOhost - printed on 2/13/2023 12:32 AM via . All use subject to https://www.ebsco.com/terms-of-use

3 A Dual and Cross-Dual interpretation of interactive coupling of conformers applied to thermally activated polarization and depolarization of polymers —— 141

I.3.1 Challenging results to the conventional models of polymer physics. Introduction to a new approach to the physics of polymer interactions: the Dual-Phase and Cross-Dual-Phase models —— **141**

I.3.2 The $T_{g,\rho}$ peak and the T_{LL} transition —— **146**

I.3.3 Application of compensations to characterize interactive coupling in the amorphous state —— **148**

I.3.3.1 Compensation laws —— **148**

I.3.3.2 Compensations of ΔH and Ln τ_o. Positive and negative compensations; the organization of the compensations in a super-compensation network. The Dual-Split model explanation —— **149**

I.3.3.3 Effect of the voltage field on the statistics of interactive coupling. The nature of what TWD is actually deconvoluting —— **164**

I.3.4 Normalization of the compensations between Ln(τ_o) and ΔH. Introduction to "grid-shifting": a collateral shifting effect due to the interaction between the voltage field, temperature, and dielectric material —— **167**

I.3.4.1 Geometrical and thermokinetic features of a Debye peak —— **169**

I.3.4.2 Shifting the Debye peak obtained at a given T_p by various amounts δ_x —— **179**

I.3.4.3 Shifting the Debye peaks obtained at various T_p by the same amount δ_x: the three temperature ranges of the voltage field–temperature interactions —— **181**

I.3.4.4 Shifting the Debye peak obtained at a given T_p to a given temperature —— **190**

I.3.4.5 Definition and description of "grid-shifting" —— **204**

I.3.4.6 Grid-shifting unifies the correlations between Ln(τ_o) and ΔH across ranges 1, 2, and 3 into a mastercurve: on the determination of the framework relating relaxation time and temperature —— **211**

I.3.4.6.1 Properties of the GRID —— **211**

I.3.4.6.2 Description of the grid shift factors —— **218**

I.3.4.6.3 The cross-dynamic structure of T_p: $T_p + \delta_{pH}$ and $T_p + \delta_{p\tau}$ —— **223**

I.3.5 Discussion and conclusions —— **233**

I.3.5.1 A survey of Chapter 3 developments —— **233**

I.3.5.2 Interpretation of the TWD results by the Dual-Phase model of polymer interactions —— **236**

I.3.5.2.1 The three ranges description of the amorphous state of polymers —— **236**

I.3.5.2.2 Conclusions regarding the physical meaning of the results of TWD —— **241**

EBSCOhost - printed on 2/13/2023 12:32 AM via . All use subject to https://www.ebsco.com/terms-of-use

I.3.5.3 General conclusions —— **243**
I.3.5.4 The search for new concepts to build up a ladder of scales —— **247**
I.3.5.4.1 The phantom variable T_x —— **247**
I.3.5.4.2 Conjugated states: [$\Delta H_c = \Delta H(T_p + \delta_{p\tau})$, $\tau_{oc} = \tau_o\,(T_p + \delta_{pH})$] —— **248**
I.3.5.4.3 The role of T, coupled to other independent external parameters, in the formulation of the interactions —— **248**
I.3.5.4.4 Is this the way to end a serious book? —— **249**

Appendix of Part I —— 251
Conventional kinetics —— **251**
Dual-Split Kinetics —— **253**
Part A. Dual-Phase Dissipative Kinetics (vertical splitting) —— **253**
A.1 Structuring between the *b* and *F* conformers —— **253**
A.2 Vertical Dual-Split Kinetics —— **254**
A.3 Examples of simulation of the vertical Dual-Split Kinetics equations (5) to (7) —— **255**
A.3.1 Cooling simulation —— **255**
A.3.2 Effect of cooling rate on the dynamics —— **260**
A.3.3 Heating at constant rate —— **261**
A.3.4 Isothermal return to equilibrium (annealing) —— **263**
Part B. Horizontal splitting of B_o: creation of $N_s(t)$ energetic kinetic systems —— **267**
B.1 Computer simulations —— **268**
B.1.1 Cooling —— **268**
B.1.2 Heating —— **271**
B.1.3 Isothermal annealing —— **272**
B.1.4 Influence of the initial number of systems N_{so} —— **275**
Part C. Compensating vertical and horizontal split constraints —— **281**
Final word —— **286**

Part II: **Application of Thermal-Stimulated Depolarization and Thermal-Windowing Deconvolution (TSD/TWD) to the characterization of the amorphous phase in polymers: case studies**

1 A comparison of TSD/TWD, DSC, DEA, and DMA for the characterization of the amorphous phase of polymers —— 289
II.1.1 General description —— **289**
II.1.2 Outputs. Resolution. Accuracy. Limitations —— **297**
II.1.2.1 DSC —— **297**
II.1.2.2 DMA and DEA —— **302**

EBSCOhost - printed on 2/13/2023 12:32 AM via . All use subject to https://www.ebsco.com/terms-of-use

II.1.2.2.1 General considerations — **302**
II.1.2.2.2 DMA — **305**
II.1.2.2.3 DMA for coatings and adhesives: severe limitations — **307**
II.1.2.2.4 DMA accuracy — **307**
II.1.2.2.5 DEA — **308**
II.1.2.2.6 Conclusion (DMA and DEA) — **309**
II.1.2.3 TSD/TWD — **309**
II.1.2.3.1 General considerations — **309**
II.1.2.3.2 TWD accuracy — **317**
II.1.2.3.3 Result of changing the baseline of integration — **317**
II.1.2.3.4 Compensation search. Accuracy to determine the DOD number — **321**
II.1.2.3.5 Isothermal depolarization experiments — **322**
II.1.2.3.6 Spontaneous depolarization current — **324**
II.1.2.3.7 The thermal-stimulated polarization current — **326**
II.1.3 Conclusion — **327**

2 Practical examples of TSD characterization — 329
II.2.1 Introduction: the nature of the peaks — **329**
II.2.2 Selective polarization — **331**
II.2.3 The $T_{g,\rho}$ peak and the measurement of “free volume” — **332**
II.2.4 Coatings, paints, pigments, and pressure-sensitive adhesives on substrates — **340**
II.2.4.1 Coatings — **340**
II.2.4.1.1 Beverage container coatings — **341**
II.2.4.1.2 Sanitary can coatings — **341**
II.2.4.1.3 Powder coatings — **343**
II.2.4.1.4 Plastic coatings — **344**
II.2.4.2 Paints — **345**
II.2.4.2.1 Case study: curing of polyester paint — **345**
II.2.4.2.2 Case study: pre-painted coil coating quality control — **347**
II.2.4.3 Pigments — **348**
II.2.4.4 Pressure-sensitive adhesive on substrates — **350**
II.2.5 Characterization of polyolefins — **351**
II.2.5.1 TSD trace of polypropylene homopolymer — **352**
II.2.5.2 TSD trace of atactic polypropylene — **352**
II.2.5.3 Effect of orientation — **353**
II.2.5.4 Polyethylenes of varying densities — **354**
II.2.5.5 Effect of additives: Irganox 1076 — **355**
II.2.5.6 Copolymers and blends (PE, HDPE, and EPR). TPOs — **356**
II.2.5.7 Conclusions — **357**
II.2.6 TSD in quality control applications — **358**
II.2.6.1 Case study: TSD of “good” and “bad” LDPE tubes — **358**

EBSCOhost - printed on 2/13/2023 12:32 AM via . All use subject to https://www.ebsco.com/terms-of-use

II.2.6.2 Case study: quality control in diaper fabrication —— **359**
II.2.7 Nucleation effect sensed by space charges —— **360**
II.2.8 Monofilaments and single strands —— **362**
II.2.9 Wood and liquid crystal polymer —— **363**
II.2.9.1 Case study: wood —— **363**
II.2.9.2 Case study: relaxation in a liquid crystal polymer: Vectra 900 —— **365**
II.2.10 Characterization of rubbers and elastomers —— **373**
II.2.10.1 Case study: vulcanized blends of crosslinked elastomers —— **373**
II.2.10.2 Case study: NR and SBR blends —— **377**
II.2.11 Conclusion —— **379**

3 Practical examples of Thermal-Windowing Deconvolution characterization —— 381
II.3.1 Internal stress and the effect of the cooling rate on the DOD of engineering thermoplastics —— **381**
II.3.2 Orientation and pressure effects on plastic materials —— **383**
II.3.3 The curing of paint and powder coating on metal —— **384**
II.3.3.1 Paints —— **384**
II.3.3.2 Determination of DOD —— **387**
II.3.3.3 Powder coatings —— **389**
II.3.4 Structure of block copolymers and blends: how to quantify the level of interpenetration and segregation by thermal-windowing —— **391**
II.3.4.1 Case study: characterization of latex copolymers by TWD —— **391**
II.3.4.1.1 DSC —— **391**
II.3.4.1.2 DMA —— **392**
II.3.4.1.3 TSD —— **392**
II.3.4.1.4 TWD —— **392**
II.3.4.2 Case study: characterization of the structure of polyether block amide resins by TWD —— **394**
II.3.4.3 Characterization of vulcanized rubber blends and crosslinked natural rubbers —— **403**
II.3.4.3.1 Case study: characterization of vulcanized blend of NR and NBR —— **404**
II.3.4.3.2 Case study: crosslinked natural rubber vulcanizates —— **408**
II.3.4.3.3 Case study: characterization of NR/SBR blends of different concentrations —— **408**
II.3.4.4 Case study: influence of LDPE blend on the relaxation map of HDPE —— **422**
II.3.5 Case study: characterization by TWD of the effect of plasticizer concentration on the amorphous state of PMMA —— **433**
II.3.6 Case study: characterization of the adhesive strength of pressure-sensitive adhesives by TWD —— **446**

EBSCOhost - printed on 2/13/2023 12:32 AM via . All use subject to https://www.ebsco.com/terms-of-use

II.3.7 Case study: characterization by TWD of the influence of the TiO_2 content on the amorphous state of polystyrene —— **450**
II.3.7.1 Discussion —— **456**
II.3.8 Case study: influence of physical aging on the DOD and other thermokinetic parameters studied by TWD —— **458**
II.3.8.1 Experimental procedure —— **459**
II.3.8.2 Results —— **460**
II.3.8.3 Discussion —— **467**
II.3.8.4 Conclusion —— **469**
II.3.9 Case study: characterization of PEEK and PEI/PEEK blends by TWD —— **470**
II.3.9.1 PEEK —— **470**
II.3.9.2 PEEK/PEI blend —— **478**
II.3.10 Chapter conclusion —— **483**

4 Multiple compensation phenomena in the amorphous phase of polymers —— 485
II.4.1 Multi-compensations in a multi-phase system —— **485**
II.4.2 Multiple compensation phenomenon in amorphous polystyrene and polycarbonate —— **487**
II.4.2.1 Polystyrene —— **487**
II.4.2.2 Polycarbonate —— **502**
II.4.2.3 Conclusion —— **504**
II.4.3 Multiple compensations in a polymer liquid crystal: Vectra —— **504**
II.4.3.1 Discussion —— **518**
II.4.4 Multi-compensations in wood samples —— **521**
II.4.5 PEBA block copolymers revisited: a multi-compensations approach —— **529**
II.4.6 Discussion and conclusion —— **535**

Book conclusions —— 537

Bibliography —— 553

Further reading —— 565

Book acknowledgments —— 577

Index —— 579

EBSCOhost - printed on 2/13/2023 12:32 AM via . All use subject to https://www.ebsco.com/terms-of-use

EBSCOhost - printed on 2/13/2023 12:32 AM via . All use subject to https://www.ebsco.com/terms-of-use

About the author

Prof. Dr. J.P. Ibar, educated at ENSCP and MIT, has spent his entire career studying, characterizing and processing the amorphous state of matter, both at an academic level (Professor of the Universities) and through 3 start-ups that he co-founded and directed as Director of Research. He is the recipient of numerous awards (Chaudron's medal, Fulbright, Sigma-Xi Society (MIT Chapter), Marie-Curie, Ikerbasque Fellowship etc.), has been granted over 300 patents worldwide (35 seminal ones) and has authored more than 15 hundred peer-reviewed papers and 3 books. He has lectured as a keynote speaker at numerous international conferences (APS, ACS, ANTEC, Gordon Conferences, ICR, SOR, SER, PPS, Cambridge University, Russian Academy of Science, Sichuan University, etc.). He is currently writing a series of books on the Duality and Cross-Duality of the interactions in polymer science and engineering, and, more generally, to describe the physics of dissipative systems.

https://doi.org/10.1515/9783110756746-203

EBSCOhost - printed on 2/13/2023 12:32 AM via . All use subject to https://www.ebsco.com/terms-of-use

EBSCOhost - printed on 2/13/2023 12:32 AM via . All use subject to https://www.ebsco.com/terms-of-use

Chapter 0
Preamble: Introduction

Introduction to the Thermal-Stimulated Depolarization (TSD) and the Thermal-Windowing Deconvolution (TWD) characterization techniques

Originally, thermal-stimulated current depolarization techniques were used to measure charge detrapping in low-molecular-weight organic and inorganic non-conductive compounds. Ever since 1967 they have been applied to the study of structural transitions in polymers, another class of non-conductive materials. The credit for the initial development must be given to C. Lacabanne at the University of Toulouse, France, J. Vanderschueren at the University of Brussels, Belgium, and J. Van Turnhout at the University of Delft, Netherlands, who all applied Thermal-Stimulated Depolarization methods to the investigation of the microstructure and properties of polymers. The result of their 20 years of dedicated research has led to the publication of hundreds of articles in leading scientific journals [1, 2]. Additionally, Lacabanne pioneered the use of the technique of "Thermal-Windowing-Deconvolution" in 1974 and applied it to the study of a wide variety of macromolecular materials, synthetic and organic. The use of "thermal-windowing" rendered possible the deconvolution of the Thermal-Stimulated Depolarization peaks and the decoupling of the relaxation modes responsible for internal motion permitting, for the first time, a better understanding of their coupling characteristics which relate to the state of the material itself, in particular its thermodynamic stability.

The methods of Thermal-Stimulated Depolarization became very popular in the early 1990s as a result of the introduction by Solomat Instruments (Stamford, CT, USA) of the automated TSD/TWD spectrometer on the thermal analysis market [3]. At Solomat, these dielectric spectrometers were called TSC/RMA.

I was the head of the Research and Development department at Solomat Instruments when the decision was taken to automate the thermal-stimulated instrument Lacabanne had developed in her lab. I met Colette Lacabanne for the first time at an ACS meeting in April 1981. A lecture she gave on that occasion, which described the results she was obtaining with a lab TSD analyzer on semi-crystalline materials, made a powerful impression on me. I realized that the instrument was at its best analyzing matter in the amorphous state. The new technology could "measure up" the amorphous state in such diverse applications as bonding and cohesion between matrices and fibers for composites, between metals and paints, or even between the phases in a blend or a block copolymer.

I had at my disposal all the best thermal analytical equipment available on the market: a DSC, a DMA, and a dielectric spectrum analyzer; but none could "measure up" the amorphous state, i. e., determine the interactive coupling molecular basis for

https://doi.org/10.1515/9783110756746-001

EBSCOhost - printed on 2/13/2023 12:32 AM via . All use subject to https://www.ebsco.com/terms-of-use

its non-equilibrium characteristics, either in the solid or in the molten temperature regions.

I could clearly see how industry engineers and scientists would welcome the arrival of an instrument to tag and measure the internal stress in injection-molded, extruded, or blow-molded parts or capable of characterizing the segregation in a blend or a block copolymer or determining the bonding strength of paints and glues. I realized that Lacabanne and Vanderschueren had developed the basic technology for such an instrument. I sought and obtained a license to develop, manufacture, and commercialize the new technology. The result was the first automated TSD/TWD spectrometer that started to sell in late 1988.

Several techniques exist to analyze the molecular response of materials to physical or chemical inputs, in order to determine their specific performance. Differential scanning calorimetry (DSC) and differential thermal analysis (DTA) are among the most popular in laboratories and on production sites. Other techniques include thermal mechanical analyzers (TMA), dynamic mechanical analysis (DMA), stress relaxation or creep analysis, thermal expansion coefficient devices, and dielectric analysis (DEA). The method of Thermal-Stimulated Depolarization (TSD) consists in putting the specimen rapidly at high temperature (above the transition temperature at which the relaxation phenomenon is expected), orient the dipoles at that temperature, and freeze in the orientation thus produced by quenching at low temperature (Figure 0.1).

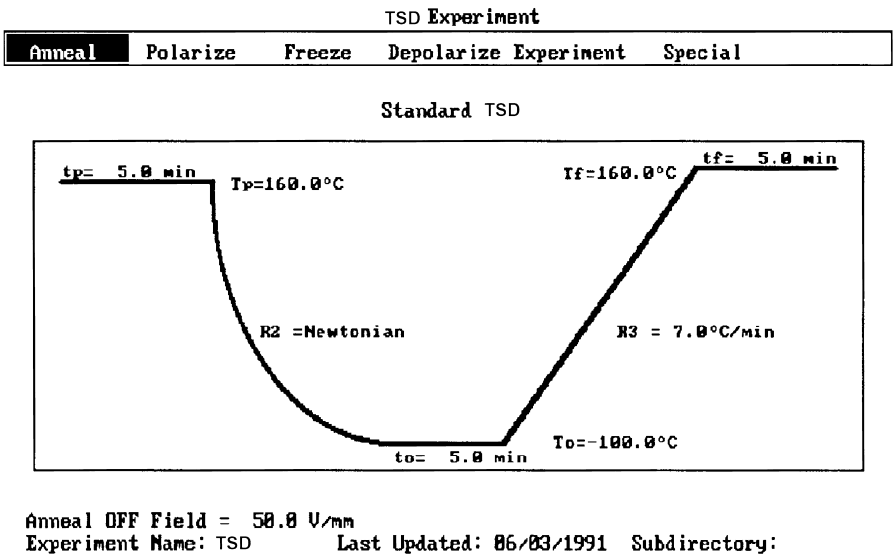


Figure 0.1: Description of the steps involved in a TSD experiment (polarization, cooling, annealing, heating) resulting in the output (a depolarization current vs. temperature) by thermal stimulation.

EBSCOhost - printed on 2/13/2023 12:32 AM via . All use subject to https://www.ebsco.com/terms-of-use

The voltage field applied is then removed and the temperature is ramped linearly back up to reveal the polarization induced at high temperature. *TSD is therefore a thermally stimulated recovery experiment*. An electrometer is connected to the sample to record the short-circuit current while heating. A current is created when the material depolarizes. This thermally stimulated depolarization current reveals the molecular mobility of the material's structure. The rate of depolarization is related to the relaxation times of the internal motions, providing a new opportunity to study the physical and morphological structure of materials.

The depolarization current, J, flowing through the external circuit is measured by a very sensitive electrometer (capable of measuring currents 10 million times smaller than those measured by a tunneling microscope) and allows determination of the "dipole conductivity."

The current peaks recorded this way (Figure 0.2a and 0.2b) are found to correlate well with the transition temperatures measured by mechanical relaxation (DMA), by DSC, or by conventional (AC) dielectric spectroscopy (DETA). A TSD output looks like a tan δ versus temperature plot, showing maxima at the transitions occurring inside the material. In fact, TSD provides very similar results to those obtained from other analytical instruments operating at the same low frequency equivalent (10^{-4} Hz), with the addition of an accrued sensitivity and a separating power unseen in other technologies.

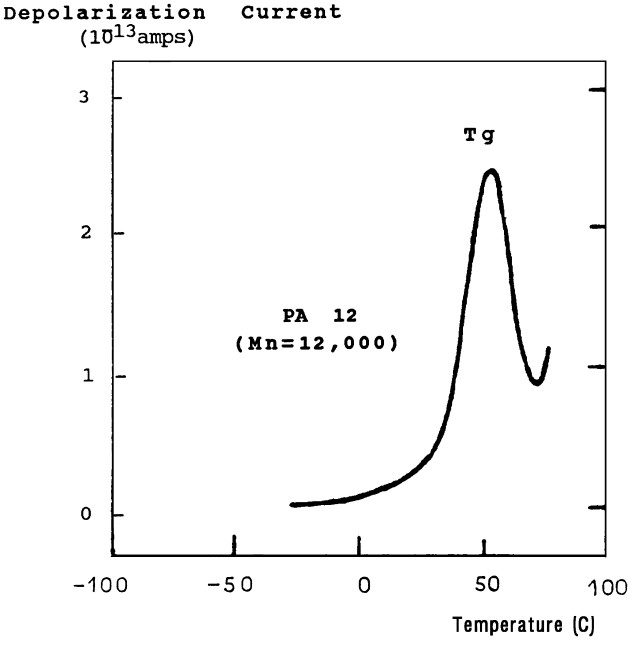


Figure 0.2a: Depolarization current vs. temperature during the thermal stimulation heating stage of polyamide 12.

EBSCOhost - printed on 2/13/2023 12:32 AM via . All use subject to https://www.ebsco.com/terms-of-use

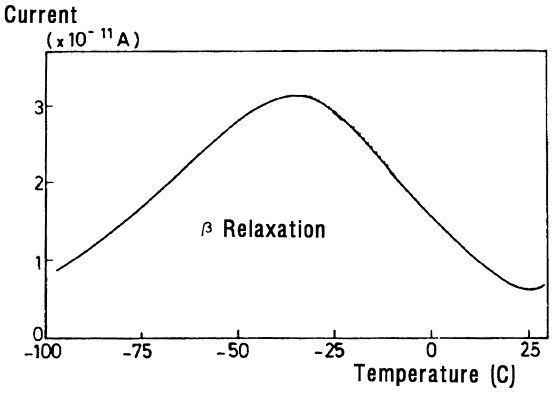


Figure 0.2b: Depolarization current vs. temperature during the thermal stimulation heating stage for a polarization temperature near the β transition of an amorphous polymer.

The concept of "thermal-windowing" gives the TSD another dimension. It consists of polarizing only a fragment of the full spectrum of relaxation and depolarizing it partially to isolate or "window" a single relaxation process. There are two types of possible windowing techniques: the first method, which can be called "partial isothermal recovery" or "isothermal windowing," consists of the following: first, polarize the sample at temperature T_p for a time t_p adjusted to allow orientation only of a certain fragment of the dipoles. At the same temperature T_p, cut off the polarizing voltage and stay at T_p for a time t_d. This allows the depolarization of a fragment of the oriented dipoles. Finally, quench the sample to $T_o \ll T_p$. Reheat at constant rate and measure the current of depolarization. Now $\Delta t = (t_p - t_d)$ is the "time window" and can vary between 1 min and about 1 hour.

The second commonly used thermal deconvolution method is the "Thermal-Windowing Deconvolution" experiment (Figure 0.3), which we designate TWD in this book. TWD essentially gives identical results as the first deconvolution method, yet it is faster to practice. In this option, a constant voltage is applied at T_p for a time t_p, commonly of the order of 2 minutes. The temperature is then lowered to T_d, at which the voltage is removed and the specimen allowed to recover partially for a time t_d, usually equal to t_p. Now $\Delta T = (T_p - T_d)$ is the temperature window and can vary between 1 °C and about 10 °C. The specimen is then quenched by 50 °C to 100 °C to a sub-temperature T_o where the amount of polarization induced in the material is frozen. A linear heating up is then performed, and the variation of current due to thermally induced depolarization or other current discharges is observed as a function of time (i. e., temperature). Since the current, J(t), is the derivative of polarization, the ratio P(t) divided by J(t) is a quantity with the dimension of time and represents, according to Bucci [24], the elementary relaxation time τ_i typical of the relaxing system. Figure 0.4 shows the result of thermal-windowing on the TSD output.

EBSCOhost - printed on 2/13/2023 12:32 AM via . All use subject to https://www.ebsco.com/terms-of-use

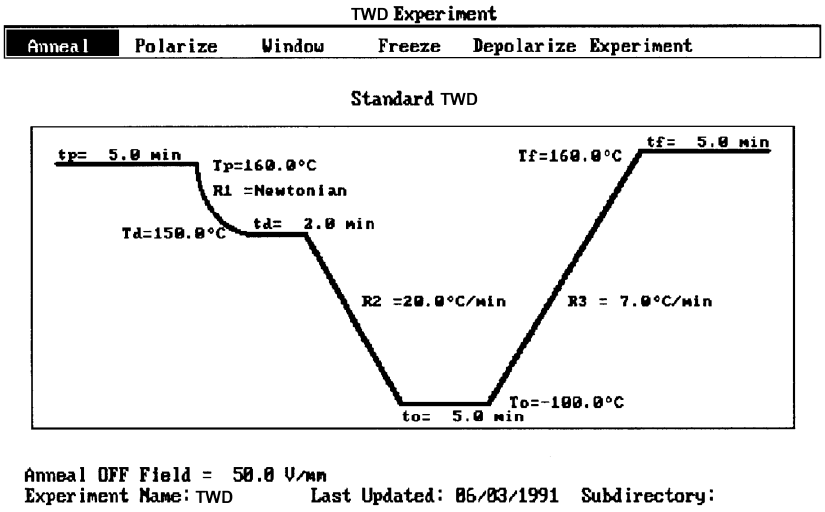


Figure 0.3: Description of the steps involved in a TWD experiment to thermally deconvolute a global TSD peak into its elementary Debye components and determine the interactive coupling between the relaxation modes.

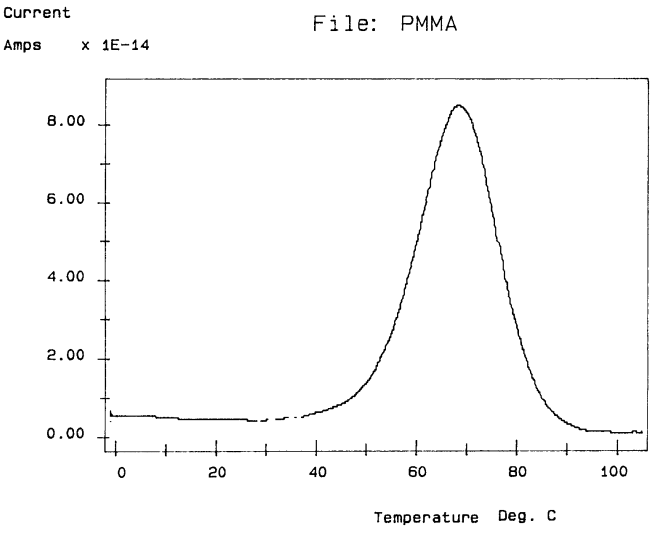


Figure 0.4: Current of depolarization vs. T for a TWD experiment. The polymer is PMMA.

When t_p, t_d, and $(T_p - T_d)$ are conveniently chosen, the depolarization current is supposed to represent the relaxation of a single Debye relaxation mode isolated from the spectrum of relaxation modes. By varying the value of the temperature of polarization T_p and repeating the above thermal-windowing process, one can isolate the elementary modes one by one (Figure 0.5).

EBSCOhost - printed on 2/13/2023 12:32 AM via . All use subject to https://www.ebsco.com/terms-of-use

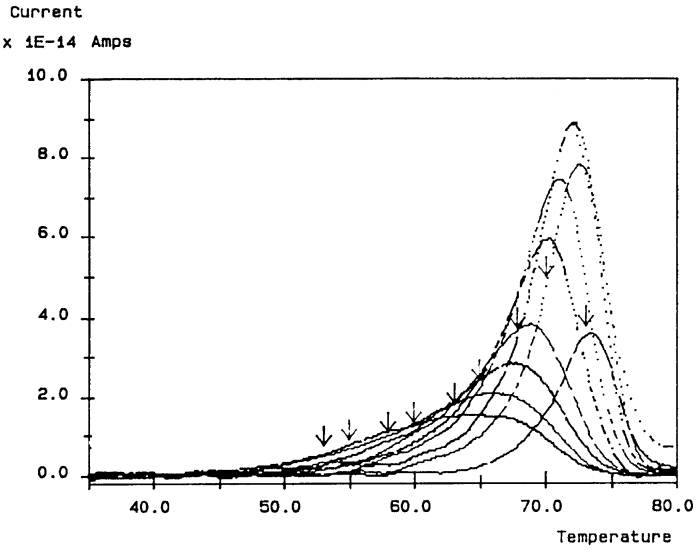


Figure 0.5: Effect of changing the polarization temperature T_p in a TWD experiment, indicated by the arrow, on the current of depolarization vs. T plot.

The computer in the automated TSD/TWD spectrometer of Solomat integrated the current vs. temperature peak for each temperature and calculated the value of the relaxation time at each temperature. The analysis, according to the Bucci's equation, of each resolved Debye peak obtained at various polarization temperature gave a temperature-dependent retardation time $\tau_i(T)$ which often followed an Arrhenius dependence (Figure 0.6).

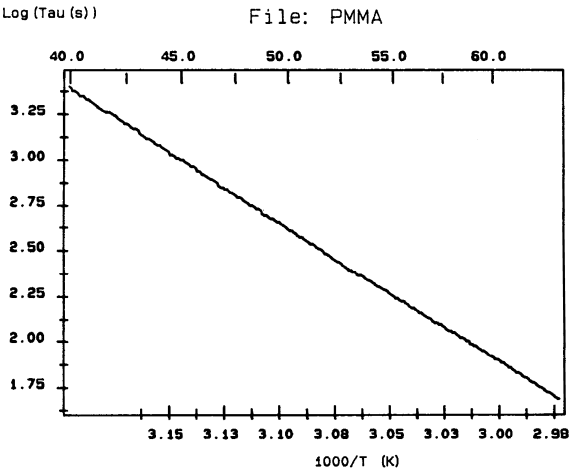


Figure 0.6: Conversion of the output in Figure 0.4 to an Arrhenius spectral line. The bottom axis is the Arrhenius scale, $1/T$ (K), in descending numbers; the top axis is the temperature in °C. The y-axis is the log of the relaxation time for the mode isolated by TWD at T_p.

EBSCOhost - printed on 2/13/2023 12:32 AM via . All use subject to https://www.ebsco.com/terms-of-use

The relaxation time is the inverse of the frequency of jump between two activated states. According to Eyring, the intercept of the Arrhenius equation is proportional to the entropy of activation for the activated process involved, and the slope is proportional to the enthalpy of activation. If a structure is "loose," the contrary of "ordered" or "compact," i. e., when molecular mobility is less hindered by the interactive intra-inter molecular surrounding, the entropy of activation will be "larger." Conversely, any parameter which acts to "organize" the structure and create a tighter environment for the bonds will cause a decrease of the entropy of activation. So, the activated entropy calculated from the intercept of Figure 0.6 gives an indication of "the degree of disorder" (DOD) of the structure.

The techniques of TSD and "Thermal-Windowing Deconvolution" (TSD/TWD) are studied in detail in this book to characterize molecular motions in non-conductive materials and to determine the degree of cooperativeness between the relaxation modes responsible for internal motions at the main transitions, revealing the state of the structure and the morphology.

A relaxation map (Figure 0.7) is obtained from a TWD experiment: it is the collection of the relaxation lines obtained for each deconvoluted Debye peak and analyzed according to Bucci's equation. Relaxation maps can be looked at as "fingerprints" of the material, being representative of its chemical structure, morphology, and non-equilibrium structure (Figure 0.8).

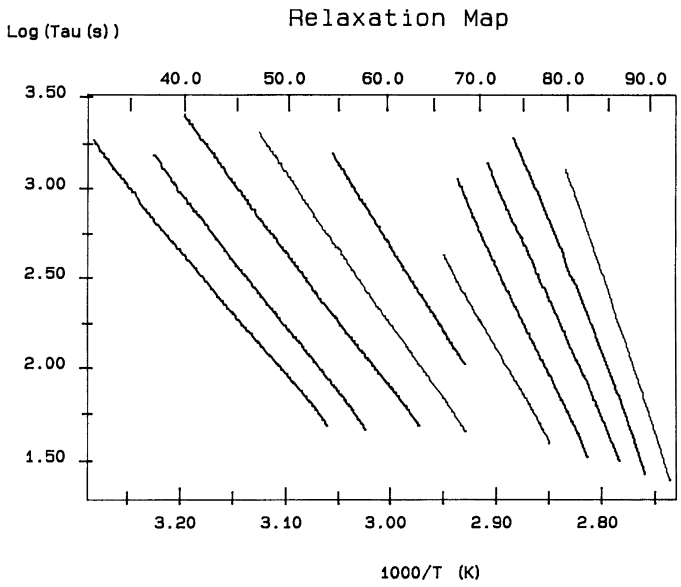


Figure 0.7: Relaxation map in the Arrhenius plane of all the relaxation modes isolated by TWD at various T_p, as shown in Figure 0.5.

EBSCOhost - printed on 2/13/2023 12:32 AM via . All use subject to https://www.ebsco.com/terms-of-use

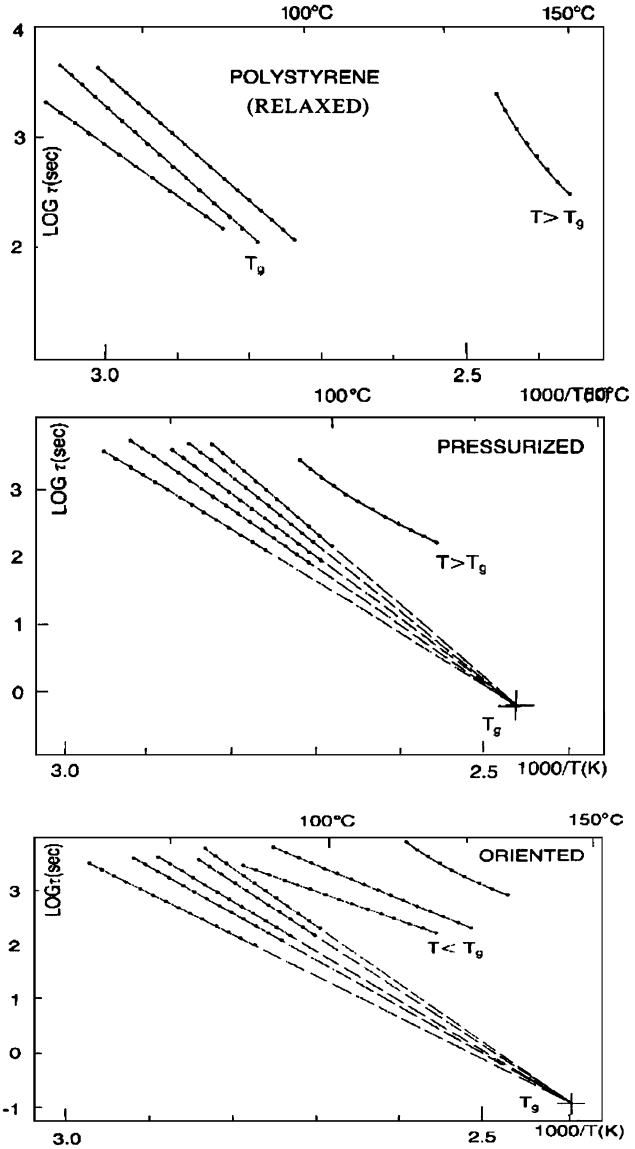


Figure 0.8: Illustration of the effect of various mechanical treatments of the melt during molding on the aspect of the relaxation map obtained by TWD of the glasses produced.

The analysis of the relaxation map determines the elementary enthalpies of activation and the pre-exponential factors (related to the entropy of activation) for all the relaxation modes obtained by varying the temperature of polarization T_p.

In summary, the relaxation observed during the recovery stage of TSD reveals the kinetics, and the powerful method of "Thermal-Windowing Deconvolution" (TWD) de-

EBSCOhost - printed on 2/13/2023 12:32 AM via . All use subject to https://www.ebsco.com/terms-of-use

convolutes the individual relaxation modes. This allows the study of their coupling characteristics, reflecting the structure and the physical state of the material. Constitutive equations can be used thereafter to reconstruct the material dielectric behavior (Figure 0.9) by calculation of the fundamental physical parameters from the spectrum of relaxation (dielectric permittivity, etc.).

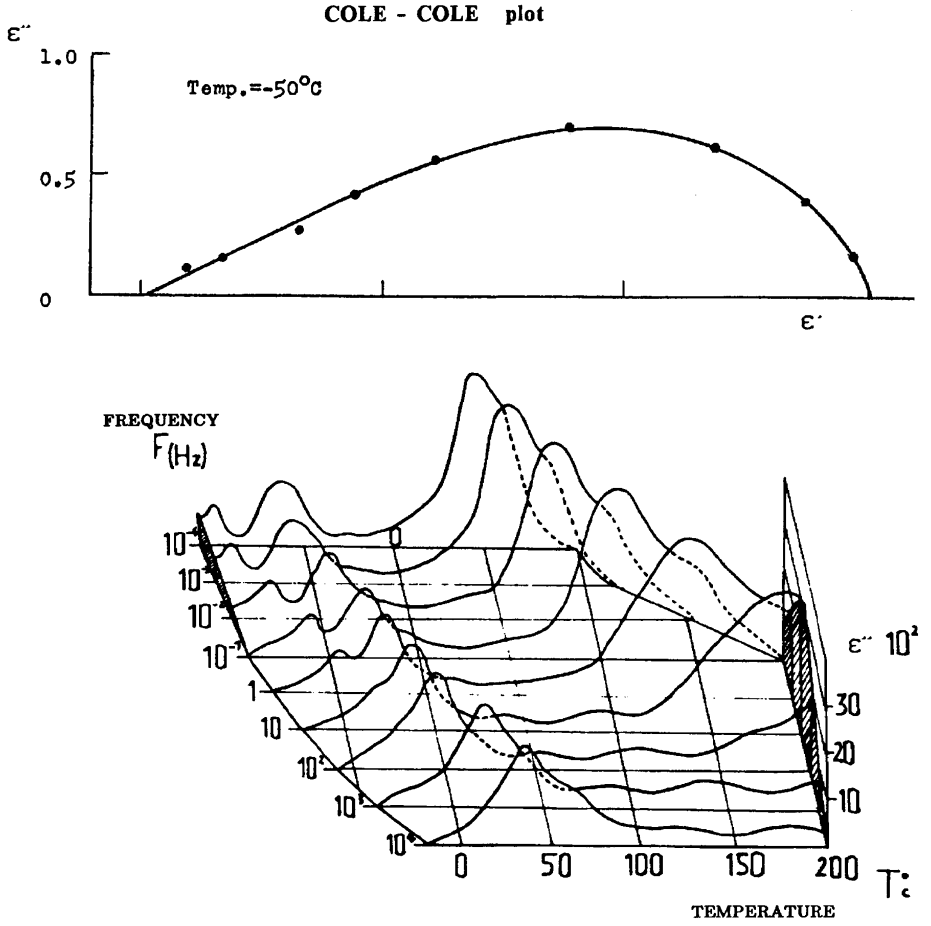


Figure 0.9: Response of a dielectric material to an AC voltage field. A Cole–Cole plot (top) consists of a plot of $\varepsilon''(f)$ vs. $\varepsilon'(f)$ at a given T. A frequency map is shown at the bottom for $\varepsilon''(f, T)$. Such plots can be calculated from the TSD/TWD response.

The various Arrhenius lines obtained by thermal-windowing at different polarization temperatures, T_p, often converge to a common point, the compensation point (Figure 0.10).

EBSCOhost - printed on 2/13/2023 12:32 AM via . All use subject to https://www.ebsco.com/terms-of-use

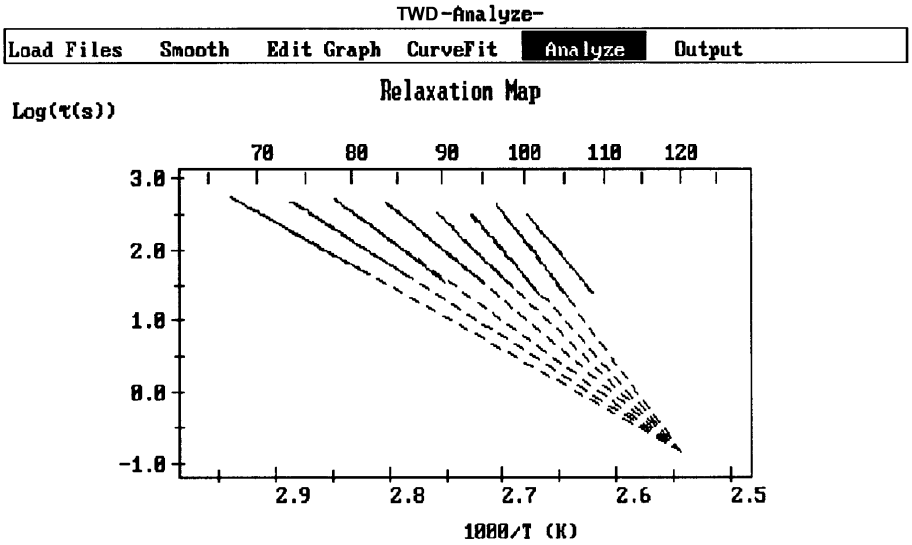


Figure 0.10: Relaxation map in the Arrhenius plane illustrated for PMMA. The spectral lines obtained at various T_p converge at a compensation point. The coordinates of the compensation point reflect the state of the amorphous phase due to the interactive coupling between the relaxation modes.

The essential focus of interest in the work of thermal-stimulated process analysis seems to lie around this phenomenon of compensation, the determination of its coordinates, the interpretation of its origin, its practical use to characterize the degree of coupling in the amorphous phase of polymeric matter, and its relationship with the state of (non)-equilibrium.

In a certain sense, one could say that a new type of thermal analysis is born with the understanding of "Thermal-Windowing Deconvolution" (TWD), since compensation phenomena apparently reflect the coupling between relaxation motions occurring cooperatively, and also because this new thermal analysis technique can describe WLF-type behavior susceptible to comparison with results observed in rheological experiments (upper temperature curve, $T > T_g$, in Figure 0.8).

Description of the content of this book

In the two parts of this book, we concentrate on two aspects of the depolarization phenomena: theoretical, in Part I, and practical, in Part II. The two parts can be read independently, although the practical chapters can be interpreted with a stronger confidence in the validation of the results after the theory of the interactions between the dipoles by the Dual-Phase model has been exposed (Part I).

In the three chapters of Part I, we cover theoretical topics: the origin of the polarization and depolarization of dipoles and of other charges induced by the voltage field (Chapter 1), the coupling effect of temperature and the voltage field on the relaxation

EBSCOhost - printed on 2/13/2023 12:32 AM via . All use subject to https://www.ebsco.com/terms-of-use

process (Chapter 2), and the understanding of the interactive coupling of the dipoles by the Dual-Phase and Cross-Dual-Phase models of the interactions (Chapter 3).

We use computer modeling to curve-fit the depolarization curves according to the Bucci et al. equation and quantify the effects of voltage, temperature of polarization or depolarization, etc. (Chapter 1). We explore in depth the technique of Thermal-Windowing Deconvolution (TWD) in Chapter 2, in particular the phenomenon of compensation of the Debye relaxation thermokinetic parameters, as T_p varies. We provide a new method to characterize the glass transition (Chapter 2) and determine the respective contribution to the entropy of the electronic and atomic vibrations of the dipoles. The interpretation of the compensation(s) of the relaxation modes in the amorphous state (positive and negative compensations across T_g) is the subject of Chapter 3 and of the Appendix. We propose in Chapter 3 a different understanding of thermal-windowing than the classical filtering of the relaxation spectrum to isolate the elementary Debye modes. We introduce a new shifting method of normalization of the compensation variables, $\mathrm{Ln}(\tau_o)$ and ΔH, to obtain a master compensation of the relaxation map covering the whole temperature range across T_g.

In Part II, we compare in Chapter 1 the TSD /TWD results with those obtained by other thermal analysis techniques (DSC, DMA, DEA). We provide in Chapters 2, 3, and 4 numerous characterization examples of use of TSD and TWD for a large variety of applications. In some cases (characterization of paints and coatings directly from the can), the measurements are actual breakthroughs in material characterization.

The presence of multi-compensations in a material might be linked to the existence of multi-phases, and we dedicate Chapter 3 of Part II to the analysis of blends and block copolymers and the other applications of TWD to which the concept of DOD applies its full force. But the presence of multi-compensations also occurs in cases where the material is known to be monophasic (Part II, Chapter 4). The comparison of the multi-compensation TWD spectra for brittle and ductile polymers or between annealed and quenched liquid crystal polymers in Chapter 4 is intriguing and has led to the theoretical developments exposed in Chapter 3 of Part I: the formulation of a new understanding of the interactions in polymers, the Dual-Phase and Cross-Dual-Phase models of polymer interactions.

Chapter 3 of Part I is the main novelty of this new edition. It provides a Dual-Phase and Cross-Dual-Phase interpretation of the results obtained by TSD and TWD. I seize the opportunity in this chapter, along with the Appendix that complements it, to expose the main ideas and concepts behind the Grain-Field Statistics (horizontal and vertical structuring), a theory that, I suggest, could be applied to describe the dynamics of open-dissipative structures in a way mathematically different from the work of I. Prigogine, who has pioneered the subject [500a]. Many aspects of the interactive coupling between the dipoles, especially those described in Part II, Chapter 4, are reminiscent of the deterministic chaos in Prigogine's work.

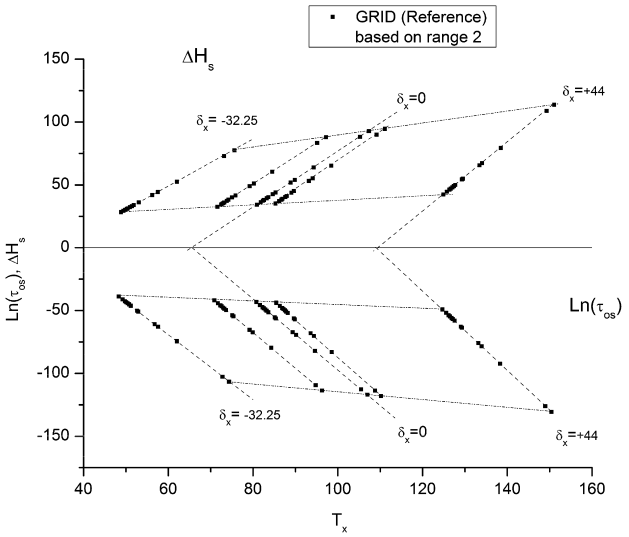
EBSCOhost - printed on 2/13/2023 12:32 AM via . All use subject to https://www.ebsco.com/terms-of-use

Although this book had been considered, initially, to be a rework by the author of the first publication on a similar subject (*Fundamentals of Thermal Stimulated Current* (*TSC*) *and Relaxation Map Analysis* (*RMA*), published by SLP Press, 1993), the new book objectives resulted in a modification of its presentation and of its content. The objective of the 1993 book was to promote the sales of the TSC/RMA spectrometer. The current objective is the dissemination of a new approach to the physics of polymer interactions describing "interactive coupling" to explain the properties. In this book, we use thermal stimulation (here applied to depolarization: TSD) and Thermal-Windowing Deconvolution (TWD) to characterize the amorphous state of matter, in particular when it is brought out of equilibrium by such thermomechanical processing procedures as to induce dissipative structures.

In the publication of 1993, I acknowledged the importance of the early contributions of C. Lacabanne [5–7, 9, 10, 13–18, 20, 26, 28, 30–46, 51–53, 56, 57, 59–68, 70–76, 78–84, 86–89, 93–97, 100–103, 105–114, 145, 146, 151–192, 205, 209–211, 219, 221], J. Vanderschueren [8, 55, 197, 231–237, 239–258, 263, 264] and J. Van Turnhout [227–230, 238] to the subject of thermal-stimulated current depolarization, as evidenced by the number of publications they have authored or co-authored. I have since taken the subject into another direction, the thermokinetics of interactive coupling to determine the parameters of the Grain-Field Statistics, yet I still acknowledge the pioneer work of these authors, without whom the science of depolarization to characterize molecular motions would have never reached this level.

EBSCOhost - printed on 2/13/2023 12:32 AM via . All use subject to https://www.ebsco.com/terms-of-use

Part I: **A Dual and Cross-Dual interpretation of interactive coupling of conformers applied to Thermal-Stimulated Depolarization (TSD) and Thermal-Windowing Deconvolution (TWD)**



EBSCOhost - printed on 2/13/2023 12:32 AM via . All use subject to https://www.ebsco.com/terms-of-use

EBSCOhost - printed on 2/13/2023 12:32 AM via . All use subject to https://www.ebsco.com/terms-of-use

Part I Chapter 1
Principle of Thermal-Stimulated Depolarization & Thermal-Windowing Deconvolution

In this chapter, we consider the outputs of Thermal-Stimulated Depolarization (TSD) and Thermal-Windowing Deconvolution (TWD) and give the equations which describe them. The first part of this chapter deals with the dielectric phenomenon in general and tries to establish the type of species capable of creating an output by application of a voltage across the material being characterized. In the second part of the chapter, model calculation of the thermal-windowing technique for TSD measurements on polymers shows how the new technique works and identifies the influential parameters.

I.1.1 The different types of polarization

Polarization can be quantified by a number, polarizability α, which is defined for an atom by the relationship $\upsilon = \alpha E_1$, where υ is the dipolar moment and E_1 is the local field. For a given atom, the total polarization is the result of several contributions which are schematically represented in Figure 1.1 and which are created as a result of

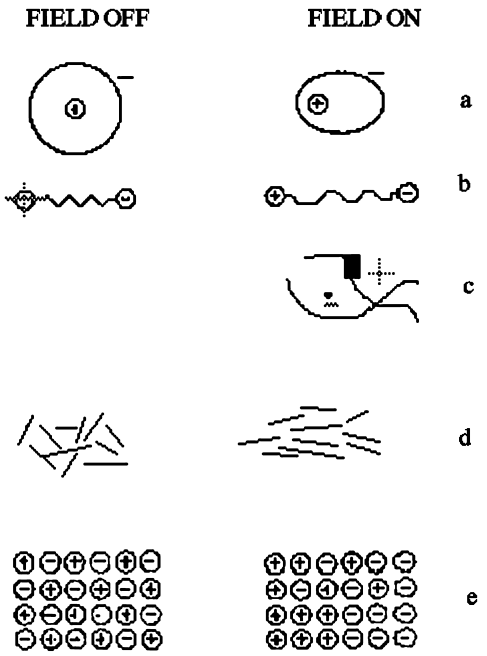


Figure 1.1: The different types of polarization. See text.

https://doi.org/10.1515/9783110756746-002

EBSCOhost - printed on 2/13/2023 12:32 AM via . All use subject to https://www.ebsco.com/terms-of-use

the following sources:

Electronic polarizability: Due to the low mass of electrons, the contribution to electronic polarizability is apparent in a very large frequency range up to the ultraviolet frequencies.

Ionic and atomic polarizability: In the case of a material where several types of atoms coexist, there might occur a transfer of one or several electrons creating an ionic dipole. In the case of a strongly ionic solid, the ions carry a charge equal to an even number of the elementary charge of the electrons. Upon application of an electric field, these charges are shifted and the resulting polarizability is called ionic polarizability. When dealing with organic substances, such as polymers, the electronic transfer is only partial. However, in the presence of an electric field, the atoms carrying a partial electronic charge are shifted along the equivalent bond, which generates a dipolar moment characterized by the "atomic polarizability." The frequency domain for such an atomic shift spreads up to the infrared spectrum.

Localized bound ionic polarizability: Some free electrons, extracted from the hydrogen atoms in regions of local lower density, may be localized at the potential holes formed by individual charge groups. Such binding (localized binding) between local electrons trapped in a free volume hole and their immediate counterions is observed in the case of polyelectrolytes [213]. Although unstable, the ionic dipoles thus created provide characterization means to evaluate the amount and properties of the free volume in polymeric phases.

Dipolar polarizability: This is created inside molecules having a permanent dipolar moment, such as in the classical molecules HCl and H_2O.

Space charge polarizability: The previous contributions to the polarizability can be met in an ideal medium that is without defects, either local or coordinated. This is largely the case of monophasic substances. However, as soon as there is a boundary, the charges which accumulate near the boundary are called "space charges." In the special case of a boundary between two phases of a heterogeneous matter, the microscopic polarization which then appears at the boundary surface yields a dielectric loss which is due to Maxwell–Wagner space charges.

Polarization by electrostatic charge: During the extrusion of polymers in the form of films, charges are often injected in the material through the contact of the polymer isolant with the metal of the barrel of the extruder. These electrostatic charges tend to accumulate under the action of an electric field in the potential wells and sites that represent the inhomogeneities or punctual defects in the material. The intensity of that electrostatic discharge might be important and mask the phenomenon of relaxation due to other depolarization effects.

In the following we will describe dipolar polarization as "orientation polarization" and electronic and atomic polarizations as "deformation polarization."

EBSCOhost - printed on 2/13/2023 12:32 AM via . All use subject to https://www.ebsco.com/terms-of-use

I.1.1.1 Deformation polarization

As shown in Figure 1.1a and b, an electric field can be applied to separate the center of gravity of positive and negative charges in the molecule or to modify the dipolar moment if that molecule is already a dipole. A force to reestablish the equilibrium is then generated and the system behaves as a simple harmonic oscillator. The equation of the return to equilibrium after the electric field is switched off can be written as

$$md^2r/dt^2 + F_t + kr = 0$$

where m is the mass of the oscillator, r is the deviation from equilibrium, k is the spring constant, and F_t is the frictional force, which can be written as $2m\beta dr/dt$, where β is the damping coefficient.

If the sample is subjected to an electric field, the charge is under the influence of a local field E_1 which will generate a force $F = qE_1$. The equation of motion then takes the form

$$d^2r/dt^2 + 2\beta dr/dt + (k/m)r = q/mE_1$$

The charge q which has been shifted from its equilibrium position by a distance r creates a dipolar moment $\upsilon = qr$. If there are N dipoles per unit volume, the polarization is $P = N\upsilon = Nqr$, and therefore the differential equation which governs the equation of motion can now be written in terms of the polarization:

$$d^2P/dt^2 + 2\beta dP/dt + (k/m)P = (q^2N/m)E_1$$

where E_1 is the local field which can be written in relationship to the external field with the Lorentz equation:

$$E_1 = E + P/\varepsilon_o \quad \text{where } \varepsilon_o \text{ is the permittivity of the vacuum}$$

The equation of motion becomes

$$d^2P/dt^2 + 2\beta dP/dt + (k/m - q^2N/3m)P = (q^2N/m)E$$

The solution to this differential equation when the excitation is an AC voltage gives for the variation of the polarization, $P(t)$, a sinusoidal function, with a resonance occurring as a function of the frequency ω of the exciting voltage. Figure 1.2 gives a schematic of the real and dissipative parts ε' and ε'', the permittivity deducted from the complex permittivity as a function of the frequency $\omega/\omega_{\max}$.

In summary, the mechanism of deformation depolarization yields a phenomenon of resonance, for which the maximum frequency is located in the infrared band as far as atomic polarization is concerned and in the optical range for electronic polarization.

EBSCOhost - printed on 2/13/2023 12:32 AM via . All use subject to https://www.ebsco.com/terms-of-use

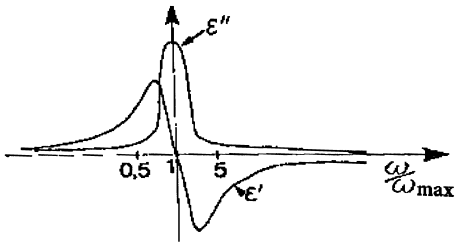


Figure 1.2: Effects of frequency, normalized by the resonance frequency, on the real and dissipative components of the permittivity, $\varepsilon'(\omega)$ and $\varepsilon''(\omega)$, respectively, for the deformation polarization type.

For this type of polarization, the response to a step function voltage field results in a pseudo-oscillatory short-term return to equilibrium, independently of temperature. This type of response is not accessible in the TSD current experiment. Infrared spectroscopy typically uses that type of polarization, and in the case of polymers this allows the identification of the various types of chemical bonds present in the material.

I.1.1.2 Dipolar orientation polarization

The polarization by orientation is due to permanent dipoles within the material. The model of this type of polarization uses the classical Debye assumption, which is in all very similar to the principles of a kinetic analysis: the orientation polarization P_s (for a given relaxing mode) increases at a rate which is proportional to the distance to equilibrium. Mathematically, this assumption can be written as

$$\frac{dP_s}{dt} = \frac{P_t - P - P_s}{\tau} \tag{1.1}$$

where P_t is the total polarization of the dielectric, P is the deformation polarization which is independent of temperature, and τ is the relaxation time. Note that $(P_t - P)$ can be expressed in terms of the two dielectric constants of the material, the static dielectric ε_s and the optical dielectric constant ε_∞, as well as the applied field E:

$$(P_t - P) = \varepsilon_o(\varepsilon_s - \varepsilon_\infty)E \tag{1.1'}$$

The differential equation can then be written as

$$\frac{dP_s}{dt} + \frac{P_s}{\tau} = \frac{\varepsilon_o(\varepsilon_s - \varepsilon_\infty)}{x}E \tag{1.2}$$

This differential equation is of the first order and can be solved for various expressions of E. If E is a sinusoidal excitation of frequency ω, Figure 1.3 represents the variation of the real and imaginary parts of the permittivity ε.

EBSCOhost - printed on 2/13/2023 12:32 AM via . All use subject to https://www.ebsco.com/terms-of-use

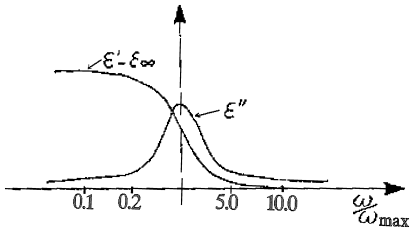


Figure 1.3: Real and dissipative components of the permittivity, $\varepsilon'(\omega)$ and $\varepsilon''(\omega)$, respectively, for the dipolar orientation polarization type (Debye polarization).

If the excitation is a Dirac function (a step function), such as in a TSD experiment, the return to equilibrium is an exponential function of time. Solutions to equation (1.2) provide an expression for the relaxation process. This type of polarization depends on temperature, and therefore the relaxation times will be temperature-dependent. That dependence of the relaxation times is a characteristic of the relaxation which takes place in the material.

In this book, the polarization by space charges and by electrostatic charge largely depends on the defects in the material which themselves are functions of the preparation of the sample. It is suggested in the following, unless otherwise stated, that the sample is prepared with the appropriate technique to be able to minimize or eliminate those charges. There are other examples where the space charges and the charges of electrostatic origin are useful and can be monitored to yield information on the structure itself. In particular, the localized bound ionic dipoles will be used to understand the role of free volume and interpret the presence of the $T_{g,\rho}$ transition.

The electronic and atomic polarizations and depolarizations are very fast phenomena which do not depend on temperature. The typical resonance frequency for those polarizations is in the ultraviolet and the infrared range. The polarization by orientation is generated by permanent dipoles associated with molecules of the material. In the classical interpretation of TSD, the dipoles "orient" in the direction of the field application and undergo viscous friction due to their interaction with their environment. Yet, the issue of the true influence of the voltage field on the creation of dipoles, on the "orientation of the dipoles," and/or on the generation of space charges needs to be addressed. The study of such a polarization/depolarization yields important information on the environment itself responsible for internal friction of the polymer. It is assumed that this type of depolarization is dominant in the study of TSD and in the following we will concentrate on the technical and theoretical aspects of TSD of the polarization induced by "orientation."

I.1.2 Thermal-Stimulated Polarization and Depolarization

Let us subject a dielectric medium to the action of an electric field. A polarization P is created by the application of the voltage (P is a vector). The dielectric is equivalent to a

EBSCOhost - printed on 2/13/2023 12:32 AM via . All use subject to https://www.ebsco.com/terms-of-use

medium with a volumetric distribution of charges with density $\rho' = \text{div}\, P$ and a surface distribution of charges equal to $\sigma' = P_N$, where P_N is the perpendicular component of the polarization at the surface.

If the dielectric is a plane capacitor, then $\text{div}\, P = 0$, hence only the surface distribution of charges remains. This charge appears with a retardation time with respect to the application of the field. This retardation (or relaxation) time characterizes the material and the state of the material.

A fundamental experiment to characterize dielectric materials consists in the measurement of the rate of polarization or depolarization of this surface charge: this rate is measured as the current of charge or discharge as a function of time. This current is the object of the analysis in the subsequent section.

I.1.3 Model calculation of the thermal-windowing steps

An equation for the thermally stimulated current due to dipolar disorientation was first given by Bucci et al. [24, 25]. For our purposes, we have adopted the set of equations derived by van Turnhout [238] and reported by Ronarc'h [215].

First we need to establish the general polarization/depolarization equation, and then we will apply it to the specific polarization and depolarization stages resulting from the application of the temperature and electric field described as "thermal-windowing" (Figure 1.4).

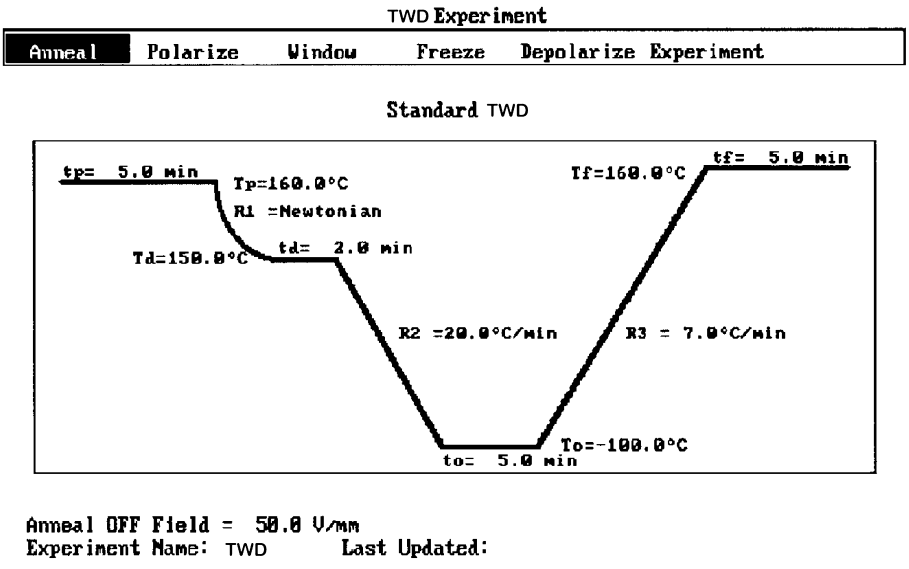


Figure 1.4: Description of the four stages of Thermal-Windowing Deconvolution: polarization at T_p, partial depolarization at T_d, cooling to T_o, and constant heating to T_f. See text.

EBSCOhost - printed on 2/13/2023 12:32 AM via . All use subject to https://www.ebsco.com/terms-of-use

I.1.3.1 General polarization equation

By using the first Debye hypothesis, for the orientation polarization (equation (1.2)) we previously obtained

$$\frac{dP_s}{dt} + \frac{P_s}{\tau} = \frac{\varepsilon_o(\varepsilon_s - \varepsilon_\infty)}{\tau}E$$

This equation is correct under isothermal conditions. However, because the windowing experiments involve thermal treatments which are not isothermal, we must hypothesize that the same equation holds true during the cooling section under an electric field:

$$\frac{dP_s}{dt} + \alpha(T)P_s = \alpha(T)\varepsilon_o(\varepsilon_s - \varepsilon_\infty)_T E \tag{1.3}$$

where $\alpha(T) = 1/\tau$ is the temperature-dependent relaxation frequency.

For most polymers $(\varepsilon_s - \varepsilon_\infty)_T$ is given by

$$(\varepsilon_s - \varepsilon_\infty)_T = \frac{N\mu^2}{3\varepsilon_o kT} \tag{1.4}$$

where N is the number of dipoles per unity of volume and μ is the dipolar moment.

On the other hand, the temperature dependence of the relaxation frequency $\alpha(T)$ can generally be described by an exponential law, $\alpha(T) = \exp(-\Delta H/kT)$, where ΔH denotes the activation energy, and thus $\alpha(T)$ varies a lot faster than $(\varepsilon_s - \varepsilon_\infty)$ in the temperature range of interest for the integration of the differential equation. This justifies considering $(\varepsilon_s - \varepsilon_\infty)$ as constant, with a good approximation.

The differential equation can now be solved, since it has separated variables:

$$\frac{1}{\alpha(T)}\frac{dP_s}{dt} = -P_s + \varepsilon_o(\varepsilon_s - \varepsilon_\infty)E \tag{1.5}$$

If we define

$$u = -P_s + \varepsilon_o(\varepsilon_s - \varepsilon_\infty)E$$

$$\frac{du}{u} = -\alpha(T)dt$$

$$u = \frac{1}{c}\exp\left(-\int \alpha(T)dt\right)$$

$$-P_s + \varepsilon_o(\varepsilon_s - \varepsilon_\infty)E = \frac{1}{C}\exp\left(-\int \alpha(T)dt\right)$$

but at $t = 0$ and $P_s = 0$, so

$$C = \frac{1}{\varepsilon_o(\varepsilon_s - \varepsilon_\infty)E}$$

EBSCOhost - printed on 2/13/2023 12:32 AM via . All use subject to https://www.ebsco.com/terms-of-use

giving the general equation which needs to be solved to find the polarization state of the material:

$$P_s(t) = \varepsilon_o(\varepsilon_s - \varepsilon_\infty)E\left[1 - \exp\left(-\int_o^t \alpha(T)dt\right)\right] \tag{1.6}$$

I.1.3.2 Polarization stage

Now let us consider the equations during the polarization stage. Referring to Figure 1.3:

- from $t = 0$ to $t = t_p$ the temperature is constant, so $\alpha(T)$ is constant,
- from $t = t_p$ to $t = t_2$ the temperature decreases linearly with time during the window:

$$T = \frac{t}{s_1} + b_1, \quad \text{thus: } dt = s_1 dT$$

and therefore

$$\begin{aligned} P_s(t) &= \varepsilon_o(\varepsilon_s - \varepsilon_\infty)E\left[1 - \exp\left(-\int_0^{t_p} \alpha(T)dt + \int_{t_p}^{t_2} \alpha(T)dt\right)\right] \\ P_s(T) &= \varepsilon_s(\varepsilon - \varepsilon_\infty)E\left[1 - \exp\left(-\alpha(T_p)t_p - s_1\int_{T_p}^{T_d} \alpha(T)dt\right)\right] \end{aligned} \tag{1.7}$$

where s_1 is negative when the temperature decreases and $\alpha(T)$ is in general of the form $\alpha(T) = \alpha_r a(T)$.

Hence,

$$P_s(T) = \varepsilon_o(\varepsilon_s - \varepsilon_\infty)E\left[1 - \exp\left(-\alpha(T_p)t_p - s_1\alpha_r\int_{T_p}^{T_d} a(T)dT\right)\right] \tag{1.8}$$

Generally, $a(T)$ varies exponentially with $-1/T$, and therefore the integral term representing the contribution to the polarization during the decrease of temperature between t_p and t_2 is negligible compared to the isothermal part of the formula.

At t_2 we have reached the end of the polarization stage. We are now going to start the process of depolarization.

EBSCOhost - printed on 2/13/2023 12:32 AM via . All use subject to https://www.ebsco.com/terms-of-use

I.1.3.3 Equations of depolarization

We assume that *no outside field* acts on the dipoles, i. e., that the applied field during the polarization stage has not induced space charges.

The differential equation of discharge is

$$dP_s/dt + \alpha(T)P_s = 0 \tag{1.9}$$

$$P_s(t) = C\exp\left(-\int_{t_2}^{t}\alpha(T)dt\right) \tag{1.10}$$

for $t = t_2$ $P_s(t) = P_s(t_2)$, so $C = P_s(t_2)$,

$$P_s(t_2) = P_s(T_d) = \varepsilon_o(\varepsilon_s - \varepsilon_\infty)E\left[1 - \exp\left(-\varepsilon(T_p)t_p - s_1\alpha_r\int_{T_p}^{T_d}a(T)dT\right)\right] \tag{1.11}$$

Looking at Figure 1.3, the depolarization stage can be split into:

- from t_2 to t_3: depolarization at constant temperature (we normally call $t_d = (t_3 - t_2)$),
- from t_3 to t_4: depolarization as we quench to T_o,
- from t_5 to t: depolarization as the temperature increases linearly. This is the depolarization stage which is normally recorded.

From t_3 to t_4 and from t_4 to t_5, there is practically no loss of polarization, so

$$\begin{aligned}\int_{t_2}^{t}\alpha(T)dt &= \int_{t_2}^{t_3}\alpha(T)dt + \int_{t_5}^{t}\alpha(T)dt\\ &= \alpha(T_d)(t_3 - t_2) + \int_{t_5}^{t}\alpha(T)dt\\ &= \alpha(T_d)(t_3 - t_2) + s_2\alpha_r\int_{T_0}^{T}a(T)dT\end{aligned} \tag{1.12}$$

where s_2 is the reciprocal of the ramp rate during the temperature increase: $dt = s_2dT$,

$$P_s(t) = P_s(T_d) = \exp\left[-\alpha(T_d)(t_3 - t_2) - s_2\alpha_r\int_{T_0}^{T}a(T)dT\right] \tag{1.13}$$

EBSCOhost - printed on 2/13/2023 12:32 AM via . All use subject to https://www.ebsco.com/terms-of-use

Let us call

$$P_s(T_0) = P_s(T_d) = \exp[-\alpha(T_d)(t_3 - t_2)] \tag{1.14}$$

This relationship gives the polarization $P_s(T_o)$ present at the beginning of the increase in temperature in the recovery experiment; it depends on the conditions of polarization at T_p and of depolarization at T_d, i. e., t_p, T_p, T_d, and $(t_3 - t_2) = t_d$.

The polarization during the thermal-stimulated recovery experiment becomes

$$P_s(T) = P_s(T_0) = \exp\left[-s_2\alpha_r \int_{T_0}^{T} a(T)dT\right] \tag{1.15}$$

I.1.3.4 Expression of the thermally stimulated current of depolarization

We can now give the formula of the current as a function of the temperature. It is necessary to specify $a(T)$ and α_r for the material. Suppose that the law which describes the temperature dependence of the relaxation time is an Arrhenius equation:

$$\begin{aligned} \alpha(t) &= \alpha_r e^{-\frac{\Delta H}{kT}} \quad a(T) = e^{-\frac{\Delta H}{kT}} \\ \tau(T) &= \tau_0 e^{+\frac{\Delta H}{kT}} \quad \alpha_r = \frac{1}{\tau_0} \end{aligned} \tag{1.16}$$

Consequently,

$$\alpha_r \int_{T_o}^{T} a(T)dT = \frac{1}{\tau_0} \int_{T_o}^{T} e^{-\frac{\Delta H}{kT}} dT \tag{1.17}$$

The exponential integral is not elementary, but can be calculated numerically.
The current is equal to the rate of change of the polarization:

$$J(t) = \frac{dP_s(t)}{dt} = -\alpha(T)P_s(t) \quad \text{(Debye equation)} \tag{1.18}$$

$$J(t) = J(T) = -\alpha(T)P_s(T_0)\exp\left[-s_2\alpha_r \int_{T_0}^{T} a(T)dT\right] \tag{1.19}$$

The density of the depolarization current is thus given by

$$J(T) = -\frac{P_s(T_0)}{\tau_0}\exp\left(-\frac{\Delta H}{kT}\right)\exp\left[-\frac{s_2}{\tau_0}\int_{T_0}^{T}\exp\left(-\frac{\Delta H}{kT}\right)dT\right] \tag{1.20}$$

EBSCOhost - printed on 2/13/2023 12:32 AM via . All use subject to https://www.ebsco.com/terms-of-use

This equation represents the variation of intensity obtained during the constant heating rate recovery of an elementary Debye process submitted to a thermal-windowing treatment, as described in Figure 1.3. Some examples of simulations derived from this equation will be presented later on.

I.1.3.5 Single Debye relaxation

In summary, for a single elementary Debye relaxation process produced with thermal-windowing as presented in Figure 1.4, one obtains an equation for the release current density $J = dP/dt$:

$$J = E\varepsilon_0(\varepsilon_s - \varepsilon_\infty)\alpha_0 a(T)[1 - \exp(-\alpha_0 x)]\exp(-\alpha_0 y) \tag{1.21}$$

where x describes the gain in polarization during the polarization and cooling period, y is related to the loss of polarization during the isothermal depolarization and TSD, α_o is the dipolar natural frequency ($\alpha_o = 1/\tau_o$), and $a(T)$ is the temperature shift of the relaxation frequency as explained in equation (1.24); ε_o, ε_s, and ε_∞ are given in equation (1.3) and represent the permittivity of vacuum and the static and high-frequency dielectric constants, respectively. We have

$$x = a(T_p)t_p + s_1 \int_{T_d}^{T_p} a(T)dT \tag{1.22}$$

$$y = a(T_d)t_d + s_2 \int_{T_0}^{T} a(T)dT \tag{1.23}$$

$$a(T) = \exp\left(-\frac{\Delta H}{kT}\right)\exp\left[-\frac{s_2}{\tau_0}\int_{T_0}^{T}\exp\left(-\frac{\Delta H}{kT}\right)dT\right] \tag{1.24}$$

where s_2 is the reciprocal of the heating rate during TSD, s_1 is the reciprocal of the cooling rate after the polarization, T_p and t_p are the polarization temperature and time, and T_d and t_d are the depolarization temperature and time. In this formulation, we only neglect a small loss in polarization during cooling between T_d and T_o, assuming the rate of cooling to be high enough.

I.1.3.6 Distributed Debye processes

In real systems, solid polymers in particular, distributed relaxation processes are the most likely to occur. The distribution of relaxation times can occur because of a distribution of enthalpy of activation, a distribution of frequency parameters, or both.

EBSCOhost - printed on 2/13/2023 12:32 AM via . All use subject to https://www.ebsco.com/terms-of-use

In order to perform any type of computer simulation, the type of distribution must be assumed (i. e., a distribution in activation energies or in natural frequencies), and prior knowledge of the natural frequency in the first case, or the activation energy in the second case, is necessary. When both activation energy and natural frequency are variable, it is necessary to tabulate the individual values of both the activation energies and the natural frequencies. The result is a discrete set of elementary Debye currents which combine into the global current,

$$J = E\varepsilon_0 \sum_{i=1}^{n} (\varepsilon_s - \varepsilon_\infty)\alpha_{0i} a_i(T)[1 - \exp(-\alpha_{0i} x_i)] \exp(-\alpha_{0i} y_i) \tag{1.25}$$

and for a distribution of natural frequencies, we obtain

$$J = E\varepsilon_0(\varepsilon_s - \varepsilon_\infty)a(T)_0 \int_0^\infty \alpha_0[1 - \exp(-\alpha_0 x)] \exp(-\alpha_0 y) f(\alpha_0) d\alpha_0 \tag{1.26}$$

while for a distribution in activation energies,

$$J = E\varepsilon_0(\varepsilon_s - \varepsilon_\infty)\alpha_0 \int_0^\infty a(T)[1 - \exp(-\alpha_0 x)] \exp(-\alpha_0 y) g(\Delta H) d\Delta H \tag{1.27}$$

in which $f(\alpha_o)$ and $g(Ea)$ denote the distribution function in α_o and activation energy ΔH, respectively.

For distributed processes, the Fuoss–Kirkwood and Cole–Cole distribution functions can be used:

$$f(u) = \frac{m \cos(m\pi/2) \cosh(\mu)}{\pi[\cos^2(m\pi/2) + \sinh^2(\mu)]} \quad \text{(Fuoss–Kirkwood)} \tag{1.28}$$

$$f(u) = \frac{\sin(m\pi)}{2\pi[\cosh(\mu) + \cos(m\pi)]} \quad \text{(Cole–Cole)} \tag{1.29}$$

where m is the width parameter of the distributions and $u = \ln(\alpha_o/\alpha_x)$ for a distribution in natural frequencies, or $u = (\Delta H - \Delta H_x)/kT$ for a distribution in activation energies; ΔH_x and α_x are the most probable values of these parameters.

I.1.4 Computer simulation

Equation (1.20) describes the variation of the current of depolarization during the linear heating stage at rate $b = 1/s_2$ from the frozen state T_o. The initial polarization is $P_s(T_o) = P_o$, which represents the integral below the current peak at the bottom of Figure 1.5. The total charge which depolarizes is equal to the initial polarization charge.

EBSCOhost - printed on 2/13/2023 12:32 AM via . All use subject to https://www.ebsco.com/terms-of-use

Figure 1.5, top and bottom, describes a pure Debye relaxation, according to equation (1.20), for which the enthalpy of activation ΔH, the pre-exponential frequency $\upsilon_o = 1/\tau_o$, and the initial polarization P_o are chosen. The derivative of the polarization is the current, which is measured by the electrometer. The bottom curve in Figure 1.5 is actually the derivative of the top curve; it allows to model the variation of the rate of change of polarization with the remaining polarization in the material.

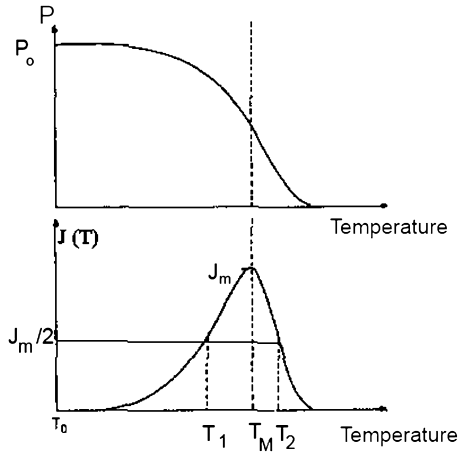


Figure 1.5: Pure Debye Thermal-Stimulated Depolarization according to equation (1.20). $P(T)$ is the polarization in the material at temperature T of the heating ramp-up and $J(T)$ is the derivative of $P(T)$, i. e., the current of depolarization.

An important feature of a pure elementary Debye relaxation is shown at the bottom of Figure 1.5. The position of T_1 and T_2 with respect to T_m, the temperature at the maximum of the peak, is asymmetrical. The area under the peak up to T_m is approximately equal to 2/3 of the area under the total peak. As explained later, this rule is used to obtain, as a first approximation, the curve-fitting constants of equation (1.20). If a peak obtained by thermal-windowing is not completely asymmetrical, say it looks like a Gaussian peak, there is probably more than just one elementary peak involved in the relaxation, hence thermal-windowing has not entirely resulted in a clean filtering of the spectrum of relaxation. In such a case, it is still possible to curve-fit the low-temperature tail of the peak with a method based on the 2/3 asymmetry of a Debye peak, allowing a description of the relaxation occurring in the lower tail of the peak. This will be further explained in detail later.

Figure 1.6 shows a computer simulation according to equation (1.20) of a thermally stimulated current depolarization peak with an activation enthalpy $\Delta H = 42.85$ kcal/m and $\tau_o = 3.25 \times 10^{-26}$ sec. The rate of heating is 7 °C/min, and $P_o = 10^{-11}$ in that simulation.

EBSCOhost - printed on 2/13/2023 12:32 AM via . All use subject to https://www.ebsco.com/terms-of-use

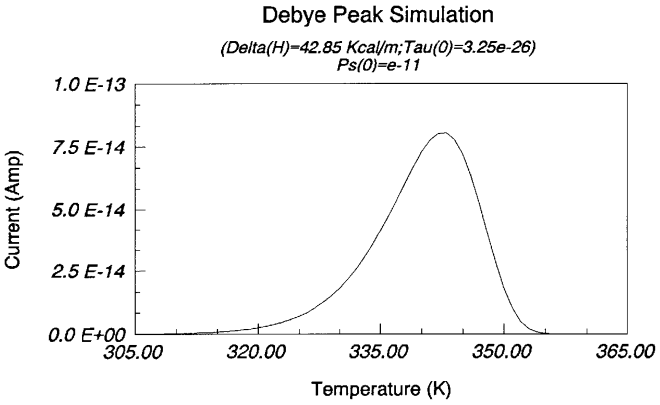


Figure 1.6: Debye Thermal-Stimulated Depolarization peak. Simulation. The values of ΔH, τ_o, and P_{so} are all that is needed to be able to simulate the TSD output of a single elementary Debye peak.

Figure 1.7 illustrates how the terms of equation (1.20) combine to create an asymmetrical peak. The exponential integral dominates the variation of $J(T)$ at the high-temperature end, but at the beginning the kinetics vary like the exponential term. The two exponential terms combine their effect to produce a peak, as drawn in Figure 1.7 (blown up in Figure 1.6). As seen in Figure 1.7, the return of the current to zero due to the exponential integral is much faster after the maximum is reached, which explains the asymmetry of the Debye relaxation.

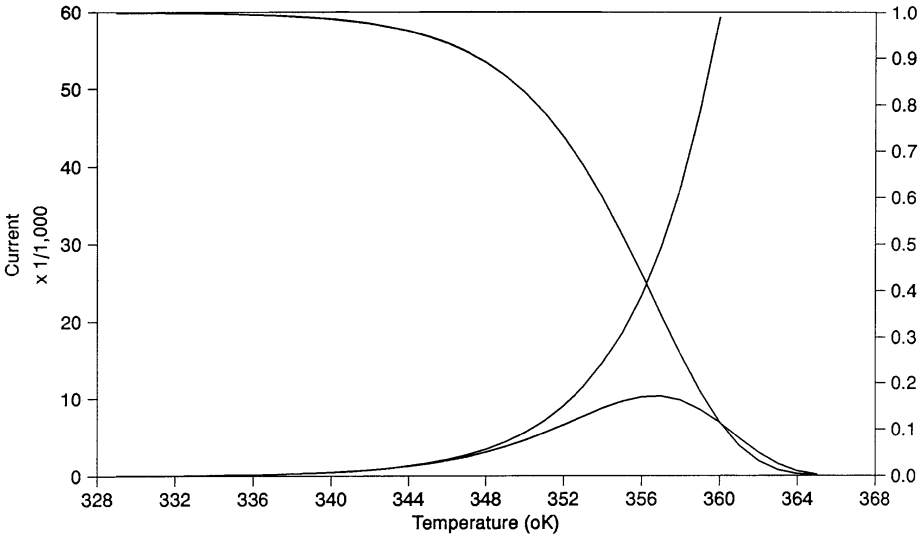


Figure 1.7: Illustration of how the two terms in equation (1.20) combine to create the asymmetry of a Debye peak.

EBSCOhost - printed on 2/13/2023 12:32 AM via . All use subject to https://www.ebsco.com/terms-of-use

I.1.5 Influence of ΔH and τ_o on a Debye relaxation peak

Figure 1.8 shows the effect of changing the activation enthalpy ΔH at constant τ_o, i. e., constant frequency front factor ($\upsilon_o = 1/\tau_o$). The two simulated Debye peaks correspond to $\Delta H = 59.7$ and 69.7 kcal/m, respectively. As the activation enthalpy increases, the peak shifts to a higher temperature. A small decrease of the intensity of the peak is also apparent, indicating that a decrease of the intensity of the peak does not necessarily relate to a decrease of the number of dipoles. The number of initial dipoles is normalized to one in Figure 1.8, and therefore, the surface area is identical (and equal to 1) for both peaks.

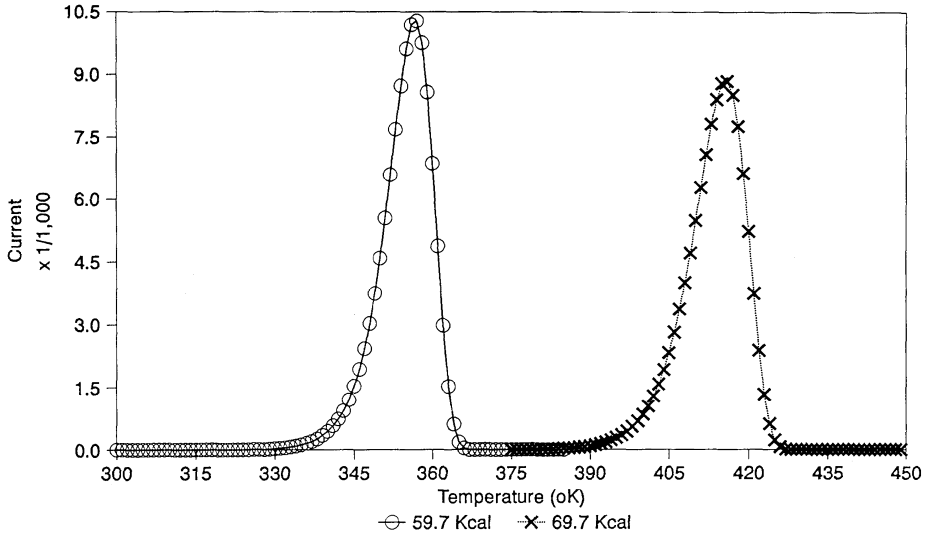


Figure 1.8: Influence of ΔH at τ_o constant (1.6×10^{-35}) on the shape and position of a Debye depolarization peak. P_{so} is normalized to 1. ΔH has the values 59.7 and 69.7 kcal/mole in the simulations.

In Figure 1.9, we show the effect of varying the frequency front factor υ_o at constant enthalpy of activation ΔH. The value of τ_o equals $(1/\upsilon_o)$ for the peak represented with crosses is 100,000 times greater than that for the peak with circles. The result of decreasing τ_o is a shift of the peak to a higher temperature and a lower peak intensity, in a manner reminiscent of the effect of an increase of the enthalpy of activation (Figure 1.8). This means that a shift of a peak to a higher temperature is not necessarily caused by an increase of the energy of activation, but can be attributed as well to a decrease of the jump frequency. The equivalence between a decrease of the frequency front factor and an increase of the enthalpy of activation is worth noting.

EBSCOhost - printed on 2/13/2023 12:32 AM via . All use subject to https://www.ebsco.com/terms-of-use

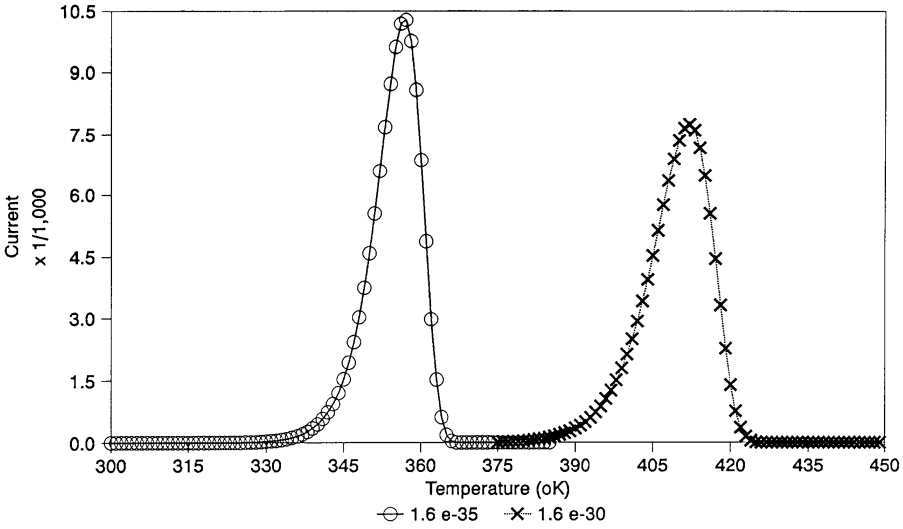


Figure 1.9: Influence of τ_o at constant ΔH (59.7 kcal/mole) on the shape and position of a Debye depolarization peak. P_{so} is normalized to 1. τ_o has the values 1.6×10^{-35} and 1.6×10^{-30} in the simulations.

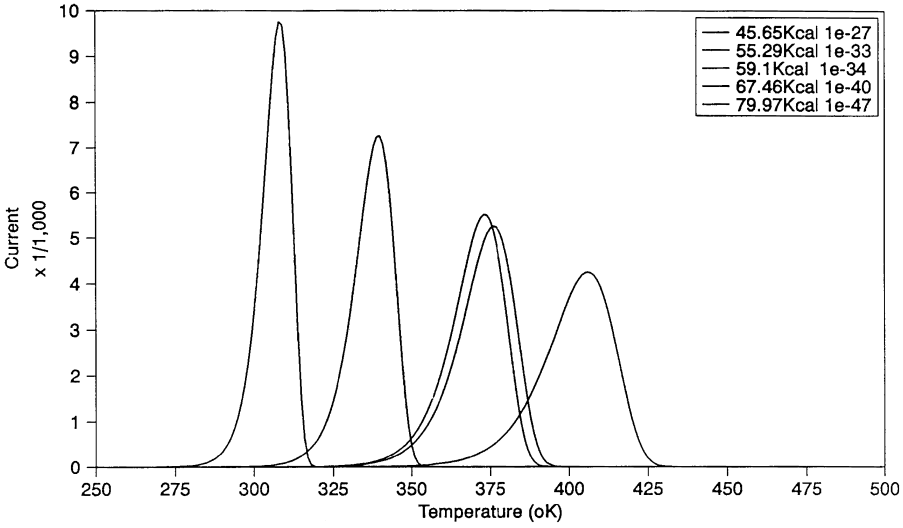


Figure 1.10: Set of simulated Debye peaks corresponding to ΔH and τ_o values shown in the inset. These values correspond to experimental curve-fits of Debye peaks obtained by TWD of PMMA with T_p varying between 65 °C and 85 °C.

In Figure 1.10 are plotted several simulated Debye relaxation curves for which both ΔH and τ_o are selected among values experimentally found applying the deconvolution technique of thermal-windowing to PMMA. Note that the simulated peaks are well

EBSCOhost - printed on 2/13/2023 12:32 AM via . All use subject to https://www.ebsco.com/terms-of-use

resolved and separated, except for the two peaks seen at $T_m \approx 375$ K, for which the ΔH and τ_o values are such that the peaks almost totally overlap. The ΔH difference is about 4 kcal/mole and the τ_o difference is a decade for these two peaks, which simulates experimental findings observed by TSD/TWD for cooperative relaxations.

Figure 1.10 provides a graph of the individual simulated Debye peaks, and Figure 1.11 also displays the total current resulting from adding up all the elementary currents. The contour of the total current closely follows the peaks themselves, except in the case of the two "cooperative" simulated peaks at 375 K for which the currents add up to a larger peak which dominates in intensity the other peaks. As said earlier, the values chosen for ΔH and τ_o for the simulated Debye peaks of Figure 1.10 correspond to experimental curve-fits found in the deconvolution of the T_g transition of PMMA, with T_p varying between 65 °C and 85 °C. The fact, in Figure 1.11, that the currents add up to a larger peak in the case of the two overlapping elementary relaxations illustrates the notion that cooperative relaxation results in larger global peaks. In essence, the presence of cooperative motion induces increased sensitivity. This statement is worth explaining because it is the fundamental reason why TSD is superior in sensitivity to other techniques such as DMA or DEA, for instance. In the case of a DMA peak obtained on a tan δ vs. temperature graph, the peak height is determined by the highest shift factor value, i. e., for the relaxation mode which gives rise to the resonance in the material. In the case of a TSD peak, the individual elementary relaxations act cooperatively, and each participates in the peak intensity, which is not limited to the current at the resonance; therefore, a better sensitivity to determine the relaxation process results. Note in Figure 1.11 that peaks which are well separated do not cooperatively add up in the global response.

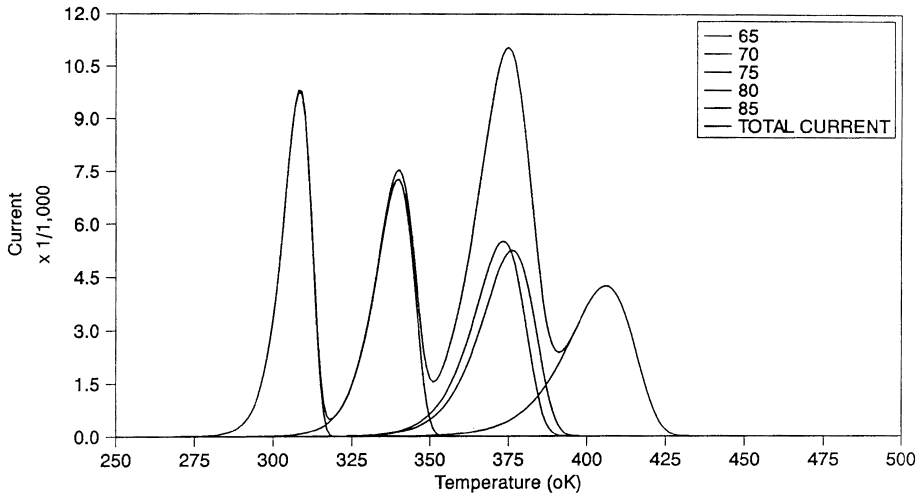


Figure 1.11: Global TSD peak obtained by current addition of elementary Debye peaks. Peaks which are well separated do not cooperatively add up in the simulated global TSD peak.

EBSCOhost - printed on 2/13/2023 12:32 AM via . All use subject to https://www.ebsco.com/terms-of-use

Figures 1.12 and 1.13 simulate what happens in the case of a spectrum of Debye peaks overlapping in a narrow temperature range due to the choice of the enthalpy of activation and the frequency front factor. The total simulated TSD response resulting from adding the effect of the elementary Debye currents is observed in Figure 1.13 as a symmetrical peak. The intensity of the total current at the maximum is at least three times the intensity of the largest individual Debye peak.

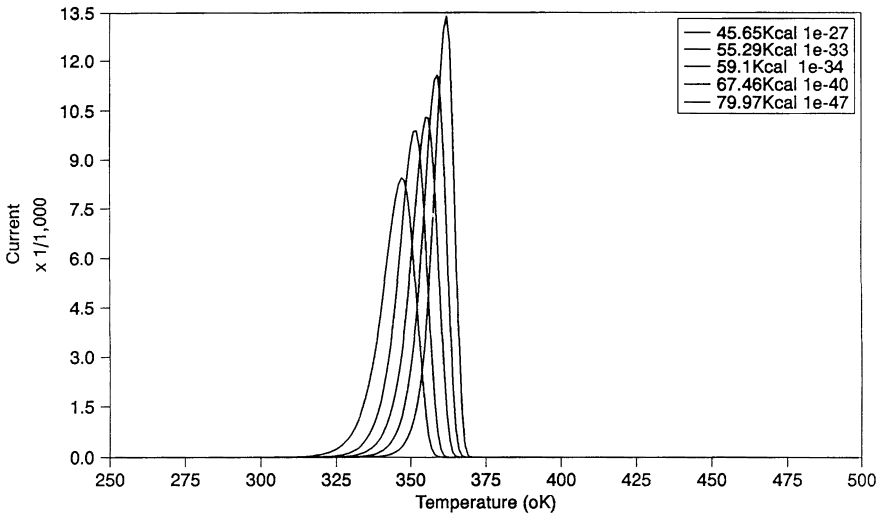


Figure 1.12: Simulation of closely interacting Debye peaks corresponding to ΔH and τ_o values shown in the inset.

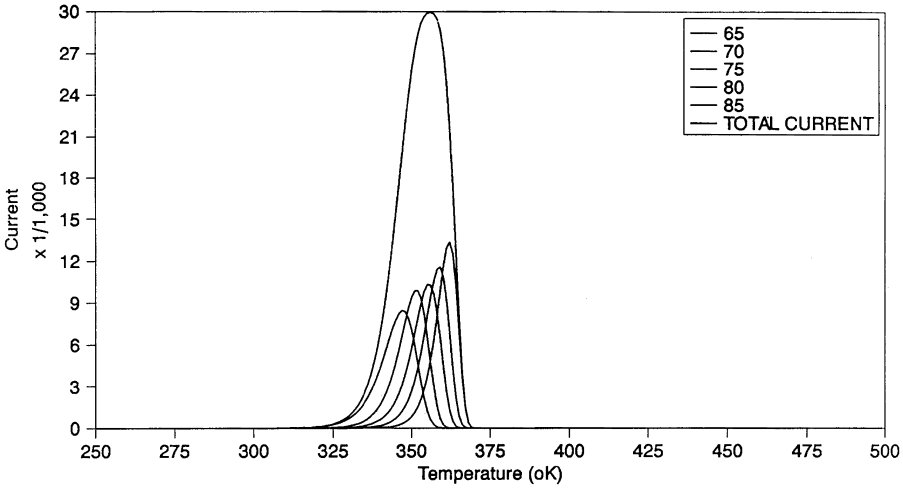


Figure 1.13: Global TSD peak calculated by current addition of the elementary Debye peaks obtained by TWD with the values of T_p in the inset.

EBSCOhost - printed on 2/13/2023 12:32 AM via . All use subject to https://www.ebsco.com/terms-of-use

An important issue of thermal analysis is raised here. Consider Figure 1.13 as a peak representative of a transition behavior. Classical curve-fitting kinetic formulations could successfully be used to describe the peak, but, in reality, the true interest lies in the determination of the elementary components of the global peak which, as we know from the simulation in Figure 1.13, is made up of several elementary asymmetrical Debye relaxations. There is a great danger in trying to model global peaks and fit them with physical models. The reason for our interest in thermal-windowing is that the method allows a physical – not mathematical – deconvolution of the relaxation spectrum to individually sort out the elementary peaks which form the global behavior. This approach is particularly well suited to cooperative kinetics which seems to be the attribute of the glass transition temperature of materials.

Another important issue is illustrated by Figure 1.13. Each elementary Debye relaxation which needs to be resolved by the technique of thermal-windowing is much lower in intensity than the global peak itself and the question of the sensitivity of the electrometer to detect much smaller peaks becomes critical. In order to successfully apply thermal-windowing, the electrometer should be able to resolve with good accuracy current levels at least 10 times smaller than those observed for global TSD peaks. This puts a restriction to the type of electrometer used and imposes a requirement on the stability in time of the electronics. The intensity of the peaks observed in depolarization current measurements depends on (1) the polarizability of the dipoles, (2) the number of dipoles excited by the voltage field, and (3) the number of relaxation modes cooperatively participating in the global relaxation. The deconvolution of a global peak into the elementary relaxation modes requires to depolarize during thermal-windowing a large number of the modes in order to isolate a single one. This results in a decrease of the throughput, the current measurement, and obviously, the better the resolution between the relaxation modes, the lower the current. Since there is a limit to the accuracy of measurement to detect any current, the technique of thermal-windowing consists in a compromise between sensitivity and resolution. The better we try to resolve the global peak, the lower the intensity of the peak detected, resulting in inaccuracies in the determination of the kinetic parameters (enthalpy of activation and frequency front factor). When the dipolar moment is low, such as for non-polar polyolefins, the intensity of current of depolarization is extremely small for thermally windowed peaks, and this becomes a limitation. In summary, the less polar the material, the more difficult it is to separate out the elementary peaks because the intensity goes down to the limit of the instrumentation.

I.1.6 Debye curve-fits

In equation (1.20), ΔH and τ_o are two curve-fitting constants which must be determined from the current vs. temperature Debye peak recorded experimentally. Curve-fitting methods are used to determine those constants. In some cases, the free energy

EBSCOhost - printed on 2/13/2023 12:32 AM via . All use subject to https://www.ebsco.com/terms-of-use

of activation ΔG is used in equation (1.20) instead of ΔH to fit the data, providing both the enthalpy and the entropy of activation (Part I, Chapter 2). In this section, we describe the various curve-fitting techniques to extract the fundamental characteristics of the relaxation process.

I.1.6.1 The Bucci–Fieschi–Guidi integral solution

The model described by Bucci et al. [24, 25] is based on equation (1.18), which states that the rate of change of depolarization at any time of the depolarization process is proportional to the remaining polarization at that instant. The proportionality constant $\alpha(T)$ is the inverse of the relaxation time at that temperature. Figure 1.14 illustrates this solution. At each temperature T the current $J(T)$ is measured, and the surface area from T to ∞, $P(T)$, is equal to the remaining dipolar activity in the sample. The ratio of the two, $J(T)/P(T)$, is equal to $-\alpha(T) = -1/\tau(T)$. The computer calculates at each temperature the value of the current $J(T)$ and the surface area $P(T)$ etched in Figure 1.14. The integration is performed, for instance every 0.1 °C or 0.5 °C, leading to a table of values of $\tau(T)$ vs. T. According to Bucci et al. [24, 25], $\tau(T)$ represents the true relaxation time of a material according to the Debye model (equations (1.18) and (1.19)). A plot of Log $\tau(T)$ vs. $1/T$ reveals the fundamental constants of the Debye peak, with either the Arrhenius or the Williams–Landel–Ferry formalism to describe the kinetic behavior. For instance, in the case of an Arrhenius curve-fit, the slope and intercept of Log τ vs. $1/T$ (Figure 1.15) yield the enthalpy of activation ΔH and Log τ_o, which is the value of the relaxation time extrapolated at $T = \infty$.

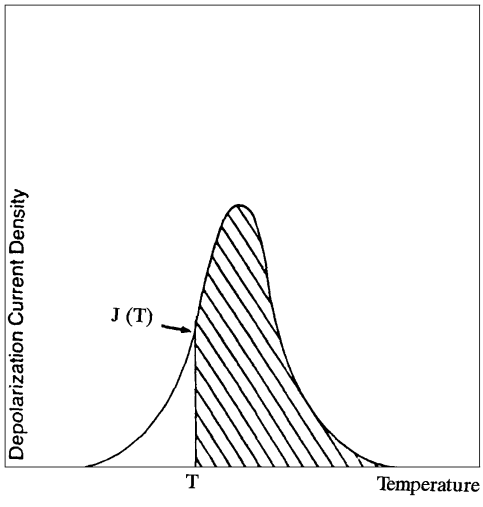


Figure 1.14: Illustration of the Bucci–Fieschi–Guidi integral solution to convert the value of $J(T)$ into $\tau(T)$.

EBSCOhost - printed on 2/13/2023 12:32 AM via . All use subject to https://www.ebsco.com/terms-of-use

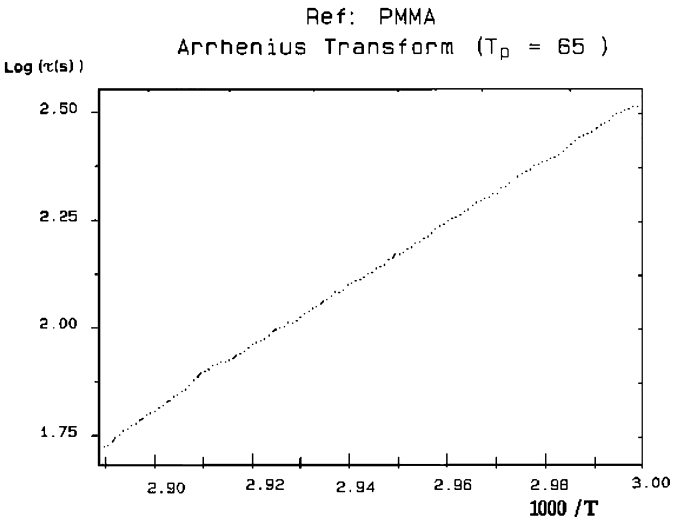


Figure 1.15: Arrhenius plot of $\log \tau(T)$ obtained from the Bucci equation versus $1/T(K)$.

In a real TSD experiment, it is unfortunately usually not possible to isolate a single unique relaxation phenomenon. The Bucci approach has been criticized by McCrum [200, 201], who tried to take into consideration a distribution of relaxation in the process of analysis. McCrum considers that $\tau(T)$ does not measure the effective relaxation time of the system at each temperature and postulates that the true relaxation time $\tau_{1/2}$ of the system is obtained when half of the depolarization process is done, that is, when $P(T)/P_o = 1/2$, where P_o is the initial polarization in the material and $P(T)$ is the polarization at temperature T of the depolarization. McCrum corrects the relaxation time obtained by the Bucci formula with a correction factor equal to $\tau_{1/2}/\tau(T)$, also equal to $\tau_{1/2}/\tau(P(T)/P_o)$. Whereas the Bucci–Fieschi–Guidi model supposes that the terms ΔH and τ_o are constant, McCrum's formalism only supposes that ΔH is constant.

I.1.6.2 The Lacabanne (2/3) rule

The method of McCrum is rather complex and somewhat arbitrary. Lacabanne has proposed a solution which accounts for the presence of a distribution of relaxation times.

This method of analysis applies to thermally windowed peaks only, since it is assumed that most of the filtering of the relaxation spectrum has already been processed. Lacabanne's (2/3) rule is a modified Bucci integration solution for which pollution from the longer relaxation times is further reduced by mathematical manipulation.

If the peak obtained experimentally contains more than *one* elementary Debye component, the method of integration of Bucci will lead to a wrong relaxation time

EBSCOhost - printed on 2/13/2023 12:32 AM via . All use subject to https://www.ebsco.com/terms-of-use

relationship since the peak is the convolution of more than one Debye relaxation. Lacabanne's idea is to concentrate on the lower tail of the relaxation peak and to integrate the peak, to obtain $P(T)$, by applying the rule already mentioned that a characteristic of a Debye relaxation is such that the area under the curve up to the summit of the peak is approximately 2/3 of the total peak. This rule allows to only integrate within the surface area up to the peak maximum and to *calculate* $P(T)$, the remaining polarization left in the material, from the 2/3 rule.

In Figure 1.16, the surface area between A and B is called S_m. According to Lacabanne's rule, the total Debye peak is equal to $S_o = (3/2S_m)$. The area located beyond the summit at T_m is 1/3 of the total area, $S_m/2$. In the application of Bucci's formula to determine $\tau(T)$, $\tau(T) = J(T)/P(T)$, it is possible to calculate $P(T)$ by limiting the integration to the summit temperature T_m, and *add* to that surface area the value of $S_m/2$, which is supposed to represent the second half of the Debye peak. In this case, $P(T)$ is not polluted by the presence of possible longer relaxation times in the calculation of $\tau(T)$ for the temperature region situated in the lower tail of the peak.

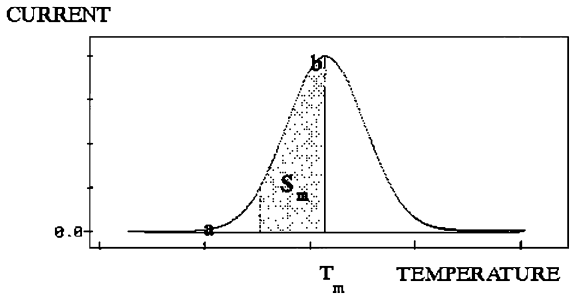


Figure 1.16: Illustration of Lacabanne's 2/3 integral rule solution to convert the value of $J(T)$ to $\tau(T)$.

We have investigated the validity of Lacabanne's 2/3 rule by computer modeling of Debye peaks using equation (1.20) and choosing pairs of values of ΔH and τ_o. The exponential integral is determined numerically by the Simpson integration routine. Table 1.1 gives the value found for the surface area ratio ($100 \times S_m/S_o$) for different pairs of ΔH and τ_o with ΔH varying between 0.7 and 2.2 eV (1 eV = 23 kcal) and Log τ_o varying between –10 and –40. Log τ_o was chosen so that the peak maximum temperature is located between 250 K and 450 K. Table 1.1 shows that the ratio S_m/S_o is approximately constant, but to a certain degree only. The "Debye ratio percent," as we call S_m/S_o, is found between 60 % and 63 % with an average value of 61.5 % for all the pairs presented in the table. The Debye ratio is not equal to 2/3, as proposed by Lacabanne, and is better described by a more accurate value around 62 %. Figure 1.17 is a plot of the Debye ratio vs. Log τ_o for various activation enthalpy values between 16 and 51 kcal/mole. All values are included in the band 60 %–63 %, scattered regularly around the average 62.25 % obtained for Log τ_o < (–20), which covers the range of Log τ_o found experimentally from thermal-windowing experiments.

EBSCOhost - printed on 2/13/2023 12:32 AM via . All use subject to https://www.ebsco.com/terms-of-use

Table 1.1: Investigation of the validity of Lacabanne's 2/3 rule by simulation using equation (1.20) of Debye peaks with ΔH and τ_o pairs given in columns 1 and 2 or 4 and 5 of Table 1.1, respectively, and integrating the corresponding simulated peaks to obtain the Debye ratio S_m/S_o in % (DB% in columns 3 and 6). According to Lacabanne's 2/3 rule this ratio should be equal to 66.67 %.

ΔH (eV)	Log τ_0	DB ratio%
0.70000000000	−9.0	60.40000000000
0.70000000000	−9.50000000000	60.11000000000
0.70000000000	−10.0	60.17000000000
0.70000000000	−10.50000000000	60.77000000000
0.70000000000	−11.0	60.90000000000
0.70000000000	−11.50000000000	60.90000000000
0.70000000000	−12.0	61.18000000000
0.70000000000	−12.50000000000	61.18000000000
0.70000000000	−13.0	61.18000000000
0.70000000000	−13.50000000000	61.55000000000
0.80000000000	−11.0	60.49000000000
0.80000000000	−11.50000000000	60.95000000000
0.80000000000	−12.0	60.49000000000
0.80000000000	−12.50000000000	61.08000000000
0.80000000000	−13.0	60.45000000000
0.80000000000	−13.50000000000	60.72000000000
0.80000000000	−14.0	61.31000000000
0.80000000000	−14.50000000000	61.39000000000
0.80000000000	−15.0	61.15000000000
0.80000000000	−15.50000000000	60.79000000000
0.90000000000	−12.0	60.42000000000
0.90000000000	−12.50000000000	60.69000000000
0.90000000000	−13.0	61.22000000000
0.90000000000	−13.50000000000	61.47000000000
0.90000000000	−14.0	60.70000000000
0.90000000000	−14.50000000000	61.12000000000
0.90000000000	−15.0	61.01000000000
0.90000000000	−15.50000000000	61.71000000000
0.90000000000	−16.0	61.09000000000
0.90000000000	−16.50000000000	61.81000000000
1.0	−14.0	61.50000000000
1.0	−14.50000000000	61.30000000000
1.0	−15.0	61.28000000000
1.0	−15.50000000000	61.76000000000
1.0	−16.0	60.77000000000
1.0	−16.50000000000	61.93000000000
1.0	−17.0	61.99000000000
1.0	−17.50000000000	60.97000000000
1.0	−18.0	61.71000000000
1.0	−18.50000000000	61.73000000000

EBSCOhost - printed on 2/13/2023 12:32 AM via . All use subject to https://www.ebsco.com/terms-of-use

Table 1.1 (continued)

Δ*H* (eV)	Log τ_0	DB ratio%
1.10000000000	−16.0	60.84000000000
1.10000000000	−16.50000000000	61.25000000000
1.10000000000	−17.0	61.54000000000
1.10000000000	−17.50000000000	61.89000000000
1.10000000000	−18.0	61.20000000000
1.10000000000	−18.50000000000	62.23000000000
1.10000000000	−19.0	61.12000000000
1.10000000000	−19.50000000000	62.22000000000
1.10000000000	−20.0	61.30000000000
1.20000000000	−17.0	61.42000000000
1.20000000000	−17.50000000000	61.79000000000
1.20000000000	−18.0	61.04000000000
1.20000000000	−18.50000000000	61.66000000000
1.20000000000	−19.0	61.44000000000
1.20000000000	−19.50000000000	61.77000000000
1.20000000000	−20.0	61.46000000000
1.20000000000	−20.50000000000	62.08000000000
1.20000000000	−21.0	62.30000000000
1.20000000000	−21.50000000000	62.23000000000
1.30000000000	−19.0	61.94000000000
1. 30000000000	−19.50000000000	61.61000000000
1.30000000000	−20.0	61.82000000000
1.30000000000	−20.50000000000	61.37000000000
1.30000000000	−21.0	61.80000000000
1.30000000000	−21.50000000000	61.83000000000
1.30000000000	−22.0	61.54000000000
1.30000000000	−22.50000000000	62.66000000000
1.30000000000	−23.0	62.03000000000
1.30000000000	−23.50000000000	61.34000000000
1.40000000000	−21.0	61.57000000000
1.40000000000	−21.50000000000	61.68000000000
1.40000000000	−22.0	61.37000000000
1.40000000000	−22.50000000000	62.25000000000
1.40000000000	−23.0	61.36000000000
1.40000000000	−23.50000000000	61.97000000000
1.40000000000	−24.0	62.63000000000
1.40000000000	−24.50000000000	61.58000000000
1.40000000000	−25.0	62.55000000000
1.40000000000	−25.50000000000	61.93000000000
1.50000000000	−23.0	62.48000000000
1.50000000000	−23.50000000000	61.10000000000
1.50000000000	−24.0	61.14000000000
1.50000000000	−24.50000000000	61.16000000000
1.50000000000	−25.0	61.27000000000

EBSCOhost - printed on 2/13/2023 12:32 AM via . All use subject to https://www.ebsco.com/terms-of-use

Table 1.1 (continued)

ΔH (eV)	Log τ_0	DB ratio%
1.50000000000	−25.50000000000	61.55000000000
1.50000000000	−26.0	62.15000000000
1.50000000000	−26.50000000000	61.17000000000
1.50000000000	−27.0	62.69000000000
1.50000000000	−27.50000000000	62.77000000000
1.60000000000	−24.0	61.54000000000
1.60000000000	−24.50000000000	62.55000000000
1.60000000000	−25.0	61.95000000000
1.60000000000	−25.50000000000	61.37000000000
1.60000000000	−26.0	62.71000000000
1.60000000000	−26.50000000000	62.55000000000
1.60000000000	−27.0	62.73000000000
1.60000000000	−27.50000000000	61.37000000000
1.60000000000	−28.0	62.56000000000
1.60000000000	−28.50000000000	62.33000000000
1.70000000000	−26.0	61.63000000000
1.70000000000	−26.50000000000	62.11000000000
1.70000000000	−27.0	62.90000000000
1.70000000000	−27.50000000000	62.17000000000
1.70000000000	−28.0	61.84000000000
1.70000000000	−28.50000000000	62.01000000000
1.70000000000	−29.0	62.84000000000
1.70000000000	−29.50000000000	62.25000000000
1.70000000000	−30.0	62.47000000000
1.70000000000	−30.50000000000	61.28000000000
1.80000000000	−28.0	61.30000000000
1.80000000000	−28.50000000000	61.85000000000
1.80000000000	−29.0	62.94000000000
1.80000000000	−29.50000000000	62.66000000000
1.80000000000	−30.0	63.08000000000
1.80000000000	−30.50000000000	62.09000000000
1.80000000000	−31.0	61.94000000000
1.80000000000	−31.50000000000	62.75000000000
1.80000000000	−32.0	62.28000000000
1.80000000000	−32.50000000000	62.95000000000
1.90000000000	−29.0	61.25000000000
1.90000000000	−29.50000000000	61.17000000000
1.90000000000	−30.0	61.68000000000
1.90000000000	−30.50000000000	62.92000000000
1.90000000000	−31.0	62.85000000000
1.90000000000	−31.50000000000	61.43000000000
1.90000000000	−32.0	63.13000000000
1.90000000000	−32.50000000000	61.26000000000
1.90000000000	−33.0	62.85000000000
1.90000000000	−33.50000000000	63.26000000000

EBSCOhost - printed on 2/13/2023 12:32 AM via . All use subject to https://www.ebsco.com/terms-of-use

Table 1.1 (continued)

ΔH (eV)	Log τ_0	DB ratio%
2.0	−31.0	61.71000000000
2.0	−31.50000000000	62.40000000000
2.0	−32.0	61.80000000000
2.0	−32.50000000000	62.08000000000
2.0	−33.0	63.43000000000
2.0	−33.50000000000	61.13000000000
2.0	−34.0	62.38000000000
2.0	−34.50000000000	62.43000000000
2.0	−35.0	61.29000000000
2.0	−35.50000000000	61.52000000000
2.10000000000	−33.0	61.78000000000
2.10000000000	−33.50000000000	61.56000000000
2.10000000000	−34.0	62.42000000000
2.10000000000	−34.50000000000	62.05000000000
2.10000000000	−35.0	62.97000000000
2.10000000000	−35.50000000000	62.68000000000
2.10000000000	−36.0	61.21000000000
2.10000000000	−36.50000000000	61.15000000000
2.10000000000	−37.0	62.69000000000
2.10000000000	−37.50000000000	63.18000000000
2.20000000000	−34. 0	62.52000000000
2.20000000000	−34.50000000000	61.82000000000
2.20000000000	−35.0	62.20000000000
2.20000000000	−35.50000000000	61.38000000000
2.20000000000	−36.0	61.84000000000
2.20000000000	−36.50000000000	61.15000000000
2.20000000000	−37.0	61.90000000000
2.20000000000	−37.50000000000	61.54000000000
2.20000000000	−38.0	62.81000000000
2.20000000000	−38.50000000000	63.02000000000

In summary, a modification of Lacabanne's 2/3 rule is obtained by computer modeling of Debye peaks to give a simple curve-fitting technique to determine the relaxation time at each temperature of the lower tail of the relaxation peak. Looking at Figure 1.16, this method of integration only applies to temperatures located below the peak maximum T_m, with a particular emphasis in choosing the limits of integration A and B to not exceed the polarization temperature T_p. Lacabanne's method has been compared – on real thermal-windowing curves – with McCrum's correction and found to provide a similar correction to the Bucci relaxation modeling.

EBSCOhost - printed on 2/13/2023 12:32 AM via . All use subject to https://www.ebsco.com/terms-of-use

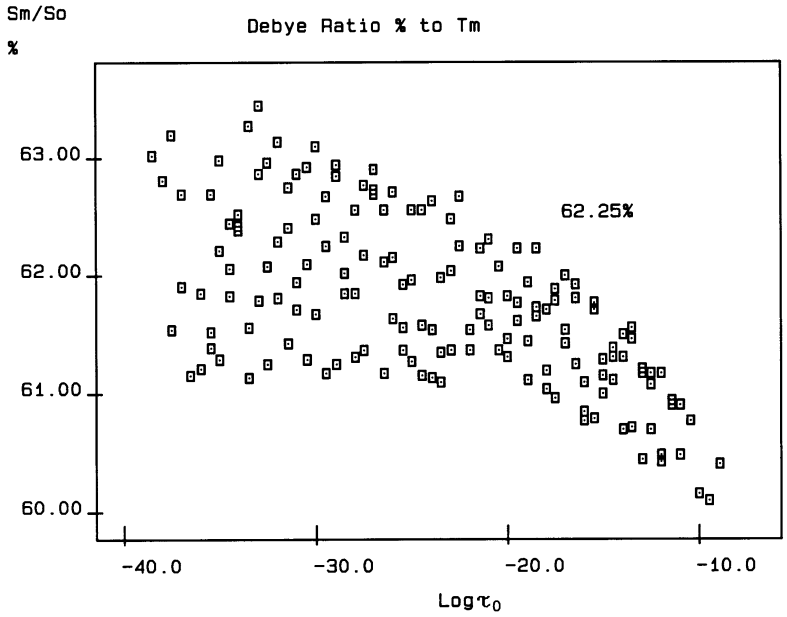


Figure 1.17: Variation of the Debye ratio S_m/S_o in % vs. log τ_o for ΔH varying between 16 and 51 kcal/mole.

I.1.6.3 Simplex curve-fitting methods

In the expression of the Debye relaxation, equation (1.20), there appears an integral of the form

$$\int F(T, \Delta H) = \int_{T_o}^{T} \exp(-\Delta H/kT')dT'$$

There have been several approximations to the exponential integral, including that of Squire [222], who suggested the approximation

$$F(T, \Delta H) = \left[\frac{T' \exp(-x)(x + 3.0396)}{(x^2 + 5.0364x + 4.1916)}\right]_{T_o}^{T}$$

with $x = \Delta H/kT$.

Another useful approximation has been given by Chen [47]:

$$F(T, \Delta H) = [T' x \exp(-1/x)(1 - 2x + 6x^2)]_{To}^{T}$$

where $x = (kT/\Delta H)$.

EBSCOhost - printed on 2/13/2023 12:32 AM via . All use subject to https://www.ebsco.com/terms-of-use

In the case of Squire's formula, the value of the current $J(T)$ becomes

$$J(T) = (P_0/\tau_0)\exp\left[-x - \frac{1}{b\tau_0}[F(T,\Delta H)]\right]$$

where $x = \Delta H/kT$ and b is the heating rate, which can be written

$$\mathrm{Log}\, J(T) + x = \mathrm{Log}(P_0/\tau_0) - \frac{1}{b\tau_0}[F(x) - F(x_0)]$$

For each value of ΔH that the curve-fitting subroutine may try (starting with Lacabanne's value of 62.25 %), a plot of $[\mathrm{Log}\, J(T) + x]$ vs. $[F(x) - F(x_o)]$ is more or less linear, with perfect linearity obtained for the correct value of x, i. e., the proper value of ΔH. We have

$$\left[\mathrm{Log}\, J(T) + x\right] = A_o + A_1\left[F(x) - F(x_o)\right]$$

From the slope A_1, we determine τ_o, $A_1 = -1/b\tau_o$, and from the intercept $A_o = \mathrm{Log}(P_o/\tau_o)$, we calculate P_o. The curve-fit consists in choosing a range of value for ΔH comprised between $0.6\Delta H_L$ and $1.4\Delta H_L$, where ΔH_L indicates the value obtained from Lacabanne's value of 62.25 %. For each value of ΔH chosen, the linearity is evaluated and a simplex method is used to find the best linear fit which renders $|r^2 - 1|$ as small as possible. The simplex algorithm is used to eliminate the possibility of secondary minima in order to find the true solution of ΔH. Once the best ΔH is obtained, the slope and intercept A_1 and A_o provide the other curve-fitting parameters τ_o and P_o. Numerical integration can be performed in this way, yielding a very accurate determination of the kinetic parameters in a relatively short time. The results can differ from the modified Lacabanne 62.25 % surface integral rule by as much as 5 %, and thus very accurate fittings should be done with the simplex method.

I.1.6.4 Curve-fitting methods based on peak half-width

Chen and Kirsh [48] provide in their book a good review of the methods to evaluate the parameters from thermally stimulated curves. A popular and simple method which involves the determination of the temperature T_1 at the half-way peak level (Figure 1.18) gives for the activation energy ΔH

$$\Delta H = 1.41R\left(\frac{T_m T_1}{T_m - T_1}\right)$$

EBSCOhost - printed on 2/13/2023 12:32 AM via . All use subject to https://www.ebsco.com/terms-of-use

where R is the gas constant (1.9872 when ΔH is in cal/m). This is the Dussel–Bube approximation [69]. Lushchik's formula [199] is also often quoted:

$$\Delta H = 2k\left(\frac{T_m^2}{T_2 - T_m}\right)$$

where T_2 is now the temperature at half-way of the peak maximum intensity for the higher-temperature region (Figure 1.18).

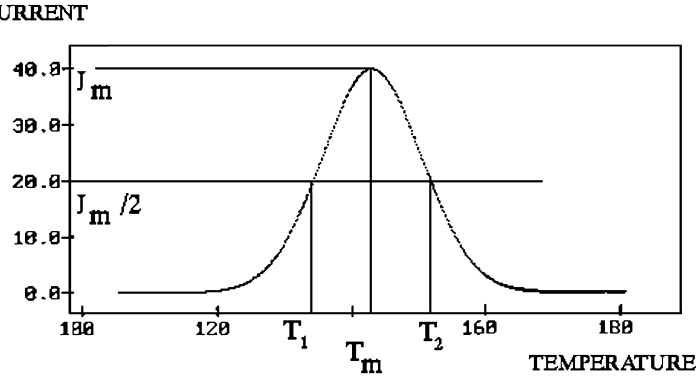


Figure 1.18: Determination of ΔH and τ_o from the curve-fitting method based on the peak half-width.

Chen [47] questioned the assumptions used to derive this formula and improved the value of the constants.

Once ΔH is known, the relaxation time τ_o can be evaluated from:

$$\tau_o = \frac{\exp\left(-\frac{\Delta H}{RT_m}\right)}{b\frac{\Delta H}{RT_m^2}}$$

where b is the heating rate in K/sec. This expression of τ_o and the Dussel–Bube expression of ΔH above will be extensively used in Part I Chapter 3.

Figure 1.19 is a plot of Log τ vs. $1000/T$ for the data already presented in Figure 1.15, but the axes have been rewritten such that the Arrhenius temperature, $1/T$, decreases from left to right, which makes T (top of the graph) increase from left to right, the classical way. In the following, for all the spectral lines of Log τ vs. $1/T$ presented in this book, the Arrhenius temperature axis will always be scaled in this way. This will make the Log τ vs. $1/T$ curves appear to go downward on the graph, the opposite of what is seen in Figure 1.15.

EBSCOhost - printed on 2/13/2023 12:32 AM via . All use subject to https://www.ebsco.com/terms-of-use

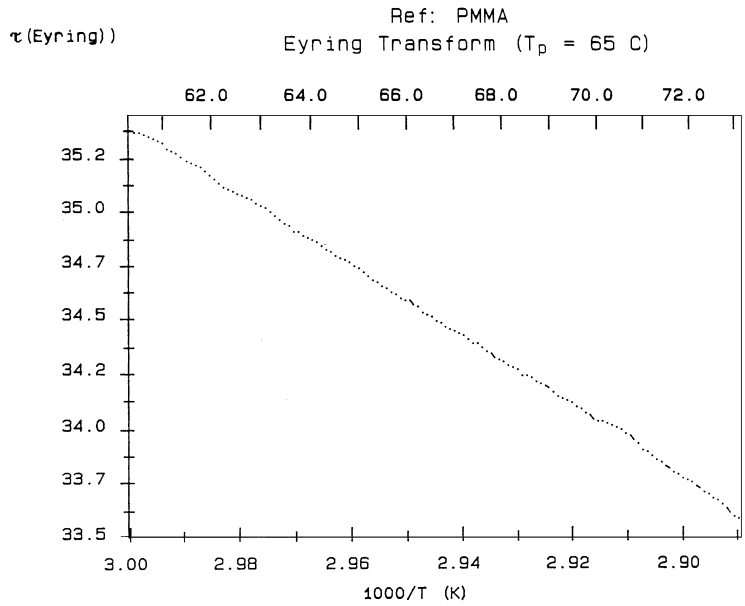


Figure 1.19: Illustration of how the $1/T$ scale will be presented, in descending numbers from left to right, in the rest of this book to display the relaxation map results. This presentation contrasts with the classical ascending approach illustrated in Figure 1.15.

I.1.7 Deconvolution of thermally windowed peaks

In the previous section, we learned how to curve-fit Debye peaks and obtain ΔH and τ_o. Thermal-windowing is supposed to experimentally deconvolute the TSD peaks into elementary Debye relaxation modes. All should now be simple! However, we have mentioned earlier that a compromise is necessary between sensitivity (the ability to read a current of depolarization) and resolution (the ability to isolate individual relaxations). Because of that, it is probable that what is called an "elementary" relaxation (Figure 1.20) is in fact made up of two, perhaps three Debye peaks. Figure 1.20 shows the current of depolarization after thermally windowing a sample of PMMA. The experimental conditions are "standard" for this polar polymer, i. e., window width 5 °C, $t_p = t_d = 2$ min. Here, $T_p = 55$ °C. The effect of variable experimental parameters is studied in the next section of this chapter.

In Figure 1.21, we show the result of a Debye curve-fit in the low tail part of the peak according to the 62.25 % rule. We obtain $\Delta H = 48.57$ kcal/mole and $\tau_o = 2.939 \times 10^{-30}$ sec. The small peak inside the figure is the theoretical Debye curve calculated numerically from equation (1.20) using the curve-fitted constant ΔH, τ_o. The fit is quite good at low temperatures, but departs even before the maximum is reached. A single Debye peak does not represent the whole experimental relaxation curve. This conclusion could be reached qualitatively by looking at the symmetry of the peak in Fig-

EBSCOhost - printed on 2/13/2023 12:32 AM via . All use subject to https://www.ebsco.com/terms-of-use

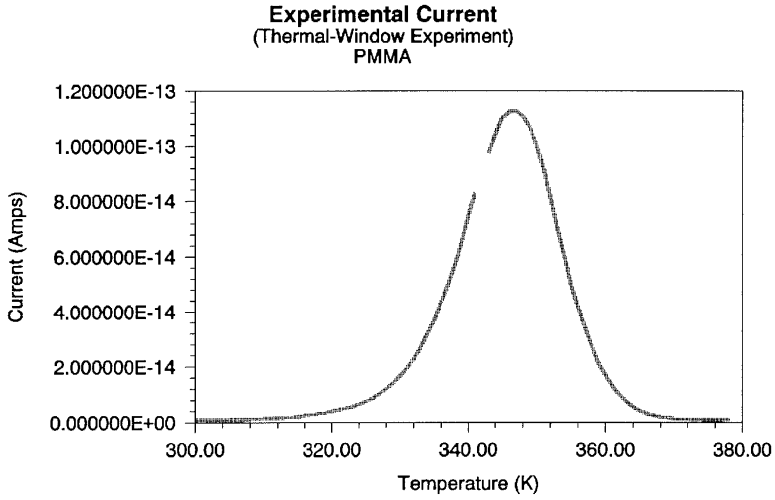


Figure 1.20: Experimental $J(T)$ for PMMA obtained by TWD using "standard" conditions: $t_p = t_d =$ 2 min, window width = 5 °C.

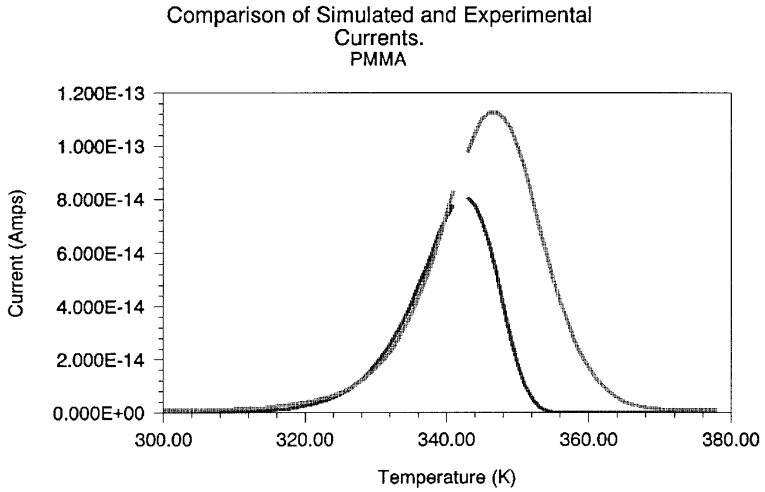


Figure 1.21: Result of a Debye curve-fit in the first half of the peak according to the modified Lacabanne rule of 62.5 %. This simulation provides the smaller of the two peaks in this figure. The other peak is the experimental TWD peak shown in Figure 1.20.

ure 1.20: Debye peaks are asymmetrical ($S_m/S_o = 62\,\%$), whereas the peak of Figure 1.20 is almost symmetrical with respect to its maximum temperature. Once we have obtained the parameters of the low-temperature Debye relaxation (P_o, τ_o, ΔH), it is possible to subtract the current due to that particular relaxation from the total current of depolarization. The remaining current should itself either be a pure Debye

EBSCOhost - printed on 2/13/2023 12:32 AM via . All use subject to https://www.ebsco.com/terms-of-use

peak or the result of another two or more peaks. The same technique of curve-fitting can be reapplied a second time to the new peak: in general, it is found that two Debye peaks describe well a 5° window relaxation, indicating that deconvolution by thermal-windowing is actually a very efficient technique. Figure 1.22 shows the two Debye relaxation peaks cooperatively making up the total current. For the second Debye peak of Figure 1.22, we find $\Delta H = 60.49\,\text{kcal/m}$, $\tau_o = 4.962 \times 10^{-37}$ sec, $P_o = 2.097 \times 10^{-12}$.

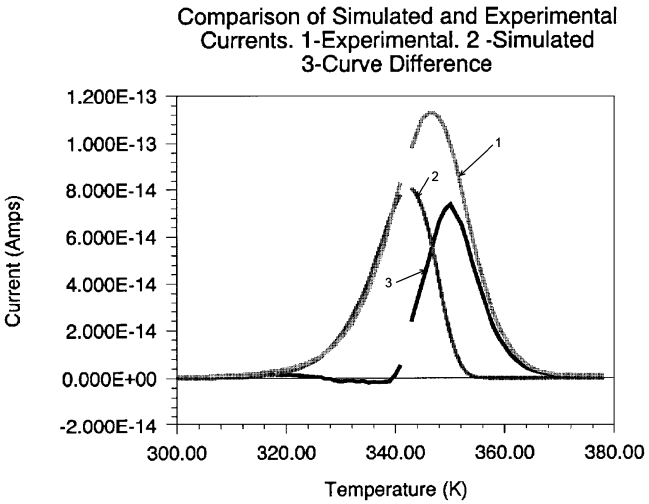


Figure 1.22: Determination of the second Debye peak by the difference between the experimental peak and the simulated peak shown in Figure 1.21.

This technique of deconvolution is easily programmable and can be performed automatically by a computer.

I.1.8 Properties of Debye peaks. Influence of peak shifting on τ_o and ΔH

A Debye peak is characterized by the values of P_{so}, s_2, ΔH, and τ_o, where P_{so} is the total polarization, s_2 the heating rate, ΔH the activation energy, and τ_o the pre-exponential constant. A Debye peak is shown at Figure 1.6. The exact formulation for the peak (equation (1.20)) does not reveal any particular property of the peak shape, which can a priori come under numerous forms. The empirical rules (Dussel–Bube approximation) which link ΔH to the half-width temperature T_1 and to the temperature of the maximum intensity T_m, and also τ_o to T_m, may come as surprisingly simple in view of the complexity of the exact formulation for the current.

EBSCOhost - printed on 2/13/2023 12:32 AM via . All use subject to https://www.ebsco.com/terms-of-use

In TSD, the main action of the voltage field seems to intensify the peaks occurring near the temperature of polarization. In thermal-windowing, the "elementary" peaks seem to vary in intensity and are shifted along the temperature axis, with T_m almost linearly related to T_p, the polarization temperature. When the peaks are analyzed, they are characterized by their values of τ_o, ΔH, and T_m.

In this section, we are interested in the relationship between τ_o, ΔH, and T_m and in particular, given a Debye peak [τ_o, ΔH, s_2, $P_{so} = 1$], whether we can fit a *shifted* peak along the temperature axis with a new set of constants [τ_o', $\Delta H'$, s_2, $P_{so} = 1$].

For this study, we simulate a Debye peak from the τ_o and ΔH values obtained from a thermal-windowing experiment conducted at constant heating rate $s_2 = 7.5\,°C/min$ (0.125 °C/s) and analyzed with Lacabanne's integration rule. For the simulation, the approximate equation by Squire is used with $\tau_o = 3.02 \times 10^{-19}$ sec and $\Delta H = 26,018.22$ cal/m. P_{so}, the total polarization of the simulated sample, is kept to 1. The peak maximum for the simulated Debye peak occurs at $T_m = 8.31\,°C$. We call this the reference state. The study consists in shifting the peak every 5° in either direction to position the maximum between –16.7° and +33.3°. The total amount of shift is 25° in both directions. For each new position of the shifted peak, a non-linear regression routine calculates the best τ_o and ΔH, starting from the approximate values provided in the empirical formulas evoked earlier. Table 1.2 provides the results of the regression. T_m is the value of the temperature chosen for the shifted maximum, $(T_m - T_{m\,ref})$ is the amount of shift from the reference state, and τ_o (sec) and ΔH (cal/m) are the Arrhenius constants; r^2 is the coefficient of non-linear regression. One sees that shifting a Debye peak to lower temperatures results in a decrease of the activation enthalpy ΔH, along with an increase of τ_o, the pre-exponential factor. Shifting in the other direction reverses the tendencies.

Table 1.2: Shifting of the curve showing $T_m = 8.308\,°C$ by ±25 °C and determination of ΔH and τ_o according to equation (1.20) for the shifted curve.

T_m	$(T_m - T_{m\,ref})$	τ_o	ΔH	r^2
−16.708	−25	2.18×10^{-17}	21527.27	0.99917
−11.705	−20	9.263×10^{-18}	22391.44	0.99935
−6.7015	−15	3.937×10^{-18}	23272.62	0.99952
−1.7	−10	1.673×10^{-18}	24170.81	0.99969
3.305	−5	7.11×10^{-19}	25086.00	0.99985
8.308	0	3.021×10^{-19}	26018.22	(ref) 0.9999959
13.31	5	1.284×10^{-19}	26967.43	0.99985
18.31	10	5.456×10^{-20}	27933.66	0.9997
23.32	15	2.319×10^{-20}	28916.90	0.99955
28.32	20	9.854×10^{-21}	29917.15	0.9995
33.32	25	4.187×10^{-21}	30934.42	0.9993

EBSCOhost - printed on 2/13/2023 12:32 AM via . All use subject to https://www.ebsco.com/terms-of-use

This is an interesting observation, because although it was predicted by the theoretical formulas, common knowledge teaches that a shift of relaxation peaks, say kinetic reactions, is produced, at constant τ_o ($\approx 10^{-13}$ sec), by a change of the enthalpy of activation only.

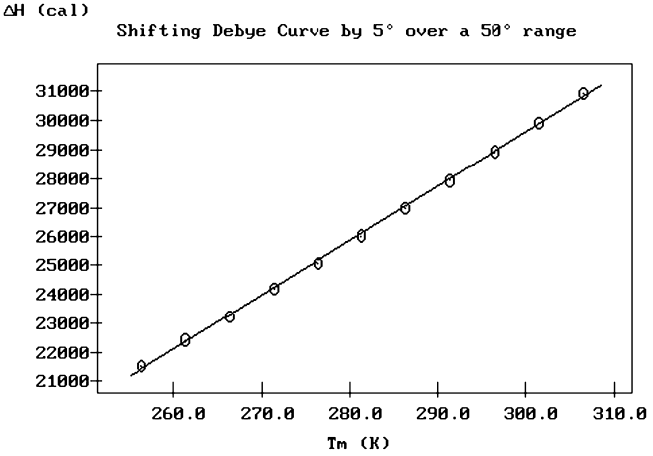


Figure 1.23: Plot of ΔH vs. T_m from Table 1.2. The reference curve ($T_m = 8.31$ °C) is shifted in steps of ±5 °C over a range of ±25 °C.

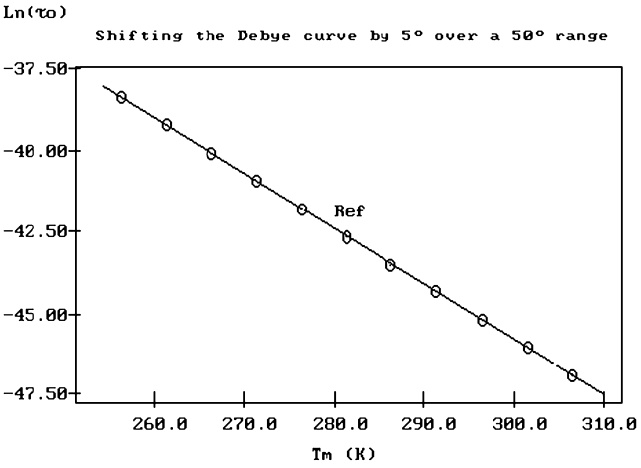


Figure 1.24: Plot of Ln τ_o vs. T_m from Table 1.2. The reference curve ($T_m = 8.31$ °C) is shifted in steps of ±5 °C over a range of ±25 °C.

Figures 1.23 and 1.24 plot ΔH and Ln τ_o against T_m for the results in Table 1.2, showing simple correlations between these variables. An exact straight line ($r^2 = 1.0000$) passes through the Ln τ_o vs. T_m data (intercept = 5.50033, slope = −0.171052). The

EBSCOhost - printed on 2/13/2023 12:32 AM via . All use subject to https://www.ebsco.com/terms-of-use

ΔH vs. T_m data are better represented by a parabolic function ($r^2 = 1.0000$), although quasi-linearity is observed in Figure 1.23 ($r^2 = 0.9994$). We have

$$\Delta H\,(\text{cal/m}) = \Delta H_{\text{ref}} + (T_m - T_{m\,\text{ref}}) \cdot A_1 + (T_m - T_{m\,\text{ref}})^2 \cdot A_2$$

where $A_1 = 188.036$, $A_2 = 0.3404$, $r^2 = 1.0000$.

Because of the quasi-linearity of the $\Delta H - T_m$ relationship, a plot of $\text{Ln}\,\tau_o$ against ΔH, a compensation plot, should be quasi-linear:

$$\text{Ln}\,\tau_o = -42.5611 - 0.9091\Delta H$$

The linearity for this plot seems excellent ($r^2 = 0.9993$) but the residuals are curved, since the function $\Delta H - T_m$ is parabolic.

A shift of the Debye peak by 1° corresponds to a shift of the Debye constants ΔH and $\text{Ln}\,\tau_o$ by 200 cal/° and −0.17/ °C, respectively.

In conclusion, when Debye peaks are shifted along the temperature axis, they can still be fitted with a Debye formula, but with a different set of ΔH and τ_o. A compensation phenomenon can be practically observed between $[\Delta H, \tau_o]$ as the peak is shifted to different temperatures.

When a compensation phenomenon is observed in a series of thermal-windowing experiments performed at various temperatures T_p, we calculate the coordinates of the compensation point from the slope and intercept of the compensation line. Here, for the shifting of the Debye peak, no particular meaning should be given to the slope and intercept of the quasi-linear compensation line. But such a study certainly helps understand experimental observations made regarding the influence of the baseline and the choice of the integration limits during the integration procedure (Part II, Chapter 1). Any factor which influences the peak characteristics and which is equivalent to the shift of the peak will result in a compensation phenomenon: this is due to the nature of the Debye peak, and no physical meaning is attached to the empirical phenomenon. For instance, the effect of polarizing at different temperatures T_p shifts the peaks on the temperature axis, in addition to a reshaping of the peak: one should expect a compensation, at least to account for the shifting part.

This raises an important issue: we observe compensations in the study of the relaxation by the method of thermal-windowing; but the effect of polarizing at different temperatures is to shift the peaks, among other things, and we know that shifting results in a compensation phenomenon for $(\Delta H, \tau_o)$: should we introduce a correction procedure to "subtract out" the shifting effect from the experimental values of $(\Delta H, \tau_o)$? In other words, should we *normalize* the curves to a new variable $(T - T_m)$ or $(T - T_p)$?

EBSCOhost - printed on 2/13/2023 12:32 AM via . All use subject to https://www.ebsco.com/terms-of-use

Let us illustrate this point with an example. Table 1.3 presents values of T_p (°C), ΔH (cal/m), $\mathrm{Ln}\,\tau_o$, and $T_{m,D}$ (°C) corresponding to Arrhenius constants isolated for thermal-window relaxations isolated at T_p, the polarization temperature. The material is polytetramethylglycol (PTMG 2000; $M_n = 2035$), a low-molecular-weight polymer which will be studied in depth in Chapter 2 of Part I. This semi-crystalline polymer has two major transition temperatures observed in a TSD scan: a glass transition temperature T_g and a pre-melting transition temperature T_α. The data of Table 1.3 refer to the Debye peaks isolated for the T_g transition by varying the polarization temperature between −105 °C and −70 °C. The table provides $T_{m,D}$, the Debye peak maximum for the fitting Debye function [τ_o, ΔH, $s_2 = 0.125$ °C/s, $P_{so} = 1$]. $T_{m,D}$ is slightly different from T_m, the temperature for the thermal-window peak maximum.

Table 1.3: Relaxation map results for PTMG 2000 obtained by TWD. The table displays the values of ΔH, $\mathrm{Ln}\,\tau_o$, and $T_{m,D}$ at the maximum of the Debye peak for each polarization temperature T_p.

T_p (°C)	ΔH (cal/m)	$\mathrm{Ln}(\tau_o)$	$T_{m,D}$ (°C) (Debye)
−105.0	11960.00	−30.68863	−98.20
−100.0	12420.00	−31.04227	−93.40
−90.0	14720.00	−34.98506	−81.60
−85.0	19550.00	−46.80672	−77.40
−80.0	21390.00	−50.39451	−73.00
−75.0	22310.00	−52.77714	−73.20
−70.0	27830.00	−65.22741	−68.35

Figure 1.25, which also includes the data for the T_α transition, plots T_m against T_p over a 100 °C span, encompassing two relaxation processes. A straight line of slope 1 is drawn in the figure, which adequately passes through the data (the intercept is 7.1 °C). The polarization stage seems to "create" the peaks observed on depolarization, so much so that Figure 1.25 does not detect any difference between the T_g and the T_α process. This will be discussed in the next chapter (Part I, Chapter 2). The change of ($\mathrm{Ln}\,\tau_o$) and ΔH due to a shift of the peaks along the temperature axis brings another concern about the influence of the depolarization stage on the compensation temperature value: this matter is explored in Chapter 3 of this volume. As will be shown in the next section, depolarization at T_d for t_d relaxes the shorter relaxation times, displacing the peaks toward the higher temperature end. Aging studies below T_g will confirm it (Part II, Chapter 3): the elimination of the low-temperature Debye peaks shifts the temperature of compensation T_c way out. We can even use that observation to characterize aging.

EBSCOhost - printed on 2/13/2023 12:32 AM via . All use subject to https://www.ebsco.com/terms-of-use

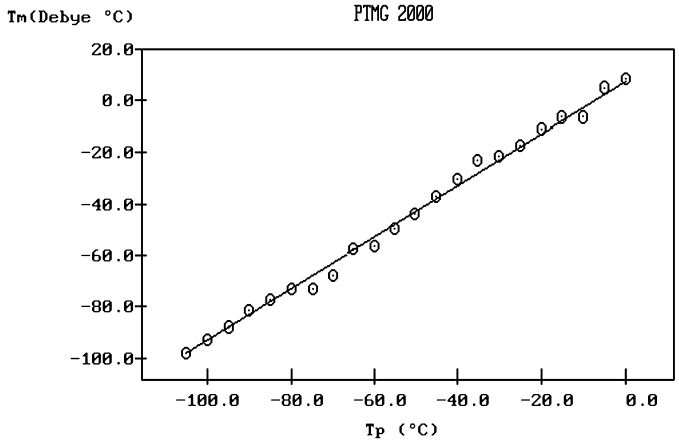


Figure 1.25: Variation of $T_{m,D}$ with T_p for the results of Table 1.3.

The depolarization at T_d below T_p – and its influence on the peak shift on the temperature scale – might also be the reason why T_m of the simulated Debye Peak versus T_p is off by 7 °C in Figure 1.25 (although the slope is correctly 1.0). The data analyzed in this figure correspond to a window width of 10 °C, and it would be interesting to verify the effect of a smaller or a zero window width on the temperature offset between $(T_c - T_g)$ on the one hand and the $T_{m,D}$ vs. T_p curve on the other hand.

We study in Table 1.4 the effect of shifting to the same temperature $T_{m,D}$ Debye peaks obtained by thermal-windowing and reconstructed by simulation. Three values of $T_{m,D}$ are selected: –98.2 °C, –68.25 °C, and –41 °C.

The operation of shifting the current–temperature curves to a given temperature is a sort of normalization of the curves to compare them: all the $T_{m,D}$ values become the same after shifting, only the shape changes. The data of Table 1.4 have the same meaning as those of Table 1.3. The same non-linear regression routine is used to curve-fit the shifted peaks to the Debye equation and extract the value of τ_o and ΔH ($P_{so} = 1$, $s_2 = 0.125$ °C/s). Plots of $\mathrm{Ln}\,\tau_o$ vs. ΔH for the three normalization temperatures are displayed in Figure 1.26.

One sees that at first approximation, these compensation plots are linear. This is expected from the formula linking τ_o, ΔH, and T_m.

Hence,

$$\tau_o = \frac{\exp(-\frac{\Delta H}{RT_m})}{s_2(\frac{\Delta H}{RT_m^2})}$$

$$\mathrm{Ln}\,\tau_o = -\frac{\Delta H}{RT_m} - \left(\mathrm{Ln}\,s_2 + \mathrm{Ln}\,\frac{\Delta H}{RT_m^2}\right)$$

EBSCOhost - printed on 2/13/2023 12:32 AM via . All use subject to https://www.ebsco.com/terms-of-use

Table 1.4: Curve-fitting values of ΔH and τ_o in equation (1.20) after shifting the experimental Debye curves obtained by TWD at different T_p values (–105 °C to –70 °C) so that their $T_{m,D}$ after shifting is the same for each T_p. (1) Shifting to $T_{m,D} = -98.2$ °C. (2) Shifting to $T_{m,D} = -68.25$ °C. (3) Shifting to $T_{m,D} = -41.0$ °C.

(1)

T_p (°C)	ΔH (cal/m)	τ_o (sec.)	T_m (°C)	r^2
–105	11959.997	4.700×10^{-14}	–98.1497	0.9999997
–100	11750.683	8.719×10^{-14}	–98.158	0.99979
–90	12230.885	2.102×10^{-14}	–98.1661	0.99931
–85	15556.643	1.164×10^{-18}	–98.147440	0.99929
–80	16270.578	1.398×10^{-19}	–98.225162	0.999237
–75	17010.525	1.642×10^{-20}	–98.1172	0.9992282
–70	20235.014	1.261×10^{-24}	–98.2027	0.9992969

(2)

T_p (°C)	ΔH (cal/m)	τ_o (sec.)	T_m (°C)	r^2
–105	16492.46	1.018×10^{-16}	–68.324	0.9987
–100	16205.83	2.092×10^{-16}	–68.33	0.9989
–90	16854.87	4.067×10^{-17}	–68.35	0.99929
–85	21389.63	4.636×10^{-22}	–68.35	0.99930
–80	22399.98	3.635×10^{-23}	–68.41	0.99922
–75	23409.61	2.999×10^{-24}	–68.304	0.99988
–70	27830.02	4.7×10^{-29}	–68.39	0.99987

(3)

T_p (°C)	ΔH (cal/m)	τ_o (sec.)	T_m (°C)	r^2
–105	21249.10	3.827×10^{-19}	–41.18	0.998
–100	20909.06	8.375×10^{-19}	–41.04	0.998
–90	21725.49	1.326×10^{-19}	–41.20	0.9986
–85	27567.72	3.269×10^{-25}	–41.23	0.99905
–80	28828.13	1.984×10^{-26}	–41.28	0.99926
–75	30119.43	1.188×10^{-27}	–41.17	0.99924
–70	35791.90	4.38×10^{-33}	–41.26	0.9995

When ΔH varies by approximately 10 kcal/m, the first term of $(\mathrm{Ln}\,\tau_o)$ vs. $\Delta H/T_{m,D}$ takes up more than 99 % of the total variation. The second term (in parenthesis) is almost constant in comparison, which explains the reason for the appearance of a compensation line when T_p varies (in reality the compensation is only a mathematical approximation). Figure 1.26 shows three $T_{m,D}$ values, thus we observe three compensation lines. The slope of these three lines is approximately equal to $(-1/RT_{m,D})$, where $T_{m,D}$ is the normalization temperature in Kelvin. The slope of a compensation line is also equal to $-1/T_c$ where T_c is the temperature of compensation; hence $T_c = T_{m,D}$. One sees in Figure 1.26 that the three compensation lines appear themselves to merge into a single "super-compensation" point as $T_{m,D}$ varies. The coordinates of this super-

EBSCOhost - printed on 2/13/2023 12:32 AM via . All use subject to https://www.ebsco.com/terms-of-use

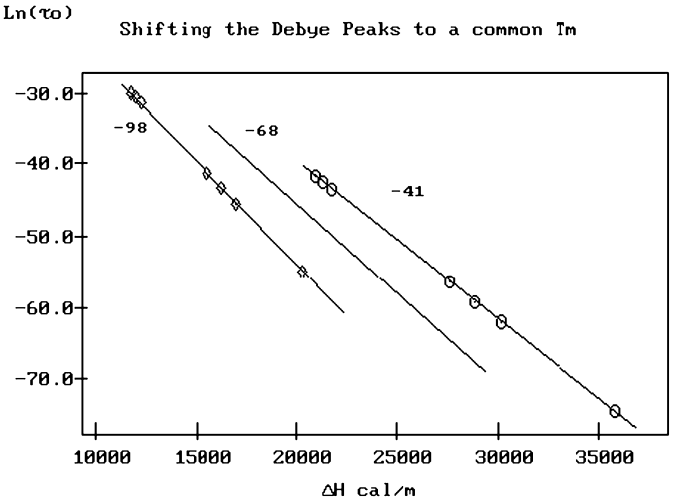


Figure 1.26: Plots of Ln τ_o (T_p) vs. ΔH (T_p) after shifting to −98.2 °C, −68.25 °C, and −41 °C, respectively. The graph shows three compensation lines.

compensation are off the chart but can be determined by plotting their intercept vs. their slope for the three $T_{m,D}$ values. Again, this super-compensation is only an approximation of the equation giving Ln τ_o against ΔH. Yet, the super-compensation provides reference values of ΔH and Ln τ_o that are independent of the choice of T_p or $T_{m,D}$. We will return to the consequences of Figure 1.26 to understand interactive coupling in Chapter 3 of this Part I. The important observation here is that one can choose the value of the temperature of compensation at will by normalizing at that temperature ($T_c = T_{m,D}$ = the temperature of the maximum chosen for the shifting). The difference between the shifted Debye peaks compared at $T_{m,D}$ can solely be expressed by their ΔH value. The compensation phenomenon is implicitly included in the use of the Debye equation to describe the relaxation peaks. What value of $T_{m,D}$, i. e., T_c, should we choose? When the glass transition temperature is under investigation, $T_{m,D} = T_g$ seems an interesting choice. For the polymer of Figure 1.26 (PTMG 2000), $T_g = -82.2$ °C. The results are shown in Table 1.5. ΔH varies between 14,295 ($T_p = -105$ °C) and 24,149 ($T_p = -70$ °C) on this compensation line. The corresponding τ_o values are found between 1.7×10^{-5} and 5.37×10^{-37}. These data should be compared with the original, unshifted data of Table 1.3, for which ΔH varies between 11,960 cal ($T_p = -105$ °C) and 27,830 cal/m ($T_p = -70$ °C). **The scale is therefore a function of the normalization temperature chosen.**

The problem with the idea of normalization at constant temperature $T_{m,D}$ is that it ignores entirely the possible physical meaning of a compensation between values obtained at different T_ps values. Hence, it does *not* seem to adequately solve our problem of separating the influence of the polarization temperature on the peak shape and position. This problem will be solved in the next chapter, Chapter 3.

EBSCOhost - printed on 2/13/2023 12:32 AM via . All use subject to https://www.ebsco.com/terms-of-use

Table 1.5: The same variables as in Table 1.4. Shifting to $T_{m,D} = -82.20\,°C = T_g$ for PTMG 2000.

T_p (°C)	ΔH (cal/m)	τ_o (sec.)	T_m (°C)	r^2
−105	14295.52	1.763×10^{-15}	−82.185	0.999268
−100	14046.335	3.454×10^{-15}	−82.193	0.99948
−90	14618.197	7.338×10^{-16}	−82.20	0.99997
−85	18578.109	1.700×10^{-20}	−82.20	0.99985
−80	19429.61	1.686×10^{-21}	−82.267	0.99974
−75	20308.742	1.639×10^{-22}	−82.16	0.99974
−70	24149.87	5.375×10^{-27}	−82.24	0.99963

Another possible way to separate out the shifting effect from the compensation results is to shift each elementary Debye peak extracted from thermal-windowing by a certain amount to position it either at exactly T_p or at a temperature between T_p and T_d, for example $(T_p + T_d)/2$.

The results are presented in Table 1.6.

Table 1.6: Effects of shifting the elementary Debye peaks by a certain amount to position its $T_{m,D}$ either at T_p or at $(T_p + T_d)/2$.

T_p (°C)	Initial $T_{m,D}$ (°C)	$(T_m - T_p)$ (°C)	$(T_{m,D} - (T_p + T_d)/2)$ (°C)	ΔH (cal/m)	τ_o (s)	$T_{m,D}$ Corrected (°C)
−105	−98.20	6.8	11.8	10366.16	5.333×10^{-13}	−109.962
−100	−93.40	6.6	11.6	10834.226	3.453×10^{-13}	−104.965
−90	−81.60	8.4	13.4	12692.784	1.072×10^{-14}	−94.963
−85	−77.40	7.6	12.6	17076.521	1.325×10^{-14}	−89.94
−80	−73.00	7.0	12.0	18864.96	3.611×10^{-21}	−85.02
−75	−73.20	1.8	6.8	20797.51	8.555×10^{-23}	−79.91
−70	−68.35	1.65	6.65	26030.44	4.575×10^{-23}	−75.04

Figure 1.27a is a plot of ΔH against T_p after the correction by $(T_m - (T_p + T_d)/2)$. A single hyperbolic function can be drawn to pass through the data, although two hyperbolas might fit the lower-temperature and higher-temperature ends better.

This is better seen in Figure 1.27b, where $(\Delta H - \Delta H_r)$ and $(\mathrm{Ln}(\tau_o/\tau_{or})$ are plotted against T_p (ΔH_r and τ_{or} refer to the unshifted data [Table 1.3]). An extremum (maximum for $\mathrm{Ln}(\tau_o/\tau_{or})$, minimum for $(\Delta H - \Delta H_r)$) is observed at $T_p = T_g \approx -82\,°C$. This is the type of response we would expect to see for the "correction factor," which should be larger when the polarization temperature matches the temperature of maximum internal motion.

EBSCOhost - printed on 2/13/2023 12:32 AM via . All use subject to https://www.ebsco.com/terms-of-use

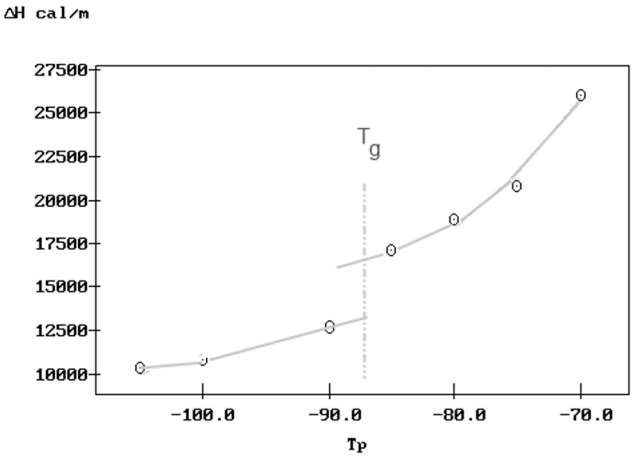


Figure 1.27a: Plot of ΔH against T_p after shifting the experimental Debye curves obtained at various T_p values by $(T_m-(T_p+T_d)/2)$. The shifted data show the T_g shifted down by −5 °C, i.e. by $-(T_p+T_d)/2$. The values are extracted from Table 1.6.

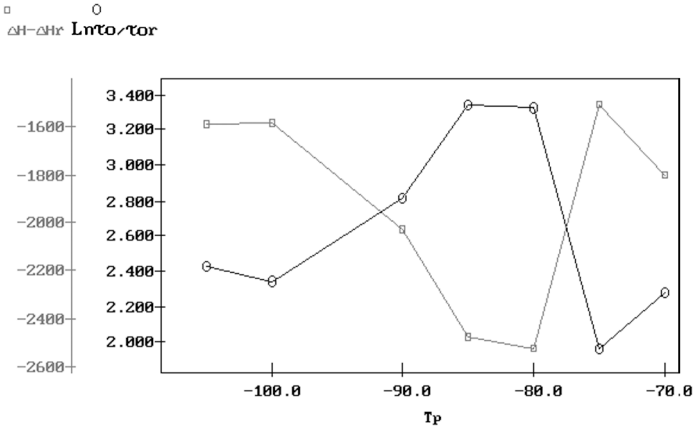


Figure 1.27b: Plots of $(\Delta H - \Delta H_r)$ and $(\mathrm{Ln}(\tau_o/\tau_{or})$ against T_p, where ΔH_r and τ_{or} refer to the unshifted data (from Table 1.3). The values of ΔH and $\mathrm{Ln}(\tau_o)$ are taken from Table 1.6.

The compensation plot $\mathrm{Ln}\,\tau_o$ vs. ΔH (not shown) is also linear for the shifted data of Table 1.6, and the compensation point coordinates are different from the unshifted data (Table 1.3). We have

$$T_c = -45.15\,°\mathrm{C}$$
$$\mathrm{Ln}\,\tau_c = -3.51 \quad \text{(uncorrected data)}$$
$$T_c = -49.11\,°\mathrm{C}$$
$$\mathrm{Ln}\,\tau_c = -4.48 \quad \text{(corrected by } (T_m - (T_p + T_d)/2)\text{)}$$

EBSCOhost - printed on 2/13/2023 12:32 AM via . All use subject to https://www.ebsco.com/terms-of-use

The temperature of compensation is closer to T_g for the corrected data, which raises the following question: what is the temperature of correction for which $T_c = T_g$? Could the correction method illustrated above provide an understanding of the difference $(T_c - T_g)$?

It becomes clear that a fundamental understanding of TWD and of the compensation phenomena requires a grasp on how to separate out the effect of the polarization T_p on the Debye peak shape (width and height) and the peak position $(T_{m,D})$. This discussion is the full focus of Chapter 3 in this volume. In the next chapter (Part I, Chapter 2), we also present an alternative way to normalize the relaxation data by using the activation free energy instead of ΔH and $\mathrm{Ln}(\tau_o)$.

I.1.9 Influence of the thermal-windowing experimental parameters on the characteristics of the depolarization peak

We study in this section the effect of the several parameters which can be selected at the initiation of a thermal-windowing experiment and which contribute to the success of the deconvolution process.

The parameters have been defined before (Figure 1.4):

- polarization voltage,
- polarization time t_p,
- depolarization time t_d,
- window width $(T_p - T_d)$,
- temperature of polarization T_p.

I.1.9.1 Polarization voltage

According to equation (1.2), the current of depolarization for a single relaxation mode is proportional to the field intensity E. The field is equal to the polarization voltage divided by the sample thickness. In Figure 1.28, we display the curves obtained by thermal-windowing a sample of PMMA under various voltage conditions during the polarization stage. The other parameters of thermal-windowing are the same: $t_d = t_p =$ 2 min, $T_p = 79$ °C, window width = 5 °C. The sample thickness is rather thick, 2 mm, but PMMA is a good dielectric and the current intensity ($\approx 10^{-13}$ A) is still considered rather large for a thermally windowed peak.

This excellent sensitivity of PMMA makes it an ideal material to analyze the effect of the thermal-windowing parameters. It also explains why PMMA is used as a standard for TWD calibration purposes. The voltage is increased in Figure 1.28 from 0 to 250 V, resulting in an increase of the intensity of the peak, as also displayed in Figure 1.29. In Figure 1.29, the current intensity at the peak maximum for each curve of Figure 1.28 is plotted against a variable which is proportional to the voltage field.

EBSCOhost - printed on 2/13/2023 12:32 AM via . All use subject to https://www.ebsco.com/terms-of-use

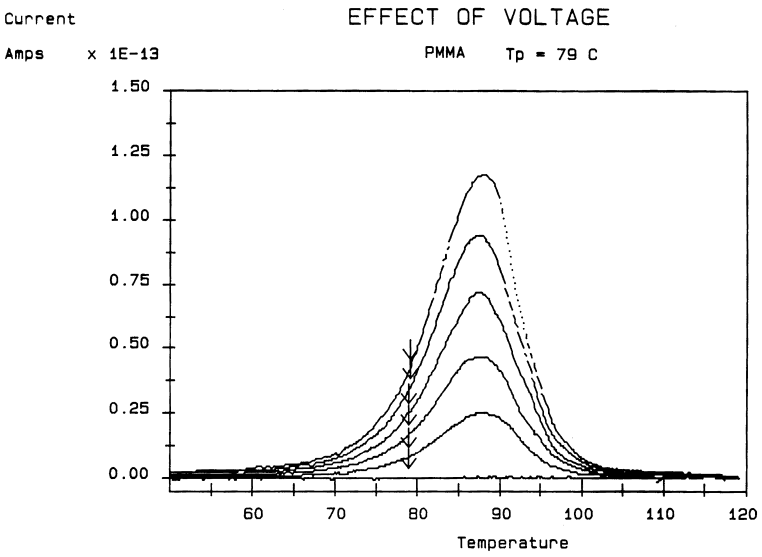


Figure 1.28: Effect of the polarization voltage on the TWD output for PMMA. The same TWD conditions apply to all curves, except for the voltage magnitude during the polarization stage. The voltage is increased from 0 to 250 V.

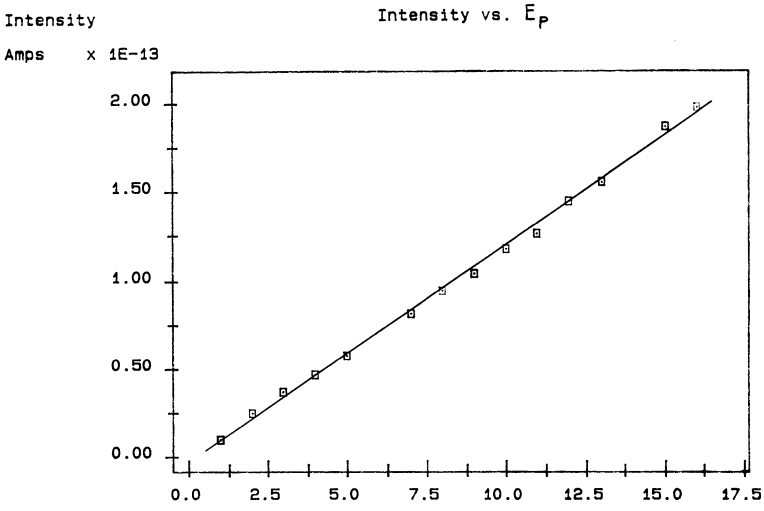


Figure 1.29: Variation of the peak intensity at the maximum of the Debye peaks in Figure 1.28 plotted versus a variable proportional to the voltage field.

EBSCOhost - printed on 2/13/2023 12:32 AM via . All use subject to https://www.ebsco.com/terms-of-use

A linear correlation seems to fit the data adequately, verifying the predictions of equation (1.22) or equation (1.25): the effect of increasing the voltage is a proportional increase of the intensity of the peak. Notice in Figure 1.28 that if we do not polarize ($V_p = 0$), there is no current of depolarization. This "baseline" test should be performed in order to determine the source of depolarization, in particular to rule out the presence of static charges or space charges which can add up to the voltage-induced depolarization current (the baseline might even be negative in some instances, as explained at the beginning of this chapter). The slope of the line in Figure 1.29 is related to the square of the dipole moment of the polarized dipoles, according to equation (1.4). Care should be exercised, however, to determine whether the peak maximum of the "elementary" thermal-window peak is really representative of a Debye relaxation or if it is made up of two or more Debye peaks (Figure 1.22).

I.1.9.2 Effect of polarization time t_p

For each elementary relaxation mode susceptible to polarization, the contribution of the time of polarization t_p to the current of depolarization comes from the term x in equations (1.22) and (1.23). According to these equations, an increase in t_p will increase the number of dipoles of type i (ΔH_i, τ_{oi}), i. e., $P_{si}(T_o)$ of equation (1.20). For a distribution of relaxation times, the longer the polarization stage, the higher the number of dipoles of all kinds that become activated, especially those with longer relaxation times and higher activation energies ΔH_i. The effect of increasing the polarization time t_p should therefore result in a broadening of the peak, especially towards the higher temperature tail, and an overall increase of the current activity during depolarization stemming from two sources:

1) each relaxation mode sees its activity increased,
2) the number of relaxation modes polarized increases.

The experimental results shown in Figure 1.30 confirm qualitatively these predictions. The polarization temperature is $T_p = 80$ °C, $t_d = 2$ min, window = 5 °C, and t_p varies between 12 seconds (smallest peak in the figure) and 2 min. By looking at the peak maximum position, it is possible to qualitatively say that up to the first half minute, the effect of increasing t_p is to "strengthen" the existing peak(s), but that beyond that time, another relaxation has entered the scene, shifting the peak maximum to the right. Of course, only a quantitative analysis could tell whether the initial peak for $t_p = 12$ sec is present in the peaks obtained for longer t_p, with a greater P_{so} value, and if the peak at 1 min and beyond includes a new term. The method of analysis presented in the preceding section is appropriate for such an investigation.

EBSCOhost - printed on 2/13/2023 12:32 AM via . All use subject to https://www.ebsco.com/terms-of-use

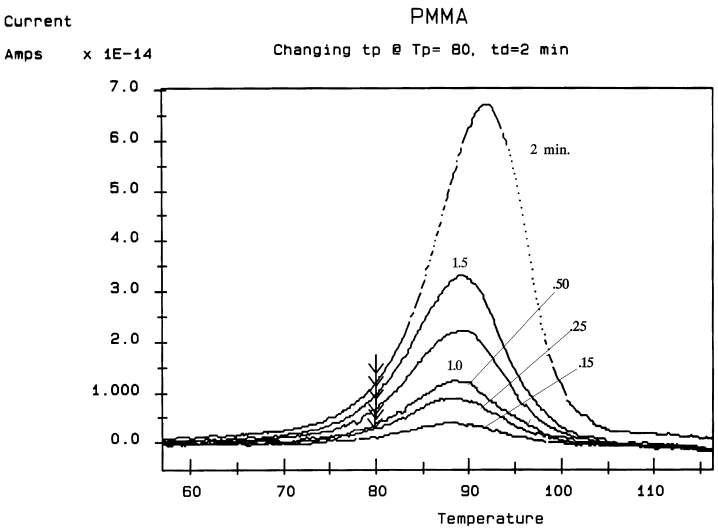


Figure 1.30: Effect of the time of polarization t_p on the TWD output for PMMA. The time of polarization is shown near the corresponding depolarization curve, varying between 12 sec and 2 min.

I.1.9.3 Effect of the time of depolarization t_d

The understanding of the quantitative effect of t_d is very similar to what was just mentioned for t_p but reversed: the number of dipoles which depolarize is directly a function of t_d in the variable y of equations (1.24) and (1.22). Increasing the time of depolarization t_d (or raising the temperature of depolarization T_d) affects the shortest relaxation times first, to the low-temperature tail of the peak, and decreases the overall current intensity by disactivating the dipoles which depolarize during the thermally stimulated stage. Figures 1.31 to 1.33 illustrate these predictions well. In Figure 1.31, the polarization temperature is 85 °C, T_d = 80 °C (window = 5 °C), t_p = 2 min, and t_d varies between 0 to 10 minutes, resulting in smaller and smaller peaks shifted to the right. Notice that the higher-temperature tail of the peak is the same for all relaxations, independently of t_d: the higher ΔH_i relaxation term, activated by the polarization condition, T_p, t_p, is the last to vanish, as t_d increases.

Figures 1.32 and 1.33 present results of zero-width thermal-windowing experiments, polarized at two different temperatures T_p = 85 °C (Figure 1.32) and T_p = 80 °C (Figure 1.33). For these settings, $T_d = T_p$, t_p = 2 min, and t_d varies between 0 and 32 minutes. It is interesting to report that although the polarization time is only 2 minutes, it takes more than half an hour to entirely depolarize the specimen! This observation indicates that the kinetics are not as simple as it may seen with the notion of a spectrum of relaxation times. It is as if the shorter relaxation times auto-catalyze the activation of longer relaxation times, as already reported by Kovacs on volumetric measurements [148, 149]. The theoretical importance of this observation is discussed

EBSCOhost - printed on 2/13/2023 12:32 AM via . All use subject to https://www.ebsco.com/terms-of-use

in the conclusions, to examine the nature of the "relaxation modes," whether the relaxation process is the result of a spectrum of molecular *motions* or a phenomenon of structuration of the free energy. The conclusions of Chapter 3 Part I discuss the differences of interpretation of the Thermal-Windowing Deconvolution results by the traditional approach and the Dual-Phase approach.

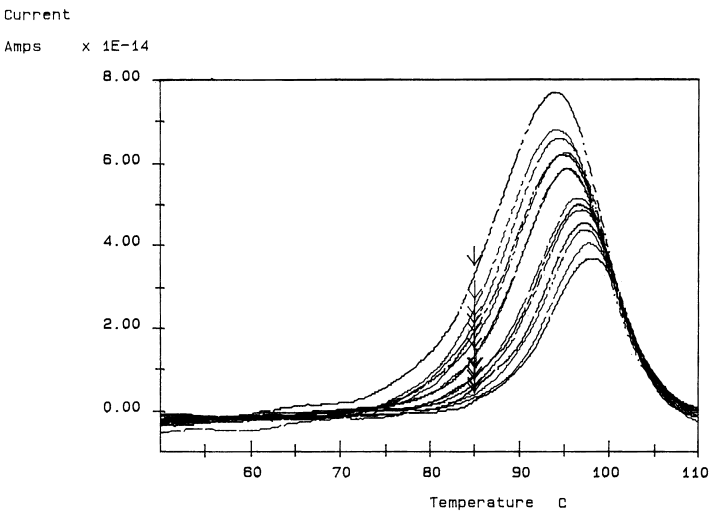


Figure 1.31: Effect of the time of depolarization t_d on the TWD output for PMMA. The time of depolarization varies between 0 and 10 min. All the other parameters of TWD are the same. The peak decreases in intensity and its lower tail "melts out" as the depolarization time increases.

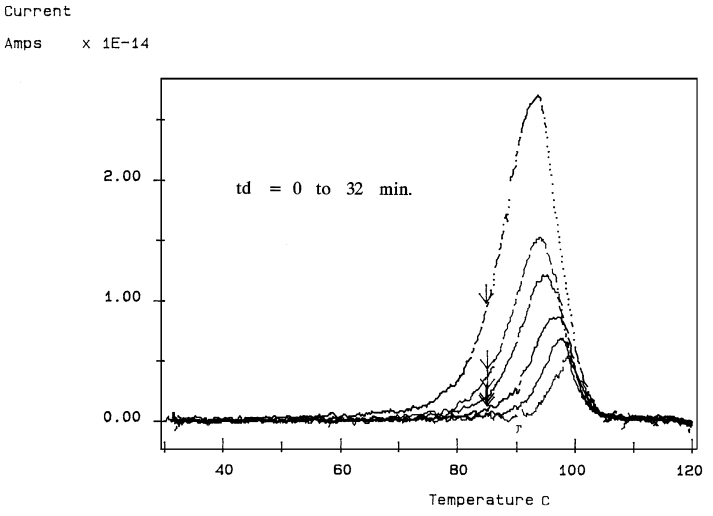


Figure 1.32: Effect of polarizing and depolarizing at the same temperature, $T_p = T_d = 85$ °C, on the TWD output. $t_p = 2$ min; t_d varies between 0 and 32 min. Compare with Figure 1.33.

EBSCOhost - printed on 2/13/2023 12:32 AM via . All use subject to https://www.ebsco.com/terms-of-use

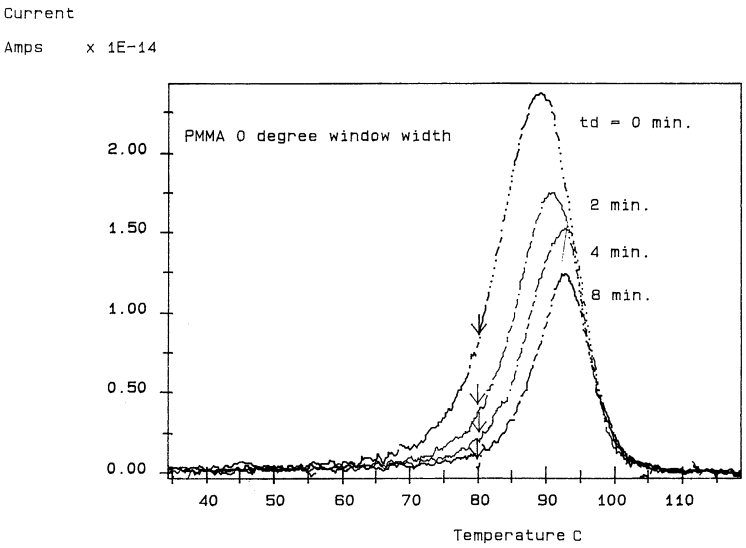


Figure 1.33: Effect of polarizing and depolarizing at the same temperature, $T_p = T_d = 80\,°C$, on the TWD output. $t_p = 2$ min; t_d varies between 0 and 8 min (indicated near each depolarization curve). Compare with Figure 1.2.

As t_d increases in Figures 1.32 and 1.33, the shape of the peak becomes more and more asymmetrical, with a Debye ratio changing from 57 % to 62.5 % after a few minutes, a sign that a true Debye relaxation has been isolated after vanishing the shorter relaxation component.

I.1.9.4 Effects of the polarization temperature T_p and the window width

T_p is the variable which is consistently varied during a probing of a transition structure by thermal-windowing. The experiment most commonly consists of choosing a voltage capable of producing a depolarization current between 10^{-15} and 5×10^{-14} Amp for a window width of 2° to 5 °C, $t_p = t_d = 2$ min. The polarization temperature T_p is then varied, say every 5 °C, in a temperature range across the transition observed in a preliminary TSD run. The influence of the temperature of polarization is quantified by its influence on $a(T_p)$ in equations (1.23) and (1.22). Increasing the temperature below the transition increases the number of dipoles which are oriented and also increases their orientation. Passed the transition, the depolarization takes place rapidly when the voltage is removed at T_d and the overall polarization left in the specimen decreases sharply.

The resolution of the several “elementary” relaxation modes by just varying the temperature T_p, keeping all the other variables constant, has become a familiar and routine method of analysis which can be conveniently performed by an automated

EBSCOhost - printed on 2/13/2023 12:32 AM via . All use subject to https://www.ebsco.com/terms-of-use

instrument. Figure 1.34 compares the peak obtained by thermal-windowing at T_p = 80 °C, T_d = 70 °C (10 °C window width) and T_p = 80 °C, T_d = 78 °C (2 °C window width). The smaller peak, corresponding to $(T_p - T_d) = 2$, has a lower amplitude and is positioned to the left of the temperature scale, i. e., at lower temperatures. It can be fitted by a Debye elementary peak. The larger peak, for $(T_p - T_d) = 10$, has frozen in additional short τ_o relaxation modes (at least one more) since T_d is lower: this makes the peak look less "elementary," much more prominent. This illustrates our point made in Part II, Chapter 1, that global techniques such as TSD, DEA, or DMA which deal with *convoluted peaks* should use caution when analyzing their data with the peak maximum temperature and its frequency dependence. Peaks are the results of interactive coupling, and the effect of increasing the rate of the measurement (thermal heating rate, or frequency for a mechanical deformation) for such peaks is to *broaden the convolution* of the elementary peaks, the opposite of the deconvolution process that we want to achieve to study interactive coupling.

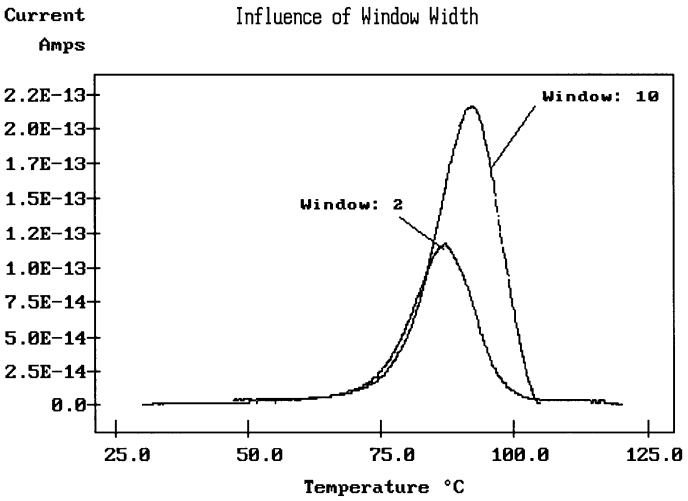


Figure 1.34: Effect of the window width of a TWD experiment on the depolarization curve. Compare the curves obtained with T_p = 80 °C, T_d = 70 °C (window width = 10 °C) and T_p = 80 °C, T_d = 78 °C (window width = 2 °C).

Figure 1.34 is interesting because it shows how "constraining" it is to deconvolute true elementary Debye peaks. Not only does it need a technique such as TSD, with its very low frequency equivalent (~ 10^{-3} Hz) that favors the separation of the peaks, but TSD also needs to operate under the TWD mode with a narrow window width.

Reducing the window width to optimize the determination of the elementary Debye peaks lengthens the overall time needed to complete a full relaxation map. In Part II of this book, TSD and TWD are devoted to the characterization of polymer sam-

EBSCOhost - printed on 2/13/2023 12:32 AM via . All use subject to https://www.ebsco.com/terms-of-use

ples, often by comparing a reference sample and another one presenting a different characteristic. The window width can then be adjusted to compromise the accuracy of the deconvolution with the running time of the relaxation maps.

However, to explore the gears of "interactive coupling" in the amorphous phase of pure amorphous polymers, or semi-crystalline polymers, or compatible vs. segregated blends of polymers and copolymers, we need the highest resolution of the Debye peaks as possible in order to determine the characteristics of the compensation lines that establish the arching bridge between the macroscopic world (the depolarizing current) and the atomic-electronic world: the inter-intra molecular bond potential energy. In Chapter 3 we discuss what "interactive coupling" means in terms of our Dual-Phase and Cross-Dual-Phase models of the interactions between conformers.

Figure 1.35 will quickly become to the reader the familiar face of a TWD transition peak deconvoluted into its several "relaxation modes" by operating at different T_p (notified by the arrow), with the window width $(T_p - T_d)$ constant and adjusted to fit the objective sought, either a fundamental research objective (Part I, Chapters 2 and 3) or an application characterization objective (Part II, Chapters 3 and 4).

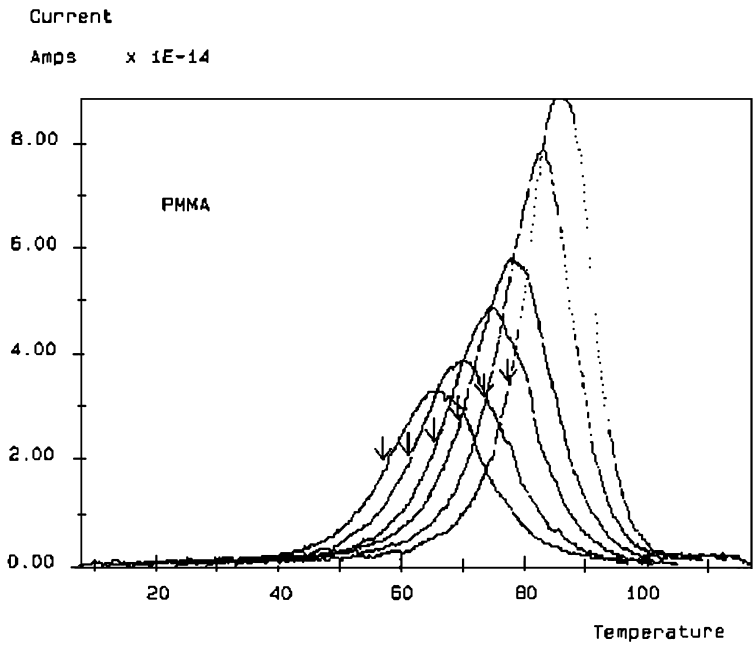


Figure 1.35: Familiar response of a Thermal-Windowing Deconvolution output for PMMA using standard parameters for T_d, t_p, t_d, and the window width (5 °C) and variable T_ps values, indicated by the arrows.

EBSCOhost - printed on 2/13/2023 12:32 AM via . All use subject to https://www.ebsco.com/terms-of-use

I.1.10 Acknowledgment

Several sections of this chapter are adapted from the thesis of Dr. D. Ronarc'h [215] and thus, indirectly, from the treatment of van Turnhout [238].

EBSCOhost - printed on 2/13/2023 12:32 AM via . All use subject to https://www.ebsco.com/terms-of-use

Part I Chapter 2
Thermal-Windowing Deconvolution, relaxation map analysis, and compensation phenomena to determine the amorphous state of polymers

I.2.1 Introduction

We try to learn in this chapter how Thermal-Windowing Deconvolution (TWD), relaxation map analysis, and compensation phenomena can be used to characterize the amorphous state of matter in a manner fundamentally different from the other traditional thermal analysis instruments.

In the previous chapters, we have introduced the relaxation map of a material as the "fingerprint" of its state. A relaxation map is obtained by TWD and consists of a spectrum of relaxation lines defined as $\mathrm{Log}\,\tau$ (relaxation time) versus Arrhenius temperature $(1000/T)$, obtained by polarizing at various temperatures T_p prior to the depolarization stage.

On both sides of the T_g of polymers, the individual Arrhenius spectral lines converge into a common point, a "compensation point." The coordinates of the compensation point are dependent on the actual state of the glass or the melt and vary with the amount of orientation or internal stress present and with the presence of diluents, plasticizer, and compatibilizers. It is also influenced by the neighboring presence of coexisting morphological structures, such as crystals, crosslinks, and segregated particles. In this chapter, we first study the thermally stimulated current characteristics of two classical polymers, PMMA and polystyrene (PS), and demonstrate the power of analysis provided by the TSD/TWD spectrometer when thermal-windowing is used. In particular, we replot the experimental results as the variation of the free energy of activation versus temperature for each polarization temperature T_p and calculate the values of the free energy, enthalpy, and entropy of activation at the value of the polarization temperature. Plots of the thermokinetic variables against T_p, when T_p varies, show characteristic results of the relaxation map: T_g is characterized by a maximum of the entropy of activation (and also of the enthalpy) and by the intercept of two compensation lines, one positive one negative, as T_g is crossed, resulting in a "Z-structure" for the relaxation lines. We show how the Z-structure and the Z-line, which it defines, relate to the corresponding positive and negative compensation lines. We also normalize the free energy map to reveal the distinct types of coupling between the dipoles below and above T_g. Normalization permits to understand quantitatively the several thermokinetic features of the depolarization process, such as the maximum of entropy at T_g, or why the free energy at T_p seems to be proportional to T_p, even sometimes across T_g. We discuss briefly the possible reasons which make coupling different below and above T_g and present quantitative equations to find the transitions T_β and T_{LL} from the variation of the entropy with T_p.

https://doi.org/10.1515/9783110756746-003

EBSCOhost - printed on 2/13/2023 12:32 AM via . All use subject to https://www.ebsco.com/terms-of-use

Finally, we analyze in this chapter the amorphous phase in semi-crystalline polymers and apply the analytical tools developed earlier to demonstrate the power of characterization of the technique in characterizing the two amorphous components of the structure for dipoles coupling inside spherulitic structures and in the interspherulitic interface.

I.2.2 Arrhenius transform. Relaxation map. Thermal-Windowing Deconvolution

The analysis of each resolved Debye peak obtained at a given polarization temperature gives a temperature-dependent relaxation time $\tau_i(T)$ which can be fitted to an Arrhenius equation:

$$\tau_i(T) = \tau_{oi} \cdot \exp(\Delta H/kT) \tag{2.1}$$

where τ_{oi} is the pre-exponential factor, ΔH is the activation enthalpy, and k is the Boltzmann constant.

It should be noted that the procedure of transforming the current vs. temperature data into its "Arrhenius transform," Log τ vs. $1000/T$, is applicable whether the fit is actually linear or not. It is also applicable to other types of thermal-window recovery processes: for instance, Lacabanne and collaborators [24] pioneered its use in the study of thermally stimulated strain recovery measurements (the ratio of strain to strain rate becomes the relaxation time). The result of an Arrhenius transform for the depolarization recovery of PMMA is shown in Figure 2.1.

In summary, each elementary relaxation curve (depolarization current vs. T of Figure 2.2) can be mathematically transformed into its Arrhenius representation, Log τ versus $1/T$, which expresses the variation of relaxation time with temperature for that particular isolated relaxation mode (Figure 2.1). A relaxation map is obtained (Figure 2.3) by transforming all the elementary peaks obtained at various T_p into their Arrhenius representation. The data of Figure 2.3 apply to PMMA, those of Figure 2.4 to mechanically treated PS (more details later). All of the relaxation curves obtained at different polarization temperatures follow an Arrhenius correlation. Table 2.1 gives the result of regression analysis for the Arrhenius lines of Figure 2.3. In this table, T_m is the temperature in degrees Celsius of the maximum of the depolarization curve, Log τ_o is the intercept of the Arrhenius lines in the relaxation map plot, ΔH (eV) equals the value of the slope of the Arrhenius line converted in electron volts, and r^2 is the statistical coefficient for the regression.

TWD results in a relaxation map of all the elementary relaxation modes and tries to correlate the single relaxation modes (relaxation time versus temperature) to thermokinetic and/or other physical variables. This is what we call relaxation map analysis.

EBSCOhost - printed on 2/13/2023 12:32 AM via . All use subject to https://www.ebsco.com/terms-of-use

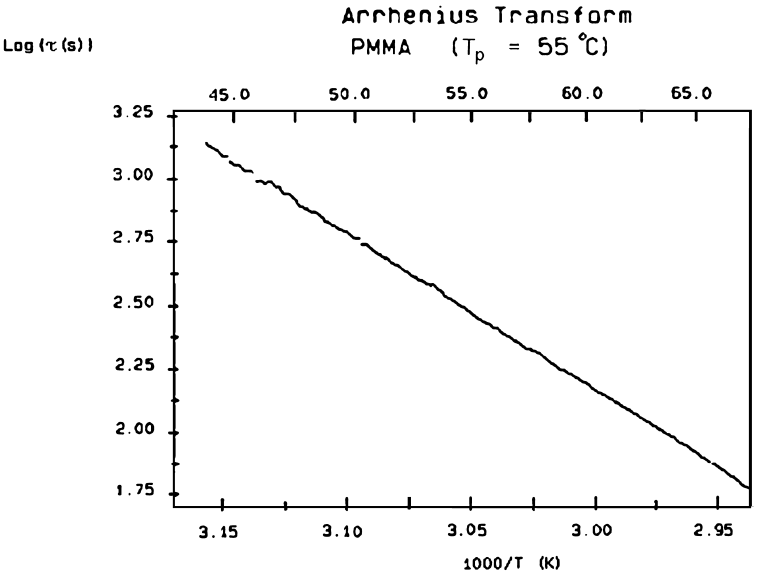


Figure 2.1: An Arrhenius transform converts the current of depolarization curve of a Debye relaxation vs. T (obtained from TWD) into its Arrhenius representation Log τ vs. $1/T$.

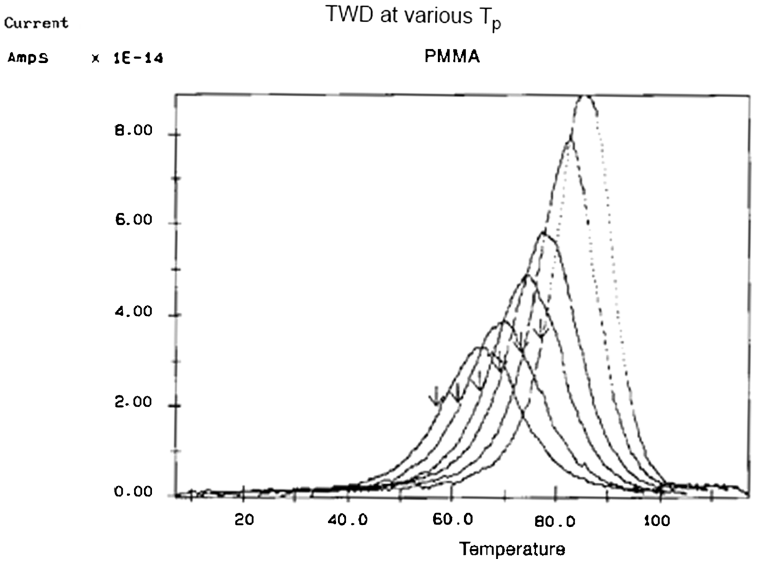


Figure 2.2: Set of TWD elementary peaks obtained by varying the temperature of polarization, T_p. The sample is PMMA. The arrows point to the value of T_p.

EBSCOhost - printed on 2/13/2023 12:32 AM via . All use subject to https://www.ebsco.com/terms-of-use

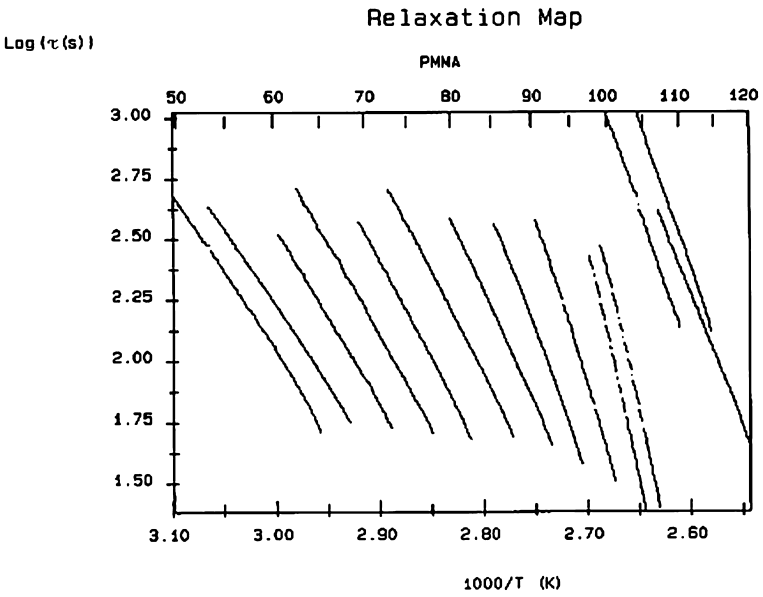


Figure 2.3: Relaxation map of all the Arrhenius transforms of the TWD curves of Figure 2.2 and those at other T_ps.

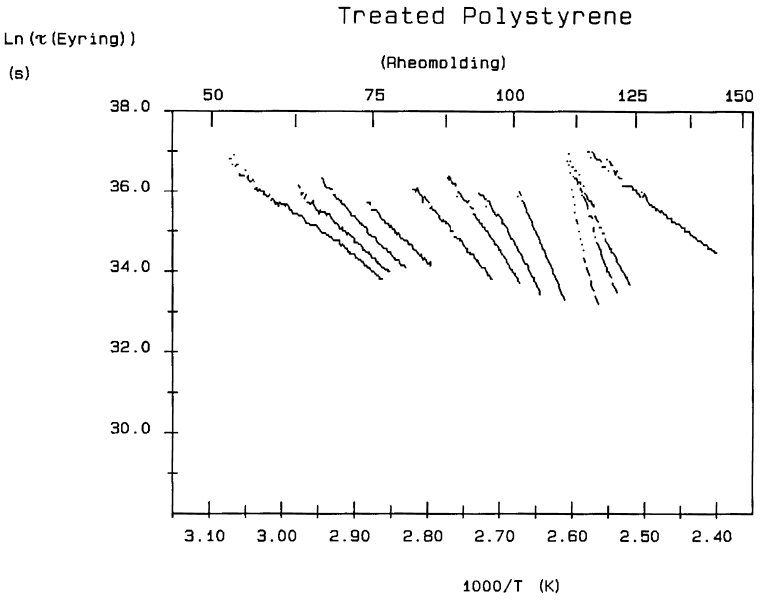


Figure 2.4: Relaxation map expressed in the Eyring plane. This representation is similar to Figure 2.3 except that the relaxation time is corrected by equation (2.5) due to Eyring. The sample is a Rheomolded PS, also studied by TSD in Part II, Chapter 2 (Figure 2.10).

EBSCOhost - printed on 2/13/2023 12:32 AM via . All use subject to https://www.ebsco.com/terms-of-use

Table 2.1: Analysis of the Arrhenius lines of Figure 2.3. The slope and intercept of the Arrhenius lines provide the value of ΔH (1 eV/m = 23.06 Kcal/m) and $\log \tau_o$. T_m (°C) is the value of the temperature at the maximum of the depolarization current in a TWD curve (Figure 2.2). R^2 is the regression coefficient for the linearity of the Arrhenius curve-fits.

T_p (°C)	T_m (°C)	$\log \tau_o$	ΔH (eV)	r^2
55.0	65.0	−18.107	1.332	0.9987
60.0	68.3	−17.307	1.292	0.9997
65.0	73.1	−19.106	1.431	0.9996
70.0	77.9	−19.944	1.508	0.9997
75.0	82.5	−21.287	1.621	0.9995
80.0	87.6	−21.761	1.679	0.9997
85.0	92.6	−24.301	1.884	0.9998
90.0	96.6	−29.887	2.309	0.9989
95.0	101.0	−35.548	2.752	0.9993
100.0	105.3	−49.910	3.851	0.9993
105.0	107.1	−48.643	3.777	0.9987
110.0	110.1	−31.052	2.522	0.9990
115.0	120.2	−25.877	2.148	0.9997
120.0	114.6	−30.081	2.477	0.9995

I.2.3 Eyring transform. Thermokinetic functions

According to Eyring, the pre-exponential factor in the Arrhenius equation is directly related to the entropy of activation of the activated states involved [133]. The entropy of activation is a statistical quantity which relates to the number of possible activated states with a potential barrier corresponding to the free energy difference ΔG. The relaxation time is the inverse of the frequency of jump between two activated states.

For a given relaxation mode isolated by polarizing at T_p, the relaxation time takes the following form:

$$\mathrm{Log}\,\tau_i = \mathrm{Log}(\tau_i)_o + \Delta G/kT \tag{2.2}$$

so

$$\begin{aligned} \Delta G &= kT \log(\tau_i/\tau_{i,o}) \\ \Delta G &= \Delta H_p - T \cdot \Delta S_p \end{aligned} \tag{2.3}$$

where the sub-index "p" implies that these variables are a function of the temperature of polarization.

Now, according to Eyring [133]:

$$\mathrm{Log}(\tau_i)_o = -\mathrm{Log}(kT/h) \tag{2.4}$$

EBSCOhost - printed on 2/13/2023 12:32 AM via . All use subject to https://www.ebsco.com/terms-of-use

so

$$\tau_i = (h/kT) \cdot \exp(-\Delta S_p/k) \cdot \exp(\Delta H_p/kT) \tag{2.5}$$

where k and h are respectively the Boltzmann and Planck constants.

A plot of $[\text{Log}\,\tau_i + \text{Log}\,T + \text{Log}(k/h)]$ vs. $1/T$ is called an "Eyring plot," and the transform of current vs. temperature data into these variables is called an "Eyring transform." We designate "Log τ_i(Eyring)" the value of the expression $[\text{Log}\,\tau_i + \text{Log}\,T + \text{Log}(k/h)]$, and, of course, one can calculate Log τ_i from Log τ_i(Eyring) at each temperature, and vice versa.

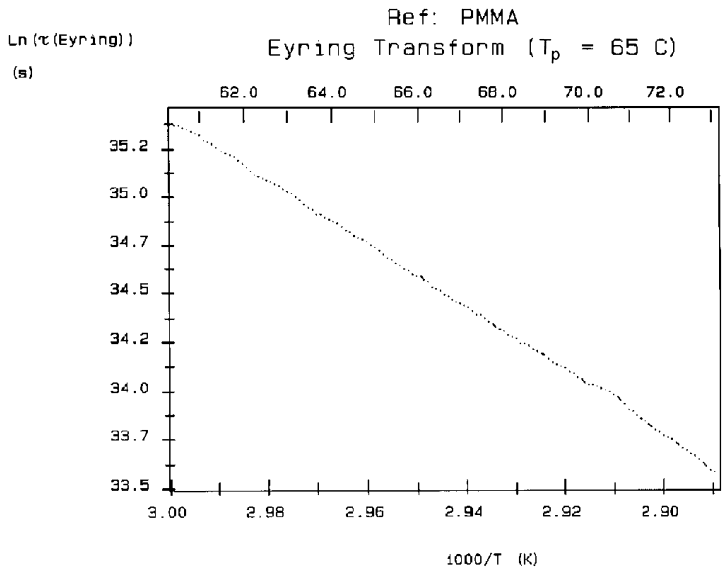


Figure 2.5: An Eyring transform converts the current of depolarization curve of a Debye relaxation vs. T (obtained from TWD) into its Eyring representation Log τ(Eyring) vs. $1/T$, where τ(Eyring) is given by equation (2.5).

Figure 2.5 displays the Eyring transform for $T_p = 65\,°\text{C}$. It is a useful way to plot the variables because from the slope $(\Delta H_p/k)$ and intercept $(-\Delta S_p/k)$ of the best linear fit through the data points, one can determine the average or mean enthalpy and entropy of activation, ΔH_p and ΔS_p, and in addition, the apparent activation entropy and enthalpy at each temperature of the depolarization curve, sub-ΔH and sub-ΔS. Finally, as shown in Figure 2.6 for PMMA, the relaxation results can be represented in a different plane, the ΔG vs. T plane, by calculating the value of ΔG at each temperature according to equations (2.2) and (2.4) or from the apparent sub-ΔH and sub-ΔS. Figure 2.7 is a relaxation map for the data of Figure 2.3 in the ΔG vs. T plane. One sees that the influence of the temperature of polarization is to raise the value of ΔG, while

EBSCOhost - printed on 2/13/2023 12:32 AM via . All use subject to https://www.ebsco.com/terms-of-use

the incidence of temperature during the recovery process reduces its value. The slope of the spectral lines in Figure 2.7 is equal to minus the entropy of activation, and the intercept is the enthalpy. The lines appear to be satisfactorily linear.

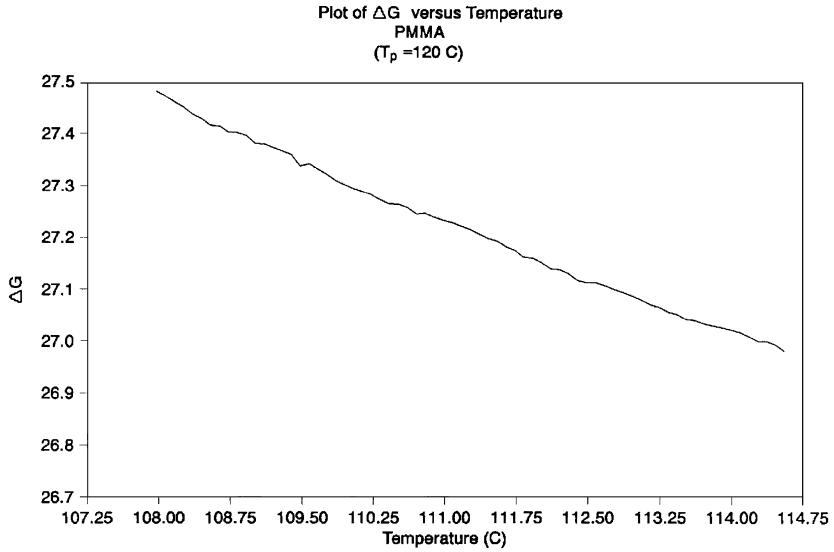


Figure 2.6: The relaxation result for a given T_p can be represented in the ΔG plane according to equations (2.2) to (2.4) which convert the Eyring relaxation time in thermokinetic terms: ΔH_p, ΔS_p, and ΔG.

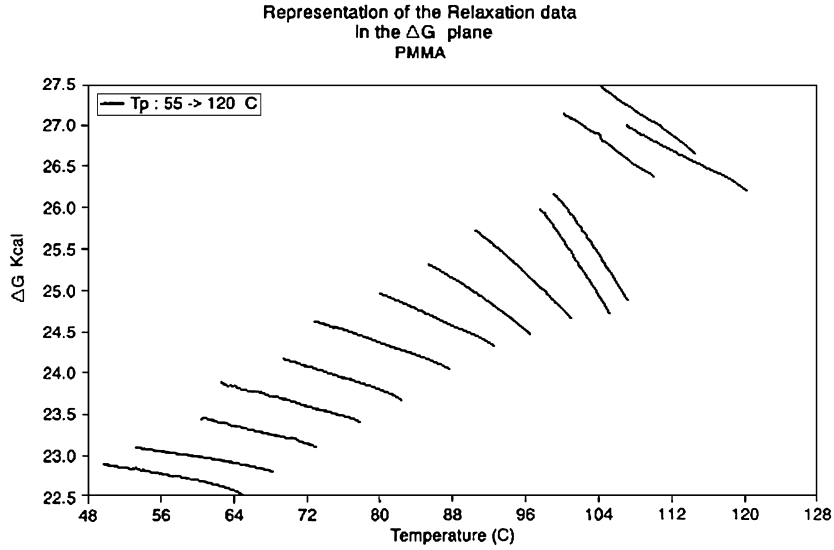


Figure 2.7: Relaxation map in the ΔG plane. All the Eyring transforms are converted in ΔG relaxation spectral lines. The x-axis is the temperature T during the depolarizing stage.

EBSCOhost - printed on 2/13/2023 12:32 AM via . All use subject to https://www.ebsco.com/terms-of-use

I.2.4 Compensation phenomena. Degree of disorder

When several Arrhenius lines converge into a single point, this point is called a "compensation point." Figure 2.8 displays such a behavior for the $T < T_g$ region in the PS sample of Figure 2.4. In general, for amorphous polymers, or for the amorphous region in semi-crystalline polymers, the behavior at T_g is characterized by at least one compensation phenomenon. The Arrhenius or the Eyring lines all converge into a single point at T_c, near T_g. The coordinates $[T_c, \text{Log}\,\tau_c]$ of the compensation point are important because they transcribe the coupling characteristics between the different modes of relaxation observed as individual activated processes in the set of converging Arrhenius lines. The coordinates of the compensation point are related to fundamental properties of the state of the polymer, as influenced by its surrounding. If a structure is "loose," the contrary of "ordered" or "compact," i. e., when molecular mobility is less hindered by the interactive intra-intermolecular surrounding, the entropy of activation is "larger." Conversely, any parameter which acts to "organize" the structure and create a tighter environment for the bonds causes a decrease of the entropy of activation. So, the activated entropy calculated from the Eyring equation, equation (2.5), gives an indication of the mobility in the structure. But the entropy of activation varies with the polarization temperature, such as shown by the variation of the slope in Figure 2.7. We would like to be able to define the "degree of disorder" (DOD) of the structure by a single number, representative of the state of the dielectric environment of the bonds. A characteristic feature of the compensation phenomenon gives us such an opportunity.

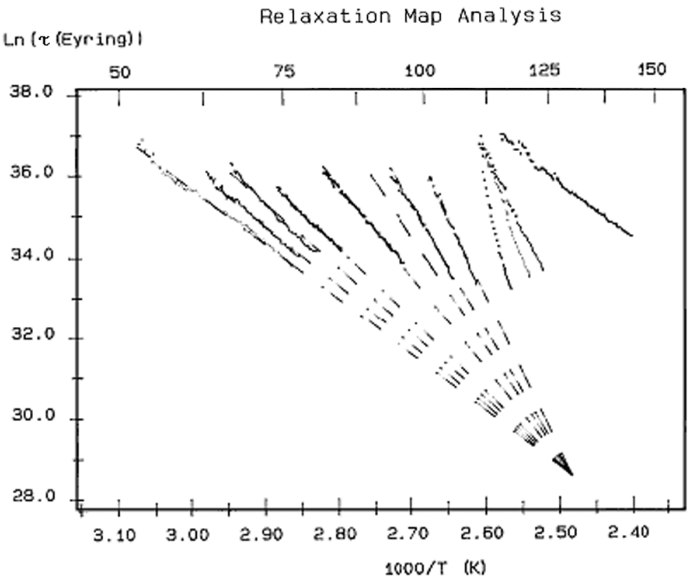


Figure 2.8: Compensation of the Eyring spectral lines $T_p < T_g$ of Figure 2.4. The point of convergence is the compensation point.

EBSCOhost - printed on 2/13/2023 12:32 AM via . All use subject to https://www.ebsco.com/terms-of-use

I.2.5 Compensation search. Z-structure. Z-line

One can prove mathematically that a very simple and practical way to see whether a set of lines obtained at various T_p converge is to plot intercept versus slope for these lines and to try to draw a straight line through the points. This type of analysis is called a "compensation search."

Let a family of straight lines, dependent on a parameter p, be

$$Y = I(p) + s(p)X$$

where $I(p)$ and $s(p)$ are intercept and slope, respectively. Let Y_c and X_c be the coordinates of the compensation point. One can write for each p

$$Y_c = I(p) + s(p)X_c$$

so

$$Y = [Y_c - s(p)X_c] + s(p)X$$

and therefore, when p varies

$$I(p) = Y_c - s(p)X_c$$

In other words, when T_p varies, a plot of $I(p)$ versus $s(p)$ should be linear with slope $(-X_c)$ and intercept Y_c. The coordinates of the compensation point Y_c, X_c are therefore calculated from the slope and intercept of "the compensation line," intercept versus slope. Figure 2.9 is the compensation line for the set of converging Eyring curves of Figure 2.8. Let us call in this case $X_c = 1/T_c$ and $Y_c = \mathrm{Ln}(\tau_c)$.

The coordinates of the compensation point are obtained by linear regression completed by a simplex to integrate all the points of the Eyring lines into the calculation of the best fit for the compensation line (Chapter 1, I.1.6.3):

$$T_c = 129.65\,^{\circ}\mathrm{C}$$
$$\mathrm{Ln}\,\tau_c(\mathrm{Eyring}) = 28.58$$

so $\mathrm{Log}\,\tau_c = -0.5$ according to equation (2.3).

For the PMMA sample of Figure 2.5, Table 2.2 gives the result of the regressional fit of the 14 individual Arrhenius lines expressed as entropy, enthalpy, and Gibbs free energy of activation, according to equations (2.5) and (2.2). The Gibbs free energy is calculated at $T = T_p$.

Notice from Table 2.2 how the thermokinetic functions vary with the polarization temperature. While both the enthalpy and entropy of activation go through a maximum for T_p around 100 °C, the Gibbs free energy seems to go smoothly across.

EBSCOhost - printed on 2/13/2023 12:32 AM via . All use subject to https://www.ebsco.com/terms-of-use

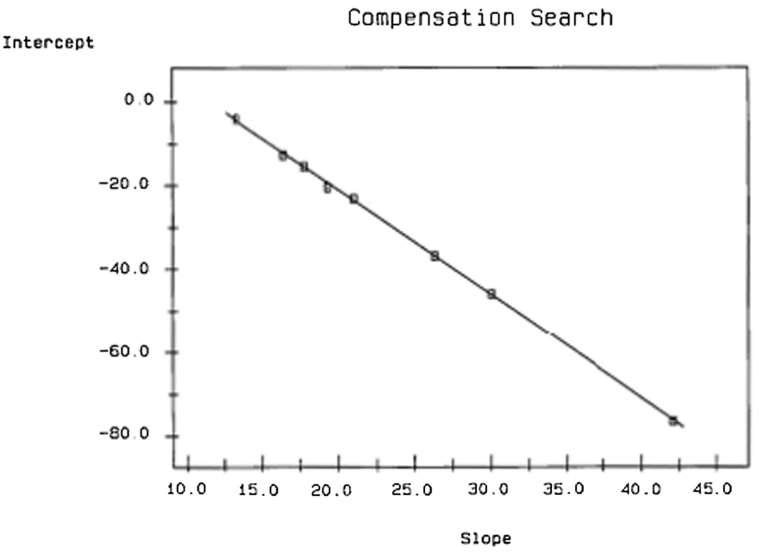


Figure 2.9: Compensation search to determine by regression the coordinates of the compensation point in Figure 2.8. The intercept and the slope in this figure, which are a function of T_p, are determined from the Eyring transforms at T_p. The intercept and slope of the compensation line passing through the points provides the coordinates of the compensation point of Figure 2.8.

Table 2.2: Thermokinetic results for the PMMA sample of Figure 2.3. This table analyzes the same results as shown in Table 2.1, using the Eyring transform instead of the Arrhenius transform to convert from the TWD current data. The Gibbs free energy in the last column is the value of ΔG calculated at $T = T_m$ (K) using equation (2.3) all caloric values are per mole.

T_p (°C)	T_m (°C)	ΔH_p (kcal/mol)	ΔS_p (cal/°C/mol)	ΔG_p (kcal/mol)
55.0	65.0	30.0154	21.9978	22.8002
60.0	68.3	29.1053	18.3919	22.9808
65.0	73.1	32.3068	26.5580	23.3302
70.0	77.9	34.0809	30.4044	23.6522
75.0	82.5	36.6546	36.4496	23.9701
80.0	87.6	38.0073	38.6547	24.3622
85.0	92.6	42.7078	50.2408	24.7216
90.0	96.6	52.4668	75.6816	24.9944
95.0	101.0	62.6732	101.5688	25.2959
100.0	105.3	87.9523	167.1228	25.6155
105.0	107.1	86.2465	161.3318	25.2631
110.0	110.1	57.4247	81.1127	26.3585
115.0	120.2	48.7469	57.2885	26.5189
120.0	114.6	56.3012	76.4458	20.2580

EBSCOhost - printed on 2/13/2023 12:32 AM via . All use subject to https://www.ebsco.com/terms-of-use

Plots of entropy, enthalpy, and ΔG versus T_p are presented in Figures 2.10 to 2.12, respectively.

The compensation search for this sample is shown in Figures 2.13 and 2.14. Figure 2.13 is the classical plot, mentioned previously, of intercept versus slope obtained from the linear regression of the Arrhenius lines. Figure 2.14 is what we call an "EE plot," entropy versus enthalpy.

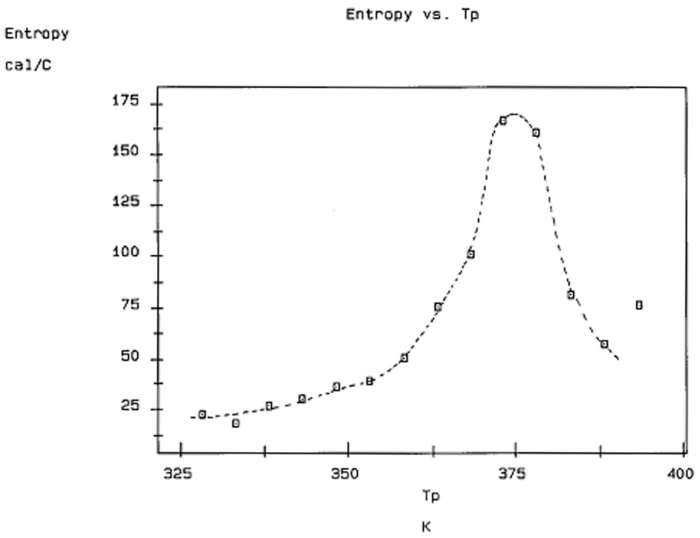


Figure 2.10: Entropy of activation, ΔS_p (cal/K) vs. T_p from the values in Table 2.2.

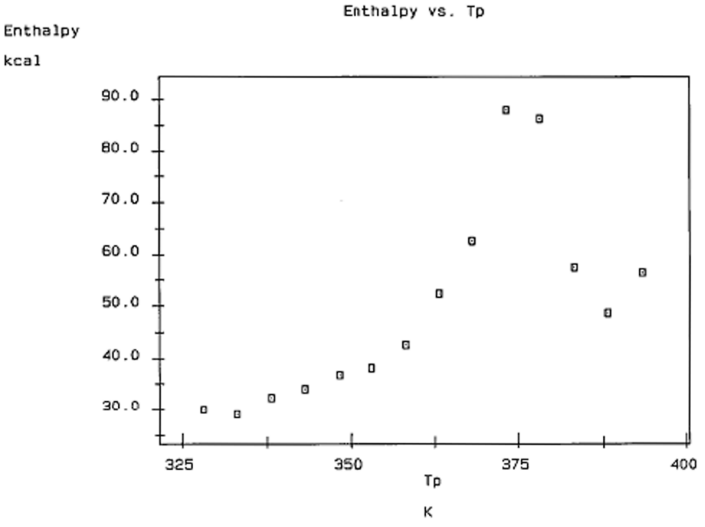


Figure 2.11: Enthalpy of activation, ΔH_p (Kcal) vs. T_p from the values in Table 2.2.

EBSCOhost - printed on 2/13/2023 12:32 AM via . All use subject to https://www.ebsco.com/terms-of-use

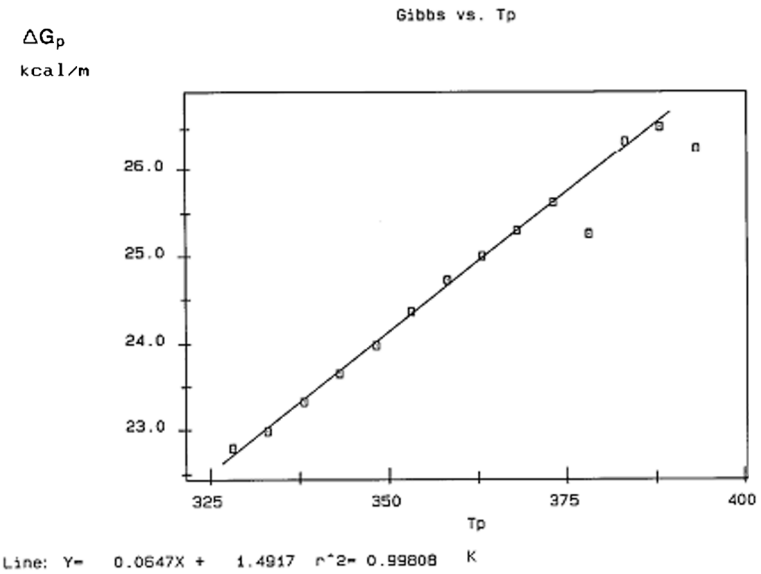


Figure 2.12: $\Delta G(T)$ vs. T_p from the values in Table 2.2. Note that the unit is Kcal, so ΔS_p in equation (2.3) must be converted to that unit; T_m is in K.

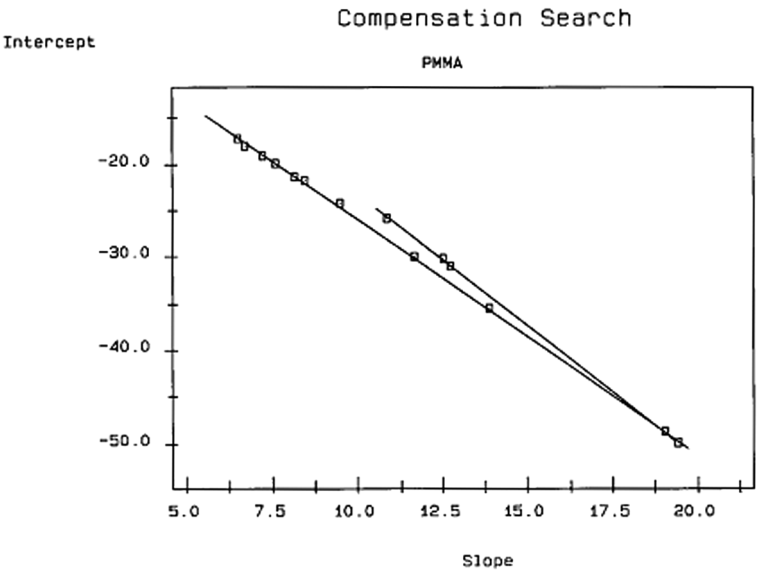


Figure 2.13: Compensation search for the relaxation map expressed in the Arrhenius plane. The plot shows two compensation lines, hence two compensation points are expected for the data of Figure 2.3.

EBSCOhost - printed on 2/13/2023 12:32 AM via . All use subject to https://www.ebsco.com/terms-of-use

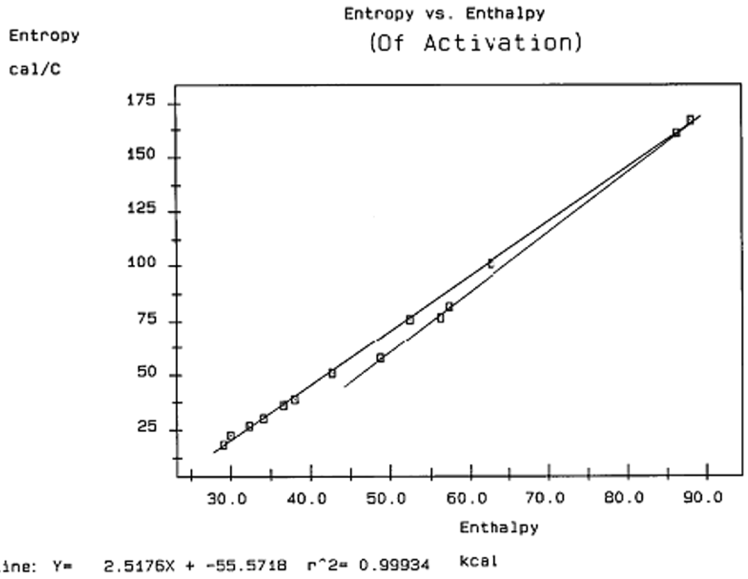


Figure 2.14: A plot of the entropy of activation vs. the enthalpy of activation, as T_p varies, extracted from the values in Table 2.2, is similar to a compensation search with the coordinates of the compensation points expressed in thermokinetic terms.

It is actually identical to a compensation search, since the entropy and enthalpy are calculated from the Eyring formulation, as expressed earlier (equation (2.5)):

$$\text{slope} = (\Delta H_p/k) \quad \text{and} \quad \text{intercept} = (-\Delta S_p/k) \tag{2.6}$$

Two important observations can be made:

1. the compensation search reveals TWO compensation lines, and
2. as T_p increases, the points in Figure 2.14 first go upward and then, as ΔH and ΔS reach their maximum, fold backward.

We can easily symbolize this phenomenon by saying that the two compensation lines observed in Figure 2.13 or Figure 2.14 do not have the same "sign," meaning that consecutive points on the compensation lines, as T_p increases, are following a pattern towards either increasing or decreasing entropy, depending on the positive or negative sign of the compensation line. We claim that this behavior is classical across a T_g. The intercept between the positive and negative compensation lines is used to determine with accuracy the value of the glass transition temperature and the values of entropy and enthalpy of activation at T_g.

We have calculated the best linear fits for the lines of Figures 2.13 and 2.14, and from them, the coordinates of the compensation points. For the positive compensa-

EBSCOhost - printed on 2/13/2023 12:32 AM via . All use subject to https://www.ebsco.com/terms-of-use

tion,

$$T_c^+ = 127.96\,°\text{C}, \quad \text{Log}\,\tau_c^+ = -0.95 \tag{2.7}$$

$$\Delta S_p^+ = 2.5176\Delta H_p^+ - 55.5718 \tag{2.8}$$

and for the negative compensation,

$$T_c^- = 82.38\,°\text{C}, \quad \text{Log}\,\tau_c^- = 4.77 \tag{2.9}$$

$$\Delta S_p^- = 2.8073\Delta H_p^- - 80.3676 \tag{2.10}$$

We can now calculate the values of ΔG_c^+ and ΔG_c^- at the corresponding compensation temperatures T_c^+ and T_c^- and the values of entropy and enthalpy at T_g, i. e., at the intercept of the positive and negative compensation lines:

$$\Delta G_c = \left[\text{Log}\,\tau_c + \text{Log}\,T_c + \text{Log}(k/h)\right] \cdot RT_c$$

where R is the gas constant (1.987 cal/m). So,

$$\begin{aligned} \Delta G_c^+ &= 22.11\,\text{kcal/m} \\ \Delta G_c^- &= 28.88\,\text{kcal/m} \end{aligned} \tag{2.11}$$

The intercept of the two compensation lines occurs for

$$\begin{aligned} \Delta H_g &= 85.59\,\text{Kcal/m} \\ \Delta S_g &= 159.91\,\text{cal/deg/m} \end{aligned} \tag{2.12}$$

which corresponds to the enthalpy and entropy of activation at T_g.

Figure 2.15 summarizes the situation for an Arrhenius system of coordinates and illustrates what we mean by a "Z-structure." The Arrhenius lines span the relaxation map drawing a kind of "Z" when the temperature of polarization T_p varies. If one considers that we have mirrored the $1/T$ temperature axis so that T increases to the right (although we plot $1/T$), the relaxation map across T_g does actually look like a Z. The "Z-line" is the line passing through the two compensation points. Its image in the EE plane (Figure 2.14) is the intercept of the two positive and negative compensation lines. Its coordinates are given by equation (2.12), and one can calculate the slope and intercept of the Z-line in Figure 2.15 from equation (2.6).

Figure 2.16 displays the Z-structure in the ΔG plane.

EBSCOhost - printed on 2/13/2023 12:32 AM via . All use subject to https://www.ebsco.com/terms-of-use

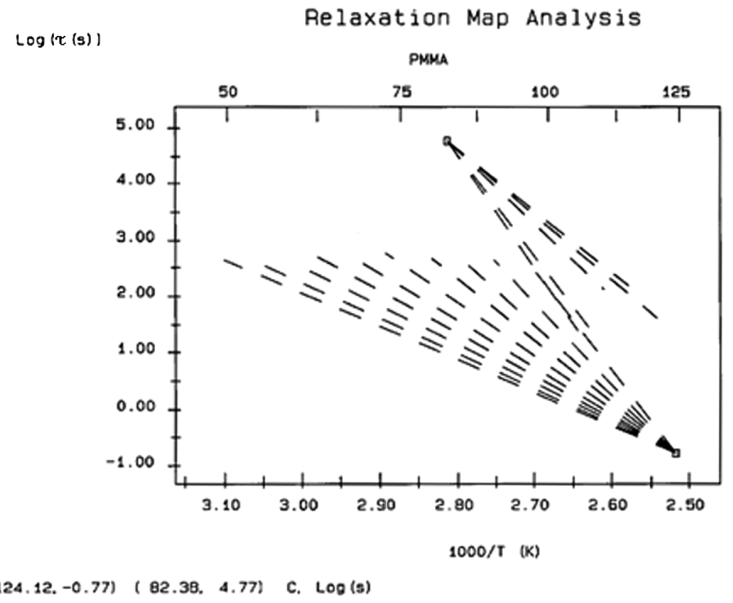


Figure 2.15: Relaxation map in the Arrhenius plane for the PMMA of Figure 2.3 showing the two sets of Arrhenius spectral lines across T_g converging to their respective positive and negative compensation points.

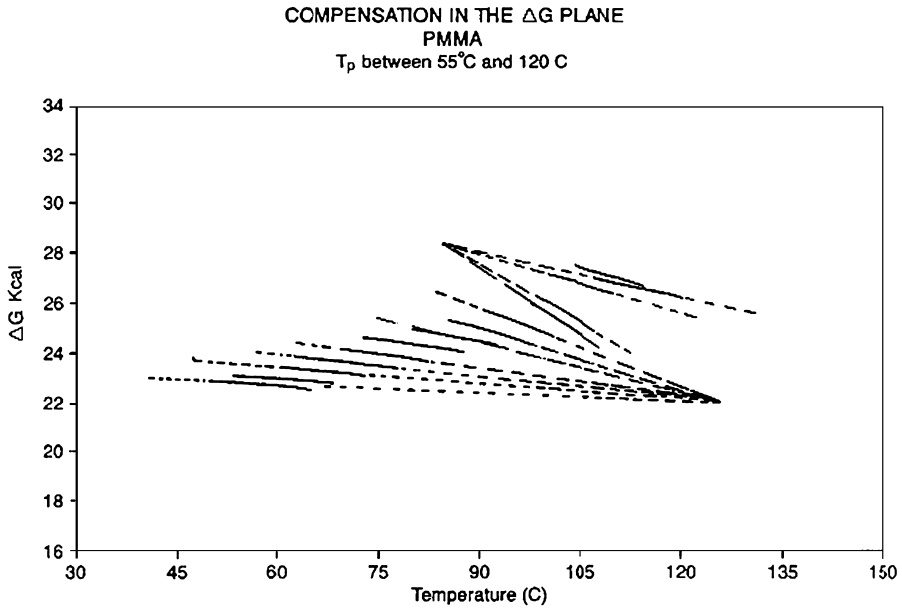


Figure 2.16: Representation of the Z-structure of the relaxation map in the ΔG plane.

EBSCOhost - printed on 2/13/2023 12:32 AM via . All use subject to https://www.ebsco.com/terms-of-use

I.2.6 Determination of T_g. Activation entropy and enthalpy at T_g

One observes that the values of the compensation temperatures are located on both sides of the value of T_g (102 °C), as determined for instance by differential scanning calorimetry (DSC), or by the value of T_p at the maximum entropy (Figure 2.10). One can stipulate, for instance, that the temperature of T_g corresponds to the medium value between the ΔG_c of the positive and negative compensation points, and therefore T_g can be calculated from the characteristics of the compensation points:

$$\begin{aligned} \Delta G_g &= (\Delta G_c^+ + \Delta G_c^-)/2 \\ \Delta G_g &= \Delta H_g - T_g \cdot \Delta S_g \end{aligned} \tag{2.13}$$

With ΔH_g and ΔS_g given by (2.12), we find $T_g = 102.64$ °C.

Another possible definition of T_g comes from the calculation of ΔG_p at $T = T_p$. Figure 2.13 shows that ΔG_p at $T = T_p$ is linearly related to T_p and that to a first approximation

$$\Delta G_p = a + b \cdot T_p \tag{2.13a}$$

where a and b are curve-fitting constants determined by regression (for many polymeric systems, it is often found that $a = 0$ and $b = 0.070$ kcal/K/m). T_g can be determined at the intercept of the Z-line in the ΔG plane and the ΔG_p vs. T_p line:

$$T_g = (\Delta H_g - a)/(\Delta S_g + b) \tag{2.13b}$$

We find 101.3 °C for PMMA, which corresponds well with the temperature of maximum entropy.

From the expression of the compensation lines formulated in the EE plane, equations (2.8) and (2.10), we can easily calculate the value of the extrapolated enthalpy $\Delta H_{o,s}$ when the entropy is zero and compare that value to ΔH_g. According to the theory of Gibbs and DiMarzio [91], the ratio $\Delta H_g/\Delta H_{o,s}$ would be representative of the number of elementary units moving at T_g.

From equation (2.8), $\Delta H_{o,s}^+ = 22.073$ kcal/m, and from equation (2.10), $\Delta H_{o,s}^- = 28.63$ kcal/m. These values are obviously equal to those calculated for ΔG_c^+ and ΔG_c^- (equation (2.11)) since $\Delta S_p = 0$ in equation (2.3). On the basis of equation (2.12), the number of units moving at T_g would be between 3 and 4.

I.2.7 DOD number

Another interesting parameter seems to be $\Delta S_{o,h}$, i. e., the extrapolated value of the entropy of activation for $\Delta H_p = 0$. This is the intercept of the compensation lines them-

EBSCOhost - printed on 2/13/2023 12:32 AM via . All use subject to https://www.ebsco.com/terms-of-use

selves, equations (2.8) and (2.10):

$$\begin{aligned} \Delta S^{+}_{o,h} &= -55.572\,\text{cal/°C/m} \\ \Delta S^{-}_{o,h} &= -80.368\,\text{cal/°C/m} \end{aligned} \tag{2.14}$$

If these values are multiplied by T_c (in K), from equations (2.7) and (2.9), we find

$$T_c \cdot \Delta S^{+}_{o,h} = -22.290\,\text{kcal/m} \tag{2.15}$$

$$T_c \cdot \Delta S^{-}_{o,h} = -28.573\,\text{kcal/m} \tag{2.16}$$

which again, obviously, equal the respective $-\Delta G_c$ since ΔH_p is zero this time.

T_c can be rewritten in a kind of thermodynamical way:

$$T_c = \Delta H_{o,s}/(-\Delta S_{o,h}) \tag{2.17}$$

which is the ratio of an enthalpic to an entropic term, as in the case of a first-order thermodynamic transition. We will show in Chapter 4 of Part II that the two terms entering equation (2.17) play a role in determining the location of the branches of a multi-compensation plot in the EE plane.

The $(-\Delta S_{o,h})$ term is as important as $\Delta H_{o,s}$ or T_c to determine the actual state of the polymeric system, and as long as we specify two parameters, the third one can be calculated from equation (2.17). We can choose any one of them, say the entropic term (the value of ΔS_p at $\Delta H_p = 0$), to define the DOD number of the material:

$$\text{DOD} = 100 + \Delta S_{o,h} \tag{2.18}$$

The number 100 is arbitrarily added to $\Delta S_{o,h}$ in order to shift all values to the positive side. Based on results obtained in the sub-EE plane (presented in the following section), it is suggested that a better physical meaning is actually achieved if we were to add 70 (i. e., subtract –70) instead of 100 to the $\Delta S_{o,h}$ values. However, one can simply consider, for the moment, equation (2.18) as a formula to define the DOD number, nothing else. Normally, only the positive compensation line is used to characterize the structure with the DOD number. For instance, the DOD for the PMMA of Figure 2.3 is 44.43, and the DOD for the mechanically treated PS of Figure 2.4 is 41.52. The coupling mode above T_g can also be characterized by the DOD number calculated from the negative compensation line, equation (2.16). The resolution and the accuracy in determining the DOD number depend on the linearity of the $\Delta G - T$ depolarization curves and the number of such curves, as explained in Chapter 1.

We also empirically observe that the value of $(T^{+}_c - T_g)$ is also significant in representing the internal state of the glass below T_g. The larger $(T^{+}_c - T_g)$, the less "internally stressed" the structure. For instance, comparing $(T^{+}_c - T_g)$ for the unstressed PMMA and for the highly mechanically stressed Rheomolded PS of Figure 2.4, 25.3 °C and

EBSCOhost - printed on 2/13/2023 12:32 AM via . All use subject to https://www.ebsco.com/terms-of-use

8.9 °C, respectively, it is clear that the PS specimen has a fair amount of internal stress present in the glassy state.

Results for PS equivalent to those presented in formulas (2.7) to (2.19) are summarized below (the compensation lines are shown in Figure 2.17 and the Z-structure is displayed in Figure 2.18):

$$T_c^+ = 124.6\,°\text{C}$$
$$\text{Ln}(\tau_c^+)_{\text{Eyr}} = 29.24$$
$$\Delta S_p^+ = 2.4884\Delta H_p^+ - 56.68$$

$$T_c^- = 108.77\,°\text{C}$$
$$\text{Ln}(\tau_c^-)_{\text{Eyr}} = 37.56$$
$$\Delta S_p^- = 2.6173\Delta H_p^- - 74.53$$

$$\Delta G_c^+ = 23.11\,\text{kcal/m}$$
$$\Delta G_c^- = 28.50\,\text{kcal/m}$$

The intercept of the two compensation lines occurs for

$$\Delta H_g = 138.48\,\text{kcal/m}$$
$$\Delta S_g = 287.91\,\text{cal/deg/m}$$

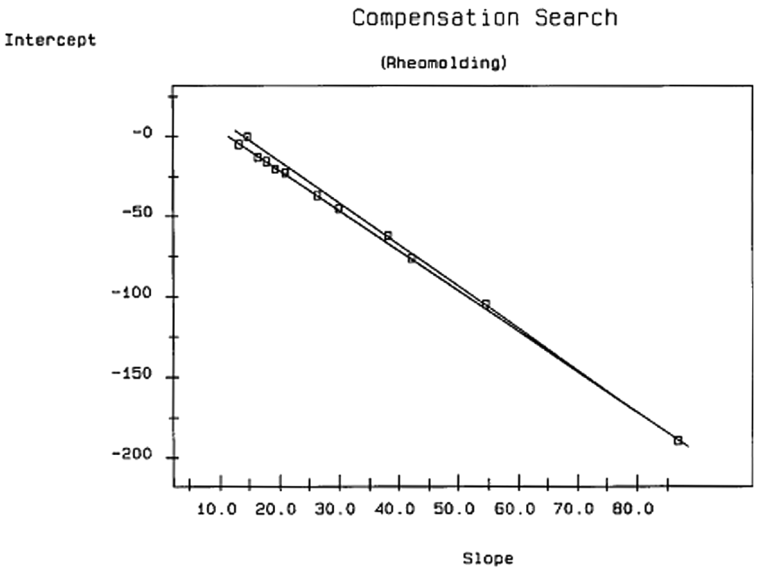


Figure 2.17: Compensation search for the Rheomolded PS data of Figure 2.4.

EBSCOhost - printed on 2/13/2023 12:32 AM via . All use subject to https://www.ebsco.com/terms-of-use

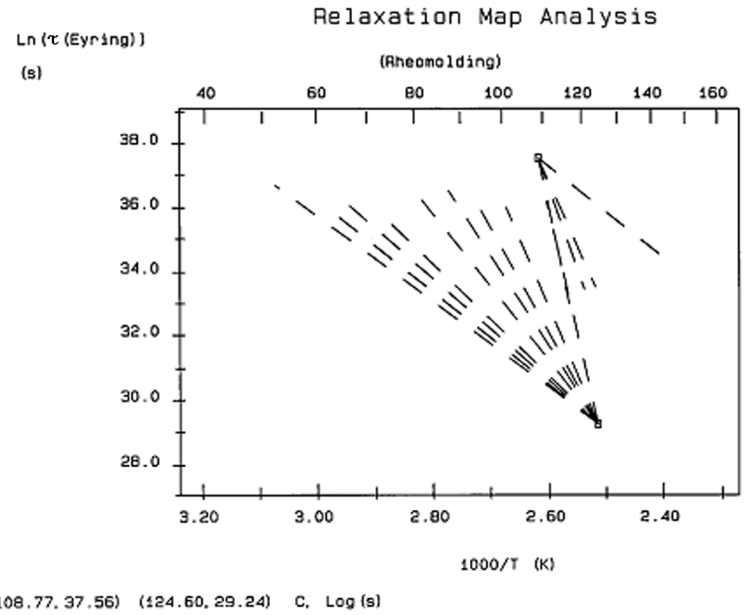


Figure 2.18: Relaxation map in the Eyring plane showing the Z-structure for the Rheomolded PS data of Figure 2.4.

which correspond to the enthalpy and entropy of activation at T_g:

$$\Delta G_g = (\Delta G_c^+ + \Delta G_c^-)/2 = 25.81\,\text{kcal/m}$$
$$\Delta G_g = \Delta H_g - T_g \cdot \Delta S_g, \quad \text{so } T_g = 118.20\,^\circ\text{C}$$

or, using the alternative method of finding the intercept of the Z-line with the ΔG_p vs. $[a + b \cdot T_p]$ line, with $a = 7.8033$ and $b = 0.0483$, $T_g = 115.7\,^\circ$C, $(T_c - T_g) = 8.9\,^\circ$C.

The number of units moving at T_g, assuming it is given by the ratio $\Delta H_g/\Delta H_{o,s}$, is equal to six units.

I.2.8 Duality at T_g

Before closing this section on the compensation phenomena in the EE plane, let us examine the possible significance of the results. Rewriting equation (2.2) at T and T_c and combining, the compensation phenomenon is often described in the literature [238] in the Arrhenius plane:

$$\text{Log}(\tau/\tau_c) = (\Delta G/k) \cdot (1/T - 1/T_c)$$

EBSCOhost - printed on 2/13/2023 12:32 AM via . All use subject to https://www.ebsco.com/terms-of-use

which puts the emphasis on the coordinates of the compensation point. How is T_c related to T_g, and (since it is empirically found that T_c^+ is often located at 23 °C above the T_g of the polymer [200], as characterized by DSC) why? Should we shift the origin of the axes to the point of compensation to rescale the data?

We prefer to emphasize the result differently and rewrite the compensation equation in the ΔG plane:

$$\begin{aligned} \Delta G_p &= \Delta H_p - T \cdot \Delta S_p \\ \Delta H_p &= T_c \cdot (\Delta S_p - \Delta S_{o,h}) \end{aligned} \tag{2.19}$$

with also

$$T_c = [\Delta H_{o,s}/(-\Delta S_{o,h})] = [\Delta H_p/(\Delta S_p - \Delta S_{o,h})] \tag{2.20}$$

By analogy, it seems interesting to define $\Delta S_{og,h}$ at T_g by

$$T_g = [\Delta H_g/(\Delta S_g - \Delta S_{og,h})] \tag{2.21}$$

We have found empirically that $\Delta S_{og,h}$ takes values between −72.0 and −62.0 cal/°C/m for a large number of polymers tested with this formula (T_g is measured at the maximum of entropy vs. T_p plot or calculated using the Z-line crossing technique explained previously, and ΔH_g and ΔS_g are given by the intercept of the two compensation lines [Figure 2.16]). For instance, for PMMA and Rheomolded PS, given their T_g equal to 101.3 °C and 115.5 °C, respectively, we find $\Delta S_{og,h} = -68.7$ for PMMA and $\Delta S_{og,h} = -68.4$ for PS.

The shifting value of approximately −70 cal/°C/m seems to play a role when studying compensation phenomena in the sub-EE plane and when determining the intercept of branches of multi-compensation lines (Part II, Chapter 4). A possible theoretical interpretation of it is given in Chapter 3 of Part I.

Our emphasis is therefore on the Z-line itself and the duality which exists at T_g: *what is happening at* $T = T_g$; which compensation "world" prevails (in choosing between the two compensations); is there a structured balance of driving forces leading to oscillation or some sort of chaotic behavior with large fluctuation? Why is the entropy going through a maximum at T_g, and should our understanding of the T_g process be improved by it? In particular, should we not use the enthalpy, entropy, and free energy of activation defined from the Z-line to compare the TSD results with those obtained by other dynamic electrical thermal analysis techniques?

EBSCOhost - printed on 2/13/2023 12:32 AM via . All use subject to https://www.ebsco.com/terms-of-use

I.2.9 Compensation in the sub-EE plane

The relaxation results can be represented in the Eyring plane (Figure 2.6) and curve-fitted with a linear regression over the whole temperature interval. When we do so, the curve-fit provides the value of ΔS_p and ΔH_p. The plot ΔG versus T is also linear, with slope ΔS_p and intercept ΔH_p. This leads to the analysis presented earlier. Suppose now that we assume linearity between ΔG and T only on a small temperature interval and determine the apparent sub-ΔH and sub-ΔS for that interval. The full temperature range can be divided up into several successive overlapping intervals, which can each be characterized by its mid-temperature and apparent sub-ΔH and sub-ΔS. The smallest temperature window pan is zero, i. e., the Eyring formula, equation (2.5), applies to the derivative of the Eyring transform at each temperature. The largest interval window spans the whole temperature range, leading to ΔS_p and ΔH_p.

For each temperature of an Eyring transform (Figure 2.5), obtained for a given T_p, we can determine the slope and intercept of the tangent to the curve. The derivative at each point can be numerically computed and provides the two parameters needed. By proceeding point by point along the Eyring curve, we calculate and tabulate the apparent sub-ΔS and sub-ΔH at each temperature T. A plot of sub-ΔS versus sub-ΔH is designated as "a sub-EE curve." Figures 2.19 to 2.22 display several of those curves (the y-coordinate is actually $-$(sub-ΔS)/R, where R is the gas constant, in Figures 2.19 to 2.21).

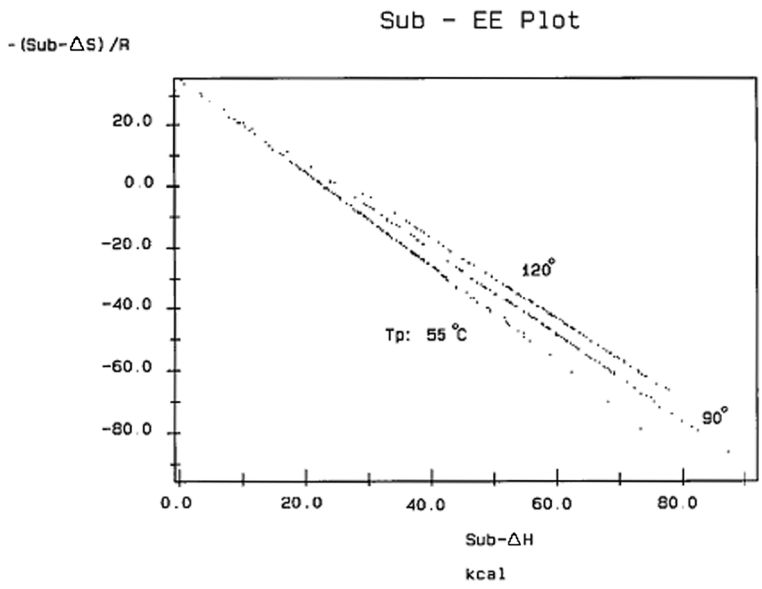


Figure 2.19: Compensation search in the sub-ΔG plane: plot of $-$sub-$\Delta S/R$ vs. sub-ΔH for the PMMA data of Table 2.2. The sub-EE plot is shown at three T_ps in this figure, each showing a series of points lining up as a straight line. The three straight lines compensate.

EBSCOhost - printed on 2/13/2023 12:32 AM via . All use subject to https://www.ebsco.com/terms-of-use

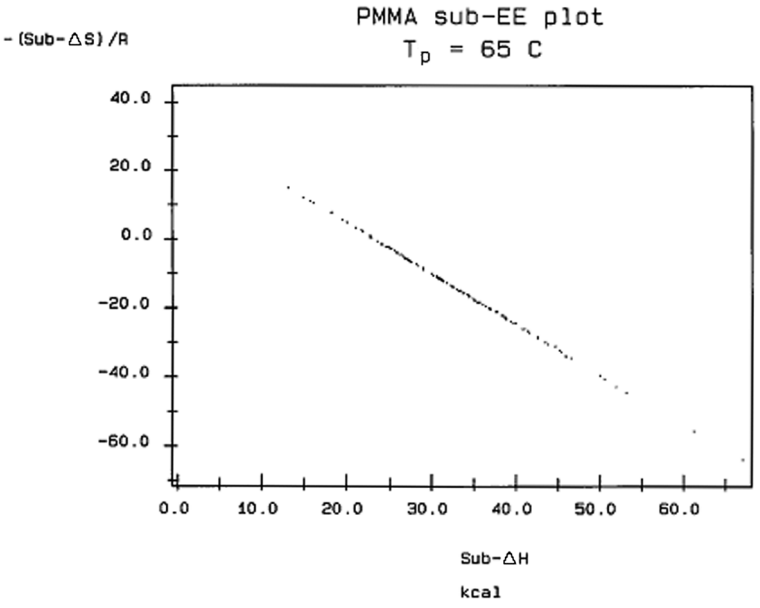


Figure 2.20: Same plot as in Figure 2.19 showing the $T_p = 65\,°C$ sub-EE relaxation.

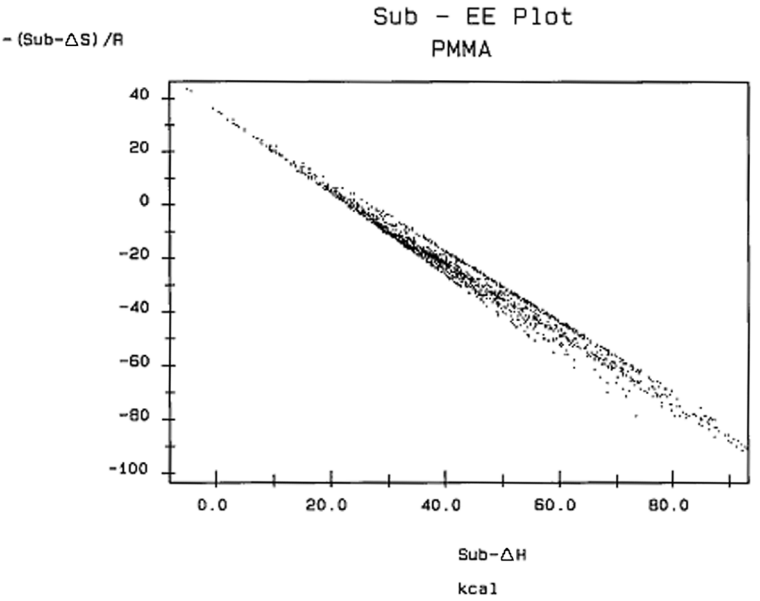


Figure 2.21: Sub-EE plot for all the T_p across T_g. All the straight lines compensate on a single compensation point, regardless if $T_p < T_g$ or $T_p > T_g$. The slope of the Sub-EE straight lines is constant and only varies with T_p. It is called T_c'. See later.

EBSCOhost - printed on 2/13/2023 12:32 AM via . All use subject to https://www.ebsco.com/terms-of-use

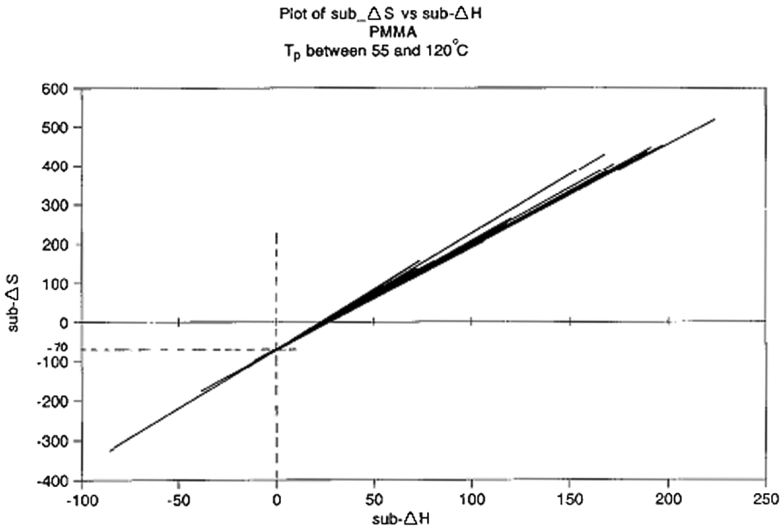


Figure 2.22: Plot of sub-$\Delta S(T_p)$ vs. sub-$\Delta H(T_p)$ for all T_p from 55 °C to 120 °C. The unique compensation corresponds to sub-$\Delta H_c = 0$ and sub-$\Delta S_c = \Delta S_{o,h} = -70$ cal/°C.

Figure 2.19 applies to $T_p = 65$ °C, Figure 2.20 shows three temperatures $T_p = 55$°, 90 °C, and 120 °C, and Figure 2.21 and 2-22 provide the full spectrum of sub-EE curves for the entire T_p span. Notice in Figure 2.19 that a sub-EE curve does not resume to a single point, which would have been the case had the relationship between free energy and temperature be perfectly linear. As expected, we observe in Figure 2.19 a linear correlation between the sub-ΔS and sub-ΔH calculated from the intercept and slope of the tangent to the relaxation curve.

We study in Figures 2.23 and 2.24 the variation of the apparent sub-ΔS with temperature for $T_p = 60$ °C and 120 °C, respectively. One observes a periodic fluctuation of the apparent sub-ΔS around an average value ΔS_{av}, which corresponds to the value calculated by regressional fit over the whole temperature range, ΔS_p. Hence the points which line up on a sub-EE curve, Figure 2.19, are not disposed in successive order along the curve, as temperature increases. The fact that the apparent sub-ΔH and sub-ΔS are linearly related is expected from the way we define the tangent to the curve by two parameters (slope and intercept) instead of just one. In fact, a plot of sub-ΔH vs. T (not shown) looks identical to that of sub-ΔS vs. T, only the scale changes.

A plot of ΔG vs. temperature, e. g., Figure 2.6, can be obtained from either [ΔG = (sub-ΔH) – T(sub-ΔS)] or from equation (2.3). (Note, in passing, that the small difference between the two calculations of ΔG would give us a good indication of how good our algorithm for the derivative is!)

EBSCOhost - printed on 2/13/2023 12:32 AM via . All use subject to https://www.ebsco.com/terms-of-use

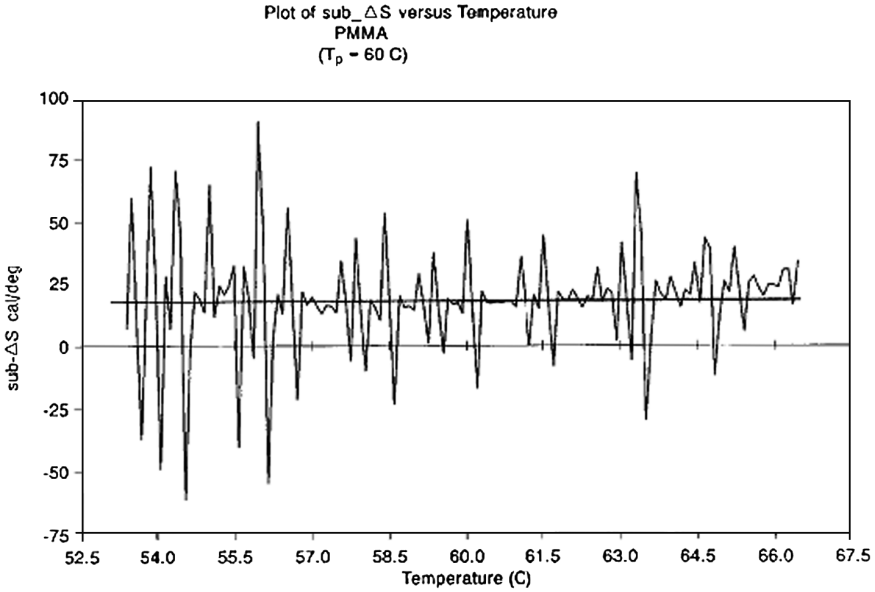


Figure 2.23: Plot of sub-$\Delta S(T_p)$ vs. T for $T_p = 60$ °C. The signal shows a fluctuation around a mean value equal to ΔS_p at that T_p.

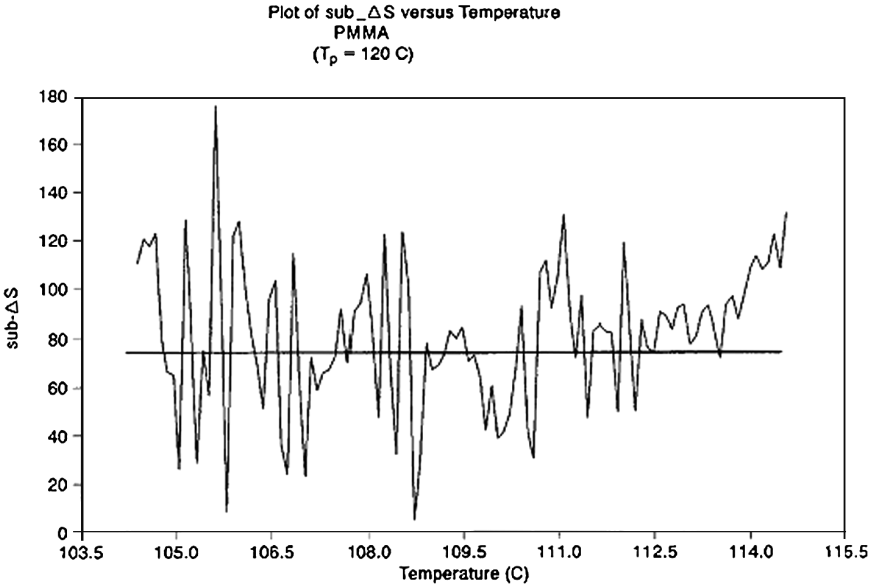


Figure 2.24: Plot of sub-$\Delta H(T_p)$ vs. T for $T_p = 120$ °C. The signal shows a fluctuation around a mean value equal to ΔS_p at that T_p. The fluctuation varies with T_p, but is the same for sub-ΔH and sub-ΔS for a given T_p, explaining the compensation line in Figure 2.20.

EBSCOhost - printed on 2/13/2023 12:32 AM via . All use subject to https://www.ebsco.com/terms-of-use

One sees in Figure 2.22 that the set of straight lines compensates into a point which is located on the sub-$\Delta H = 0$ axis at –70 cal/°C/m. It is not certain that the intercept is exactly on the 0 enthalpy axis. It might be converging to a point of low enthalpy value, which might have some meaning (the discussion is beyond the scope of this chapter). Table 2.3 gives the value of the slope and intercept of the sub-EE curves of Figure 2.21 with T_p changing between 55 °C and 120 °C.

Table 2.3: Values of the slope and intercept of the straight lines in Figure 2.21 as a function of T_p varying across T_g from 55 °C to 120 °C. See text for the meaning of the column headers.

T_p (°C)	T_m (°C)	T_c' (°C)	Slope	log(τ)	r^2
55.0	65.0	54.9	–1.535	35.075	0.9998702
60.0	68.3	56.6	–1.528	35.233	0.9998748
65.0	73.1	65.1	–1.489	34.777	0.9998525
70.0	77.9	65.0	–1.489	35.472	0.9998845
75.0	82.5	73.7	–1.452	34.936	0.9998932
80.0	87.6	77.5	–1.437	35.181	0.9998989
85.0	92.6	84.7	–1.407	34.850	0.9999441
90.0	96.6	89.1	–1.390	34.913	0.9999461
95.0	101.0	93.9	–1.372	34.941	0.9999344
100.0	105.3	100.7	–1.347	34.435	0.9999710
105.0	107.1	102.7	–1.340	34.444	0.9999812
110.0	110.1	103.4	–1.338	35.993	0.9999659
115.0	120.2	109.6	–1.316	35.341	0.9999334
120.0	114.6	107.7	–1.322	36.006	0.9999389

The third column of Table 2.3 relates to a temperature T_c' (which we calculate from the slope of the sub-EE curve), so in effect $T_c' = [\text{sub-}\Delta H/\text{sub-}\Delta S]$, and which increases with the temperature of polarization T_p. The fifth column is the intercept of the sub-EE lines plotted as $-(\text{sub-}\Delta S)/R$ vs. (sub-ΔH).

Figure 2.25 is a compensation search to determine the best set of coordinates for the sub-EE curves compensation point. The best compensation point is obtained with a simplex regressional analysis, from the slope and intercept of the best regression line passing through the data points in Figure 2.25. The best regression line is *not* exactly a horizontal line, but it is very close to it, hence we have drawn in Figure 2.25 the best horizontal line passing through the data. We find $(\text{sub-}\Delta H)_c = 0$ and $(\text{sub-}\Delta S)_c = -69.84 = 1.987 \cdot 35.15$ cal/deg/m (the "1.987" comes from the gas constant).

Alternatively, one could also consider two temperature zones, one below and one above T_g, and find $(\text{sub-}\Delta H)_c$ different from zero for both zones. In such a case, $(\text{sub-}\Delta S)_c$ is larger than –69.84 for $T_p < T_g$ and smaller than –69.84 above T_g. We have observed that $(\text{sub-}\Delta S)_c$ is almost equal to the value found for $\Delta S_{o,h}$ (equation (2.14)).

EBSCOhost - printed on 2/13/2023 12:32 AM via . All use subject to https://www.ebsco.com/terms-of-use

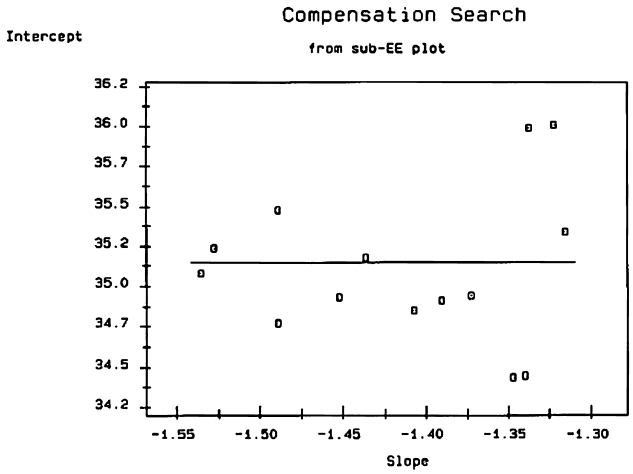


Figure 2.25: Compensation search (intercept vs. slope) for the determination of the compensation point in Figure 2.21 as T_p varies across T_g.

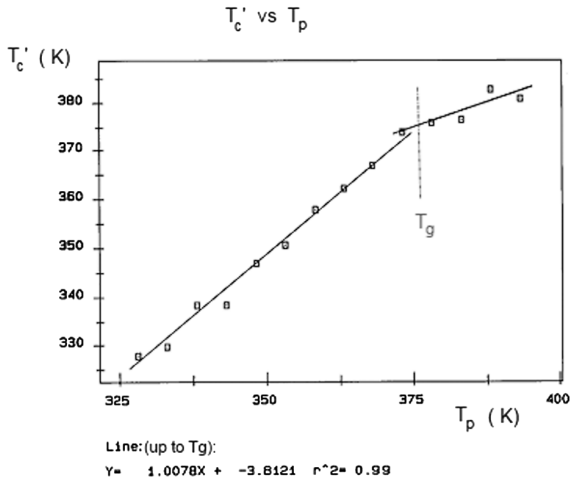


Figure 2.26: Plot of T_c' vs. T_p from the values of Table 2.3. T_c' is defined by (sub-ΔH/sub-ΔS).

Figure 2.26 is a plot of T_c' vs. T_p from the values of Table 2.3. Two temperature zones across T_g are clearly visible. It seems that for $T < T_g$, $T_c' = T_p$ (or actually $(T_p + T_d)/2$) with good accuracy.

The slope is approximately 0.5 above T_g.

Before going into the discussion section and explaining all these "compensation features," let us first quickly explain why ΔG versus temperature does not show any fluctuation, although sub-ΔS and sub-ΔH both vary with temperature with a certain amount of "noise."

Intuitively, this can be explained by the fact that both sub-ΔH and sub-ΔS are issued from a single quantity, the tangent to the ΔG-T curve. In quantitative terms, if we describe the "noise" with a sine function, the cancelation of the fluctuating terms in

EBSCOhost - printed on 2/13/2023 12:32 AM via . All use subject to https://www.ebsco.com/terms-of-use

the expression of ΔG is clear:

$$\begin{aligned} \Delta G &= (\text{sub-}\Delta H) - T \cdot (\text{sub-}\Delta S) \\ \text{sub-}\Delta H &= \Delta H_{\text{av}} + \Delta H_f \cdot \sin(2\pi f_h \cdot t) \\ \text{sub-}\Delta S &= \Delta S_{\text{av}} + \Delta S_f \cdot \sin(2\pi f_s \cdot t) \end{aligned} \tag{2.22}$$

with

$$\{\Delta H_f \cdot \sin(2\pi f_h \cdot t) - T \cdot \Delta S_f \cdot \sin(2\pi f_s \cdot t)\} = 0$$

so

$$\begin{aligned} &(\Delta H_f - T \cdot \Delta S_f) \cdot \sin(2\pi f \cdot t) = 0, \\ &\Delta G = \text{sub-}\Delta H - T \cdot \text{sub}\Delta S = \Delta H_{\text{av}} - T \cdot \Delta S_{\text{av}} \end{aligned} \tag{2.23}$$

with

$$\Delta H_{\text{av}} = \Delta H_p, \quad \text{and} \quad \Delta S_{\text{av}} = \Delta S_p$$

Figure 2.27 is a plot of $[(\text{sub-}\Delta H - \Delta H_p)/(\text{sub-}\Delta S - \Delta S_p)]$ against temperature for $T_p = 60$ °C. The slope of the straight line in this figure is 1.0, indicating that sub-$\Delta G(T)$ equals ΔG for the whole depolarization curve.

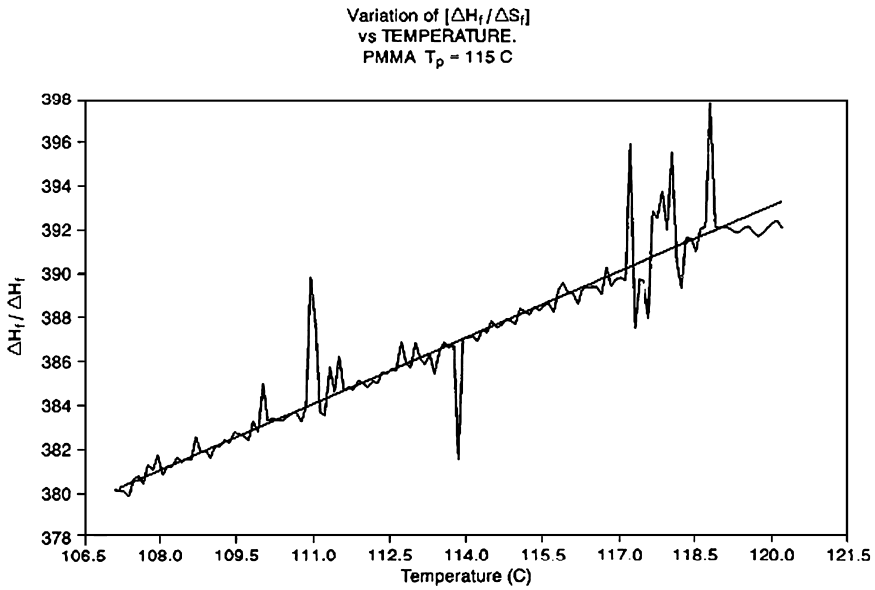


Figure 2.27: Plot for $T_p = 60$ °C of $(\text{sub-}\Delta H - \Delta H_p)/(\text{sub-}\Delta S - \Delta S_p)$ vs. T during the depolarization stage.

EBSCOhost - printed on 2/13/2023 12:32 AM via . All use subject to https://www.ebsco.com/terms-of-use

I.2.10 Normalization of the $\Delta G - T$ curves. Discussion

In the calculation of the temperature-dependent apparent activation entropy and enthalpy, sub-ΔS and sub-ΔH, the fluctuation (noise) around the mean value is probably the result of normal random errors due to the digitizing of the temperature and current variables. The observation that the sub-EE plots compensate and that their slope is practically equal to T_p ($T_c' = T_p$) indicates that we should be interested in normalizing the ΔG versus temperature curves, both on the vertical and horizontal axes. It actually suggests normalizing the ΔG axis by dividing it by T_p and the temperature axis by using $(T - T_p)$ instead of T or T_p. Such a plot is shown in Figure 2.28 for $T_p = 110$ °C and in Figures 2.29 and 2.30 for several polarization temperatures, respectively below and above T_g.

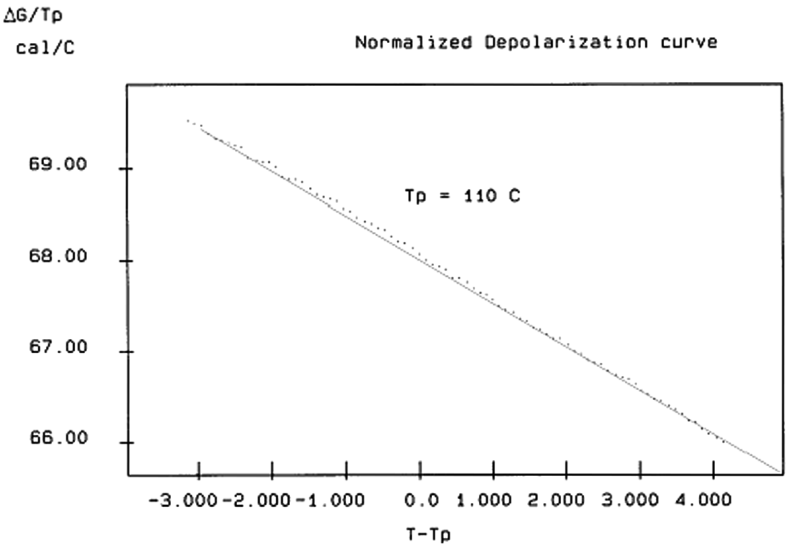


Figure 2.28: Normalized depolarization curve at T_p: $\Delta G/T_p$ vs. $(T - T_p)$. The polymer is PMMA.

We observe (Figures 2.29 and 2.30) that the normalized ΔG relaxation curves compensate. For instance, Figure 2.29 shows the compensation for the polarization temperatures below T_g (T_p between 60 °C and 100 °C). The point of convergence of all these normalized lines can be calculated with a compensation search using a simplex regression routine, as is normally done with the relaxation map. We find that the normalized thermokinetic relaxation lines converge to a point very near the $[T - T_p] = 0$ axis (the real value is $\delta_c = [T - T_p]_c = -1.18$ °C) for a value of $[\Delta G/T_p]_c = A_c = 68.72$ cal/°C.

EBSCOhost - printed on 2/13/2023 12:32 AM via . All use subject to https://www.ebsco.com/terms-of-use

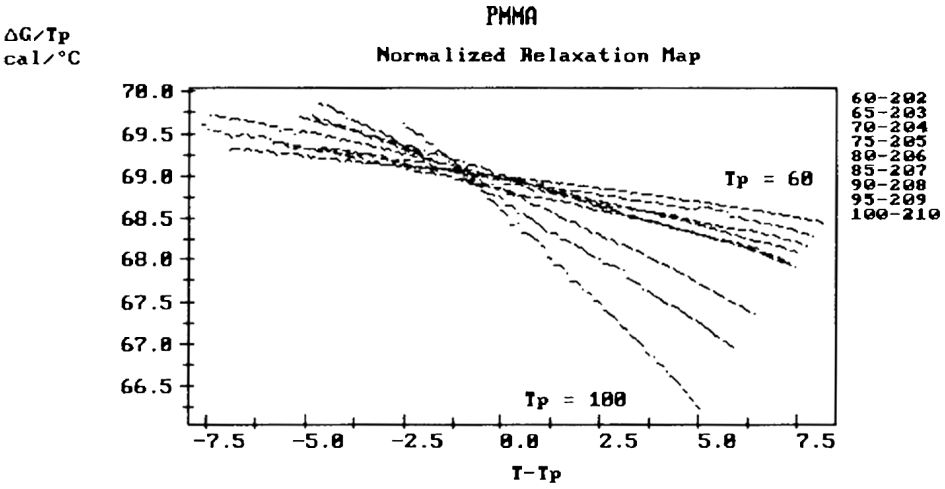


Figure 2.29: Normalized relaxion map for all T_p below T_g using the normalization variables of Figure 2.28 (PMMA).

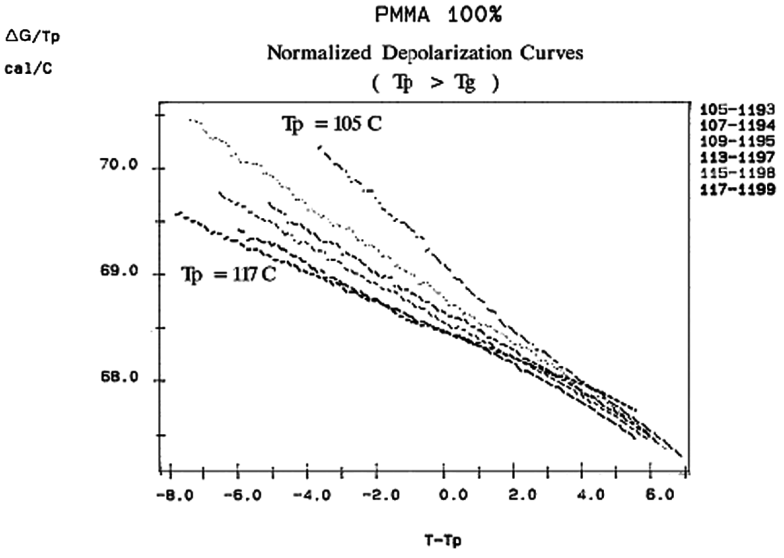


Figure 2.30: Normalized relaxion map for all T_p above T_g using the normalization variables of Figure 2.28.

The normalized ΔG relaxations for the T_p above T_g (Figure 2.32) also compensate (A_c = 67.53 cal/°C; δ_c = 5.74 °C), although we have also been able to observe for other systems and for higher T_ps ($T_p > T_{LL}$) that the normalized lines become parallel to one another, implying that the effect of polarization changes from a compensation phenomenon to a superposition of the relaxation curves above T_{LL} [135].

EBSCOhost - printed on 2/13/2023 12:32 AM via . All use subject to https://www.ebsco.com/terms-of-use

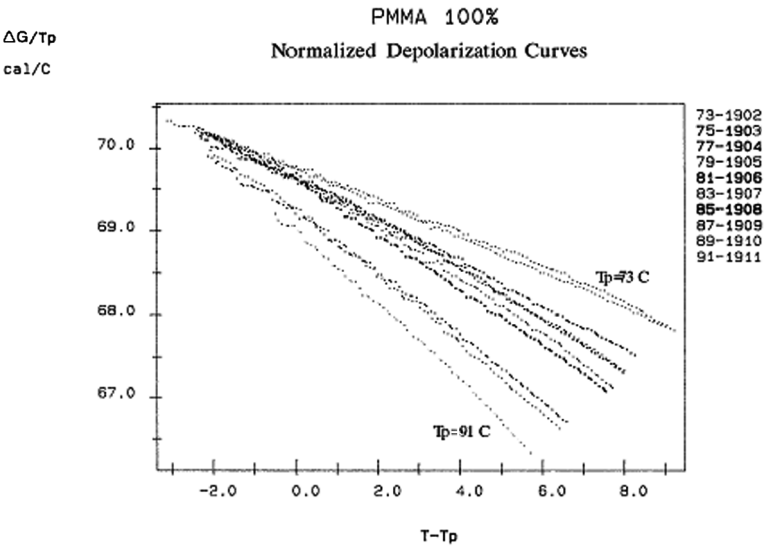


Figure 2.31: Normalized relaxation map similar to the one in Figure 2.29 for a different PMMA. $T_p < T_g$.

In Figure 2.31 is shown another PMMA system, with different thermal history, analyzed below T_g (T_p varies between 73 °C and 91 °C here). We find $A_c = 70.41$ cal/°C; $\delta_c = -2.98$ °C.

These results are quite spectacular, and although they have not been investigated for enough systems, they seem to be quite general and descriptive of the different inner mechanism of the action of the voltage field below and above T_g and beyond T_{LL}. The convergence of the normalized $(\Delta G/T_p)$ depolarization curves occurs for $T = T_p$ or slightly less than T_p, perhaps $(T_p + T_d)/2$. The intercept $(\Delta G/T_p)_c$ is equal or close to the 70 cal/deg which we found for the mirror of the compensation of the sub-EE lines. This explains why we find ΔG_p linearly related to T_p (Figure 2.15), with, as commonly observed, zero intercept and a slope equal to 70 cal/deg for the T_ps below T_g, as reported previously (equation (2.13a)).

I.2.10.1 Expression of the entropy ΔS_p vs. T_p

The equation of the $\Delta G/T_p$ normalized curves can be rewritten:

$$\Delta G/T'_p = A_c - \Delta S_p/T'_p(T - T'_p) \tag{2.24}$$

If we call $T'_p = (T_p + \delta_c)$, now, the ΔG vs. T lines also converge to a compensation point, $[T_c, \Delta G_c]$. For instance, for the PMMA data of Figure 2.31, which correspond to the T_ps of the positive compensation in Figure 2.18, $T_c = 127.96$ °C, $\Delta G_c = 22.11$ kcal/m.

EBSCOhost - printed on 2/13/2023 12:32 AM via . All use subject to https://www.ebsco.com/terms-of-use

The equation of the ΔG vs. T lines can be written as a function of the coordinates of the compensation point coordinates:

$$\Delta G = \Delta G_c - \Delta S_p(T - T_c) \tag{2.25}$$

so

$$\Delta G/T'_p = \Delta G_c/T'_p - \Delta S_p/T'_p(T - T_c) \tag{2.26}$$

Combining (2.24) and (2.26) yields

$$\Delta S_p = (\Delta G_c - A_c T'_p)/(T'_p - T_c) \tag{2.27}$$

This expression indicates that the entropy of activation for the depolarization curves polarized at temperature T_p, ΔS_p, varies with T_p as a hyperbolic function. The temperature which renders the entropy of activation infinite is $T'_p = T_c$, i. e., for T_p slightly off the value of the compensation temperature T_c. This is an important result, shining light on the meaning of the temperature T_c: *T_c is the temperature at which the entropy of interactive coupling between the dipoles becomes infinite*.

From equation (2.27), one can calculate the temperature T_p for which ΔS_p is zero, perhaps indicating the beginning of coupling of the dipoles. If T_β is such a temperature,

$$T'_\beta = \Delta G_c^+/A_c \tag{2.28a}$$

or

$$(T_p)_\beta = (\Delta G_c^+/A_c) - \delta_c \tag{2.28b}$$

and

$$(\Delta H_p)_\beta = \Delta G_c^+$$

For instance, for the PMMA sample of Figure 2.31, $\Delta G_c = 22.11$ kcal/m, $A_c = 68.75$ cal/°C; therefore, $T_\beta = 322.8$ K, i. e., 49.6 °C. Interactive coupling in the glassy state, for PMMA, would start as low as 50 °C below T_g and culminate at T_c if such a temperature could be reached with the same mechanism of coupling the dipoles. Above T_g, the association between the dipoles seems to be governed by other coupling laws. The negative compensation of the $\Delta G - T$ relaxations above T_g (Figure 2.18), with compensation point coordinates $[\Delta G_c^-, T_c^-]$, corresponds to a compensation in the normalized plane (Figure 2.32) with apparently the same or not very different A_c, but different δ_c (T_p offset). Above T_{LL}, there seems to be no compensation of the relaxation data neither in the ΔG plane nor in the normalized $\Delta G/T_p$ plane, where the depolarization curves superpose horizontally instead. This needs to be confirmed, in

EBSCOhost - printed on 2/13/2023 12:32 AM via . All use subject to https://www.ebsco.com/terms-of-use

the future, for other systems and for larger temperature spans. In particular, is there a difference observed, in that regard, between samples below M_c and above M_c, with M_c being the molecular weight for entanglement?

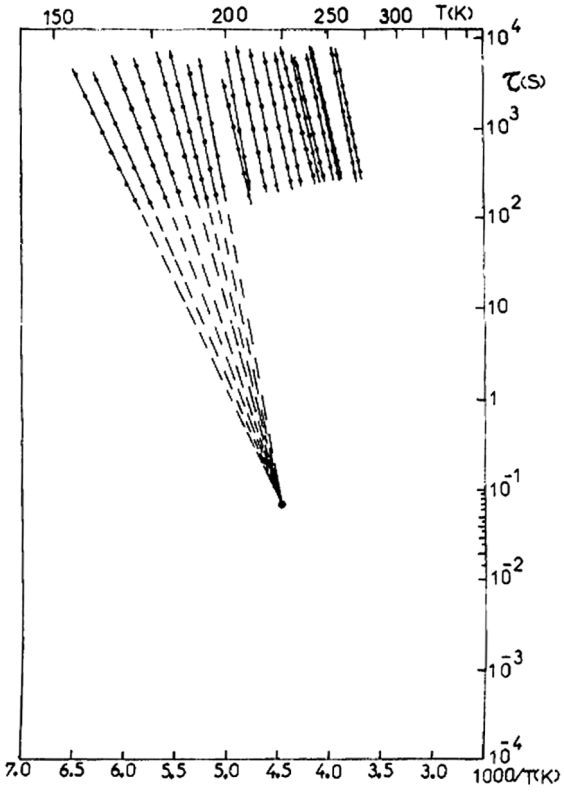


Figure 2.32: Relaxation map in the Arrhenius plane for PTMG 2000 (after Faruque, [77]). The data are in Table 2.4.

The entropy ΔS_p varies with T_p above T_g according to (2.27), with the appropriate values of ΔG_c, T_c, δ_c, and A_c. The negative compensation coordinates should be used in (2.27). If A_c is taken to be identical below and above T_g, which is not true for PMMA according to Fig. 2.26, we can calculate T_p for which $\Delta S_p = 0$ in this expression. We call this temperature T_{LL}:

$$T'_{LL} = \Delta G_c^- / A_c^- \tag{2.28}$$

or

$$(T_p)_{LL} = (\Delta G_c^- / A_c^-) - \delta_c^-$$
$$(\Delta H_p)_{LL} = \Delta G_c^-$$

EBSCOhost - printed on 2/13/2023 12:32 AM via . All use subject to https://www.ebsco.com/terms-of-use

These formulas are identical to (2.28a) for the calculation of $(T_p)_\beta$ and $(\Delta H_p)_\beta$, but for the negative compensation. The temperature $(T_p)_{LL}$ marks the end of coupling above T_g. For PMMA analyzed here, we find 414 K, i. e., 141 °C, and 28.5 Kcal/m. Also note that the value of the enthalpy of activation at T_β and T_{LL} is not very dissimilar, by a few kilocalories, in contrast to the value found for T_g, which is typically 3 to 4 times larger. We will show in Chapter 3 of Part I how to fine tune the value of T_{LL} for PMMA since, as we said, A_c is different below and above T_g for this amorphous polymer.

Equation (2.27) can be written differently:

$$-Ac + (\Delta G_c - A_c T_c)/(T_p' - T_c) \tag{2.28c}$$

This expression shows that the other asymptote is $-A_c$, which is approximately −70 for both the positive and negative compensations, and explains why we said for the DOD number definition that it would be preferable to add 70, instead of 100, to the value of the entropy.

For the PMMA of Figures 2.32 and 2.33, which correspond to the normalized depolarizations for respectively the negative and positive compensations for a PMMA with the same thermal history, let us calculate the value of $(\Delta G_c - A_c \cdot T_c)$, i. e., the numerator in equation (2.28a):

$$\begin{aligned}(\Delta G_c - A_c \cdot T_c)^+ &= -5.446\,\text{kcal/m}\\ (\Delta G_c - A_c \cdot T_c)^- &= 5.272\,\text{kcal/m}\end{aligned} \tag{2.28d}$$

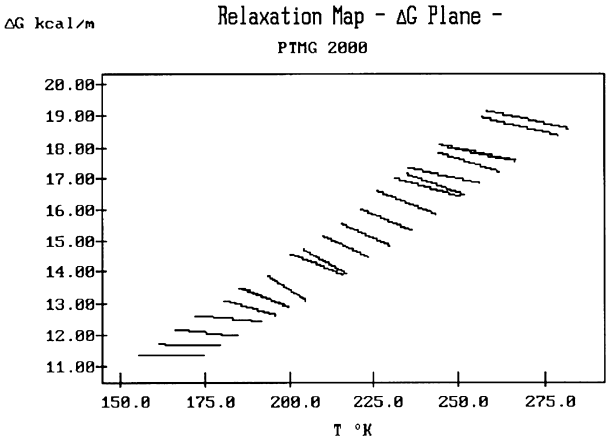


Figure 2.33: Relaxation map in the ΔG plane for the data of Table 2.4.

At first approximation, these two quantities have the same absolute value, 5.360 cal/m. This might be significative of the mechanisms responsible for coupling on both sides of T_g. See Chapter 3 of Part II to refine this conclusion.

EBSCOhost - printed on 2/13/2023 12:32 AM via . All use subject to https://www.ebsco.com/terms-of-use

T_g is obtained by equating the value of ΔS_g in equation (2.28c):

$$T_g = T_c^- - \delta_c^- + \frac{(\Delta G_c^- - A_c T_c^-)}{(\Delta S_g + A_c)}$$

$$T_g = T_c^- - \delta_c^- + \frac{(\Delta G_c^- - A_c T_c^-)}{(\Delta S_c + A_c^-)}$$

or else by elimination of ΔS_g between the two hyperbolas. This provides a quantitative calculation of T_g when the coordinates of the compensation points are known.

It is important to stress that the observed maximum of entropy of activation corresponds in fact to the intercept of two hyperbolas crossing at T_g, where there is interruption of a certain mode of coupling and the switching to another mechanism.

Another important conclusion arises from the observation that the spread ($T_g - T_c$), which we said earlier is related to the measurement of the internal stress in the material, is proportional to ($\Delta G_c - A_c \cdot T_c$). A possible explanation is that ($\Delta G_c - A_c \cdot T_c$) represents a potential energy gap which can be affected by thermomechanical or thermoelectrical history. At this stage, any comment or conclusion on the meaning of this finding would be pure speculation. A large number of polymeric systems must be elucidated with the intention to determine ($\Delta G_c - A_c \cdot T_c$) with great accuracy before any quantitative conclusion can be drawn from the previous result (some examples will be provided in tables of Chapter 4, Part II). The theoretical development of TWD in terms of the Dual-Phase model presented in Chapter 3, Part I will permit to conclude about the meaning of these considerations involving A_c (mechanism 2 of the grid-network).

I.2.10.2 Expression of the enthalpy ΔH_p vs. T_p

Rewriting the compensation law in the EE plane,

$$\Delta H_p = \Delta G_c + T_c \cdot \Delta S_p \tag{2.29}$$

and substituting the expression of ΔS_p into equation (2.27),

$$\Delta H_p = \frac{T_p'(\Delta G_c - A_c T_c)}{(T_p' - T_c)} \tag{2.30}$$

which can also be rewritten as follows:

$$\frac{T_p' T_c}{(T_p' - T_c)}(\Delta G_c / T_c - A_c) \tag{2.30a}$$

For instance, $(\Delta G_c - A_c \cdot T_c)/T_c$ equals –0.013615 for the positive compensation and 0.012559 for the negative compensation.

EBSCOhost - printed on 2/13/2023 12:32 AM via . All use subject to https://www.ebsco.com/terms-of-use

$\Delta H_p = 0$ for $T'_p = 0$, and from (2.27), $\Delta S_p = -(\Delta G_c/T_c)$. This is the value of the DOD number, without the 100 added to it (equation (2.18)). This demonstrates, once again, that the DOD number describes fundamental characteristics of the state of the polymeric system in the glassy temperature region.

I.2.10.3 Expression of the free energy ΔG vs. T_p

For a given T_p, the depolarization free energy can be written

$$\Delta G = \Delta G_c + (T_c - T) \cdot \Delta S_p \tag{2.31}$$

and substituting from (2.27),

$$\Delta G = \Delta G_c + (T_c - T)\frac{(\Delta G_c - A_c T'_p)}{(T'_p - T_c)} \tag{2.31a}$$

The value of ΔG at T'_p, which is slightly off T_p, can easily be calculated:

$$\Delta G'_p = \Delta G_c - (\Delta G_c - A_c \cdot T'_p) = A_c \cdot T'_p \tag{2.32}$$

This is a remarkable result. The free energy at T_p is independent of the coordinates of the compensation point, or even the type of compensation when A_c is identical for both the positive and negative compensations. This explains why the free energy of activation crosses T_g without passing through a maximum, unlike ΔH_p and ΔS_p. A good verification of equation (2.32), when $T_p = T'_p$, is given in Chapter 4 in Part II in the study of liquid crystals (Figure 4.29). In other cases, A_c is different below and above T_g. Examples of this kind of behavior will be presented in Chapters 3 of Part I, 3 and 4 of Part II.

I.2.10.4 Discussion

If we think of $(\Delta G/T_p)$ as a quantity related to the interactive coupling between the dipoles, coupling below T_{LL} seems to occur with a change of the way the voltage field influences the potential energy barrier responsible for coupling. Interactive coupling above T_{LL} does not seem to exist (the lines are parallel). In essence, this means that the voltage field modifies the value of the potential energy barrier below T_{LL}, to an extent which depends on T_p; this would explain the existence of compensations observed below T_{LL}. Polarization of the dipoles above T_{LL} would not involve a modification of the potential energy barrier of the conformers. From T_β to T_{LL}, passing through a scale change at T_g, interaction between the dipoles would occur by a purely energetic kinetic mechanism which is slightly modified by the voltage field, thus creating

EBSCOhost - printed on 2/13/2023 12:32 AM via . All use subject to https://www.ebsco.com/terms-of-use

the compensation phenomena observed. This is fully explained in the next chapter by the Dual-Phase model of the interactions.

Above T_{LL}, the sole voltage role is to excite the dipoles off their equilibrium position, and thermal stimulation depolarizes the dipoles, which occurs without their interaction: the properties of uncoupled Debye relaxations are revealed above T_{LL}. Below T_{LL}, both above and below T_g, the voltage interferes with the potential energy barrier between the conformers carrying the dipoles. In essence, the voltage not only excites the dipoles off their equilibrium position, but also modifies the free energy structure responsible for the dissipative features observed upon cooling or heating. Compensations exist because of the perturbation of the potential energy barrier by the voltage field (Part I, Chapter 3, equation (3.7)). Two types of compensation exist because of the change of scale across T_g that modify the value of Δ_m, $\mathrm{Ln}(\upsilon_m)$ in the master compensation plot of $\mathrm{Ln}(\tau_o)_p$ vs. ΔH_p describing the Dual-Phase thermokinetic parameters $(\mathrm{Ln}(\upsilon_x), \Delta_x)$. See Chapter 3. Under certain circumstances (Part II, Chapter 4), it is even possible to observe as many as three to six compensations from T_β to T_{LL}. A possible interpretation of the results is presented in Chapter 3 of this Part I.

I.2.10.5 Conclusion

Compensation phenomena, below T_g and above T_g, have the same common origin, although they might represent different thermokinetic solutions to the problem of interactive coupling between dipoles.

The entropy of activation ΔS_p raises hyperbolically from 0 at T_β to infinity at T_c, but cannot reach T_c, because at T_g begins another mechanism of interactive coupling involving a different scale: the energetic kinetic systems start to modulate the kinetics above T_g.

Below T_g, the temperature T_p at which the free energy is equal to ΔG_c^+, i. e., for which $\Delta S_p = 0$, marks the beginning of interactive coupling. Above T_g, the temperature T_p for which $\Delta S_p = 0$ corresponds to the end of interactive coupling, i. e., what is defined as T_{LL} in Chapter 3. For this temperature T_p, the free energy ΔG_p is equal to ΔG_c^-. It is possible to calculate the value of T_{LL} from a relaxation map by extrapolation of the ΔG_p vs. T_p plot [135].

In Chapter 3 we show that the transitions T_β, T_g, and T_{LL} are related and originate from the duality and cross-duality of the interactions between the conformers and the free volume. Equations (2.28a) and (2.28b) and the equations of T_g can be rewritten to quantify the interdependence. By the same token, the formula for the enthalpy and entropy of activation can be rewritten in terms of T_c^+, T_c^-, T_β, T_g, and T_{LL}.

EBSCOhost - printed on 2/13/2023 12:32 AM via . All use subject to https://www.ebsco.com/terms-of-use

I.2.11 Characterization of the amorphous phase in semi-crystalline polymers by TWD spectroscopy

Analysis of semi-crystalline polymers by TWD can provide detailed information that is complementary to, yet can hardly be matched by, any other single analytical technique. This section will discuss (i) the use of TWD and of the corresponding relaxation maps in characterizing the amorphous phases in semi-crystalline polymers and (ii) the influence of the degree of orientation on the state of the amorphous material. Three semi-crystalline polymers will be considered as examples: polytetramethylglycol of low molecular weight (M_n = 2035), polyamide 12, and drawn or undrawn polypropylene.

I.2.11.1 PTMG 2035

The data considered here are chosen in the literature [77–79, 82] and reanalyzed with the concepts studied earlier in this chapter. In all the examples presented, the original data were in the form of tables of values of [τ_o, ΔH] obtained from the slope and intercept of the Arrhenius transforms.

Figure 2.32 is an example of the original plot for the relaxation map of polytetramethylglycol (PTMG 2000). The table of data is obtained from the original thesis of Faruque [77] and is reproduced in Table 2.4.

The polarization temperature varies between –105 °C and 0 °C, encompassing two transition zones: the T_g transition and the T_α process generally associated with motions within the semi-crystalline texture. The relaxation map shown in Figure 2.32 presents a compensation characteristic for the low T_ps and a series of quasi-parallel Arrhenius lines covering the temperature region between –70 °C and 0 °C. In the following study, we have proceeded as follows: the constants τ_o and ΔH obtained from Table 2.4 are reintroduced into a Debye equation (equation (2.20)) to generate the curve-fitted Debye peak for each polarization T_p. The peak is then analyzed as described in this chapter to determine the entropy and enthalpy of activation according to the Eyring formula. The activation energy ΔG is calculated at each temperature, for a given T_p, from equation (2.2). A plot of the relaxation map in the ΔG plane is shown in Figure 2.33. The plot consists of a series of straight lines, the slope in this figure being the representation of the entropy, whereas a plot in the Arrhenius plane produces a representation of the slope as the enthalpy.

Figures 2.34 and 2.35 display the reconstructed Debye peaks calculated for the values of τ_o and ΔH isolated from TWD.

EBSCOhost - printed on 2/13/2023 12:32 AM via . All use subject to https://www.ebsco.com/terms-of-use

Table 2.4: Analysis of the data of Faruque [77] in the Arrhenius plane giving the values of ΔH and τ_o for PTMG 2000 for T_p varying between −105 °C and 0 °C.

T_p (°C)	τ_o (sec.)	ΔH (eV)	T_m (°C)
−105	4.7×10^{-13}	0.55	−96
−100	3.3×10^{-14}	0.54	−92
−95	2.8×10^{-16}	0.63	−86
−90	6.4×10^{-16}	0.64	−82
−85	4.7×10^{-21}	0.85	−78
−80	1.3×10^{-22}	0.93	−74
−75	1.2×10^{-23}	0.97	−70
−70	4.7×10^{-29}	1.21	−66
−65	1.7×10^{-23}	1.04	−60
−60	6.9×10^{-27}	1.19	−57
−55	2.1×10^{-24}	1.12	−49
−50	1.2×10^{-24}	1.16	−41
−45	6.6×10^{-24}	1.16	−30
−40	3.9×10^{-23}	1.16	−29
−35	1.4×10^{-20}	1.07	−22
−30	1.7×10^{-22}	1.17	−19
−25	6.9×10^{-19}	1.01	−18
−20	1.5×10^{-21}	1.17	−12
−15	7.5×10^{-19}	1.05	−6
−10	1.1×10^{-18}	1.04	−5
−5	1.9×10^{-19}	1.13	5
0	3.1×10^{-19}	1.13	7

Original data. Table for PTMG 2000, activation energy ΔH and τ_o for the Arrhenius transforms obtained by thermal-windowing.

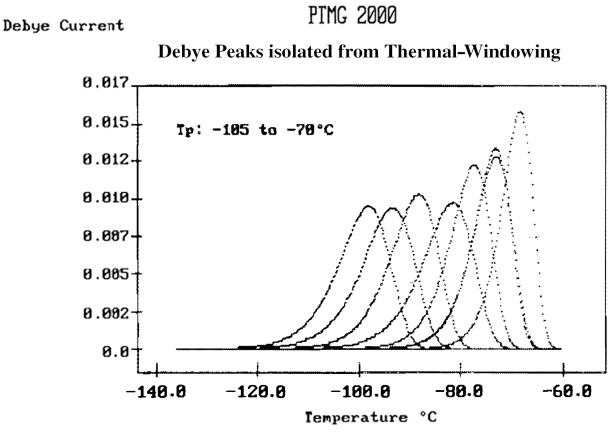


Figure 2.34: TWD Debye peaks for $T_p < -70$ °C recalculated from Table 2.4.

EBSCOhost - printed on 2/13/2023 12:32 AM via . All use subject to https://www.ebsco.com/terms-of-use

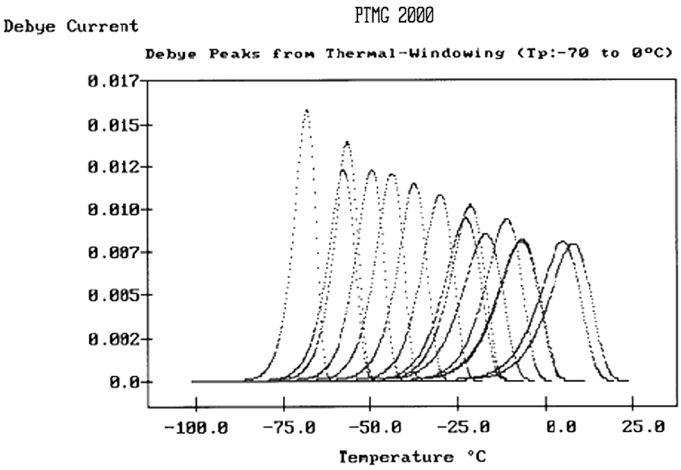


Figure 2.35: TWD Debye peaks for $T_p > -70$ °C recalculated from Table 2.4.

Figure 2.34 concentrates on the elementary Debye peaks for the T_g relaxation process and Figure 2.35 applies to the T_α process for which T_p is chosen between –70 °C and 0 °C. An interesting observation concerns the displacement of the temperature peaks along the temperature axis in a manner which seems to directly depend on the temperature of polarization (this observation is analyzed in depth in Chapter 2). One also sees that the peak maximum amplitude varies with the polarization temperature. For instance, the peak amplitude seems to increase as T_p approaches T_g, yet decrease from T_g on for the T_α process (Figure 2.35). The variable plotted in Figure 2.34 and Figure 2.35 is the "Debye current," which is the simulated current calculated from the Debye equation assuming $P_{so} = 1$. In other words, we are comparing Debye functions with different $[\tau_o, \Delta H]$ characteristics without any consideration for the number of dipoles which were activated during the excitation stage at T_p. One sees that the Debye characteristics vary with the polarization temperature and that tendencies for the width and height of the Debye peaks are seemingly following the occurrence of transitions or specific relaxation processes in the material. As a first approximation, it appears that the relaxation process leading to the T_g transition (Figure 2.34) can be characterized by both a shift of the Debye peaks and a thinning of the peaks as T_p approaches T_g. This is coupled with a decrease of the half-width of the peak along with an increase of its peak maximum intensity at T_g. The T_α process, on the contrary, seems to display a flattening and broadening of the elementary Debye peaks as T_p moves towards higher temperatures (Figure 2.35).

Figure 2.36 is an EE plot for PTMG 2000 with a compensation line drawn passing through the lower polarization temperatures, as the dots appearing on the right-hand side of the legend indicate. The compensation line slope and intercept provide the coordinates of the compensation point, indicative of a coupling between the relaxation

EBSCOhost - printed on 2/13/2023 12:32 AM via . All use subject to https://www.ebsco.com/terms-of-use

modes isolated by the thermal-windowing process. Many other points of the EE plot, representative of the $T > -70\,°C$ temperature range, are seemingly dispersed in a disordered way with no apparent compensation phenomena emerging from the position of the points. These points are representative of the relaxation modes occurring in the relaxation temperature range where the T_α process occurs.

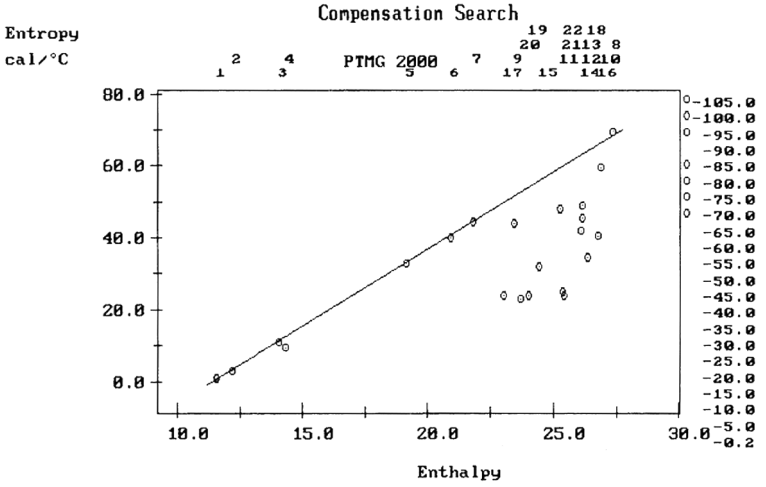


Figure 2.36: Compensation search $\Delta S_p(T_p)$ vs. $\Delta H_p(T_p)$ for the data in Table 2.4. The small numbers above the graph relate to the row position in Table 2.4 starting with 1 for $T_p = -105\,°C$. The numbers at the top correspond vertically to the points on the graph.

We find for the compensation point

$$T_c = -40.78\,°C$$
$$\Delta G_c = 11.42\,\text{kcal/m}$$
$$\text{DOD} = 50.86$$

The compensation phenomenon is displayed in Figure 2.37.

Notice that the lower relaxation mode, corresponding to $T_p = -105\,°C$, gives a horizontal line with zero entropy, which would locate the β transition for this material at approximately this temperature of –105 °C.

In Figure 2.38, we plot the temperature found for the maximum of the Debye peak (Figures 2.34 and 2.35) against the temperature of polarization T_p. A linear relationship with slope 1 is observed all the way from the T_β transition across the T_g transition and the T_α process. This observation led us to conclude earlier in this chapter that the action of the voltage field at the polarization T_p was to modify the free energy in a manner which primarily influenced the relaxation process at T_p. See section I.2.10.

EBSCOhost - printed on 2/13/2023 12:32 AM via . All use subject to https://www.ebsco.com/terms-of-use

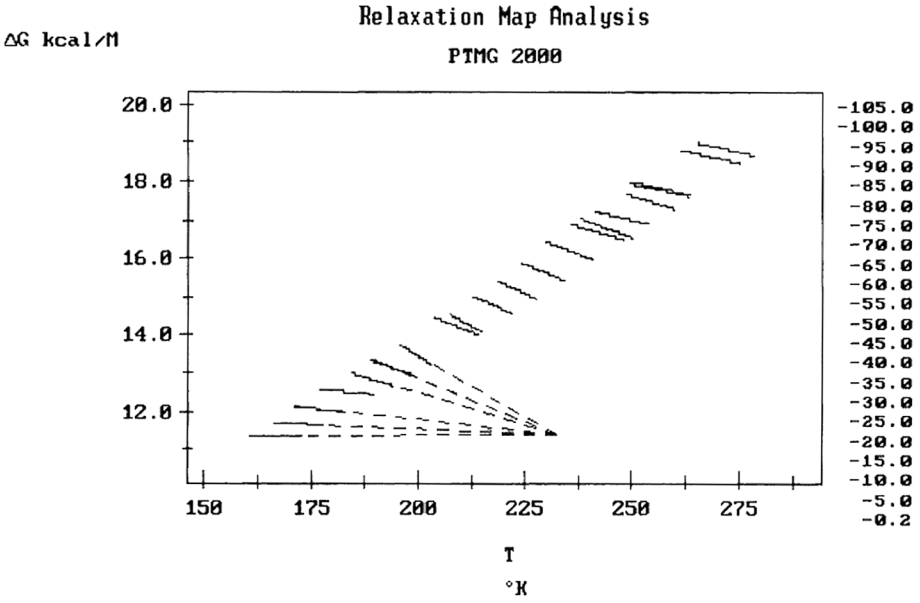


Figure 2.37: Relaxation map in the ΔG plane showing the compensation corresponding to the straight line in the compensation search (Figure 2.36).

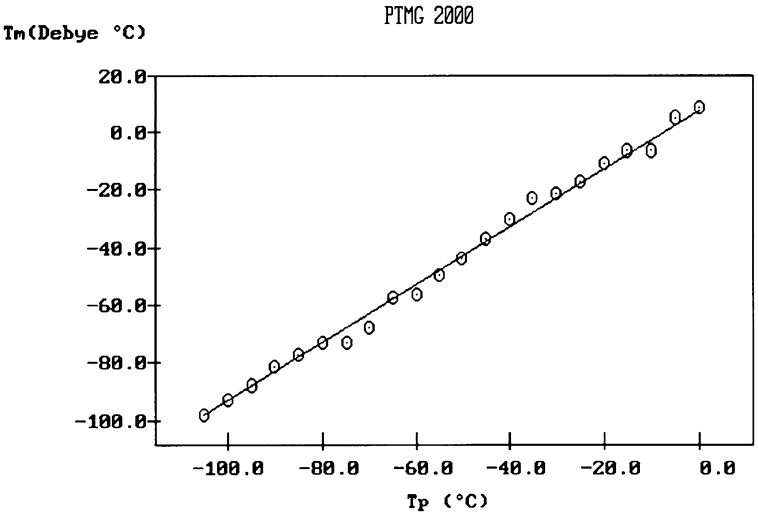


Figure 2.38: Plot of T_m, the temperature at the maximum of the Debye peaks in Figures 2.34 and 2.35 and Table 2.4, against T_p for PTMG 2000.

EBSCOhost - printed on 2/13/2023 12:32 AM via . All use subject to https://www.ebsco.com/terms-of-use

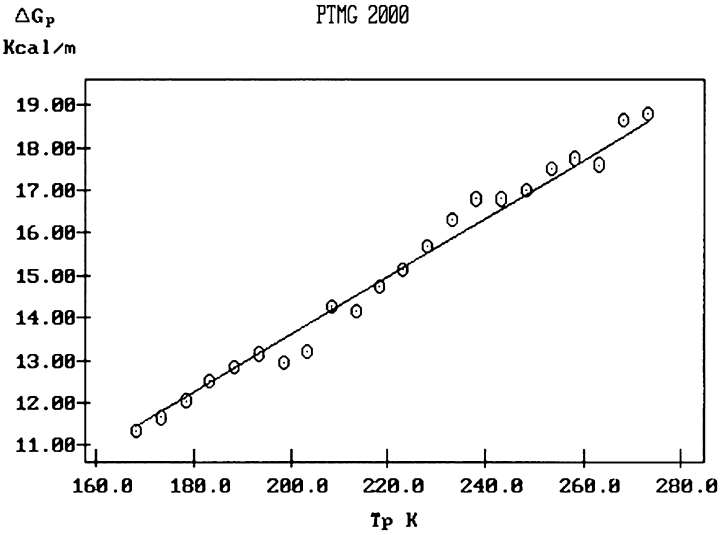


Figure 2.39: Plot of ΔG_p vs. T_p for the data of PTMG 2000 in Table 2.4.

The value of ΔG_p, which is the value of the energy of activation at $T = T_p$, is plotted against T_p in Figure 2.39, showing a straight line behavior passing through 0 when T_p is in Kelvin. The apparent slope for the line passing through the T_g process and the T_α process is 0.0681. This behavior is identical to what was observed in the case of amorphous polymers. The resultant conclusion is that the crossing over the T_α process does not make any difference to this empirical and simple law. The value of the free energy during depolarization, when the temperature reaches the temperature of polarization, seems to be very simply related to the temperature of polarization itself. This is true regardless of the relaxation mode under consideration, whether it participates cooperatively in a relaxation of either the T_g or the T_α type. Initially, this seems to be a universal finding for amorphous polymers as well.

Figure 2.40 provides another interpretation of the results shown in Figure 2.39. In this plot, we examine the temperature zone just above T_g and find that a more accurate fit is obtained if a straight line with a slope different from the average 0.068 is drawn up. Following this thinking, we find for the first six points of Figure 2.40 a slope of 0.0754 and an intercept close to 0. The second line passing through the points between –70 °C and –35 °C (shown in Figure 2.40) has a slope of 0.1027 and an intercept of –7.682. The last seven points of the graph are described by a line with a slope and intercept reminiscent of the slope and intercept for the first T_ps (T_p between –105 °C and –70 °C). Thus, the amorphous matter polarized just above T_g for this semi-crystalline polymer might be considered at slight variance with the overall universal behavior observed for "classical" amorphous polymers. Beyond a temperature of approximately 240 K, which corresponds to the T_α peak maximum temperature in a TSD scan, the behavior of ΔG_p vs. T_p becomes "normal" again.

EBSCOhost - printed on 2/13/2023 12:32 AM via . All use subject to https://www.ebsco.com/terms-of-use

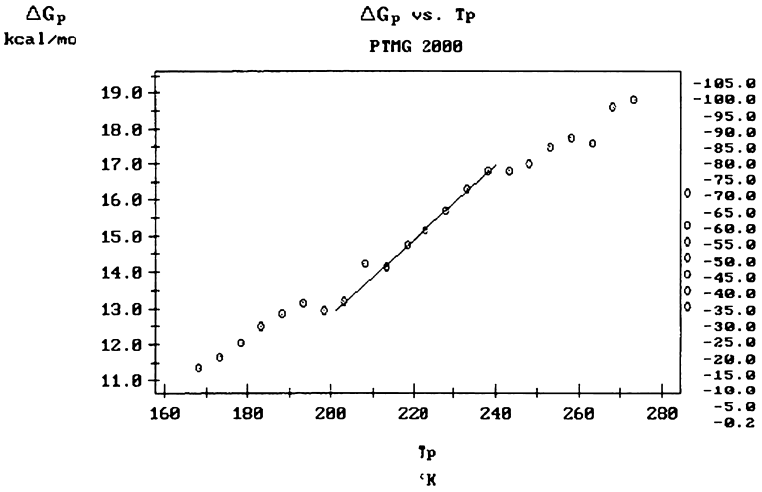


Figure 2.40: Same graph as in Figure 2.39, with a different partition of the regions of interactive coupling.

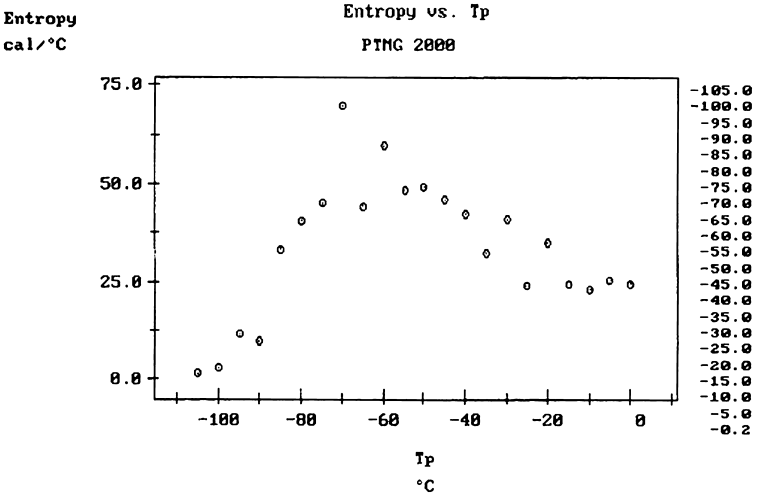


Figure 2.41: Plot of the entropy of activation ΔC_p vs. T_p for PTMG 2000.

Figure 2.41 displays the variation found for the entropy of activation (the slope of the lines in Figure 2.33) against the temperature of polarization. The entropy appears to increase from below T_g to reach a maximum at T_g and then exponentially or hyperbolically decrease after that. The behavior below T_g is identical to what is observed for an amorphous phase in a classical amorphous polymer.

EBSCOhost - printed on 2/13/2023 12:32 AM via . All use subject to https://www.ebsco.com/terms-of-use

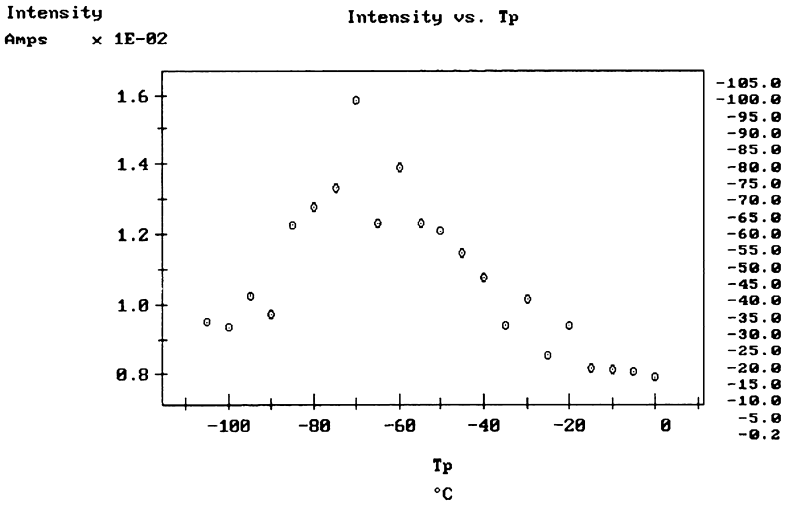


Figure 2.42: Plot of the Debye peak intensity at T_m vs. T_p for PTMG 2000.

Figure 2.42 is an interesting plot when it is compared to Figure 2.41. In Figure 2.42, the intensity at the *Debye peak* maximum is plotted against the polarization temperature. In other words, the variable presented in this figure is nothing else than the peak maximum of the synthesized curves shown in Figures 2.34 and 2.35. The entropy vs. T_p plot seems to be identical to the Debye intensity vs. T_p plot, as if one could associate the activation entropy with the peak height of the Debye peaks. We have already provided in Chapter 2 approximate formulas which link the half peak width to the activation enthalpy ΔH, following the approximation by Dube. The comparison between Figures 2.41 and 2.42 leads us to make another approximation and associate the entropy of activation with the peak height of the Debye peak.

An attempt to find the constant of proportionality between entropy and peak height is made by plotting entropy of activation versus Debye peak intensity (this is displayed in Figure 2.43). Two straight lines can be drawn through the data set in Figure 2.43. The lower line gathers points representative of the T_g process and the upper line concerns the $T > T_g$, the T_α, and the $T > T_\alpha$ temperature regions. The upper straight line passing through the data has a substantial amount of scatter which might invalidate the use of only one single straight line in this wide temperature range. We find two constants of proportionality between entropy and peak height depending on the temperature region. For the T_g relaxation process and the relaxation mode below T_g, the slope and intercept of the line in Figure 2.43 are 1269.56 and −92.36, whereas these constants become 5848.54 and −22.67 for the relaxation modes involved in the T_α transition region, respectively (assuming a single line for the behavior above T_g).

EBSCOhost - printed on 2/13/2023 12:32 AM via . All use subject to https://www.ebsco.com/terms-of-use

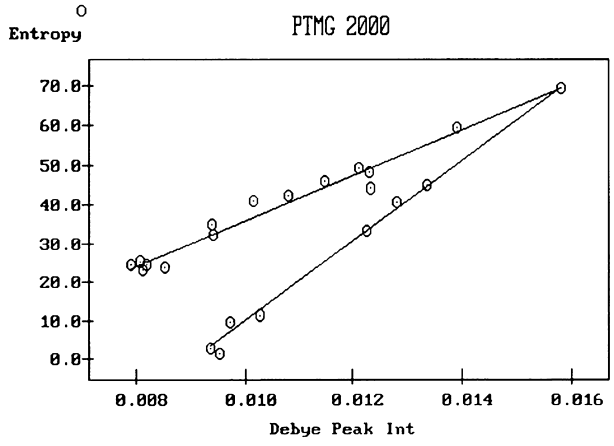


Figure 2.43: Cross-plot of entropy of activation vs. the Debye peak intensity for all the T_p.

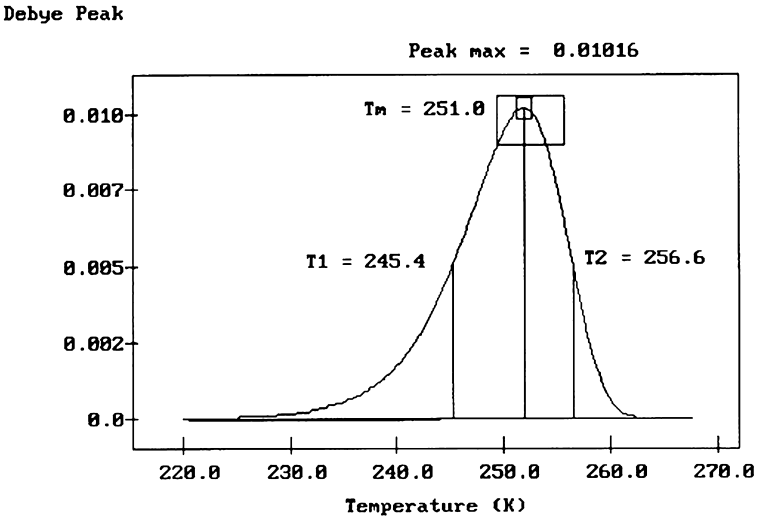


Figure 2.44: Assignment of the features of a Debye peak (intensity, half-width) to compute the thermokinetic characteristics.

The Debye relaxation process during thermally stimulated current depolarization can be summarized in Figure 2.44 with the following qualitative statements. The peak height is proportional to the activation entropy, the enthalpy of activation is directly related to the peak width according to Dube's formula, the temperature of peak maximum T_m is directly proportional to the free energy at T_p, and T_m is itself equal to T_p. These observations qualitatively lead us to a simple interpretation of the Debye peaks. The universal aspect of the influence of voltage field on the relaxation process is perceived as a linear relationship between ΔG_p and T_p, and the position of the Debye relaxation is known from the temperature of polarization T_p. The shape of the peak,

EBSCOhost - printed on 2/13/2023 12:32 AM via . All use subject to https://www.ebsco.com/terms-of-use

its width, and its height are directly related to two thermodynamic quantities derived from the peak itself: the enthalpy of activation and the entropy of activation. A compensation phenomenon is, therefore, the relationship between the peak height and the peak width of a Debye curve, and, as is true in human morphology, it says that that which is thin is usually long, and that which is fat is usually short…

If the peak height of the Debye peaks is related to the entropy, plots of peak height versus T_p could be viewed as the influence of the internal mobility in the material, an attribute normally assigned to the intensity of the peaks of current themselves. As already mentioned previously, and illustrated further in Part II, Chapter 3, the plots of intensity at the peak maximum for the raw data obtained by thermal-windowing do not match the curve obtained from plotting the Debye peak intensity at the maximum against the temperature of polarization T_p. This latter plot corresponds to a plot of entropy against T_p, as mentioned in this section. It now becomes apparent that when the two variables – the peak maxima obtained from an entropy versus T_p plot and the intensity at current maximum versus T_p – do not coincide, it is because either the thermal-window width is large enough to accommodate more than one single peak when curve-fitting with Debye, or the material is highly polar. The maximum of the Debye peak height is obtained for a $T_p = T_g$, and apparently the peak height increases hyperbolically on both sides of this transition. The T_g occurs for a maximum of both the entropy and enthalpy, which are both related to shape features of the Debye peak. The enthalpy of activation increases to very large values as the Debye peak becomes narrow, and the peak height simultaneously increases in a proportion which is dictated by a compensation law.

In this section we have learned how to assign thermokinetic attributes to the peak shape characteristics when the relaxation is simulated with a simple Debye formula. The position on the temperature axis of the peak at $T_{m,D}$ gives the value of the free energy of activation at T_p, $\Delta G_p = 0.07T_p$, with $T_p = T_{m,D}$. The enthalpy of activation is proportional to $[T_1 T_{m,D}/(T_{m,D} - T_1)]$, and the entropy of activation is proportional to the peak height at T_m. The value obtained for the proportionality between ΔG_p and T_m might be a function of the heating rate during the ramp-up in thermal-windowing. In the experiments and simulations reported in this book, the heating rate is invariably 7 °C per minute and the universal constant used is 70 cal/°C.

In conclusion, the same type of analysis used for the characterization of amorphous polymers by TWD spectroscopy can be applied to the study of the amorphous phase in semi-crystalline polymers. The same phenomenon of compensation is observed for the amorphous phase located at the lower temperature. However, it is not clear from the study of the spectrum for PTMG 2000 whether a negative compensation is observed or whether a positive compensation only characterizes the amorphous state in semi-crystalline polymers. This question is solved by studying another classical semi-crystalline polymer, polyamide 12, in the next section.

EBSCOhost - printed on 2/13/2023 12:32 AM via . All use subject to https://www.ebsco.com/terms-of-use

I.2.11.2 Polyamide 12

Polyamide 12 is produced by a molten state poly-condensation reaction to produce chains of average molecular weight $M_n = 12{,}000$. These polyamide chains are used in the synthesis of block copolymers studied in more detail in Chapter 3 of Part II (section II.3.4.2). The results analyzed here are taken from the thesis by Faruque [77]. Thermal-windowing is accomplished with a window width of 10 °C and a time of polarization and depolarization of 2 minutes. The polarization temperature varies between 10 °C and 65 °C.

The relaxation map plotted in the Arrhenius plane is shown in Figure 2.45. The Arrhenius transforms are obtained from the simulated Debye peaks created mathematically from the value of τ_o, and ΔH is read from the table in Faruque's thesis. This is the reason for the excellent linearity of the Arrhenius lines, which correspond to the ideal Debye case.

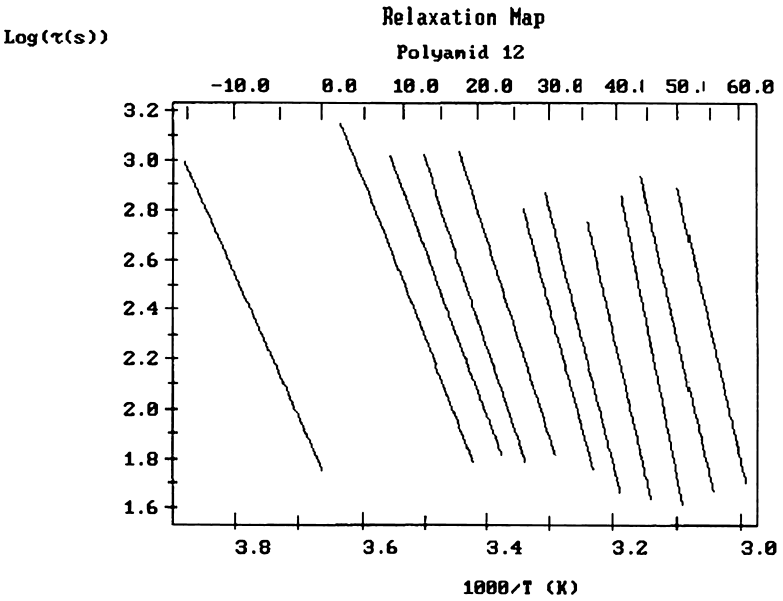


Figure 2.45: Relaxation map in the Arrhenius plane for polyamide 12. T_p varies between 10 °C and 65 °C with steps of 5 °C.

Figure 2.46 displays the relaxation map in the ΔG plane and Table 2.5 provides the value of the thermokinetic constants for each T_p. The enthalpy and entropy values go through a maximum for $T_p = 50$ °C, a behavior similar to what is observed for true amorphous polymers.

EBSCOhost - printed on 2/13/2023 12:32 AM via . All use subject to https://www.ebsco.com/terms-of-use

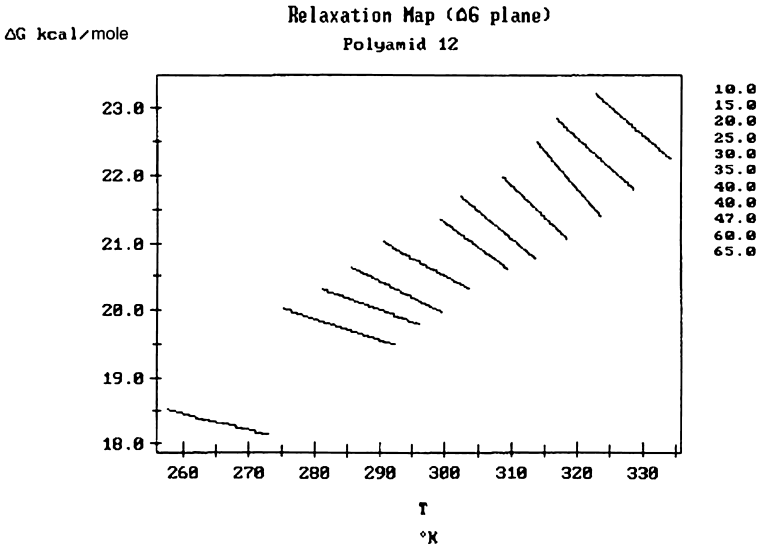


Figure 2.46: Relaxation map in the ΔG plane for the data of Figure 2.45.

Table 2.5: Thermokinetic parameters derived from the analysis of Figure 2.46.

	T_p (°C)	T_m (°C)	ΔH_p (kcal/mol)	ΔS_p (cal/°C/mol)	ΔG_p (kcal/mol)
1	10.0	1.3	25.3833	26.6001	17.8512
2	15.0	20.9	28.7700	31.7737	19.6141
3	20.0	25.1	30.1463	34.9648	19.8960
4	25.0	28.5	34.2545	47.6783	20.0387
5	30.0	33.1	36.2535	52.4843	20.3423
6	35.0	38.5	42.6384	71.1518	20.7123
7	40.0	41.9	45.9400	80.2462	20.8100
8	45.0	46.6	50.5165	92.4839	21.5543
9	50.0	51.9	58.0945	113.4378	21.7763
10	55.0	56.9	50.8605	88.4659	21.3872
11	60.0	62.9	50.3188	84.0191	21.9069

The compensation search is described in the EE plot of Figure 2.47: two compensation lines, one positive and one negative, are observed on this plot. The compensation coordinates are calculated from the slope and intercept of the compensation lines. We find for the positive compensation

$$T_c = 84.71\,^{\circ}\mathrm{C}$$
$$\Delta G_c = 17.39\,\mathrm{kcal/m}$$
$$\mathrm{DOD} = 51.40$$

EBSCOhost - printed on 2/13/2023 12:32 AM via . All use subject to https://www.ebsco.com/terms-of-use

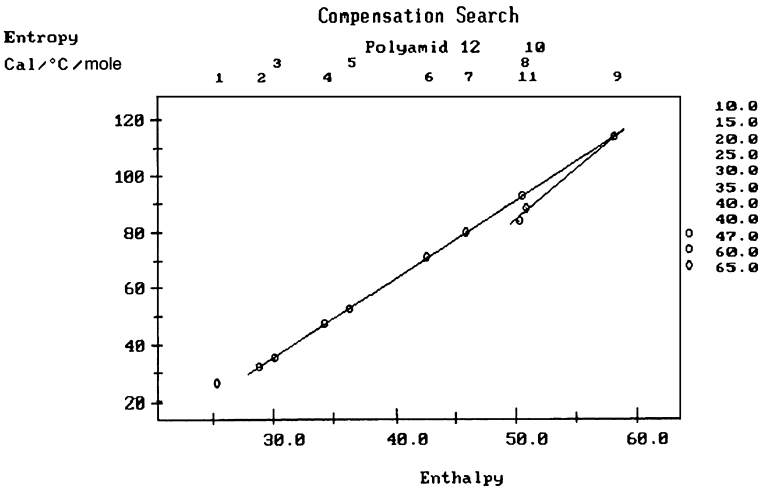


Figure 2.47: Compensation search for finding the compensations in Figure 2.46. The small numbers correspond to the first column numbers in Table 2.5 relative to T_p.

and for the negative compensation

$$T_c = 1.45\,°\text{C}$$
$$\Delta G_c = 26.92\,\text{kcal/m}$$
$$\text{DOD} = 1.97$$

It is interesting to note that the value of T_c is far away from T_g, which is located at 53 °C for this polymer (as measured by TSD). $(T_c - T_g) = 31.71\,°\text{C}$ for the positive compensation and 51.55 °C for the negative compensation. These numbers are approximately twice as big as those found normally for amorphous materials. The same observation could be made in the case of PTMG 2000 presented previously, for which $(T_c - T_g)$ is equal to 42.20 °C for the positive compensation. A possible explanation for these large numbers can be found after we study the effect of orientation in the plane perpendicular to the polarization by the voltage field. This will be covered in more detail in the next section on drawn and undrawn polypropylene. It is possible that for semi-crystalline polymers, the amorphous phase for which the compensation phenomenon is observed is submitted to a certain amount of orientation if the amorphous phase is trapped between spherulites. The positive and negative compensations are displayed in Figures 2.48 and 2.49, respectively.

The spread between the ΔG_c values (over 10 kcal/m) is also due to the spread of the compensation points on both sides of T_g. The further away the compensation temperatures, the lower and higher the negative and positive compensations.

Figures 2.50 and 2.51 display the result of the relaxation map analysis in the normalized ΔG plane.

EBSCOhost - printed on 2/13/2023 12:32 AM via . All use subject to https://www.ebsco.com/terms-of-use

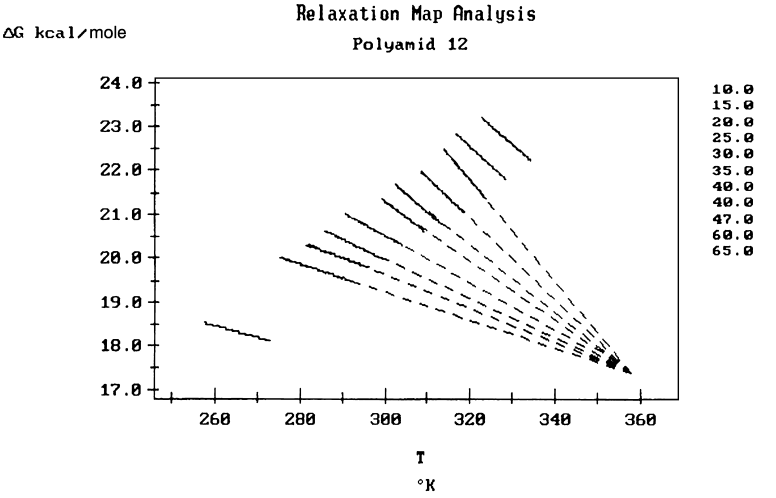


Figure 2.48: Same relaxation map in the Δ*G* plane as in Figure 2.46 with the positive compensation resulting from Figure 2.47 transcribed in the graph.

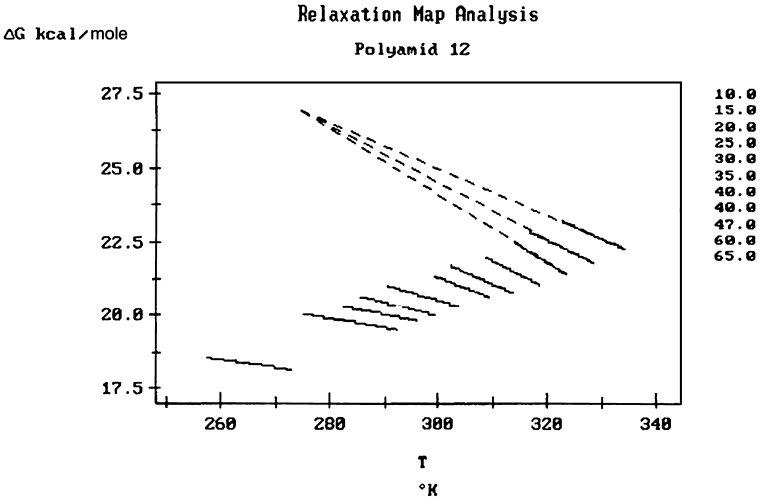


Figure 2.49: Same relaxation map in the Δ*G* plane as in Figure 2.46 with the negative compensation resulting from Figure 2.47 transcribed in the graph.

The relaxation data are plotted as $\Delta G/T_p$ vs. $(T - T_p)$ in Figure 2.50. The compensation search for these normalized data (Figure 2.51) reveals that only a few relaxation modes converge to the same A_c point. We find $\delta_c = -12.65\,°C$ and $(\Delta G_c/T_p)_c = 69.38\,cal/°C$. Notice that the value obtained for δ_c is rather large compared to values obtained previously in the case of pure amorphous polymers. The question can be raised whether we can justify normalizing to the temperature T_p when the value of δ_c becomes so

EBSCOhost - printed on 2/13/2023 12:32 AM via . All use subject to https://www.ebsco.com/terms-of-use

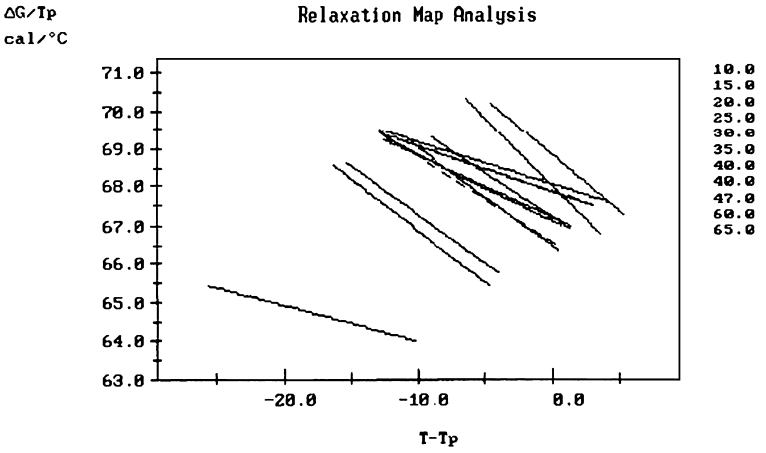


Figure 2.50: Relaxation map for polyamide 12 in the normalized Δ*G* plane. The two types of compensations are visible. Only a compensation search – shown in Figure 2.51 – permits to fine-tune our assessment of the amorhous phase structures.

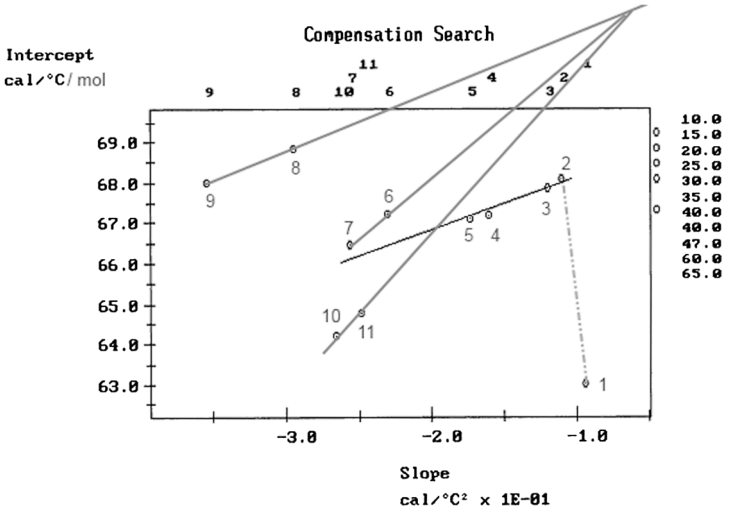


Figure 2.51: Compensation search for the data of Figure 2.50. The existence of two phases and their compensations only hinted in Figure 2.50 is now visible as a pair of positive and negative compensations at low T_ps, points (1,2) and points (2–5), and 3 other compensations that themselves participate in a super-compensation: (6,7), (8,9) and (10,11). The pair of compensations can be associated with the amorphous phase outside spherulites and the other compensations relate to amorphous phases entrapped within crystalline structures.

large. It might be preferable to divide by $T_p' = T_p - 12\,°C$. This will raise the ordinate value for the normalized Y-axis to 70.2 cal/°C and the X-coordinate for the compensation point in the normalized relaxation map will then of course become zero. The

EBSCOhost - printed on 2/13/2023 12:32 AM via . All use subject to https://www.ebsco.com/terms-of-use

caption of Fig. 2.51 shows that it is possible to distinguish the environment of the amorphous phases (inside or outside the crystalline structures) from the analysis of the compensation search in Figure 2.50.

In Figures 2.52 to 2.54, we examine the data in the previously introduced sub-EE plane to see whether an analogy with the results obtained for PMMA can be derived. In particular, it was asked before whether the linear correlations obtained in the sub-EE planes at each temperature of polarization T_p were due to a fluctuation in the electrometer during the digitization process or due to some other mathematical round-off error of the same type during the derivation process. By starting from simulated Debye functions which are calculated with a double precision in the computer, we can be certain that the results are not dependent on the measurement of the electrometer.

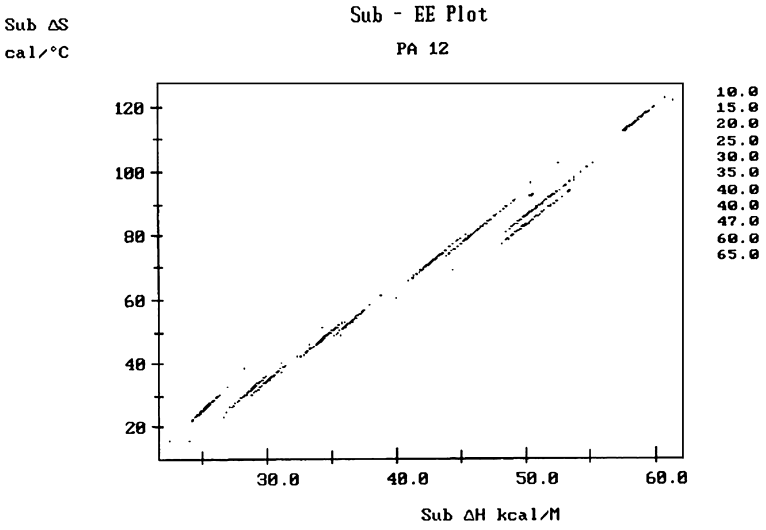


Figure 2.52: Sub-EE plot for polyamide 12.

Figure 2.52 is a plot of sub-ΔS versus sub-ΔH for the 11 temperatures of polarization. The same behavior is observed for this semi-crystalline polymer as for PS or PMMA. These EE lines are small temperature spreads around a min value determined approximately by the min entropy and min enthalpy of activation. The integration technique used to integrate the exact Debye peaks is the straight baseline technique [245], which does not require the improved Lacabanne approximation to integrate. However, we have limited ourselves to the temperature maximum of a Debye peak for the upper limit of integration. This is to conform to what is normally done in real experimental integration procedures [245, 252]. It is seen that all lines seem to converge to an identical compensation point.

EBSCOhost - printed on 2/13/2023 12:32 AM via . All use subject to https://www.ebsco.com/terms-of-use

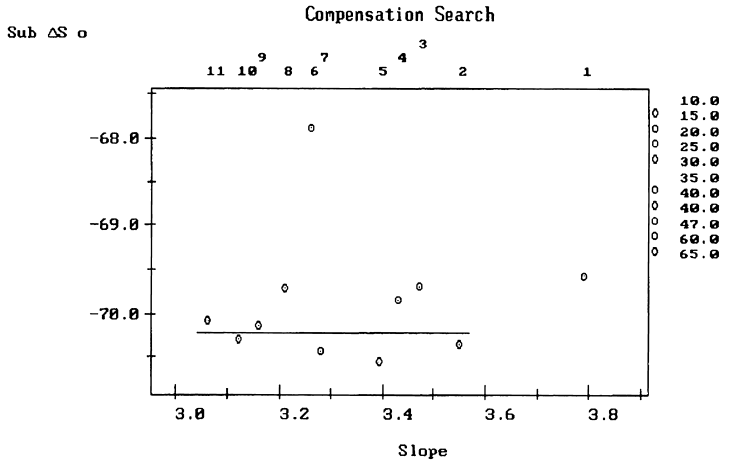


Figure 2.53: Compensation search for the data of Figure 2.52.

Figure 2.53 is a compensation search to determine the best coordinates of the point of conversion of the lines in Figure 2.52. A simplex algorithm is performed to find the best horizontal line going through the data. For the zero slope, we find an intercept equal to sub-$\Delta S_c = -70.23$ cal/°C. The analogy with amorphous polymers is complete.

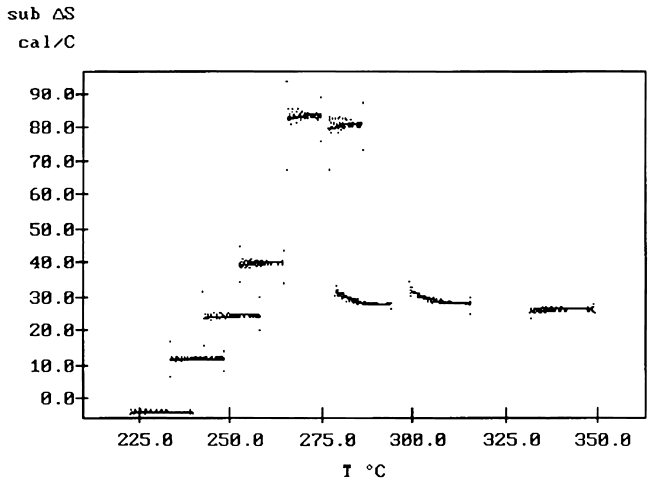


Figure 2.54: Sub-$\Delta S(TK)$ during depolarization for $T_p = 20$ °C to 65 °C. The steady-state value is equal to ΔS_p for each depolarization step.

In Figure 2.54, we plot, for each temperature T during the depolarization, the variation of sub-ΔS. The results show that it remains approximately constant, but with a small fluctuation around a min value equal to ΔS_p over the interval of depolarization.

EBSCOhost - printed on 2/13/2023 12:32 AM via . All use subject to https://www.ebsco.com/terms-of-use

The level for the plateau for each segment obtained at a given T_p varies as plotted in Figure 2.55, which is the traditional plot of entropy of activation (at T_p) vs. T_p. Significantly, T_p is located among the temperature range of depolarization, and sub-ΔS remains approximately constant during the return of ΔG to its equilibrium value (the effect of voltage field during the polarization stage is to inflate the ΔG, and depolarization allows a return to equilibrium with a rate which is the activation entropy).

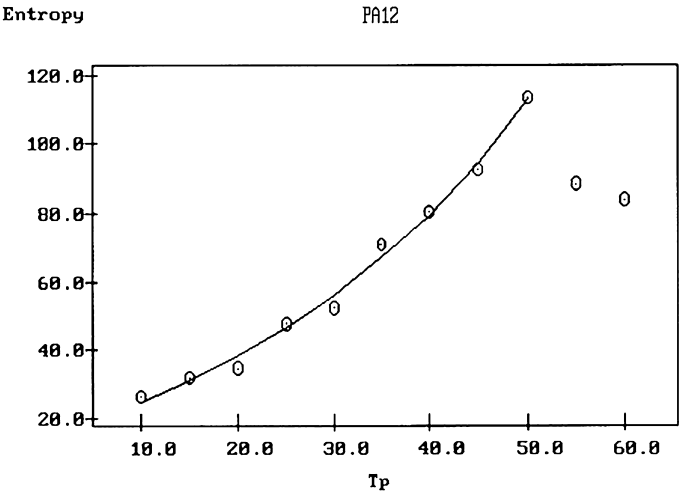


Figure 2.55: Steady-state value of sub-$\Delta S(T)$ in Figure 2.54 plotted against T_p.

In Figure 2.55, we have drawn a hyperbolic function among the data up to T_g. This behavior has been explained earlier, and the asymptotic value found for T_p should be the temperature of compensation. The hyperbola of Figure 2.55 has the following constants:

$$\Delta S_p = -96.73 - \frac{11259.3}{T_p - 103.77}$$

Notice that the value found for T_c' from the hyperbolic variation of ΔS_p is different by 19 °C from the T_c found from the compensation search ($T_c = 84.71$ °C, $T_c' = 103.77$ °C). The curve-fits to obtain these values are excellent. We have seen that compensation in the normalized ΔG plane results in a shift of δ_c to larger than usual values (–12.65 °C), yet not enough to explain the difference of 19° between the two T_c values. This would need further investigation.

Figure 2.56 is the plot of the entropy of activation versus the Debye peak height at the peak maximum. We observe two lines which we can assign to the compensation lines. This confirms the positive and negative coupling across T_g, which is found at the intercept of the two lines for $T_g = 50$ °C. In Figure 2.56, the intercept and slope

EBSCOhost - printed on 2/13/2023 12:32 AM via . All use subject to https://www.ebsco.com/terms-of-use

for the lower line (corresponding to the positive compensation) are A_o = –104.33 and A_1 = 16715.98. For the upper line (corresponding to the negative compensation), the intercept and slope are respectively A_o = –49.81 and A_1 = 12566.87. Note in Figure 2.56 that the negative compensation is clearly defined, whereas it was less obvious in the case of the EE plot in Figure 2.47, because the last two points in this graph were very close to one another. Therefore, another interesting way to determine the belonging of relaxations to one compensation group or another is to utilize plots of entropy versus peak height of the Debye fitting curve.

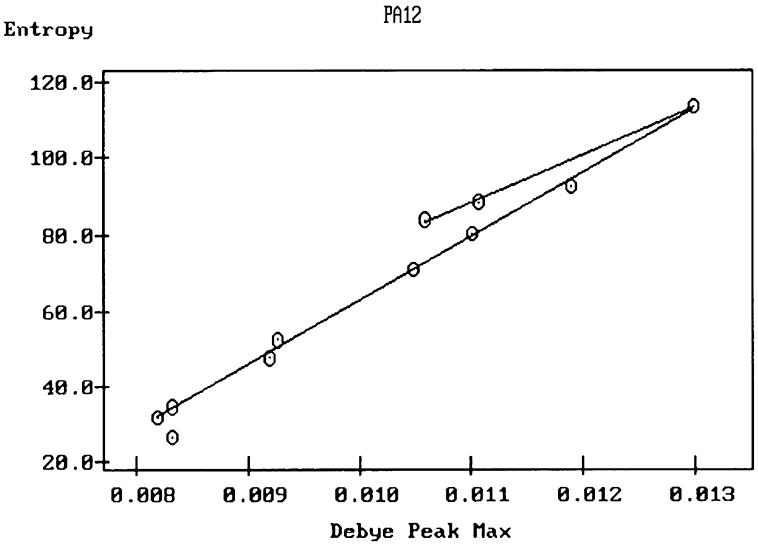


Figure 2.56: Entropy of activation, ΔS_p, plotted against the peak height maximum current showing the different linearities in the two compensation zones.

In summary, overall, the behavior of the amorphous phase in the polyamide 12 semi-crystalline polymer is totally reminiscent of the amorphous matter in pure amorphous polymers. Three features are typical of the behavior of the amorphous phase: the existence of positive and negative compensations, the possibility to find a compensation behavior in the normalized ΔG plane, and the variation with T_p of the entropy as a hyperbolic function. Only in Figure 2.51 do we find for this polymer evidence of the existence of two amorphous phases distinctively positioned in the morphology with respect to the texture of the spherulites. The distinction between the amorphous matter within spherulites or in-between spherulites more apparent in the next study, where the temperature of polarization range is extended beyond T_g.

EBSCOhost - printed on 2/13/2023 12:32 AM via . All use subject to https://www.ebsco.com/terms-of-use

I.2.11.3 Polypropylene (undrawn and drawn)

I.2.11.3.1 Undrawn polypropylene

The data reanalyzed in this section, in light of the characterization tools developed in this chapter, are from Jarrigeon et al. [146]. We selected to reanalyze these particular data from the literature because the material had been thoroughly studied by the authors using "more traditional" thermal analysis techniques (infrared dichroism, DSC, inverse gas chromatography, dilatometry, dynamic mechanical analysis [DMA], and dielectric spectroscopy). Our purpose is to use the method of analysis presented for PTMG 2000 and polyamide 12 on these well-characterized polypropylene samples and to determine whether the TWD technique is capable of detecting differences due to orientation on the cooperative kinetics, and on the distinction between the amorphous components located within spherulites or between spherulites.

The polarization voltage (550 V) is applied for 2 minutes at temperatures T_p between −40 °C and +70 °C. The thermal-windowing width is 10 °C, and the time of polarization and depolarization is 2 minutes. The results were reanalyzed from the data provided in Table 4 in the article by Jarrigeon et al. [146]. As done before, the values obtained for τ_o and ΔH are inserted into a Debye equation to create the Debye peaks extracted from thermal-windowing. The Debye peaks are integrated to calculate the entropy, enthalpy, and free energy. The work presented here looks at the data in light of the variables presented in this chapter: relaxation map in the ΔG plane, normalized compensation, sub-EE plots, etc.

Figure 2.57 is a reproduction of Figure 11 from reference [146]. It is a relaxation map in the Arrhenius plane showing characteristic features of the undrawn polypropylene film studied. The TSD traces for the two undrawn and drawn samples are provided in Chapter 3 (Figure 3.23). The orientation effect is easily detected by TSD, but TSD only provides a qualitative distinction between the drawn and undrawn specimens and does not yield to an understanding of the assignment of the peaks, either at T_g or just above T_g. The relaxation map analysis helps to further understand the coupling between the relaxation modes and the influence of orientation on the different amorphous phases present.

Figure 2.57 reveals the presence of a strong compensation for the low T_p relaxation modes, followed by a set of relaxations which are more or less parallel above T_g. Two relaxations modes are curved, describing a Williams–Landel–Ferry (WLF) dependency generally associated with the presence of free volume. We discuss in Chapter 3 the relationship between free volume and the presence of $T_{g,\rho}$. The $T > T_g$ peak observed in TSD for drawn and undrawn polypropylene is probably the result of a combination of dipolar relaxations and free volume-dependent relaxations. This explains why the relaxation taking place above T_g is displayed in the map (Figure 2.57) with both Arrhenius and WLF lines. In this case $T_{g,\rho}$ seems to have two components, observed in the relaxation map with two non-Arrhenius relaxations. This is the first in-

EBSCOhost - printed on 2/13/2023 12:32 AM via . All use subject to https://www.ebsco.com/terms-of-use

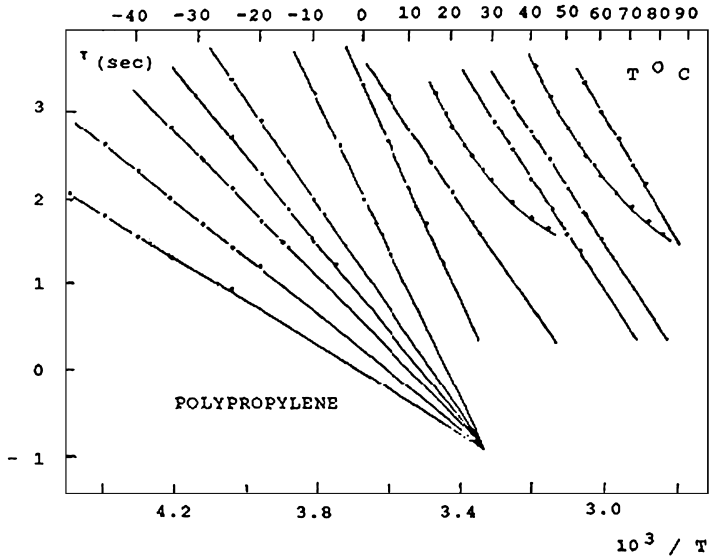


Figure 2.57: Relaxation map in the Arrhenius plane for undrawn polypropylene from $T_p = -50$ °C to 90 °C.

dication that two amorphous phases are present in the morphology. Each $T_{g,\rho}$ would be related to an independent amorphous phase.

The set of Debye peaks extracted from the thermal-windowing experiment for undrawn polypropylene is displayed in Figure 2.58 (we have eliminated from the presentation the Debye peak simulations corresponding to the two WLF relaxations). One observes an increase of the peak height as the temperature of polarization moves closer to T_g. The peaks become very thin at T_g and decrease in intensity afterwards.

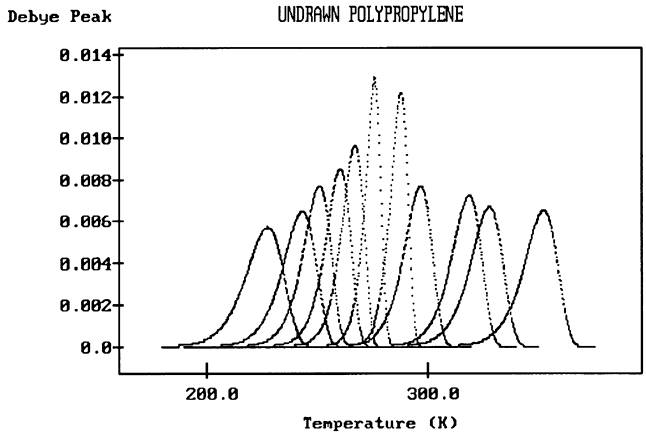


Figure 2.58: Masterplot of the elementary peaks obtained from TWD for undrawn polypropylene.

EBSCOhost - printed on 2/13/2023 12:32 AM via . All use subject to https://www.ebsco.com/terms-of-use

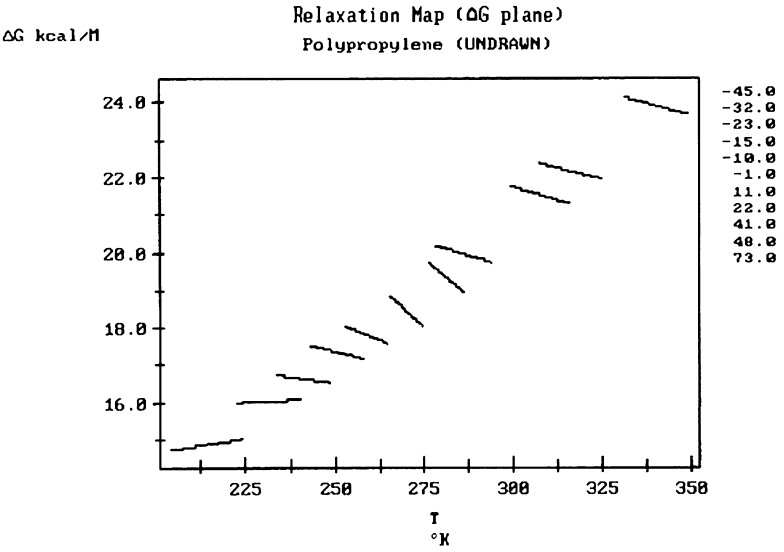


Figure 2.59: Relaxation map in the ΔG plane for the data of Figure 2.58.

Table 2.6: Thermokinetic parameters derived from the analysis of Figure 2.59.

	T_p (°C)	T_m (°C)	ΔH_p (kcal/mol)	ΔS_p (cal/°C/mol)	ΔG_p (kcal/mol)
1	−45.0	−45.7	11.6731	−15.0073	15.0972
2	−32.0	−30.2	15.1255	−3.9745	16.0840
3	−23.0	−22.4	19.4603	11.6883	16.5363
4	−15.0	−12.9	23.4417	24.3091	17.1661
5	−10.0	−6.3	28.1334	39.8879	17.6365
6	−1.0	3.0	40.9396	83.2789	18.2744
7	11.0	15.1	42.0647	80.7553	19.1172
8	22.0	23.9	28.0975	28.4115	19.7115
9	41.0	45.8	30.3789	28.7942	21.3329
10	48.0	54.9	29.6800	23.8095	22.0334
11	73.0	79.0	32.8002	26.2257	23.7219

The relaxation map in the ΔG plane for the Arrhenius relaxations of Figure 2.57 is shown in Figure 2.59.

The thermokinetic table, which is reproduced in Table 2.6, and Figures 2.60 to 2.63 provide the traditional plots associated with the study of the interactive coupling between the relaxation modes.

The compensation search (EE plot) in Figure 2.60 reveals a compensation line for the polarization temperature between −45 °C and 0 °C, which is displayed in Fig-

EBSCOhost - printed on 2/13/2023 12:32 AM via . All use subject to https://www.ebsco.com/terms-of-use

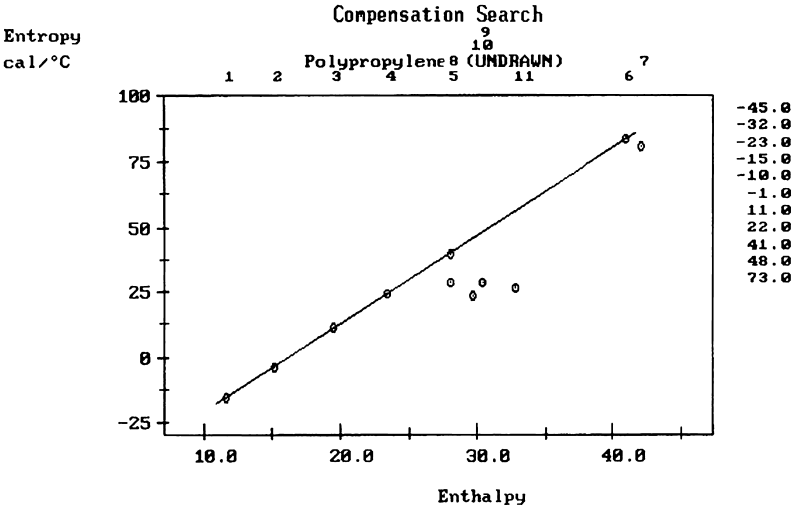


Figure 2.60: Compensation search for finding the compensations in Figure 2.59. The small numbers correspond to the first column numbers in Table 2.6 relative to T_p.

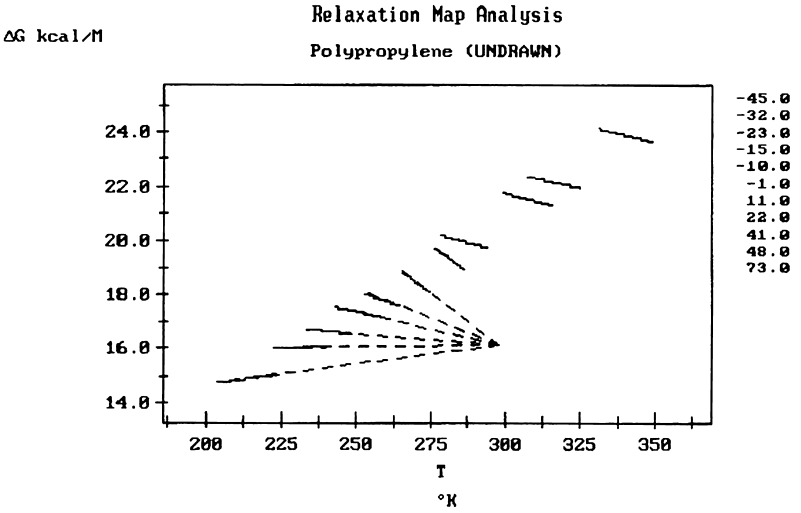


Figure 2.61: Same relaxation map in the ΔG plane as in Figure 2.59 with the positive compensation resulting from Figure 2.60 transcribed in the graph.

ure 2.61. We find

$$T_c = 24.53\,^{\circ}\mathrm{C}$$
$$\Delta G_c = 16.17\,\mathrm{kcal/m}$$
$$\mathrm{DOD} = 45.66$$

EBSCOhost - printed on 2/13/2023 12:32 AM via . All use subject to https://www.ebsco.com/terms-of-use

A negative compensation can also be drawn through points 7 and 8 in Figure 2.60 (the line has not been drawn in the figure) with the following characteristics:

$$T_c = -6.3\,°\text{C}$$
$$\Delta G_c = 20.51\,\text{kcal/m}$$
$$\text{DOD} = 23.11$$

The last four relaxation lines of Figure 2.61, corresponding to the highest T_ps, are almost parallel to one another which means that they have approximately the same entropy of activation. This is also well demonstrated in Figure 2.62, which plots the entropy of activation against T_p. The hyperbolic variation of the entropy for the coupled relaxation modes corresponding to the compensation at lower T_ps is clearly visible in this figure. We find for the hyperbolic equation:

$$\Delta S_p = -62.57 - \frac{3121.80}{T_p - 20.42}$$

In this case, the value found for the asymptote T_c' matches well the temperature of compensation found from the EE plot (24.53 °C) (the difference is due to the window width divided by two).

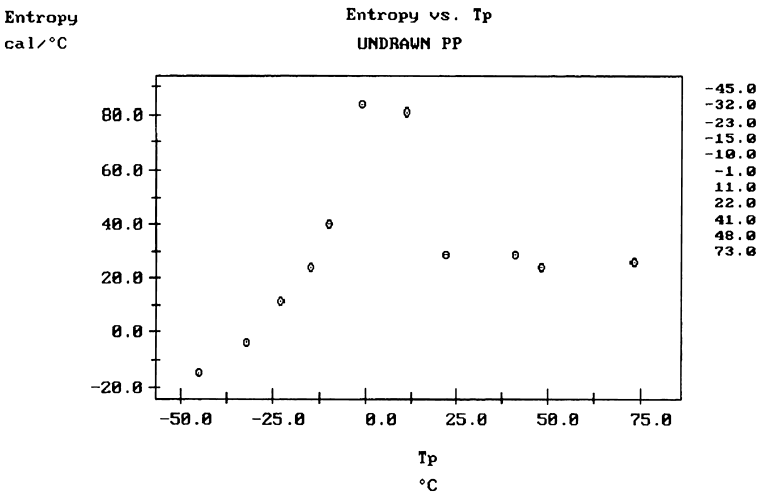


Figure 2.62: ΔS_p vs. T_p for undrawn polypropylene.

The free energy of activation at T_p is plotted against T_p in Figure 2.63, showing the classical straight line with slope 0.070 and intercept 0. There seems to be no difference in behavior below, above, and across T_g. The representation of the relaxation map in the normalized plane (Figure 2.64) shows that compensation occurs for the lower T_p

EBSCOhost - printed on 2/13/2023 12:32 AM via . All use subject to https://www.ebsco.com/terms-of-use

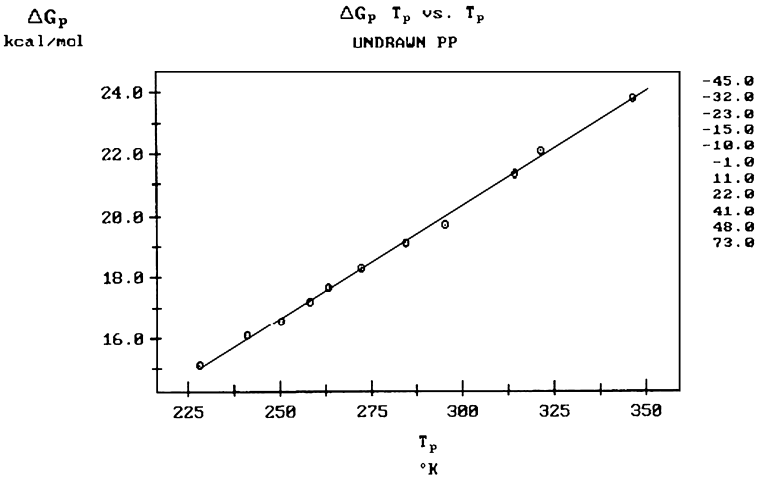


Figure 2.63: ΔG_p vs. T_p (K) for undrawn polypropylene.

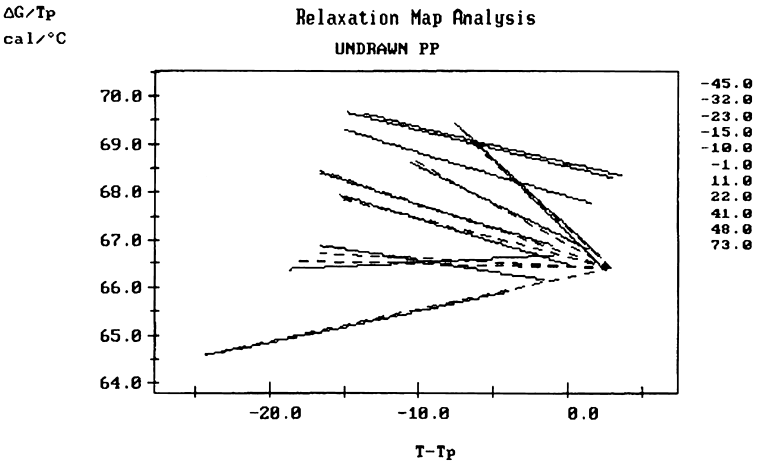


Figure 2.64: Relaxation map in the normalized ΔG plane for undrawn polypropylene.

($\delta_c = 2.5\,°C$, $(\Delta G/T_p)_c = 66.4\,cal/°C$). The sub-EE plot for undrawn polypropylene is shown in Figures 2.65 and 2.66. The compensation of all the sub-EE lines is revealed in Figure 2.67. The best intercept for all the lines seems to be on the sub-$\Delta H = 0$ axis with sub-$\Delta S_c = -70.48\,cal/°C$. The reason for obtaining a different value of conversions for the sub-EE lines and the normalized $(\Delta G/T_p)$ lines needs clarification. In one case (Figure 2.64), the compensation occurs for a $(\Delta G/T_p)$ value 3.5 cal/°C lower than the 70.5 cal/°C found for the sub-EE line compensation. The significance of the difference is unclear, except perhaps for one observation: normally, for a positive compensation in the ΔG plane, we observe compensation in the normalized plane to a point with

EBSCOhost - printed on 2/13/2023 12:32 AM via . All use subject to https://www.ebsco.com/terms-of-use

a negative δ_c. Conversely, a negative compensation in the ΔG plane corresponds to a positive δ_c (and a lower value of $(\Delta G/T_p)_c$). In the case here, δ_c is positive, although it is a positive compensation. This unusual behavior might have to do with the presence of two amorphous phases, which is further interpreted in the following section for drawn polypropylene.

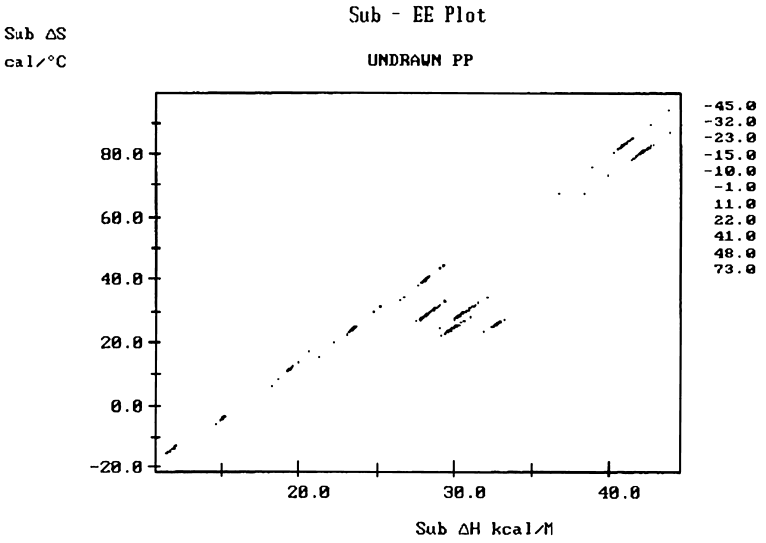


Figure 2.65: Sub-EE plot for undrawn polypropylene.

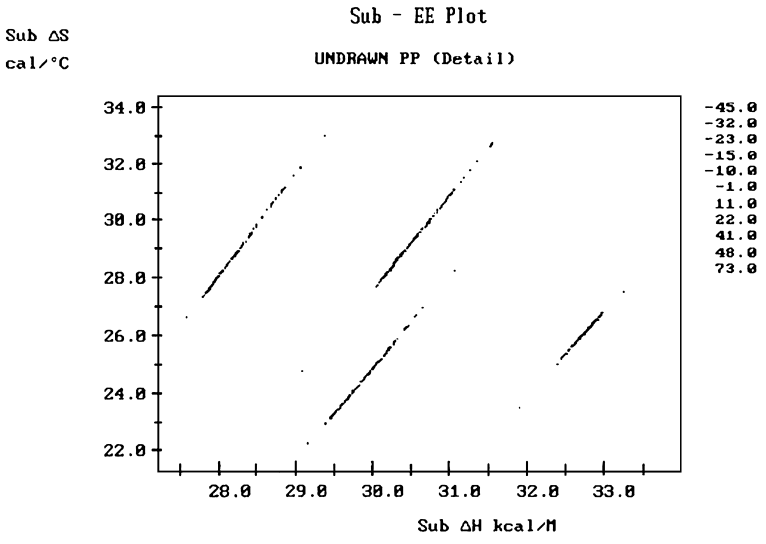


Figure 2.66: Detail of Figure 2.65, zooming on the response for four T_ps.

EBSCOhost - printed on 2/13/2023 12:32 AM via . All use subject to https://www.ebsco.com/terms-of-use

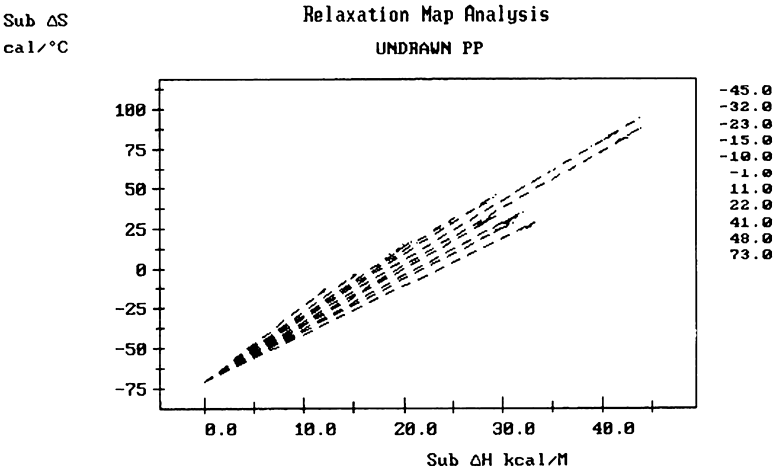


Figure 2.67: Compensation of the data of Figure 2.65 for undrawn polypropylene.

I.2.11.3.2 Drawn polypropylene

We present in the next set of figures the equivalent analysis for the case of a drawn polypropylene film. The film is oriented in the direction perpendicular to the voltage field applied during its characterization by TSD/TWD. The original article does not describe the amount of orientation present in the film.

Figure 2.68 displays all the relaxation Debye peaks reconstructed from the table of values found in reference [146].

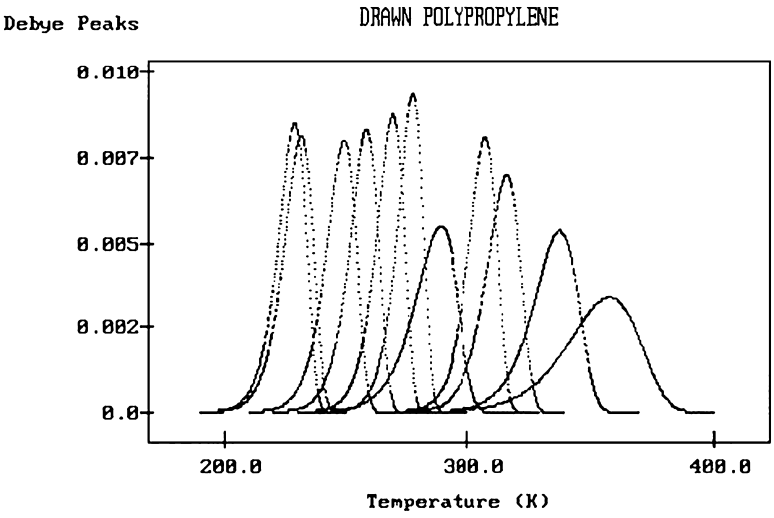


Figure 2.68: Masterplot of the elementary peaks obtained from TWD for drawn polypropylene.

EBSCOhost - printed on 2/13/2023 12:32 AM via . All use subject to https://www.ebsco.com/terms-of-use

The two relaxations corresponding to the $T_{g,\rho}$ peak are not included in this figure. Also refer to Chapter 2 of Part II for the discussion concerning the respective evolution of the $T_{g,\rho}$ peak intensities for drawn and undrawn polypropylene. The thermokinetic results are confined in Table 2.7.

Table 2.7: Thermokinetic parameters derived from the analysis of the relaxation map in the ΔG plane for drawn polypropylene.

	T_p (°C)	T_m (°C)	ΔH_p (kcal/mol)	ΔS_p (cal/°C/mol)	ΔG_p (kcal/mol)
1	−45.0	−44.3	17.8957	12.6703	15.0049
2	−42.0	−41.7	17.4308	9.6609	15.1976
3	−26.0	−24.3	20.2608	15.6515	16.3924
4	−17.0	−15.1	22.7342	22.3531	17.0082
5	−9.0	−4.5	25.6031	29.5447	17.7986
6	0.1	3.5	29.2364	39.9941	18.3076
7	12.0	15.0	18.0198	−4.3583	19.2628
B	31.0	34.4	31.5535	36.4428	20.4691
9	38.0	43.2	28.2742	22.8019	21.1792
10	56.0	65.0	24.7102	5.8550	22.7829
11	67.0	85.0	16.7614	−21.5340	24.0864

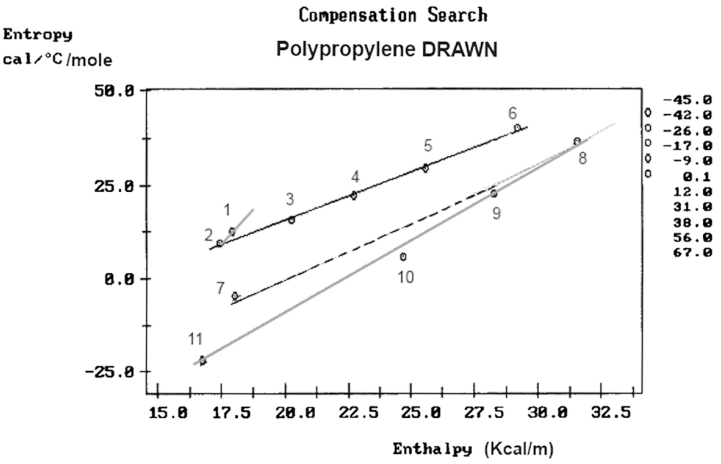


Figure 2.69: Compensation search in the EE plane for finding the compensations in Table 2.7. The small numbers correspond to the first column numbers in Table 2.7 relative to T_p. This is for drawn polypropylene. The choice of the drawn lines for the compensation (1,2), (2–6) and (7,8), (8–11) results from the analysis of Figures 2.70 to 2.73.

The compensation search of Figure 2.69 reveals a more complex behavior for drawn polypropylene. A positive compensation line clearly joins points 2 to 6 (T_p between

EBSCOhost - printed on 2/13/2023 12:32 AM via . All use subject to https://www.ebsco.com/terms-of-use

−42 and 0 °C). Another main compensation, negative, is found between points 8 and 11, joining the T_ps between 31 °C and 67 °C. We have also drawn two other compensations lines (1,2) and (7,8). Of course, we are lacking points to ascertain the correct position of these compensation lines, but we believe that point 7 actually belongs to at least one compensation: the positive compensation associated with the T_g process for the higher T_ps. The negative compensation drawn through points 8 to 11 is probably associated with the positive compensation through points points (7,8). This will become more apparent in Fig. 2.72 below with a further study of entropy versus Debye peak height.

The main compensations (positive and negative) found from the compensation search are drawn up in Figure 2.70 and Figure 2.71. The compensation point coordinates for the positive compensation (Figure 2.70) are

$$T_c = 113.74\,°\text{C}$$
$$\Delta G_c = 13.99\,\text{kcal/m}$$
$$\text{DOD} = 63.84$$

and for the negative compensation (Figure 2.71)

$$T_c = -16.88\,°\text{C}$$
$$\Delta G_c = 22.32\,\text{kcal/m}$$
$$\text{DOD} = 12.92$$

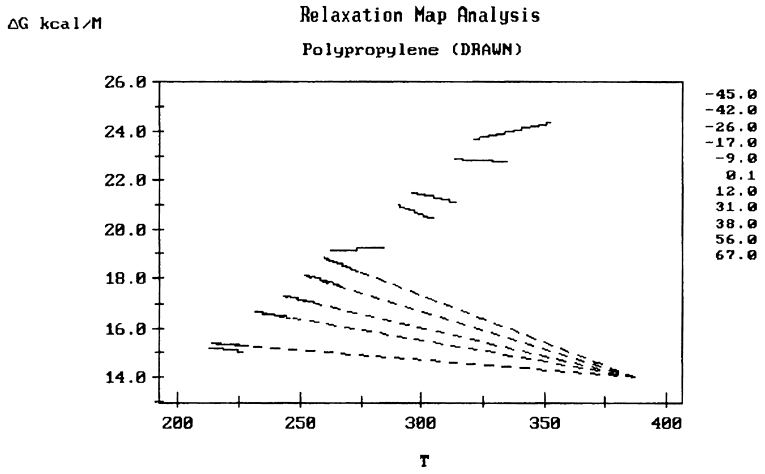


Figure 2.70: Relaxation map in the Δ*G* plane for drawn polypropylene showing the positive compensation resulting from Figure 2.69 (points 2 to 6).

EBSCOhost - printed on 2/13/2023 12:32 AM via . All use subject to https://www.ebsco.com/terms-of-use

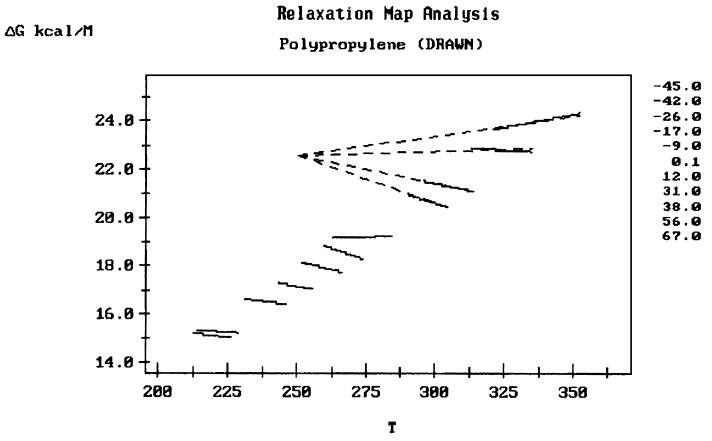


Figure 2.71: Relaxation map in the Δ*G* plane for drawn polypropylene showing the negative compensation resulting from Figure 2.69 (points 8–11).

The value found for the positive compensation should be compared with those found for undrawn polypropylene. The remarkable difference in the value of T_c and in the DOD number is significant to the effect of drawing. T_c increases from 24.53 °C to 113.14 °C and the DOD number increases from 45.66 to 63.84. Recall that the amorphous phase studied here under the voltage direction is the amorphous phase perpendicular to the orientation plane. When a polymer is stretched in one direction, or even in two directions in the case of biaxial orientation, the perpendicular direction is disoriented. This is probably the reason for the large increase in the DOD number for the amorphous phase perpendicular to the stretching direction.

Before drawing any conclusion, we will need to analyze the whole set of graphs to compare the behavior of the drawn and undrawn samples. We said earlier that the Debye peak height at the peak maximum could be used, when plotted against entropy, to determine the compensation lines. Figure 2.72 is such a plot, more clearly showing the existence of two amorphous phases.

The lower T_ps, points (1 to 6), are associated with the compensation behavior at the right of the figure, and the upper T_ps correspond to the left compensation behavior (points 7 to 11). Interestingly, the first two polarization temperatures, points 1–2, correspond to a line, and the second group gathers points 2, 3, 4, 5, and 6, which is conform to the compensation search in Figure 2.69. The intercept of the first two lines in Figure 2.72 is incidentally on the entropy = 0 line, a behavior that we will also encounter for other polymers in Chapter 4, Part II. The upper T_p behavior shows the gathering of points 8 to 11 into the compensation, and we have drawn up another compensation joining points 7 and 8. This analysis corresponds to our analysis in Figure 2.69. In this present analysis, the first two points, points 1 and 2, correspond to a negative compensation, and the next four gather into a positive compensation, which matches the positive compensation observed in Figure 2.69. These two compensations represent

EBSCOhost - printed on 2/13/2023 12:32 AM via . All use subject to https://www.ebsco.com/terms-of-use

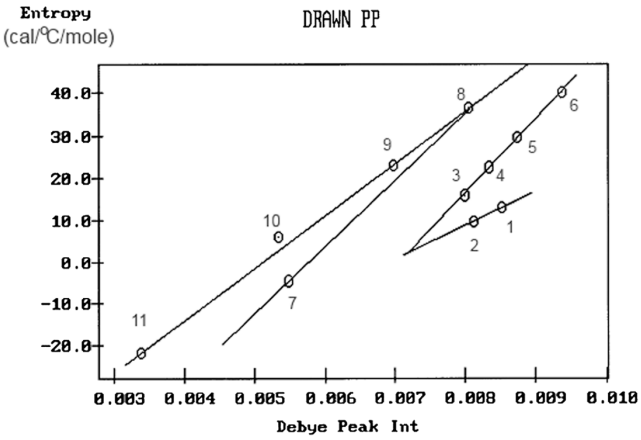


Figure 2.72: Entropy of activation, ΔS_p, vs. Debye peak intensity at T_m for drawn polypropylene. The follow through of the position of the row numbers near the points permits to confirm the main positive and negative compensations and the assumed respective (1,2) and (7,8) compensation lines. See text.

the first amorphous phase of the drawn polypropylene. Points 7 to 11 create another phase for which the positive compensation will be characterized by the line joining points 7 and 8, and the negative compensation is the line joining points 8 to 11.

The analysis of drawn polypropylene in the normalized ΔG plane leads to a very simple compensation search shown in Figure 2.73.

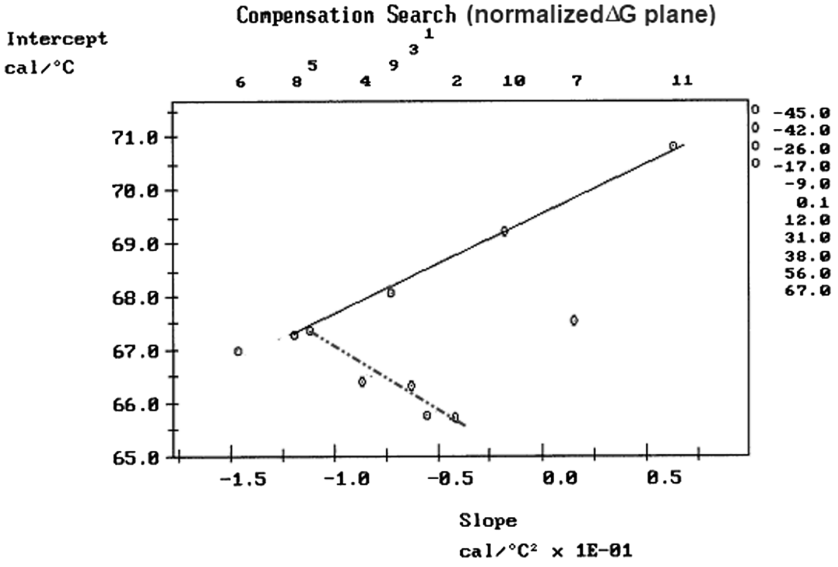


Figure 2.73: Compensation search in the Normalized ΔG plane for drawn polypropylene.

EBSCOhost - printed on 2/13/2023 12:32 AM via . All use subject to https://www.ebsco.com/terms-of-use

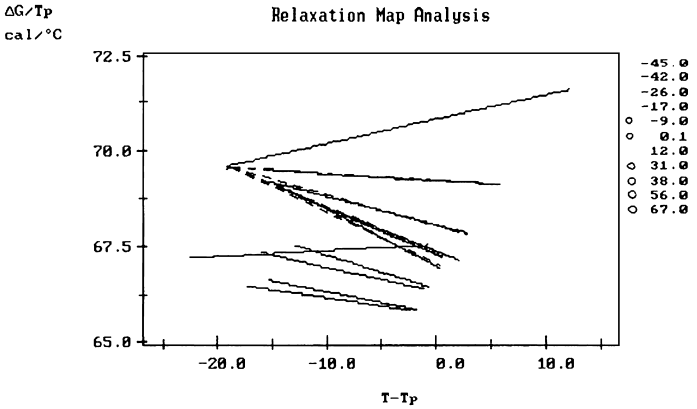


Figure 2.74: Relaxation map in the normalized Δ*G* plane for drawn polypropylene showing the negative compensation (T_p = −9 °C to 67 °C).

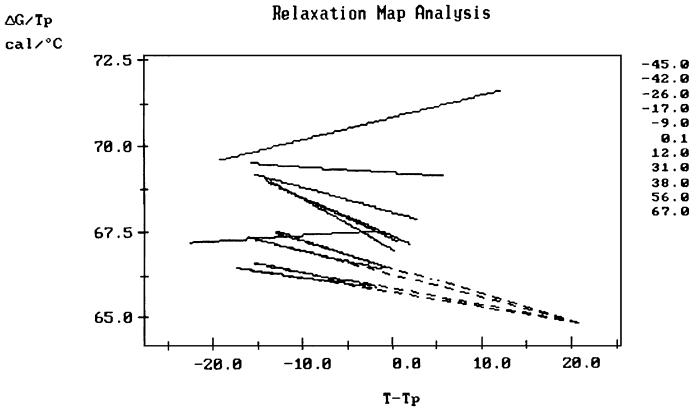


Figure 2.75: Relaxation map in the normalized Δ*G* plane for drawn polypropylene showing the positive compensation (T_p = −45 °C to −17 °C).

There are basically two lines joining respectively the low T_ps (T_p = −45 to −17 °C) and the higher T_ps, points 6 to 11 (T_p = 0 to 67 °C). The compensation in the normalized Δ*G* plane is shown in Figure 2.74 for the higher T_ps and in Figure 2.75 for the lower T_ps. The coordinates of the compensation points in Figures 2.71 and 2.72 are for the higher T_ps δ_c = −18.70 °C and $(\Delta G/T_p)_c$ = 69.56 cal/°C and for the lower T_ps δ_c = 20.75 °C and $(\Delta G/T_p)_c$ = 64.80 cal/°C. It is interesting to note that the convergence to the negative δ_c is associated with the highest T_p and, conversely, that the positive δ_c is associated with the lower T_ps. This is contrary to what is observed for the amorphous phase in a true amorphous material, unless the behavior observed describes, as previously suggested, two amorphous phases. The positive and negative compensations detected on the normalized Δ*G* plane would not belong to the same amorphous component in the structure. For instance, it is assumed that the interspherulitic region amorphous com-

EBSCOhost - printed on 2/13/2023 12:32 AM via . All use subject to https://www.ebsco.com/terms-of-use

ponent is associated with the lower T_p compensation. Thus, the negative compensation observed in Figure 2.75 should be associated to a positive compensation which is not observed here, perhaps because the temperature of polarization was not started low enough (points 1 and 2 could be considered on that compensation). Likewise, if we consider that the compensation observed in Figure 2.74 corresponds to a positive compensation for the upper T_ps amorphous phase, then there should be associated with it a negative compensation, which is not clearly observed in this figure. This compensation would be found for intermediate T_p values which have not been investigated in this thermal-windowing series. It is, indeed, regrettable that there are no more T_ps to confirm our breakdown of the relaxation map into two phases.

In summary, the results observed here are in favor of the coexistence of two amorphous components in the structure. Another interesting observation in Figures 2.74 and 2.75 is the large difference observed for δ_c: more than 20 °C for both the positive and negative compensations for each respective amorphous component. These values are much larger than those normally found for the amorphous phase in true amorphous polymers. However, as we already suggested in the study of polyamide 12, the presence of orientation and the elongation of the dipoles in the direction perpendicular to the voltage field might be the reason for this behavior. In such a case, both amorphous components would be affected by the orientation process since both the negative and positive δ_c are far from zero.

The sub-EE plot for drawn polypropylene (Figures 2.76 and 2.77) does not present any specific particularities or difference with the plot obtained for undrawn polypropylene. The compensation of the sub-EE lines occurs on the sub-$\Delta H = 0$ line with an intercept sub-$\Delta S_o = -70.35$ cal/°C, which is exactly the same value found for undrawn polypropylene.

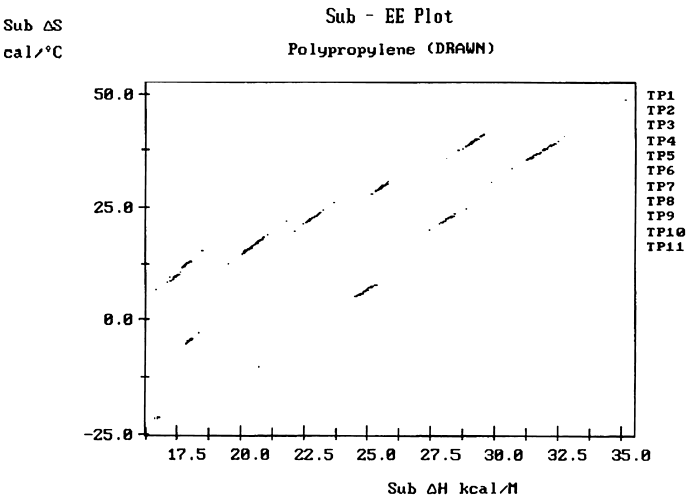


Figure 2.76: Sub-EE plot for drawn polypropylene.

EBSCOhost - printed on 2/13/2023 12:32 AM via . All use subject to https://www.ebsco.com/terms-of-use

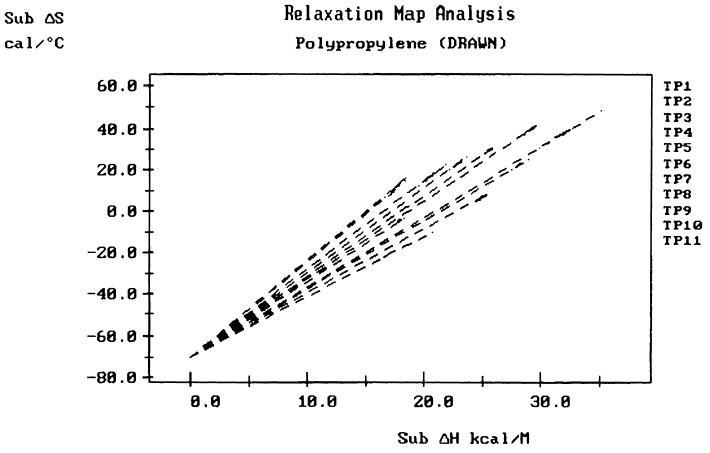


Figure 2.77: Compensation of the data of Figure 2.76 for drawn polypropylene.

I.2.11.3.3 Comparison between undrawn and drawn polypropylene

Figure 2.78 and Figure 2.79 compare respectively the positive and the negative compensations for drawn and undrawn polypropylene.

The most spectacular result from the change in the compensation line is the change of slope and therefore of T_c, the temperature of compensation (T_c increases by approximately 90 °C). The effect of orientation on the internal mobility is particularly well displayed in the plots of entropy against T_p, both below and above T_g (Figures 2.80 and 2.81).

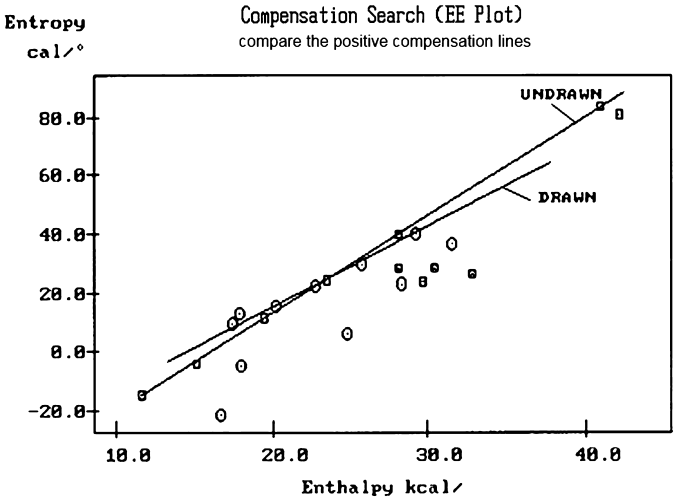


Figure 2.78: Comparison of undrawn and drawn polypropylene in the EE plane, showing the positive compensation differences.

EBSCOhost - printed on 2/13/2023 12:32 AM via . All use subject to https://www.ebsco.com/terms-of-use

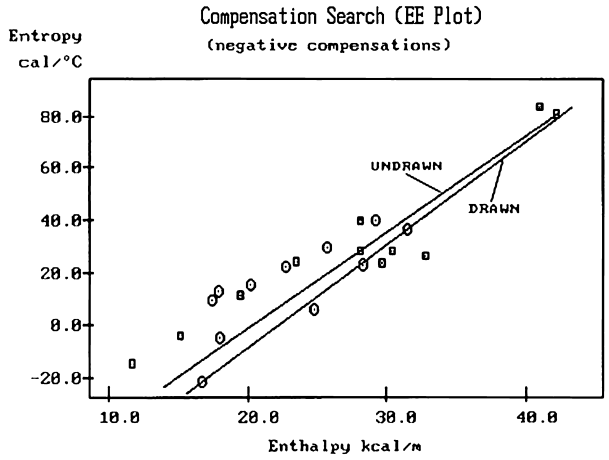


Figure 2.79: Comparison of undrawn and drawn polypropylene in the EE plane, showing the negative compensation differences.

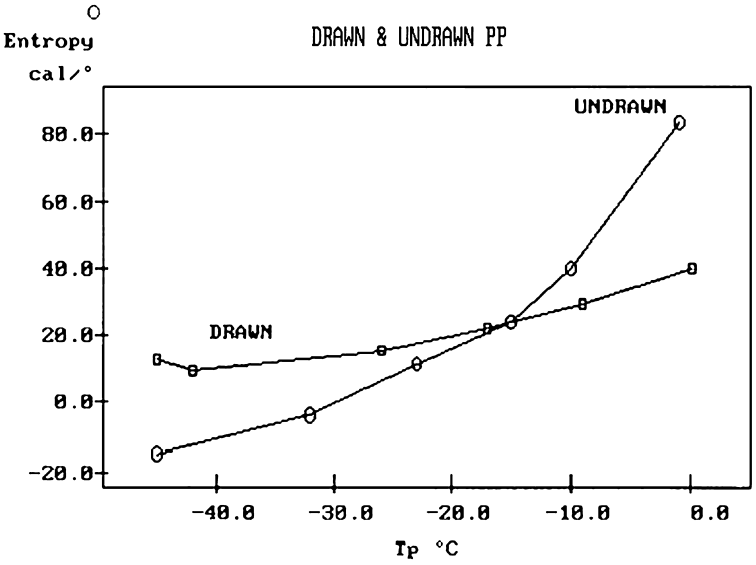


Figure 2.80: Comparison of ΔS_p vs. T_p for drawn and undrawn polypropylene for $T_p < T_g$.

The hyperbolic description of the polarization temperature dependence of the entropy is observed for both drawn and undrawn polypropylene samples (Figure 2.80), but the variation of the entropy of activation for the same T_p span below T_g is much reduced in the case of the drawn specimen. The asymptote value found for the drawn sample (T_p = 40.85 °C) is higher than for the undrawn specimen. For undrawn polypropylene;

$$\Delta S_p = -62.57 - \frac{3121.80}{T_p - 20.42}$$

EBSCOhost - printed on 2/13/2023 12:32 AM via . All use subject to https://www.ebsco.com/terms-of-use

and for drawn polypropylene,

$$\Delta S_p = -20.58 - \frac{2475.21}{T_p - 40.85}$$

Note that the asymptote found for the drawn specimen is not the temperature of compensation because the value of δ_c is not close to zero in this case.

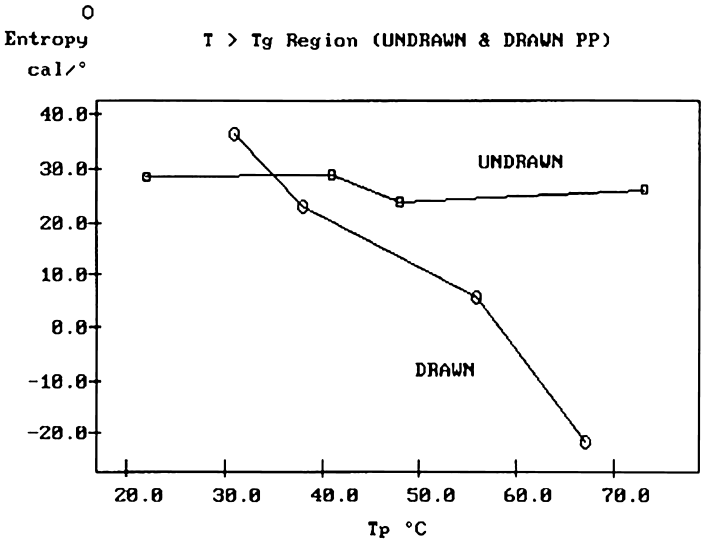


Figure 2.81: Comparison of ΔS_p vs. T_p for drawn and undrawn polypropylene for $T_p > T_g$.

Figure 2.80 is spectacular in demonstrating the power of TWD spectroscopy. The effect of orientation on the mobility is well characterized by this technique. For the amorphous phase analyzed above T_g (Figure 2.81), it is remarkable to see that only the behavior for drawn polypropylene shows a decrease of entropy as T_p is raised. One would expect to see a "melting" of the orientation of the amorphous phase when the polymer is reheated above its T_g. The entropy was raised by the orientation effect in the direction perpendicular to the orientation direction. Entropy is lost as the polymer is "annealed" above T_g, which occurs as the polarization temperature of higher values is used to perform thermal-windowing. Incidentally, the value obtained for $T_p = 65$ °C is –20 cal/°C, which matches the initial value in Figure 2.80 for the undrawn specimen at lower T_ps.

The free energy of activation against T_p is shown in Figure 2.82, demonstrating that, although the entropy and enthalpy for the two amorphous components are very different in drawn and undrawn polypropylene, the action of the voltage field on the interaction between the dipoles remains identical and independent of the state of the amorphous component within the structure.

EBSCOhost - printed on 2/13/2023 12:32 AM via . All use subject to https://www.ebsco.com/terms-of-use

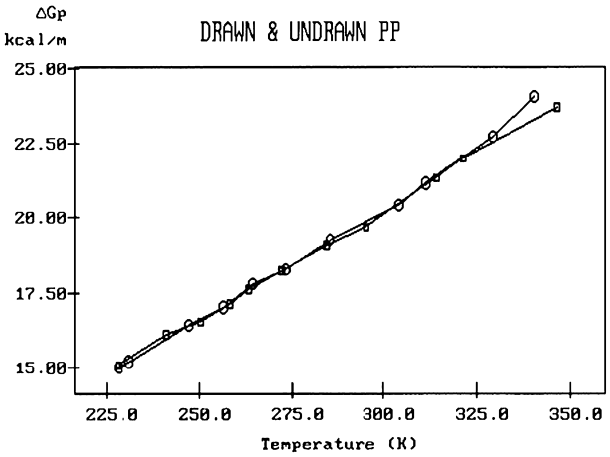


Figure 2.82: Comparison of ΔG_p vs. T_p for drawn and undrawn polypropylene for T_p below and above T_g.

Mechanical strain does not influence the interaction between the voltage field and the dipoles attached to the amorphous component on the structure. It will be shown in Chapter 4 of Part II that this is not always the case and that multi-component systems with blends and/or block copolymers can have different free energy of activation at various T_ps. A good example will be provided with a blend of low-density polyethylene (LDPE) and high-density polypropylene (HDPE).

In summary, TWD spectroscopy has been shown to provide a level of detail about the coupling kinetics between the dipoles due to the material structure that is unmatched by any other single technique, including TSD. In addition to identifying the main amorphous component situated between spherulites and its dependence on orientation by mechanical means, the technique allows the quantitative study of the amorphous phase included within the spherulites, perhaps those dipoles located at the turn of the lamella forming regions. The influence of the crystalline structure on the amorphous regions can be investigated by TWD spectroscopy. Many of the analytical tools developed in this chapter can be used to provide important detail related to the structure of the amorphous phase imbedded in complex crystalline structures. The information is critical to physical properties such as impact strength, since the amorphous matter is located at the boundary of the rigid spherulites, and the plasticity of a material also depends on the amorphous component inside the spherulites.

I.2.12 Conclusion

Thermally stimulated current allows an in depth understanding of the intermolecular coupling involved in the process of glass transition. Windowing polarization techniques represent a new tool to separate out the different elementary relaxation modes which couple up to create the global TSD output at T_g. The classical instruments tra-

EBSCOhost - printed on 2/13/2023 12:32 AM via . All use subject to https://www.ebsco.com/terms-of-use

ditionally used in thermal analysis (TMA, DMA, DSC, DETA) can only reveal the global aspect of molecular motion. Relaxation map analysis provides a detailed understanding of the coupling mode between the elementary molecular motions involved and helps quantify the degree of coupling and its relation to the state of the glass with the introduction of the concept of compensation. The compensation phenomenon can be studied directly in the Arrhenius plane, with plots of $\log \tau$ versus 1 / T, or it can be studied in the ΔG plane, in the sub-EE plane, or in the normalized ΔG plane. ΔG can be calculated from the apparent enthalpy and entropy of activation at each temperature, which we call sub-ΔH and sub-ΔS, respectively, and the compensation phenomenon can be looked at from a different perspective, as a converging set of lines of activation free energy ΔG plotted against temperature crossing at the compensation point.

Replotting the depolarization data with normalized variables allowed us to find mathematical relationships between the entropy of activation, the enthalpy of activation, and the polarization temperature. The mathematics proved to be extremely simple and useful to explain some of the experimental results which seemed puzzling. The question remains whether the analytical treatment of this chapter has any physical sense or is merely a mathematical description of the variation of the shape of relaxation curves with the polarization temperature. The answer relies on the meaning of compensation. We will present in the next chapter (Part I, Chapter 3) a possible interpretation for its observation based on the Dual-Phase model of the interactions.

What about the meaning of $A_c = -\Delta S_{o,h} = 70$ cal/°C? The question remains asked. It is possible that this entropic term is associated with the electronic entropy due to the spinning of the electrons on their orbitals. The reason is that 70 cal/°C corresponds to a frequency of 10^{15}, which is precisely the frequency of vibration of the electrons. Also, this number seems to be approximately constant, plus or minus 2 cal/°C, and one would not expect any influence from external means to the electronic entropy by more than 2% to 3%. The influence of heating rate on the value of A_c has not been investigated in this work.

Another important question should be raised. Suppose that all of the above findings, derived from a mathematical understanding of thermal-windowing by the Debye formula, are entirely created by the technique of thermal-windowing itself and the technique used to analyze. Suppose that the need to heat up to the polarization temperature, in order to apply the voltage field, perturbs the state of the system so much that it is the reason for the maximum entropy, because once T_p is superior to T_g, the polymer can relax to the equilibrium state prior to the application of the field. Could the technique of analysis of the curves be also the reason for compensation phenomena? After all, is it not intriguing to find compensation phenomena for the sub-EE plots and for the normalized free energy plots? Could it be that the regression analysis of the "Debye" peaks is nothing more than a fitting technique and that no meaning should be given to the derived activation energy and entropy? The very small value found for τ_o in the Arrhenius curve-fits does not seem to be realistically related to the vibration of the atoms (although we just mentioned the possibility that the frequency of the

EBSCOhost - printed on 2/13/2023 12:32 AM via . All use subject to https://www.ebsco.com/terms-of-use

electrons on their orbitals might be included). These questions are all addressed and answered in the next chapter of Part I, where it is shown that the Dual-Phase nature of the interactive coupling between the dipoles is responsible for the compensations observed.

Nevertheless, should it be the case that thermal-windowing creates the features which we observe and explain quantitatively in this chapter, it remains that the cascade of new structural parameters that it defines can help characterize the structure of polymeric materials, with all the power of comparison that this implies. This will be demonstrated in Part II through case studies.

EBSCOhost - printed on 2/13/2023 12:32 AM via . All use subject to https://www.ebsco.com/terms-of-use

EBSCOhost - printed on 2/13/2023 12:32 AM via . All use subject to https://www.ebsco.com/terms-of-use

Part I Chapter 3
A Dual and Cross-Dual interpretation of interactive coupling of conformers applied to thermally activated polarization and depolarization of polymers

The reason for naming this book "*Dual-Phase Depolarization Analysis. Interactive coupling in the amorphous state of polymers*" starts to become apparent: the previous two chapters cover the fundamentals involved to characterize *interactive coupling in the amorphous state of polymers* by Thermal-Stimulated Depolarization spectroscopy (TSD/TWD). This chapter concentrates on the part of the main title of the book that attempts to find an interpretation of the results found by TSD/TWD using the Dual-Phase model of the interactions introduced for polymers in previous publications [128, 134, 135, 139, 140] and other publications pending to be published [137, 138, 143, 144]. The general subject of the coupling of the interactions – local and collective – is also introduced at the end of the discussion and in Appendices A and B at the end of this Chapter 3 and in the CONCLUSIONS chapter of the book.

I.3.1 Challenging results to the conventional models of polymer physics. Introduction to a new approach to the physics of polymer interactions: the Dual-Phase and Cross-Dual-Phase models

In many ways, the results obtained by TSD or TWD represent a challenge to the classical views on macromolecules. The $T_{g,\rho}$ peak (Figure 3.5) is in dispute: some scientists claim it is T_{LL}, but we present a different explanation in this text; the compensation of the relaxation modes extracted from the Debye peaks obtained at variable T_p is simulated in Chapter 1 (Figure 1.13), yet its implication on the meaning of compensations must be clarified; the existence of the negative compensations found for $T_p > T_g$ is a novelty without interpretation from the classical views of polymer physics (Part II, Figure 1.25, top, or Part II, Figure 3.61); the existence of the T_{LL} relaxation-transition, which, in the context of TSD/TWD, we derive from relaxation maps in the ΔG plane (equation (2.28b)), is still a well-known controversial issue [21, 135]; the network of multi-compensations and super-compensations found for the organization of the enthalpy and entropy in Part II, Chapter 4 (Figures 4.8 to 4.10) represents the greatest challenge to any theory of polymer physics, including our own model: why would all the relaxation modes describing interactive coupling in the amorphous phase resume to a network of positive or negative compensations as sketched in Part II, Figure 4.14?

It is not our intention to present here the details of our model of the physics of interactions in polymers. The interested reader can refer to an introduction of the

https://doi.org/10.1515/9783110756746-004

EBSCOhost - printed on 2/13/2023 12:32 AM via . All use subject to https://www.ebsco.com/terms-of-use

Dual-Phase and Cross-Dual-Phase models of polymer physics interactions in references [128, 134, 135, 137, 138].

We will limit ourselves in this text to presenting the general principles and fundamentals of the theory.

In our view, "conformers," the constituents of the macromolecules, gather into statistical systems which go beyond belonging to individual macromolecules. A conformer is shown in Figure 3.1, duplicated from reference [128]. The macromolecules themselves represent a chain of "covalent conformers" put together as an entity. The problem is to determine whether the chain properties, derived from its statistics, control *entirely* the dynamics of the collection of chains making up a polymer. This is what has been assumed by all the other theories, and this is what the Dual-Split Kinetics and the Grain-Field Statistics challenge.

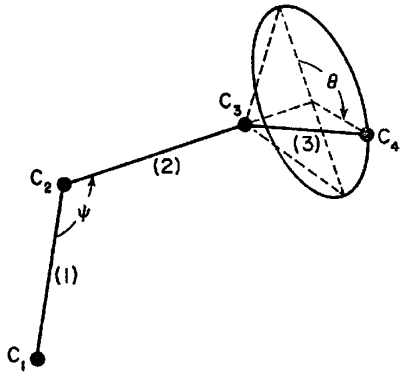


Figure 3.1: Sketch of a conformer ([128], after Flory's three-bond unit [90]).

Also in our view, the free energy of the collection of chains assembled as a polymer is not equal to the scaled-up free energy of a macromolecule embedded in a mean field created by the influence of the other macromolecules; at least not below the temperature T_{LL} (see below), which itself is a function of the dynamics of the experiment and the chain characteristics. In fact, for many experimental conditions, depending on temperature and other factors, our model of polymer interactions does not require, in its hypotheses and derivations, a description of the changes which occur to the individual macromolecules. The dynamic statistical systems dealt with, to determine the free energy and its structure (enthalpy and entropy), are not macromolecules in our approach. However, the fact that macromolecules compose the basic structure *is essential*, for instance to understand the basis of our new Dual-Phase statistics and to explain "entanglements," for which our model provides a completely different interpretation than the ones offered by the conventional spaghetti bowl or tube models [128].

A "covalent conformer" is not the same as a "free conformer" (Figure 3.1), such as a small molecule used as the monomer in the polymerization process. Its interaction

EBSCOhost - printed on 2/13/2023 12:32 AM via . All use subject to https://www.ebsco.com/terms-of-use

to other conformers by covalent bonding modifies the conformational potential energy of a free conformer, and this governs the statistical properties of a "free chain." Here we are still "classical," yet when dealing with a collection of chains put together, our approach differs from the classical one. Conformers belong to two types of sets: they belong to macromolecules, which link them via covalent forces, as we just said, and they belong to the grand ensemble of conformers which are linked by *inter-intra* molecular forces, van der Waals, dipole-dipole, and electrostatic interactions which affect and define the viscous medium. That duality is intrinsic to conformers, which we could call the "dual-conformers" to mark this specificity. The potential energy of a dual-conformer is different from the potential energy of a conformer part of a free chain.

To simplify, one could view the difference between our statistical model and the classical model to describe the properties of polymers as follows: according to the classical views, the statistical systems are the macromolecules, i. e., a network of chains; the properties of the chains are disturbed by the presence of other chains and by the external conditions (temperature, stress tensor, electric field, etc.). The classical definition of the statistical system contrasts with our approach whereby the statistical systems are the "*dual-conformers*," not the macromolecules. The interactive coupling between the dual-conformers is defined by a new field of statistics, the Grain-Field Statistics, that explores the correlation between the local conformational property of the dual-conformers and their collective behavior as a dissipative network. In the following, for simplicity we will just call the dual-conformers "conformers."

Again to simplify, the statistics that are used by the classical models and our model to describe the rotational isomeric states (RISs) of the conformers are fundamentally different: the classical molecular dynamic statistics is the Boltzmann statistics, famous for its kinetic formulation of the properties of gases. The Dual-Split or Dual-Phase statistics, leading to the Grain-Field Statistics, is inspired by the classical Boltzmann concept but departs from it by defining a dissipative term in the equations and assuming that the free energy remains always equal to its minimum value, that of the equilibrium state, even for transient states. The kinetics created by such changes in the fundamental equations result in the formation of free energy structures, which we have once called "the energetic kinetic dissipative network of conformers (EKNET)" ([117–122]) and more recently, while dealing with rheology, "the elastic dissipative network" ([128, 134]).

In our analytical formulation of the dynamics of these "*open dissipative systems of interactions*" generated by our two modifications of the classical formula, we realized that essentially two mechanisms of structuration of the free energy prevail and compete: a "vertical structuring" and a "horizontal structuring," each specifically applying its own version of the basic equations. This distinction increases the complexity of the analytical solution but is, in our opinion, a fundamental aspect of the way interactions work. The vertical structuring refers to a split of the units (collectively interacting in the system) into two compensating sub-systems having each a different statistical

EBSCOhost - printed on 2/13/2023 12:32 AM via . All use subject to https://www.ebsco.com/terms-of-use

partition. The horizontal structuring offers a different split of the collective set, via the generation of N_s identical sub-systems, each with the same statistical partition. Each split mechanism generates a dissipative function. The total dissipative function ought to be minimized (it is 0 at stable equilibrium), a condition that creates their compensation, i. e., whether they work independently, in sequence, or together.

By applying these general principles to polymers, specifically, we can now summarize our model in one sentence:

> We define a polymer as a set of "dual-conformers," i. e., a set of three-bond elements belonging or not to the same macromolecule, submitted to *intra-inter* molecular forces described by an energy potential to which the equations of the Dual-Split and Grain-Field Statistics theory apply.

The details of the simulations performed using this model of polymer interactions shows that there is a temperature, which we associate with T_{LL}, that is the dynamic transition temperature beyond which the classical molecular models based on the Boltzmann statistics and our open dissipative network model are compatible and coherent. This stipulates that molecular theories of polymeric materials will provide the same results as our model for $T > T_{LL}$, a temperature at which the dissipative function kinetically collapses. Below T_{LL}, the behavior that results from the interactions is dominated by the statistics of the Dual-Phase and Cross-Dual-Phases; thus, below T_{LL}, the macromolecular aspect does not statistically dictate the properties. The projections of these macromolecular statistical models (reptation, for instance) are physically unfounded below T_{LL}, in our opinion, which explains their failure to describe the experimental results (Chapter 7 of [128], also [135]).

If one tests the predictions of the classical approach under conditions that bring its state above T_{LL}, one may conclude that those data validate the classical views since they provide correct answers in the range tested. This is not an easy task, because T_{LL} is rate-dependent, pressure- and-shear dependent, and molecular weight-dependent. Thus, although one will find in the literature convincing experimental evidence of success for the classical models, which is the reason for their acceptance, we claim that these successes are due to the use of conditions that bring the state of the polymer above its T_{LL} transition.

The amount of experimental evidence of failure of the macromolecular dynamic models is growing ([212, 259, 260]), and those experimental facts can no longer be ignored or designated artifacts. The $T_{g,\rho}$, the T_{LL}, and the multi-compensation network described in this book are experimental facts that theories cannot ignore.

Besides, in most experimental set-ups used by the industry, T_{LL} is raised to such high values, due to the high rates and pressures, that the range of validation of the macromolecular dynamics to predict the properties is in default: the use of such classical models in such conditions would provide the wrong answers.

Additionally, although the subject is beyond the objectives addressed in this book, the Dual-Phase and Cross-Dual-Phase theory can be applied successfully to the inter-

EBSCOhost - printed on 2/13/2023 12:32 AM via . All use subject to https://www.ebsco.com/terms-of-use

pretation of rubber elasticity, linear and non-linear viscoelasticity viscous behavior (shear-thinning, strain softening), relaxation of enthalpy (DSC) and volume, thermo-mechanical memory effects, and crystallization from the amorphous state ([128, 136]). This novel approach of the physics of polymer interactions leads to the new world of processing technology called "Rheomolding" and "Rheo-fluidification" or disentanglement/sustained-orientation" ([124, 128]). These technologies are being licensed and are practiced by the injection molding and compounding industries. The acceptance of these new technologies has been endorsed slowly though, much more slowly than it should have in view of their practical benefits, simply because the dominant classical models could not explain the results, a typical reason for rejection, unfortunately.

We have advocated elsewhere (Chapter 7 of [128]) to abandon the classical interpretation of polymer physics by single-chain macromolecular dynamics because of its inability to describe the full range of its behavior and other essential properties of polymers such as the dielectric TSD/TWD responses analyzed in this book.

A quantitative description of the results obtained in this book using the equations of Dual-Split and Grain-Field Statistics has not been attempted. However, as will be introduced in the Appendix of this book and fully presented in the book dedicated to the grain-field theory ([137]), we have performed a great number of simulations based on the equations of the Dual-Split models (horizontal and vertical structuring) that lead, by analogy, to the understanding of the coupling between the free volume and the conformational energy characterizing the interactions between the dual-conformers. We symbolize this duality by $[(b/F) \leftrightarrow (c, g, t)]$, where b and F represent two conjugated states of the inter-intra duality and (c, g, t) refers to three conformational states of the dual-conformers (Chapter 1 of [128]).

This local duality, described by the Dual-Split Kinetics (equations (5) to (7) of the Appendix, for instance), provides a reason for the existence and characteristics of the b grains surrounded by the F conformers, our explanation for the $T_{g,\rho}$ peak observed in TSD (Part II, Chapter 2). In a certain way, the presence of the $T_{g,\rho}$ peak may be considered an indirect validation of the local duality (b/F) in our model.

The Appendix can be read as a short quantitative introduction to the terms and assumptions of the Dual-Split Kinetics models (vertical and horizontal structuring) that we will refer to in the following sections: Appendix Part A deals with vertical structuring and Appendix Part B with horizontal structuring.

The reader's comprehension of the $T_{g,\rho}$ peak and the T_{LL} transition, described in the next section, will benefit from reading the Appendix, since the simulation equations give rise to (b/F) and its stability, i. e., to our interpretation of these two transition-relaxations, by analogy.

EBSCOhost - printed on 2/13/2023 12:32 AM via . All use subject to https://www.ebsco.com/terms-of-use

I.3.2 The $T_{g,\rho}$ peak and the T_{LL} transition

The characteristics of $T_{g,\rho}$ and T_{LL} are discussed in Part II, Chapter 2. The presence of the $T_{g,\rho}$ peak is universal in the characterization of polymers by TSD. We find that peak just above T_g for all polymers tested. The position of $T_{g,\rho}$ with respect to T_g depends, to a large extent, on the choice of the polarization temperature T_p, which enhances the respective magnitude and the resolution of the peaks by the effect of polarization selectivity mentioned in Part II, Chapter 2.

TSD, which works at a very low frequency equivalent (~10^{-5} to 10^{-3} Hz, see Part II, Chapter 1), is capable of resolving the $T_g/T_{g,\rho}$ kinetic presence with far higher resolution and sensitivity than other techniques. However, it is not uncommon to observe that the T_g and $T_{g,\rho}$ peaks merge into a broad intense peak for certain polarization temperatures, complicating their fine analysis.

The transition T_{LL} should not be confused with $T_{g,\rho}$, as has many times been the case [21]. Its manifestation by a peak in TSD, located at a higher temperature than $T_{g,\rho}$, is not systematic and depends on the thermomechanical treatment of the specimen. In some instances, the mechanical history of the specimen and the temperature of polarization are such that $T_{g,\rho}$ and T_{LL} merge or overlap. TWD normally allows a good separation of all the peaks, which can be isolated and deconvoluted individually (Part II, Figure 1.13).

The Dual-Phase theory suggests a common *dynamic* origin to T_g, $T_{g,\rho}$, and T_{LL}, and even to T_β (Chapter 2 and reference [122]). The apparent complexity of the relaxation behavior arises for two reasons:

(1) The kinetics are due to the interactive coupling between horizontal structuring (Appendix Part B) and vertical structuring (Appendix Part A) that combine to create the structure of the free energy. The dissipative wave generates the compensation between the two structuring modes: the solutions are, indeed, not simple. However, Figure C.4 in Appendix B explains how the modulation of the structure of the N_s systems by the b and F conformers kinetics can result in a split of the peaks observed at the occurrence of the main relaxation. Therefore, one could say that $T_{g,\rho}$ is inherently reflecting the duality of the b/F conformers; the presence of a shoulder on the main TSD or DSC peak might just be related to that: kinetic effects.

(2) But, even if the T_g and $T_{g,\rho}$ are kinetically related, their dielectric origin is most of the time different, because the effect of voltage field on the b and F conformers is different. The T_g peak is due to the relaxation of dipole moments attached to the b conformers, and the kinetic complexities might reveal some modulations on the peak itself. The dipolar moment for $T_{g,\rho}$ is probably associated with ionic dipoles, or perhaps space charges attached to the interfacial tissue created by the F conformers. There is much evidence in Part II, Chapter 2 to suggest that the $T_{g,\rho}$ peak is related to the free volume in the sample, which the Dual-Phase interpretation redefines as the volume around the F conformers. Either local unstable ionic dipoles or space charges get trapped in the free volume characteristic of the surrounding of the F conformers.

EBSCOhost - printed on 2/13/2023 12:32 AM via . All use subject to https://www.ebsco.com/terms-of-use

These charges are injected by the voltage field, or enhanced by it, and relax at $T_{g,\rho}$. In some instances, the $T_{g,\rho}$ peak is broad and contains a combined effect of molecular dipoles and free volume relaxations (Figure 2.10 of Part II, Chapter 2). In such cases, two or more additional compensations are observed in the ($T > T_g$) region up to T_{LL}. The existence of this special F conformer tissue in the structure is also revealed by the response of polymers during the TSPC experiments either on heating or cooling (Part II, Chapter 1). During thermally stimulated polarization experiments, the $T_{g,\rho}$ peak is not observed, but volume or surface conductivity starts at that same onset temperature.

According to the Dual-Phase views ([134], Chapter 1 of [128]), the local density difference between the b grains and the F conformers is "time-averaged" by the constant wiping (above T_g) of a "dissipative elastic wave" having a frequency ω_o that is a function of temperature and molecular weight and thus is different from the Brownian dissipation, i. e., the thermal fluctuation characteristic of the Boltzmann mean field (the classical kT/h term). As a consequence of the dissipative elastic wave in the rubbery state and in the melt, the F conformers become the source of formation of a tree-type channel of nano-conduction for the injected charges from the electrodes across the non-conductor. About 20 °C below T_g, the F conformers are frozen in, which makes the boundaries around the b grains to become localizable (and the source of crazes when submitted to axial stresses).

We have proposed in Chapter 2 how to calculate the value of T_{LL} from the negative compensation, by extrapolation of the entropy vs. T_p results for $\Delta S_p = 0$ (or towards a minimum asymptotic value). In this sense, we can consider T_{LL} as the temperature marking the end of the relaxation behavior due to the modulation by the dissipative term in the Dual-Phase dynamics. This is seen in Figure 3.2 when the rate of $dN_b(t)/dt$ becomes 0, ending the modulation of $n_{tb}(t)$ by $N_b(t)$. This figure is understood from the explanations given in the Appendix regarding Figures A.1 to A.3 related to vertical Dual-Split structuring. $N_b(t)$ is the sum of the population n_{tb} and n_{cgb} and Figure 3.2 plots the derivative of $N_b(t)$ and $n_{tb}(t)$ to show the modulation that starts on cooling ($q = -1$ K/s) at T_{LL}.

We propose that the mechanism of relaxation in polymers is due to the dynamic coupling of two types of splitting processes of the total statistical population of conformers in interactions: the creation of $N_s(t)$ energetic kinetic systems (horizontal splitting) and the modulation of the conformational structure of these systems by the dissipative function (vertical splitting).

This applies to the coupling of cooperatively interactive dipolar motions and to the modulation of both the sub-T_g and the ($T > T_g$) kinetics. It might be more appropriate to categorize T_{LL} as one of the kinetic manifestations resulting from the cooperative kinetic process already giving rise to T_β, T_g, and $T_{g,\rho}$. Beyond $T_p = T_{LL}$, the organization of the inter-intra molecular interactions between the various dipoles as a dissipative network is kinetically inefficient and hence has ended. As we said earlier,

EBSCOhost - printed on 2/13/2023 12:32 AM via . All use subject to https://www.ebsco.com/terms-of-use

a description of the properties of the polymer by invoking the properties of the individual macromolecules embedded in a mean field is acceptable from this point on. T_β is the temperature for the onset of energetic kinetic coupling. It should be a function of thermal history. The temperature of infinite viscosity defined by the WLF equation, fitted to the $T_{g,\rho}$ Arrhenius transform, should characterize the lower limit for T_β. The intercept of the ($T > T_g$) Z-lines, either from multi-compensations or for specimens with variable thermal history, should also define $T_{\beta o}$, the lowest T_β achievable.

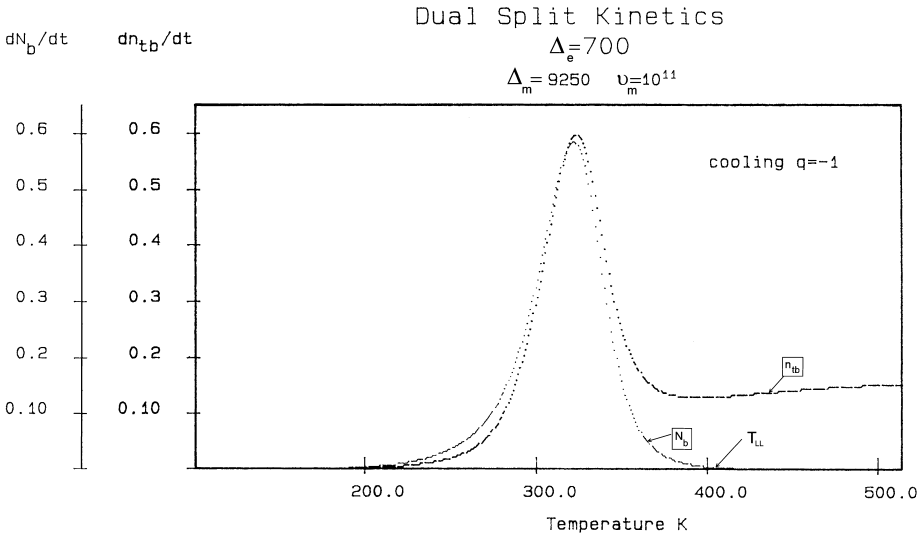


Figure 3.2: Dual-Split Kinetics simulation (solution of equations (5) to (7) of Appendix Section A.2) for $\Delta_m = 9250$, $u_m = 10^{11}$, $\Delta_e = 700$. COOLING simulation from $T_o = 515$ K with cooling rate $q = -1$. The two curves designate the kinetic rates for the population of n_{tb} and N_b.

I.3.3 Application of compensations to characterize interactive coupling in the amorphous state

I.3.3.1 Compensation laws

In this book we make use of compensations as a quantitative characterization tool to evaluate the interactive coupling between the Debye relaxation modes. Compensation of the Debye characteristics (ΔH, Ln τ_o) means that their modes of relaxation, stimulated at various temperatures, T_p, are interdependent. The interdependence is clearly visible graphically: a series of plots of $\log \tau(T)$ vs. $1/T$ in the Arrhenius plane or of ΔS_p vs. ΔH_p in the ΔG plane, when T_p varies, shows a set of spectral lines that converge to a single point, the compensation point. Hence, the compensation point coordinates appear to define the interactive coupling between the relaxation modes.

EBSCOhost - printed on 2/13/2023 12:32 AM via . All use subject to https://www.ebsco.com/terms-of-use

We will show in Part II of this book how to apply the concept of compensation to the analysis of complex TWD results, when the amorphous phase is made up of cooperative relaxation modes of different origins, for semi-crystalline polymers, for copolymers, and for blends of polymers, as well as when additives are added. In every such case the compensation characteristics of the amorphous state(s) is modified and this modification can be quantified by comparing its compensation point coordinates with a reference value.

This is why the TWD characterization technique offers a unique value in the spectrum of thermal analysis instruments available to determine the properties of non-conductive materials.

But, beyond the practical usefulness of the use of compensations to characterize the amorphous state of non-conductive matter, the theoretical value of compensation laws is a full debate on its own. We refer to the appropriate literature for the details ([50, 115, 116, 218]).

In this section, we examine the possible links between the compensation results in Chapter 2 and Part II, Chapter 4 and their possible interpretation in terms of the horizontal- and/or vertical-split structuring models introduced in the Appendix. In particular, what do we mean by "several relaxation *modes*"? Is it the manifestation of the same relaxation process, such as vertical structuring, when it is submitted to a series of thermal stimulations, controlled by one parameter, say T_p? The analogy that comes to mind is the study of an object by the observation of its shadow, varying the angle of illumination of the object.

We want to address three aspects of the problem:

- What gives rise to the compensations of the slope and intercept of the Arrhenius lines? What gives rise to positive and negative compensations and the possibility to organize them in super-compensation networks?
- What is the effect of the voltage field on the statistics of interactive coupling?
- Can we determine the fundamental parameters of the Grain-Field Statistics by voltage field stimulation? What is a network of compensations?

It should be made clear that the following proposed answers to these important questions are incomplete and that the subject requires much more additional details and research to be signed off.

I.3.3.2 Compensations of ΔH and Ln τ_o. Positive and negative compensations; the organization of the compensations in a super-compensation network. The Dual-Split model explanation

The first thing to understand is the compensation of the $\mathrm{Ln}(\tau_o)$ and ΔH variables when T_p varies: are we revealing the existence of several relaxation kinetics or of a single relaxation like the object under several illumination angles?

EBSCOhost - printed on 2/13/2023 12:32 AM via . All use subject to https://www.ebsco.com/terms-of-use

Both the vertical and horizontal structuring kinetics described in the Appendix result in a compensation law between kinetic variables that can be assimilated to ΔH and $\mathrm{Ln}\,\tau_o$. In the following, we choose to simplify the situation by considering that the coupling between the fundamental parameters of a conformer, $[(b/F) \leftrightarrow (c, g, t)]$, are derived from the vertical structuring and that the role of the horizontal structuring is limited to the organization of the b conformers in N_s b grains.

The fundamental constants of the Dual-Split Kinetics model (equations (5) to (7) of Appendix Part A) are Δ_m, υ_m, and Δ_e. When these constants are known, we can characterize the system of interactions by the statistical population of the conformers, their cis, gauche, and trans conformation, and their b/F state, which controls the free volume in the system. The interactive coupling between the conformational states and the b/F state is described by Δ_x, υ_x, which are functions of Δ_m, υ_m, and Δ_e. At equilibrium, the system of interactions is stable and the b and F populations are "transparent," i. e., undistinguishable, statistically speaking. As soon as non-equilibrium conditions occur, such as by cooling or heating, the b/F population becomes asymmetric, which is governed by a self-generated kinetics. This auto-catalytic kinetics can be expressed by a single constant, k_x, which varies only with T, for a given set of Δ_m, υ_m, and Δ_e (Figure A.11 of the Appendix). As explained in the Appendix, for a given value of Δ_e, we run simulated annealing experiments after quenching from the same temperature down to a series of five lower temperatures at which the value of (k_x) is determined from a phase plot of dN_b/dt vs. N_b at $t \rightarrow 0$. Figure A.12 shows that the temperature dependence of k_x follows an Arrhenius variation, which corresponds to the linearity of $\mathrm{Ln}(k_x(T))$ with $1/T$. From the intercept and slope of such an Arrhenius plot, we determine $\mathrm{Ln}\,\upsilon_x$ and Δ_x, respectively, that we could hypothetically associate with an entropy and enthalpy of activation for the $(b/F \leftrightarrow (c, g, t))$ interactive coupling kinetics, the way we did to convert the current of depolarization into a relaxation time and determine $\mathrm{Ln}(\tau_o)$ and ΔH from the Arrhenius temperature dependence of $\tau(T)$. We repeat the simulations for a series of Δ_e values at constant Δ_m and υ_m. This procedure establishes the value of $\mathrm{Ln}\,\upsilon_x$ and Δ_x for various Δ_e for a given set of Δ_m and υ_m. Finally, we change the values of Δ_m and υ_m and repeat the entire procedure.[1]

Figure 3.3 displays the influence of Δ_e on the k_x statistics: for a given set of Δ_m and υ_m ($\Delta_m = 9250$ and $\upsilon_m = 10^{11}$ in Figure 3.3), a compensation law is observed between $\mathrm{Ln}\,\upsilon_x$ and Δ_x when Δ_e varies. The compensation between $\mathrm{Ln}\,\upsilon_x$ and Δ_x when Δ_e varies is similar to the compensation between $\mathrm{Log}\,\tau_o$ and ΔH when T_p varies in a TWD experiment. The compensation means that the Arrhenius lines of $\mathrm{Ln}(k_x)$ vs. $1/T$ converge to a single point, the compensation point, when Δ_e varies. This is similar to the situation observed in a relaxation map showing the compensation of the spectral

1 Note that in the TWD experiments the variables are τ_o and ΔH, i. e., a relaxation time and an enthalpy, whereas in the simulation υ_x and Δ_x refer to a frequency and an enthalpy. This difference results in a change of sign for the log axis variable, since $1/\upsilon_x = \tau_x$.

EBSCOhost - printed on 2/13/2023 12:32 AM via . All use subject to https://www.ebsco.com/terms-of-use

Arrhenius lines when T_p varies. As we saw in Chapter 2 (Figures 2.8 and 2.9), the coordinates of the compensation point of $\mathrm{Ln}(k_x)$ vs. $1/T$ can be determined by the slope and intercept of the corresponding compensation line in a compensation search, in our case – $\mathrm{Ln}\,\upsilon_x$ vs. Δ_x obtained by regression.

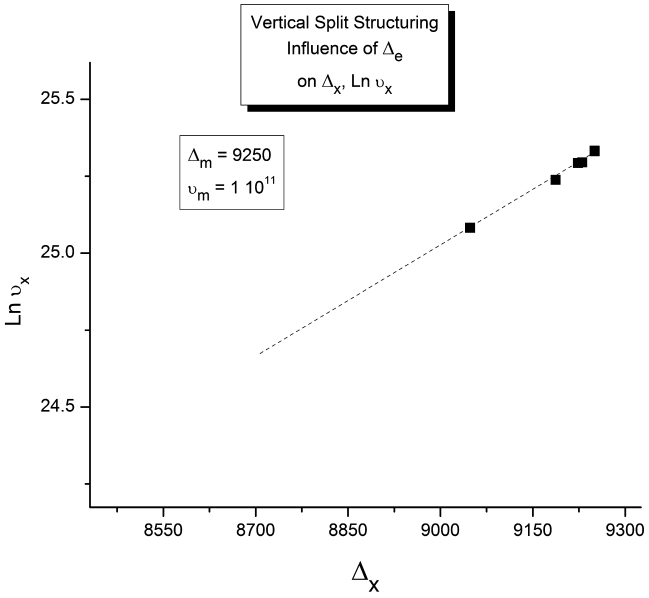


Figure 3.3: $\mathrm{Ln}\,\upsilon_x$ vs. Δ_x for $\Delta_m = 9{,}250$, $\upsilon_m = 10^{11}$ and Δ_e variable.

Figure 3.4 shows the influence of changing the value of Δ_m and υ_m on the compensation line for various Δ_e. Note that the variables in Figure 3.4 have been "normalized," i. e., have become $(\Delta_x - \Delta_m)$ and $(\mathrm{Ln}(\upsilon_x) - \mathrm{Ln}(\upsilon_m))$. When Δ_e varies, for a given pair of (Δ_m, υ_m), this is Δ_x and υ_x which vary. This will be important to remember when we will simulate the behavior of $(\Delta H, \mathrm{Ln}(\tau_o))$ with T_p by the behavior of $(\Delta_x, \mathrm{Ln}(1/\upsilon_x))$ with Δ_e. It should also be noted in this figure that the Δ_e values are rather small (from 5 to 150) with respect to Δ_m and that Δ_e decreases from left to right on the compensation lines that all pass through the origin. The origin corresponds to $(\Delta_x - \Delta_m) = 0$ and $(\mathrm{Ln}(\upsilon_x) - \mathrm{Ln}(\upsilon_m)) = 0$, obtained for $\Delta_e = 0$. All of these particular features are important to note to be able to correlate the effect of T_p on the $\mathrm{Ln}(\tau)$ vs. $1/T$ kinetics with the effect of Δ_e on the $\mathrm{Ln}(k_x)$ vs. $1/T$ kinetics. In particular, we need to know if the Dual-Split model of the interactions can simulate the switch from a positive compensation law to a negative compensation law when T_p crosses the T_g of the polymer *or if this results from another cause*. This implies to understand how Δ_e and T_p are related.

EBSCOhost - printed on 2/13/2023 12:32 AM via . All use subject to https://www.ebsco.com/terms-of-use

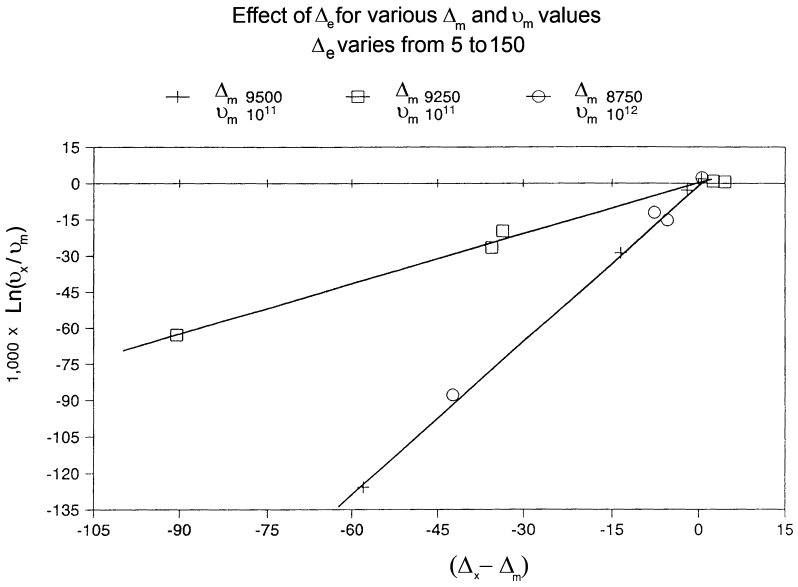


Figure 3.4: Effect of Δ_e for various Δ_m and υ_m values. Note that Δ_e decreases from left to right (from 150 to 5).

It is clear in Figure 3.4 that changing the values of Δ_m and/or υ_m in this low value of Δ_e range modifies the slope only. The inverse of the slope gives the value of T_c, the temperature of compensation for the Ln(k_x) vs. $1/T$ lines when Δ_e varies (since we have equated the gas constant to 1 in the simulations, we need to divide (1/slope) by 1.987 cal/mole if ΔH_x is expressed in such units). One sees in Figure 3.4 that T_c for Δ_m = 9,250 (squares) is greater than for Δ_m = 9,500 (the "+" symbol), at υ_m constant (10^{11}). The same slope can be obtained if we change Δ_m and υ_m simultaneously. Compare the dots (8,750, 10^{12}) and the "+" symbols (9,500, 10^{11}). Figures 3.5 to 3.7 show the effect of increasing Δ_e for these three sets of Δ_m and υ_m parameters.

Figure 3.5 applies to Δ_m = 9,500, υ_m = 10^{11}. Δ_e is now extended to 400 (4.21% of Δ_m). We observe two compensation lines, the one passing through the origin, point O, at low values of Δ_e, corresponding to the "+" symbols in Figure 3.4, and another straight line to cover the greater values of Δ_e, ending at point G in the figure. We have written the equation of the compensation lines on the graph $y = \alpha_o + \alpha_1 x$ for the larger values of Δ_e and $y = \alpha_1' x$ for the low Δ_e values. We can express the coordinates of the compensation points of [Ln(k_x), T_c] for these two compensation lines:

$$\begin{aligned} T_{c1} &= (1/1.987\alpha_1) \\ \mathrm{Ln}(k_x)_{c1} &= \alpha_o + \mathrm{Ln}(\upsilon_m) - \alpha_1 \Delta_m \end{aligned} \tag{3.1}$$

EBSCOhost - printed on 2/13/2023 12:32 AM via . All use subject to https://www.ebsco.com/terms-of-use

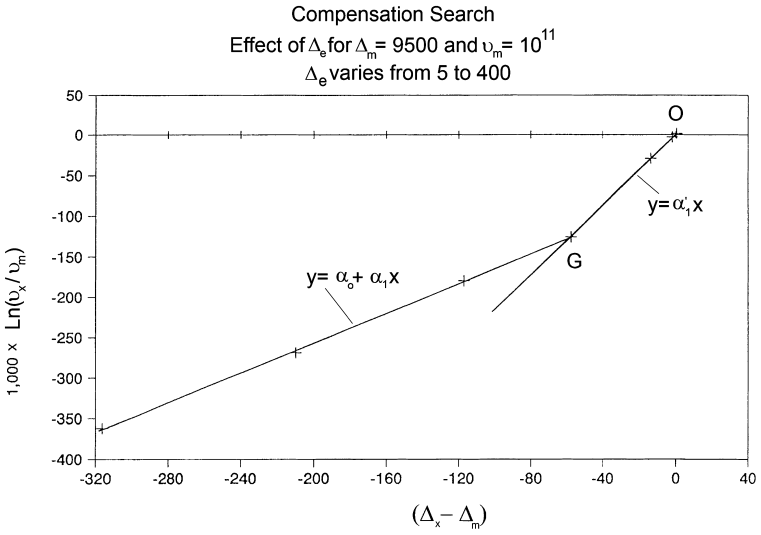


Figure 3.5: Normalized compensation search of $\mathrm{Ln}(\upsilon_x/\upsilon_m)$ vs. $(\Delta_x - \Delta_m)$ for $\Delta_m = 9500$, $\upsilon_m = 10^{11}$. Effect of varying Δ_e. Here Δ_e decreases from $\Delta_e = 400$, at the left, to $\Delta_e = 5$, at the far right. See text.

with $\Delta_e > \Delta_{eg}$, where Δ_{eg} is the value of Δ_e at point G,

$$T_{c2} = (1/1.987\alpha'_1)$$
$$\mathrm{Ln}(k_x)_{c2} = \mathrm{Ln}(\upsilon_m) - \alpha'_1\Delta_m \tag{3.2}$$

with $\Delta_e < \Delta_{eg}$.

Could the two compensation lines of Figure 3.5 simulate the change of behavior at T_g for an amorphous phase analyzed by TWD?

Let us consider the experimental evidence first: for a Debye relaxation map, scanning T_p from a low value below T_g, crossing T_g, and above T_g, we go from a positive compensation to a negative compensation, meaning that the value of ΔH_p, the slope of the Arrhenius line, increases first with T_p, passes through a maximum value at T_g, and then decreases towards a minimum value. As we show in Part II, Chapter 1, this maximum of ΔH_p describes the typical response of an amorphous phase submitted to a voltage field stimulation according to the thermal-windowing protocol (Introduction Chapter, Figure 0.3).

Now, assuming that we can simulate the effect of T_p on the depolarization kinetics by a change of Δ_e on the k_x relaxation kinetics, we can formulate and test the hypothesis that the compensation line below point G in Figure 3.5, corresponding to the higher values of Δ_e, simulates the $T_p < T_g$ positive compensation and that the compensation line above point G, corresponding to lower and vanishing values of Δ_e, simulates the

EBSCOhost - printed on 2/13/2023 12:32 AM via . All use subject to https://www.ebsco.com/terms-of-use

negative compensation. This would only occur if

$$T_{c2} < T_{c1} \quad \text{and} \tag{3.3a}$$

$$\text{Ln}(k_x)_{c2} > \text{Ln}(k_x)_{c1} \tag{3.3b}$$

The first requirement is met since $\alpha_1' > \alpha_1$ in Figure 3.5, which, plugged into equations (3.1) and (3.2), means that (3.3a) is true.

The second requirement, (3.3b), will be met if and only if

$$\text{Ln}(k_x)_{c2} = \{\text{Ln}(\upsilon_m) - \alpha_1'\Delta_m\} > \text{Ln}(k_x)_{c1} = \{\alpha_o + \text{Ln}(\upsilon_m) - \alpha_1\Delta_m\} \tag{3.4}$$

where the expressions of $\text{Ln}(k_x)_{c1}$ and $\text{Ln}(k_x)_{c2}$ are brought in from (3.1) and (3.2), respectively.

Equation (3.4) simplifies to

$$\text{Ln}(\upsilon_m/\upsilon_{xg}) + \alpha_1(\Delta_{xg} - \Delta_m) < (\alpha_1' - \alpha_1)\Delta_m \tag{3.5}$$

where υ_{xg} and Δ_{xg} are the values of υ_x and Δ_x at point G, at which $\Delta_e = \Delta_{eg}$.

Hence, we must demonstrate that

$$\text{Ln}(\upsilon_m/\upsilon_{xg}) < \alpha_1'\Delta_m - \alpha_1\Delta_{xg}$$

But at point G, we also have

$$\text{Ln}(\upsilon_{xg}/\upsilon_m) = \alpha_1'(\Delta_{xg} - \Delta_m) \quad \text{which is the transposition of } y = \alpha_1'x$$

Finally, the second requirement in equation (3.3b) resumes to test if equation (3.6) is true:

$$\alpha_1'(\Delta_m - \Delta_{xg}) < \alpha_1'\Delta_m - \alpha_1\Delta_{xg} \tag{3.6}$$

Equation (3.6) simplifies to

$$-\alpha_1'\Delta_{xg} < -\alpha_1\Delta_{xg}$$

or

$$\alpha_1' > \alpha_1$$

which is always true when $T_{c2} < T_{c1}$.

In summary, the two conditions (3.3a) and (3.3b) *are verified* and we could conclude that Figure 3.5 is the correct representation of the positive and negative com-

EBSCOhost - printed on 2/13/2023 12:32 AM via . All use subject to https://www.ebsco.com/terms-of-use

pensations observed for describing interactive coupling in the amorphous phase of a homopolymer across its T_g. This analogy implies that Δ_e decreases as T_p increases, which is observed in Figure 3.5 since Δ_e decreases from left to right.

But there is one remaining question to consider: even if this solution seems to work, is it the only plausible solution? In other words, is the solution offered by Figure 3.5 the only possible explanation for the switchover at T_g from a positive to a negative compensation? Here are a few good reasons to remain cautious:

1. The simulation in Figure 3.5 is not exactly a simulation of the TWD experiment (we will get back to that point). In particular, the depolarization stage in a TWD experiment is obtained under a thermal temperature ramp at constant rate. This is not the case for the simulations, done isothermally.

2. If equations (3.3) to (3.6) were truly simulating the TWD two-compensation split at T_g, point G in Figure 3.5 would correspond to the T_g of the polymer system of interactions. At this point $\Delta_e = \Delta_{eg}$, which can be obtained from the simulation data, and the values of Δ_x and $\mathrm{Ln}\, \upsilon_x$ are those at point G. The crossing of the positive and the negative compensations in an amorphous polymer occurs at $T_p = T_g$, defining the characteristics of the Z-line, the line joining the two compensation points. But, the existence and the position of the break in Figure 3.5 is determined by the choice of the values of Δ_m and υ_m. As we will see, for certain pairs of Δ_m and υ_m, the break observed at point G in Figure 3.5 is not observed (see Figure 3.7 discussed later). This could, of course, simply mean that the choice of Δ_m and υ_m to simulate polymers should be restricted to those values that display a break conform to Figure 3.5 in their compensation search when Δ_e varies.

The fact that the choice of Δ_m and υ_m is not unlimited, but rather should correspond to some criteria to meet the requirements that they simulate polymers, is, indeed, a reasonable proposition that we believe is true, regardless of the issue considered here.

3. But the fact that we need to assign a certain value of Δ_e equal to Δ_{eg}, the value of Δ_e when $T_p = T_g$, faces various objections. The first reason is that T_g is a kinetic phenomenon observed whether a voltage field is applied or not. In the Appendix, we attribute to kinetic reasons the freezing of the statistical populations at low temperatures. This occurs for all values of Δ_e, not just a specific one. The second reason is that we attribute the break in Figure 3.5 to the interference on the kinetics of k_x of the coupling between Δ_e and (Δ_m, υ_m): this is what we mean by interactive coupling between the conformational states and free volume (the b/F state). The coupling is more prominent at large values of Δ_e, for $\Delta_e > \Delta_{eg}$ in Figure 3.5, and simplifies to a pure influence of Δ_e alone at lower values of Δ_e, vanishing to 0. This has nothing to do with a T_g transition which shows up for all values of Δ_e. Besides, in the simulations, the value of Δ_e is constant during cooling or heating; it is not a function of T. Even if, in our explanation of the compensation of ΔH and $\ln \tau_o$, it has been said that the value of

EBSCOhost - printed on 2/13/2023 12:32 AM via . All use subject to https://www.ebsco.com/terms-of-use

T_p during the polarization stage fixes the value of Δ_e, this value remains constant during the simulation of the cooling and depolarization stages. It is possible, obviously, to change this assumption in the simulations and make Δ_e a function of T, but this was not the case in the simulations that led to Figure 3.5.

Our conclusion is that despite the remarkable and simple explanation provided by the break in Figure 3.5, we need to find another explanation for the split of the compensation slopes at T_g that results in the positive and negative compensations. As we shall reveal in Section I.3.4.5, which describes "grid-shifting," we have found such an explanation and it is not based on the change of slope in Figure 3.5. As we will discover then, the "coalescence" at T_g of the localized (b/F) pockets of free volume around the b grains is responsible for a change of the polarization efficiency at T_p, changing from electronic and atomic polarization to orientation polarization and increasing $\Delta_e(E, T_p)$ as T_p increases, instead of decreasing it below T_g. This, we will show, is the true suggested cause resulting in the negative compensation of the TWD response.

For the moment, we want to develop the connection between the Dual-Phase model parameters and the TWD depolarization results to show how the phenomenon of compensation itself of $\ln \tau_o$ vs. ΔH *is correctly described* by the interactive coupling between the conformational states, (c, g, t), and the free volume, (b/F) state, that can be quantitatively modeled by the vertical Dual-Split Kinetics equations. In this model, the interactive coupling is characterized by the values of Δ_x and $\ln \upsilon_x$, which depend, in particular, on the value of Δ_e, itself determined by the coupling of the voltage field and the polarization temperature, T_p. We propose, as a first approximation, how to quantify this coupling below.[2]

Point O in Figure 3.5 can be associated with a temperature T_x of the polymer system of interactions for which $\Delta_e = 0$. We assume that T_x is the thermodynamic value of T_{LL}. In other words, T_x is the T_p value corresponding to $\Delta_e = 0$. We still need to understand the physical meaning of T_x.

At the origin O, $x = y = 0$ and thus $\upsilon_x = \upsilon_m$ and $\Delta_x = \Delta_m$. Therefore, this state does not generate asymmetric b/F statistics, which is our definition of T_{LL}. We view T_x as the thermodynamic (rate-independent) transposition of T_{LL} that can only be experimentally measured by extrapolation of T_{LL} at zero rate. Regarding the T_{LL} transition, we have made previous statements that it is the temperature of "superposition" of the b and F states; borrowing an expression from quantum mechanics, we have called it "the temperature at which the b and F states become 'transparent' or 'undistinguishable'." Yet, in the Dual-Split statistics, a system of interactions at equilibrium is de-

2 As we said before, the true simulation of the TWD polarization and depolarization stages, done in equations (1.21)–(1.24) in Chapter 1, was not performed for the effect of Δ_e on Δ_x and υ_x in the Appendix, in which isothermal relaxation takes place to determine Δ_x and $\mathrm{Ln}(\upsilon_x)$; hence, the first approximation statement.

EBSCOhost - printed on 2/13/2023 12:32 AM via . All use subject to https://www.ebsco.com/terms-of-use

fined by three fundamental constants, Δ_m, υ_m, and Δ_{eo}, not simply Δ_m and υ_m. We, therefore, suggest that T_{LL} is the temperature at which $\Delta_e(T_p) = \Delta_{eo}$, which provides a dynamic character to the "superposition" transition.

By combining the statements above regarding the value of Δ_e at T_g, T_{LL}, and T_x, we can tentatively conclude that Δ_e varies with T_p and the voltage field E such as

$$\Delta_e\left(E, T_p\right) = \Delta_{eo} + kF(\alpha, \mu, N)E\frac{\left(T_{LL} - T_p\right)}{T_{LL}} \tag{3.7}$$

where E is the normalized voltage field (V/m), F is a transfer function, α, μ and N are polarization Debye parameters expressed in equation (3.20) found in the discussion, k is a scaling constant

At $T_p = T_{LL}$:

$\Delta_e = \Delta_{eo}$

$\Delta_e = 0$ for $T_p = T_x$

T_x is the thermodynamic value of T_{LL}

Δ_{eo} is also the value of Δ_e when the material is not dielectrically stimulated ($E = 0$). Note that $F(\alpha, \mu, N)$ in equation (3.7) is a transfer function between the macroscopic and the molecular world, which, for the present purpose, does not need to be elaborated, but which can be derived from the expression of the dielectric constant, ε, as a function of the total dipole moment, permanent and induced, and the number of dipoles, N. See equation (3.20) in the Discussion.

Equation (3.7) can be rewritten as a function of Δ_{eg}:

$$\Delta_e\left(E, T_p\right) = \Delta_{eo} + \left(\Delta_{eg} - \Delta_{eo}\right)\frac{\left(T_{LL} - T_p\right)}{\left(T_{LL} - T_g\right)} \tag{3.8}$$

with:

$$\Delta_{eg} = \Delta_e\left(E, T_g\right) = \Delta_{eo} + kF(\alpha, \mu, N)E\frac{\left(T_{LL} - T_g\right)}{T_{LL}}$$

When Δ_m and υ_m vary, the aspect of the normalized compensation search shown in Figure 3.5 presents notable changes, as evidenced in Figures 3.6 and 3.7.

Figure 3.6 applies to the couple $\Delta_m = 8{,}750$ and $\upsilon_m = 10^{12}$ and Figure 3.7 to the couple $\Delta_m = 9{,}250$ and $\upsilon_m = 10^{11}$ already analyzed in Figure 3.3, but now presented with an extended range of Δ_e values (from 5 to 900).

EBSCOhost - printed on 2/13/2023 12:32 AM via . All use subject to https://www.ebsco.com/terms-of-use

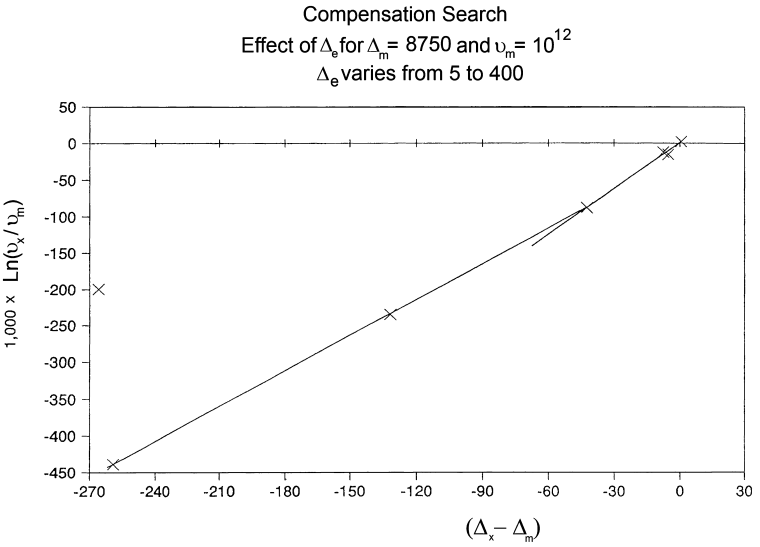


Figure 3.6: Influence of Δ_e on Δ_x, Ln u_x. The same graph as Figure 3.5, except that $\Delta_m = 8{,}750$ and $u_m = 10^{12}$.

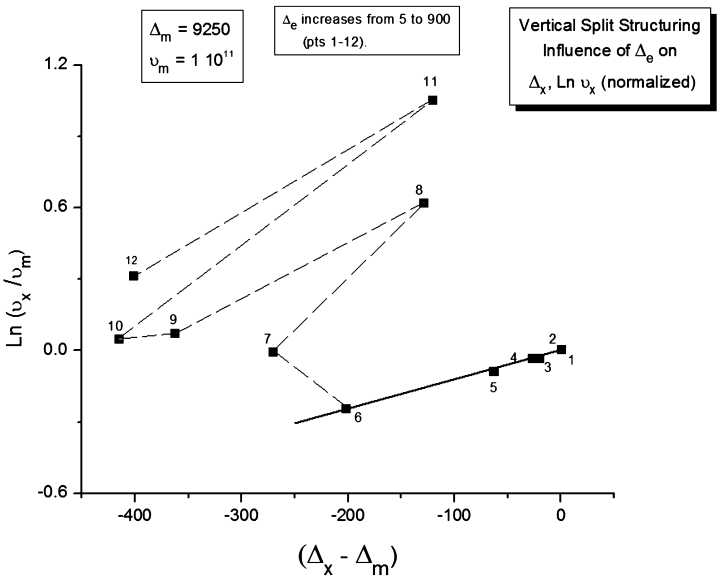


Figure 3.7: The same graph as Figure 3.5 except that Δ_e decreases from 900 to 5 as the index of the points continuously decreases from point #12 to point #1.

EBSCOhost - printed on 2/13/2023 12:32 AM via . All use subject to https://www.ebsco.com/terms-of-use

Figure 3.6 provides the same information as Figure 3.5: the existence of two compensation lines defined by points G and O and the slopes α_1 and α_1' such that $\alpha_1' > \alpha_1$. Again, the simulation results for a different set of Δ_m and υ_m values corresponds to positive and negative compensations for $\mathrm{Ln}(k_x)$ vs. $1/T$. The differences bear on the relative positions of the compensation lines, their intercept defining Δ_{eg}, and the relative magnitude of T_{c1} and T_{c2}. The other observable difference is the last point (corresponding to $\Delta_e = 400$) on the higher Δ_e side of the $y = \alpha_o + \alpha_1 x$ compensation line. *This point is totally off the compensation line*, as if it was due to an error. But the simulation for this particular Δ_e is entirely similar to the other simulations, at lower values of Δ_e, with the same regression accuracy in the determination of the values of $k_x(T)$ to find the corresponding Δ_x, $\mathrm{Ln}\,\upsilon_x$. Thus this point is not due to a simulation error; it is real.

We further analyze this apparently erratic phenomenon in Figure 3.7. As we said, this figure explores the same Δ_m, υ_m settings as in Figure 3.3, yet with a much broader range of Δ_e values: 12 values ranging from $\Delta_e = 5$ to $\Delta_e = 900$. Table 3.1 provides the results of the simulation.

Table 3.1: Results of a simulation by equations (5) to (7) of Appendix Part A with $\Delta_m = 9250$, $\upsilon_m = 10^{11}$, and Δ_e constant varying between 5 and 900. Δ_x and $\mathrm{Ln}(\upsilon_x)$ are the dissipative Dual-Phase kinetic parameters corresponding to $\mathrm{Ln}(k_x)$ vs. $1/T$, where k_x is determined from $N_b(t)$.

	Δ_e	Δ_x	$\mathrm{Ln}(\upsilon_x)$	$\Delta_x - \Delta_m$	$\mathrm{Ln}(\upsilon_x) - \mathrm{Ln}(\upsilon_m)$
1	5	9250.75	25.33095	0.75	0.00251
2	25	9250.5	25.33285	0.5	0.00442
3	75	9230.38	25.29485	−19.62	−0.03359
4	100	9223.42	25.29295	−26.58	−0.03548
5	150	9187.16	25.23795	−62.84	−0.09048
6	300	9048.21	25.08195	−201.79	−0.24649
7	500	8979.68	25.32185	−270.32	−0.00658
8	600	9121.68	25.94725	−128.32	0.61882
9	650	8887.69	25.40105	−362.31	0.07262
10	700	8835.45	25.37655	−414.55	0.04812
11	800	9129.59	26.38035	−120.41	1.05191
12	900	8849.11	25.64155	−400.89	0.31312

Figure 3.7 is a normalized compensation search apparently showing only one compensation line for points 1–6. These points are labeled according to their row number listed in the first column of Table 3.1. They are sorted by increasing Δ_e values. The overall view of the effect of an increase of Δ_e for these Δ_m, υ_m settings is that beyond a certain value, say corresponding to the end of the compensation line, the system becomes chaotic. We have drawn dashed lines linking the successive points, following a continuous increase of Δ_e, and we observe the typical response of scattering. The conclusion is that this choice of Δ_m and υ_m values is not particularly suitable, beyond

EBSCOhost - printed on 2/13/2023 12:32 AM via . All use subject to https://www.ebsco.com/terms-of-use

$\Delta_e \sim 400$, to simulate the kinetics of depolarization by TWD. The only compensation that we observe does not even show the behavior of Figures 3.5 and 3.6, which we used to explain the difference between positive and negative compensation.

A second view of the scattered data of Figure 3.7, exhibited in Figure 3.8, imagines a certain order of the chaos by drawing a series of possible positive and negative compensations, if we were allowed to extend such definitions to the compensation search plot (for Figures 3.5 and 3.6, we made sure to apply these definitions to the $\mathrm{Ln}(k_x)$ vs. $1/T$ relaxation results themselves).

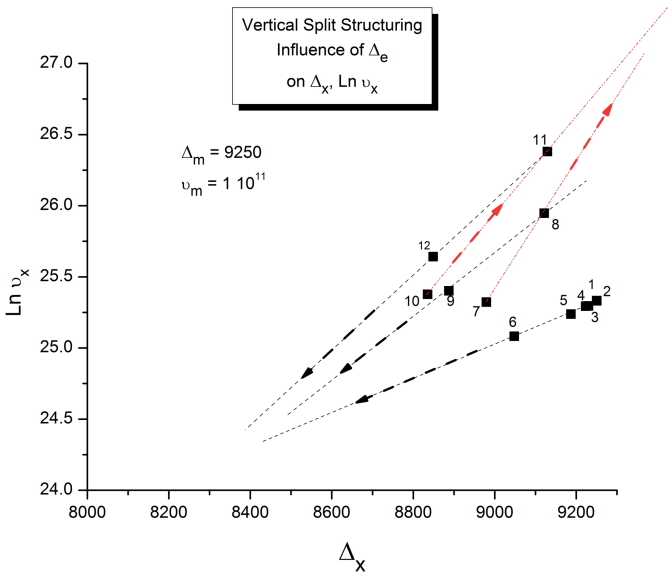


Figure 3.8: Same compensation search as in Figure 3.7, *without* the normalization of the axes by Δ_m, u_m. Note that Δ_e decreases continuously between 900 (point #12) and 5 (point #1). One can define positive compensations (black arrows pointing downward, showing an increase of Δ_e) and negative compensations (red arrows pointing upward, with a decrease of Δ_e).

Figure 3.8 uses the same data of Table 3.1, replotted without the normalization of the axes. We have drawn three black lines with an arrow pointing down and two red lines with arrows pointing up. The arrows follow the tendency for the y-variable to decrease or increase within a range. Indeed, the ranges are determined arbitrarily since the lines only join two points; an exception is for the first six points. It would, indeed, be quite useful to increase the number of Δ_e values to resolve the definition of the ranges. But the idea is that the apparent chaos might still have a certain structure. For instance, the "positive" lines (1–6, 8–9, 11–12) may compensate into a super-compensation, and the same applies for the "negative" lines (3–8 and 10–11).

EBSCOhost - printed on 2/13/2023 12:32 AM via . All use subject to https://www.ebsco.com/terms-of-use

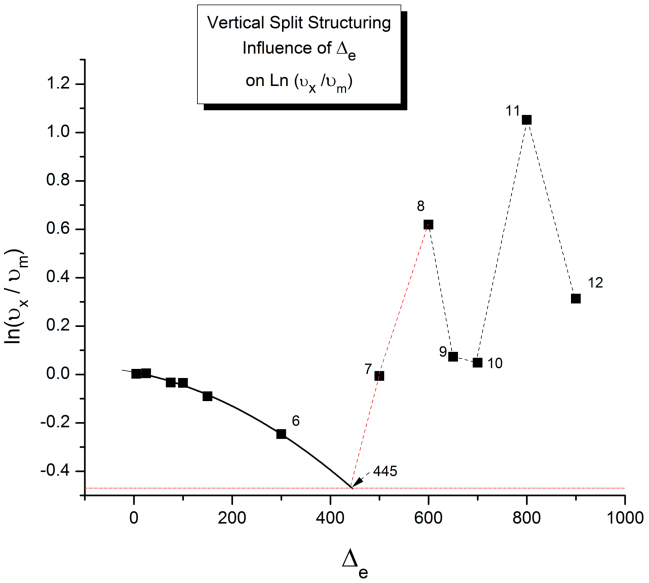


Figure 3.9: Variation of $\mathrm{Ln}(u_x/u_m)$, at u_m constant, against Δ_e for the data of Figure 3.7.

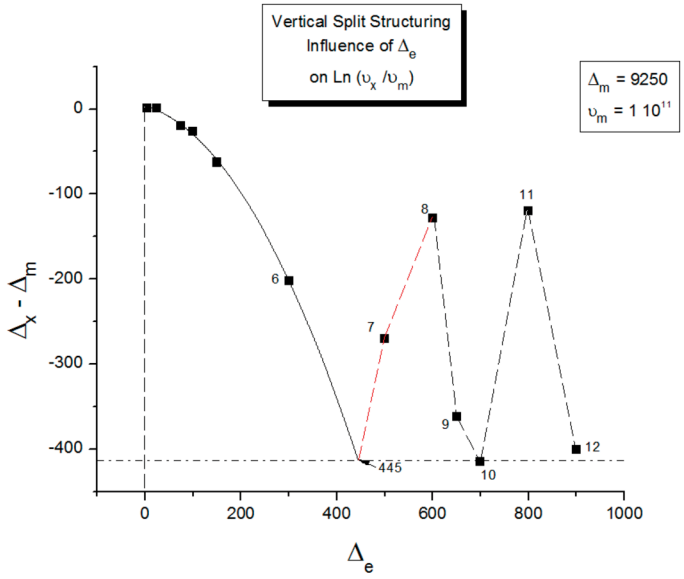


Figure 3.10: Variation of $(\Delta_x - \Delta_m)$, at Δ_m constant, against Δ_e for the data of Figure 3.7.

Figures 3.9 and 3.10 present another angle to reveal the possible structure of Δ_x and $\mathrm{Ln}\,\upsilon_x$ at higher values of Δ_e. These figures plot the variation of the normalized $\mathrm{Ln}\,\upsilon_x$ and Δ_x data against Δ_e: Figures 3.9 and 3.10, respectively.

EBSCOhost - printed on 2/13/2023 12:32 AM via . All use subject to https://www.ebsco.com/terms-of-use

The first observation is that Δ_x or $\mathrm{Ln}(\upsilon_x)$ decreases when Δ_e increases in range 1 [points 1–6], and vice versa. This will serve to explain positive and negative compensation in the discussion. A second observation is that both Figures 3.9 and 3.10 reveal that in range 1 a quadratic equation can be used to fit the Δ_e dependence of either $\mathrm{Ln}\,\upsilon_x$ or Δ_x. This permits to evaluate the value of Δ_e that ends the first range or starts the second range: we find $\Delta_e = 445$. The third observation is that there seems to be a periodic oscillation of the values, up and down, with the down values possibly aligned, for Figure 3.9, on the zero horizontal line, or not far from it for the arbitrary choice of the current Δ_e values chosen. See points 7 (right on the 0 axis), point 9, and points 10 and 12. Similarly, in Figure 3.10, we see two "peaks" showing the same periodicity and possibly the same alignment of points 10 and 12 with the intercept of range 1 and 2, at point $\Delta_e = 445$.

It should be emphasized, of course, that this tentative structuring of the chaotic behavior is totally speculative, at this time, and that without the recourse of many more points to (in)validate it, it will remain so.

However, we show in Part II, Chapter 4, e. g., Figure 4.17, that the relaxation map for a classical amorphous polymer, polystyrene, can be broken down into separate groups, each with a characteristic compensation point. The number and sign of the multi-compensations depend on the thermomechanical history on cooling. Figure 4.17 revealed a simple relationship between the various compensation lines in the compensation search plane, from 50 °C below to approximately 60 °C above T_g. We concluded that the relaxation process described by the individual relaxation modes, i. e., occurring below T_g, at T_g, and above T_g, was correlated as a structure of compensations and super-compensations.

In view of Figures 3.8 to 3.10, particularly Figure 3.8, the temptation is now strong to suggest that this network of compensations is generated by a combination of thermomechanical history during the processing of the sample coupled with the thermal dielectric history during its TWD characterization, both affecting the value of $\Delta_e(T_p)$ in a way that brings its value in the range of values that make the system's response apparently chaotic, but in fact structured as suggested in Figure 3.8.

Our conclusion is that the characterization of the depolarization current response of dielectric samples, such as polymers, by the TWD method may lead to the determination of the fundamental parameters of the statistical model of polymer interactions that we have introduced in the Appendix: the Dual-Split (vertical) structuring and the horizontal structuring (of the b conformers in N_s b grains). The value of Δ_e is equal to Δ_{eo} at equilibrium, but we cannot measure it directly; we must modify its value by mechanical means and/or by dielectrical means in order to access it by extrapolation.

Essentially, we assume that the TWD characterization technique reveals the dissipative mechanisms of structuration of the interactions in polymers.

In other words, our assumption is that a polymer material behaves like a self-dissipative statistical system that generates its own dissipative statistics (the b/F variation) at Δ_{eo} constant when it is brought out of equilibrium by simple thermal acti-

EBSCOhost - printed on 2/13/2023 12:32 AM via . All use subject to https://www.ebsco.com/terms-of-use

vation alone (heating, cooling, annealing), yet that in order to determine the values of Δ_{eo}, Δ_m, and υ_m, we need to modify the original value of Δ_{eo} by imposing either a voltage field, in the instances of this book, or a mechanical stress field (shear and/or pressure) in other instances, on top of the thermal activation. The statistical system has the same Δ_m, υ_m set but a different value of Δ_e, a thermally dielectrically stimulated value of Δ_{eo}. Polarizing at various T_p allows doing precisely that: changing the value of Δ_{eo} in the simulation before quenching and thermally depolarizing the material. By repeating the process at various T_p, we can simulate the effect of various Δ_e and finally extrapolate to $\Delta_e = \Delta_{eo}$ by determining T_{LL}. The variation with Δ_{eo} of the dissipative Dual-Split pair (Δ_x, $\mathrm{Ln}(1/\upsilon_x)$) simulates the variation with T_p of the experimental TWD pair (ΔH, $\mathrm{Ln}(\tau_o)$).

By scanning sequentially at various T_p from a low temperature below T_g to a high temperature in the solid or the liquid state, the TWD procedure essentially reveals the interactive coupling between the conformers, the coupling between the conformational interactions and the free volume, and the organization of the collective set of all the interactions as a network, i. e., the existence of a global dissipative network of the interactions.

We acknowledge that this interpretation of the thermally stimulated depolarization results is new and unconventional.

As far as the traditional interpretations of compensations observed by TWD [50, 115, 116] some reservations should be raised: these models stipulate that the entropy and enthalpy calculated from the Arrhenius spectral lines are equal to N times the value of a basic elementary unit with entropy and enthalpy $\Delta S^{\#}$, $\Delta H^{\#}$. In our opinion, these interpretations of the physically "unreasonable" large values for the magnitude of ΔH and $\mathrm{Ln}(\tau_o)$ obtained from the TWD analysis are incomplete and need further refinement (see later). Besides, these authors do not recognize the interactive coupling character of the relaxation modes for $T_p > T_g$, leading their analysis to ignore the negative compensation in this temperature range. Beyond the theoretical interpretation of the split of the compensation line slope at T_g, a discussion initiated in the previous section, the distinction between a positive and negative compensation at the crossing of T_g is crucial to understand the reason why the entropy and enthalpy pass through a maximum at transitions, such as T_g. We develop in another section below another important argument showing the difference of understanding of the meaning of TWD itself: does it deconvolute elementary Debye peaks, the traditional interpretation, or does it deconvolute the Dual-Split complexity of the interactions, as we suggest?

Furthermore, the unfortunate confusion between $T_{g,\rho}$ and T_{LL} often made by these same authors does not help consolidate the arguments in favor of the existence of T_{LL}, a transition consensually ignored by the polymer science community for lack of clear evidence ([21, 135]). By being incomplete and/or confusing, these traditional explanations of the TSD/TWD results may be damaging the credibility of the TSD/TWD characterization technique itself and of its findings: the importance of the T_{LL} transition

EBSCOhost - printed on 2/13/2023 12:32 AM via . All use subject to https://www.ebsco.com/terms-of-use

and of $T_{g,\rho}$, for instance, or the compensation of the relaxation mode characteristics ΔH and $\mathrm{Ln}(\tau_o)$.

We believe that a correct model of the interactions in polymers must take into consideration the existence of the T_{LL} transition and of $T_{g,\rho}$. This implies a clear and straightforward presentation of the facts regarding their experimental manifestations and a solid theoretical explanation of how their physical presence can be integrated with the rest of the properties.

In the next section, we further discuss the implications of our Dual-Split statistics proposed view to describe the effect of the voltage field on a dielectric medium.

I.3.3.3 Effect of the voltage field on the statistics of interactive coupling. The nature of what TWD is actually deconvoluting

TWD involves a sophisticated thermal dielectrical "treatment" of the sample in order to characterize it (Figure 2.4). The sample is heated to a certain temperature, T_p, to polarize it for a certain time t_p, and then the field is turned off. The second step is a succession of annealing treatment stages: first, the temperature is lowered to a lower temperature, T_d, and kept there for a time t_d; then it is rapidly cooled to a temperature T_o. The final step is to heat it up at a constant rate and let it depolarize. We measure and record the current of depolarization during the temperature increase.

It is clear that the TWD thermal-dielectrical history of the sample including its final depolarization step at constant heating rate is not what is simulated in the relaxation simulations presented in Figures 3.3 to 3.10 (see our footnote 2). In these simulations, Δ_e remains constant all the way through cooling and the subsequent annealing stage. The relaxation towards equilibrium is what yields the (Δ_x, $\mathrm{Ln}\,\upsilon_x$) kinetic constants and it is done isothermally, not during a ramp-up heating step. This is why we stated at the onset of the Appendix:

> This Appendix does not pretend to provide equations that will directly apply to the results obtained by TSD or TWD. However, working by analogy, one can recognize some identical patterns of behavior between the computer simulations and the real response of polymers using the TSD and TWD stimulation techniques.

Indeed, it is possible to simulate step by step the TWD procedure, considering that the dielectrically stimulated value of Δ_e is given by equation (3.7) and that it is equal to Δ_{eo} otherwise. This more complex stimulation was not done. The simulation performed corresponds to the isothermal depolarization curves discussed in Part II, Chapter 1 (Figures 1.32 and 1.33). Nevertheless, we have shown (unpublished results) that the kinetic results ($\mathrm{Ln}(k_x)$ vs. $1/T$) extracted either from a series of relaxations done at various temperatures or under thermally scanning conditions (such as in the depolarization step in TWD) provided very similar compensation search results (such as those in Figures 3.7), with only a change in the values of the slopes and intercepts.

EBSCOhost - printed on 2/13/2023 12:32 AM via . All use subject to https://www.ebsco.com/terms-of-use

If the Grain-Field Statistics theory of the interactions (vertical and horizontal structuring) can successfully predict the properties of polymers by simulation, it becomes essential to know how to find the fundamental constants of the theory, Δ_m, υ_m, and Δ_{eo}. Is the TWD protocol or even a modified TWD protocol (a quench/isothermal annealing experiment) capable of extracting the fundamental constants of the Grain-Field Statistics from its own characteristic parameters: the free energy ΔG_p, its structure ΔH_p and ΔS_p, the coordinates of the compensation points, the value of these parameters at T_g and at T_{LL}, etc.?

For instance, equation (3.7) proposes a physical correlation between the value of Δ_e, T_p, the voltage field E, and the dipole moment μ. Equation (3.8) incorporates the effect of the voltage in the expression of Δ_e via Δ_{eg}, so the unknown constant k can disappear from the expression. Δ_{eg} itself can be expressed in terms of T_g and Δ_{eo} (Δ_e at $T = T_{LL}$) and the equation of the Z-line can be deducted from equations (3.1) and (3.2).

The slopes and intercepts of the $\mathrm{Ln}(k_x)$ vs. $1/T$ Arrhenius plots at various Δ_e (aka various T_p) can also be converted into enthalpy–entropy variables, using the same equation used to convert the $\mathrm{Ln}(\tau_o)$, ΔH plots (equations (2.2) to (2.4) of Chapter 2). This permits to define the free energy ΔG_e (aka ΔG_p) and write the compensation line equations in terms that are the same as those used to characterize the relaxation modes in the ΔG planes. We seem to be ready to find the fundamental constants of the Dual-Split model: Δ_m, υ_m, and Δ_{eo}.

Actually, the task is more complex than that and *it is impossible at this stage to achieve such a goal*.

The reason must be reemphasized again: the $\mathrm{Ln}(k_x)$ vs. $1/T$ Arrhenius plots at various Δ_e do not provide the kinetic constants that could simulate the dynamic depolarization stage of the TWD, which is done at a constant heating rate and not under isothermal annealing conditions.

The TWD thermal history is not a two-stage straightforward polarize/anneal process. As we said, it involves an intermediary stage, at T_d, where the state of the melt is allowed to relax, partially. In effect, the TWD procedure includes a short isothermal annealing step, the kind that we use in the simulation. This extra step makes the TWD procedure a three-step process. It is regrettable that this annealing step was not recorded in the TSD/TWD instrument, although it is straightforward to implement such an operation. This has, expectedly, an influence on the results, which we will try to evaluate in the discussion Section (I.3.5).

In fact, in the entire book, up to this chapter, we sided with Lacabanne's interpretation of thermal-windowing *as a filtering process*, a physical deconvolution of the spectrum of relaxations to isolate the elementary Debye peaks. And we still agree with the general statement of deconvoluting competing mechanisms, yet we now offer a different approach to what is being deconvoluted.

Our Dual-Split interpretation of the effect of the voltage field at temperature T_p is to modify the value of Δ_e, which itself perturbs the statistical state of the conformers

EBSCOhost - printed on 2/13/2023 12:32 AM via . All use subject to https://www.ebsco.com/terms-of-use

and of their (b/F) free volume duality by putting it out of its original state. The mechanism of perturbation and the magnitude of this perturbation essentially depend on the original state of the material being polarized at T_p, whether it is a frozen glass below its T_2 temperature[3] or above its T_2 temperature, or a rubbery or molten polymer above its T_g. So, in order to evaluate the amount of disturbance by the application of the voltage at T_p, we need to position T_p with respect to T_2, to T_g, and, as we have seen, to T_{LL}.

The other steps of TWD are done *without an electric field*, and the return to the equilibrium step is activated by temperature and time, at T_d, t_d, and during the ramp-up at constant ramp rate. We are able to observe the return to equilibrium because it involves the depolarization of what was polarized. It should be clear that the polarization step is not the only cause of the non-equilibrium state of the material. The material processing history also created a non-equilibrium state for the interactions between the bonds. This is true for all amorphous matter cooled below their T_g. In summary, the return to equilibrium as temperature activates the relaxation to this stable state does not simply involve the return of what was disturbed dielectrically, but also, on top of that and/or besides that, the return of the stable state of the conformers. The analysis of the depolarization stage is, therefore, the deconvolution of the dielectric disturbance due to the voltage and of the conformer statistical state disturbance due to temperature.

This summarizes the effect of polarizing at T_p, depolarizing at T_d, and ramp-up to create the depolarization current–temperature curve. Then we change T_p and repeat the same operation several times.

Now, going back to the analogy of the illumination of an object by a light and turning the light in all directions to study the evolution of its shadow, it appears that changing T_p is like changing the light direction. We are not talking of a different relaxation process in this explanation; this is still the same object that is illuminated. We are talking about the same relaxation process disturbed (illuminated) in many ways, by changing T_p, and this explains the compensation between the kinetics parameters of the kinetics of the return to the undisturbed state (Δ_{eo}). In other words, the TWD does not consist in isolating elementary peaks from other elementary peaks; it is deconvoluting the Dual-Split complex nature of the interactions that is the result of kinetic and energetic concerns working in duality. TWD reveals the gears of the Grain-Field Statistics.

This is a major difference in the theoretical interpretation of TWD. We will get back to this subject in the Discussion.

3 T_2 is the value of the temperature that makes the Newtonian viscosity infinite in the Vogel–Fulcher equation (sometimes designated T_∞). It is assumed that the free volume is zero at T_2, resuming any possible motion left to single conformers' internal rotation.

EBSCOhost - printed on 2/13/2023 12:32 AM via . All use subject to https://www.ebsco.com/terms-of-use

I.3.4 Normalization of the compensations between Ln(τ_o) and ΔH. Introduction to "grid-shifting": a collateral shifting effect due to the interaction between the voltage field, temperature, and dielectric material

The initial investigation that led to the results that are developed in this section started with the inquiry of the influence of the shifting of Debye peaks along the temperature axis on the determination of the peak characteristics, ΔH_{os} and Ln τ_{os}. This study was reported in Chapter 1 of this Part I, Table 1.2, Figures 1.23 and 1.24. We concluded the following:

> when Debye peaks are shifted along the temperature axis, they can still be fitted with a Debye formula, but with a different set of ΔH and τ_o. A compensation phenomenon can be practically observed between [ΔH, Ln τ_o] as the peak is shifted to different temperatures.

The shifting of the Debye peak by a certain amount (+10 °C) and the incidence it has on the value of ΔH and Ln(τ_o) is illustrated in Figure 3.11. The values are taken from Table 1.2 of this Part I.

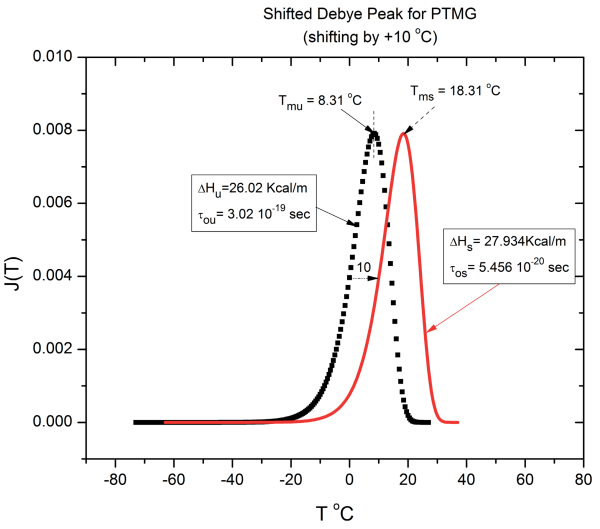


Figure 3.11: Shifting by +10 °C the simulated Debye Peak for PTMG 2000 (black squares) corresponding to T_{mu} = 8.31 °C (with the values of ΔH_u and τ_{ou} given in the box) to give the shifted $J(T)$ red curve, with a maximum at T_{ms} = 18.31 °C, and new values of ΔH_s and τ_{os} after the shift.

Furthermore, in the same section of Part I, Chapter 1, in Table 1.4 and Figure 1.26, we studied the effect of shifting Debye peaks to the same temperature, starting from their original position at T_m after performing a TWD at various T_p (the starting values for the Debye peaks before shifting them were given in Table 1.3). Again, it was found that the

EBSCOhost - printed on 2/13/2023 12:32 AM via . All use subject to https://www.ebsco.com/terms-of-use

shifted ΔH_s and $\mathrm{Ln}(\tau_{os})$ new values compensated and that the slope and intercept of the compensation line depended on the temperature to which the Debye peaks were shifted (Figure 2.26). Figures 3.11 and 3.12 below are new plots for these same data that concern a semi-crystalline polymer, PTMG 2000.

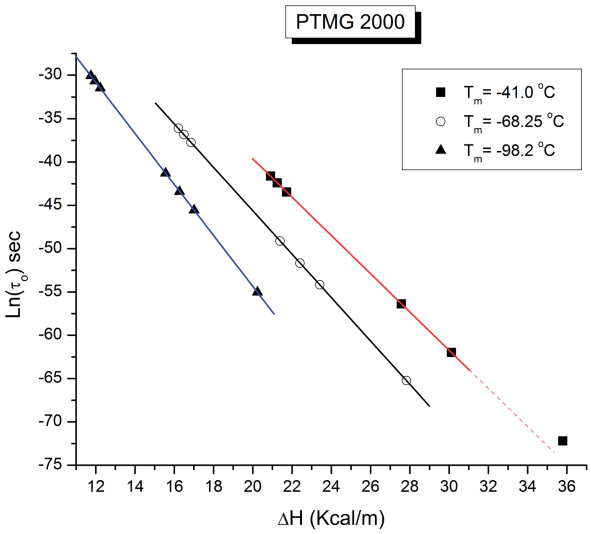


Figure 3.12: For PTMG 2000, shifting the elementary Debye peaks obtained at seven values of T_p so that the shifted Debye peaks have all the same value of T_m. The graph explores three values of T_m: −41 °C, −68.25 °C, and −98.2 °C. Note the compensation, for each T_m, of the associated Arrhenius lines of $\mathrm{Ln}(\tau(T))$ vs. $1/T$ when T_p varies.

PTMG is not a "simple" polymer. By that we mean that it is not made up of a single amorphous phase like we observe in simple polymers such as polystyrene (PS) or polymethyl methacrylate (PMMA). PTMG is a semi-crystalline polymer with an amorphous phase and a crystalline phase. The crystalline phase represents 57 % of the structure. The T_g listed for PTMG is −88 °C, and its T_m, for M = 2000, is 32 °C. Its aspect at room temperature is a malleable soft wax.

What we say for PEEK in Part II, Chapter 3 (Figures 3.106 to 3.111) also applies to PTMG: it has two amorphous phases, not just one, and therefore two T_{gs}: a T_{gL} and a T_{gU}, as coined by Boyer, who pioneered the concept [22]. In addition, as we have said in Section I.3.2, amorphous matter above T_g has two characteristic states depending on whether it is above or below its T_{LL} temperature. So, in fact, the situation of PTMG is not just "not simple," it appears to be awfully complex. We will publish separately the analysis of the shifting of the Debye peaks in PTMG that permits to resolve the various amorphous phases in the different temperature ranges. However, our objective in this chapter is of a more fundamental nature: define, describe, and explain the in-

EBSCOhost - printed on 2/13/2023 12:32 AM via . All use subject to https://www.ebsco.com/terms-of-use

teractions between the voltage field and temperature by following the compensation characteristics of ΔH and Ln(τ_o) as T_p varies.

This is the reason we chose to study a much simpler polymer, PMMA, which is fully amorphous and already well characterized by TWD. In the following, we use the data of PMMA already presented in Table 2.1 of Chapter 2 and will proceed to shift the Debye peaks like it was introduced for PTMG in Chapter 1 and shown in Figures 3.11 to 3.13.

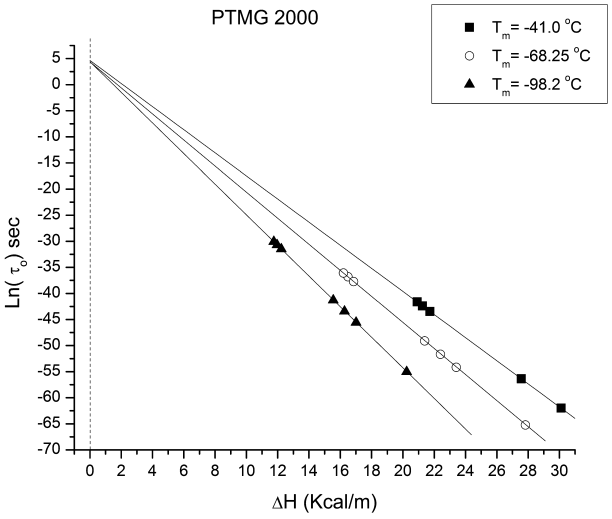


Figure 3.13: Super-compensation of the straight lines of Figure 3.12; the super-compensation coordinates are $\Delta H_c = 0$, Ln(τ_{oc}) ~ 5.

As we shall discover, by studying the shifting effect of the TWD Debye peaks for a simple amorphous polymer, we will derive the "grid-shifting" procedure, a way to correct the original unshifted Debye characteristics, ΔH_u and Ln(τ_{ou}), eliminate the slope split observed at T_g, and hence provide a novel explanation for the manifestation of the negative compensation.

I.3.4.1 Geometrical and thermokinetic features of a Debye peak

When the values of ΔH and τ_o are known, a Debye peak, $J(T)$ vs. T, can be calculated using equation (1.20) of Chapter 1. The equation also requires the total polarization, P_{so}, and the heating rate, s_2, but we can assume that $P_{so} = 1$ and that the heating rate is the standard value, 7 °C/min, which was the value used to obtain the results of Table 4.1 on the PMMA of concern. Assuming $P_{so} = 1$ does not affect the features of a Debye peak; it simply normalizes the integral of the peak to 1. Figure 3.14 shows the simulated Debye peak corresponding to $T_p = 55$ °C in Table 4.1.

EBSCOhost - printed on 2/13/2023 12:32 AM via . All use subject to https://www.ebsco.com/terms-of-use

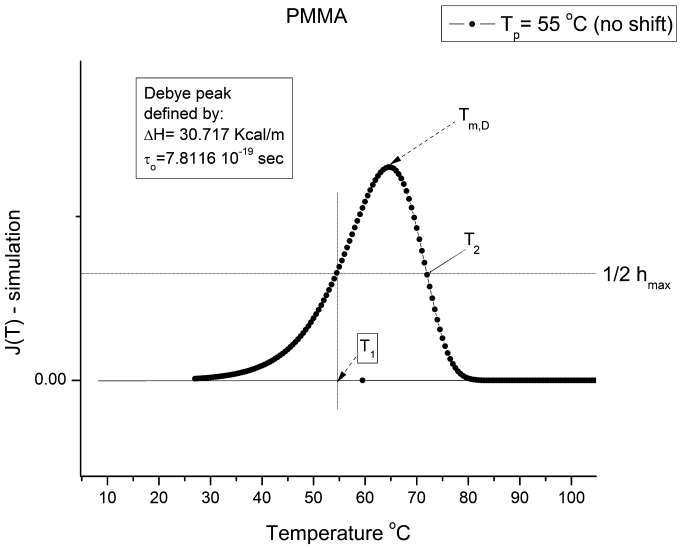


Figure 3.14: Simulation of $J(T)$ vs. T (°C) for a PMMA Debye peak at $T_p = 55$ °C showing the characteristic features of the peak and their determination.

We can define several geometrical features of the peak in Figure 3.14: the value of the temperature at the peak maximum, $T_{m,D}$, the peak height at the maximum, $h_{\max}$, and the values of T_1 and T_2 at half peak height that characterize the half-peak width: $T_2 - T_1$. Notice that we have called $T_{m,D}$ and not T_m the temperature of the maximum of the peak. This is done to distinguish the value found for the simulation using equation (1.20) and the experimental value found by TWD.

As T_p is varied, the geometrical peak features vary, along with the thermokinetic values of ΔH and $\mathrm{Ln}(\tau_o)$. It is interesting to see how these various features are interrelated. For instance, Figure 3.15 compares the variation of $T_{m,D}$ and T_m with T_p, showing a small departure between the calculated and the experimental peak temperatures starting at T_g.

In Figure 3.16, we plot the variation of T_1, T_2, and T_m as a function of $T_{m,D}$ when T_p varies.

T_1 and T_2 vary linearly with $T_{m,D}$, with a marked change of slope at 111.2 °C, near T_g. For $T_p < T_g$ these two lines are convergent and appear to merge when T_p reaches a value, 156.45 °C, that can be calculated from the regression of the T_1 and T_2 data below T_g. This point of convergence is located on the $Y = X$ black line extrapolated outside of the data range investigated, thus at that point $T_1 = T_2$ and the corresponding Debye peak width collapses to zero. The convergence of the T_1 and T_2 lines is interrupted at T_g to reverse to a set of diverging straight lines seemingly emerging from the focal point also located on the Y-X black line, and at that point $T_1 = T_2 = 94.4$ °C; this temperature could be assigned to the onset of the T_g transition.

EBSCOhost - printed on 2/13/2023 12:32 AM via . All use subject to https://www.ebsco.com/terms-of-use

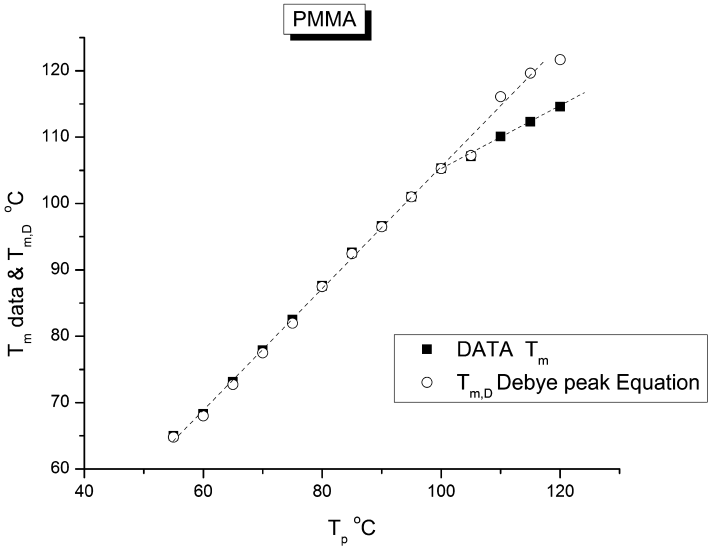


Figure 3.15: Compare T_m (data) and $T_{m,D}$ (simulation Debye peak) plotted vs. T_p for PMMA.

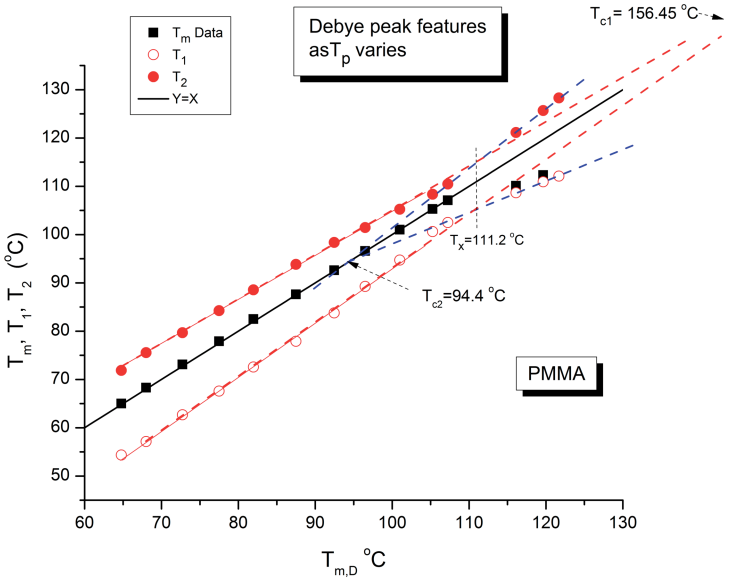


Figure 3.16: PMMA graph of the Debye peak features (T_m, T_1, T_2) vs. $T_{m,D}$ as T_p varies.

EBSCOhost - printed on 2/13/2023 12:32 AM via . All use subject to https://www.ebsco.com/terms-of-use

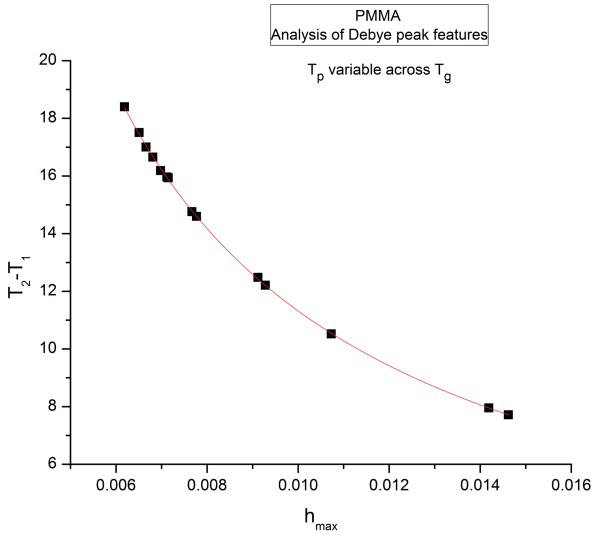


Figure 3.17a: PMMA graph of $(T_2 - T_1)$ vs. h_{max} at various T_p across T_g showing a unique curve. The reversibility at T_g is explained in Figure 3.17b.

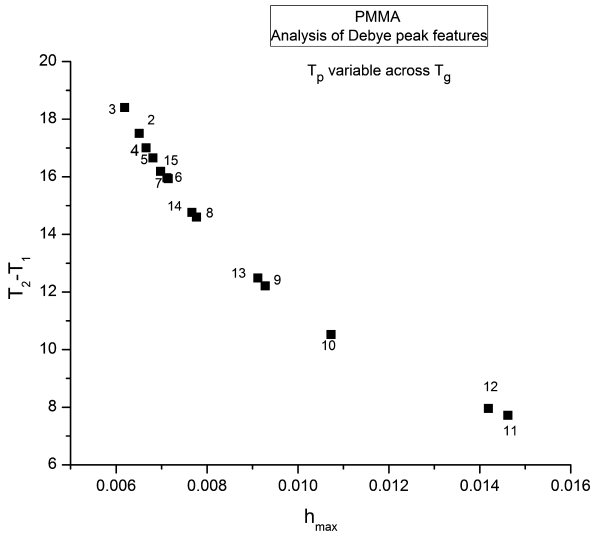


Figure 3.17b: Same plot of $T_2 - T_1$ vs. h_{max} as in Figure 3.17a; the data points corresponding to $T_p > T_g$ are moving backward on the same curve as $T_p < T_g$, as T_p increases.

Figure 3.17a and b correlates for all the values of T_p the peak height at the maximum, h_{max}, and the half peak width: $T_2 - T_1$. It is remarkable that there is only one curve in Figure 3.17a, and not two as could be expected across T_g from plotting ΔH vs. $\ln(\tau_o)$ for instance (Figure 3.20), showing a split of the slope of the lines at T_g. Figure 3.17b indexes all the data points according to their row number in the spreadsheet, with T_p increasing as the index increases. One sees that at T_g, the points change direction to fall back on the same curve, unlike in Figure 3.20. The curve going through the data points in Figure 3.17a is a hyperbolic function showing that the peak half-width

EBSCOhost - printed on 2/13/2023 12:32 AM via . All use subject to https://www.ebsco.com/terms-of-use

is inversely proportional to the peak height maximum: $T_2 - T_1 = -0.0432 + 0.113/h_{\max}$ ($r^2 = 0.99985$). At $T_p = 156.45$ °C, where the half peak width collapses, $h_{\max} = 2.618$, which is 164 bigger than its value observed at T_g (Figure 3.18). This indicates that at this hypothetical temperature the Debye peak has become a Dirac peak (infinite height, no width). It is interesting to note that this temperature is located near the expected T_{LL} temperature of PMMA according to the criteria of Figure 4.16 ($\Delta S_p = 0$).

In Figure 3.18, the peak height at $T_{m,D}$ is plotted against T_p, showing the typical increase up to T_g and decrease beyond T_g observed for ΔH and Ln(τ_o). Figure 3.19a and b precisely displays those curves, fitted by hyperbolic functions, as explained in Chapter 2 (equations (2.28) to (2.30)), across T_g, with the value of T_g calculated at the crossing of these hyperbola: 103.20 °C. Figure 3.20 is a typical compensation search in the Arrhenius plane, showing the two compensation lines below T_g and above T_g, the positive and negative compensations, respectively.

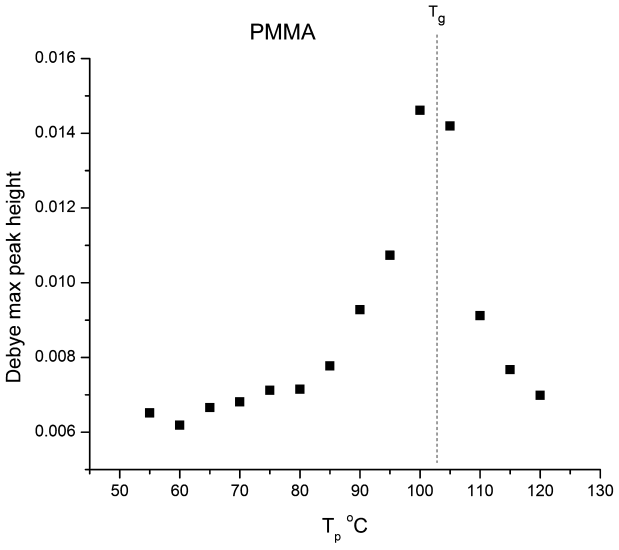


Figure 3.18: Plot of $h_{\max}$, the Debye peak height value at $T_{m,D}$ vs. T_p for PMMA.

Up to now, all the teaching of Chapter 2 is validated. Figure 3.21a and b motivated the need to pursue our inquiry further, showing a plot of ΔH or Ln(τ_o) vs. $h_{\max}$ as T_p varies. The difference with Figure 3.20 is observed for the first five T_ps, in what is called region 1 in the figure. These points, [3–6], with a green line passing through them, are not aligned with points [7–11], the red line called region 2 in Figure 3.21, meaning that the points [2–11] corresponding to $T_p < T_g$ *have a structure*. The [2–6] points are systematically off the extrapolated line 2. This is in contrast with what is observed in Figure 3.20: all the points [2–11] appear to be aligned on the positive compensation line. Region 3, [12–15], describes the $T_p > T_g$ behavior: it is similar to the negative compensation observed in Figure 3.20.

EBSCOhost - printed on 2/13/2023 12:32 AM via . All use subject to https://www.ebsco.com/terms-of-use

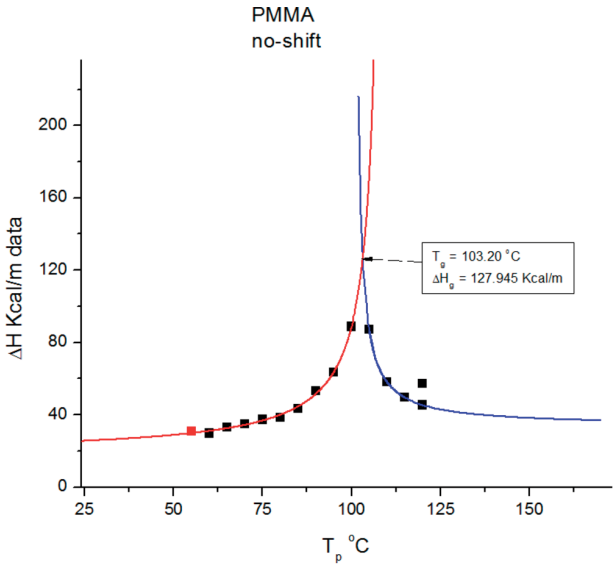


Figure 3.19a: The two curves: ΔH data (unshifted) vs. T_p below and above T_g can be fitted by hyperbolic regressions. Their intercept determines the value of T_g and ΔH_g at T_g.

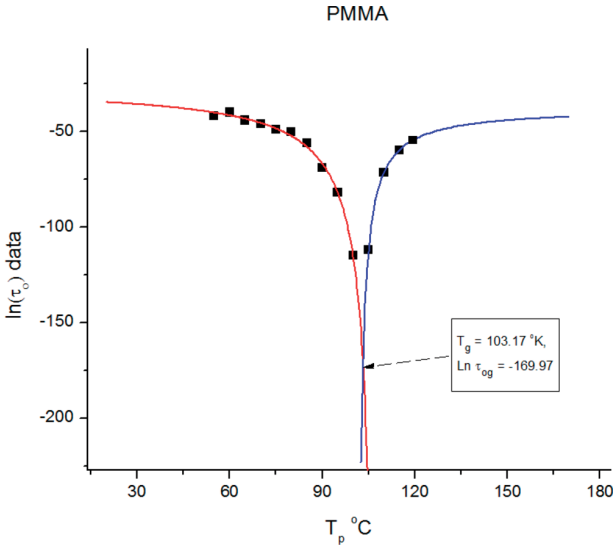


Figure 3.19b: Same plot as in Figure 3.19a, now applied to the Ln τ_o vs. T_p data to determine the intercept coordinates at T_g. The same value of T_g is found.

In summary, two new characteristics of the Debye peaks appear to be important (Figures 3.17a and 3.21a and b). Both figures involve the peak height at the maximum. Fig-

EBSCOhost - printed on 2/13/2023 12:32 AM via . All use subject to https://www.ebsco.com/terms-of-use

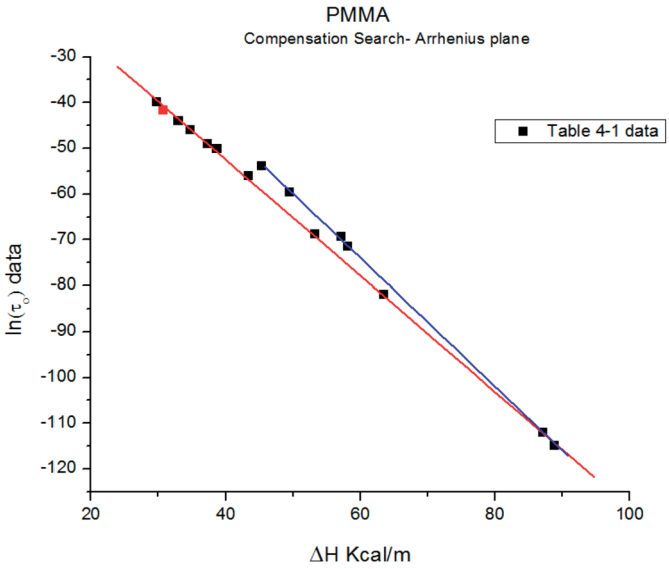


Figure 3.20: Compensation search in the Arrhenius plane of Ln τ_o data vs. ΔH for the PMMA data of Figure 3.19 showing two compensation lines: a positive compensation (bottom red straight line) and a negative compensation (blue straight line). The data in this plot will be reanalyzed several times in the text, revealing the existence of another compensation line.

ure 3.17a plots two geometrical features of the peak, its half width and its height; Figure 3.21 plots a thermokinetic variable, here ΔH for (a) and Ln(τ_o) for (b), against a geometrical variable. In Figure 3.17a we do not observe the presence of any temperature range, not even T_g. Figure 3.21 reveals the presence of three temperature ranges, two ranges below T_g, [2–6] and [7–11], and one range above T_g, [12–15], which we have designated 1, 2, and 3. Both ΔH vs. $h_{\max}$ and Ln(τ_o) vs. $h_{\max}$ show the two ranges 1 and 2 below T_g, but when Ln(τ_o) is plotted vs. ΔH (Figure 3.20), ranges 1 and 2 merge into apparently one range [2–11]. This needs to be elucidated.

In studying the effect of the shifting of the Debye peak, these three ranges appear distinctively and can be made to merge, revealing their possible origin. We analyze two possibilities:

- The peaks at various T_p are shifted by the same amount, δ_x.
- The peaks at various T_p are shifted to the same temperature, for instance T_g, or $T_g + 23$ °C, etc. In this case the amount of shift, δ_x, is variable for each T_p.

As mentioned earlier, we use the "simplex curve-fitting methods" described in Chapter 1 (Part I, Chapter 1, Tables 1.2 to 1.4) to obtain the simulation of the Debye peaks at T_p, and of their ΔH_s and Ln(τ_{os}) characteristics after shifting by δ_x. The shifted values of ΔH_s and Ln(τ_{os}) at four values of δ_x (–32.25, –10, +4, +44 °C) as T_p varies from 55 °C to 115 °C are given in Table 3.2.

EBSCOhost - printed on 2/13/2023 12:32 AM via . All use subject to https://www.ebsco.com/terms-of-use

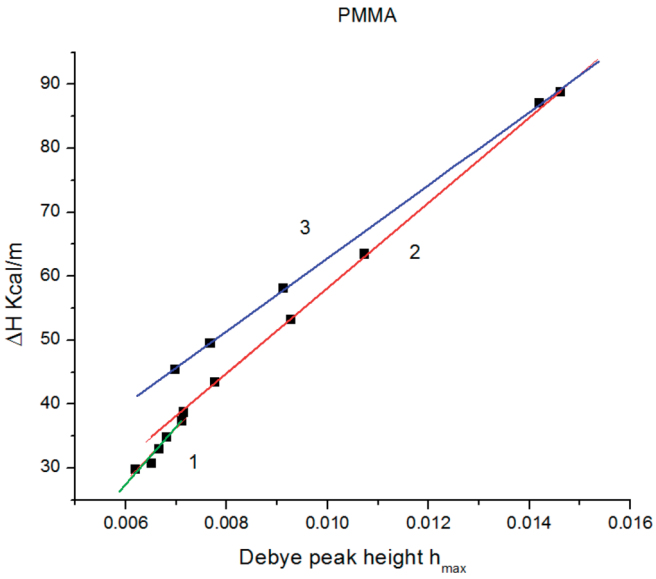


Figure 3.21a: For PMMA, $\Delta H(T_p)$ is plotted against the Debye peak height, showing three zones of proportionality: range 1 (green straight line), range 2 (red straight line), and range 3 (blue straight line, with the points moving backward).

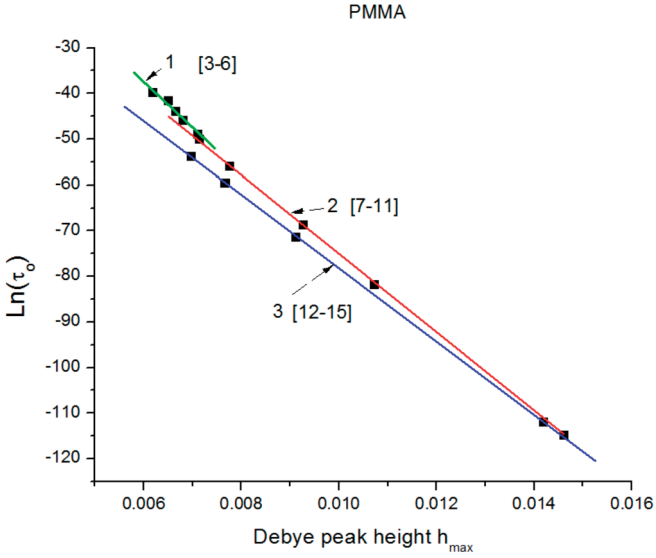


Figure 3.21b: Equivalent plot as in Figure 3.21a, now for $\mathrm{Ln}(\tau_o(T_p))$ vs. the Debye peak height, $h_{\max}$, showing the three ranges of T_p values 1, 2, and 3, and their point assignments: [3–6] for range 1, etc.

EBSCOhost - printed on 2/13/2023 12:32 AM via . All use subject to https://www.ebsco.com/terms-of-use

Table 3.2: PMMA – Value of ΔH_s and Ln(τ_{os}) after shifting the Debye peaks at various T_p by δ_x.

	L	M	N	O	P	Q	R	S	T
	T_p	ΔH_s kcal/m (−32.25)	τ_{os} for δ_x = −32.25	ΔH_s (−10)	τ_{os} (−10)	ΔH_s (+4)	τ_{os} (+4)	ΔH_s (+44)	τ_{os} (+44)
1	°C	ΔH shift by −32.25	τ_o shift by −32.25	ΔH shift by −10	τ_o shift −10	ΔH shift by 4	τ_o shift by 4	ΔH shift by 44	τ_o +44 shift
2	55	25.1715	5.82658E-17	29.04063	2.55189E-18	31.61681	3.56545E-19	39.58034	1.28889E-21
3	60	24.64094	2.224E-16	28.38978	1.10489E-17	30.88456	1.67114E-18	38.5912	7.57742E-21
4	65	27.5223	3.68645E-18	31.63721	1.44094E-19	34.37321	1.87414E-20	42.81535	5.52115E-23
5	70	28.82784	8.92355E-19	33.06895	3.31984E-20	35.8866	4.18568E-21	44.57159	1.12822E-23
6	75	31.33534	3.17949E-20	35.8744	9.87642E-22	38.88771	1.11161E-22	48.16655	2.16629E-25
7	80	31.73341	4.01399E-20	36.25053	1.34095E-21	39.24674	1.57995E-22	48.46268	3.50914E-25
8	85	36.18552	9.01088E-23	41.2485	2.12216E-24	44.60403	2.00664E-25	54.91409	2.37703E-28
9	90	44.68017	4.49448E-28	50.83933	5.00996E-30	54.9185	2.95878E-31	67.44048	9.1329E-35
10	95	53.11443	3.77528E-33	60.32475	2.10667E-35	65.09671	8.04982E-37	79.7316	7.16152E-41
11	100	74.15131	3.7467E-46	84.06346	3.31607E-49	90.61892	3.97777E-51	110.7048	1.29178E-56
12	105	73.21986	2.732E-45	82.95113	2.8535E-48	89.38527	3.79883E-50	109.09257	1.6615E-55
13	110	48.75794	5.72872E-29	55.09636	7.17944E-31	59.28302	4.56435E-32	72.08953	1.73905E-35
14	115	42.23087	1.20335E-24	47.67501	2.8806E-26	51.26964	2.75184E-27	62.25975	3.35632E-30
15	120	38.84501	2.03004E-22	43.82947	6.75869E-24	47.1199	7.94603E-25	57.17721	1.75375E-27

EBSCOhost - printed on 2/13/2023 12:32 AM via . All use subject to https://www.ebsco.com/terms-of-use

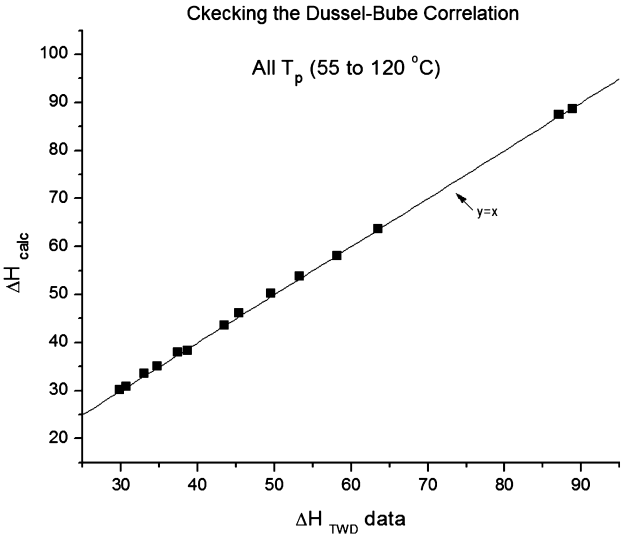


Figure 3.22a: Compare the ΔH_{calc}, calculated with the new Dussel–Bube constant for the PMMA data, with the ΔH data obtained by TWD. The straight line passing through is $Y = X$, validating the use of the Dussel–Bube equation with the modified constant.

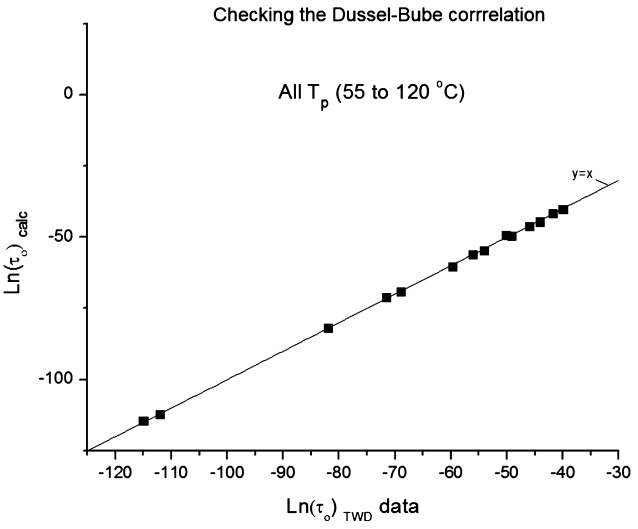


Figure 3.22b: Equivalent plot as in Figure 3.22a, now using the $\text{Ln}(\tau_o)$ calculated (on the Y-axis) and the TWD data (on the X-axis) to validate the new Dussel–Bube constant. The validation is perfect.

We have checked that the shifted peak characteristics follow the Dussel–Bube approximation (Chapter 1, see equation (3.9) below). This is demonstrated in Figure 3.22a and b.

EBSCOhost - printed on 2/13/2023 12:32 AM via . All use subject to https://www.ebsco.com/terms-of-use

In these figures, we plot the calculated value of ΔH and Ln(τ_o) against their TWD data value as T_p varies. Figure 3.22a is for ΔH_{calc}, calculated by a modified Dussel–Bube equation, replacing their constant 1.41 by 1.4642 to fit the data perfectly. Figure 3.22b is the corresponding calculated Ln(τ_o) value, which is determined from ΔH and $T_{m,D}$ (Chapter 1, p. 42, also see equation (3.9) below). The straight line in Figure 3.22a and b is $Y = X$, validating the use of the modified Dussel–Bube correlation to fit the shifted data.

I.3.4.2 Shifting the Debye peak obtained at a given T_p by various amounts δ_x

Once the correlation of Figure 3.22 is established, the values of ΔH_s and Ln(τ_{os}) for the shifted Debye peak are found very simply by plugging in the Dussel–Bube equation the value of $T_{m,D}$ and T_1 shifted by δ_x:

$$\Delta H = 1.4642R\frac{(T_m + \delta_x)(T_1 + \delta_x)}{(T_m - T_1)}$$
$$\tau_o = \frac{\exp\left(-\frac{\Delta H}{RT_m}\right)}{b\frac{\Delta H}{RT_m^2}} \tag{3.9}$$

To simplify, $T_{m,D}$ is written T_m in the following.

Figures 3.23 and 3.24 are compensation search plots at constant T_p, for $T_p = 55\,°C$ in Figure 3.23 and 115 °C in Figure 3.24. Plots of Ln(τ_o) vs. ΔH when δ_x varies would be linear if there was a compensation.

There is no compensation visible across the full range of δ_x variation in either Figure 3.23 or Figure 3.24. For the low T_p case (55 °C), however, one could divide the range into two regions across $\delta_x = 0$ and define a compensation for each range. One could also fit the compensation line with a parabolic fit, resulting in no compensation. Above T_g, in Figure 3.24, the two regions separated by $\delta_x = 0$ are quadratic fits with different parameters, as expected from equation (3.9). In conclusion, the Dussel–Bube equation predicts no compensation at constant T_p (constant T_1 and T_m) and δ_x variable.

In the next section, the crossing of the effect of δ_x and T_p reveals the presence of three different ranges of T_p corresponding to the three mechanisms of polarization–depolarization already hinted in Figure 3.21. In essence, the coupling of the effect of T_p and δ_x can serve as a magnifier of the details, inducing us to fine-tune our understanding of the voltage field interactions with the dielectric medium.

EBSCOhost - printed on 2/13/2023 12:32 AM via . All use subject to https://www.ebsco.com/terms-of-use

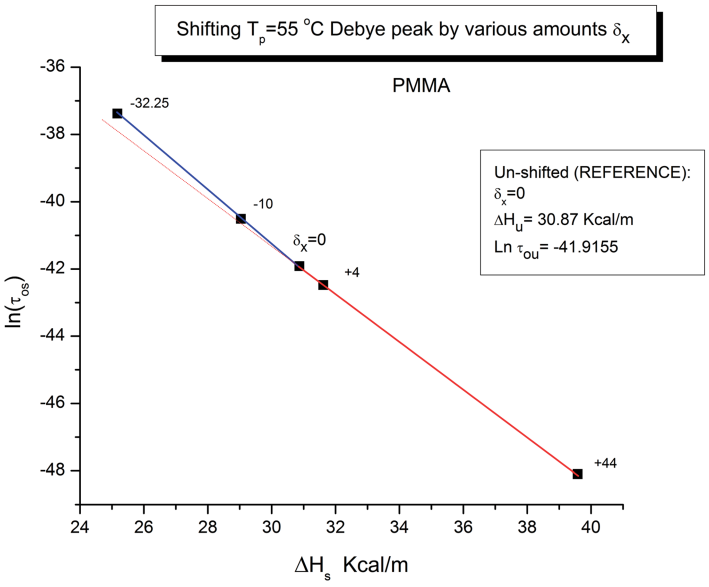


Figure 3.23: Compensation search of Ln(τ_{os}) vs. ΔH_s for shifting the T_p = 55 °C Debye peak by various amounts δ_x (written on the curve). The data can be fitted either by two perfect straight lines intercepting at δ_x = 0 or by a parabolic function.

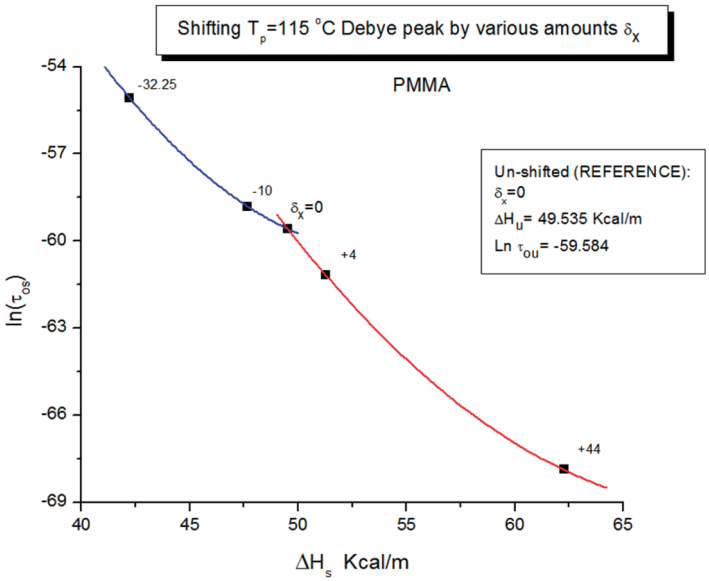


Figure 3.24: Compensation search of Ln(τ_{os}) vs. ΔH_s for shifting the T_p = 115 °C Debye peak by various amounts δ_x (written on the curve). This results in two parabolic fits across δ_x = 0, i. e., no overall compensation.

EBSCOhost - printed on 2/13/2023 12:32 AM via . All use subject to https://www.ebsco.com/terms-of-use

I.3.4.3 Shifting the Debye peaks obtained at various T_p by the same amount δ_x: the three temperature ranges of the voltage field–temperature interactions

As T_p varies, we now shift each Debye peak obtained by TWD by the same amount δ_x. T_1 and T_m, are T_p-dependent as formulated in equation (3.10) below. *As a first approximation*, we can assume the linearity of T_1 and T_m with T_p in two ranges across T_g (Figure 3.15):

$$T_1\,(\mathrm{K}) = d_o + d_1 \cdot T_p\,(\mathrm{K}) \tag{3.10}$$

with $d_o = -30.4$, $d_1 = 1.082$ for $T_p < T_g$ and $d_o = 250$, $d_1 = 0.344$ for $T_p > T_g$,

$$T_m\,(\mathrm{K}) = c_o + c_1 \cdot T_p\,(\mathrm{K})$$

with $c_o = 39.28$ and $c_1 = 0.9082$.

Let us call ΔH_u the unshifted value of ΔH: it is only a function of T_p; we have already called ΔH_s the shifted value of ΔH, which is a function of δ_x and T_p. It is straightforward to write ΔH_s as a function of ΔH_u:

$$\begin{aligned}
\Delta H_U &= 1.4642R\frac{T_m T_1}{(T_m - T_1)}\\
\Delta H_s &= 1.4642R\frac{(T_m + \delta_x)(T_1 + \delta_x)}{(T_m - T_1)}\\
\Delta H_s &= \frac{(T_m + \delta_x)(T_1 + \delta_x)}{(T_m T_1)}\Delta H_U = \left(1 + \frac{\delta_x}{T_1}\right)\left(1 + \frac{\delta_x}{T_m}\right)\Delta H_U\\
\text{Slope of } \Delta H_s/\Delta H_u &= \left(1 + \frac{\delta_x}{d_0 + d_1 T_p}\right)\left(1 + \frac{\delta_x}{c_0 + c_1 T_p}\right)
\end{aligned} \tag{3.11}$$

The slope of $\Delta H_s/\Delta H_u$ is an example of "crossing functions" capable of revealing structures that are otherwise invisible without the analytical magnifying effect. We have used such functions in other circumstances to invalidate the separation of the variables of temperature and molecular weight in the formulation of the Newtonian viscosity (Chapter 3 of [128], [138]) or to demonstrate the existence of the T_{LL} transition in the amorphous state of polymer melts [135]. For our current concern, we only see two compensation lines in Figure 3.20; there is no discernment of a structure [2–6] and [7–11] for $T_p < T_g$, although such a structure is visible in Figure 3.21. Let us explain how to use the crossing of δ_x and T_p in equation (3.11) to make this structure appear requiring an explanation.

Figure 3.25 is a plot of ΔH_s vs. ΔH_u for the T_p range above T_g corresponding to rows [12–15] in Table 3.2. Each symbol corresponds to a certain value of δ_x. One clearly sees that within this limited span of T_p, the correlation between ΔH_s and ΔH_u formally written by equation (3.11) can be approximated by a set of straight lines with the separation of the effect of δ_x and T_p. For a given δ_x, the effect of T_p appears as a linear relationship

EBSCOhost - printed on 2/13/2023 12:32 AM via . All use subject to https://www.ebsco.com/terms-of-use

between ΔH_s and ΔH_u with slope α_1 and intercept α_o. Although the straight lines are perfectly defined ($r^2 = 1.0$), equation (3.11) says it is only an approximation, not real.

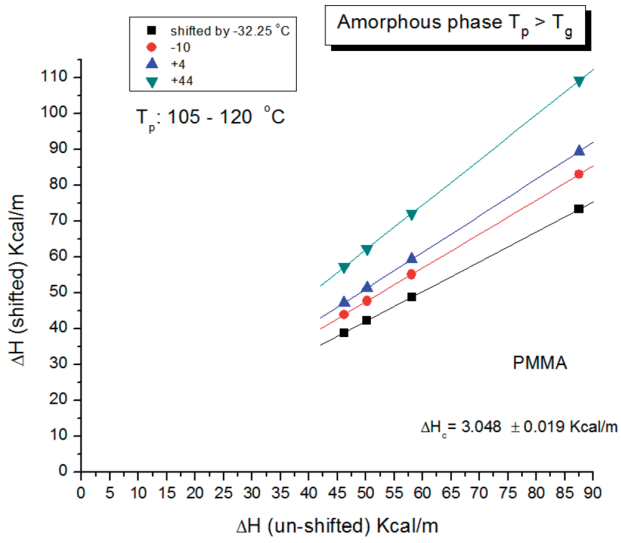


Figure 3.25: Plots of ΔH_s (shifted) vs. ΔH_u (unshifted) at various δ_x for points [12–15], i. e., points of range 3 ($T_p > T_g$). The straight lines are perfect and compensate for the value shown as ΔH_c.

The effect of changing δ_x is to vary the values of α_1 and α_o. Figure 3.25 hints that a compensation may exist between these lines, when δ_x varies, with a compensation point that is found by plotting α_o vs. α_1, our classical way to find the coordinates of the compensation point. This procedure has been explained several times so we will only concentrate on the results.

The α_o vs. α_1 compensation search is fitted by a straight line passing through the point (1, 0), corresponding to $\delta_x = 0$, with a regression coefficient $r^2 = 0.9996$ and a standard deviation SD = 0.019. The value of the slope of α_o vs. α_1 gives -3.0554 ± 0.06 kcal/m, which is equal to $-\Delta H_{uc}$, and that of its intercept is 4.0404 ± 0.06 kcal/m, equal to ΔH_{sc}. If we force fit $\Delta H_{sc} = \Delta H_{uc}$ in the regression of the super-compensation line, we find $\Delta H_{sc} = \Delta H_{uc} = 3.048 \pm 0.09$, with $r^2 = 0.9982$ and a $\chi^2/\text{DoF} = 8.1 \times 10^{-4}$.

Once again, equation (3.11) does not support such a finding: these compensations and super-compensations are only approximations. Yet, the statistical errors of the regressions, both at δ_x constant and T_p variable (Figure 3.25) and for the super-compensation search when δ_x varies (not shown), are good enough that one can easily be convinced of the validation of the linearity of the lines in Figure 3.25 and of their convergence on the $Y = X$ axis at a super-compensation point, independent of the effect of T_p and δ_x.

Figure 3.26 plots the values of $\text{Ln}(\tau_{os})$ vs. $\text{Ln}(\tau_{ou})$ found in Table 3.2 limited to the same range of T_p as in Figure 3.25: they apply to the $T_p > T_g$ amorphous phase. This time the compensation of the straight lines gives $\text{Ln}(\tau_{osc}) = 1.6356 \pm 0.0014$, $\text{Ln}(\tau_{ouc}) =$

EBSCOhost - printed on 2/13/2023 12:32 AM via . All use subject to https://www.ebsco.com/terms-of-use

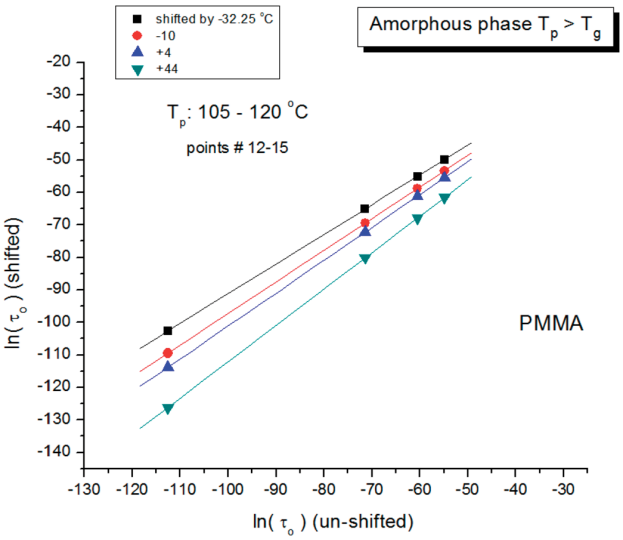


Figure 3.26: Plots of Ln(τ_{os}) (shifted) vs. Ln(τ_{ou}) (un-shifted) at various δ_x for points [12–15], i. e., points of range 3 ($T_p > T_g$). The straight lines are perfect and compensate for Ln(τ_{oc}).

1.6354 ± 0.0014 with $r^2 = 1.0$ and SD $= 2.2 \times 10^{-4}$. We conclude that Ln(τ_{oc}) = 1.6355 with an accuracy lower than 1 %.

In summary, for this $T_p > T_g$ range,

$$\begin{aligned} \Delta H_c &= 3.048 \\ \text{Ln}(\tau_{oc}) &= 1.6355 \end{aligned} \tag{3.12}$$

These coordinates are the values found for the super-compensations in Figures 3.25 and 3.26, and they do not depend on the values of T_p and δ_x. They can therefore be used to "normalize" the ΔH, Ln(τ_o) data in this range: (ΔH-ΔH_c) and (Ln(τ_o) – Ln(τ_{oc})), respectively. We will show such a plot after we normalize the $T_p < T_g$ range in the next section.

For the $T_p < T_g$ data, displayed in rows 2–11 of Table 3.2, we address the issue of the existence of a range structure by studying separately, for both ΔH_s vs. ΔH_u and Ln(τ_{os}) vs. Ln(τ_{ou}), the case [2–11] – for no structure – and the case of a structure, [2–6] and [7–11]. To compare the two possible options, either [2–11] or [2–6] + [7–11], we look at the quality of the regressions, the r^2, the SD, the χ^2/DoF, and the statistical errors found for the slopes and intercepts of the straight lines at δ_x constant and of the compensation searches. The regression results are summarized in Table 3.3.

First, looking at the statistical errors and the r^2 of the regressions in Table 3.3, it is clear that splitting the $T_p < T_g$ range [2–12] into two ranges, [3–6] and [7–11], improves very significantly the quality of the fits. The tolerances and errors speak for themselves. Yet, such improvements are expected, to a certain degree, when the fits themselves are supposed to approximate curvatures by linear segments. The response is a matter of appreciation of the tolerance levels. The χ^2/DoF result for [2–12] is, how-

EBSCOhost - printed on 2/13/2023 12:32 AM via . All use subject to https://www.ebsco.com/terms-of-use

ever, 30 to 80 times bigger than for the split ranges [3–6] and [7–11], respectively. We consider this large increase a relevant argument to back up our claim that the $T_p < T_g$ range should be split in two.

Table 3.3: PMMA – Regression results for the compensation plots of ΔH_s vs. ΔH_u and $\text{Ln}(\tau_{os})$ vs. $\text{Ln}(\tau_{ou})$ for various T_p ranges defined by their order number (from $T_p = 55\,°C$ to $120\,°C$): [2–6] and [7–11] for T_p below T_g or [2–11] and [12–15] above T_g.

T_p range	ΔH_c	$\text{Ln}(\tau_{oc})$	$R^{2(*)}$	$\chi^2/\text{DoF}^{(*)}$
[2–12]	−5.84 ± 0.22	14.5408 ± 0.003	0.9972	3.8 E-3
[3–6]	−8.03 ± 0.11	21.033 ± 0.0007	0.99975	1.1 E-4
[7–11]	−3.92 ± 0.04	11.1352 ± 0.0018	0.99979	5.0 E-5
[12–15]	3.048 ± 0.09	1.6355 ± 0.0014	0.9982	8.1 E-4

(*) These values correspond to the constrained linear regression of α_o vs. α_1, the super-composition search for ΔH_s vs. ΔH_u. The same values for the $\text{Ln}(\tau_o)$ columns are even better: $r^2 = 1.0$ and $\chi 2/\text{DoF} \sim 10^{-7}$, respectively.

Another way to reveal the three zones is to normalize the unshifted $\text{Ln}(\tau_o)$ vs. ΔH axes of Figure 3.20 by the respective values of $\text{Ln}(\tau_{oc})$ and ΔH_c, in each range, and compare the normalized Arrhenius compensation plot to Figure 3.20. This is shown in Figure 3.27.

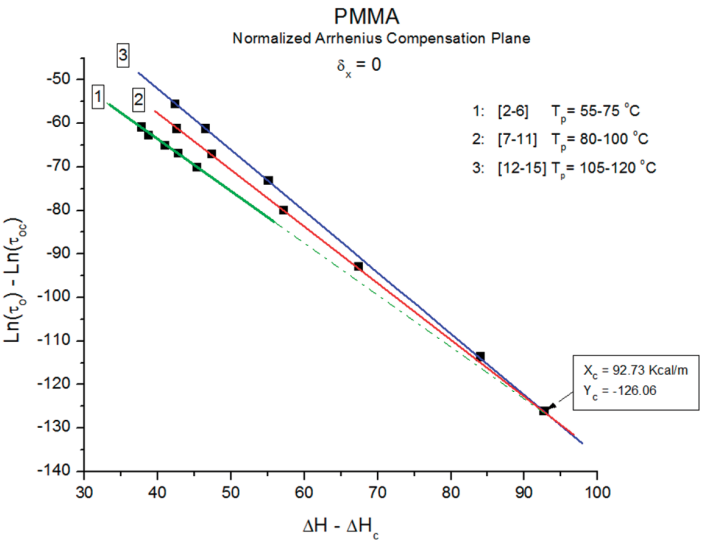


Figure 3.27: Compensation search for $\delta_x = 0$, using normalized axes: $\text{Ln}(\tau_{oc})$ and ΔH_c are the values of the compensation coordinates determined in Figures 3.25 and 3.26 for range 3 and similar plots for ranges 1 and 2. It appears that the three compensation lines describing ranges 1, 2, and 3, respectively, super-compensate at T_g.

EBSCOhost - printed on 2/13/2023 12:32 AM via . All use subject to https://www.ebsco.com/terms-of-use

We clearly observe three ranges in this plot: range 1 (the green straight line) applies to [2–6], range 2 (the red straight line) applies to [7–11], and range 3 (the blue straight line) covers [12–15]. These three straight lines appear to converge to the same super-compensation point: X_c = 92.73 Kcal/m, Y_c = –126.06. The slope of the compensations lines for the three zones determines the temperature of compensation for the Ln(τ_o) vs. $1/T$ spectral lines in the Arrhenius plane. T_c (K) is equal to –1000/(1.9872 slope).

In summary, normalization by the respective values of ΔH_c and Ln(τ_{oc}) in each range clearly identifies two temperature ranges below T_g. These ranges are characterized by their compensation temperature, T_c, and the values of their ΔH, Ln(τ_o) at the super-compensation point, back-calculated from the values of X_c and Y_c and of ΔH_c, Ln(τ_{oc}) in each range. Using the sub-index 1, 2, 3 to characterize ranges 1, 2, and 3, we have

$$\begin{aligned} T_{c1} &= 432.79\,\text{K}(159.8\,°C); \quad \Delta H_1 = 84.7\,\text{Kcal/m}; \quad \text{Ln}(\tau_{o1}) = -105.03 \\ T_{c2} &= 388.4\,\text{K}(115.4\,°C); \quad \Delta H_2 = 88.81\,\text{Kcal/m}; \quad \text{Ln}(\tau_{o2}) = -114.92 \\ T_{c3} &= 360.86\,\text{K}(87.9\,°C); \quad \Delta H_3 = 95.78\,\text{Kcal/m}; \quad \text{Ln}(\tau_{o3}) = -124.424 \end{aligned} \tag{3.13}$$

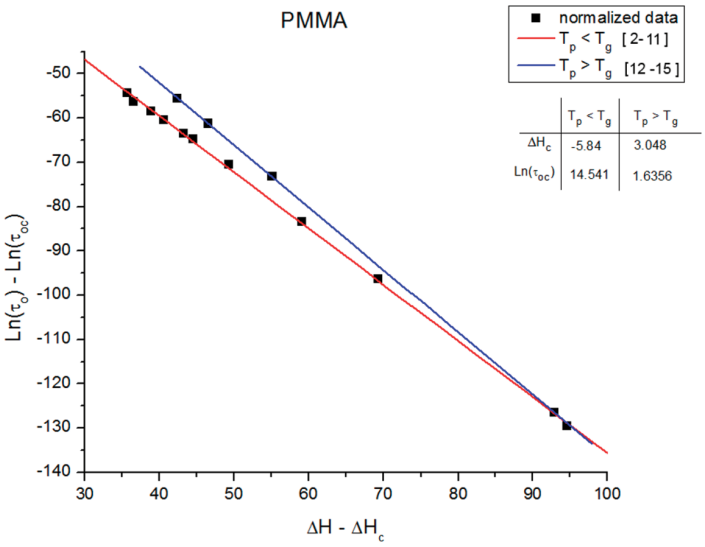


Figure 3.28: Same graph as in Figure 3.27, assuming no split in two ranges below T_g. In this range, Ln(τ_{oc}) and ΔH_c are the values of the compensation coordinates determined for points [2–11] considered as a single range below T_g. Above T_g, the values of Ln(τ_{oc}) and ΔH_c are the values for range 3 in Figure 3.27.

Figure 3.28 shows the normalized compensation in the Arrhenius plane for the no-split option below T_g: range [2–11]. This time, the values of ΔH_c and Ln(τ_{oc}) applicable in

EBSCOhost - printed on 2/13/2023 12:32 AM via . All use subject to https://www.ebsco.com/terms-of-use

the $T_p < T_g$ range are those in the first row of Table 3.3, the $T_p > T_g$ remaining the same. We see that in this case, zones 1 and 2 stay merged, although a fine statistical analysis of the residuals of the regression line passing through the ten points of [2–11] shows a systematic departure from the line for the first five points. Interestingly, the value of T_c for the $T_p < T_g$ no-split solution is 392.2 K (124.2 °C), which is about 21 °C higher than T_g, an observation constantly made for positive compensations, yet the T_{c2} reported in equation (3.13) for the normalized value is only 12 °C greater than T_g, which makes it almost T_g and not T_g + 23, as often observed for the unnormalized compensation search. Note also that the ΔH_{c2} of the no-split range, [2–12], is 88.33 Kcal/m, the same value found in range 2 of equation (3.13). The $\ln(\tau_{oc})$ value is not the same, though, and equal to –113.7. As already mentioned before, the standard deviation for the [2–11] compensation line between ΔH and $\mathrm{Ln}(\tau_o)$ is three times the value found for [2–6] and [7–11] separately.

In conclusion, although we know that equation (3.11) implies that the effects of T_p and δ_x are not analytically separable, it appears remarkable that we can formulate the relationship between ΔH_s and ΔH_u (or $\mathrm{Ln}(\tau_{os})$ vs. $\mathrm{Log}(\tau_{ou})$) as if these two effects were actually separable. The use of compensation laws and super-compensation laws is remarkably simple, yet is this elegant mathematical simplicity misleading us by making the illusion credible? Is the formulation of correlations between parameters with help of compensations an illusion that disguises the knowledge of the true interactive dependence between these parameters? At the end, the mathematical description of the data should help understand the physical reality behind the data, but it should not misguide us. For instance, in the exercise above, we have found a mathematical way (Figure 3.27) that suggests that the interactions of the voltage field with the polymer dielectric characteristics consist of three mechanisms of interactions. Is this real?

In all the chapters of this book, we have never discussed this reality; why not?

We have abundantly analyzed the differences between the positive and negative compensations of amorphous polymers or amorphous phases in semi-crystalline polymers or blends. Our objectives, practical and theoretical, to demonstrate the power of the TWD method of characterization were served well by focusing our analysis on the compensation search figures, such as Figure 3.20 or Figure 3.27, that seemingly validate a homogeneous temperature range below T_g. Perhaps we should have paid more attention to the details, for instance by looking more closely at the low T_p range in Figure 3.19a, a plot of enthalpy vs. T_p, or in Figure 3.18, a plot of the peak height vs. T_p, or even in Figure 3.21a and b, which clearly reveals a difference of behavior in the low T_p range. Case in point: in Figure 3.19a, the hyperbolic fit should have been limited to the range [7–11], the range [2–6] displaying a different behavior (linear). Figure 3.29 unambiguously proves the split of the $T_p < T_g$ behavior in two ranges (ΔH is normalized by the values of ΔH_c found in Table 3.3).

The phenomenon of compensations itself, as a topic for mathematicians to research in depth, does not appear to have been the subject of any significant interest, such as holograms did, for instance. And there might be good reasons to investigate

EBSCOhost - printed on 2/13/2023 12:32 AM via . All use subject to https://www.ebsco.com/terms-of-use

the source and the intricacy of compensations mathematically. Figure 3.30, also issued from equation (3.11), is a good illustration of the intrinsic simplicity of the compensation solutions to describe the more complex case of independent interactive variables.

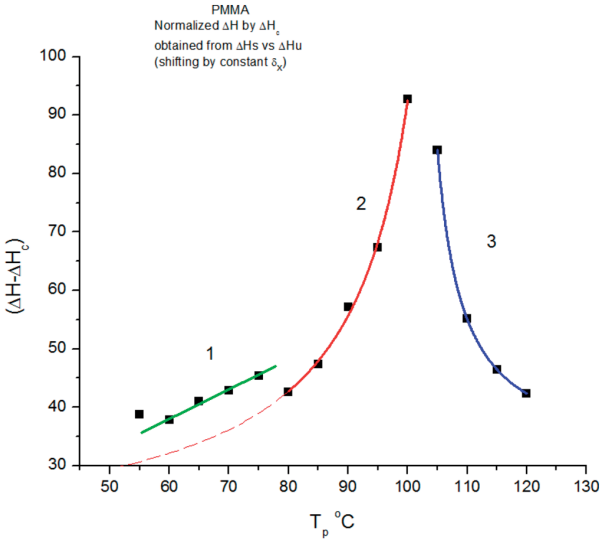


Figure 3.29: Plot of the normalized ΔH, i. e., $(\Delta H\text{-}\Delta H_c)$, vs. T_p showing three very distinct ranges, 1, 2, and 3, with a specific behavior for ranges 1 and 2 below T_g.

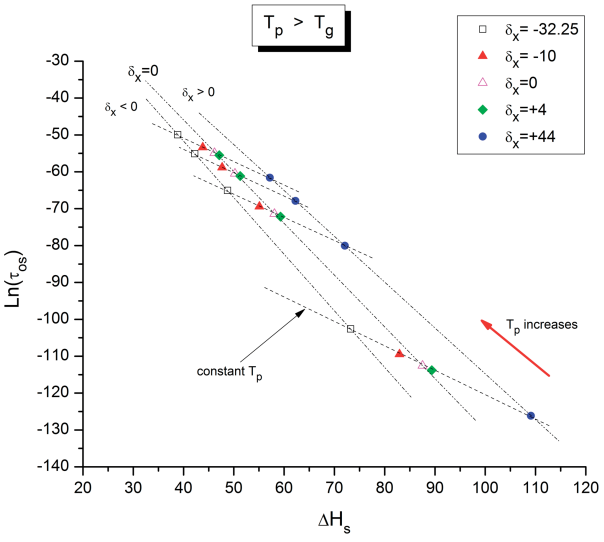


Figure 3.30: Compensation search of Ln(τ_{os}) vs. ΔH_s at various T_p above T_g (in range 3) and various δ_x. This plot can be studied either at T_p constant or at δ_x constant, providing two sets of compensations.

EBSCOhost - printed on 2/13/2023 12:32 AM via . All use subject to https://www.ebsco.com/terms-of-use

Whereas compensation plots, such as those in Figures 3.20 and 3.26, are applied to the variation of one single variable, T_p, at $\delta_x = 0$, Figure 3.30 handles the more complex situation, here illustrated for the $T_p > T_g$ range, of δ_x and T_p varying simultaneously. Figure 3.30 shows the "cross-compensation" of the effect of δ_x and T_p. By cross-compensation, it is meant that each independent variable participates in the build-up of a network of two interdependent compensations: the compensation at T_p constant, illustrated by the transversal small dash lines passing through five different symbols, and the compensation at δ_x constant, illustrated by the transversal dash dot dot lines passing through sets of identical symbols (like the blue dots at the far right). Note that Figures 3.20 and 3.27 correspond to one of these compensation lines of the latter kind with T_p variable and $\delta_x = 0$ (the open up triangles in Figure 3.30). Interestingly, the transversal compensations at T_p constant also appear to converge to a super-compensation point as T_p varies. In other words, for each range of T_p – here in Figure 3.30 the $T_p > T_g$ range corresponding to [12–15] – we can define two super-compensation coordinates, one for the compensations at δ_x constant and T_p variable and one for the compensations at T_p constant and δ_x variable. Equation (3.13) above recaps the constants associated with the "T_p network of compensations," at $\delta_x = 0$, leading to a total of nine constants: six constants for the super-compensation coordinates and three T_c constants specifically assigned to define the three T_p ranges for the effect of T_p. Likewise, we can define the "δ_x network of compensations" and its lot of fundamental constants.

Table 3.4 provides the SLOPE and INTERCEPT of the compensations of $\mathrm{Ln}(\tau_{os})$ vs. ΔH_s at T_p constant and δ_x variable from –32.25 °C and +44 °C. These are the transversal

Table 3.4: PMMA – SLOPE and INTERCEPT of the compensations of $\mathrm{Ln}(\tau_{os})$ vs. ΔH_s at T_p constant and δ_x variable. T_p varies across T_g from 55 °C to 120 °C.

	RANGE	T_p (°C)	shifted $T_p - T_g$	SLOPE	Intercept
1				–	–
2	$T_p < T_g$	55	−48.2	−0.73945	−18.93407
3		60	−43.2	−0.73302	−18.13709
4	–	65	−38.2	−0.72216	−20.43361
5	–	70	−33.2	−0.71226	−21.19512
6	–	75	−28.2	−0.70282	−23.04605
7	–	80	−23.2	−0.69236	−22.85901
8	–	85	−18.2	−0.68214	−26.26002
9	–	90	−13.2	−0.67338	−33.09879
10	–	95	−8.2	−0.66447	−39.60938
11	–	100	−3.2	−0.65562	−56.31095
12	$T_p > T_g$	105	1.8	−0.65235	−55.16539
13	–	110	6.8	−0.63998	−34.02486
14	–	115	11.8	−0.63536	−28.41372
15		120	16.8	−0.63282	−25.52006

EBSCOhost - printed on 2/13/2023 12:32 AM via . All use subject to https://www.ebsco.com/terms-of-use

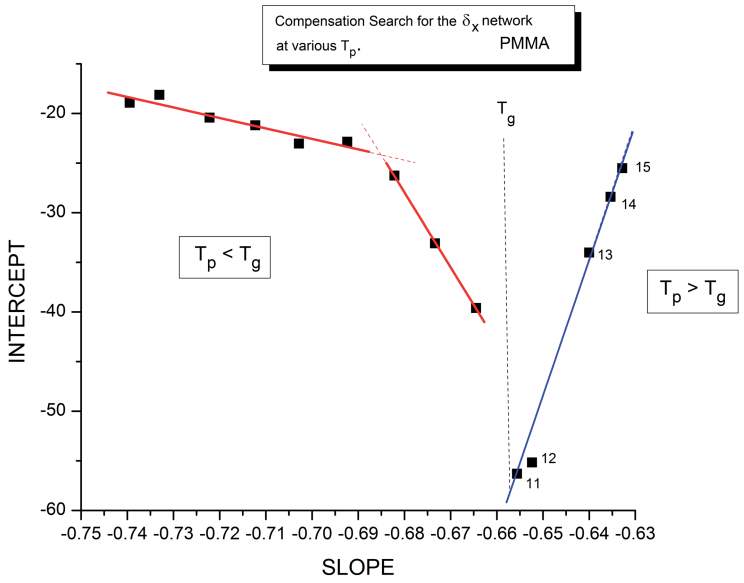


Figure 3.31: Super-compensation search for the δ_x network at constant T_p in the previous figure. The INTERCEPT and SLOPE values are those of the dashed lines at T_p constant. There are three ranges of super-compensation, two below T_g (the two red straight lines) and one above T_g, the straight blue line passing through points [11–15]. These three super-compensation lines determine the coordinates of three super-compensation points (ΔH_c, Ln(τ_{oc})), one pair for each range.

small dash lines of Figure 3.30. Table 3.4 shows the results for each T_p, when it varies from 55 °C to 120 °C.

Figure 3.31 is the compensation search for the δ_x network, i. e., a plot of INTERCEPT vs. SLOPE from Table 3.4 when T_p varies. We clearly observe three ranges for which INTERCEPT and SLOPE are linearly related: [2–7], [8–10], and [13–15]. For each of these ranges, which we notice are sliced slightly differently from the ranges established for the T_p network of compensations, linearity in Figure 3.31 implies the convergence of the corresponding compensations for that range. This is what we have designated a super-compensation. Table 3.5 gives the coordinates Ln(τ_{oc}), ΔH_c for the three super-compensations points of the δ_x network.

Table 3.5: Coordinates of the compensation points: Ln(τ_{oc}), ΔH_c, for the δ_x network, i. e., at T_p constant and δ_x variable.

Range for the δ_x network	ΔH_c for the δ_x network	Ln(τ_{oc}) for the δ_x network
[2–7]	105.62468	−96.50162
[8–10]	755.41	−541.63
[13–15]	−1191.07	728.263

EBSCOhost - printed on 2/13/2023 12:32 AM via . All use subject to https://www.ebsco.com/terms-of-use

We will let the reader calculate the slope of the normalized [Ln(τ_{os}) – Ln(τ_{oc})] vs. [ΔH_s – ΔH_c] for each range of the δ_x network, from which he or she will deduct the corresponding T_{c1}, T_{c2}, and T_{c3} for this δ_x network. In summary, the cross-network is defined by 18 constants. This number can be considered as the "mesh size" of the cross-network.

It is clear that using equations (3.9) and (3.11) to describe the effect of δ_x and T_p is not only extremely simple to implement, but mathematically rigorous. It only requires to know the constants of T_1 (T_p) and T_m(T_p) in each T_p range. This modified Dussel–Bube approach is the "analog" version to characterize the interactive coupling between the effects of T_p and δ_x. Conversely, the use of the cross-network of compensations, which might be considered as the "digital" version of the solution, is based on approximations and requires the combination of logic (to determine the range of T_p in order to choose which constants apply) and a set of 18 constants; this looks unnecessarily laborious and complex. However, conceptually, this digitization by a process of compensations and super-compensations, at two levels, of a continuous function of two variables might open up a new way to analyze physical problems and should deserve further mathematical scrutiny, in our opinion.

Our investigation in this section of the effect of shifting the Debye peaks by δ_x *did not lead to the normalization of the positive and negative compensation lines into a single compensation*. On the contrary, yet most importantly, it led us to reveal the existence of another compensation line, at lower T_p, on top of the positive and negative ones.

I.3.4.4 Shifting the Debye peak obtained at a given T_p to a given temperature

In this section, instead of shifting the peaks at constant δ_x, we proceed to shift them to a constant temperature, the same for all T_ps. For instance, we shift all the peaks to the T_g temperature. This small variation creates a dependence between T_p and δ_x through the choice of the "reference" temperature, the temperature of shifting. In Figure 3.30, studied in the previous section, we correlated the effect of two independent parameters, T_p and δ_x, but now, in this section, the two parameters are linked by a dependence to T_g, or to any other reference temperature we choose. In this study, the shifting temperature references are T_g –23, T_g, T_g +23, and T_g +70. Note that this choice makes it different than simply shifting to a list of temperatures chosen at random, e. g., 85 °C, 95 °C, 120 °C, etc. For polymers, it is known that T_g determines the onset of the free volume expansion in the material, so shifting to T_g or to $T_g + 23$ amounts to study the effect of shifting to a given constant free volume state.

To obtain the shifted values, ΔH_s and Ln(τ_{os}), of the shifted Debye peak to temperature T, we use the Dussel–Bube equation, equation (3.11), as before, with now $\delta_x = T - T_{(m,D)_u}$, where the sub-index u points to the unshifted peak at T_p. Both $T_{(m,D)_s}$

EBSCOhost - printed on 2/13/2023 12:32 AM via . All use subject to https://www.ebsco.com/terms-of-use

and T_{1s} are shifted by δ_x:

$$\begin{aligned} T_{(m,D)_s} &= T = T_{(m,D)_u} + \delta_x \\ T_{1s} &= T_{1u} + \delta_x = T_{1u} + (T - T_{(m,D)_u}) \end{aligned} \tag{3.14}$$

Once ΔH_s is determined, its value is plugged into equation (3.9) to find the corresponding value of Ln(τ_{os}) after shifting the Debye peak to T. As we said, we consider four values for the shifting to T study: $T = T_g - 23$, $T = T_g$, $T = T_g + 23$, and $T = T_g + 70$. Notice, for the following, that only one of these values is located below T_g and also that the last one among the three above T_g is located just above T_{LL} (estimated at around 155–165 °C).

In the six following figures, we analyze the results the same way we did for the effect of T_p at δ_x constant. We analyze ΔH_s vs. ΔH_u at T constant and vary the value of T, the same for Ln(τ_{os}) vs. Ln(τ_{ou}), and finally for Ln(τ_{os}) vs. ΔH_s. Since the aim of these figures is similar to that of the ones presented in the case of a shift by δ_x constant, we will limit ourselves to only presenting the specific differences between working at δ_x constant or at T constant.

Figure 3.32 is a plot of ΔH_s vs. ΔH_u after shifting to $T = T_g$ constant. The plot is done for all values of T_p from $T_p = 55$ °C to 120 °C. Since T_g is between 103 °C and 107 °C, one T_p, point 12, is located at T_g or very near it. One distinctively observes the three zones, 1, 2, and 3, that slice the total range; a quasi-perfect straight line is found by regression for each range. This tendency is general for all the figures that follow, from Figure 3.33 to Figure 3.37. Note that we have also performed a linear regression through the full $T_p < T_g$ range, [2–11], and those results are included in some of the graphs, although the r^2 and standard deviations for those plots are three to four times worse than those obtained for the split [3–6], [7–11].

Figure 3.33 is the same plot as Figure 3.32 except that it concerns the Ln(τ_{os}), Ln(τ_{ou}) variables. The shifting temperature is T_g.

Figure 3.34 is the same plot as Figure 3.33 except that the shifting temperature is lowered to $T_g - 23$, i. e., below T_g. The change of direction of the straight lines, pointing towards positive values of ln(τ_{ou}), has the same explanation as the slope change at T_g passing from a negative compensation ($T_p > T_g$) to a positive one ($T_p < T_g$).

Figure 3.35 is a compensation search of INTERCEPT vs. SLOPE for the values of ΔH_s vs. ΔH_u at constant T. The main difference we observe with the same results at constant δ_x is that these curves compensate at the origin for all the ranges: [3–6], [7–11], and [12–15]. This is conforming to equation (3.11), stating the proportionality between ΔH_s and ΔH_u. A minor observation should be made about the points for $T = T_g + 70$: it is hard to see visually, but these points are very slightly off the line passing through them and the origin. We believe that this is due to the fact that this T is above the T_{LL} temperature, for which a different (shifted) ΔH_s applies. Figure 3.36, below, confirms that finding more affirmatively.

EBSCOhost - printed on 2/13/2023 12:32 AM via . All use subject to https://www.ebsco.com/terms-of-use

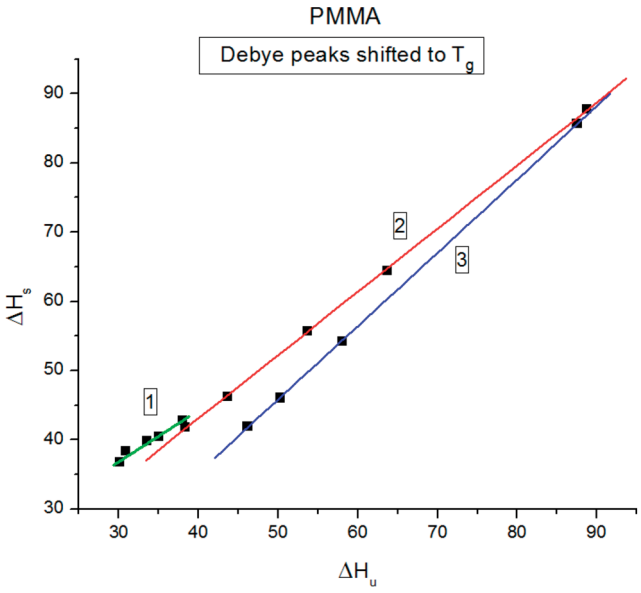


Figure 3.32: Shifting all Debye peaks to T_g: a plot of ΔH_s vs. ΔH_u shows a split of the T_p range across T_g in three distinct ranges: 1, 2, and 3.

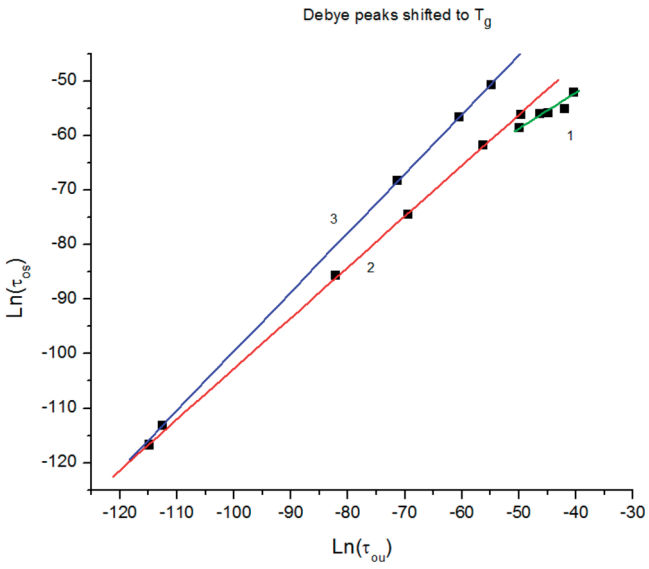


Figure 3.33: Shifting all Debye peaks to T_g: a plot of $\mathrm{Ln}(\tau_{os})$ vs. $\mathrm{Ln}(\tau_{ou})$ shows a split of the T_p range across T_g in the same three distinct ranges, 1, 2, and 3, as in Figure 3.32. Also compare this plot with Figure 3.34 showing the shift of the same data to $(T_g - 23)$.

EBSCOhost - printed on 2/13/2023 12:32 AM via . All use subject to https://www.ebsco.com/terms-of-use

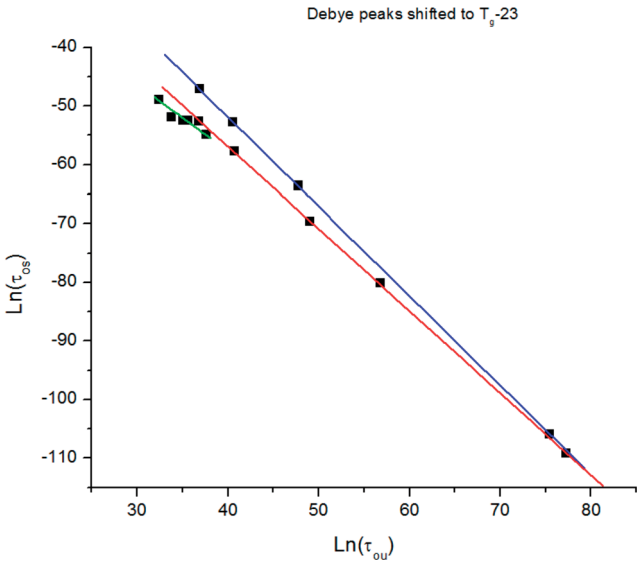


Figure 3.34: The same plot of Ln(τ_{os}) vs. Ln(τ_{ou}) for the Debye peaks now shifted to $T_g - 23$. See text.

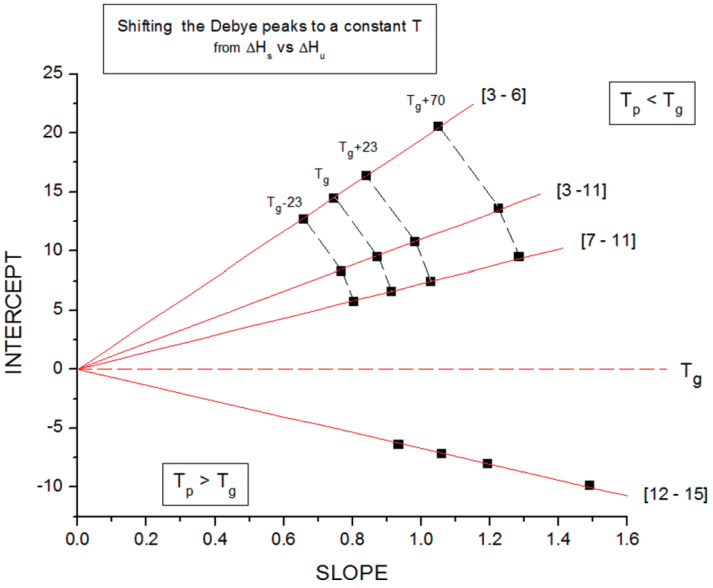


Figure 3.35: Super-compensation search of INTERCEPT vs. SLOPE for shifting the Debye peaks to a constant $T = T_g + X$. This plot concerns the ΔH_s vs. ΔH_u data.

EBSCOhost - printed on 2/13/2023 12:32 AM via . All use subject to https://www.ebsco.com/terms-of-use

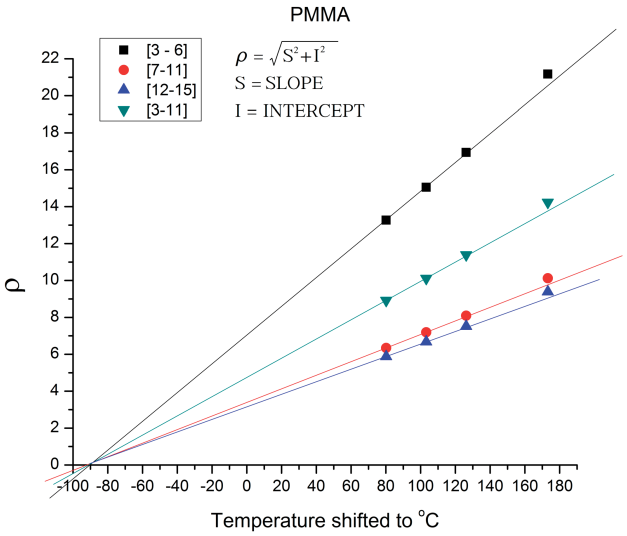


Figure 3.36: Analysis of ρ (defined in the graph insert) vs. T for the three shifting temperature ranges (and range [3–11]). The INERCEPT and SLOPE values are those in Figure 3.35.

In Figure 3.35, we see that the points corresponding to different T values, for the four ranges shown, align radially and axially, like in a polar plot, and therefore we can define the polar coordinates of these points, in particular their amplitude $\rho = (S^2 + I^2)^{0.5}$, where I = INTERCEPT and S = SLOPE. The angle of the polar coordinate is determined from the slope. The slope remains the same for a given range, as T varies. The slope is the highest for range [3–6], decreases as the T_p values in the range increase, and becomes negative for the range above T_g: [12–15]. A zero slope separates the $T_p < T_g$ from the $T_p > T_g$ ranges, and thus may be assigned to T_g itself, although the range would be assimilated to a single temperature in this case. Also interesting is the fact that range [2–11] holds its place nicely in the polar plot, as if it was a legitimate point. If we were to define a "representative temperature" for a range, for instance its T_c value from a compensation search of $\mathrm{Ln}(\tau_o)$ vs. ΔH, or a compounding average of the T_ps of the points participating in that range, we could assign a slope to each of the "real ranges," such as the slopes in Figure 3.35, and a virtual slope by way of a mixing law for all the combinations of smaller ranges, such as [2–11] composed of a mix of [3–6] and [7–11]. This is perhaps the interpretation for the integration of the range [2–11] in the polar plot defined by the real ranges in Figure 3.35.

The assignment of a zero slope for T_g seems to define T_g as a critical transition. It would be interesting to explore this subject further by submitting the T_g range to a series of T_p only separated by 1 °C or 1.5 °C and observe the fluctuations, if any, of the ΔH and $\mathrm{Ln}(\tau_o)$ values. Figure 3.29 shows that the T_g range might be defined by two hyperbolic boundaries going towards infinity within a very small margin of changes (100–110 °C).

EBSCOhost - printed on 2/13/2023 12:32 AM via . All use subject to https://www.ebsco.com/terms-of-use

We plot ρ vs. T in Figure 3.36. T is the shift temperature and ρ is the polar amplitude defined from the slope and intercept. We observe a compensation of the four straight lines in Figure 3.36; the compensation point occurs for $\rho = 0$ for a temperature $T = -90$ °C. What is the physical meaning of the collapse of ρ? Its definition implies that both the intercept and the slope must be equal to 0 for ρ to collapse. We suggested in Figure 3.35 that the zero slope line also passing through the origin was the T_g of the material, so $\rho = 0$ at T_g, according to the definition of ρ. This suggests that the temperature of the compensation of the lines in Figure 3.36 is the "core T_g," whatever that means; perhaps its most elementary representation? We will return to this question after we have covered the last shifting option in the next section: shifting to T_x constant with $T_x = T_p + \delta_x$. That study will also reveal the existence of an elementary core enthalpy, $\Delta H\#$. Is the "core T_g" related to the "core enthalpy"?

Also notice in Figure 3.36 the slight offset for the points corresponding to $T = T_g + 70$. Like we already said for Figure 3.35, this offset might be due to the presence of the T_{LL} transition. We have demonstrated in another publication that working at constant free volume while studying the crossed effect of two independent variables, in that instance T and M (molecular weight), permitted to define T_{LL} quantitatively. It is possible that the crossed effect of T_p and δ_x, while working at $T = T_g + X$ constant, produced the same result.

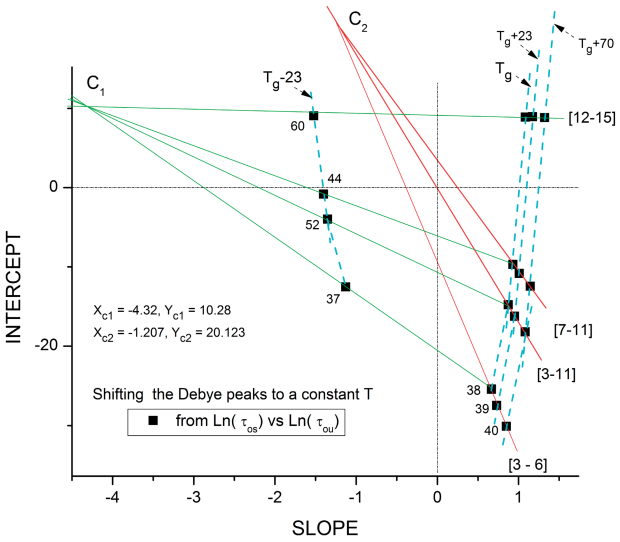


Figure 3.37: Equivalent of Figure 3.35 but for Ln(τ_{os}) vs. Ln(τ_{ou}): Super-compensation search of INTERCEPT vs. SLOPE for shifting the Debye peaks to a constant $T = T_g + X$.

Figure 3.37 is the equivalent of Figure 3.35, INTERCEPT vs. SLOPE, but now applied to the analysis of Ln(τ_{os}) vs. Ln(τ_{ou}) at T constant, when T varies. This figure looks

EBSCOhost - printed on 2/13/2023 12:32 AM via . All use subject to https://www.ebsco.com/terms-of-use

much more complicated to analyze than Figure 3.35 for the enthalpies. The dash lines (cyan) in Figure 3.37 join the points at constant T, and although we have drawn dash segments between the points, we might have curved lines instead. We have labeled a few points, such as points 37, 52, 44, and 60, which make up the $T = T_g - 23$ curve passing through. Other points in the figure, 38, 39, and 40, are aligned and belong to the group [3–6]. Each of these points also belongs to a dash line that connects points of different ranges having the same T: the T_g dash line, the $T_g + 23$ dash line, and the $T_g + 70$ dash line. These three dash lines are located on the positive side of the zero slope axis, while the equivalent dash line for $T = T_g - 23$ is located on the negative side of the graph. The curvatures of these dash lines on each side of the zero vertical line are seemingly the mirror of each other, like the two branches of a parabolic fit passing through (if we were to compare $T_g + 23$ and $T_g - 23$, for instance). Point 37 on the $T_g - 23$ dash line also belongs to the [3–6] group, yet it is not aligned with the three other points, 38, 39, and 40. The same situation occurs for point 52 that belongs to dash line $T_g - 23$ and to the group [7–11], and similarly for point 44 of the group [7–11] and point 60 of the group [12–15].

Finally, we have organized the points in the figure to be part of a cross-network of two super-compensations, the C_1 super-compensation gathering four straight lines (green) and the C_2 super-compensation gathering three straight lines (red). We have determined (graphically) the coordinates of the two super-compensation points:

$$X_{c1} = -4.32 \quad Y_{c1} = 10.28 \quad \text{for } C_1$$
$$X_{c2} = -1.207 \quad Y_{c2} = 20.123 \quad \text{for } C_2$$

We have mentioned earlier the need to have mathematicians look at the origin of compensation and study their properties. Figure 3.37 motivates that need. This book on the interactive coupling between activated dipoles is not the place to discover how the coupling of equations (3.9) and (3.11) leads to such an organization as in Figure 3.37. If we compare the compensation searches for ΔH_s vs. ΔH_u, on the one hand, and for $\text{Ln}(\tau_{os})$ vs. $\text{Ln}(\tau_{ou})$ calculated from ΔH_s, ΔH_u by equation (3.9), on the other hand, the difference in the maps of INTERCEPT vs. SLOPE is, indeed, intriguing (Figures 3.35 and 3.37). There is only one compensation in Figure 3.35, passing through the origin; by contrast, in Figure 3.37, a second compensation (C_1) is observed resulting from the singularity of the points at $T = T_g - 23$ which are not located on the straight lines compensating on the red compensation (C_2). Here is the paradox: how is it possible that Figure 3.37 clearly sees a distinct behavior at $T < T_g$ that is not observed in Figure 3.35, although the values in Figure 3.37 are all calculated from those in Figure 3.35? Both compensation searches, though, single out the behavior above T_{LL} for $X = 70$.

EBSCOhost - printed on 2/13/2023 12:32 AM via . All use subject to https://www.ebsco.com/terms-of-use

With such differences observed between the behavior of (ΔH_s vs. ΔH_u) and (Ln(τ_{os}) vs. Ln(τ_{ou})), we are intrigued to investigate the "crossing" of ΔH_s and Ln(τ_{os}), i. e., how is the compensation between Ln(τ_{os}) vs. ΔH_s affected when shifting at T constant?

Table 3.6: Intercept and slope of Ln(τ_{os}) vs. ΔH_s for shifting at $T = T_g + X$ constant.

	RANGE	T_p (°C)	shifted $X = T - T_g$	SLOPE	INTERCEPT	T_c (K)	$T_g + X$ (K)
1	SHIFTING TO	A GIVEN T		–	–	–	–
2	–	$T = T_g + X$	–	–	–	–	–
3	–	–	–	–	–	–	–
4	$T < T_g$ 2 zones	SPLIT T_g range	–	–	–	–	–
5	[3–6]	–		–	–	–	–
6	GREEN ZONE	–	–	–	–	–	–
7	–	$T_g - 23$	−23	−1.12769	−12.54417	446.2402	355.5
8	–	T_g	0	−1.08243	−12.38823	464.89899	378.5
9	–	$T_g + 23$	23	−0.98121	−13.27323	512.8572	401.5
10	–	$T_g + 70$	70	−1.05439	−13.0961	477.26231	448.5
11	–	–	–	–	–	–	–
12	[7–11]	–	–	–	–	–	–
13	RED ZONE	–	–	–	–	–	–
14	–	$T_g - 23$	−23	−1.41546	0	355.51737	355.5
15	–	T_g	0	−1.33226	0	377.71952	378.5
16	–	$T_g + 23$	23	−1.16923	0	430.38633	401.5
17	–	$T_g + 70$	70	−1.28753	0	390.84185	448.5
18	–	–	–	–	–	–	–
19	$T < T_g$	–	–	–	–	–	–
20	[3–11]	NO SPLIT	–	–	–	–	–
21	RED ZONE	–	–	–	–	–	–
22	–	$T_g - 23$	−23	−1.35112	−3.97762	372.44702	355.5
23	–	T_g	0	−1.27601	−3.94884	394.37043	378.5
24	–	$T_g + 23$	23	−1.12318	−4.52059	448.03203	401.5
25	–	$T_g + 70$	70	−1.23223	−4.35002	408.38205	448.5
26	–	–	–	–	–	–	–
27	$T > T_g$	–	–	–	–	–	–
28	[12–15]	–	–	–	–	–	–
29	BLUE ZONE	–	–	–	–	–	–
30	–	$T_g - 23$	−23	−1.52283	9.05253	330.45094	355.5
31	–	T_g	0	−1.427	9.06933	352.64233	378.5
32	–	$T_g + 23$	23	−1.23707	9.3358	406.78427	401.5
33	–	$T_g + 70$	70	−1.37197	9.23076	366.78689	448.5

Table 3.6 provides the values of the INTERCEPT and SLOPE for such compensations, for the three ranges [3–6] (green), [7–11] (red), and [12–15] (blue). The colors refer to

EBSCOhost - printed on 2/13/2023 12:32 AM via . All use subject to https://www.ebsco.com/terms-of-use

the various groups of T_p values participating in the linear regressions between $\text{Ln}(\tau_{os})$ vs. ΔH_s. The split below T_g in two groups [3–6] and [7–11] is also compared to results obtained for the no-split solution, group [3–11].

Figure 3.38 provides for group [7–11] the four compensations obtained between $\text{Ln}(\tau_{os})$ vs. ΔH_s after shifting the T_p Debye peaks to the constant $T = T_g + X$, with $X = -23$ (black square), $X = 0$ (T_g: red dots), $X = +23$ (blue square), and $X = 70$ (green triangle). For all the T_ps within that range (T_p between 80 °C and 100 °C), the $\text{Log}(\tau_{os})$ values compensate with the ΔH_s values quasi-perfectly ($r^2 = 1.0$); also, these different compensation lines all compensate at the origin (0,0) when X varies. For this group of T_ps just below T_g (corresponding to the hyperbolic fit #2 in Figure 3.29), $\text{Ln}(\tau_{os})$ is proportional to ΔH_s and when $\Delta H_s = 0$, $\tau_{os} = 1$ sec. One can calculate the temperature of compensation, T_c, in K, from the slope of the compensation lines: $T_c = -1000/(1.9872 \cdot \text{SLOPE})$. The values of T_c are provided in Table 3.6 and compared to the values of $T = T_g + X$ (in the last column). See the Discussion.

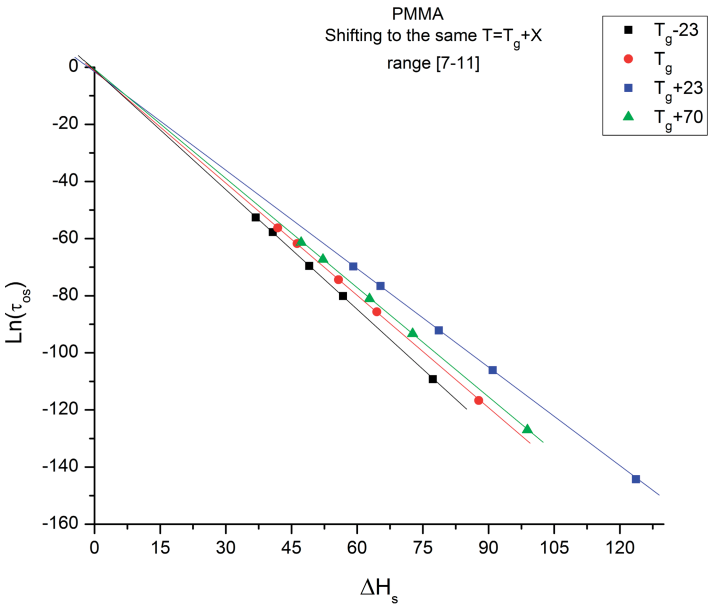


Figure 3.38: Masterplot in range [7–11] of $\text{Ln}(\tau_{os})$ vs. ΔH_s after shifting to the same $T = T_g + X$. The super-compensation coordinates are (0,0), the origin.

The compensation lines of Figure 3.38 themselves compensate in a super-compensation point $\Delta H_c = 0$, $\text{Ln}(\tau_{oc}) = 0$, which implies that a super-compensation search of INTERCEPT vs. SLOPE for the straight lines of Figure 3.37 should have a zero slope and a zero intercept. This is confirmed in Figure 3.39, a super-compensation search,

EBSCOhost - printed on 2/13/2023 12:32 AM via . All use subject to https://www.ebsco.com/terms-of-use

for all the groups [3–6], [7–11], [12–15], and [3–11], of the INTERCEPT vs. SLOPE values in Table 3.6.

In Figure 3.39, we confirm the linearity of all the super-compensation lines, whose slope and intercept provide the coordinates of the super-compensations for each group. The super-compensation coordinates are confined in Table 3.7 below.

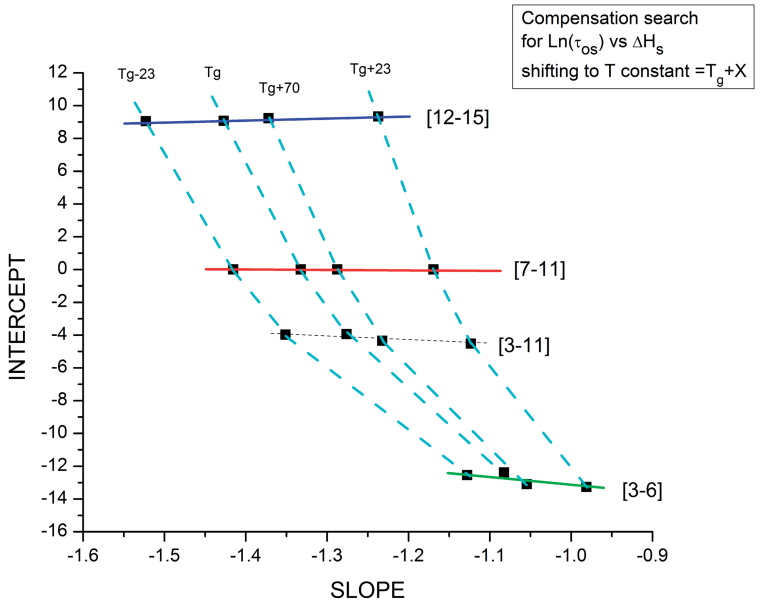


Figure 3.39: Super-compensation search for plots of Ln(τ_{os}) vs. ΔH_s after shifting to $T = T_g + X$ constant. The super-compensation line for range 2 ([7–11]) has zero slope and a zero intercept, confirming the coordinates of the super-compensation point (0,0) for this range. This range 2 will serve as reference for grid-shifting (Figure 3.54).

Table 3.7: The ΔH_c and Ln(τ_{oc}) in the table are the coordinates of the compensations of Ln(τ_{os}) vs. ΔH_s shifted at T constant and split in four T_p ranges: [3–6], [7–11], [12–15], and [3–11].

Range	ΔH_c of super-compensation	Ln(τ_{oc}) super-compensation
[3–6]	5.80	18.983
[7–11]	0	0
[12–15]	−1.07	10.66
[3–11]	2.66	7.51

EBSCOhost - printed on 2/13/2023 12:32 AM via . All use subject to https://www.ebsco.com/terms-of-use

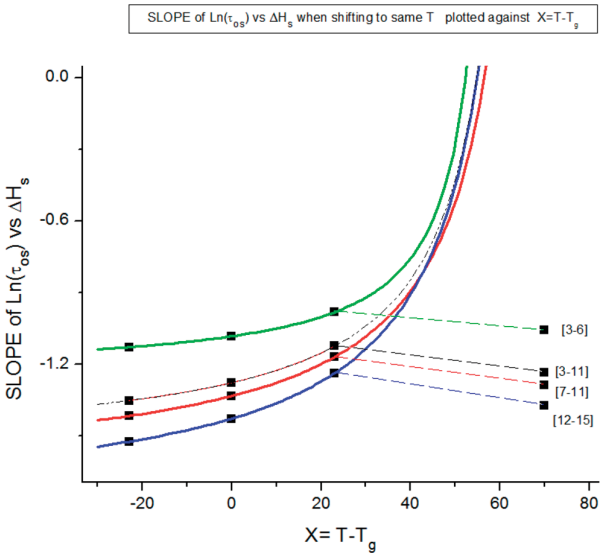


Figure 3.40: SLOPE of Ln(τ_{os}) vs. ΔH_s, when shifting to the same T, plotted against $X = T - T_g$ when X varies. The four curves correspond to the ranges [3–6], [7–11], [12–15], and [3–11].

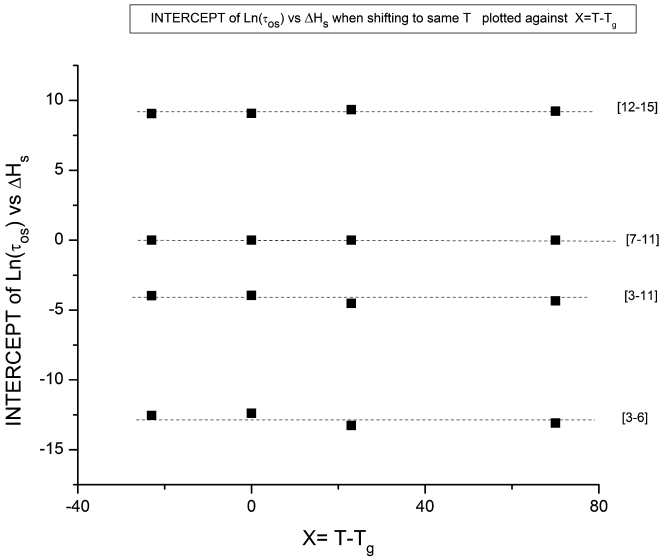


Figure 3.41: INTERCEPT of Ln(τ_{os}) vs. ΔH_s, when shifting to the same T, plotted against $X = T - T_g$.

In Figures 3.40 and 3.41 we show the variation of the SLOPE and INTERCEPT of Figure 3.39 with $X = T - T_g$, respectively. Only the slope displays a discontinuity for $X \sim 60\,°C$; the intercept remains continuous, actually practically constant across T_g.

EBSCOhost - printed on 2/13/2023 12:32 AM via . All use subject to https://www.ebsco.com/terms-of-use

We have drawn hyperbolic fits of the data in Figure 3.40 for $X \neq 70$ °C. These curves correspond to the four ranges [3–6], [3–11], [12–15], and [3–11]. The slope becomes 0 for X approximately 60 °C, and within a few more degrees goes towards infinity. As a consequence, we can now confirm that the point at $X = 70$ does not belong to the other points below $X \sim 60$ °C, revealing without doubt a distinct behavior. We speculate that the transition observed at these values of the shifting temperature characterizes the T_{LL} behavior, only timidly observed previously.

Figure 3.42 is the same type of graph of Ln(τ_{os}) vs. ΔH_s shown in Figure 3.38 for the group [7–11], now applied to group [12–15], for $T_p > T_g$. Our purpose is to again point out the cross-compensation between two independent variables, here T_p and X, the way we observed it for δ_x and T_p in the previous section (Figure 3.30). We see the similarity of the cross-compensation phenomenon in Figures 3.30 and 3.42. In Figure 3.42 we work either at T_p variable (within a range) and X constant or at T_p constant and X variable. We observe that the points with different symbols corresponding to the latter case align perfectly transversally the way we saw it for δ_x at T_p constant in Figure 3.30. Yet, there is an important difference: in Figure 3.30, the transversal compensations at T_p constant formed a super-compensation when T_p varied, but not in Figure 3.42, in which the transversal compensations are all parallel to one another when T_p varies.

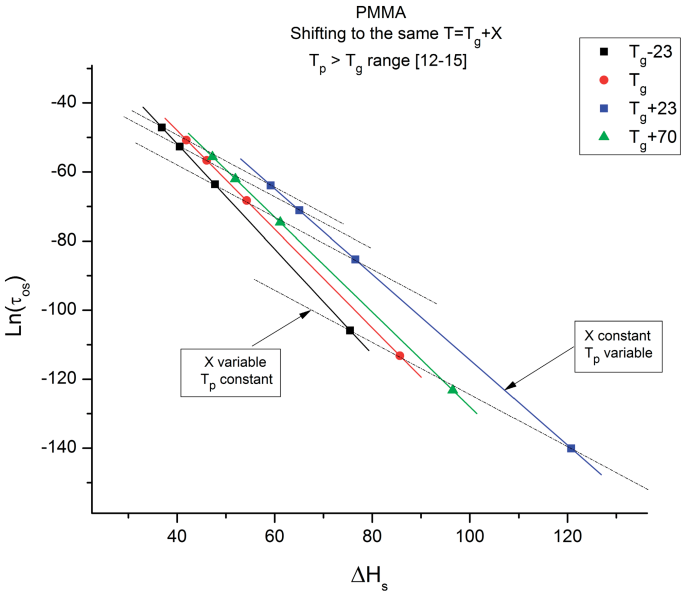


Figure 3.42: Compensation search plot for range 3, [12–15], of Ln(τ_{os}) vs. ΔH_s after shifting the T_p Debye peaks to the same $T = T_g + X$. This graph shows a cross-compensations grid, at X constant and at T_p constant.

EBSCOhost - printed on 2/13/2023 12:32 AM via . All use subject to https://www.ebsco.com/terms-of-use

Finally, to close this section on the effect of shifting the Debye peaks to a common temperature T ($T = T_g + X$), Figure 3.43 presents the normalized compensation search plot of $\mathrm{Ln}(\tau_o)$ vs. ΔH for the unshifted data, using the specific values of ΔH_c and $\mathrm{Ln}(\tau_{oc})$ found in Table 3.7 for the three ranges 1, 2, and 3, to provide the coordinates, ΔH-ΔH_c, and $\mathrm{Ln}(\tau_o) - \mathrm{Ln}(\tau_{oc})$, respectively. This normalized plot should be compared with Figure 3.27 obtained by shifting the Debye peaks by constant δ_x.

In Figure 3.43, the disposition of the three compensation lines representing the three ranges of T_p is very different than in Figure 3.27. The same annotations are used: 1 for the lower (green) group [2–6], 2 for the red [7–11] group, and 3 for the blue [12–15] group. Groups 1 and 2 correspond to $T_p < T_g$ and group 3 to $T_p > T_g$.

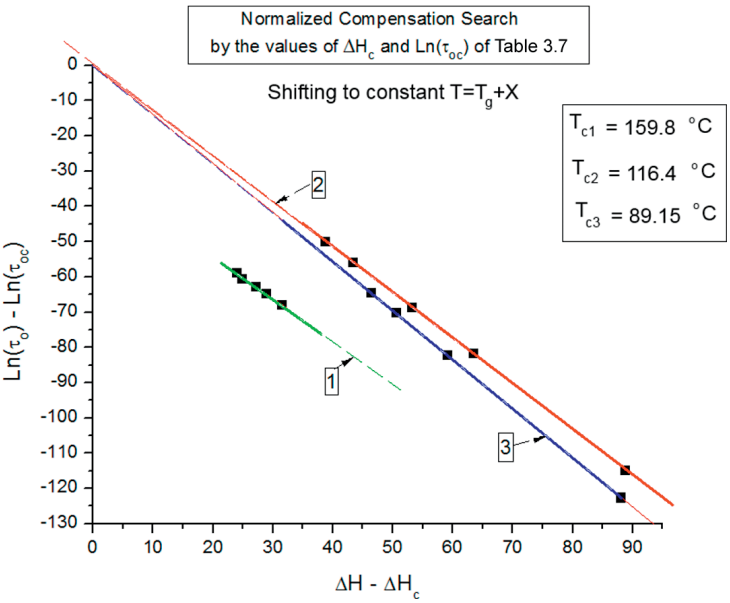


Figure 3.43: Normalized compensation search of $[\mathrm{Ln}(\tau_o) - \mathrm{Ln}(\tau_{oc})]$ vs. $(\Delta H - \Delta H_c)$ with values of $\mathrm{Ln}(\tau_{oc})$, ΔH_c in Table 3.7. The T_c are calculated from the slopes. See text. Note that both range 2 and range 3 compensate to (0,0). T_{c2} is the value of T_g of PMMA quoted in reference books [85]. T_{c1} is the value of T_{LL} found in Figure 3.16. The value of T_{c3} is explained in the Discussion.

One clearly sees that the two different modes of shifting the Debye peaks, either at δ_x constant or at $T = T_g + X$ constant, result in a profound modification of the compensation search pattern. In Figure 3.43, the compensation lines 2 and 3 go through the origin (so this is where they intercept), whereas they intercept at T_g in Figure 3.27. Besides, in Figures 3.43 and 3.27, the disposition of 2 and 3 is reversed: 2 is on top of 3 in Figure 3.43 and below 3 in Figure 3.27. We have written as an insert in the graph the

EBSCOhost - printed on 2/13/2023 12:32 AM via . All use subject to https://www.ebsco.com/terms-of-use

values of T_c determined from the slopes of the three compensation lines: T_{c2} (116.4 °C) is close to T_g + 13, with T_g = 103.2 °C, and T_{c3} (89.15 °C) is close to T_g – 13. The T_c of range 1, T_{c1} = 159.8 °C, is almost equal to the value we assigned to the T_{LL} transition in Figure 3.40, although we believe the origin of these two temperatures is totally different (see the Discussion). One may have a clue to the understanding of the physical meaning of range 1 by looking at the intercept of compensation 1 (green line), corresponding to the normalized $\Delta H = 0$: it is equal to –31.296, which translates into a relaxation time of 2.56×10^{-14} s. The corresponding radial frequency is 3.9×10^{13}, the same frequency as the thermally induced vibration of the atoms composing the dipoles. For the compensation lines 2 and 3, the equivalent frequency is 2.72 rad/s (0.43 Hz). This value certainly corresponds to the activation of a different kind of mechanism of interactions between the dipoles than in range 1. See the Discussion.

To summarize, we have studied in this and the previous section how the forced shifting of the Debye peaks by an amount δ_x resulted in a modification of the thermokinetic characteristics of the peak, ΔH_s, Ln(τ_{os}), that revealed, or at least hinted to, the origin of the differences between the various compensations observed between Ln(τ_o) vs. ΔH. Throughout this book, until this Chapter 3, only two compensations were necessary to fully describe the relaxation of the elementary Debye peaks generated at various temperatures T_p across T_g: the positive compensation, below T_g, and the negative compensation, for T_p above T_g. We are talking in this chapter about a simple amorphous phase for an amorphous polymer, and, of course, the situation can become much more complicated for blends, semi-crystalline polymers, etc.

We have realized, by shifting the peaks by a chosen amount δ_x, that there was actually an additional compensation at low T_p temperatures, so that the T_p range below T_g was actually split into two compensations, not just the single positive compensation we have described throughout this book. We called this new T_p zone "range 1."

Shifting the Debye peaks to a constant $T = T_g + X$, instead of a constant δ_x, revealed that the *nature* of the interactions in range 1 was different than in zones 2 and 3 (Figures 3.29 and 3.43).

What are the different mechanisms of interactions between the voltage field and the induced rearrangements of the dipoles in the structure that cause the observation of these three distinct ranges of T_p polarizing behavior?

As is developed below, the method of "grid-shifting" sheds some light onto the similarities and the differences between the three ranges, providing a possible theoretical interpretation of the mechanisms of interactions between voltage field and temperature, revealing the nature of the interactions in amorphous polymers.

EBSCOhost - printed on 2/13/2023 12:32 AM via . All use subject to https://www.ebsco.com/terms-of-use

I.3.4.5 Definition and description of "grid-shifting"

In Figure 3.44 we have plotted Ln(τ_{os}) vs. $T_x = T_p + \delta_x$ for all T_p values from 55 °C to 120° and all values of δ_x already analyzed in the section at δ_x constant (–32.25 °C, –10 °C, +4 °C, +44 °C). These values of Ln(τ_{os}) were already presented in Table 3.2 and are now rearranged to be plotted against T_x instead of δ_x at T_p constant. Plotting against δ_x constant or against T_p constant does not reveal the common ground between the various ranges, but plotting against T_x in Figure 3.44 or Figure 3.48 does, as we explain below.

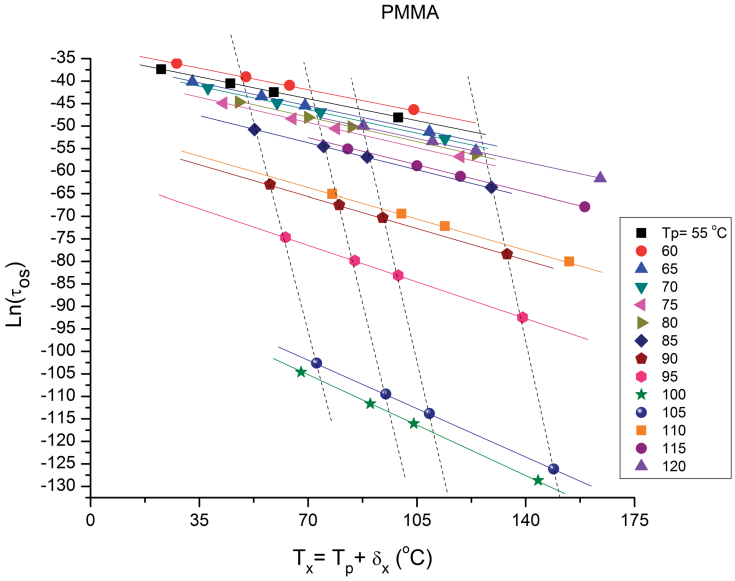


Figure 3.44: Ln(τ_{os}) vs. $T_x = T_p + \delta_x$ at various values of T_p (the dash lines are explained in the text).

Figure 3.44 displays a grid of points that we have joined in two directions, either at T_p constant and δ_x variable or at δ_x constant and T_p variable. The four points at T_p constant are aligned on a straight line, visually perfectly passing through the points. A regression analysis confirms ($r^2 = 1.0$) the perfection of this linear assessment for all T_p values.

The effect of T_p on these lines, which look pretty parallel, but actually are not, is to essentially shift their intercept: one sees that starting at the low T_p, at the top, the intercept becomes more negative as T_p increases, reaches a minimum for the star symbols, and then reverses its course as T_p increases above T_g. This is the classical behavior described in Figure 3.19b, for instance.

Figure 3.44 also shows four dash lines drawn upward, each line joining T_x points at various T_p that have the same value of δ_x. We see that this happens for only four

EBSCOhost - printed on 2/13/2023 12:32 AM via . All use subject to https://www.ebsco.com/terms-of-use

T_p temperatures: 105 °C, 95 °C, 90 °C, and 85 °C, all part of range 2. Some other points appear to fall on a given dash line, but they do not have the same δ_x value and therefore are disqualified.

Now, take a temperature, say T_p = 110 °C (the yellow filled squares). The points on this constant T_p line seem to be "shifted to the right" by a certain amount of δ_x, such that they miss to be located on the dash lines like all the points of the line just below do, corresponding to T_p = 90 °C. Visually, it seems that if we were to slide back to the left these four points by a certain amount, they would fall back in place to belong to the constant δ_x dash lines.

We can do the same for T_p = 115 °C (the purple filled dots) and T_p = 120 °C (the blue upper triangles), i. e., for all the $T_p > T_g$, which we call range 3: sliding back to the left, albeit with a different sliding amount, variable with T_p.

Now, for the points of range 1, which are all packed at the top of Figure 3.44, creating a density of points more difficult to access visually, we need to slide the points along their constant T_p line by an amount to the right, this time, so that they all fall onto the respective dash lines at constant δ_x of range 2..

Altogether, one can shift the points of the T_p constant grid, either to the left (for range 3, $T_p > T_g$) or to the right (for the T_p of range 1) so that they fall onto the δ_x constant grid made up by the points of range 2 [3–11].

The resulting grid of crossed parallel lines (4*14) then perfectly aligns all the 56 points in the two directions. We call this process "grid-shifting." We analyze below some of its characteristics.

The action of submitting the material to a polarization at T_p is reflected in two ways in Figure 3.44: it affects the value of the intercept of the lines of the grid at T_p constant, and it also affects the position of the δ_x points on the T_x temperature axis, as if the temperature was $T_p + \delta_p$, not T_p, with δ_p a function of T_p and of the voltage field. See the Discussion in Section I.3.5.

We determine by regression the SLOPE and INTERCEPT of all the straight lines at T_p constant passing through the Ln(τ_{os}) vs. T_x data. Table 3.8 provides the results for this figure, Figure 3.44, and for Figure 3.48, ΔH_s vs. T_x, which is studied below. Figures 3.45 and 3.46 plot the variation of the INTERCEPT and SLOPE with T_p (°C). Figure 3.47 is a compensation search, a plot of INTERCEPT vs. SLOPE to determine if the straight lines of Figure 3.44 compensate into a compensation point.

Figures 3.45 and 3.46 look very similar, distinctively showing the three ranges; they project that the intercept and the slope are linearly related when T_x varies, which is confirmed in Figure 3.47. Note that the three ranges are no longer discernable in Figure 3.47, all points being collected on the same line. The linearity of the intercept vs. the slope implies that the straight lines of Figure 3.44 compensate. The coordinates of the compensation point is X_c = −273 °C, i. e., the absolute zero temperature, and Y_c = 4.20.

The analysis of Ln(τ_{os}) vs. T_x done for Figures 3.44 to 3.47 can be duplicated for ΔH_s vs. T_x, which is presented in Figures 3.48 to 3.50.

EBSCOhost - printed on 2/13/2023 12:32 AM via . All use subject to https://www.ebsco.com/terms-of-use

Table 3.8: Values of Intercept and slopes of Ln(τ_{os}) and ΔH_s vs. T_x.

	A	B	C	E	H	F	K	I	J
1	–	T_x vs. ΔH_s	T_x vs. ΔH_s	slope of ΔH_s vs. T_x	intercept of ΔH_s vs. T_x	ΔS_u from Fig. 3.19b	ΔH_u from Fig. 3.19a	Ln(τ_{os}) vs. T_x	Ln(τ_{os}) vs. T_x
2	T_p (°C)	INTERCEPT	SLOPE	1/SLOPE of T_x vs.	= −1/S of T_x vs. ΔH_s	–	–	INTERCEPT	SLOPE
3	55	−108.4794	5.26012	0.19011	20.62299	−40.04665	29.81098	−34.18363	−0.14058
4	60	−104.9685	5.43338	0.18405	19.31919	41.48126	31.02314	−32.29849	−0.13491
5	65	−102.526	4.95683	0.20174	20.68378	−43.24711	32.51039	−35.37068	−0.14569
6	70	−99.9362	4.81539	0.20767	20.7535	−45.4739	34.37836	−35.97691	−0.14791
7	75	−97.29	4.50468	0.22199	21.59754	−48.36919	36.7947	−38.22527	−0.15602
8	80	94.98594	4.53259	0.22062	20.95622	−52.28719	40.04244	−37.36821	−0.15275
9	85	−92.68773	4.04912	0.24697	22.89083	−57.88602	44.63982	−41.87463	−0.16847
10	90	−90.063	3.3324	0.30008	27.02647	−66.54264	51.64878	−51.2992	−0.20209
11	95	−87.549	2.84955	0.35093	30.7238	−81.70312	63.64143	−60.02453	−0.23319
12	100	−85.085	2.07513	0.4819	41.00225	−115.10724	88.8655	−83.19394	−0.31594
13	105	−81.04562	2.11458	0.47291	38.32705	−112.00467	87.10134	−80.16797	−0.3085
14	110	−79.7773	3.25158	0.30754	24.53493	−71.49983	58.15983	−49.72671	−0.19682
15	115	−76.21186	3.78792	0.264	20.11971	−59.58396	49.53502	−41.19704	−0.16773
16	120	−72.0128	4.1386	0.24163	17.40028	−53.88462	45.39175	−36.53132	−0.15291

EBSCOhost - printed on 2/13/2023 12:32 AM via . All use subject to https://www.ebsco.com/terms-of-use

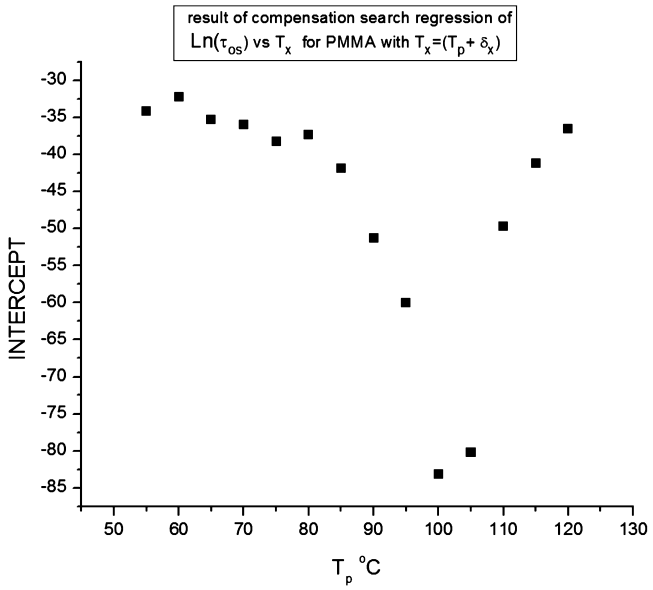


Figure 3.45: INTERCEPT of (Ln(τ_{os}) vs. T_x) plotted against T_p, for the effect of shifting by δ_x the T_p Debye peaks.

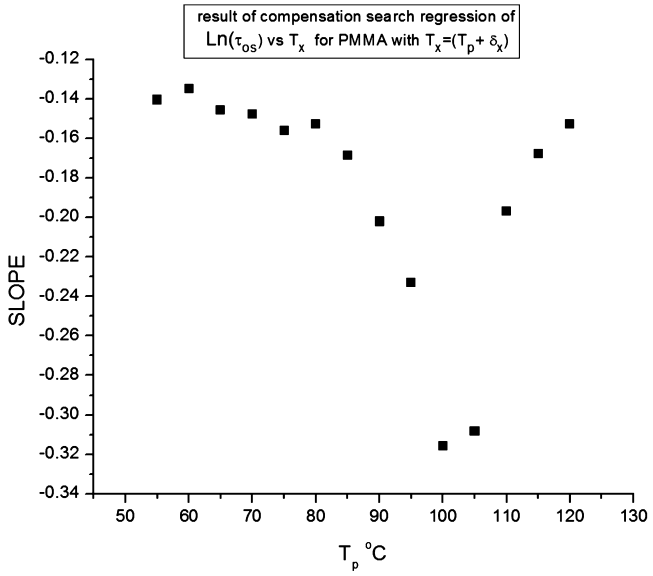


Figure 3.46: SLOPE of (Ln(τ_{os}) vs. T_x) plotted against T_p, for the effect of shifting by δ_x the T_p Debye peaks.

EBSCOhost - printed on 2/13/2023 12:32 AM via . All use subject to https://www.ebsco.com/terms-of-use

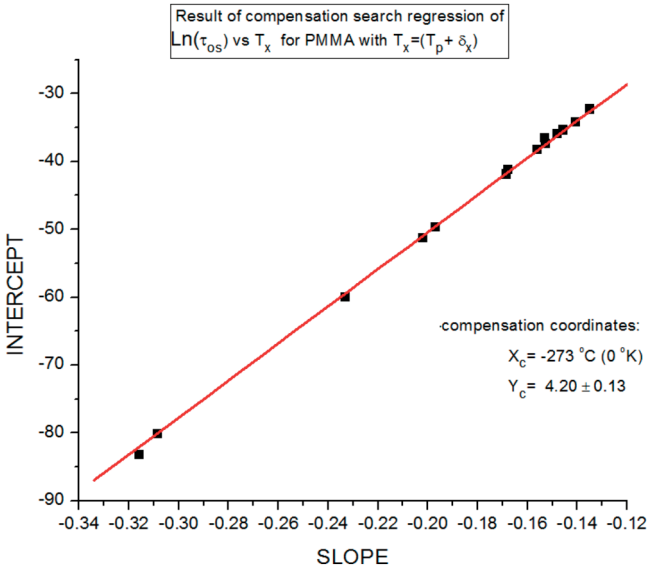


Figure 3.47: INTERCEPT vs. SLOPE of (Ln(τ_{os}) vs. T_x) for the effect of shifting by δ_x the T_p Debye peaks.

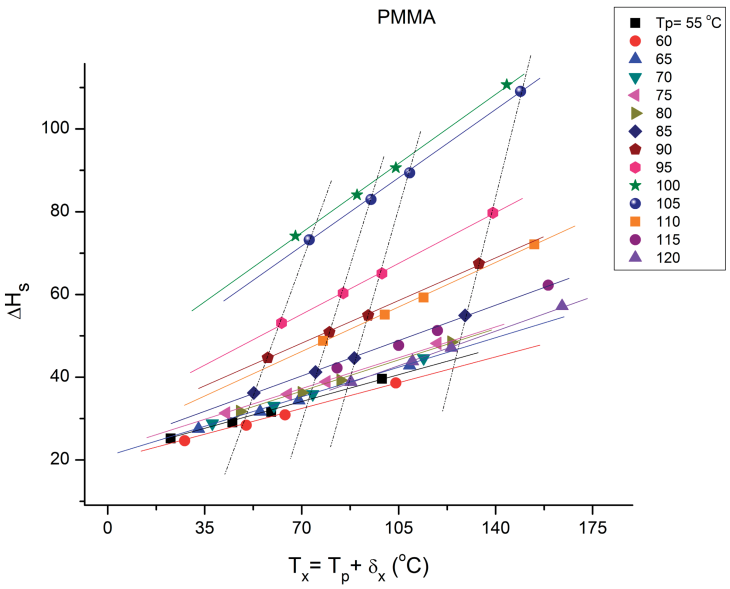


Figure 3.48: ΔH_s vs. $T_x = T_p + \delta_x$ at various values of T_p (the dash lines are explained in the text).

EBSCOhost - printed on 2/13/2023 12:32 AM via . All use subject to https://www.ebsco.com/terms-of-use

Figure 3.48 presents the same features that were described for Ln(τ_{os}) vs. T_x in Figure 3.44: the linearity of the lines at constant T_p joining the points at various δ_x; the effect of T_p on the value of the INTERCEPT of these lines (up until T_g is reached, then down); the presence of the four dash lines, corresponding to the same values of T_p in range 2, joining points for the same value of δ_x; and the possibility to slide along the T_p line the entire set of δ_x points either to the left (for the points of range 3) or to the right (for the points of range 1). In summary, except for the reversal of the direction of the changes, ΔH_s vs. T_x in Figure 3.48 provides the same qualitative information as Ln(τ_{os}) vs. T_x in Figure 3.44, in particular the possibility to shift ranges 1 and 3 onto range 2 (as reference) to form a perfect grid of cross-points. We will provide the value of the shifts in Table 3.9 below, but before that, we want to show the differences between ΔH_s and Ln(τ_{os}), before the shift of ranges 1 and 3 occurs.

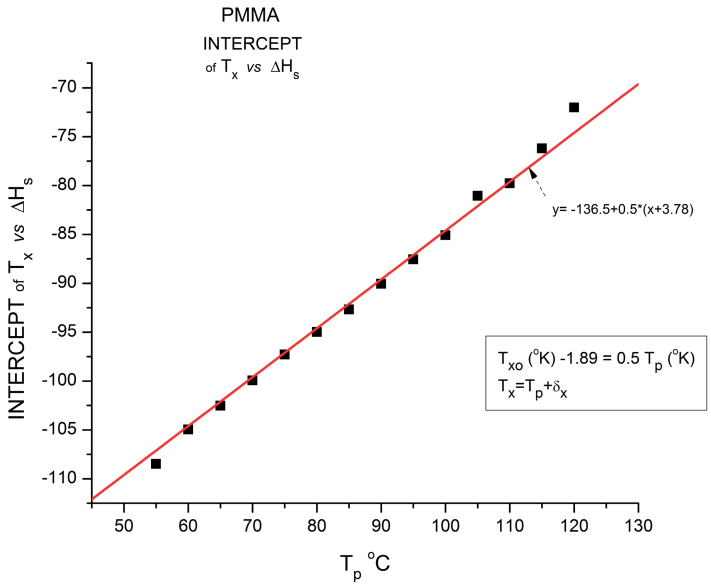


Figure 3.49: INTERCEPT of T_x (°C) vs. ΔH_s (calculated from regressions of T_x vs. ΔH_s) plotted against T_p in °C.

Figure 3.49 is the INTERCEPT of the lines of T_x vs. ΔH_s plotted against T_p. Notice that INTERCEPT is not the intercept of the lines in Figure 3.48 because the axes have been inverted. We use caps, INTERCEPT and SLOPE, for T_x vs. ΔH_s and lower cases, intercept and slope, for ΔH_s against T_x. The conversion between the two intercepts and slopes is obvious. The reason for doing the reversal of the axes is given in Figure 3.49: whereas a plot of intercept vs. T_p provides the classical features of the three ranges (like in Figures 3.45 or 3.46), INTERCEPT vs. T_p "eliminates" the presence of the three

EBSCOhost - printed on 2/13/2023 12:32 AM via . All use subject to https://www.ebsco.com/terms-of-use

ranges. Besides, the equation of the straight line in Figure 3.49 is actually remarkably simple:

$$y = -136.5 + 0.5(x + 3.78), \quad \text{where } y \text{ and } x \text{ are in °C} \tag{3.15}$$

This gives, converted to K,

$$T_{xo}\,(\mathrm{K}) = 1.89 + 0.5T_p\,(\mathrm{K})$$

where T_{xo} is the value of the INTERCEPT, $T_p + \delta_x$, in K, at $\Delta H_s = 0$.

In Figure 3.50 we plot 1/SLOPE of (T_x vs. ΔH_s) against T_p (°C). This plot is the slope of ΔH_s vs. T_x, i. e., the variation of the slope of the T_p constant straight lines in Figure 3.48. The values of 1/SLOPE vary between 0.15 and 0.5. We have drawn two hyperbolic fitted curves through the data for $T_p < T_g$ and $T_p > T_g$. This is what we had done in Figure 3.19a and b, assuming that there was no split below T_g. The curve in Figure 3.50 looks very similar, indeed, to both Figure 3.19a and Figure 3.19b (although flipped negatively in the latter case). Figure 3.51 displays a straight line correlation between Ln(τ_{ou}) and 1/SLOPE, by elimination of T_p: this means that the three ranges have superposed into a single one. The same plot done with ΔH_u (not shown) reveals the three ranges.

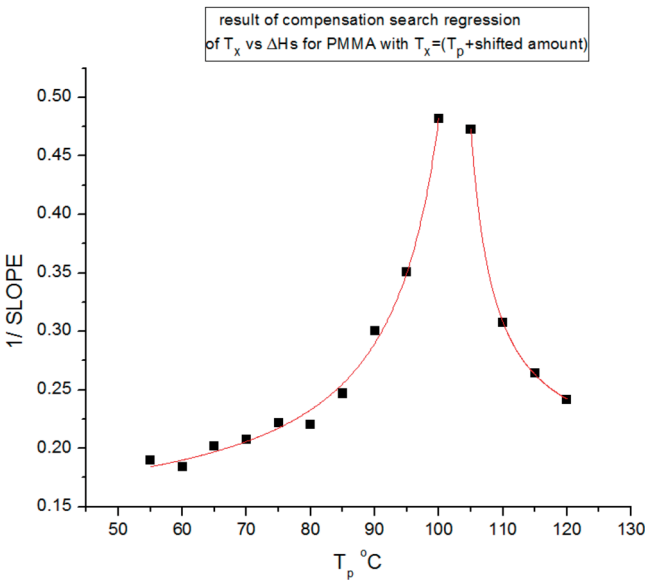


Figure 3.50: Slope of (T_x vs. ΔH_s), also equal to (1/SLOPE), with a SLOPE of (ΔH_s vs. T_x), plotted against T_p in °C for characterizing the effect of shifting the T_p Debye curves by δ_x.

EBSCOhost - printed on 2/13/2023 12:32 AM via . All use subject to https://www.ebsco.com/terms-of-use

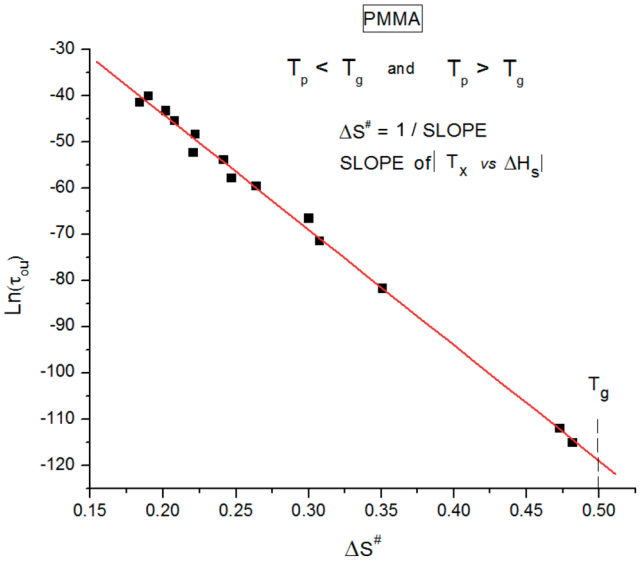


Figure 3.51: Single line correlation between Ln(τ_{ou}) vs. $\Delta S^{\#}$ at various T_p, with $\Delta S^{\#}$ defined from the SLOPE of (T_x vs. ΔH_s): $\Delta S^{\#}$ = 1/SLOPE.

We call $\Delta S^{\#}$ the x-axis in Figure 3.51. The reason is that in a plot of T_x vs. ΔH_s, the SLOPE has the unit of the inverse of an entropy. Note that in this book, we have associated the variation of Ln(τ_o) to an entropy, ΔS_p, via the equation of Eyring (equation (2.5) of Chapter 2). Hence, Figure 3.51 correlates this entropy to a basic reference entropy $\Delta S^{\#}$ with a scaling factor $N = 250$ from Figure 3.51. Additionally, while $\Delta S^{\#}$ varies only between 0 and 0.5, the T_g state can be determined by a novel criterion: $\Delta S^{\#} = 0.5$.

So far, we have discovered several correlations describing the variations of Ln(τ_{os}) vs. T_x and, separately, ΔH_s vs. T_x: we have learned how certain variables correlate that make the three-range structure collapse into one. On their own, these separate analyses are rich in new information, yet we are interested in the direct correlations between Ln(τ_o) and ΔH.

I.3.4.6 Grid-shifting unifies the correlations between Ln(τ_o) and ΔH across ranges 1, 2, and 3 into a mastercurve: on the determination of the framework relating relaxation time and temperature

I.3.4.6.1 Properties of the GRID

Figure 3.52 shows Ln(τ_{os}) vs. T_x for the four T_p values belonging to range 2 for which the T_p and T_x values match coherently with their definition: $T_x = T_p + \delta_x$, whatever the value of δ_x. For any other value of T_p outside range 2, T_x does not match the value of $T_p + \delta_x$, whatever the value of δ_x. The grid is made up of the crossing of the (p)

EBSCOhost - printed on 2/13/2023 12:32 AM via . All use subject to https://www.ebsco.com/terms-of-use

lines, at constant δ_x, and of the (x) lines, at constant T_p. First, we need to determine by regression the equations of the (p) lines and of the (x) lines, in particular for the values of T_p defining range 2.

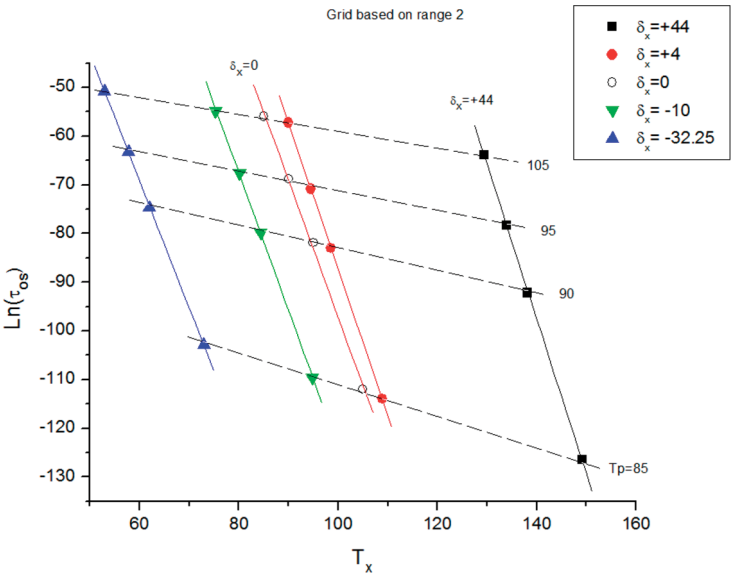


Figure 3.52: Basic grid in range 2 for Ln(τ_{os}) vs. T_x and display of the cross-grid lines at δ_x constant (five values are shown in the insert) and at T_p constant (within range 2).

Table 3.9 provides the values of T_x, ΔH_s, and Ln(τ_{os}) for the four values of T_p of range 2 defining the reference grid: T_p = 105 °C, 95 °C, 90 °C, and 85 °C. The table is divided into two parts: the top part refers to ΔH_s vs. T_x and the bottom part to Ln(τ_{os}) vs. T_x. The columns go by pairs. Each pair refers to a value of δ_x; for instance, in columns B and C δ_x = +44. We also have δ_x = +4, 0, –10, –32.25 in the other columns, moving to the right of the table.

The values in Table 3.9 are the crossing coordinates in range 2 calculated from the intercept of the straight lines obtained by regression at T_p constant and variable δ_x and at δ_x constant and T_p variable. We have seen in the previous section that the regressions of the cross-lines were almost perfect (r^2 = 1), and thus recalculating the grid-crossing coordinates of the reference grid appears to be the most accurate way to optimize grid-shifting for the points belonging to ranges 1 and 3. Yet, this recalculation of the data points is the reason we do not see exact numbers when we know we should have one, such as in cell B1, where T_x is 149.33 when it is the sum of T_p = 105 and δ_x = 44. The small residual errors, in this instance 0.33, are due to the crossing of the two variables T_p and δ_x.

EBSCOhost - printed on 2/13/2023 12:32 AM via . All use subject to https://www.ebsco.com/terms-of-use

EBSCOhost - printed on 2/13/2023 12:32 AM via . All use subject to https://www.ebsco.com/terms-of-use

Table 3.9: Value of the crossing coordinates of the GRID lines obtained at T_p constant and δ_x variable and at δ_x constant and T_p variable. These values are based on the regressions of the lines passing through the data points for T_p in range 2 (85 °C, 90 °C, 95 °C, 105 °C).

	A	B	C	D	E	S	R	F	G	H	I
	T_p (°C)	$\delta_x = 44$ ΔH_s vs. T_x T_x	$\delta_x = 44$ ΔH_s vs. T_x ΔH_s	$\delta_x = 4$ ΔH_s vs. T_x T_x	$\delta_x = 4$ ΔH_s vs. T_x ΔH_s	$\delta_x = 0$ ΔH_s vs. T_p $T_x = T_p$	$\delta_x = 0$ ΔH_s vs. T_x $\Delta H_s = \Delta H_u$	$\delta_x = -10$ ΔH_s vs. T_x T_x	$\delta_x = -10$ ΔH_s vs. T_x ΔH_s	$\delta_x = -32.25$ ΔH_s vs. T_x T_x	$\delta_x = -32.25$ ΔH_s vs. T_x ΔH_s
1	105	149.33	109.0197	109.302	90.2626	105	88.146	95.1586	83.60783	73.15724	73.33165
2	95	138.51432	79.58403	98.44032	65.28404	95	64.227	84.89746	60.4245	62.34144	52.16024
3	90	134.26186	67.48166	94.23417	55.59595	90	54.043	80.09044	51.35548	57.81175	44.70072
4	85	129.45484	54.79119	89.70448	45.1031	85	44	75.8843	41.69834	53.00473	36.43644
5	–	–	–	–	–	–	–	–	–	–	–
6	–	–	–	–	–	–	–	–	–	–	–
7	–	–	–	–	–	–	–	–	–	–	–
8	–	$\delta_x = 44$ Ln(τ_{os}) vs. T_x	$\delta_x = 44$ Ln(τ_{os}) vs. T_x	$\delta_x = 4$ ln(τ_{os}) vs. T_x	$\delta_x = 4$ Ln(τ_{os}) vs. T_x	$\delta_x = 0$ Ln(τ_{os}) vs. T_x	$\delta_x = 0$ Ln(τ_{os}) vs. T_x	$\delta_x = 10$ Ln(τ_{os}) vs. T_x	$\delta_x = -10$ Ln(τ_{os}) vs. T_x	$\delta_x = -32.25$ Ln(τ_{os}) vs. T_x	$\delta_x = -32.25$ Ln(τ_{os}) vs. T_x
9	–	T_x	ln(τ_{os})	T_x	ln(τ_{os})	T_x	Ln(τ_{os})	T_x	Ln(τ_{os})	T_x	Ln(τ_{os})
10	105	149.1467	−126.4752	108.89434	−113.94473	105	−112.00465	94.78144	−109.50392	72.93712	−102.88512
11	95	138.18373	−92.19321	98.50397	−82.97215	95	−81.85229	84.39107	−79.86075	62.01496	−74.68451
12	90	133.92941	−78.3899	94.49509	−70.83768	90	−68.81736	80.13675	−67.5	57.7606	−63.28547
13	85	129.42964	−63.8229	89.9953	−57.20409	85	−55.95512	75.30972	−54.7998	52.93361	−50.755

The grid itself can be extended outside range 2 to other values of T_p and other values of δ_x. We know that for ranges 1 and 3 the points defining ΔH_s and $\mathrm{Ln}(\tau_{os})$ do not fall at the crossing of any (p) and (x) lines; they fall shifted on the (x) line defined by the value of T_p. Figure 3.53, which is identical to Figure 3.52, except that it concerns ΔH_s vs. T_x instead of $\mathrm{Ln}(\tau_{os})$ vs. T_x, illustrates, for $T_p = 75$ °C, how to perform numerically the shifting of the points.

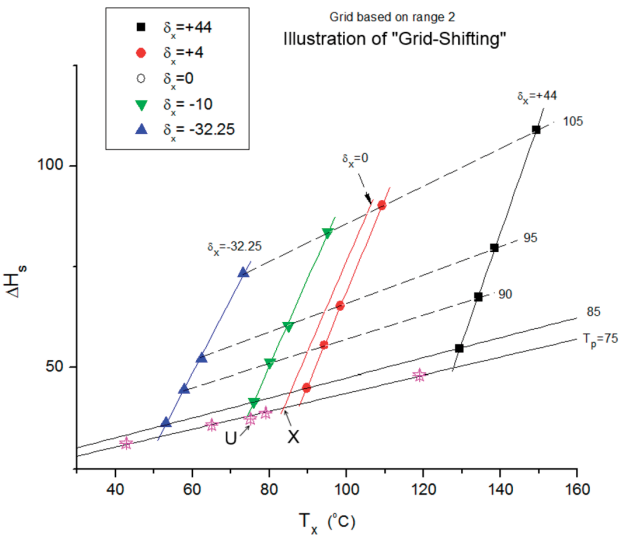


Figure 3.53: Grid-shifting illustrated at $T_p = 75$ °C for the ΔH_s vs. T_x grid.

The data points for $T_p = 75$ °C are the stars (magenta) lining up on the last (x) bottom grid line. The reference (p) grid line corresponding to $\delta_x = 0$ (we have removed the cross-points for convenience) intercepts the $T_p = 75$ (x) line in X. The star point for $\delta_x = 0$ is the third point from the left (or right) and appears as U. Grid-shifting consists of sliding U on X. Since we know the coordinates of X and U, the sliding involves a δT_x and a $\delta\Delta H_x$ change such that $\delta T_x = (T_x)_x - (T_x)_u$ and $\delta\Delta H_x = (\Delta H_s)_x - (\Delta H_s)_u$. The amount of shifting occurring on the (x) line is δs given by equation (3.16); its value depends on the grid type, either ΔH_s or $\mathrm{Ln}(\tau_{os})$:

$$\begin{aligned} \delta s_H &= \sqrt{(\delta T_x^2 + (\delta\Delta H_x)^2)} \\ \delta s_\tau &= \sqrt{(\delta T_x^2 + (\delta\,\mathrm{Ln}(\tau_{ox}))^2)} \end{aligned} \tag{3.16}$$

We said earlier that the shifting, here to the right for $T_p = 75$ °C, involved the sliding of all the points, all with the same amount of sliding, whatever δ_x. This is a first approximation only; there is a small variation of δs with δ_x, but we are not going to be concerned with that here, focusing on a single δ_x value, $\delta_x = 0$.

EBSCOhost - printed on 2/13/2023 12:32 AM via . All use subject to https://www.ebsco.com/terms-of-use

Of course, grid-shifting is performed for both the ΔH grid and the Ln(τ_o) grid. As we said the shifting is done numerically since we know accurately the coordinates of all the crossings of the grids and the experimental values of ΔH_s and Ln(τ_{os}) at each T_x. Once grid-shifting is done, all points are located on the grid, so the "normalized relationship" between ΔH and Log(τ_o) resumes to the study of the grid itself.

Figure 3.54 is the general grid presentation of the interactions between ΔH and Ln(τ_o) for all values of δ_x and of T_p. The graph is divided in two parts: at the top is the grid for ΔH_s and at the bottom the grid for Ln(τ_{os}). One sees that the top and bottom grids interact through the zero horizontal line, for which ΔH = Ln(τ_o) = 0. This is true whatever δx: in fact, the value of the intercept on the zero axis characterizes δ_x. We have drawn the connection between the grids for δ_x = 0 and δ_x = +44.

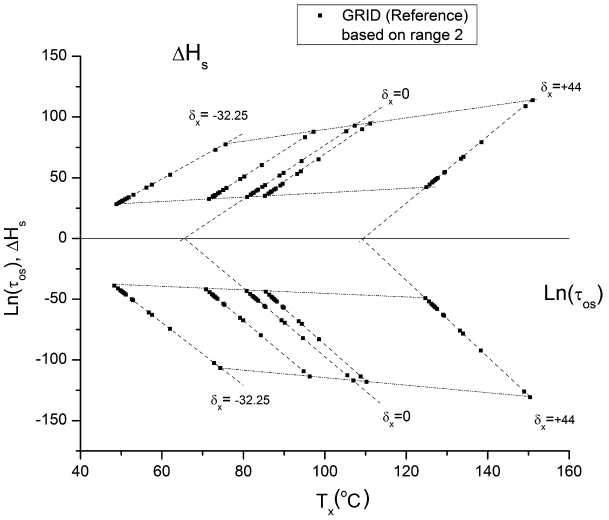


Figure 3.54: General grid (reference) based on range 2 showing both ΔH_s and Ln(τ_{os}) vs. T_x.

The grid is remarkably simple and summarizes our shifting by δ_x results to express the relationship between the two fundamental parameters of a relaxation map: the polarization temperature and the relaxation time τ_o. Another interesting feature of the general grid concerns the compensations of all the (x) lines of the grids, which differentiates the top and bottom grids, i. e., the ΔH from the Ln(τ_o) behavior. For the Ln(τ_o) grid, the (x) lines, at T_p constant, all compensate to the compensation point (–273 °C, 4.20), in other words to T_{xc} = 0 K, Ln(τ_{osc}) = 4.20. This was already mentioned in Figure 3.47.

For the ΔH_s grid, the (x) lines also compensate but not to the absolute zero temperature. The compensation point is (–65.50 °C, 8.68 kcal/m), on the average. The details and the corresponding graph showing the respective compensations for the ΔH_s and Ln(τ_{os}) grids are provided in the Discussion section below.

EBSCOhost - printed on 2/13/2023 12:32 AM via . All use subject to https://www.ebsco.com/terms-of-use

Notice the characteristic feature of a cross-duality representation: the search of a third variable, here T_x, as a way to create an implicit function of two dependent variables, here ΔH and $\mathrm{Ln}(\tau_o)$. This procedure may be generalized, especially as an alternative solution to the separation of variables, such as often encountered in physics, offering a new way to describe interactions [138].

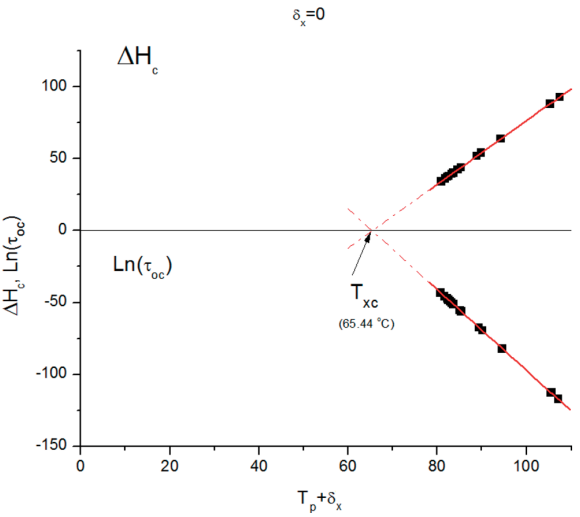


Figure 3.55: Particular case of $\delta_x = 0$. Plots of ΔH_c and $\mathrm{Ln}(\tau_{oc})$ vs. $T_x = T_p + \delta_x$ are linear, both lines intercepting on the x-axis (Y = 0 line) for $T_{xc} = 65.44\,°C$. Note that the data are located on these grid lines only for T_p values of range 2. See text.

Figure 3.55 shows the detail of the reference grid for $\delta_x = 0$. The two lines are perfectly linear and cross for $T_x = T_p + \delta_x = T_{xc} = 65.44\,°C$. This temperature is a characteristic temperature for the material investigated (PMMA) and corresponds to $\Delta H_c = \mathrm{Ln}(\tau_{oc}) = 0$. The subscript "c" designates "corrected," and by that we mean that all the experimental values of ΔH_s and $\mathrm{Ln}(\tau_{os})$ have been shifted on the general grid by a dual-shift factor that is a function of T_p only (in Figure 3.55, $\delta_x = 0$). Not only do we no longer see the presence of ranges 1 and 3, but also the ΔH and $\mathrm{Log}\,\tau_o$ grid lines pass through $T_{xc}, 0$. T_{xc} can be eliminated between the equations of the two lines in Figure 3.55, and therefore ΔH is proportional to $\mathrm{Ln}(\tau_o)$. The proportionality constant is the ratio of the two slopes of the straight lines in Figure 3.55. The regression of the lines give

$$\begin{aligned} \Delta H_c &= -144.938 + 2.21378 T_x \quad (r^2 = 1.0\ \mathrm{SD} = 7.8 \times 10^{-9}) \\ &= 2.21378(T_x - T_{xc}) \quad \text{with } T_{xc} = 65.47\,°C \\ \mathrm{Ln}(\tau_{oc}) &= 183.7835 - 2.81004 T_x \quad (r^2 = 1.0\ \mathrm{SD} = 8.9 \times 10^{-9}) \\ &= -2.8100(T_x - T_{xc}) \quad \text{with } T_{xc} = 65.40\,°C \end{aligned} \tag{3.17}$$

EBSCOhost - printed on 2/13/2023 12:32 AM via . All use subject to https://www.ebsco.com/terms-of-use

And thus

$$\begin{aligned} \mathrm{Ln}(\tau_o) &= -1.26934\Delta H \\ T_{xc} &= 65.44\,°C \end{aligned} \tag{3.18}$$

These are the fundamental characteristics of the grid at $\delta_x = 0$. As we shall elaborate in the Discussion, this temperature may correspond to the value of T_2 for PMMA (also see footnote 3).

We plot in Figure 3.55 the "corrected" compensation search of $\mathrm{Ln}(\tau_{oc}) = \mathrm{Ln}(\tau_{ou}) + \delta\,\mathrm{Ln}(\tau_{ox})$ versus $\Delta H_c = \Delta H_u + \delta\Delta H_x$ for all T_p values covering the three ranges. The straight line has a slope of –1.27 and passes through the origin. As we have done many times, the value of the slope can be converted into a temperature, T_c, the compensation temperature for all the Arrhenius lines Ln(τ_o) vs. $1/T$ when T_p varies.

$$T_c = -1000/(1.987 \cdot \text{slope}) = 396.44\,\mathrm{K}(123.44\,°C) \tag{3.19}$$

Since the gas constant is 1.987(2) cal/m and ΔH is in Kcal/m, the 1000 in the numerator is included to convert the two units.

In summary, the grid in Figure 3.55 represents the true "masterplot" of the shifted results. It is characterized by two fundamental temperatures: T_{xc} and T_c. Derived from the masterplot, and thus less general, is the "mastercurve" displayed in Figure 3.56. This classical representation of the compensation between Ln(τ_o) and ΔH misses the existence of T_{xc}. Obviously, more results are needed to link T_c and T_{xc} in amorphous matter, which should be an objective for future investigation.

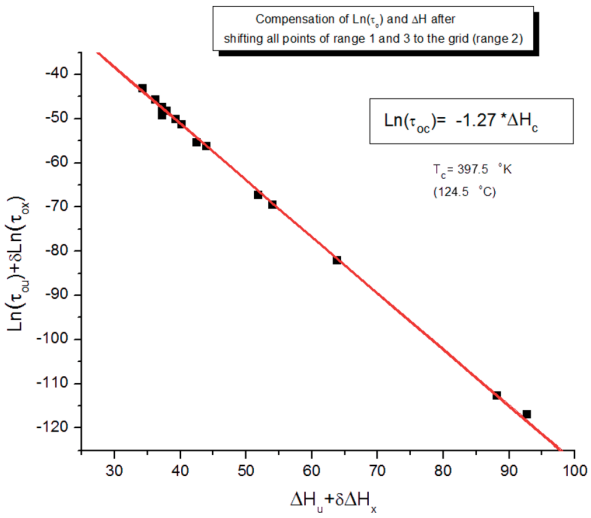


Figure 3.56: Master compensation of Ln(τ_o) vs. ΔH after shifting to the ΔH and Ln(τ_o) grids the points of ranges 1 and 2. The master compensation passes through the origin.

EBSCOhost - printed on 2/13/2023 12:32 AM via . All use subject to https://www.ebsco.com/terms-of-use

The properties of the grid are not sufficient to describe the complexity of the several mechanisms revealed by the presence of the three ranges. The unification of the ranges into a masterplot, making the ranges disappear, should be completed by the study of the variation of the grid shift factors with the polarization temperature. This is presented in the next section.

I.3.4.6.2 Description of the grid shift factors

Table 3.10 gives the results of the grid-shifting process done numerically as explained in Figure 3.53.

This table applies to $\delta_x = 0$. It is separated in two sections: columns C24 to C30 relate to the ΔH_s grid shift factors and columns C34 to E to the $\mathrm{Ln}(\tau_{os})$ grid shift results. The two shift factors per grid, δT_x and $\delta\Delta H_s$ for the ΔH grid and δT_x and $\delta\,\mathrm{Ln}(\tau_{os})$ for the $\mathrm{Ln}(\tau_o)$ grid, are in columns C26, C27, C35, and D1, respectively. The other columns provide δs, ΔH_c, and $\mathrm{Ln}(\tau_{oc})$, the value of the corrected ΔH_u and $\mathrm{Ln}(\tau_{ou})$, u standing for unshifted, and the value of T_x after the shift, $T_p + \delta T_x$.

Figure 3.57 is a plot of the sliding shift, δs, against T_p. The two values of δs in each grid, δs_H and δs_τ, given by equation (3.16), are almost undistinguishable in comparison to their variation with T_p. The difference between the two is larger in range 3, especially as T_p increases. The amount of sliding shift is linearly related to T_p in all three ranges (it is 0 in range 2, the reference range). δs is decreasing with T_p in range 1 and increasing in range 3.

Figure 3.58 displays the variation of $\delta\Delta H_x$ with T_p. One sees that $\delta\Delta H_x$ values are positive in range 1 and negative in range 3, explaining the sliding to the right and to the left, respectively, for these two ranges. The separation of the ranges is clearly visible; the behavior within a range looks straightforward too. We notice, however, some intriguing differences regarding the definition and the continuity of the ranges observed between Figure 3.58 and Figure 3.57. In Figure 3.57, range 1 has six points well aligned, range 2 connects the four points of range 2, as expected, and range 3 has four points, also as expected. This structure is different in Figure 3.58: range 1 has only five points, not six, and the line passing through these points does not intercept range 2 at the first point of range 2, but rather at the last point, leaving a discontinuity gap of $\delta\Delta H_x = 2$ at $T_p = 85\,°\mathrm{C}$. Likewise, the first point of range 3 is also showing a discontinuity with its junction between range 2 and range 3. The definition of the points belonging to range 2 seems to also be different in Figures 3.58 and 3.57. The same phenomenon occurs, but reversed, for the variation of $\delta\,\mathrm{Ln}(\tau_{ox})$ with T_p. This apparent contradiction in comparing the ranges between Figures 3.57 and 3.58 is important to reveal because it puts into evidence the phenomenon of cross-compensations. The compensation for δs can occur *within* a grid, between the two terms entering either δs_H or δs_τ in equation (3.16), or it can occur *across* the grids, between ΔH and $\mathrm{Ln}(\tau_o)$. The entanglement between the cross-compensations is a subject of its own, beyond the present scope, but explains apparent contradictions. At the end, the cross-compensations of the effects of

EBSCOhost - printed on 2/13/2023 12:32 AM via . All use subject to https://www.ebsco.com/terms-of-use

Table 3.10: Grid-shifting values $\delta\Delta H_x$ and d Ln(τ_{ox}) to shift all points of the ΔH_s vs. T_x grid and of the Ln(τ_{os}) vs. T_x grid onto the grid crossing interceptions.

C24	C25	C26	C27	C28	C29	C30	C33	C34	C35	D1	D2	D3	E
ΔH values	$\delta_x = 0$				ΔH_c	–	Ln(τ_o) values					Ln(τ_{oc})	
T_p (°C)	ΔH_u no-shift	δT_x ($\delta_x = 0$)	$\delta\Delta H_s$ ($\delta_x = 0$)	δ_s shift	$\Delta H_u + \delta\Delta H_s$	$T_p + \delta T_x$	T_p (°C)	ln(τ_{ou}) no-shift	δT_x ($\delta_x = 0$)	δ ln(τ_{os}) ($\delta_x = 0$)	δ_s shift	Ln(τ_{ou}) + δ Ln(τ_{os})	$T_p + \delta T_x$
55	30.71725	26.81232	5.45908	27.36242	36.17633	81.81232	55	−41.69291	26.65214	−3.96938	26.9461	−45.66229	81.65214
60	29.79481	20.9257	4.41876	21.38716	34.21357	80.9257	60	−39.85084	20.77438	−3.34492	21.04194	−43.19576	80.77438
65	33.00029	17.31542	4.2898	17.8389	37.29009	82.31542	65	−43.99319	17.25427	−3.36111	17.57859	−47.3543	82.25427
70	34.77599	12.5935	3.1297	12.97656	37.90569	82.5935	70	−45.92275	12.55059	−2.26421	12.75319	−48.18697	82.55059
75	37.38188	8.61106	2.77648	9.04761	40.15836	83.61106	75	−49.01513	8.64999	−2.26121	8.94066	−51.27634	83.64999
80	38.71942	3.23183	0.59941	3.28695	39.31883	83.23183	80	−50.10656	3.22452	0.0258	3.22463	−50.08076	83.22452
85	43.44692	0.33055	0.51799	0.61447	43.96491	85.33055	85	−55.95512	0.42575	−0.31119	0.52736	−56.26631	85.42575
90	53.24785	−0.14025	0.74373	0.75684	53.99158	89.85975	90	−68.81736	0.14079	−0.69839	0.71244	−69.51575	90.14079
95	63.46387	−0.70258	0.35172	0.78571	63.81559	94.29742	95	−81.8523	−0.38525	−0.23545	0.4515	−82.08774	94.61475
100	88.80791	7.36332	3.93272	8.34774	92.74063	107.36332	100	−114.92202	7.04359	−2.09127	7.34749	−117.01329	107.04359
105	87.1014	0.27219	1.00992	1.04596	88.11132	105.27219	105	−112.00465	0.51558	−0.71488	0.88141	−112.71953	105.51558
110	58.15984	−21.09563	−6.28326	22.01147	51.87658	88.90437	110	−71.49987	−20.64274	4.18587	21.06286	−67.31401	89.35726
115	49.53503	−30.3454	−7.06651	31.15732	42.46852	84.6546	115	−59.584	−29.85461	4.10552	30.13558	−55.47848	85.14539
120	45.39175	−37.68455	−8.10159	38.54557	37.29016	82.31545	120	−53.88466	−37.08543	4.67487	37.37892	−49.20979	82.91457

EBSCOhost - printed on 2/13/2023 12:32 AM via . All use subject to https://www.ebsco.com/terms-of-use

the two shift factors within a grid and on both grids results in the smooth and continuous variation of δs. This observation indicates that the coordinates (the structure) of a continuous variable (here δs against T_p) can mathematically behave differently, showing discontinuities, than the function that integrates its variation. The mathematical contradiction is resolved when the solution integrates all the coordinates of the entangled parts participating in the integration. This is an important property of Dual-Phase and Cross-Dual-Phase physics.

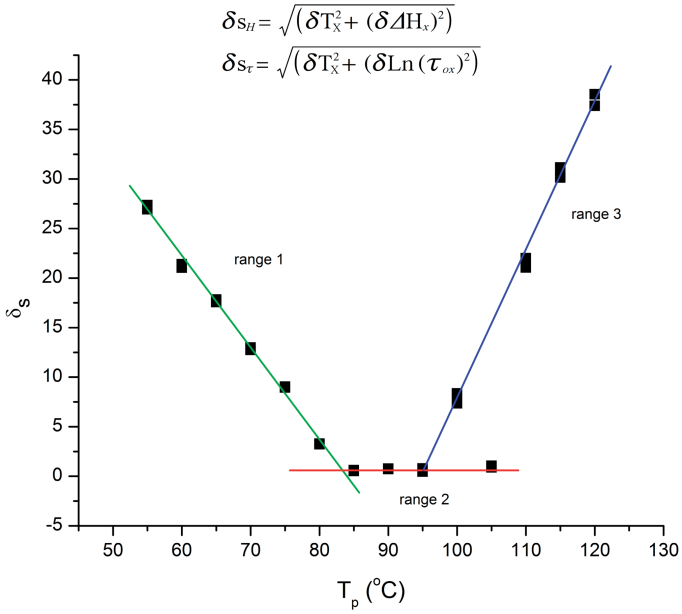


Figure 3.57: Grid-shifting (sliding) value, δs, along the (x) line of the grid at T_p constant to obtain superposition of the points on the grid. The shift factors, δs_H and δs_τ, are slightly different for the ΔH and the Ln(τ_o) grids, except in range 2 (reference), where they are 0.

In Figure 3.59 we have plotted the variation of T_x, defined in columns C30 and E of Table 3.10 for the ΔH and Ln(τ_o) grids, against T_p. T_x is the sum of T_p and δT_x, with δT_x itself varying with T_p as given in columns C26 and C35. This graph makes it clear how the grid physically works. In range 2, $T_x = T_p$, which is shown by the straight line $Y = X$ passing through the four points of range 2. The points in range 1 are located above the $Y = X$ line, and in range 3 they are below this line. For all the points $\delta_x = 0$, but δT_x is only 0 in range 2, being positive in range 1 and negative in range 3.

EBSCOhost - printed on 2/13/2023 12:32 AM via . All use subject to https://www.ebsco.com/terms-of-use

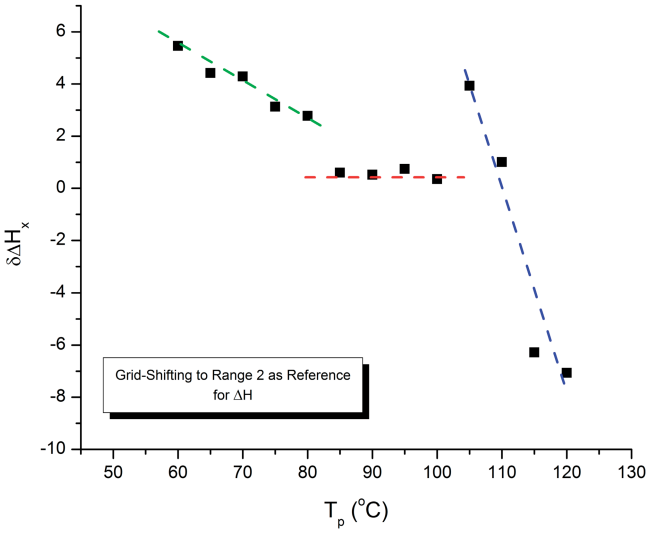


Figure 3.58: Grid-shifting ΔH shift factor, $\delta\Delta H_x$, plotted against T_p. The change of sign between range 1 and range 3 is due to the shifting to the left or to the right. See text.

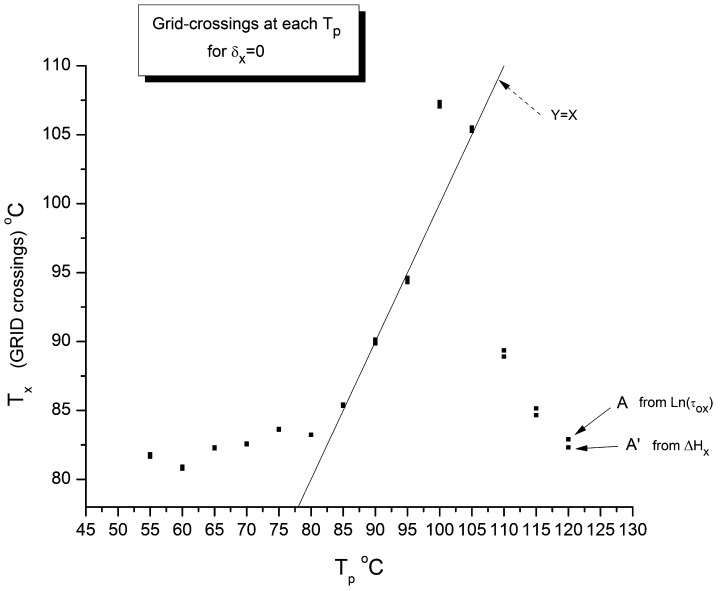


Figure 3.59: Plot of T_x of the grid-crossings vs. T_p at $\delta_x = 0$ showing $T_x = T_p$ for range 2 only. The A points are from Ln(τ_{os}) vs. T_x and the A' points are from ΔH_s vs. T_x.

EBSCOhost - printed on 2/13/2023 12:32 AM via . All use subject to https://www.ebsco.com/terms-of-use

Another observation concerns the difference between $(T_x)_H$ and $T_{x(\tau)}$. We had to use a smaller dimension than usual for the symbols in the graph to be able to make the difference appear. In range 1, no difference is visible; some difference starts to be visible in range 2, but it is randomly scattered, showing that the difference denotes the random background noise of the grid calculations. A systematic non-random difference between $(T_x)_H$ and $T_{x(\tau)}$ is seen in range 3. In this regime, the relaxation process for the ΔH and the $\mathrm{Ln}(\tau_o)$ grids shows a growing divergence with $(T - T_g)$. This is not the case in regime 1 or in regime 2. Range 3 is the only regime polarized above T_g; this appears to create a small shift between the behavior according to ΔH or $d\,\mathrm{Ln}(\tau_o)$, with the amount of shift growing with $(T - T_g)$, the free volume.

Figure 3.60 is a plot of δT_{xH} and $\delta T_{x\tau}$ against $(\delta T_{xH} - \delta T_{x\tau})$ that makes visible another definition and a different correlation structure across the three ranges. The difference is not so much between the two grids, the dots and the squares, which we discussed in the previous figure, separating range 3 from ranges 1 and 2, the difference in the rezoning of range 1 and 2 into a new structure: the appearance of a different structure for range 1 that now involves six points and for range 2 which extends to five points. As we said before, the complexity of the cross-compensations is responsible for these redefinitions of the zones.

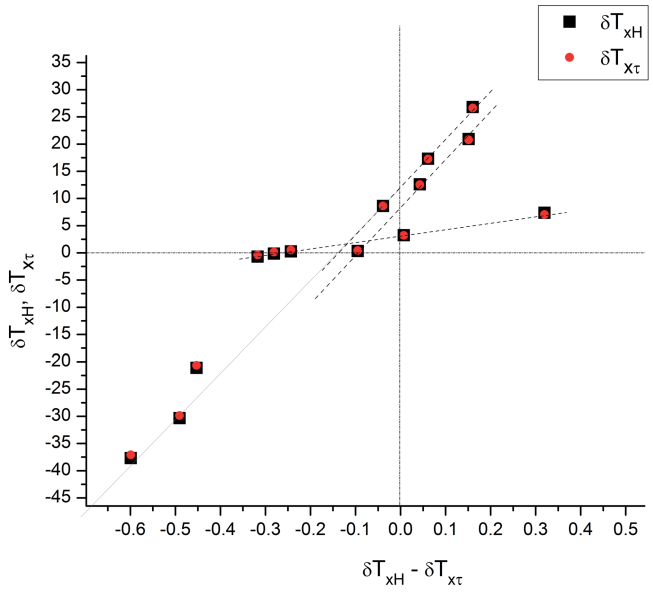


Figure 3.60: Plot of δT_{xH} and $\delta T_{x\tau}$ vs. $(\delta T_{xH} - \delta T_{x\tau})$ showing sub-structural trends.

EBSCOhost - printed on 2/13/2023 12:32 AM via . All use subject to https://www.ebsco.com/terms-of-use

I.3.4.6.3 The cross-dynamic structure of T_p: $T_p + \delta_{pH}$ and $T_p + \delta_{p\tau}$

A possible way to study this entanglement of various cross-compensations is to analyze the grid results from the point of view of T_p and not T_x. The idea is exposed in Figure 3.61, which is a plot of both ΔH_u (black square) and ΔH_c (red dots) plotted against T_p, where ΔH_u is the unshifted value of ΔH and ΔH_c is the "corrected value," as we defined it in column C29 of Table 3.10, i. e., the grid crossing value at T_p after shifting.

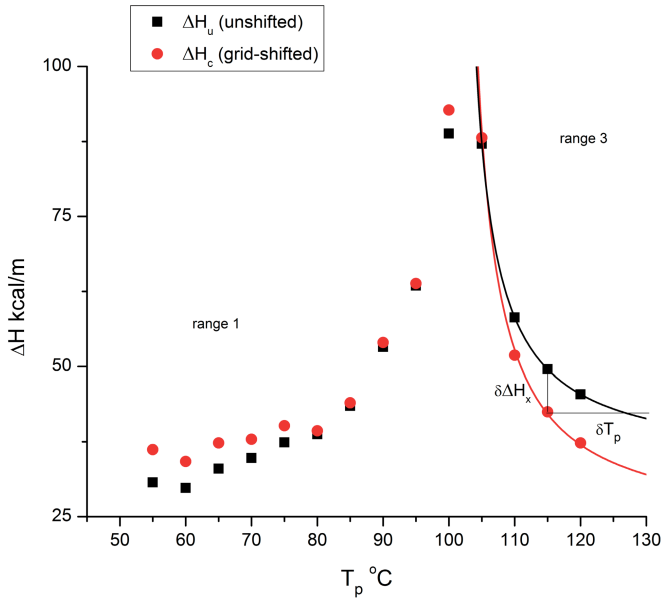


Figure 3.61: Compare ΔH_u (unshifted) vs. T_p with ΔH_c (corrected) vs. T_p after grid-shifting to the reference grid (range 2). $\delta\Delta H_x$ is the shift factor for the ΔH_s vs. T_x grid for T_p = 115 °C (in range 3).

In Figure 3.61, we focus on range 3 to illustrate what we want to study. The ΔH_c curve is below the ΔH_u curve in this range (it is the opposite in range 1), and we know from grid-shifting the value of $\delta\Delta H_x$ at any T_p. The value of $\delta\Delta H_x$ at T_p = 115 °C is shown in Figure 3.61. We are interested to know the value of $T_p + \delta T_p$ that makes ΔH_u equal to ΔH_c. The determination of δT_p, which we call δ_p to drop the "T," is simplified if we know the equation of the curves of $\Delta H_u(T_p)$ and $\Delta H_c(T_p)$. These curves turn out to be well described by simple hyperbolas that we can curve-fit by regression.

The same exercise can be accomplished for the curves of Ln(τ_{ou}) and Ln(τ_{oc}) versus T_p, which are shown in Figure 3.62. We can extend our hyperbolic description of these curves to range 1, so we can also perform in this range the same determination of $T_p + \delta_p$ at various T_p.

EBSCOhost - printed on 2/13/2023 12:32 AM via . All use subject to https://www.ebsco.com/terms-of-use

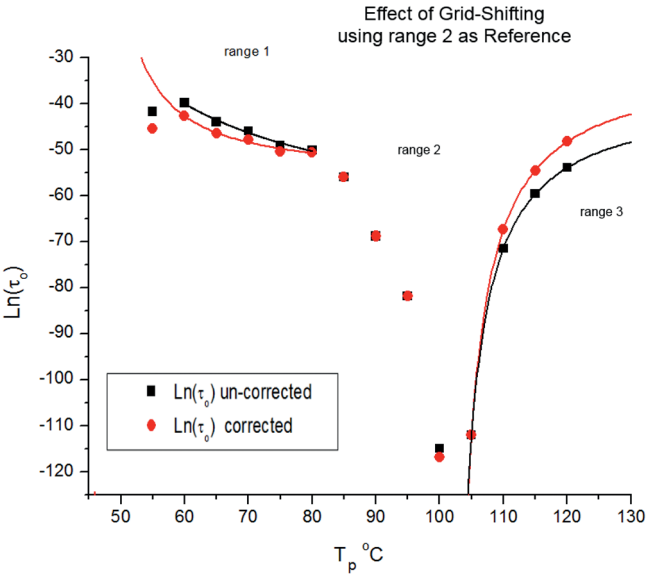


Figure 3.62: Plot similar to Figure 3.61 for Ln(τ_o) vs. T_p.

Once all the ranges are quantified by hyperbolic expressions obtained by regression, for both ΔH and Ln(τ_o) data, unshifted and shifted, it is possible to synthesize a new set of data with a larger number of data points than those obtained experimentally. For instance, for range 1, we chose 13 points between T_p = 50 °C and 80 °C, and for range 3, we chose eight points between T_p = 120 °C and 105 °C, with an addition of five more points to extend the range to 130. The simulated data are tabulated in Table 3.11 and the results are illustrated in Figure 3.62 in range 1 by the black and red traces passing through the points.

Note that the values of calc ΔH_u, calc Ln(τ_{ou}) and calc ΔH_c, calc Ln(τ_{oc}) at the various T_p shown in Table 3.11 are slightly different than those in Table 3.10, because of the regressions, but this does not affect our conclusions here.

Table 3.11 is, like Table 3.10, divided in two sections: columns A to J for the Ln(τ_o) grid results and columns L to P for the ΔH grid results. Additionally, the rows are also sectioned in two parts: rows 1 to 12 apply to the simulated data set for range 3 and rows 15 to 27 apply to range 1.

Figures 3.63 and 3.64 test our formulas in the simulation by checking that the compensation search for the simulated ΔH_u, Ln(τ_{ou}) in Figure 3.63 and the corrected ΔH_c, Ln(τ_{oc}) in Figure 3.64 provide the same results as what we found before (Figure 3.56). Figure 3.63 shows that range 1 and range 3 compensation searches are linear, but with different slopes and intercepts, consistent with what is expected, and yet the normalization of the results by δH_x and δ Ln(τ_{ox}) results in the merging of ranges 1 and 3, with the same slope and passing through the origin, as expected from Figure 3.56.

EBSCOhost - printed on 2/13/2023 12:32 AM via . All use subject to https://www.ebsco.com/terms-of-use

EBSCOhost - printed on 2/13/2023 12:32 AM via . All use subject to https://www.ebsco.com/terms-of-use

Table 3.11: Simulation of data in range 1 and range 3, at $\delta_x = 0$, after the grid-shifting factors at various T_p of Table 3.10 have been curve-fitted by regression in each range by hyperbolic functions.

	A	B	C	E	F	H	I	J	L	M	N	O	P
1	T_p (°C)	calc ΔH_u	calc Ln(τ_u)	calc $T_p(H)$	calc $T_p(\tau_o)$	$\delta_p(H)$	$\delta_p(\tau_o)$	$\delta_p = \delta_p(H) - \delta_p(\tau_o)$	calc ΔH_c	calc Ln(τ_{oc})	δT_x	ΔH @ $T_p(\tau_o)$	Ln(τ_o) @ $T_p(H)$
2	130	41.35545	−48.3479		169.61706		39.61706	–	31.66171	−42.23536		36.88643	−35.11272
3	127.5	42.08157	−49.3428		156.31607		28.81607	–	32.52721	−43.31422		37.6762	−36.29087
4	125	42.95743	−50.54354		145.81438		20.81438	–	33.5718	−44.61675		38.62914	−37.71374
5	122.5	44.03468	−52.02136		137.31241		14.81241	–	34.8575	−46.22057		39.80165	−39.46641
6	120	45.3918	−53.88466	179.32894	130.28866	59.32894	10.28866	49.04028	36.47867	−48.2439	−37.2702	41.27953	−41.67857
7	117.5	47.15416	−56.30691	146.20046	124.38842	28.70046	6.88842	21.81204	38.5863	−50.87608		43.1999	−44.55818
8	115	49.53509	−59.584	129.69244	119.36209	14.69244	4.36209	10.33035	41.43801	−54.44062	−30.1022	45.79649	−48.461
9	112.5	52.92961	−64.26538	119.80555	115.0289	7.30555	2.5289	4.77665	45.51229	−59.53952		49.5028	−54.05017
10	110	58.15995	−71.49987	113.22174	111.25472	3.22174	1.25472	1.96702	51.80984	−67.43515	−20.8478	55.22357	−62.71991
11	107.5	67.26739	−84.15914	108.52266	107.93793	1.02266	0.43793	0.58473	62.83333	−81.29808		65.21403	−77.98595
12	105	87.10163	−112.00464	105.00034	105.00014	3.37956E-4	1.35245E-4	2.02711E-4	87.09737	−112.00223	0	87.09993	−111.99862
13								–					
14								–					
15	80	38.70083	−50.36948	83.15121	81.17016	3.15121	1.17016	1.98105	39.55	−50.74748	3.0565	21.98765	−20.22694
16	77.5	37.95508	−49.50581	81.89512	79.78626	4.39512	2.28626	2.10885	39.22272	−50.2987		22.75322	−21.38826
17	75	37.13526	−48.55634	80.48986	78.2481	5.48986	3.2481	2.24176	38.83912	−49.7727	8.588	23.49366	−22.51751
18	72.5	36.22974	−47.50763	78.90719	76.52835	6.40719	4.02835	2.37884	38.3833	−49.14766		24.21018	−23.61601
19	70	35.22435	−46.34325	77.11127	74.59286	7.11127	4.59286	2.51841	37.83274	−48.39271	12.5247	24.90392	−24.68498
20	67.5	34.1016	−45.04295	75.05585	72.39829	7.55585	4.89829	2.65756	37.15446	−47.46263		25.57595	−25.7256
21	65	32.83967	−43.58146	72.68034	69,88891	7.68034	4.88891	2.79143	36.29822	−46.28852	17.279	26.22728	−26.73899
22	62.5	31.41097	−41.92683	69.90364	66.99174	7.40364	4.49174	2.9119	35.18337	−44.7598		26.85884	−27.72619
23	60	29.7801	−40.03806	66.61473	63.60935	6.61473	3.60935	3.00538	33.67195	−42.68728	20.9293	27.47153	−28.68822
24	57.5	27.90087	−37.86166	62.65751	59.60873	5.15751	2.10873	3.04878	31.50653	−39.71799		28.06618	−29.62603
25	55	25.71189	−35.32652	57.80522	54.8033	2.80522	−0.1967	3.00192	28.14549	−35.10921	26.99287	28.64357	−30.54051
26	52.5	23.12969	−32.33598	51.71545	48.92306	−0.78455	−3.57694	2.79239	22.22094	−26.98525		29.20444	−31.43253
27	50	20.03785	−28.75522	43.84565	41.56201	−6.15435	−8.43799	2.28365	8.99215	−8.84546		29.7495	−32.3029

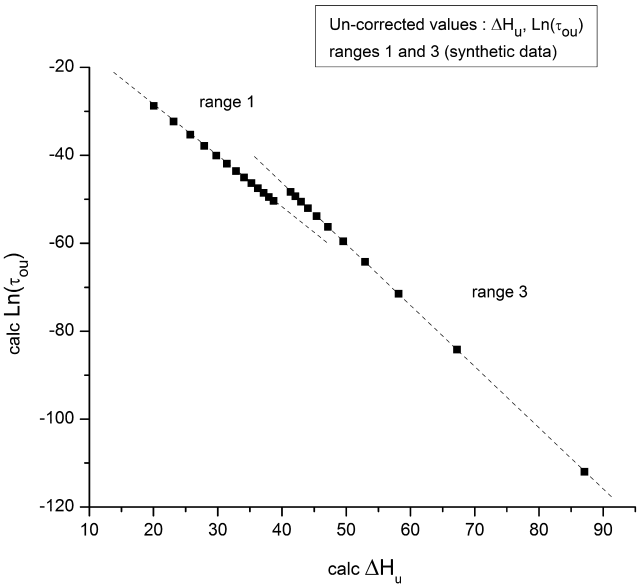


Figure 3.63: Compensation search using calculated synthetic data in ranges 1 and 3 for the un-shifted ΔH_u and $\mathrm{Ln}(\tau_{ou})$.

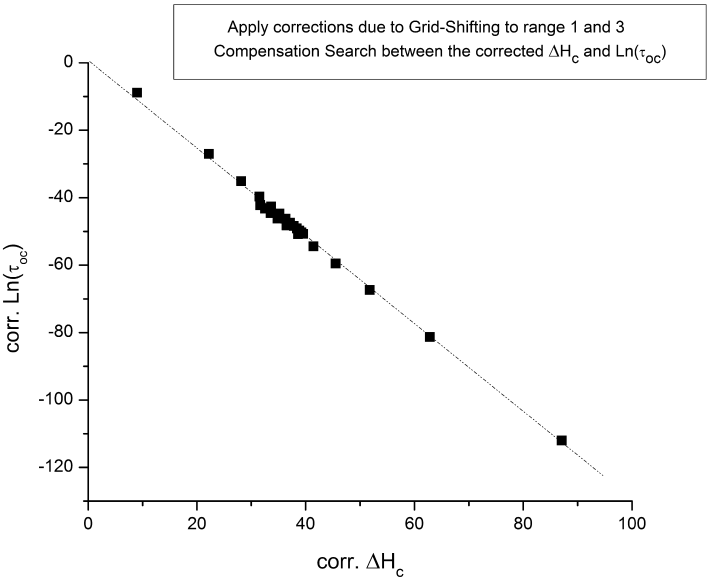


Figure 3.64: Compensation search using calculated synthetic data in ranges 1 and 3 after applying corrections on both axes according to the grid-shifting procedure (superposition of the data onto range 2 grid). The result is a unique compensation line going through the origin.

EBSCOhost - printed on 2/13/2023 12:32 AM via . All use subject to https://www.ebsco.com/terms-of-use

We now seek to analyze the influence of T_p on the value of $\Delta H(T_p + \delta_{p\tau})$ when $\text{Ln}(\tau_{oc}) = \text{Ln}(\tau_{ou})$ @ $(T_p + \delta_{p\tau})$, and conversely, the influence of T_p on the value of $\text{Ln}(\tau_o(T_p + \delta_{pH}))$ when $\Delta H_c = \Delta H_u$ @ $(T_p + \delta_{pH})$. We first describe these conditions and their solutions in more detail by explaining the columns in Table 3.11 and then illustrate the results graphically.

Columns B, C, L, and M have already been discussed: they are the values calculated from the hyperbolic regressions for ranges 1 and 3.

Columns E and F provide calc $T_p(H)$ and calc $T_p(\tau_o)$ for each value of T_p. This was explained earlier. The value of T_{pH} is determined by $\delta\Delta H_x = \Delta H_c(T_p) - \Delta H_u(T_p)$ and the corresponding value of $\text{Ln}(\tau_{ou})$ at $T_{pH} = T_p + \delta_{pH}$ is in column P; the value of δ_{pH} is in column H. Likewise, $T_p\tau_o$ is determined by $\delta\,\text{Ln}(\tau_{ox}) = \text{Ln}(\tau_{ou})$ @ T_p – $\text{Ln}(\tau_{ou})$ @ T_p and the corresponding value of ΔH at $T_p\tau_o$ is in column O. The value of $\delta_p\tau_o$ is in column I.

In column J we calculate the difference $\delta_p = \delta_{pH} - \delta_p\tau_o$ at each T_p.

One sees some blanks in Table 3.11: the first four rows of column E do not indicate any value. This is because in Figure 3.61, the hyperbolic asymptote of $\Delta H_u(T_p)$ creates a limit to the solutions of T_p to maintain the value of ΔH_c at $T_p+\delta_{pH}$ above the asymptote.

The second observation is that δ_{pH} is always bigger than $\delta_p\tau_o$. This is seen in Figure 3.65 in a plot of $\delta_p\tau_o$ vs. δ_{pH} for both range 1 (green linear line) and range 3 (blue hyperbolic curve). In range 1, the slope of the straight line is very close to 1 so $\delta_p\tau_o = \delta_{pH} - 2.5$. In range 3, $\delta_p\tau_o$ varies between 0 and 10, and δ_{pH} six times that. There is no solution beyond $\delta_{pH} = 60$.

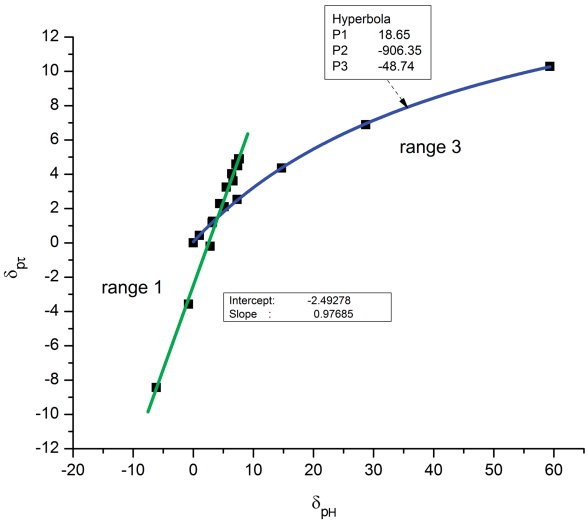


Figure 3.65: Plot of $\delta_{p\tau}$ vs. δ_{pH} in range 1 (green straight line) and range 3 (hyperbolic blue curve) against T_p. $\delta_{p\tau}$ and δ_{pH} are defined by $\text{Ln}(\tau_{ou})$ @ $(T_p + \delta_{p\tau}) = \text{Ln}(\tau_{oc})$ @ T_p; and conversely, ΔH_u @ $(T_p + \delta_{pH}) = \Delta H_c$ @ T_p.

EBSCOhost - printed on 2/13/2023 12:32 AM via . All use subject to https://www.ebsco.com/terms-of-use

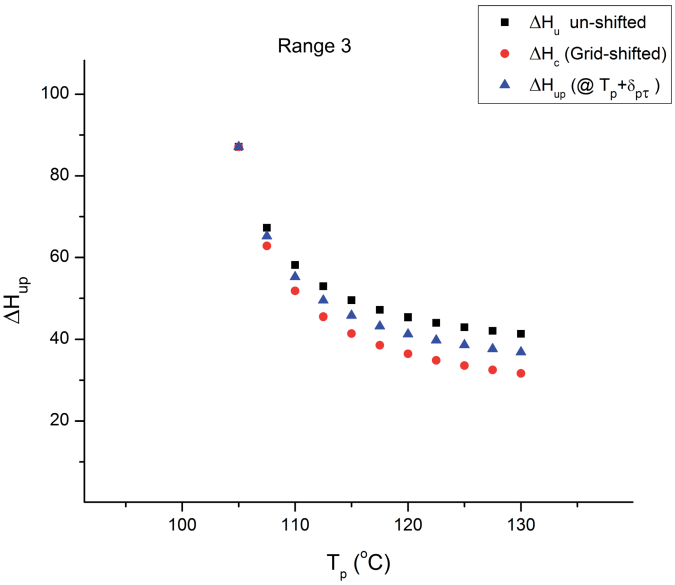


Figure 3.66: Compare values of δH_u (unshifted), ΔH_c (grid-shifted), and ΔH_{up}(@ $T_p + \delta_{p\tau}$) against T_p (°C).

Figure 3.66 compares, in range 3, the values of ΔH_u, ΔH_c and of ΔH_{up}, which is the value of ΔH_u at $T_p + \delta_{p\tau}$ (we drop the subscript "o" in τ_o for simplification). ΔH_u is the experimental unshifted value of ΔH determined by TWD at T_p. ΔH_c is the corresponding grid value at the same temperature T_p, obtained by grid-shifting. $T_p + \delta_{p\tau}$ is the temperature that makes $\mathrm{Ln}(\tau_{ou}) = \mathrm{Ln}(\tau_{oc})$ where $\mathrm{Ln}(\tau_{oc})$ is the value on the grid corresponding to ΔH_u (at T_p). Finally, ΔH_{up} is the value of ΔH_u at $T_p + \delta_{p\tau}$. We know from Figure 3.65 that in range 3, $\delta_{p\tau}$ is smaller than δ_{pH}, so we expect ΔH_{up} to be somewhere between the values of ΔH_u and ΔH_c. This is verified in Figure 3.66: the blue triangles (ΔH_{up}) are between the black rectangles (ΔH_u) and the red dots (ΔH_c). But why is ΔH_{up} exactly in the middle of ΔH_u and ΔH_c, whatever the value of T_p? The same result is true when we use $\mathrm{Ln}(\tau_{ou})$, $\mathrm{Ln}(\tau_{oc})$, and $\mathrm{Ln}(\tau_{oup})$ with $T_p + \delta_{pH}$. Is this a coincidence?

Figure 3.67 examines the question from a different angle. This figure is a compensation search plot of $\mathrm{Ln}(\tau_o)$ vs. ΔH for three types of configuration: ΔH_u, $\mathrm{Ln}(\tau_{ou})$ at T_p, ΔH_c, $\mathrm{Ln}(\tau_{oc})$ at T_p, and the association of ΔH_{up} at $T_p+\delta_{p\tau}$ and $\mathrm{Ln}(\tau_{oup})$ at $T_p+\delta_{pH}$, determined as explained above. As a matter of fact, for the blue triangles of Figure 3.67, the temperature for ΔH and $\mathrm{Ln}(\tau_o)$ is not the same, so this association can be considered as virtual. However, what is interesting is the particular perfect symmetry observed between these three compensation lines. First, although it is not surprising to see that ($\mathrm{Ln}(\tau_{ou})$, ΔH_u) and ($\mathrm{Ln}(\tau_{oc})$, ΔH_c) compensate, with the red dots aligned with the origin as expected (there are on the grid), it is surprising to discover that the ($\mathrm{Ln}(\tau_{oup})$, ΔH_{uo}) pair also compensates, despite the fact that these coordinates are not obtained

EBSCOhost - printed on 2/13/2023 12:32 AM via . All use subject to https://www.ebsco.com/terms-of-use

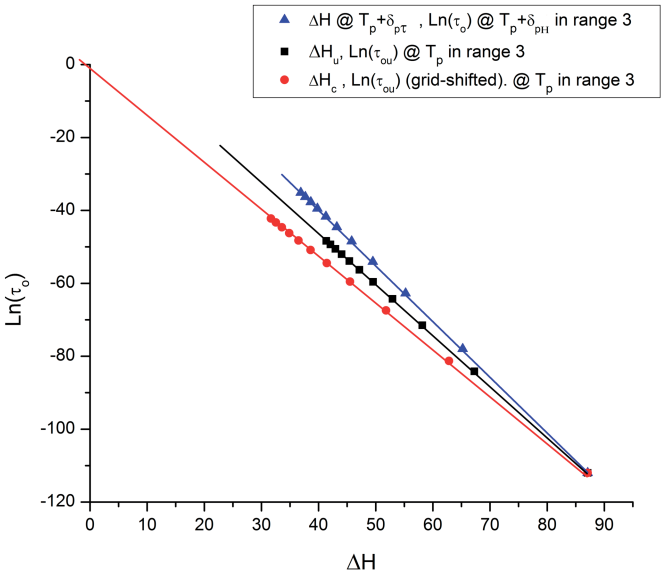


Figure 3.67: Compensation search to compare three pairs of Ln(τ_o), ΔH values in range 3. See the inset box in the graph to characterize the pairs: unshifted, grid-shifted, and conjugated.

at the same temperature, $T_p + \delta_{pH}$ and $T_p + \delta_{p\tau}$, respectively. Besides, the three compensation lines of Figure 3.67 super-compensate themselves in a super-compensation point at $\Delta H_{cc} = 87.5$, $\mathrm{Ln}(\tau_{occ}) = -115$. We can determine the equations of the lines by regression and from their slopes calculate the angle between them. We find at less than 1 % error that the black square compensation (the U line) is exactly in the middle of the "C" red dot line and the "UP" blue triangle line. Is it still a coincidence or the expression of a physical significance between $\delta_{p\tau}$ and δ_{pH}, revealed through the cross-duality between ΔH, Ln(τ_o), and T_p?

Even more intriguing is the result observed in Figure 3.68. While the previous figure dealt with range 3 only, we have added the "UP" blue triangle points calculated for range 1 in Figure 3.68: now, is it fortuitous that the (Ln(τ_{oup}), ΔH_{up}) pairs as T_p varies in range 1 are located on the compensation line of the black square U data located in range 3? This, of course, may still be a coincidence (and it shall remain so until we are capable of explaining it), yet it is definitely intriguing.

If we rotate the blue triangle range 3 compensation line around its super-compensation point so that its range 3 is now superposed on the "U" range 3 black square line, then the rotation will also bring the blue triangle range 1 onto the "C" range 3 compensation line. This is obvious since the three compensation lines in range 3 are separated by the same angle with respect to the super-compensation pole. Since a simple rotation expresses a mathematical link between the coordinates of a system, here ΔH and Ln(τ_o), it appears that the result of Figure 3.68 provides an additional

EBSCOhost - printed on 2/13/2023 12:32 AM via . All use subject to https://www.ebsco.com/terms-of-use

characteristic of the interactions between the shift factors by synchronizing, in a complex way still to be mathematically tracked, the results of range 1 and range 3. In other words, grid-shifting established a way to normalize the different aspects of the interactions in ranges 1, 2, and 3, with range 2 as reference, but remained to be understood the interrelationship between the shift factors of ranges 1 and 3. The results of Figure 3.68 appear to describe such a link.

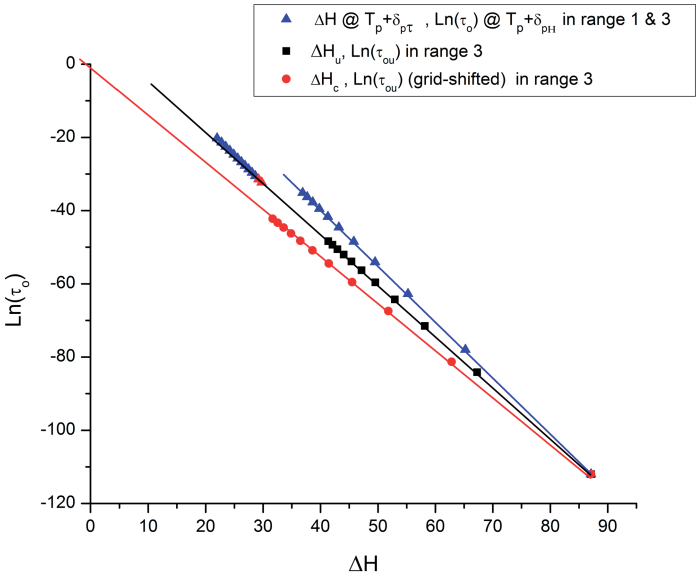


Figure 3.68: The same graph as in Figure 3.67 except for the conjugated pairs (blue triangles) which are shown in ranges 1 and 3.

In the following three figures, Figures 3.69 to 3.71, we want to introduce other "intriguing" relationships between the δH and $\mathrm{Ln}(\tau_o)$ variables and the way to discover their interdependence by way of the cross-dynamic structure of T_p: $T_p + \delta_{p\tau}$ and $T_p + \delta_{pH}$. The purpose is to give a glimpse to possible new tools to explore interactive coupling. Some general comments about this new research can be found in the Discussion and conclusion section that follows.

Figure 3.69 is inspired by Figure 3.54, assembling on the same Y-coordinate the variation of $\mathrm{Ln}(\tau_o)$, ΔH vs. T_x (in Figure 3.54) and T_p in Figure 3.69. The difference is that $\mathrm{Ln}(\tau_{oup})$ and ΔH_{up} are not obtained at the same T_p, but at $T_p + \delta_{pH}$ and $T_p + \delta_{p\tau}$, respectively. Like in Figure 3.54, the ΔH values are at the top (black squares) and the $\mathrm{Ln}(\tau_o)$ ones at the bottom (blue triangles). The same scale is used for both ΔH_u and $\mathrm{Ln}(\tau_o)$. The graph includes the ranges of T_p for range 1 and range 3. There are two remarkable features that emerge from looking at Figure 3.69:

EBSCOhost - printed on 2/13/2023 12:32 AM via . All use subject to https://www.ebsco.com/terms-of-use

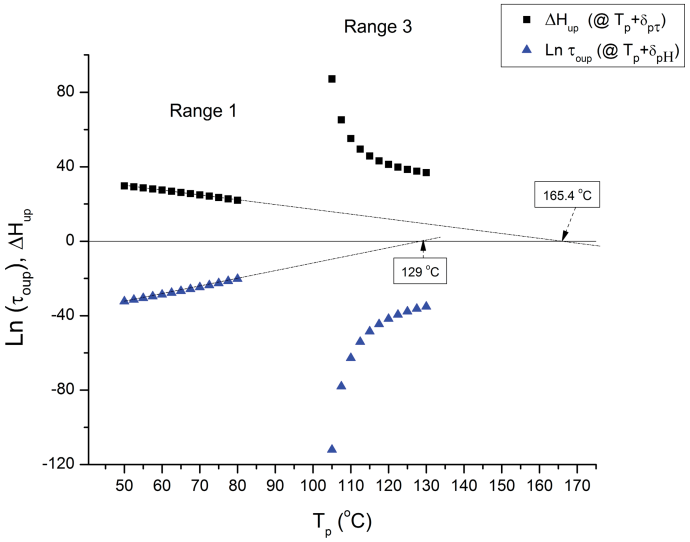


Figure 3.69: Compare values of Ln(τ_{oup}) obtained at $T_p + \delta_{pH}$ and ΔH_{up} obtained at $T_p + \delta_{p\tau}$.

- In range 1 the relationship between Ln(τ_o) or ΔH and T_p is linear. T_p can be eliminated between the equations of the two straight lines to explain the compensation of the range 1 data in Figure 3.68. However, unlike Figure 3.54, the two straight lines of range 1 do not intercept on the zero horizontal axis. This is expected since the ΔH and Ln(τ_o) values are not established at the same temperature. The difference observed between 129 °C and 165.4 °C for the intercepts with the zero axis can be related to the cross-dynamic structure of T_p.
- Further, in range 3, the two curves (black squares and blue triangles) are proportional to one another, after eliminating T_p between the hyperbolic functions that describe their function of T_p. As a consequence, this explains the success of the compensation search in range 3 for these values of Ln(τ_{oup}) and ΔH_{up} in Figures 3.67 and 3.68.

In Figure 3.70, we are keeping ΔH_{up} vs. T_p for the upper part of the graph, and therefore the two black square curves are the same as in Figure 3.69. However, for the Ln(τ_o) lower side of the graph (red dots), we switch to Ln(τ_{oc}), such that now, the two variables ΔH and Ln(τ_o) are set at the same temperature $T_p + \delta_{p\tau}$.

We observe that in range 3 the two hyperbolic curves are scalable and their values are linearly related, explaining the compensation in range 3 at $T_p + \delta_{p\tau}$. This is the first observation. The second observation is the similarity of the red dot range 1 curve with the black square range 3 curve. These curves seem to be parallel and can be fitted by parallel hyperbolic functions with good accuracy ($r^2 > 0.99$). This means that another mathematical correlation can be added to express the interdependence of ranges 1 and 3.

EBSCOhost - printed on 2/13/2023 12:32 AM via . All use subject to https://www.ebsco.com/terms-of-use

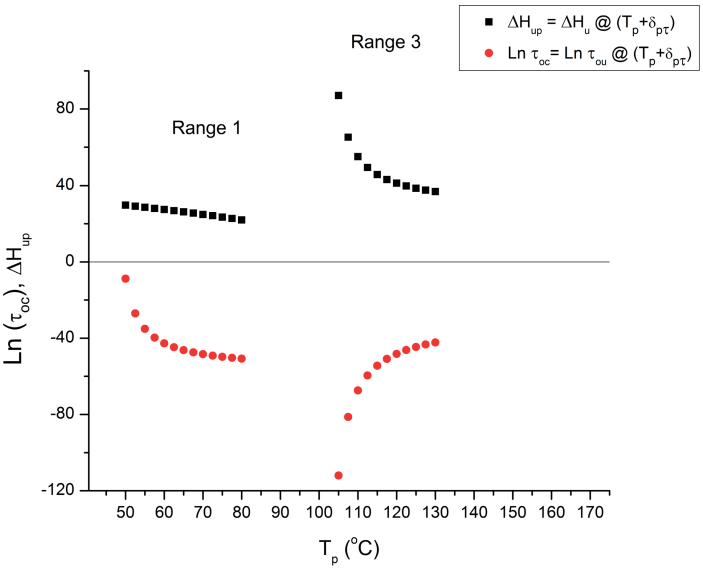


Figure 3.70: Associate values of $\mathrm{Ln}(\tau_{oc}) = \mathrm{Ln}(\tau_{ou})$ obtained at $T_p + \delta_{p\tau}$ and ΔH_{up} also obtained at $T_p + \delta_{p\tau}$.

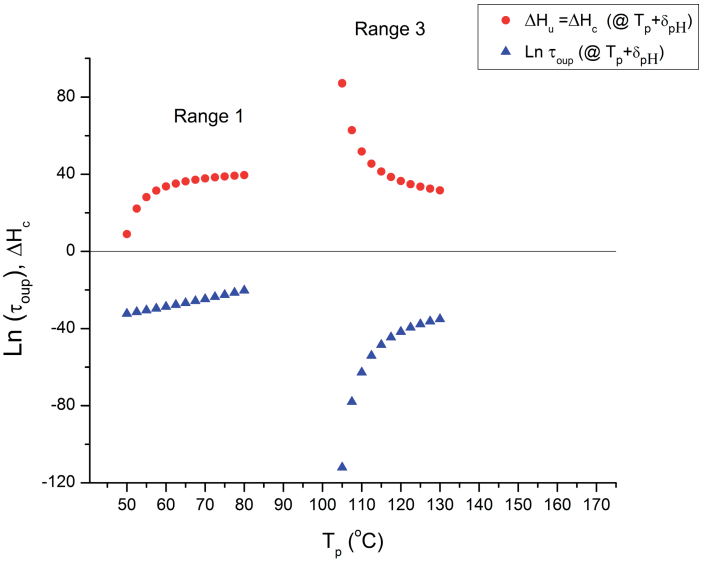


Figure 3.71: Compare values of $\mathrm{Ln}(\tau_{oup})$ obtained at $T_p + \delta_{pH}$ and ΔH_{up} obtained at $T_p + \delta_{p\tau}$.

Finally, in Figure 3.71, we use the same analysis as in Figure 3.70 but inverting the roles of ΔH and $\mathrm{Ln}(\tau_o)$, with ΔH_u at the top for ΔH_u at $T_p + \delta_{pH}$ represented by the red dots and $\mathrm{Ln}(\tau_{oup})$ at the bottom at the same $T_p + \delta_{pH}$ represented by the blue triangles.

EBSCOhost - printed on 2/13/2023 12:32 AM via . All use subject to https://www.ebsco.com/terms-of-use

Hence the situation is crossed twice: reversing the role of ΔH and $\mathrm{Ln}(\tau_o)$ and reversing the role of the cross-dynamic structure of T_p: $T_p + \delta_{pH}$ instead of $T_p + \delta_{p\tau}$.

The result in Figure 3.71 is remarkably symmetrical to the one in Figure 3.70: in range 3, we still have the linearity between the values that translate into a compensation. And, for range 1, it is now the red dot representing ΔH that is parallel to the blue range 3 triangle representing $\mathrm{Ln}(\tau_o)$.

I.3.5 Discussion and conclusions

I.3.5.1 A survey of Chapter 3 developments

We have already covered in Sections I.3.2 and I.3.3.2 several aspects of the depolarization response of a dielectric material due to the interactions between the voltage field and temperature during polarization: we explained the origin of the $T_{g,\rho}$ peak manifestation from the locality of the space charges in the F conformers surrounding the b grains; we explained the T_{LL} manifestation by the collapse of the collective dissipative network stability at T_{LL}. Both explanations are backed by concepts defined in the Dual-Phase and Cross-Dual-Phase models of conformer interactions introduced in the Appendix.

The same model provided an explanation, the $[(b/F) \leftrightarrow (c,g,t)]$ interactive coupling explanation, for the compensation of the Arrhenius lines, $\mathrm{Ln}(\tau_o)$ vs. $1/T$, when T_p varies. We introduced equations that determined the coupled influence of the voltage field and the temperature of polarization T_p on the value of Δ_e, a fundamental parameter of the vertical split aspect of the Grain-Field Statistics that allows to determine, at any time, the conformational state (c,g,t) and the free volume state (b/F) of the conformers in collective interactions.

We showed that interactive coupling could be quantitatively described by the five fundamental constants: Δ_m, υ_m, Δ_x, υ_x, and Δ_e, and that plots of $\mathrm{Ln}(\upsilon_m/\upsilon_x)$ vs. $(\Delta_m - \Delta_x)$ at various Δ_e (T_p) compensated. We also showed that the true fundamental constants were only three constants: Δ_m, υ_m, and Δ_{eo}, because Δ_x and υ_x express the dissipative nature of the collective interactive dynamics, an auto-catalytic process generated by Δ_m, υ_m, and Δ_{eo}. We associated the variation of $(\Delta H, \mathrm{Ln}(\tau_o))$ with T_p to the variation of $(\Delta_x, \mathrm{Ln}(1/\omega_x))$ with Δ_e, suggesting the dissipative nature of the compensation interdependence between $\mathrm{Ln}(\tau_o)$ and ΔH in a TWD experiment.

Section I.3.4 addressed the issue of the negative compensation. Interestingly, resolving this issue took more than 60 % of this chapter's length, showing that what initially looked like an apparently simple problem to solve turned out to be a very subtle and quite new challenge to crack.

EBSCOhost - printed on 2/13/2023 12:32 AM via . All use subject to https://www.ebsco.com/terms-of-use

The TWD challenge can be summarized in this simplified manner:

- Can the model of Dual-Phase interactive coupling satisfactorily explain the change of slope between the positive and negative compensations of $\mathrm{Log}(\tau_o)$ vs. ΔH when T_p varies across T_g?
- Can the model of Dual-Phase interactive coupling satisfactorily explain the increase of both $\mathrm{Ln}(\tau_o)$ and ΔH with T_p for the positive compensation line as well as the decrease of both $\mathrm{Ln}(\tau_o)$ and ΔH with T_p for the negative compensation line, the intersection between the two occurring at $T_p = T_g$?

In short, the success of our Dual-Phase interactive coupling model in understanding the TWD results is still awaiting our explanation of the two above issues.

First, let us summarize our findings about the slope change issue at $T_p > T_g$.

Figure 3.17a and Figure 3.17b are both plots of the Debye peak half width, $T_2 - T_1$, against the peak height at the maximum, $h_{\max}$. These figures suggested that an explanation for the apparent change of slope of the compensation between $\mathrm{Ln}(\tau_o)$ and ΔH at T_g was probably inherent to features specific to the nature of the elementary Debye peaks when they are polarized at two shifted T_p. The graphs in Figure 3.17a and b clearly showed reversibility for various T_p across T_g by plotting against each other two characteristics of the Debye peak that entered the calculation of ΔH and $\mathrm{Ln}(\tau_o)$ through the Dussel–Bube equation, equation (3.9).

We made the hypothesis that the same dissipative phenomenon generated by the Dual-Split equations (equations (5) to (7) of Appendix Section A.2), made apparent when correlating the pairs $(\Delta_m, \ln(\upsilon_m))$ and $(\Delta_x, \mathrm{Ln}(\upsilon_x))$ in a compensation plot of $\mathrm{Ln}(\upsilon_m/\upsilon_x)$ vs. $(\Delta H_m - \Delta H_x)$ at various Δ_e (see Figure 3.4), could also be made apparent by comparing pairs of $(\Delta H, \mathrm{Ln}(\tau_o))$ taken in several ranges of the value of T_p. In other words, we assumed that it was possible to find $(\Delta H_x, \mathrm{Ln}(\tau_{ox}))$, such that the normalization of the compensation search plots by these dissipative variables would reduce the difference between the negative and positive compensation to a single mastercurve of $(\mathrm{Ln}(\tau_o/\tau_{ox})$ vs. $(\Delta H - \Delta H_x)$ when T_p varied. The various pairs of ΔH_x, $\mathrm{Ln}(\tau_{ox})$ found in the different T_p ranges would describe the equivalent of (Δ_m, υ_m) associated with the *mechanism of interaction* involved in the ranges between the dielectric material, the voltage, and the temperature.

In studying the effect of the shifting of the Debye peak to try to achieve the merging of the positive and negative compensations on a dissipative compensation mastercurve, such as the ones in Figure 3.4, *we never anticipated finding the presence of three ranges of* T_p *values*, we expected to find just two ranges: the $T_p < T_g$ range for the positive compensation and the $T_p > T_g$ range for the negative compensation. However, three ranges of T_p appear distinctively (Figure 3.29) and can be made to merge in a dissipative compensation plot, revealing their possible specific origin (Figure 3.56).

The study of the effect of shifting Debye peaks by pure translation on the T_p axis turned out to be fecund in discovering the gears of the cross-duality interlock in

EBSCOhost - printed on 2/13/2023 12:32 AM via . All use subject to https://www.ebsco.com/terms-of-use

the process of dissipation itself. This statement needs, indeed, further development, which will be provided below and in future publications.

To briefly explain what we mean, consider the Dual-Split equations that drive the vertical structuring of the Grain-Field Statistics, equations (5) to (7) of Appendix Part A. The values of Δ_x, $\mathrm{Ln}(\upsilon_x)$ are dissipative variables, auto-catalytically generated by the dissipative system; they only exist when the system is made dynamic, out of equilibrium. Their pairing with Δ_m, $\mathrm{Ln}(\upsilon_m)$, brought about by Δ_{eo}, is the description of the cross-duality between (b/F), the first duality, and (c, g, t), the second duality. Each duality is described by its own kinetic equations, but the system is dissipative and can only be solved because of the cross-duality between the energy equation (to keep the free energy constantly equal to the equilibrium energy) and the kinetic equations. Duality and cross-duality are intrinsically interlocked.

In Section I.3.4, we analyzed three options:

- The Debye peaks at various T_p are shifted by the same amount, δ_x. We determine and study the thermokinetic parameters, ΔH_s, $\mathrm{Ln}(\tau_{os})$, of the shifted peaks when T_p and δ_x vary (independently).
- The peaks at various T_p are shifted to the same temperature, for instance T_g, or $T_g + 23\,°C$, etc. In this case the amount of shift, δ_x, is variable for each T_p.
- As a third option we reanalyzed the results of shifting by the same amount δ_x by plotting the results at constant $T_x = T_p + \delta_x$ instead of constant T_p or constant δ_x.

This analysis led, for a specific range of T_p values, to the definition of a reference grid for ΔH_s and $\mathrm{Ln}(\tau_{os})$ and the possibility to "grid-shift" the other T_p ranges onto the reference grid, *resulting in a compensation search mastercurve* matching, in all aspects, the Dual-Phase dissipative compensation plot results of Figure 3.4 for one given pair of (Δ_m, υ_m).

One could claim QED for the first issue: there is no change of slope of the compensation of $\mathrm{Ln}(\tau_o)$ vs. ΔH at $T_p = T_g$, there is simply a change of the mechanism of dissipation between three ranges of T_p values, two mechanisms of dissipation below T_g and one above T_g.

The second issue of the challenge can now be expanded to include range 1 and rephrased in the following terms:

- Why do we have three ranges of T_p values? Are the three ranges only for PMMA or is this structure universally expected for all amorphous phases in polymeric materials?
- Can the Dual-Phase model explain the change of behavior between ranges 1 and 2 and separately for range 3? Is the variation of $\mathrm{Ln}(\tau_o)$ and ΔH with T_p satisfactorily described in the three ranges, and what is the meaning of the grid-shift factors?
- What is the Dual-Phase interpretation of the results of the measuring technique of TSD/TWD to deconvolute interactions between dipoles in purely amorphous polymers?

EBSCOhost - printed on 2/13/2023 12:32 AM via . All use subject to https://www.ebsco.com/terms-of-use

I.3.5.2 Interpretation of the TWD results by the Dual-Phase model of polymer interactions

I.3.5.2.1 The three ranges description of the amorphous state of polymers

First, we look again at the plot that defined the reference grid, based on the values of ΔH_s, $\mathrm{Ln}(\tau_{os})$ in range 2, and the five arbitrarily chosen δ_x values studied in Section I.3.4. Figure 3.72 is the expansion of Figure 3.54 to extrapolate to $T_x = 0\,\mathrm{K}$, the absolute temperature (T_x is in degrees Celsius in the figure). This large-scale overview allows to compare the ΔH_s and the $\mathrm{Ln}(\tau_{os})$ grids starting from the absolute zero temperature. The dash lines cross to determine the grids. As we said, these are of two types: the (x) lines at T_p constant and the (p) lines at δ_x constant.

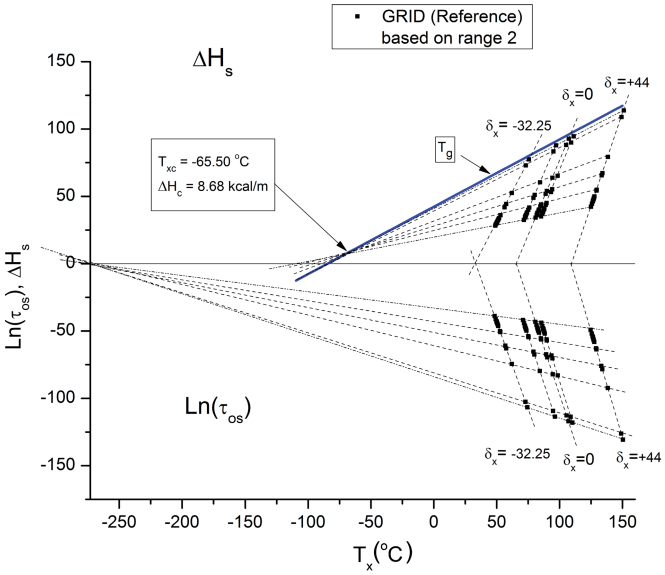


Figure 3.72: Grid reference (range 2) for T_x in degrees Celsius.

The ΔH_s and $\mathrm{Ln}(\tau_{os})$ grids are clearly different: this is the main observation of this large-scale overview. The individual compensations at T_p constant of ΔH_s vs. T_x or $\mathrm{Ln}(\tau_{os})$ vs. T_x are fundamentally different: the (x) lines of $\mathrm{Ln}(\tau_{os})$ compensate at the origin (0,0) or close to it (this point will be discussed), and the (x) lines of ΔH_s apparently compensate to a finite point of the grid (–65.5 °C, 8.68 Kcal/m). The asymmetry between the two grids raises the question of comparing the (p) lines up to the point of compensation of the ΔH_s grid.

We saw in Figure 3.55 that the (p) lines in each grid, for a given δ_x, compensate on the T_x axis, a fundamental property that defines the cross-correlation between ΔH_s

EBSCOhost - printed on 2/13/2023 12:32 AM via . All use subject to https://www.ebsco.com/terms-of-use

and Log(τ_{os}) and causes the compensation line in Figure 3.56 to pass through the origin. In Figure 3.56, $\delta_x = 0$, but we see in the overview figure, Figure 3.72, that this same property remains valid whatever the value of δ_x: all the (p) lines across the top and bottom grids meet on the T_x axis (for $\delta_x = 0$, $T_{xc} = 65.44$ °C, see equation (3.18)). We could even think of decreasing the value of δ_x below –32.25 (the lowest value of δ_x that we have studied), until the corresponding ΔH_s grid (p) line passes through the compensation point, corresponding to $T_x = -65.5$ °C. One sees that for such a value of δ_x, the upper grid would have collapsed onto its compensation point, which is independent of the value of T_p.

But turning now to the Ln(τ_{os}) grid at the bottom of Figure 3.55, the compensation of the (x) lines being at $T_x = 0$, the collapse of the bottom grid occurs for that value and, therefore, not for the value of δ_x that collapses the ΔH_s grid. We see that the asymmetry of the ΔH_s and Ln(τ_{os}) grids causes problems of boundaries, a subject which we are not going to discuss further here. For our purpose, we will admit that the coherence of the reference grid at its boundaries need to be investigated.

The reference grid corresponds to range 2, so there are no grid-shift factors for this range: this is why it is called the reference grid. This means that there is no need to apply any "dissipative" shift factors $\delta\Delta H_x = \delta \,\mathrm{Ln}(\tau_{ox}) = 0$ in this range of T_p to ΔH_s and Ln(τ_{os}) to obtain the compensation line passing through the origin.

The resolution to determine the compensation points in Figure 3.72 is itself in question.

For the Ln(τ_{os}) grid, Figure 3.72 indicates (0,0) for the compensation of the (x) lines. Yet, Figure 3.47, which is a compensation search of INTERCEPT vs. SLOPE of the Ln(τ_{os}) grid (x) lines, gives (0, 4.20), as is mentioned on the graph. This is the more precise evaluation of the Y-coordinate of the compensation point (off by 1 % on the Y scale of the overview). When converted into an entropy, using the Eyring formulation of the relaxation times (equation (2.5) of Chapter 2), this value of $\mathrm{Ln}(\tau_{oc}) = 4.20$ becomes $\Delta S_{pc} = 67$ cal/m/K, which is very close to the $(\Delta G_p/T_p) = 70$ cal/m/K that we have assumed corresponds to the entropic distortion of the electronic clouds of the dipoles. This means that all the values of entropy determined by TWD are shifted by –0.070 kcal/K/m. This confirms our conclusions of Chapter 2 (Figure 2.22).

Likewise, the coordinates of the ΔH_s grid compensation point can be determined more accurately by a compensation search of the INTERCEPT vs. SLOPE of the (x) dash lines at various T_p. The compensation search is shown in Figure 3.73.

Three lines are drawn in Figure 3.73, not just a single one, as expected from the overview scale of Figure 3.72: the three ranges 1, 2, 3 are, indeed, visible; especially range 3 stands out. If there are three compensation lines, then three compensation points are replacing the one drawn in Figure 3.72.

- In range 1: $\Delta H_{c1} = 6.05$ kcal/m $T_{c1} = -72.4$ °C;
- in range 2: $\Delta H_{c2} = 3.963$ kcal/m $T_{c2} = -76.7$ °C; and
- in range 3: $\Delta H_{c3} = -5.16$ kcal/m $T_{c3} = -95.2$ °C.

EBSCOhost - printed on 2/13/2023 12:32 AM via . All use subject to https://www.ebsco.com/terms-of-use

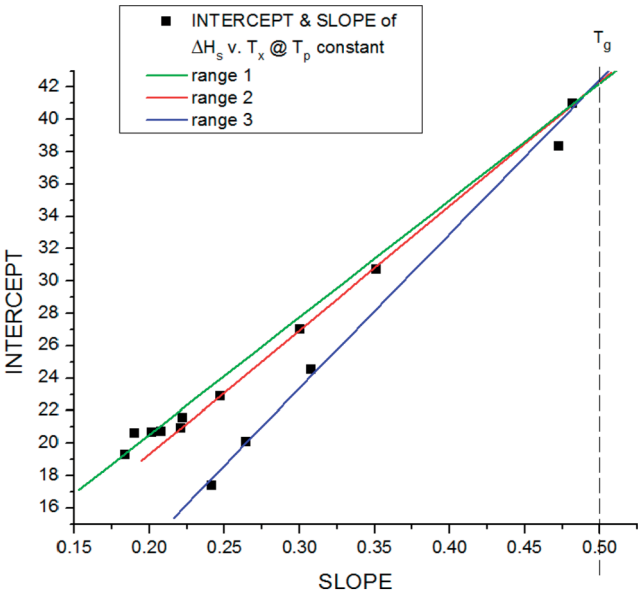


Figure 3.73: Compensation search INTERCEPT vs. SLOPE for ΔH_s vs. T_x at T_p constant, the (x) lines of the ΔH_s grid.

Also note in Figure 3.73 that the three compensation lines corresponding to the three ranges themselves compensate into a super-compensation point with SLOPE=0.5 and INTERCEPT=42.32 kcal/m. The straight line corresponding to this super-compensation point is drawn in thick blue color in Figure 3.72. It marks the upper boundary for all the (x) dash lines of ΔH_s. We have written T_g to designate that line. It is because the X-coordinate of the super-compensation point is 0.5, which we have assigned in Figure 3.51 to the T_g state. The three compensation points for ranges 1, 2, and 3 are positioned on that T_g boundary straight line, and, at least for ranges 1 and 2, they are located very near each other, which explains the lack of resolution to separate them when using the overview scale in Figure 3.72.

It is also interesting to note that while ΔH_{c1} and ΔH_{c2} are positive, with $\Delta H_{c2} < \Delta H_{c1}$, the value of ΔH_{c3} is negative, and, therefore, the corresponding compensation point is located in the bottom half of the general grid figure. This last point will be explained by the change of mechanism responsible for range 3.

Range 1 and range 2

As far as the enthalpy of the interactions is concerned, the mechanism of interactions in range 1 and range 2 originates by the value of their respective ΔH_c, which is 6.05 kcal/m for range 1, dropping by 2 kcal/m to 3.963 kcal/m for range 2. These values can be interpreted as the potential energy of conformer rotation for the CO-O bond

EBSCOhost - printed on 2/13/2023 12:32 AM via . All use subject to https://www.ebsco.com/terms-of-use

in PMMA under two environmental conditions: first, in range 1, with local frozen-in b grains incapable of providing new F conformers; and second, with b grains capable of releasing F conformers in their immediate local surrounding but with no coalescence of the local F conformers' free volume surroundings of the b grains until the T_g state is reached. Note that range 1 concerns the T_p values between 55 °C and 70 °C. We have mentioned $T_{cx} = 65.44$ °C as possibly the T_2 value for this PMMA with $T_g \sim 103.4$ °C (at the frequency equivalent[4] of the TWD test, around 3.5×10^{-4} Hz). This implies that range 1 concerns T_p values below T_2: the mechanism of polarization is mostly involving electronic and atomic polarization terms, with no orientation of the dipoles. In range 2, still below T_g, there is a release of local free volume due to the unfreezing of the $b \rightarrow F$ kinetics, yet no dipoles' collective orientation with the voltage field.

Our interpretation of the difference between range 1 and range 2 is supported qualitatively by several arguments. The conformational energy computation is 8.7 kcal/m for the CO-O bonds in PMMA and 2.7 kcal/m for the C-C bond, according to Gorin and Monnerie [92]. This could be compared to the value of ΔH_c found in range 1: 6.05 kcal/m. The lower value found for ΔH_{c2} in range 2 could be due to the starting of the $b \rightarrow F$ kinetic process at these high temperatures, producing more F conformers, with more free space to move around, creating a less rigid surrounding for the rotational isomerism to take place. This explains the lower ΔH_c and the lower T_c value found for this range (−76.7 °C instead of −72.4 °C, an increase by 5 °C of the free volume, expressed on the temperature scale). The 2 kcal/m drop in ΔH_c could be related to the b/F enthalpic change.

Range 3 (T_p above T_g)

The mechanism of interactions between the dipoles involved in range 3 is different from ranges 1 and 2 because the locality of the b grains (and of their surrounding free volume) starts collapsing at T_g. The b grains are now submitted to the elastic dissipative wave sweeping motion that tries to compensate for the local density difference between the b grains and their F conformers' surrounding. This elastic dissipative sweeping motion occurring above T_g influences the distribution of free volume throughout the sample, and this has an effect on the polarizing and depolarizing steps at T_p and T_d, due to a large increase of the mobility above T_g. The continuous sweeping of the elastic dissipative wave moves around the polarized F conformers which now tend to align in the field direction instead of holding still their polarization charge locally. The net result is that $[\Delta_e(E, T_p) - \Delta_{eo}]$ in equation (3.7), which kept decreasing as T_p increased in ranges 1 and 2 (below T_g) because $(T_{LL} - T_p)$ decreased, at μ quasi-constant, now increases because a larger and larger fraction of the activated dipoles

4 The frequency equivalent of the TWD technique is $f = \frac{0.113 b \Delta H}{2\pi k T_m^2}$, where b is the heating rate. Such low frequencies lower the value of the transitions by as much as 15–20 °C.

EBSCOhost - printed on 2/13/2023 12:32 AM via . All use subject to https://www.ebsco.com/terms-of-use

have relaxed out, making μ much bigger for the remaining dipoles that orient in the direction of the voltage field: this increase of μ overcomes the opposite effect of $(T_{LL} - T_p)$ as T_p continues to increase above T_g. As a result, not only does $[\Delta_e(E, T_p) - \Delta_{eo}]$ increase when T_p increases, but the number of activated dipoles decreases because of the faster relaxation of the dipoles in the structure back to equilibrium. The situation is presented in Figure 3.74, which follows the variation of $\mu(T_{LL} - T_p)/T_{LL}$ against T_p across T_g.[5]

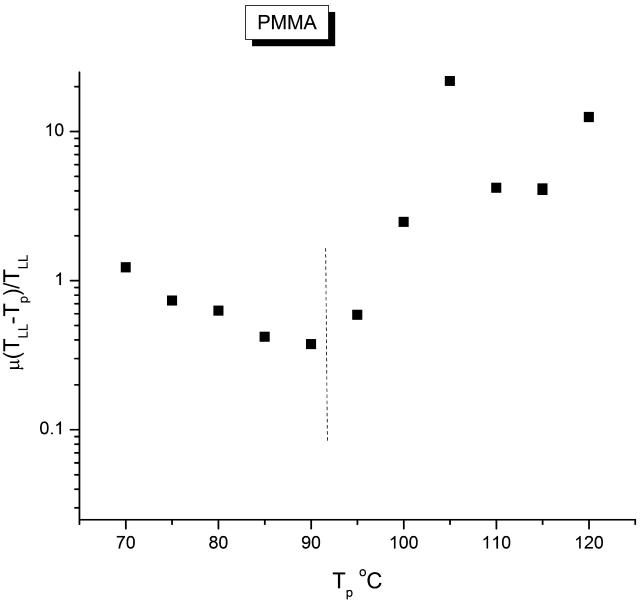


Figure 3.74: Variation of the Δ_{eo} step increment, $\Delta_e - \Delta_{eo}$, calculated at T_p, plotted against T_p.

Remember that the simulation has postulated the analogy between the variation of ΔH and $\mathrm{Ln}(\tau_o)$ with T_p and the variation of Δ_x, $\mathrm{Ln}(1/\upsilon_x)$ with Δ_e. Referring now to Figures 3.9 and 3.10, it should be clear that d $[\Delta_e(E, T_p) - \Delta_{eo}]/dT_p < 0$ corresponds to the situation of a positive compensation because Δ_x is increasing when Δ_e decreases and, conversely, that $d[\Delta_e(E, T_p) - \Delta_{eo}]/dT_p > 0$ corresponds to the negative compensation case because Δ_x decreases when Δ_e increases.

5 We have chosen $T_{LL} = 159.4$ °C according to its evaluation in Figure 3.16 and 5.663×10^5 for the ratio between the dielectric strength, $(\varepsilon_s - \varepsilon_a)$ and P_{so}, the polarization in the sample before the ramp-up depolarization step. The values of the dielectric strength and of P_{so} vs. T_p can be found in Table 3.12 at the end of this chapter.

EBSCOhost - printed on 2/13/2023 12:32 AM via . All use subject to https://www.ebsco.com/terms-of-use

I.3.5.2.2 Conclusions regarding the physical meaning of the results of TWD

In conclusion, we have demonstrated that:

1. In ranges 1 and 2, we have a positive compensation that matches an increase of ΔH with T_p, the slope of the Arrhenius lines in an Arrhenius relaxation map.
2. In range 3, occurring above approximately 95 °C for PMMA, we have a negative compensation that results in the opposite effect of decreasing the slope of ΔH as T_p increases.
3. The compensations of $\mathrm{Ln}(\tau_o)$ vs. ΔH in ranges 1, 2, and 3 can be superposed into a mastercurve compensation (Figure 3.56) passing through the origin. This master compensation corresponds to the basic mechanism of the interactive coupling described by the Dual-Phase dissipative model of conformers interactions: $[(b/F) \leftrightarrow (c, g, t)]$.
4. The shift factors, $\mathrm{Ln}(\tau_{ox})$, ΔH_x, are constant within a range and characterize the specific mechanism of interaction between the voltage field and temperature in that range (electronic and atomic polarization, orientation polarization). The shift factors can be determined by grid-shifting.
5. The properties of the reference grid can be explained in terms of the Dual-Phase dissipative model of conformers interactions.
   5.1 The $\mathrm{Ln}(\tau_o)$ grid converges at $T = 0$ K to a point that matches the value of the electronic polarization entropy found for $\Delta G_p/T_p$ in all polarized amorphous polymers studied by TWD in this book.
   5.2 The ΔH grid shows three compensations merging into a super-compensation at T_g. The characteristics of ΔH_c for these three compensations permit to differentiate the three ranges and identify their origin according to a Dual-Phase interactive coupling explanation: only ΔH_c in range 2 corresponds to the description of the unrestricted conformational energy of a conformer, say in "a theta-solvent like" type of environment.

A better picture of the fundamental mechanism for the overall relaxation process starts to emerge from this study. The phenomena observed in TSD and TWD experiments are the result of the energetic and kinetic nature of the interactions between the conformers. The concepts of the energetic and kinetic structure of the dissipative network of conformers in interactions are explained in this chapter using a simple approach of the Grain-Field Statistics, assuming that only the equations of the vertical structuring of the free energy of the collective system are at play. This simplification helps understand the physical reality of the compensations between $\mathrm{Ln}(\tau_o)$ and ΔH, the features observed at T_g, the multiple compensations, their sign, and the apparent alternation between them. This represents a coherent set of explanations modeled by a simple mathematic formulation.

Only the grain-field statistical entire energetic kinetic approach can address the general solution that determines how the collective dissipative structure has been af-

EBSCOhost - printed on 2/13/2023 12:32 AM via . All use subject to https://www.ebsco.com/terms-of-use

fected, how many horizontal dynamic systems have been created and modified, and how they have structured themselves by vertical structuring between their b and F state and their (c, g, t) state. As we said, we simplified the solution by assuming that only one dynamic horizontal system existed and remained invariant to let us focus on the vertical structure only. In our simplified approach, the voltage field only modifies the Dual-Phase potential energy Δ_e by an amount equal to the dipolar moment times the voltage field and a temperature term that we made a function of $(T_{LL} - T_p)$ in equation (3.7). Only by simulating the more general solution, letting the voltage field also potentially modify the horizontal structuring, can we be confident that the vertical structuring is dominant, even exclusive.

The fact that the relaxation curves in the normalized ΔG plane (Chapter 2) all converge to the same value $(\Delta G/T_p)_c \sim 66–70$ cal/K/mole for a temperature equal to T_p is probably indicative of the way the voltage field interacts with the dielectric medium. It also reveals that the dielectric medium is the internal viscosity, i. e., is entirely responsible for the relaxation behavior. By probing the dissipative network structure at different T_ps, the voltage field energy modifies the Dual-Phase potential well of the existing dipolar groups, distorting it to store the electrical energy, and this energy is released by thermal stimulus on reheating. The value of $A_c = (\Delta G/T_p)_c = 70$ cal/K/m corresponds to the spinning of the electrons around their orbitals, converting the disorder created by the vibration into entropy. Therefore, the primary mechanism of polarization is by energetic kinetic coupling distortion, which is responsible for the $\Delta G_p - T_p$ linear behavior, and not by dipolar orientation, which can only partially occur above T_g.

Beyond T_g, some polarization by orientation occurs for polar materials, which explains the departure from the linear $\Delta G_p - T_p$ behavior in this region. The voltage energy is dissipated between two mechanisms, the distortion of the potential well of conformers and the structuring of the dissipative network to allow rotation of the dipoles in the direction parallel to the field: this is dipolar orientation. The distortion of the free energy at T_p by the voltage field induces a free energy structure at that temperature, different from the equilibrium free energy structure.

Below T_g, even if we had several systems created by horizontal structuring, the systems would all be dependent, and the assumption that the voltage field directly affects the potential well Δ_e is probably a good hypothesis. Above T_g, the modification of the potential well is through the interlock kinetics, and therefore the total electrical energy is not stored in the distortion of the potential well, which becomes a less efficient process (the free energy at T_p remains approximately constant in a certain temperature zone). By comparing the starting free energy, when the dipoles start to relax, and the final free energy, at the end of the Debye relaxation, one can calculate not only the amount of free energy released during depolarization (in addition to the value of the equilibrium free energy for a particular temperature), but also the amount of energy stored by distortion during the polarization stage. This amount depends on the free energy structure, which itself is function of the voltage field energy, in a recur-

EBSCOhost - printed on 2/13/2023 12:32 AM via . All use subject to https://www.ebsco.com/terms-of-use

sive way. This is, therefore, above T_g, that the activation of the horizontal structuring dynamics would affect the formulation of equation (3.7).

The voltage field does *not* isolate elementary molecular motions by thermal-windowing. The complex kinetics (see Appendix Parts A and B) takes its source in the coupling between kinetic and energetic equations and is essentially due to a minimum principle applied at two different levels (horizontal and vertical structuring). The return to equilibrium specifies the changes which occur to the free energy structure and reveals the modification of the potential well Δ_e by the coupling between the voltage field and the temperature, at T_p, T_d and during the ramp-up depolarization stage. By varying T_p, T_d, and t_d we activate or deactivate a part of the cooling (or heating) pattern of the free energy structure (Figure 3.51) and freeze it to lower temperatures. The ramp-up depolarization output, coming right after the partial relaxation stage that brings the system closer and closer to equilibrium, step after step as T_p increases, reveals the fundamental characteristics of the mechanisms of interactive coupling, as modeled by the Dual-Phase and the Grain-Field Statistics. We concluded that TWD was, *de facto*, a method to discover the gears of the vertical and horizontal energetic and kinetics interplays. The current analysis only introduces the methodology, yet the refined research still lies ahead.

I.3.5.3 General conclusions

This research also initiates the use of another language to describe interactions. Classical physics formulates interactions by introducing a potential function, V, often expressed in terms of the distance separating the interacting entities; the force of the interaction is the gradient of the potential $F = -\text{Grad}(V)$, using vectors to imply a field of action, not scalars.

We do not specifically deal in this text with the force, covalent or inter-intra molecular, that bonds the conformers together; we assume certain general rules regarding the result of their interactions:

- Locally, the isomeric rotation of the conformers occurs and is governed by their conformational potential energy, as well as their ability to agglomerate as nanometric grains, creating a local inhomogeneity.
- The local density inhomogeneity is "compensated" – this is the way we call this dual aspect of the interactions in the Dual-Phase model – by a collective action of all the interactive conformers working as a dynamic dissipative set. In our statistical model, the dissipative energy is introduced via equations that link the kinetic and the energetic aspect of the conformers statistics variations, and it leads to the definition and the quantification of a new dynamic entity: the dissipative pair (Δ_x, υ_x). This term describes the collective aspect of the duality of the conformers under dynamic conditions ($\Delta_e \neq 0$), whereas (Δ_m, υ_m) represents its local aspect

EBSCOhost - printed on 2/13/2023 12:32 AM via . All use subject to https://www.ebsco.com/terms-of-use

(the local conformational energy properties of the conformers). Δ_x, υ_x define the kinetics of $\mathrm{Ln}(N_b/N_f)$, the dissipative term.

– We find invariably that Δ_x and $\mathrm{Ln}(\upsilon_x)$ compensate when Δ_e varies or Δ_m, υ_m vary. We also find that the two dualities (Δ_m, υ_m) and (Δ_x, υ_x) compensate through the origin when Δ_e varies in a normalized plot of ($\mathrm{Ln}(\upsilon_m) - \mathrm{Ln}(\upsilon_x)$) vs. ($\Delta_m - \Delta_x$). We call this property of the dissipative Dual-Phase model of the dynamics of the interactions: "a cross-duality."

We believe that this duality and cross-duality property of interactions may be applied to many other entities in interactions, not simply conformers.

There is perhaps even another dimension to dissipative energy, duality, and cross-duality.

In physics, most of the complex interactive problems involving time we know how to solve are in steady-state and not in transient-state conditions, and this simplifies their mathematical description a great deal: the reason is the separation of the variables. The separation of time from the other variables is, obviously, validated under steady-state conditions, yet the procedure has been generalized to many implicit functions of several variables. In addition, there are instances when time is intrinsically linked to other variables and the separation of the variables to resolve such implicit functions becomes questionable: this is the case for the wave function in quantum mechanics, $\Psi(r,t) = f(r)g(t)$, when the potential energy is a function of both r and t: $V(r,t)$.

Likewise, we have given the proof elsewhere [138] of the inadequacy of the separation of variables hypothesis in the case of the temperature and molecular weight dependence of the Newtonian viscosity in polymer melts rheology. $\eta(M,T) = F(M).A(T)$. We showed that the separation of M and T only occurred for specific period doubling values of M ([138]).

The technique of the separation of the variables has, indeed, demonstrated its remarkable utility of simplification over the last 200 years, permitting, as if these variables were independent functions, to easily use the tools of calculus (differentiation or integration) to express their interdependence. Its validity, however, should be carefully verified and their use not systematically generalized.

Let us illustrate this point using the variables studied in this book: the voltage field, E, and the polarizing temperature T_p. A priori, these two variables are independent: one can choose arbitrarily the value of E and T_p. Yet, this is not counting for the interactions induced by the dielectric nature of the material exposed to such a voltage at such a temperature.

In fact, the external field, E_o, triggers the presence of a different field, E, in the material and their ratio is the dielectric constant, $\varepsilon = E_o/E$, expressing the "polarizability," i. e., the tendency of a material to polarize in response to an applied electric field. The field inside the dielectric, E, is the vector sum, $\mathbf{E} = \mathbf{E}_o + \mathbf{E}_p$, where E_p is generated

EBSCOhost - printed on 2/13/2023 12:32 AM via . All use subject to https://www.ebsco.com/terms-of-use

by the polarization P of the dipoles in the dielectric: $E_p = -P/\varepsilon_o$, where ε_o is the permittivity of the vacuum. The polarization is usually proportional to the macroscopic field: $E_p = -\chi E$, where χ is called the macroscopic susceptibility of the dielectric. The susceptibility, χ, or the polarizability $P = \varepsilon_o(\varepsilon - 1)E_o/\varepsilon$ are equivalent constants to express the polar nature of the chemical structure of the polymer: PMMA, PC, PET, PVC, nylons, etc., are polar polymers, while PS, PE, PP, PTFE, etc., are non-polar. Debye [23] quantified the induced and the permanent contributions of the polarizability of non-polar and polar molecules (here the conformers) in a modified generalization of the Clausius-Mossotti expression of the dielectric constant:

$$\frac{(\varepsilon - 1)}{(\varepsilon - 2)}\frac{M}{\rho} = \frac{4\pi N}{3}\left(\alpha + \frac{\mu_o^2}{3k_BT}\right) \tag{3.20}$$

where M is the molar mass of the conformer, ρ its density, N the total number of activated dipoles, α the induced moment divided by E_o, μ_o the permanent moment, and k_BT the Boltzmann thermal energy.

In other words, the dielectric constant, ε, primarily depends upon the chemical nature of the conformer, which controls the type and the magnitude of the polarizability, P, but it also varies with the physical state of the polymer, i. e., whether it is a solid, a paste, a liquid, a liquid crystal, in equilibrium or out of equilibrium, etc., all of which are controlled by the temperature at polarization and by the thermomechanical history of the sample that also determines its non-equilibrium state.

In summary, T_p, E, and ε are interactively coupled in a circular way, and the best way to describe it is with an implicit function of the type $H(\varepsilon, T_p, E) = 0$.

This expression would greatly simplify if we could find a simple expression for the temperature dependence of ε. But ε is the sum of various contributions: the electronic permittivity, the atomic permittivity (both quasi-time-independent, i. e., rapidly found in steady state) and the dipolar (orientation) permittivity, with its characteristic spectrum of relaxation and its sluggish time dependence, characterized by $\tau(T)$.

Here we are: back to the purpose of this book of characterizing the temperature dependence of all the relaxation times of the atomic and molecular motions and their interdependence to create the cohesion of the bonds and its dielectric response as temperature varies.

We can rewrite the implicit equation by inserting the two constants that define the temperature dependence of $\tau(T)$:

$$I(\tau_{oc}, \Delta H_c, T_p, E) = 0$$

The subscript "c" in τ_{oc} and ΔH_c is included to summarize the general result found in this chapter, c standing for "compensation." The master compensation result is materialized by Figure 3.56.

EBSCOhost - printed on 2/13/2023 12:32 AM via . All use subject to https://www.ebsco.com/terms-of-use

In the newly written implicit equation, the emphasis has shifted from the expression of ε to describe the behavior of dielectrics, the classical approach, to the compensation approach, so to speak, i. e., the description of the interactive couplings between the enthalpy and entropy at different scales. By enthalpy and entropy, we, of course, relate to the physical sense attributed to the slope and intercept in the Arrhenius plane of $\mathrm{Ln}(\tau(T))$ vs. $1/T$, but also to the x- and y-coordinates of compensation plots such as $\mathrm{Ln}(\tau_o)$ vs. ΔH when T_p varies. By "different scales," we symbolize the observed changes of the mechanism of interaction between the voltage field, temperature, and the dielectric material, in a way similar to, but fundamentally different from, the classical school description of the various contributions to the dielectric constants (electronic, atomic, and dipolar). In our Dual-Phase dissipative model of interactive coupling, the normalized variables of the masterplot have two similar terms: $\Delta_m - \Delta_x$ for the x-axis and $\mathrm{Ln}(\upsilon_m) - \mathrm{Ln}(\upsilon_x)$ for the y-axis. But the "m" and the "x" terms do not play the same role. Only Δ_x and $\mathrm{Ln}(\upsilon_x)$ vary with Δ_e; Δ_m and $\mathrm{Ln}(\upsilon_m)$ remain constants within the "scales," i. e., within the "ranges of T_p" the way we called ranges 1, 2, and 3 in our discussion of the dielectric interactive coupling in this chapter. Δ_m, υ_m define the scale and Δ_x, $\mathrm{Ln}(\upsilon_x)$ define the dissipation term of the Dual-Phase dissipative statistics.

And, as we have seen in this chapter, *we need both the dissipative contribution and the scale contribution to complete the masterplot, which goes through the origin at all scales*.

This is where we wanted to land: our approach of the interactions tries to find the way to unify the various scales participating in the process of interaction.

It is not surprising, using the language just proposed, to see that the three scales describing ranges 1, 2, and 3 compensate at T_g (in Figure 3.73). The reason is (i) that the dielectric fields defined by the clouds of the electrons in the orbitals, by the geometric disposition of the atoms in a conformer in isomeric conformation rotation, and by the dipolar moment vector submitted to orientation are all interrelated and (ii) that they share the same dissipative term, $\mathrm{Ln}(N_b/N_F)$, related to the (b/F) free volume structure, coalescing at T_g, whatever the scale. This collective coalescence of the dissipative term at the T_g phase-transition, melting the spatial locality of the b grains, occurs with an increase of the degree of freedom of the statistics dynamics. The last and ultimate increase of the degree of freedom of the Dual-Phase statistics occurs at T_{LL}, where the space-time difference between the b and F conformers collapses, marking the end of the materialization of the Dual-Phase dissipative elastic wave and marking a return to the Boltzmann statistics. The T_g spatial delocalization of the b grains touches all scales related to electrons and their surroundings: this is the reason this is perceived as a super-compensation of ΔH in Figure 3.73.

We have noted before the difference between the ΔH grid and the $\mathrm{Ln}(\tau_o)$ grid in Figure 3.72: the ΔH vs. T_x (x) lines all compensate in three compensation points, themselves lined up on the T_g (x) line as a super-compensation; there is no trace of the ranges for the (x) lines of the $\mathrm{Ln}(\tau_o)$ grid. Since the $\mathrm{Ln}(\tau_o)$ grid is related to entropy,

EBSCOhost - printed on 2/13/2023 12:32 AM via . All use subject to https://www.ebsco.com/terms-of-use

the compensation y-axis value at $T = 0$ K is the basic entropic value of the distortion of the electronic orbitals due to the field voltage. Any other entropy value related to any point in the $\mathrm{Ln}(\tau_o)$ grid is a multiple of this basic value, proportional to the absolute T_p temperature. The absence of a scale structure for the entropy reference grid, like it is observed for the ΔH enthalpy grid, must have a fundamental importance (provided these results are validated for other polar polymers). We speculate that the equivalent of the T_g state blue line drawn for the ΔH grid is, for the $\mathrm{Ln}(\tau_o)$ grid, another blue line, located at the bottom of the set of (x) lines, actually the lowest (x) line passing through the (0,4.2) super-compensation. The difference between this T_g state blue line and the ΔH blue line is that the ΔH T_g state blue line passes through three compensation points defining the three scales on the energy axis, while there are no such three corresponding compensation points on the entropy axis. The absence of correspondence must be elucidated.

I.3.5.4 The search for new concepts to build up a ladder of scales

In our investigation of the fundamentals of interactive coupling via the TWD relaxation map, we realized, at least for a polar amorphous polymer like PMMA, that we could unify the types of interactions present into a single concept, the compensation of $\mathrm{Ln}(\tau_o)$ vs. ΔH, provided we also divided the temperature range into three ranges, defining three scales of (Δ_m, υ_m) values. The objective of finding the differences between scales 1, 2, and 3 and relate the findings to a unification scheme that would permit to designate T, the temperature, as the fundamental parameter to pass from one scale, say scale 1 identified by $(\Delta_m, \upsilon_m)_1$, to other scales, say scale 2 identified by $(\Delta_m, \upsilon_m)_2$, etc., is an important objective of its own that appears a challenging one, yet worth the effort. The final result will look like a ladder of scales, three scales in this instance, perhaps more complex when the polymer can crystallize or form liquid crystal phases.

We initiated this investigation in Section I.3.4.6.3, Figures 3.61 to 3.71.

The results we presented, though, were preliminary and clearly raise more questions than answers. In this last section of the book, we will allow ourselves to be imaginative, perhaps even provocative. Here are a few of those provocative thoughts/questions.

I.3.5.4.1 The phantom variable T_x

The introduction of $T_x = T_p + \delta_x$ to study separately $\Delta H(T_x)$ and $\mathrm{Ln}(\tau_o(T_x))$ led to important discoveries (Figures 3.59 and 3.72). In Figure 3.59, not only do we see how the T_x vs. T_p grid works, but also emerges the distinction between points A and A' which introduces the concept of a temperature drift between the enthalpic and the entropic term of an interaction: $T_{xH} \neq T_{x\tau}$. This concept is also explicated in Figure 3.60.

EBSCOhost - printed on 2/13/2023 12:32 AM via . All use subject to https://www.ebsco.com/terms-of-use

One could argue that in the definition of T_x, δ_x plays a role similar to a derivative in elementary algebra. This is partially equivalent but not true. First, δ_x does not need to be infinitely small, like dT_p needs to be, and second, its value is chosen independently of T_p, which is not the case for dT_p, for which the dependence with T_p characterizes the function (the derivative is associated with the slope of the curve at the point). We prefer to call δ_x "a phantom variable." By varying it in an astute way, like in Figure 3.72, we could obtain unique information regarding the differences between the ΔH and $\mathrm{Ln}(\tau_o)$ grids compensation structure.

The use of the phantom variable also led to the unique discovery of T_{xc} at $\delta_x = 0$ in Figure 3.55 and of the two equations defining the master compensation for the reference grid, equation (3.17).

I.3.5.4.2 Conjugated states: $[\Delta H_c = \Delta H(T_p + \delta_{p\tau}), \tau_{oc} = \tau_o\,(T_p + \delta_{pH})]$

From simple arguments based on Figures 3.61 and 3.62, we showed that grid-shifting for ΔH and $\mathrm{Ln}(\tau_o)$ permitted to define conjugated states, ΔH_c at $T_p + \delta_{p\tau}$ and $\mathrm{Ln}(\tau_{oc})$ at $T_p + \delta_{pH}$. Conjugated states show surprising properties, as illustrated by the blue triangles in Figures 3.66 to 3.68. Conjugated compensation states at one scale (range 1) can assume real data compensation states of another scale (range 3). There are several other properties of the conjugated states at different scales that are remarkable in Figures 3.69 to 3.71.

Could it be that the temperature drift, $\delta = \delta_{pH} - \delta_{p\tau}$, shown to exist between "conjugated variables," such as those coupled in Figure 3.67, is the key to define the ladder of scales, completing the unification of the network of the interactions at all scales?

I.3.5.4.3 The role of T, coupled to other independent external parameters, in the formulation of the interactions

Does the imposition of a voltage field on a dielectric material at temperature T_p induce a coupling effect that slightly shifts the temperature scale, as if temperature would have a different scale when acting alone or coupled with a voltage field? This question calls for a possible relativity effect in materials due to the interactions. In a sense, it suggests that it is impossible to measure directly and alone the effect of the voltage field on the dielectric properties of a material, since the measurement is always done at a certain temperature T_p at which the voltage field and temperature couple up to trigger a dissipative response.

The impact of this relativity effect inside materials may be critical as far as our knowledge of reality via measurements is concerned. Our knowledge of reality occurs *through measurements done above the absolute zero temperature* (0 K),[6] so coupling

6 The current record is held by scientists at MIT who have reached 10^{-7} K. This value is still very hot compared to the Planck T fluctuation value for birthing photons from the atoms, which we have evaluated at 7.6384×10^{-12} K.

EBSCOhost - printed on 2/13/2023 12:32 AM via . All use subject to https://www.ebsco.com/terms-of-use

between the absolute temperature T and any other measured parameter must be reflected in the equations describing any of their correlations.

Shall we include the dissipative effect of coupling with temperature in *the definition of the units* that are used as reference values to be able to quantify the other independent variables, such as voltage (in Volts), distances (in meters), time intervals (in sec), etc., as well as the fields in the physics of interactions (in the latter case by introducing a dissipative term accounting for the coupling between T and the field)?

For instance, should temperature T appear in the description of the potential field function in the Schrödinger equation, $V(r, t, T)$ instead of presently $V(r, t)$, and do we need to add a dissipative term in the equations to solve when the potential includes T?

These are iconoclastic questions, of course, the last question being the most provocative one: it suggests to rescale the *unit* of a physical quantity to account for the dissipative coupling between it and T, implying a radical modification of the equations in physics by incorporating the interaction of absolute temperature and the physical entity in question. To illustrate this simply, the meter, the reference unit for length, would have a different value (1) when distance and voltage are combined in a measurement and when (2) distance and optical measurements are involved. All fundamental "independent" units (time, space, temperature, mass) would need to be defined relative to another, i. e., interactively and coupled, at least in their Planck state.

I.3.5.4.4 Is this the way to end a serious book?

No, there is one more question: what is the most striking idea to be remembered of the vertical split structuring defining the Dual-Phase statistics?

Two ideas, in fact:

First, the fact that it defines a dissipative factor from the coupling between energetic and kinetic constraints and that this dissipative factor, $\mathrm{Ln}(N_b/N_F)$, regards the collective response, dynamically represented by Δ_x, υ_x, the quantities that are measured. Our knowledge of the local properties, Δ_m, υ_m, is filtered through the collective response, Δ_x, υ_x, and not the opposite. Should we not reverse our methodology of investigation and focus on determining the fundamental laws of the whole first, since this is what we measure, and learn how to transmit them down to the local scale *rather than doing the opposite*: starting from the local laws (the elementary particles and forces of the standard model, for instance) and constructing the whole (astronomy)?

Second, the local will be derived from the whole at phase-transitions, where the scales synchronize, i. e., when the Δ_e of the collective set collapses ($\Delta_e = 0$ for $\Delta_m = \Delta_x$; $\upsilon_m = \upsilon_x$).

To seriously end this book's Part I, it should be added that the last question above lacks completeness since it did not factor in the interlocking between the horizontal and the vertical structuring solutions, a more complex problem, indeed, to be dealt with in due course.

EBSCOhost - printed on 2/13/2023 12:32 AM via . All use subject to https://www.ebsco.com/terms-of-use

Table 3.12: PMMA – Frequency table with P_o and dielectric strength.

	T_p (°C)	T_m (°C)	Frequency (Hz)	Intensity (Amps)	P_o (c/m^2)	$\varepsilon_s - \varepsilon_\infty$
1	70.0	81.9	3.449E-04	2.675E-14	1.49E-07	8.40E-02
2	75.0	86.3	3.891E-04	4.550E-14	2.27E-07	1.28E-01
3	80.0	90.3	4.410E-04	6.444E-14	2.78E-07	1.57E-01
4	85.0	95.2	4.620E-04	9.153E-14	3.86E-07	2.18E-01
5	90.0	98.7	5.419E-04	1.280E-13	4.51E-07	2.55E-01
6	95.0	101.8	6.640E-04	1.245E-13	3.62E-07	2.04E-01
7	100.0	105.3	7.040E-04	5.604E-14	1.51E-07	8.54E-02
8	105.0	108.6	6.414E-04	1.309E-14	3.86E-08	2.18E-02
9	110.0	120.8	3.775E-04	2.681E-14	1.27E-07	7.17E-02
10	115.0	122.3	4.012E-04	3.137E-14	1.41E-07	7.94E-02
11	115.0	122.3	3.979E-04	3.137E-14	1.43E-07	8.09E-02
12	120.0	123.1	4.162E-04	1.708E-14	7.49E-08	4.23E-02

EBSCOhost - printed on 2/13/2023 12:32 AM via . All use subject to https://www.ebsco.com/terms-of-use

Appendix of Part I

This Appendix does not pretend to provide equations that will directly apply to the results obtained by TSD or TWD. However, working by analogy, one can recognize some identical patterns of behavior between the computer simulations and the real response of polymers using the TSD and TWD stimulation techniques. The mathematical details are avoided as much as possible to concentrate on the meaning of the concepts that could be useful to the study of interactive coupling in the amorphous state, the subject of this book.

The dynamic equations presented here can easily be applied to simulate many specific problems of physics, including the action of a voltage or a mechanical stress field on the interactions between the dual-conformers in polymers. There are several ways to set up the simulation: for instance, by making the value of Δ_e appearing in the equations the only variable (as a function of stress or voltage), keeping υ_m and ΔH_m independent of these external actions. In other simulations, both Δ_m and Δ_e vary when the external action, other than a change of temperature, is imposed on the dynamics. We limit ourselves, within the scope of this appendix, to dynamic situations that simulate simple cooling and/or heating or annealing experiments after the system's initial conditions have been defined; these simulations imply that the value of Δ_e has been pre-determined by the effect of an electrical or mechanical field applied prior to the dynamic thermal stimulation. Hence, it is assumed that Δ_m, υ_m, and Δ_e remain constant during the dynamic simulations illustrated below. We show how the system dynamics result from the imposition of non-equilibrium conditions or the recovery of equilibrium ones by thermal stimulation.

We discuss in Part I, Chapter 3 how a thermoelectrical history procedure, such as the TWD characterization studied in this book, can be simulated by a modification of Δ_e with the temperature of polarization, T_p, and with the intensity of a voltage field. Once the value of Δ_e is set by these pre-conditions, the depolarization step of TWD can be simulated by a return to equilibrium at Δ_e constant in the dynamic equations of this Appendix.

The simulation is presented in a shortened and simplified way (Δ_m, υ_m constant) to let the reader quickly grasp that the complex relaxation behavior observed by TSD or TWD to characterize interactive coupling may derive from simple Dual-Phase or more sophisticated Cross-Dual-Phase principles.

Conventional kinetics

The study of kinetics is a discipline that describes the evolution of the units of a population of, say, chemical molecules that participate in chemical reactions. Another example would be to describe the evolution of units of a population which could occupy different "states." Many other terms have been used to describe the same objective:

https://doi.org/10.1515/9783110756746-005

EBSCOhost - printed on 2/13/2023 12:32 AM via . All use subject to https://www.ebsco.com/terms-of-use

"statistics," or "dynamics," for instance, as shown in the following definitions: the population partition that evolves with time can be studied with the tools of "statistics," a transient statistics in fact, a field also regarded as "dynamics." All these definitions are used in our presentation. The important thing here is to define the terms quantitatively.

Consider a simple dynamic process such as a first-order reversible kinetic equation between two states, $t \leftrightarrow cg$, controlled by an activated process with direct and reverse kinetic constants k_1 and k_2, with activation energy Δ_1 and Δ_2, respectively. One can write the following elementary set of kinetic and thermodynamic equations to describe the evolution of the system:

$$B_o = (n_t + n_{cg}) \tag{1}$$

where B_o = total number of units in state energy levels t, cg,

$$\begin{aligned} \Delta G &= RT \cdot \mathrm{Ln}(n_t/n_{cg}) \quad \text{is the free energy of the system with} \\ \Delta G_e &= RT \cdot \mathrm{Ln}(n_{te}/n_{cge}) = RT \cdot \mathrm{Ln}(k_2/k_1) \quad \text{the equilibrium value} \end{aligned} \tag{2}$$

(the sub-index "e" corresponds to the equilibrium value) and R is the gas constant,

$$\begin{aligned} dn_t/dt &= -k_1 \cdot n_t + k_2 \cdot (B_o - n_t) \\ dn_{cg}/dt &= -k_2 \cdot n_{cg} + k_1 \cdot (B_o - n_{cg}) \\ &\text{with } k_1 = \upsilon_m \exp(-\Delta_1/RT) \text{ and } k_2 = \upsilon_m \exp(-\Delta_2/RT) \end{aligned} \tag{3}$$

where υ_m is the frequency front factor.

In the following, we call $\Delta_e = (\Delta_1 - \Delta_2)/2$ and $\Delta_m = (\Delta_1 + \Delta_2)/2$.

When the total number of units in the two levels, B_o, is constant, the statistics applies to a *closed* thermodynamic system.

If the system is cooled at a constant cooling rate $q = dT/dt$, the now non-linear system of differential equations above can easily be solved (for instance with a Runge–Kutta fifth-order algorithm) to produce at each temperature a set of n_t and n_{cg} values, which can be compared to those of equilibrium at the same temperature. This will determine the effective departure from equilibrium due to non-isothermal cooling. Notice in the equation which gives the free energy that the term $\mathrm{Ln}(n_t/n_{cg})$ reflects the departure of the free energy from its equilibrium value and that n_t, n_{cg} are being determined by solving the kinetic set. Therefore, under non-isothermal conditions, the free energy plays a very subordinate role, and its magnitude is driven by the kinetic aspect.

For a classical set of kinetic equations it is clear that the transient free energy is not at its minimum value, since the value of the minimum free energy at any given temperature is known: it is the equilibrium value at that temperature, $\Delta G_e = RT \cdot \mathrm{Ln}(k_2/k_1)$. When the system is brought out of equilibrium and then allowed to relax,

EBSCOhost - printed on 2/13/2023 12:32 AM via . All use subject to https://www.ebsco.com/terms-of-use

the kinetic equations drive the system back to the equilibrium state, which implies that the value of the equilibrium free energy is implicit in the formulation of the kinetic constants. In fact, the ratio of the two kinetic constants is equal to the thermodynamic constant, a quantity which gives the partition function for the two energy levels at equilibrium:

$$\Delta G_e = RT \cdot \mathrm{Ln}(n_{te}/n_{cge})$$

In conclusion, for classical kinetic equations under non-isothermal conditions, for which the solution is driven by kinetic considerations only, the free energy of the system is not equal to its minimum – equilibrium – value.

Dual-Split Kinetics

Can we modify the set of equations driving the kinetics so the system free energy *stays at its minimum value at all times*? The Dual-Split Kinetics model describes new sets of kinetic equations fulfilling these conditions. There are two types of solutions that we have studied, vertical and horizontal splitting, and several possible hybrid combinations of the two. As stated above, we will briefly introduce these three in this appendix.

Part A. Dual-Phase Dissipative Kinetics (vertical splitting)

It is assumed that we can split each state *cg* and *t* into an *F* and *b* category, giving four states, *cgF*, *cgb*, *tF*, and *tb*; the result is a *dual partition*, between *cg* and *t* units on the one hand and between the *F* and *b* units on the other hand. The two partition functions are coupled.

In this section we present the assumptions driving the new non-equilibrium statistics and study the difference between its results and results obtained classically. The new equations converge to traditional kinetic equations at long times or under "true" equilibrium conditions. Under non-isothermal conditions the system becomes self-dissipative, and the duality is responsible for a structure of the free energy.

A.1 Structuring between the *b* and *F* conformers

Suppose the total B_o population is split into two sets of units, N_b and N_f, with $N_b(t)$ and $N_f(t)$ transient or steady-state. The total population $(N_b + N_f) = B_o$ remains constant, and for this reason, the rate of change of N_b is equal to minus the rate of change of N_f. The kinetics of n_{tb} and n_{cgb} in sub-set N_b are different from the kinetics of n_{tf} and n_{cg} in sub-set N_f, and we can define a sort of intrinsic partition between these two sub-sets

EBSCOhost - printed on 2/13/2023 12:32 AM via . All use subject to https://www.ebsco.com/terms-of-use

$N_b(t)/N_f(t)$, for each set a situation corresponding to open-system dynamics:

$$\begin{aligned} B_o &= N_b + N_f \\ N_b &= (n_{tb} + n_{cgb}) \\ N_f &= (n_{tf} + n_{cgf}) \end{aligned} \tag{4}$$

It is clear that under equilibrium conditions $N_{be} = N_{fe} = B_o/2$ and that the population of each level is n_{tbe}, n_{cgbe}, n_{tfe}, n_{cgfe}, and, of course,

$$\begin{aligned} n_{tbe} &= n_{tfe} \\ n_{cgbe} &= n_{cgfe} \\ \mathrm{Ln}(n_{tbe}/n_{cgbe}) &= \mathrm{Ln}(n_{tfe}/n_{cgfe}) = \mathrm{Ln}(k_2/k_1) \end{aligned}$$

The free energy is equal to

$$0.5RT \cdot \mathrm{Ln}(n_{tbe}/n_{cgbe}) + 0.5RT \cdot \mathrm{Ln}(n_{tfe}/n_{cgfe}) = RT \cdot \mathrm{Ln}(k_2/k_1) = 2\Delta_e$$

where R is the gas constant. In the equilibrium state the two types of units become indistinguishable; only non-isothermal kinetics will populate them distinctively.

A.2 Vertical Dual-Split Kinetics

Let us now consider the following modified system of equations, the "vertical Dual-Split statistics" system of equations, and comment on the assumptions made:

$$\begin{aligned} N_b &= n_{tb} + n_{cgb} \\ N_f &= n_{tf} + n_{cgf} \\ B_o &= (N_b + N_f) \end{aligned} \tag{5}$$

$$\begin{aligned} dn_{tb}/dt &= (dN_b/dt)/2 - k_1 \cdot n_{tb} + k_2 \cdot (N_b - n_{tb}) \\ dn_{tf}/dt &= (dN_F/dt)/2 - k_1 \cdot n_{tf} + k_2 \cdot (N_f - n_{tf}) \\ k_1 &= \upsilon_m \exp(-\Delta_1/T) \\ k_2 &= \upsilon_m \exp(-\Delta_2/T) \end{aligned} \tag{6}$$

(the gas constant R is equated to 1 here and from now on),

$$\begin{aligned} &\mathrm{Ln}(n_{tb}/n_{cgb}) + \mathrm{Ln}(n_{tf}/n_{cgf}) + \mathrm{Ln}(N_b/N_f) = 2\,\mathrm{Ln}(k_2/k_1) = 4\Delta_e/T \\ &q = dT/dt \quad \text{(under isothermal relaxation } q = 0) \end{aligned} \tag{7}$$

Note the presence of an additional term, $\mathrm{Ln}(N_b/N_f)$, in the expression of the free energy. This function is what we designate the "**dissipative term**."

EBSCOhost - printed on 2/13/2023 12:32 AM via . All use subject to https://www.ebsco.com/terms-of-use

Its introduction is fundamental in our work on interactions; it is the source of the originality of the new statistics and results in the study of a new generation of dynamics of open self-dissipative systems.

At equilibrium, $N_{be} = N_{Fe} = (B_o/2)$ and therefore $\mathrm{Ln}(N_b/N_f)$ is equal to zero.

Also note that in equation (6), another important modification of the original kinetic equations, which now includes an extra term, $(dN_b/dt)/2$ for the b conformers and $(dN_F/dt)/2$ for the F conformers. This term is introduced to make the different rates consistent with the belonging of the units into one single closed system. Hence, the presence of this term is not an assumption: it is a requirement.

When B_o is constant in equation (6), $(dN_F/dt)/2 = -(dN_b/dt)/2$.

There is no assumption in equations (5)–(7) regarding the variation of dN_b/dt and its temperature dependence: the solutions come directly from equations (5) to (7), as illustrated in Figure A.1 discussed in the next section. The coupling between energetic and kinetic constraints driving the new kinetic model is now apparent: the solutions for n_{tb}, n_{cgb}, n_{tf}, n_{cgf}, and N_b are not obtained from a simple kinetic assumption (the expression of the kinetic constants and the proportionality between rate and population concentration). There is a real coupling between the free energy constraint and the kinetic constraints. The condition regarding energy is nothing other than a minimal principle, since it is assumed that the free energy remains that of the equilibrium state at the corresponding temperature. In conventional kinetics a system always evolves towards its minimum free energy, and therefore the minimum value is given by the equilibrium value. In the Dual-Split Kinetics, the free energy remains equal to its equilibrium value when it evolves, which is a fundamental new assumption.

As we said at the beginning of this Appendix, we are not covering here the simulations of the influence of an external variable (voltage polarization field, mechanical shear stress, or pressure) on the parameters of dual-split equations. This is the object of a dedicated book in the works [137]. We discuss the case of an electrical field in some details in Chapter 3, Part I of this book.

A.3 Examples of simulation of the vertical Dual-Split Kinetics equations (5) to (7)

The solution of equations (5)–(7) is done by solving the system of equations numerically using a fifth-order Runge–Kutta algorithm.

A.3.1 Cooling simulation

Let us consider a system of $B_o = 1000$ units, with a statistics corresponding to the following parameters: $\Delta_e = 250$, $\Delta_m = 9250$, and $\upsilon_m = 10^{11}$. Recall that Δ_m is equal to $(\Delta_1 + \Delta_2)/2$ and Δ_e equal to $(\Delta_1 - \Delta_2)/2$. The system cools at a rate of $q = -1$ Kelvin per

EBSCOhost - printed on 2/13/2023 12:32 AM via . All use subject to https://www.ebsco.com/terms-of-use

second from an initial temperature $T_o = 400$ K. The system is assumed to be *initially* at equilibrium at that temperature, so $N_b = N_f = B_o/2$.

In Figure A.1, the rate of change of N_b, dN_b/dt, is plotted against cooling temperature. The rate does not remain equal to zero: the rate increases rapidly at first, goes through a maximum, and decreases back to zero at lower temperatures. Figure A.2 shows the variation of the dissipative term, $\mathrm{Ln}(N_b/N_f)$, which rises from its equilib-

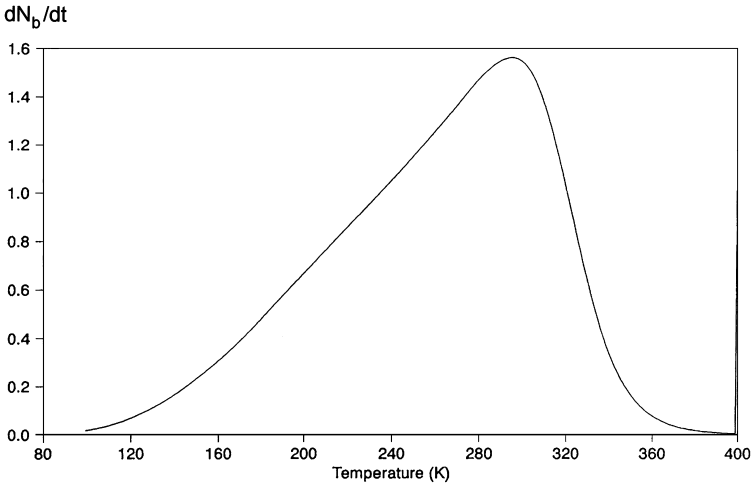


Figure A.1: Variation dN_b/dt during cooling ($q = -1$) $\Delta_m = 9250$, $\Delta_e = 250$, $u_m = 10^{11}$, $B_o = 1000$, $T = 400$ °K. The 1st peak observed (at ~300 °K) is influenced by the value of the pair (Δ_m, u_m), whereas the 2nd peak, only visible by a small hump at $T \sim 200$ °K in this figure, is the reflection of the value of Δ_e on the kinetics.

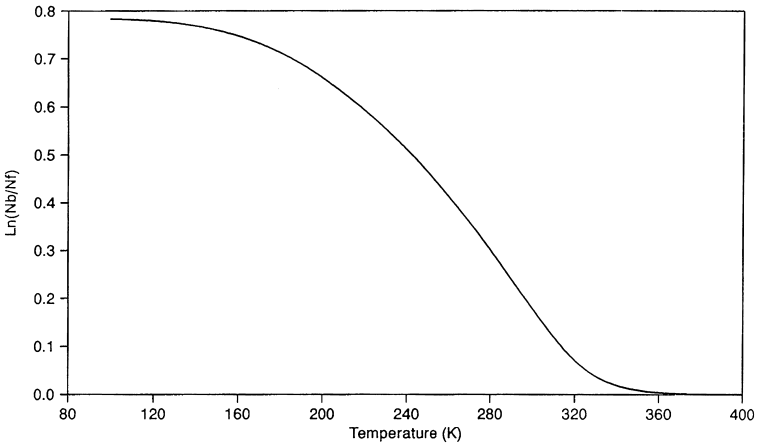


Figure A.2: Dual-Split Kinetics Simulation. Variation of dN_b/dt during cooling ($q = -1$). $\Delta_m = 9250$, $\Delta_e = 250$, $u_m = 10^{11}$, $B_o = 1000$, $T = 400$ °K.

EBSCOhost - printed on 2/13/2023 12:32 AM via . All use subject to https://www.ebsco.com/terms-of-use

rium value (0) to a plateau value at lower temperature. This figure clearly demonstrates that the minimal principle of the free energy implies a structuring of the b/F population as non-equilibrium triggered by cooling proceeds: cooling favors the production of b conformers. Conventional kinetics (equations (1)–(3)) also creates non-equilibrium values for the cg and t populations, but the interactive coupling between the b/F kinetics and the (c, g, t) kinetics in equations (5) to (7) generates significant large differences. The differences between the conventional kinetics ("classical") and the Dual-Split Kinetics (DSK) are illustrated in Figures A.3, A.4, and A.5.

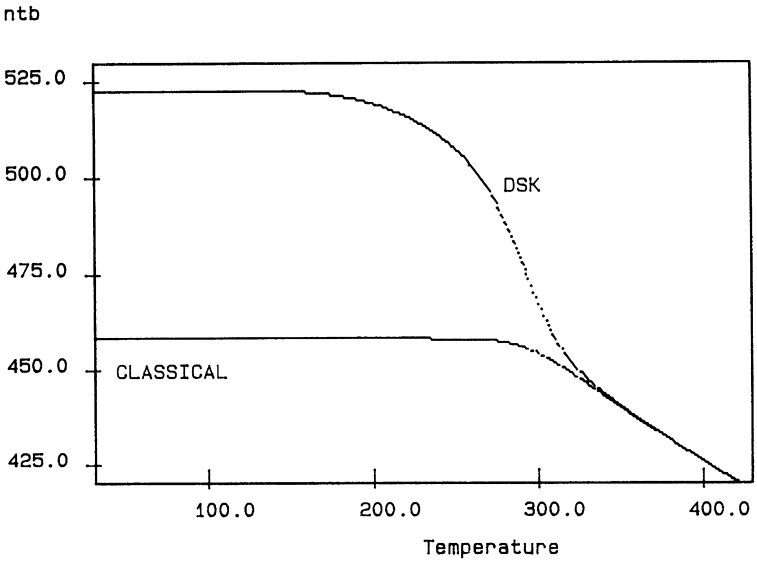


Figure A.3: Dual-Split Kinetics (cooling at $q = -1$): Compare the simulations of the Dual-Split Kinetics (DSK), in Eqs. (5)–(7), and of a CLASSICAL kinetics, in Eqs. (1)–(3), using the same parameters ($\Delta_m = 9250$, $\Delta_e = 250$, $\upsilon_m = 10^{11}$, $B_o = 1000$, $T = 400$ °K).

Figure A.3 is a plot of n_t and n_{tb} vs. temperature for a system of $B_o = 1{,}000$ conformers submitted either to the conditions of equations (1)–(3) for the classical kinetics or to equations (5)–(7) for the Dual-Split Kinetics ("DSK" in Figure A.3). The values of Δ_m, υ_m, and Δ_e are the same for both simulations, given in the captions of Figures A.1 and A.2. The cooling rate is also the same, $q = -1$ K/sec; n_t reaches a non-equilibrium plateau at a low temperature of 458.3, which is 22 % lower than the plateau value of n_{tb} (Figure A.3) and 45 % lower than the total plateau number of trans conformers $(n_{tb} + n_{tf})$ shown in Figure A.4. The modulated effect of dN_b/dt on the dynamics of n_{tb}, n_{tf}, n_{cgb}, and n_{cgf} is quite significant.

In Figure A.4, both n_{tb} and n_{tf} are plotted vs. T (n_{tb} is the top curve). One sees that the increase of the trans conformers is only favored in the b-state but actually decreases in the free volume interfacial tissue in the F state. The variation of n_{tF} (lower

EBSCOhost - printed on 2/13/2023 12:32 AM via . All use subject to https://www.ebsco.com/terms-of-use

curve of Figure A.4) suggests that the flexed conformations, the cis-gauche, are favored by the cooling process for the free volume conformers. As a result, the total trans population, $(n_{tb} + n_{tF})$, although we said is much larger than what classical kinetics could produce, plateaus at a low temperature to a value that is only 12% greater than the equilibrium value at $T_o = 400$ K.

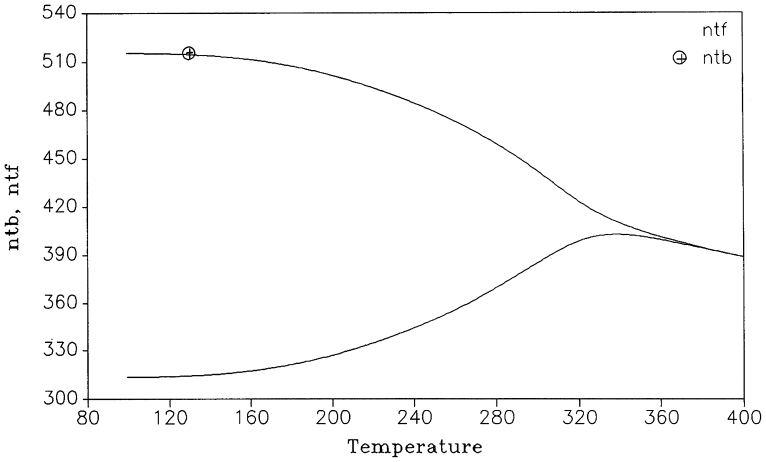


Figure A.4: Variation of the energetic kinetic variables n_{tb}, n_{tf} on cooling ($q = -1$). $\Delta_m = 9250$, $\Delta_e = 250$, $u_m = 10^{11}$.

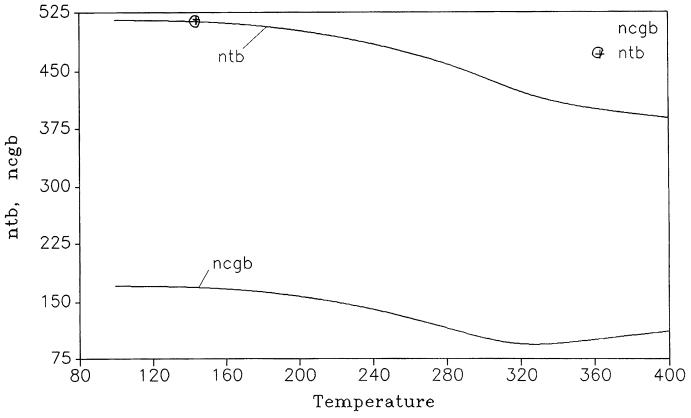


Figure A.5: Variation of n_{tb}, n_{cgb} on cooling. $\Delta_m = 9250$, $\Delta_e = 250$, $u_m = 10^{11}$.

The difference between the transient behavior for the n_{tb} and the n_{cgb} conformers during cooling is shown in Figure A.5. From $T = 400$ K down to 320 K, n_{cgb} decreases while n_{tb} rises towards a plateau; then, as T continues to decrease, n_{cgb} rises slightly

EBSCOhost - printed on 2/13/2023 12:32 AM via . All use subject to https://www.ebsco.com/terms-of-use

towards its own frozen plateau value. The sum $(n_{tb}+n_{cgb})$, which is equal to the total of b conformers, increases and plateaus off to 685, which is 49.6 % greater than the corresponding value obtained assuming classical kinetics $(n_t + n_{cg})$. Figures A.4 and A.5 provide and compare the populations at various "levels" and demonstrate that the kinetics of $(cg \leftrightarrow t)$ are coupled and modulated by the kinetics of $(b \leftrightarrow F)$ and vice versa.

In summary, the coupling of pure kinetic considerations with a minimal principle, resulting in the splitting of B_o into the b and F sub-sets, has a considerable effect on the kinetics of the transient dynamics and on the non-equilibrium values obtained at low temperature (by analogy with a glass, corresponding to the glassy state values). The b and F sub-systems are *conjugated open dissipative systems* because their individual total number of units is not a close set, but it varies with time. Only the number of units of the overall system, B_o, is closed. This Dual-Split Kinetics mode, the vertical structuring mode, gives rise to self-dissipative effects, quantified by the dissipative parameter $\mathrm{Ln}(N_b/N_f)$, which transcribes the departure from a pure equilibrium state. The minimum principle of the free energy establishes the value of the free energy at all times as that of equilibrium, yet pure equilibrium is obtained when the statistics of the populations are also at equilibrium.

Grain-Field Statistics is the study of all the possible ways that the interactions could organize to minimize the value of the dissipative factor. This gives rise to the concept of a dissipative wave and to the finding of other compensating modes of structuration such as the horizontal structuring mode described in Part B of this Appendix.

The energy equation, equation (7), breaks down the total value at equilibrium, $(4\Delta_e/T)$, into three components, I_b, I_F, and I_{ds}, which are defined in equation (8) and shown to all vary with time in Figure A.6:

$$\begin{aligned} I_b &= \mathrm{Ln}(n_{tb}/n_{cgb}) \\ I_F &= \mathrm{Ln}(n_{tf}/n_{cgf}) \\ I_{ds} &= \mathrm{Ln}(N_b/N_F) \end{aligned} \tag{8}$$

Figure A.6, a plot of these functions vs. $1000/T$, shows that, during cooling, I_F and I_b depart quickly from each other and from the equilibrium condition value (at the left of the plot) when the dissipative term, I_{ds}, sharply takes off after remaining zero until a certain temperature is reached (thus defining the equivalent of the T_{LL} temperature for the simulation – see Chapter 3 of Part I).

One also sees that, when plotted against $1/T$, both I_b and I_{ds} seem to rapidly level off and stay constant at lower temperatures, whereas I_F takes most of the value of the total energy and varies almost linearly with $1/T$, continuing the high temperature –equilibrium – trend.

EBSCOhost - printed on 2/13/2023 12:32 AM via . All use subject to https://www.ebsco.com/terms-of-use

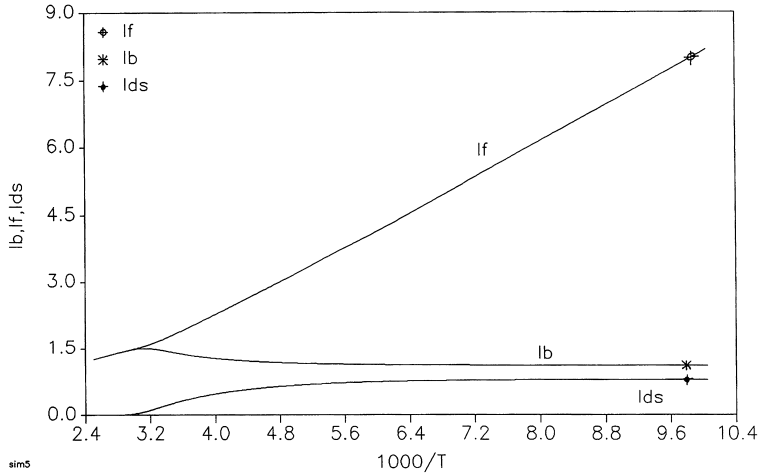


Figure A.6: Variation of I_b, I_f, I_{ds} with temperature (cooling curves).

A.3.2 Effect of cooling rate on the dynamics

The effect of cooling rate on the kinetics rate of dN_b/dt and on the "glassy" value of $N_b(t)$ found at low T are shown for three cooling rates ($q = -1, -10, -100$ K/s) in Figures A.7 and A.8.

In summary, the cooling rate, which is responsible for bringing the system out of equilibrium in the first place, modifies the kinetic and energy structuring, allowing dissipative effects to take place at higher temperature. By analogy, the same situation is observed for the glassification process from the liquid state across the glass transition temperature of materials.

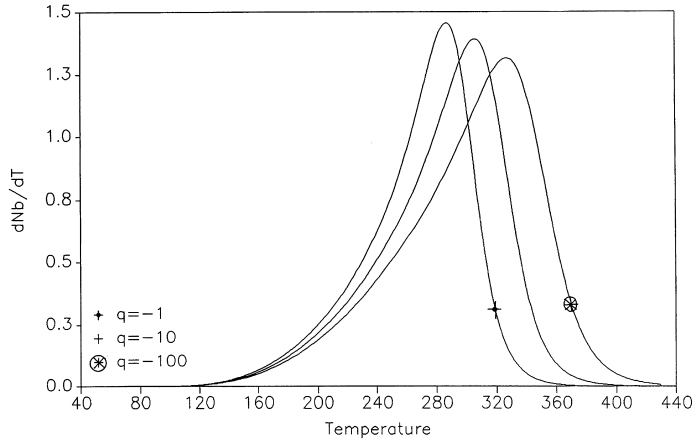


Figure A.7: Variation of dN_b/dT vs. T during cooling. Effect of cooling rate.

EBSCOhost - printed on 2/13/2023 12:32 AM via . All use subject to https://www.ebsco.com/terms-of-use

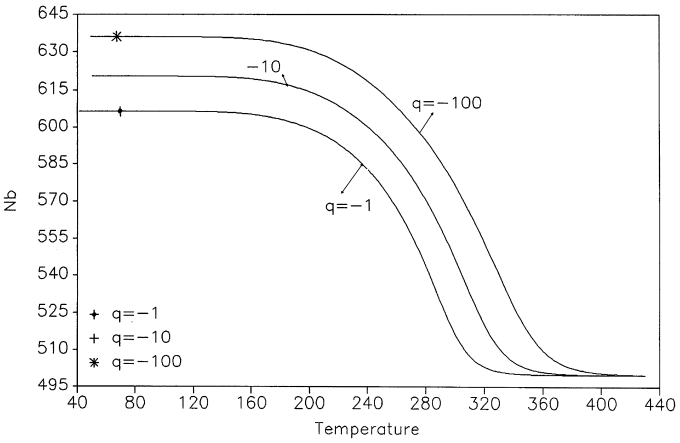


Figure A.8: Variation of N_b vs. T during cooling. Effect of cooling rate.

A.3.3 Heating at constant rate

Figures A.9 to A.11 provide plots of non-isothermal returns to equilibrium, and a comparison of the kinetic paths obtained during cooling and heating. In Figure A.9 the system is first cooled at constant rate (–1 K/sec) until a temperature of 100 K is reached. Taking the system variables at that temperature as initial conditions, the rate is reversed and one records the variation of N_b with temperature (Figure A.9), n_{tb} (Figure A.10), and their derivative (Figure A.11). It is clear that N_b behaves like n_{tb}, yet modulated, and one observes the classical undershoot on heating which is common to dynamic kinetic systems studied by thermal analysis (DSC traces for instance) [216].

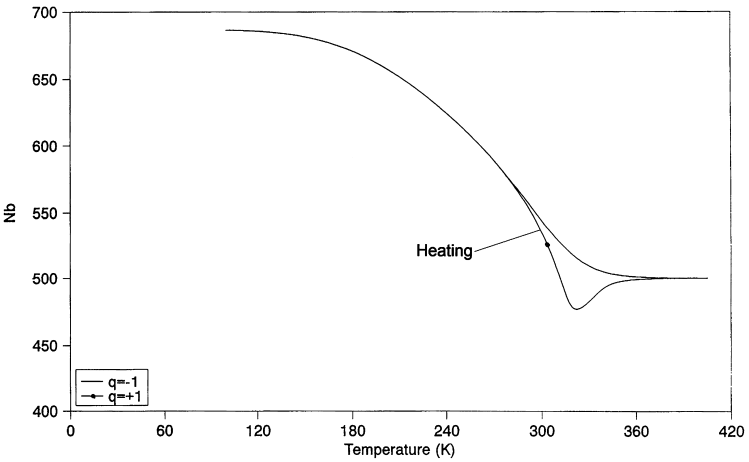


Figure A.9: Compare N_b during heating and cooling. $\Delta_m = 9250$, $\Delta_e = 250$, $u_m = 10^{11}$, $B_o = 1000$.

EBSCOhost - printed on 2/13/2023 12:32 AM via . All use subject to https://www.ebsco.com/terms-of-use

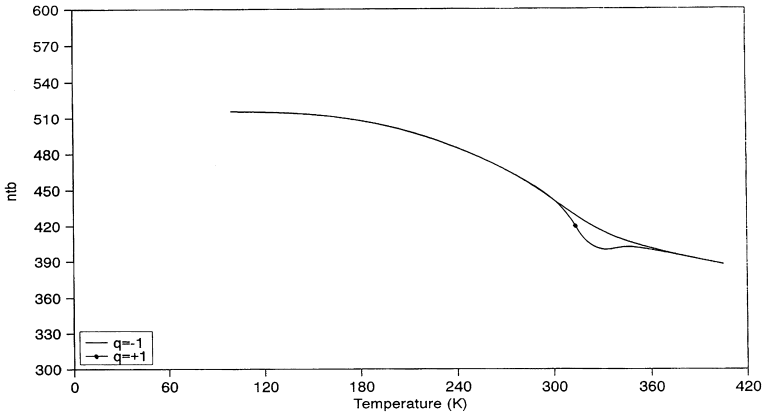


Figure A.10: Compare n_{tb} during heating and cooling. $\Delta_m = 9250$, $\Delta_e = 250$, $\upsilon_m = 10^{11}$, $B_o = 1000$.

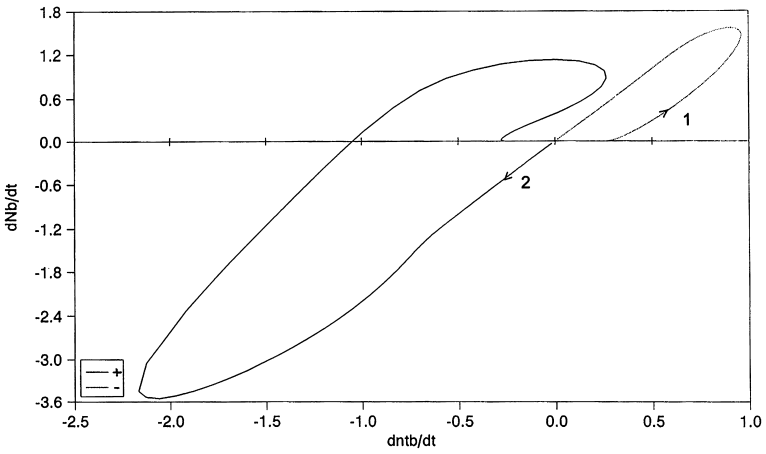


Figure A.11: Phase-plot dN_b/dt versus dn_{tb}/dt for a cooling step ($q = -1$) followed by a heating step ($q = +1$), both steps followed by the arrows 1 and 2 on the curve, respectfully. $\Delta_m = 9250$, $\Delta_e = 250$, $\upsilon_m = 10^{11}$, $B_o = 1000$, $T = 400$ °K.

It is difficult to decide whether the kinetics of N_b "drag" the kinetics of n_{tb} or vice versa. It is probably more appropriate to say that the two are interactively coupled in some recursive fashion and that this coupling is a feature that describes the properties of a self-dissipative system (see the next section on annealing).

Figure A.11 is a "phase-plot" of dN_b/dt vs. dn_{tb}/dt. We compare in this plot the cooling and heating cycles. Cooling corresponds to the loop on the right end side of the plot (designated by "1"). The small upward arrow follows the cooling pattern. In the first section of this loop, the plot is non-linear, due to the strong influence of the kinetic equations in equation (6) since the kinetic constants are not frozen in this temperature range. Also notice the value of dn_{tb}/dt at time $t = 0$: it does not seem to be zero. The

EBSCOhost - printed on 2/13/2023 12:32 AM via . All use subject to https://www.ebsco.com/terms-of-use

initial system was, however, at equilibrium ($dn_{tb}/dt = 0$), but it instantaneously jumps to the value 0.25, and as a result, the other values seem to emerge from this state. Once the top of the loop is passed, the two derivatives are proportional to one another: the energetic constraint, equation (7), now dominates the overall kinetics. Both rates converge towards zero as the temperature decreases.

Let us now turn to the heating loop, on the left of the plot (designated as "2"). The small downward arrow follows the heating path this time. The system starts to relax right away, dN_b/dt being proportional to dn_{tb}/dt. The system starts to imitate the process previously described for the cooling path, but in reverse. Actually, there is a large difference with the cooling path: the loop is much bigger, with almost double the magnitude for the maximum rates, as if the process was self-accelerating. The system finally undershoots, probably due to the excess of "speed" on its return to equilibrium, and closes in on a positive loop, which also exhibits a characteristic asymmetry with the cooling loop. We stipulate that this behavior is typical of a self-dissipative system.

A.3.4 Isothermal return to equilibrium (annealing)

This simulation consists of letting the system relax at a given temperature and study the kinetics of return to equilibrium. The initial state is taken from the cooling path (cooling rate –1 K/s for all curves), and the system is allowed to relax according to the same set of equations (5)–(7), except that $q = dT/dt$ is now zero.

Figure A.12 shows the variation of $N_b(t)$ with time for two temperatures of isothermal relaxation $T_1 = 313.90$ K and $T_2 = 305.51$ K. The figure demonstrates that N_b decreases back to the equilibrium value of $B_o/2$ in a "kinetically controlled" manner: the rate of change of N_b is dependent on the temperature of isothermal relaxation. Since there is no specific kinetic assumption regarding the variation of N_b, its temperature dependence should reveal the nature of the intercoupling between the kinetic and energetic constraints. Figures A.13 and A.14 cast some light on this issue.

The decay of $N_b(t)$, in Figure A.12, looks exponential, and, therefore, the first equation we try to fit the data with is a first-order kinetic expression of the form

$$dN_b/dt = k_x^1 \cdot N_b - k_x^2 \cdot N_F \tag{9}$$

where k_x^1 and k_x^2 would be kinetic constants. Equation (9) can be rewritten to graphically test its validity, so Figure A.13 plots $[(dN_b)/dt]/N_b$ vs. $(B_o - N_b)/N_b$, since $B_o = (N_b + N_f)$; one sees that for these two temperatures, equation (9) is only valid as we approach equilibrium, i. e., as dN_b/dt tends toward zero. In the near equilibrium zone (98 % to 100 %), we find that the first-order fit is excellent with $k_x^1 = k_x^2$ (0.009737 for $T = 305.90$ and 0.0216275 for $T = 313.90$). The fit gets non-linear below 96 %, as clearly observed in the figure and explained later.

EBSCOhost - printed on 2/13/2023 12:32 AM via . All use subject to https://www.ebsco.com/terms-of-use

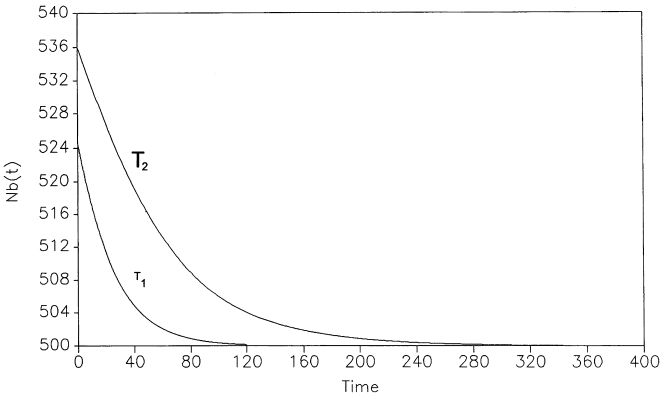


Figure A.12: Variation of $N_b(t)$ on annealing at two temperatures (T_1 = 313.90 K, T_2 = 305.51 K).

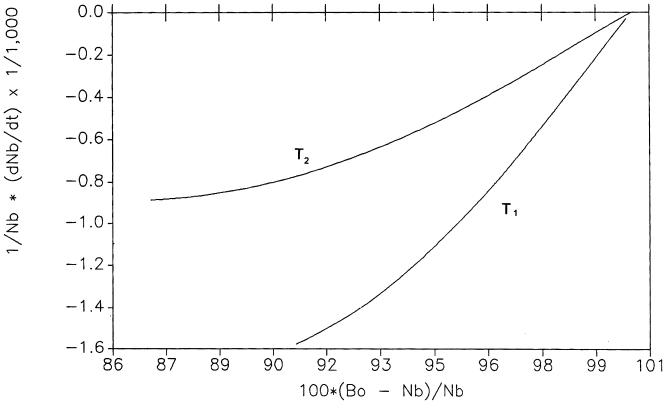


Figure A.13: Kinetics study for $N_b(t)$ on annealing at two temperatures (T_1 = 313.90 K, T_2 = 305.51 K).

Figure A.14 studies the return to equilibrium for n_{tb} at the temperature T_1 = 313.90 K. The graph is also not linear, showing non-linear kinetics. As we lower the temperature of relaxation, the non-linearity becomes predominant. But let us turn our attention to the region where first-order kinetics apply well to the description of the variation of $N_b(t)$. The situation is favorable as the temperature of relaxation is raised or as we study systems with smaller Δ_e values.

Let us call k_x the value of the kinetic constant found from a plot of N_b versus dN_b/d_t (Figure A.15) when $(dN_b/dt) \to 0$; k_x is the Dual-Split Kinetics constant, equal to k_x^1 and k_x^2 of equation (9):

$$(N_b - B_o/2) = -[1/(2 \cdot k_x)] \cdot dN_b/dt \tag{10}$$

By varying the temperature of relaxation and curve-fitting the N_b vs. dN_b/dt plots as $dN_b/dt \to 0$, we calculate k_x at several temperatures. Figure A.15 is a plot of $\mathrm{Ln}(k_x)$

EBSCOhost - printed on 2/13/2023 12:32 AM via . All use subject to https://www.ebsco.com/terms-of-use

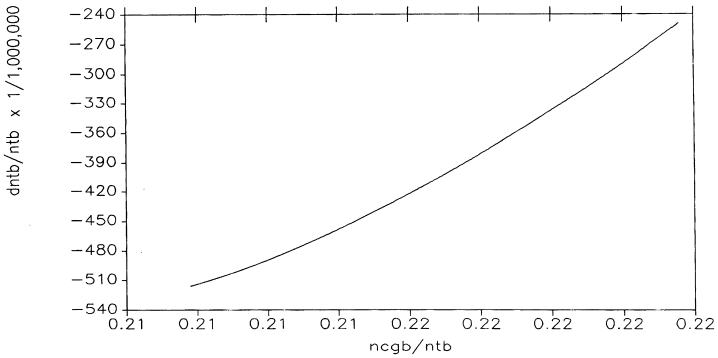


Figure A.14: Study of n_{tb} kinetics $\Delta_e = 250$, $\Delta_m = 9250$, $\upsilon_m = 10^{11}$. Annealing at $T = 313.896$ K.

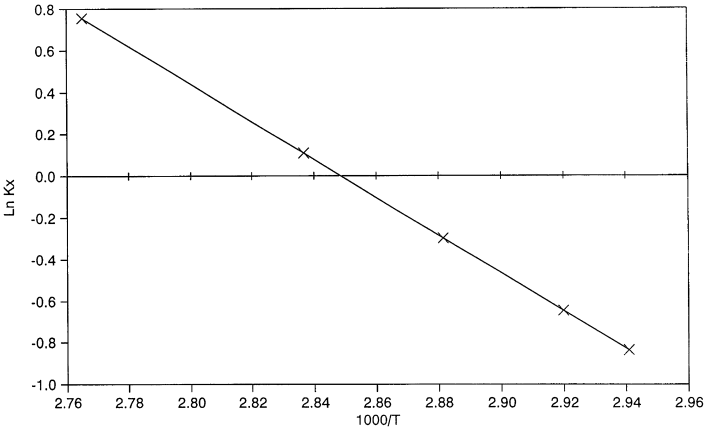


Figure A.15: Apahenius plot of Ln(k_x) vs. $1000/T$. $\Delta_m = 9250$, $\upsilon_m = 10^{11}$, $\Delta_e = 300$.

versus $1/T$ to attempt to fit the temperature dependence of k_x by an Arrhenius equation. *The plot is linear* with an activation energy Δ_x and a frequency front factor υ_x respectively equal to 9048.2 and 7.815×10^{10} ($r^2 = 0.999989$).

One can write

$$dN_b/dt = (B_o - 2N_b) \cdot \upsilon_x \exp(-\Delta_x/T) \tag{11}$$

The vertical Dual-Split Kinetic model produces a structuring of the total population of conformers which, as a result of non-equilibrium cooling, kinetically behaves like a rate process with activation energy and frequency front factor easily derivable, but *different* from the kinetic parameters of the main statistics. Note that υ_x and Δ_x are not equal to the parameters of the kinetic constants, either υ_m or Δ_m. It is interesting that the frequency front factor is found different from the main kinetics' υ_m. The coupling between kinetic and energetic constraints literally generates a cross-dynamic

EBSCOhost - printed on 2/13/2023 12:32 AM via . All use subject to https://www.ebsco.com/terms-of-use

partition: the "dissipative partition" between the F conformer types and the b conformer types which varies in a kinetically controlled manner, just as the kinetics between the cg conformer types and the t conformer types, albeit with a different set of kinetic constants. The auto-catalytic effect observed for the kinetics is due to the self-generated split of the conformers into the b and F types. A thermally activated transition between a "t" and a "cg" conformation, described by Δ_m, υ_m, and Δ_e, cannot occur without a change between the F and b populations, and the statistics b/F is itself thermally activated with an activation energy, Δ_x, and a frequency front factor, υ_x, generated by and coupled with the activation energy, Δ_m, and the frequency front factor, υ_m, that characterize the $t \leftrightarrow cg$ conformational transition. This defines and describes the duality characteristics of the conformers submitted to coupled *intra- and intermolecular* interactions.

When this vertical Dual-Split statistics is applied to real time-dependent relaxation phenomena (say the relaxation of dipoles below or above the glass transition temperature of polymeric materials), the question to raise is whether the kinetic response observed corresponds to the "Δ_m, υ_m" kinetics, from which one can derive the Dual-Split Kinetics parameters; the "by-product" kinetics (Δ_x, υ_x), which seems to be a self-created image of the inner mechanism; or a combination of both. In other words, are we dealing with the $F \leftrightarrow b$ kinetics, the $t \leftrightarrow cg$ kinetics, or both? If what we measure is υ_x and Δ_x, then we need to find a correlation between these variables to obtain the real kinetic constants υ_m and Δ_m. The search of this correlation is essentially the objective of Chapter 3 of Part I of this book. We show in Part I, Chapter 3 that a change of the value of Δ_e, keeping υ_m and Δ_m constant, results in a compensation between the corresponding variation of Δ_x and $\ln(\upsilon_x)$. See Figure 3.3 of Part I. This is also expanded in Chapter 2 of reference [138]. This compensation means that the $\mathrm{Ln}(k_x)$ vs. $1/T$ Arrhenius lines compensate when Δ_e varies. This situation is similar to the compensation of the $-\log \tau_o$ vs. $1/T$ lines in the Arrhenius plane when T_p varies.

As explained in Chapter 3, Part I, this is a key result for the comprehension of interactive coupling between the conformers and the use of the compensation phenomenon to characterize it by TWD.

Many classically incomprehensible features observed in this book, such as the differences between the positive and negative compensations across T_g or the existence of a converging network of super-compensation lines in the relaxation maps of mechanically treated amorphous samples (PS), submitted to vibration during their cooling from the melt (Figures 4.17 to 4.19 of Part II), can be qualitatively understood from the normalized plots of $(\mathrm{Ln}(\upsilon_x) - \mathrm{Ln}(\upsilon_m))$ vs. $(\Delta H_x - \Delta H_m)$ obtained at various values of Δ_e, as illustrated in Chapter 3 (Figure 3.7) of Part I, for instance.

In summary, simple relationships between $\mathrm{Ln}\,\upsilon_x$, Δ_x, and Δ_e exist which are revealed by varying Δ_e in equations (5) to (7). The vertical splitting kinetics is, on its own, powerful enough to simulate the effect of activating the dipoles (permanent and/or induced) at the polarizing temperature T_p and observing its thermally activated depolarization as a Debye current.

EBSCOhost - printed on 2/13/2023 12:32 AM via . All use subject to https://www.ebsco.com/terms-of-use

As further explicated in reference [137], the conclusions drawn from using the vertical Dual-Split statistics appear to be applicable to the understanding of other results obtained by other authors in other disciplines of physics or physical chemistry (e. g., [214]).

In Part B of this Appendix, we provide a short presentation of "horizontal splitting," which is an alternative solution to the problem of minimization of the free energy, leading to a different structuring process. This will allow the reader to decide whether compensation laws, observed when dipoles relax, are due to a modification of the energy gap Δ_e in the Dual-Split Kinetics model, or due to the structuring of the free energy into cloning systems, or perhaps both. For the Dual-Split Kinetics, the energy gap Δ_e could vary, either because of a distribution of Δ_e due to the several isomeric states, or perhaps because of the influence of the voltage field at T_p on the value of Δ_e.

Part B. Horizontal splitting of B_o: creation of $N_s(t)$ energetic kinetic systems

There are many variations concerning "horizontal splitting" (Chapter 5 of [137]). We provide below the simplest one.

Let us consider the following set of differential equations and apply the principle of minimum free energy to it:

$$dn_t/dt = \delta_k \cdot (dB_{os}/dt) - (k_1 + k_2) \cdot n_t + k_2 \cdot B_{os} \tag{12}$$

$B_{os} = B_o/N_s$

$I_s = RT \cdot \mathrm{Ln}(n_t/(B_{os} - n_t))$

$N_s \cdot I_s = RT \cdot \mathrm{Ln}(k_1/k_2) = N_{se} \cdot 2\Delta_e$, i. e., the equilibrium value at T

B_o = total number of units for the statistics

$k_1 = \upsilon_m \exp(-\Delta_1/RT)$ and $k_2 = \upsilon_m \exp(-\Delta_2/RT)$

υ_m is the frequency front factor, R is the gas constant

$q = dT/dt$, and

δ_k is the Kronecker number, either 0 or 1. In this book, $\delta_k = 0$

In this option of the structuration of the interactions by the Grain-Field Statistics, the free energy still remains equal to the equilibrium value at the same temperature (basic principle of the model), but it is allowed to subdivide into $N_s(t)$ *identical* "energetic kinetic systems" (EKS). The total number of units in the statistics, B_o, therefore subdivides into $B_{os} = (B_o/N_s)$ units for each system. The splitting is called "horizontal" because in this option of the splitting process, splitting does not require, unlike for vertical splitting, a dissipative function that compensates for the split. The reason is simple: in vertical splitting, more statistical states are created, and this is not the case

EBSCOhost - printed on 2/13/2023 12:32 AM via . All use subject to https://www.ebsco.com/terms-of-use

in horizontal splitting. Horizontal splitting creates more *identical* statistical sets, with no vertical splitting occurring, i. e., no sub-sets (N_b and N_F) like for vertical splitting. We have speculated that because of that fundamental difference, horizontal splitting does not require a dissipative term. We will study in Part C of this Appendix a hybrid solution that combines the requirements of vertical and horizontal splitting.

The total free energy is simply the free energy of each EKS times the number of EKS. This is the case for homogeneous fields in thermodynamics: the property of the whole system is described by the property of its identical constituents scaled up by the number of constituents. The scaling variable here is $N_s(t)$, and its value is determined by solving equation (12); no further kinetic or energetic assumption is needed except the equilibrium value at higher temperature prior to cooling.

B.1 Computer simulations

Note that the simulations illustrated in the figures in this section are functions of the initial conditions; the initial state of the variables is designated by either the subscript "o" or the subscript "A" in the figures.

B.1.1 Cooling

Figure B.1 plots the number of EKS as we simulate cooling at a very fast rate, $q = -1000$ K/sec, from a temperature $T_o = 400$ K. The initial value for N_s (N_{so} at $t = 0$) is equal to the assumed equilibrium value $N_{se} = 1$ (we also assume that the equilibrium value is not temperature-dependent). The kinetic parameters are $\upsilon_m = 10^{11}$, $\Delta_m = 8250$, $\Delta_e = -250$, $N_{se} = 1$. The total number of conformers is $B_o = 1{,}000$. One sees that as soon as cooling starts, the free energy subdivides into $N_s(t)$ EKS. The number of systems, in this case, rapidly reaches a plateau value ($N_s = 15$), which remains fairly constant all the way down to lower temperatures.

In Figures B.2 to B.4 we present various cooling patterns which are functions of the cooling rate q, the initial temperature T_o, the total number of conformers B_o, the initial value of N_s, the equilibrium value of N_{se}, and of course the kinetic parameters υ_m, Δ_m, and Δ_e. For instance, in Figure B.2, $T_o = 300$ K, $B_o = 1{,}000{,}000$, $N_{so}(t = 0) = N_{se} = 10$, $q = -0.1$, and $\upsilon_m = 10^{11}$, $\Delta_m = 9250$, $\Delta_e = -250$. In this case, the number of systems rises very quickly, seemingly towards an asymptotic value for $T = 264$ K or so. Since the product of energy of a system and the number of systems is finite (constant in this simulation), it must be that the free energy of the individual systems, $I_s = RT \cdot \mathrm{Ln}(n_t/(B_{os} - n_t))$, goes towards zero, a situation which occurs for $n_t = (B_{os} - n_t)$. In Figure B.3 the total number of conformers in the statistics is 1,000. But the other parameters are those of Figure B.2. Figure B.4 is a plot of $N_s(t)$ versus cooling time for a system cooled at –1000 K/sec with $\upsilon_m = 10^{11}$, $\Delta_m = 11{,}250$, $\Delta_e = -250$, $N_{se} = 10$.

EBSCOhost - printed on 2/13/2023 12:32 AM via . All use subject to https://www.ebsco.com/terms-of-use

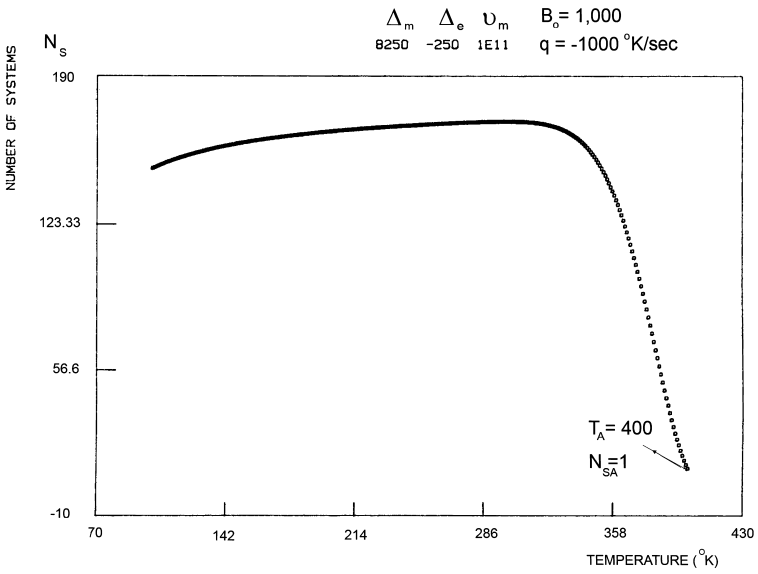


Figure B.1: Horizontal structuring simulation. Variation of the number of energetic kinetic systems, N_S, on COOLING, submitted to Dual-Phase parameters and cooling conditions expressed in the header. See text.

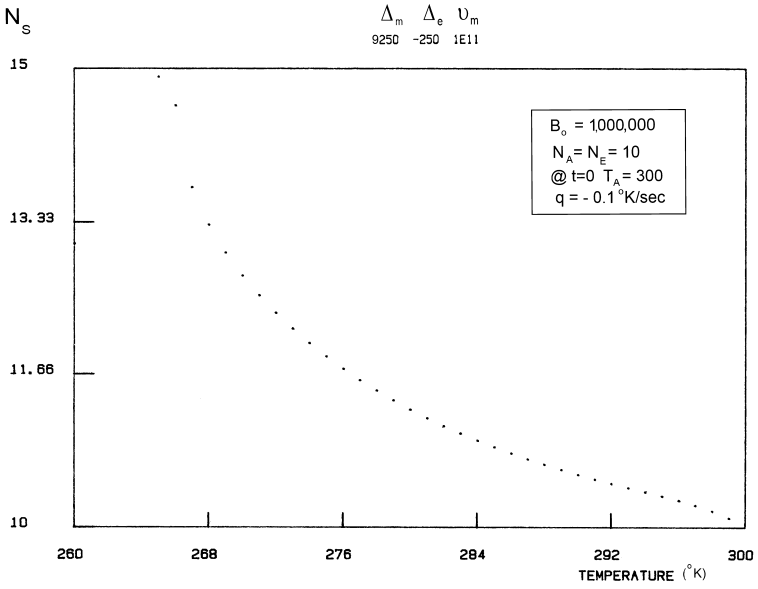


Figure B.2: Horizontal structuring simulation. Same as in Figure B.1 submitted to a different set of Dual-Phase parameters ($\Delta_m = 9250$, $B_o = 1{,}000.000$) and cooling conditions (T_A, N_A, q) expressed in the header. See text.

EBSCOhost - printed on 2/13/2023 12:32 AM via . All use subject to https://www.ebsco.com/terms-of-use

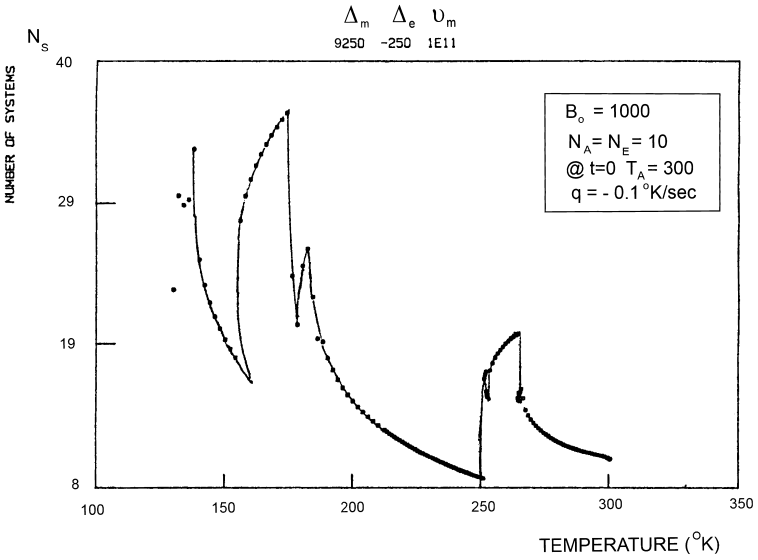


Figure B.3: Horizontal structuring simulation. Same as in Figure B.1 submitted to the same Dual-Phase parameters yet different cooling conditions (T_A, q) expressed in the header. See text.

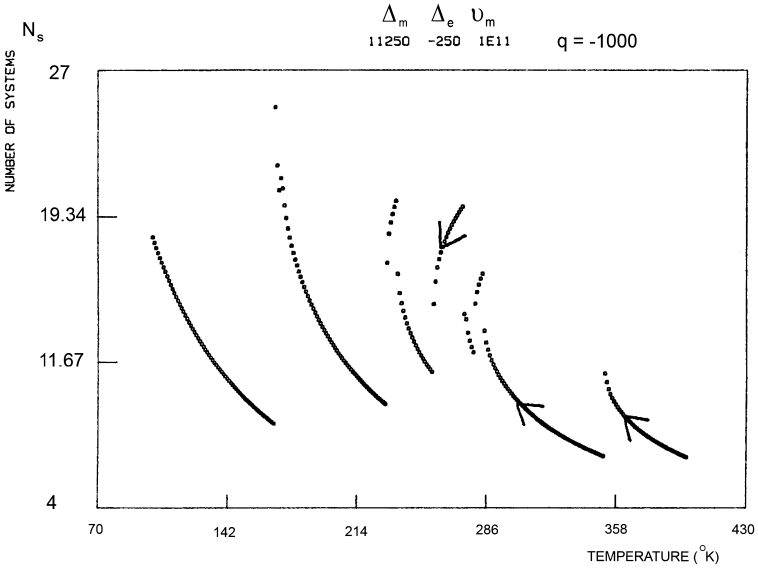


Figure B.4: Horizontal structuring simulation. Variation of the number of energetic kinetic systems, N_S, on COOLING, submitted to a different Δ_m (11,250) Dual-Phase parameter yet the same cooling conditions expressed in the header. See text.

EBSCOhost - printed on 2/13/2023 12:32 AM via . All use subject to https://www.ebsco.com/terms-of-use

It is seen in the last two figures that the number of EKS increases as temperature decreases and that it goes through sudden "discontinuities," although the total free energy remains a monotonous continuous function of temperature across these apparent "jumps" of $N_s(t)$. Notice that the jumps occur either as the number of systems $N_s(t)$ increases or decreases. This is represented by upward or downward arrows in Figure B.4. The apparent chaos observed on cooling might be explained by a combination of things: the algorithm used to solve equation (12) and the influence of the initial value of (T_o, N_{so}) on the cooling pattern. As said before, the tendency towards asymptotic $N_s(t)$ values comes from $n_t = (B_{os} - n_t)$, which can occur for several couples of n_t and B_{os}.

The solutions obtained in Figures B.3 and B.4 are not Runge-Kutta solutions, to avoid that the computer gets stuck in stiffness problems: when we use for the simulation a fifth-order "intelligent" Runge-Kutta algorithm, which automatically adjusts the time step to the stiffness of the solution, the step for the numerical integration becomes extremely small when the solution approaches an asymptotic value, resulting in the impossibility to cross "transitions." When a simpler first-order approach is used (based on the Newtonian approximation of the derivative), the accuracy depends on the choice of the fixed numerical step, but transitions can be crossed, as demonstrated in Figures B.3 and B.4. However, the point just after the transition depends on the tolerance and step size chosen. We might as well consider the solution beyond the transition as a cooling path started from a different initial condition of T_o and N_{so}, showing that it influences the variation of $N_s(t)$ either towards an increase or decrease.

In summary, depending on the cooling rate, the values of Δ_m, υ_m, and Δ_e, the initial temperature, the initial condition, and the size of the statistics, one can generate a very different energetic kinetic structure for the free energy.

B.1.2 Heating

Figure B.5 compares $N_s(t)$ vs. T curves obtained on cooling or heating. The system is first cooled from $T = 300$ K until the number of systems reaches approximately $N_s = 12$. It is then heated at the same rate $q = 0.1$. Figure B.5 displays a strong hysteresis effect, with an undershoot below the value of N_{se} and a gradual return to equilibrium thereafter. For other systems heated up from low temperature, the same behavior observed during cooling takes place, showing many "discontinuities" all the way (figure not shown). A study of the isothermal return to equilibrium allows us to understand the kinetics underlying the variation of N_s and therefore of I_s.

EBSCOhost - printed on 2/13/2023 12:32 AM via . All use subject to https://www.ebsco.com/terms-of-use

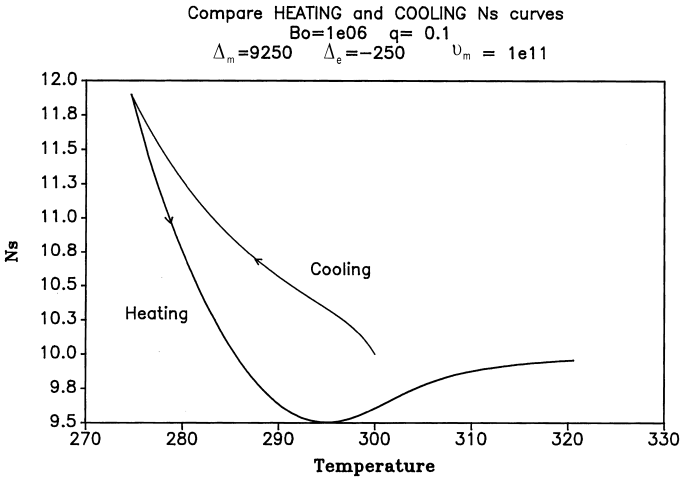


Figure B.5: Horizontal structuring simulation. Compare the effect of cooling and heating on the variation of the number of energetic kinetic systems, N_s, submitted to Dual-Phase parameters and the same heating cooling rate, both expressed in the header. See text.

B.1.3 Isothermal annealing

One can try to see if the horizontal splitting kinetics (the variation of $N_s(t)$) can be curve-fitted with a kinetic equation, as is done for the Dual-Split Kinetics.

The variation of $N_s(t)$ with time upon annealing at $T = 305$ K for ($\upsilon_m = 10^{11}$, $\Delta_m = 9{,}250$, $\Delta_e = -250$, $N_{se} = 10$, $N_{so} = 1$) is shown in Figure B.6. One sees that equation (12) behaves like a spring, i. e., N_s rushes back to its equilibrium value (here 10), when it is departed from it. The kinetics of return to equilibrium are best analyzed by plotting the derivative against the spread $(N_s - N_{se})$. This is shown in Figure B.7. The slope of the plot at $(N_s - N_{se}) \to 0$ provides the kinetic constant for a first-order kinetic curve-fit. The same thing can be accomplished for the kinetics of n_t, which is influenced by the kinetics of N_s, and this is shown in Figure B.8.

The isothermal return to equilibrium for several temperatures, $T = 285$, 290, and 300 K, is compared in Figure B.9. The higher the temperature, the faster the return to equilibrium, as expected. Table B.1 and Figure B.10 summarize the kinetic analysis. The figure plots the Log of the kinetic constant k_x against $1/T$. Each value of k_x is the slope of n_t vs. (dn_t/dt) at $n_t \to n_{te}$. The plot is linear, and from its slope and intercept one can define an activation energy and a frequency front factor. We find $\Delta_x = 9426.1$ and $\upsilon_x = 1.333 \times 10^{12}$. Interestingly, we find values for Δ_x and υ_x which are *larger* than Δ_m and υ_m, whereas the vertical Dual-Split Kinetics gave *smaller* values. The same analysis can be performed on $N_s(t)$, yielding another Arrhenius straight line, from which we can extract another activation energy Δ'_x and frequency front factor υ'_x. The kinetics of n_t are modulated by the variation of $N_s(t)$, thus the population of the two levels assumes a dynamic statistics which strongly differs from classical kinetics.

EBSCOhost - printed on 2/13/2023 12:32 AM via . All use subject to https://www.ebsco.com/terms-of-use

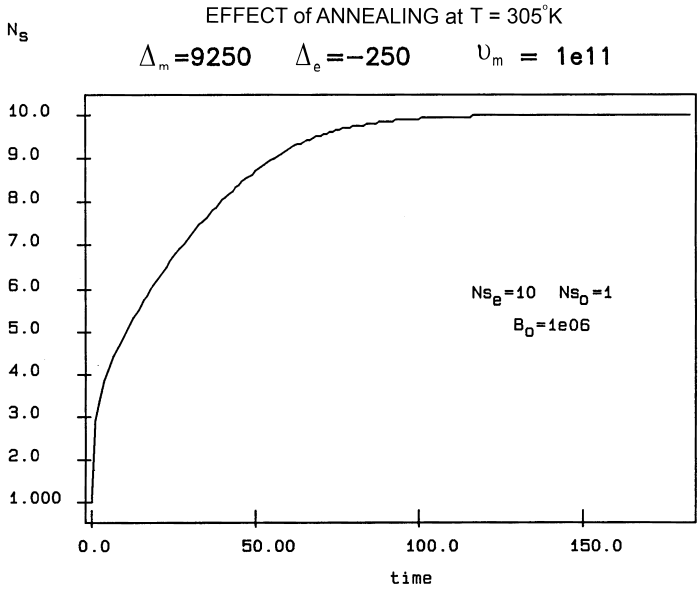


Figure B.6: Horizontal structuring simulation. Variation of the number of energetic kinetic systems, N_s, while ANNEALING at $T = 305$ °K to trigger the return to equilibrium. The Dual-Phase parameters and simulation conditions are given in the header and the figure.

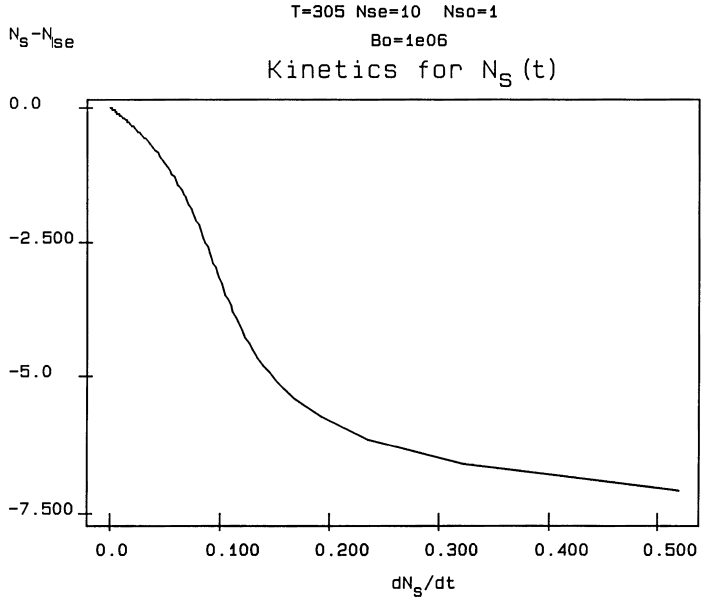


Figure B.7: Horizontal structuring simulation. Phase plot of $(N_s - N_{se})$ vs. dN_s/dt to study the kinetics of N_s during ANNEALING at $T = 305$ °K to trigger the return to equilibrium. The Dual-Phase parameters and simulation conditions are the same as in Figure B.6.

EBSCOhost - printed on 2/13/2023 12:32 AM via . All use subject to https://www.ebsco.com/terms-of-use

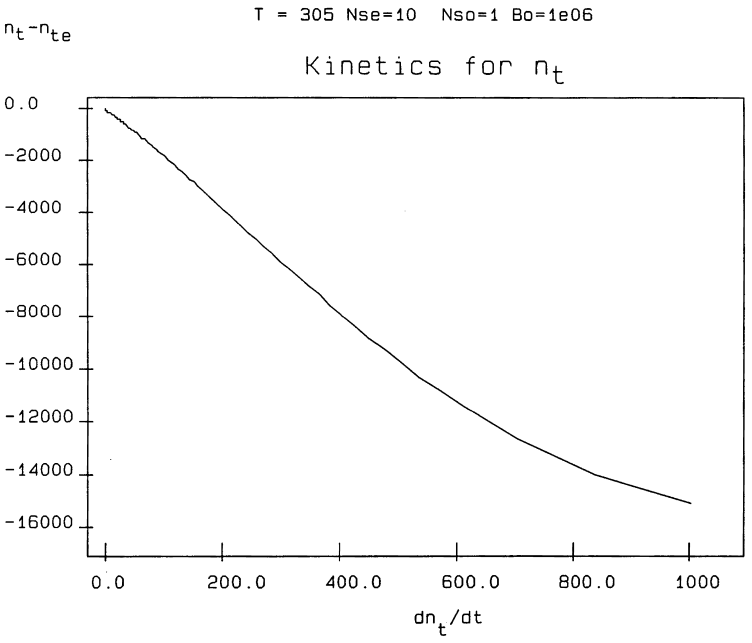


Figure B.8: Horizontal structuring simulation. Phase plot of $(n_t - n_{te})$ vs. dn_t/dt to study the kinetics of n_t during ANNEALING at $T = 305$ °K to trigger the return to equilibrium. The Dual-Phase parameters and simulation conditions are the same as in Figure B.6.

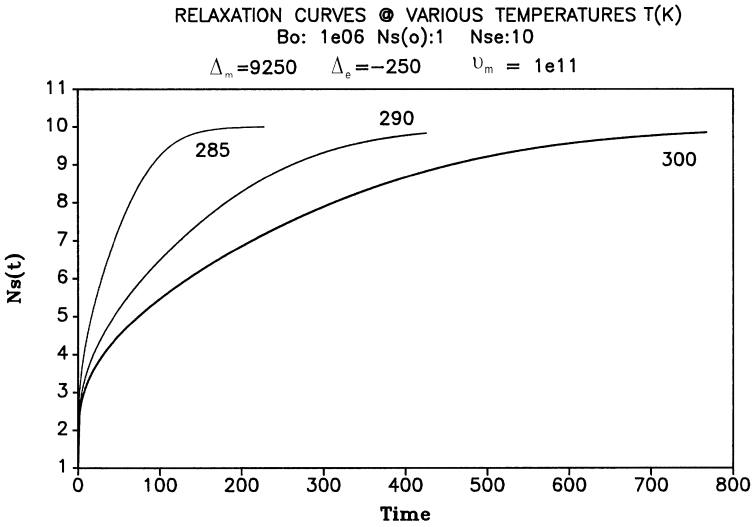


Figure B.9: Horizontal structuring simulation. Kinetics of the return to equilibrium for $N_s(t)$ at 3 different annealing temperatures. The Dual-Phase parameters and simulation conditions are the same as in Figure B.6 except for the temperature.

EBSCOhost - printed on 2/13/2023 12:32 AM via . All use subject to https://www.ebsco.com/terms-of-use

Table B.1: Isothermal study of n_t vs. dn_t/dt near equilibrium ($n_t \rightarrow n_{te}$). $\Delta_m = 9250$, $\Delta_e = -250$, $\upsilon_m = 10^{11}$.

T	$k = n_t/(dn_t/dt)$	r^2	Ln $-k$	$1000/T$
285.000000000	−172.840800000	0.999690000	5.152370940	3.508771930
290.000000000	−97.930851000	0.999580000	4.584261628	3.448275862
300.000000000	−34.204506000	0.999940000	3.532357390	3.333333333
305.000000000	−19.376358000	0.998520000	2.964053663	3.278688525
315.000000000	−7.325495400	0.998570000	1.991360784	3.174603175
325.000000000	−2.992149300	0.999240000	1.095991959	3.076923077

N_{so} is smaller than 14

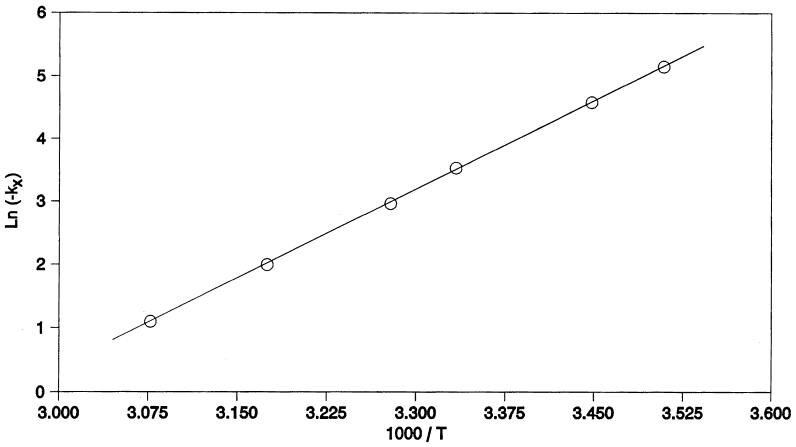


Figure B.10: Horizontal structuring simulation. Analysis of the kinetics of $N_s(t)$ when $N_{so} < 14$ (return to the 1st attractor). Ln $(-k_x)$ vs. $1000/T$. Kinetic study for n_t. $N_{se} = 10$, N_{so} lower than 14.

B.1.4 Influence of the initial number of systems N_{so}

Figures B.11 to B.13 simulate the isothermal returns at a same temperature, $T = 300$, for various initial N_{so} values, 13 (Figure B.11), 14 (Figure B.12), or 20 (Figure B.13). The equilibrium value is the same for all, $N_{se} = 10$, which is also the value in Figure B.6. Also identical are the kinetic parameters: $\upsilon_m = 10^{11}$, $\Delta_m = 9{,}250$, $\Delta_e = -250$. While the case of $N_{so} = 13$ results in a "normal" return to the equilibrium value $N_{se} = 10$, the other figures show N_s to increase with time until it becomes equal to the total number of B_o conformers (Figure B.13)!

The kinetics for that particular situation ("return to new attractor") is displayed in Figure B.14, as a plot of dN_s/dt against N_s. This phase-plot is linear. The kinetics for n_t is shown at Figure B.15.

EBSCOhost - printed on 2/13/2023 12:32 AM via . All use subject to https://www.ebsco.com/terms-of-use

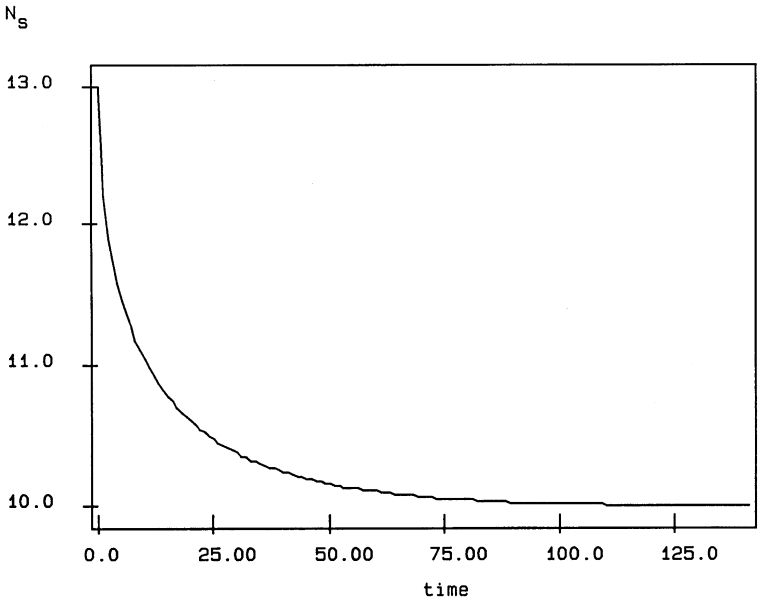


Figure B.11: Horizontal structuring simulation. Kinetics of $N_s(t)$ when $N_{so} = 13$ (< 14). Note that the return to the attractor is a decay function. $B_o = 10^6$, $T = 300$, $N_{se} = 10$, $N_{so} = 13$.

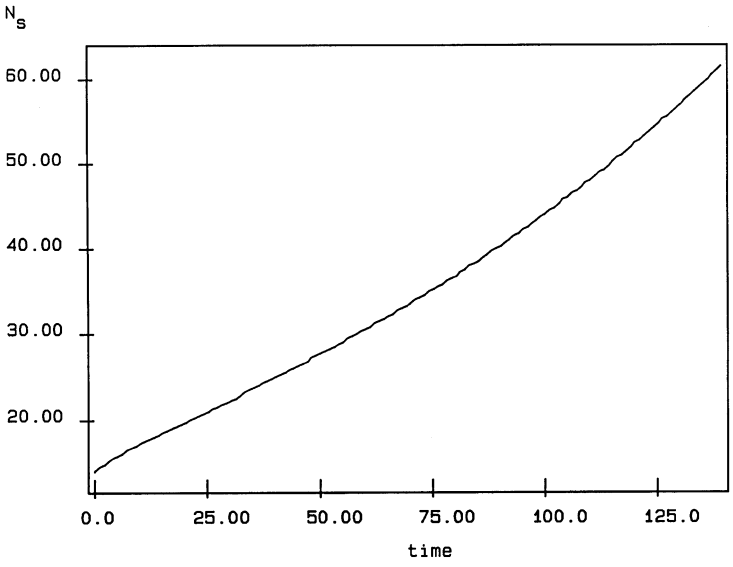


Figure B.12: Horizontal structuring simulation. Kinetics of $N_s(t)$ when $N_{so} = 14$. Note that the variation is now an increase, not a decay. $N_{se} = 10$, $N_{so} = 14$, $B_o = 10^6$, $T = 300$.

EBSCOhost - printed on 2/13/2023 12:32 AM via . All use subject to https://www.ebsco.com/terms-of-use

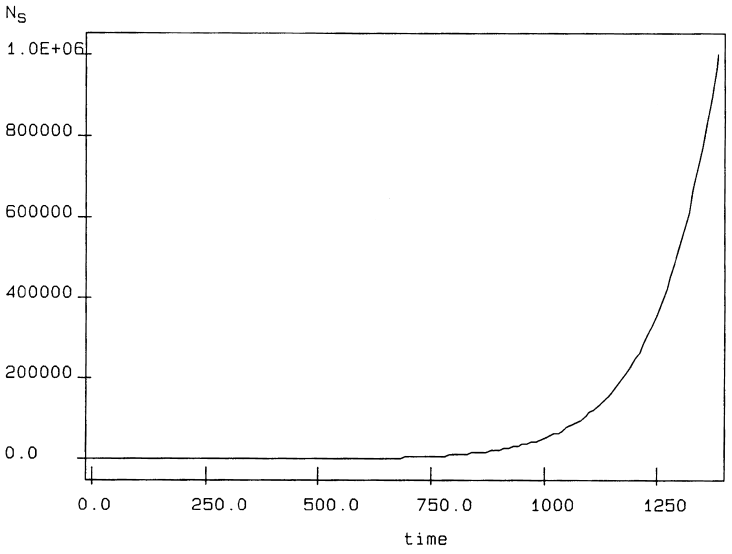


Figure B.13: Horizontal structuring simulation. Kinetics of $N_s(t)$ when $N_{so} = 20$ (>14). The system exponentially returns to a 2nd attractor ($N_{se2} = B_o$), not the initial equilibrium value. $\Delta_m = 9250$, $\Delta_e = -250$, $\upsilon_m = 10^{11}$, $B_o = 10^6$, $N_{se} = 10$, $N_{so} = 20$, $T = 300$.

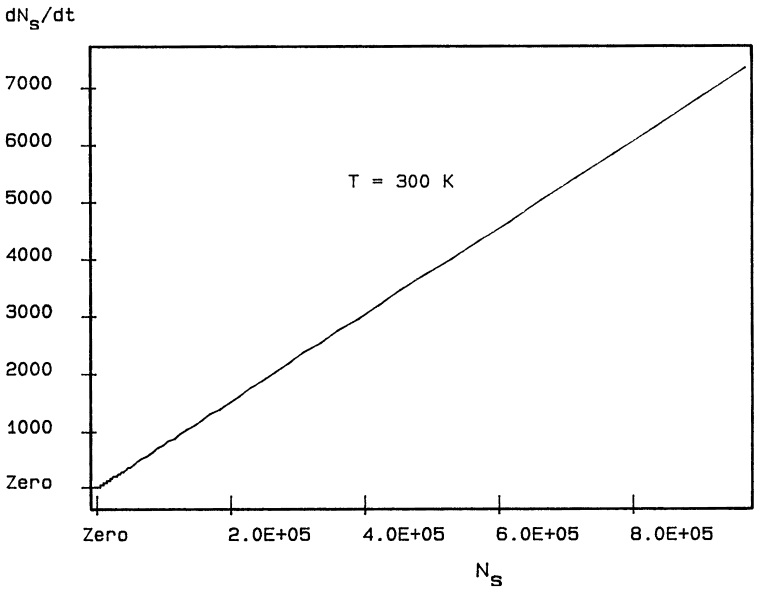


Figure B.14: Horizontal structuring simulation. Analysis of the kinetics of the return to the 2nd attractor for $N_{so} = 20$ (phase-plot). The straight line implies an exponential function for $N_s(t)$. Return to NEW ATTRACTOR. $B_o = 10^6$, $N_{so} = 20$, $N_{se} = 10$.

EBSCOhost - printed on 2/13/2023 12:32 AM via . All use subject to https://www.ebsco.com/terms-of-use

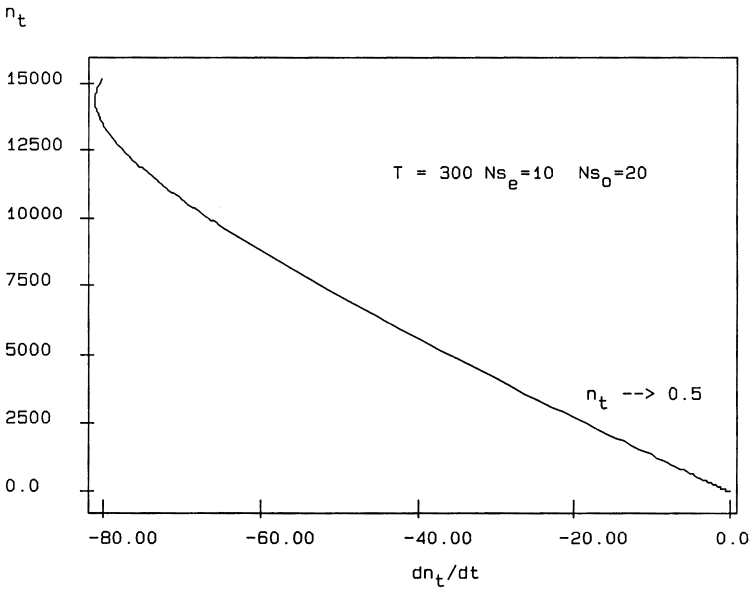


Figure B.15: Horizontal structuring simulation. Analysis of the kinetics for $n_t(t)$ with a new attractor $n_{te} = 0.5$. Return to NEW ATTRACTOR. Study of n_t kinetics.

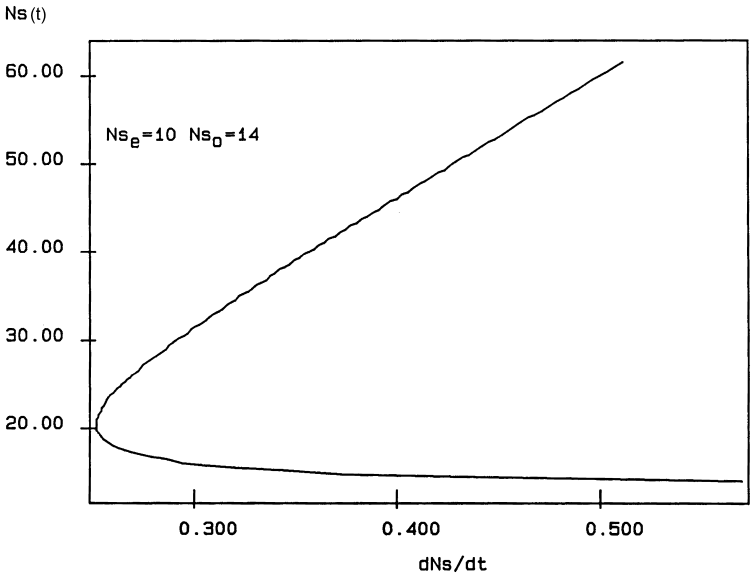


Figure B.16: Horizontal structuring simulation. Phase-plot to analyze the kinetics of $N_s(t)$ in Figure B.12. $T = 300$. Kinetics for $N_s(t)$, $N_{so} = 14$.

In the case of $N_{so} = 14$ (Figure B.16), the rate decreases at first, passes through a minimum for $N_s = 21$, and then increases exponentially with time. $N_{so} = 14$ seems to be

EBSCOhost - printed on 2/13/2023 12:32 AM via . All use subject to https://www.ebsco.com/terms-of-use

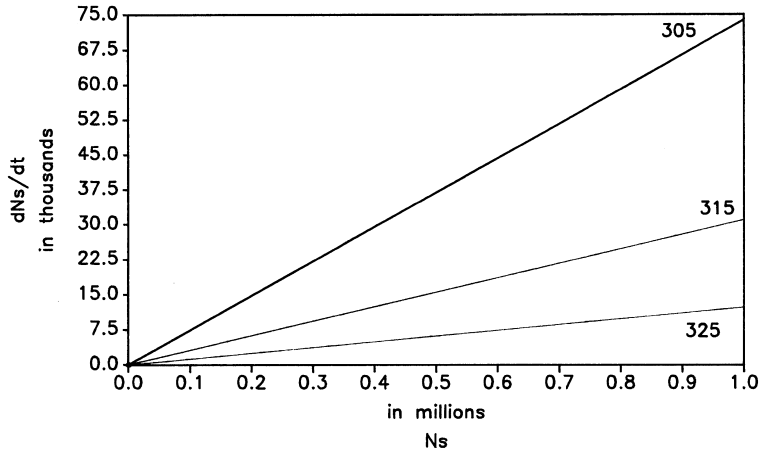


Figure B.17: Horizontal structuring simulation. Phase plots for $N_s(t)$ to analyze the kinetics of return to the 2nd attractor for $N_{so} = 20$ ($N_{se} = 10$) at different temperatures.

Table B.2: $B_o = 10^6$, $N_{se} = 10$, $N_{so} = 20$. $\Delta_m = 9250$, $\Delta_e = -250$, $\upsilon_m = 10^{11}$.

$\mathbf{Ln}(\tau_x)$	$\mathbf{1000}/T$	$T_{\mathbf{relax}}$
2.6056	3.0769	325.0000
3.4717	3.1746	315.0000
4.3955	3.2787	305.0000
5.9025	3.4483	290.0000
6.4404	3.5088	285.0000

Regression coefficients: intercept: −24.7197, slope: 8.8804.

the border line, separating the return behavior towards either the first attractor N_{se} or the second attractor $N_s = B_o$. Figure B.17 presents the return kinetics for $N_{so} = 20$ at different temperatures, $T = 305$, 315, and 325 K. All plots are linear, with slope equal to a kinetic constant. Table B.2 gives the value of Log τ_x, where τ_x is the slope in Figure B.17, at various isothermal temperatures between 285 and 325 K. Log τ_x vs. $1/T$ is linear in Figure B.18, from which one can extract an activated energy of $\Delta_x = 8{,}880.4$ cal/m and a frequency front factor of $\upsilon_x = 5.441 \times 10^{10}$ Hz. This time, both Δ_x and υ_x are *smaller* than Δ_m and υ_m, respectively.

Let us summarize the situation: horizontal splitting equations, equation (12), result in a structure of the free energy of the individual systems which present many interesting features worth studying in detail, but necessarily beyond the scope of this Appendix.

EBSCOhost - printed on 2/13/2023 12:32 AM via . All use subject to https://www.ebsco.com/terms-of-use

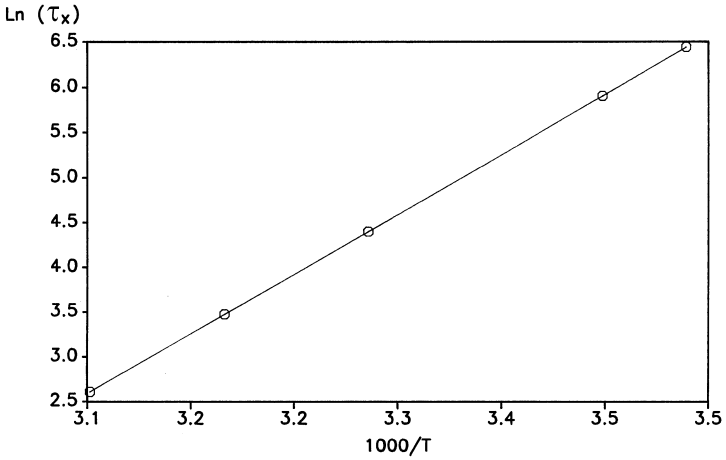


Figure B.18: Horizontal structuring simulation. Ln (τ_x) vs. 1000/T with τ_x determined for the return to the 2nd ATTRACTOR ($N_s = B_o$, $n_t = 0.5$).

The so-called "second attractor" is a set of B_o systems, as if the units in interactions themselves could be *viewed as systems*. The other attractor would be to consider $N_{se} = 1$, i. e., that the set of unit *structures as a whole*. In the presentation here, the equilibrium value N_{se} is assumed to remain constant, irrespective of temperature. This is probably not a realistic assumption.

In conclusion, the kinetics on cooling, heating, or annealing are not the same. The free energy structure depends on the rate q and on the initial state with respect to the equilibrium position.

Most interestingly, one sees in horizontal splitting kinetics that I_s, the system free energy, goes through "peak transitions," such as depicted with the variation of N_s in Figures B.3 and B.4. By plotting I_s against temperature and calculating the slope and intercept at each T, one might want to call the slope the apparent entropy ΔS and the intercept the apparent ΔH. Such a definition presumes that thermodynamic quantities, which are valid for equilibrium conditions, can also be used for dynamic systems. This is the same situation as in Chapter 2, where it was stipulated that the Debye formula, which one should normally only apply to isothermal depolarization systems, could also be used to describe non-isothermal depolarization phenomena, such as TSD (see Chapter 2). Plots of ΔS versus ΔH are of course linear, since the two quantities plotted are formulated from the derivative at T. If we apply this technique across a "peak transition" of I_s, we obtain two compensation laws intercepting at or near the temperature of the extremum. Furthermore, when there are several branches for the $N_s - T$ behavior (Figure B.4), one will associate several compensation laws, and they will seemingly appear to converge, such as displayed in a multi-compensation map (Chapter 4 of Part II). The behavior observed at T_g by thermal-windowing seems to be somehow related to the kinetics of the EKS N_s.

EBSCOhost - printed on 2/13/2023 12:32 AM via . All use subject to https://www.ebsco.com/terms-of-use

Part C. Compensating vertical and horizontal split constraints

We now imagine solutions that combine the vertical and horizontal Dual-Split Kinetics to simulate the dynamics of statistical units in interactions. In this Appendix we just want to illustrate one of the solutions of the Grain-Field Statistics that we have explored extensively to simulate the thermal properties and the rheology of polymers. More generally, the description of the several possible combinations and their simulation constitutes a vast and fascinating program of investigation. Additionally, among the various solutions, the challenge is to recognize what combination could possibly correctly simulate the specific interactions in a given field of the physics of interactions, not just polymer physics.

As an illustration for polymer physics, we can combine the equations driving the split between the b and F conformers, equations (5) to (7), and the equations of the formation of the energetic kinetic systems, equation (12). Even for polymers there are several ways to do the combination. Here are a few examples.

In one of the solutions, the vertical Dual-Split Kinetics "drives" the split of the total population B_o into $N_F(t)$ and $N_b(t)$, two compensating open systems, and the horizontal split kinetics structures the $N_b(t)$, whereas the $N_F(t)$ and its structure are still controlled by the vertical Dual-Split Kinetics. A variant of this b-structuring solution will be presented in equations (13) to (16) below.

Alternatively, it is possible to imagine a solution in which horizontal splitting is the driving force, producing N_s open dissipative systems that are vertically structured by dual-split. Such a case illustrates perfectly *the cross-duality of horizontal and vertical structuring*, and their compensation, since B_{os}, the size, is controlled by the equations of the horizontal split kinetics and the structure of B_{os} is controlled by the vertical split kinetics.

In still another solution, the equations combine the kinetics of the vertical dual-split and the cloning attributes of the horizontal split and apply the minimum principle to the total free energy. This *hybrid solution* is transcribed as follows:

$$\begin{aligned} B_o &= (N_b + N_f) \\ N_b &= N_s \cdot B_{os} \\ n_{tb} &= N_s \cdot n_{tbs} \\ N_f &= (n_{tf} + n_{cgf}) \\ B_{os} &= (n_{tbs} + n_{cgbs}) \end{aligned} \tag{13}$$

$$\begin{aligned} dn_{tb}/dt &= (dN_b/dt)/2 - k_1 \cdot n_{tb} + k_2 \cdot (N_b - n_{tb}) \\ dn_{tf}/dt &= (dN_f/dt)/2 - k_1 \cdot n_{tf} + k_2 \cdot (N_f - n_{tf}) \\ dn_{tbs}/dt &= (dB_{os}/dt)/2 - k_1 \cdot n_{tbs} + k_2 \cdot (B_{os} - n_{tbs}) \end{aligned} \tag{14}$$

$$N_s \cdot \mathrm{Ln}(n_{tbs}/n_{cgbs}) + \mathrm{Ln}(n_{tf}/n_{cgf}) + \delta_p \,\mathrm{Ln}(N_b/N_f) = 2\,\mathrm{Ln}(k_2/k_1) = 4\Delta_e/RT \tag{15}$$

EBSCOhost - printed on 2/13/2023 12:32 AM via . All use subject to https://www.ebsco.com/terms-of-use

$$
\begin{aligned}
k_1 &= \upsilon_m \exp(-\Delta_1/RT) \\
k_2 &= \upsilon_m \exp(-\Delta_2/RT) \\
q &= dT/dt \quad \text{(under isothermal relaxation } q = 0\text{)}
\end{aligned}
\tag{16}
$$

where B_{os} is the total number of b conformers *per* N_s*-system*, N_s is the number of systems, and B_o is the grand total of conformers; δ_p is the Kronecker constant, either –1 or +1 in the simulations.

This set of equations permits to horizontally structure the sub-set of N_b b conformers into N_s b grains, a hypothesis that we have talked about in many parts of this book and in many other references: it leads to the Dual-Phase description of the interactions in polymers [128]. Note that this solution is only a hybrid solution and not a cross-duality since it does not apply the energetic kinetics specificities of horizontal structuring, but it uses the energetic kinetic drivers of vertical structuring.

One can use a fifth-order Runge-Kutta algorithm to solve the set of equations (13) to (16). The solutions are stable. Our findings will be presented in the book dedicated to that purpose [137]. Figure C.1a and b sketches the solution obtained by solving equations (13) to (16). These figures were also what we described when we discussed the solutions of equations (5) to (7). We mentioned the structure of the N_b set of conformers into a sub-set of b grains surrounded by F conformers. Yet, equations (5) to (7) only provide N_b/N_f and the structure $n_{tbs}/(N_b - n_{tbs})$, called "the structure of B_{os}" in Figure C.1a, but not the size nor the numbers of the b grains. This information is provided by solving equations (13) to (16), completing the dynamic picture of the formation of the b grains and of their F conformers surroundings (Figure C.1b).

In each of the combinations of vertical and horizontal structuring mentioned above, we are dealing with *auto-generated open dissipative systems* driven by the energetic kinetics assumptions, i. e., by solutions of the structure of the free energy so that the minimization of the total free energy, for the collective set, always remains equal to the equilibrium value at that temperature. An open system occurs when its total population is not kept constant. Such a system compensates its openness by modulating the structures of its free energy at various levels (scales).

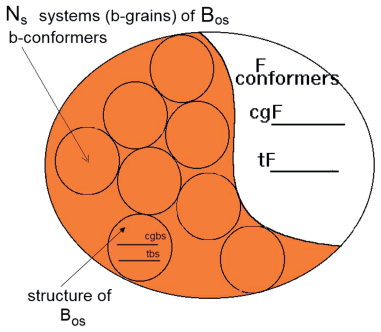


Figure C.1a: Combining vertical and horizontal structuring simulations. See text.

EBSCOhost - printed on 2/13/2023 12:32 AM via . All use subject to https://www.ebsco.com/terms-of-use

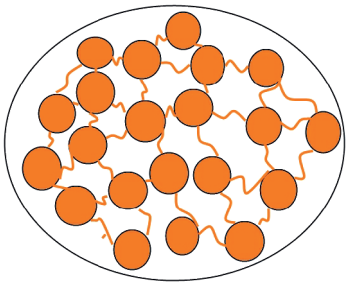


Figure C.1b: Combining vertical and horizontal structuring simulations (the Dual-Phase system of *b*-grain conformers surrounded by *F*-conformers) by dissipative statistical re-organization of the solution sketched in Figure C.1a.

Before closing this section on the Dual-Split Kinetics, let us look at a couple of graphs obtained by making B_o vary with time in equation (12), the simple horizontal split simulator. This exercise of modeling a simple open system has the purpose to illustrate how coupling between the vertical and the horizontal split kinetics can give rise to kinetic features which are reminiscent of real systems, in thermal analysis for instance.

Figure C.2 is the solution of equation (12) when B_o varies linearly with time, i. e., the total number of units in the statistics is modulated in the simplest way possible (dB_o/dt = constant). The function of modulation can take more complex forms, indeed, for instance in equations (13) to (16) when the vertical dual kinetics modulates the variation of N_b that becomes the $N_s B_{os}$ units of a system responding to a horizontal structuring mode.

Figure C.2 studies the effect of an increase or decrease of B_o with rate ±100, respectively, on the number of systems N_s. It is seen that when the total population of conformers decreases ($dB_o/dt < 0$), the number of systems N_s increases faster, and the asymptotic temperature is reached sooner on cooling.

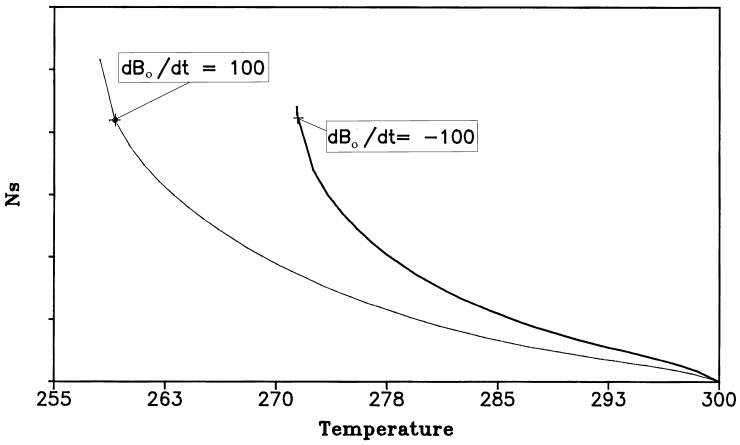


Figure C.2: Horizontal structuring simulation. Effect of varying B_o at constant rate during cooling. $B_o = 10^6$ @ $T = 300$, $q = -0.1$, $\Delta_m = 9250$, $\Delta_e = -250$, $u_m = 10^{11}$.

EBSCOhost - printed on 2/13/2023 12:32 AM via . All use subject to https://www.ebsco.com/terms-of-use

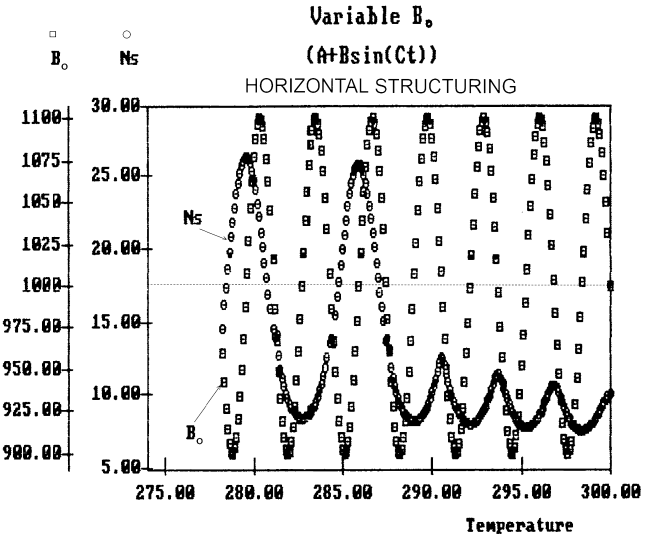


Figure C.3: Horizontal structuring simulation. Variation of $N_s(t)$ during cooling when $B_o(t)$ is varied sinusoidally. See text.

Figure C.3 provides another interesting perspective of the open-system dynamics when their total population, B_o, is submitted to a *fluctuation around a mean value*. The system is again defined by equation (12), but we now suppose that the value of B_o varies with time like a sine wave as it is cooled at rate $q = -1\,\mathrm{K/s}$:

$$B_o = A + B\sin(Ct) \quad \text{and} \quad T = T_o - qt$$

where $A = 1000$ and $B = 100$ are used in Figure C.3.

The problem is more complex to resolve numerically, but is still quite tractable. The solution for $N_s(T)$ is plotted on the same graph as $B_o(T)$ for comparison. The temperature decreases from right to left in the figure, where $B_o(t)$ is represented by the squares and $N_s(t)$ by the open dots.

We see in Figure C.3 that N_s varies periodically but nothing like a sine wave.

What is interesting, however, is to follow the period of the oscillation and the maximum and the minimum of the amplitude of $N_s(T)$, from right to left: the amplitude of N_s has difficulty to rise up beyond its initial value at high temperature, showing a slow increase of the peak maximum value and a strong non-linear oscillating system with lots of harmonics. Beyond the fourth oscillation of $B_o(t)$, however, the peak maximum value increases rapidly and levels off to a plateau value, and the oscillation becomes cleaner, indicating the muting of many harmonics. *The other remarkable feature is the period doubling of the oscillation at lower temperature*. At high temperature, the periods of $N_s(t)$ and $B_o(t)$ are the same, but as we cross the transition tempera-

EBSCOhost - printed on 2/13/2023 12:32 AM via . All use subject to https://www.ebsco.com/terms-of-use

ture on cooling, the period of $N_s(t)$ becomes twice the period of $B_o(t)$, a phenomenon observed for "time crystals," for instance.

This horizontal dynamic system is capable to produce a transition separating two temperature regions presenting very unique characteristics in material physics [137].

Finally, Figure C.4 provides an example of a dynamic response for the hybrid kinetics. We plot the rate of change of n_{tbs} against temperature during a heating cycle (q = 1 K/sec) for a simulation described by equations (13) to (16), i. e., a combination of horizontal attributes and vertical dynamic structuration.

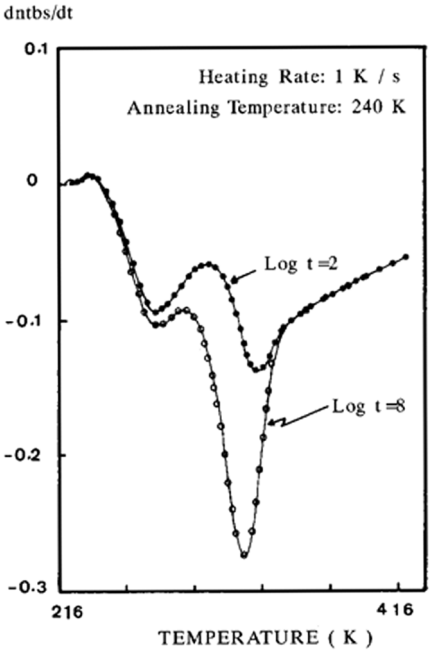


Figure C.4: Horizontal structuring simulation. Rate of variation of dn_{tbs}/dt vs. temperature. This is an example of thermally activated (heating) return to equilibrium of a system first cooled to be out of equilibrium, then annealed, then heated at constant rate, showing a typical DSC trace crossing T_g after annealing below T_g (for instance for PS or PC).

The system is first quenched to 200 K from 425 K at a very high rate (q = –1000 K/s) and annealed at 240 K for either 100 sec or 10^8 sec. The annealed systems are quenched at an infinite rate and heated up to reveal the kinetics of Figure C.3. One observes two peaks in the figure, and the two peaks have the tendency to merge on annealing; for $logt$ = 2 (annealing time = 100 sec) the two peaks are prominent; for $\log t$ = 8 (3.17 years), the lower peak has become a shoulder on the main peak. After 5 years (not shown), i. e., $t = 1.58 \times 10^8$ s, the two peaks have fully merged into a single one.

EBSCOhost - printed on 2/13/2023 12:32 AM via . All use subject to https://www.ebsco.com/terms-of-use

The peak height also varies with annealing. Obviously, the timing in these results is controlled by the simulation values chosen for Δ_m, υ_m, Δ_e, etc.

Qualitatively, the dynamic response in Figure C.4 is reminiscent of kinetic effects observed by DSC ([139], also Figure 3.12) or TSD when the heights of two peaks compensate in time to finally merge (Chapter 3, Figure 3.8). The details are beyond the present scope, but it is already interesting to note that two peaks may emerge at a "transition" on heating or cooling, and not simply a single peak, although the kinetics are driven by a single activation process (Δ_m, υ_m). The appearance of a relaxation spectrum for the relaxation process may, in fact, be due to the compensation between the vertical and horizontal dissipation responses to minimize the total free energy (remaining equal to the equilibrium value). The whole dynamics may just be revealing the gears of the Grain-Field Statistics options.

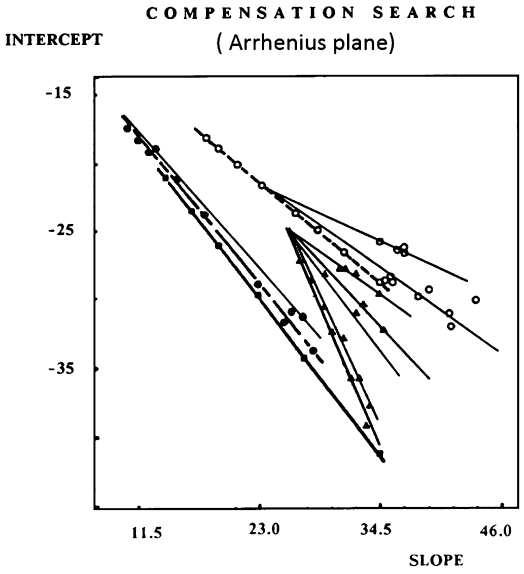
Final word

This challenge of finding the correct combination of horizontal and vertical splitting to describe interactions requires a dedicated book [137], my last book of the series.

An important chapter of that book (Chapter 12) is titled "The Dynamics of Open-Dissipative Systems of Interactions: the Question of their Finitude and Stability." This chapter, whose title, obviously, resonates with the work of Prigogine in the 1970s [214], although it totally differs from it for its mathematical treatment, should lay down the basic map of what needs to be resolved by the next generation of research scientists interested in these solutions to better understand how the local and the global interactions structure one another to generate transient and steady-state events in time-space, i. e., describe what we call reality (time vs. space, matter vs. vacuum). This could offer new perspectives on the description of the different types of interactions and of their unification as solutions of the network of open dissipative cooperative systems. The first Renaissance in physics, from Newton to Einstein for gravitational interactions to the standard model of interactions to describe the infinitely small, may have exhausted the resources of closed-system statistics to complete a grand unification. Should the second Renaissance, inspired by Prigogine [214] to expand the resources of open-dissipative-system statistics, now take the baton?

EBSCOhost - printed on 2/13/2023 12:32 AM via . All use subject to https://www.ebsco.com/terms-of-use

Part II: **Application of Thermal-Stimulated Depolarization and Thermal-Windowing Deconvolution (TSD/TWD) to the characterization of the amorphous phase in polymers: case studies**



EBSCOhost - printed on 2/13/2023 12:32 AM via . All use subject to https://www.ebsco.com/terms-of-use

EBSCOhost - printed on 2/13/2023 12:32 AM via . All use subject to https://www.ebsco.com/terms-of-use

Part II Chapter 1
A comparison of TSD/TWD, DSC, DEA, and DMA for the characterization of the amorphous phase of polymers

II.1.1 General description

In the introduction we suggested that Thermal-Windowing Deconvolution (TWD) and the understanding of compensation phenomena can be used to characterize the amorphous state of matter in a manner fundamentally different from the other traditional thermal analysis instruments: differential scanning calorimetry (DSC), dynamic mechanical analysis (DMA), and dielectric analysis (DEA). Yet, TSD/TWD gives very similar results to the other thermal analysis techniques when used with the TSD mode. This chapter reviews some of the issues of TSD/TWD spectroscopy: is it similar, complementary, or significantly more powerful than existing instrumentation technology [142]?

Relaxations take place in materials as the result of internal motions, which are induced by either thermal, mechanical, or electrical energy disturbances. The materials processed in the industry by the usual molding methods have mechanical and electrical properties which depend on the local motions within their internal structure. It is therefore of paramount importance to be able to characterize those motions, which might take their origin from the atomic (electronic), molecular, or macromolecular level.

Essentially, there are three types of methods for studying relaxation times in materials: (1) resonance methods, (2) damping methods, and (3) the thermal-activated methods.

In the resonance method, the material is subjected to a periodic excitation, either mechanical or electrical in nature (Figure 1.1, top), applied at a determined temperature and pressure. The frequency of the excitation can be swept, and the storage and loss mechanical or dielectric constants can be determined at each frequency. Plots of the storage and loss functions versus the log of frequency display peaks which characterize the motions occurring in the structure (Figure 1.1, bottom). The value of the frequency at the maximum of loss corresponds to the resonance frequency for that particular internal motion. Working at different temperatures (Figure 1.2) shifts the curves, a feature which can be used to determine the fundamental parameters of the rate-dependent process giving rise to internal motion.

An alternative method which is frequently used consists in subjecting the material to an excitation at a determined frequency while programming a linear variation in temperature (Figure 1.3). When the temperature reaches a level capable of thermally inducing the internal relaxation process, a resonance peak for the selected ex-

https://doi.org/10.1515/9783110756746-006

EBSCOhost - printed on 2/13/2023 12:32 AM via . All use subject to https://www.ebsco.com/terms-of-use

citation frequency is observed. It is possible to operate at various (fixed) frequencies (Figure 1.4), and thus analyze the dependence between time and temperature or frequency and temperature, which provides knowledge on the mechanism responsible for internal motion.

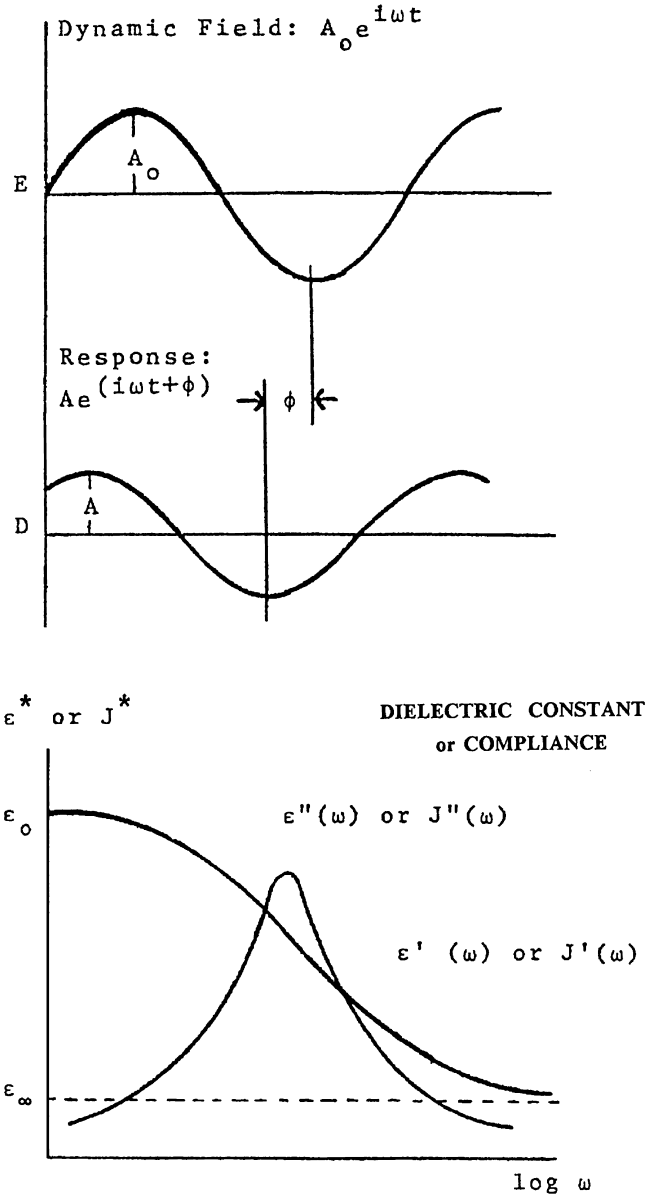


Figure 1.1: Definition and effect of a dynamic field of activation (electric, mechanical) on a material response. Top: dynamic field versus time, defining the amplitude and the frequency of the excitation signal. Middle: amplitude and phase difference of the response curve. Bottom: defining the two components of the response signal treated as a complex number: a real and an imaginary component.

EBSCOhost - printed on 2/13/2023 12:32 AM via . All use subject to https://www.ebsco.com/terms-of-use

Note that in these techniques the mechanical or electrical "deformation" is applied as the measurement is made. The field induces polarization or orientation within the sample, causing oscillation which is at the same frequency as the field but with a phase angle shift δ (Figure 1.1). In the case of dielectric measurement (DEA), the phase angle shift is measured by comparing the applied voltage to the measured current (which is separated into capacitance and conductance components). In the case of mechanical measurement (DMA), the stress and strain are compared to provide the elastic and loss moduli. The resolution depends on the ability to measure changes in these variables, in particular in the tan δ vs. temperature (or frequency) loss peak.

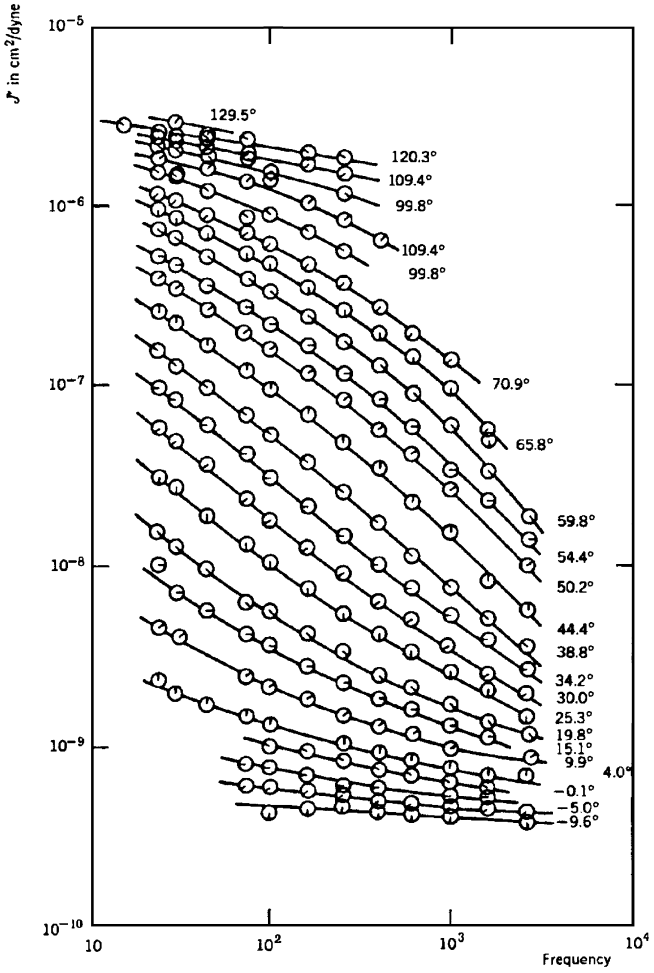


Figure 1.2: Variation of the compliance, J, of a dynamic mechanical test versus frequency at various temperatures, from −9.6 °C to 129 °C, across T_g of the material in this case. Shifting horizontally the isothermal curves onto one of them, selected as a reference, produces a mastercurve having an extended frequency range for the chosen reference temperature.

EBSCOhost - printed on 2/13/2023 12:32 AM via . All use subject to https://www.ebsco.com/terms-of-use

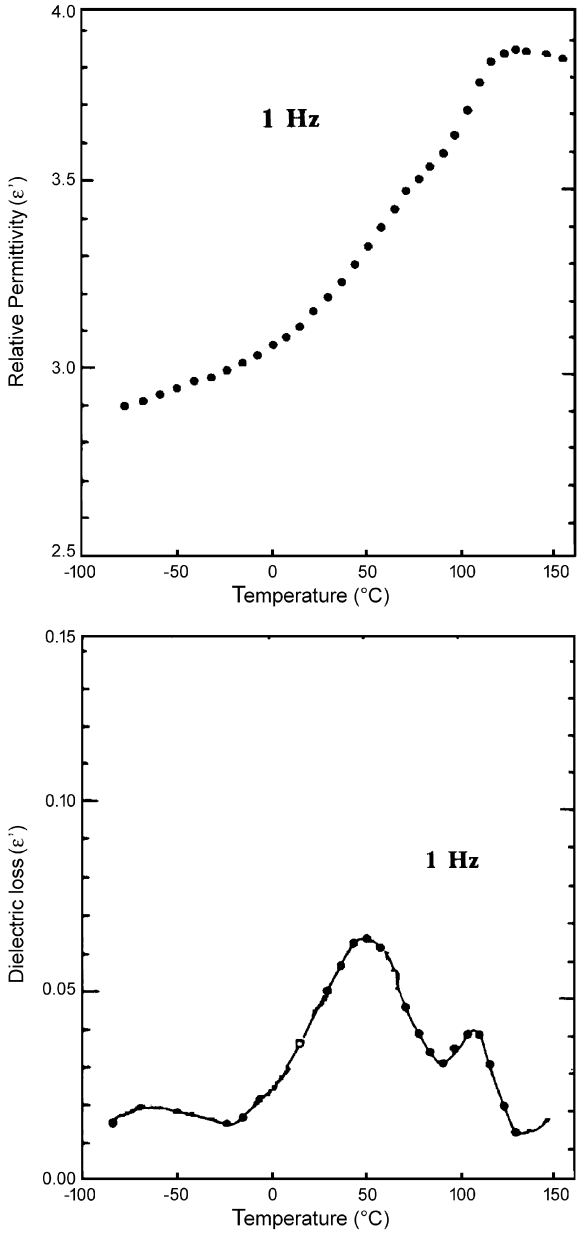


Figure 1.3: Plots of ε' and ε'' versus temperature, relative permittivity (top), and dielectric loss (bottom), at a frequency of 1 Hz for a dynamic electrical output signal.

The methods using damping analysis consist of an excitation stage, for instance submitting the specimen to a sudden torsion at a given temperature, followed by the interruption of the excitation and subsequent recording of the recovery curve, showing the return to equilibrium. The damping characteristics are directly a function of the internal state at this temperature, and the molecular relaxations which govern the kinetics

EBSCOhost - printed on 2/13/2023 12:32 AM via . All use subject to https://www.ebsco.com/terms-of-use

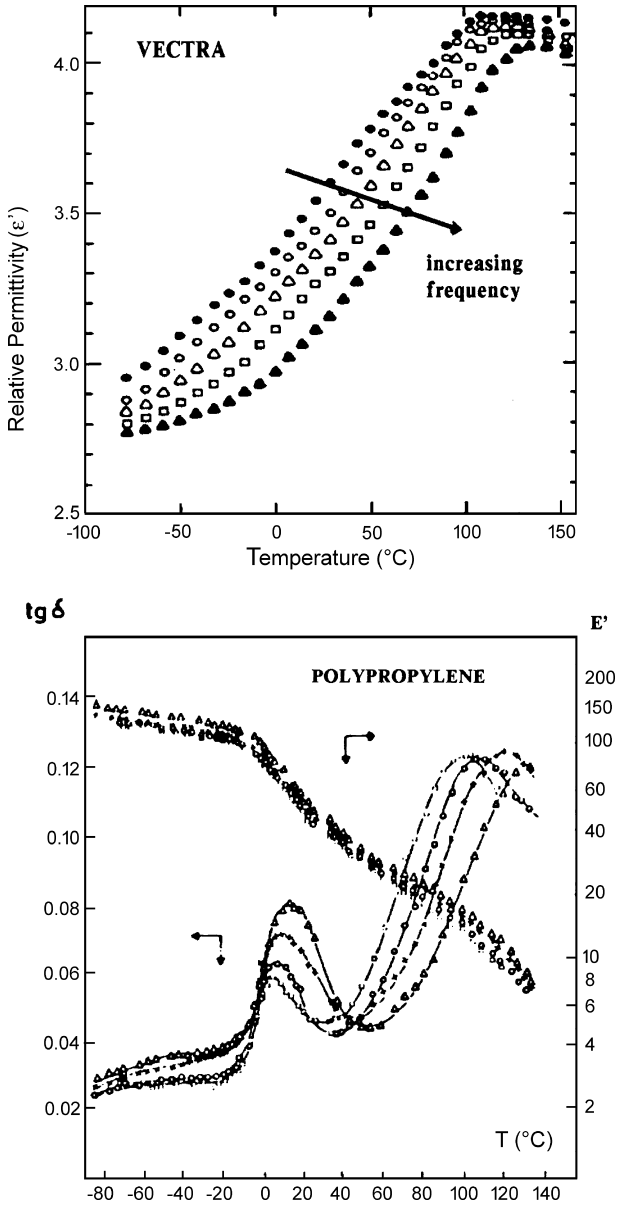


Figure 1.4: Effect of the frequency of the excitation on the temperature dependence of the relative permittivity (ε') of Vectra (top) and of the loss modulus (E'', right axis) and tan δ (left axis) of polypropylene (bottom).

can be determined. The excitation stage may be a creep experiment or a sinusoidal deformation. The first case corresponds to the classical torsional pendulum which was much used in the 1950s to study "internal friction." In the case a sinusoidal pulse was generated at ultrasonic frequency, analysis of the damping of the wave propagating across the specimen leads to the complex modulus and complex viscosity at that frequency.

EBSCOhost - printed on 2/13/2023 12:32 AM via . All use subject to https://www.ebsco.com/terms-of-use

The so-called "thermal-activated" methods include purely calorimetric measurements (DSC and differential thermal analysis [DTA]) and the thermal-stimulated methods which combine the influence of temperature and another variable, which may be a mechanical (thermal-stimulated creep recovery [TSR]), electrical (TSD), or electromagnetic (light) variable. In this book, only thermally stimulated current characterization techniques are described, leaving to other publications [160, 204, 231, 238] the description of the less popular and less sensitive TSR and thermal-stimulated luminescence (TSL).

Differential microcalorimetry is a rapid and streamlined method to determine phase transitions in materials, for example in order to determine fusion and solidification temperatures, and vitreous transitions in the amorphous phases of noncrystalline or semi-crystalline materials. DSC is the most widely used of all thermoanalytical techniques. In this analysis technique, temperature essentially plays two roles: that of stimulator, by contributing thermal energy capable of initiating activated internal movements, and that of sensor, by comparative measurement of the temperature.

A DSC measures the temperatures and the heat flow associated with transitions in materials as a function of time and temperature (Figure 1.5).

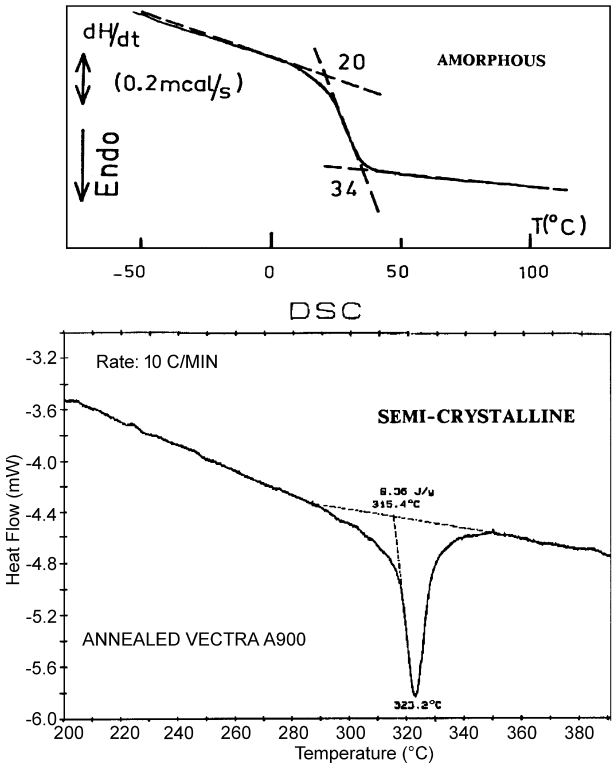


Figure 1.5: DSC outputs of heat flow vs. temperature for an amorphous (top) and a semi-crystalline material (bottom) showing a T_g between 20 °C and 34 °C at the middle of the drop-off of the heat flow variation (top) and a temperature of fusion of the crystals of Vectra at T = 323.2 °C (bottom).

EBSCOhost - printed on 2/13/2023 12:32 AM via . All use subject to https://www.ebsco.com/terms-of-use

DSC consists in comparing the heat flux supplied to two pans located in the same thermostatic atmosphere, a device in which one of the two pans contains the material to be studied. The temperature in the chamber may be programmed to increase or decrease linearly or to stay constant (isothermal mode). The furnace is regulated in such a way that the temperature of the two pans is exactly the same. The variable heat flux supplied or subtracted from the pan containing the material under investigation is recorded as a function of the temperature of the heat chamber. DSC measurements provide quantitative and qualitative information about physical or chemical changes that involve endothermic or exothermic processes or changes in heat capacity.

In a variant of the DSC process, DTA, the difference in temperature between the two pans is recorded as a function of the furnace temperature. The difference in temperature between the two pans changes when there is an alteration in the physical structure accompanied by the variation in enthalpy within the material.

The TSD technique is relatively original with respect to the previously described methods of characterization. In this technique temperature plays the role of "developer" during the recovery stage, whilst the external variable (the electric field) imposed during the excitation stage plays the role of "marker." In a variant of the process, described in further detail below, temperature also plays the role of "filter" for the relaxation times; this is the "thermal-windowing" method, sometimes also described by other authors as "thermal-sampling" or "thermal-cleaning."

As already described in the Introduction (Figures 0.1 and 0.3), the purpose of the excitation, in the form of an electric field imposed on the material at a given temperature, is primarily to "polarize dipoles." In a more general sense, the action of the field is to create a state of non-equilibrium at temperature T_p. The field is applied for a given time t_p, and the temperature is then lowered very quickly (tempering) to a temperature T_o at which internal motions are prevented for kinetic reasons. As a consequence, a more or less frozen-in image of the disturbed state produced at T_p is preserved at T_o. The field is suppressed at T_o and the material is reheated at constant heating rate to allow the thermal energy to flow in to free up molecular motions in order to complete a full return to the equilibrium state. Hence TSD consists of a recovery test performed at constant heating rate. The current of depolarization is measured (Figure 1.6) as a function of temperature.

At each onset of molecular motion a peak is observed, which corresponds to a given type of relaxation. The temperature at which the peaks become visible is a function of the chemical structure of the material, its morphology, and processing parameters. Like the other characterization methods DMA and DEA, the thermal-stimulated techniques disclose the relaxation movements in a global manner, i. e., it is generally *impossible* to define a *single relaxation time* to characterize the kinetics of return to the equilibrium state. The output of a global TSD (Figure 1.6) looks like a tan δ vs. T plot from a DMA or DEA instrument working at very low frequencies (10^{-4} Hz). *This is the result of an interactive cooperation between various molecular relaxations*. The relaxation process at T_g, for instance, is due to a distribution of relaxation times, and the

EBSCOhost - printed on 2/13/2023 12:32 AM via . All use subject to https://www.ebsco.com/terms-of-use

technique of "Thermal-Windowing Deconvolution (TWD)" is used for the experimental deconvolution of the global TSD spectra into the individual elementary relaxation modes (Figure 1.7).

TWD can be viewed as an important variant of the TSD technique. Its purpose is to isolate the individual relaxations of the spectrum of relaxation times and *study their coupling characteristics*.

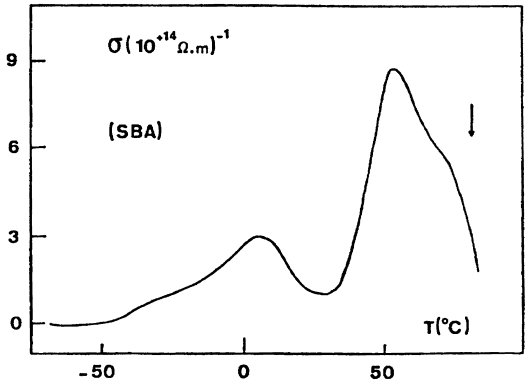


Figure 1.6: Illustration, for SBA, of the output signal obtained by TSD. The depolarization current is plotted against temperature at constant ramp rate (10 °C/min) after the material has been polarized at temperature T_p, shown by the arrow. The current is normalized to show conductivity.

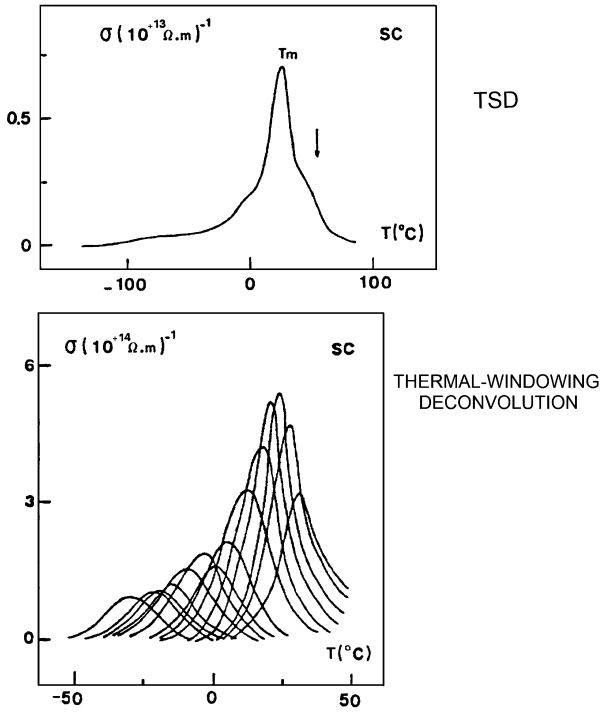


Figure 1.7: Difference between the depolarization outputs from a single polarization temperature (TSD, top) and TWD (bottom), the result of the deconvolution of a global TSD peak into elementary peaks.

EBSCOhost - printed on 2/13/2023 12:32 AM via . All use subject to https://www.ebsco.com/terms-of-use

TWD consists of polarizing (orienting) only a fragment of the full spectrum of relaxation and depolarizing (desorienting) it partially to isolate or "window" a single relaxation process (Introduction, Figure 0.3). Using this process repeatedly and varying the temperature of polarization T_p each time, one can isolate the elementary relaxation modes one by one (Figure 1.7).

Each elementary relaxation curve (depolarization current vs. T) can be mathematically transformed into its Arrhenius representation, Log τ versus $1/T$, which expresses the variation of relaxation time with temperature for that particular isolated relaxation mode (Introduction, Figure 0.6). A relaxation map (Introduction, Figure 0.7) is the result of transforming all the elementary peaks obtained at various T_p into their Arrhenius representation.

TWD tries to correlate the single relaxation modes (relaxation time versus temperature) to thermokinetic and/or other physical variables (Introduction, Figure 0.10). The description of the elementary relaxation modes, their thermokinetic characteristics (activation energy and entropy), and the description of the coupling law are essential for a full understanding of the macroscopic properties of materials (Table 1.1).

Table 1.1: Thermodynamic coefficients (per mole).

	T_p (°C)	T_m (°C)	ΔH_p (kcal/mol)	ΔS_p (cal/°C/mol)	ΔG_p (kcal/mol)
1	40.0	53.8	31.2769	29.2527	22.1208
2	45.0	57.8	33.3621	34.4723	22.3999
3	50.0	63.3	34.5037	36.1144	22.8388
4	55.0	68.4	37.8845	44.5958	23.2571
5	60.0	73.4	42.2965	55.8746	23.6903
6	65.0	77.9	45.6562	63.9224	24.0504
7	70.0	82.3	55.2875	89.7271	24.5111
8	75.0	86.2	59.0795	98.6349	24.7546
9	80.0	89.4	67.4594	120.5010	24.9225
10	85.0	92.4	79.9679	153.4386	25.0369

II.1.2 Outputs. Resolution. Accuracy. Limitations

II.1.2.1 DSC

The classical output from a DSC is shown at Figure 1.5, which is a plot of heat capacity versus temperature. The heat capacity increases across the glass transition temperature of polymeric materials, showing kinetic features along the way which can be analyzed as a change of slope of the baseline or as the formation of an endothermic peak. Melting and solidification phenomena are characterized by endothermic or exother-

EBSCOhost - printed on 2/13/2023 12:32 AM via . All use subject to https://www.ebsco.com/terms-of-use

mic peaks. The nature of the peaks is global, i. e., the peaks represent the integrated output of cooperative thermally active motions inside the material.

The problems of baseline stability, surface effects, and sensitivity (in the case of amorphous polymers) plague microcalorimetry. The inability to study recovery of oriented materials because of recoiling in the pan and the surface effects it induces presents a severe limitation of DSC in quality control applications.

In order to increase the resolution, the temptation to increase the size of the sample should be resisted because a gradient within samples causes poor resolution, distortion of the peaks, and possibly a temperature error. Also, large samples may result in self-heating in the case of exothermic reactions, which will modify the kinetic rates. The use of small samples is unavoidable but limits the sensitivity.

Another main disadvantage of differential microcalorimetry, or DTA, is that the instrument output is a global response which converts the cooperative plurality of internal relaxations without sensing their individual origins.

A further main disadvantage is the low sensitivity in detecting "secondary" internal movements for which the activation enthalpy is low or in separating out the T_gs of segregated phases in a block copolymer (Figure 1.8). Finally, this technique also presents difficulties in studying certain phenomena such as the physical aging of plastic materials. It is not uncommon to observe great variations in the mechanical properties of plastic materials, such as the ductile to brittle transition of polycarbonate, and to be unable to see any difference on the corresponding traces in DSC analyses [216]. In fact, differential microcalorimetry appears to be rather insensitive to internal stresses induced by the thermal history, as illustrated in Figure 1.9, which compares the outputs obtained by DSC and TWD for polystyrene samples cooled in a mold under various cooling rate conditions.

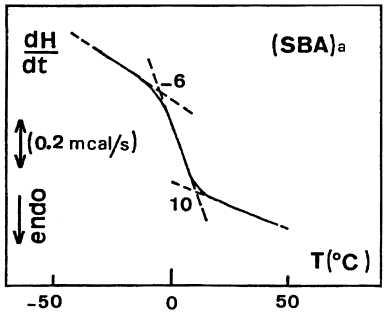


Figure 1.8: Output from DTA or DSC showing the endothermal drop-off of the heat flow at T_g for an amorphous material.

In the case of blends or block copolymers, the melting of one of the phases often obstructs the appearance of the T_g of the higher T_g component (Figure 1.10). So, if one of the polymers in the blend does not crystallize, the situation might arise that it is impossible with a DSC to determine whether the two phases actually mix or segregate (only one melting peak is visible and the T_gs cannot be detected).

EBSCOhost - printed on 2/13/2023 12:32 AM via . All use subject to https://www.ebsco.com/terms-of-use

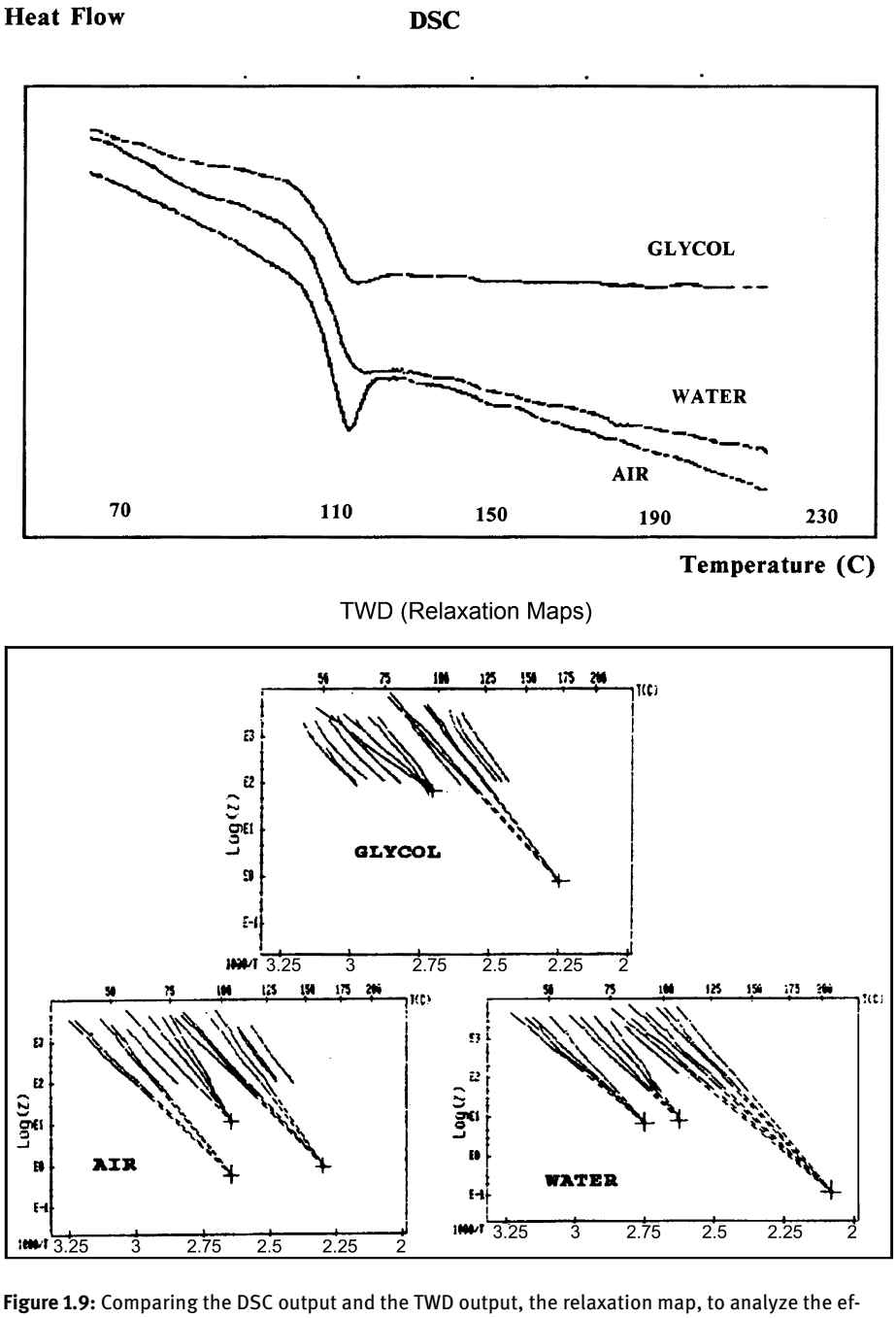


Figure 1.9: Comparing the DSC output and the TWD output, the relaxation map, to analyze the effect of cooling rate (air cooling, water cooling, glycol refrigerant cooling) on the amorphous state of polystyrene samples. Details are discussed in Section II.4.2.1.

EBSCOhost - printed on 2/13/2023 12:32 AM via . All use subject to https://www.ebsco.com/terms-of-use

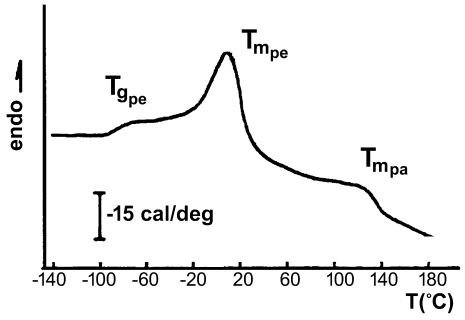


Figure 1.10: DSC trace (heat capacity vs. T) for a block copolymer of polyethylene (PE) and polyamide (PA) segments showing T_g of the PE blocks and the melting temperatures, $T_{m_{PE}}$ and $T_{m_{PA}}$, of the PE and PA blocks, respectively.

The TSD technique's super-sensitivity makes the detection of some transitions that DSC cannot see or cannot define well enough possible. This is illustrated in Figures 1.11 and 1.12. The DSC traces shown in Figure 1.11 apply to block copolymers of acrylate n-butyl and styrene. The sample "SC" is a statistical copolymer, and the other two, "A.S.S." and "S.A.S.," refer to two block copolymers for which the order of introduction of the monomers differs. DSC curves show the classical drop-off of the baseline at T_g, for the statistical copolymer, and somewhat the same thing, but with a wider effect, for the block copolymers. It is not clear from the DSC traces whether there is segregation of the phases for the two block copolymers. TSD traces solve the dilemma

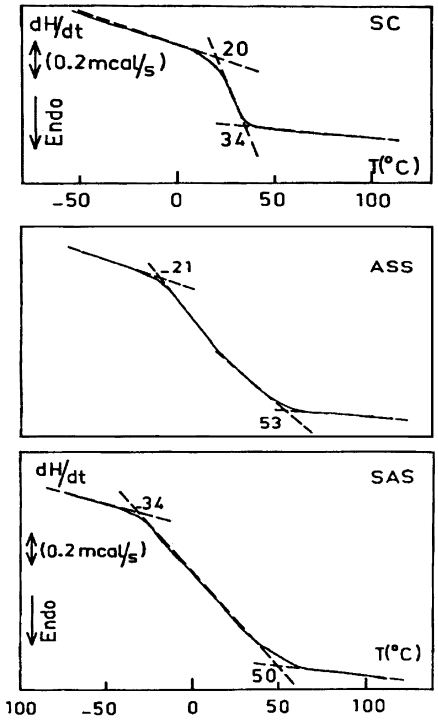


Figure 1.11: DSC traces (heat flow vs. T) of three copolymers of styrene and acrylate n-butyl: a statistical copolymer (SC) at the top and A.S.S and S.A.S., which are two block copolymers with different introduction of the comonomers, at the bottom.

EBSCOhost - printed on 2/13/2023 12:32 AM via . All use subject to https://www.ebsco.com/terms-of-use

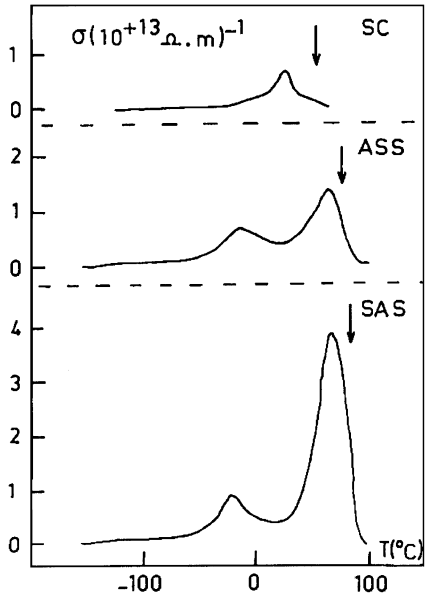


Figure 1.12: TSD traces (conductivity vs. *T*) for the same copolymers as in Figure 1.11. Also refer to Figure 1.19 for the DMA traces relative to the same materials.

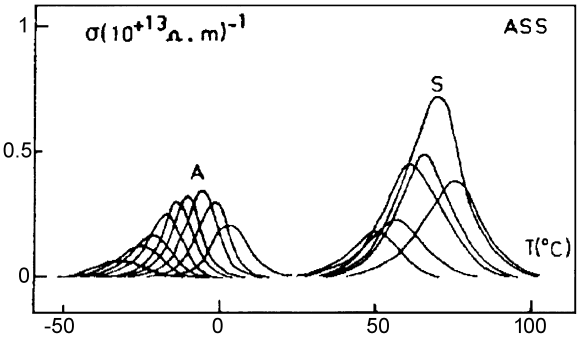


Figure 1.13: Deconvolution via Thermal-Windowing of the Thermal-Stimulated Depolarization trace of the A.S.S. block copolymer. The analysis of the deconvolution of the two main peaks into elementary peaks provides the relaxation map of the relaxation modes describing the state of interactive coupling between the bonds. This type of analysis (TWD) quantifies the amorphous state of the material.

easily (Figure 1.12). The relative intensity of the T_gs TSD peaks and their width can be analyzed in detail with TWD (Figure 1.13), and this allows the complete decoupling of the relaxation modes participating in the relaxation processes. The amount of segregation and the interpenetration of the phases can be quantified from TWD, as we shall see in Chapter 3 of this Part II.

In conclusion, DSC seems to be particularly appropriate to study semi-crystalline materials, in particular the melting or solidification temperatures. It is the perfect tool

EBSCOhost - printed on 2/13/2023 12:32 AM via . All use subject to https://www.ebsco.com/terms-of-use

to detect the presence of thermally active impurities, when those are present in sufficient quantity. *The method is not selective enough to characterize the amorphous state in partially or totally miscible blends, and a DSC is almost useless to analyze paints, coatings, adhesives, films, fibers, and composites*.

II.1.2.2 DMA and DEA

II.1.2.2.1 General considerations

The outputs from DMA or DEA working at constant frequency of excitation are normally three types of curves: G' (or ε'), G'' (or ε''), and tan δ, the ratio of the loss component G'' to the elastic or in-phase component G', all plotted against temperature. The three curves are usually plotted together on the same graph (Figure 1.14). G' and tan δ give rise to global peaks, and G' looks like a modulus versus temperature plot

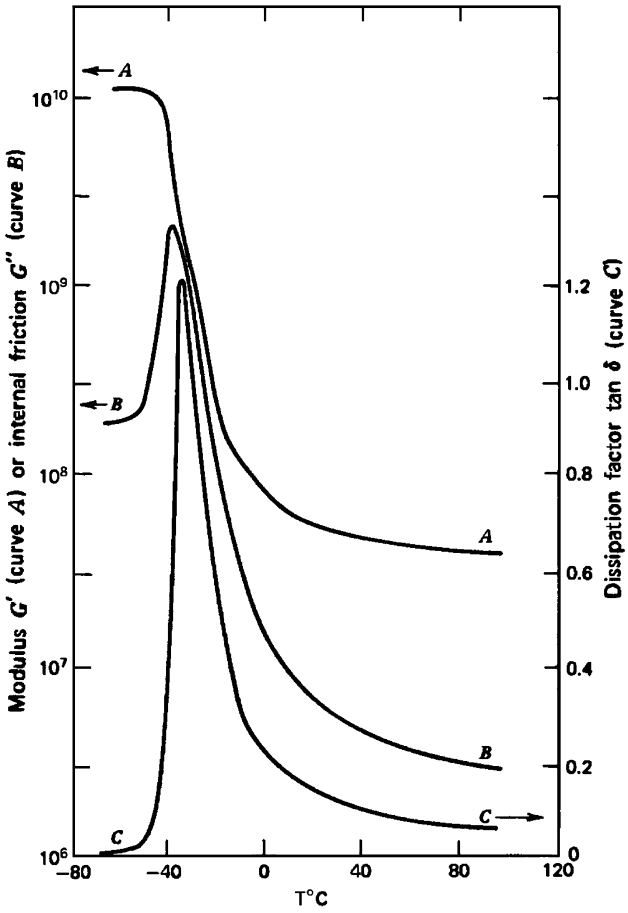


Figure 1.14: Outputs G', G'', and tan δ from DMA plotted against temperature as curves A, B, and C, respectively. The frequency of the excitation is fixed, often 1 Hz.

EBSCOhost - printed on 2/13/2023 12:32 AM via . All use subject to https://www.ebsco.com/terms-of-use

obtained from a relaxation experiment for a given time of relaxation (Figure 1.15). By varying the frequency, the peaks' positions are shifted, in particular the peaks' maxima, and a "pseudo-activation energy" can be calculated from the value of the shifts (Figure 1.16). An alternative method is to work at constant temperature and scan the frequency across the full relaxation time spectrum (Figure 1.2).

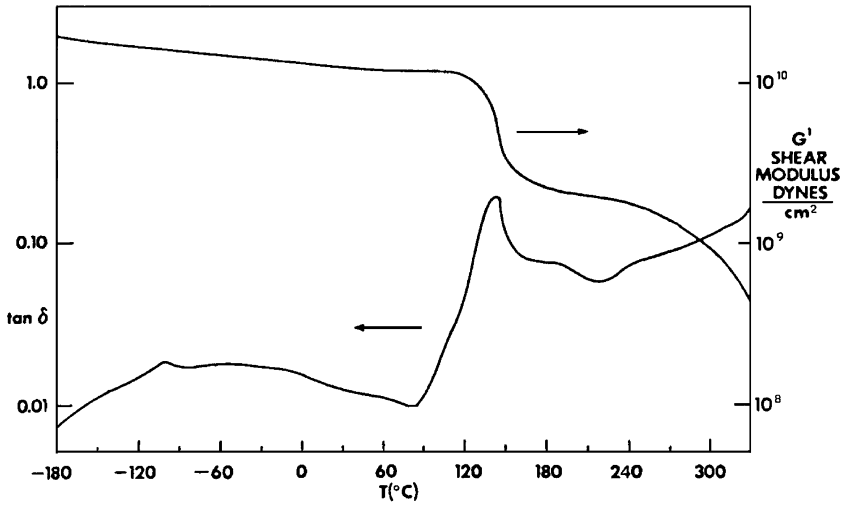


Figure 1.15: DMA traces of $G'(T)$ and tan δ vs. T for polycarbonate ($T_g \sim 145$ °C) showing the display of peaks of tan δ at molecular relaxations and transitions.

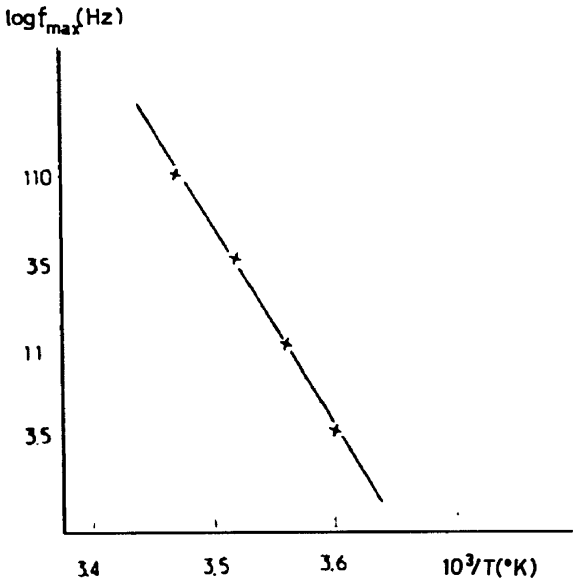


Figure 1.16: Plot of the log of frequency (Hz) vs. the Arrhenius temperature ($1/T$ K) at the maximum of tan δ for a series of four DMA runs performed at frequencies of 3.5, 11, 35, and 110 Hz. The slope of the Arrhenius line gives the activation energy of the molecular relaxation giving rise to the peak shifted by the frequency.

EBSCOhost - printed on 2/13/2023 12:32 AM via . All use subject to https://www.ebsco.com/terms-of-use

The peaks observed in DMA and DEA are often much more sensitive to the influence of structural parameters than what can be observed by DSC. Furthermore, the techniques have proven very useful in determining the properties of the amorphous phase near T_g and of secondary transitions at cryogenic temperatures and above. The commercial success of DMA and DEA is due to this ability to pick up information invisible to the most popular DSC. Unfortunately, there are many drawbacks and limitations to the universal use of these instruments.

Since the excitation applied is AC, the first question to ask concerns the frequency range and the number of instruments required to cover a range adequate for studying transitions in polymeric materials.

According to Hedvig [104], the low frequency range is most useful to study transitions in polymers by dynamic spectroscopy. One reason for this is that by measuring transitions at high frequencies as a function of the temperature the loss peaks are shifted to high temperatures at which either chemical decomposition processes, depolymerization, or morphological changes (crystallization) begin to be effective. On the other hand, for studying cryogenic transitions and problems connected with lattice vibrations the high-frequency methods are more useful. For many authors studying polymers, it seems that the very low frequency range and the very high frequency range are most important. Figure 1.17 demonstrates the effect of frequency on the α, β, and γ transitions of polyethylene. The ability to resolve the transitions is increased at lower frequencies. It is clear in Figure 1.17 that DMA and DEA experiments conducted

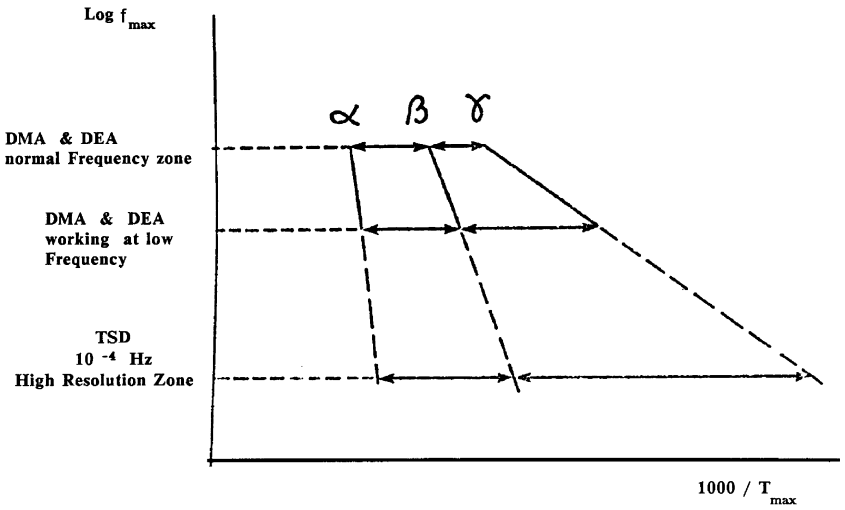


Figure 1.17: This graph shows that the power of separation of molecular relaxation characteristics (α, β, γ) increases as the frequency decreases. This positions TSD as a high-resolution peak deconvolution method compared to DMA and DEA because it works at a low frequency (equivalent) of 10^{-4} Hz.

EBSCOhost - printed on 2/13/2023 12:32 AM via . All use subject to https://www.ebsco.com/terms-of-use

in the normal frequency range of use of these instruments result in a fair amount of overlap between the three peaks. The TSD technique, by working at a low frequency equivalent (10^{-4} Hz), provides a comfortable zone of high resolution.

In summary, an important limitation of DMA and DEA devices is the inability to separate thermally activated peaks with close activation energies. The effect of frequency is to merge neighboring peaks instead of resolving their fine differences.

DMA and DEA are not useful techniques to study the coupling between elementary relaxation modes making up cooperative relaxation processes.

II.1.2.2.2 DMA

DMA has been very popular because the technique is simple to realize and to analyze, and the physical meaning for the input and output (stress and strain) is straightforward. Furthermore, it yields fundamental elastic constants of the materials since the deformation is chosen in the linear viscoelastic region. However, the frequency range is limited to the medium range (0.01 to 100 Hz) and the time-temperature must be applied in order to extrapolate to a reasonable frequency range. The time-temperature superposition principle may lead to gross misapplications [132], and furthermore plastics are never used in the linear viscoelastic region in practical applications. The time-temperature (or frequency-temperature) shift is applied to either tan δ vs. T, G' vs. T, or G'' vs. T, or even G^* (complex modulus) vs. T plots. The temperature dependence of the shift factor, which is used to derive the activation energy, varies with the variable chosen to perform the shift: it is actually not clear which variable should be used to apply the frequency-temperature superposition principle in order to extrapolate results from the mastercurve. Figure 1.18 displays mastercurves obtained by choosing different superposing functions, demonstrating that the extrapolation of the modulus at frequencies outside the experimental range is hazardous, to say the least. Furthermore, if the choice of the superposing variable makes a difference in the value of the activated energy found, one should also question whether this superposing exercise is capable of providing the real fundamental constants of the relaxation mechanism.

If the reason for using a DMA is to get the elastic constants of the materials, a stress-strain curve obtained with a universal tensile testing machine seems more adequate, since it will cover a more practical deformation range. If, however, the DMA is primarily used to plot tan δ vs. temperature, in order to determine the number and type of motions relaxing in the structure, or the number of phases present, then the TSD technique is much more sensitive and provides a better physical insight. Figure 1.19, compared to Figure 1.12, clearly illustrates the superiority of TSD for the block copolymer samples of acrylate and styrene reported previously (Figures 1.11 and 1.12). The E' and E'' DMA curves, obtained with a rheometrics instrument [29], do not conclusively reveal the number of phases present in the block copolymer structure.

EBSCOhost - printed on 2/13/2023 12:32 AM via . All use subject to https://www.ebsco.com/terms-of-use

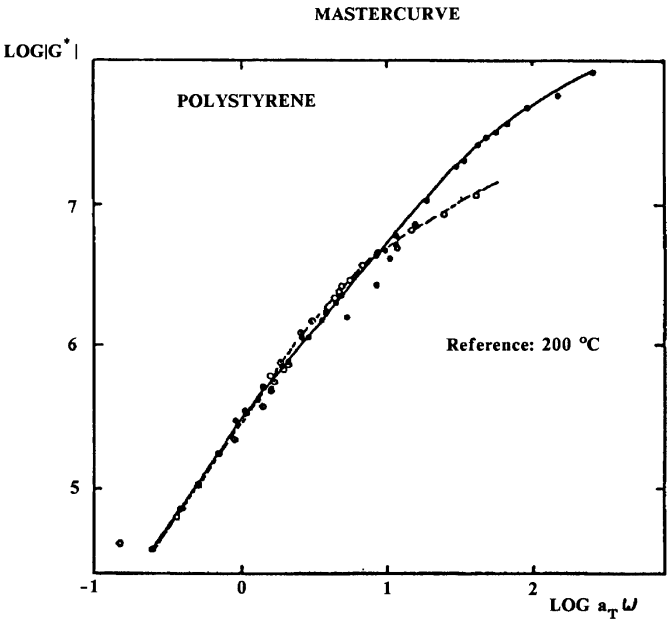


Figure 1.18: Mastercurves at $T_{ref} = 200\,°C$ obtained for polystyrene by extrapolation from DMA results near T_g and from rheometry near $T_g = 100\,°C$. The superposing variable is the complex modulus G^*. The extrapolated mastercurves are notably different.

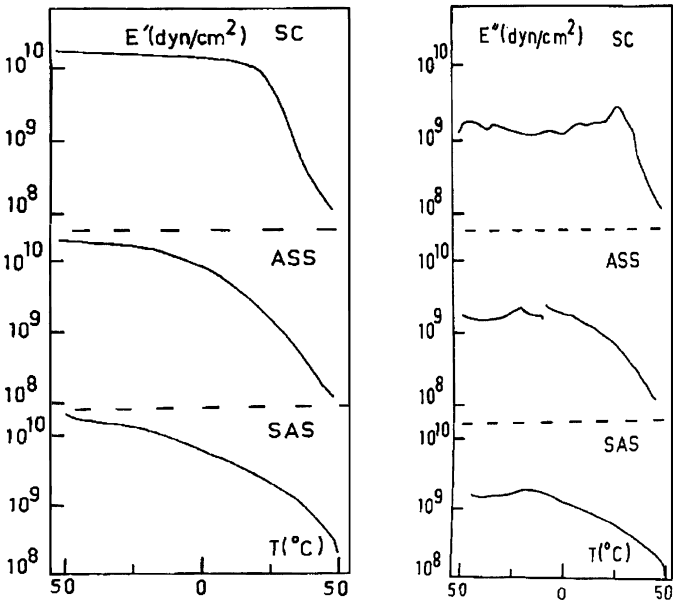


Figure 1.19: Storage (E') and loss (E'') moduli from DMA plotted against T for the samples studied by DSC and TSC in Figures 1.11 and 1.12, respectively.

EBSCOhost - printed on 2/13/2023 12:32 AM via . All use subject to https://www.ebsco.com/terms-of-use

Problems of slippage or breakage in the grips, possible self-heating as the sample gets close to its maximum loss, and the ongoing debate about the respective merits and limitations of the type of deformation to apply (torsion, three-point bending, or tension) are typical worries of DMA users.

The dynamic mechanical behavior of most polymers can be measured with a DMA provided the modulus exceeds 10^6 dynes/cm^2 and tan δ is in the range of 0.0001 to 1.7. The upper limit of use is therefore just above T_g (Figure 1.14), which probably explains why DMA is often considered inappropriate to the study, *without a braid support*, of the rubbery and rubbery flow regions for uncrosslinked amorphous thermoplastics.

II.1.2.2.3 DMA for coatings and adhesives: severe limitations

Many materials such as coatings and adhesives require support for DMA measurements. Glass fiber ribbons have been conveniently used as support, but they suffer from inconsistency of the ribbon itself and are difficult to coat uniformly and to a consistent thickness.

For coatings and adhesives characterization, a minimum damping signal is necessary to yield a detectable damping curve; below this minimum only instrument noise is observed. Maximization of the signal from the coating requires as thin a substrate as possible. However, a minimum-substrate-thickness-to-arm-spacing ratio below which no damping behavior can be detected exists. As the coating thickness decreases, the interface makes a larger contribution to the DMA measurements, which alters the results. The major drawback for coatings and adhesives is the irreproducibility of the DMA data, a secondary concern being the lack of a quantitative measurement technique of the modulus. Quantitative measurements of storage and loss moduli require thick layers (100–255 μm) and preferably a range of thickness, which are severe limitations.

Insufficient machine stiffness can affect dynamic measurements. The difference between actual and measured phase angle is non-linear and becomes significant as the sample stiffness gets near the DMA stiffness. Sample clamping creates a softening or stiffening in the sample tested, which might result in systematic errors. Also, the ratio of clamped to unclamped sample length must be small to eliminate end effects. The thermal expansion during non-isothermal heating causes buckling (in torsion and dual cantilever bending tests). For low frequencies (which are desired to improve resolution), the transducer drift during a cycle may be important relative to signal amplitude, limiting the use of low frequencies. Finally, transducer resonance can result in modulus changes and phase shifts.

II.1.2.2.4 DMA accuracy

The wide diversity in the samples used and the intense reliance of the modular and damping behavior on molecular and structural parameters make it difficult to stipu-

EBSCOhost - printed on 2/13/2023 12:32 AM via . All use subject to https://www.ebsco.com/terms-of-use

late accuracy in DMA experiments. For a given sample, however, measurements can be reproduced to within 2 % to 4 %.

II.1.2.2.5 DEA

The dielectric method is applicable to all polymers, provided that their conductivity is low, which is generally the case, that their dissipation factor falls in the proper range of the instrument, and that the sample can be prepared in a thickness giving a capacitance within the range of measurement available. In a DEA experiment, ε' and ε'' are calculated from the capacitance and dissipation factor of a condenser with the polymer as the dielectric. The temperature of the experiment is selected so that the relaxation times of the motion are comparable to the frequencies used in the experiment. The great advantage of the dielectric method is the possibility to explore an extended frequency range and therefore to avoid having to rely on the predictions of the time-temperature superposition principle. But several techniques and instruments must be combined in order to achieve that.

The bridge method of measuring dielectric permittivity is useful in the frequency range from 0.1 Hz up to about 10 Mhz. The direct phase-separation technique can be used also approximately [104] in this frequency range, mainly from 20 Hz up to 1 Mhz. At higher frequencies up to the sub-millimeter wave region (10^{12} Hz) the resonance method can be used. In the frequency range between 10^8 Hz and 10^{11} Hz the conventional RLC circuits are no longer useful; waveguides and resonators are exclusively used.

Since the frequency range of the commercially available DEA instruments is limited, the range 0.1 Hz to $1 \cdot 10^5$ Hz being most convenient, it is necessary to select a polymer or an operating temperature so that the glass transition falls in the proper range for observation at these high frequencies. Most determinations of T_g (by dilatometry or thermal measurements, for example) are usually so slow that the relaxation times involved are not below 100 sec, in contrast to the range 10 to 10^{-5} seconds for the dielectric method. Small voltages (1 Volt) are normally applied to the dielectric samples, small enough to stay in the linear region, but insufficient to alter non-polar materials dielectrically in order to display transitions. This is the case for polyethylene and polypropylene and their derivatives. Low voltages constrain the use of films almost exclusively, which is not practical for QC/QA applications out of pellets, granules, or bulky samples.

In most instances, sample preparation consists of vacuum deposition of a thin film of conductor on the surface. This process requires the purchase of expensive equipment.

For DEA results, precision and accuracy are determined largely by the care taken in preparing the sample and carrying out the experiment. For the determination of ε', a precision of about ±0.5 % can be achieved with a highly uniform sample of accurately known dimensions. For ε'', the dimensions need not be known precisely but sample

EBSCOhost - printed on 2/13/2023 12:32 AM via . All use subject to https://www.ebsco.com/terms-of-use

uniformity is still important; a precision of about ±2 % can be reached. The precision of the apparatus itself is of the order of ±0.01 %.

II.1.2.2.6 Conclusion (DMA and DEA)

An important question for both DMA and DEA concerns the true physical meaning of the entropy and enthalpy of activation determined from the frequency dependence of the loss peak. If the peak observed is "elementary," i. e., it describes a pure and unique relaxation process, then the value obtained by DMA and DEA is founded. When a non-negligible degree of cooperativeness (interactive coupling) is responsible for the global aspect of the peak, it is difficult to use any classical model to fit the data. Both the thermally activated and free volume equations become empirical linearizing equations which should not be fitted to theoretical models. In that case, the only certainty is that the process giving rise to internal relaxation is rate-dependent and complex.

II.1.2.3 TSD/TWD

II.1.2.3.1 General considerations

The TSD/TWD instrument outputs can either be "classical" or entirely new for polymer characterization. In the classical mode (TSD), the output trace is the current of depolarization versus temperature, showing global peaks for every motion taking place during the recovery process: the output is very similar to a plot of tan δ vs. T obtained with a DMA working at very low frequency.

Figure 1.20 compares the tan δ vs. T output from a DMA for the γ transition of polycarbonate with the TSD output. Although the peaks from the two techniques look very much alike, we notice that the TSD peak is shifted to lower temperatures by about −30 °C. This is explained in Figure 1.21, which shows that, because of the very low frequency equivalent, peaks are expected to be found lower for TSD. As a matter of fact, the extrapolation of the DMA frequency-temperature measurements to 10^{-3} Hz gives −132 °C, which is right where the TSD peak maximum is found in Figure 1.20. The shifting to lower temperatures is prominent for secondary relaxations, because the activation energy is small, but very limited for T_g types of transitions, because the apparent activation energy for these highly cooperative processes is much bigger, resulting in almost no shift at all between the DMA and TSD outputs.

The sensitivity is much superior with a TSD instrument. We can mathematically estimate that the equivalent resolution needed for tan δ in DMA or DEA, to be able to match the resolution of a TSD peak (10^{-16} Amp), given a certain sample mass is 0.0000001 radians, i. e., up to 5,000 times better than what is currently available for these two techniques, and presumably impossible to match in future instruments of the same kind.

EBSCOhost - printed on 2/13/2023 12:32 AM via . All use subject to https://www.ebsco.com/terms-of-use

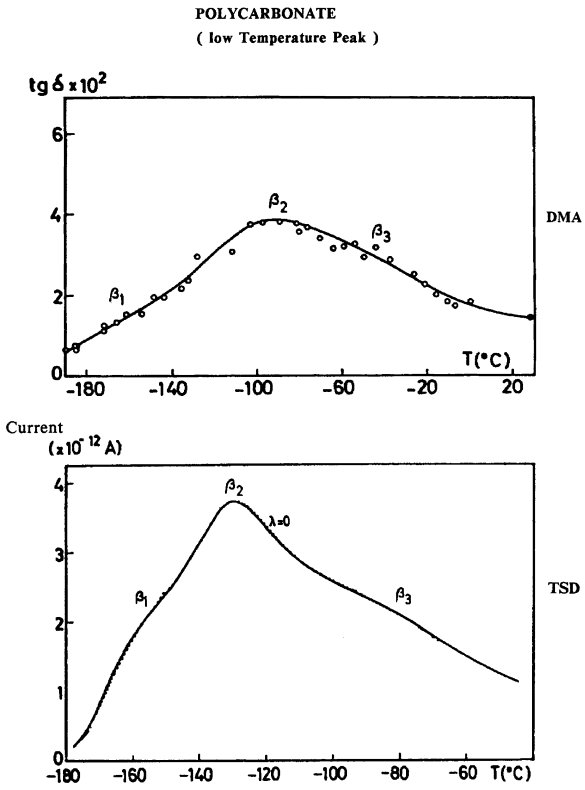


Figure 1.20: Comparison of the DMA tan δ vs. T γ-relaxation peak for polycarbonate (top) and of the TSD depolarization current vs. T response (bottom).

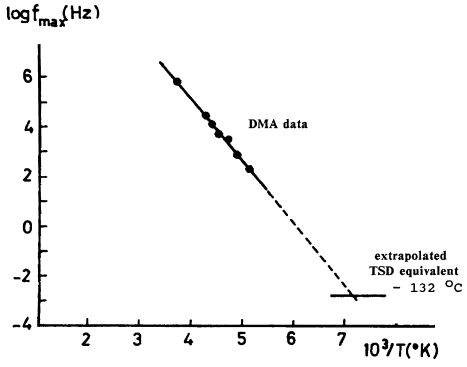


Figure 1.21: Shift of the DMA peak of Figure 1.20 (top) to a lower temperature (–132 °C) for the low frequency equivalent applicable to TSD.

The voltage is much higher for TSD than for DEA (up to 1500 Volts). When the material is non-polar, we increase the voltage until dipoles (or space charges) are created from the displacement of electron clouds within the structure. *This feature enables the study of polyolefins and other non-polar materials*.

Another important feature of TSD is the ability to "coat" the interface between phases (polar or not) with a layer of space charges (free electrons), created at the sur-

EBSCOhost - printed on 2/13/2023 12:32 AM via . All use subject to https://www.ebsco.com/terms-of-use

face, for instance, by application of fast cooling rates during the preparation stage. This is the case for the surface of non-polar polymers. The difference between the thermal expansion coefficient of the electrode surface and the plastic film enables the creation of surface tension, during quenching, which presumably results in free radicals at the surface. Upon reheating, a surface conductivity current is revealed at the onset of the major transitions within the bulk of the material, because of the change in the free energy at the surface, resulting from the motions in the bulk of the material.

Figures 1.22 and 1.23 are TSD plots of a low-density polyethylene heated up at 7 °C/min, after it has been quenched from 160 °C, the temperature at which the material was allowed to sit under the small pressure exerted by the weight of the top electrode. In Figure 1.22, the two LDPE samples *have not been submitted to any voltage*, either during annealing or cooling. This depolarization without the polarization stage is called "instantaneous depolarization." Figure 1.22 displays a pronounced current discharge at the melting temperature of samples A and B. This method of detecting the melting temperature, T_m, of a non-conductor is rather similar to that of DSC. Since the TSD melting peaks are sharp, reproducible, and obtained with a high resolution, one can use the melting of known standard films to calibrate the instrument within a specified temperature zone.

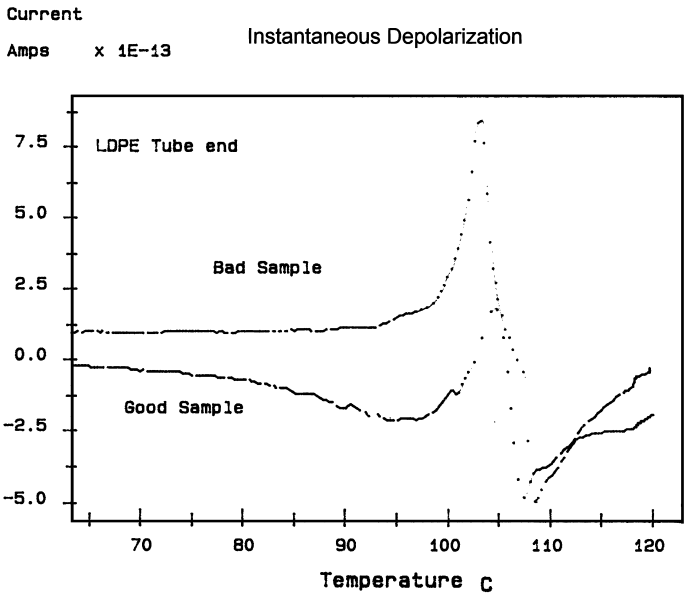


Figure 1.22: Instantaneous depolarization (no polarization before cooling) for a "bad" and a "good" sample taken from an LDPE tube end. Comparison of the TSD traces versus *T*. See text.

EBSCOhost - printed on 2/13/2023 12:32 AM via . All use subject to https://www.ebsco.com/terms-of-use

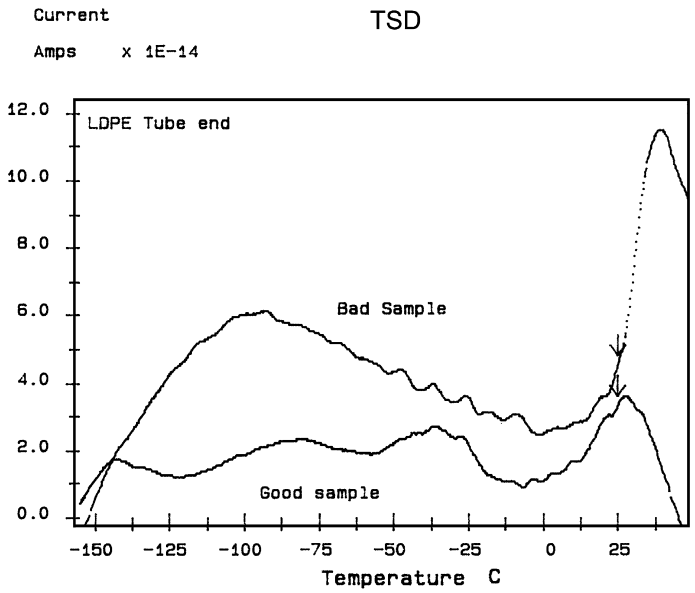


Figure 1.23: Depolarization after polarizing at $T = 25\,°C$ for the same "bad" and "good" samples taken from an LDPE tube end. The height of the T_α peaks observed is related to the amount of amorphous matter in the sample. The traces permit to differentiate the two samples' crystallinity.

In Figure 1.23, the same LDPE samples are polarized at $T_p = 25\,°C$ prior to cooling. Figure 1.23 compares the α peaks which depend on the amount of crystals present in the morphology. One sees large differences between samples A and B: the specimen with the higher α peak has fewer crystals, i. e., it is more amorphous. This concurs also with the value of T_m, which is lower for sample B.

TSD is applicable to a large variety of sample states: films, strands or fibers, up to 3-mm-thick bulk specimens, pasty and rubbery materials, latexes, paints, glues, resins, and even pellets. The great advantage is in the sample preparation, which is simpler than for a normal DEA experiment and does not run into the geometrical and temperature restrictions imposed by DMA. In the case of paints, glues, and other coatings, the material can be studied directly on its support, which presents a definite advantage for quality control applications [207].

Temperature can be scanned from the temperature of liquid nitrogen to 400 °C, across T_g, exploring the rubbery and rubbery flow regions as easily as the solid state or even the liquid state, but with some restrictions.

In the TWD mode, the output is a spectral line either of $\log \tau$ vs. $1/T$ obtained from an Arrhenius transfer of the elementary Debye depolarization curve (Introduction, Figure 0.10) or of the free energy of activation ΔG versus temperature calculated from the Eyring model (Figure 1.24; also see Figure 2.24 in Part I, Chapter 2).

EBSCOhost - printed on 2/13/2023 12:32 AM via . All use subject to https://www.ebsco.com/terms-of-use

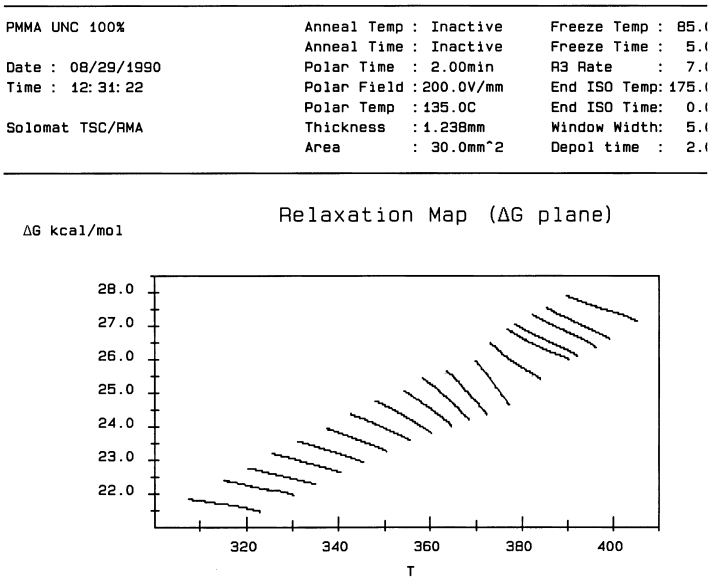


Figure 1.24: Relaxation map (from TWD) in the ΔG plane for pure PMMA. This graph was the output of the relaxation modes obtained by thermal-windowing (T_p between 55 °C and 120 °C) using the automated TSC/RMA spectrometer of Solomat Instruments in the 1990s. Also see Figure 4.16.

Plots and tables of free energy ΔG, entropy ΔS, and enthalpy ΔH of activation versus polarization temperature T_p represent the thermokinetic outputs. Another interesting output is the variation with T_p of the intensity of the current of depolarization at the maximum of the thermal-windowed elementary peaks (Figure 1.25, bottom right). This is further discussed in Part I, Chapters 1 and 2. T_g is the temperature at the maximum of entropy of activation (Figure 1.25, bottom left). Compensation search plots (Figure 1.25, top), or EE plots (ΔS vs. ΔH), determine the degree of cooperation between the coupled relaxation modes, which describes the thermokinetic state of the amorphous phase (Part I, Chapter 2).

The thermal-windowing data can easily be converted into ε' and ε'' values (Figure 1.26), thus allowing a comparison with ordinary dielectric data. The great advantage of getting the individual relaxation times and their distribution by thermal-windowing is not only being able to study their cooperativeness (compensation search), but also to be able to calculate the response of the material at any other frequency and temperature. Agreement with AC data is remarkably good, provided the various thermal-windowed peaks are correctly fitted. The equations of conversion are as follows:

$$\varepsilon' - \varepsilon_\infty = \sum_{i=1}^{n} (\varepsilon_s - \varepsilon_\infty) i \frac{1}{1 + \omega^2 \tau_i (T_p)^2}$$
$$\varepsilon'' = \sum_{i=1}^{n} (\varepsilon_s - \varepsilon_\infty) i \frac{\omega \tau_i (T_p)}{1 + \omega^2 \tau_i (T_p)^2} \tag{1.1}$$

EBSCOhost - printed on 2/13/2023 12:32 AM via . All use subject to https://www.ebsco.com/terms-of-use

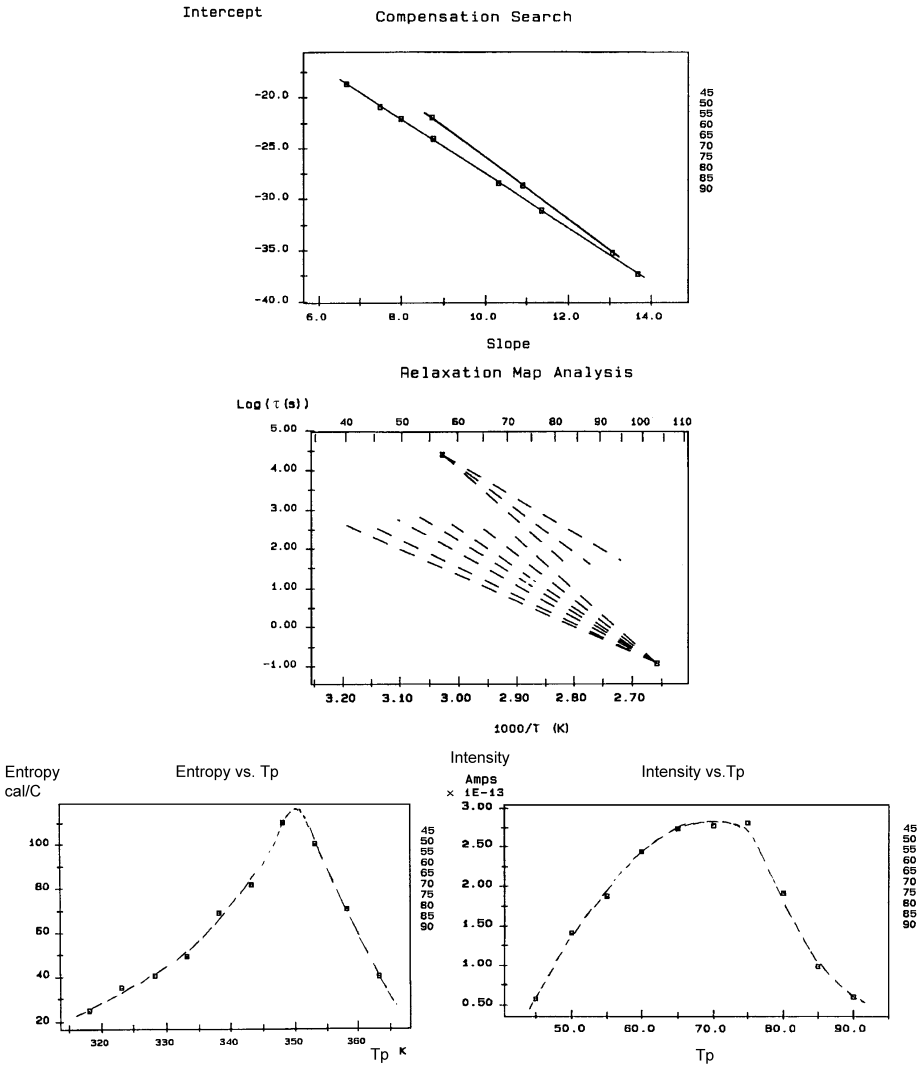


Figure 1.25: Several outputs obtained from thermal-windowing. Top: compensation search (intercept vs. slope at various T_p of the Debye elementary relaxation modes plotted as Arrhenius lines). Middle: relaxation map analysis in the $\log \tau$ vs. $1/T$ plane of all the relaxation modes. Bottom: entropy of the Debye peaks vs. T_p (K) (left) and peak intensity of the Debye peaks vs. T_p (right); both graphs show the change of the mechanism of interactive coupling across the T_g of the polymer.

where ω is the radial frequency and the parameters $(\varepsilon_s - \varepsilon_\infty)_i$ and $\tau_i(T_p)$ are found from a series of thermal-windowing experiments at different T_p.

Two other chapters of this book (Part I, Chapter 2 and Part II, Chapter 3) clearly demonstrate the power of information inherent to TWD, either theoretically (Part I)

EBSCOhost - printed on 2/13/2023 12:32 AM via . All use subject to https://www.ebsco.com/terms-of-use

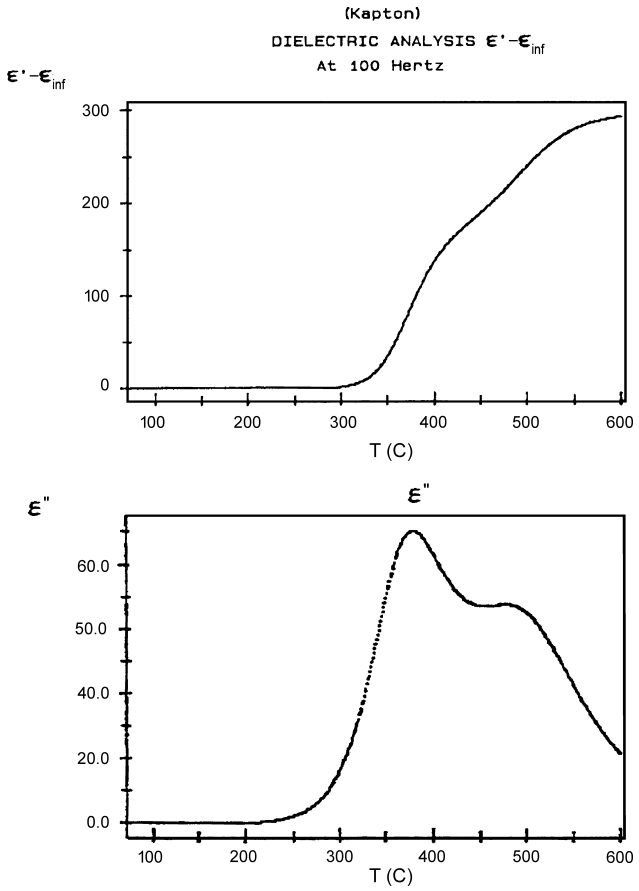


Figure 1.26: Example of DEA for analyzing the molecular motions in Kapton at a frequency of 100 Hz. The top graph shows $\varepsilon' - \varepsilon_{\text{inf}}$ vs. T (°C) and the bottom graph shows the dielectric loss, $\varepsilon''(T)$.

or practically (Part II). For paints, coatings, and glues, the TWD technique provides a unique opportunity to quantify the bonding strength, not only to the metallic support, but also to other materials, such as paper for labels (Part II, Chapter 3). The value of $(T_c - T_g)$, where T_c is the compensation temperature for the T_g transition, and the DOD number characterize the state of non-equilibrium for plastic parts which are oriented or thermally treated. Note, for oriented specimens, that the recoiling of the specimen above T_g does not distort the results: the return to equilibrium in the structure is what we want to observe through the motion of the dipoles.

The repeatability of a TSD is excellent (2%) provided the samples are located precisely at the same place between the electrodes. Gradients exist in the TSD cell but are minimized by a specific design by the manufacturers.

The resolution is absolutely outstanding in this technique, and can be further increased by lowering the heating rate upon depolarization.

EBSCOhost - printed on 2/13/2023 12:32 AM via . All use subject to https://www.ebsco.com/terms-of-use

The accuracy in determining the DOD number, or the compensation point coordinates, depends on the number of points used to characterize the compensation line. This is developed in more detail in the next section on TWD accuracy. T_g is located at the maximum of the entropy versus T_p plot, and the accuracy to locate it depends on the interval chosen between the T_ps. Another quantitative treatment, explained in Part I, Chapter 2, uses the intercept of the Z-line with the ΔG_p vs. T_p curve, leading to very accurate results to determine T_g and the obtention of ΔH_g and ΔS_g at T_g.

Despite all its merits, the thermal-stimulated method has a major drawback: TSD cannot be applied to conductors or semi-conductor materials for which the resistance is smaller than 10^9 ohms/meter of thickness.

The presence of space charges in the structure needs to be dealt with carefully and with knowledge to avoid certain pitfalls and artifacts. Note, however, that the doping of space charges at the interface between distinct morphological entities (fiber/matrix in a composite) can be used to probe the interface. Another important application of space charges to the characterization of the melting temperature is demonstrated in Figures 1.22 and 1.23.

For a classical use of the instrument and for "normal" sample preparation techniques, the upper temperature limit of analysis is located at the onset of melting of the sample, which shows up as a large current discharge – Figure 1.27 – (the sample behaves as a battery which drains the charges accumulated at the surfaces). In that respect, a DSC and a TSD are complementary since one technique (DSC) characterizes well semi-crystalline materials while the other (TSD) excels with amorphous ones.

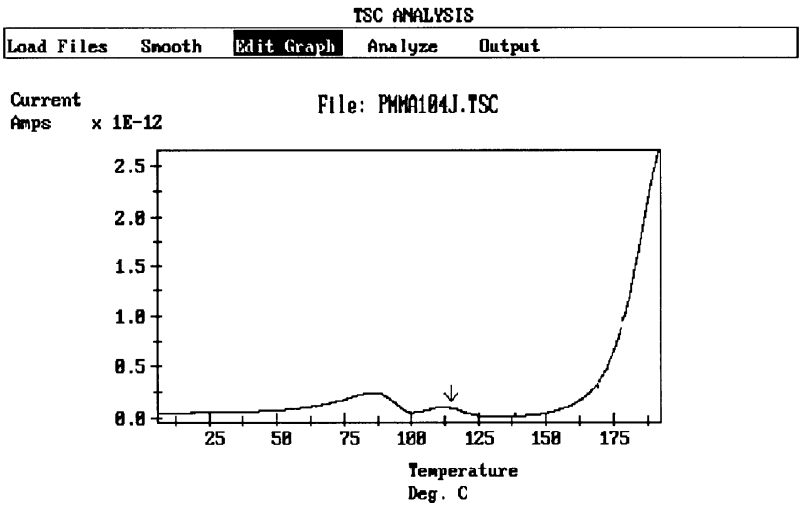


Figure 1.27: TSD output for PMMA from the automated TSC/RMA spectrometer from Solomat Instruments. The arrow indicates the temperature of polarization, T_p.

EBSCOhost - printed on 2/13/2023 12:32 AM via . All use subject to https://www.ebsco.com/terms-of-use

The thermal-stimulated methods consist in applying an electric or mechanical field at a temperature T_p in the vicinity of the temperature at which the internal movements occur. The effect of bringing the material to this temperature T_p enables the latter to relax from its internal stresses, if any are present, or to modify its rate of crystallization, if it is capable of crystallizing, or to modify its degree of curing, if it is a thermoset. It is clear that the stimulated methods are restricted to the study of internal movements which are not disturbed by morphological changes at the "probing temperature" T_p.

There are ways around this problem, for instance, improving the thermal controls of the TSD instrument to minimize the time spent to reach T_p and cool to T_o. One can also use several samples, one for each T_p, which unfortunately results in a rather long and expensive process. Alternatively, the same sample is programmed to be tested in a batch mode to undergo in the cell a series of TWD scans across several T_ps. But the best approach in this case is to consider *isothermal* polarization–depolarization methods, spontaneous depolarization, or the thermal-stimulated polarization current (TSPC) mode. These techniques are available in commercial TSD/TWD instruments and are described in Sections II.1.2.3.5 to II.1.2.3.7 below.

II.1.2.3.2 TWD accuracy

In Part I, Chapter 1, we studied in detail the methods of integration, which can produce an uncertainty in the determination of the kinetic parameters. In this section, we study the regression parameters which influence the compensation results and, in particular, we show that, once the correct integration method is perfected, critical attention should also be exercised in the definition of the baseline, when integrating the data to obtain the Arrhenius transform of the raw depolarization data.

We have claimed that compensation phenomena and the DOD number are new analytical tools to characterize the amorphous state of polymers. The questions that we must address to qualify the phenomenon of compensation as a legitimate tool for studying the amorphous state of polymeric matter are as follows: what is the decisive argument which tells with certainty that the relaxation curves obtained from thermal-windowing converge into a point? Could it be a mathematical approximation, a forced artifact? Could the $\log \tau$ vs. $1/T$ curves be replotted in a manner which would make them superpose by traditional models instead? What is the accuracy expected in determining the coordinates of the compensation point, and could it be that relaxation curves, which apparently compensate on an Arrhenius diagram, also superpose on a $\mathrm{Log}\,\tau$ vs. T plot? What is the influence of the choice of the baseline in the determination of the relaxation times, and how does this affect the accuracy in the determination of the compensation point coordinates?

II.1.2.3.3 Result of changing the baseline of integration

We first study the effect of making a possible error in the evaluation of the baseline before integration of the window-cleaned peaks. The relaxation time is evaluated at

EBSCOhost - printed on 2/13/2023 12:32 AM via . All use subject to https://www.ebsco.com/terms-of-use

each temperature as the ratio of the current to the remaining polarization (see Introduction), and it is, therefore, crucial to determine the integral of current over the first half of the peak with a good accuracy, assuming an integration according to a Debye approximation.

Figure 1.28 is a current of depolarization output for polycarbonate polarized at 130 °C (indicated by the arrow in the figure). We have chosen this particularly bad thermal-window peak to prove our point (the experimental conditions of thermal-windowing *should* be modified to obtain a better "Debye peak").

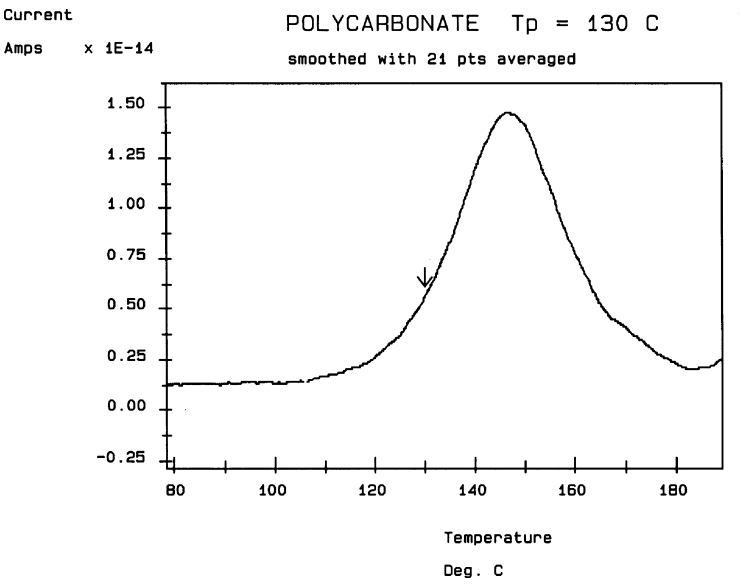


Figure 1.28: TWD output showing the current of depolarization for polycarbonate polarized at T_p = 130 °C and submitted to the thermal-windowing procedure.

In a first trial, the raw data are smoothed with a 21-point smoothing average technique. The smoothed curve is integrated using the modified Lacabanne integration technique explained in Part I, Chapter 1: this produces the Arrhenius transform, Log τ vs. $1/T$ shown in Figure 1.29 for a baseline of 1.476×10^{-15}. The slope of the Arrhenius line is equal to 1.85 eV and the intercept is –20.45. In order to study the effect of selecting several horizontal lines for the baseline, we draw another baseline at 1.18×10^{-15}, a baseline choice which is qualitatively "as good," with the reservations already mentioned regarding the poor quality of the Debye peak obtained by thermal-windowing. The new fit gives a slope of 1.8 eV and an intercept of –19.81.

If the integration is performed from the unsmoothed data instead, but using the same baseline (1.18×10^{-15}), another set of values are found for the slope (1.74 eV) and

EBSCOhost - printed on 2/13/2023 12:32 AM via . All use subject to https://www.ebsco.com/terms-of-use

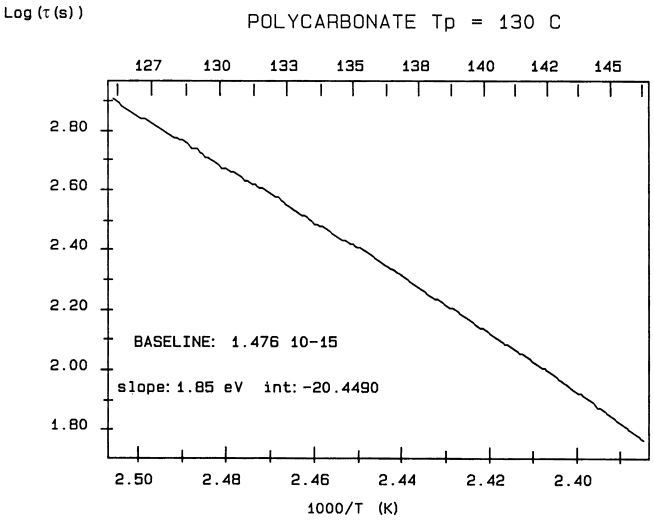


Figure 1.29: Conversion of the current of depolarization shown in Figure 1.28 into a log τ vs. $1/T$ elementary relaxation mode in the Arrhenius plane. This relaxation is characterized by the slope and intercept of the Arrhenius line.

the intercept (–19.04). Finally, if we integrate the peak with a different choice for the integration limits, we obtain other values for the slope and intercept.

The results of changing the baseline and the integration limits are confined in Figure 1.30, which is a plot of intercept versus slope.

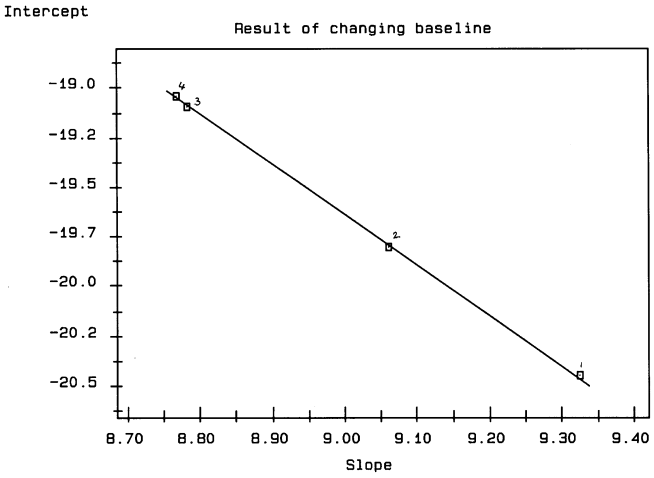


Figure 1.30: Effect of redefining the baseline in Figure 1.28 on the values of the characteristics (slope and intercept) of the relaxation mode. Four possible baselines have been considered, numbered 1 to 4 on this plot of intercept vs. slope (a compensation search type of plot).

EBSCOhost - printed on 2/13/2023 12:32 AM via . All use subject to https://www.ebsco.com/terms-of-use

One sees in Figure 1.30 that the slope varies between 8.75 kcal/m and 9.35 kcal/m and that slope and intercept are in a first approximation linearly related to one another. Therefore, the error due to a wrong assignment of the baseline corresponds, in this extreme situation of a bad experiment, to an error of ±3 % in the determination of the slope and intercept. It is interesting to note that a change of the baseline results in a compensation phenomenon for the intercept and slope. While there is, a priori, no real physical reason for it (and some people will use that result to disqualify the compensation phenomenon altogether), there is a good explanation for such a behavior. In Part I, Chapter 1, we study the effect of shifting the Debye peaks along the temperature axis and/or changing the total polarization on the activation enthalpy and the value of the pre-exponential factor. We observe a compensation behavior for the intercept–slope coordinates as the result of either temperature shifting of the Debye depolarization curves or the increase of the total polarization. These compensations are extensively analyzed in Part I, Chapter 3: they are not artifacts and correspond to physical reality. The choice of a different baseline, however, is equivalent to changing the total integral below the peak and, therefore, it should result in a compensation effect, but this compensation has "no physical reality"; it merely describes how the uncertainties of measurement have the same apparent look as a true effect. The artifacts can be quantified easily by simulation, and although they may affect the accuracy in the determination of the *true* compensation points, they can be eliminated by using a careful and systematic integration method. For instance, the effect of changing the integration limits when using the modified Lacabanne integration rule is identical to selecting a slightly different curve-fitting Debye peak: once again, we should expect a compensation for those values obtained by integrating differently. However, the compensation coordinates in this case, like for the baseline effects, is physically meaningless.

The software of an automated TSD/TWD instrument incorporates means to avoid errors from the integration routine, for instance, a regression determination of the baseline and an automatic integration of the peak based on an understanding of the Debye equation. The automatic integration leads to point #2 in the compensation search diagram shown in Figure 1.30. It is estimated that an automatic curve-fit of the Debye relaxation peaks leads to the minimization of the error due to an estimate of the location of the baseline before integration. The software also provides a mathematical baseline subtraction routine and means to check that the values obtained by the Debye integration curve-fit well the depolarization peak. As an illustration of the intelligence built in the software of the TSD/TWD instruments currently commercialized, the software notifies the user during the analysis of Figure 1.28 to modify the experimental TWD set-up (T_d, t_d) to obtain a better elementary Debye peak in order to improve the accuracy of the peak analysis. Both mathematical curve-fitting criteria and physical understanding considerations interact to optimize the accuracy.

When the conditions of the experiment and integration are optimum, which is easily provided by the software nowadays, the accuracy in the determination of enthalpy and entropy of activation at a given polarization temperature can be as low as 1 %.

EBSCOhost - printed on 2/13/2023 12:32 AM via . All use subject to https://www.ebsco.com/terms-of-use

II.1.2.3.4 Compensation search. Accuracy to determine the DOD number

In a compensation search, each point has as coordinates the slope and intercept of an Arrhenius line. The best determination of the compensation point coordinates can be done by finding the best line passing through the data points. This can be performed by simple regression analysis, taking each data point (slope–intercept) as a single point of the regression statistics. The more data points for the regression, the better the determination of the compensation point. This implies that the DOD number, which is obtained from the equation of the compensation line, is better determined if many temperatures of polarization are used. Another approach consists in considering that each data point of a compensation search is in fact representative of a set of approximately 300 data points of the Arrhenius line itself. Each Arrhenius line might not be linear with the same accuracy, and therefore their respective influence on the characterization of the compensation point should not be dealt with identically. One can use a linear simplex method to determine the best straight line (with the best regression coefficient r^2) taking all the points representing the Arrhenius lines.

In Figure 1.31, the simplex line (full line) passes through data points 1, 3, 4, and 5 only, and grossly misses data points 2 and 7. The dotted line is obtained by simple regression. This seems to indicate that points 2 and 7 were obtained with an error associated with a poor determination of the baseline. These two data points were fabricated by us to illustrate our point of concern here: in effect, we purposely and erroneously chose the baseline in the integration of data points 2 and 7. The simplex correctly ignored those data, which could be eliminated from a subsequent recalculation set.

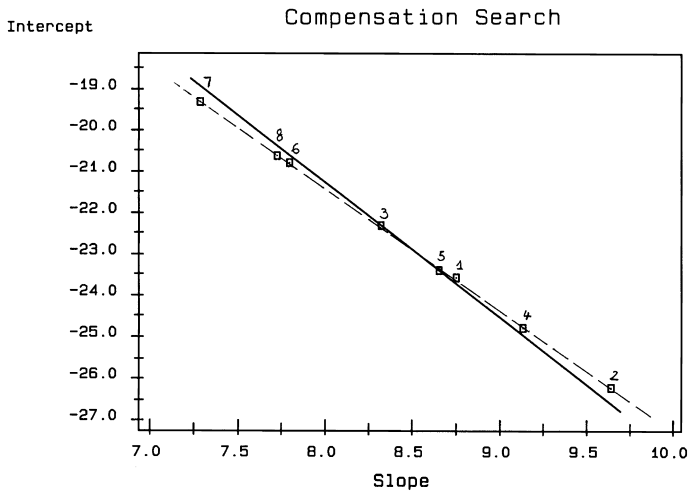


Figure 1.31: Analytical procedure coupling a regression and a simplex technique to determine a compensation search with accuracy by eliminating results that are corrupted by the wrong definition of the baseline of the Debye peak.

EBSCOhost - printed on 2/13/2023 12:32 AM via . All use subject to https://www.ebsco.com/terms-of-use

In other words, bad data can be eliminated by comparing results obtained from a simple linear curve-fitting regression and a simplex regression. If the compensation lines obtained with the two methods are very close to one another, then we choose the value obtained by the simplex method which usually gives the best determination and the best correlation coefficient. If the results are largely different, we reexamine the integration routine and check the validity of the peak to be a real Debye. In some instances, we might have to reselect the thermal-windowing variables and rerun the experiment.

Most of the uncertainty in the assignment of an accurate DOD number comes from the positioning of the sample in the dielectric cell. The suspended technique of holding the sample in the cell is often used because it eliminates or greatly reduces surface and space charges in the sample. But the suspension of the specimen in the cell must be prepared carefully to avoid the effect of temperature gradients. The existence of temperature gradients in the cell, although minimized in the central region by a specific design, results in most of the error in a TSD or TWD experiment. The location of a depolarization peak on the temperature axis depends on the temperature of polarization of the sample, which, for a given T_p, depends on the position of the sample in the cell, because of the presence of temperature gradients. As mentioned in the previous paragraph, a slight shift of the peak on the temperature axis results in a change of both the activation enthalpy and the pre-exponential factor of the corresponding curve-fitting Debye, resulting in an error. When the experimental procedure is well defined and the operator is well aware of the consequences of his or her set-up, the repeatability and accuracy of the technique are excellent, leading to a reliable definition of the DOD.

With only five temperatures of polarization, the error in the determination of the DOD number is ±1 % if the experimenter's potential errors are under control. This improves to 0.5 % for nine T_ps and to 0.3 % for 11 or more T_ps. This proves that the accuracy of the TWD technique is linked to its repeatability. When optical instrumentation to fine-tune the alignment of the specimen in the cell is used, the operator's errors can be further eliminated.

In conclusion, we advocate the use of automatic data integration to eliminate errors due to baseline selection, at least nine temperatures of polarization per compensation line, and linear programming solutions (simplex) to obtain the best accuracy for the determination of the compensation point coordinates.

II.1.2.3.5 Isothermal depolarization experiments

In isothermal depolarization experiments, the material is quickly brought up (or down) to the temperature of interest, say to a temperature of crystallization, and polarized for a certain time. The depolarization curve is then directly recorded at that same temperature by automatically switching to reading mode (Figure 1.32). Cycles of polarization–depolarization can easily be programmed to follow the evolution of the structure at that temperature. The TSD can be looked at as a "camera" which takes pictures at regular intervals.

EBSCOhost - printed on 2/13/2023 12:32 AM via . All use subject to https://www.ebsco.com/terms-of-use

cotb	Anneal Temp : Inactive	Depolarization Ti
COTB.BTC	Anneal Time : Inactive	10.0min
Date : 01/03/1991	Polar Time : 2.00min	
Time : 11:28:09	Polar Field : 1000.0V/mm	
	Polar Temp : 10.0C	
Solomat TSC/RMA	Thickness : 0.040mm	
	Area : 38.0mm^2	

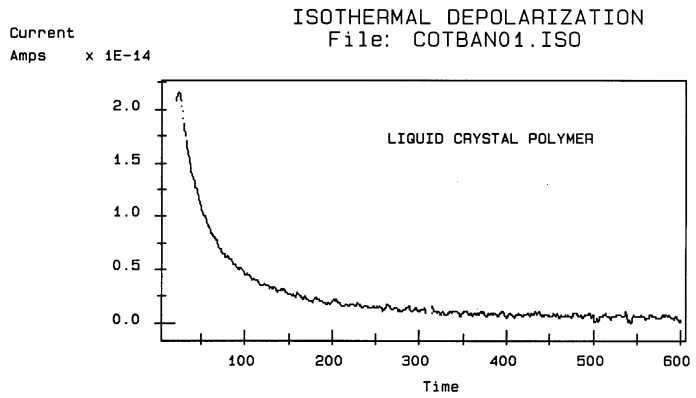


Figure 1.32: Isothermal depolarization. After the polarization stage at T_p, the current of depolarization is measured in time, defining a relaxation time at that temperature.

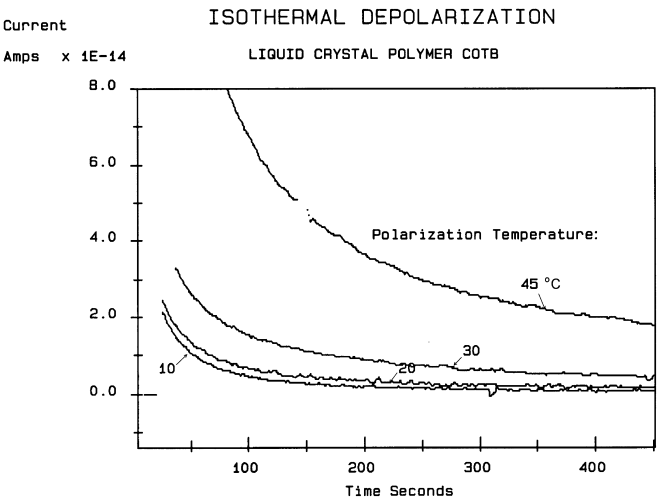


Figure 1.33: Effect of polarizing at different temperatures, T_p, for the same polarization time, on the current of depolarization kinetics.

Figure 1.33 displays the relaxation curves at several temperatures of isothermal operation, showing the classical decrease of the relaxation times at lower temperatures. The relaxation curves can be analyzed with the classical models of thermokinetics, e. g.,

EBSCOhost - printed on 2/13/2023 12:32 AM via . All use subject to https://www.ebsco.com/terms-of-use

the stretched exponential formula, and the kinetic parameters compared with those found from thermal-windowing.

II.1.2.3.6 Spontaneous depolarization current

It is well known that polymers generally assume, in the glassy temperature region, a state of non-equilibrium. In addition to the presence of internal stress, essentially resulting from cooling rate effects, orientation of the chains is often observed in parts which are processed by injection or extrusion. Trapped delocalized charges form during thermoforming or extrusion, which can be observed on reheating in a simple experiment of spontaneous depolarization.

In this mode of depolarization of the charges, the sample is positioned in the dielectric cell without prior exposure to any voltage field. The cell is heated up at constant heating rate and the specimen is shorted through the electrometer. The current of discharge during heat-up is measured by the electrometer and plotted against temperature, revealing negative or positive peaks at the onset of molecular or dipolar mobility in the material structure. When a polar specimen is oriented, the disorientation of the dipoles occurs when the chains recoil back to their random coiled state. A current is generated during the disorientation process.

The peaks generated during spontaneous depolarization are very sensitive to the initial non-equilibrium state of the material, its thermomechanical history, and its processing and aging conditioning. The presence of thermal gradients across the thickness during cooling also results in the creation of local charges, which can be trapped at dipolar sites.

Spontaneous depolarization current (SDC) is, in many respects, complementary to DSC, which measures the calorimetric relaxation during the return to equilibrium, and can be used to characterize the initial state of specimens as a function of processing conditions, orientation, etc. The technique does not perturb the non-equilibrium state to be characterized because, unlike TSD, no preliminary heating to the polarization temperature takes place.

Figures 1.34 and 1.35 give two examples of practical use of SDC. In Figure 1.34, two films of PET, provided by ICI Co., are compared, one with a special corona treatment. The amount of "static" charges left in the samples (proportional to the surface area under the peak) is much reduced for the treated specimen.

Figure 1.35 is the SDC for a biaxially stretched film of PET, heated at 7 °C/min in the TSD cell. The dipoles are oriented in the two directions perpendicular to the film thickness, i. e., the current flow direction. The uncoiling, which starts to occur at 55 °C, consists of three stages, each represented by a peak in the SDC diagram. The current first decreases slightly, followed by an important increase in the form of a large positive peak. Before the peak can reach its maximum, a negative peak comes into play, which drives the current downwards. The composite curve is the sum of these two peaks –

EBSCOhost - printed on 2/13/2023 12:32 AM via . All use subject to https://www.ebsco.com/terms-of-use

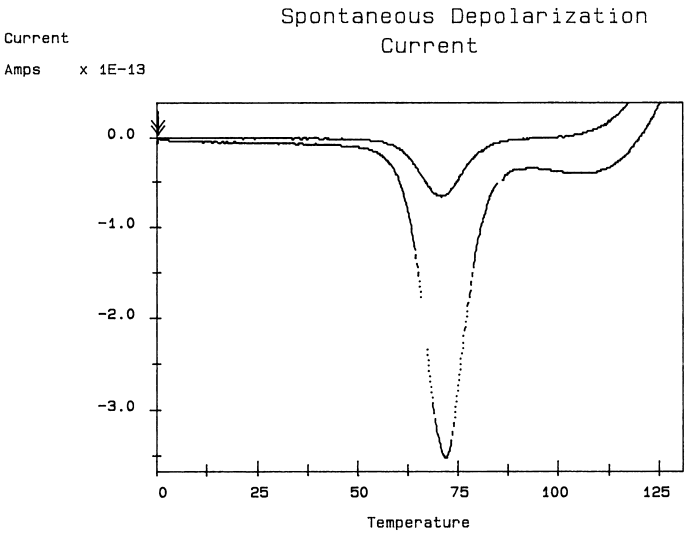


Figure 1.34: Example of SDC runs for two PET films heated at 7 °C/min without prior polarization. The large peak corresponds to a film without any corona treatment. The small peak is obtained for a film treated with a special corona procedure.

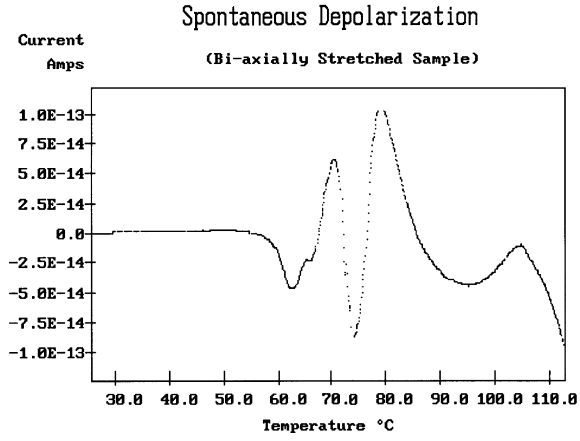


Figure 1.35: SDC plotted versus temperature for a biaxially stretched film heated at 7 °C/min in the TSC cell.

one positive and one negative – which possibly reveals a non-uniform draw ratio in the plane of biaxial stretch.

The SDC technique is simple and extremely sensitive, but more delicate to interpret. The distribution of charges in the thickness might vary from spot to spot in the specimen and between specimens. However, by averaging over several samples or specimens, the technique can be suitably applied to determine the *distribution of internal stress and orientation* in molded thermoplastics and resins.

EBSCOhost - printed on 2/13/2023 12:32 AM via . All use subject to https://www.ebsco.com/terms-of-use

II.1.2.3.7 The thermal-stimulated polarization current

In the TSD experiments described in this chapter, current peaks are recorded while the sample is under short-circuit during heating. This allows the measurement of current discharge and depolarization current. An alternative method consists in recording the current which arises when an unpolarized specimen is heated in the TSD cell under an external field. The sample is cooled from room temperature to some initial temperature T_o in the absence of a voltage field. At T_o, the field is applied to the sample, and the material is heated under the field while the current, through the electrometer, is recorded against temperature. This gives rise to current peaks, which appear when the sample becomes polarized at the onset of molecular or dipolar mobility in the material structure. This current is called the TSPC. The current measurement is actually equivalent to measuring the conductance in the material. Figure 1.36 shows the polarization current arising from heating PET cut-outs from blow-molded bottles to reveal the internal stress in the material.

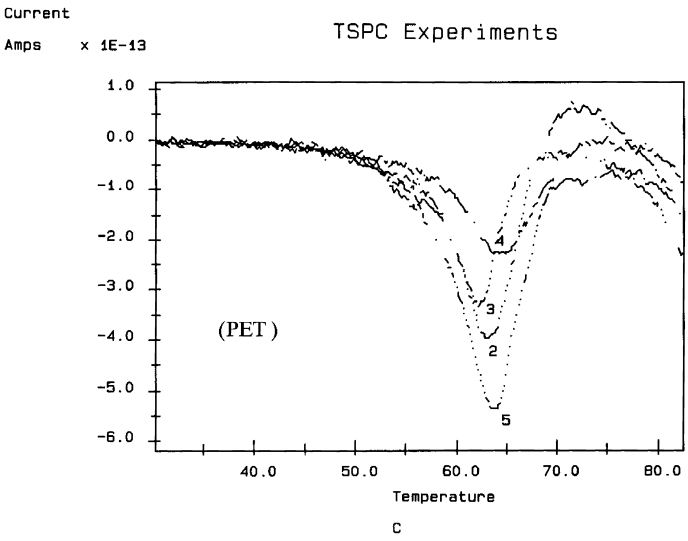


Figure 1.36: Examples of thermally polarized current (TSPC) runs in the TSC cell for a PET sample.

TSPC has received less attention in the literature than the TSD technique. One reason is perhaps the apparent signal-to-noise ratio, which is better in the case of TSD where no external field is applied during the measurement. However, TSPC measurements may reveal information on the nature of the peaks observed, which could not be obtained from TSD measurements alone. In particular, if a given peak is observed as a positive current in TSD, an equivalent negative peak should be observed in TSPC in the case of a dipolar transition (e. g., T_g transition). If the depolarization peak observed in a TSD run is due to the motion of trapped charges (vacancies or interstitial ionic dipoles),

EBSCOhost - printed on 2/13/2023 12:32 AM via . All use subject to https://www.ebsco.com/terms-of-use

an exponential rise of conductivity will appear at the same temperature range during heating in the TSPC experiment. In the case of the $T_{g,\rho}$ transition, the TSPC does not produce any peak and the temperature associated with $T_{g,\rho}$, during a TSD run, is actually the start-up of conductivity in a TSPC experiment. This is a crucial observation for the interpretation of the nature of the $T_{g,\rho}$ peak, as explained further in Part II, Chapter 2 and Part I, Chapter 3.

II.1.3 Conclusion

In conclusion, we have briefly compared the merits and limitations of the most popular techniques DSC, DMA, and DEA with the less-known thermal-stimulated techniques, TSD and TWD, only introduced commercially since the late 1990s. The TSD technique's super-sensitivity makes the detection of some transitions that other techniques cannot see or cannot define well enough possible. While the theory of thermal-stimulated processes has been known for years, its use has been delayed by a lack of effective instrumentation, particularly the lack of adequate electrometers, experiment controls, automation, and analysis software. Advances in microelectronics and software analysis and a good 40 years of back-up experience in the lab [160] from the scientists who put the method together make the technique a practical reality.

The thermal-stimulated current instrument generates quantitative reproducible results with ease. The quasi-absence of requirements (size, shape) for sample preparation makes it possible to characterize samples taken directly from their sites of practical use. This is unique to this instrumentation. But a TSD/TWD spectrometer is more than just a thermal analyzer: it is both a thermal analyzer and a rheological instrument, capable of probing the local motions and also determining their interactive cooperation, which dictates the macroscopic viscosity. Research scientists who have used other techniques (DMA, DEA, DSC) will recognize the benefits of a thermally stimulated dielectric instrument which, when simply used as a TSD, combines the outputs from the traditional apparatus, yet, when switched to the TWD spectrometer mode, allows a new understanding of the structure and behavior of polymers. In particular, it becomes rapidly clear to the users that the description of the elementary relaxation modes, their thermokinetic characteristics (activation enthalpy and entropy), and the description of the *interactive coupling dynamics* is essential for a complete understanding of the macroscopic properties of polymeric materials (Part I Chapter 3).

EBSCOhost - printed on 2/13/2023 12:32 AM via . All use subject to https://www.ebsco.com/terms-of-use

EBSCOhost - printed on 2/13/2023 12:32 AM via . All use subject to https://www.ebsco.com/terms-of-use

Part II Chapter 2
Practical examples of TSD characterization

II.2.1 Introduction: the nature of the peaks

Let us first go back to the principle of thermally stimulated current analysis, to be sure that the nature of the peaks observed in this technique is well understood. It should be clear that the sample to be tested is a dielectric capacitor charged by application of a voltage at high temperature and then quenched to freeze the charges. The polarization stage consists, therefore, in producing a thermal electret. The depolarization stage, which is induced by thermal energy as temperature ramps up at a given rate, occurs by shorting the sample via the electrometer. The electrometer is nothing more than a current amplifier of exceptional characteristics, capable of detecting infinitesimal current discharge. Recent advances in metal–oxide–silicon (MOS) field-effect transistors (FETs) and the development of bipolar FETs and MOS operational amplifiers have made possible the detection of ultralow current (down to 10^{-17} Amp). Figure 2.1 (after Vanderschueren) schematically describes a possible configuration for the TSD cell.

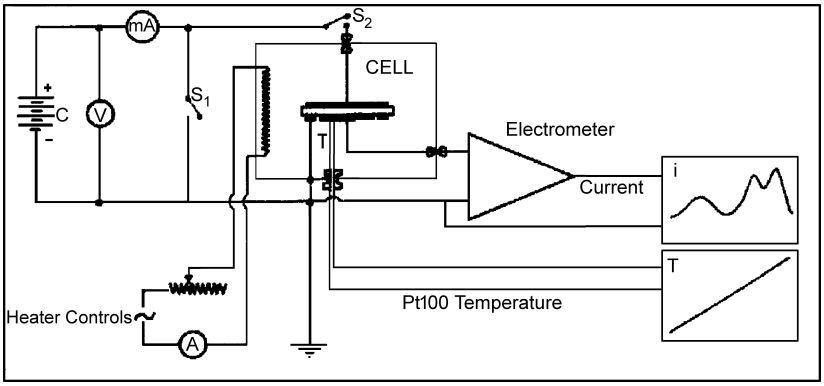


Figure 2.1: Schematic of a possible configuration for a TSD instrument (after Vanderschueren).

The electrometer in a TSD/TWD instrument is so sensitive that it measures currents one million times smaller than those measured in tunneling microscopes. Dipolar, ionic, and space charges create the thermally stimulated current output (Figure 2.2).

In this figure are shown (a) the polarization stage and (b) the depolarization stage. In case (a), the power supply (battery) charges up the capacitor, creating a current of polarization I_p. The thermally stimulated discharge of the charges results in current I_d in (b), flowing in the sensitive electrometer A.

The effect of the voltage field is to stretch and/or orient the dipoles (either molecular or ionic), distort the orbitals, and create new charges either at interfaces be-

https://doi.org/10.1515/9783110756746-007

EBSCOhost - printed on 2/13/2023 12:32 AM via . All use subject to https://www.ebsco.com/terms-of-use

tween heterogeneous surfaces or at internal local places of microdensity differences (Figure 1.1 of Part I, Chapter 1). The current measured in the electrometer is the total of all contributions, space charge and dipolar relaxations combined (Figure 2.3 [after Vanderschueren]).

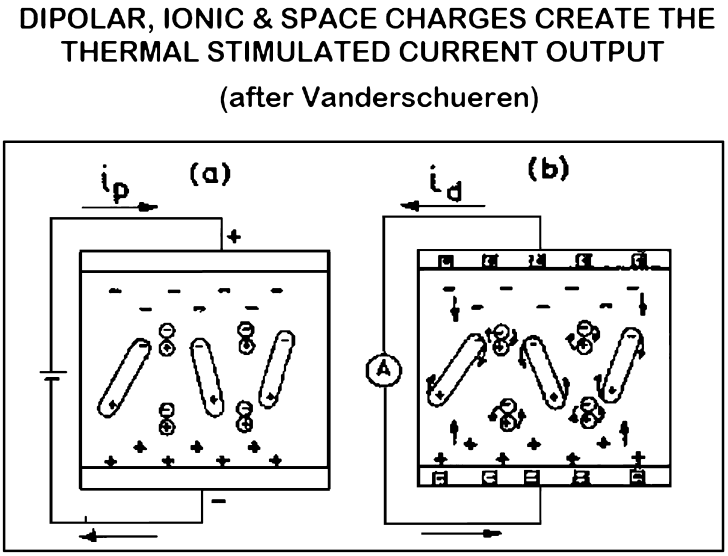


Figure 2.2: Schematic of all possible charges created by the polarization voltage and flowing out as current in the depolarization stage (after Vanderschueren).

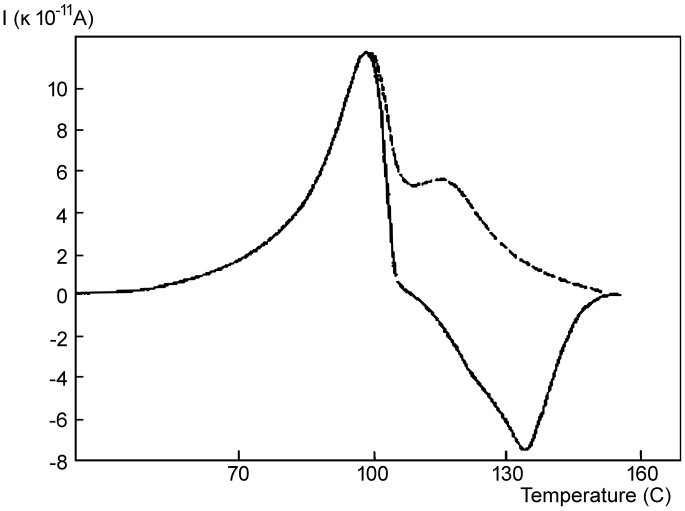


Figure 2.3: Examples of TSD currents observed: negative current discharges may occur due to surface charges. Their elimination is successful using the correct sample mounting procedure.

EBSCOhost - printed on 2/13/2023 12:32 AM via . All use subject to https://www.ebsco.com/terms-of-use

When there is no good contact between the electrode and the polymer, accumulation of surface charges at their point of contact may occur, resulting in a negative current peak just after T_g, or interfering with it, as shown in Figure 2.3, bottom curve. The negative peak can be eliminated (top curve) by applying a small pressure to the surface of contact, by changing the metal of the electrode, by vacuum deposition of thin film metallic layers, or simply by using silver lacquer to paint both surfaces of the sample and suspending it with thin copper wires between the electrodes.

II.2.2 Selective polarization

Figure 2.4 is a TSD depolarization curve obtained for acrylonitrile–butadiene–styrene (ABS), polarized at –40 °C for 1.5 minutes under 200 V/mm. The peak at –75 °C represents T_g for the butadiene phase. It is important to emphasize that the choice of the temperature of polarization T_p determines the focus of molecular or relaxational mo-

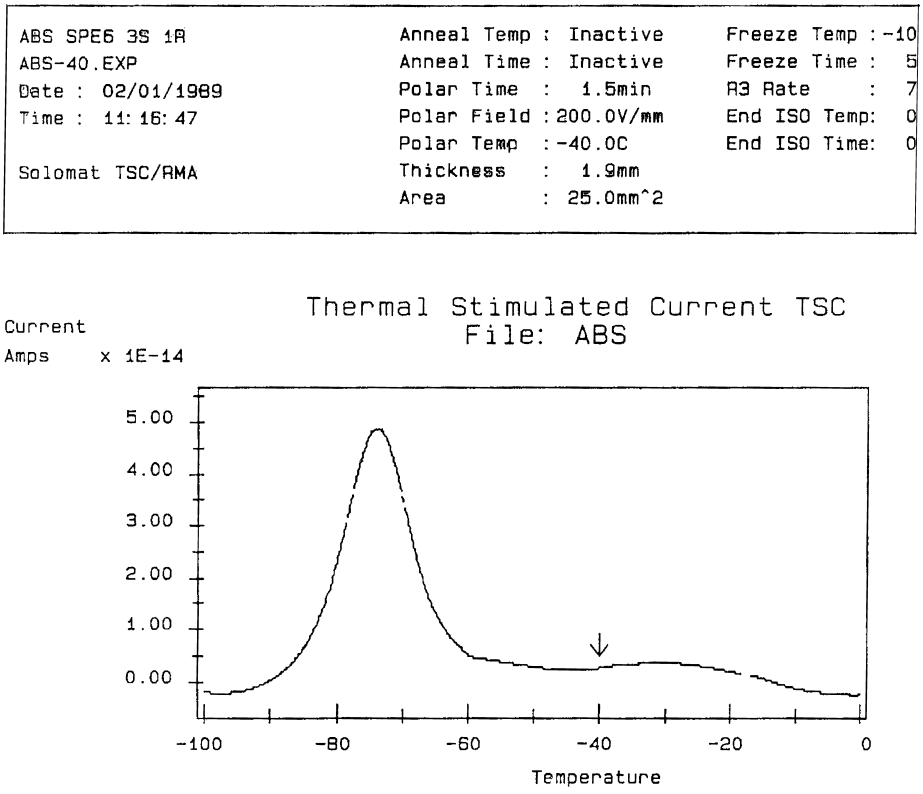


Figure 2.4: TSD depolarization curve obtained for ABS polarized at –40 °C (arrow) for 1.5 min under 200 V/mm of sample thickness. This illustration is the output curve of the TSC/RMA spectrometer by Solomat Instrument (1989).

EBSCOhost - printed on 2/13/2023 12:32 AM via . All use subject to https://www.ebsco.com/terms-of-use

tion. For instance, T_g of the styrene phase is around 80 °C; if we polarize at –40 °C we will not be able to excite, orient, or polarize the styrene dipoles. But, that temperature of polarization activates the butadiene dipoles, and through this selective polarization, we are capable of focusing on that T_g transition. Polarizing closer to the peak maximum, say between –95 °C and –60 °C, would enhance the peak intensity even further. TSD allows the user to zoom in on a given transition "by putting his finger on it," so to speak, i. e., by adjusting the temperature of polarization.

II.2.3 The $T_{g,\rho}$ peak and the measurement of "free volume"

Figure 2.5 is a typical TSD curve for polyethylene terephthalate (PET). Two peaks are clearly visible, which we call T_g and $T_{g,\rho}$. The two peaks are separated by about 50 °C in this figure, and the intensity of the higher peak, $T_{g,\rho}$, is higher than the intensity of the first peak T_g.

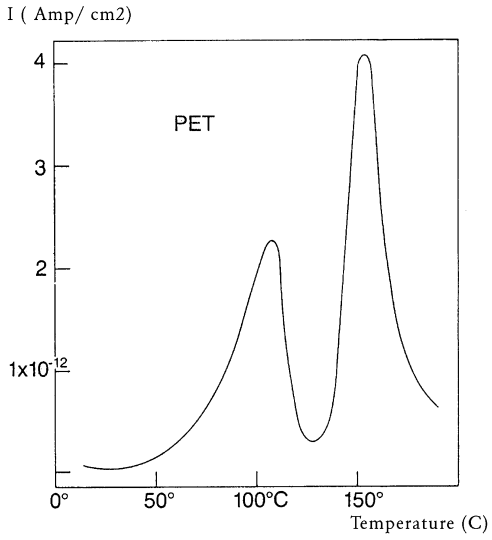


Figure 2.5: TSD depolarization curve obtained for PET showing the T_g and $T_{g\rho}$ peaks. The $T_{g\rho}$ manifestation can be correlated to the free volume content in the material.

Figure 2.6 displays the TSD curve for polycarbonate (PC), showing $T_{g,\rho}$ only 16 °C above the T_g peak, and Figure 1.27, in the first chapter, shows $T_{g,\rho}$ (114 °C) located near the polarization temperature (designated with an arrow) in the case of atactic PMMA.

The value of $T_{g,\rho}$ observed by TSD is designated differently by various authors. Lacabanne and Boyer call that peak T_{LL} [170] and associate its existence with local order. Vanderschueren and other authors call it T_ρ [27, 98, 228, 231] and speculate that it originates from the discharge of space charges delocalized in the structure. Extensive studies have shown that the relative intensity of the T_g and $T_{g,\rho}$ peaks, as well as their

EBSCOhost - printed on 2/13/2023 12:32 AM via . All use subject to https://www.ebsco.com/terms-of-use

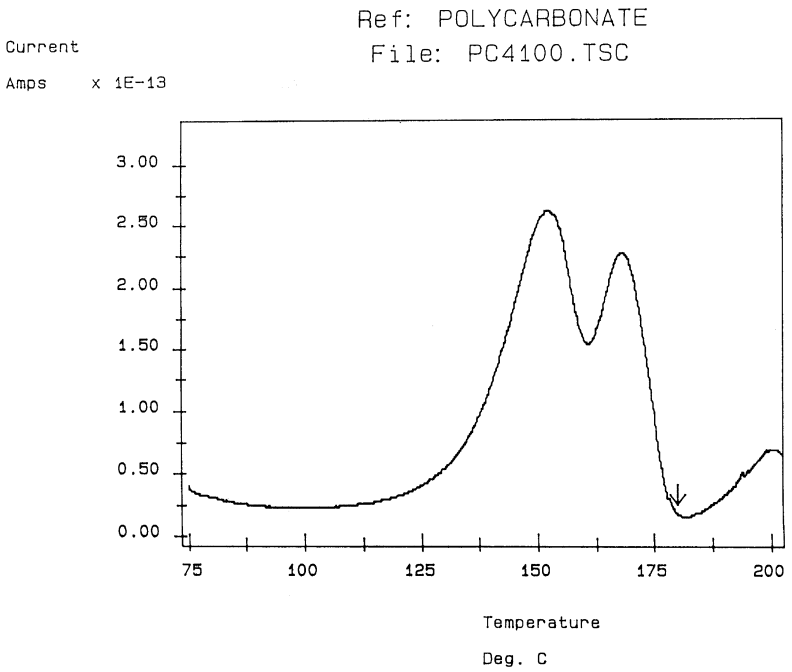


Figure 2.6: TSD depolarization curve obtained for PC showing the T_g and $T_{g\rho}$ peaks. The arrow indicates the temperature of polarization.

respective position, depends on the thermal and mechanical history of the polymer, in particular physical aging. The magnitude of the $T_{g,\rho}$ peak is also a function of the voltage field, increasing first and then leveling off as the voltage increases.

The presence of the $T_{g,\rho}$ peak is universal in the characterization of polymers by TSD. We find that peak just above T_g for all polymers tested: from paints to thermoplastics, from thermosets to rubbers, and for non-polar plastics as well as polar ones. This peak is apparently absent in the characterization of the same polymers by dynamic mechanical analysis (DMA) or DEA. It is stipulated here that differential scanning calorimetry (DSC) experiments can show $T_{g,\rho}$ under special cooling and processing conditions which enhance its manifestation (see later).

The position of $T_{g,\rho}$ with respect to T_g depends, to a large extent, on the choice of the polarization temperature T_p, which enhances the respective magnitude and the resolution of the peaks by the effect of polarization selectivity mentioned in the previous section. Thus it is not uncommon to observe the T_g and $T_{g,\rho}$ peaks merge into a broad intense peak for certain polarization temperatures, complicating their fine analysis. The transition T_{LL} is also found by TSD, but it is located at a higher temperature, and it should not be confused with $T_{g,\rho}$. In some instances, the mechanical history of the specimen and the temperature of polarization are such that $T_{g,\rho}$ and T_{LL} merge or overlap, making the analysis even more complicated (Figure 2.7). Fortunately,

EBSCOhost - printed on 2/13/2023 12:32 AM via . All use subject to https://www.ebsco.com/terms-of-use

thermal-windowing normally allows a good separation of all the peaks, which can be isolated and deconvoluted individually. The only drawback with thermal-windowing at temperatures of polarization above T_g is that it modifies and partially erases the kinetic effects which are responsible for the relaxations under investigation. In other words, the manifestation of both T_{LL} and $T_{g,\rho}$ is favored by thermal history treatments which bring the specimen far out of equilibrium, but this is quickly erased by annealing above T_g, which occurs when the sample in the TSD cell is brought up to the polarization temperature.

In Figure 2.7, the specimen is a compression-molded 2-mm-thick polystyrene rapidly cooled to room temperature. A platen pressure of 226 bars is applied at 122 °C prior to and during cooling. The polarization temperature is 115 °C. Three peaks are clearly visible: T_g at 97 °C, $T_{g,\rho}$ at 112 °C, and T_{LL} at 150 °C.

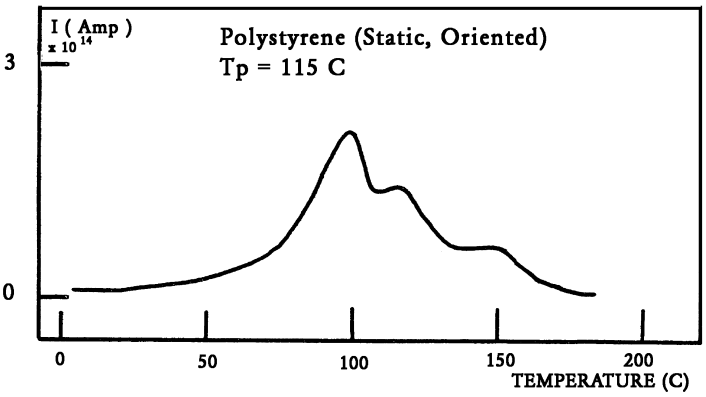


Figure 2.7: TSD depolarization curve obtained for an oriented compression-molded PS sample showing T_g and two other peaks above T_g.

The intensity of the $T_{g,\rho}$ peak is enhanced by fast cooling or any other thermomechanical process which creates a state of non-equilibrium in the polymer.

The intensity of $T_{g,\rho}$ decreases with annealing time, as is demonstrated in Figure 2.8. In this figure, PC is subjected to a compression molding treatment involving a mechanical vibration as it is being cooled. This type of treatment is called Rheomolding and is described elsewhere [124]. In the TSD experiments shown in Figure 2.8, a Rheomolded PC is rerun three times in a row without changing specimen. The same polarization conditions are used each time. Each run partially erases the initial thermal history of the specimen. We focus on the intensity and position of the T_g and $T_{g,\rho}$ peaks. The first trace (first polarization) displays a very intense $T_{g,\rho}$ peak relative to the T_g peak, but the intensity of this peak rapidly decreases for traces 2 and 3, as the initial state of PC returns to more traditional non-equilibrium conditions (cooling in the TSD cell, although rather fast, is no match to the severe cooling conditions imposed

EBSCOhost - printed on 2/13/2023 12:32 AM via . All use subject to https://www.ebsco.com/terms-of-use

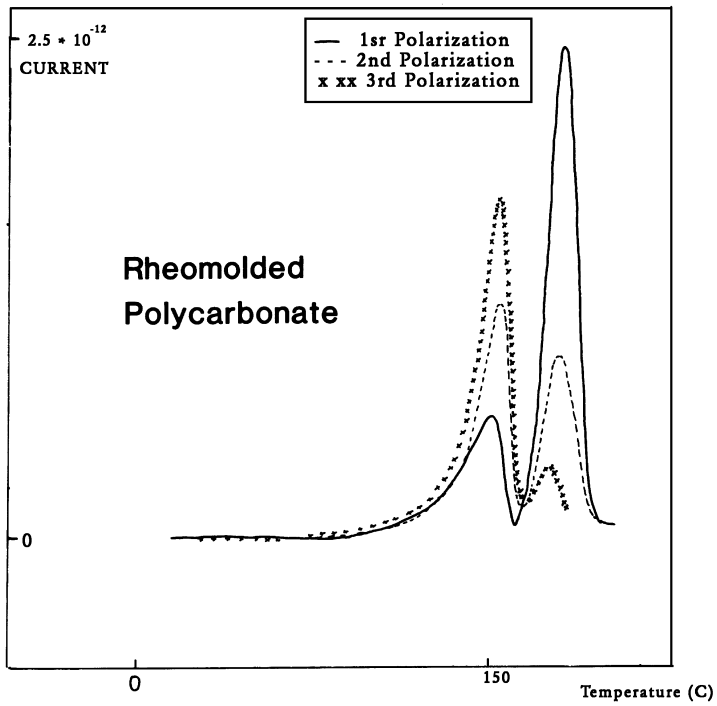


Figure 2.8: TSD depolarization curve obtained for a mechanically pressurized and vibrated PC sample during its compression molding showing the compensation between the T_g and $T_{g\rho}$ peak intensity when the sample is annealed due to repeated polarizations done above T_g on the same sample.

by Rheomolding). It is interesting to observe that as the intensity of $T_{g,\rho}$ decreases, the intensity of the T_g peak increases, in a kind of complementary manner. The position of the T_g and $T_{g,\rho}$ peaks also changes in a reverse way: as T_g maximum increases slightly, $T_{g,\rho}$ decreases, giving the impression of fusion of the two peaks.

The understanding of the existence of $T_{g,\rho}$ and T_{LL} is offered in Part I, Chapter 3. As far as we are concerned, the $T_{g,\rho}$ peak is real, big, often stronger than T_g, and located a few degrees after T_g. In this chapter, which deals with the applications of TSD, it is important to introduce the existence of peaks T_g, $T_{g,\rho}$, and T_{LL} and suggest that their presence is universal in the context of the TSD characterization technique. It is not essential, however, to speculate about their origin. Let us just mention that Part I, Chapter 3 suggests a common kinetic origin to T_g, $T_{g,\rho}$, and T_{LL}, and even to T_β. The apparent complexity of the relaxation behavior arises for two reasons: even if T_g and $T_{g,\rho}$ are kinetically related, their dielectric origin is different, because the effect of voltage field on the kinetic units responsible for their respective relaxation is different. In the case of T_g, the dipole moment relaxing is associated with a molecular dipole, but probably not so for $T_{g,\rho}$. The electric moment for $T_{g,\rho}$ seems to be associated with ionic dipoles, or perhaps space charges. There is much evidence to confirm that the

EBSCOhost - printed on 2/13/2023 12:32 AM via . All use subject to https://www.ebsco.com/terms-of-use

$T_{g,\rho}$ peak is related to the "free volume" in the sample, which suggests that either local unstable ionic dipoles or space charges get trapped in the free volume of the polymer under the influence of the voltage field and relax at $T_{g,\rho}$. More details will be provided in Part I, Chapter 3, where the "free volume" is defined in the morphology in terms of statistical units of the polymer chains.

The difference between the characteristics of $T_{g,\rho}$ and T_{LL} is definitive: hydrostatic pressure lowers the value of $T_{g,\rho}$ and increases the value of T_{LL}. This is shown for $T_{g,\rho}$ in Figure 0.8 of the introductory chapter. In this figure, polystyrene samples are prepared by compression molding under various conditions. In the top graph, a relaxed specimen is cooled under no mechanical stress at a very slow cooling rate. The Arrhenius transform of the $T_{g,\rho}$ peak is shown at the extreme right of the graph; it is curved and can be fitted with a WLF type of equation, providing the free volume thermal expansion coefficient above T_g, and the temperature of infinite viscosity (the values found match well viscosity data). In the middle graph, corresponding to the "pressurized" specimen, the WLF curve is shifted towards a lower temperature. Another thermomechanical treatment is shown in the bottom graph. Figure 2.9 displays the Arrhenius transforms of the $T_{g,\rho}$ peak for the several processing conditions: static

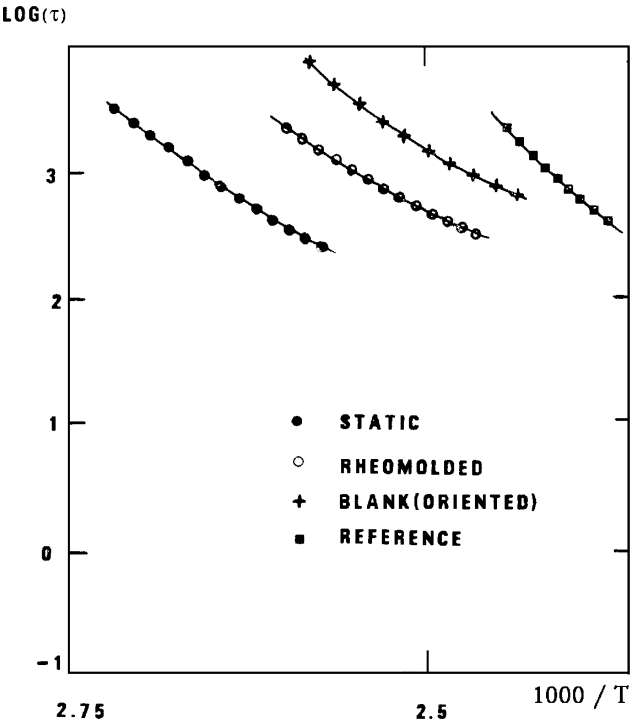


Figure 2.9: Variation with the thermomechanical history of the molded PS of the $T_{g\rho}$ peak perceived as a WLF curve in the Arrhenius plane after conversion by the Bucci equation.

EBSCOhost - printed on 2/13/2023 12:32 AM via . All use subject to https://www.ebsco.com/terms-of-use

pressure, Rheomolding treatment, oriented sample, and the relaxed polystyrene. The relaxational mode obeys a free volume criterion for all conditions, but the content of free volume and the mobility at a given temperature, given by the horizontal position of the WLF curve, is a strong function of the state of polymer due to processing conditions.

In some instances, the $T_{g,\rho}$ peak is broad and contains a combined effect of molecular dipoles and free volume relaxations (Figure 2.10). In such cases, thermal-windowing around the $T_{g,\rho}$ peak produces several relaxation modes (Figure 0.8, bottom curve), and sometimes one or two additional compensations are observed in the $(T > T_g)$ region up to T_{LL} (see Figure 1.9, the relaxation maps at the bottom and Part II, Chapter 4).

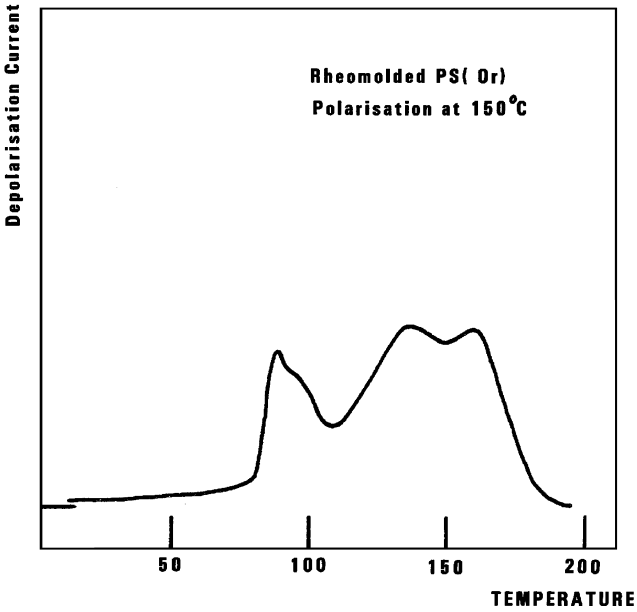


Figure 2.10: TSD depolarization curve obtained for a vibrated oriented compression-molded PS sample (Rheomolded) after polarization at $T_p = 160$ °C showing T_g and two other peaks above T_g.

We consider T_{LL} as the temperature marking the end of a certain type of relaxational behavior due to cooperative kinetic interactions. Whether or not it actually corresponds to a TSD peak is irrelevant to our definition. For instance, we mentioned that T_{LL} shows up in Figure 2.7 as a peak at 150 °C. It might be more appropriate to categorize this peak as one of the kinetic manifestations resulting from the cooperative kinetic process already giving rise to T_β, T_g, and $T_{g,\rho}$. It is suggested in Part I, Chapter 3 and in references [122, 130, 131] that the mechanism of relaxation is due to the coherence between the collective behavior defining the statistical ensemble and the

EBSCOhost - printed on 2/13/2023 12:32 AM via . All use subject to https://www.ebsco.com/terms-of-use

local existence of Dual-Phases (the b and F phases) which describes the interactive coupling between the conformers belonging to the macromolecules modulating both the sub-T_g and the ($T > T_g$) kinetics. In that regard, T_{LL} is probably more at 175 °C than 150 °C in Figure 2.7, and the peak at 150 °C should be considered as a manifestation of the modulation by the network (collective) of b/F interactions occurring in the phase richer in free volume and responsible for the $T_{g,\rho}$ relaxation manifestation. This point is further illustrated in Figure 2.11.

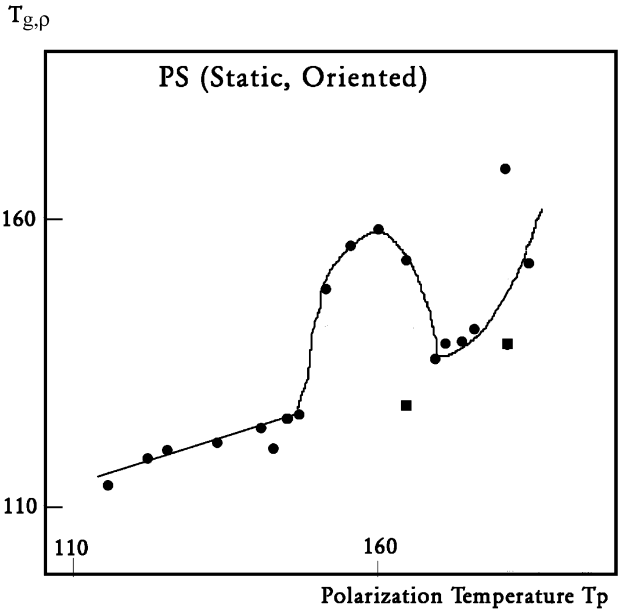


Figure 2.11: Variation of the position of the $T_{g\rho}$ peak with T_p for a static (no vibration) oriented compression-molded PS sample, exhibiting the T_{LL} transition at 160 °C.

In this figure, we plot the variation of $T_{g,\rho}$ with T_p, $T_{g,\rho}$ being considered the "first" peak observed above T_g. When a second peak appears, which we call $T'_{g,\rho}$, we indicate its temperature on this graph with square dots. One sees that $T_{g,\rho}$ increases slowly and linearly with T_p (the slope is much less than 1), at least until $T_p = 145$ °C, a temperature at which $T_{g,\rho}$ rises quickly to a maximum. The first split of $T_{g,\rho}$ into two peaks occurs for $T_p = 165$ °C, and the second split occurs for 180 °C. In the case of a split, the temperatures of the two peaks are located on both sides of the "expected" $T_{g,\rho}$ extrapolated from the lower values. The departure from the baseline at 145 °C reveals the kinetic presence of the network modulating collectively the interactions (Part I, Chapter 3). Beyond $T_p = 170$ °C, the modulation by the elastic dissipative network of the inter-intra molecular interactions between the various dipoles **is over**. T_{LL} would be 170 °C, according to our definition.

EBSCOhost - printed on 2/13/2023 12:32 AM via . All use subject to https://www.ebsco.com/terms-of-use

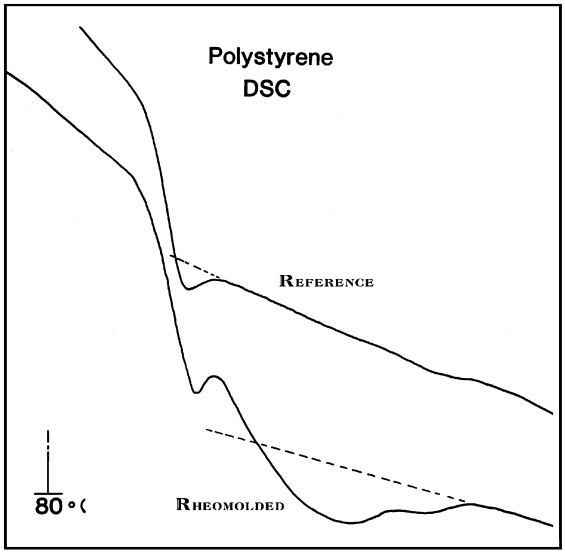


Figure 2.12: DSC trace comparison of two PS samples: the reference at the top is a compression-molded general-purpose PS. The bottom trace gives the response for a Rheomolded sample, compression-molded and vibrated at the same time while cooled. The cooling conditions were the same for both samples.

The DSC trace for a Rheomolded polystyrene showing cooperative relaxation above T_g is compared in Figure 2.12 with a reference trace (obtained by cooling the same sample in the DSC cell after the first run). The difference between the Heat Flow of the two curves is significant just above the T_g peak, and until the T_{LL} temperature is reached. The thermal history of the Rheomolded sample, revealed during the first run, creates a thermal activity above T_g clearly similar to what is observed by TSD (Figure 2.10). The thermal history is erased as the sample is heated in the DSC cell, and both reference and Rheomolded DSC traces are identical above T_{LL}.

We consider Figure 2.12 as an important illustration by DSC of the existence of $T_{g,\rho}$ and T_{LL}. However, the sample preparation conditions imposed on the material, in order to reveal the thermal history, are quite severe in the case of a DSC technique. TSD, which works at a very low frequency equivalent (Part II, Chapter 1), is capable of resolving the $T_g/T_{g,\rho}$ kinetic presence with far higher resolution and sensitivity (note how thermal history of the Rheomolded PC of Figure 2.8 is still revealed after the successive runs).

The thermal analyst should be gratified: the $T_{g,\rho}$ peak gives us a new parameter to characterize polymers. It varies with the processing conditions, and thus can be used to characterize the effect of processing variables (pressure, orientation, thermal history); it is often stronger than T_g and exists for non-polar materials when the free volume can be trapped with charges. It is perhaps the only peak which one can observe

EBSCOhost - printed on 2/13/2023 12:32 AM via . All use subject to https://www.ebsco.com/terms-of-use

to characterize thick non-polar polymers. In that case, the "T_g" found is possibly a $T_{g,\rho}$, several degrees higher than what would have been expected from a DSC comparison (the TSD T_g peak matches well the T_g obtained in a DSC experiment at a 20 °C/min heating rate).

II.2.4 Coatings, paints, pigments, and pressure-sensitive adhesives on substrates

II.2.4.1 Coatings

In this section, four sets of experiments are designed to provide a cursory overview of the TSD characterization capabilities in the area of coating and cure. The coating systems analyzed include two water-borne systems, a solvent-borne system, and an appliance powder coating. The experimental details can be found in reference [207].

In the experiments reported below the coating is very thin; it is studied directly on the substrate which is used for the application (Figure 2.13). It is remarkable to be able to cut out samples directly from the can and, without any further sample preparation, study the degree of cure of the coating. One of the electrodes is the conductor used as substrate (say aluminum), and the results are not sensitive to the shape of the sample, at least for a qualitative comparison analysis. *TSD allows the thermal analyst to directly characterize actual samples, not just laboratory-prepared samples*. This could be crucial for quality assurance in the beverage and canned food industries. TSD curves of different pieces cut at random from the coated can could be compared to a reference curve in order to qualify the curing process before the cans are filled with beverage or food.

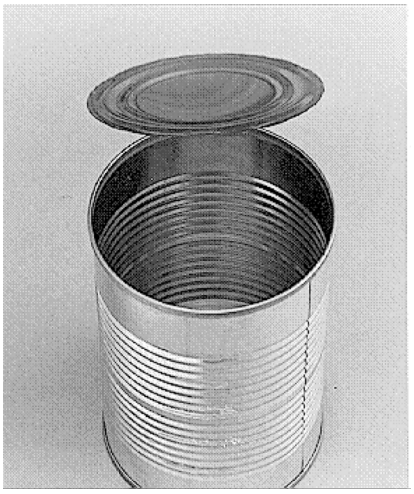


Figure 2.13: TSD characterization of coatings applied to aluminum surfaces inside a can.

EBSCOhost - printed on 2/13/2023 12:32 AM via . All use subject to https://www.ebsco.com/terms-of-use

II.2.4.1.1 Beverage container coatings

In this study very thin coatings over aluminum are analyzed to distinguish between various cure levels. Cans were coated and baked at 204 °C. Samples were punched from can bottoms using a 1-cm punch; total film thicknesses were estimated at less than 0.01 mm.

In general, simple TSD results produced a DMA-like response for this coating. Figure 2.14 shows TSD peaks at about 85 °C and 120 °C. Well-controlled studies in similar materials using DMA and transmission electron microscopy have shown that the first peak corresponds to a low-temperature acrylic component and the second peak to an epoxy-acrylic component.

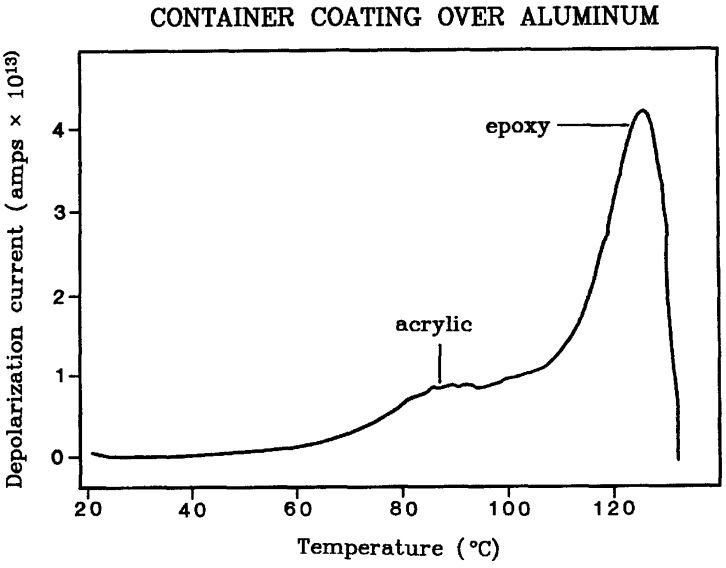


Figure 2.14: TSD analysis of the degree of cure of a very thin coating over an aluminum can. The acrylic and epoxy components are distinctively observed.

Other TSD experiments (not shown) revealed a β transition centered around –45 °C, which probably stems from the motion of side groups pendant to the backbone. The position and relative intensity of these peaks were very similar in the two coatings.

II.2.4.1.2 Sanitary can coatings

This experiment was designed to distinguish between epoxy-based coating samples which had either passed or failed a production quality control test. In these tests, opacity in the coating indicates improper cure, while a coating which remains transparent after cure passes the test. “Good” and “bad” samples were punched from production cans. The good samples (labeled “bu”) were removed from the bottom of the can and

EBSCOhost - printed on 2/13/2023 12:32 AM via . All use subject to https://www.ebsco.com/terms-of-use

acted as a control for this work. Two samples were removed from the bad end of the can; one (labeled "tb") was opaque after testing while the other (labeled "tu") was transparent even though it was removed from an area immediately adjacent to the opaque sample of the bad can.

TSD analysis indicated that epoxy-based can end coatings which failed Q/C tests in production were under-cured. Figure 2.15 shows the results for three samples. The large peaks probably coincide with segmental motion at T_g of each sample. The depolarization curves labeled "tb," "bu," and "tu" describe the bad coating, the good sample, and a "good" sample taken from an area immediately adjacent to the bad area, respectively. The curve labeled "tu3" illustrates the effect of rebake on the bad sample.

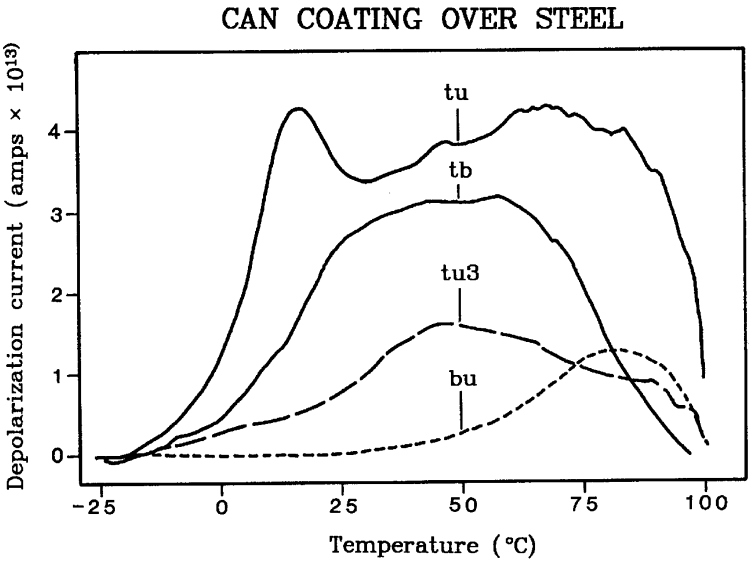


Figure 2.15: Characterization of a can coating over steel, distinctively separating the characteristic of the molecular mobility for tb, bu, and tu samples designating the bad coating, the good coating, and a good sample in an area close to a bad sample, respectively.

Generally, the depolarization peak temperature corresponds to T_g, and the higher the T_g, the greater the extent of cure. By using this crude measure of the extent of cure, the lower relative peak position in the problem sample (tb) indicates that it was undercured in comparison to the good sample (bu). Moreover, the shift in the peak position from roughly 15 °C (tu) to about 50 °C (tu3) after rebake further corroborates the conclusion that the problem coating was under-cured. The analysis of identical materials by DSC provided no indication of any difference in cure or any other pertinent morphological information.

EBSCOhost - printed on 2/13/2023 12:32 AM via . All use subject to https://www.ebsco.com/terms-of-use

II.2.4.1.3 Powder coatings

An epoxy/polyester appliance coating was sprayed over a Bonderite 1000 steel substrate and cured for 5, 10, 15, and 20 minutes at 193.3 °C in a forced air oven. These samples measured approximately 1 cm^2. This experiment was designed to test the sensitivity of the TSD technique to different cure levels over a thick metal substrate.

Figure 2.16 shows the TSD depolarization peaks observed for powders sprayed over a steel substrate and baked for 5 and 20 minutes at 193 °C. The peak temperature increases from 83 °C after the short bake to 91 °C after the longer bake. Since this increase in relative peak position corresponds to an increase in T_g, it indicates that the degree of cure is increasing with bake time.

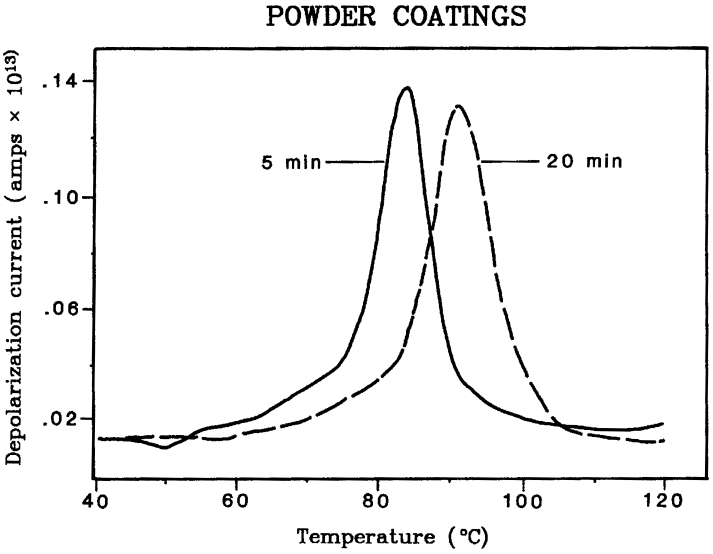


Figure 2.16: TSD depolarization traces for powders sprayed over a steel substrate and baked for 5 and 20 min at T = 193 °C.

The TSD relaxation peaks – correlated with the glass transition T_g – once again increase in temperature as the bake time increases, strongly suggesting that crosslink density increased with bake time.

Any change in the degree of cure with bake time should also produce a change in the peak depolarization current intensity. This occurs because an increase in crosslink density restricts segmental motion and reduces the number of dipoles which align in the electric field. Thus, if a system has a relatively high crosslink density, the total depolarization current will be low. As Table 2.1 shows, the peak depolarization current intensity decreases by some two orders of magnitude as the bake time increases, strongly suggesting an increase in crosslink density.

EBSCOhost - printed on 2/13/2023 12:32 AM via . All use subject to https://www.ebsco.com/terms-of-use

Table 2.1: Depolarization current intensity for powder coatings baked for different intervals at 380 °F (193 °C).

Bake time (min)	Peak intensity (femtoamps)
5	1000
10	96
15	77
20	6

II.2.4.1.4 Plastic coatings

Two acrylic urethane system-based coatings were used in these experiments. The addition of catalyst distinguished the two systems. One system (labeled H) included catalyst, while the other (labeled E) did not. Each sample was applied over SMC and cured. These experiments were designed to quantify differences in (1) T_g, (2) cure levels, and (3) adhesion levels. TSD traces for the two samples are compared in Figure 2.17.

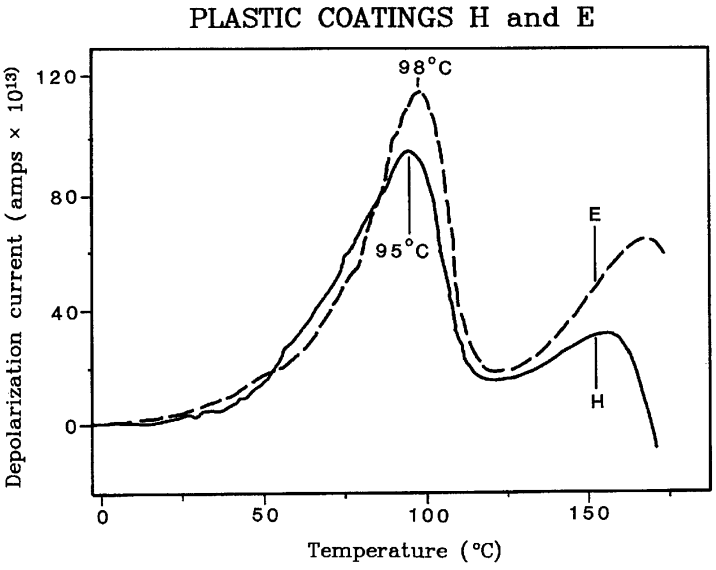


Figure 2.17: TSD depolarization traces for two acrylic urethane system base coatings prepared with a catalyst (sample H) or without the catalyst (sample E).

The TSD results strongly suggest that the addition of the catalyst alters the crosslinking chemistry and the total degree of cure reached under standard cure cycles. A comparison of the two systems reveals that T_g is 3 °C lower in the amine-added system. Surprisingly, the total depolarization current was significantly lower in sample H, even

EBSCOhost - printed on 2/13/2023 12:32 AM via . All use subject to https://www.ebsco.com/terms-of-use

though T_g was lower. Normally a decrease in T_g would imply less crosslinking, greater dipolar mobility, and a consequent increase in depolarization current. These results show the opposite, strongly suggesting that significant changes in the crosslinking chemistry occurred with the addition of the catalyst – most likely affecting both the nature of the crosslink and the total degree of cure. In particular, the decrease in depolarization current with the addition of the amine indicates a more highly crosslinked network. If these changes in chemistry carry through to the coating–substrate interface, then it is likely that the adhesive bond formed between the coating and substrate has also improved.

In conclusion, TSD proves a sensitive technique for characterizing T_g, the general morphology, and relative cure levels in a variety of coatings. The instrument also yields quantifiable differences in the level of cure for powder coatings and an in-mold plastic coating.

II.2.4.2 Paints

II.2.4.2.1 Case study: curing of polyester paint

The study of the crosslink density and/or cure ratio for paint on metal is vital not only in the final quality inspection of a finished part, but also in the development of new resins and processes for paints and coatings.

The material studied in this case study is a polyester that is crosslinked with a melamine resin and catalyzed with a sulfonic acid. The 0.001 coating is applied with a wire-wound draw-down bar over cold rolled steel that has been pre-treated with iron phosphate and primed with a urethane primer. These samples are processed differently, varying the bake time to produce under-cured, correctly cured, and over-cured samples. Each sample is cut into small squares approximately 1.613×10^{-4} m.

TSD experiments are carried out on the three samples using the following parameters: heat to 120 °C, the temperature of polarization T_p; polarize with 100 Volts for 2 minutes; lower the temperature to 25 °C with the polarization field applied; remove the field and hold there for 2 minutes; and finally, heat up to 200 °C at a rate of 7 °C/min. During the ramp-up in temperature, the electrometer reads the current generated by the relaxation of the disorienting dipoles (Figure 2.18a).

The peak observed near 35 °C corresponds to the expected T_g transition for the polyester component in the paint. The occurrence observed above the peak (near 75 °C) is interesting in that it also changes as a result of processing. However, the influence of the degree of cure on the peak at 35 °C is the only focus here.

As shown in the case of coatings, when a material is subjected to a longer cure time, or a higher temperature of cure, the peak generated by TSD shows up at higher temperatures with a lower intensity as curing increases. This is clearly demonstrated in Figure 2.18a. Figure 2.18b is a blow-up of the lower region of Figure 2.18a, illustrating the temperature and intensity shift as influenced by differing cure time.

EBSCOhost - printed on 2/13/2023 12:32 AM via . All use subject to https://www.ebsco.com/terms-of-use

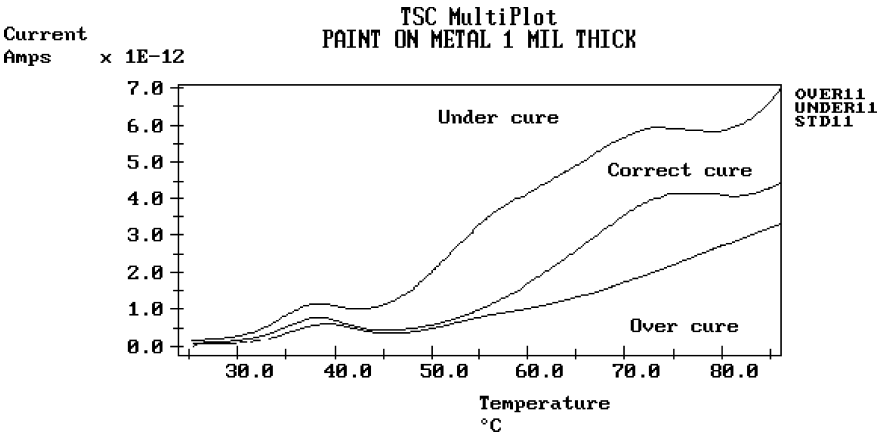


Figure 2.18a: TSD characterization of the crosslinking quality or cure ratio for paints on metal.

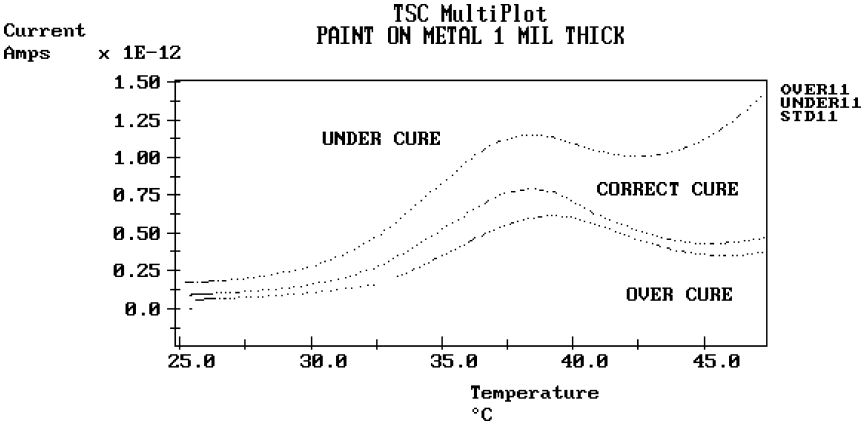


Figure 2.18b: Blow-up of the lower region in Figure 2.18a to detail the shift of the peak intensity and temperature due to the curing time.

Another very useful parameter to characterize the degree of cure or crosslink density is P_o, the area under the TSD curve, which provides the value of the initial polarization in the sample (P_o) (normalized for surface area and heating rate). If the sample has a greater degree of cure (more crosslinking present), there are fewer dipoles excited by application of the field, and therefore P_o is smaller. In summary, TSD alone provides substantial information about the relative cure or crosslink density in each sample, although the test is simple and quick. In this fashion, the instrument is being used for incoming quality assessment and process control in many different fields and industries for a number of years. A typical example of such use is presented in our next case study.

EBSCOhost - printed on 2/13/2023 12:32 AM via . All use subject to https://www.ebsco.com/terms-of-use

II.2.4.2.2 Case study: pre-painted coil coating quality control

Until recently, "because it was always done that way" was reason enough to continue post-painting appliances' metallic surfaces. However, volatile organic compound emissions, pre-treatment slouch disposal, requirements for costly space and working process inventory, metal finishing, touch-up stations, and the high energy cost of heat curing are rendering the process of post-painting more difficult. In the process of coil coating, steel coils are continuously dirt-decontaminated, brushed, and coated with paints yielding pre-painted steel sheets ready for their assembly in different appliances. Recent advances and automation in pre-painted metals have resulted in more efficient methods to improve quality and productivity while lowering in-plant costs [58]. The on-line quality control of the paint degree of cure can be done by a TSD analyzer in less than 5 minutes of testing, virtually resulting in no interruption of the continuous process. The end product is TSD-controlled at random intervals in a lab station placed on-line, which allows one to determine and quantify the quality of the primer and paint, replacing the less reliable pencil test and rub and scratch tests.

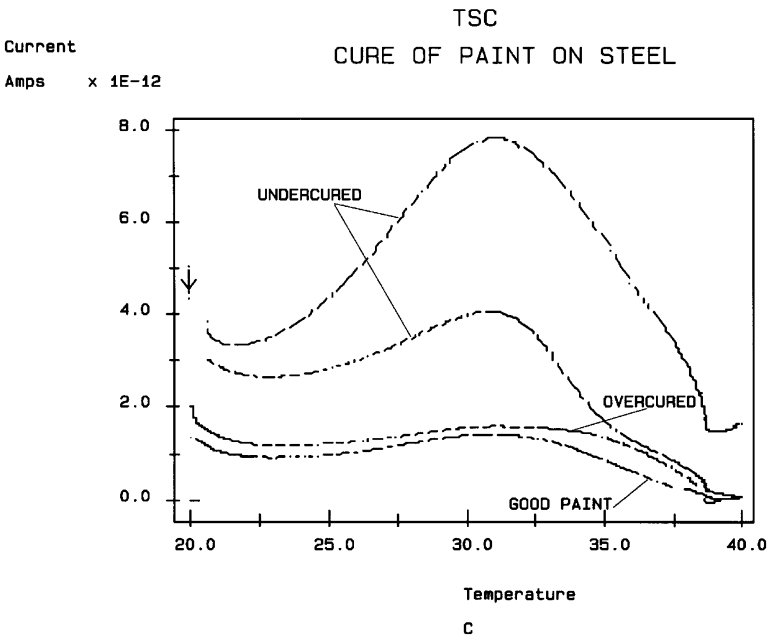


Figure 2.18c: On the use of TSD characterization for quality control purposes with regard to the cure of paint on steel.

Figure 2.18c illustrates four cases of paint obtained from on-line specimens, corresponding to an under-cured paint, an over-cured paint, and a perfect paint. As shown in the figure, the process control consists in comparing the peak intensity of the depo-

EBSCOhost - printed on 2/13/2023 12:32 AM via . All use subject to https://www.ebsco.com/terms-of-use

larization of the relaxation obtained by polarization at room temperature. The ramp-up rate is boosted to 10 °C/min in this case, and a temperature span of only 50 °C is needed to compare the degree of cure. The intensity of the depolarizing current is related to the number of dipoles polarized at room temperature, in direct correlation with the degree of cure of the paint. It has been demonstrated in laboratory experiments that the intensity of the current at the peak maximum and the position of the peak correlate reliably with the test normally done to determine the quality of the paint. A "good paint" TSD curve is normalized and used as reference, easily stored in a database for a given type of paint, and compared to random tests obtained on-line to determine whether the conditions of manufacturing are yielding a correct paint. This fail/pass test can be installed in the process itself, at the end of the fabrication line, to modify the parameters of the paint coating whenever necessary. This sophisticated control minimizes the rejects level, reducing to its minimum the number of coils which do not pass the quality test before being sent to the appliance manufacturer.

II.2.4.3 Pigments

The use of pigments in plastic materials is to improve their optical performance, usually by giving them a pleasing appearance. The effectiveness of a given pigment is determined by the way in which the pigment particles scatter and absorb light. This is determined by the morphological characteristics of the pigment such as size, shape, and surface texture and the way these factors affect the compatibility with the medium it fills.

The use of titanium dioxide (TiO_2) pigment for opacifying paints, plastics, paper, inks, rubber, and other materials is due primarily to its high reflective index that produces a high level of light scattering at pigment particle surfaces [65]. Interparticle forces in pigments involve primarily Van der Waals or London attractions which operate when the molecules in different surfaces approach each other at close range, as well as electrostatic forces [65]. The dielectric constant of the medium surrounding a particle modifies the magnitude of the Van der Waals or London forces. Commercial pigments are normally modified by surface coatings (alumina, silica [or both], phosphates, zinc oxide, precipitated titanium, and organic coatings) that are applied in various ways so that the surfaces may be chemically modified, physically coated, or both. The behavior of a TiO_2 pigment, as a particle in dispersions, is influenced by the charge residing from the surface, induced electrostatically.

The TSD/TWD technology can be used to identify the effect of the pigment on the surrounding, and the presence of electrostatic charges around the TiO_2 particles can easily be detected in a simple TSD run, producing a negative peak on heating.

EBSCOhost - printed on 2/13/2023 12:32 AM via . All use subject to https://www.ebsco.com/terms-of-use

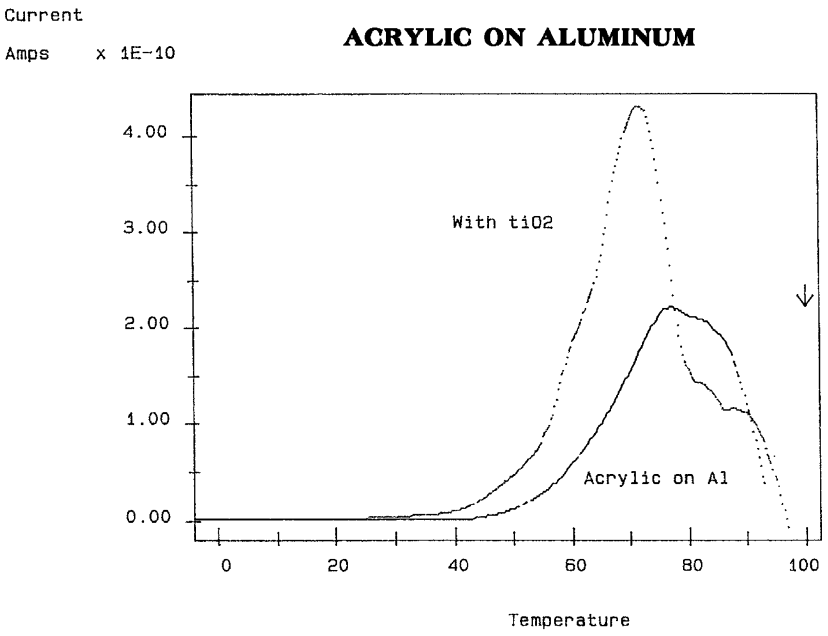


Figure 2.19: Comparison using TSD characterization of the effect of the presence of a TiO_2 pigment filler for an acrylic film.

In Figure 2.19, the TSD traces for a pigment-loaded acrylic film are compared to the trace for acrylic without the filler. The presence of the TiO_2 particles is readily seen by a large increase of the relaxation peak compared to the pure acrylic resin. The increase of intensity is due to the increase in the polarizability of the material in the presence of the TiO_2 particles. An interesting observation in this figure is the shift to a substantially lower temperature of the relaxation taking place in the material on the material loaded with TiO_2. This result can be interpreted by the influence of the TiO_2 particle size on breaking the Van der Waals and London bonds. These create the electronic medium responsible for the relaxation peak observed at T_g. In a simple manner, the shifting of the temperature maximum indicates that there is an interaction between the pigment (or the filler) and the matrix characteristics and viscous properties. In the case of a very small amount of pigment, the peak intensity increases but the peak position remains at the same temperature. Thermal-stimulated current analysis can also detect the effect of particle size and concentration. Fine TiO_2 particles have the tendency to pack into the voids of a coarse extended system, and their proximity exaggerates the interference effect. Packing effects are determined by criteria which describe the volume relationship of pigment to binder, as described by the ASTM method D281 as the critical pigment volume concentration (CPVC). Thermal-windowing practiced on films loaded with pigments allows the user to fully understand the nature of the interaction between this pigment and the polymeric substrate (Part II, Chapter 3).

EBSCOhost - printed on 2/13/2023 12:32 AM via . All use subject to https://www.ebsco.com/terms-of-use

II.2.4.4 Pressure-sensitive adhesive on substrates

The primary function of adhesives is to join parts together. Adhesives do this by transmitting stresses from one member to another in a manner that distributes the stresses much more uniformly than can be achieved with conventional mechanical fasteners.

Pressure-sensitive adhesives (PSAs), in the dry state, are aggressively and permanently tacky at room temperature and firmly adhere to a variety of dissimilar surfaces without the need for more than finger or hand pressure. They require no activation by water, solvent, or heat in order to exert a strong adhesive holding force. Adhesives based on acrylic polymers have become commercially important and are now probably as much used as natural rubber (NR). Unfortunately, they do have poor creep properties compared to NR. Blends of NR and styrene–butadiene rubber (SBR) also provide excellent PSAs. PSAs are frequently used on tapes. In the case study presented here, TSD experiments are carried out on samples of PSA on its paper substrate. The nature of the adhesive has not been revealed by the manufacturer. The user has problems of quality control of his production, with apparently no analytical tool at his disposal to test the product once made, other than an unsatisfied customer who rejects a lot based on real-life peeling performance. Thermal-windowing results will be presented in Part II, Chapter 3 on five different specimens, allowing their classification by degree of tackiness. Figure 2.20 provides the TSD traces for paper alone and for the adhesive

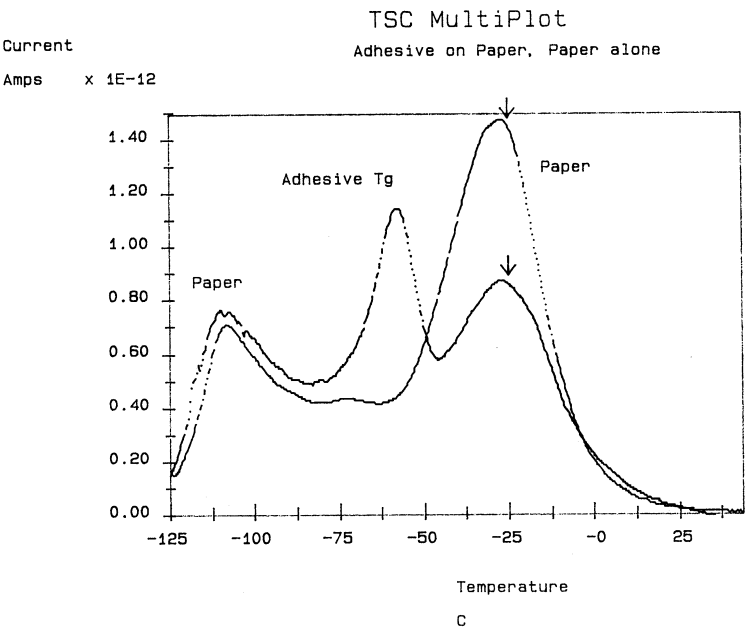


Figure 2.20: TSD characterization of the quality of an adhesive on paper by comparison of the TSD traces of the paper alone and the adhesive + paper.

EBSCOhost - printed on 2/13/2023 12:32 AM via . All use subject to https://www.ebsco.com/terms-of-use

on paper. The thickness of the glue is approximately 10 µm. The specimen is laid flat between the two electrodes and the same amount of pressure is exerted on the PSA to avoid the effect of pressure sensitivity. We observe the two main relaxations for paper in both samples. In addition, the T_g of the tacky phase in the case of the PSA sample is clearly characterized. The technique separates very well the relaxation due to the glue from the relaxations due to the paper. TWD experiments carried out by polarizing around the T_g transition of the glue allow the user to determine how strong the bonding between the paper and the glue is and how well the PSA adheres to the metallic surface of the electrode. This application of TSD/TWD seems quite remarkable (Part II, Chapter 3).

II.2.5 Characterization of polyolefins

We have abundantly described examples of characterization of "amorphous" polymers and thermosets, and it seems appropriate to now turn our attention to the case of semi-crystalline polymers, in particular polyolefins, which represent a huge class of commercial plastics.

We have already given an example of a TSD graph for a commercial semi-crystalline polymer, Nylon 12 (Figure 0.2a). This figure illustrates the ability of the TSD technique to characterize T_g in a semi-crystalline polymer. Remember that it is very difficult to detect T_g of a semi-crystalline polymer by DSC (Part II, Chapter 1). DMA works well with semi-crystalline polymers, because the crystals create crosslinks, which does not allow the mechanical strength to prevail above T_g. In the case of unsupported, uncrosslinked amorphous materials such as polystyrene or PMMA, which do not have any crystals to hold the structure, the DMA test specimen sags and starts to melt and flow as T_g is passed. This explains why all the graphs from DMA, tan δ vs. temperature or G' or G'' vs. temperature, always stop at T_g, disqualifying the technique for the study of the ($T > T_g$) region. TSD/TWD is capable of measurement about 100 °C above T_g.

Polyolefins are, generally speaking, more difficult to study by TSD, because of the absence of local polar groups. An increase of the voltage and the time of polarization, the use of thinner samples, and the additive of polar molecules, which are often included as stabilizers, solve the problem.

In our design, we are limited to a maximum voltage of 1500 V, because the helium starts to ionize in the TSD cell beyond this high voltage. Besides, the use of high voltage, resulting in the creation of artifacts, various spurious discharge peaks of unknown origin, and non-linear distortions of the Debye relaxations, is not recommended. The use of thinner samples or longer polarization times is preferable. Despite these experimental difficulties, analysis of polyolefins by TSD/TWD can provide a level of detailed information that cannot be matched by any other single analytical technique. The examples below discuss the use of TSD in determining the level

EBSCOhost - printed on 2/13/2023 12:32 AM via . All use subject to https://www.ebsco.com/terms-of-use

of atactic material, the degree of orientation, the presence of additives, the type of polyethylene (PE), the and identification/characterization of blends. These figures are selected from the thesis of [215] and modified to conform to our normal presentation of TSD results in this book.

II.2.5.1 TSD trace of polypropylene homopolymer

A typical TSD spectrum of polypropylene (PP) homopolymer is shown in Figure 2.21. A strong peak at 267.5 K is due to the glass transition of the PP. A weak peak associated with the γ transition can also be observed at a lower temperature. This peak is a result of localized PP side chain motions. We expect this low-temperature transition to be sensitive to the type and activity of the polymerization catalyst.

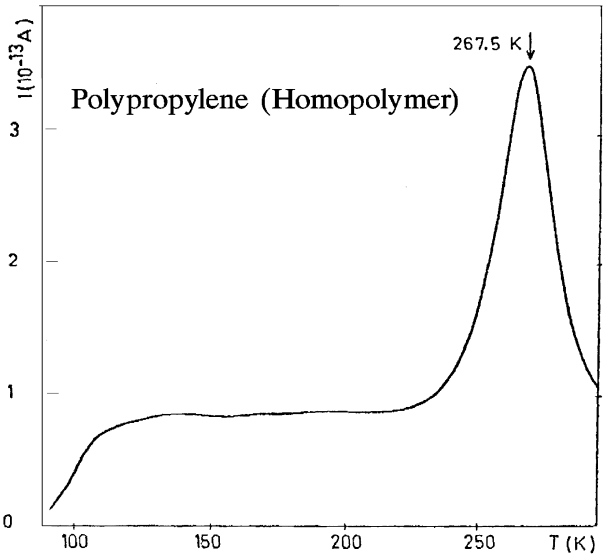


Figure 2.21: TSD trace for a typical PP homopolymer. T_p is shown by the arrow.

II.2.5.2 TSD trace of atactic polypropylene

In Figure 2.22, we find the TSD spectrum of atactic PP. Several important differences are observed between the atactic and isotactic homopolymers. T_g shifts from 267.5 to 266.0 K. As expected, the T_g peak is more than fourfold more intense for the atactic material due to the higher amorphous PP content. TSD is very sensitive to the level of atactic material. This may be useful as a quality control method for monitoring the level of atactic material produced during polymerization.

EBSCOhost - printed on 2/13/2023 12:32 AM via . All use subject to https://www.ebsco.com/terms-of-use

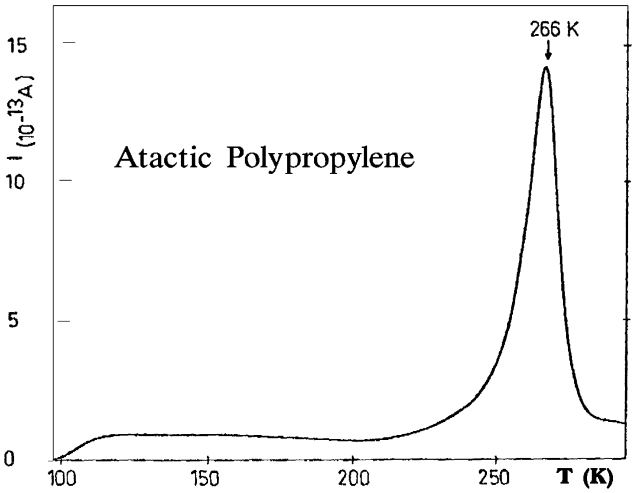


Figure 2.22: TSD trace for atactic PP (aPP) using the same T_p for comparison with Figure 2.21.

II.2.5.3 Effect of orientation

The impact of orientation of PP is easily detected by TSD. In Figure 2.23 (after reference [146]), the TSD traces of drawn and undrawn PP are compared. Both have T_g at 0 °C, which is typically observed for amorphous PP. The higher temperature peak is believed to be due to the combination of $T_{g,p}$ and amorphous PP which has been constrained by crystallites within a spherulitic structure. A detailed TWD of the drawn

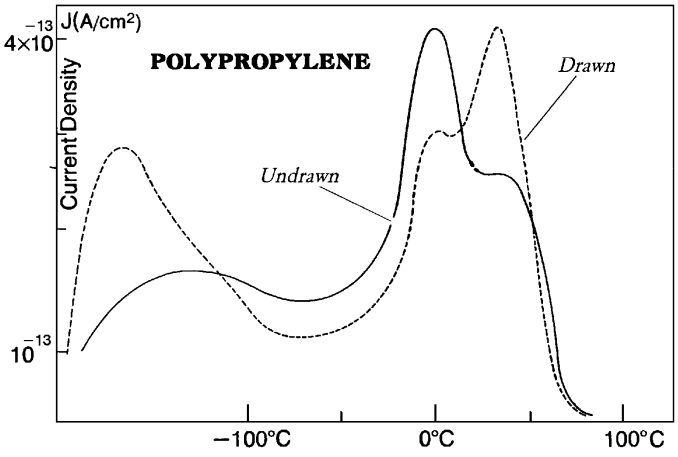


Figure 2.23: TSD trace comparison to study the effect of orientation on the internal mobility. The traces show the drawn and undrawn samples. The TWD relaxation maps for these two samples are given in Chapter 4 of Part II.

EBSCOhost - printed on 2/13/2023 12:32 AM via . All use subject to https://www.ebsco.com/terms-of-use

and undrawn samples in Part II, Chapter 4 will confirm the existence of two amorphous phases. Drawing results in a reorganization of the dipoles in the structure, a decrease in the number of unoriented dipoles in the direction parallel to the field, for the amorphous matter contained in between spherulites (which explains the lower intensity for the first T_g peak), and an increase of the free volume withdrawing, which explains an increase of the intensity of the second T_g peak which contains $T_{g,\rho}$. Quantitative measurements are provided by thermal-windowing in Chapter 4 Part II.

II.2.5.4 Polyethylenes of varying densities

Four PEs of various densities are compared in Figure 2.24. TSD easily differentiates between the PEs of different densities by the position of the peak due to the glass transition (250 K). The highest T_g corresponds to the highest density. The peaks associated with the γ transition (125 K) are also significantly different for low-density PE (LDPE). The shape of the γ peak is related to the extent of branching in PE. This lower-temperature transition might be expected to be quite sensitive to changes in polymerization conditions.

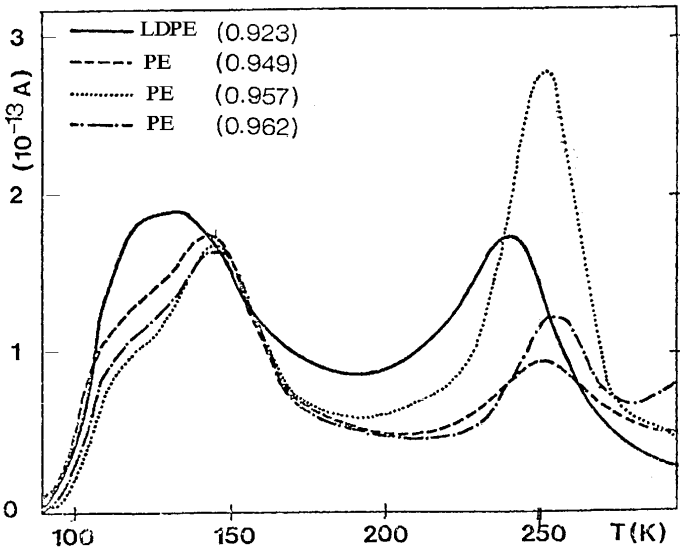


Figure 2.24: TSD trace comparison for four PE samples of various densities from 0.923 (LDPE) to 0.962 (HDPE).

EBSCOhost - printed on 2/13/2023 12:32 AM via . All use subject to https://www.ebsco.com/terms-of-use

II.2.5.5 Effect of additives: Irganox 1076

The effect of phenolic antioxidant on TSD peak intensity is shown in Figure 2.25. The sample is LDPE and the stabilizer is Irganox 1076 with a concentration varying from 0 (pure) to 1.0 %. Peak intensity increases dramatically with stabilizer concentration. This effect is due to relaxations of the relatively strong dipoles associated with Irganox 1076. While the polar additive is soluble within the PE and is generally considered quite mobile on the time scale of the experiment, the antioxidant is entrapped in the polymer and only capable of relaxing when polymer motion becomes possible. Therefore, the intensities of the transitions normally observed are increased by the presence of even low concentrations of soluble polar additives. This technique may be useful as a quality control method for ensuring the presence of stabilizers. It is interesting to note that the influence of the additive is only detected in peak intensity. The relative positions of the peaks are unaffected. This suggests that even at a concentration of 1 %, Irganox 1076 does not appear to affect polymer relaxation at or below T_g.

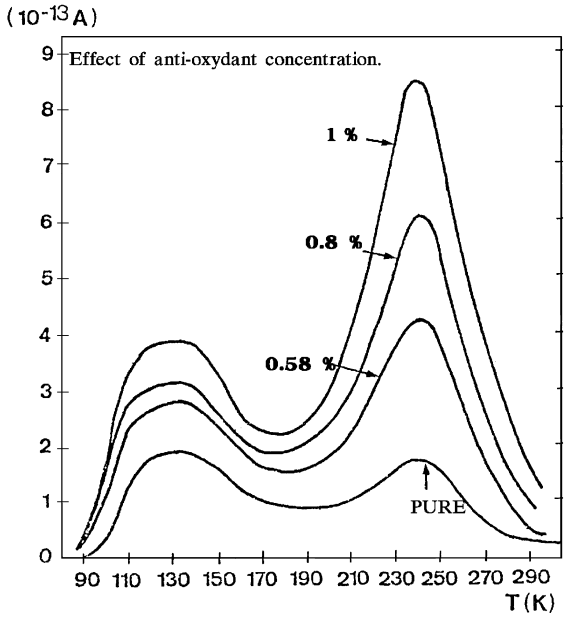


Figure 2.25: TSD characterization of the effect of the concentration of Irgonox on the internal mobility in LDPE.

One word of caution – the levels used in the samples presented here are an order of magnitude larger than those normally used in most applications. Generally, PE will contain 0.1 % phenolic antioxidant (Irganox 1076 or Irganox 1010) and often a phosphite (Irgafos 168).

EBSCOhost - printed on 2/13/2023 12:32 AM via . All use subject to https://www.ebsco.com/terms-of-use

II.2.5.6 Copolymers and blends (PE, HDPE, and EPR). TPOs

In Figure 2.26, the TSD traces of PP, high-density PE (HDPE), and ethylene/propylene random copolymer (EPR) are compared. Again, TSD easily differentiates these polymers. The EPR trace contains a single T_g, indicating that the material exists as a single phase, as expected.

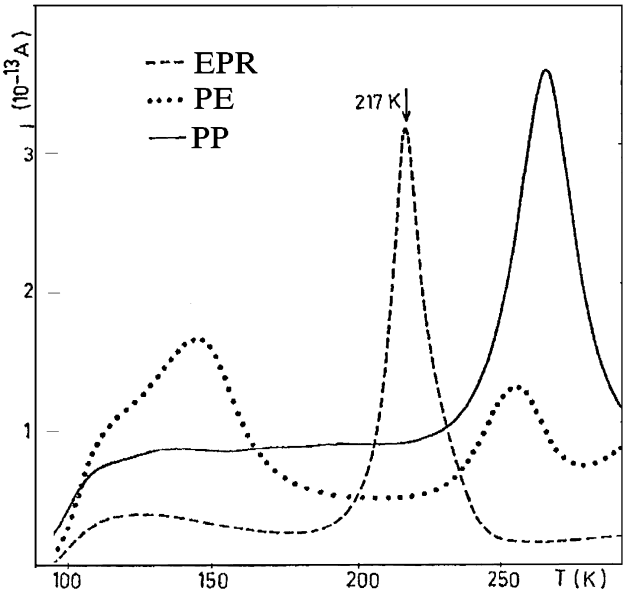


Figure 2.26: Comparison of the TSD traces for industrial polyolefins: PP, HDPE, and EPR (ethylene/propylene random copolymers).

Figure 2.27 compares three different tertiary polymer blends. These blends contain PP, EPR, and PE and are known as thermoplastic polyolefins (TPOs) or impact-modified PP. TPOs are becoming increasingly important in the automotive industry for use as bumpers and body paneling. The upper temperature peak can be assigned to the phase containing primarily PP. The chief component of the middle peak is EPR and the low temperature peaks are due to γ transitions of PP and PE.

From the TSD analysis, it is obvious that the three blends are significantly different. Copolymer III and Copolymer II show a large difference in the position of the EPR peak. The observed shift from 217 to 228 K suggests a greater degree of interpenetration between the EPR and PP. Copolymer II would therefore be expected to have increased long-term stability (and compatibility) due to its reduced internal stress at the EPR–PP phase boundary. Comparing Copolymer III and Copolymer I, we immediately see that Copolymer I has much less EPR than does Copolymer III. The extent of interpenetration between III and I appears similar.

EBSCOhost - printed on 2/13/2023 12:32 AM via . All use subject to https://www.ebsco.com/terms-of-use

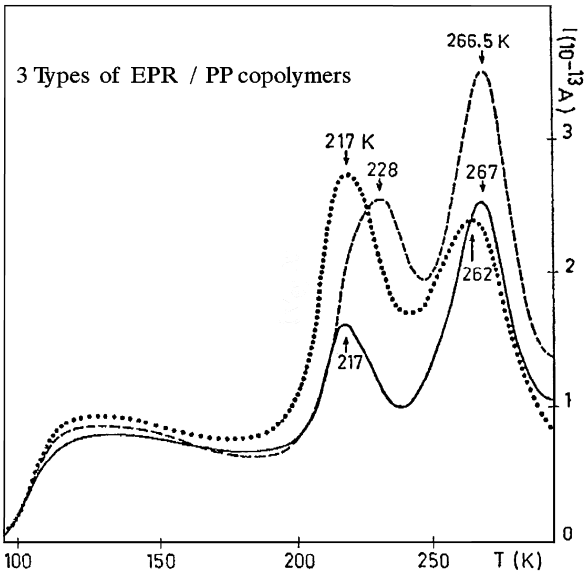


Figure 2.27: Comparison of the TSD traces for three types of EPR/ PP copolymers. See text.

The results of this study are useful in selecting the proper match between copolymer and application. For many polymer blend systems, it has been shown that impact strength is increased with increasing distinctness of phase separation. This suggests that Copolymer I and Copolymer III would provide the best impact strength. If the application requires resistance to UV exposure, Copolymer II may be the preferred choice due to its enhanced compatibility. The impact of compatibility on long-term stability is well established [265]. TSD can be used as a fast, effective tool in the development and application of copolymers and polymer blends.

II.2.5.7 Conclusions

TSD is a powerful tool for the characterization of polyolefins. As a quality control method, this technique can be used to easily identify changes in tacticity, molecular weight, crystallinity, phase configuration of blends, etc. In addition to identifying a simple T_g, other important transitions related to side chain motion and the influence of crystallinity on amorphous regions are easily investigated. Evaluation of the α transition provides important details related to branching and crosslinking of the polyolefins and can be used to evaluate relative quantities of blend components. In polymer blends such as TPOs, the degree of interpenetration between components of the blend can be assessed through examination of the position and breadth of T_g. This information is critical to physical properties such as impact strength and long-term stability.

EBSCOhost - printed on 2/13/2023 12:32 AM via . All use subject to https://www.ebsco.com/terms-of-use

Finally, it should be noted that application of TWD spectroscopy to polymer blends (Part II, Chapter 3) will permit to develop quantitative measurement of the degree of interpenetration between blend and copolymer components.

II.2.6 TSD in quality control applications

II.2.6.1 Case study: TSD of "good" and "bad" LDPE tubes

A customer reported a problem with bad seals in a series of LDPE tubes. Figures 1.22 and 1.23 of Part II, Chapter 1 show TSD traces of "good" and "bad" seals. The bad sample is shown at the top of both figures, showing transitions at –100 °C and 37 °C (both shown in Figure 1.23), followed by a sharp peak at 102.6 °C (Figure 1.22). The good sample does not show any transition at –100 °C; it shows a peak at 29 °C and a sharp decrease of the baseline (96 °C) before a sharp peak at 98.79 °C.

The peak located at –100 °C for the bad sample corresponds to the lower glass transition temperature of LDPE; it is absent, or much weaker, for the good sample. The peak, observed at 37 °C for the bad sample, 29 °C for the good one, is a classical transition observed for LDPE called T_α. It is much less intense for the good sample. The sharp peak observed around 100 °C is related to the melting transition of the crystals resulting in a sharp discharge of current.

One clearly sees important differences between the good and bad samples in the TSD results. The bad sample has a stronger peak at T_g and T_α. The T_g peak is almost non-existent in the case of the good sample. The intensity of these two peaks is related to the amount of amorphous content and, therefore, it can be said right away that the amount and type of crystallization in the good sample are different from those of the bad sample. Also, clearly visible in Figure 1.22 is the difference of several degrees between the onset of melting of the good and the bad samples. This is a relatively large difference which is due to the crystallization texture and to the amount of crystallization present in the morphology of the LDPE. Any process involving pressure and temperature to seal the tube in order to create an enclosure would require that the material's morphology and melting temperature are the same in order to obtain the same quality seal. A change (increase) in the melting temperature of about 3 °C is matched by an increase of pressure by approximately 2268 kg (Clapeyron's equation). In our case, the processing conditions should have changed to maintain a quality seal with the bad LDPE: either decrease the sealing temperature by 3 °C at the same pressure or increase the pressure by 340 bars (3.4×10^7 Pa) at the same temperature. It is obvious that applying the same processing conditions to seal these two tubes would result in a seal of variable quality. The reason for the different crystallinity in the two tubes is unknown, perhaps due to differences in the extrusion process to produce these tubes. One tube might have been cooled faster than the other, resulting in a larger content

EBSCOhost - printed on 2/13/2023 12:32 AM via . All use subject to https://www.ebsco.com/terms-of-use

of amorphous matter and a significant difference in the size of crystallites. This is evidenced by the larger T_g and T_α peaks.

In conclusion, a simple TSD test reveals that the extrusion parameters to produce these two tubes had varied. The final product should have been tested ahead of the sealing procedure to either reject the bad tube or change the sealing conditions: lower the temperature at which the pressure is applied for creating the seal or increase the pressure by at least 340 bars (3.4×10^7 Pa).

II.2.6.2 Case study: quality control in diaper fabrication

Figures 2.28 and 2.29 relate to the TSD relaxation of two hot melt adhesives used in the manufacturing of diaper tape. One adhesive, sample A, provides PSA tapes which perform well in creep tests, while the other adhesive, B, fails the test. The customer does not have at his or her disposal a method to determine whether the adhesive will be good or bad before the diaper tapes are actually produced, and he or she does not relate the difference in creep performance between the adhesives to any variation of the processing variables. The objective of this study is to differentiate the two samples to provide a quantitative quality control tool.

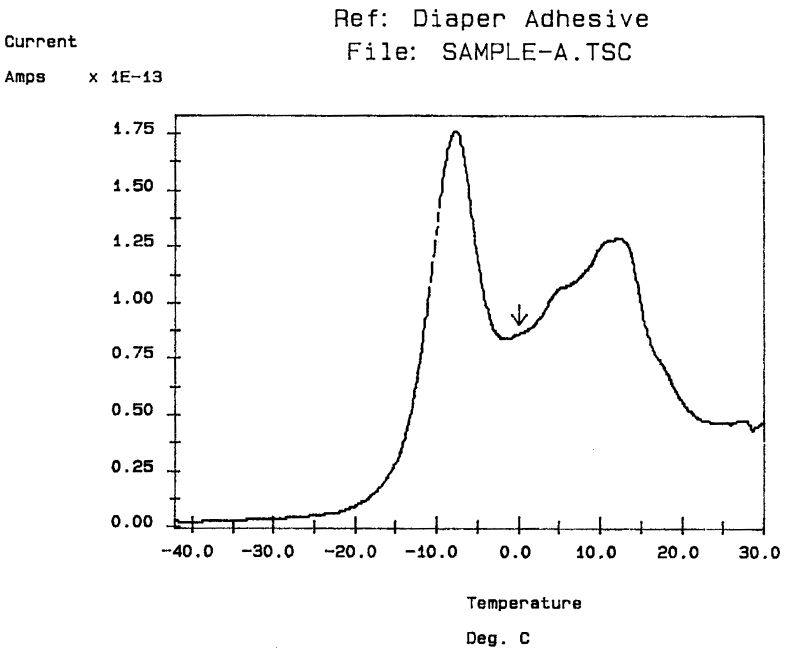


Figure 2.28: TSD trace for a "good" hot melt adhesive (PSA) which performs well in creep tests when used on diapers. See Figure 2.29 for comparison.

EBSCOhost - printed on 2/13/2023 12:32 AM via . All use subject to https://www.ebsco.com/terms-of-use

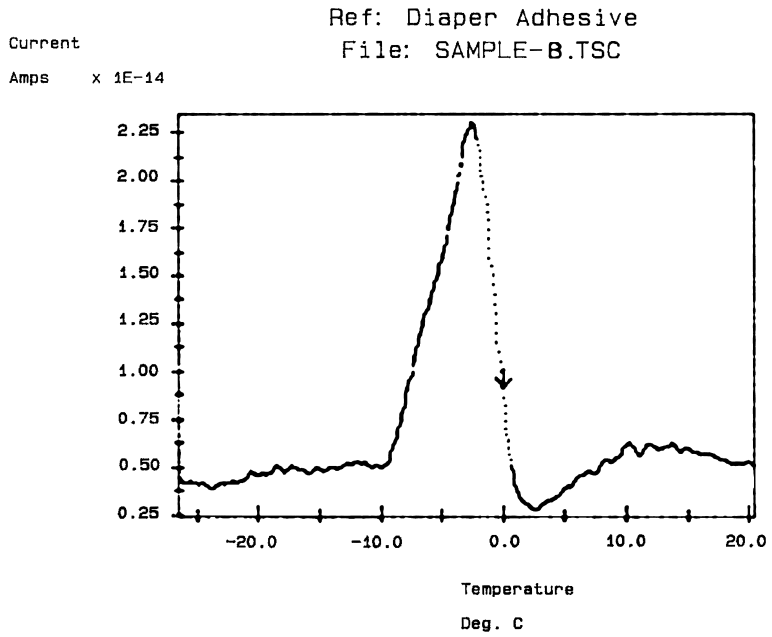


Figure 2.29: TSD trace for a "bad" hot melt adhesive (PSA) which performs poorly in creep tests when used on diapers. See Figure 2.28 for comparison.

The adhesive is a low-molecular-weight PP, and the peaks observed in the figures correspond to T_g and $T_{g,\rho}$. For sample B, $T_{g,\rho}$ is almost non-existent, and the intensity of the peak at T_g is approximately 10 times smaller than for sample A. The possibility to differentiate samples A and B is therefore straightforward. One can speculate that the better adhesive corresponds to the sample with the more prominent $T_{g,\rho}$, perhaps because it relates to the amount of free volume left in the material.

II.2.7 Nucleation effect sensed by space charges

In this section, space charges are used to detect the presence of heterogeneities in the structure of PET. When a small amount of nuclei starts to form, in the solid state, it is extremely difficult to detect their presence by any known method of characterization. A voltage field applied to a heterogeneous structure creates Maxwell–Wagner space charges around the heterogeneous sites, resulting in strong negative discharges in TSD runs. Let us investigate nucleation effects occurring in amorphous PET pellets.

Figure 2.30a displays the type of granules which can be directly analyzed by TSD without sample preparation.

Figure 2.30b shows the TSD traces, using a log scale for the current intensity, for three samples having various thermomechanical history. The two peaks observed at 70 °C and 110 °C correspond to T_g and $T_{g,\rho}$. Maxwell–Wagner effects are shown at 175 °C

EBSCOhost - printed on 2/13/2023 12:32 AM via . All use subject to https://www.ebsco.com/terms-of-use

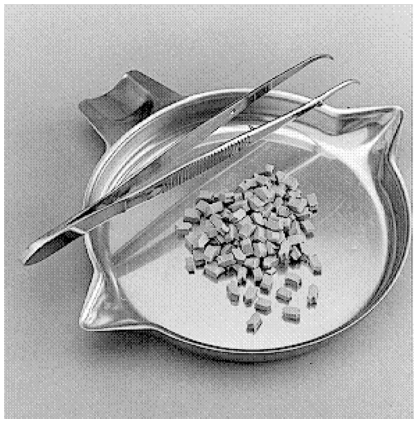


Figure 2.30a: A set of PET pellets. Pellets can be analyzed "as is" by TSD/TWD spectrometry.

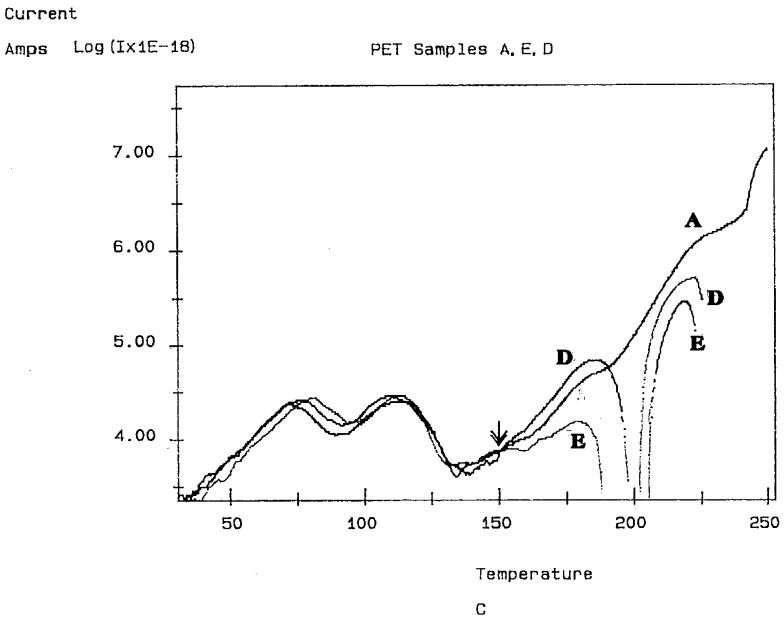


Figure 2.30b: TSD traces for three PET pellets with different thermomechanical history during processing. See text.

(sample E) and 182 °C (sample D). Sample A does not display any discharge activity in this temperature range. Space charge effects are large in amplitude compared to dipolar relaxations. The space charges are created during the polarization at $T_p = 150$ °C and arise from changes occurring in the morphology as PET anneals at this temperature. Upon annealing, PET starts to crystallize, initially by the formation of nuclei which are sites for attracting electrons when the voltage field is applied. These side effects can be utilized to characterize the morphology and the incidence of the pro-

EBSCOhost - printed on 2/13/2023 12:32 AM via . All use subject to https://www.ebsco.com/terms-of-use

cessing variables on the microstructure. For instance, in the case of Figure 2.30b, pellets A show marked differences with pellets D and E when submitted to the process of blow-molding.

II.2.8 Monofilaments and single strands

Figures 2.31 and 2.32 are two examples of the use of TSD on single strands. Figure 2.31 is a 10-µm-diameter Lycra® fiber polarized at 200 °C. The small peak at 22 °C is the glass transition temperature for this highly oriented and crystalline monofilament ($T_{g,\rho}$ is seen as a shoulder on the high-temperature side of the T_g peak). The large peak found between 75 °C and 210 °C is probably associated with the complex intermingled morphological and disorientation changes induced by the temperature rise.

TSD can be run on monofilaments, braids, mats, or fabrics to compare the differences. In Figure 2.32, we observe some amount of background noise associated with surface charges. The strand here is a single fiber of liquid crystal polymer. The current level is still quite acceptable but, due to the noise, it is not possible to perform thermal-windowing on this single fiber (it is possible for the Lycra fiber). As mentioned in Part II, Chapter 1, thermal-windowing reduces the intensity of the current during the selective depolarization of the shorter relaxation times, making impossible the measurement of current below a certain level.

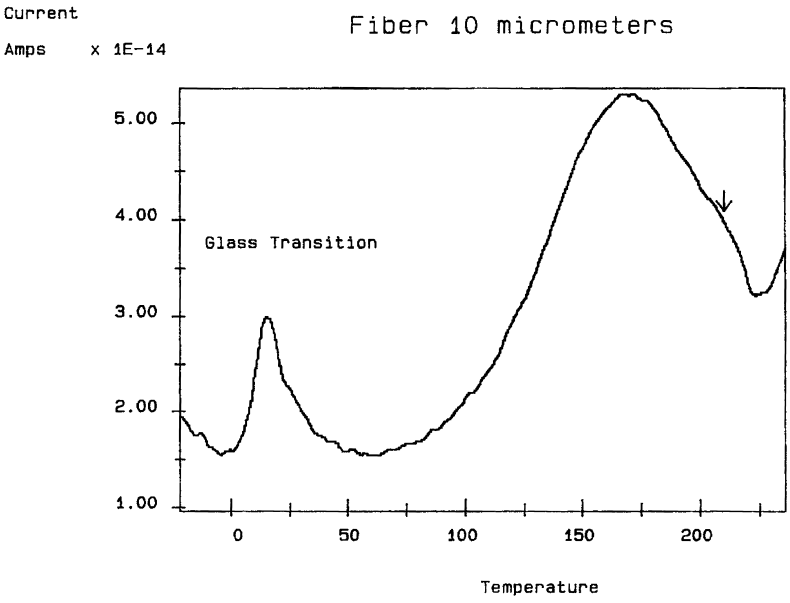


Figure 2.31: TSD characterization can be performed on single strands, such as a 10-µm-diameter fiber of Lycra polarized at $T_p = 200$ °C.

EBSCOhost - printed on 2/13/2023 12:32 AM via . All use subject to https://www.ebsco.com/terms-of-use

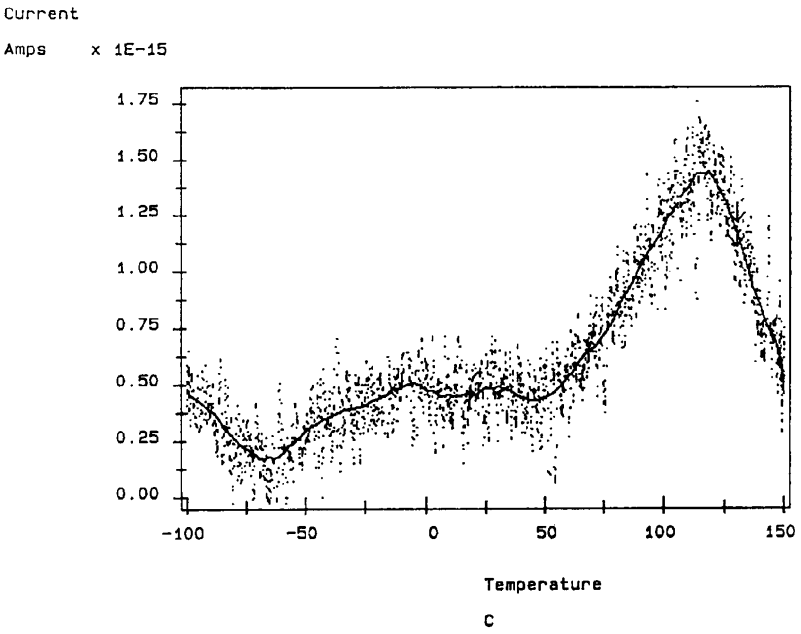


Figure 2.32: TSD trace obtained using a single fiber of LCP. The background noise is due to surface charges.

II.2.9 Wood and liquid crystal polymer

II.2.9.1 Case study: wood

In wood, cellulose crystals, which comprise only 50 % to 60 % of the volume, take the form of tubular cells. The cellulose crystals are bonded with an amorphous lignin composed of carbohydrate compounds. The cell cavities furnish passageways for sap and moisture to flow during the growth process. We believe that lignin is the material which dielectrically relaxes in Figures 2.33 and 2.34.

Most of our quantitative work on wood is presented in Part II, Chapter 4, where it is suggested by the relaxation behavior that wood and Vectra 900 have much in common. In Figure 2.33, the two TSD traces relate to a plain and boiled wood sample polarized at 50 °C, respectively. Boiling has the apparent effect of sharply reducing the amount of amorphous matter (the peak intensity decreases), although the peak position remains unchanged. Some type of organization of the structure takes place during boiling.

The effect of stressing pine wood is shown in Figure 2.34 (polarization temperature 150 °C). The unstressed sample exhibits a higher intensity at 50 °C, but the peak at 165 °C is more intense for the stressed sample. The nature of this higher peak has not been investigated and might be influenced by the moisture content.

EBSCOhost - printed on 2/13/2023 12:32 AM via . All use subject to https://www.ebsco.com/terms-of-use

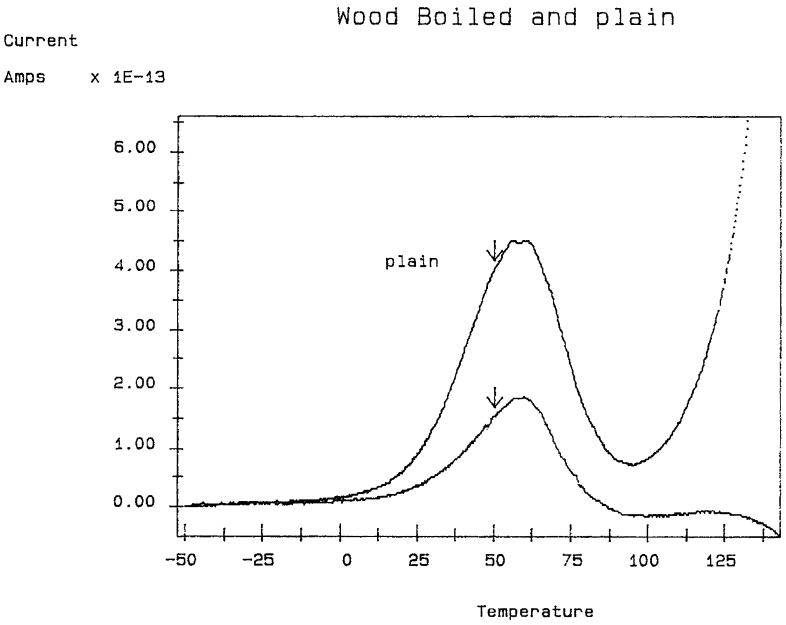


Figure 2.33: TSD traces for plain wood and boiled wood to modify the amount of crystalline/amorphous content. The TSD signal is the response of the amorphous component: the lignin.

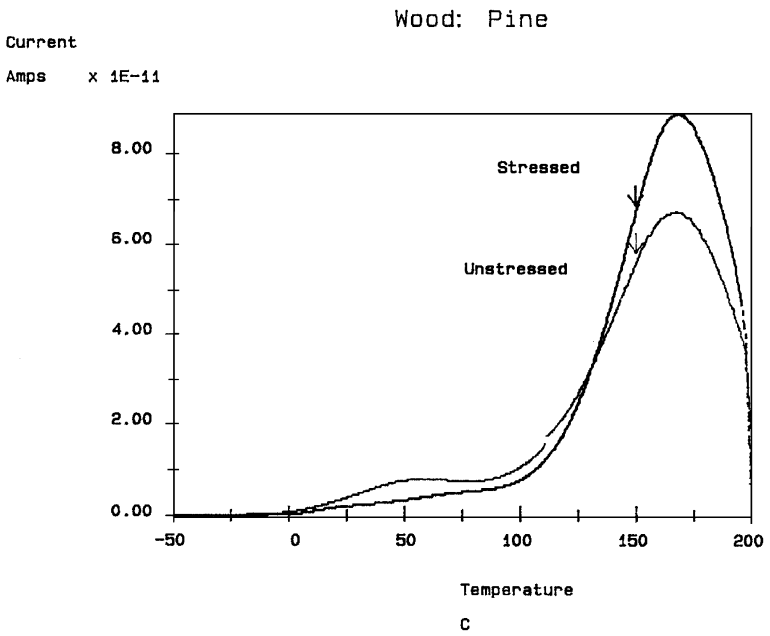


Figure 2.34: Effect of stressing pine wood on the TSD trace after polarization at $T_p = 150$ °C (arrow).

EBSCOhost - printed on 2/13/2023 12:32 AM via . All use subject to https://www.ebsco.com/terms-of-use

II.2.9.2 Case study: relaxation in a liquid crystal polymer: Vectra 900

As an example of the use of TSD to characterize the relaxations in a commercial liquid crystal polymer, we report below the result of our investigation on Vectra. The TWD analysis will be described in Part II, Chapter 3.

Vectra A900 is the commercial tradename for the Hoechst Celanese liquid crystal polymer material composed of 73 % 4-hydroxybenzoic acid and 27 % 6-hydroxy-2-naphthoic acid. Films with a thickness of 25.4 µm are melt-extruded at the Hoechst Celanese film division. The "unannealed" specimens refer to the untreated extruded films. The "annealed" films were heat-treated for 4 hours at 230 °C followed immediately by 16 hours at 270 °C in nitrogen. In the following, we compare the results of annealed and unannealed samples. Some of the DSC, DMA, and DEA outputs have already been reported for this polymer in Part II, Chapter 1, to illustrate the comparison with the TSD results. We will refer to those graphs here, when appropriate.

In DSC, the endothermal peak found at 315.4 °C (Figure 1.5, bottom curve) corresponds to the melting of crystallites or other ordered structures grown during the annealing treatment of the extruded film. The amount of crystallization induced by annealing can be calculated from the heat of fusion determined from the area under the curve. The amount of energy absorbed is rather small, perhaps indicating that annealing under those conditions does not predominantly result in the formation of large crystals. The unannealed Vectra does not have any substantial amount of crystals, as demonstrated by the absence of an endothermic process on reheating (Figure 2.35).

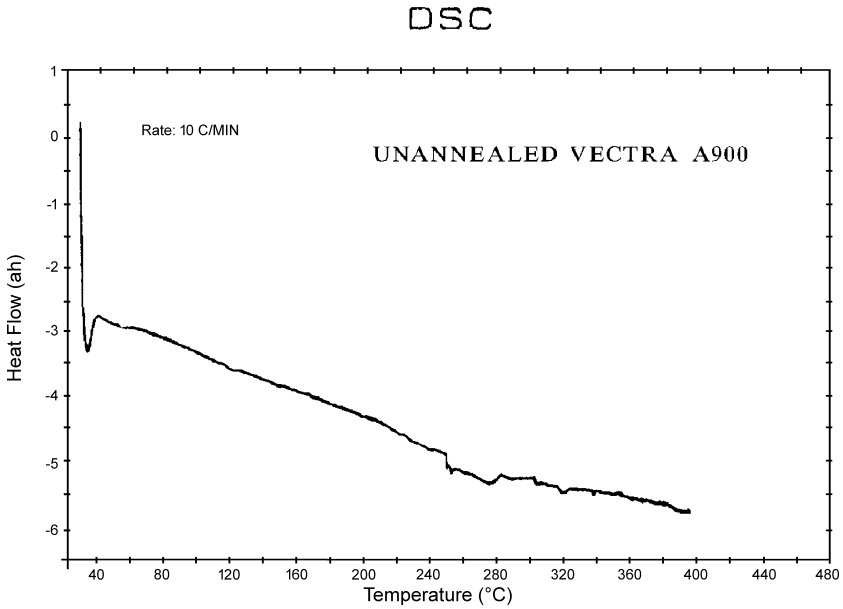


Figure 2.35: DSC scan of Vectra A900 (see Chapter 1 for the DMA and DEA results). T_g is hardly visible at around $T = 60$ °C.

EBSCOhost - printed on 2/13/2023 12:32 AM via . All use subject to https://www.ebsco.com/terms-of-use

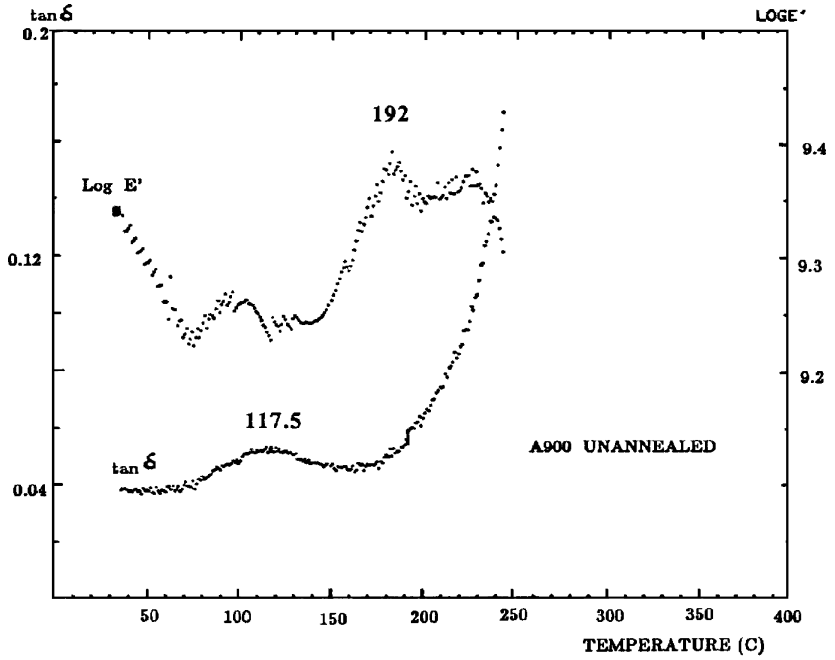


Figure 2.36: DMA scan for the unannealed Vectra A900.

It is not very clear from Figure 2.35 where T_g of Vectra is located. A small change of slope around 60 °C is hardly visible and could be confused with baseline instability or a surface effect.

The DMA results shown in Figures 2.36 and 2.37 are obtained in a tensile mode at 3 Hz of oscillation. The analysis of these curves is not simple: a peak is observed at 117 °C for both the annealed and unannealed Vectra from tan δ data, and second and third peaks are seen for the unannealed sample at 240 °C and 330 °C. For the unannealed specimen, the elastic modulus seems to decrease first and then increase starting at around 150 °C. This might be due to crystallization taking place during the measurement of the mechanical data. Also note that the modulus of the annealed Vectra varies more smoothly, i. e., the data seem to be somewhat more "noisy" for the unannealed sample.

The DEA results obtained by Ward et al. [4] are reproduced in Figures 1.3 and 1.4 (top) of Part II, Chapter 1. Figure 1.3 (top) is a plot of the relative permittivity, and the dielectric loss at 1 Hz is shown in Figure 1.3 (bottom). Two loss peaks are observed at 50 °C and 112 °C. Another secondary peak is visible at a lower temperature (–65 °C). By varying the frequency (Figure 1.4, top), the peaks position are shifted, in particular their maximum, and a "pseudo-activation energy" can be calculated from the value of the shifts, yielding the "frequency map" shown in Figure 2.38.

Figure 2.39 is the TSD depolarization trace obtained on the annealed Vectra after polarization at 130 °C under 5000 V/mm. Four peaks are clearly visible at 122 °C,

EBSCOhost - printed on 2/13/2023 12:32 AM via . All use subject to https://www.ebsco.com/terms-of-use

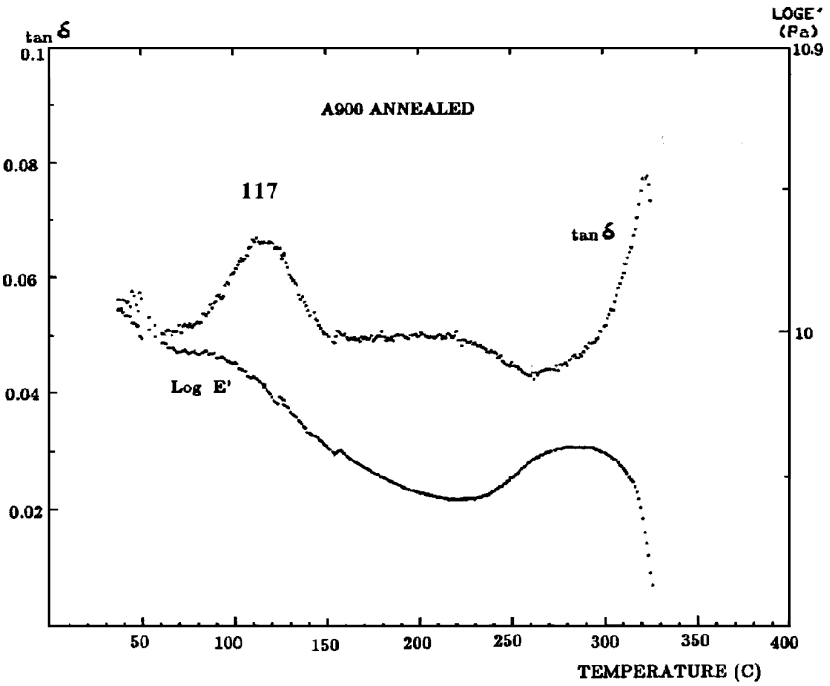


Figure 2.37: DMA scan for the annealed Vectra A900.

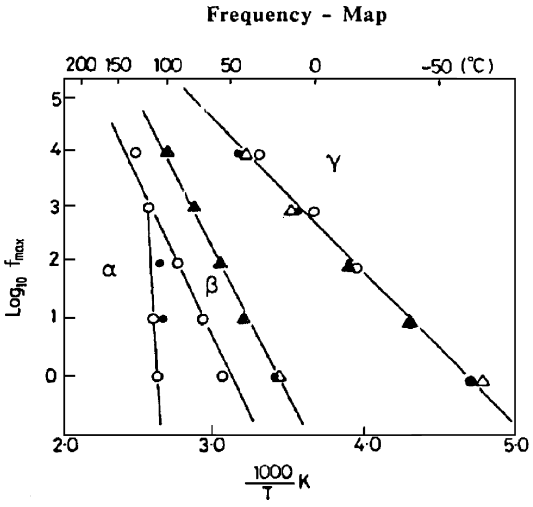


Figure 2.38: Frequency map obtained by DEA [4] to show the α, β, and γ transitions of Vectra A900.

185 °C, 229 °C, and 315 °C. Polarizing at a lower temperature (T_p = 65 °C in Figure 2.40) moves the lower peak downwards (71.5 °C instead of 122 °C for T_p = 130 °C) and reveals lower temperature peaks at –16 °C and –78 °C. The unannealed Vectra is presented in Figures 2.41 to 2.43.

EBSCOhost - printed on 2/13/2023 12:32 AM via . All use subject to https://www.ebsco.com/terms-of-use

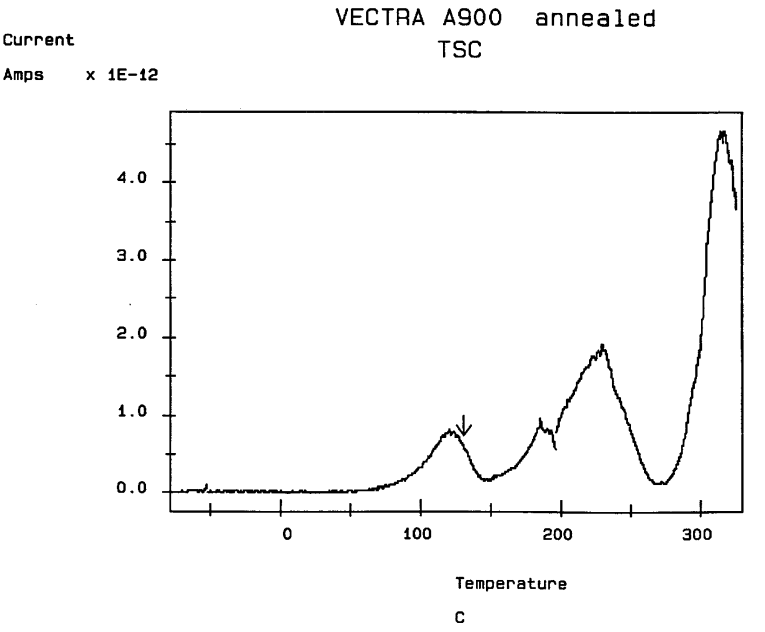


Figure 2.39: TSD trace for the annealed Vectra A900 after polarization at T_p = 130 °C under a voltage field of 5,000 V/mm.

hoechst annealed	Anneal Temp : Inactive	Freeze Temp : -100.
65.EXP	Anneal Time : Inactive	Freeze Time : 5.
Date : 04/04/1990	Polar Time : 2.00min	R3 Rate : 7.(
Time : 11:30:05	Polar Field : 5000.0V/mm	End ISO Temp: 150.(
	Polar Temp : 65.0C	End ISO Time: 0.(
Solomat TSC/RMA	Thickness : 0.025mm	
	Area : 78.0mm^2	

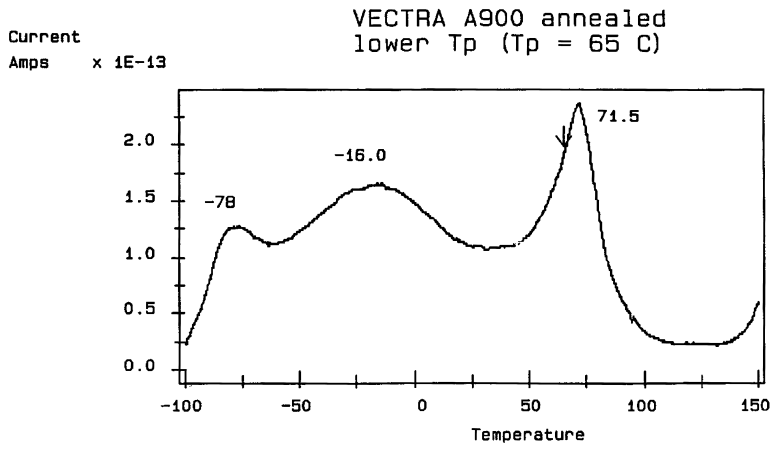


Figure 2.40: TSD trace like in Figure 2.39 after polarization at T_p = 65 °C.

EBSCOhost - printed on 2/13/2023 12:32 AM via . All use subject to https://www.ebsco.com/terms-of-use

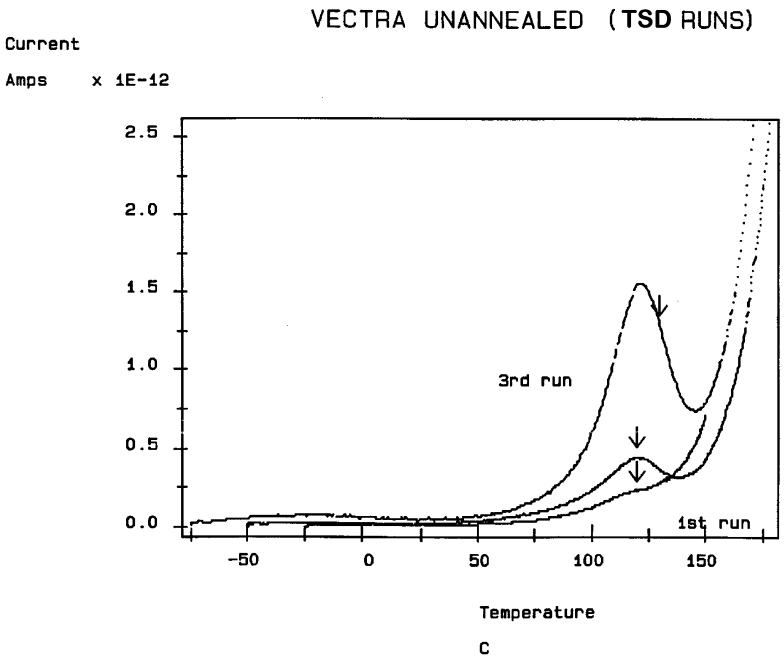


Figure 2.41: TSD trace for the unannealed Vectra A900 after polarization at $T_p = 130\,°C$ under a voltage field of 5000 V/mm. The three traces correspond to successive TSD runs on the same sample. As the unannealed sample is rerun, it ages and hence becomes annealed: its TSD trace converges to that of the annealed sample. Compare to Figure 2.39 for the annealed sample.

Figure 2.41 presents the result of successive TSD runs on the same sample, showing that the peak observed at 122 °C grows to a well-defined peak out of an initial shoulder for the first run, as the sample is rerun in the TSD cell, i. e., as it is annealed after runs 1 and 2.

Figure 2.42 displays the same behavior for the lower peak at –18 °C, which is only visible starting at the third rerun. Figure 2.43 represents the third TSD rerun on the full temperature range, up to 320 °C: only two well-defined peaks at 122 °C and 222 °C are visible, compared to four peaks for the annealed Vectra in Figure 2.39. Additionally, the behavior above 240 °C seems to be "noisy" for this specimen, with sudden current discharges, possibly related to the presence of space charges accumulating around germinating and growing nuclei inside the morphology.

Figure 2.44 compares the relative intensity of the peaks for the annealed and unannealed Vectra polarized under identical conditions. The peak intensities are much larger for the unannealed sample, revealing an interesting feature of the TSD technique: the peaks, contrary to DSC peaks, are more prominent when there is more amorphous matter in the morphology.

EBSCOhost - printed on 2/13/2023 12:32 AM via . All use subject to https://www.ebsco.com/terms-of-use

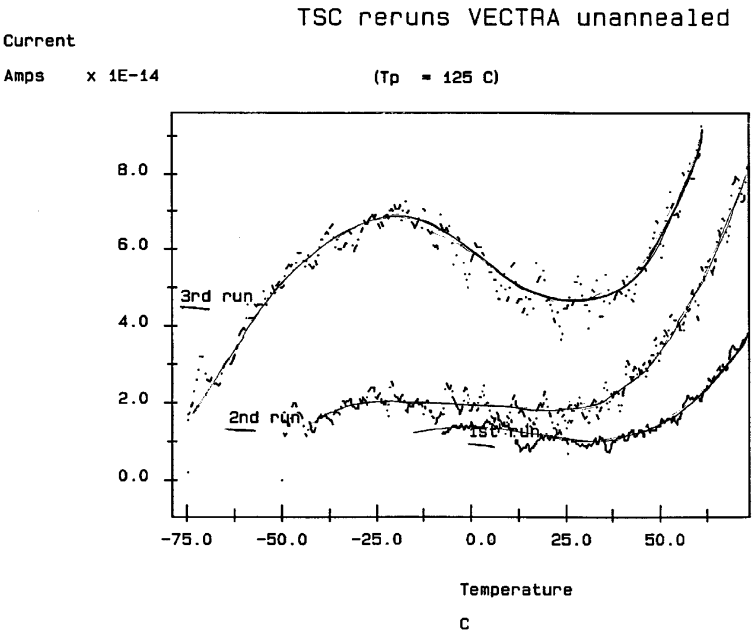


Figure 2.42: Detail of Figure 2.41 in the low-temperature region, near the −18 °C transition. The same observation is made regarding the increase of the signal intensity as the system anneals after each rerun.

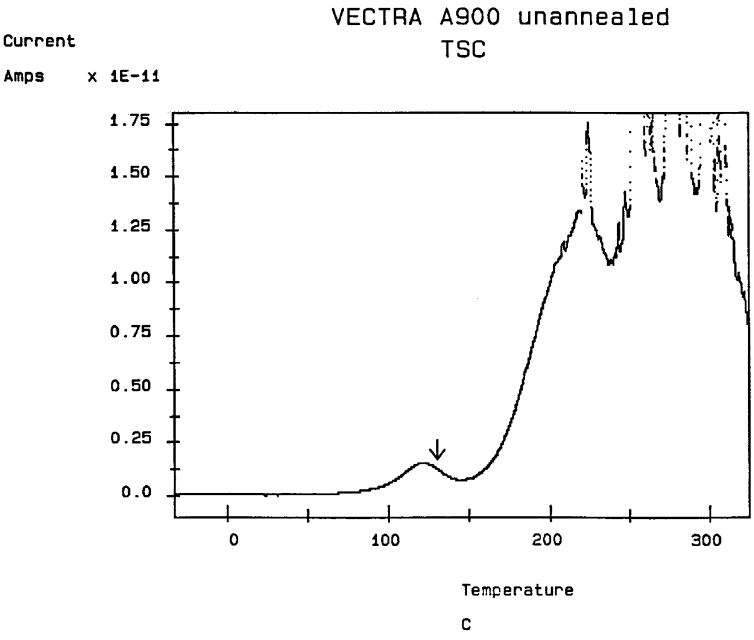


Figure 2.43: Full scale of the TSD trace for the third rerun of Figure 2.42. The temperature range is expanded to higher temperatures showing the discharge of space charges accumulating around the crystals.

EBSCOhost - printed on 2/13/2023 12:32 AM via . All use subject to https://www.ebsco.com/terms-of-use

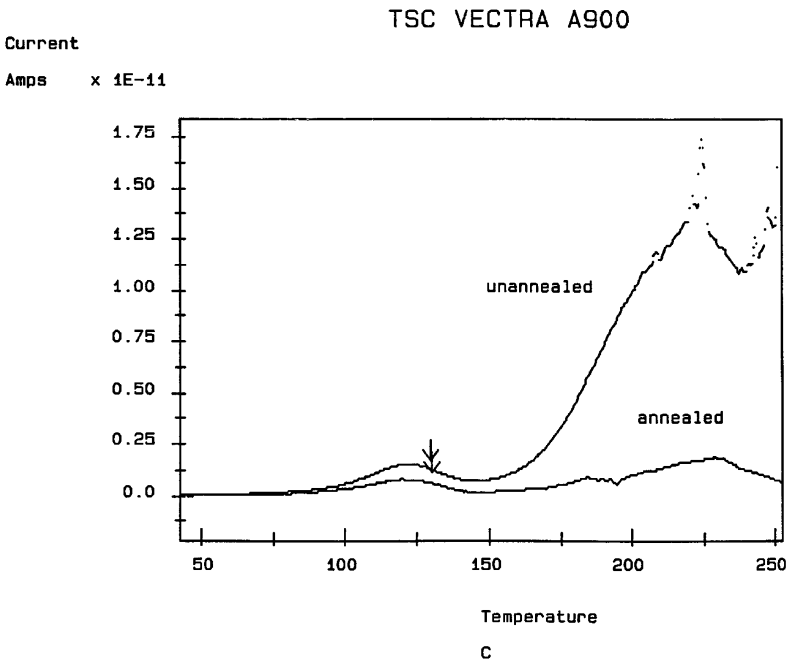


Figure 2.44: Comparison of the TSD traces polarized under similar conditions for the annealed and unannealed samples. The TSD output is more intense for the sample with the most amorphous matter present.

Figure 2.45 is a plot of the current of polarization versus temperature, as temperature is raised at 5 °C/min from 0 °C upward *while a field of* 1000 *V/mm is applied* on the sample. This "thermal-stimulated polarization current" (TSPC) is important since it differentiates the behavior of the annealed and unannealed samples. Only the unannealed Vectra displays mobility at around 57.8 °C. This is confirmed in Figure 2.46, where the unannealed Vectra is annealed in the TSD cell during the first heating run and subsequently rerun (second run in Figure 2.45). The intensity of the peak at 57.8 °C has largely decreased between the two runs.

Two important characteristics of the unannealed Vectra film due to the processing variables are: (1) the film is extruded, i. e., it presents a certain amount of orientation, and (2) it is quenched, which implies a low (if any) percentage of crystals in the structure (Figure 2.35), as well as an amorphous phase out of equilibrium relative to the statistical distribution of the conformers, resulting in internal stress.

Annealing can induce several phenomena depending on temperature: (1) reduce or destroy the orientation present, (2) relax the internal stress, and finally (3) permit nucleation and/or growth of crystals, especially under thermal conditions which approach the maximum rate of crystallization (normally at $0.82T_m$, i. e., 184 °C).

EBSCOhost - printed on 2/13/2023 12:32 AM via . All use subject to https://www.ebsco.com/terms-of-use

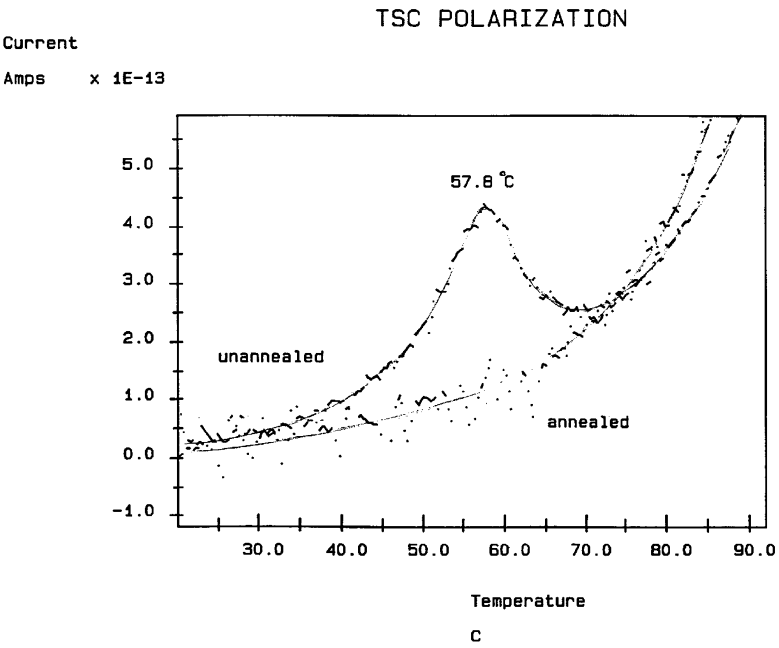


Figure 2.45: TSPC traces for the annealed and unannealed Vectra films. This is a polarization trace (not a depolarization trace) under a field of 1000 V/mm. See text.

In addition to these structural and morphological difficulties, the method of thermal-stimulated current itself may induce other complications. First, bringing the sample to the temperature of polarization anneals it to a certain extent. Secondly, the polarization field might interfere with the polar groups, as is known to be the case for non-polymeric liquid crystals.

In view of the above, it is expected that the response to the orientation of the dipoles by the voltage field, the so-called polarization, varies with the thermal treatment, the thermal history, and the analysis technique (TSD, TSPC, TWD) which is applied.

Take Figure 2.41, for example: the peak at 120 °C grows in intensity between runs for the unannealed Vectra. It is possible that the annealing treatment, inherent to the successive runs performed, loosens up the orientation present in the film in the direction perpendicular to the voltage field. As more and more amorphous matter becomes available in the direction parallel to the field, because the macromolecules unstretch from the other direction, the number of dipoles which can be polarized at 120 °C increases, resulting in a larger peak upon depolarization. This peak, at 120 °C, is located at the same temperature than the peak obtained by DMA (Figure 2.36) and is associated with a depreciation of the modulus, which makes it a strong candidate for T_g. It is well known that annealing an oriented material at T_g, or slightly above it, will disorient it. Figure 2.41 is, therefore, well understood. But Figure 2.44 shows that the

EBSCOhost - printed on 2/13/2023 12:32 AM via . All use subject to https://www.ebsco.com/terms-of-use

intensity of the peaks for the annealed specimen is smaller, apparently in contradiction with what we just said. This is now the effect of the crystallization, well perceived by the endothermic peak in a DSC scan (Figure 1.5, bottom). Crystallization traps amorphous matter into ordered structures, resulting in a reduced availability of the dipoles to the polarization effect: when there are fewer units to polarize, the current of depolarization is smaller. Notice that in Figure 2.41 the maximum temperature between runs is 175 °C, away from crystallization effects; annealing produces available amorphous dipoles in this case.

A TSD ramp-up may induce crystallization, probably nucleation in the case of unannealed Vectra. Figures 2.39 and 2.43 display such a behavior. The peaks observed correspond to the motion of dipoles due to a modification of the morphology, for instance during the migration of amorphous matter to the crystallization sites. Maxima of motion occur, resulting in TSD peaks, at the temperature of occurrence of maximum diffusion in the structure and at the melting temperature (Figure 2.39). The permanent dipoles which rotate in the structure at these higher transitions do not need to be polarized by the voltage field in order to create a current. The peaks actually occur in a temperature zone beyond the influence of the temperature of polarization (marked by an arrow in the figures). It is unclear in Figure 2.39 whether the current is generated by motions which are primarily diffusion-based, as the mobile units would need to have a strong dipolar moment to be visible without polarization, or the voltage field creates dipolar entities ("nodular dipoles") which become thermally unstable at higher temperatures, thus creating the visible peaks. This assumption is also mentioned in Part II, Chapter 4, where the relaxation maps are analyzed. Another possibility, beyond the effect of crystallization or other phase-ordering processes, is that trans-esterification occurs in the solid phase, resulting in an increase of the molecular weight of the chains.

II.2.10 Characterization of rubbers and elastomers

II.2.10.1 Case study: vulcanized blends of crosslinked elastomers

In an effort to gain more insight into the degree of crosslinking and the macromolecular structure of NR and related blends, four samples are analyzed by TSD. In these tests, an initial polarization (250.0 V/mm) is applied for a period of 2 minutes, followed by a quench to –100 °C. The samples are then heated at a rate of 7 °C/min, during which the current resulting from the dipole relaxation is recorded.

The TSD traces for two NR vulcanizates, A and B, with crosslink densities of 18 and 49 mol/m^3 (as determined by equilibrium stress-strain measurements), are shown in Figures 2.46 and 2.47. The polarization conditions and the sample dimensions are shown in the header of Figure 2.46. In Figure 2.47, we focus on the glass transition T_g, which is located in the low-temperature portion of the data. Sample B, the more highly

EBSCOhost - printed on 2/13/2023 12:32 AM via . All use subject to https://www.ebsco.com/terms-of-use

crosslinked material, is shifted to a slightly higher temperature, which is consistent with the increased molecular weight resulting from the high degree of crosslinking. Additionally, we observe a significantly higher level of intensity in Sample B. The cur-

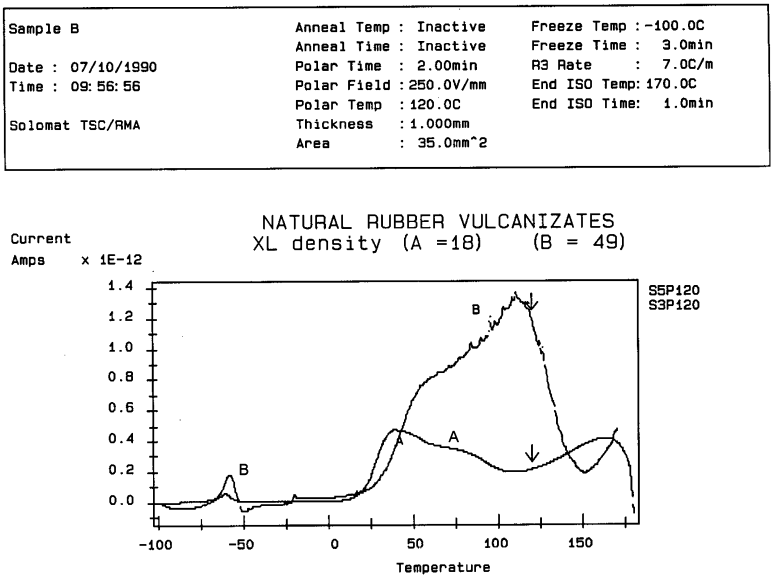


Figure 2.46: TSD traces for two NR vulcanizates, A and B, with crosslink densities of 18 and 49 mole/m^3, respectively.

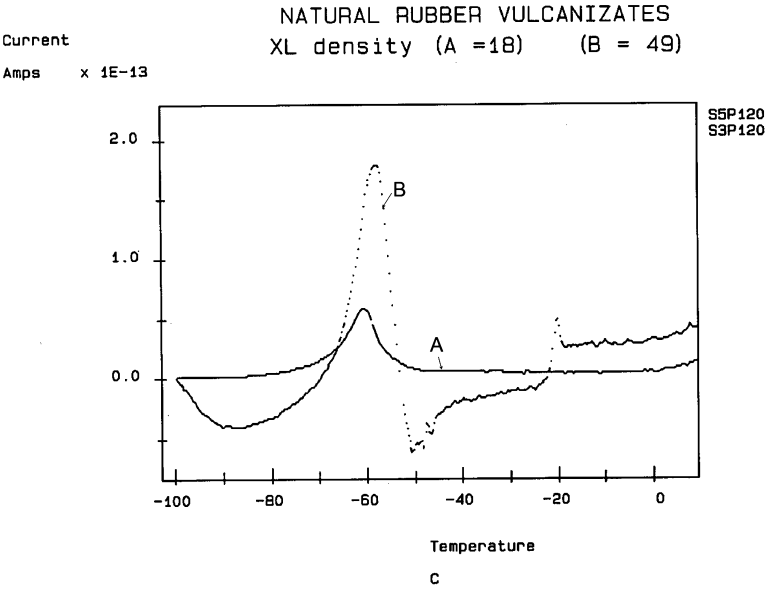


Figure 2.47: Detail of Figure 2.46 in the low-temperature region (–100 °C to 0 °C).

EBSCOhost - printed on 2/13/2023 12:32 AM via . All use subject to https://www.ebsco.com/terms-of-use

rent response of the TSD measurement is directly related to the number and type of dipoles; the presence of sulfur groups inserted between the chains probably enhances the dipolar activity at the T_g relaxation, perhaps in a manner similar to the role played by the Irganox stabilizer for HDPE. However, an increase of the degree of crosslinking should counteract this effect by decreasing the molecular mobility, so, while we would expect intensity to increase with the degree of vulcanization due to the increase in the concentration of polar groups on the NR, the crosslinking of the chains should level off or even decrease this tendency for higher crosslinking densities. TWD spectroscopy is a much better tool to assess the crosslinking density, as reported further in Part II, Chapter 3.

The higher temperature peaks observed in Figure 2.46 are also of great interest as they are believed to be related to motions in the macromolecular structure of the rubber vulcanizate. The behavior is remarkably different for the two vulcanizates, with peaks shifted and more intense for the higher sulfur content (sample B).

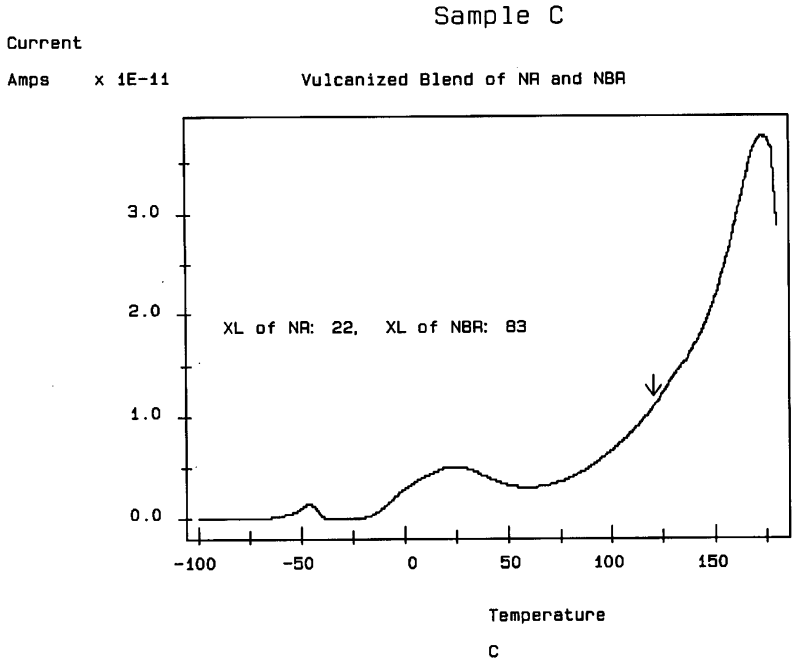


Figure 2.48: TSD trace for a vulcanized blend of NR and NBR with crosslink densities of 22 for NR and 83 for NBR.

Figure 2.48 displays the TSD for a vulcanized blend of NR and acrylonitrile–butadiene rubber (NBR; sample C) with crosslink densities estimated to be 22 and 83 mol/m^3, respectively. As with samples A and B, we observe higher temperature peaks which

EBSCOhost - printed on 2/13/2023 12:32 AM via . All use subject to https://www.ebsco.com/terms-of-use

are presumably related to motion in the macromolecular structure. Figure 2.49 is a blow-up of the low-temperature relaxation: we see two peaks at –59.5 °C and –46.0 °C, indicating that two distinct phases exist in the sample. The two T_gs are rather fused in this figure because of the high polarization temperature (T_p = 120 °C). By polarizing between the two peaks, separation becomes better resolved. The best method is to use thermal-windowing, polarizing between –80 °C and –30 °C. The results are presented in Part II, Chapter 3, and confirm the segregation into two phases.

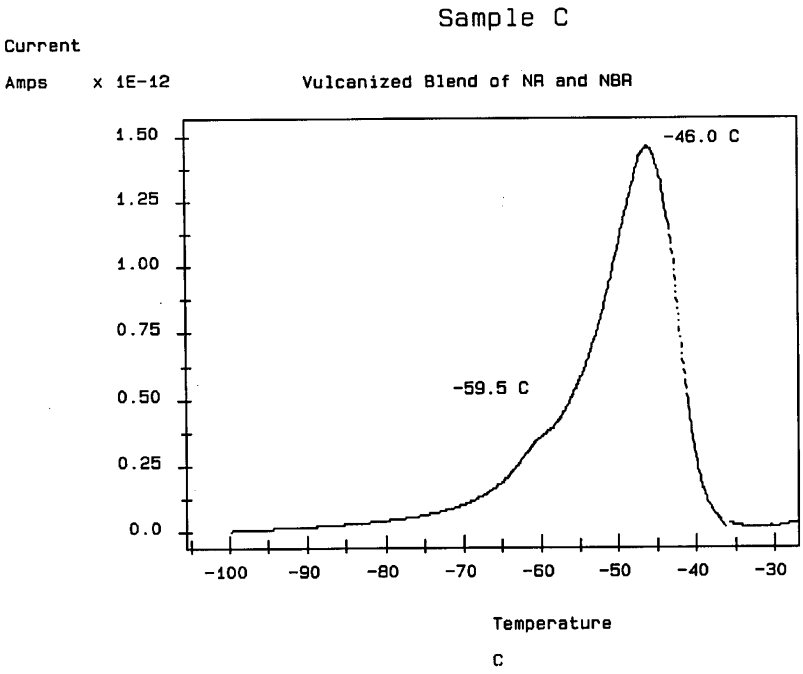


Figure 2.49: Detail of Figure 2.48 in the low-temperature region (–100 °C to –30 °C). The trace shows two peaks corresponding to two segregated phases. The deconvolution by TWD will be discussed in Chapter II.3.4.3.

Finally, the TSD trace of an unvulcanized blend of NR and NBR is shown in Figure 2.50.

Here we observe T_g at –59 °C with a weak poorly resolved shoulder at slightly lower temperature. Higher-temperature transitions at –13.5 °C and 48.2 °C are also observed. The vulcanization process has perhaps merged these two peaks into the single peak observed at 25 °C (with a shoulder at 0 °C) in Figure 2.48. Note that the intensity of this sample (Figure 2.50) is two orders of magnitude lower than that of sample C (Figure 2.48). This can be attributed to the absence of the polar groups in the rubber resulting from the vulcanization.

EBSCOhost - printed on 2/13/2023 12:32 AM via . All use subject to https://www.ebsco.com/terms-of-use

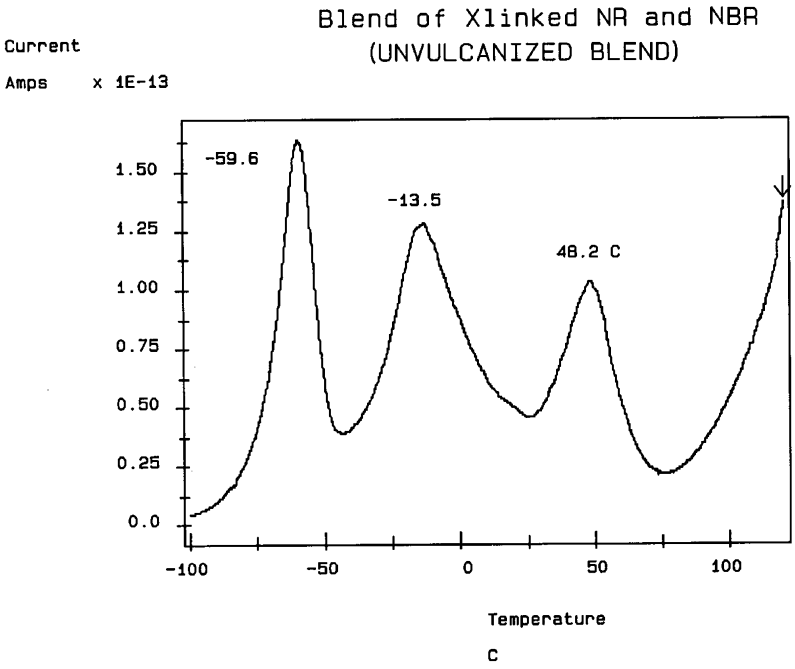


Figure 2.50: TSD trace of an unvulcanized blend of NR and NBR. Compare with the vulcanized blend in Figure 2.48.

II.2.10.2 Case study: NR and SBR blends

A series of NR and SBR blends were provided by Bridgestone Japan and characterized by TSD and TWD. The TWD results are presented in Part II, Chapter 3. The TSD plots (Figure 2.51) clearly resolve the glass transition temperature (T_g) of both blend components, indicating segregation. T_g for 100 % NR and 100 % SBR are –62 °C and –50 °C, respectively.

Figure 2.52 displays the effect of blend ratio on T_g of both phases in the blends. The T_g values of both phases seem to indicate a certain amount of solubility of one segment in the other phase, as attributed to the decrease (for SBR) or increase (for NR) of the T_gs.

In Figure 2.53, the peak intensity versus blend ratio is shown. A significant decrease in intensity is observed for the NR upon the addition of 25 % SBR. Beyond this 25:75 ratio, the intensity is relatively linear with NR concentration as expected. This unexpectedly large loss of intensity may be due to a large-scale migration of polar impurities from the NR into the SBR. TSD peak intensity is proportional to the number of dipoles polarized in a sample. Migration of polar impurities would therefore be expected to result in a decrease in the NR peak and an increase in the SBR peak intensity, as observed. The TWD results, in Part II, Chapter 3, will clearly identify the migration

EBSCOhost - printed on 2/13/2023 12:32 AM via . All use subject to https://www.ebsco.com/terms-of-use

process and assign the slight variations of T_g observed in Figure 2.52 to the respective plasticization of the phases by the impurities. Virtually no dissolution of NR into SBR or vice versa occurs. Migration of impurities seems to dominate their observed relaxation effects.

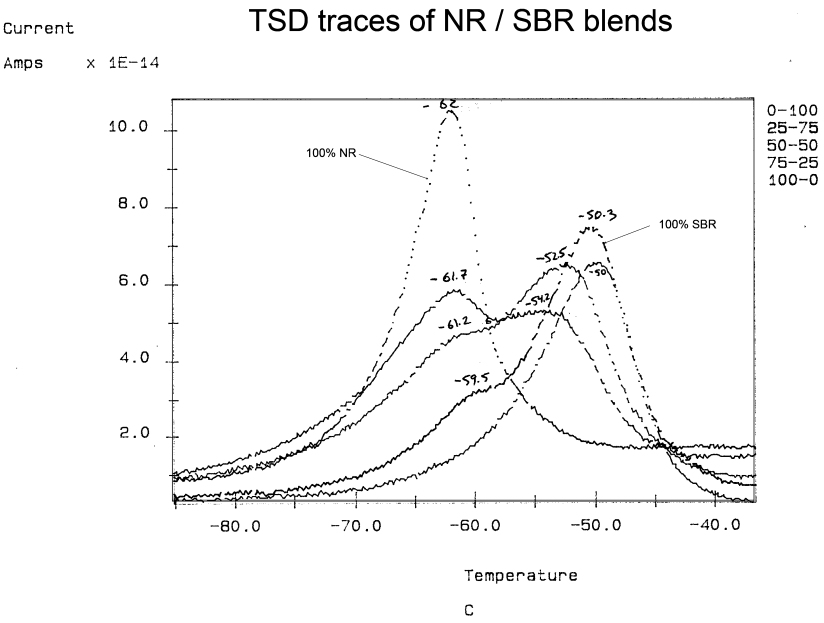


Figure 2.51: TSD traces for blends of NR and SBR at various blend ratios.

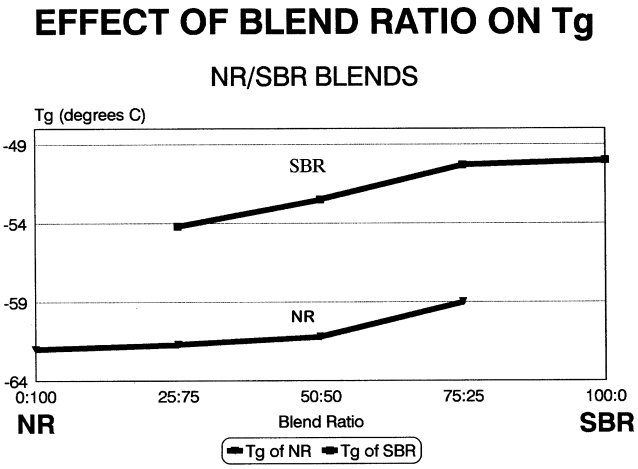


Figure 2.52: Effect of the blend ratio on the value of T_g of both phases in the NR/SBR blends. T_g of the SBR-rich phase is shown at the top; T_g of the NR-rich phase is shown at the bottom.

EBSCOhost - printed on 2/13/2023 12:32 AM via . All use subject to https://www.ebsco.com/terms-of-use

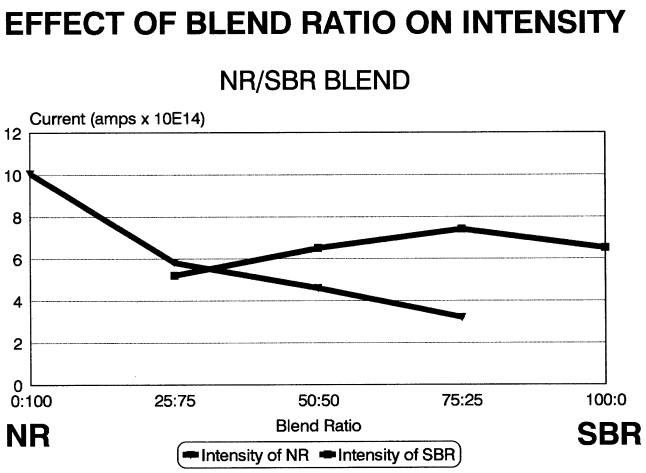


Figure 2.53: Effect of the blend ratio on the value of the peak intensity for both phases in the NR/SBR blends.

These results are significant because they open the possibility of monitoring additive migration between phases or layers of a multi-layer system. This cannot be easily accomplished through any other technique.

II.2.11 Conclusion

Thermally stimulated current is a useful tool in the analysis of many practical characterization processes. We have shown in this chapter several examples where the technique is unique and can be used in the case of samples in situ, in their lifetime application format. TSD has been shown to be useful in the in-polymer analysis of additives. Concentrations of soluble additives can be determined based on the peak intensity or area. The most important aspect of additive analysis by TSD may be the ability to identify the state of the additive within the polymer matrix. Soluble stabilizers such as Irganox 1076 can be identified based on their positive effect on peak intensity. Insoluble or partially soluble stabilizers can be clearly differentiated by their negative effect on peak intensity. Additionally, it appears that TSD will be useful in monitoring migration of soluble additives between polymer phases. No other analytical technique appears to offer these unique capabilities.

EBSCOhost - printed on 2/13/2023 12:32 AM via . All use subject to https://www.ebsco.com/terms-of-use

EBSCOhost - printed on 2/13/2023 12:32 AM via . All use subject to https://www.ebsco.com/terms-of-use

Part II Chapter 3
Practical examples of Thermal-Windowing Deconvolution characterization

In Chapter 2 of Part I we have defined characteristic parameters of the Thermal-Windowing Deconvolution (TWD) depolarization kinetics to quantify the local and modulated coupled interactions between the dipoles. One such "practical" parameter is the degree of disorder (DOD). There are many other parameters, also described in Part I, Chapter 2, that can adequately be used to specify the state of interaction between the dipoles. In particular, by working in the ΔG plane or in the normalized ΔG plane, important correlations between the mechanism of relaxation of the polarized dipoles and the collective behavior of interactive coupling become apparent (equations (2.25) to (2.32) of Part I, Chapter 2). In this chapter, we concentrate on the *practical applications of these concepts* to characterize materials. Whenever possible, we use the simple DOD number instead of other variables to analyze changes observed in the relaxation map of a TWD experiment, because the interpretation of the results makes it straightforward, although, in a few instances, the DOD number is too simplistic and other complementary parameters of the relaxation map must also be considered.

The DOD is influenced by any parameter which changes the overall interactive structure of the material, as long as it can be perceived as a change in the glassy state of the amorphous phase. TWD is particularly useful as a quantitative way to describe:

- internal and thermal stress,
- curing of thermosets (in coatings and composite materials), and
- interpenetration and segregation of phases for blends and block copolymers.

We present in this chapter several examples to illustrate the use of TWD characterization in thermal analysis. The characterization of materials by TWD is still not widely used. We try, in the case studies reported here, to provide as much experimental information as possible to incite the reader to develop his/her own views on the subject and help further the understanding. For this reason, a great number of plots and tables, always alike, are reported, showing the similarities and differences between samples of a same material and between materials.

II.3.1 Internal stress and the effect of the cooling rate on the DOD of engineering thermoplastics

It is often critical to control thermally induced residual stresses in blow-molded or injection-molded parts through optimization of the thermal history of the process.

https://doi.org/10.1515/9783110756746-008

EBSCOhost - printed on 2/13/2023 12:32 AM via . All use subject to https://www.ebsco.com/terms-of-use

In some instances, internal stress, resulting in birefringence patterns, must be eliminated (compact discs), and in other circumstances (PET bottle necks), they ought to be optimized to induce strength.

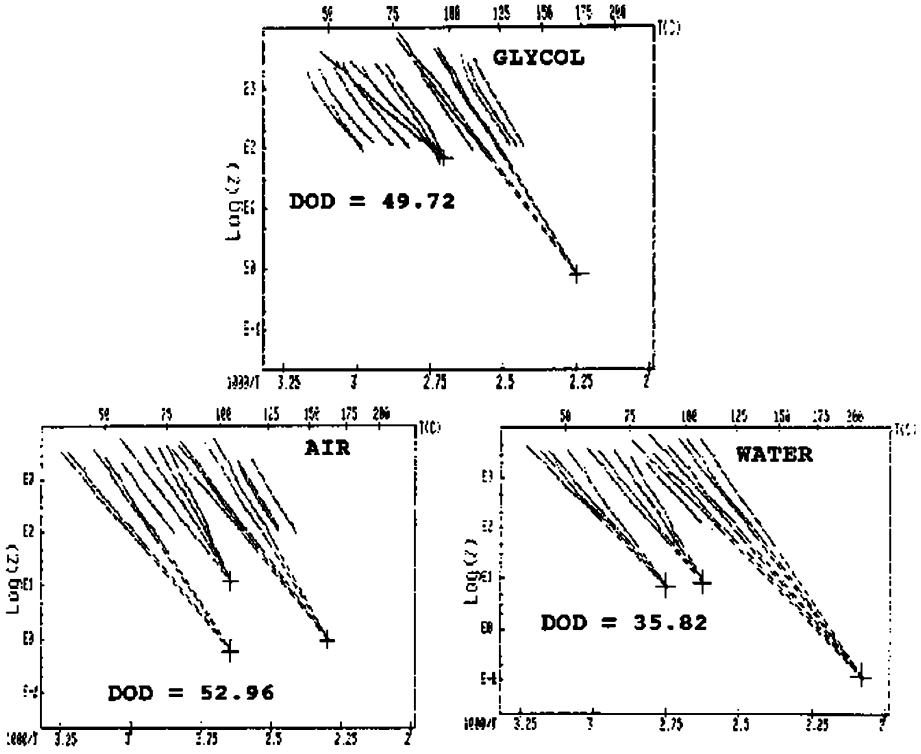


Figure 3.1: Relaxation maps in the Arrhenius plane showing the effect of cooling polystyrene compression-molded samples at different cooling rates. The cooling rate is controlled by the nature of the fluid flowing in the cooling pipes embedded in the mold: air, glycol, and water. The DOD is associated with the state of non-equilibrium of the amorphous matter below its T_g.

Figure 3.1 illustrates that the DOD number is related to the amount of internal stress induced by the speed of cooling. The DOD is calculated here from the low-temperature compensation, which is representative of the state in the glass (an interpretation for the existence of multiple compensations in polymeric systems is proposed in Part I, Chapter 3). The three relaxation maps shown in Figure 3.1 apply to polystyrene specimens which are cooled in a mold under various cooling conditions obtained by varying the cooling agent circulating through the internal cooling circuits of the mold halves. Water (at a temperature of 10 °C), glycol mixed with water (at −22 °C), and compressed air (1 bar (10^5 Pa)) are used alternatively. Quenching (with water) seems to induce the more "ordered" glassy state, resulting in the lowest DOD: 35.82. Glycol

EBSCOhost - printed on 2/13/2023 12:32 AM via . All use subject to https://www.ebsco.com/terms-of-use

is less effective than water (DOD = 49.72), although cooler (–22 °C), and air-cooled specimens have the highest DOD (DOD = 52.96), indicating a glassy structure closer to equilibrium. Upon annealing the water-quenched sample, the DOD increases correspondingly, and the aging process can be quantified with the DOD changes (see later).

II.3.2 Orientation and pressure effects on plastic materials

There have been great advances in the production of polymer morphologies with a high degree of chain extension and orientation, with resultant with material high tensile modulus and strength. While the result of orientation is primarily to stretch the macromolecules, hydrostatic pressure is thought to exert a greater influence on the free volume, ultimately producing densification. Careful TWD measurements [14] on oriented and pressurized polystyrene specimens (Figures 3.2 and 3.3) show that the DOD is very sensitive to the actual state of the plastic and can be used for quality controls.

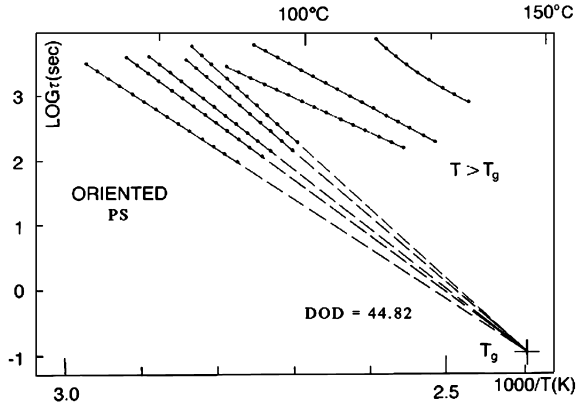


Figure 3.2: Relaxation map in the Arrhenius plane for a polystyrene compression-molded sample after initial orientation.

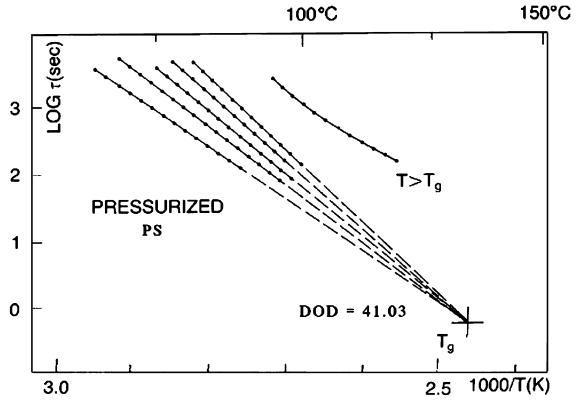


Figure 3.3: Relaxation map in the Arrhenius plane for a pressurized polystyrene compression-molded sample (no orientation).

EBSCOhost - printed on 2/13/2023 12:32 AM via . All use subject to https://www.ebsco.com/terms-of-use

In Figures 3.2 and 3.3 the difference between the two specimens consists in their mode of preparation in the mold. Both samples are prepared from the same plaque, which has been extruded and presents a certain amount of orientation (15 %). The specimen designated "pressurized" has been released from the initial orientation present by raising first the mold temperature to 180 °C and annealing it there for 20 minutes. The specimens are brought up to a molding temperature of 160 °C, pressurized in the mold cavity to 667 bars (6.7×10^7 Pa), and quenched to room temperature under pressure.

The relaxation maps are obtained from cut-outs of the treated specimens, one cut-out for each temperature of polarization [14]. The DOD number is calculated from the positive compensation at T_g; DOD = 41.03 for the pressurized polystyrene and 44.82 for the oriented polystyrene. One sees that the DOD for the oriented polystyrene is greater than for the "pressurized" sample by about 9 %. The reason for the higher DOD for the oriented material is the direction of the polarizing voltage field, which was perpendicular to the direction for the mechanical orientation: the material is actually more disordered, i. e., with a higher DOD, in the direction *perpendicular* to the biaxial orientation. This was also observed in Part I, Chapter 2 in the case of the low-temperature amorphous component of the drawn polypropylene. Also note that the curved $T_{g,\rho}$ relaxation is shifted towards lower temperatures by the pressure applied during the process (T_∞ is lower for the pressurized sample). The free volume parameters can be found in reference [14].

II.3.3 The curing of paint and powder coating on metal

The manufacture of aerospace structures depends heavily on (i) the bonding of reinforced thermoplastic components and (ii) the bonding strength of paints and other coatings on their metallic substrate. Relaxation maps can be analyzed to develop methods to achieve good bond strength without deconsolidation and warping and follow the degree of crosslinking. DOD numbers can be compared for cured and uncured resins and coatings to determine a quantitative scale for the degree of curing.

II.3.3.1 Paints

In this first example, the material studied is the polyester already analyzed by TSD in Part II, Chapter 2, crosslinked with a melamine resin and catalyzed with a sulfonic acid. Samples are processed under three conditions by varying the bake time: under-cured, correctly cured, and over-cured. Each sample is cut into small squares of approximately 6.35 mm square.

The peaks detected by TSD (Figure 2.18a–c of Part II, Chapter 2) in the three samples are now subjected to thermal-windowing experimentation using the following

EBSCOhost - printed on 2/13/2023 12:32 AM via . All use subject to https://www.ebsco.com/terms-of-use

parameters:

range of study:	20 °C to 40 °C
window width:	2 °C
polarization voltage:	50 Volts
polarization and depolarization time:	2 minutes

Figures 3.4 to 3.6 illustrate the deconvolution of the global peaks into elementary, cooperative relaxation modes.

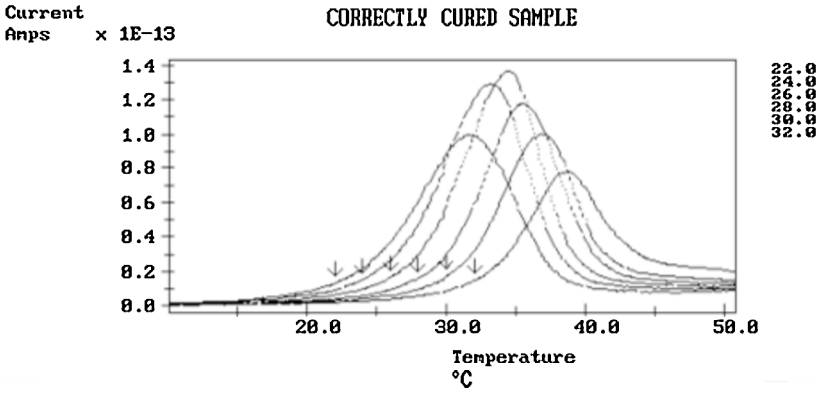


Figure 3.4: TWD multiplot of a paint: correctly cured sample. This sample was studied by TSD in Figure 3.18a.

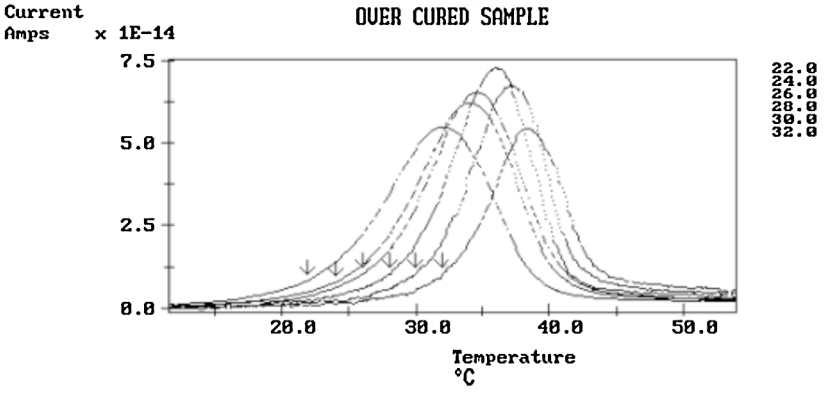


Figure 3.5: TWD multiplot of a paint: over-cured sample. This sample was studied by TSD in Figure 3.18b.

EBSCOhost - printed on 2/13/2023 12:32 AM via . All use subject to https://www.ebsco.com/terms-of-use

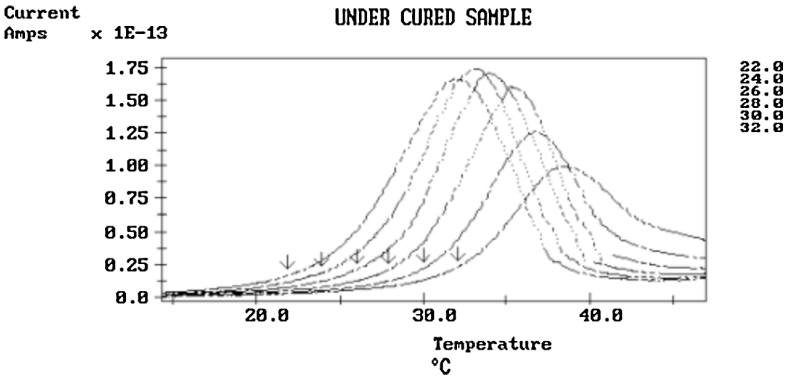


Figure 3.6: TWD multiplot of a paint: under-cured sample. This sample was studied by TSD in Figure 3.18c.

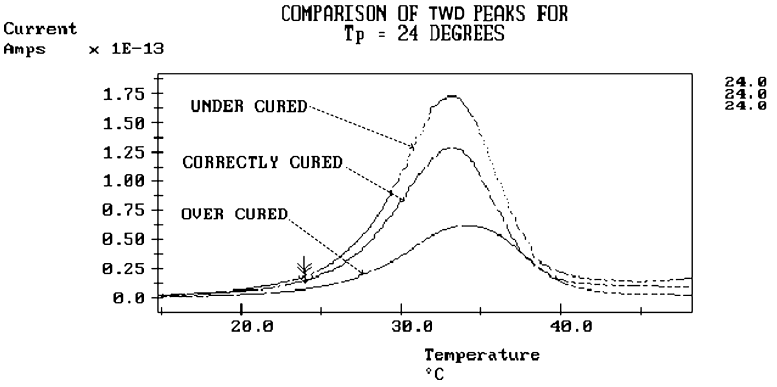


Figure 3.7: Comparison of the TWD at $T_p = 24\,°C$ for the under-cured, correctly cured, and under-cured samples.

Figure 3.7 compares the elementary peaks of the three samples obtained at the same temperature of polarization $T_p = 24\,°C$. The under-cured is the top curve, the over-cured is at the bottom, and the correctly cured is in the middle. The same general phenomenon as in the TSD scan is observed: the peak intensity goes down with cure and the peak temperature goes up slightly.

Looking at the Arrhenius transforms in Figure 3.8 for each of the three curves of Figure 3.7, the under-cured and correctly cured samples appear to be very close while the over-cured sample has a significantly different slope than the other samples. This comparison is done at the same $T_p = 24\,°C$. It is interesting to note that the slope for the over-cured sample is less steep than for the other two. This would imply a lower activation energy for this relaxation mode, although the specimen is more cured, an apparent contradiction. In fact, it is crucial to realize that the individual relaxation modes, isolated from the spectrum, do not represent the environment of the bonds.

EBSCOhost - printed on 2/13/2023 12:32 AM via . All use subject to https://www.ebsco.com/terms-of-use

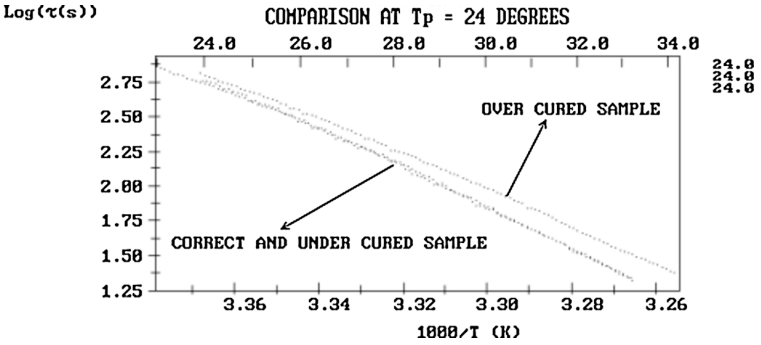


Figure 3.8: Comparison of the Arrhenius transforms of the TWD curves in Figure 3.7.

Only the coordinates of the compensation, especially the DOD, play that role. The relaxation modes cannot be associated with elementary molecular motions in the structure; they represent the same phenomenon, kinetic coupling, viewed from different "angles," as T_p is varied. Comparing individual relaxation modes obtained at the same T_p has very little value.

II.3.3.2 Determination of DOD

A true indication of the influence of the cure on the bonds environment can be determined by the DOD resulting from the compensation search.

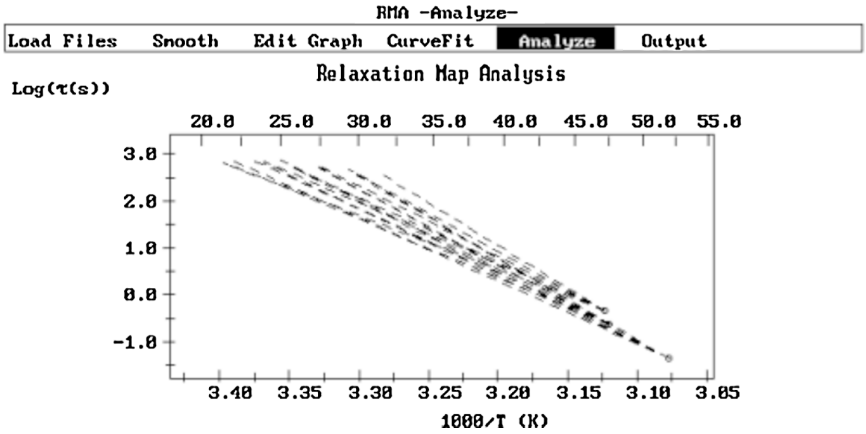


Figure 3.9: Master plot of the relaxation map in the Arrhenius plane for all three samples showing the compensations associated with the advance of the curing process. See Table 3.1 results.

Figure 3.9 displays the relaxation map, and Table 3.1 provides the DOD numbers. We immediately see that the less cured sample has the highest DOD number. This follows

EBSCOhost - printed on 2/13/2023 12:32 AM via . All use subject to https://www.ebsco.com/terms-of-use

Table 3.1: Coordinates of the compensation points for the different levels of cure and the corresponding DOD numbers.

	T_c (°C)	Log τ_c	DOD	ΔG_c (kcal/m)
Under-cured	51.94	−1.35	47.47	17.08
Good cure	47.52	−0.61	43.34	18.17
Over-cured	47.2	−0.32	42.78	18.33

logically as there is less restriction or order in the under-cured system than in the correctly and over-cured systems.

It is interesting to note that once the material approaches and exceeds correct cure, the difference in the compensation behavior (Figure 3.9) and in the DOD number (Table 3.1) becomes less substantial. As the crosslink density approaches saturation, the rate of crosslinking diminishes due to kinetic effects.

Figure 3.10 is a plot of entropy vs. T_p to illustrate that curing of the paint decreases the entropy substantially and that it is possible to quantify the crosslink effect from these entropy calculations (the lower curve is the over-cured sample, the top one is the under-cured one).

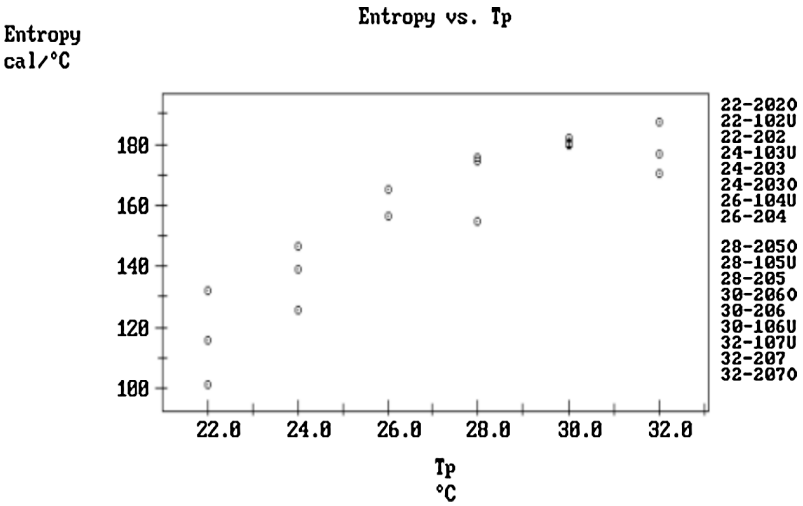


Figure 3.10: Entropy of activation vs. T_p for the three paint samples. Lower curve: over-cured; top curve: under-cured; middle curve: correctly cured.

Another very useful parameter to characterize the degree of cure or crosslink density is P_o, the area under the elementary thermal-windowing curve which provides the value of the initial polarization in the sample P_o (normalized for surface area). For the sam-

EBSCOhost - printed on 2/13/2023 12:32 AM via . All use subject to https://www.ebsco.com/terms-of-use

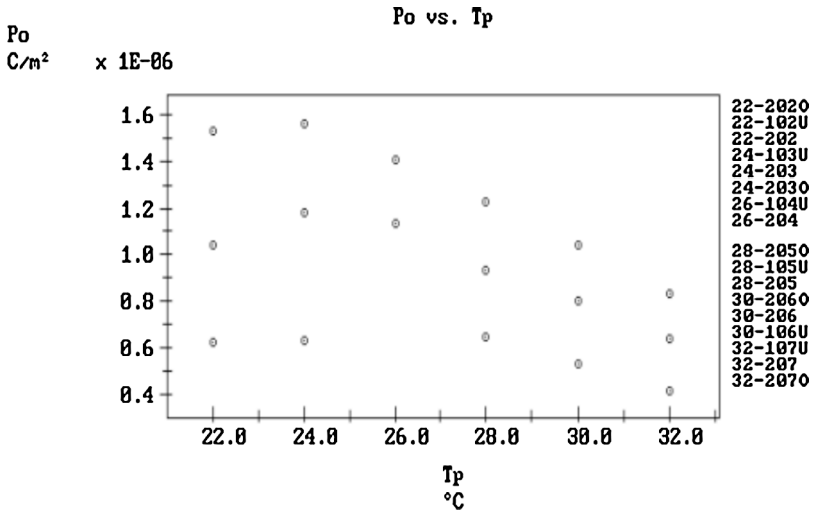


Figure 3.11: Mobility in the paint samples measured by the initial number of dipoles during the TWD depolarization: P_o. P_o is plotted against T_p, very distinctively separating the levels of cure in the three samples.

ple with the greatest degree of cure, there are fewer activated dipoles by application of the field, and therefore P_o is smaller, as indicated in Figure 3.11.

II.3.3.3 Powder coatings

In our second example, an epoxy/polyester appliance, coating is sprayed over a Bonderite 1000 steel substrate and cured for 5, 10, 15, and 20 minutes at 193 °C in a forced air oven. These samples were already studied by TSD in Part II, Chapter 2 (Figure 2.16 and Table 2.1).

The results shown in Figure 3.12 were obtained using a polarization temperature T_p between 50 °C and 85 °C and a window width of 5 °C. The time of polarization and depolarization is 2 min. Thermal-windowing experiments yield a quantifiable difference in the apparent level of cure in two of these samples. Relaxation map analysis of the samples cured for 5 and 10 minutes reveals that the DOD for the sample cured for 5 min is 47.95, while that of the sample cured for 10 min is 44.84. The lower DOD value in the sample cured for 10 minutes indicates less entropy, a higher crosslink density, and a higher degree of cure. A one-tenth unit difference in DOD is considered significant; the total error is less than 0.1 units for the seven relaxation curves used in these experiments. A typical compensation search plot is shown in Figure 3.13.

EBSCOhost - printed on 2/13/2023 12:32 AM via . All use subject to https://www.ebsco.com/terms-of-use

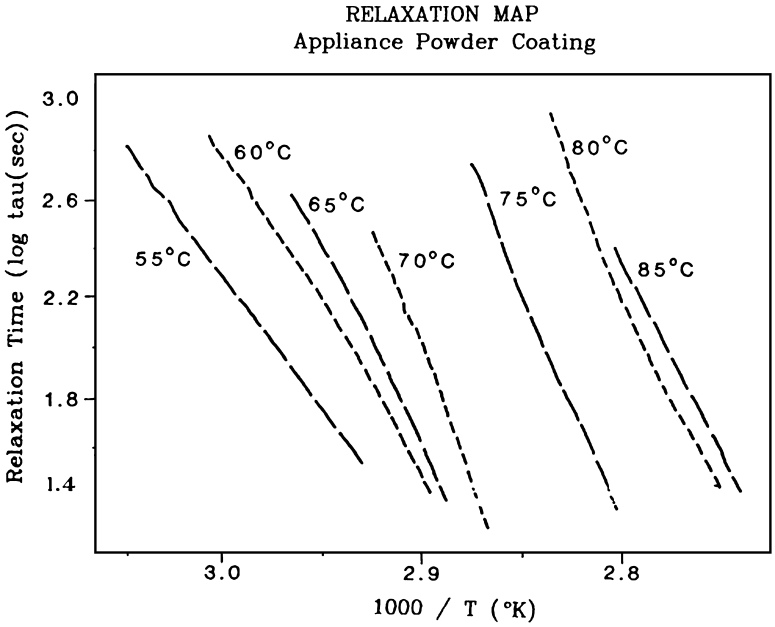


Figure 3.12: Relaxation map in the Arrhenius plane for an appliance powder coating studied in Figure 3.16 and Table 3.1 by TSD.

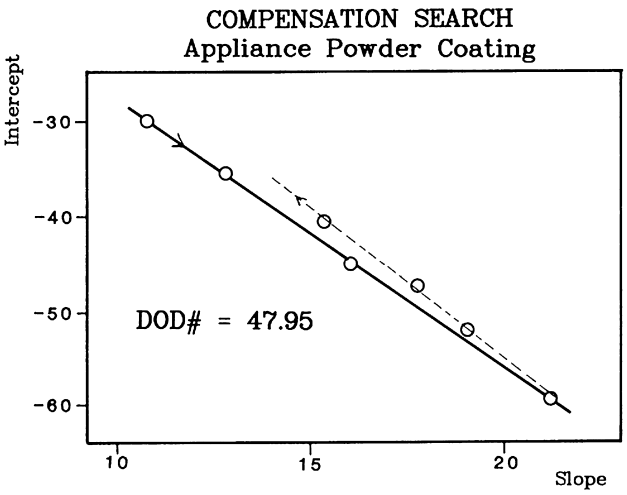


Figure 3.13: Compensation search for the results of Figure 3.12 showing the positive and negative compensations across T_g and the determination of the DOD number for the $T_p < T_g$ compensation.

EBSCOhost - printed on 2/13/2023 12:32 AM via . All use subject to https://www.ebsco.com/terms-of-use

II.3.4 Structure of block copolymers and blends: how to quantify the level of interpenetration and segregation by thermal-windowing

The microstructure of alloys and blends and of statistical or block copolymers is the key to their macroscopic behavior. The amount of alloying and/or segregation and the degree of interpenetration of the phases are crucial questions to answer. Yet, in several instances, the traditional techniques of microstructure analysis such as DSC, TMA, and DMA have reached their limit of resolution, sometimes to the point that it is even impossible to answer the fundamental question whether there is segregation of the phases or not (Part II, Chapter 1). Our objective in this section is to characterize and compare the microstructure of blends and block copolymers by TWD spectroscopy. We will determine the "degree of disorder" (DOD) of the phases present and discuss the extent of interpenetration from the value of the DOD and other parameters defined in Part I, Chapter 2.

II.3.4.1 Case study: characterization of latex copolymers by TWD

The original work is published in P. Cebeillac's thesis [29]. We consider here three types of amorphous copolymers of styrene (S) and acrylate n-butyl (A). The conditions of polymerization are responsible for the change in the microstructure of these three latexes. The statistical copolymer (S.C.) is prepared by a method of emulsion copolymerization where both monomers are fed randomly in a semi-continuous manner. Block copolymers are prepared by step emulsion copolymerization of A first and then S to form A.S.S. block copolymers or S first and then A to synthesize the S.A.S. block copolymers. Our objective is to characterize and compare the microstructure of these three latexes by several thermal analysis techniques. Some of the results obtained by thermal analysis (DSC, TSD, and DMA) have already been introduced in Part II, Chapter 1 (Figures 1.11 to 1.13 and 1.19). Also consult the original work in reference [29] and references [132, 203, 217].

II.3.4.1.1 DSC

Figure 1.11 of Part II, Chapter 1 displays the three traces of heat capacity C_p versus temperature (heating rate 20 °C/min) recorded on a Dupont 990, for the S.C., A.S.S., and S.A.S. samples. The thermogram for the S.C. is characteristic of a quasi-homogeneous structure, with only one single T_g drop observed at 20 °C, a temperature located between the T_gs of the polyacrylate and polystyrene homopolymeric phases. This behavior is indicative of the presence of a single homogeneous phase for this copolymer. The drop of the baseline for the A.S.S. block copolymer spreads over 70 °C, and a kink is

EBSCOhost - printed on 2/13/2023 12:32 AM via . All use subject to https://www.ebsco.com/terms-of-use

visible around 15 °C, which we might take as an indication of the presence of a heterogeneous microstructure, but it is difficult to assess where the respective T_g of the two phases is located, perhaps –21 °C and +15 °C. The case of the alternate block copolymer S.A.S. is even more troublesome to analyze. Again, the drop at T_g is very broad, over 85 °C, but there is apparently no indication of the presence of two T_gs. In such a case, we can only guess that there are two segregated phases, but we have no indication of the microstructural differences between the S.A.S. and A.S.S. samples.

II.3.4.1.2 DMA

Figure 1.19 of Part II, Chapter 1 is a representation of the storage modulus E' and loss modulus E" for the three latexes (S.C., A.S.S., and S.A.S.) as a function of temperature. The figure does not reveal much at all. The case of the statistical random copolymer (S.C.) is the only conclusive one: the semi-continuous introduction of monomers gives a relatively homogeneous phase with a single T_g. The other graphs of Figure 1.19 of Part II, Chapter 1 do not indicate the influence of polymerization conditions on the microstructure of those block copolymers. As for DSC, only very vague statements on the presence of at least two phases can be made.

II.3.4.1.3 TSD

The TSD spectra in Figure 1.12 of Part II, Chapter 1 are recorded after polarization (E_p = 3 MV/m) for 2 minutes at the temperatures indicated by the arrows. The variation of the dipolar conductivity in the temperature range from –150 °C to –100 °C shows a single TSD peak for the S.C. and two resolved peaks for both A.S.S. and S.A.S. The low-temperature peak observed for both A.S.S. and S.A.S. is associated with the glass transition of butyl acrylate sequences, and the high-temperature is associated peak with the glass transition of styrene sequences.

II.3.4.1.4 TWD

The TSD analysis reveals the global microstructure of the materials under investigation: S.C. is a relatively homogeneous statistical random copolymer with T_g located between the T_gs of the homopolymers and both S.A.S. and A.S.S. are block copolymers with a segregation of two phases. One phase is rich in the styrene component, and the other phase is rich in acrylate sequences. The amount of styrene in acrylate (or acrylate in styrene) is, however, unknown. TWD can be used here to answer this question.

For resolving the global TSD spectra of Figure 1.12 of Part II, Chapter 1, TWD is applied in the temperature range –45 to +75 °C, with a temperature window of 5 °C. The electrical voltage applied is the same as for the global TSD thermogram. Figure 1.13 of Part II, Chapter 1 shows, for A.S.S., the deconvolution of the global peaks into elementary Debye peaks for the two T_gs.

EBSCOhost - printed on 2/13/2023 12:32 AM via . All use subject to https://www.ebsco.com/terms-of-use

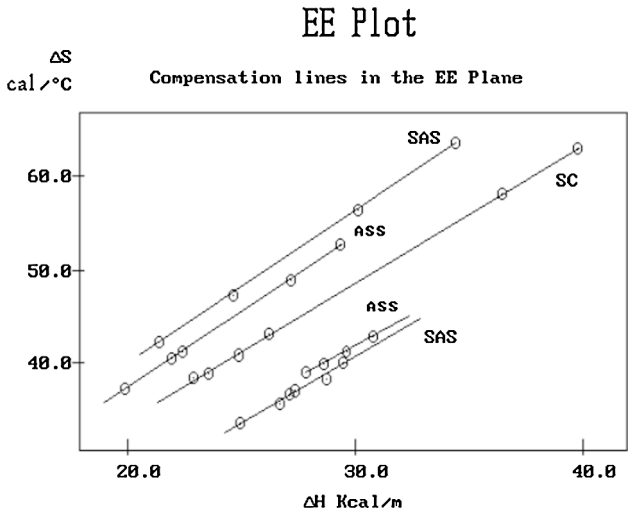


Figure 3.14: EE plot for determining the compensation lines in the block copolymers S.A.S., A.S.S., and S.C. already presented by TSD in Figure 1.12.

Figure 3.14 is a compensation search in the EE plane for all the Arrhenius lines obtained for all the copolymers studied. In the case of the S.C. (the straight line in the middle of Figure 3.14), there is just one compensation line (positive), which corresponds to only one single phase, one single T_g. In the case of the A.S.S. and S.A.S. copolymers, the existence of two positive compensation lines is observed, corresponding to two T_gs. They correspond to the low (A) and high (S) temperature peaks observed by TSD (Figure 1.12 of Part II, Chapter 1). This phenomenological behavior is characteristic of a biphasic structure. It is important to note that the microstructure of the two phases in A.S.S. and S.A.S. is different, as evidenced by the respective location of the compensation lines associated with the two phases A and S. Each compensation line can be compared to the compensation found for the S.C., which corresponds to a good mix between the two phases. The "distance" between the compensation lines is a direct measurement of the interpenetration of the phases for each segregated phase. One sees in Figure 3.14 that the activation entropies are closer to the statistical (good mix) values for A.S.S. than for S.A.S.: the segregation is lower in A.S.S. than in S.A.S.. These results are indicative of a core shell structure and suggest a morphology in which latex particles have a butyl acrylate-rich core and a styrene-rich shell for both A.S.S. and S.A.S.. It also suggests that the phase segregation is more pronounced for S.A.S. These conclusions concur with other results published separately [203, 220].

In conclusion, it is clear, in this example, that the power of resolution and of characterization of the TSD/TWD technique far exceeds that of the other methods. The copolymer polymerized with a semi-continuous feed of monomers is statistical. Its phenomenological behavior is typical of a monophasic polymer: its structure is char-

EBSCOhost - printed on 2/13/2023 12:32 AM via . All use subject to https://www.ebsco.com/terms-of-use

acterized by a single drop off of the DSC or DMA storage modulus baseline, and there is only one single compensation line in a compensation search diagram: one T_g, one single homogeneous phase.

The copolymers polymerized by the monomer step feed method are block copolymers. In DSC and DMA, a broad transition region is observed. Nothing much can be learned from these two analytical methods, which have both reached their limit of resolution. By contrast, we found in TSD, two well-resolved relaxations respectively associated with the glass transition of styrenic and acrylic sequences. On the compensation diagram, two compensation lines confirm the existence of a biphasic structure. The core shell structure depends on the chemical composition of the core: the styrene-rich core is more segregated than the acrylate-rich one. These data may be explained by the higher reactivity of styrene and its hydrophobic character.

II.3.4.2 Case study: characterization of the structure of polyether block amide resins by TWD

In this example, several polyether block amide (PEBA) resins are characterized by TSD and TWD. The original work is published in H. S. Faruque's thesis [77] and in references [78–82].

PEBA resins are used as based polymers for structural applications, paints, and hot-melt adhesives. The overall chemical structure of PEBAX copolymers is explained in Figure 3.15. This kind of block copolymers consists of sequences of soft oligo-ether and hard oligo-amide segments. The polytetramethylglycol (PTMG), which represents the soft segment, has an average degree of polymerization $n = 28$, which gives an average soft-segment molecular weight of 2035. This polymer has already been studied in Part I, Chapter 2 under the label PTMG 2000. The polyamide 12 (PA) hard segment was prepared for values of p in Figure 3.15 varying from 7 to 21, giving an average hard-

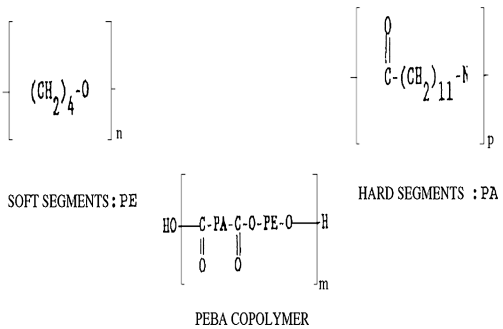


Figure 3.15: Description of the chemical formulation for the PEBA copolymers formed of soft segments (PE) and hard segments (PA).

EBSCOhost - printed on 2/13/2023 12:32 AM via . All use subject to https://www.ebsco.com/terms-of-use

segment molecular weight range of 600 to 4000. The total molecular weight of the block copolymers (which determines the value of m in Figure 3.15) was 20,000. The PEBAX will be labeled according to the molecular weight of the PA segment. Table 3.2 (top) provides a summary of the structural parameters for the samples reported here. The nature of the PA sequence has an influence on melting points, specific gravity, and chemical resistance [82]. The study consists of comparing the effect of increasing the molecular weight of the amide blocks on the intermiscibility of the phases.

Table 3.2: Characteristics of the PEBAX obtained by DSC and TSD.

Samples	Hard segment Weight %
4200–2000	68
2100–2000	51
900–2000	31
600–2000	23

Samples	$T_{g_{PE}}$ (°C)	$T_{m_{PE}}$ (°C)	$T_{m_{PA}}$ (°C)		X_{PE} (%)		X_{PA} (%)
			PEBA	Oligomers		PEBA	Oligomers
4800–2000	−83	24	172	(173)	16.8	21.5	(39)
2100–2000	−83	30	162	(163)	30.2	21.2	(37)
900–2000	−82	9	141	(141)	30	22.4	(36)
600–2000	−80	13	127	(128)	28.9	16.2	(34)
PTMG 2000	−83	25	/	/	57	/	/

It is reported [82] that the unique properties of the copolymers are directly related to its two-phase microstructure, with the hard domain acting as a reinforcing filler and as a thermally reversible crosslink. The soft segment is responsible for the rigidity of the copolymer. At room temperature, the PTMG segment is above its glass transition temperature and is semi-crystalline; the hard segment PA12 is below its glass transition, and is also semi-crystalline. Table 3.2 (bottom) provides some of the characteristics of the PEBAX copolymers obtained by TSD and DSC. The DSC experiments provided the values for the melting temperatures of the crystalline phases and for the calculation of the crystallinity percentage from the enthalpy of fusion. The table shows a large decrease of the PE segment crystallinity in the PEBAX samples compared to the corresponding pure PTMG 2000 (crystallinity = 57 %). It is assumed that the joints between the hard and soft segments put a constraint on the PE segment mobility and reduce the crystallization ability of the PE segments.

The TSD analysis for different PEBAX (Figure 3.16 for PEBA 900 and PEBA 2100) reveals a complex interaction between the segments of PE and PA as the molecular weight of the hard segments increases.

EBSCOhost - printed on 2/13/2023 12:32 AM via . All use subject to https://www.ebsco.com/terms-of-use

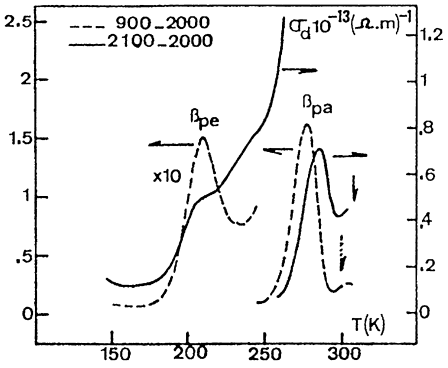


Figure 3.16: TSD curves for PEBA 900 and PEBA 2100.

In Figure 3.16, the glass transition temperature β_{PE} is clearly visible as a unique relaxation process for PEBA 900 (the intensity of the peak has been magnified 10 times to be able to compare it with the corresponding peak for PEBA 2100). The glass transition for the PA phase β_{PA} is also well defined at around 275 K. The case of PEBA 2100 shows an increase of the intensity of the peak at T_g for the PE phase along with a shoulder occurring at 240 K, which is probably associated with the T_α transition of the PTMG segments. The glass transition temperature for the PA phase is shifted to higher temperatures due to the increase in length of the PA block. It is important to note that TSD allows the detection of the T_g phases (and even of the T_α phase) in a complex biphasic structure where spherulites of different types and amorphous phases of different nature and type are mixed.

The complexity of the relaxation process leads to the use of TWD to separate out the different relaxation modes in the structure. It also helps to understand the influence of the surrounding on the coupling characteristics due to the interpenetration and blending of the phases at the segregated sites.

As mentioned previously, the DOD reflects the influence of the surrounding of the bonds which can be influenced by several factors: the internal stress, the orientation, the degree of crosslinking or crystallization, the molecular weight, and the degree of compatibility between the two phases of a block copolymer.

Figures 3.17 and 3.18 give the result of thermal-windowing for the PTMG 2000 homopolymer. A main compensation is observed at low temperature corresponding to the positive compensation for the amorphous component located between spherulites. The DOD number for this amorphous phase is 50.65. Figure 3.18, which shows the compensation search to determine the coordinates of the compensation point, displays the complexity above T_g of the relaxation behavior. This graph has already been discussed in Part I, Chapter 2.

EBSCOhost - printed on 2/13/2023 12:32 AM via . All use subject to https://www.ebsco.com/terms-of-use

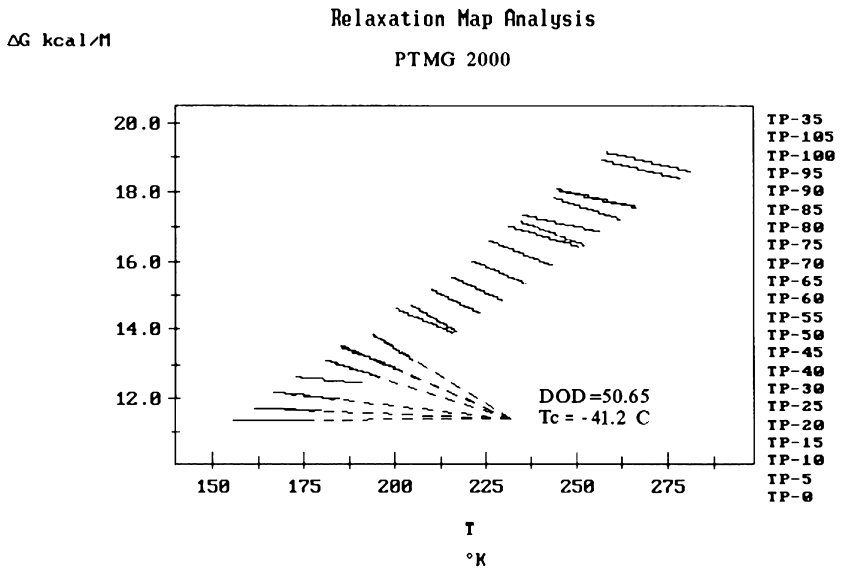


Figure 3.17: Relaxation map in the Δ*G* plane for PTMG 2000. The compensation shown corresponds to interactive coupling in the amorphous phase located *between* the sherulites.

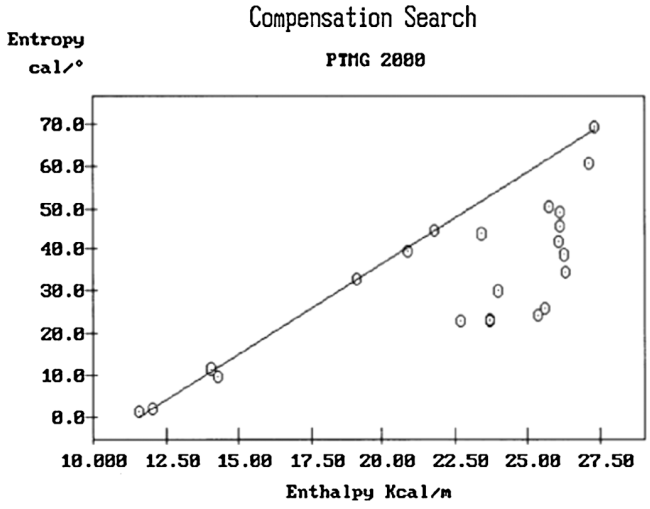


Figure 3.18: Compensation search for the determination of the compensation coordinates of the compensation in Figure 3.17.

For the PA12 phase, the EE plot for the homooligomer $M_n = 2000$ is shown in Figure 3.19. For each of the other oligomers of the hard PA phase, thermal-windowing is applied to determine the compensation line in order to find the DOD number for that amorphous phase. The results are tabulated at the top of Table 3.3.

EBSCOhost - printed on 2/13/2023 12:32 AM via . All use subject to https://www.ebsco.com/terms-of-use

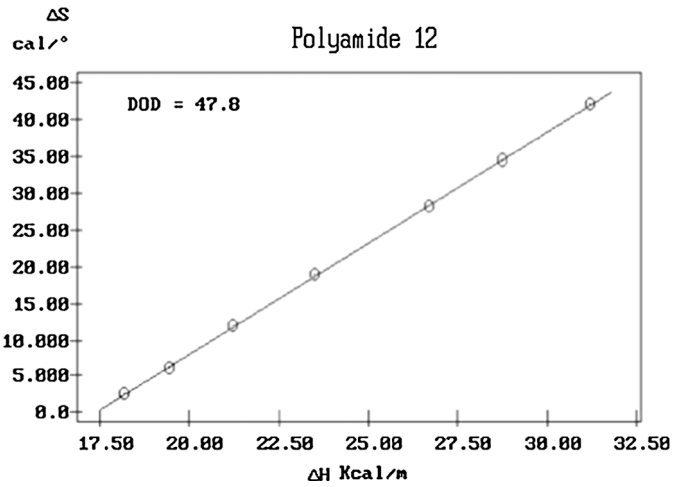


Figure 3.19: EE plot for the PA12 rigid block to determine the DOD number of the amorphous phase in this component of the block copolymer.

Table 3.3: Results of the compensation characteristics for PA homopolymers and for PA block copolymers when the molecular weight of the PA blocks increases.

For the PA Homopolymers

$M_{n_{PA}}$	DOD_{PA}	$\Delta G_{c_{PA}}$	T_c^+ (°C)
600	45.25	16.3	24.66
850	47.61	16.91	49.6
2,000	47.8	17.35	59.24
4,000	46.54	17.71	58.19
12,000	51.4	17.39	84.71

For the PA Block Copolymers

$M_{n_{PA}}$	DOD_{PE}	DOD_{PA}
600	51.07	58.3
850	53.27	58.86
2,000	56.09	77.18
4,000	52.74	60.74

The TWD results for the various PEBAX expressed by their relaxation maps and thermokinetic constants are presented in Figures 3.20 to 3.22 and in Table 3.3 (bottom part).

Figure 3.20 relates to PEBA 2535 and displays the result of the compensation search, revealing four compensations for two phases. One phase at lower temperatures is associated with the PE segments, and the other phase at higher temperatures

EBSCOhost - printed on 2/13/2023 12:32 AM via . All use subject to https://www.ebsco.com/terms-of-use

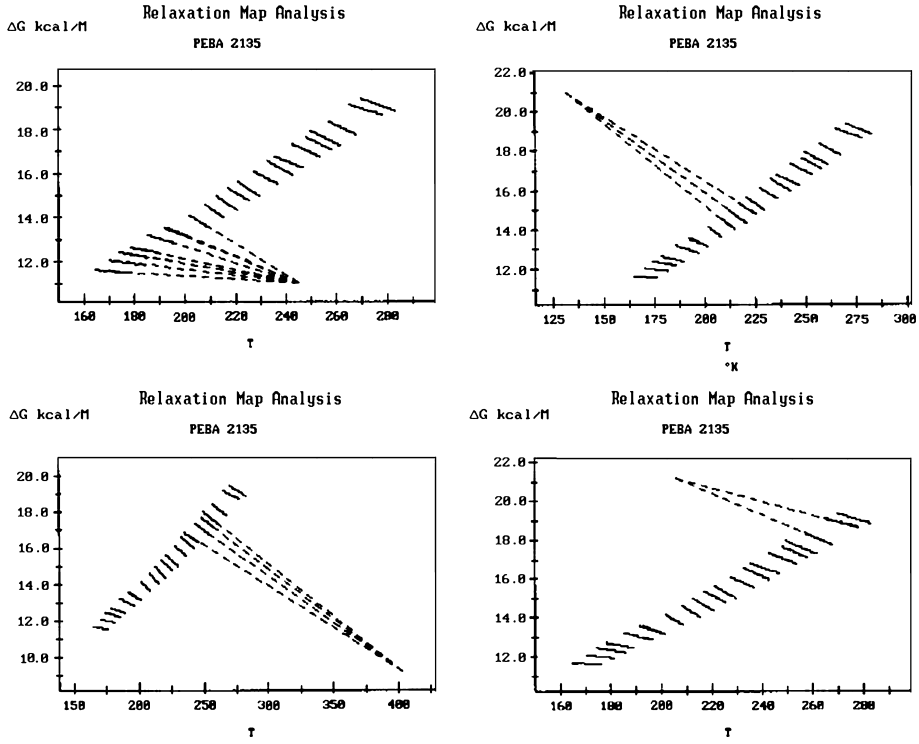


Figure 3.20: Determination for PEBA 2135 of the positive and negative compensations for the two types of amorphous phases present, a total of four compensations. See text.

is associated with the PA segments. The positive and negative compensations observed across the glass transition temperature for each of the phase are well defined for this apparently complex structure of PEBAX. One can apply all the mathematical tools developed in Part I, Chapter 2 to determine T_g, ΔS_g, ΔH_g, T_c, ΔG_c, etc. The DOD number is useful in this case since it summarizes most of the results in a clear fashion.

Table 3.3 shows the variation of the DOD number for each phase when the molecular weight of the PA blocks increases. The DOD numbers can also be compared with the DOD for the homooligomers with identical molecular weight (at the top of the table).

The compensation search for the PEBAX copolymers is shown in Figure 3.21, again revealing the relatively classical relaxation behavior observed for this apparently complex copolymer. In some instances, the four compensations (one positive and one negative for each phase) are observed (Figure 3.21c and d), but in some other cases, only three compensations can be determined with accuracy (Figure 3.21b). These results with multi-compensations showing the existence and the characteristics of two amorphous phases are commented on in Part II, Chapter 4 and Part I, Chapter 3.

EBSCOhost - printed on 2/13/2023 12:32 AM via . All use subject to https://www.ebsco.com/terms-of-use

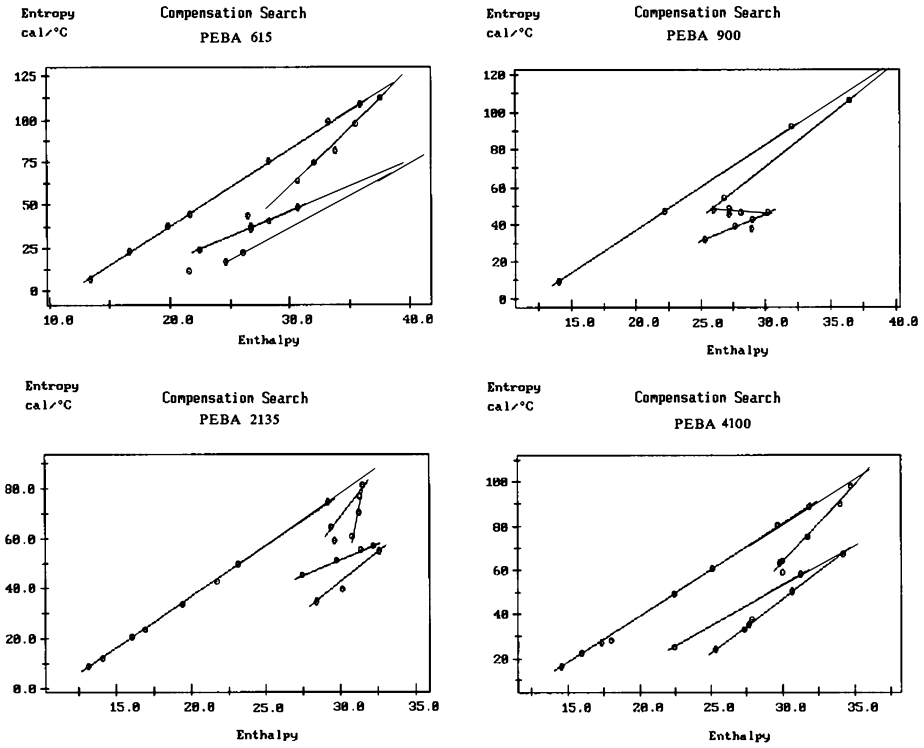


Figure 3.21: Compensation search in the EE plane for the PEBAX copolymers showing the characteristics of the amorphous phases associated with the biphasic system.

The most spectacular result in Table 3.3 relates to the large increase in DOD number for the PA segments in PEBAX compared to the respective values found for the homooligomers. The trend is identical for the PE phase, but to a much lower degree. The DOD increases with the molecular weight for both the copolymers and the homopolymers. A singularity seems to arise for $M_n = 4000$ for both the homopolymer series and the PEBA series. The anomaly is perceived in the values of the DOD number, ΔG_c, T_c, and the DOD numbers for both phases in the case of the block copolymer. The increase of the DOD number with molecular weight is reminiscent of the increase of free volume with molecular weight attributed to chain ends. Not shown in Table 3.3 is the variation of ΔG_c and T_c for the two phases in PEBA samples. T_c in PE increases steadily by approximately 10 °C for every increase in molecular weight, except for the 4000 sample, for which T_c slightly decreases from the value of PEBA 2000. The value of ΔG_c in the PE phase decreases from 11.59 (PEBA 600) to 10.73 (PEBA 4000). In the PA phase, T_c increases rapidly from 66.95 °C (PEBA 600), 72.98 °C (PEBA 900), 129.47 °C (PEBA 2000), and decreases for PEBA 4000. The values of T_c and ΔG_c for the homooligomers of increasing molecular weight for PA are shown at the top of Table 3.3. The value of ΔG_c increases steadily with molecular weight and T_c also in-

EBSCOhost - printed on 2/13/2023 12:32 AM via . All use subject to https://www.ebsco.com/terms-of-use

creases with molecular weight (with the exception of PEBA 4000). The value of ΔG_c is found much higher for the homooligomers than for the PEBA block copolymers in the PA phase. The ΔG_c values found for the PA phase in the PEBAX block copolymers are 14.18 kcal/m (PEBA 600), 14.24 kcal/m (PEBA 900), 9.19 kcal/m (PEBA 2000), and 12.62 kcal/m (PEBA 4000), which could be compared to the values between 16.30 and 17.71 found for the homopolymers.

In the PE phase, the comparison is less obvious. The value for the PE homopolymer ($\Delta G_c = 11.44$) falls in the middle of the range found for the block copolymers. Another observation concerning the spread between the positive and negative compensation values found for ($\Delta G_c^+ - \Delta G_c^-$) is that it is constant to 10 kcal/m independently of a molecular weight of the PEBA in the PA phase. The amount of depreciation of ΔG_c might be directly related to the amount of interpenetration of the PE elements in the PA phase. The DOD number is also supposed to be related to the same factor. In this case, comparing respectively the value obtained for the homopolymer and PEBA for the same molecular weight, one could quantitatively describe the amount of blending of PE in PA and, by the same token, the amount of interpenetration of PA segments in the PE-rich segregated phase. The fine analysis of the results in Table 3.3 shows that the DOD numbers contain information about the environment of chain segments involved in relaxation. The modification of the fine structure of $T_{g,\mathrm{PE}}$ and $T_{g,\mathrm{PA}}$ relaxation modes, as a function of the molecular weight of the PA segments, can be interpreted in terms of the degree of phase separation. The large increase in the DOD for the amorphous regions, for both the PE and PA sequences, is possibly due to a decrease of the percentage of crystallinity, as shown in Table 3.2 (bottom), according to the DSC data. It can also be due to the ability to alloy blocks from the two groups. In fact, the intensity of the TSD peak itself increases as the total fraction of amorphous matter is made more available during the polarization stage. The area underneath the melting peaks observed in DSC also decreases correspondingly, and the peak appears broader (Figure 1.10 of Part II, Chapter 1).

The mobility inside the structure can also be ascertained by plotting the variation of the entropy of activation against T_p. Such a plot is shown in Figure 3.22a for PEBA 4100. The two peaks observed in this figure are clear evidence of the biphasic structure of the block copolymer. T_g can be calculated either by the crossing of the positive and negative compensations in the compensation search diagram and application of equation (2.13b) in Part I, Chapter 2 or by the intercept of the positive and negative ΔS_p vs. T_p hyperbolas crossing at T_g.

The mobility in the amorphous phase might be a different parameter to analyze from the degree of blending between the two phases. For instance, there might be an increase of the DOD number due to the blending in one phase but a decrease of the overall mobility in the amorphous component of that new phase. Figure 3.22b compares the entropy of activation for PEBA 695 and PEBA 2135. The plot is interesting because it demonstrates the respective mobility in each phase for the two PEBAX. The increase of T_g for the PE phase and the decrease of T_g for the PA phase is also apparent

EBSCOhost - printed on 2/13/2023 12:32 AM via . All use subject to https://www.ebsco.com/terms-of-use

in this figure. The respective increase or decrease of T_g is traditionally related to the amount of interpenetration of one component into the phase of the other component. This information is complementary to the variation of the DOD number or the variation of ΔG_c. In Figure 3.22b, the mobility in the PE phase is lower for PEBA 2135 than PEBA 695, but it is higher in the PA phase due to the increase of the molecular weight.

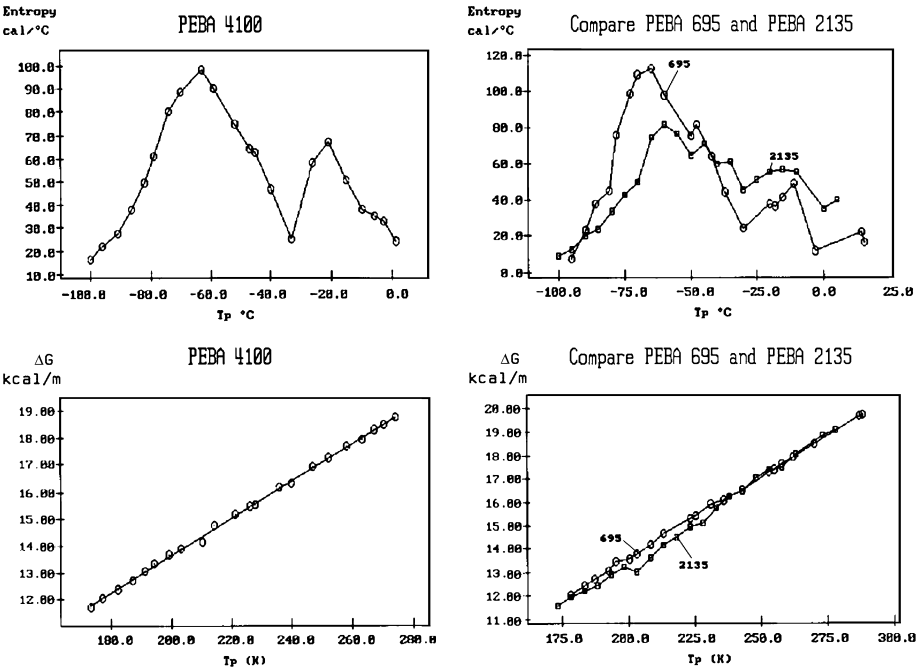


Figure 3.22: Entropy of activation vs. T_p (top) for PEBA 4100, PEBA 695, and PEBA 2135. ΔG_p vs. T_p (bottom) for the same polymers.

The free energy of activation at T_p, ΔG_p, varies linearly with T_p across the two T_gs of the two phases, as displayed in Figure 3.22c for PEBA 4100. However, comparing PEBA 695 and PEBA 2135 in Figure 3.22d reveals that the two free energies are very different, except for the higher temperature end beyond $T_p = 237$ K. The ΔG_p values are always found higher for the lower molecular weight. In Figure 3.22d, the decrease of the free energy for the PE phase ($T_p < 237$ K) corresponds to an increase of the miscibility of the phases which is associated with a decrease of the mobility due to the influence of the hard segments on the sub-segments.

In Figure 3.22b, the decrease of the activation entropy in the $T_{g,\mathrm{PE}}$ relaxation process, coupled with an increase of the molecular weight of the PA segment, indicates a loss of the mobility in the amorphous phase of the corresponding copolymer. We conclude that the mobility of the soft segment is restricted by the presence of PA seg-

EBSCOhost - printed on 2/13/2023 12:32 AM via . All use subject to https://www.ebsco.com/terms-of-use

ments in the PTMG amorphous phase. This conclusion is consistent with the shift of the $T_{g,\mathrm{PE}}$ peak towards higher temperatures observed in Figure 3.22b for the shift of the peak maximum of the entropy. The progressive influence of the hard segment on the mobility of the amorphous of the PE segments is also noted by the gradual broadening of the values found for ΔH_p and ΔS_p on both sides of T_g. This can also be observed on the compensation line by a broadening of the values between the maximum and minimum for both the ΔH and ΔS axes. The large increase in the DOD number for the PA phase, in particular for the sample PEBA 2000 (in Table 3.3), implies that the PA phase contains a high concentration of polyether units. This also results in a large decrease of the crystallinity in this phase (Table 3.2, bottom). It is assumed that the miscibility decreases for PEBA 4000 and that the short PA blocks contain a crystalline PA phase, an amorphous PTMG-rich phase, and an amorphous PA-rich phase. The compositions of these two amorphous phases depend on the molecular weight of the PA block present in the block copolymer.

In conclusion, the characterization of PEBA copolymers by relaxation map spectroscopy shows that the deconvolution by thermal-window polarization of the global TSD peaks, observed at the glass transition for each phase of a block copolymer, allows the quantitative determination of the state of the glassy structures present in the morphology. The DOD influenced by the miscibility of the phases can be used to describe the influence of molecular weight of the amide sections on the extent of segregation, their miscibility at the boundary, and the mobility in the structure. It is determined, for instance, that the low-molecular-weight PA sequences correspond to the most appropriate PEBA resins for adhesive applications, because of the increased mobility due to a disordered structured. As the miscibility from the PA segments in the PE amorphous phase increases, decreasing the overall mobility, the PEBA resins would become more appropriate for thermoplastic elastomeric applications. These resins could then be used as latex.

II.3.4.3 Characterization of vulcanized rubber blends and crosslinked natural rubbers

The majority of rubber is used in the form of blends, and the optimization of blends to obtain the best all-around performance is a vital part of the successful development of these materials. Rubber blends differ from thermoplastic blends because they require vulcanization in order to be serviceable. The most common form of vulcanization – accelerated sulfur vulcanization – involves complex chemistry, a considerable number of species, and competing reactions. It is reasonable to expect that in some, if not most, blends, the presence of one rubber will affect the vulcanization of the other. Until recently, there was no accurate method of estimating the extent of crosslinking in the individual rubber phases of a vulcanized blend [225]. A technique based on NMR spectroscopy of swollen vulcanizates was recently developed at the Malaysian

EBSCOhost - printed on 2/13/2023 12:32 AM via . All use subject to https://www.ebsco.com/terms-of-use

Rubber Producers' Research Association, and results obtained using the technique have been published [198, 224]. The technique is based on the correlation between the peak broadening in the continuous wave ^{1}H NMR spectra of swollen vulcanizates and the degree of crosslinking. The papers [198, 224] apply the technique to the investigation of the degree of crosslinking in the individual phases of a vulcanizate of a blend of two rubbers, natural rubber (NR) and acrylonitrile–butadiene rubber (NBR). The technique requires up to 2 hours to accumulate a spectrum having suitable signal-to-noise ratio for highly crosslinked samples [225]. Typically, 2 days are allowed to swell the sample to equilibrium prior to obtaining the spectrum. The results obtained show a marked preferential distribution of crosslinks in favor of one of the component rubbers. The ability to measure the degree of crosslinking in the individual phases of a vulcanized blend enables identification of alternative vulcanization systems (alternative accelerators for instance) which will reduce or eliminate the uneven distribution of crosslinks. This characterization technique can be used to investigate whether a slight change in the distribution of crosslinks provides an overall improvement in properties.

TWD offers an alternative approach to the estimation of crosslinks in the vulcanized blend phases.

In the case study presented here, we first study a vulcanized blend of NR and acrylonitrile–butadiene rubber ("sample C"), for which the crosslink densities of the two rubbers in the blend have been estimated by the swollen-state NMR spectroscopy technique to be 22 and 83 mol/m^3, respectively. In a second part of this study, two NR vulcanizates, "sample A" and "sample B," are analyzed. The crosslink densities, as determined from established equilibrium stress–strain measurements, are 18 and 49 mol/m^3, respectively.

II.3.4.3.1 Case study: characterization of vulcanized blend of NR and NBR

Thermal-windowing was applied on 1-mm-thick cut-outs of samples provided by the Tun Abdul Razak Laboratory. The voltage field was 200 V/mm; the polarization and depolarization time was 2 min; the freeze temperature was –100 °C; the window width was 5 °C; and the temperature of polarization scanned the range across the T_gs of the material, i. e., the peak observed in the TSD experiment (Figure 3.23). T_p was selected between –85 °C to –30 °C. The TSD run displays two maxima at –59.5 °C and –46.0 °C, as already discussed in Part II, Chapter 2.

The relaxation map in the Arrhenius plane for this material is shown in Figure 3.24, along with the experimental conditions at the top of the plot.

Table 3.4 provides the thermal kinetic parameters for each polarization temperature T_p. The enthalpy of activation, entropy of activation, and ΔG_p, the activation energy at T_p during the depolarization stage, are calculated by regression analysis.

EBSCOhost - printed on 2/13/2023 12:32 AM via . All use subject to https://www.ebsco.com/terms-of-use

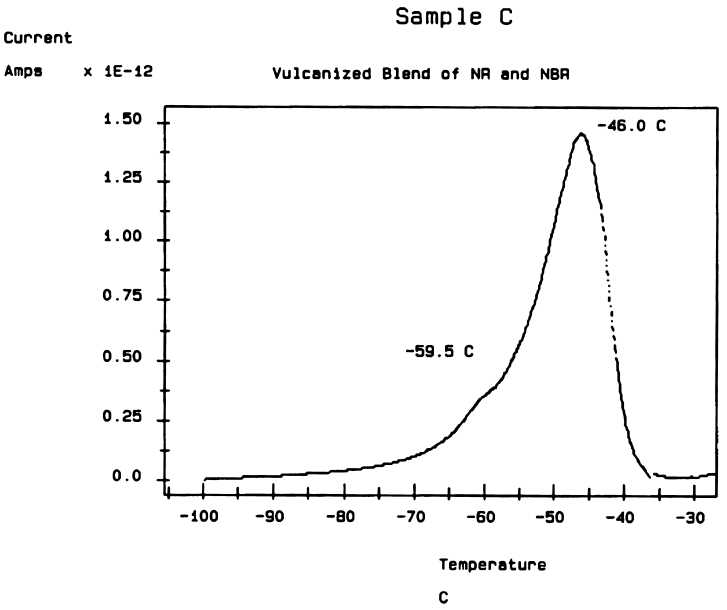


Figure 3.23: TSD trace for a vulcanized blend of NR and NBR. This graph is a duplicate of Figure 3.49 reproduced here for convenience.

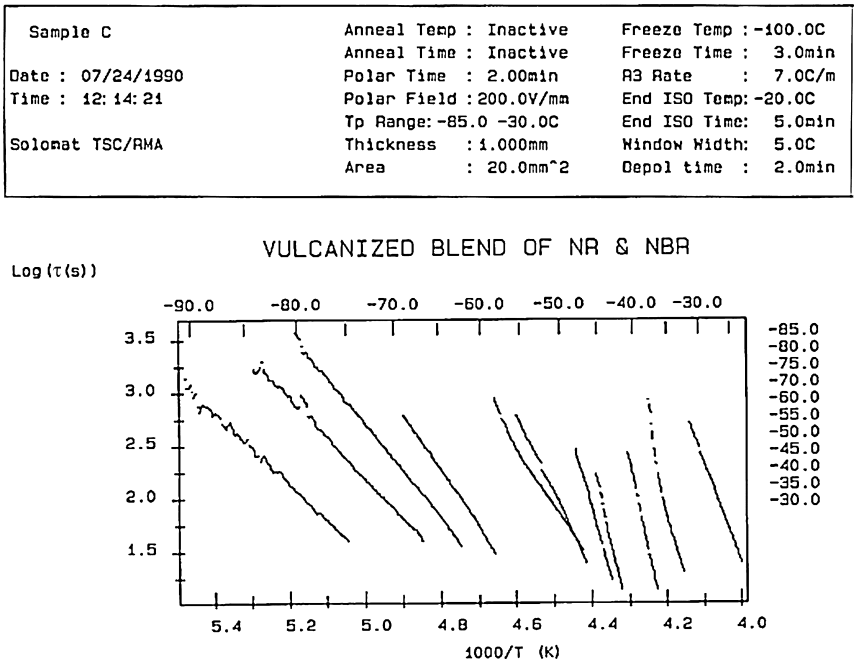


Figure 3.24: Relaxation map in the Arrhenius plane to deconvolute the two peaks shown in the TSD trace reproduced in Figure 3.23. The TWD conditions are shown in the header.

EBSCOhost - printed on 2/13/2023 12:32 AM via . All use subject to https://www.ebsco.com/terms-of-use

Table 3.4: Thermokinetic parameters for the relaxation map in the ΔG plane (not shown) derived from the relaxation map in the Arrhenius plane by Eyring transform (equation (2.5) of Part I).

Vulcanized blend of NR and NBR

T_p (°C)	T_m (°C)	ΔH_p (kcal/mol)	ΔS_p (cal/°C/mol)	ΔG_p (kcal/mol)
−85.0	−74.4	15.1608	11.4069	13.0144
−80.0	−66.1	17.1958	18.1883	13.6826
−75.0	−61.8	20.0651	30.1884	14.0829
−70.0	−57.9	23.7157	45.6337	14.4448
−60.0	−46.6	26.0083	50.2397	15.2992
−55.0	−46.1	34.1087	86.1197	15.3208
−50.0	−42.7	59.3086	194.2446	15.9610
−45.0	−41.3	74.0909	257.0255	15.4480
−40.0	−36.2	77.1799	263.0340	15.8509
−35.0	−31.8	81.5420	275.5779	15.9104
−30.0	−22.6	42.9236	107.1316	16.8735

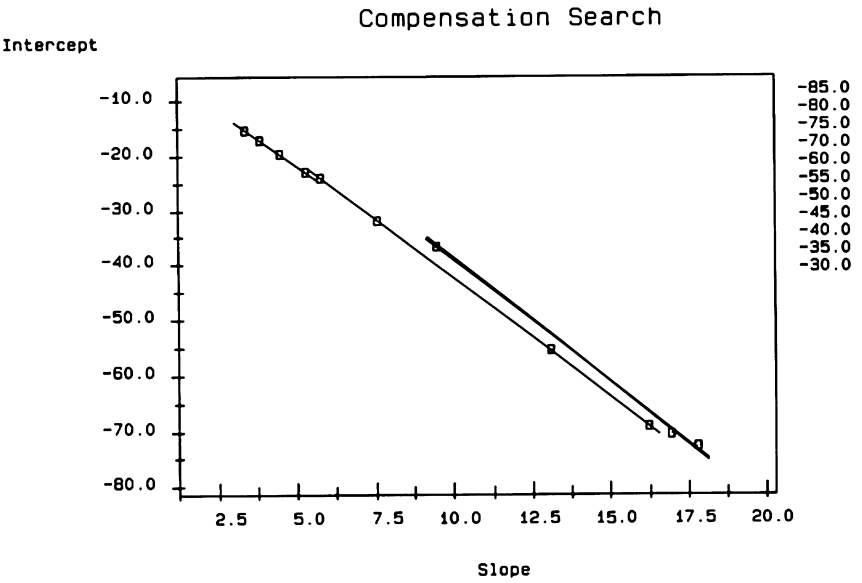


Figure 3.25: Compensation search in the Arrhenius plane to determine the compensations in Figure 3.24. Three compensation lines are defined. Table 3.5 provides their characteristics and the DOD number of the glassy phase.

The compensation search in the Arrhenius plane (intercept vs. slope) is displayed in Figure 3.25. The first four points form a compensation line. The second four polarization temperatures provide another compensation line, and the last three points gather into a negative compensation.

EBSCOhost - printed on 2/13/2023 12:32 AM via . All use subject to https://www.ebsco.com/terms-of-use

Table 3.5: Characteristics of the compensation coordinates for the three compensation lines of Figure 3.25.

Line	Compensation T_c (°C)	$\log(\tau_c)$ (Second)	DOD Number
1	−22.45	−1.83	50.21
2	−40.35	0.64	39.03
3	−51.75	6.65	11.54

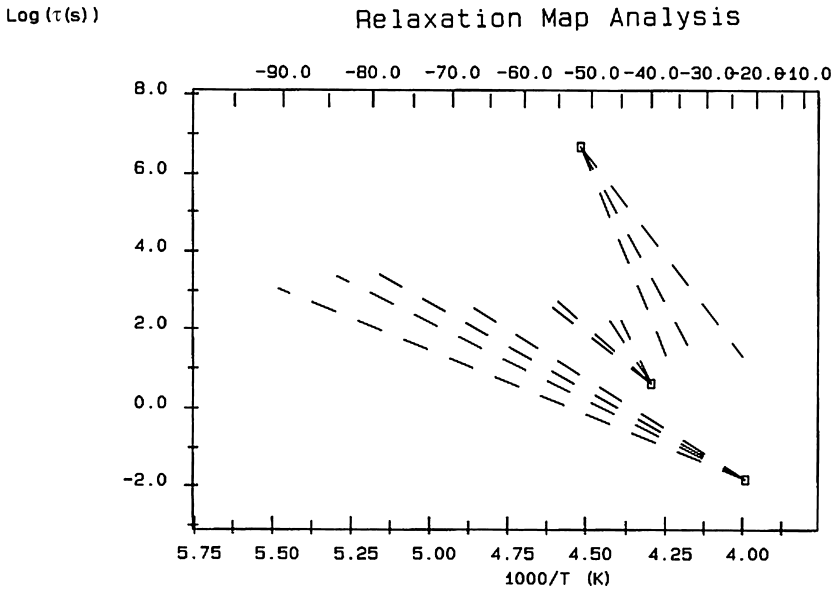


Figure 3.26: Representation of the compensations in the Arrhenius plane after the compensation search result of Figure 3.25. One negative and two positive compensations are observed. See text.

Table 3.5 lists the coordinates of the compensation points in the Arrhenius plane with the DOD numbers.

Figure 3.26 shows a summary of the compensation search analysis displaying the three compensations. The two rubber phases are clearly visible and correspond to the two positive compensations in this plot. It is assumed that the negative compensation observed is associated with the NBR phase. The DOD number found for the NR phase is 50.21, and the DOD found for the NBR phase is 39.03. These values should be compared to the crosslink density obtained by the NMR technique, i. e., 22 and 83 mol/m^3, respectively. The decrease of the DOD value, with an increase of the crosslink density, is expected. The thermal-windowing approach to the determination of the crosslink densities in the two rubber phases is straightforward and requires little time and attention from the technician using the spectrometer. The advantage of the TSD/TWD technique in this case is remarkable.

EBSCOhost - printed on 2/13/2023 12:32 AM via . All use subject to https://www.ebsco.com/terms-of-use

II.3.4.3.2 Case study: crosslinked natural rubber vulcanizates

The TSD traces for two NR vulcanizates, A and B, with crosslink densities of 18 and 49 mol/m^3 (as determined by equilibrium stress–strain measurements), have already been presented in Figures 2.47 and 2.48 of Part II, Chapter 2. Thermal-windowing is performed on the glass transition temperature located around –60 °C. The compensation phenomenon transcribes the coupling between the relaxation modes and allows to extract the DOD number representative of the environment of the bonds and reflective of the crosslink density for that environment. For sample A, we find

$$\begin{aligned} \Delta G_c^+ &= 12.70\,\text{kcal/m} \\ T_c &= -63.20\,°\text{C} \\ \text{DOD} &= 43.25 \end{aligned}$$

and for sample B, we find

$$\begin{aligned} \Delta G_c^+ &= 13.38\,\text{kcal/m} \\ T_c &= -56.58\,°\text{C} \\ \text{DOD} &= 38.22 \end{aligned}$$

As in the case of the vulcanized blend of NR/NBR, the DOD decreases with the crosslink density by a significant amount, allowing the characterization of the crosslink density by TWD spectroscopy.

In conclusion, the outstanding resolution and sensitivity of TWD spectroscopy provides a valuable tool to quantitatively determine the degree of crosslinking for each phase in a rubber vulcanizate. The technique can be applied to individual rubber vulcanizates to determine a scale of the value between the crosslink density and DOD number and then be used to characterize the crosslink density in a blend by comparison with the corresponding DOD number. Also note in the results obtained for samples A and B that the value of ΔG_c at the compensation point increases with the crosslink density and that the temperature of compensation T_c also increases. These variables can also be quantitatively related to the crosslink density.

II.3.4.3.3 Case study: characterization of NR/SBR blends of different concentrations

A series of elastomeric blends made of NR and styrene–butadiene copolymer rubber (SBR) were blended in different proportions and analyzed by TWD spectroscopy. The material was provided by the Bridgestone Company (Japan). The NR concentration varied between 0 % and 100 % by increments of 25 %. In the following, the samples will be labeled in the order of NR:SBR content: 0:100, 25:75, 50:50, 75:25, and 100:0. The mechanical properties of the elastomers – stiffness, hardness, and abrasion resistance – are dependent on the concentration in the blend. The stability of the blend

EBSCOhost - printed on 2/13/2023 12:32 AM via . All use subject to https://www.ebsco.com/terms-of-use

is also a function of concentration. No information was provided with respect to the mechanical properties of these samples.

The physical behavior of blends, in general, is related to its solid-state morphology. Phase separation typically gives rise to a dispersed phase (consisting of one block type) in a continuous matrix (consisting of a second block type). In many applications, the dispersed phase consists of hard domains, which are crystalline or glassy and amorphous, and the matrix is soft and rubber-like. A compatible blend of one crystalline homopolymer and a second homopolymer (amorphous or crystalline) is rarely possible (we will show one example in the case study of PEEK/PEI later on). Phase separation in block copolymers or blends is dependent on the factors governing crystallization in homopolymers. Mixing in a binary system occurs when the Gibbs free energy ΔG is negative. In general, various types of morphology are possible. When one homopolymer is present in large excess (>70 %), it will form a continuous phase containing dispersed discrete aggregates of the second homopolymer. The state of the two phases is temperature-dependent, and stability or lack of stability results. The state of miscibility or segregation is also a function of the thermal history and the processing conditions. No such information was provided for the elastomeric blends characterized by TWD spectroscopy.

It is known that the difference between different blends is related to the calculation of the entropy of mixing. This is due to the requirement of placing segments A and B at the interface between the phases and from the requirement that one block of segments (A) is excluded from the phase of the second block (B). Segments of types A and B (here NR and SBR) tend to separate because they are incompatible, but are prevented from doing so by the chemical bonds linking segments together. It has become common practice to describe the morphology for phase-separated systems as domains composed of groups of one type of bonds dispersed in a continuous matrix of segments of the second type. The size of the domains is an important factor of correlation to determine the mechanical behavior and the stability. Domain size is dependent on the conformational entropy and on the interfacial energy, which will also determine domain geometrical shape [54].

For random copolymers, or miscible blends, a single glass transition temperature characteristic of the intimate mixing of the units is observed, usually intermediate between those of the homopolymers participating in the blend. For segregated blends or immiscible block copolymers, the number of glass transition temperatures is determined by the domain type and number. For instance, if two glass transitions are observed, two types of domain are expected to coexist in the structure. The degree of local miscibility of segments of one type in the domain of the other type depends on the concentration, processing condition, presence of compatibilizer, and thermal aging. The location of the glass transition temperature and the thermodynamic parameters (enthalpy and entropy) that characterize the glassy amorphous state are both important variables which can be monitored to follow the extent of miscibility within the microdomains of the segregated blend.

EBSCOhost - printed on 2/13/2023 12:32 AM via . All use subject to https://www.ebsco.com/terms-of-use

TSD/TWD seems a powerful characterization tool to determine the microproperties within the complex structure. When the two phases of a blend are completely compatible, a homogeneous polyblend results, which behaves like a plasticized one-phase homopolymer. If the two phases are incompatible, the resulting product is usually opaque and rather friable. When the two phases are partially compatibilized at their interfaces, the resulting polyblend system may then assume a hard, impact-resistant character.

Considering the number of variables possible in preparing two-phase polymers, it is not surprising that many types of blends can be prepared. The results discussed in this section unfortunately lack any knowledge of the detail of the sample preparation and also any intimate information regarding the polymers used in the blend. Only the respective concentrations are known, in addition to the fact that the two polymers which are blended here have no crosslink and are not vulcanized. This makes our approach very difficult "a priori." However, as will be demonstrated, the power of thermal-windowing and TWD spectroscopy is still apparent in this case study. The experimental conditions for thermal-windowing were identically kept constant for all five samples studied: surface area under the voltage field, 25 mm^2; sample thickness, 1.19 mm; voltage field, 200 V/mm; polarization time and depolarization time, 2 min; freeze time, 1 min; heating rate during depolarization: 7 °C/min; window width, 2 °C; and polarization temperature range, –85 °C to –40 °C.

We give an example of the results obtained for the NR/SBR 50:50 blend in Figures 3.27 to 3.32. Figure 3.27 is the relaxation map in the Arrhenius plane. Table 3.6 provides the analysis of the Arrhenius lines in thermokinetic terms.

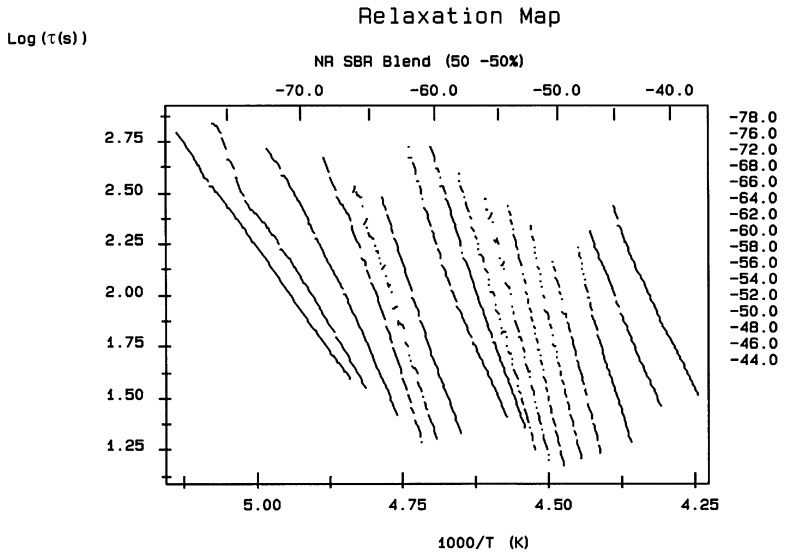


Figure 3.27: Relaxation map in the Arrhenius plane for the NR/SBR blend studied by TSD in Figures 3.51 to 3.53.

EBSCOhost - printed on 2/13/2023 12:32 AM via . All use subject to https://www.ebsco.com/terms-of-use

Table 3.6: Thermokinetic results derived from the relaxation map in Figure 3.27 for the NR/SBR 50:50 blend.

T_p (°C)	T_m (°C)	ΔH_p (kcal/mol)	ΔS_p (cal/°C/mol)	ΔG_p (kcal/mol)
−78.0	−66.4	18.0252	22.1729	13.6979
−76.0	−65.1	20.9627	35.9606	13.8727
−72.0	−62.9	26.3526	60.9191	14.0981
−68.0	−61.0	37.1210	111.1686	14.3137
−66.0	−59.9	40.0481	124.0785	14.3440
−64.0	−58.0	38.8326	116.7644	14.4101
−62.0	−54.3	34.3150	92.7656	14.7266
−60.0	−52.8	37.9239	108.1575	14.8691
−58.0	−51.9	45.3127	141.2058	14.9309
−56.0	−50.7	53.0288	175.1006	15.0040
−54.0	−49.5	60.5659	207.6915	15.0482
−52.0	−47.9	58.0457	194.5480	15.0195
−50.0	−46.3	50.4487	158.8505	14.9996
−48.0	−43.6	45.6210	135.0405	15.2152
−46.0	−40.9	31.7358	72.0586	15.3669
−44.0	−37.4	27.3895	51.2907	15.6358

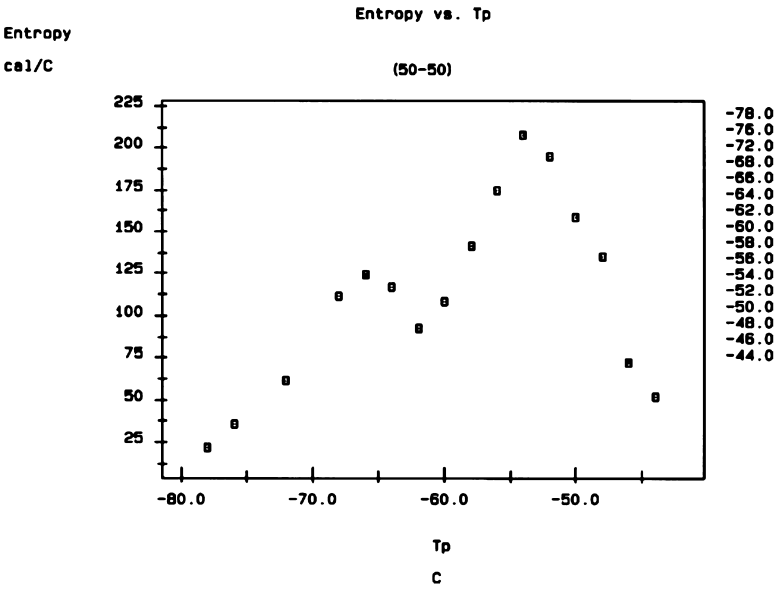


Figure 3.28: Entropy of activation vs. T_p for the NR/SBR 50:50 blend showing the biphasic system.

Figure 3.28 demonstrates the biphasic structure of the blend and its segregation into two distinct domains, with T_gs characterized at the maximum of entropy for both peaks.

EBSCOhost - printed on 2/13/2023 12:32 AM via . All use subject to https://www.ebsco.com/terms-of-use

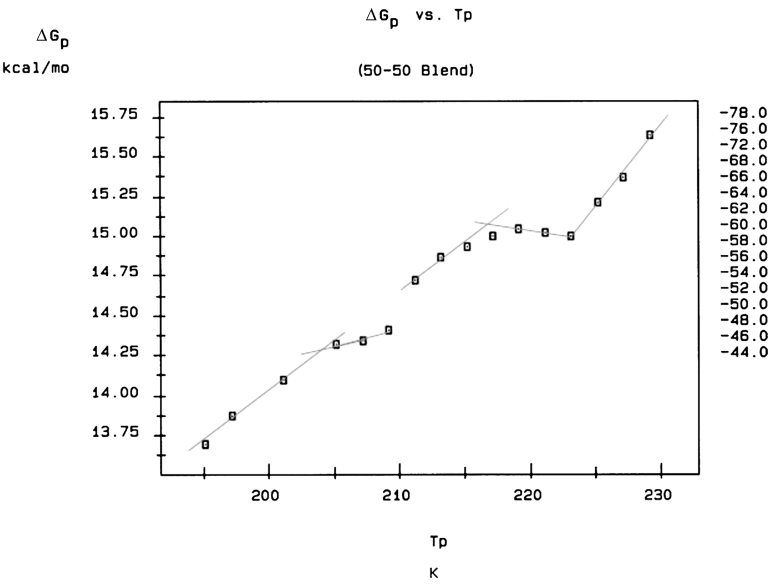


Figure 3.29: ΔG_p vs. T_p for the NR/SBR 50:50 blend.

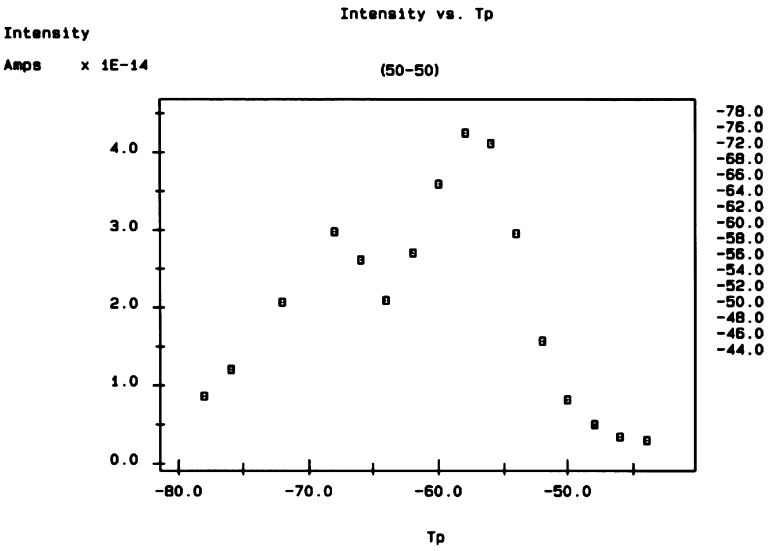


Figure 3.30: Intensity of the Debye peak at T_m plotted against T_p showing the analogy with the entropy results in Figure 3.28.

Figure 3.29, a plot of ΔG_p against T_p, shows the distinct behavior for the two microdomains and the more traditional linear relationship above 222 K.

The intensity at the maximum of the thermal-window peaks is plotted against polarization temperature in Figure 3.30, showing that if the current is used as a variable

EBSCOhost - printed on 2/13/2023 12:32 AM via . All use subject to https://www.ebsco.com/terms-of-use

to determine mobility, we do not find the correct temperature for the glass transition of the two domains. Only entropy can give us the true value of the glass transition temperatures. One sees, comparing Figure 3.30 and Figure 3.28, that a 2 °C difference for the NR phase and a 4 °C difference for the SBR phase exist if current is used as the variable. This remark leads to an important conclusion regarding the use of TWD spectroscopy for truly investigating segregation characteristics in complex blends and block copolymers. DMA, DSC, and even TSD global techniques deal with the combined relaxation from the different modes and may wrongly lead to conclusions regarding miscibility at the interface of the microdomains based on the respective shift of the T_g peaks on the temperature scale. In Part II, Chapter 2, for instance, it was observed that T_g of the NR phase was shifted to a higher temperature as the concentration of SBR increased. As we will see with the more precise thermal-windowing technique, which determines T_g from the elementary Debye peaks extracted from the current vs. temperature measurements, the variation of T_g in the NR phase is not as obvious as a global technique would lead to believe. The miscibility of the phases can be misled by the use of the wrong technique when the T_g transitions of the two blends are close. This is the case for the two elastomers NR and SBR studied here.

Figure 3.31 is a composite graph of compensation search to determine the compensation lines (positive and negative) among the relaxation modes excited at different T_ps.

The result of the compensation search is illustrated in Figure 3.32, which is also a composite graph of the compensations found for the NR/SBR 50:50 blend.

Figure 3.32a and b displays the positive compensations for the NR and SBR domains and Figure 3.32c and d shows the negative compensations for these segregated microdomains. The overall conclusion is that segregation is very neat, allowing a classical characterization by thermal-windowing with a well-defined positive and negative compensation for each phase. This is indicative of a frank separation between the two microdomains. We are not showing the relaxation maps for the other concentrations and for the pure homopolymers NR and SBR, but the behavior is essentially identical to that represented in Figures 3.27 to 3.32. Only the compensation parameters and the position of the Z-lines separating the positive and the negative compensations vary with the concentration.

Figures 3.33 to 3.43 summarize the comparison between the different blends and help derive conclusions regarding the influence of the concentration on the blend characteristics. Figure 3.33 shows the variation of T_g in each phase against the NR content present in the blend. The intercept between the positive and negative compensations in a compensation diagram allows the determination of the characteristics at the glass transition temperature for each domain. ΔS_g, ΔH_g, and T_g are determined this way. The glass transition for the pure NR is given for 100 % NR. As can be seen in Figure 3.33, blending with an increasing amount of SBR results in a *decrease* of T_g (except for the 25:75 blend, for which T_g is raised a little bit). This tendency for T_g

EBSCOhost - printed on 2/13/2023 12:32 AM via . All use subject to https://www.ebsco.com/terms-of-use

to decrease in the presence of segments of another material with a higher T_g is indicative of the mechanism which occurs at the interface: as the concentration of SBR increases, impurities which act as a plasticizer to the NR phase start to extract out from the NR domain, inducing a decrease of T_g for this phase. The effect of blending moderates the decrease of T_g by trying to raise T_g as the segments from the two types of rubber become more compatible. This might explain the small raise of T_g for the 25:75 blend. What kind of impurities can be extracted from the rubber phase? It was already observed in Part II, Chapter 2 that the higher-temperature tail of the TSD peak does not come down to zero before a plateau is maintained for some temperature range. It was assumed in that chapter that a certain amount of mineral or organic impurities was present in the NR phase which could be detected by TSD. The impurities are combined in the NR in a miscible fashion, which creates the impression of a true miscible homopolymer with a doped low-molecular-weight compound mixed with it.

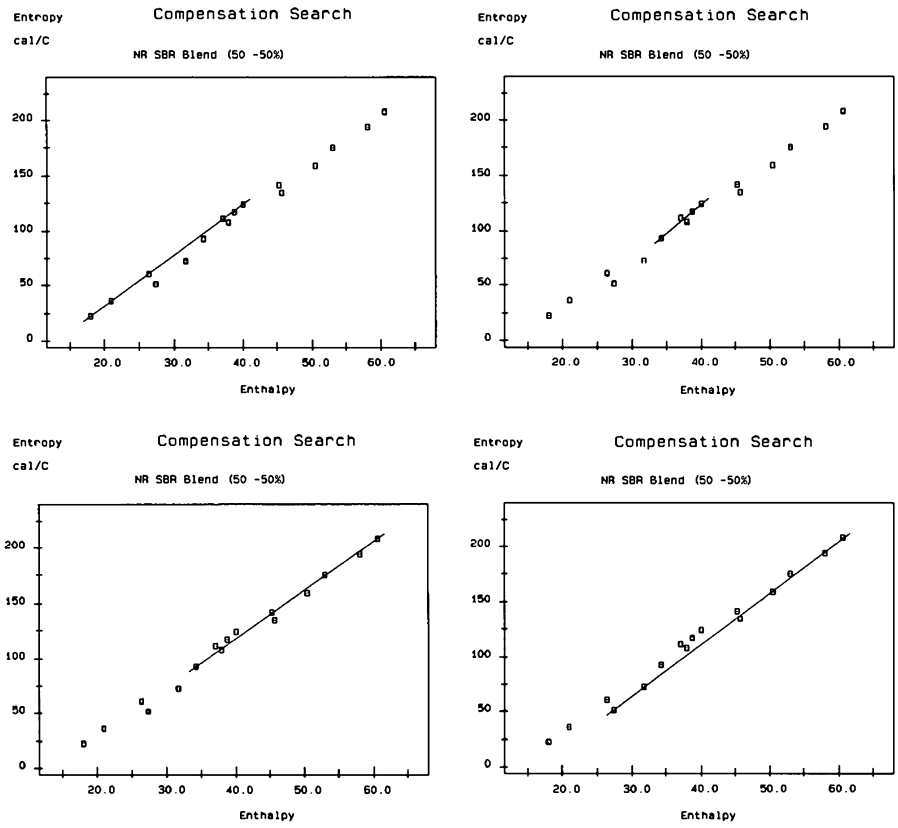


Figure 3.31: Series of four compensation search analyses dedicated to the determination of the positive and negative compensations of the amorphous phases in the biphasic components of the NR/SBR 50:50 blend.

EBSCOhost - printed on 2/13/2023 12:32 AM via . All use subject to https://www.ebsco.com/terms-of-use

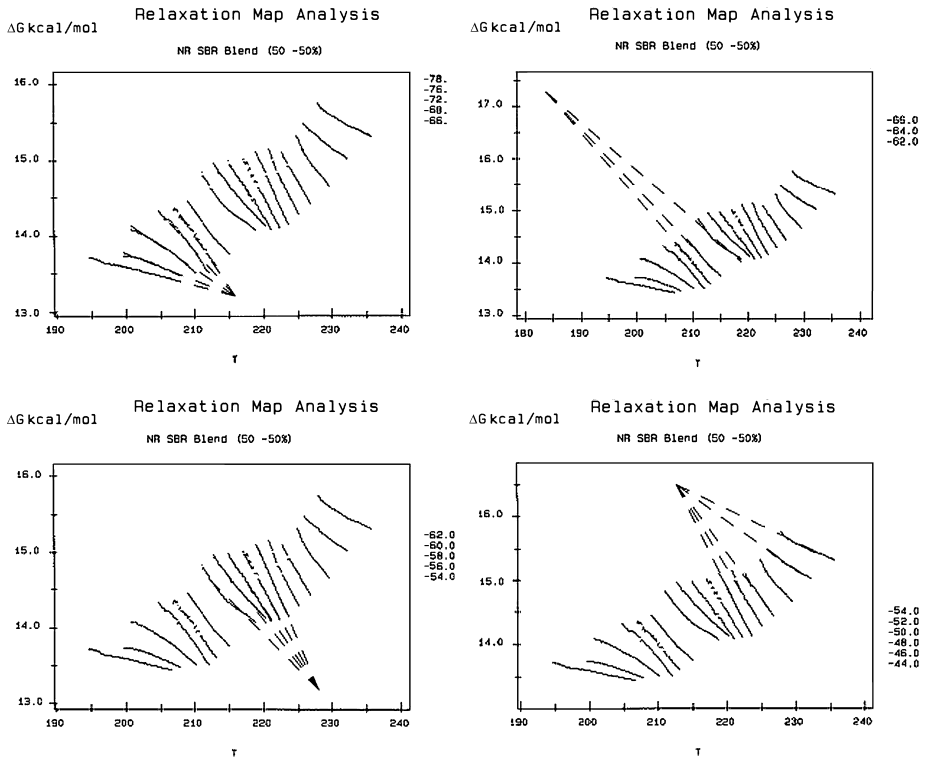


Figure 3.32: Reconstruction of the relaxation map in the ΔG plane for the NR/SBR 50:50 blend showing the results of the compensation search of Figure 3.31.

As far as the SBR-rich phase is concerned (upper curve of Figure 3.33), T_g remains approximately constant, and even raises slightly as the concentration of NR increases up to 50 %, and then sharply drops for the 75:25 blend. The constancy or even increase of T_g is also indicative that the two phases in presence are quite separated and not compatible at their interface. The case of 75 % NR remains doubtful on this matter of compatibility. It is unlikely that the impurities of the NR phase have migrated to the SBR domains, since the plasticizing effect on that phase would have lowered the temperature and not increased the temperature up to 50 % NR. Based on the T_g results, only the 75:25 blend could be thought of as a blend with segregated phases, with a slight improvement of the compatibility between NR and SBR for the SBR phase.

Figure 3.34 analyzes the variation of the DOD number for the positive compensations of both the NR and SBR domains against the NR content. The overall tendency, except for the 50:50 blend, is a decrease of the DOD number for the SBR phase as the NR content increases and a slight increase for the NR phase as the SBR content increases. Interpretation of the variation of the DOD in each phase is not obvious, especially in view of the competing mechanism which may occur from the migration of

EBSCOhost - printed on 2/13/2023 12:32 AM via . All use subject to https://www.ebsco.com/terms-of-use

the impurities out of the NR domain, and the miscibility of the segments from the two types of rubbers.

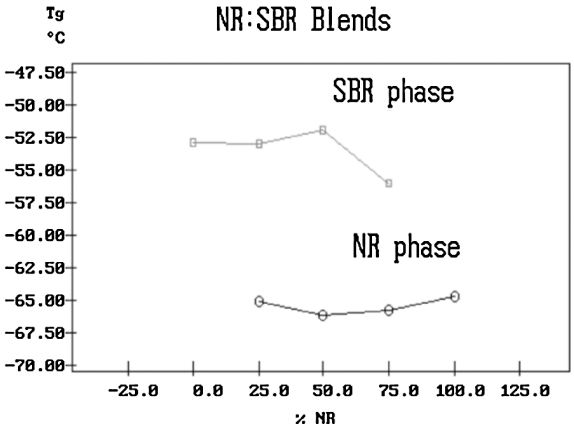


Figure 3.33: Variation of T_g for each of the two phases against the relative NR content. T_g is determined by the intercept of the two compensation lines in a compensation search.

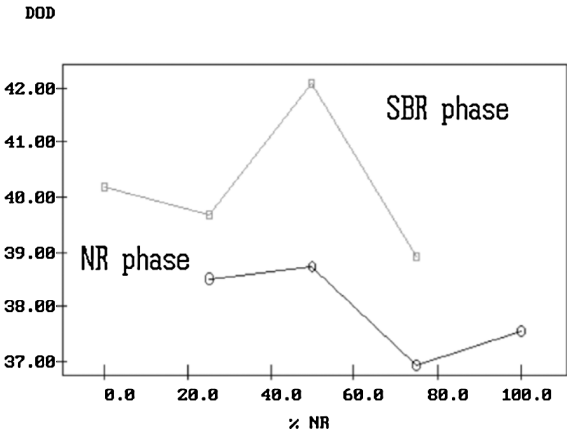


Figure 3.34: Variation of the DOD number for the SBR and NR phases as a function of the relative NR content. The DOD numbers are determined by the positive compensations in each phase.

In many aspects, the blends behave as separate microdomains, as illustrated in Figures 3.35 and 3.36, which display the entropy of activation against T_p for either pure SBR or the NR/SBR 25:75 blend. The hyperbolic variation commonly observed for homopolymers in the sub-glass transition temperature region is also visible for the blend. Very clearly defined behaviors of the entropy of activation vs. T_p are observed for both phases, with a clear break for the separation between the relaxation in one domain or the other.

EBSCOhost - printed on 2/13/2023 12:32 AM via . All use subject to https://www.ebsco.com/terms-of-use

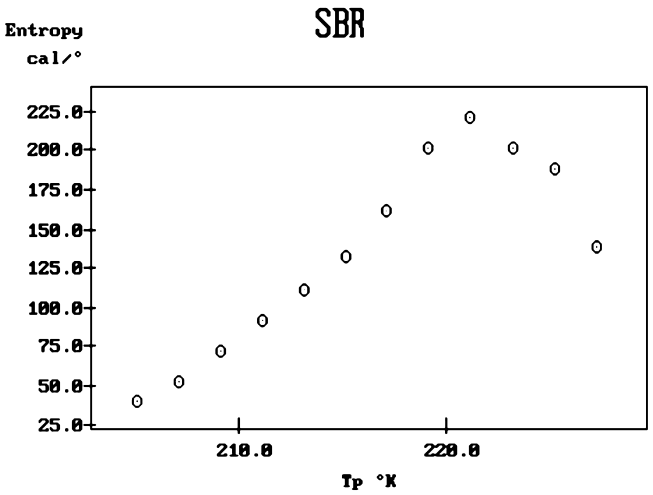


Figure 3.35: Entropy of activation vs. T_p for pure SBR.

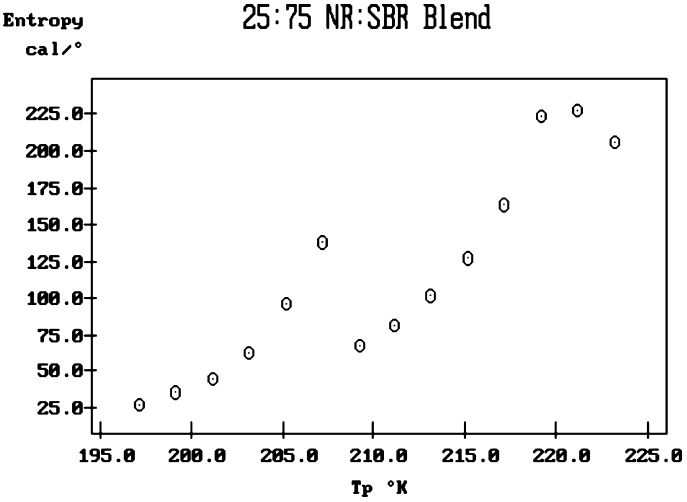


Figure 3.36: Entropy of activation vs. T_p for the NR/SBR 25:75 blend.

This is well evidenced in Figures 3.36 and 3.37 for the 25:75 and 50:50 NR/SBR blends. We attempted without success to quantify from the equation of the hyperbolic variations of ΔS_p vs. T_p the effect of the concentration in the blend on the thermokinetic characteristics.

There is no doubt that blending the two elastomers can result in various types of properties, as illustrated in Figure 3.38. In this figure, we compare the mobility in the structure, associated with the variation of entropy with T_p, due to the presence of 75 % NR in the blend. The NR phase is well defined in Figure 3.38. So is the SBR phase, for

EBSCOhost - printed on 2/13/2023 12:32 AM via . All use subject to https://www.ebsco.com/terms-of-use

which the variation of ΔS_p vs. T_p is identical to the pure SBR polymer. However, the entropy of activation seems to have decreased at higher T_ps for the blend compared to the pure SBR sample. This should probably result in a change of mechanical behavior in this temperature range.

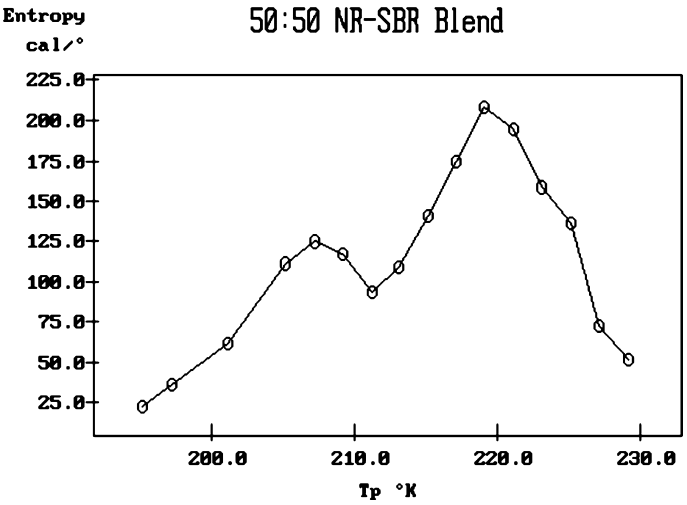


Figure 3.37: Entropy of activation vs. T_p for the NR/SBR 50:50 blend.

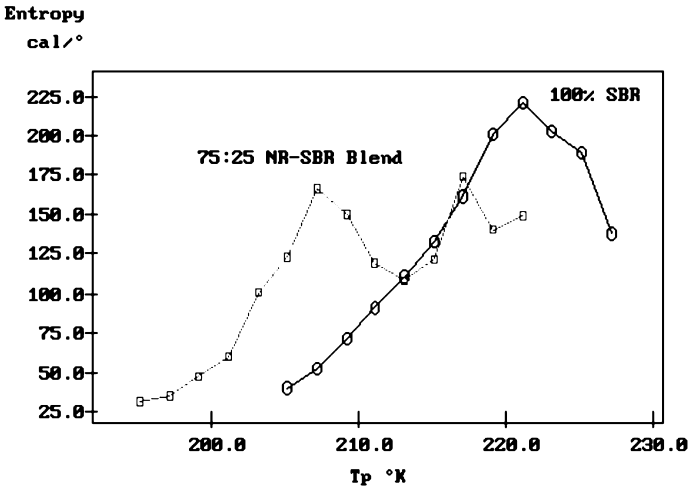


Figure 3.38: Entropy of activation vs. T_p for the NR/SBR 75:25 blend and comparison with 100 % SBR.

Figure 3.39 is a plot of ΔS_g (ΔS_p at $T_p = T_g$) for the two phases as a function of the NR content. The variation for the SBR phase is particularly interesting. If one extrap-

EBSCOhost - printed on 2/13/2023 12:32 AM via . All use subject to https://www.ebsco.com/terms-of-use

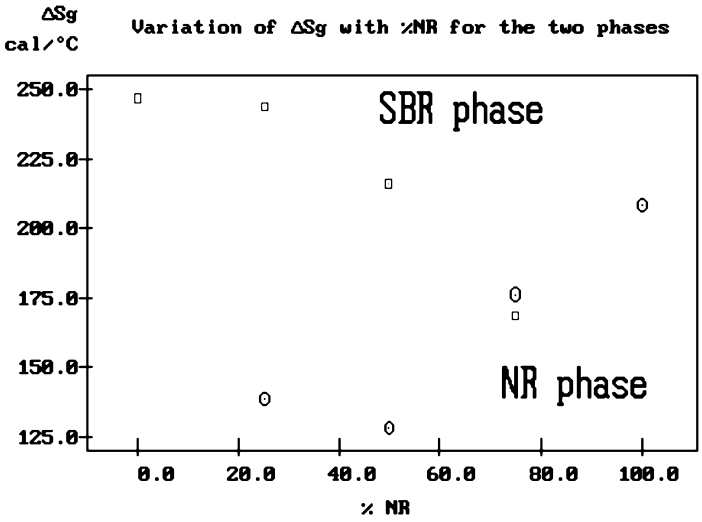


Figure 3.39: Variation of ΔS_g at T_g vs. relative NR content determined from the Z-line for the SBR phase (squares) and for the NR phase (dots).

olates the continuously decreasing curve of ΔS_g vs. %NR to the case where NR content = 100 %, a difference of approximately 110 cal/ °C is found. The entropy of activation at T_g for pure NR is too large by 110 cal/ °C compared to the extrapolated value found by blending this phase with SBR. It could be concluded that the excess entropy ΔS_g is due to the presence of impurities and that as the NR content decreases, these impurities are extracted from the NR phase by the presence of the SBR phase in the structure in the surrounding of the NR. This assumption would also explain the decrease of ΔS_g of the NR phase as the content of SBR increases. Incidentally, the extrapolated value found for 100 % SBR (0 % NR) is also different from the value found for pure SBR by 110 cal/ °C. It might be speculated that the blending of NR/SBR in various proportions results in a segregated blend with different percentages of impurities entering the domains and acting as dopant for both phases. As the concentration of the impurities decreases from one microdomain, it increases in the other domain, perhaps according to a diffusion mechanism. When the NR domains are surrounded by an increasing amount of SBR phase, the migration to the SBR phase becomes preponderant and the entropy in the NR phase decreases by the amount it increases in the SBR phase.

The mechanism of migration and plastification of the two rubber phases by the impurities seems to be the major mechanism influencing the overall relaxation process, and no direct miscibility or almost no miscibility between the elastomeric phases occurs. If it could be confirmed by other techniques, this result would certainly be remarkable, allowing us to say that TWD spectroscopy is capable of analyzing migration effects from one solid phase to another.

EBSCOhost - printed on 2/13/2023 12:32 AM via . All use subject to https://www.ebsco.com/terms-of-use

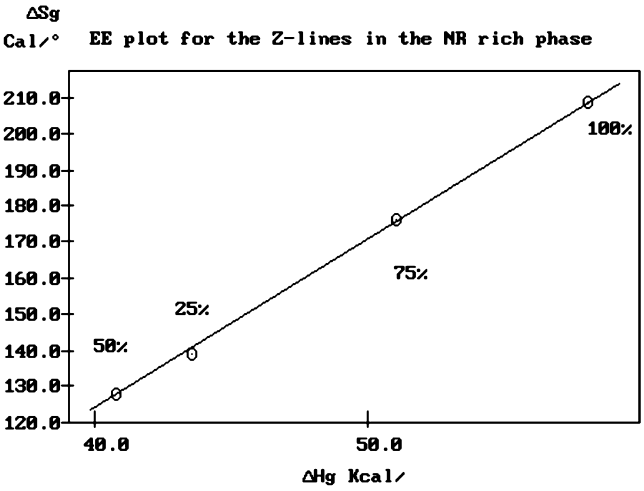


Figure 3.40: ΔS_g vs. ΔH_g in the NR-rich amorphous phase for the four concentrations of NR in the blend.

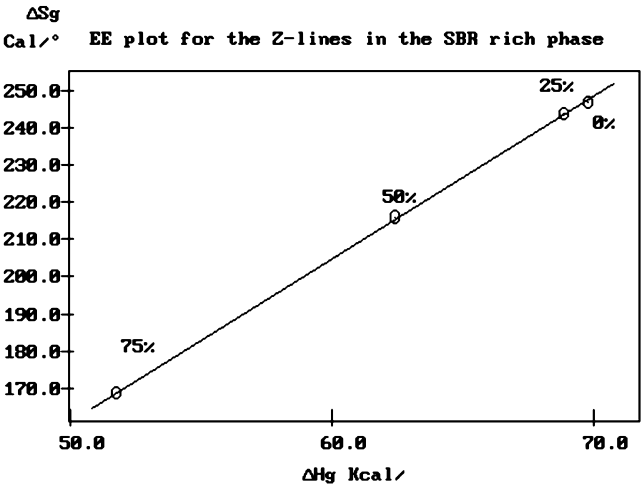


Figure 3.41: ΔS_g vs. ΔH_g in the SBR-rich amorphous phase for the four concentrations of NR in the blend.

Another reason for our assertion of a diffusion-controlled migration mechanism, which makes the impurities act as a diffused filler or plasticizer, is explained in Figures 3.40 and 3.41. In these figures, we plot ΔS_g against ΔH_g for each phase for the various blends when the NR content varies between 0 and 100 %. Figure 3.40 applies to the NR-rich phase, and Figure 3.41 concentrates on the SBR-rich phase. These two figures are actual EE plots for the Z-lines obtained by the intersection of the respective positive and negative compensations in the relaxation maps. ΔS_g and ΔH_g are,

EBSCOhost - printed on 2/13/2023 12:32 AM via . All use subject to https://www.ebsco.com/terms-of-use

respectively, the slope and intercept of the Z-line which joins the two compensation points in the relaxation map plotted in the ΔG plane. The linearity in Figures 3.40 and 3.41 implies that Z-lines for various blends compensate themselves. The point of compensation can be found from the slope and intercept of the EE lines in Figures 3.40 and 3.41. This behavior is identical to what we observe for a plasticized PMMA system, which will be reported later in another case study. The influence of the content of plasticizer is perceived as a EE plot for the Z-lines as the concentration varies. The identical behavior observed in Figures 3.40 and 3.41 seems to validate our assumption that relaxation occurs as the result of migration of impurities from one phase to another. The two EE plots for the Z-lines in the blend for both phases are compared in Figure 3.42. This figure is remarkably simple, and quantitative analytical conclusions can be derived from it to determine from TWD spectroscopy the actual relative content of any given NR/SBR blend.

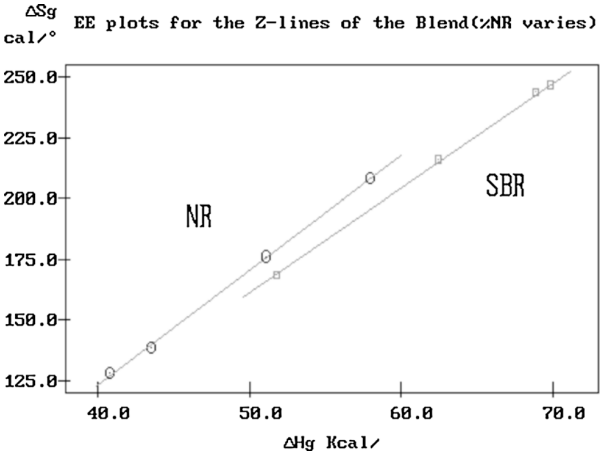


Figure 3.42: Comparison of the graphs in Figures 3.40 and 3.41.

Figure 3.43 is a plot of $(T_c^+ - T_g)$ against SBR content in the blend for the NR and SBR phases. Remember that SBR is the "hard" segment in the blend and NR is the "soft" segment. This means that T_g of the SBR phase is higher (actually by approximately 13 °C) than T_g of the NR phase. Figure 3.43 suggests an increase of $(T_c - T_g)$ when the SBR content increases. At higher concentrations of SBR (>70 %), the soft segments are in small domains surrounded by a matrix of hard SBR segments. In the blend, at a temperature where SBR is already below its glass transition temperature (thus becoming mechanically glassy and hard), the small microdomains of the NR segments are being pressurized under the stress from the hard segments. It is expected, under these conditions, that the internal stress in the soft rubber phase increases. This is probably the reason for the tendency of $(T_c - T_g)$ to increase in Figure 3.43.

EBSCOhost - printed on 2/13/2023 12:32 AM via . All use subject to https://www.ebsco.com/terms-of-use

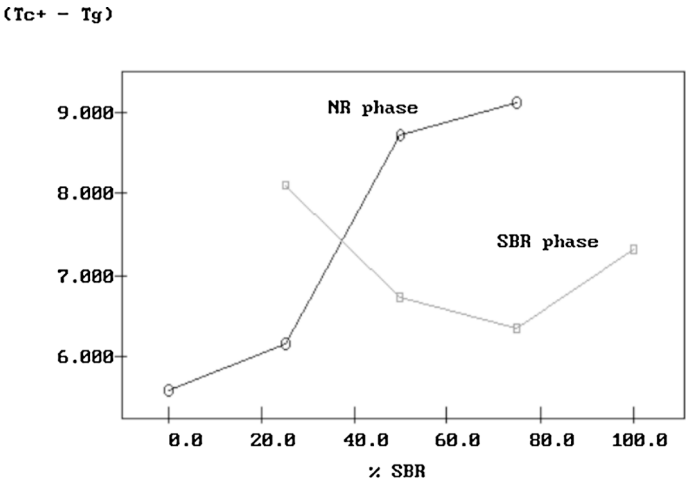


Figure 3.43: Plot of $(T_c^+ - T_g)$ vs. relative SBR content for both the NR-rich and the SBR-rich phases of the blends.

In conclusion, we were able to easily detect the migration of soluble purities from one rubber phase to another in a series of NR/SBR blends. The same technique could be useful in detecting the migration of additives between layers of a multi-layer sample. The analysis reveals that very little direct compatibility between the segments of the two elastomers NR and SBR is achieved in the blend at almost any concentration.

II.3.4.4 Case study: influence of LDPE blend on the relaxation map of HDPE

Figure 3.44 presents the TSD trace for a pure high-density polyethylene (100 % HDPE) and a polyblend of 5 % low-density polyethylene (LDPE) in a matrix of 95 % HDPE. The polarization temperature in the figure is $T_p = 50$ °C. The most spectacular effect of adding 5 % LDPE to the blend is an increase of the peak intensity for T_g and T_γ, a decrease of the intensity for T_α, and the presence of a shoulder on the T_α peak observed at 42 °C. T_α is associated with relaxations and movements occurring in the crystalline phase and is not the subject of the present report. For the T_g process (–55 °C to 0 °C), there is not only an increase of the peak intensity, but a broadening of the peak in the lower-temperature tail region. Thermal-windowing is carried out around the T_g found for the pure HDPE and the blend in order to separate out the various relaxation modes which combine into the T_g TSD relaxation around –25 °C in Figure 3.44.

The relaxation map in the Arrhenius plane for 100 % HDPE is shown in Figure 3.45. The experimental conditions and the sample thickness and area are also displayed in the header of this figure. The samples were provided by Thai Ciba-Geigy. Please note the large magnitude of the field in the case of this non-polar material.

EBSCOhost - printed on 2/13/2023 12:32 AM via . All use subject to https://www.ebsco.com/terms-of-use

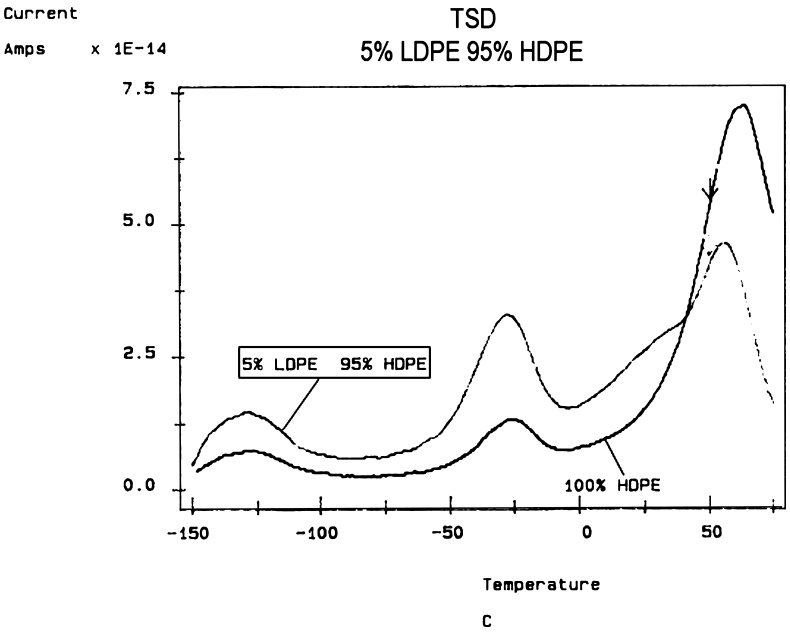


Figure 3.44: TSD trace for 100 % HDPE and for a blend of 5 % LDPE and 95 % HDPE. Comparison of the traces. T_p is 50 °C.

100% HDPE	Anneal Temp : Inactive	Freeze Temp : -73.0C
	Anneal Time : Inactive	Freeze Time : 1.0min
Date : 10/30/1992	Polar Field : 2500.0V/mm	R3 Rate : 7.0C/m
Time : 19:36:58	Polar Time : 2.00min	End ISO Temp: 17.0C
	Tp Range: -50.0 -23.0C	End ISO Time: 0.0min
Solomat TSC/RMA	Thickness : 0.152mm	Window Width: 2.0C
	Area : 25.0mm^2	Depol time : 2.0min

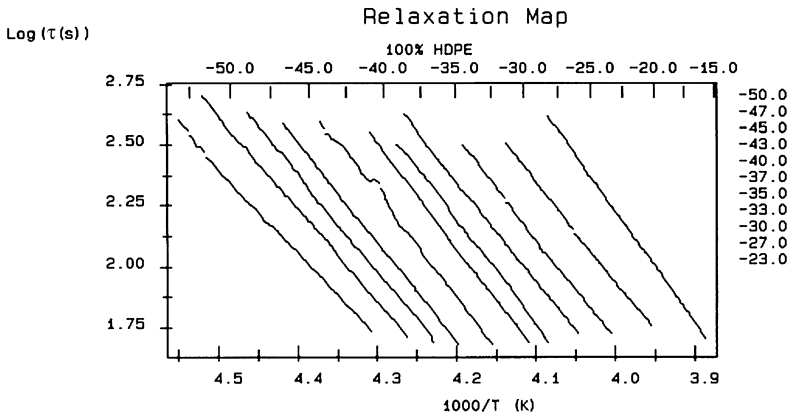


Figure 3.45: Relaxation map in the Arrhenius plane for 100 % HDPE. The TWD conditions are shown in the box header. T_p focuses on the T_g region: −50 °C to −23 °C.

EBSCOhost - printed on 2/13/2023 12:32 AM via . All use subject to https://www.ebsco.com/terms-of-use

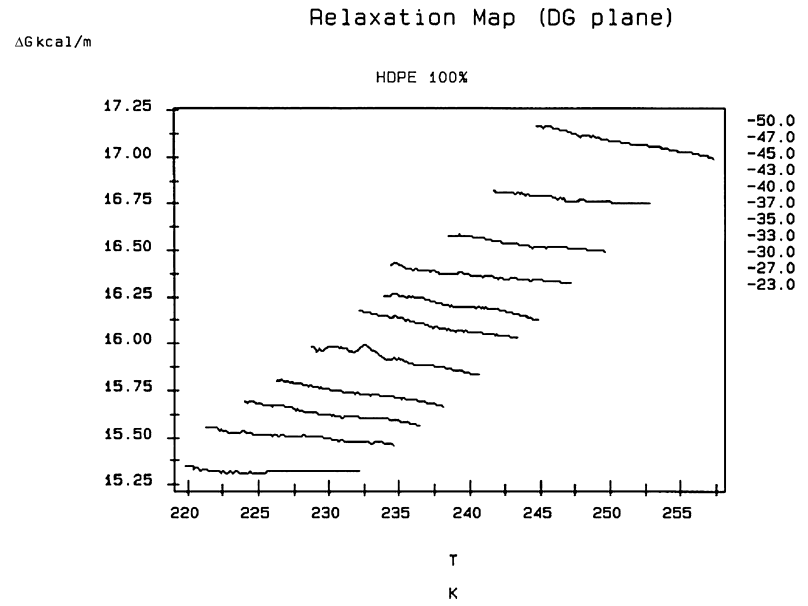


Figure 3.46: Relaxation map in the ΔG plane for 100 % HDPE. The conversion of the Arrhenius spectral lines to the Eyring format is done via equation (2.5) of Part I.

The relaxation map is presented in the ΔG plane in Figure 3.46. This representation puts the emphasis on the entropy of activation, perceived as the rate of free energy recovery during the depolarization stage. The slope of the lines in Figure 3.46 is proportional to the entropy of activation. The first observation is that the lines seem to be almost horizontal, which indicates that the entropy of activation is very small.

The compensation search (EE plot) is displayed in Figure 3.47, showing that a positive and a negative compensation are found for the glass transition temperature of the pure HDPE studied.

The positive and negative compensations are shown in Figures 3.48 and 3.49, respectively.

The compensation coordinates for the positive compensation are

$$T_c = 10.61\,^{\circ}\mathrm{C}$$
$$\Delta G_c = 15.19\,\mathrm{kcal/m}$$
$$\mathrm{DOD} = 46.47$$

and for the negative compensation they are

$$T_c = -138.98\,^{\circ}\mathrm{C}$$
$$\Delta G_c = 17.46\,\mathrm{kcal/m}$$
$$\mathrm{DOD} = -30.10$$

EBSCOhost - printed on 2/13/2023 12:32 AM via . All use subject to https://www.ebsco.com/terms-of-use

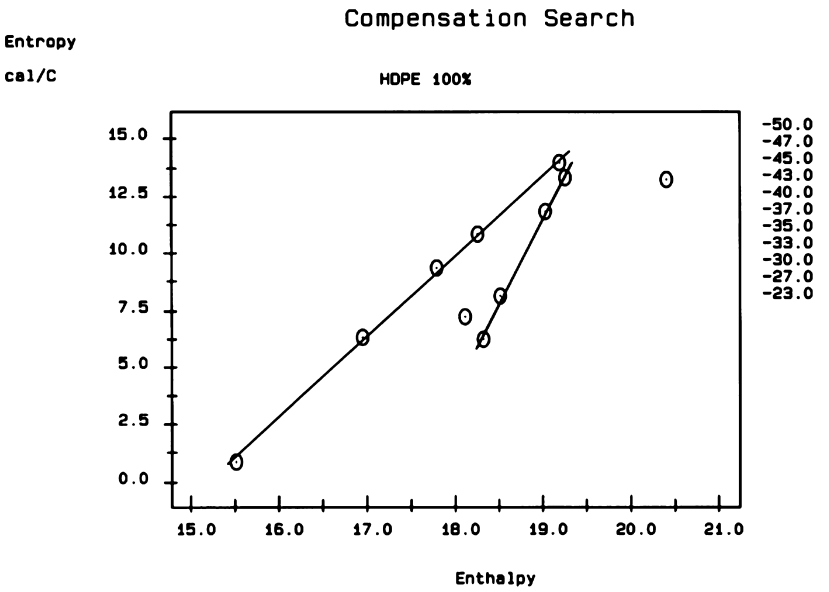


Figure 3.47: Compensation search in the EE plane for 100 % HDPE. The positive and negative compensation lines characterize interactive coupling in this amorphous component located outside the spherulites.

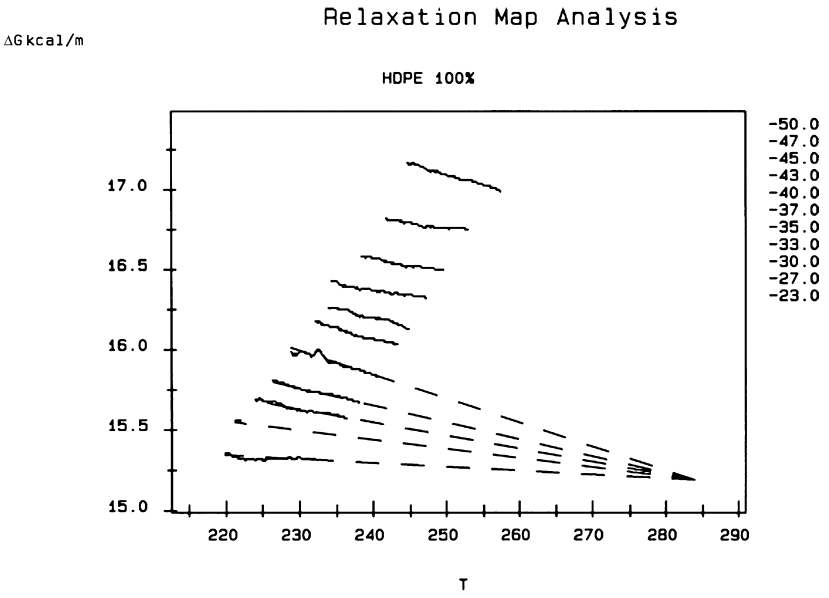


Figure 3.48: Relaxation map in the ΔG plane for 100 % HDPE showing the positive compensation determined by the positive compensation line in the compensation search of Figure 3.47.

EBSCOhost - printed on 2/13/2023 12:32 AM via . All use subject to https://www.ebsco.com/terms-of-use

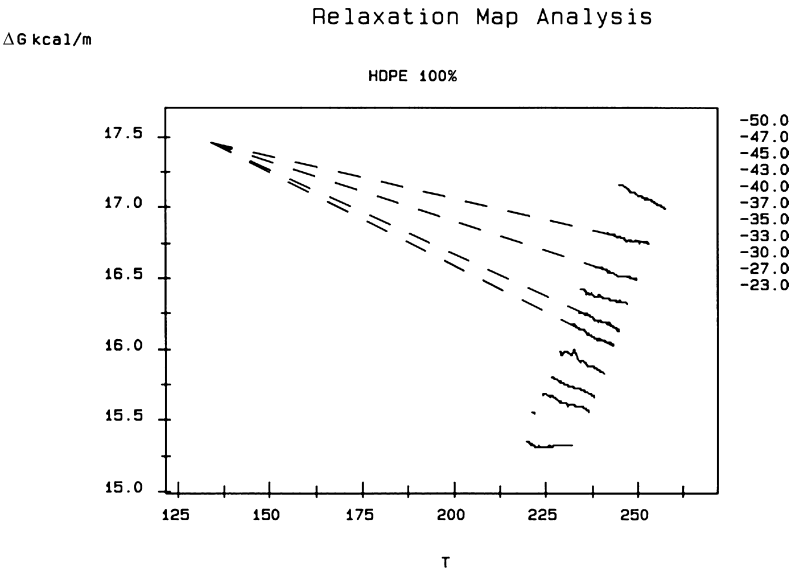


Figure 3.49: Relaxation map in the Δ*G* plane for 100 % HDPE showing the negative compensation determined by the negative compensation line in the compensation search of Figure 3.47.

Note that T_c for the negative compensation is located almost exactly at the *γ* transition for polyethylene. The difference $(T_c - T_g)$ is large for both the positive and negative compensations, an indication that the relaxation lines are almost parallel. The difference between ΔG_c^+ and ΔG_c^- is also very small.

Table 3.7 confirms that the entropy is very small for all temperatures of compensation and that it contributes very little to the free energy of activation at T_p. However, a plot of the entropy against T_p (Figure 3.50) displays a maximum at T_g which occurs

Table 3.7: Thermokinetic results derived from the relaxation map in Figure 3.46 for 100 % HDPE.

T_p (°C)	T_m (°C)	ΔH_p (kcal/mol)	ΔS_p (cal/°C/mol)	ΔG_p (kcal/mol)
−50.0	−40.9	15.5151	0.8580	15.3236
−47.0	−38.3	16.9398	6.3007	15.5149
−45.0	−36.5	17.7813	9.3593	15.6459
−43.0	−34.9	18.2508	10.8307	15.7580
−40.0	−32.3	19.1896	13.9356	15.9403
−37.0	−29.7	19.2523	13.2779	16.1166
−35.0	−28.1	19.0345	11.8248	16.2183
−33.0	−25.9	18.1007	7.2047	16.3705
−30.0	−23.5	18.5167	8.1221	16.5418
−27.0	−19.9	18.3209	6.2425	16.7842
−23.0	−15.7	20.3989	13.2198	17.0918

EBSCOhost - printed on 2/13/2023 12:32 AM via . All use subject to https://www.ebsco.com/terms-of-use

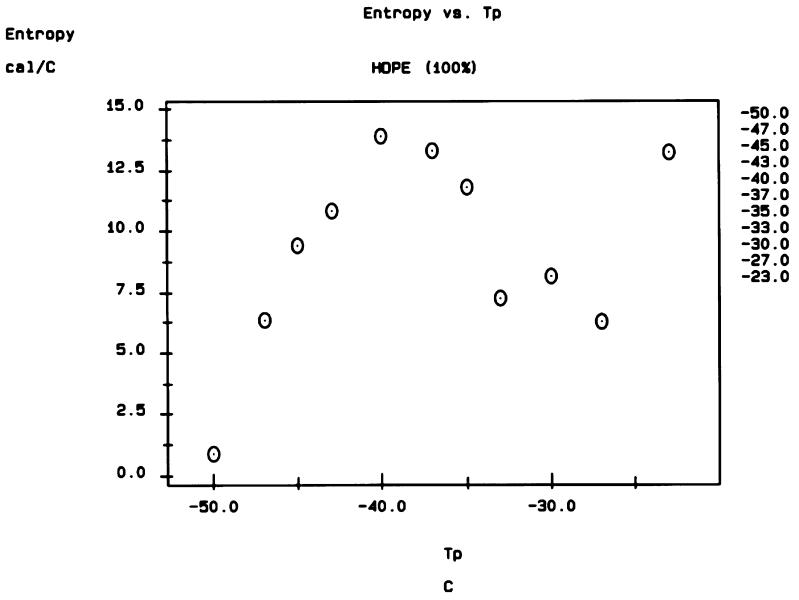


Figure 3.50: Entropy of activation vs. T_p for the T_g transition peak observed at low T for 100 % HDPE.

here for $T_p = -39$ °C. Also note that a hyperbolic function can be drawn through the data in the lower-temperature ($T < T_g$) region, but the curvature is different that of from normal systems. The compensation temperature does not seem to correspond at all to the asymptotic value for the hyperbola. This singular behavior across T_g for the amorphous phase in HDPE results in a non-classical variation of ΔG_p vs. T_p, as illustrated in Figure 3.51. The straight line drawn in Figure 3.51 has a slope of 0.064 and an intercept of 11. This contrasts with the "normal" values found for many systems: slope 0.070 and intercept 0.

In Figure 3.52, we observe that the intensity at the thermal-window peak maximum is indeed very low (from 5×10^{-15} for $T_p = -15$ °C to a maximum of 8×10^{-15} for $T_p = -40$ °C). The maximum in Figure 3.52 is not located very far from the maximum found from the entropy plot (Figure 3.50). This is also at variance with typical behavior found for polar systems, for which the difference between the two maxima is sometimes as great as 10 °C to 15 °C.

Turning now to the blend of 5 % LDPE in 95 % HDPE, the relaxation map in the ΔG plane is shown in Figure 3.53.

The temperature range for the polarization is lowered to −60 °C to span the range up to −33 °C. The compensation search in Figure 3.54 reveals the presence of two positive compensations. One compensation is close to the one found for the pure HDPE, and the other compensation is probably associated with the LDPE phase. The behavior in Figure 3.54 is conclusive of a two-phase structure. The presence of 5 % LDPE in the blend results in segregation of the two segments.

EBSCOhost - printed on 2/13/2023 12:32 AM via . All use subject to https://www.ebsco.com/terms-of-use

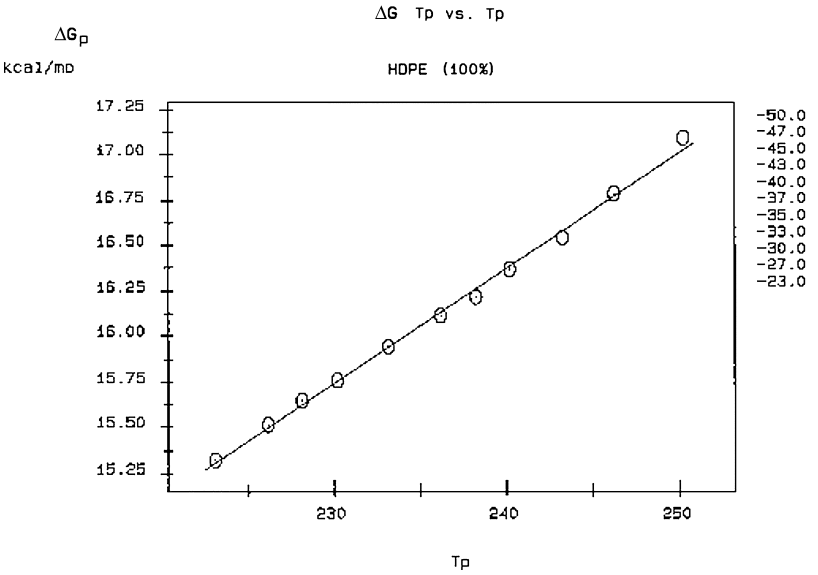


Figure 3.51: The ΔG_p vs. T_p (K) straight line shown for the data of 100 % HDPE has a slope of 0.064 and an intercept of 11: these are unclassical values compared to those found for the unstrained amorphous phase of amorphous polymers.

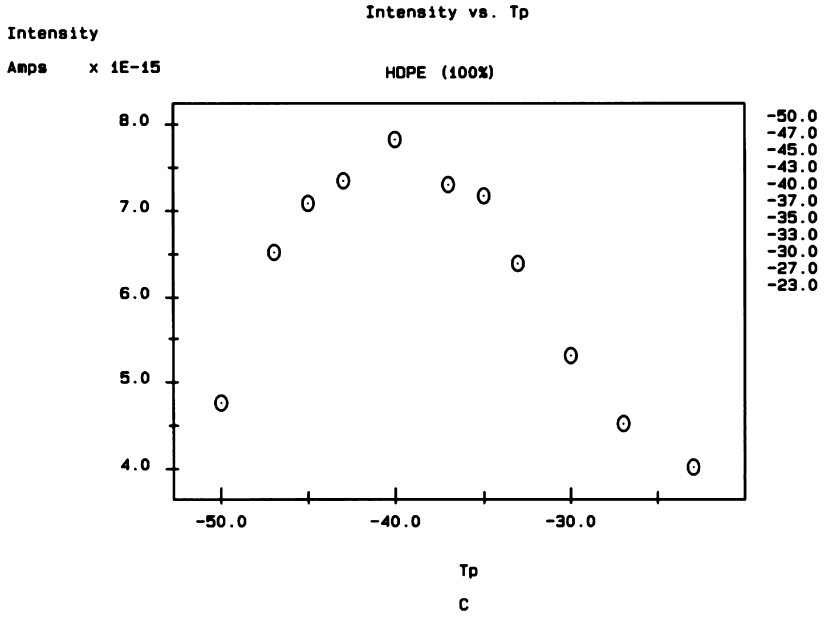


Figure 3.52: Intensity of the TWD peaks at their T_m values for 100 % HDPE.

EBSCOhost - printed on 2/13/2023 12:32 AM via . All use subject to https://www.ebsco.com/terms-of-use

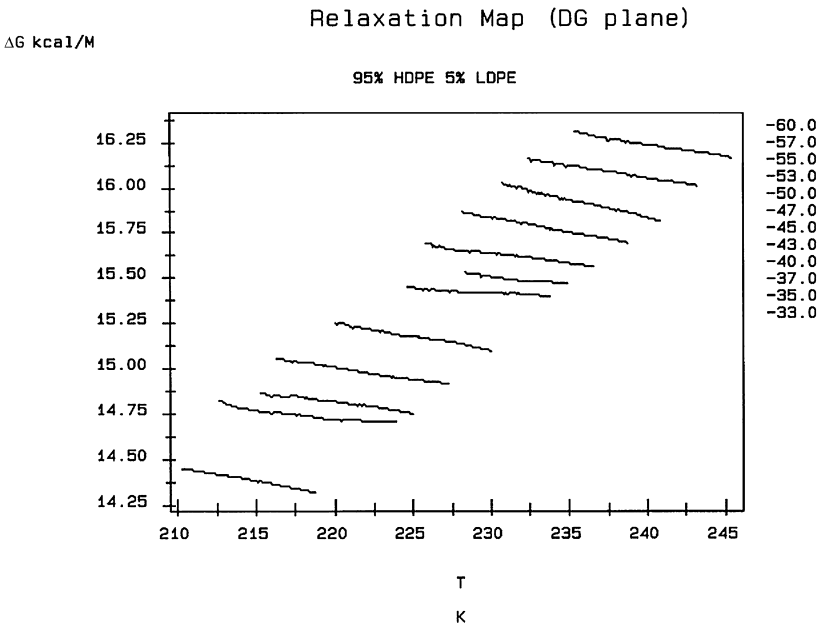


Figure 3.53: Relaxation map in the ΔG plane for the 95 % HDPE/5 % LDPE blend. T_p spans the extended range −60 °C to −23 °C.

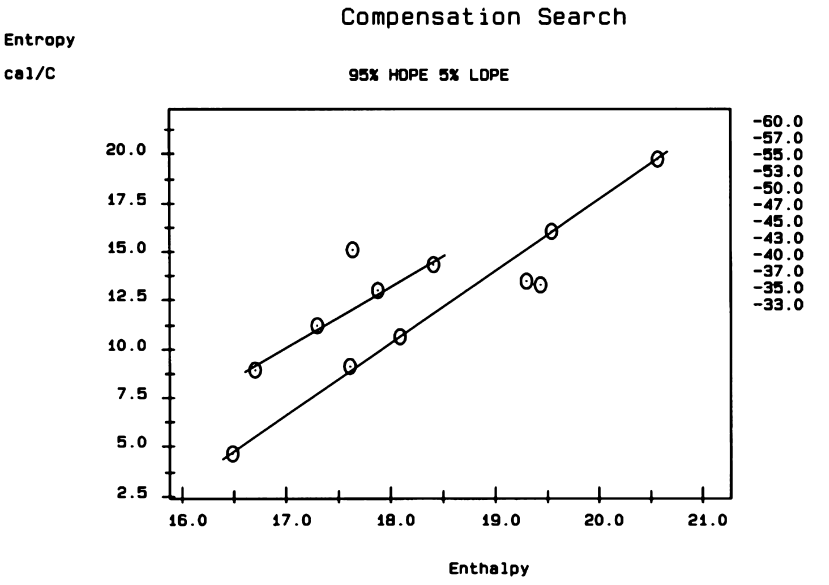


Figure 3.54: Compensation search in the EE plane for the 95 % HDPE/5 % LDPE blend. The two lines are positive compensations demonstrating a two-phase structure.

EBSCOhost - printed on 2/13/2023 12:32 AM via . All use subject to https://www.ebsco.com/terms-of-use

The compensation coordinates for the two positive compensations are shown in Table 3.8. The values for the second compensation ("2 Comp") apply to the HDPE phase and should be compared with the pure HDPE: ΔG_c remains the same for both (15.19 kcal/m), the DOD number decreases (from 54.10 to 46.47), and at the same time the temperature of compensation decreases in the blend.

Table 3.8: Coordinates and DOD numbers for the two positive compensations observed in Figure 3.54.

Line	Compensation Coordinates		DOD Number
1	$T_c = 46.84°C$	$\Delta G_c = 13.76$ kcal/mol	56.99
2	$T_c = -1.41°C$	$\Delta G_c = 15.19$ kcal/mol	44.10

Table 3.9: Thermokinetics results from the relaxation map in the ΔG plane for the 95 % HDPE/5 % LDPE blend.

T_p (°C)	T_m (°C)	ΔH_p (kcal/mol)	ΔS_p (cal/°C/mol)	ΔG_p (kcal/mol)
−60.0	−54.1	17.6306	15.1102	14.4098
−57.0	−49.1	16.7120	9.0147	14.7634
−55.0	−48.0	17.2843	11.2193	14.8366
−53.0	−45.8	17.8706	13.0149	15.0052
−50.0	−42.9	16.4148	14.3839	15.2049
−47.0	−39.2	16.4906	4.6593	15.4369
−45.0	−38.1	17.6045	9.1070	15.5266
−43.0	−36.5	18.0888	10.6571	15.6359
−40.0	−34.3	19.5392	16.1003	15.7852
−37.0	−32.2	20.5684	19.7176	15.9118
−35.0	−29.9	19.2955	13.5064	16.0788
−33.0	−27.6	19.4352	13.3191	16.2365

Table 3.9 provides the detail of analysis for the kinetic results. This table should be compared with Table 3.7.

Figure 3.55 is such a comparison plot in the case of the entropy of activation. The round dots in the plot apply to 100 % HDPE and the squares indicate values for the 5 % LDPE/95 % HDPE blend. The location of the maximum for the HDPE phase, either in the pure material or in the blend, seems to be unchanged. However, the intensity has increased for the mobility in the blend. This might be due to either a decrease of the crystallinity in the HDPE phase due to the presence of the LDPE segments or the presence of stabilizers or fillers in the LDPE, which have migrated to the HDPE phase. The decrease of crystallinity hypothesis is consistent with an increase of the peak intensity

EBSCOhost - printed on 2/13/2023 12:32 AM via . All use subject to https://www.ebsco.com/terms-of-use

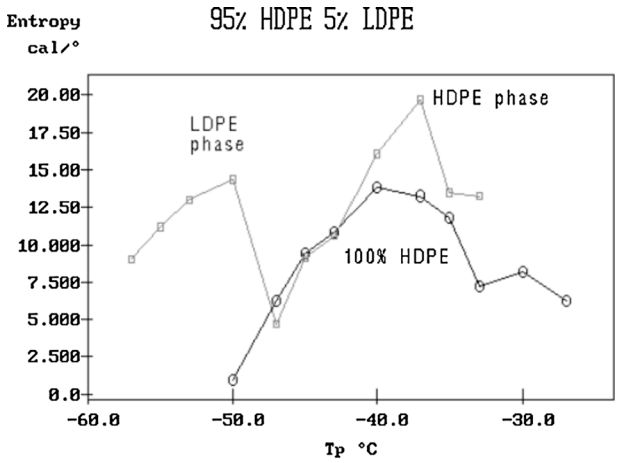


Figure 3.55: Entropy of activation vs. T_p for both 100 % HDPE (open dots) and the 95 % HDPE/5 % LDPE blend (open squares). The blend shows the two phases: the LDPE-rich phase and the HDPE-rich phase.

at T_g and T_β, which is observed in Figure 3.44. However, the DOD would also increase in such a case, and it does not. As it turns out, the 5 % LDPE/95 % HDPE blend also includes a certain amount of carbon black, which raises the dipolar conductivity, as it is commonly observed in carbon black-filled rubbers. This explains the increase in intensity of the current peaks. The decrease of DOD observed here might be caused by orientation and/or internal stress in the amorphous segments, due to a fine dispersion of the LDPE phase in the HDPE matrix, or the ordering of the structure by the carbon black component. This is perhaps confirmed by the sharp reduction of $(T_c - T_g)$, 10 °C, between 100 % HDPE and the 5 % LDPE/95 % HDPE blend.

The ΔG_p against T_p plots are compared in Figure 3.56 for the pure material and the blend. Surprisingly, in view of the fact that we almost invariably find a universal line for this plot, the presence of only 5 % LDPE results in a very different behavior for the effect of the field on the interactions between the bond segments. The decrease of ΔG_p in the blend indicates an overall increase of the entropic term, which might be significant of a decrease of the crystallinity or the presence of more polar carbon black filler. We commonly observe that the ΔG_p vs. T_p relationship is sensitive to the degree of crystallinity in the system, the polarizability (increased here by the presence of carbon black), and the voltage field.

Figure 3.57 is a comparison EE plot combining the results obtained for pure HDPE and the 95 % HDPE/5 % LDPE blend. The upper compensation line refers to the LDPE phase and is quite separate from the rest of the points in the graph. The compensation line for the HDPE interactive coupling is shifted slightly for the blend, indicating that the presence of the LDPE domains in the structure slightly affects the environment of the bonds in the matrix of HDPE. For a given enthalpy of activation, the entropy is

EBSCOhost - printed on 2/13/2023 12:32 AM via . All use subject to https://www.ebsco.com/terms-of-use

higher for the blend than for the pure material, confirming that the interaction results in a slight increase of the mobility in the polymer. The increase of mobility comes along with an increase in the polarizability of the blend due to the presence of carbon black. This is shown in Figure 3.58, which plots the intensity at the thermal-window peak maximum vs. T_p. The difference in polarizability for the two materials, which implies a large difference in the dielectric strength, is proportional to the percentage of carbon black present.

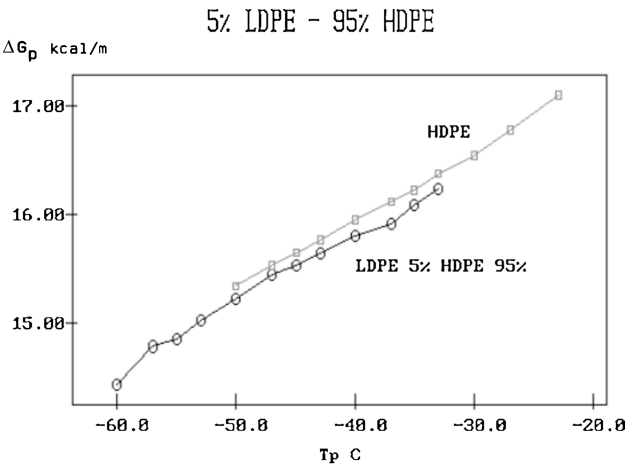


Figure 3.56: Comparison of ΔG_p vs. T_p (K) for 100 % HDPE and the 95 % HDPE/5 % LDPE blend. These curves are significantly different. See text.

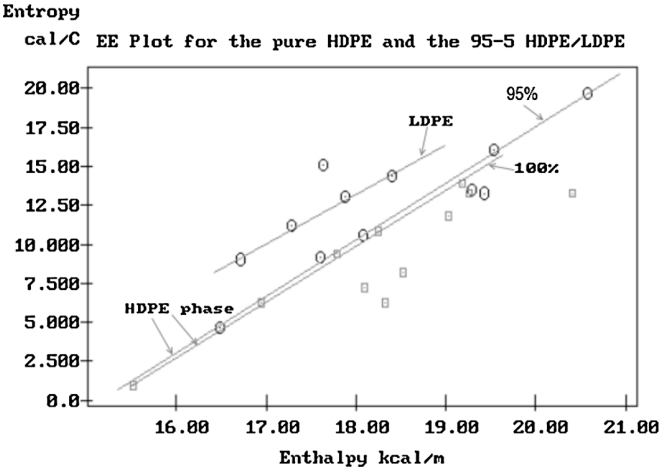


Figure 3.57: Compensation search in the EE plane to compare the two positive compensations of the 95 % HDPE/5 % LDPE blend and the positive compensation for 100 % HDPE.

EBSCOhost - printed on 2/13/2023 12:32 AM via . All use subject to https://www.ebsco.com/terms-of-use

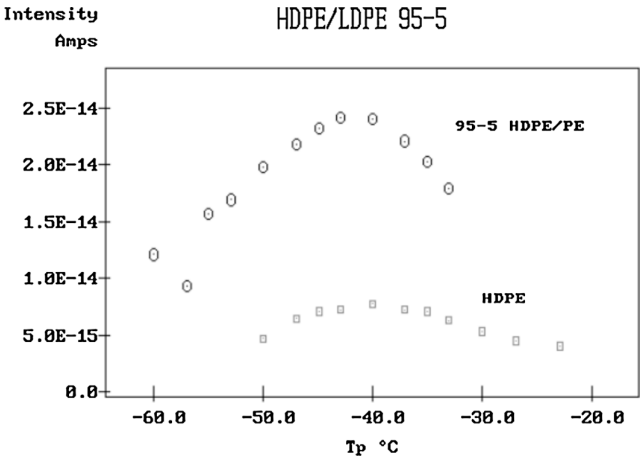


Figure 3.58: Intensity of the Debye peaks at T_m plotted against T_p to compare the mobility in 100 % HDPE and the 95 % HDPE/5 % LDPE blend. The increase of the mobility is due to the two-phase segregation.

In conclusion, TWD spectroscopy predicts phase separation and immiscibility between LDPE and HDPE, which was not revealed, for some reason, by TSD. In fact, incompatibility between LDPE and HDPE has already been reported. It is related to the extent of branching in the low-density material, which can be monitored to achieve full compatibility. TWD can certainly uniquely be used to determine a quantitative criterion to the degree of compatibility.

II.3.5 Case study: characterization by TWD of the effect of plasticizer concentration on the amorphous state of PMMA

The polymers analyzed in this case study were provided by the University of North Carolina [147]. The MMA monomer was obtained from Edrich and was submitted to gamma radiation for 6 hours at 4.8 MHz (Cesium-134) to produce the PMMA polymer [147]. The characterization is carried out on three types of samples: 100 % pure PMMA, 85 % pure PMMA, and 70 % pure PMMA, with dibutylphtalate (DBT) as plasticizer. The increasing amount of plasticizer depreciates the glass transition temperature T_g of the PMMA, as measured by DMA. The T_g characterized by the peak maximum of the loss tangent in a DMA experiment provides the following T_gs:

PMMA (%)	T_g (°C) by DMA
100	124
85	78
70	68

EBSCOhost - printed on 2/13/2023 12:32 AM via . All use subject to https://www.ebsco.com/terms-of-use

The purpose of this case study is to investigate the effect of the increasing plasticizer content on the TWD parameters. One of the consequences of this study is a better understanding of the physical parameters measured by the thermal-windowing and TWD techniques.

The relaxation map in the ΔG plane for PMMA 100 % is displayed in Figure 3.59. All the depolarization lines are quasi-linear except for T_p = 135 °C, for which the curve is badly curved (at the top of Figure 3.59).

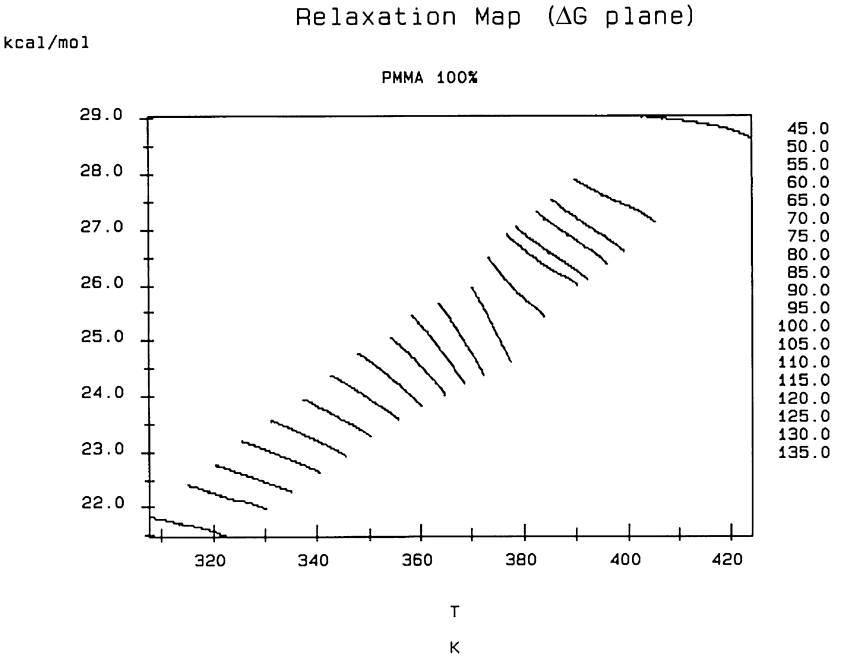


Figure 3.59: Relaxation map in the ΔG plane for pure PMMA. This will provide the reference thermokinetic constants for different blends of PMMA and dibutylphtalate.

The compensation search in Figure 3.60 displays the classical two-compensation behavior across T_g: one positive and one negative compensation.

The two compensations are shown in Figure 3.61, and the Z-line is the line joining the two compensation points. The slope and intercept of the Z-line provide the entropy and enthalpy at T_g for the pure PMMA 100 %.

The coordinates of the compensation points for the positive and negative compensations are shown in Table 3.10.

The equivalent figures for 85 % PMMA (15 % DBP) are shown in Figures 3.62 to 3.64.

Table 3.11 provides the coordinates for the compensation point and the DOD number.

EBSCOhost - printed on 2/13/2023 12:32 AM via . All use subject to https://www.ebsco.com/terms-of-use

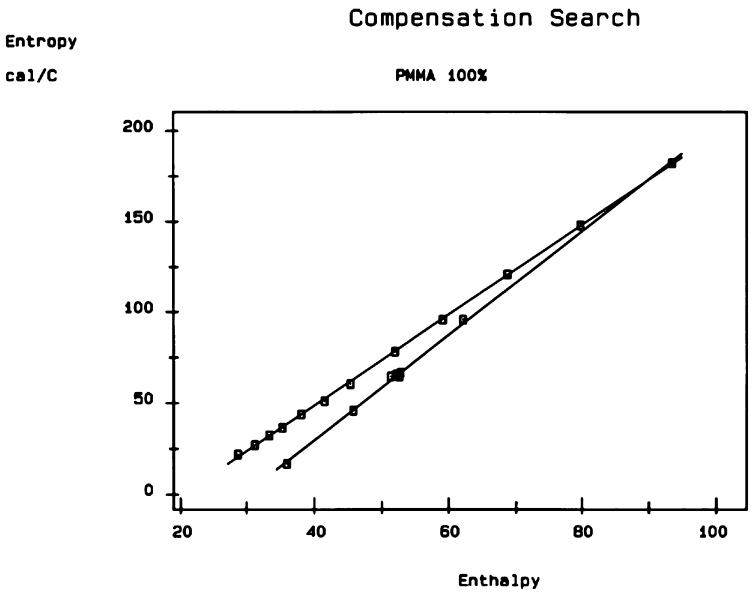


Figure 3.60: Compensation search in the EE plane to determine the positive and negative compensation coordinates of the amorphous state.

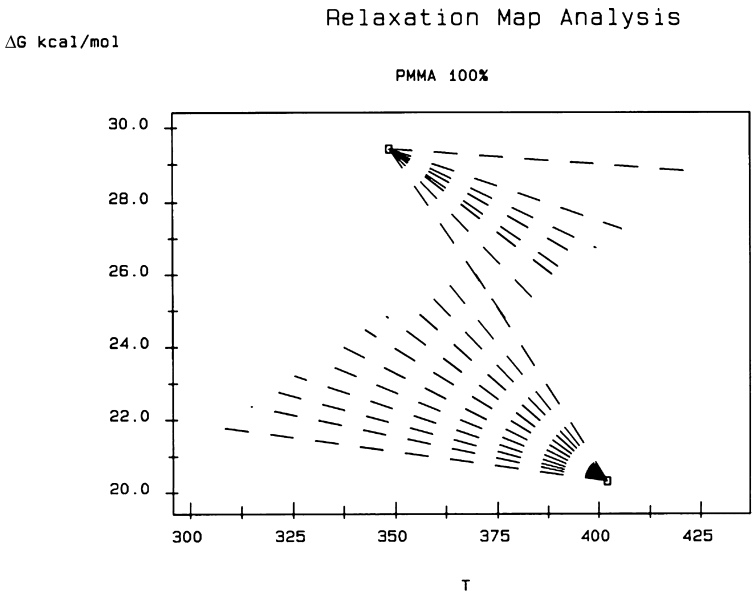


Figure 3.61: Reconstruction of the positive and negative compensations of the spectral lines in Figure 3.59 as a result of the compensation search in Figure 3.60.

EBSCOhost - printed on 2/13/2023 12:32 AM via . All use subject to https://www.ebsco.com/terms-of-use

Table 3.10: Values of the compensation coordinates in Figure 3.60 obtained by simplex regression.

Line	Compensation Coordinates		DOD Number
1	T_c = 129.02 °C	ΔG_c = 20.32 kcal/mol	49.45
2	T_c = 75.69 °C	ΔG_c = 29.44 kcal/mol	15.57

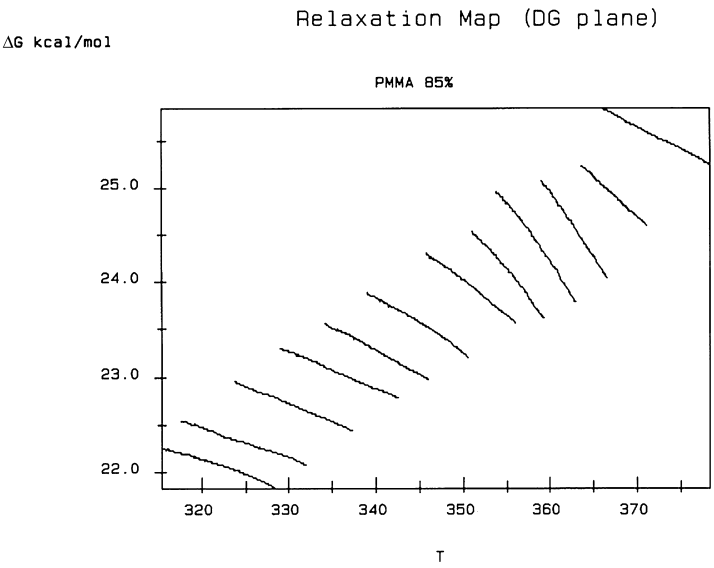


Figure 3.62: Relaxation map in the ΔG plane for 85 % PMMA.

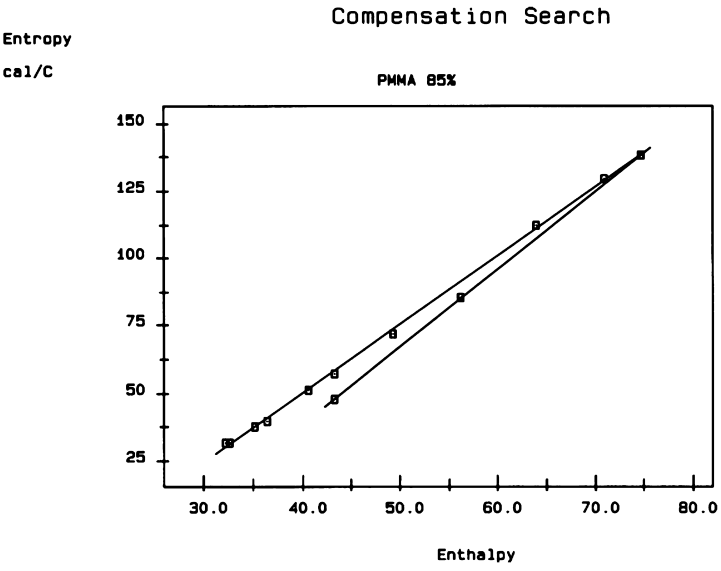


Figure 3.63: Compensation search in the EE plane for 85 % PMMA.

EBSCOhost - printed on 2/13/2023 12:32 AM via . All use subject to https://www.ebsco.com/terms-of-use

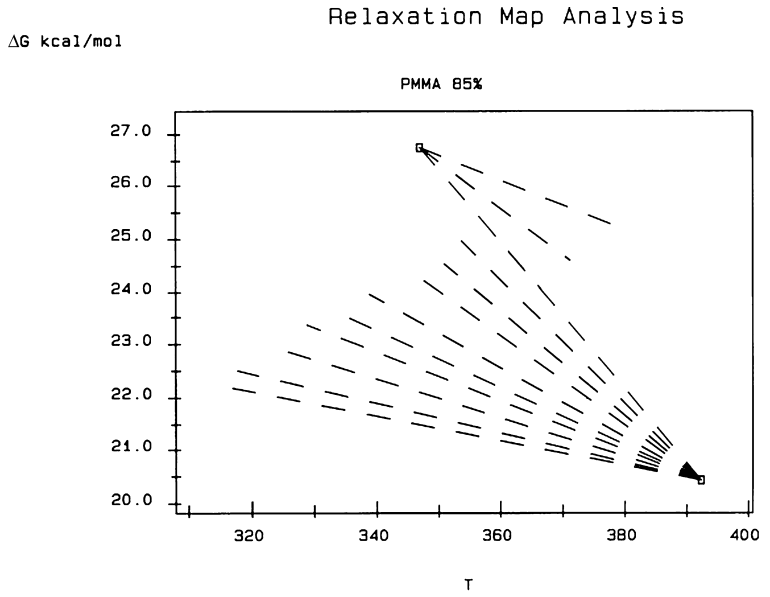


Figure 3.64: Reconstruction for 85 % PMMA of the positive and negative compensations of the spectral lines in Figure 3.62 as a result of the compensation search in Figure 3.63.

Table 3.11: Values of the compensation coordinates in Figure 3.63 for 85 % PMMA.

Line	Compensation Coordinates		DOD Number
1	T_c = 119.25 °C	ΔG_c = 20.45 kcal/mol	47.87
2	T_c = 73.98 °C	ΔG_c = 26.74 kcal/mol	22.95

The ΔG_p vs. T_p plot is shown in Figure 3.65. It is interesting to note in this figure the departure observed from the straight line behavior at lower T_p. The value of ΔG_p seems to reach a plateau zone before starting up again. This behavior is observed in several instances for many polymers. The departure from the straight line is associated, in Part I, Chapter 3, with an orientation polarization process where modulated systems kinetics takes over in the transmittal of the voltage energy to the bonds interaction.

The case of 70 % PMMA (30 % DBP) is presented in Figures 3.66 to 3.69.

Table 3.12 provides the compensation points in the ΔG plane. As seen in the case of 85 % PMMA, the ΔG_p vs. T_p linear behavior is only typical at lower temperatures (the straight line of Figure 3.69). Above 60 °C, the variation of ΔG_p could be fitted with a smooth curve, such as a hyperbolic function, or with a pair of straight lines.

The summary of the TWD results is confined in Table 3.13.

EBSCOhost - printed on 2/13/2023 12:32 AM via . All use subject to https://www.ebsco.com/terms-of-use

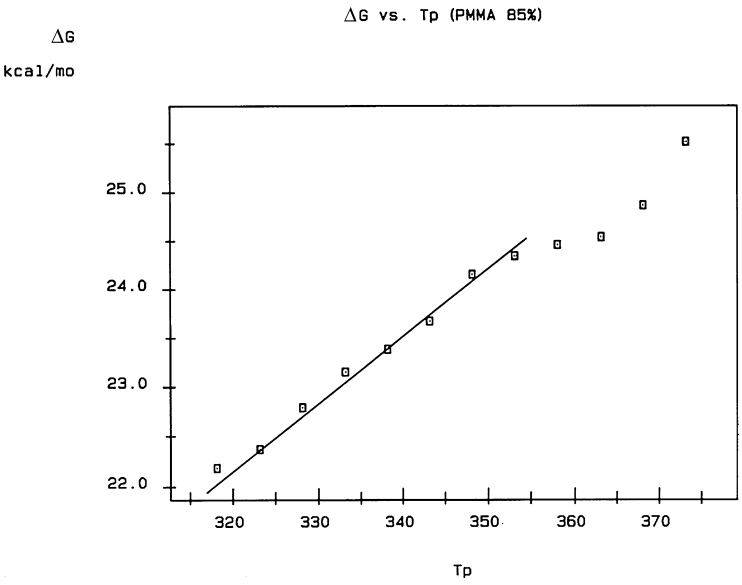


Figure 3.65: ΔG_p vs. T_p (K) for 85 % PMMA.

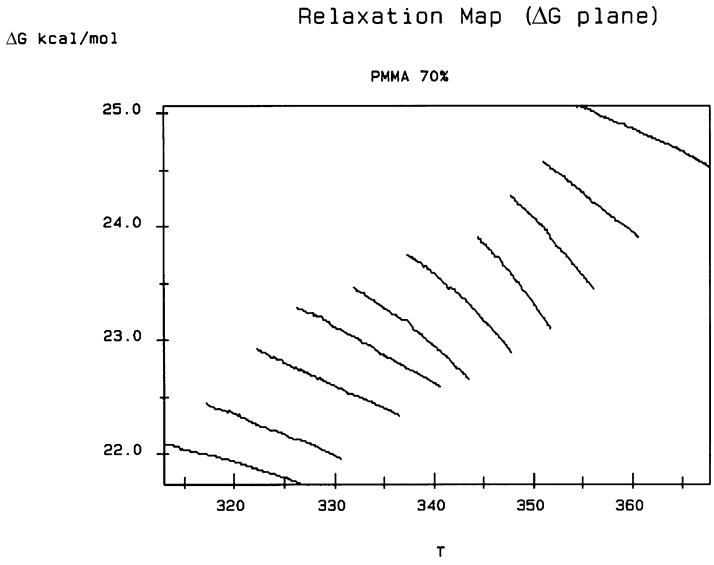


Figure 3.66: Relaxation map in the ΔG plane for 70 % PMMA.

Table 3.12: Values of the compensation coordinates in Figure 3.67 for 70 % PMMA.

Line	Compensation Coordinates		DOD Number
1	T_c = 103.10 °C	ΔG_c = 20.61 kcal/mol	45.19
2	T_c = 52.04 °C	ΔG_c = 26.32 kcal/mol	19.02

EBSCOhost - printed on 2/13/2023 12:32 AM via . All use subject to https://www.ebsco.com/terms-of-use

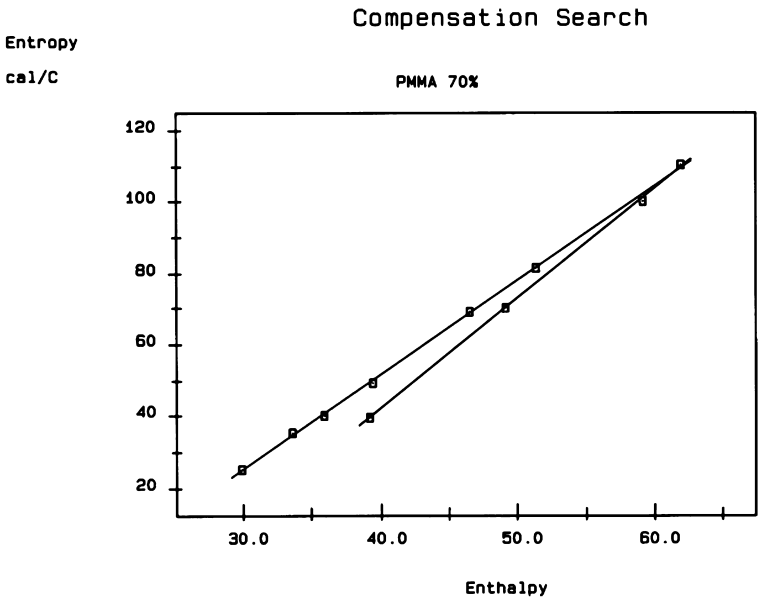


Figure 3.67: Compensation search in the EE plane for 70 % PMMA.

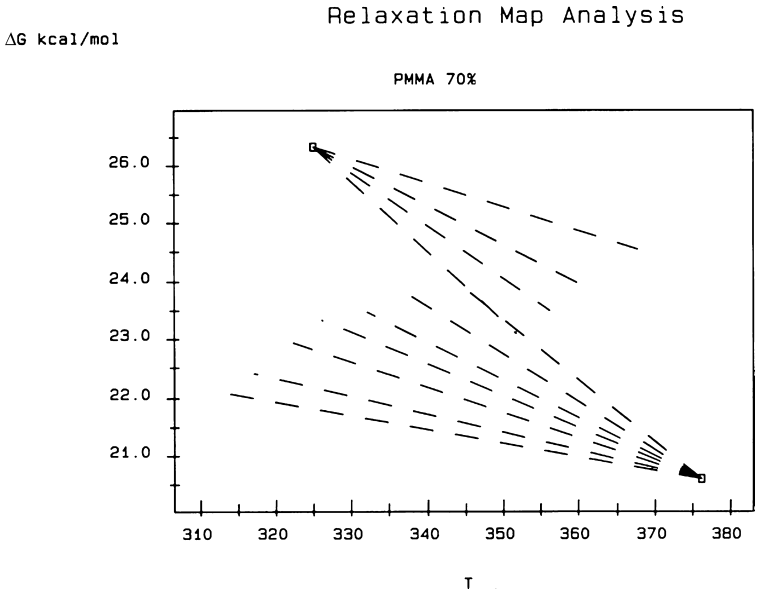


Figure 3.68: Reconstruction for 70 % PMMA of the positive and negative compensations of the spectral lines in Figure 3.66 as a result of the compensation search in Figure 3.67.

EBSCOhost - printed on 2/13/2023 12:32 AM via . All use subject to https://www.ebsco.com/terms-of-use

Table 3.13: Recapitulation of all the TWD and thermokinetic results for plasticized PMMA.

	T_g (K)	ΔH_g (kcal/m)	ΔS_g (cal/°C/m)	T_c^+ (K)	ΔG_c^+ (kcal/m)	DOD	T_c^- (K)	ΔG_c^- (kcal/m)	A_c (cal/°C/m)	$(\Delta G_c - A_C T_C)$ (kcal/m)	ΔG_g (kcal/m)	$(\Delta G_g - \Delta G_c^+)$ (kcal/m)	$(\Delta G_c^- - \Delta G_g)$ (kcal/m)
0 %	371.72	89.095	171.01	402.17	20.32	49.45	348.84	29.44	69.65	−7.8319	25.52	5.2	3.92
15 %	360.53	74.970	138.94	392.40	20.45	47.87	347.13*	26.74*	70.04	−7.018	24.88	4.43	1.86
30 %	347.22	62.686	111.82	376.25	20.61	45.19	325.19	26.32	69.57	−5.7275	23.85	3.24	2.47

*Note: Only 3 points to determine negative compensation for 15 %.

EBSCOhost - printed on 2/13/2023 12:32 AM via . All use subject to https://www.ebsco.com/terms-of-use

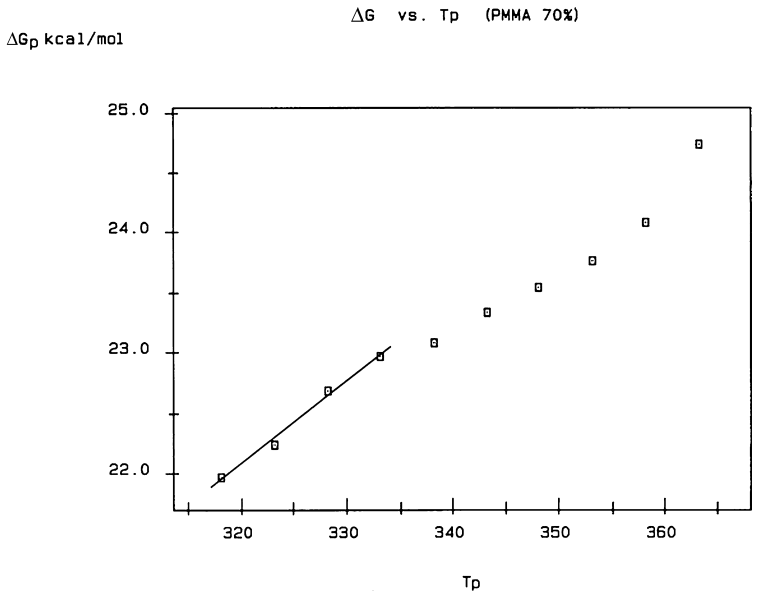


Figure 3.69: ΔG_p vs. T_p (K) for 70 % PMMA.

Table 3.13 contains the calculated values of T_g, ΔH_g, and ΔS_g, along with the values found for the positive and negative compensations and the DOD numbers. The values of ΔH_g and ΔS_g are calculated from the Z-line, which is drawn to pass through the positive and negative compensations for a given percentage of DBP. T_g is calculated according to the method proposed in Part I, Chapter 2: by the intercept of the ΔG_p vs. T line with the Z-line. For determining the value of T_g with accuracy, the Z-line is plotted on the same graph as the ΔG_p vs. T_p, and the intercept of these two curves is assumed to represent T_g of the plasticized PMMA. Table 3.13 also includes A_c and $(\Delta G_c - A_c T_c)$ to derive the expression of the entropy, enthalpy, and free energy as a function of T_p. A_c is obtained from a compensation search in the normalized ΔG plane (Part I, Chapter 2). The column labeled ΔG_g in the table is the calculated free energy of activation at T_g, which is a point on the Z-line. The difference between this value and the positive or negative compensation ΔG_c is also tabulated in the last two columns of Table 3.13. Some of the results from the table are graphically represented in Figures 3.70 to 3.76.

The influence of the percentage of plasticizer is to depreciate the values of T_g, T_c^+, and T_c^- (Figure 3.70). The lowering of T_g in proportion to the percent plasticizer content is classical.

What is less expected is the decrease of the DOD number with the percentage of plasticizer (Figure 3.71). The classical understanding would be that the dopant favors entropic disorder in the structure and that an increase of the DOD would result. There is no experimental error which could justify such a steady decrease of the DOD with the percentage of plasticizer. The effect is real and needs an additional explanation.

EBSCOhost - printed on 2/13/2023 12:32 AM via . All use subject to https://www.ebsco.com/terms-of-use

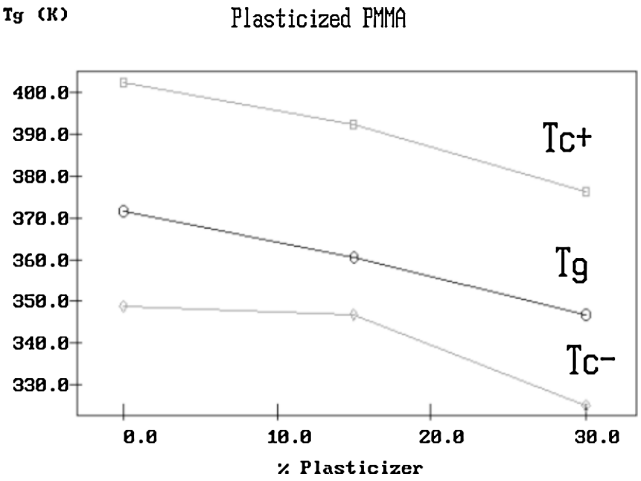


Figure 3.70: Influence of the relative plasticizer content on the depreciation of T_g, T_c^+, and T_c^-.

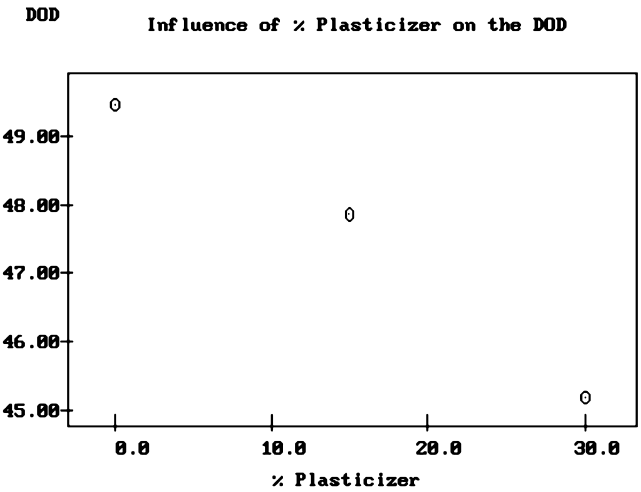


Figure 3.71: Influence of the relative plasticizer content on the DOD characteristic of the positive compensation.

Figure 3.72 shows how the compensation point is shifted to higher ΔG_c values and lower T_c temperatures as the percentage of plasticizer increases in the PMMA. One of the possible reasons for a decrease of the DOD number could have been the processing condition. However, the difference $(T_c - T_g)$ remains approximately equal to 30 °C as the percentage of plasticizer increases. One other possible reason might be the polymerization method used to create the polymer network. The use of radiation to polymerize might result in a three-dimensional network, which has a certain amount of crosslinks. The decrease of the DOD would essentially be due to the increase of

EBSCOhost - printed on 2/13/2023 12:32 AM via . All use subject to https://www.ebsco.com/terms-of-use

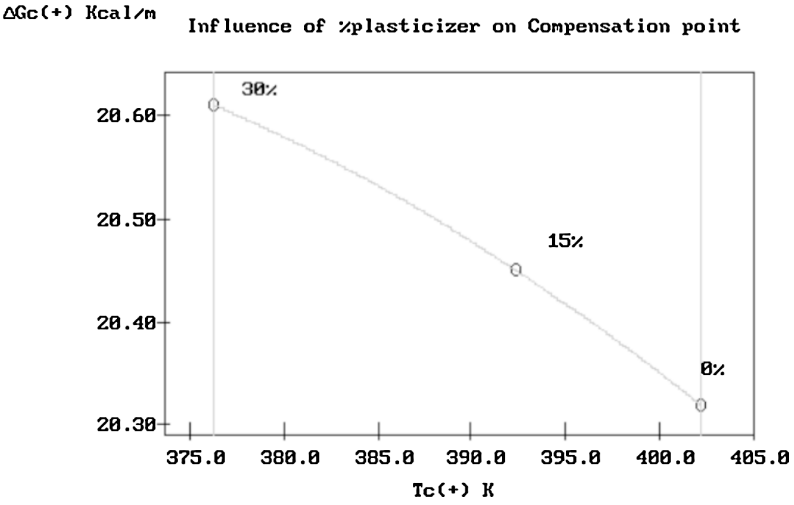


Figure 3.72: Influence of the relative plasticizer content on the ΔG_c, T_c^+ compensation point coordinates.

the crosslink density in the case of the more plasticized PMMA. Such an explanation would not be incompatible with the smooth departure from the straight line behavior normally observed for the ΔG_p vs. T_p relationship. The dopant could very well swell the network structure created by the crosslinks, resulting in the curvature observed in Figures 3.65 and 3.69.

Figure 3.73 plots $(\Delta G_c - A_c \cdot T_c)$ against plasticizer content. We submitted in Part I, Chapter 2 the idea that this quantity could be related to the true intermolecular energy barrier which needs to be overcome by thermal energy, since $(A_c \cdot T_c)$ seems to be equal to the energy pumped into the free energy by action of the voltage field. The absolute value of $(\Delta G_c - A_c \cdot T_c)$ actually decreases with the percentage of plasticizer. This sounds more like the effect of a true plasticizer. The DOD number is proportional to the value of $(\Delta G_c - A_c \cdot T_c)$. This is shown in Figure 3.74. This relationship is to be expected when A_c is constant since DOD = 100 – $(\Delta G_c / T_c)$ with ΔG_c in cal/m. This shows, once again, that the DOD might be related to the true fundamental property of the coupling kinetic relaxation.

The enthalpy and entropy of activation at T_g are determined from the slope and intercept of the Z-line. A plot of ΔH_g vs. ΔS_g when the plasticizer content varies is shown in Figure 3.75. The fact that the points in Figure 3.75 align on a straight line indicates that the corresponding Z-lines in the ΔG plane compensate. The slope and intercept of the straight line in Figure 3.75 provide the coordinates of the point of compensation for the Z-lines in the ΔG plane. We find

$$\Delta G_{g,c} = 12.88 \text{ kcal/m}$$
$$T_{g,c} = 446.0 \text{ K} (173 \text{ °C})$$

EBSCOhost - printed on 2/13/2023 12:32 AM via . All use subject to https://www.ebsco.com/terms-of-use

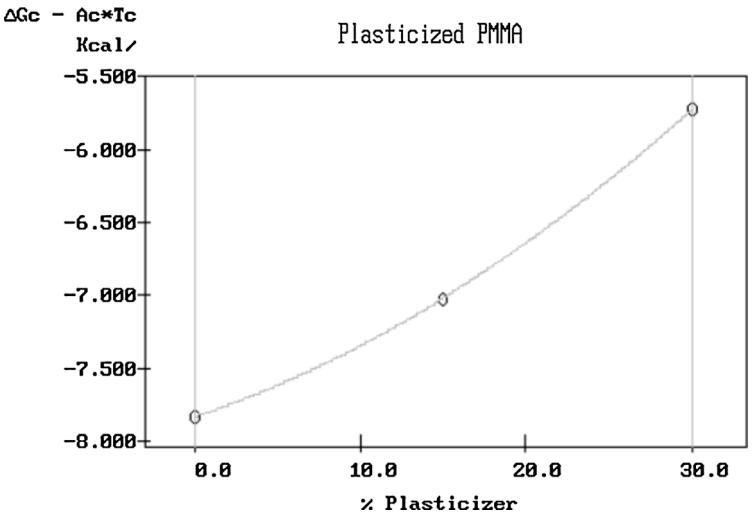


Figure 3.73: Influence of the relative plasticizer content on the value of $(\Delta G_c - A_c T_c)$, where $A_c T_c$ has been considered in Chapter 4 as the increase of ΔG by the voltage field due to the entropic polarization of the electronic clouds of the atoms.

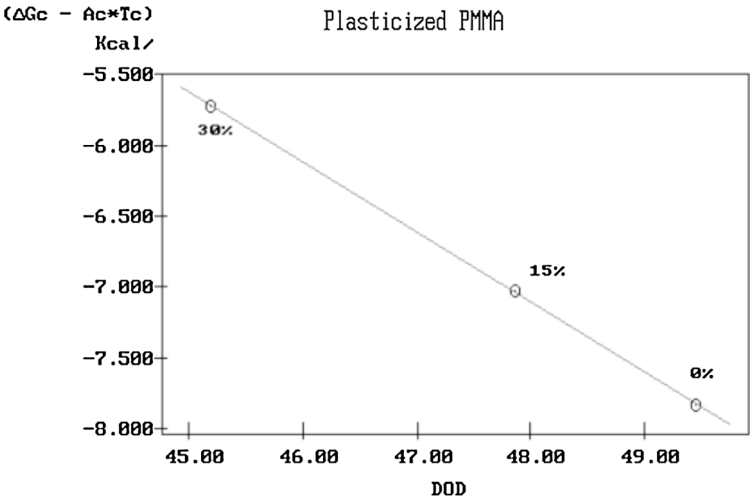


Figure 3.74: Proportionality between the DOD and $(\Delta G_c - A_c T_c)$ at all relative plasticizer contents. See text.

The point of compensation of the Z-lines is independent of the concentration of plasticizer. The value of $T_{g,c}$ seems to be related to the thermodynamic value of the T_{LL} transition, T_X, considered in Part I, Chapter 3, as the rate independent endset temperature for the structuring of the free energy (Dual-Phase model).

EBSCOhost - printed on 2/13/2023 12:32 AM via . All use subject to https://www.ebsco.com/terms-of-use

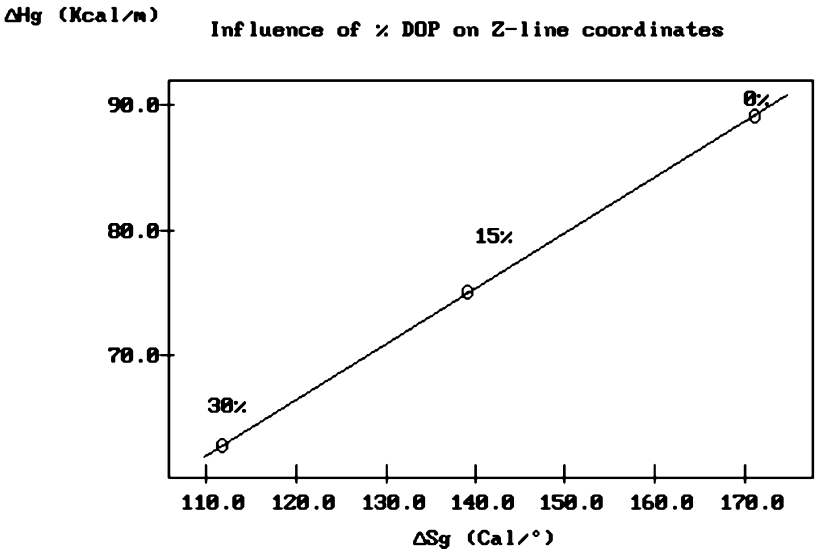


Figure 3.75: Influence of the relative plasticizer content on the value of ΔH_g vs. ΔS_g for the plasticized PMMA.

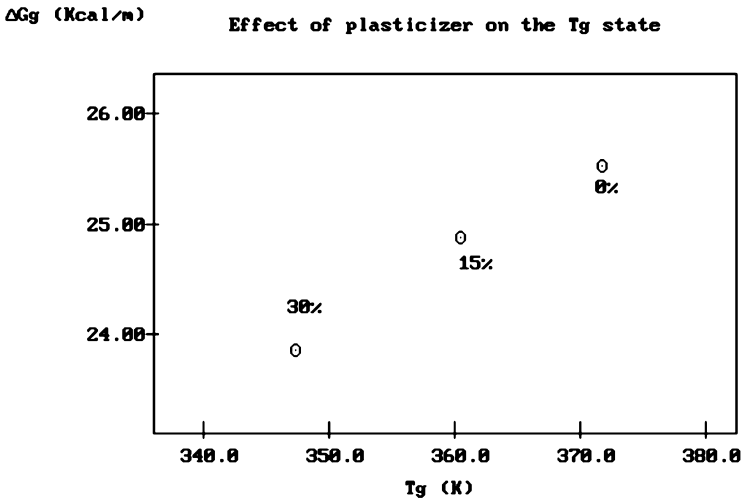


Figure 3.76: Quasi-proportionality between the value of ΔG_g (at T_g) and T_g (K) when the relative plasticizer content varies.

Another possible interesting correlation is displayed in Figure 3.76. The value of the free energy of activation at T_g decreases with T_g, as the percentage of DBP increases.

The compensation of the Z-lines for the PMMA doped at various content of plasticizer is an interesting and very simple observation. This correlation can be quan-

EBSCOhost - printed on 2/13/2023 12:32 AM via . All use subject to https://www.ebsco.com/terms-of-use

titatively used to determine the plasticizer content. The same remarkable result was found in the case study of NR/SBR rubber phases in blends of various concentrations. We concluded at the time that impurities acting as plasticizer were migrating from one phase to another, facilitated by the relative concentration of the phases in presence. It is certainly true that in the case of PMMA plasticized by DBP, the Z-lines also compensate. However, the question remains to see whether the compensation of the Z-lines occurs when any other external parameter varies, and thus is a common feature characteristic of the inner relaxation process giving rise to the overall kinetics. In other words, to discern whether compensation of the Z-lines is a general phenomenon is the key to finding the kinetic parameters needed to generate the Dual-Phase solutions (Part I, Chapter 3).

For the case study under consideration in this section, thermal-windowing analysis provides additional information regarding the structure compared to DMA or DSC, which only report the location of T_g. An indication of the presence of crosslinks in 100 % PMMA due to the use of the gamma ray polymerization technique is found in the high value of T_g reported for DMA, 124 °C, which is rather high for a PMMA. The decrease of the DOD number with the plasticizer content seems to suggest that a certain amount of crosslinks is created in the morphology: the more, the higher the plasticizer content. All other factors which are expected to vary with an increase of plasticizer content actually behave as such, including a depreciation of T_g, ΔG_g, and ΔS_g.

II.3.6 Case study: characterization of the adhesive strength of pressure-sensitive adhesives by TWD

This work, conducted in collaboration with Moore Research Co., was introduced in Part II, Chapter 2 (Figure 2.20), which provided the TSD curve for the glue on a paper substrate. The present thermal-windowing study is carried across the adhesive T_g peak observed in Figure 3.20, for a temperature of polarization between −78 °C and −52 °C. The experimental conditions used during thermal-windowing are displayed in the header of Figure 3.77. The thickness of the material is 0.1 mm and the voltage field applied is 400 V/mm. The window width is 2 °C. Independent adhesive strength tests conducted at Moore Research have determined a classification between three samples into three groups: NS ("not sticky"), TS ("too sticky"), and GS ("good stickiness"). Since the stickiness of pressure-sensitive adhesives (PSAs) relates to the amount of intermolecular bonding at the interface between the glue and the substrate they stick to, it is believed that TWD spectroscopy can play a quantitative role in determining the amount of stickiness to a given substrate. The substrate chosen was the stainless steel surface of the bottom electrode of the TSD cell. The pressure applied from the top electrode is monitored, so as to be identical for the three specimen tested. Figures 3.77 and 3.78 display thermal-window elementary peaks isolated at the T_g relaxation process for one of the samples subjected to this analysis.

EBSCOhost - printed on 2/13/2023 12:32 AM via . All use subject to https://www.ebsco.com/terms-of-use

moore 313	Anneal Temp : Inactive	Freeze Temp : -114.0C
MOORE.BTC	Anneal Time : Inactive	Freeze Time : 5.0min
Date : 02/08/1991	Polar Time : 2.00min	R3 Rate : 7.0C/m
Time : 15:13:42	Polar Field : 4000.0V/mm	End ISO Temp: -24.0C
	Polar Temp : -64.0C	End ISO Time: 0.0min
Solomat TSC/RMA	Thickness : 0.100mm	Window Width: 2.0C
	Area : 78.0mm^2	

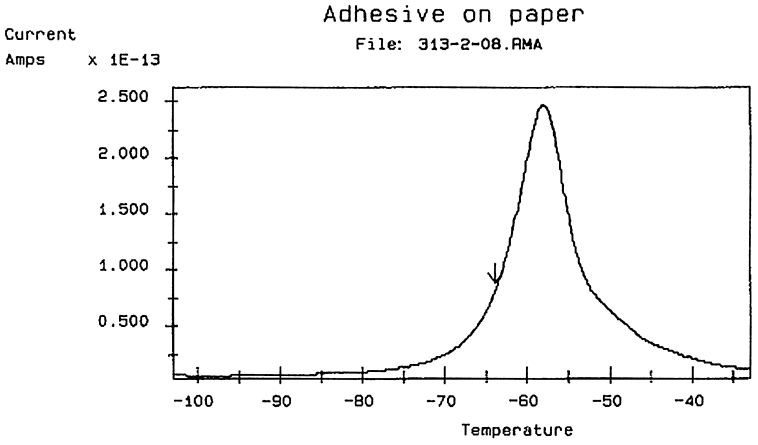


Figure 3.77: TWD trace at $T_p = -64\,°C$ for a pressure-sensitive adhesive (PSA) on paper. See Figure 3.20 for the TSD study.

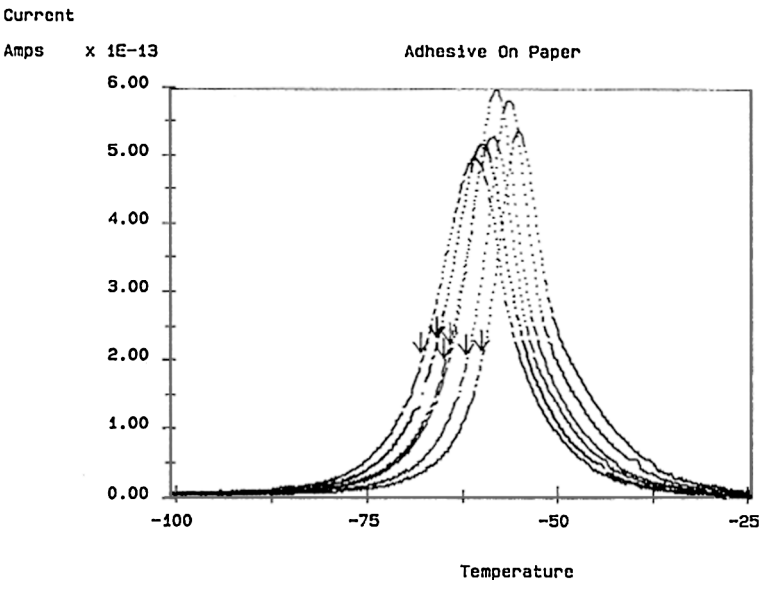


Figure 3.78: TWD multiplot at several T_p values around T_g of the PSA showing the deconvoluted elementary peaks.

EBSCOhost - printed on 2/13/2023 12:32 AM via . All use subject to https://www.ebsco.com/terms-of-use

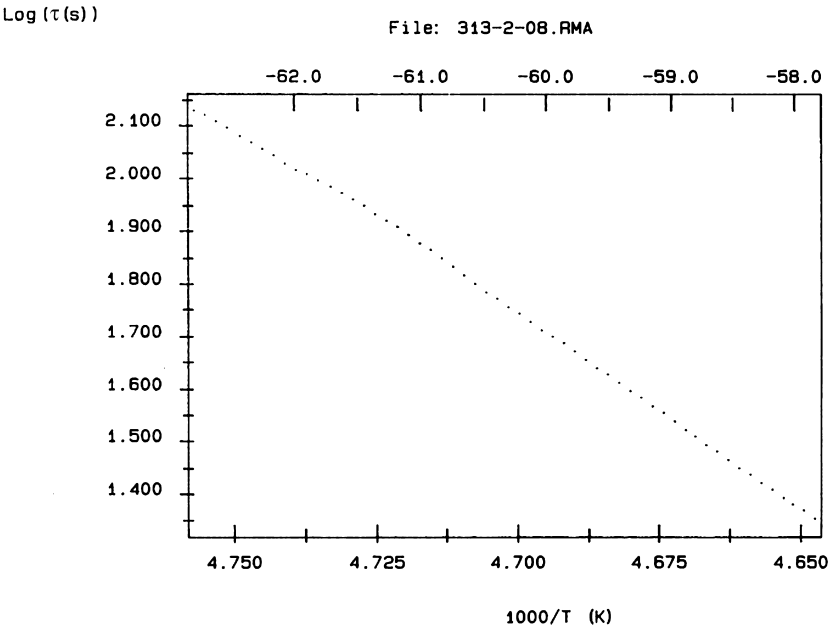


Figure 3.79: Arrhenius transform for the TWD peak of Figure 3.77.

Note that although the glue on the paper is extremely thin (a simple single coat), the current is quite large and there is no problem of sensitivity or resolution. The Arrhenius transform for the peak of Figure 3.77 is a very good straight line (Figure 3.79), from which we calculate the kinetic parameters for that temperature of polarization.

The thermokinetic constants for samples NS, TS, and GS are found in Figure 3.80.

The compensation search for one of the samples (GS) is shown in Figure 3.81.

The behavior is typical of a glass transition temperature, with the display of positive and negative compensation lines crossing at T_g. The intercept of the positive and negative compensations provides the coordinates of the Z-line and the calculation of T_g can then proceed from the intercept of the ΔG_p vs. T_p plot and the Z-line. Table 3.14 summarizes our results.

The T_g values do not vary significantly from a too sticky to a non-sticky specimen. This is probably the reason why other characterization techniques, such as DMA or DSC, are at the limit of their capabilities in determining the peeling strength of labels or identical PSAs, since the characterization information is almost exclusively based on the shift of the glass transition temperature. The DOD number is tabulated in the fifth column of Table 3.14. The DOD is lower for the non-sticky material and is larger for the too sticky material, the good material falling in between. The same trend is observed for the values of ΔG_c and $(\Delta G_c - A_c \cdot T_c)$. Although the difference between these samples is indeed rather small, it is much beyond the error of measurement and is related to the adhesive strength to the substrate. Notice that ΔH_g and ΔS_g do not

EBSCOhost - printed on 2/13/2023 12:32 AM via . All use subject to https://www.ebsco.com/terms-of-use

Thermokinetics (NS)

T_p °C	T_m °C	Enthalpy kcal/m	Entropy cal/°C	ΔG_p kcal/m
-78.0	-72.1	14.9441	9.3657	13.1178
-76.0	-68.3	15.5451	10.8106	13.4154
-74.0	-66.6	17.5528	20.0681	13.5593
-72.0	-64.4	18.9843	26.1528	13.7276
-70.0	-63.0	21.0242	35.3053	13.8573
-68.0	-61.1	26.7307	61.7992	14.0618
-66.0	-60.2	28.3154	68.7511	14.0839
-64.0	-58.7	31.3650	82.2284	14.1792
-62.0	-57.3	34.5603	96.1284	14.2772
-60.0	-55.8	39.7642	119.2560	14.3627
-58.0	-54.3	37.1540	105.9305	14.3789
-56.0	-52.2	33.4675	87.3860	14.5047
-54.0	-50.6	29.5506	68.3465	14.5827
-52.0	-48.1	25.0992	46.7699	14.7630

Thermokinetics (TS)

T_p °C	T_m °C	Enthalpy kcal/m	Entropy cal/°C	ΔG_p kcal/m
-76.0	-68.7	16.5118	15.8871	13.3820
-74.0	-66.9	17.5730	20.3663	13.5201
-70.0	-63.3	21.0169	35.4705	13.8164
-68.0	-61.7	23.9629	48.8529	13.9480
-66.0	-60.2	26.6685	60.9500	14.0518
-64.0	-58.9	30.1976	76.8408	14.1378
-62.0	-57.6	33.9702	93.6441	14.2113
-60.0	-56.1	38.1856	112.1940	14.2883
-58.0	-54.7	36.7404	104.2773	14.3208
-56.0	-53.1	35.0283	95.1315	14.3848
-54.0	-51.0	29.5450	68.5947	14.5228
-52.0	-48.3	24.6346	44.8141	14.7307
-50.0	-44.2	18.5418	15.6176	15.0591

Thermokinetics (GS)

T_p °C	T_m °C	Enthalpy kcal/m	Entropy cal/°C	ΔG_p kcal/m
-76.0	-71.8	14.3680	6.2526	13.1488
-76.0	-67.7	16.3819	14.7932	13.4676
-74.0	-66.2	17.2874	18.6416	13.5778
-72.0	-64.1	19.5568	28.8517	13.7595
-70.0	-62.8	21.7600	38.8661	13.8702
-68.0	-61.4	24.3469	50.5379	13.9865
-66.0	-59.9	27.3935	64.1041	14.1139
-64.0	-58.8	31.4289	82.5933	14.1669
-62.0	-57.2	33.6123	91.7393	14.2559
-60.0	-55.8	35.1763	97.9451	14.3140
-58.0	-54.3	35.5009	98.2729	14.3722
-56.0	-52.4	28.8242	66.1492	14.4698
-54.0	-50.3	25.0807	47.7854	14.6157
-52.0	-47.5	21.0957	28.4415	14.8101
-50.0	-43.2	16.4314	5.8618	15.1242

Figure 3.80: Thermokinetic constants for the three samples studied by TSD in Figure 3.20: samples NS (non-sticky), TS (too sticky), and GS (good stickiness).

provide the proper order. The reason why the DOD acquires a larger value for the too sticky specimen is unclear. A linear dependence is also observed between $(\Delta G_c - A_c \cdot T_c)$ and the DOD, as was already mentioned in the case of the PMMA plasticizer effect. It is simpler to reason from the $(\Delta G_c - A_c \cdot T_c)$ parameter if this parameter is truly representative of the energy barrier to overcome for thermal motion to occur. The too

EBSCOhost - printed on 2/13/2023 12:32 AM via . All use subject to https://www.ebsco.com/terms-of-use

sticky material has a greater amplitude for this parameter, which can be attributed to the more intense intermolecular bonding at the interface.

In conclusion, the TWD spectroscopy technique can be used with ease and reliability to classify adhesives on substrate with regard to their bonding strength. This application of the TWD technique seems remarkable.

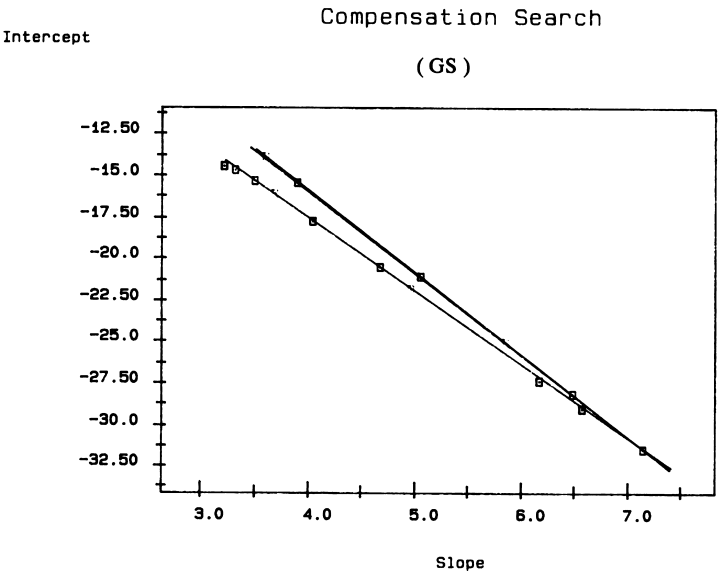


Figure 3.81: Compensation search in the Arrhenius plane for sample GS showing the positive and negative compensation lines crossing at T_g.

Table 3.14: Results from the analysis of Figure 3.80. See text.

	T_g (K)	ΔG_c^+ (kcal/m)	T_c^+ (K)	$(\Delta G_c - A_c T_c)$ (kcal/m)	DOD	ΔH_g (kcal/m)	ΔS_g (cal/°C/m)	$(\Delta G_g/T_g)$
NS	210.02	13.095	222.84	−2.504	41.24	41.08	125.60	0.070
TS	210.24	12.994	224.27	−2.704	42.05	40.48	122.55	0.070
GS	210.33	13.060	224.14	−2.630	41.73	40.04	120.36	0.070

Note: $A_c = 0.070$ kcal/m.
Legend: NS “Not sticky”, TS “Too sticky”, GS “Good stickiness”.

II.3.7 Case study: characterization by TWD of the influence of the TiO_2 content on the amorphous state of polystyrene

In Part II, Chapter 2, the TSD traces for a pigment-loaded acrylic film were provided (Figure 2.19). The purpose of the present case study is to investigate the influence of the

EBSCOhost - printed on 2/13/2023 12:32 AM via . All use subject to https://www.ebsco.com/terms-of-use

relative TiO_2 content on the glass transition relaxation characteristics of polystyrene. The samples were provided by DuPont Co., which specified that the TiO_2 is an R902 TiO_2, i. e., TiO_2 coated with a mixture of alumina and silicone. The polystyrene was not characterized, but its TSD trace (not shown) does not reveal anything in particular about the material. The TSD traces for the filled polystyrene do not reveal much either on the change of mobility due to TiO_2.

The relaxation map for the 5 % TiO_2-filled polystyrene is displayed in Figure 3.82. The thermal-window conditions are provided in the header. The temperature of polarization is below T_g in this case, from 70 °C to 90 °C, covering the temperature range below T_g only.

PS+tio2 5%	Anneal Temp : Inactive	Freeze Temp : 25.0C
	Anneal Time : Inactive	Freeze Time : 1.0min
Date : 05/06/1992	Polar Field : 600.0V/mm	R3 Rate : 7.0C/m
Time : 13:26:16	Polar Time : 2.00min	End ISO Temp: 105.0C
	Tp Range: 70.0 90.0C	End ISO Time: 0.0min
Solomat TSC/RMA	Thickness : 0.638mm	Window Width: 2.0C
	Area : 25.0mm^2	Depol time : 2.0min

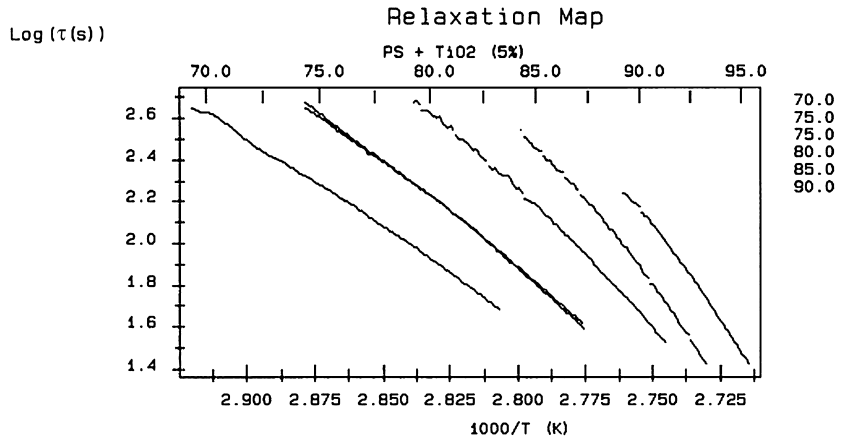


Figure 3.82: Relaxation map for T_p between 70 °C and 90 °C for a pigment-loaded (5 % TiO_2) polystyrene film. The TSD traces were provided in Figure 3.19 for TiO_2-loaded acrylic film.

The thermokinetic parameters are tabulated in Table 3.15 for the six polarization temperatures.

The compensation search (EE plot) is seen in Figure 3.83, and the resulting compensation for this particular filler content is shown at Figure 3.84.

EBSCOhost - printed on 2/13/2023 12:32 AM via . All use subject to https://www.ebsco.com/terms-of-use

Table 3.15: Thermokinetic parameters calculated from Figure 3.82 after conversion to the Eyring plane via equation (2.5) of Part I. TiO_2 loading: 5 %.

T_p (°C)	T_m (°C)	ΔH_p (kcal/mol)	ΔS_p (cal/°C/mol)	ΔG_p (kcal/mol)
70.0	83.3	38.3753	41.0157	24.3003
75.0	87.3	46.7533	63.4229	24.6720
75.0	87.2	45.1644	58.9305	24.6472
80.0	91.2	56.0614	87.8061	25.0518
85.0	93.2	72.6214	132.5771	25.1376
90.0	95.4	81.0696	154.4781	24.9694

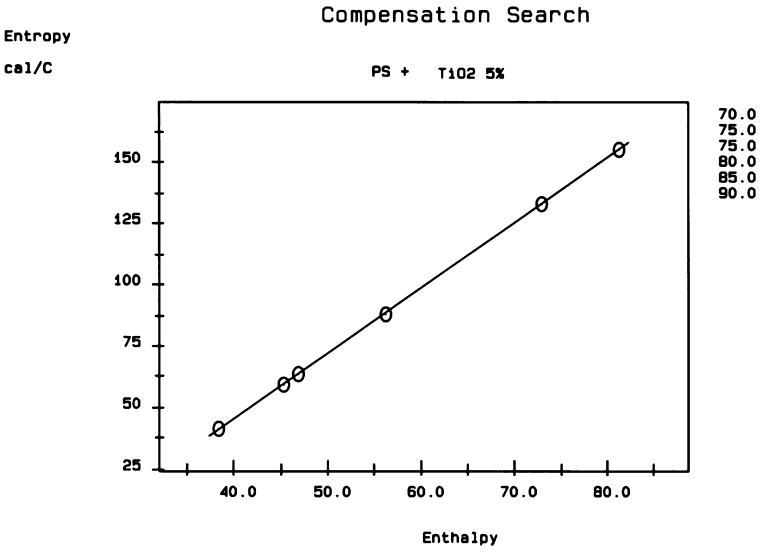


Figure 3.83: Compensation search in the EE plane according to Table 3.15. One positive compensation line is observed for this T_p range. TiO_2 loading: 5 %.

The only compensation observed in this temperature range is a positive compensation with the following characteristics:

$$T_c = 102.31\,°\text{C}$$
$$\Delta G_c = 22.99\,\text{kcal/m}$$
$$\text{DOD} = 38.37$$

Table 3.16 provides the thermokinetic parameters at various polarization temperatures for the 10 % filler content.

EBSCOhost - printed on 2/13/2023 12:32 AM via . All use subject to https://www.ebsco.com/terms-of-use

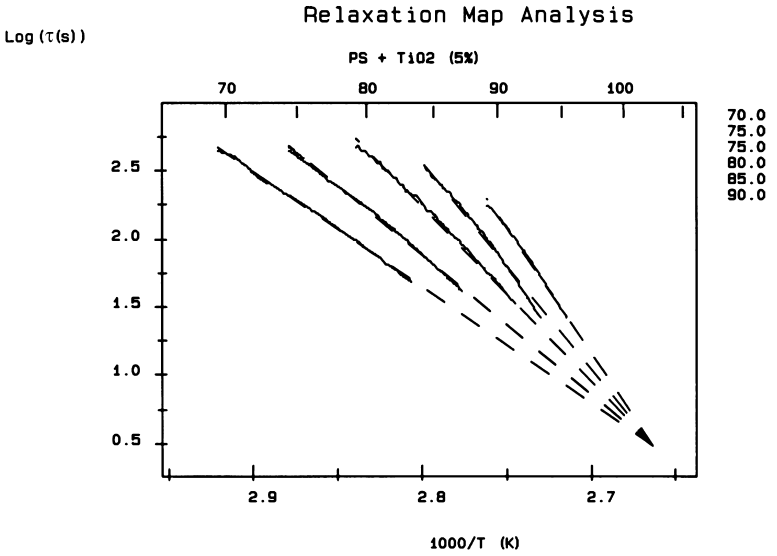


Figure 3.84: Reconstruction in the Arrhenius plane of the compensation of the spectral lines according to the compensation search in Figure 3.83. One sees that the spectral lines are only approximately linear.

Table 3.16: Thermokinetic parameters for a 10 % TiO_2-loaded polystyrene film.

T_p (°C)	T_m (°C)	ΔH_p (kcal/mol)	ΔS_p (cal/°C/mol)	ΔG_p (kcal/mol)
65.0	77.1	28.0489	12.9653	23.6645
70.0	83.2	32.1743	23.3185	24.1724
75.0	87.3	43.6764	54.6961	24.6335
80.0	90.6	59.1223	96.6369	24.9940
85.0	93.3	74.9116	138.8659	25.1754
90.0	95.2	92.1752	185.0530	24.9714

The compensation search for this 10 % TiO_2 is studied in Figure 3.85. Notice a group of points situated below the zero entropy line in this figure, which corresponds to polarization temperatures located between −40 °C and −10 °C.

The TWD in the ΔG plane for the 10 % TiO_2 is displayed in Figure 3.86. The low-temperature relaxation modes gather into lines which have apparently positive slopes (negative entropies), whereas the line for $T_p = -10$ °C is horizontal (zero entropy of activation). The coordinates of the compensation point for this material are

$$T_c = 98.43\,°\text{C}$$
$$\Delta G_c = 23.34\,\text{kcal/m}$$
$$\text{DOD} = 37.18$$

EBSCOhost - printed on 2/13/2023 12:32 AM via . All use subject to https://www.ebsco.com/terms-of-use

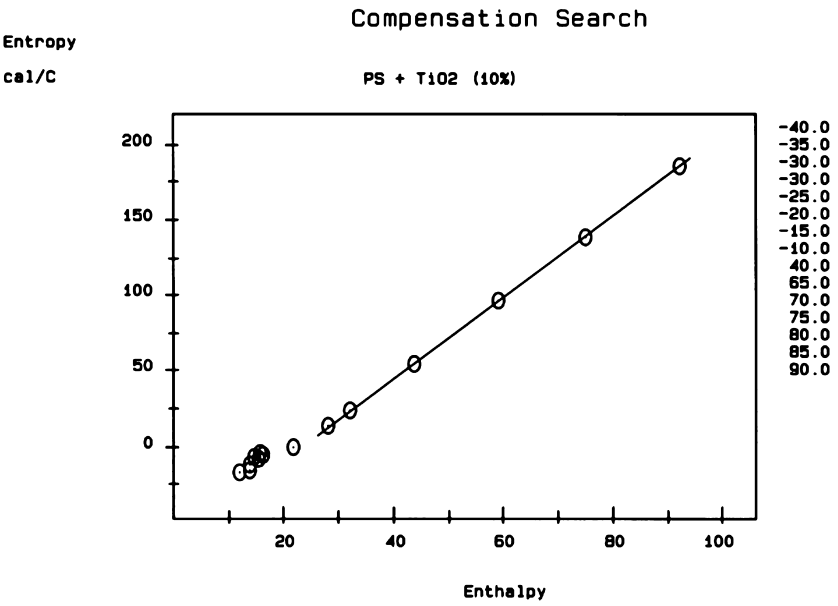


Figure 3.85: Compensation search in the Arrhenius plane according to Table 3.16. One positive compensation line is observed for this T_p range. TiO_2 loading: 10 %.

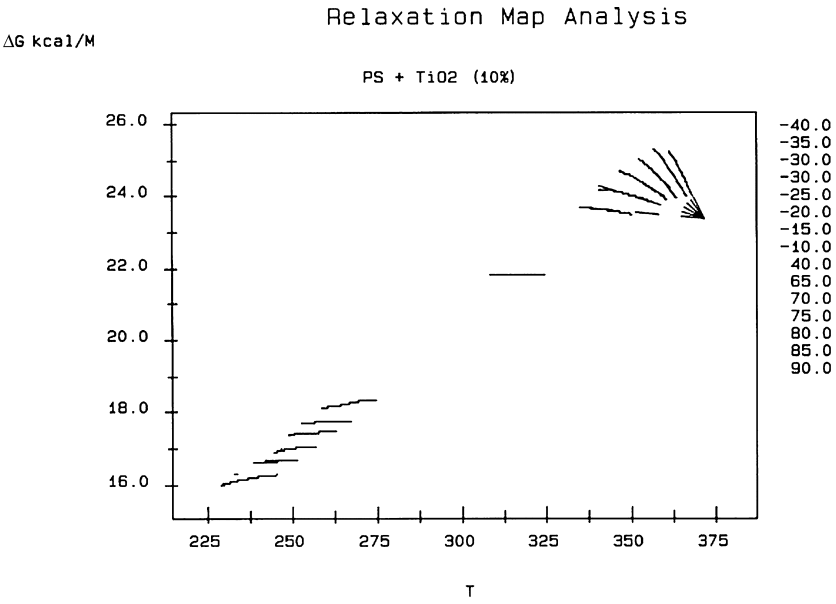


Figure 3.86: Reconstruction in the ΔG plane of the compensation of the spectral lines according to the compensation search in Figure 3.85. Like for the 5 % loading, the spectral lines are approximately linear. The spectral lines at the low T_p values (with negative entropies) are discussed in the text.

EBSCOhost - printed on 2/13/2023 12:32 AM via . All use subject to https://www.ebsco.com/terms-of-use

Table 3.17: Thermokinetics for the pure polystyrene film (0 % loading). T_p is below T_g.

T_p (°C)	T_m (°C)	ΔH_p (kcal/mol)	ΔS_p (cal/°C/mol)	ΔG_p (kcal/mol)
70.0	82.6	40.8472	48.3997	24.2383
75.0	86.6	48.4261	68.3867	24.6166
80.0	89.0	67.3818	120.4209	24.8539
85.0	90.9	86.0170	171.0736	24.7453

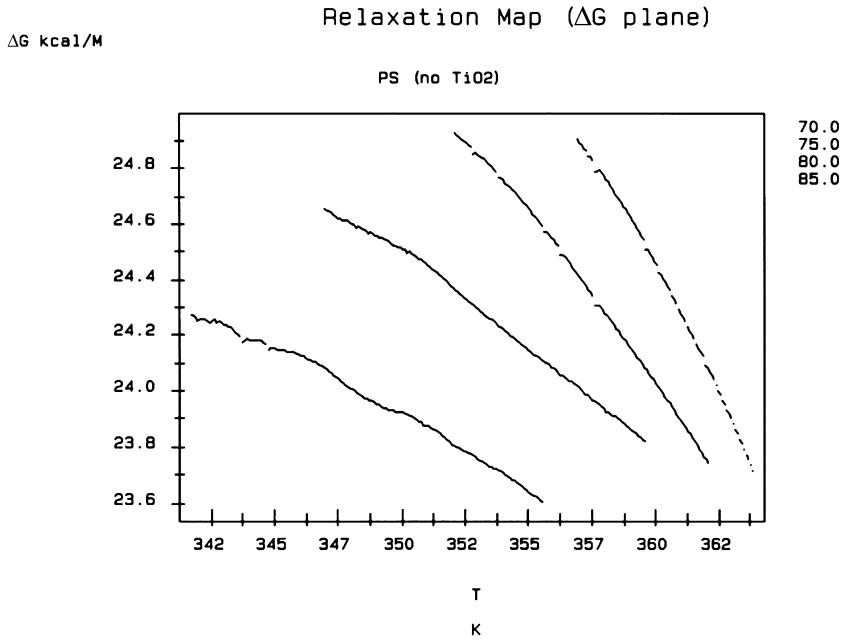


Figure 3.87: Relaxation map in the ΔG plane for the data in Table 3.17.

For the unfilled polystyrene, the equivalent results are confined in Table 3.17 (thermokinetic parameters), Figure 3.87 (relaxation map in the ΔG plane), and Figure 3.88 (compensation search). The coordinates of the compensation point for the unfilled polystyrene are

$$T_c = 94.33\,°\mathrm{C}$$
$$\Delta G_c = 23.16\,\mathrm{kcal/m}$$
$$\mathrm{DOD} = 36.97$$

EBSCOhost - printed on 2/13/2023 12:32 AM via . All use subject to https://www.ebsco.com/terms-of-use

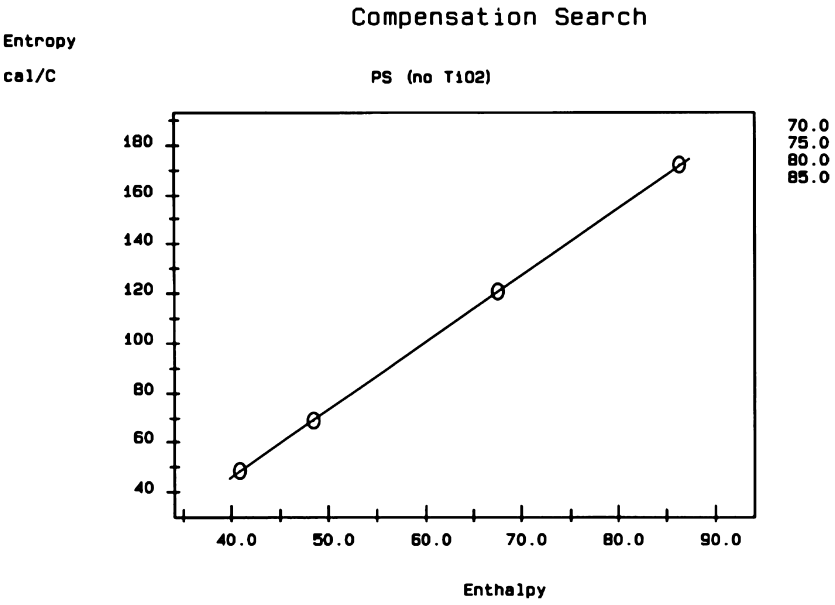


Figure 3.88: Compensation search in the EE plane for the pure polystyrene film. One positive compensation line is observed.

II.3.7.1 Discussion

Both the DOD and T_c vary in the same way, increasing from the unfilled polystyrene to reach a maximum for 5 % TiO_2 and decreasing slightly thereafter. The variation of ΔG_c shows a minimum for 5 %. The influence of the TiO_2 content on the mobility is best seen graphically in Figures 3.89 and 3.90. Figure 3.89 is the intensity at the elementary peak maximum against T_p, showing that the polarizability of the system is greater for the 5 % TiO_2 content.

The mobility, which is followed with the entropy of activation (Figure 3.90), shows that the TiO_2 presence actually results in a reduction of the mobility with respect to the unfilled polymer. The increase of the current intensity up to 5 % filler content (Figure 3.89) is due to the polarizability of the filler which first increases as the filler content increases. However, the current is also dependent on the mobility, and Figure 3.90 demonstrates that the mobility actually decreases with TiO_2 content. This is probably due to the bulkiness of the filler inside the styrene structure.

The free energy of activation at T_p is plotted against T_p in Figure 3.91. Low T_ps do not separate the different polystyrenes. However, the plateau reached for either 0 % or 5 % and 10 % TiO_2 content are very different. The curves are actually seemingly shifted along the $0.07T_p$ line by an amount which corresponds to approximately 0.4 kcal/m on the ΔG_p axis. The effect of the filler is to increase T_g (by approximately 5 °C), increase the value of ΔG_g (the value of the plateau zone in Figure 3.91), decrease the internal

EBSCOhost - printed on 2/13/2023 12:32 AM via . All use subject to https://www.ebsco.com/terms-of-use

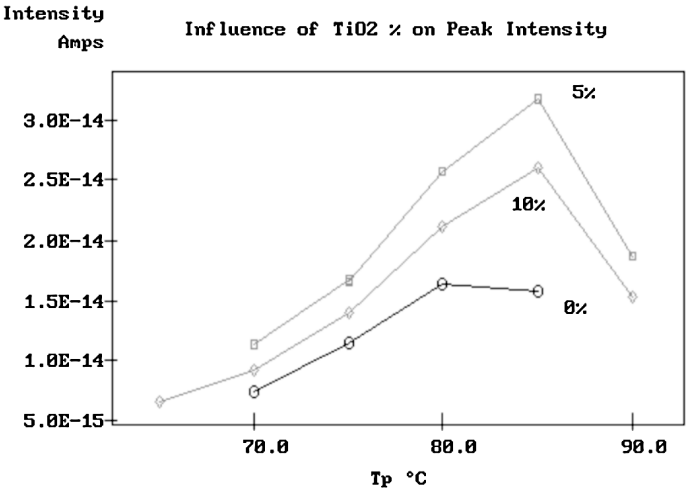


Figure 3.89: Influence of the relative loading content (0 %, 5 %, 10 %) on the intensity of the Debye peak at the maximum T_m (plotted against T_p).

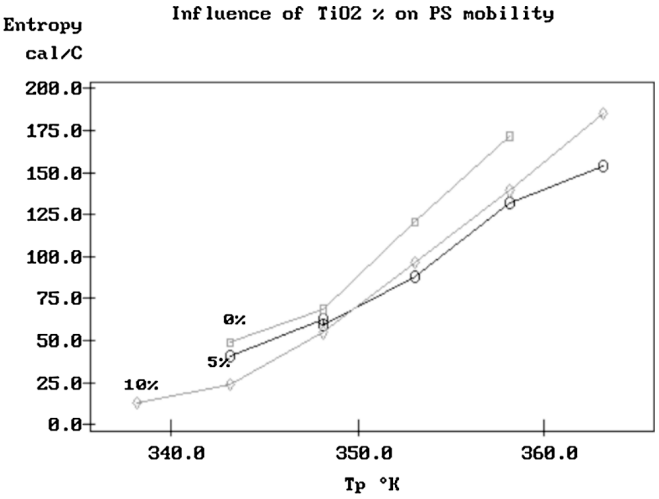


Figure 3.90: Entropy of activation vs. T_p for the three TiO_2 loading contents.

mobility (Figure 3.90), and increase to a certain extent (up to 5 % filler content) the polarizability, which should have an influence on the dielectric properties.

We plot in Figure 3.92 the dielectric strength calculated from the relaxation map against the polarization temperature. The dielectric strength can be increased by as much as 100 % by the addition of 5 % TiO_2 filler. This might have industrial applications.

EBSCOhost - printed on 2/13/2023 12:32 AM via . All use subject to https://www.ebsco.com/terms-of-use

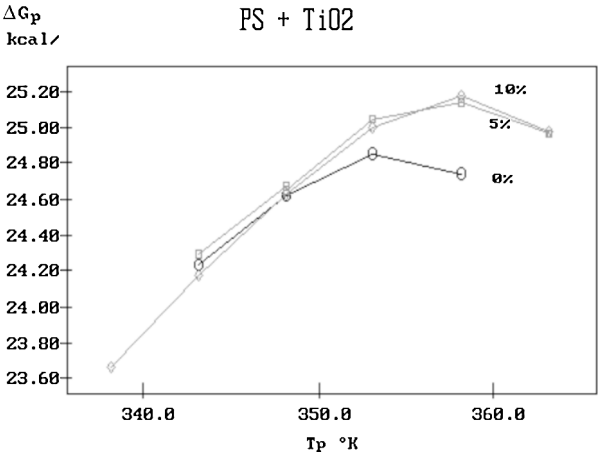


Figure 3.91: ΔG_p vs. T_p for the three TiO_2 loading contents.

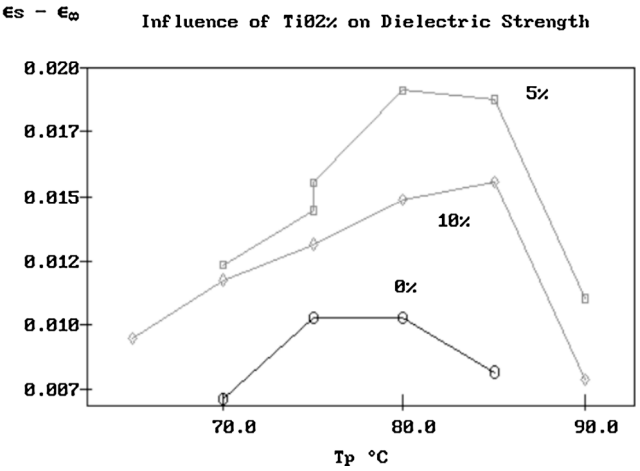


Figure 3.92: Influence of the TiO_2 loading content on the dielectric strength, $\epsilon_s - \epsilon_\infty$, of the polystyrene film. The maximum changes occur for 5 %.

II.3.8 Case study: influence of physical aging on the DOD and other thermokinetic parameters studied by TWD

A few studies of the use of TSD to characterize physical aging can be found in the literature [99, 150, 229, 264]. The method of spontaneous depolarization (Part II, Chapter 1) seems to be ideally fitted to aging studies in the case of polar materials for which the sample spontaneously depolarizes in the TSD cell as it is thermally stimulated. No polarization is necessary; no pre-heating to the polarization temperature is required either. However, for short aging times or low aging temperatures, the material polar-

EBSCOhost - printed on 2/13/2023 12:32 AM via . All use subject to https://www.ebsco.com/terms-of-use

ization states differ very little, and it seems difficult to measure any change due to either aging or disorientation. By quenching a polymer from above T_g to the glassy state, the cooperative motions between the conformers (Part I, Chapter 3) are frozen in, but the glass obtained is thermodynamically unstable. The system tries to return to the equilibrium state, resulting in a gradual decrease of mobility due primarily to a shift of the relaxation time spectrum to longer time scales. It has been reported [223] that the decrease in free volume accompanying aging is responsible for the lowering of the segmental mobility which influences the polarizability during the polarization stage and the relaxation rate during the depolarization phase.

In this section, we present original data on the use of thermal-windowing to characterize physical aging. It may seem a bit odd, at first, to consider thermal-windowing as a good candidate to study aging, because the polarization stage ages the sample at T_p, in a sense influencing what we try to characterize. However, since the mechanism of aging below T_g is essentially the same as the relaxation of dipoles occurring during the polarization and depolarization stages of thermal-windowing, it seems that if we modify (in a characteristic and systematic way) the structure during the polarization stage, we might be off the true initial state, but still in line with the kinetics of relaxation which we want to characterize. Our objective is to demonstrate that coupling between the relaxation modes is affected by quenching and physical aging, resulting in a systematic variation of the relaxation map parameters, including the DOD, ΔG_c, and T_c.

II.3.8.1 Experimental procedure

Physical aging of a quenched PMMA sample at different annealing temperatures and times was carried out automatically on the Solomat TSD/TWD spectrometer by programming the instrument to work on its own for 2 months without interruption while performing the aging experiments and analyzing the data. The aging cycles were initially entered in a DOS batch file which was stored in the memory of the computer (which monitors the spectrometer), and the instrument performed the experiments for the following 1350 hours without the need of any operator.

The machine was programmed to carry out the following cycle. PMMA was first brought up to 180 °C for 40 min and quenched to the aging temperature T_a. It was annealed at that temperature for a time t_a and then submitted to the process of TWD at temperature T_p in order to obtain the corresponding Arrhenius transform $\mathrm{Log}\,\tau$ versus $1/T$ isolated at T_p. The variables studied are the temperature and time of annealing and the temperature of polarization T_p. Water cooling was used, instead of liquid nitrogen, to allow the unattended and continuous use of the spectrometer. For each aging experiment, all variables, except time, were kept constant (i. e., heating and cooling rates, polarization time, and voltage were strictly identical). The results were analyzed in terms of the variation of the entropy and enthalpy of activation for the

EBSCOhost - printed on 2/13/2023 12:32 AM via . All use subject to https://www.ebsco.com/terms-of-use

individual relaxation modes occurring in the glass and isolated at the various T_p with aging conditioning.

II.3.8.2 Results

Figure 3.93 is a plot of the elementary relaxation curves versus temperature for the PMMA. It is aged at 50 °C for several times varying between 10 minutes and 36 hours, studied at the same polarization temperature T_p = 70 °C. One sees that the result of aging at 50 °C, as studied with the thermal-windowing method, is to decrease the intensity of the peak height. The value of T_m remains practically unchanged with annealing time.

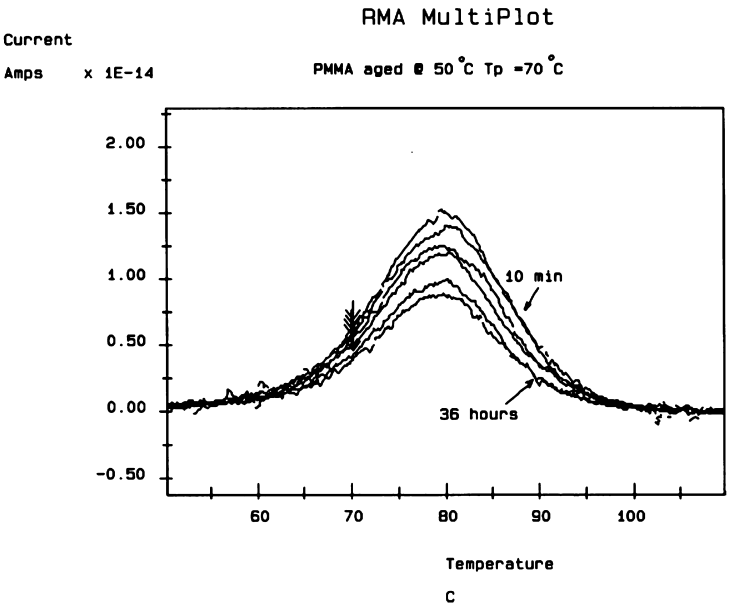


Figure 3.93: Study of the aging process below T_g in PMMA glass. Annealing temperature: 50 °C. T_p = 70 °C. Annealing time: 10 min to 36 hours prior to running a TWD trace. The graph displays the variation of the TWD output with the annealing time.

Figure 3.94 is an identical plot for a higher temperature of polarization, 80 °C. In this figure, the reversed effect for the intensity is observed, i. e., the intensity of the peak at the maximum increases with the aging time between 10 minutes and 36 hours, with a tendency to level off after 7 hours. The T_m values remain unchanged.

Figure 3.95 is a plot of the peak intensity at T_m versus aging time in hours for the three values of the polarization temperature T_p = 65 °C, 75 °C, and 80 °C. The trend across T_p = 77 °C is reversed in this figure.

EBSCOhost - printed on 2/13/2023 12:32 AM via . All use subject to https://www.ebsco.com/terms-of-use

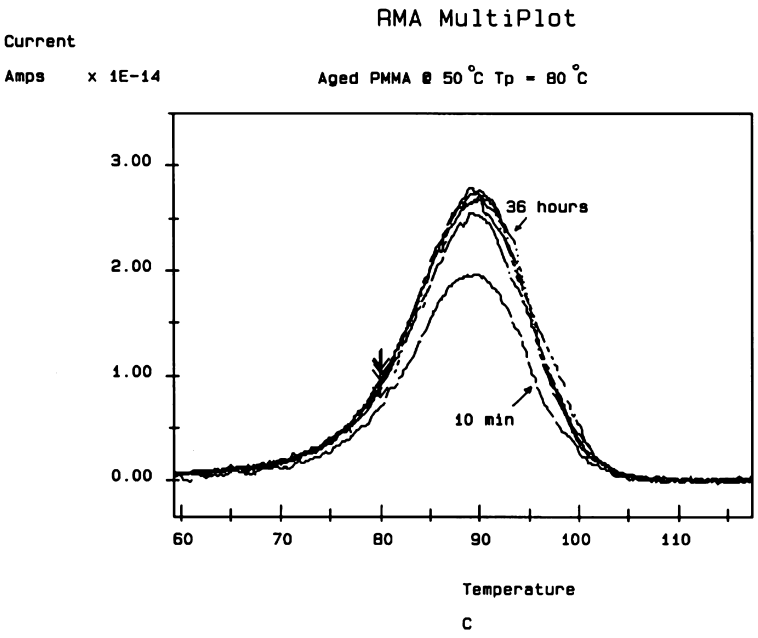


Figure 3.94: The same experiment as in Figure 3.93 but the temperature of polarization, T_p, is increased to 80 °C. The annealing time has the reverse effect of increasing the intensity of the Debye peak.

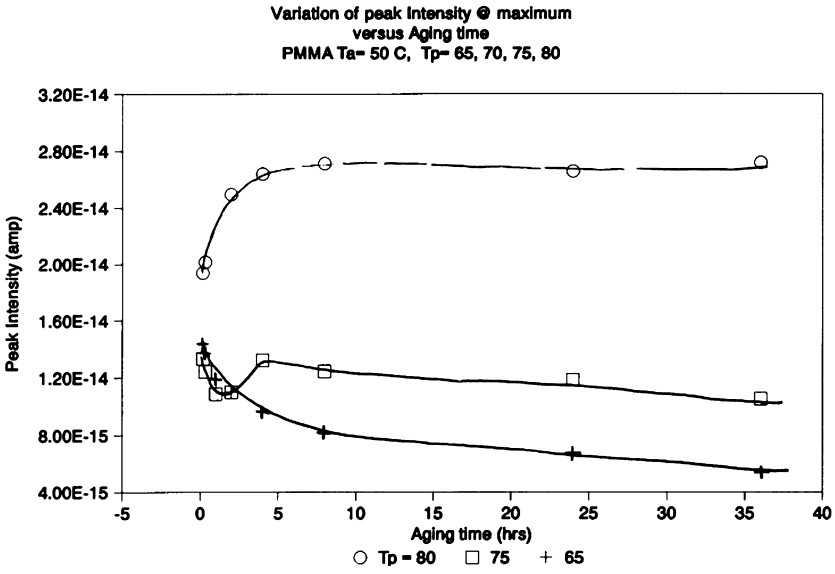


Figure 3.95: Intensity of the current at T_m for the TWD peaks at three values of T_p: 80 °C, 75 °C, and 65 °C.

EBSCOhost - printed on 2/13/2023 12:32 AM via . All use subject to https://www.ebsco.com/terms-of-use

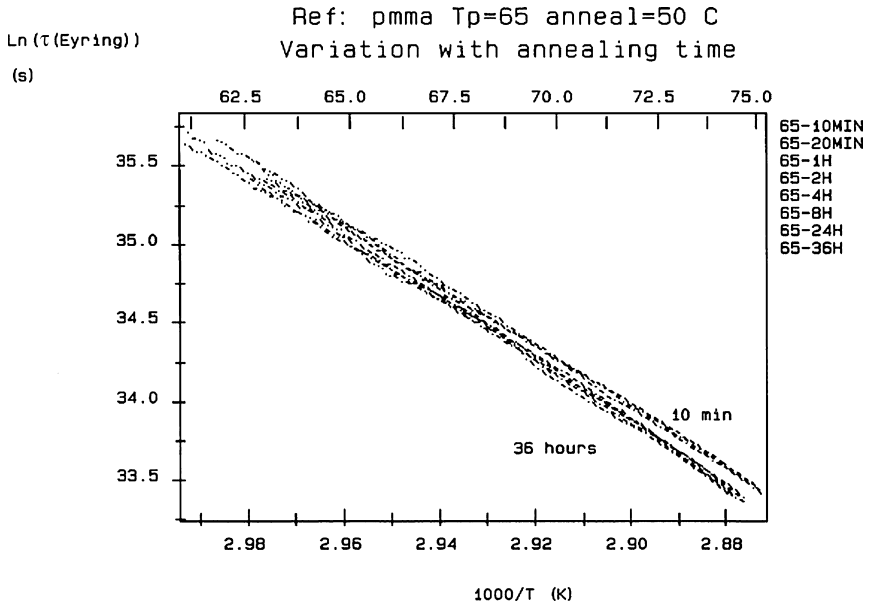


Figure 3.96: Eyring transforms of the TWD for PMMA samples annealed at $T = 50\,°C$ for times between 10 min and 36 hours. $T_p = 65\,°C$.

Figure 3.96 is a plot of $\log \tau$ versus $1/T$ for the various PMMA specimens aged at $T_a = 50\,°C$, polarized at a constant $T_p = 65\,°C$. The tendency is for the Arrhenius lines to be displaced, especially horizontally, although we also observe a certain amount of tilt (slope change). Notice that the curve obtained for an aging time of 10 minutes is located above the curve corresponding to a longer aging time at 36 hours at the bottom of the plot. The respective position of these curves is reversed at $T_p = 80\,°C$. Figure 3.97 is a relaxation map for a sample aged between 10 minutes and 24 hours at 50 °C for various T_p between 65 °C and 80 °C. Each of the bundle of lines corresponds to a given T_p, the spread for each bundle is due to aging.

Figure 3.98 plots the same results differently: we establish compensations for the data aged for the same time t_a at $T_a = 50\,°C$ and polarized at various polarization temperatures. Since there are five aging times, we obtained five compensations. The effect of the polarization is an additional amount of aging at the corresponding temperature (the time of polarization is 2 minutes). Figure 3.98 displays the compensations and the compensation points. We calculate the DOD number for a given set of T_ps and the same aging time and observe that the DOD number and the compensation temperature T_c increase with aging time (the DOD number goes from 49.39 to 53.09 and T_c varies from 124.78 °C to 150.31 °C). This result indicates that the value of the DOD number can be used to quantitatively describe the state of a glass, and in particular it shows that a larger DOD number relates to a glass closer to its equilibrium state.

EBSCOhost - printed on 2/13/2023 12:32 AM via . All use subject to https://www.ebsco.com/terms-of-use

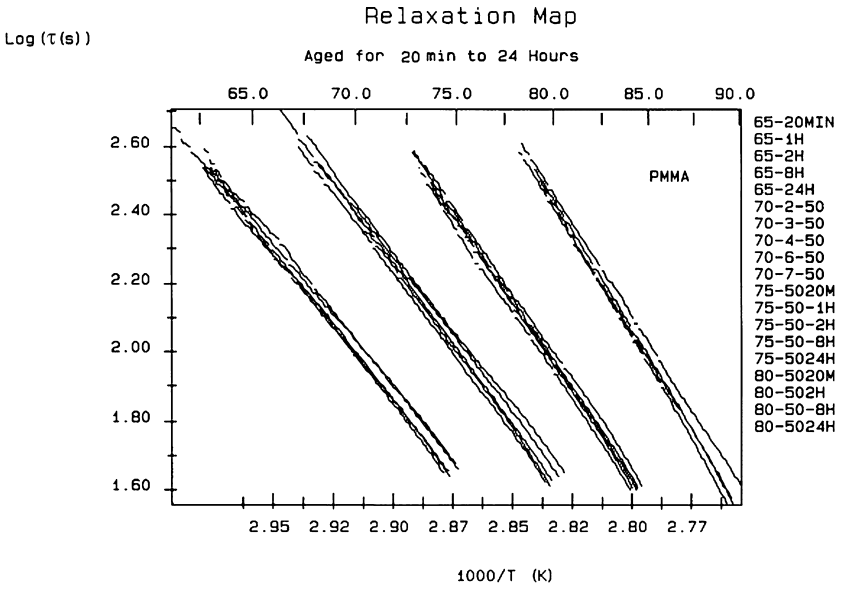


Figure 3.97: Relaxation map in the Arrhenius plane for PMMA samples annealed at $T = 50\,°C$ for times between 20 min and 24 hours and then submitted to a TWD at various T_p (65 °C, 70 °C, 75 °C, and 80 °C).

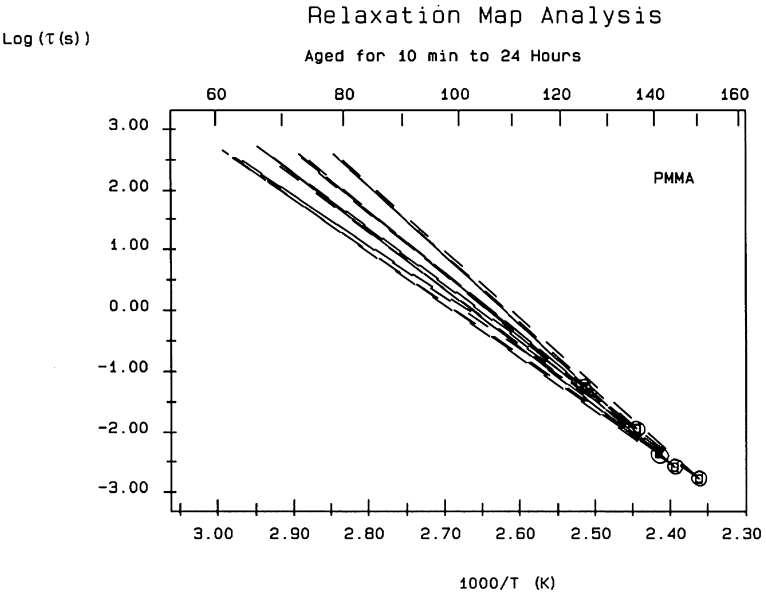


Figure 3.98: Relaxation map in the Arrhenius plane for the same data as in Figure 3.97, but plotted differently. Here, the same annealing time is selected and the various Arrhenius spectral lines are obtained by varying T_p. A compensation is observed, the characteristics of which vary with the annealing time.

EBSCOhost - printed on 2/13/2023 12:32 AM via . All use subject to https://www.ebsco.com/terms-of-use

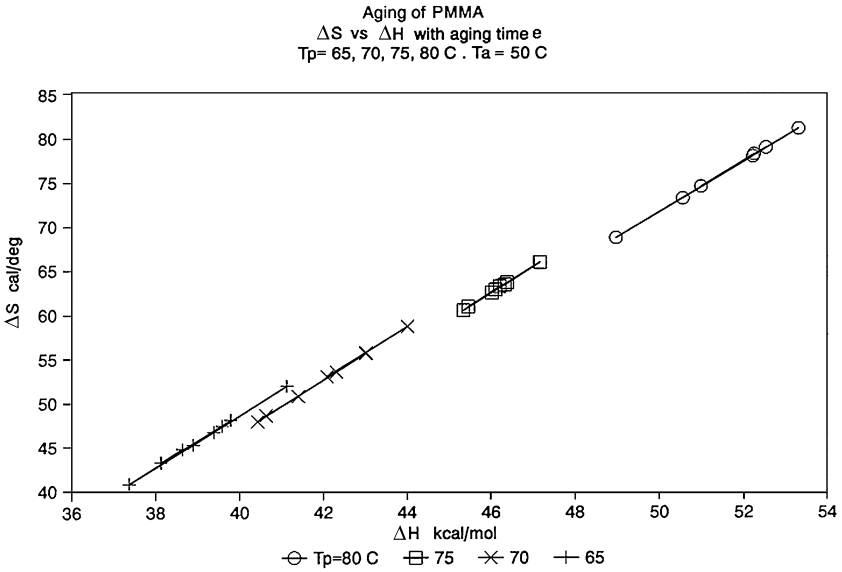


Figure 3.99: Compensation search in the EE plane. The compensations at the four T_p values were identified using data at various annealing times and the same annealing temperature (50 °C).

Another way to present the aging effect is shown in Figure 3.99, which corresponds to a compensation search in the EE plane: ΔS against ΔH. One sees that the ΔS and ΔH values obtained at different aging times compensate on a compensation line whose slope and intercept vary with the temperature of polarization. In particular, it seems that the effect of the polarization temperature is to increase the value of both ΔS and ΔH. The effect of aging is to displace (predominantly decrease) values along the compensation line corresponding to each polarization temperature.

In Figure 3.100, ΔS is plotted against ΔH for PMMA samples aged at two different temperatures, $T_a = 50\,°C$ and $T_a = 65\,°C$, and the same polarization temperature, $T_p = 70\,°C$. Most significantly, we observe that the values obtained for the higher annealing temperature are located at the bottom of the plot, so the basic influence of aging seems to affect the position along the compensation line with a decrease for both the entropy and enthalpy of activation as the aging process proceeds. The aging process is accelerated at higher aging temperatures, as expected. The fact that one is moving downward on the compensation line makes it a negative compensation, according to Part I, Chapter 2. The negative compensation is illustrated in the Arrhenius plane for $T_p = 70\,°C$ in Figure 3.101 (the same plot is shown in the $\Delta G - T$ plane in Figure 3.102).

Figure 3.103 is a plot of the free energy ΔG versus annealing time for the specimen aged at 50 °C and studied at different temperatures between 65 °C and 80 °C. One seems to observe some reversal of the value of ΔG at the beginning of the aging process, a phenomenon which has been reported for DSC data [122] (see later).

EBSCOhost - printed on 2/13/2023 12:32 AM via . All use subject to https://www.ebsco.com/terms-of-use

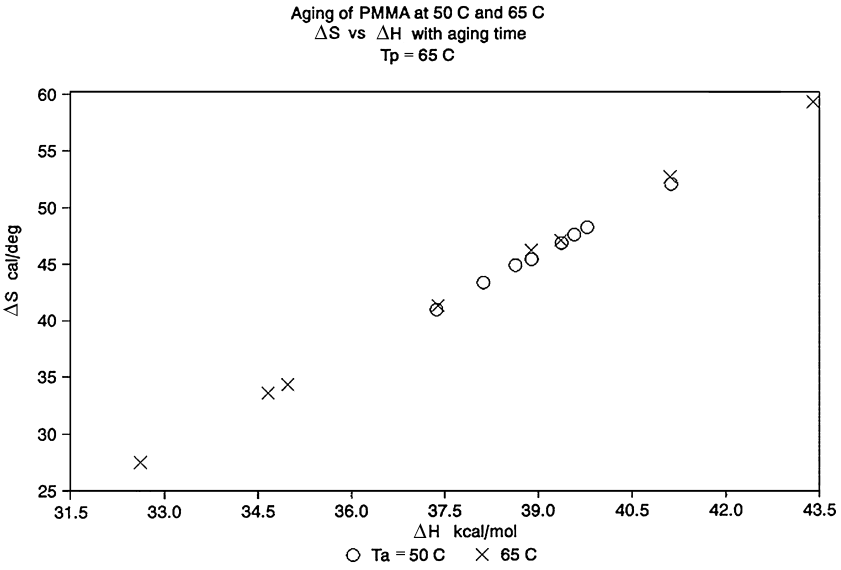


Figure 3.100: ΔS (annealing time) vs. ΔH (annealing time) for samples annealed at two temperatures, 50 °C and 65 °C, for various times. The TWD is obtained after polarization at the same T_p = 70 °C.

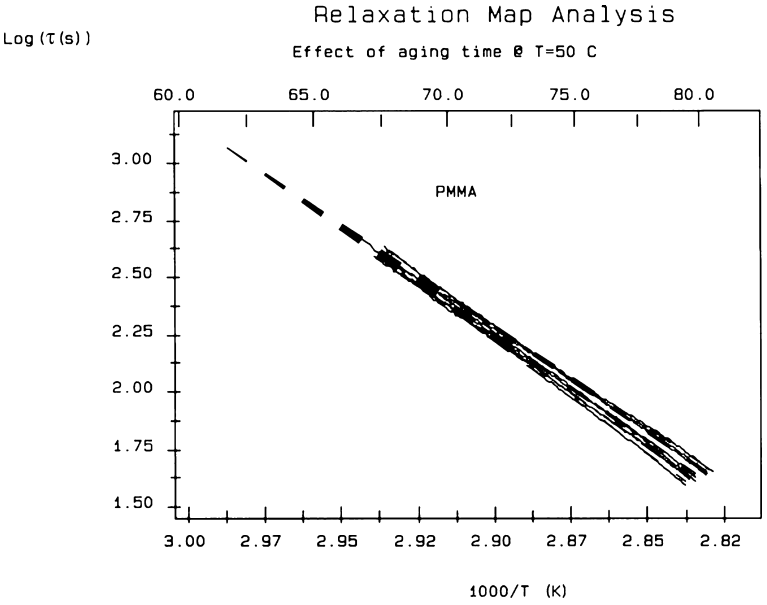


Figure 3.101: Negative compensation observed in the Arrhenius relaxation map for the effect of the annealing time at T_a = 50 °C, studied after polarizing at T_p = 70 °C.

EBSCOhost - printed on 2/13/2023 12:32 AM via . All use subject to https://www.ebsco.com/terms-of-use

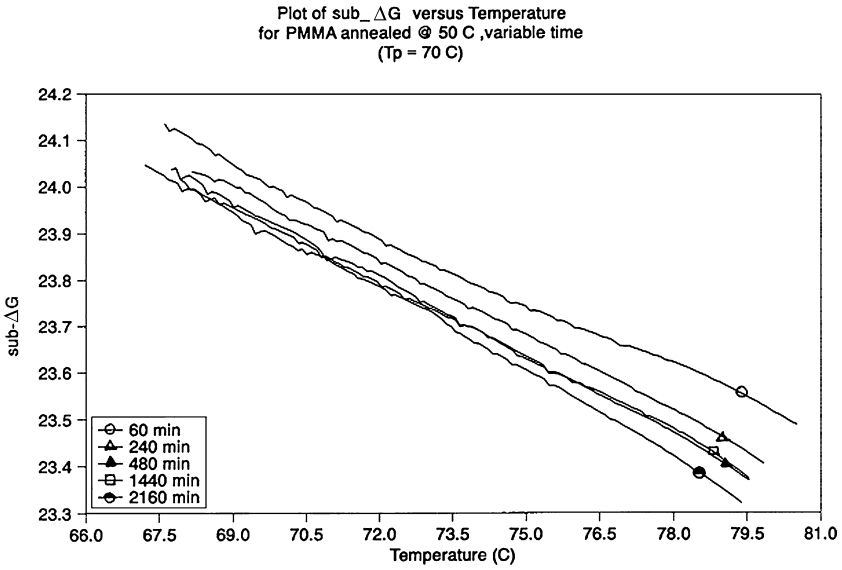


Figure 3.102: The same compensation as in Figure 3.101 plotted in the Δ*G* plane, showing details at high temperatures (the spectral lines are more separated, confirming the negative status of the compensation).

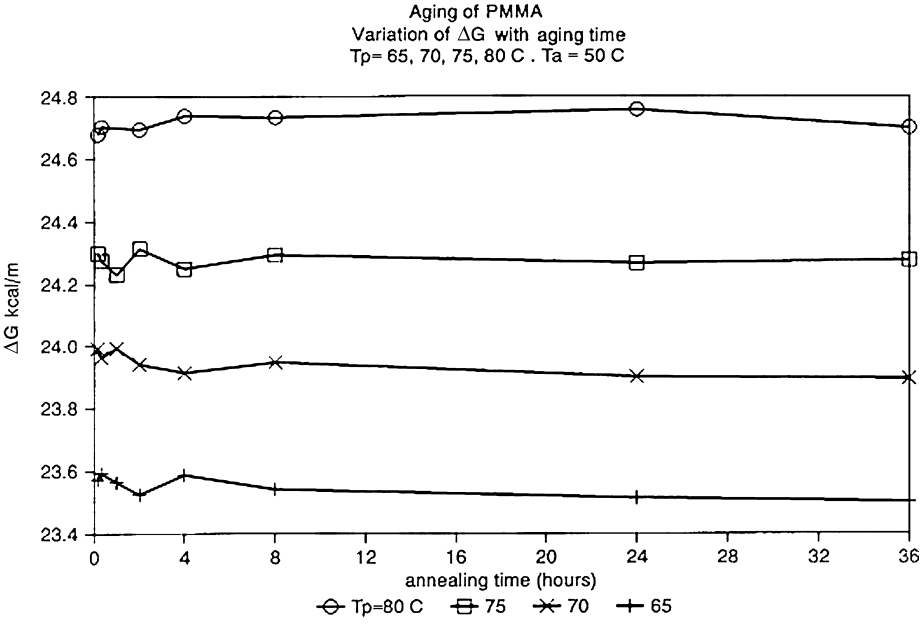


Figure 3.103: Plot of Δ*G* vs. annealing time with T_a = 50 °C. T_p varies between 65 °C and 80 °C.

EBSCOhost - printed on 2/13/2023 12:32 AM via . All use subject to https://www.ebsco.com/terms-of-use

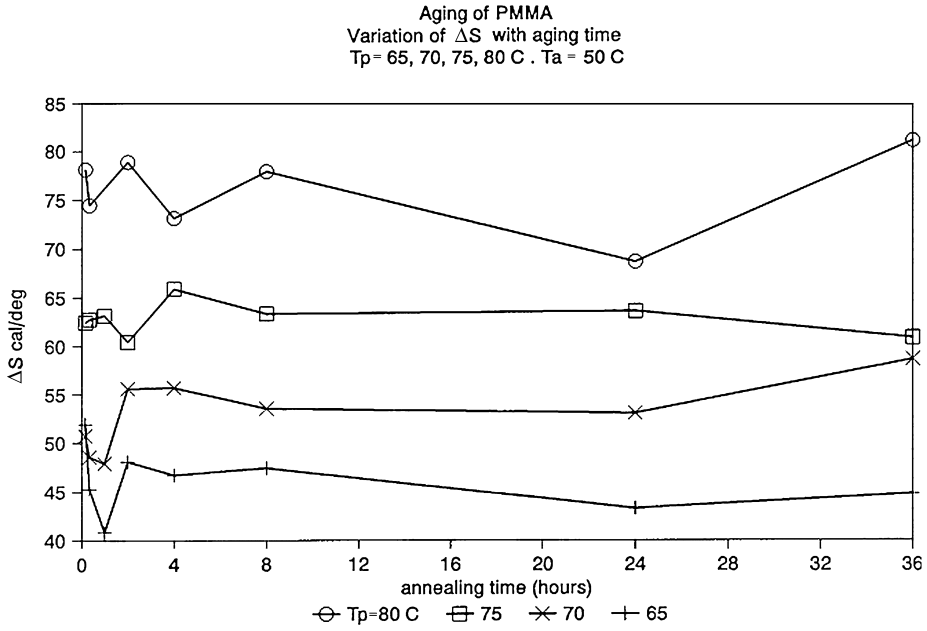


Figure 3.104: Plot of ΔS vs. annealing time with T_a = 50 °C. T_p varies between 65 °C and 80 °C.

Figure 3.104 is a plot of ΔS versus annealing time, again showing a long-term stabilization of ΔS, which does not seem to vary much with aging time, and a decay of the entropy for aging times between 10 minutes and 2 hours.

II.3.8.3 Discussion

This study clearly demonstrates that the incidence of aging in the glassy state is to increase the value of the DOD number (from 44.39 for no aging to 53.09 for 36 hours of aging), increase the value of T_c (from 124.8 °C for 10 min to 150.3 °C for 36 hours), and decrease the value of ΔG_c (from 21.65 to 21.09 kcal/m). In other words, the Arrhenius lines tend to become parallel as aging proceeds to completion. These results are consistent with our interpretation of the compensation phenomenon as the reflection of the state of non-equilibrium of the coupled interactive kinetics (Part I, Chapter 2 and Part I, Chapter 3). A plot of ΔG_c against T_c (not shown) for annealing time between 10 min and 36 hours is practically linear, defining a common activation energy and entropy for the relaxing process: 51 kcal/m and 76 cal/deg.

Another interesting observation concerns the reversal of the aging effect passed 70 °C. Below this temperature, aging decreases the intensity of the relaxation peak

EBSCOhost - printed on 2/13/2023 12:32 AM via . All use subject to https://www.ebsco.com/terms-of-use

(Figure 3.93). This translates in a positioning of the corresponding Arrhenius lines from right to left, such as shown in Figure 3.96: the short aging times correspond to the lower slopes, i. e., the lower activation energies and entropies. As the aging process continues, the Arrhenius lines become steeper and the entropy of activation increases, i. e., the rate of decrease of the free energy increases. This is as if the shortest relaxation times occurred after the long ones, a classical paradox observed by many authors working on the lower glass [148]. Above 70 °C, everything is reversed: the intensity of the peaks increases as aging occurs (Figure 3.94), and this means that the short aging time Arrhenius lines are now with steeper slopes on a relaxation map, positioned on the left. This also means that for these higher polarization temperatures, the initial free energy is higher the longer the annealing time, and the rate of decrease of the free energy is lower as annealing time increases. This phenomenon can be understood.

The action of the voltage field is clearly to "activate" the dipoles, i. e., increase their free energy, which translate into an excess of free energy which is then released during the non-isothermal depolarization. The rate at which the free energy is released is given by, or is, the entropy of activation. The higher the entropy, the higher the rate. For any given temperature of polarization and temperature of annealing (Figure 3.102), the initial value of the free energy and the rate of change of the free energy of activation either increase ($T_p < 70$ °C) or decrease ($T_p > 70$ °C) with the aging time, resulting in both cases in a positive compensation (Figure 3.101, for instance). The value of the free energy at the compensation point seems to indicate a maximum disturbed value obtainable at that temperature of polarization, irrespective of the aging time, thus giving an indication of the initial state (note that we cannot know the true saturation value at T_p because the system relaxes during thermal-windowing, as explained before).

The behavior above $T_p = 70$ °C is classical, in the sense of an exponential decay. The longer the annealing time, the more relaxed the structure becomes. The closer it is to its equilibrium state, the slower it is to reach that final state: the entropy of activation decreases with annealing time. The behavior at lower T_ps is more typical of a kinetic process (Part I, Chapter 3), controlled by the minimization of the total free energy of the collective set, the grand ensemble of bond interactions. The change of behavior between the short and longer annealing times has been observed by several authors [206] and has been commented on by us before. The system first loses entropy and free energy at the beginning of annealing, as clearly demonstrated on the left of Figures 3.99 and 3.103 and even more clearly in Figure 3.105.

EBSCOhost - printed on 2/13/2023 12:32 AM via . All use subject to https://www.ebsco.com/terms-of-use

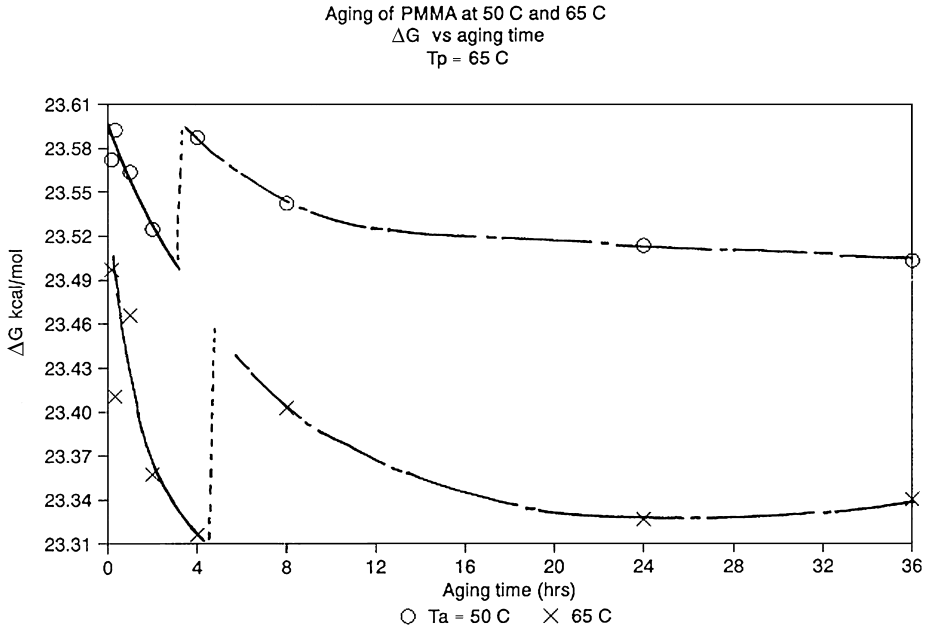


Figure 3.105: Comparison of ΔG vs. annealing time for $T_a = 50\,°C$ and $65\,°C$ analyzed with $T_p = 65\,°C$.

II.3.8.4 Conclusion

In this section we have shown that an automatic experimental procedure can be set up by software to run aging experiments in a batch form in the TSD/TWD spectrometer. The study is done unattended, and the automatic analysis features of the software can also be activated to obtain very good accuracy.

The study of the aging phenomenon in PMMA by TSD/TWD spectroscopy provides very interesting results regarding the evolution of the Dual-Phase state of the conformers with aging time and temperature (see Part I, Chapter 3). The DOD number, which is assumed to characterize the state of *disorder* of the glass ("*order*" being the mark of a collective interaction), has been verified to increase with aging time and temperature. The study also shows that a return to equilibrium due to aging corresponds to an increase of the compensation temperature, T_c. This appears to be logical if we assume that the perfect theoretical equilibrium state of the glass is reached when the Arrhenius spectral lines are parallel, i. e., in the absence of a compensation below T_g. In other words, following these thoughts, the collective aspect of the interactive process could be measured by the characteristics of the compensation between the relaxation modes. Quantitative measurements of the non-equilibrium state can be evaluated from the difference in values between the temperature of compensation T_c and the temperature of T_g, defined as T_p at the maximum of entropy (or the temperature defined at the Z-line). In this sense, the thermokinetic features displayed in a

EBSCOhost - printed on 2/13/2023 12:32 AM via . All use subject to https://www.ebsco.com/terms-of-use

relaxation map are correlated to the state of cooperative coupling between the dipoles. Many important results on the kinetic structure can be derived from the study of the relaxation map as a function of aging conditions.

II.3.9 Case study: characterization of PEEK and PEI/PEEK blends by TWD

Samples of pure PEEK and PEEK/PEI 50:50 blend were prepared by the Virginia Polytechnic Institute and submitted to thermal-windowing analysis. Blends of PEEK/PEI are reported to be miscible, although the PEEK elements are crystallizable. PEI is the high-T_g component in the blend, with a T_g of 220 °C, as determined by TSD.

II.3.9.1 PEEK

We first analyzed the pure PEEK material. Figure 3.106a shows a DSC trace obtained with a Perkin-Elmer IIB showing T_g, the cold crystallization peak, and the melting peak. Figure 3.106b shows a TSD trace for both the pure PEEK and the PEEK/PEI 50:50 blend to be studied later.

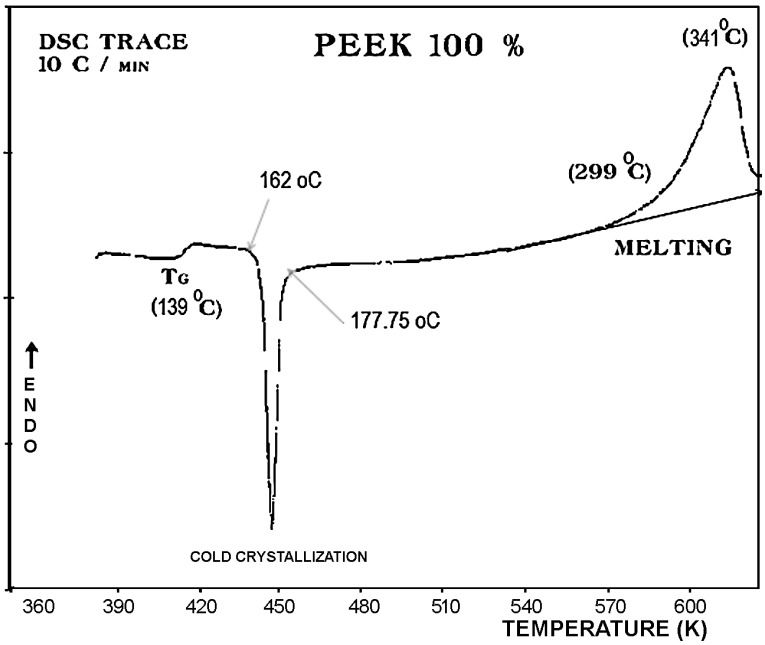


Figure 3.106a: DSC trace for pure PEEK showing T_g, the exothermic cold crystallization, and the melting peak.

EBSCOhost - printed on 2/13/2023 12:32 AM via . All use subject to https://www.ebsco.com/terms-of-use

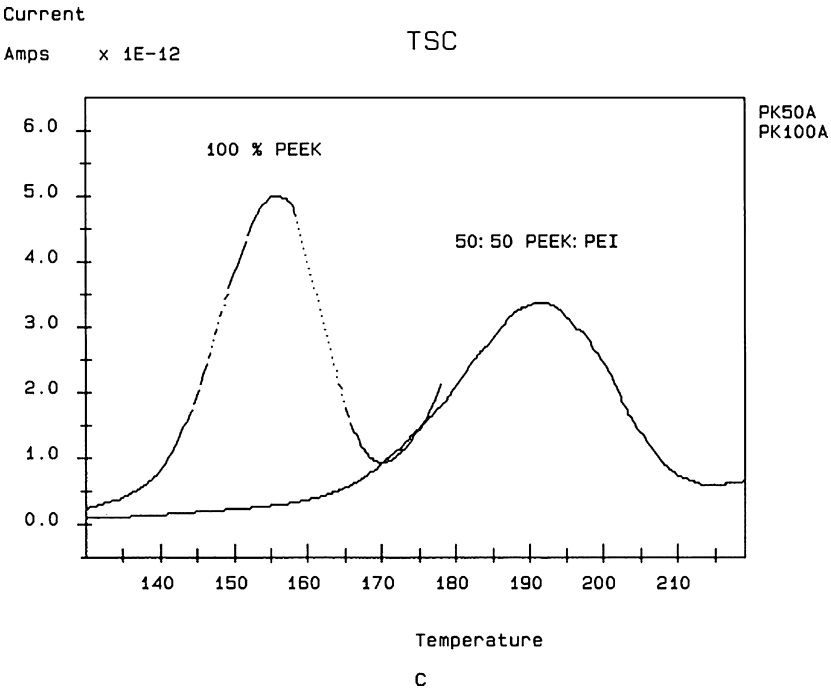


Figure 3.106b: Comparison of the TSD traces for pure PEEK (100 %) and a PEEK/PEI 50:50 blend. The two T_g peaks should be compared.

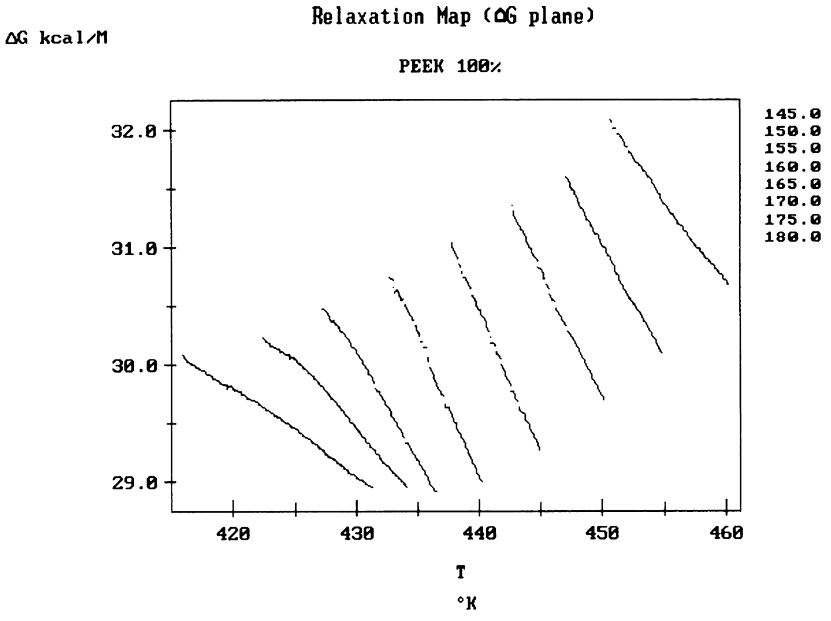


Figure 3.106c: Relaxation map in the Δ*G* plane for 100 % PEEK.

EBSCOhost - printed on 2/13/2023 12:32 AM via . All use subject to https://www.ebsco.com/terms-of-use

The thermal-windowing parameters are as follows: sample thickness, 0.25 mm; sample area, 7.0 mm^2; heating rate, 7.0 °C/min; polarization time and depolarization time, 2 min; and window width, 2 °C. The voltage field is 200 V/mm. The temperature of polarization is varied across the T_g of the PEEK amorphous region, between 145 °C and 180 °C.

The relaxation map in the ΔG plane for the pure PEEK material is displayed in Figure 3.106c. All relaxation curves are good straight lines, except for the polarization at 150 °C, which shows a slight upturn at the beginning of depolarization. The small departure from linear behavior was ignored during the analysis.

The thermokinetic parameters are provided in Table 3.18.

Table 3.18: Thermokinetics for 100 % PEEK for T_p between 145 °C and 180 °C.

	T_p (°C)	T_m (°C)	ΔH_p (kcal/mol)	ΔS_p (cal/°C/mol)	ΔG_p (kcal/mol)
1	145.0	158.3	60.4401	72.9708	29.9266
2	150.0	161.1	78.8015	114.7811	30.2307
3	155.0	163.6	106.5275	177.8076	30.3973
4	160.0	167.3	134.4429	239.5426	30.6826
5	165.0	171.9	140.4626	249.9742	30.9339
6	170.0	177.1	128.5290	219.6118	31.2058
7	175.0	181.8	118.0526	193.4087	31.3746
8	180.0	187.3	98.1301	146.6425	31.6776

The EE plot of Figure 3.107 shows positive (top, blue line) and negative (bottom, red line) compensation behavior. The positive compensation includes points 1 to 4 (these numbers are those of Table 3.18 in the first column near the T_p column). The negative compensation links points 5 to 8. For an amorphous polymer, the intercept of the two compensation lines "normally" corresponds to the T_g transition, but in the present case, it corresponds to a T_p located between points 4 and 5, i. e., approximately 162 °C, which is 23 °C above the T_g found by DSC (139 °C in Figure 3.106a). In Figure 3.106a, 162 °C marks the onset of the cold crystallization process, but, as we propose below, it is also a glass transition temperature, the $T_g(U)$ of Boyer [22].

The slope and intercept of the compensation lines provide the coordinates of the two compensation points in the ΔG plane.

For the positive compensation, we find

$$T_c = 173.46\,°\mathrm{C}$$
$$\Delta G_c^+ = 27.39\,\mathrm{kcal/m}$$
$$\mathrm{DOD} = 38.67$$

EBSCOhost - printed on 2/13/2023 12:32 AM via . All use subject to https://www.ebsco.com/terms-of-use

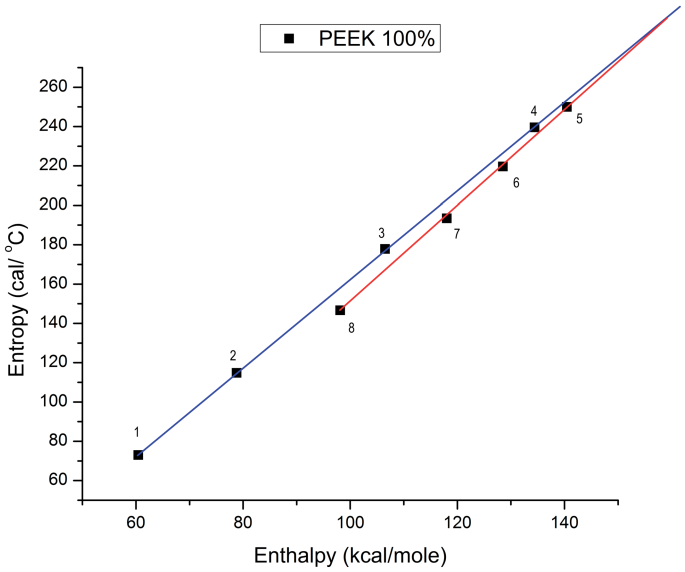


Figure 3.107: Compensation search in the EE plane for 100 % PEEK showing a positive and a negative compensation.

and for the negative compensation, we find

$$T_c = 135.78\,°\text{C}$$
$$\Delta G_c^- = 38.47\,\text{kcal/m}$$
$$\text{DOD} = 5.94$$

The values of T_c for the two compensations appear to be close to the crystalline and amorphous phase temperature characteristics of the melt found by DSC (Figure 3.106a): the end of the cold crystallization process, 177 °C, matches approximately the positive compensation temperature (T_c = 173.46 °C), and T_g of the material, 139 °C, appears equal to the negative compensation temperature (T_c = 135.78 °C).

We calculate the coordinates of the intercept of the two compensation lines in Figure 3.107 to determine ΔH_{gl} and ΔS_{gl}, the subscript "gl" standing for "g-like," i. e., a behavior like a glass transition, but not the traditional glass transition, which is observed at T_g = 139 °C. We find

$$\Delta S_{gl} = 294.06\,\text{cal/m/°C}$$
$$\Delta H_{gl} = 158.72\,\text{kcal/m}$$

These values are *very high* compared to the values found for the T_g of other amorphous phases analyzed by TWD in this book (Part I, Chapter 2). We will see in Part II, Chapter 4 that special mechanical treatments during processing ("Rheomolding") are

EBSCOhost - printed on 2/13/2023 12:32 AM via . All use subject to https://www.ebsco.com/terms-of-use

capable to modify the amorphous state of classical thermoplastics such as polystyrene to induce such high performance ΔS_g and ΔH_g values when tested by TWD.

Suppose now that this intercept of the two compensations lines of Figure 3.107 is a glass transition, for instance that it is the upper glass transition, $T_g(U)$, of Boyer's two T_gs for semi-crystalline polymers [22]. Then $T_g(U)$, like the normal T_g for an amorphous polymer, can be determined in TWD by the temperature of maximum of the entropy vs. T_p, as shown in Figure 3.109 ($T_g(U) = 162\,°C = 435\,K$), while $T_g(L)$ is the T_g of the amorphous phase outside and between spherulites, equal to 412 K (139 °C) in the DSC run of Figure 3.106a.

We can determine ΔG of the amorphous phase at $T_g(U)$ as

$$\Delta G_g(U) = \Delta G_{gl} = \Delta H_{gl} - T_g(U)\Delta S_{gl} = 30.80\,\text{kcal/mole}$$

a value located between ΔG_c^+ (27.39 kcal/mole) and ΔG_c^- (38.47 kcal/mole).

Unfortunately, we cannot compare this value with $\Delta G_g(L)$, the value of ΔG at $T_g(L)$, since the polarization temperatures selected for this experiment did not cover the range across $T_g(L)$, the values of T_p starting at $T = 145\,°C$ while $T_g(L) = 139\,°C$.

Another attribute of the T_g transition for amorphous polymers is the fact that ΔG_p vs. T_p remains identical across T_g when T_p is chosen to vary from below to above T_g.

The relationship between ΔG_p and T_p (K) for the transition observed for PEEK, when $T_p = 145\,°C$ to 180 °C, is linear, as shown in Figure 3.108a, yet the slope and intercept of that classical plot are not typical. We find for the slope 0.0492 and for the intercept 9.39. The "classical" numbers are 0.07 ± 0.003 for the slope and 0 for the intercept. There is no doubt that this departure from the normal behavior is significant of the special nature of the amorphous phase observed. Notice, however, that the straight line in Figure 3.108a does not differ from what we always observe across a T_g for the other polymers studied by TWD: there is no break in the curve of ΔG_p vs. T_p for the whole range of T_p covered: from T_g, indicated by the first arrow in Figure 3.108a, all the way up to the end of the range. This means that the presence of the cold crystallization process, which starts at the second arrow in Figure 3.108a, 162 °C, and ends at $T = 177\,°C$, according to the DSC trace of Figure 3.106a, does not affect the plot of ΔG_p vs. T_p. And since this is the same line that is observed from $T_g = 139\,°C$ to 162 °C, for which there is no crystalline activity, based on the DSC trace, we conclude that the characteristics of ΔG_p vs. T_p are not due to the cold crystallization process, but, instead, to another glass transition.

In fact, as suggested above, we conclude that the transition observed, which has all the T_g-like characteristics of amorphous polymers analyzed by TWD, is the $T_g(U)$ glass transition of Boyer [22], known to describe the state of a constrained amorphous phase within the spherulites of semi-crystalline polymers. Being a constrained phase is possibly the reason we do not find the classical slope of 0.07 across T_g in Figure 3.108a: the present thermal-windowing polarization range overlaps the negative compensation range of $T_g(L)$ and the positive compensation range of $T_g(U)$.

EBSCOhost - printed on 2/13/2023 12:32 AM via . All use subject to https://www.ebsco.com/terms-of-use

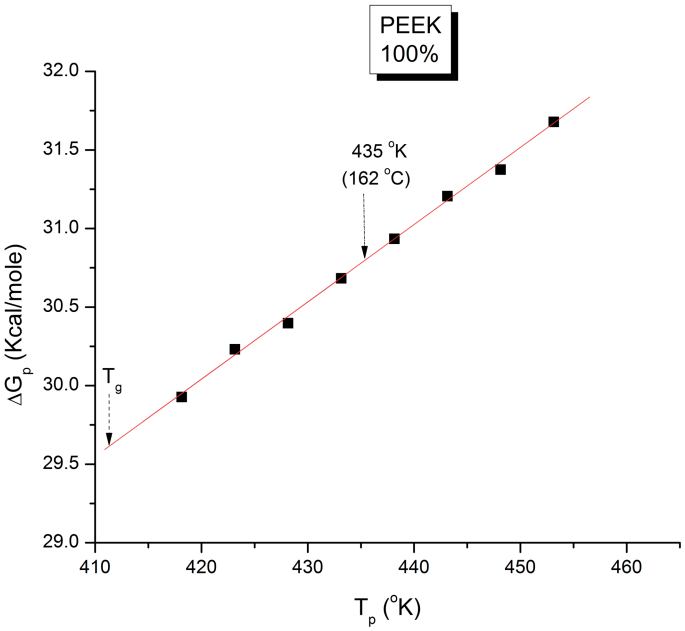


Figure 3.108a: ΔG_p vs. T_p (K) for 100 % PEEK.

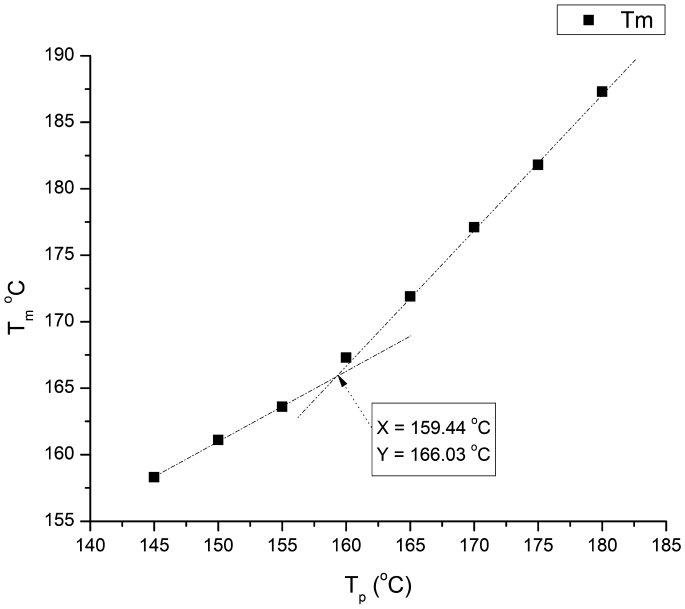


Figure 3.108b: Variation of T_m vs. T_p, both in °C, for 100 % PEEK.

EBSCOhost - printed on 2/13/2023 12:32 AM via . All use subject to https://www.ebsco.com/terms-of-use

In Figure 3.108b, a plot of T_m vs. T_p, where T_m is the temperature at the maximum of the Debye peak induced by the polarization at T_p in the TWD, we observe a break at (T_p = 159.5 °C, T_m = 166.0 °C), which is in close vicinity of the onset of cold crystallization (~162 °C). This proves that TWD is, indeed, affected by the crystallization process, but not ΔG_p.

The mobility in the amorphous structure, describing the intermolecular coupling, is studied in Figure 3.109, a plot of the entropy of activation against T_p. The classical hyperbolic variation of ΔS_p vs. T_p is observed here for the $T_p < T_g(U)$ transition, and the maximum mobility occurs at $T_g(U)$ found for T_p = 161.9 °C by the method of intercept of the Z-lines and the ΔG_p vs. T_p line.

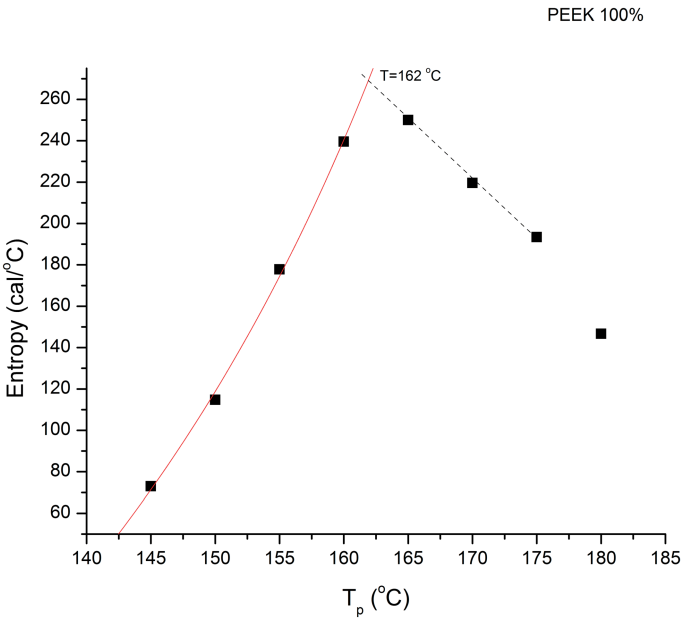


Figure 3.109: Entropy of activation, ΔS_p, vs. T_p for 100 % PEEK.

The intensity of the Debye elementary peak at its maximum is plotted in Figure 3.110 and also displays a maximum, but the peak maximum occurs for T_p = 175 °C, which corresponds to the end of cold crystallization and is 14 °C higher than the value of $T_g(U)$ found from the entropy plot or the EE lines. Therefore, the cold crystallization process influences both the peak intensity (Figure 3.110) and its position, T_m, on the temperature scale (Figure 3.108b), but not the compensation line characteristics (Figures 3.108a and 3.109).

The comparison between the intensity and the entropy plots is reemphasized in Figure 3.111. The spread between the maxima relates to the polarizability of the seg-

EBSCOhost - printed on 2/13/2023 12:32 AM via . All use subject to https://www.ebsco.com/terms-of-use

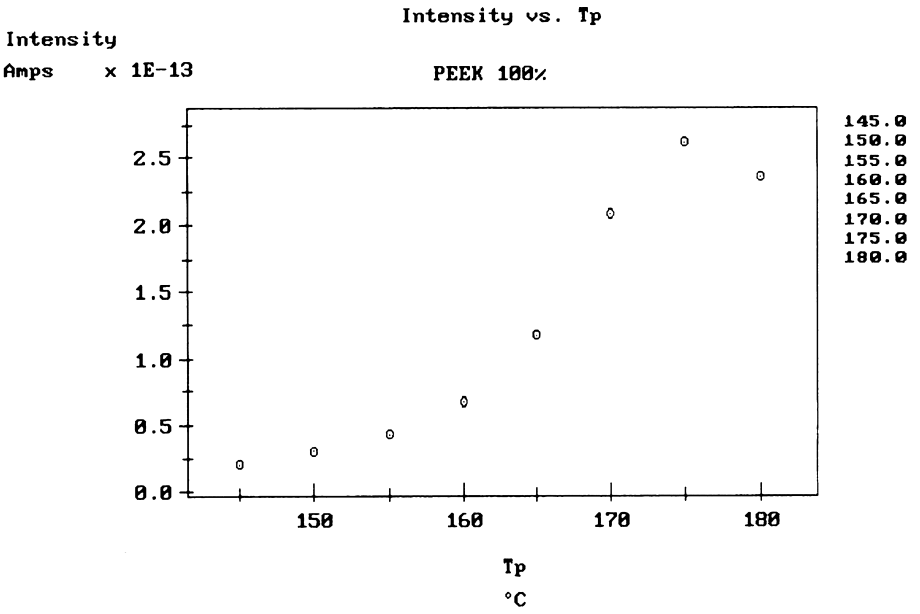


Figure 3.110: Intensity of the Debye peak at T_m vs. T_p for 100 % PEEK.

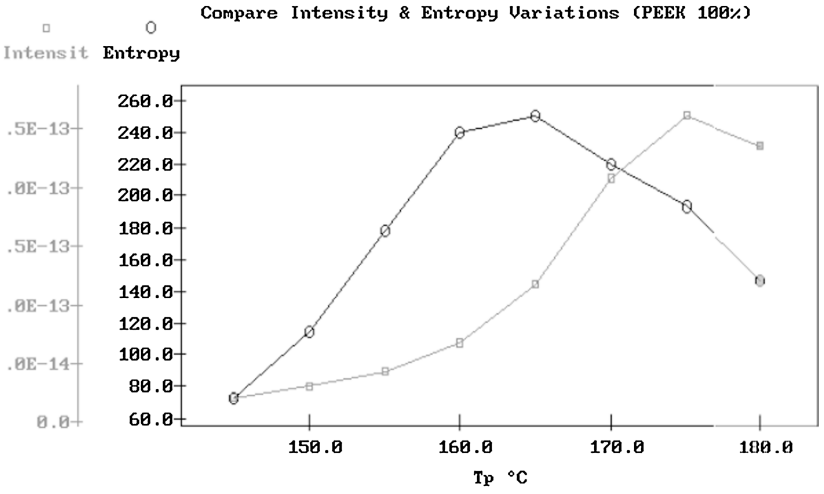


Figure 3.111: Comparison of the intensity vs. T_p and the entropy vs. T_p for 100 % PEEK. Note the T-shift difference between these two variables to reach the maximum.

ments activated by the voltage field and to the experimental thermal-windowing parameters. We have observed in the case study of 100 % HDPE that for non-polar materials the two maxima occur at almost the same temperature. For highly polar materials, such as PEEK or polyesters, the difference between the two maxima is sometimes very

EBSCOhost - printed on 2/13/2023 12:32 AM via . All use subject to https://www.ebsco.com/terms-of-use

large. As explained in Part I, Chapter 2, the true mobility of the dipoles in the material is described by the variation of the entropy of activation, and not the intensity of the current at the peak maximum. When the elementary peak obtained by thermal-windowing is not a true single true Debye peak, the peak maximum evidenced from thermal-windowing, even for small window widths, is not the maximum for the curve-fitted Debye peak, which fits the low-temperature region of the elementary thermal-window peak. If we were to plot the intensity of the current at, say, two-thirds of the peak maximum temperature, against the polarization temperature, the two maxima, for both intensity and entropy, would possibly coincide. Therefore, the difference between the two maxima relates to the number of Debye peaks which make up an "elementary" thermal-window depolarization peak. As studied in Part I, Chapter 1, it is sometimes difficult to obtain a single Debye peak for polar materials and, more than often, the Debye peak is coupled with another peak for a single "elementary" thermal-window depolarization peak. The technique of integration can take this into account to deconvolute the thermal-window peak into its elementary Debye components.

II.3.9.2 PEEK/PEI blend

A blend of 50:50 of PEEK and PEI is analyzed with the thermal-windowing technique for a temperature of polarization between 150 °C and 220 °C. The samples studied in this case are slightly thicker than the PEEK samples (0.51 mm). We kept the same area under the voltage field (7.0 mm^2) and kept all the other variables the same, in order to compare with the PEEK reference sample. Before giving the TWD spectroscopy results, let us examine briefly, with two illustrative figures, what DSC and TSD teach us. Figure 3.112a shows a DSC trace and Figure 3.106b, presented earlier, provides the TSD trace for the PEI/PEEK blend. The DSC and TSD graphs seem to favor the assumption of compatibility between the PEI and PEEK segments. The DSC trace, in particular, is typical of a quenched semi-crystalline homopolymer with a single T_g, the cold crystallization, and the fusion peak. The relaxation map in the ΔG plane is provided in Figure 3.112b.

Table 3.19 summarizes the thermokinetic results.

Two compensation lines, one positive and one negative, can be drawn through the data in the EE plane. In addition, in the higher-T_p region, some points do not seem to belong to any compensation, as often observed for the T_α process. The coordinates of the positive compensation line give

$$T_c = 202.04\,°C$$
$$\Delta G_c = 30.345\,\text{kcal/m}$$
$$\text{DOD} = 36.13$$

EBSCOhost - printed on 2/13/2023 12:32 AM via . All use subject to https://www.ebsco.com/terms-of-use

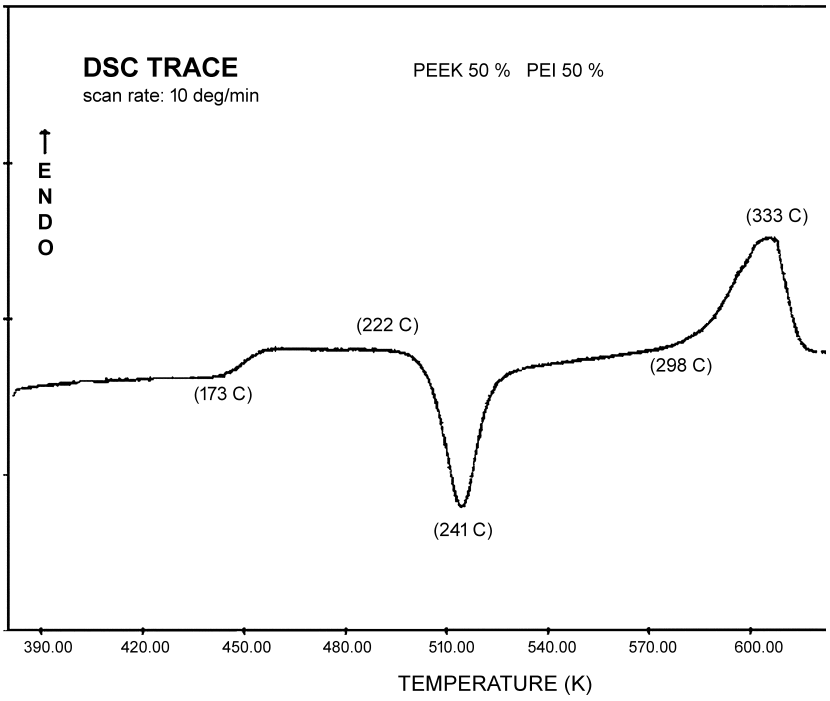


Figure 3.112a: DSC trace for the PEEK/PEI 50:50 blend showing T_g, the exothermic cold crystallization, and the melting peak. Compare with Figure 3.106a for 100 % PEEK.

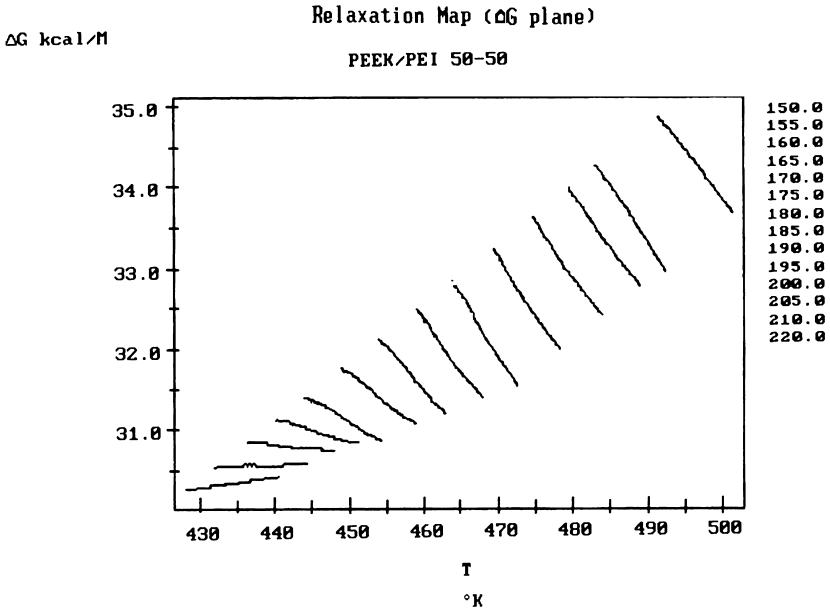


Figure 3.112b: Relaxation map in the Δ*G* plane for the PEEK/PEI 50:50 blend.

EBSCOhost - printed on 2/13/2023 12:32 AM via . All use subject to https://www.ebsco.com/terms-of-use

Table 3.19: Thermokinetics for the PEEK/PEI 50:50 blend for T_p between 150 °C and 220 °C.

	T_p (°C)	T_m (°C)	ΔH_p (kcal/mol)	ΔS_p (cal/°C/mol)	ΔG_p (kcal/mol)
1	150.0	167.6	24.4811	−13.4784	30.1846
2	155.0	171.3	29.4113	−2.6232	30.5344
3	160.0	175.1	35.0907	9.7221	30.8795
4	165.0	178.3	44.0085	29.2424	31.1956
5	170.0	181.3	56.4915	56.4378	31.4806
6	175.0	185.9	65.0675	74.1479	31.8374
7	180.0	190.1	80.0316	105.5120	32.2178
8	185.0	195.0	90.0285	125.3591	32.5940
9	190.0	199.6	104.0280	153.4291	32.9658
10	195.0	205.3	99.4781	141.1705	33.3878
11	200.0	211.0	95.5100	130.4386	33.7917
12	205.0	216.0	94.9473	127.1853	34.1324
13	210.0	219.5	103.1036	142.4345	34.2849
14	220.0	228.3	94.2146	120.7262	34.6773

and for the negative compensation we have

$$T_c = 82.05\,°\text{C}$$
$$\Delta G_c = 29.45\,\text{kcal/m}$$
$$\text{DOD} = -39.22$$

Notice the very unusual values found for this compensation. The DOD is very low, ΔG_c^- is *smaller* than ΔG_c^+, and T_c^- is far too low a value to be associated with the normal negative compensation coupled with the positive compensation passing through the first nine points (up to $T_p = 190\,°\text{C}$). Somehow, the behavior does not seem to be representative of a true monophasic structure.

Figure 3.113 compares the positive compensations found for both PEEK and PEEK/PEI in a compensation search performed as an EE plot. The values found for the enthalpy of activation and entropy of activation start at much lower values for the blend, and the compensation line for the blend is located below the compensation line for the PEEK sample. The ΔH_g (33.89 kcal/m) and ΔS_g (7.5 cal/ °C) values, calculated from the intercept and slope of the Z-line passing through the positive and negative compensation points, are far too low to be correct. T_g is calculated at 164.36 °C, which seems to be very close to the T_g of the PEEK phase, as if the system was segregated.

Before we can decide whether the blend behaves as a true monophasic system, let us consider Figure 3.114, which plots the intensity against T_p, and Figure 3.115, which compares the entropy of activation vs. T_p for PEEK and PEEK/PEI. We will also compare the compensation characteristics.

EBSCOhost - printed on 2/13/2023 12:32 AM via . All use subject to https://www.ebsco.com/terms-of-use

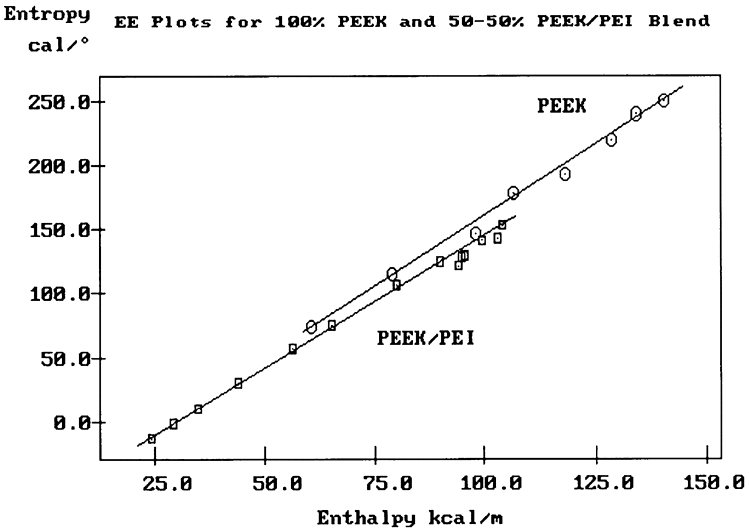


Figure 3.113: Compensation search in the EE plane for 100 % PEEK (dots) and the PEEK/PEI 50:50 blend (squares).

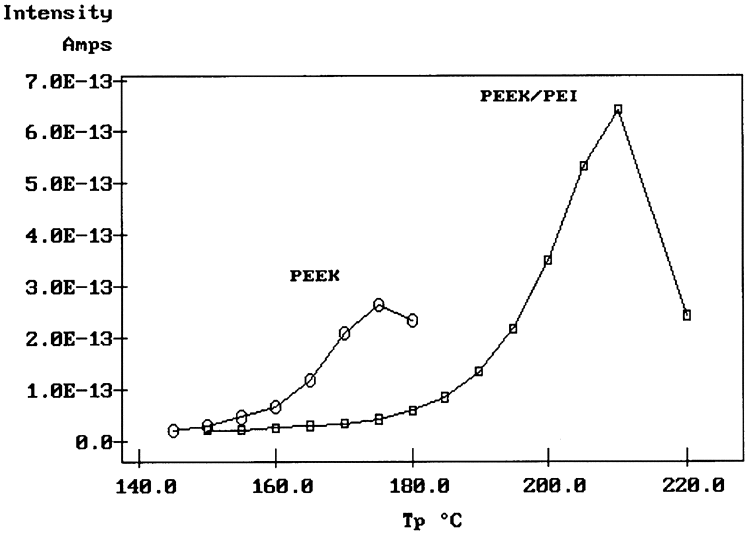


Figure 3.114: Intensity of the Debye peak at T_m vs. T_p for 100 % PEEK (dots) and the PEEK/PEI 50:50 blend (squares).

The behavior for the PEEK/PEI blend in Figure 3.114 gives credit to the position that the system is a monophasic system. There is no trace whatsoever of the presence of a T_g at 170 °C or of a higher temperature in the lower tail of the peak in the blend of Figure 3.114. The peak maximum occurs surprisingly very near the T_g of PEI, which

EBSCOhost - printed on 2/13/2023 12:32 AM via . All use subject to https://www.ebsco.com/terms-of-use

demonstrates the dominance of the dipolar groups belonging to the PEI segments. However, the mobility in the material displays a very different pattern in Figure 3.115. This figure compares the mobility in the pure PEEK and in the 50:50 blend. We observe that the values for the blend are lower than those obtained for 100 % PEEK. The second observation is that the hyperbolic variation which is clearly visible below T_g in the blend is not occurring above T_g. Actually, the tendency above T_g (which is observed at T_p = 190 °C) is a downward curve interrupted by an upturn which itself reaches a maximum for T_p = 210 °C. This post-T_g behavior is not typical of a completely miscible blend in this region. Furthermore, the second hump of increase of mobility at 210 °C is reminiscent of the presence of T_g of PEI in this region. The comparison of the behavior for a true amorphous system, PEEK, and the blend of PEEK and PEI is instructive. It is not necessarily in favor of a totally miscible behavior, which is the claim from other characterization techniques that are unable to work at the level of the true mobility in the material. The overall decrease of mobility in the PEEK/PEI blend is perhaps related to an ordering in the glassy phase, which could also be the reason for a decrease of the DOD number for the blend. Another sign that the macrostructure is not as simple as claimed comes from the value found for the negative compensation. The temperature of compensation is far too low for a true negative compensation behavior. Also, the presence of points on the EE plot which do not belong to any compensation might be the result of an ordering through a cold crystallization process occurring as T_p is increased. However, the DSC trace for the PEEK/PEI 50:50 blend (Figure 3.112a) demonstrates that cold crystallization occurs in a temperature region located to the right of the range studied here.

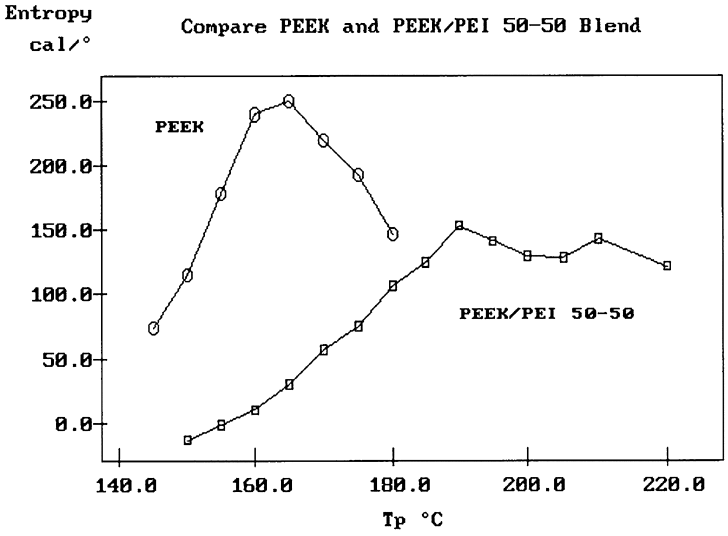


Figure 3.115: Entropy of activation, ΔS_p, vs. T_p for 100 % PEEK (dots) and the PEEK/PEI 50:50 blend (squares).

EBSCOhost - printed on 2/13/2023 12:32 AM via . All use subject to https://www.ebsco.com/terms-of-use

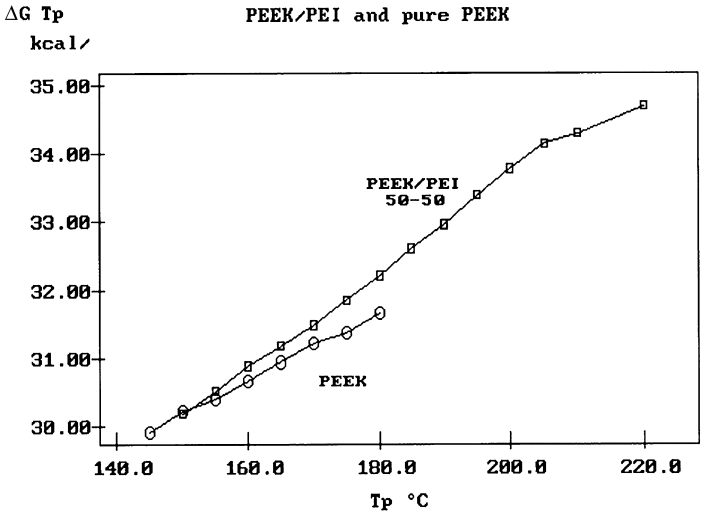


Figure 3.116: Comparison of ΔG_p vs. T_p (K) for 100 % PEEK (top) and the PEEK/PEI 50:50 blend (squares).

Finally, the influence of the voltage field on the interaction between dipoles, normally analyzed in plots of ΔG_p vs. T_p, as shown in Figure 3.116, reveals that the blend behaves in a typical amorphous polymer fashion up to 205 °C. Here an upturn and a change of slope is clearly observed. The slope and intercept found for the 50:50 blend are 0.070 kcal/ °C and 0, the "classical" values found for true amorphous glassy phases. The properties of PEEK and the blend with PEI certainly need more investigation. However, it is clear that the TWD technique provides insight into the bond interaction level which is unprecedented by any other thermal analysis technique.

II.3.10 Chapter conclusion

We have tried in this chapter to provide a multitude of examples of analysis using the TWD technique applied to a wide and diversified range of materials and sample shapes. As mentioned at the beginning of this book, the full *understanding* of TWD spectroscopy is still far from completion, yet, as a characterization technique, TWD is extremely powerful, as hopefully evidenced by the multiple examples presented in this chapter.

We have introduced, in this Part II, the use of a *qualitative language* ("interactive coupling" between "conformers," "*b* grains," "dynamic free volume," "thermokinetic" parameters, "compensation") to describe the commonalities and the differences between samples of various nature and processing history. Many of the parameters derived from the relaxation map of TWD can be interpreted using this qualitative language of "interactive coupling," without the need to precisely correlate these terms

EBSCOhost - printed on 2/13/2023 12:32 AM via . All use subject to https://www.ebsco.com/terms-of-use

with their fundamental statistical origin: the interactive coupling Dual-Phase model. The correlation is done in Part I and this is why we claimed, in the preface of this book, that the two parts could be studied separately.

The theoretical background giving a precise definition of all the terms, the correspondence between the depolarization current and the Arrhenius relaxation map, the compensation of the Arrhenius lines, and the Dual-Phase understanding of the compensation itself is developed in Part I. However, none of these quantitative developments are required to use TWD as a quantitative characterization tool to specify the state of the amorphous phase as a function of its interactive environment. The interactive environment of the conformers can be quantified by the compensation characteristics of the Arrhenius or Eyring lines of a relaxation map of the sample as T_p is varied from the solid to the liquid state. The interactive environment polarizability is very sensitive to the structure of the amorphous phase (oriented or isotropic), its homogeneity (detected by the presence of segregated phases), the presence of crystals or nematic phases, and its non-equilibrium state induced by the processing conditions.

This TWD dielectric measurement will certainly complement or even supplement other thermal analysis methods that are more traditionally used to characterize the texture, the morphology, or the relaxation state in complex polymeric systems.

EBSCOhost - printed on 2/13/2023 12:32 AM via . All use subject to https://www.ebsco.com/terms-of-use

Part II Chapter 4
Multiple compensation phenomena in the amorphous phase of polymers

In this chapter, we present examples of multi-compensations for polystyrene, polycarbonate, liquid crystal polymer, wood, and a block copolymer. The objective is to explore the complexity of the phenomenon of compensation to better understand its origin.

In the case of a multi-phase system, such as a segregated blend, the relaxation map displays multi-compensations, each associated with the T_g of the corresponding phase. In the case of crystallizable polymers or liquid crystal polymers, multi-compensations are sometimes visible, both below and above the glass transition temperature of the polymer. It will be shown that for true monophasic amorphous polymer, e. g., polystyrene, (1) it is possible to observe several compensations and (2) the number of compensation points observed on the relaxation map depends on the thermomechanical history: the processing variables, the cooling rate, the amount of pressure, orientation, etc. Lacabanne et al. [153] have suggested that the several compensation points observed for polystyrene and polycarbonate are caused by the presence of several amorphous phases, the indication of "local ordering," a subject of great controversy. Furthermore, these authors suggest that T_{LL} is the melting transition for these local microordered structures.

In the following pages, we debate the origin of multi-compensations in monophasic amorphous systems and in ordered morphological systems, and propose an alternative explanation for the existence of multiple compensation laws based on the Dual-Phase model of the inter-intra molecular potential energy barrier of the polymers.

II.4.1 Multi-compensations in a multi-phase system

Lacabanne and collaborators have published extensively on this subject [13, 77, 78, 81]. Chapter 3, Part II has provided many examples of systems (copolymers and blends) with several compensations. Figures 4.1 and 4.2 summarize the issue. In the case of a homopolymer (Figure 4.1), only one T_g is observed. The compensation search leads to a single pair of compensation lines, one positive and one negative. The presence of two phases in the morphology is clearly revealed by two T_gs, and thus two pairs of compensation lines (Figure 4.2). Comparison of the respective position of the compensation lines for the homopolymer and the block copolymer leads to a better understanding of the segregation characteristics between the phases and, in particular, of the degree of interpenetration and local compatibility (Chapter 3). It is clear that in this case, there is a direct relationship between the number of compensation lines and the number of phases in the morphology.

https://doi.org/10.1515/9783110756746-009

EBSCOhost - printed on 2/13/2023 12:32 AM via . All use subject to https://www.ebsco.com/terms-of-use

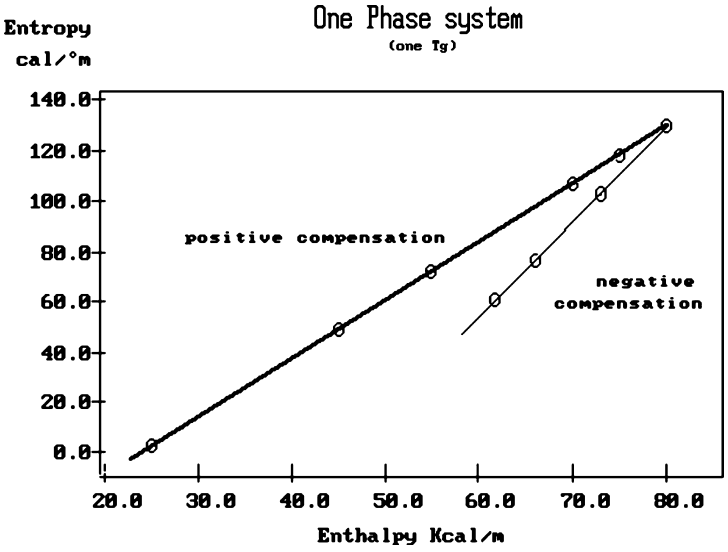


Figure 4.1: Schematic description of a compensation search in the EE plane to characterize the amorphous phase across T_g for a single-phase system; typically for an amorphous homopolymer.

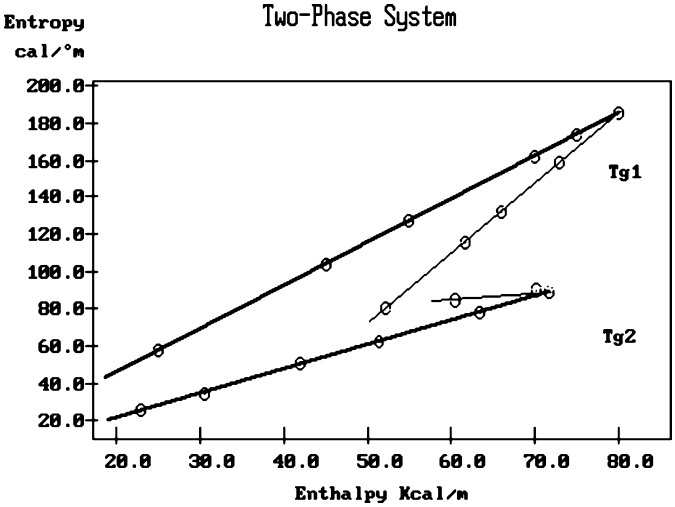


Figure 4.2: Schematic description of a compensation search in the EE plane to characterize the amorphous phases across their respective T_g for a two-phase system; typically for a block polymer.

EBSCOhost - printed on 2/13/2023 12:32 AM via . All use subject to https://www.ebsco.com/terms-of-use

II.4.2 Multiple compensation phenomenon in amorphous polystyrene and polycarbonate

Forty or so years ago, there was great controversy about the existence of local order in the structure of amorphous polymers, such as polystyrene and polycarbonate [208, 261, 262], but the debate soon cooled off on the evidence of structureless glass presented by Benoit [11] by small-angle neutron scattering (SANS) results, and because of the possibility of generating the nodular pictures observed by Yeh [261] and Geil [208] by defocusing the electro spectro-microscopy beam [226]. Atactic polystyrene is now considered to be a totally amorphous monophasic system [19]. Polycarbonate tends to crystallize under certain circumstances, and therefore only quenched specimens are considered totally amorphous without local ordering present.

The data of Figures 4.3 to 4.22 are sourced in the theses of A. Bernes (polystyrene) and A. Bettacchioli (polycarbonate), who both worked on samples provided by Solomat and characterized them by TSD/TWD spectroscopy [12, 19]. Bernes and Bettacchioli's data are plotted differently and analyzed with a different focus here to draw attention to multi-compensations and their characteristics and meaning. Our view and analysis does not necessarily represent the opinion of these respective authors. In particular, Lacabanne and Bernes have inferred the existence of local ordering of the amorphous phase of polycarbonate based on the results which we reanalyze here [153]. We disagree with their interpretation of these results and of the T_{LL} transition, by extension.

II.4.2.1 Polystyrene

Figure 4.3 is a relaxation map in the Eyring plane (Part I, Chapter 2) of a polystyrene very slowly cooled from 180 °C in a platen pressure mold. There is virtually no pressure applied on the specimen during the cooling stage. The mold is cooled by shutting off the power to the heater cartridges (Newtonian cooling). It took approximately 7 hours to cool the mold down to 50 °C. Table 4.1 gives the thermokinetic parameters as a function of T_p. Figure 4.4 is the compensation search in the EE plane. The polarization temperature is varied between 60 °C and 125 °C (the window temperature is 10 °C). The numbers on the figure apply to increasing polarization temperatures. We clearly observe two negative compensation lines. The first compensation line is made up of points 1, 2, 3, and 4, point 5 (T_p = 95 °C) seems to be lost between the two lines, and points 6, 7, and 8 are aligned on another negative compensation line.

We will go back to a more detailed analysis of this polystyrene specimen later, but, at this stage, we might want to question the reasoning which consists in equating the number of glassy phases or "transitions" with the number of compensation points and ask whether negative compensation points "count"?

EBSCOhost - printed on 2/13/2023 12:32 AM via . All use subject to https://www.ebsco.com/terms-of-use

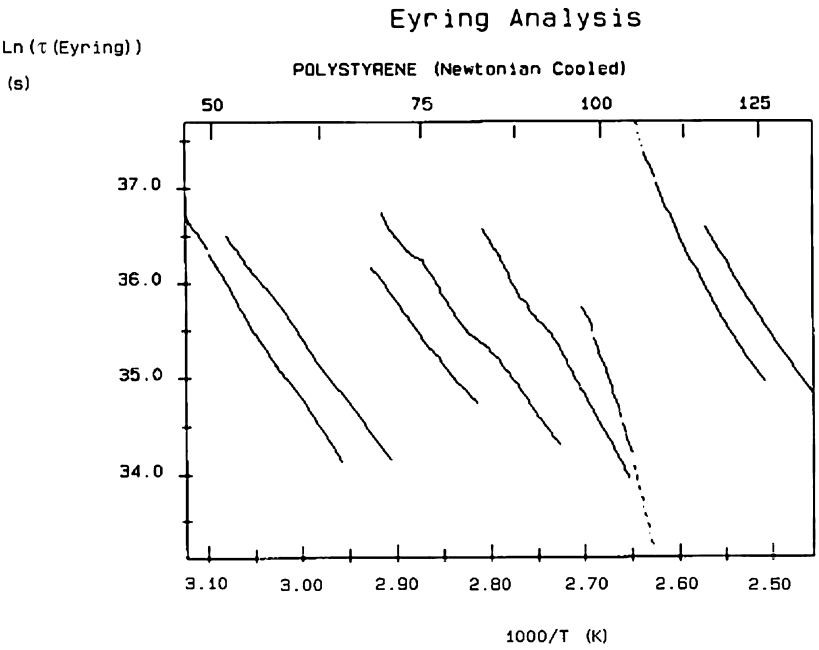


Figure 4.3: Relaxation map in the Eyring plane for a very slowly cooled compression-molded polystyrene sample (sample called PS_VA in subsequent figures).

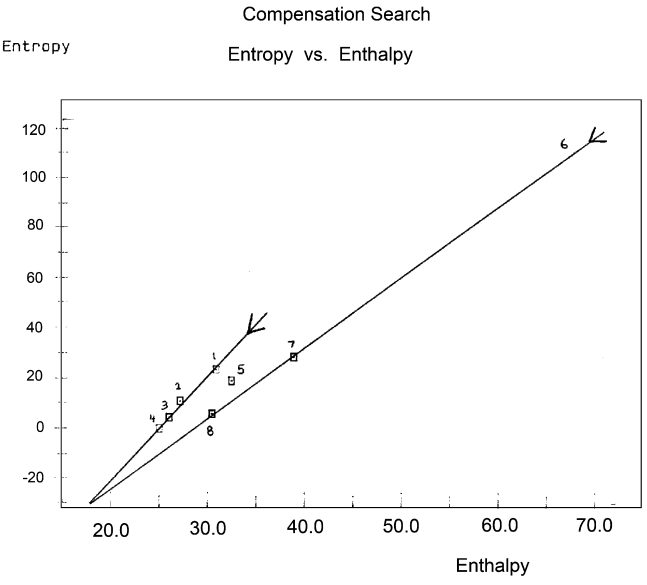


Figure 4.4: Compensation search in the EE plane for the data of Figure 4.3.

EBSCOhost - printed on 2/13/2023 12:32 AM via . All use subject to https://www.ebsco.com/terms-of-use

Table 4.1: Thermokinetics for sample PS_VA of Figure 4.3.

T_p (K)	T_m (K)	ΔH_p (kcal/mol)	ΔS_p (cal/°C/mol)	ΔG_p (kcal/mol)
333.2	344.0	30.8906	23.6368	23.0196
338.2	349.8	27.1823	11.1923	23.3993
348.2	367.5	25.9793	4.2110	24.5138
353.2	372.7	25.0293	0.0593	25.0084
368.2	380.5	32.4905	10.5915	25.6488
378.2	382.0	67.5262	111.1845	25.4985
388.2	411.9	38.8583	28.3365	27.8637
398.2	418.1	30.5001	5.8074	28.1887

Figures 4.5 to 4.10 relate to the same polystyrene, but mechanically pressurized during a fast cooling treatment. The mechanical treatment includes the application of vibration to induce specific thermal history patterns, a process known as "Rheomolding" [124]. The mold is cooled in approximately 30 seconds. The rate of cooling when the glass transition temperature is crossed is around 7 °C/sec.

Using the notations and definitions presented in Part I, Chapter 2, we can make the following remarks.

Figure 4.5 is the relaxation map in the Eyring plane. Figure 4.6 is the "unanalyzed" EE plot based on the Entropy and Enthalpy data of Table 4.2. See the caption of Figure 4.6.

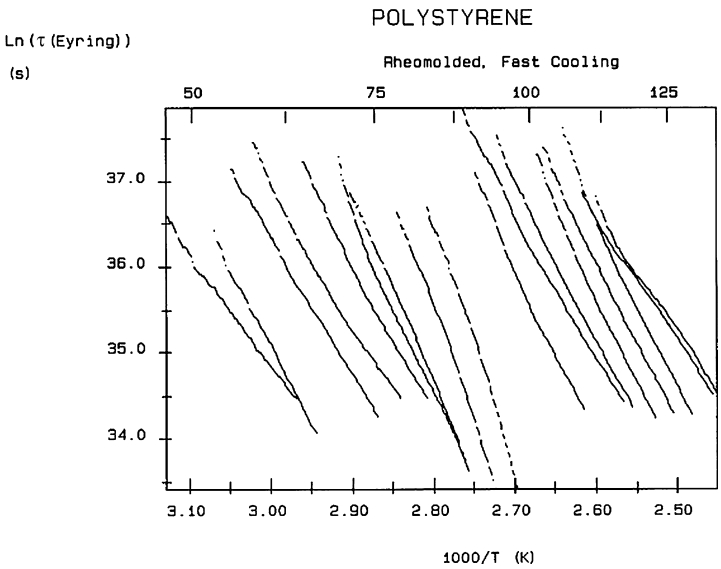


Figure 4.5: Relaxation map in the Eyring plane for a "Rheomolded" compression molded PS sample. The sample is pressurized and vibrated during fast cooling in the mold. This sample is designated PS_RL.

EBSCOhost - printed on 2/13/2023 12:32 AM via . All use subject to https://www.ebsco.com/terms-of-use

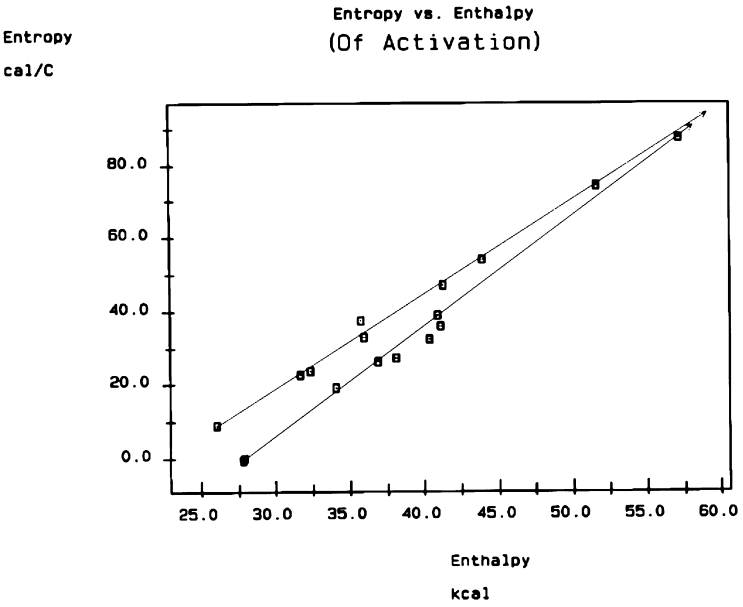


Figure 4.6: Compensation search in the EE plane for the PS_RL sample of Figure 4.5. The analysis appears complex. The 2 straight lines drawn in the graph are not joining consecutive T_p points and thus cannot represent the solution. The finding of the true positive and negatives compensation for this complex situation is shown in Figures 4.8 and 4.9.

Table 4.2: Thermokinetics for sample PS_RL.

T_p (°C)	T_m (°C)	ΔH_p (kcal/mol)	ΔS_p (cal/°C/mol)	ΔG_p (kcal/mol)
65.0	69.7	26.0444	8.9170	23.0304
70.0	70.2	35.7053	37.4304	22.8666
75.0	79.8	31.6927	22.8775	23.7313
80.0	84.6	32.3430	23.6549	23.9928
85.0	88.8	35.9299	32.5990	24.2595
90.0	90.2	41.3196	47.1144	24.2171
95.0	90.6	43.9499	54.2181	23.9976
100.0	94.6	51.6467	74.0286	24.0340
105.0	98.8	57.1351	37.3810	24.1051
115.0	113.5	40.9335	36.9967	25.8028
120.0	120.4	34.0003	19.0242	26.5237
125.0	121.9	36.8776	26.0567	26.5070
130.0	125.4	41.0596	35.8890	26.5964
135.0	129.0	38.0933	27.3621	26.9295
140.0	132.5	40.3364	32.1720	27.0494
145.0	137.3	27.7921	−0.3743	27.9485
150.0	138.5	27.8984	−0.3003	28.0254

EBSCOhost - printed on 2/13/2023 12:32 AM via . All use subject to https://www.ebsco.com/terms-of-use

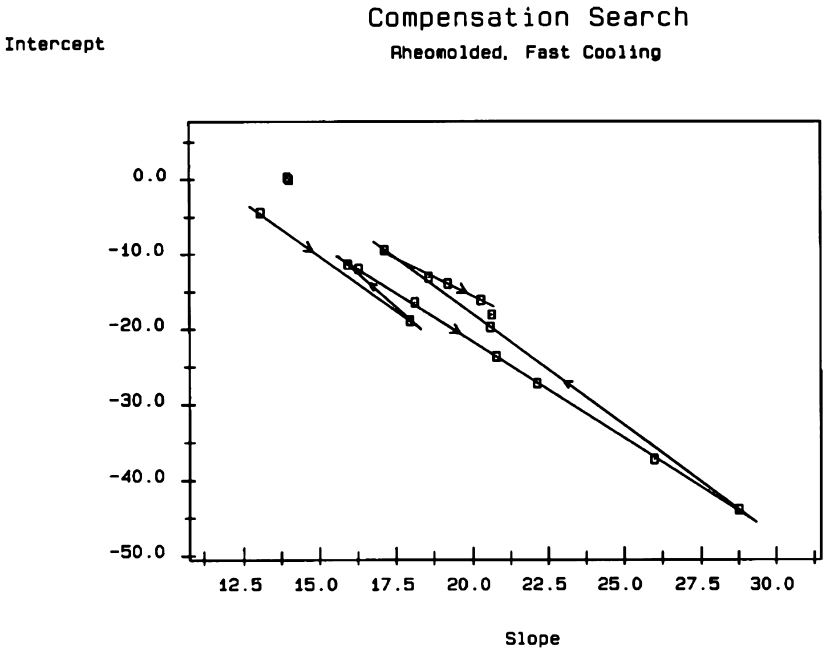


Figure 4.7: Compensation search in the Arrhenius plane for PS_RL to find the compensation(s) in Figure 4.5. Several positive and negative compensations emerge from what initially looked complex (in Fig. 4.6). The down arrows indicate positive compensations, the up arrows a negative compensation.

Figure 4.7 shows an attempt to find the compensation lines in Figure 4.6, both positive and negative compensations. For this, we use the intercept vs. slope system of coordinates. We have drawn two lines in Figure 4.6, but these did not take into account the position of the points lining up in Table 4.2. Only successive points can participate in a compensation line. Such an analysis is shown in Figure 4.7 and it reveals a series of positive followed by negative compensation lines (indicated by the direction of the arrows).

Figure 4.8 reveals that the positive compensation lines *converge on the* $\Delta S = 0$ *axis*. The corresponding value of ΔH at the intercept point is 23 kcal/mole.

Figure 4.9 concentrates on the negative compensation lines. This analysis is more difficult because of the lack of points to define the lines accurately. Nevertheless, it is possible to draw three negative compensation lines (two with confidence). Interestingly, it seems possible to force the negative compensation lines – in the EE plane – to intercept on either the $\Delta S = 0$ axis or the $\Delta H = 0$ axis (we have attempted to draw such a feature in Figure 4.9). We do not have enough accuracy in the determination of the negative compensation lines to conclude, at this stage, which procedure, if any, is well founded.

EBSCOhost - printed on 2/13/2023 12:32 AM via . All use subject to https://www.ebsco.com/terms-of-use

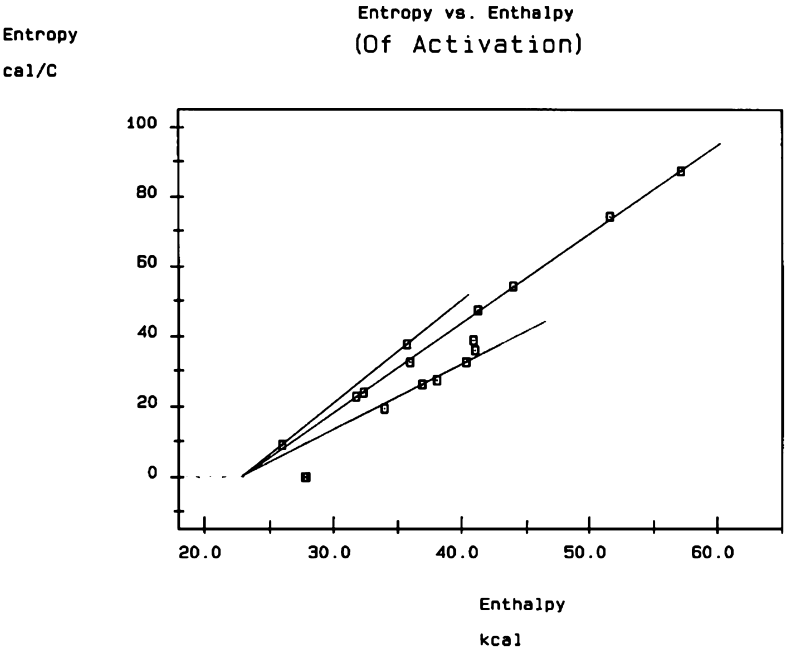


Figure 4.8: Compensation search in the EE plane for PS_RL showing only the *positive* compensation results and a new (partial) analysis of Figure 4.6. The rest of the analysis is in Figure 4.9 for the negative compensations.

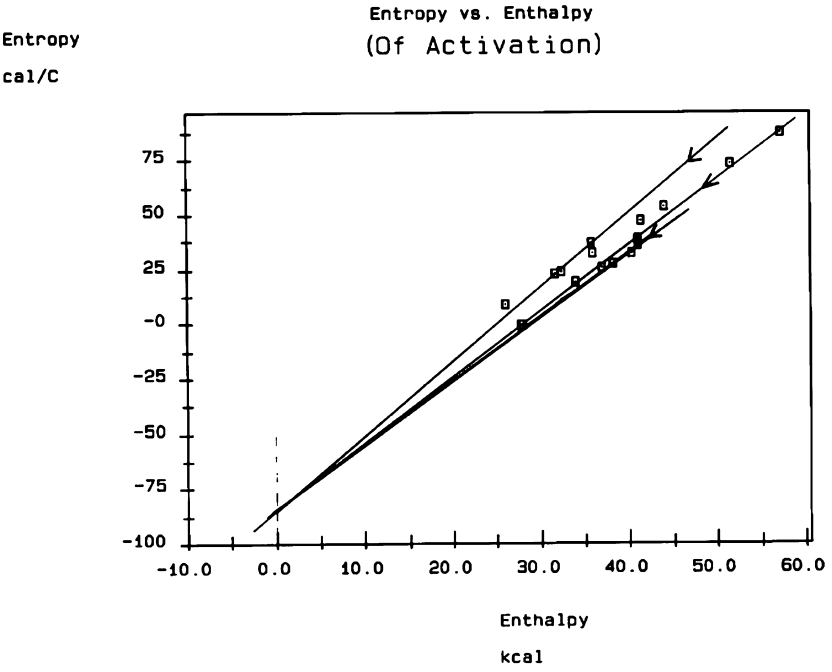


Figure 4.9: Compensation search in the EE plane for PS_RL showing only the *negative* compensation results of the analysis conducted in Figure 4.6.

EBSCOhost - printed on 2/13/2023 12:32 AM via . All use subject to https://www.ebsco.com/terms-of-use

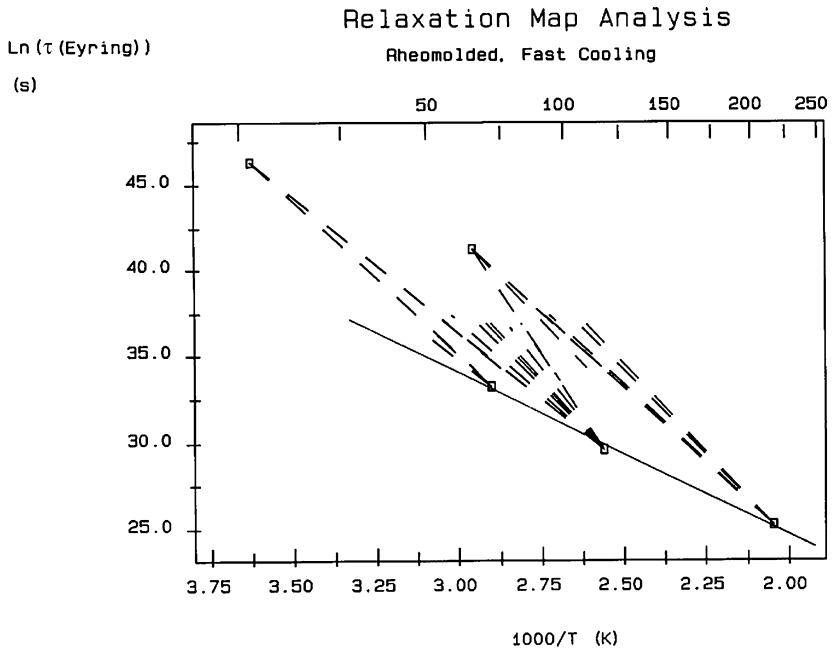


Figure 4.10: Schematic reconstruction for PS_RL of the compensations of the spectral lines in Figure 4.5 following the compensation search results of Figures 4.8 and 4.9.

Figure 4.10 represents a summary of our compensation search, displaying a triple-Z-structure with several Z-lines and six compensation points (three positive and three negative). Note that we have drawn a single line through the positive compensation points: this feature expresses, in the Eyring plane, the convergence of the positive compensation lines in the EE plane (Figure 4.8).

We have found the following results (with ΔS_p in cal/°C/m and ΔH_p in kcal/m):

$$\Delta S_p = 2.9514\Delta H_p - 67.95 \quad \text{for } T_p \text{ [65–70 °C]}$$
$$\Delta S_p = 3.6268\Delta H_p - 92.06 \quad T_p \text{ [70–75 °C]}$$
$$\Delta S_p = 2.5720\Delta H_p - 59.19 \quad T_p \text{ [75–105 °C]}$$
$$\Delta S_p = 2.9603\Delta H_p - 81.85 \quad T_p \text{ [105–120 °C]}$$
$$\Delta S_p = 2.3862\Delta H_p - 62.04 \quad T_p \text{ [120–135 °C]}$$
$$\Delta S_p = 2.6381\Delta H_p - 73.74 \quad T_p \text{ [140–150 °C]}$$

EBSCOhost - printed on 2/13/2023 12:32 AM via . All use subject to https://www.ebsco.com/terms-of-use

The free energy of activation energy and the temperature of compensation at the compensation points ΔG_c, T_c can be derived from the regressional analysis:

	ΔG_c (kcal/m)	T_c (°C)
Comp $(1)^+$	23.02	65.7
Comp $(1)^-$	25.38	2.57
Comp $(2)^+$	23.01	115.6
Comp $(2)^-$	27.65	64.6
Comp $(3)^+$	26	145.9
Comp $(3)^-$	27.95	105.9

At first sight, the relaxation behavior looks chaotic. However, it appears that the Gibbs free energy at the compensation points alternates between two values, approximately 23 and 27.75 kcal/m. It also seems that whatever goes on at T_g itself is not inherent to that temperature, and that we can define several Z-lines, one above and one below T_g. We call T_g^- and T_g^+ the "transitions," as defined by the corresponding Z-lines, which are observed in the sub-T_g and the $T > T_g$ regions: their values can be determined from the crossing of the positive and negative compensation lines:

$$\Delta S_g^- = 37.42\,\text{cal/°C/m}, \quad T_g^- = 66.2\,\text{°C}$$
$$\Delta H_g^- = 35.70\,\text{kcal/m}$$

$$\Delta S_g = 90.93$$
$$\Delta H_g = 58.37, \quad T_g = 102.6\,\text{°C}$$

$$\Delta S_g^+ = 48.72, \quad T_g^+ = 140.0\,\text{°C}$$
$$\Delta H_g^+ = 46.42$$

Figure 4.11 is a plot in the ΔG plane of the three Z-lines corresponding to T_g^-, T_g, and T_g^+. The intercept of the T_g and T_g^- lines occurs for $\Delta G_c = 20$ kcal/m, $T_c = 150$ °C, and the intercept between the T_g^+ and T_g Z-lines is at $\Delta G_c = 32.5$ kcal/m, $T_c = 25$ °C. The low Tc, 25 °C, may be associated with $T_{\beta,o}$, and the upper T_c, 150 °C, could either be a second T_g, such as the one observed for PEEK, without the presence of crystallites to induce its stability, a kind of $T_g(U)$ formed and stabilized under "sustained orientation" due to the Rheomolding treatment during cooling, or it could be associated with the T_{LL} transition, as defined in Part I, Chapter 2, but this appears at variance with the criteria proposed in that chapter of a temperature making $\Delta S_p = 0$. Note that $T_{\beta,o}$ is the lowest value (at zero rate) that can be found experimentally for T_β, i. e., the temperature of infinite viscosity found from the Gibbs–DiMarzio analysis of rheological data [91]. We propose that the "transitions" revealed by multi-compensation analysis in Figure 4.11 correspond to the T_β, $T_g(L)$, and $T_g(U)$. This appears to be the first time that is mentioned that two states of amorphous matter can subsist in sustained condi-

EBSCOhost - printed on 2/13/2023 12:32 AM via . All use subject to https://www.ebsco.com/terms-of-use

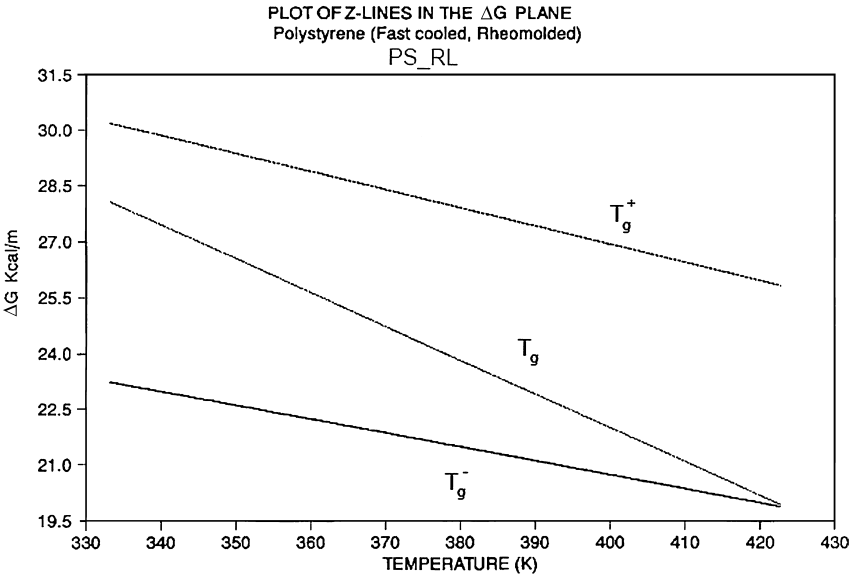


Figure 4.11: Recapitulation of the interactive coupling map for PS_RL shown as Z-lines in the ΔG plane.

tions without the need of crystals to stabilize them, at least up to the T_{LL} temperature which marks the end of the stability of the cross-duality of the interactions defined by the Grain-Field Statistics (Part II, Chapter 3).

Figure 4.11 could be compared with a "frequency map" [202], obtained with a dynamical AC device (dielectric or mechanical). However, the depolarization data collected and analyzed by TWD are much richer in details than what is available from other thermal analysis techniques: this is demonstrated in Figures 4.12 and 4.13, which plot the variation of entropy and free energy of activation versus T_p. TWD seems to indicate that the transitions perceived below and above T_g have the same relaxation origin as T_g itself. This is the same overall mechanism of relaxation which seems to unfold with T_p, perhaps as a result of structuring of the free energy into a network, as suggested by the Dual-Phase and Cross-Dual-Phase theory ([118, 137], also see Part I, Chapter 3). Furthermore, the detailed structure of the kinetic of relaxation is suggested by the way the compensation lines of the EE plot gather into two sets, one possibly emerging from the $\Delta S = 0$ axis, and the other from the $\Delta H = 0$ axis.

Figure 4.14 shows an attempt to schematize this speculative situation. Another interesting question concerns the number of discrete compensation lines in the EE plane and also their absolute value. Can we obtain a continuous series of discrete compensation lines by changing the thermomechanical history of the polymer, or is this effect discontinuous, framed to only correspond to certain given values?

EBSCOhost - printed on 2/13/2023 12:32 AM via . All use subject to https://www.ebsco.com/terms-of-use

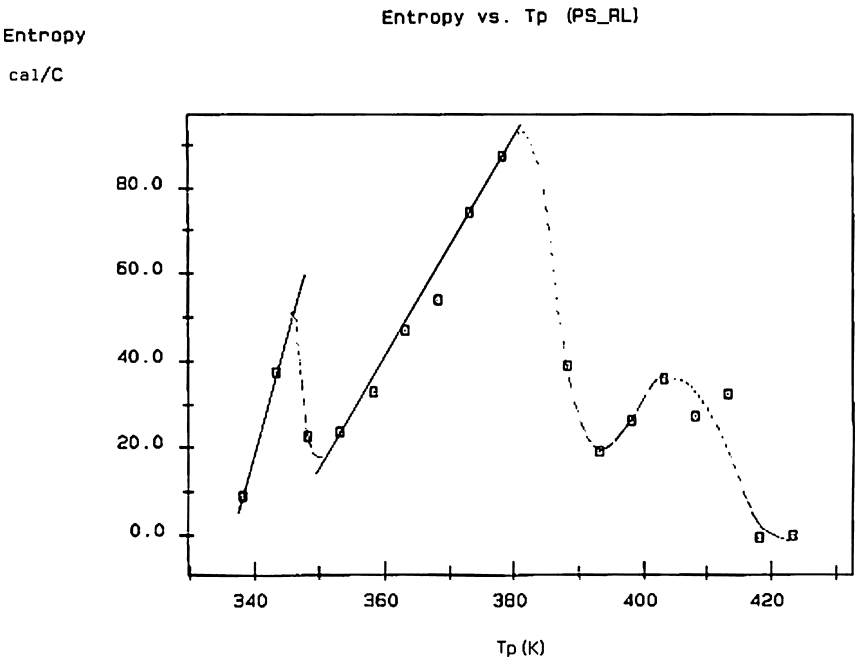


Figure 4.12: ΔS_p vs. T_p for PS_RL.

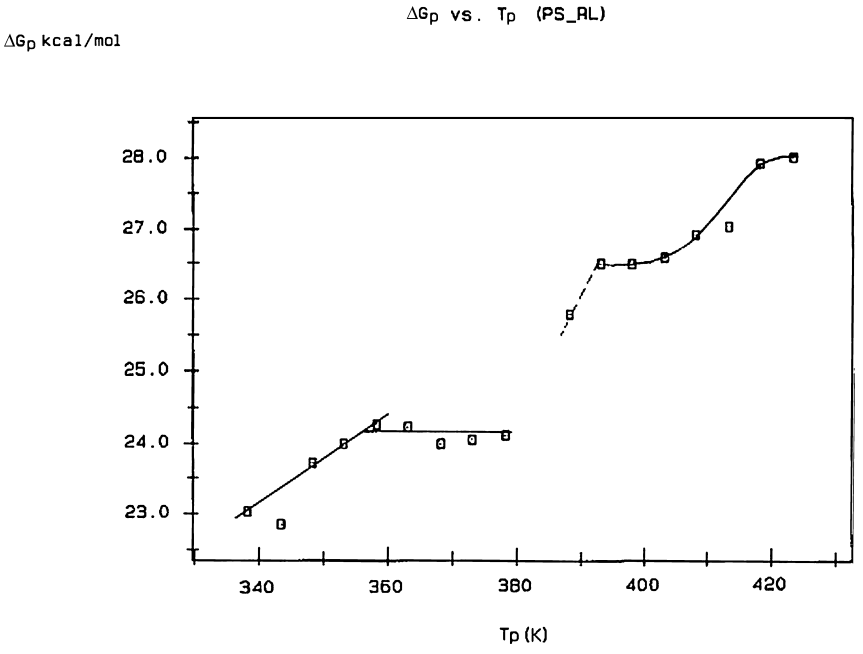


Figure 4.13: ΔG_p vs. T_p for PS_RL. There is a gap of 2.3 Kcal/m for ΔG_p over a temperature range from 360 to 395 K.

EBSCOhost - printed on 2/13/2023 12:32 AM via . All use subject to https://www.ebsco.com/terms-of-use

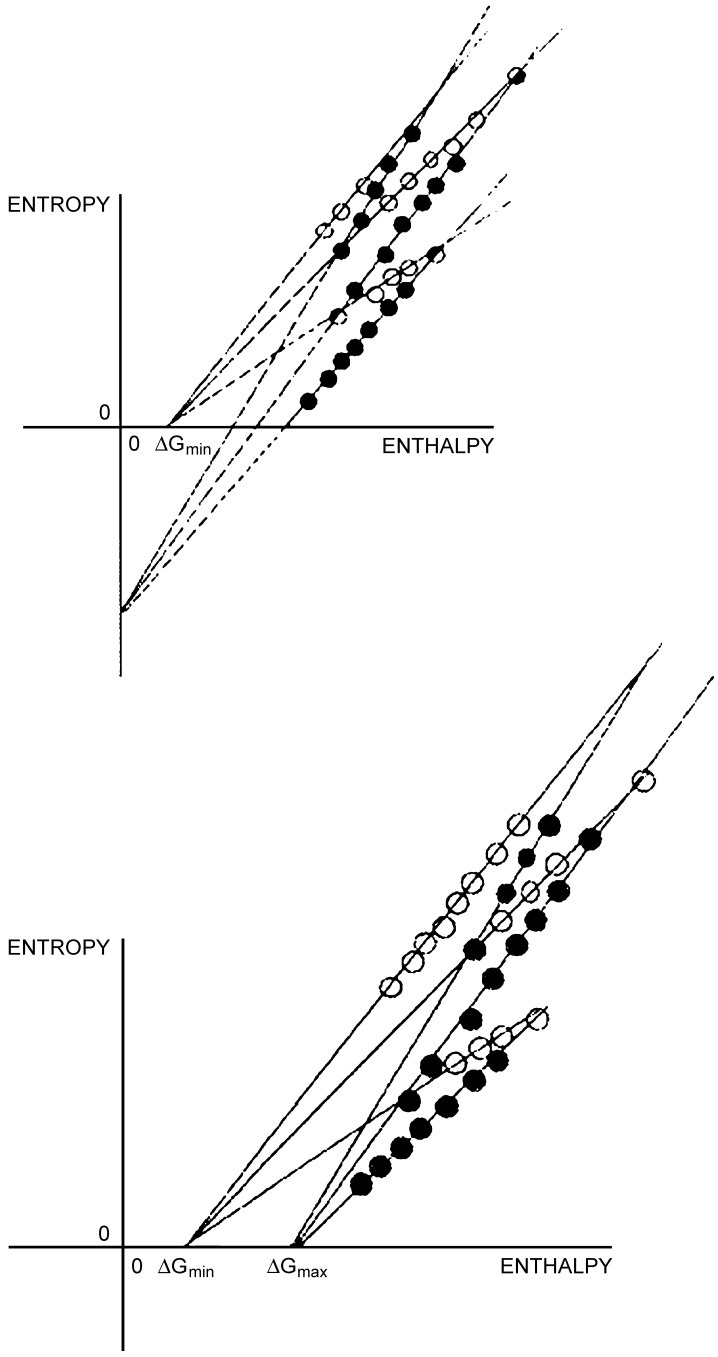


Figure 4.14: Speculative interpretation of the entropy vs. enthalpy results showing the existence of a Cross-Dual-Phase network to describe the interactive coupling between the dipoles as induced by a thermomechanical treatment during molding (Rheomolding).

EBSCOhost - printed on 2/13/2023 12:32 AM via . All use subject to https://www.ebsco.com/terms-of-use

Let us now go back to the analysis of the slowly cooled sample PS_VA (Figure 4.4). We said earlier that two negative compensations are clearly visible (Figure 4.4). We can now reexamine the situation: point 5 (T_p = 95 °C) seems to line up with point 4 and 6 to form a positive compensation line. The positive compensation line is not defined with certainty in this case since we only have one intermediate point between 4 and 6 to determine its slope and intercept. We have calculated the following parameters:

$$\text{Comp}(1)^- \ \Delta S_p = 3.9900\Delta H_p - 99.03 \quad \text{for } T_p \text{ [60–80 °C]}$$
$$\text{Comp}(2)^+ \ \Delta S_p = 2.6236\Delta H_p - 66.08 \qquad T_p \text{ [80–105 °C]}$$
$$\text{Comp}(3)^- \ \Delta S_p = 2.8573\Delta H_p - 81.93 \qquad T_p \text{ [105–125 °C]}$$

The coordinates of the compensation points are found from the equation of the EE curves:

	ΔG_c (kcal/m)	T_c (°C)
Comp $(1)^-$	24.83	−22.37
Comp $(2)^+$	25.23	108.08
Comp $(3)^-$	28.67	75.47

The intercept of lines 1^- and 2^+ is apparently point 4, *which is located on the* $\Delta S = 0$ *horizontal line*. Therefore, the free activation energy of the first two compensation points is approximately the same: $\Delta G(1)^- = \Delta G(2)^+ = 25.0$ kcal/m. This is an intriguing result: how could the free energy of activation be the same – or approximately the same – for two adjacent compensation points? In the case of the fast cooled Rheomolded polystyrene, the free energy is the same every other compensation point, which suggests a periodic return to the same state after a cycle.

Figure 4.15 shows the result of the compensation search in the Eyring plane. The Z-line for the transition between the first (negative) and the second (positive) compensation lines is represented in the Eyring plane as the straight line joining the first two compensation points. It is almost obvious from Figure 4.15 that the two compensation points do not represent the same state. We know from Part I, Chapter 2 that ΔH_p and ΔS_p appear to be infinite at the compensation points (at least at T_g). There must be different infinite values at the two compensations, suggesting, perhaps, that ΔH_p and ΔS_p are related to functions of temperature with periodic singularities.

The temperature = T_g^- corresponding to the first Z-line is 80 °C. Up to that temperature, the Gibbs free energy of activation (Figure 4.16) varies linearly with T_p:

$$\Delta G_p = 0.1018 T_p - 10.96$$

The slope and intercept are not "classical" (0.070 and 0).

EBSCOhost - printed on 2/13/2023 12:32 AM via . All use subject to https://www.ebsco.com/terms-of-use

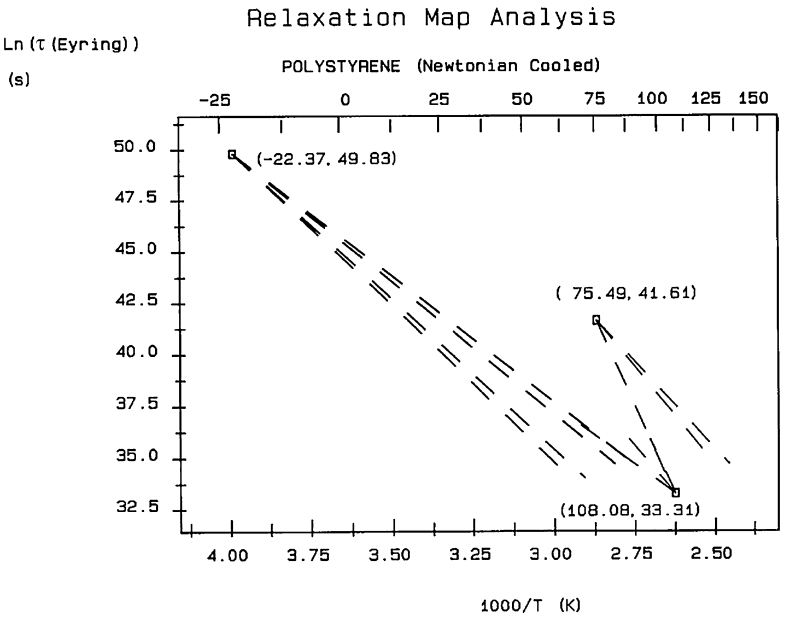


Figure 4.15: Reexamination of the compensation results of Figure 4.4 regarding the slowly cooled PS_VA sample as a consequence of the interpretation of sample PS_RL.

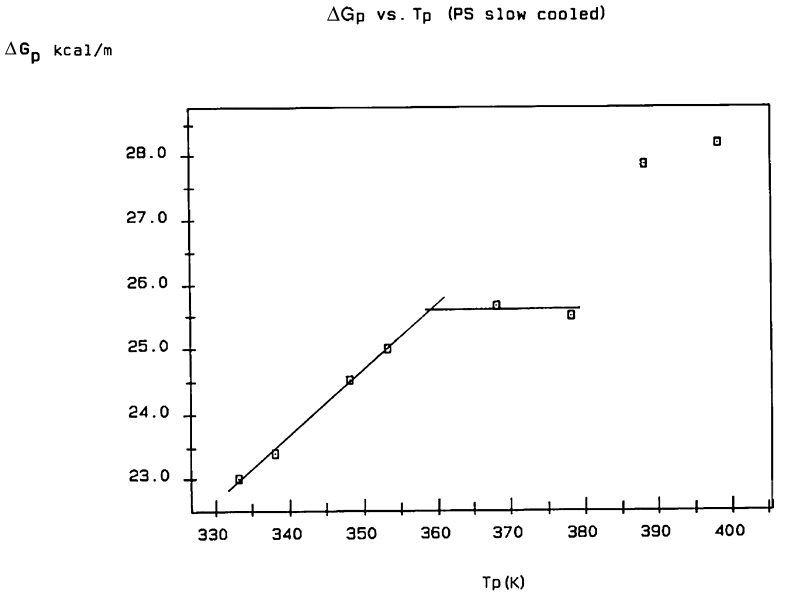


Figure 4.16: ΔG_p vs. T_p (K) for sample PS_VA. See text.

EBSCOhost - printed on 2/13/2023 12:32 AM via . All use subject to https://www.ebsco.com/terms-of-use

Between 80 °C and 105 °C, the free energy seems to be approximately constant to 25.52 kcal. Then the second Z-line occurs, at T_g, which shows up as a discontinuous change of ΔG_p, and a return to a linear relationship between ΔG_p and T_p. Hence, as the first Z-line is crossed, at 80 °C, there is a radical change in the structure of the free energy.

The free energy of activation at the third compensation point is: $\Delta G(3)^{-} = 8.675$ kcal/m. This time, the alternation from one compensation line to the next seems to result in a more substantial change of free energy at the compensation point.

In conclusion, the *relaxation behavior for the slowly cooled specimen presents interesting characteristics which are not observed for the fast quenched sample*. Again, we observe a series of positive and negative compensation lines which can be analyzed in the same systematic way. The analogy between what goes on in the EE plane and the Log τ vs. $1/T$ plane is striking: we observe a Z-structure in the EE plane.

Figures 4.17 to 4.20 are EE plots obtained on the same polystyrene specimen submitted to a variety of thermomechanical treatments. These samples are Rheomolded specimens [124] called PS_RG, PS_RF, PS_RO, and PS_RM. For each sample, the Rheomolding conditions are varied during cooling. We are providing these relaxation maps without further comments to illustrate the generality of the phenomenon of multicompensations for a monophasic amorphous system and to present some of their additional features.

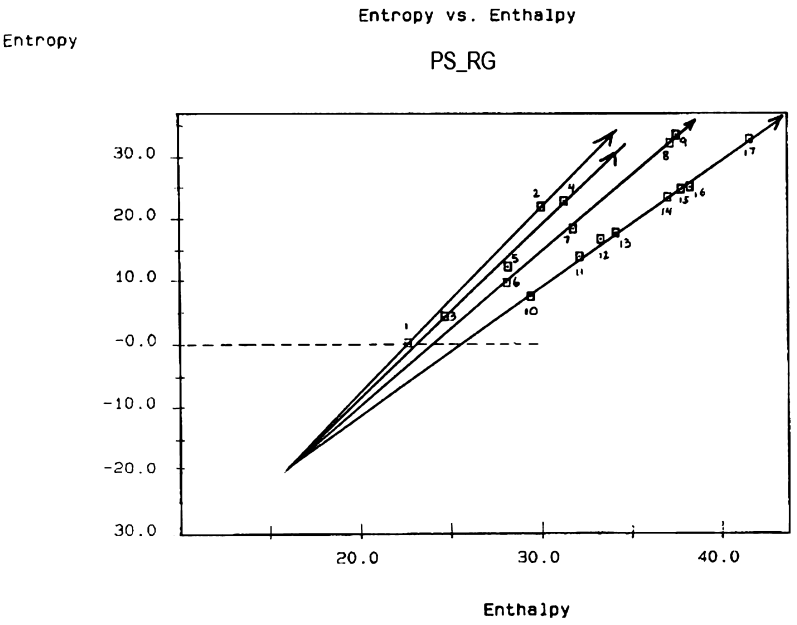


Figure 4.17: Compensation search in the EE plane for a different thermomechanical treatment during molding: sample PS_RG.

EBSCOhost - printed on 2/13/2023 12:32 AM via . All use subject to https://www.ebsco.com/terms-of-use

Figure 4.17 shows the PS_RG EE plot. It is observed that points 1 and 2, 3 and 4, 6–9, and 10–17 gather into four positive compensation lines which themselves *compensate*. The lack of points to determine the first two compensation lines with accuracy limits the validity of our findings. However, it seems that the compensation lines converge into a point which is located on neither the $\Delta H = 0$ nor the $\Delta S = 0$ axis (we could force the fit differently, but we do not know which way is justified). We find –8 cal/°C/m and 20 kcal/m for the point of convergence between the compensation lines.

The behavior for the polystyrene sample of Figure 4.18 (PS_RF) is quite similar, with approximately the same value for the converging point of the compensation lines in the EE plane, although the individual compensation lines do not have the same T_c and they do not collect the same T_ps. In other words, the fragmentation of the T_p temperature span is different. Figure 4.19 gives the case of PS_RO for another thermal treatment: a set of compensation lines emerges from a point located on the $\Delta S = 0$ axis ($\Delta H_c = 23$ kcal/m), and Figure 4.20 (PS_RM) illustrates an example of compensation lines seemingly compensating from a point on the $\Delta H = 0$ axis.

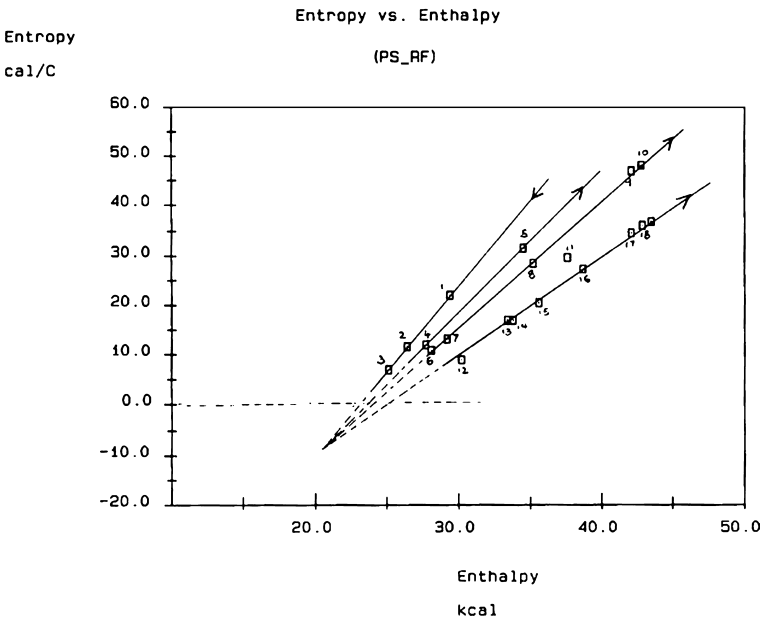


Figure 4.18: Compensation search in the EE plane for a different thermomechanical treatment during molding: sample PS_RF.

EBSCOhost - printed on 2/13/2023 12:32 AM via . All use subject to https://www.ebsco.com/terms-of-use

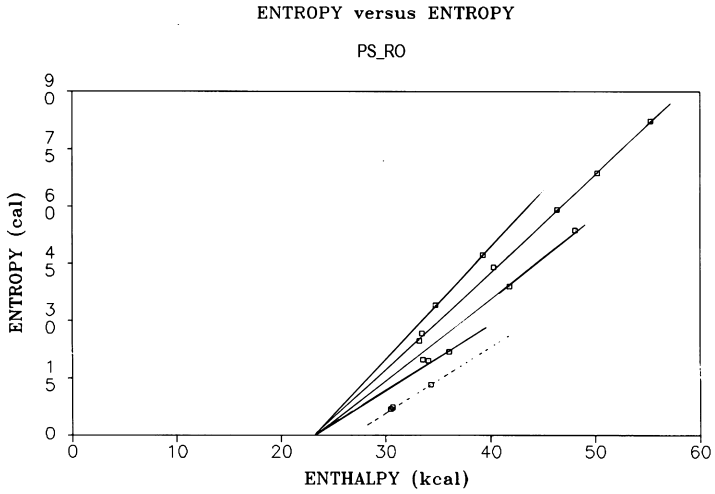


Figure 4.19: Compensation search in the EE plane for a different thermomechanical treatment during molding: sample PS_RO.

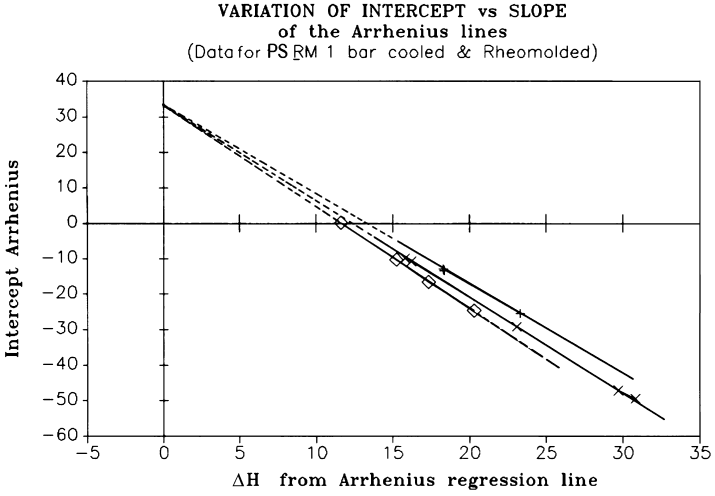


Figure 4.20: Compensation search in the Arrhenius plane (notice the difference with the EE plane used for similar Figures). for a different thermomechanical treatment during molding: sample PS_RM.

II.4.2.2 Polycarbonate

Figures 4.21 and 4.22 are the EE plots for two polycarbonate specimens which have been annealed either at 175 °C for 1 minute (Figure 4.21) or at 265 °C for 5 minutes (Figure 4.22). Although Izod impact tests were not performed to check our assertion, it is

EBSCOhost - printed on 2/13/2023 12:32 AM via . All use subject to https://www.ebsco.com/terms-of-use

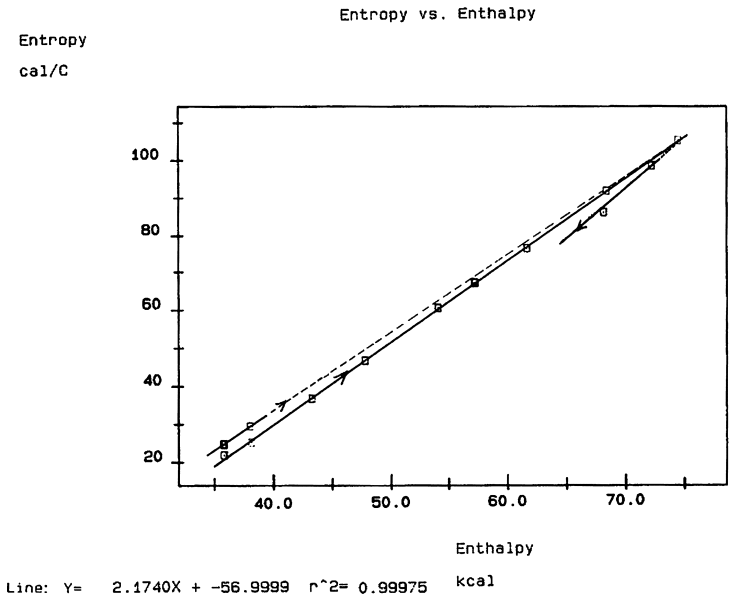


Figure 4.21: Compensation search in the EE plane for polycarbonate annealed at $T = 175\,°C$ for 1 min.

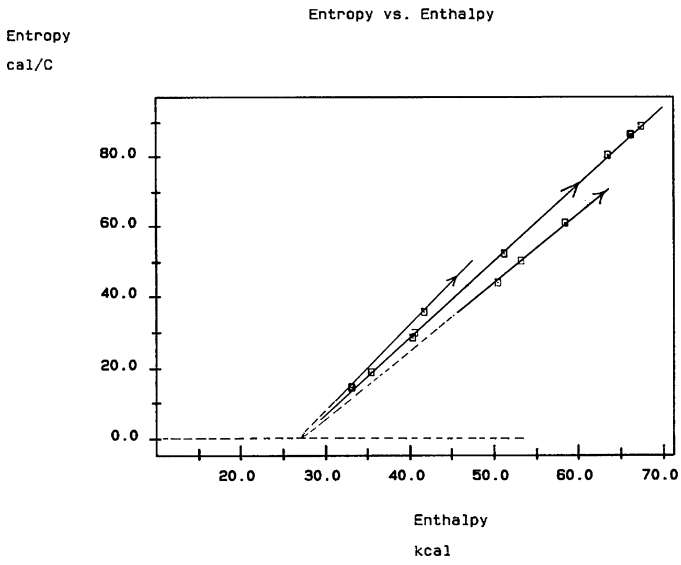


Figure 4.22: Compensation search in the EE plane for polycarbonate annealed at $T = 265\,°C$ for 5 min.

believed that the first annealing treatment has not induced any change in the mechanical ductility of the polymer, whereas the second treatment has induced brittleness [193–197]. The two EE plots are very different: the compensation lines for the more ex-

EBSCOhost - printed on 2/13/2023 12:32 AM via . All use subject to https://www.ebsco.com/terms-of-use

tensively annealed PC converge on a point of minimum entropy, i. e., on the $\Delta S = 0$ axis (Figure 4.22). This behavior is reminiscent of polystyrene. The case of the ductile polymer reveals that the compensation lines now emerge from the point of maximum of entropy (or enthalpy) of activation. This behavior is unique and unforeseen for brittle amorphous polystyrene. Based on this observation, could we set up a simple criterion for the ductility of amorphous polymers, and could we devise means to treat the material in order to induce ductility (for instance by a particular Rheomolding treatment [124])?

II.4.2.3 Conclusion

In conclusion, the most interesting observation in this first part of this chapter is the possibility to find a common kinetic origin to the various relaxation mechanisms found below T_g, at T_g, and above T_g. The phenomenon of compensation of the compensation lines seems to be a key to the understanding of the fundamental mechanism responsible for this apparently diversified and complex behavior (Chapter 3, Part I). Apparently, it also seems to play an important role in determining the mechanical properties in the material, separating distinctively brittle from ductile behavior.

II.4.3 Multiple compensations in a polymer liquid crystal: Vectra

The liquid crystal polymer analyzed here is Vectra 900 provided by Hoechst Celanese. Some of the TSD results obtained on this material have already been presented in Chapter 1 of this Part II. The focus in this chapter is on the multi-compensation behavior. We compare the results for annealed and quenched (unannealed) samples. Note that the experiments reported here were the initial results. Extensive characterization work done by the Hoechst Celanese Group by TSD/TWD has been reported elsewhere [49].

For each of the TSD peaks observed for Vectra A900 between –50 °C and 320 °C (Figures 2.35 to 2.45 of Chapter 2, Part II), the global TSD response – tan δ vs. T type – is the result of an interactive cooperation between various molecular relaxations.

In this section, we focus on the lower transition observed around 122 °C in Figure 2.43 of Part II, Chapter 2 for the corresponding polarization condition. Remember from Chapter 1 that this peak is observed near the temperature of polarization, shifts with the value of T_p, and seems to be induced or influenced by the voltage field in a manner uncharacteristic of a T_g transition. The thermal-windowing conditions are given in the header of Figure 4.23: the polarization temperature is chosen every 5 °C, between 15 °C and 120 °C, i. e., all around the peak. The voltage field across the film

EBSCOhost - printed on 2/13/2023 12:32 AM via . All use subject to https://www.ebsco.com/terms-of-use

hoechst unannealed	Anneal Temp : Inactive	Freeze Temp : 70.0
	Anneal Time : Inactive	Freeze Time : 5.0
Date : 04/13/1990	Polar Time : 2.0min	R3 Rate : 7.0
Time : 05: 40: 21	Polar Field : 5000.0V/mm	End ISO Temp: 160.0
	Tp Range: 15.0 120.0C	End ISO Time: 0.0
Solomat TSC/RMA	Thickness : 0.0mm	Window Width: 5.0
	Area : 78.0mm^2	

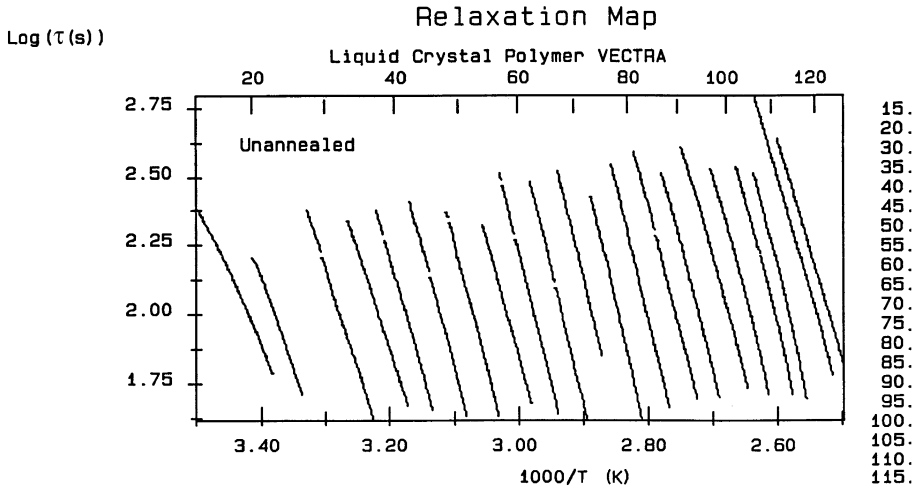


Figure 4.23: Relaxation map in the Arrhenius plane for the liquid crystal polymer Vectra A900.

is 5000 V/mm. The polarization and depolarization times are $t_p = t_d = 2$ min. The temperature window width is 5 °C and the heating rate is 7 °C /min.

Figure 4.24, for the annealed Vectra, displays two compensations: a positive compensation, which collects the low temperature T_p ($T_p < 75$ °C), corresponds to a low value of τ_c (approximately 10^{-4} sec) and describes coupling of the local dipoles, and a negative compensation gathers the higher-T_p relaxation modes ($T_p > 75$ °C) and is characterized by a long relaxation time $\tau_c = 10^{11}$ sec at the corresponding compensation point. The same type of behavior will be observed for the unannealed sample (Figure 4.32).

It has been speculated in Part I, Chapter 2 that the nature of the coupling between the local dipoles, giving rise to the relaxation process below the transition, is modulated above T_g by another large-scale ordering process, possibly the coordination of the dipoles due to the presence of the macromolecules, and that this type of coupling explains the long relaxation time observed for the negative compensation. This large-scale coupling corresponds to a dissipative "collective" aspect of the vertical structuring model, designated by Δ_x, Ln(υ_x) in Part I, Chapter 3. Figure 4.24 is reexamined and discussed in more detail later on.

EBSCOhost - printed on 2/13/2023 12:32 AM via . All use subject to https://www.ebsco.com/terms-of-use

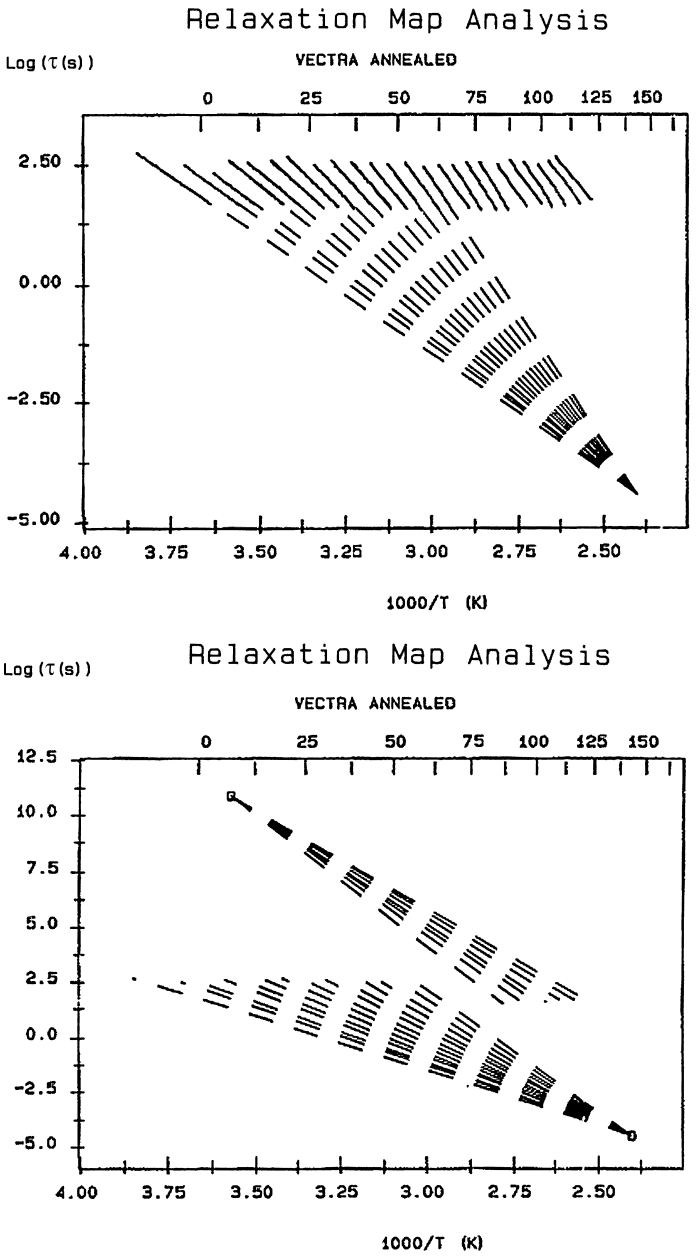


Figure 4.24: Relaxation map analysis for annealed Vectra A900: positive compensation (top) and positive and negative compensations (bottom).

EBSCOhost - printed on 2/13/2023 12:32 AM via . All use subject to https://www.ebsco.com/terms-of-use

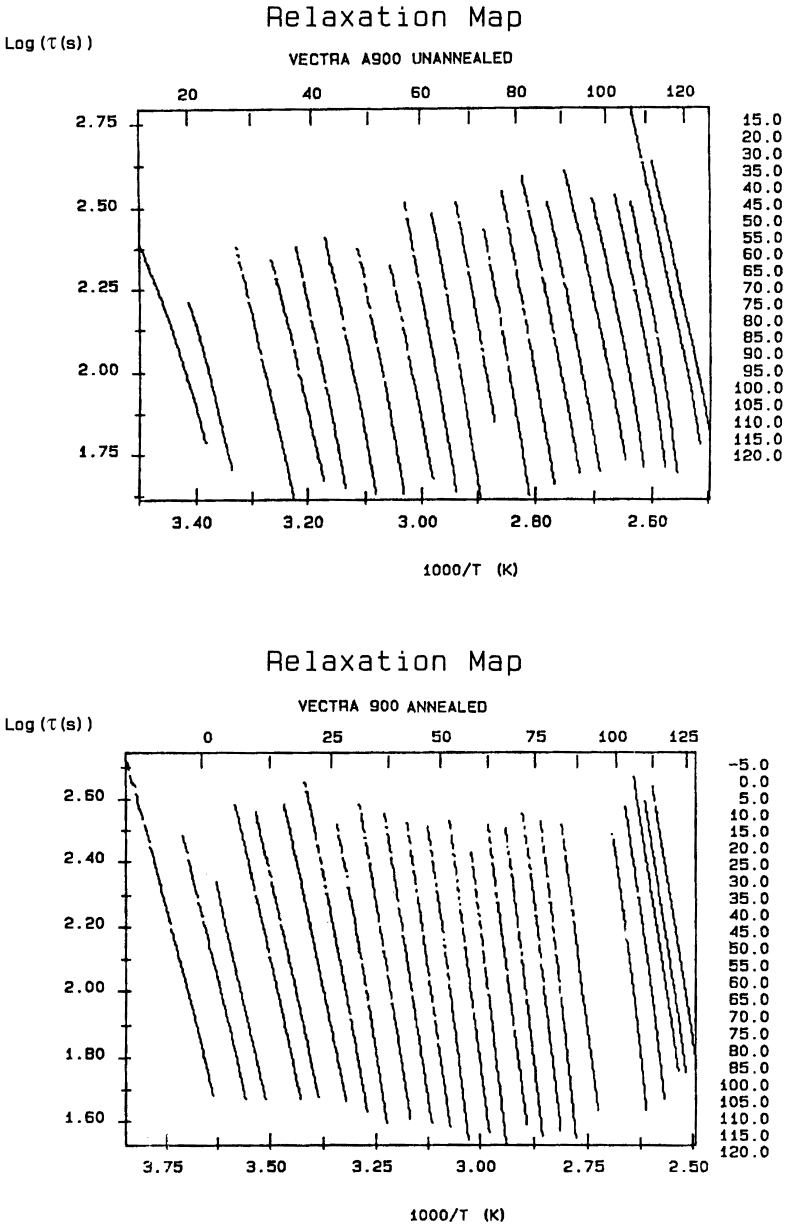


Figure 4.25: Relaxation maps in the Arrhenius plane for the unannealed Vectra (top) and for the annealed Vectra (bottom).

Figure 4.25 compares the relaxation maps for the annealed and unannealed Vectra films. It is clear that a *quantitative* analysis of the maps is necessary in order to differentiate them. Tables 4.3 and 4.4 provide the thermokinetic constants which determine

EBSCOhost - printed on 2/13/2023 12:32 AM via . All use subject to https://www.ebsco.com/terms-of-use

the value of the enthalpy, entropy, and Gibbs free energy of activation at T_p for various polarization temperatures T_p.

Table 4.3: Thermokinetic parameters for unannealed Vectra.

T_p (°C)	T_m (°C)	ΔH_p (kcal/mol)	ΔS_p (cal/°C/mol)	ΔG_p (kcal/mol)
15.0	22.6	23.0905	11.3125	19.8325
20.0	26.8	29.6980	32.6740	20.1245
30.0	37.0	33.1219	40.7925	20.7618
35.0	42.2	32.8185	37.8317	21.1663
40.0	46.0	37.6467	51.7749	21.4412
45.0	51.3	39.4906	55.5255	21.8335
50.0	56.7	40.2225	55.7394	22.2187
55.0	62.3	38.2236	47.5337	22.6325
60.0	67.2	42.3863	58.2948	22.9741
65.0	72.3	44.0847	61.4076	23.3289
70.0	77.7	44.1039	59.3750	23.7383
75.0	82.6	46.3405	63.9370	24.0904
80.0	88.3	44.0476	55.4253	24.4825
85.0	93.8	41.0338	45.1172	24.8818
90.0	98.4	41.0293	43.6202	25.1952
95.0	104.6	38.2017	34.1308	25.6416
100.0	109.3	40.1249	37.9171	25.9818
105.0	114.9	41.0806	38.8398	26.3992
110.0	118.1	43.9279	45.3075	26.5751
115.0	124.5	36.7485	25.1108	27.0055
120.0	127.3	35.5653	21.3979	27.1559

Figure 4.26 is a plot of the entropy of activation versus T_p for unannealed Vectra. The tendency of that plot is shown at the top of Figure 4.27, showing a maximum for $T_p = 340$ K (67 °C). The apparent large scatter will be explained later. Figure 4.27 compares the average curves obtained for both the annealed and unannealed Vectra. The entropy of activation is always greater for the annealed sample, which seems in contradiction with the aging studies of Chapter 3 (see later). Figure 4.27 (bottom) compares the intensity of the current at the peak maximum for the individual thermally windowed relaxation modes at various T_ps. It is clear that both the polarizability (Figure 4.27 bottom) and the internal mobility (Figure 4.27 top) are greater for the annealed Vectra, although TSD and TSDP outputs (Figures 2.44 and 2.45 of Chapter 2,

EBSCOhost - printed on 2/13/2023 12:32 AM via . All use subject to https://www.ebsco.com/terms-of-use

Table 4.4: Thermokinetic parameters for annealed Vectra.

T_p (°C)	T_m (°C)	ΔH_p (kcal/mol)	ΔS_p (cal/°C/mol)	ΔG_p (kcal/mol)
−5.0	1.9	22.3459	15.1375	18.2891
0.0	8.0	23.8845	18.9037	18.7238
5.0	11.6	25.0782	21.9862	18.9660
10.0	18.5	26.2810	23.9548	19.5018
15.0	22.3	26.5124	23.5823	19.7207
20.0	28.0	28.1567	27.3390	20.1464
25.0	32.5	31.2456	36.1395	20.4760
30.0	37.1	35.1746	47.4436	20.7992
35.0	42.7	35.7443	47.1848	21.2113
40.0	47.8	37.9507	52.2807	21.5869
45.0	52.4	41.1641	60.5221	21.9181
50.0	57.3	44.7687	69.6962	22.2569
55.0	62.8	45.0265	68.1450	22.6749
60.0	67.3	49.6982	80.2190	22.9853
65.0	72.8	46.5235	68.4130	23.4000
70.0	77.3	51.2853	80.4405	23.6942
75.0	82.6	50.8939	77.0463	24.0818
80.0	87.0	54.2602	84.6454	24.3803
85.0	93.8	47.3495	62.6803	24.9099
100.0	109.9	46.2715	54.1260	26.0825
105.0	116.4	42.2088	41.4913	26.5251
110.0	121.6	37.6995	28.3574	26.8386
115.0	124.5	38.0427	28.5303	26.9729
120.0	128.2	36.4548	23.5152	27.2133

respectively) apparently show the opposite phenomenon, less mobility for the annealed sample. This requires clarification. Figure 4.28 is a reexamination of the low-tail ($T_p < 75$ °C) entropy of activation for both the unannealed (top) and annealed (bottom) Vectra. The variation of entropy versus T_p displays some "structure," which is not explainable by data scatter. The structure is more pronounced for the unannealed Vectra, which has three small but well-defined humps. These humps are still clearly visible at the same location but more or less smoothed out for the annealed specimen.

EBSCOhost - printed on 2/13/2023 12:32 AM via . All use subject to https://www.ebsco.com/terms-of-use

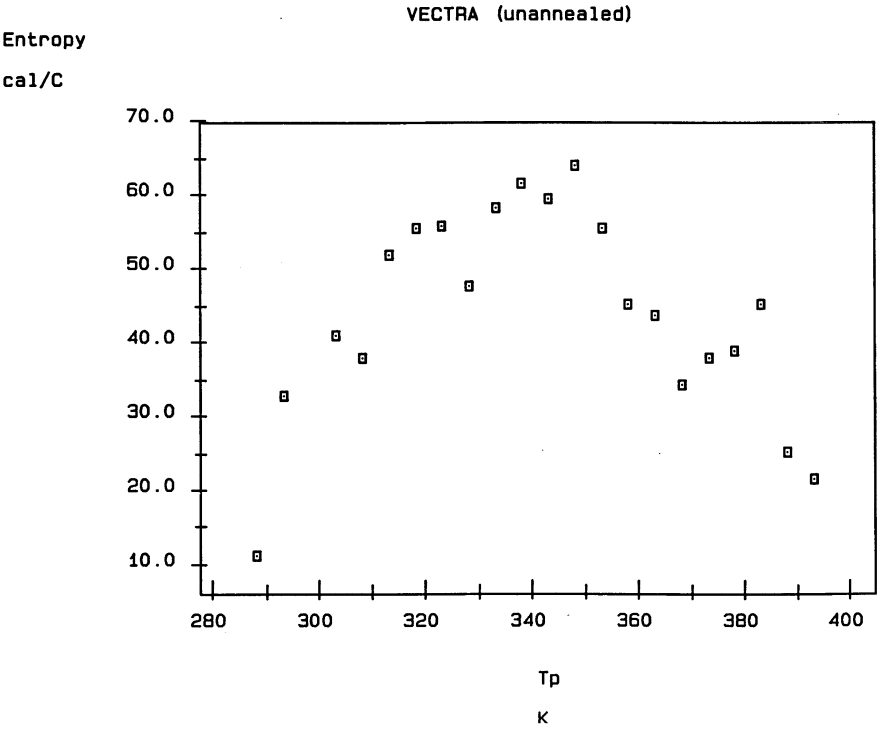


Figure 4.26: ΔS_p vs. T_p (K) for unannealed Vectra.

Figure 4.29 shows that although the entropy of activation presents certain "structures" as T_p is increased, the Gibbs free energy, ΔG_p, calculated as $(\Delta H_p - T_p\,\Delta S_p)$ remains structureless and is strictly the same for both samples; furthermore, it is shown to vary proportionally with the polarization temperature ($\Delta G_p/T_p = 72$ cal/m/K). As explained in Part I, Chapter 2, this behavior is typical of materials across a transition such as at a glass transition temperature ($T_p = T_p'$ and $A_c = 72$ in equation (2.32) of Part I, Chapter 2). It also indicates that annealing Vectra 900 results in a "restructuring" of the enthalpy and entropy of activation of the relaxation modes coupling up in the amorphous phase, but that the value of A_c itself at various T_ps remains independent of the changes in the amorphous phase resulting from the annealing treatment. Another interesting observation comes from the examination of Figure 4.30. Although the entropy of activation (the mobility) shows several humps (top figure) when plotted against the polarization temperature, the intensity at the peak maximum of the elementary relaxations (Figure 4.30, bottom) does not display any structure; furthermore, the maximum observed for the entropy at around 70 °C (Figure 4.27, top) is not observed for the peak intensity (Figure 4.27, bottom) before a much higher temperature is reached (110 °C for the annealed sample, 115 °C for the unannealed one). The

EBSCOhost - printed on 2/13/2023 12:32 AM via . All use subject to https://www.ebsco.com/terms-of-use

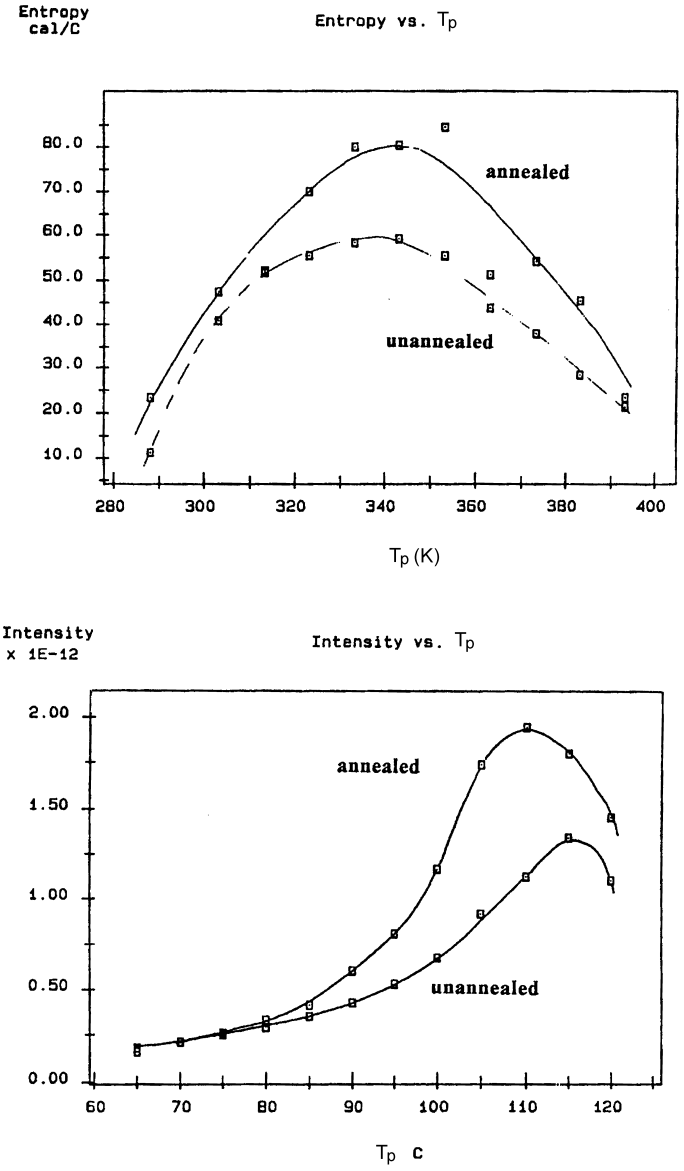


Figure 4.27: Comparison of the unannealed and annealed Vectra: plots of entropy vs. T_p (top) and of intensity of the Debye peaks at T_m vs. T_p (bottom).

possible reasons for the spread between these two maxima has already been discussed in Part I, Chapter 1 and Part II, Chapter 3. However, a spread of 40 °C seems very unusual and must have a different origin.

EBSCOhost - printed on 2/13/2023 12:32 AM via . All use subject to https://www.ebsco.com/terms-of-use

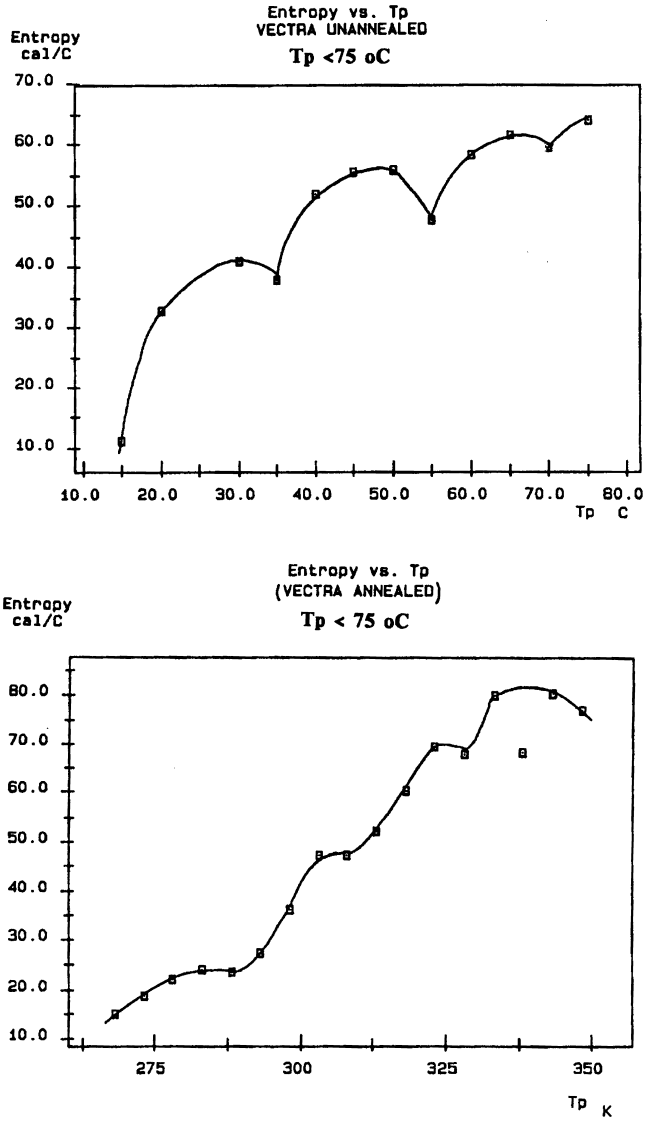


Figure 4.28: ΔS_p vs. T_p with $T_p < 75$ °C (348 K) for unannealed Vectra (top) and annealed Vectra (bottom).

In order to understand further what might be responsible for the structuring of the relaxation modes, let us study the compensation between the modes and concentrate, first, on the case of the unannealed Vectra. Figure 4.31 is a compensation search, a plot of intercept versus slope for the Arrhenius lines of Figure 4.25 (top). We have drawn

EBSCOhost - printed on 2/13/2023 12:32 AM via . All use subject to https://www.ebsco.com/terms-of-use

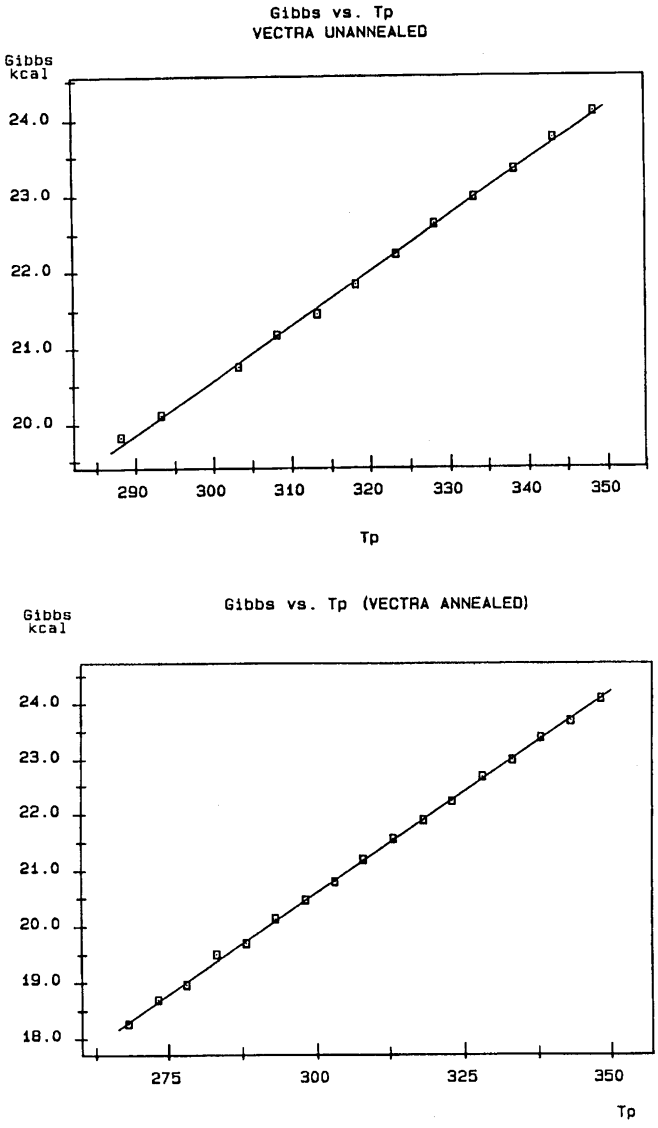


Figure 4.29: ΔG_p vs. T_p (K) with $T_p < 348$ K for unannealed Vectra (top) and annealed Vectra (bottom).

in Figure 4.31 two compensation lines, one positive and one negative, and Figure 4.32, the equivalent for the unannealed sample of Figure 4.24 presented earlier, is the result of the compensation search dividing the data into two groups, one which compensates at a low log τ_c^+ value and one which compensates at a high log τ_c value.

EBSCOhost - printed on 2/13/2023 12:32 AM via . All use subject to https://www.ebsco.com/terms-of-use

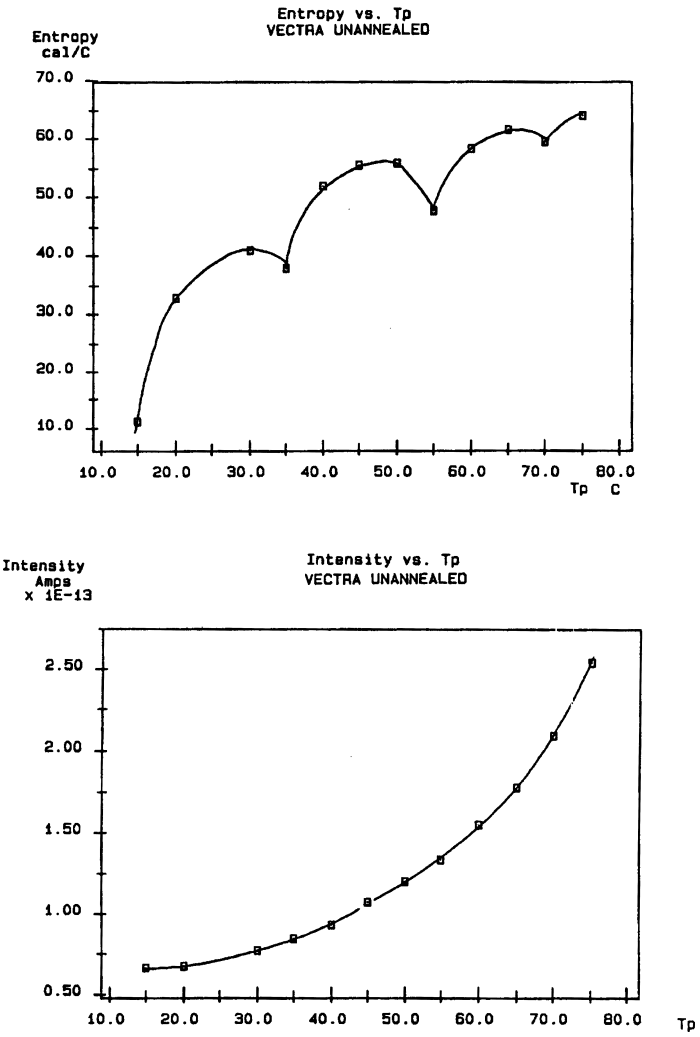


Figure 4.30: ΔS_p vs. T_p (top) and intensity of the Debye peak at T_m (bottom) for the unannealed Vectra. Details at low T_p (T_p between 15 °C and 80 °C).

Figure 4.33 shows that, in fact, the situation is rather more complex than the simple compensation lines drawn up in Figure 4.31. One observes in Figure 4.33a and b a series of compensation lines with characteristic jumps between compensation lines at specific temperatures along T_p. Figure 4.33a identifies the structure for the low-end temperature region ($T_p < 75$ °C), and Figure 4.33b concentrates on the upper region ($T_p > 75$ °C). Table 4.5 summarizes the compensation search, providing the coordinates of the compensation points for all the compensation lines and the DOD numbers calculated for both the unannealed and annealed specimens.

EBSCOhost - printed on 2/13/2023 12:32 AM via . All use subject to https://www.ebsco.com/terms-of-use

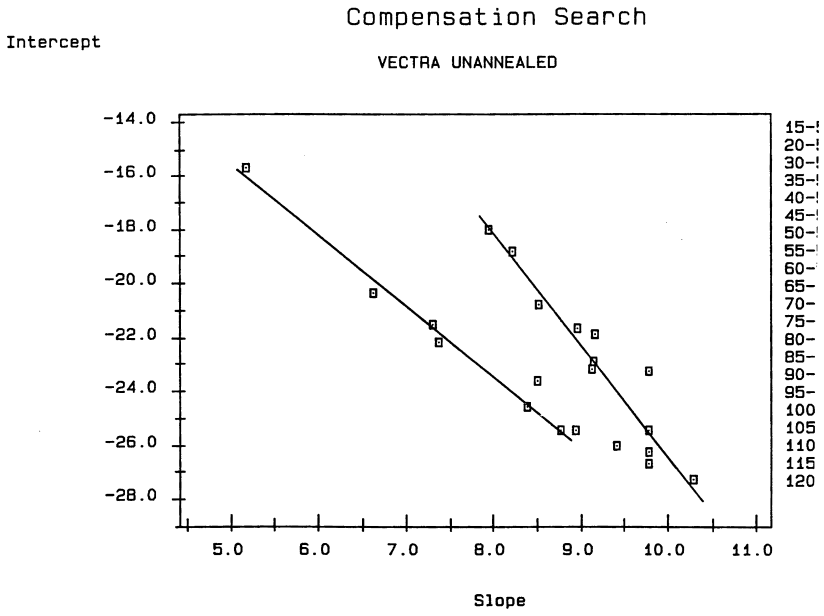


Figure 4.31: Compensation search in the Arrhenius plane for the unannealed Vectra showing a main positive and a main negative compensation among other points left behind.

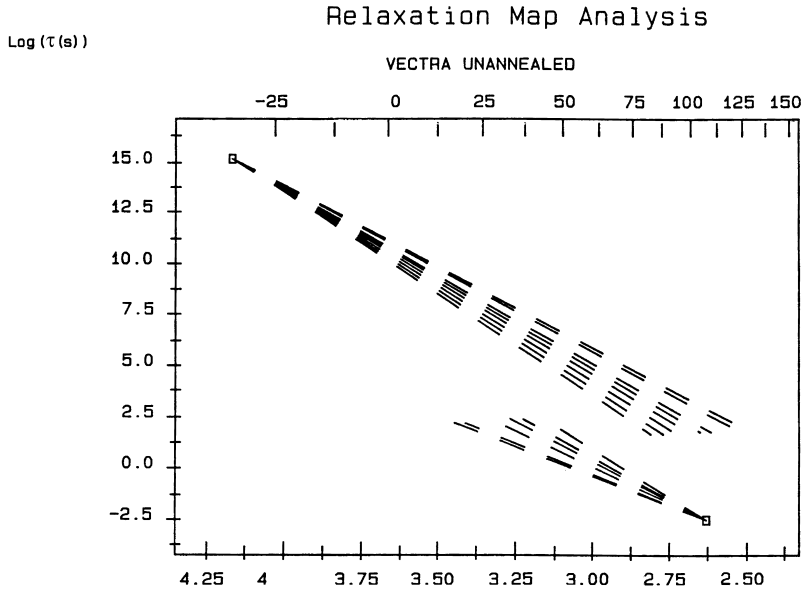


Figure 4.32: Reconstruction of the compensations in the Arrhenius plane for unannealed Vectra according to the main compensation search results of Figure 4.31. The entire solution is not complete.

EBSCOhost - printed on 2/13/2023 12:32 AM via . All use subject to https://www.ebsco.com/terms-of-use

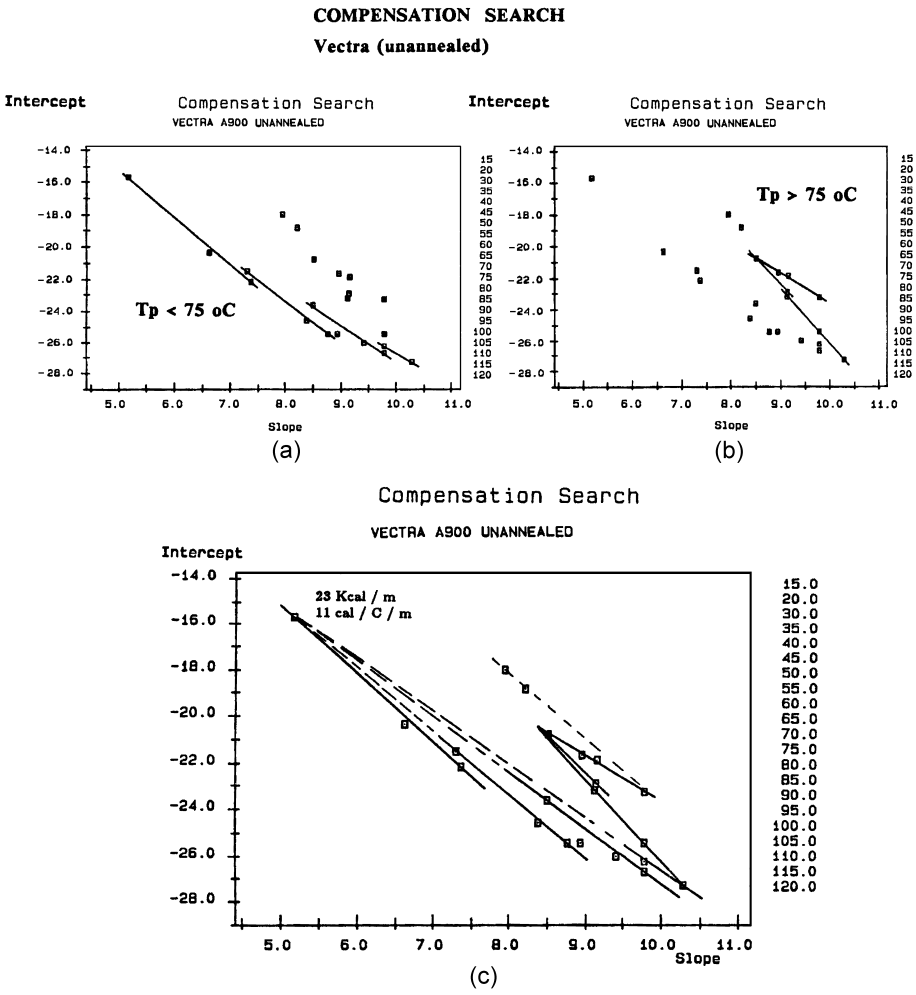


Figure 4.33: Construction of the various steps leading to the complete solution for the unannealed Vectra interactive coupling map. (a) $T_p < 75$ °C: four compensations. (b) $T_p > 75$ °C: three compensations. (c) Cross-Dual-Phase network showing two super-compensations.

The compensation lines which are observed in Figure 4.33a and b are described quantitatively in Table 4.5 (top) (unannealed Vectra). One sees a gradual increase of the DOD number for each consecutive compensation line when T_p increases from $T_p = 15$ °C to $T_p = 75$ °C. The compensation lines seem themselves to compensate, as observed in Figure 4.33c, i. e., they seem to emerge from a common single point: 23 kcal/m for the enthalpy of activation and 11.31 cal/°C/m for the entropy of activation. Figure 4.33b shows an identical structuring of the compensation lines for the polarization temperatures $T_p > 75$ °C. The common intercept of the compensation lines is 38 kcal/m and

EBSCOhost - printed on 2/13/2023 12:32 AM via . All use subject to https://www.ebsco.com/terms-of-use

Table 4.5: Results of the compensations ($T_p < 75$ °C and $T_p > 75$ °C) for the unannealed Cross-Dual-Phase network (top) and for the annealed Cross-Dual-Phase network (bottom).

Line	Compensation T_c (°C)	Log(τ_c) (Second)	DOD Number
$T_p < 75$ °C			
1	72.53	−0.82	44.58
2	108.02	−2.43	51.80
3	159.31	−4.13	59.37
4	213.28	−6.14	68.36
5	−39.33	16.07	−32.41
$T_p > 75$ °C			
1	9.58	9.14	−0.91
2	24.72	7.81	5.14
3	240.85	−4.19	59.29

Line	Compensation T_c (°C)	Log(τ_c) (Second)	DOD Number
$T_p < 75$ °C			
1	169.47	−5.22	64.34
2	87.78	−1.87	49.33
3	126.22	−3.62	57.15
4	113.10	−2.31	51.20
5	122.35	−2.14	50.40
$T_p > 75$ °C			
1	35.07	7.16	8.03
2	43.83	7.16	8.01

14.7 cal/°C in this case. A summary of the compensation search for the unannealed specimen is proposed in Figure 4.33c, which shows "super-compensation order" for the structure both below T_g and above T_g.

The treatment of annealed Vectra is presented in Figures 4.34 and 4.35. Figure 4.24, previously presented, also refers to the analysis of this specimen.

The equivalent figure to Figure 4.33, in the case of the annealed Vectra, is Figure 4.35 (Figure 4.35a for $T_p < 75$ °C and Figure 4.35b for $T_p > 75$ °C). As for Figure 4.31, as a first approximation, two compensation lines can be drawn up through the data showing a positive and a negative compensation (Figure 4.34). The result of this analysis is illustrated in Figure 4.24. Table 4.5 (bottom) provides the compensation points and the DOD numbers.

EBSCOhost - printed on 2/13/2023 12:32 AM via . All use subject to https://www.ebsco.com/terms-of-use

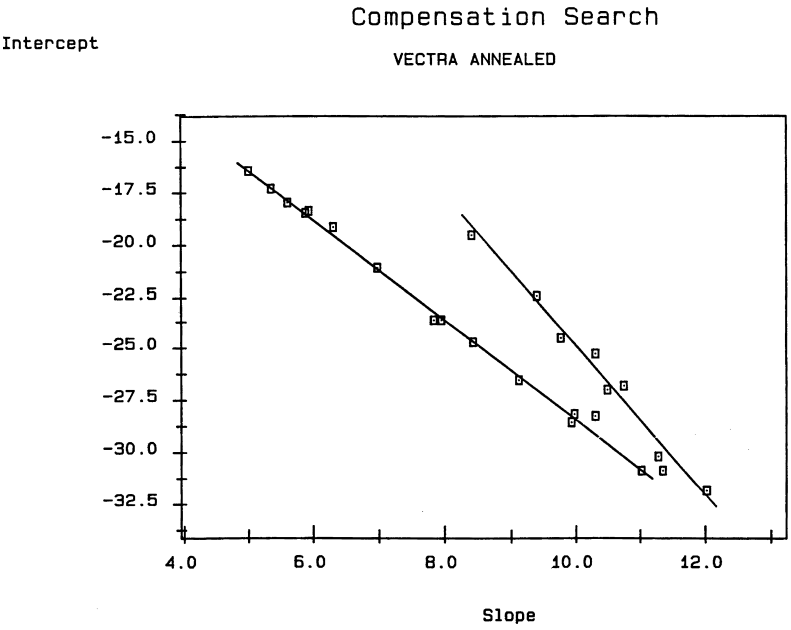


Figure 4.34: Compensation search in the Arrhenius plane for the annealed Vectra showing a main positive and a main negative compensation among other points left behind (7).

Figure 4.35 reveals that much less structure characterizes the temperature region below $T_p < 75\,°C$ and that there does not seem to be any super-compensation order in the rubbery state above $T_p > 75\,°C$. That is as if the apparent super-compensation order had dissolved out into the structure during the annealing stage.

We observe in Table 4.5 that for a given value of the DOD number, for the annealed or unannealed samples, T_c is always greater for the annealed specimen. Also, if one compares the DOD numbers for the low-T_p (positive) compensation lines shown in Figures 4.31 and 4.34, one sees that the compensation temperature is higher for the annealed specimen (recall from Part I, Chapter 2 that T_c is related to T_g) and the DOD number is bigger for the annealed specimen, an indication that the structure has gained disorder as it is annealed.

II.4.3.1 Discussion

The nature of the "transition" at around 75 °C is unclear. In some respects it has characteristics of a glass transition, with a maximum of the entropy of activation and a Z-structure associated with it (Part I, Chapter 2, positive and negative compensations). But the value of the entropy at the maximum is small, say half, compared to what is observed at the T_g of classical polyesters, indicating that a large constraint is imposed

EBSCOhost - printed on 2/13/2023 12:32 AM via . All use subject to https://www.ebsco.com/terms-of-use

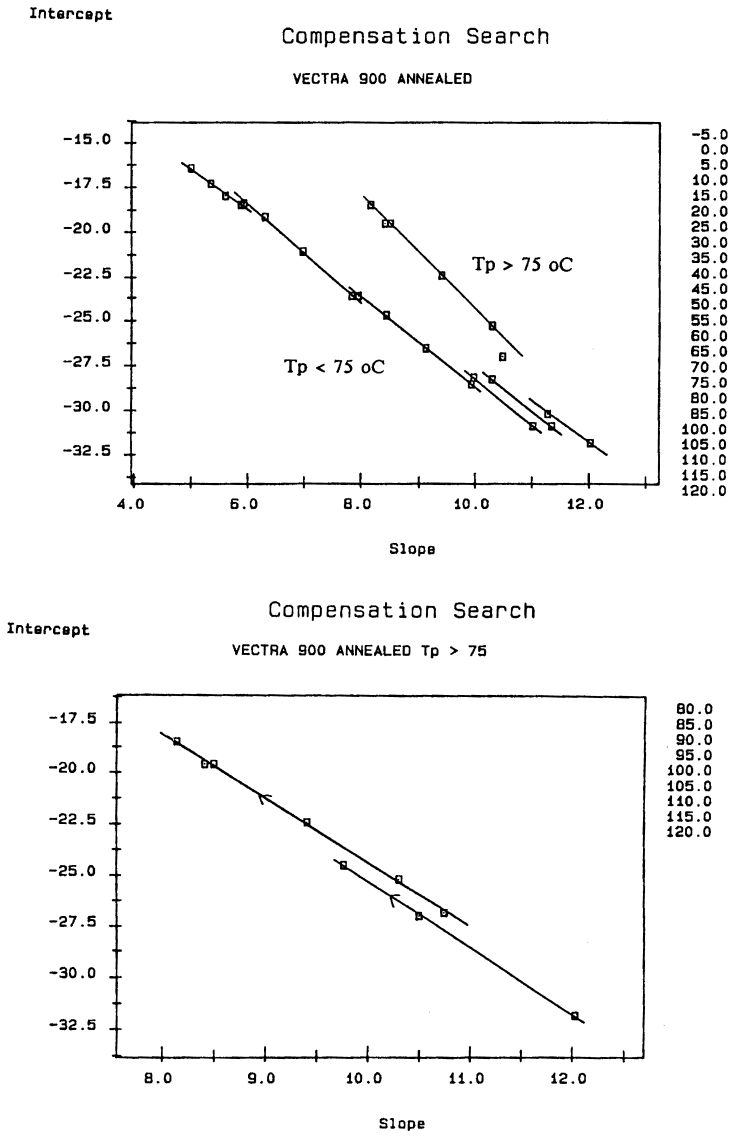


Figure 4.35: Compensation search in the Arrhenius plane for the annealed Vectra showing a different definition of the composition lines than in Figure 4.34. The graph at the top includes all T_ps from −5 °C to 120 °C. The graph at the bottom focuses on the $T_p > 75$ °C spectral lines and reveals two compensation lines.

by the surrounding of the dipoles, preventing the extent of their mobility. Furthermore, the characteristics of the compensation points, both for the positive and negative compensations, are not in line with what is normally associated with a glass transition. The value of the positive compensation relaxation time is very small ($10^{-2.5}$ sec

EBSCOhost - printed on 2/13/2023 12:32 AM via . All use subject to https://www.ebsco.com/terms-of-use

in Figure 4.32), indicating a very local type of coupling, like amorphous matter trapped in a crystalline phase or in a very ordered environment, and the negative "average" compensation relaxation time (10^{15} sec) is very large (10^4 to 10^5 are more classical values), which suggests that coupling above 75 °C occurs much beyond the entanglement scale, perhaps even involving the entire system of bonds. These observations are not consistent with a classical glass transition temperature. It reminds us of TWD results obtained on wood (see next section).

In Figure 4.27 the mobility of the dipoles seems to be enhanced by the thermal treatment: the current at the peak maximum is bigger for the annealed Vectra. This observation apparently contradicts previous statements that crystallization, and possibly other ordering processes taking place during thermal treatment, restricts the mobility. A possibility is that although local mobility of the individual dipoles is restricted by the annealing treatment, there is concurrently taking place an ordering process of the dipoles into nodular entities, "nodular dipoles," which are oriented by the voltage at the polarization stage. The voltage perhaps even helps induce the creation of these nodular dipoles, and so does the local crystallization of some of the bonds belonging to oriented chains already strongly tied up to one another by the relative bulkiness and stiffness of the medium.

A certain image of the morphology might arise from these various observations: the Vectra chains are rather stiff and elongated, parallel to the direction of flow during extrusion. Because of these configurational constraints and the stiffness of the conformers due to the presence of the aromatic components, lateral ordering and restricted two-dimensional crystallization are likely to occur, creating small bundles along the oriented chains and, under the influence of the voltage, nodular dipoles. The nodular dipoles are grown from the ordered regions, from the proximity of the local dipoles. These parts of the chains are ordered amorphous chains. Some regions along the fibrillated packs of chains remain purely amorphous and unordered, say random-coiled, although they might be oriented mechanically and have internal stress accumulating, which can be released by annealing close to the glass transition. Another aspect of these "truly amorphous" bonds is that they might serve as the flexible joints, at higher temperatures of annealing, allowing the nodular dipoles to rotate as whole packs from the direction of extension of the chains, in the plane of the film, to the third dimension, across the thickness, thus creating an availability of nodular dipoles in the direction of the voltage field, upon polarization. This interpretation explains why the intensity of the thermally windowed peaks is higher for the annealed (treated) Vectra. It also explains all the other features observed in the TSD/TWD, DSC, and DMA experiments.

Further research would help verify these interpretations. We suggest to pursue the research and the analysis by varying the intensity of the voltage and perform a complete TWD from −20 °C to 170 °C, varying the intensity of the voltage, to confirm whether the voltage field is actively involved, along with thermal activation energy, in the ordering process which seems to structure the morphology in the solid phase.

EBSCOhost - printed on 2/13/2023 12:32 AM via . All use subject to https://www.ebsco.com/terms-of-use

II.4.4 Multi-compensations in wood samples

Wood, a natural polymer, is a material whose mechanical properties are dominated by the fact that its molecular chains are both strongly oriented and crystalline. In wood, cellulose crystals, which comprise only 50 % to 60 % of the volume, take the form of tubular cells. The cellulose crystals are bonded with an amorphous lignin composed of carbohydrate compounds.

We have given in Chapter 2 of this Part II (Figures 2.33 and 2.34) the TSD peaks obtained for two wood samples (provided by the University of Mississippi). It is believed that lignin is the material which dielectrically relaxes here, and in this section, we present thermal-windowing results of the relaxation behavior in order to stress the structural differences between the boiled and unboiled samples.

The relaxation maps given in Figures 4.36 (unboiled sample) and 4.37 (boiled sample) are obtained by transforming all the elementary peaks obtained at various T_p into their Arrhenius transform. The conditions of polarization are specified in the header of Figures 4.36 and 4.37.

Wood not boiled	Anneal Temp : Inactive	Freeze Temp : 40
	Anneal Time : Inactive	Freeze Time : 5
Date : 04/05/1990	Polar Time : 2.0min	R3 Rate : 7
Time : 23: 38: 12	Polar Field : 100.0V/mm	End ISO Temp: 130
	Tp Range: 20.0 90.0C	End ISO Time: 0
Solomat TSC/RMA	Thickness : 0.6mm	Window Width: 5
	Area : 30.0mm^2	

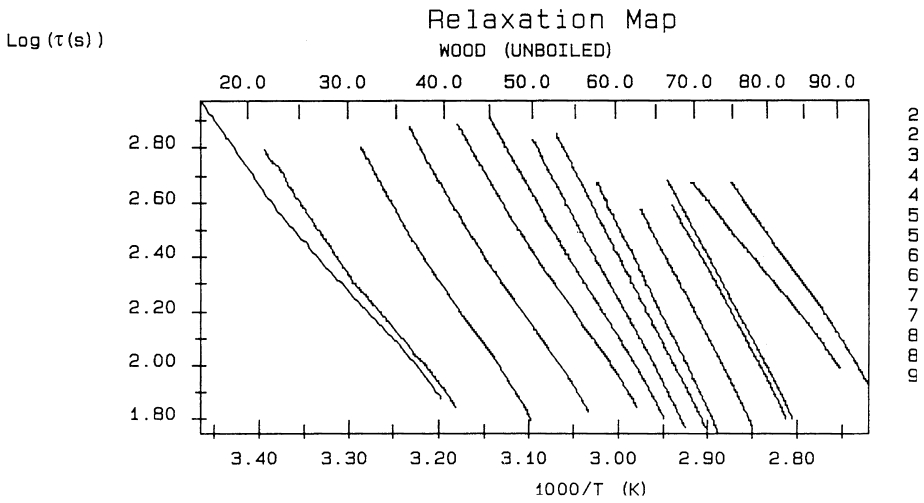


Figure 4.36: Relaxation map in the Arrhenius plane for an unboiled wood specimen. Refer to Figure 3.33 for the TSD trace. T_p varies between 20 °C and 90 °C.

EBSCOhost - printed on 2/13/2023 12:32 AM via . All use subject to https://www.ebsco.com/terms-of-use

od boiled	Anneal Temp : Inactive	Freeze Temp : 50.0
	Anneal Time : Inactive	Freeze Time : 5.0
te : 04/07/1990	Polar Time : 2.0min	R3 Rate : 7.0
me : 00:06:05	Polar Field : 100.0V/mm	End ISO Temp: 140.0
	Tp Range: 20.0 100.0C	End ISO Time: 0.0
lomat TSC/RMA	Thickness : 0.6mm	Window Width: 5.0
	Area : 30.0mm^2	

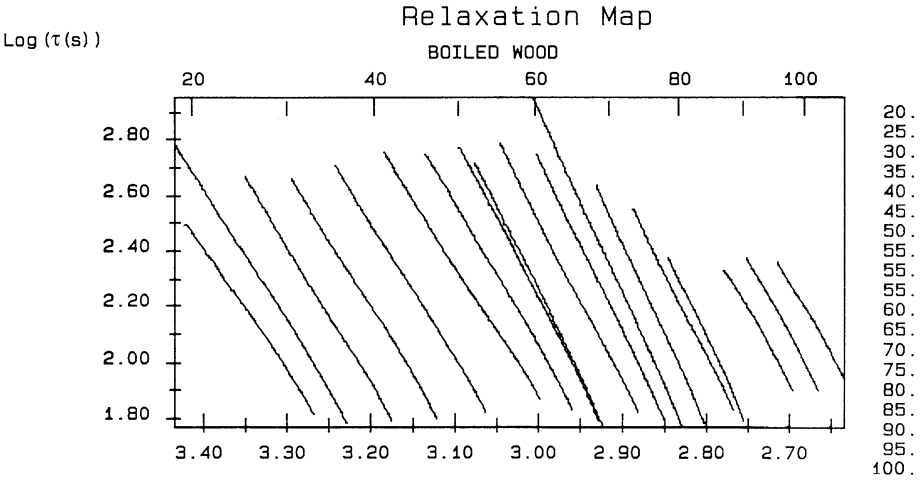


Figure 4.37: Relaxation map in the Arrhenius plane for a boiled wood specimen. Refer to Figure 3.33 for the TSD trace. T_p varies between 20 °C and 90 °C.

Table 4.6 provides the values of the enthalpy, entropy, and Gibbs free energy for various polarization temperatures T_p for the two samples. Figures 4.38a and 4.38b are plots of the entropy of activation versus T_p for unboiled and boiled wood. The comparison for the two samples is shown in Figure 4.39. The entropy of activation seems to be shifted to a higher temperature for the boiled sample, by about 10 °C. It should also be noted that the value obtained for the entropy maximum around 20 cal/°C/mole is very low compared to "normal" synthetic polymers for which we find values between 80 and 150 cal/°C/mole. This is very similar to what was reported for Vectra. This might be due to the highly organized tubular structure of the crystalline regions in the wood materials. Note that the entropy versus T_p curves are just shifted along the temperature scale and that there is no increase of the magnitude of the entropy due to boiling.

The ΔG_p free energy at T_p (Figures 4.40 and 4.41) seems to be identical for both the unboiled and boiled specimens. In a manner similar to what is observed for Vectra, what seems to occur is a change of the scale for the entropic state, not a change of A_c

EBSCOhost - printed on 2/13/2023 12:32 AM via . All use subject to https://www.ebsco.com/terms-of-use

Table 4.6: Thermokinetic parameters for the boiled (top) and unboiled (bottom) wood specimen.

T_p (°C)	T_m (°C)	ΔH_p (kcal/mol)	ΔS_p (cal/°C/mol)	ΔG_p (kcal/mol)
20.0	33.1	19.4242	−3.4916	20.4473
25.0	36.9	21.1919	1.5448	20.7315
30.0	41.9	24.8084	2.3445	21.0980
35.0	47.3	21.5749	0.3449	21.4686
40.0	53.4	21.5439	−1.1323	21.8983
45.0	60.5	20.7642	−5.0693	22.3763
50.0	64.9	22.8395	0.3347	22.7314
55.0	68.6	25.9119	8.7661	23.0366
55.0	69.1	27.2443	12.6332	23.1006
55.0	68.6	26.0599	9.2018	23.0417
60.0	74.2	25.6538	6.7144	23.4179
65.0	77.8	27.7583	12.0024	23.7015
70.0	80.4	29.5512	16.5765	23.8654
75.0	83.7	29.2287	14.8216	24.0708
80.0	88.3	26.3320	5.5699	24.3658
85.0	89.9	27.8432	9.4909	24.4455
90.0	97.9	22.8871	−6.0231	25.0734
95.0	102.1	24.1960	−3.2540	25.3934
100.0	106.6	22.7156	−8.1150	25.7425

T_p (°C)	T_m (°C)	ΔH_p (kcal/mol)	ΔS_p (cal/°C/mol)	ΔG_p (kcal/mol)
20.0	39.6	17.4539	−11.4132	20.7979
25.0	41.3	19.4912	−5.0413	20.9935
35.0	49.9	22.8936	3.9815	21.6673
40.0	56.8	22.4231	0.9017	22.1408
45.0	62.7	22.3145	−0.7557	22.5548
50.0	66.1	24.6329	5.5265	22.8478
55.0	68.7	27.3561	13.0473	23.0766
60.0	71.7	28.9199	16.9999	23.2590
65.0	73.3	30.1664	20.2354	23.3268
70.0	77.7	28.2340	13.4358	23.6255
75.0	82.5	27.1548	9.1595	23.9673
80.0	83.4	27.6567	10.3865	23.9903
85.0	90.3	17.9092	−18.8034	24.6408
90.0	94.7	20.9513	−10.8805	24.9009

in equation (2.32) of Part I, Chapter 2, when T_p varies. This seems to indicate that the effect of voltage on the free energy is identical for both samples as T_p varies across the relaxation transition. The system seems to have acquired more order after boiling, at least in the direction parallel to the voltage field.

EBSCOhost - printed on 2/13/2023 12:32 AM via . All use subject to https://www.ebsco.com/terms-of-use

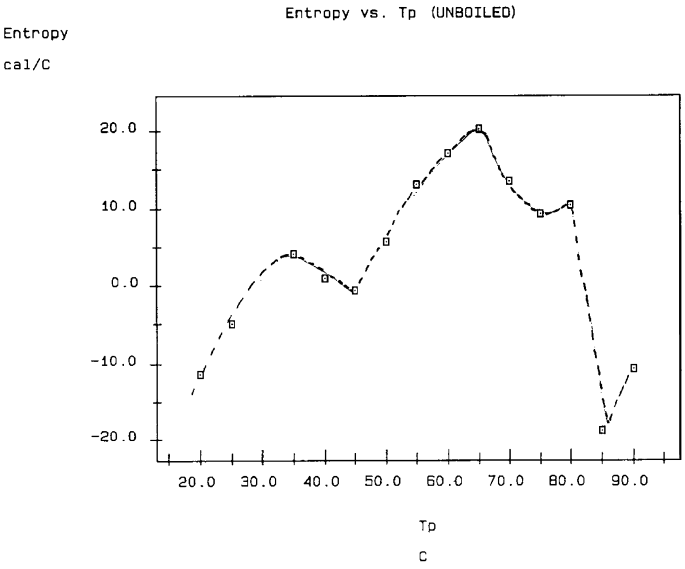


Figure 4.38a: ΔS_p vs. T_p for the unboiled wood.

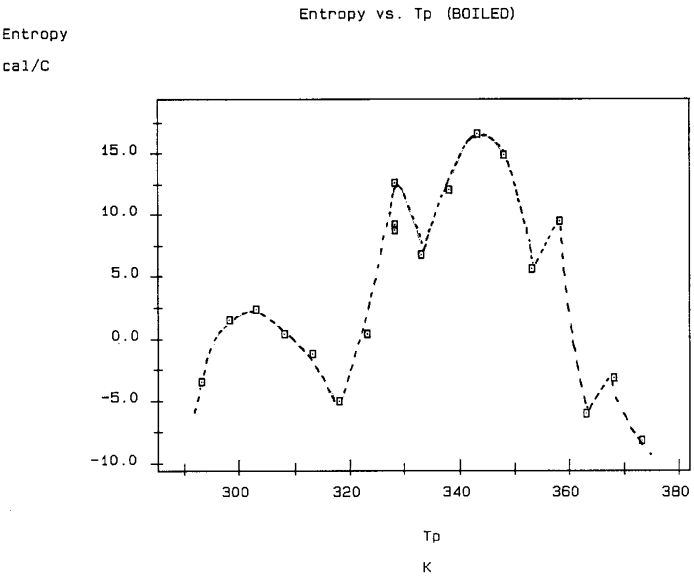


Figure 4.38b: ΔS_p vs. T_p for the boiled wood.

Figure 4.42 compares the intensity versus T_p for the boiled and unboiled samples showing large differences for these two specimens: the intensity is lower for the boiled specimen, showing a decrease of mobility, and a shift of 10 °C to higher temperatures, in agreement with the entropy results.

EBSCOhost - printed on 2/13/2023 12:32 AM via . All use subject to https://www.ebsco.com/terms-of-use

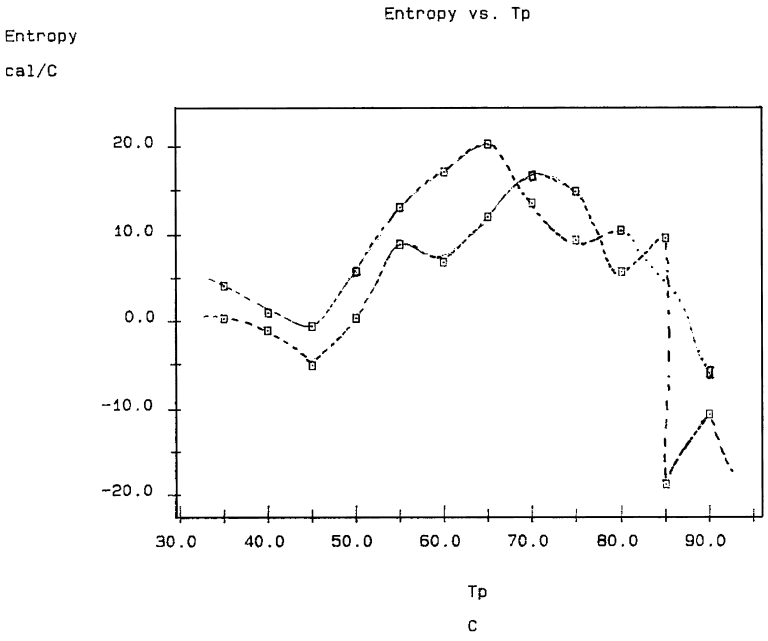


Figure 4.39: Comparison of the ΔS_p vs. T_p for the boiled and unboiled wood.

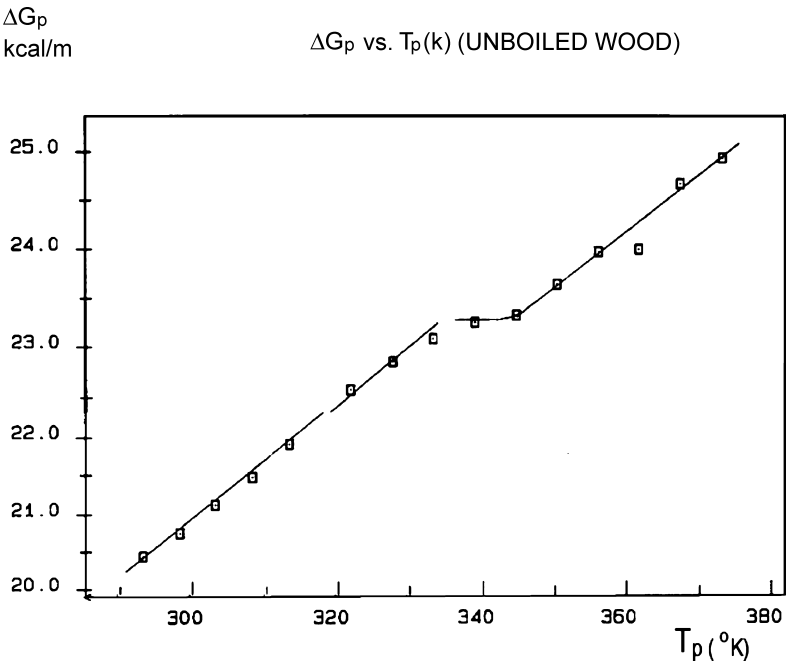


Figure 4.40: ΔG_p vs. T_p (K) for the unboiled wood.

EBSCOhost - printed on 2/13/2023 12:32 AM via . All use subject to https://www.ebsco.com/terms-of-use

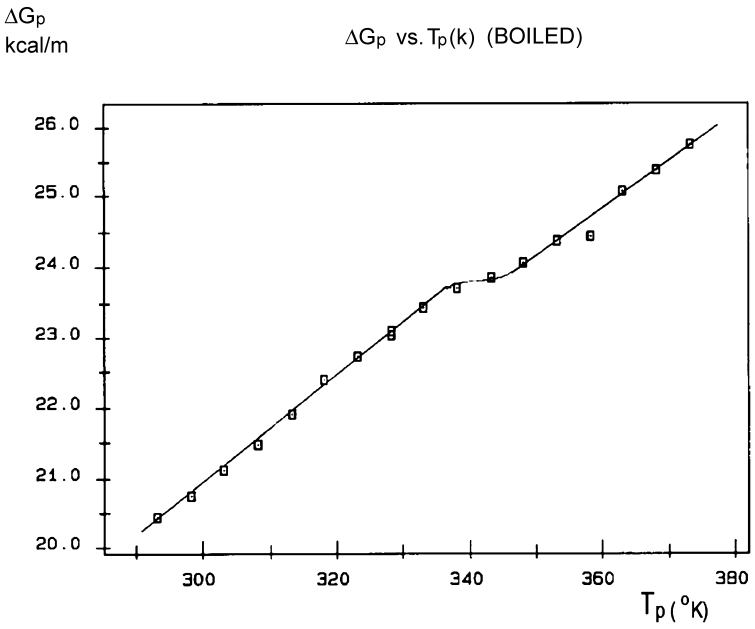


Figure 4.41: ΔG_p vs. T_p for the boiled wood.

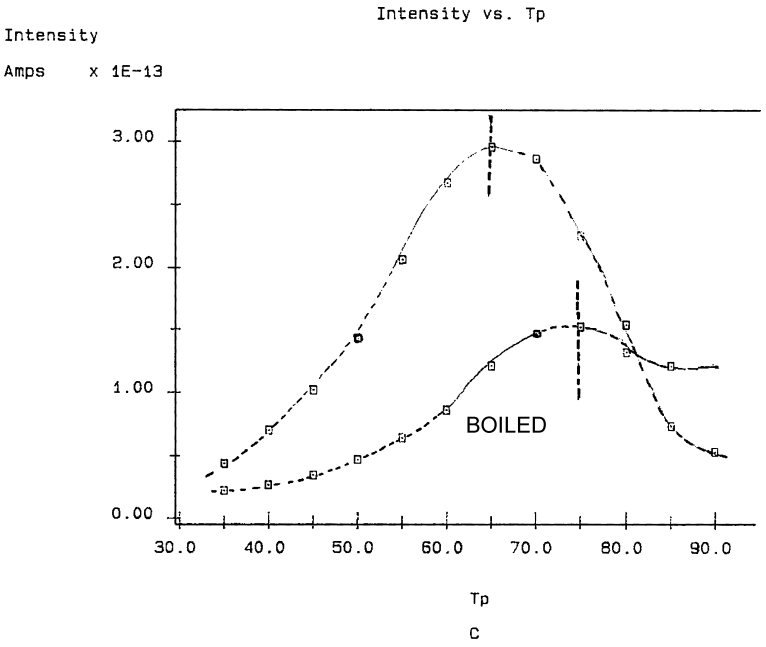


Figure 4.42: Intensity of the deconvoluted peak at T_m vs. T_p to compare the boiled and unboiled wood samples.

EBSCOhost - printed on 2/13/2023 12:32 AM via . All use subject to https://www.ebsco.com/terms-of-use

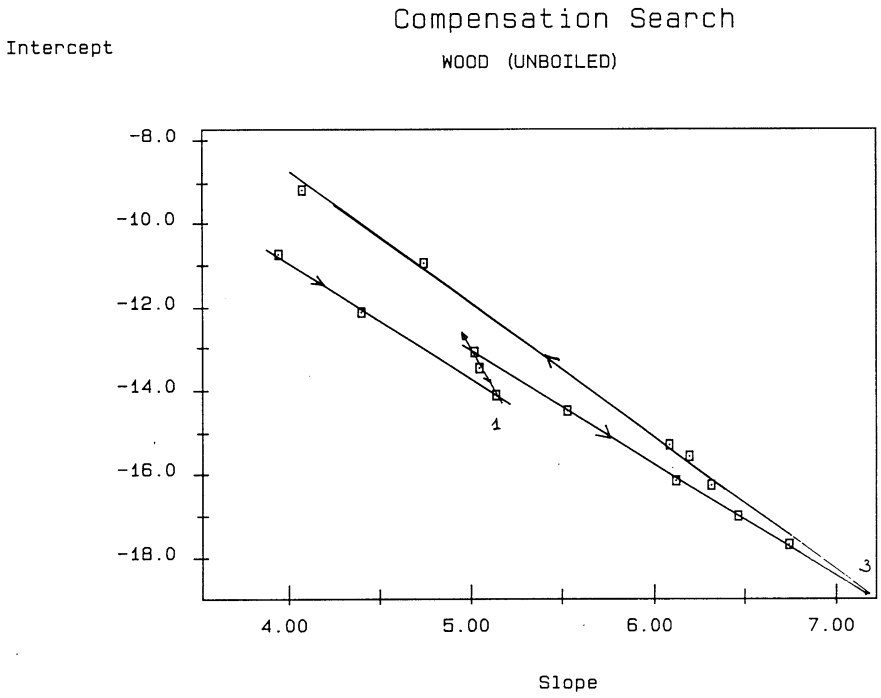


Figure 4.43: Compensation search in the Arrhenius plane for the unboiled wood showing two pairs of (positive/negative) compensations.

Both the boiled and unboiled samples show compensation phenomena for the peaks observed in the temperature range from –5 °C to 120 °C. The complexity of the structure is revealed in the analysis of the compensation search. Figure 4.43 shows a compensation search for the *unboiled* specimen. We have drawn in Figure 4.43 four compensation lines, two "positive" and two "negative."

It might be claimed from Figure 4.43 that we have *two* glassy phases with two transitions (let us call them T_g for convenience), not just one. This is seen by the fact that there are two pairs of positive–negative compensation lines. The first "T_g" occurs at the intercept of the first two compensation lines, 35 °C, and the second T_g at the intercept of the second pair around 67.5 °C. Looking back at Figure 4.38a, which gives the entropy vs. T_p, we confirm the presence of a secondary maximum at around 35 °C for the unboiled specimen.

Figure 4.44 is the compensation search for the *boiled* specimen: three pairs of positive/negative compensations (six compensation lines), associated with three "glass transitions," shown as 1, 2, and 3 in Figure 4.44, are now visible. Table 4.7 provides the values found for the compensation lines. A very interesting observation is that the points of intercept of the three pairs also line up. This is the mark of a super-

EBSCOhost - printed on 2/13/2023 12:32 AM via . All use subject to https://www.ebsco.com/terms-of-use

compensation. One notices that the effect of boiling is to create an additional "phase" (three pair junctions instead of two in Figure 4.43) and to lower the value of enthalpy and entropy at the pair junctions, predominantly at pair junction 3.

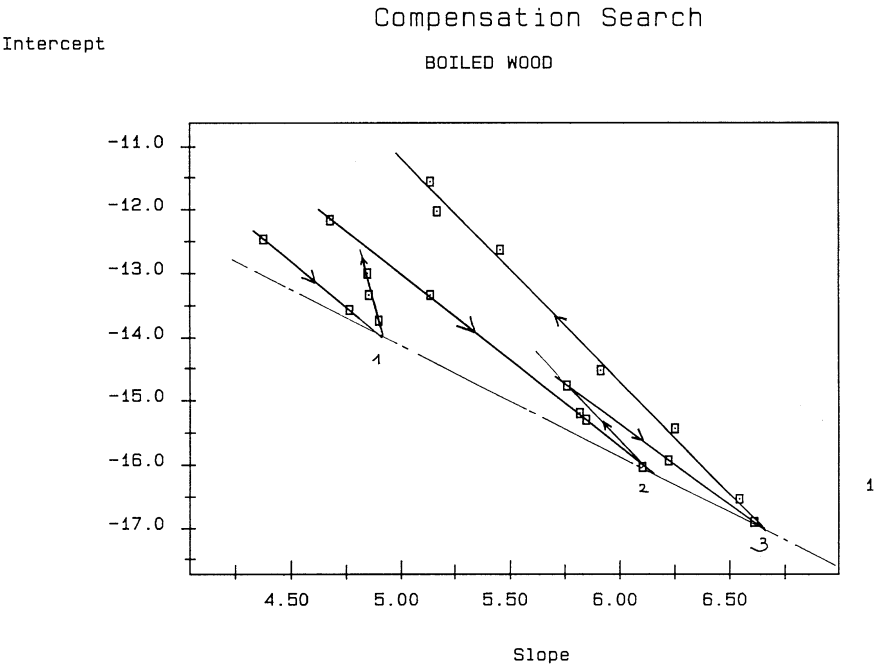


Figure 4.44: Compensation search in the Arrhenius plane for the boiled wood showing three pairs of (positive/negative) compensations modulated by a super-compensation.

The DOD number for the boiled and unboiled samples should be compared off the positive compensation lines only, for instance the designated "1 comp" in Table 4.7. One sees that the compensation temperature T_c is higher for the unboiled specimen (87.8 °C vs. 78.08 °C), although T_g for that resin phase (35 °C) is identical for the unboiled and boiled specimens, an indication that the resin structure of the unboiled sample has less internal stress built up. Once again, it seems that boiling has resulted in a more complex, more ordered structure, whatever the reason for it.

Another important parameter is the difference between T_g (as determined by the maximum entropy) and T_c (the compensation temperature). As explained in Part I, Chapter 2, this difference is believed to be a characteristic of the state of non-equilibrium induced by the thermomechanical history. The $(T_c - T_g)$ values confirm our conclusion regarding the increased order in the structure of boiled wood.

In wood, the cell cavities furnish passageways for sap and moisture to flow during the growth process. If it is confirmed that lignin is the material which dielectrically

EBSCOhost - printed on 2/13/2023 12:32 AM via . All use subject to https://www.ebsco.com/terms-of-use

Table 4.7: Results of the compensation search (Figures 4.43 and 4.44) for the boiled and unboiled wood samples.

Line	Compensation T_c (°C)	Log(τ_c) (Second)	DOD Number
Unboiled			
1	87.80	0.11	40.17
2	100.25	0.32	39.14
3	41.86	3.94	22.81

Line	Compensation T_c (°C)	Log(τ_c) (Second)	DOD Number
Boiled			
1	78.08	−0.01	40.79
2	94.43	0.60	37.91
3	121.97	−0.18	41.36
4	11.99	6.36	11.90

relaxes here, the results discussed might indicate that there are several amorphous phases present assuming several thermokinetic states depending on the location of the lignin in the wood structure. Another interpretation is that there is an overall order of the amorphous lignin due to the presence of ordered tubular cells glued together by the elongated and stressed lignin. The analogy with the relaxation map obtained for the liquid crystal in the previous section is remarkable. The analogy with the stressed polystyrene is also worth noting.

II.4.5 PEBA block copolymers revisited: a multi-compensations approach

PEBA block copolymers have been thoroughly investigated by TWD in Chapter 2 of this Part II (e. g., Figures 2.20 and 2.21). The search for compensation (Figure 2.21) led to the breakdown of the relaxation maps into two sets of compensation (one positive and one negative for each set), corresponding to the two segregated phases. In the present section, we reanalyze the relaxation maps with the intent to present an explanation for the points which are "left out" in the compensation search, i. e., the points of the EE plot which do not belong to any of the "main" compensation lines. We see several of those unconnected points in each graph of Figure 2.21. In the case of PEBA 2135, for instance (bottom left), we have drawn four compensation lines, and three points are left unconnected in between. For PEBA 900 (top right), five points are left out unconnected.

EBSCOhost - printed on 2/13/2023 12:32 AM via . All use subject to https://www.ebsco.com/terms-of-use

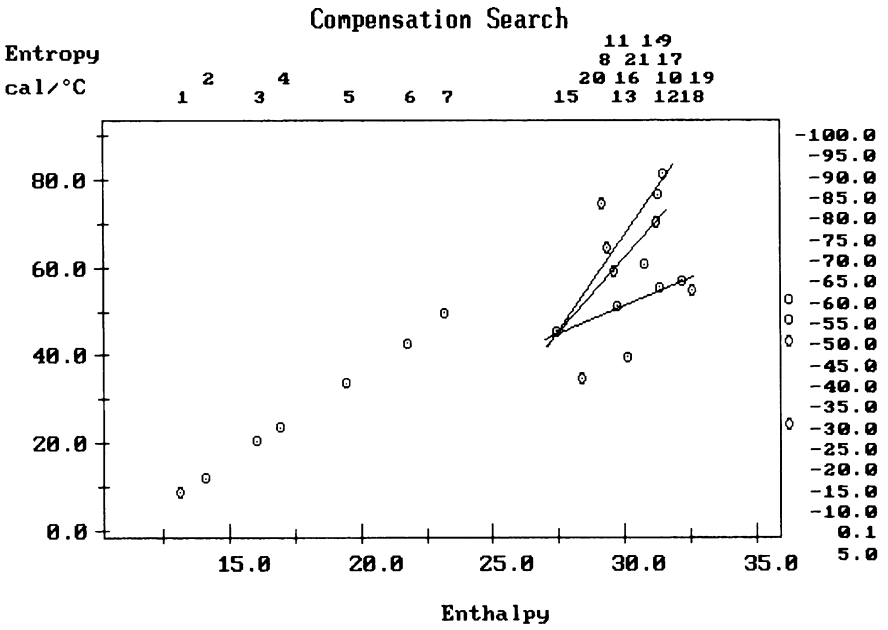


Figure 4.45: Revisited compensation search for PEBA block copolymers (see Figures 3.20 and 3.21). EE plot for PEBA 2135. A super-compensation is observed.

Figure 4.45 is the EE plot for PEBA 2135. We observe that a super-compensation links the points in-between, the high and low T_ps, nine points altogether. We have not drawn the main positive (or negative) compensation line in this figure for clarity, our main interest lying in demonstrating the possible existence of a super-compensation for some of the lines. The coordinates of the super-compensation point, the point of intercept of the compensation lines, can be found in Figure 4.46 by plotting ΔG_c against T_c obtained from the slope and intercept of the three compensation lines. The figure shows that the three points are on a straight line, which gives for the super-compensation coordinates

$$\Delta S_{sc} = 45\,\text{cal/°C/m}$$
$$\Delta H_{sc} = 27.45\,\text{kcal/m}$$

The corresponding compensations in the ΔG plane are displayed in Figure 4.47. One sees that the compensation points associated with the compensation lines of Figure 4.45 line up nicely and that the overall picture is a reversed Z-line structure, negative compensation first followed by positive compensation.

EBSCOhost - printed on 2/13/2023 12:32 AM via . All use subject to https://www.ebsco.com/terms-of-use

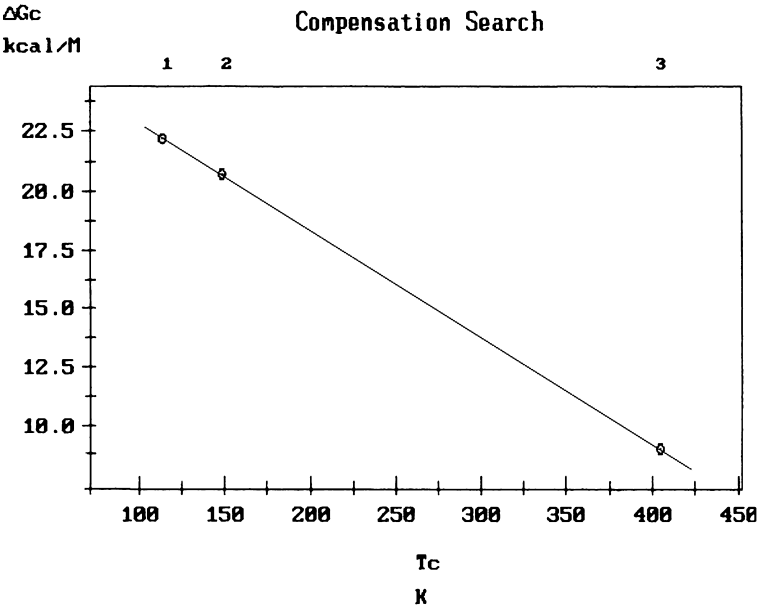


Figure 4.46: Determination in the Δ*G* plane of the coordinates of the super-compensation in Figure 4.45.

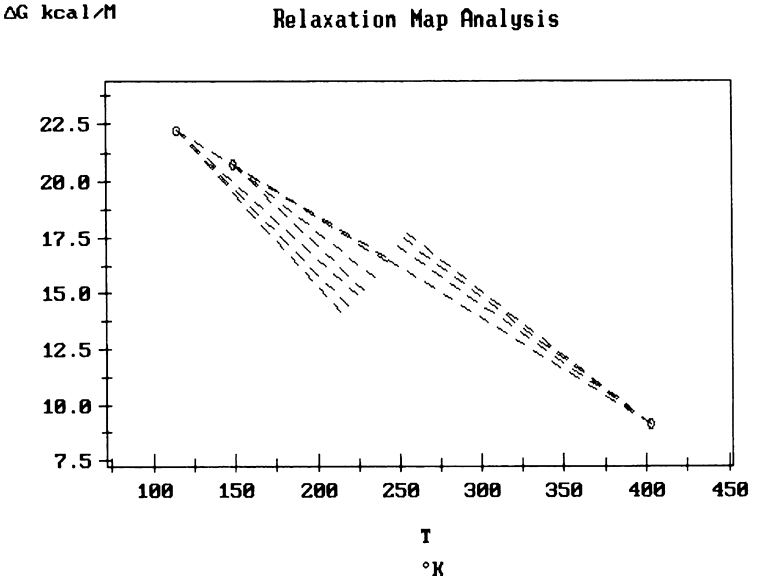


Figure 4.47: Reconstruction in the Δ*G* plane of the spectral lines showing the three compensations (two negative and one positive) and the super-compensation (line-up of the compensation points).

EBSCOhost - printed on 2/13/2023 12:32 AM via . All use subject to https://www.ebsco.com/terms-of-use

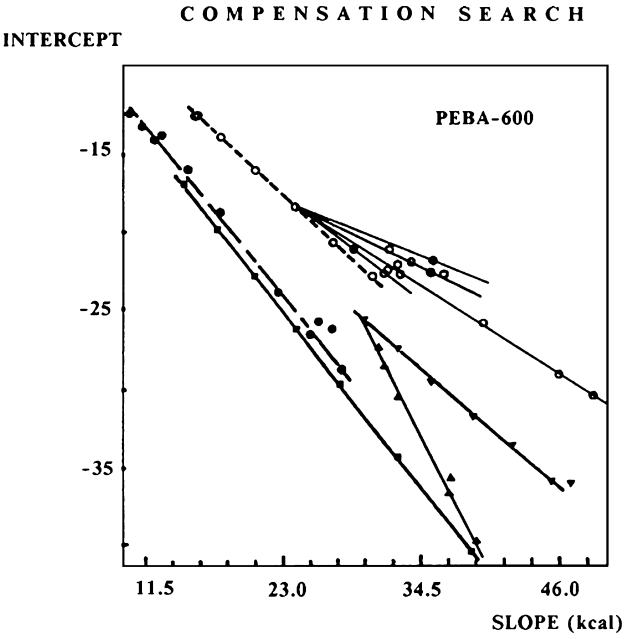


Figure 4.48: Multiple compensations and super-compensation organized as an interactive coupling network for PEBA 600.

Figures 4.48 to 4.51 present the result of our super-compensation search for a series of PEBA block copolymers, for which the molecular weight of both the polyamide (PA) and PE segments varies. The compensation search is conducted from data in the Arrhenius plane, i. e., the intercept and slope are rows of Arrhenius transforms. The various symbols in the figures have the following meaning: the open circles at the top apply to the PA homopolymers; the black dots at the bottom represent PTMG homopolymers; the triangles, the PA segments in PEBA; and the rectangles, the PE segments in PEBA.

In Figure 4.48, which applies to PEBA-600, we have found a super-compensation for the PE homopolymer and, knowledgeably with only two compensation lines, another super-compensation in the PA-rich phase for PEBA. Evidence for these two super-compensations is better shown in Figure 4.49. The two super-compensations are well defined in this figure. It is interesting to note the influence of the block copolymerization on the super-compensation coordinates in the PA phase. For the homopolymer, the super-compensation occurs for

$$\tau_{o,sc} = 10^{-18}\,\text{sec}$$
$$\Delta H_{sc} = 28.75\,\text{kcal/m}$$

EBSCOhost - printed on 2/13/2023 12:32 AM via . All use subject to https://www.ebsco.com/terms-of-use

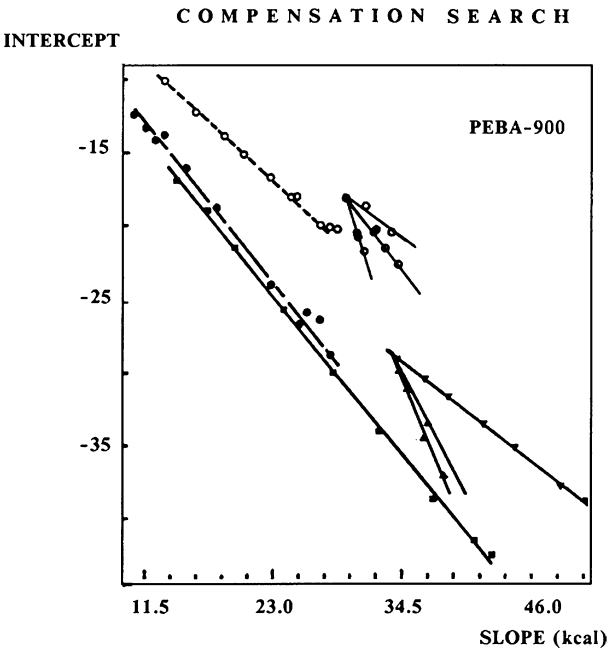


Figure 4.49: Multiple compensations and super-compensation organized as an interactive coupling network for PEBA 900.

and for PEBA, the super-compensation occurs for

$$\tau_{o,sc} = 10^{-29}\,\text{sec}$$
$$\Delta H_{sc} = 32.2\,\text{kcal/m}$$

Only one clear super-compensation (for the PEBA block PA phase) is evidenced in Figures 4.50 and 4.51. Possibly a second super-compensation is observed in Figure 4.51 for the PE phase at the bottom. The coordinates of the super-compensation point are dependent on the molecular weight of the PA block segment (Figure 4.48) and also on the presence of the PE segments.

The existence of the super-compensation(s) in these figures is still speculative at this stage, and the meaning is unclear. Could it be possible that the relaxations occurring in the PA-rich amorphous phase are submitted through its surrounding medium to a thermomechanical history, similar to what is observed in the case of classical amorphous matter such as polystyrene or polycarbonate? Further investigation is necessary to ascertain the assumption of super-compensation taken in this section.

EBSCOhost - printed on 2/13/2023 12:32 AM via . All use subject to https://www.ebsco.com/terms-of-use

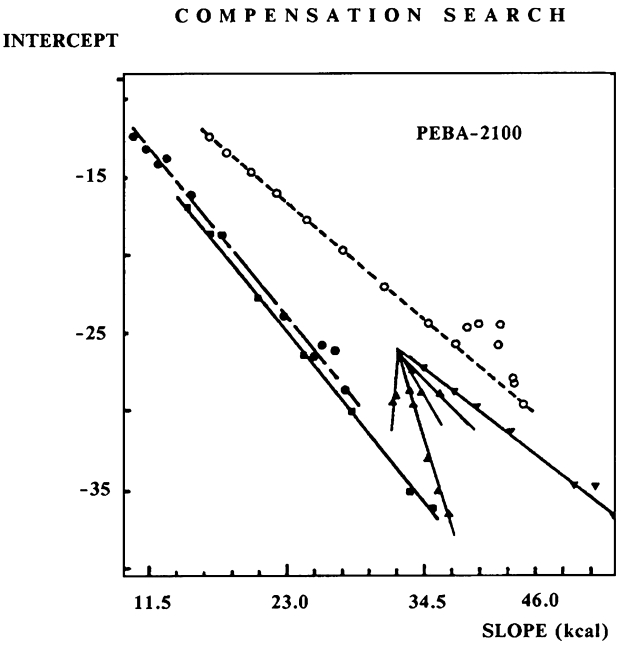


Figure 4.50: Multiple compensations and super-compensation organized as an interactive coupling network for PEBA 2100.

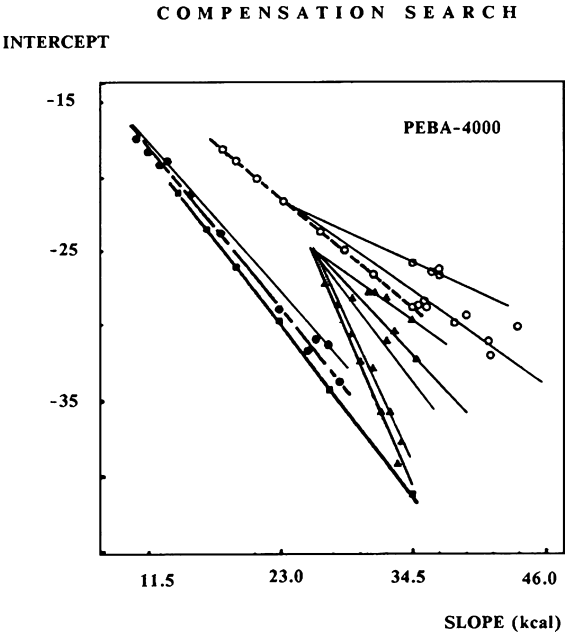


Figure 4.51: Multiple compensations and super-compensation organized as an interactive coupling network for PEBA 4000.

EBSCOhost - printed on 2/13/2023 12:32 AM via . All use subject to https://www.ebsco.com/terms-of-use

II.4.6 Discussion and conclusion

In this chapter, we demonstrate that the relaxation behavior is, overall, far from simple, even for classical amorphous polymers. In the first two sections of this chapter, multiple compensations are found, across T_g, for systems which are apparently rheologically simple: polystyrene or polycarbonate. In the case of a true monophasic amorphous polymer, e. g., polystyrene, the number of compensation points observed on the relaxation map depends on the thermomechanical history: the processing variables, the cooling rate, the amount of pressure, orientation, etc. The phenomenon of super-compensation, which is observed here, represents a remarkable finding for the understanding of the *kinetic* model responsible for the relaxation process. *The fact that relaxation modes well below T_g, at T_g, and above T_g are gathered into compensation lines which themselves compensate is an important finding and an essential finding for determining the mechanism of non-equilibrium in amorphous polymers*. It is, therefore, strongly suggested that, for these polymers, the relaxation processes described by the individual compensation lines, i. e., occurring below T_g, at T_g, and above T_g, are all interrelated, perhaps an indication that it is the same process which repeats itself several times. A possible interpretation of super-compensation is presented in Part I, Chapter 3 and its Appendix.

It could also be claimed [153] that the structure of polystyrene or polycarbonate is made up of several "phases," each corresponding to a specific compensation diagram. It is true that in the case of segregated phases, such as in incompatible blends or block copolymers, the separate phases show up on the relaxation map as separate compensations. In the case of an ordered morphological structure, such as a liquid crystal polymer, separate multi-compensations are observed below and above T_g. Does it suggest the presence of several phases? In the context of liquid crystal polymers, it seems that annealing at higher temperature, such as to produce the annealed Vectra, destroys the super-compensation above 75 °C. For wood, boiling seems to create more compensations, although a super-compensation is also clearly visible. For PEBAX, the presence of hydrogen bonds probably results into this super-structural order which marks the amorphous content in a manner that only thermalomechanically strained amorphous phases can display in the case of rheologically simple polymers.

A better picture of the fundamental mechanism for the overall relaxation process starts to emerge from this study, and it looks more and more like the unfolding, by the effect of temperature, of an apparent chaotic phenomenon whose inner structure seems to be relatively simple. The distinct and complementary role played by the enthalpy and the entropy of activation is implied in the unfolding mechanism.

We stipulate in Part I, Chapter 3 that the phenomenon of multiple compensations can be the result of the energetic and kinetic nature of the interactions between the conformers belonging to the macromolecules (Figure 3.1 of Part I). The Dual-Phase theory proposes an explanation of the existence of compensation laws based on the

EBSCOhost - printed on 2/13/2023 12:32 AM via . All use subject to https://www.ebsco.com/terms-of-use

inter-intra molecular potential energy barrier ([123–131, 139], Part I, Chapter 3). The apparent multi-compensation order of the chaotic behavior observed for multiple compensations, their sign, and the apparent alternation between them might be modeled by the vertical structuring brought out of equilibrium by special thermomechanical conditions (Rheomolding) inducing large initial values of Δ_e (T_p, E). See Part I, Chapter 3, Figures 3.8 to 3.10.

EBSCOhost - printed on 2/13/2023 12:32 AM via . All use subject to https://www.ebsco.com/terms-of-use

Book conclusions

This book is about the understanding of "interactive coupling" between molecular motions in polymers determined by their dielectric relaxation behavior when submitted to thermally induced polarization by a voltage field followed by its depolarization at constant heating rate.

The characterization methods described in this book, thermally stimulated depolarization (TSD) and Thermal-Windowing Deconvolution (TWD), provide the best way to study local and cooperative relaxations in the amorphous state of matter that are, in my opinion, essential to understand the glass transition, molecular motions in the rubbery and molten states, and even the processes leading to crystallization.

In 1993 I wrote a manual of use for a thermally stimulated current (TSC) spectrometer that Solomat Instrumentation Corp. commercialized; and in one example of use of the instrument, I disclosed that the relaxation map of the interactive relaxation modes of the dipoles of a series of Rheomolded PS samples structured as a network of compensation lines, themselves compensating into a super-compensation macrostructure (Figures 4.8 to 4.14 of Chapter 4, Part II). The pattern of the macrostructure was a function of the Rheomolding thermomechanical history. This discovery, that no current theory could explain, was the motivation to write this book: could the model of Dual-Phase address and explain such a high level of relaxation order across T_g for a pure amorphous polymer?

This book is composed of two specific parts published in one single volume.

Part I deals with the physics of interactions under a voltage field excitation. The first two chapters are dedicated to the fundamentals of this dielectric characterization technique: the origin of the dipole formation, induced or permanent dipoles, the origin of the Wagner space charges, of the $T_{g,\rho}$ transition, and of the T_{LL} manifestation, the origin of the Debye elementary relaxations of the relaxation map and of their compensation, and finally, the origin of their super-compensations. The science of activation and deactivation of dipoles to produce an understanding of the coupling forces of interactions that control molecular motions is the subject of Chapters 1 and 2. For instance, these chapters describe the thermokinetic features of the relaxation of dipoles as a function of temperature, in particular how the depolarization current can be converted to a relaxation time (the Bucci equation) that generally varies with temperature in an Arrhenius fashion. The last chapter of Part I, Chapter 3 introduces the new physics of polymer interactions and applies it to the relaxation of dual-conformers that carry the dipoles. This chapter provides the Dual-Phase description of interactive coupling and shows that this model is compatible with the manifestation of compensations of the Arrhenius relaxation modes observed in a relaxation map. The super-network of compensation structures found for the Rheomolded PS samples mentioned above can also be simulated (in the Appendix).

https://doi.org/10.1515/9783110756746-010

EBSCOhost - printed on 2/13/2023 12:32 AM via . All use subject to https://www.ebsco.com/terms-of-use

Part II is practical and filled with case studies giving examples on how to apply the characterization techniques of Thermal-Stimulated Depolarization (TSD) and Thermal-Windowing Deconvolution (TWD) described and explained in Part I. In Part II we characterize a multitude of samples given to our lab because other thermal analysis techniques (DSC, DMA, DEA) have had a hard time to characterize them. This part is dedicated to help the engineers and researchers of the industry find answers: the characterization of interfaces in blends, two-phase copolymers, coated films, wood samples, paints, the migration of impurities from one phase to another, etc.

In Chapter 1 of Part II we briefly compare the merits and limitations of the most popular techniques, DSC, DMA, and DEA, with TSD/TWD.

The TSD technique's super-sensitivity makes the detection of some transitions that other techniques cannot see or cannot define well enough possible. While the theory of the thermal-stimulated processes has been known for years, its use has been delayed by lack of effective instrumentation, particularly the lack of adequate electrometers, experiment controls, automation, and analysis software. Advances in microelectronics and software analysis and a good 40 years of backup experience in the lab [160] from the scientists who put the method together make the technique a practical reality nowadays.

The thermal-stimulated current instrument does not require any specific sample preparation to generate quantitative reproducible results. The quasi-absence of requirements (size, shape) for sample preparation makes it possible to characterize samples taken directly from their sites of practical use. This is unique to this instrumentation.

But a TSD/TWD spectrometer is more than just a thermal analyzer: it is both a thermal analyzer and a rheological instrument, capable of probing "interactive coupling," i. e., the *local motions* and their *interactive cooperation* that dictate the macroscopic properties such as viscosity. Research scientists who have used other techniques (DMA, DEA, DSC) will recognize the benefits of a thermally stimulated dielectric instrument which, when simply used as a TSD, combines the outputs from the traditional apparatus, yet, when switched to the TWD spectrometer mode, allows a new understanding of the structure and behavior of polymers. In particular, it becomes rapidly clear to the users that the description of the elementary relaxation modes, their thermokinetic characteristics (activation enthalpy and entropy), and the *coupling kinetics* is essential to complete the understanding of what underlies the macroscopic properties of polymeric materials.

In Chapters 2 and 3 of Part II, for instance, we demonstrate the power of TSD (Chapter 2) and TWD (Chapter 3) in characterizing a series of natural rubber (NR) and styrene–butadiene copolymer rubber (SBR) blends. The TSD plots (e. g., Figure 2.51) clearly resolve the glass transition temperature (T_g) of both blend components, indicating segregation.

EBSCOhost - printed on 2/13/2023 12:32 AM via . All use subject to https://www.ebsco.com/terms-of-use

The T_g of both phases seems to indicate a certain amount of solvability of one segment in the other phase, as attributed to the lowering (for SBR) or the heightening (for NR) of the T_gs.

We demonstrate the large-scale migration of polar impurities from the NR into the SBR by the unexpected large decrease of the TSD peak intensity versus blend ratio (Figure 2.53). The TSD peak intensity is proportional to the number of dipoles polarized in a sample. Migration of polar impurities results in a decrease in the NR's peak intensity and an increase in the SBR's peak intensity, *as observed*. The TWD results in Chapter 3 clearly identify the migration process and assign the slight variations of T_g observed in Figure 2.52 to the respective plasticization of the phases by the impurities. There is virtually no dissolution of NR into SBR or vice versa. Migration of impurities seems to dominate the relaxation effects observed. The results discussed in this example are typical of the complementary nature of TSD and TWD and their unique ability to draw conclusions that cannot easily be obtained through any other characterization technique. Additionally, this example suggests that TSD will be useful in monitoring migration of soluble additives between polymer phases in general. Concentrations of soluble additives can be determined by using peak intensity or area. The most important aspect of additive analysis by TSD may be the ability to identify the state of the additive within the polymer matrix. Soluble stabilizers such as Irganox 1076 can be identified based on their positive effects on peak intensity. Insoluble or partially soluble stabilizers can be clearly differentiated based on their negative effect on peak intensity. No other analytical technique appears to offer these unique capabilities.

In conclusion, Thermally Stimulated Depolarization (TSD), on its own, is a useful tool in the analysis of many practical characterization processes. We have shown in Chapter 2 of Part II several examples where the technique is unique and can be used in the case of samples in situ, in their lifetime application format.

In Chapter 3 of Part II we provide a multitude of examples of analysis using the Thermal-Windowing Deconvolution (TWD) technique applied to a wide and diversified range of materials and sample shapes. As mentioned at the beginning of this book, our *understanding* of TWD spectroscopy is still far from complete, yet, as a characterization technique, TWD is extremely powerful and straightforward to apply to characterize challenging characterization issues (the role of interfaces in phase separation). In Chapters 3 and 4 of Part II we use a qualitative, simple, and intuitive "translation" of the concepts of the Dual-Phase model ("interactive coupling" between "conformers," "b grains," "dynamic free volume") to describe the characteristics of the relaxation map ("thermokinetic" parameters of the Arrhenius lines of the relaxation modes, "compensation," transitions, etc.). All of the parameters derived from the relaxation map of TWD can be interpreted using this qualitative language of "interactive coupling," without the need to precisely correlate these terms with their fundamental statistical origin, the interactive coupling Dual-Phase model. None of the quantitative theoretical developments of Part I of the book are required to use TWD as a quantitative characterization tool to specify the state of the amorphous phase as a function

EBSCOhost - printed on 2/13/2023 12:32 AM via . All use subject to https://www.ebsco.com/terms-of-use

of its interactive environment. The interactive environment of the conformers can be quantified by the compensation characteristics of the Arrhenius or Eyring lines of a relaxation map of the sample as T_p is varied from the solid to the liquid state. The introduction of the DOD number to determine the state of the amorphous phase permits that simplification. The interactive environment polarizability is very sensitive to the structure of the amorphous phase (oriented or isotropic), its homogeneity (detected by the presence of segregated phases), the presence of crystals or nematic phases, and its non-equilibrium state induced by the processing conditions.

In other words, the creation and the use of a *qualitative language* (such as the DOD number) to present the correspondence between the depolarization current and the Arrhenius relaxation map, the compensation of the Arrhenius lines, and the Dual-Phase understanding of the compensation itself permits to express a complex theoretical background developed in Part I in simple terms, more adapted to easily describe the commonalities and the differences between samples of various nature and processing history.

Chapter 4 of Part II gives a good demonstration of the usefulness of this "qualitative language" applied to complex situations. We show in that chapter that the relaxation behavior is, overall, far from simple, even for classical amorphous polymers. In the first two sections of this chapter, multiple compensations are found, across T_g, for systems which are apparently rheologically simple: polystyrene and polycarbonate. In the case of a true monophasic amorphous polymer, e. g., polystyrene, the number of compensation points observed on the relaxation map depends on the thermomechanical history: the processing variables, the cooling rate, the amount of pressure, orientation, etc. The phenomenon of super-compensation, which is observed in Figures 4.8 and 4.9 for instance, represents a remarkable discovery for the understanding of the *kinetic* model responsible for the relaxation process. The fact that relaxation modes well below T_g, at T_g, and above T_g are gathered into compensation lines which themselves compensate is an important finding, even an essential finding, for determining the mechanism of non-equilibrium in amorphous polymers. We concluded that, at least for these polymers, the relaxation processes described by the individual compensation lines, i. e., occurring below T_g, at T_g, and above T_g, are all interrelated, perhaps an indication that it is the same process which repeats itself several times. A possible interpretation of super-compensation is given in Chapter 3 of Part I and is also summarized below for three other materials that we analyzed in depth: a liquid crystal polymer (Vectra), wood, and PEBAX.

In the case of an ordered morphological structure, such as a liquid crystal polymer, separate multi-compensations are observed below and above T_g. Does it suggest the presence of several phases? In the context of liquid crystal polymers, it seems that annealing at higher temperatures, such as to produce the annealed Vectra, destroys the super-compensation above 75 °C. For wood, boiling seems to create more compensations, although a super-compensation is also clearly visible. For PEBAX, the presence of hydrogen bonds probably results in this super-structural order which marks

EBSCOhost - printed on 2/13/2023 12:32 AM via . All use subject to https://www.ebsco.com/terms-of-use

the amorphous content in a manner that only thermomechanically strained amorphous phases can display in the case of rheologically simple polymers.

A better picture of the fundamental mechanism for the overall relaxation process emerges from the study of multi-compensations in Chapter 4 of Part II: the analogy with the unfolding, by the effect of temperature, of an apparent chaotic phenomenon whose inner structure seems to be relatively simple is what comes to mind. The distinct and complementary role played by the enthalpy and the entropy of activation is implied in the unfolding mechanism.

We stipulate in Part I, Chapter 3 that the phenomenon of multiple compensations can be the result of the energetic and kinetic nature of the interactions between the conformers belonging to the macromolecules (Figure 3.1 of Part I). The Dual-Phase theory proposes an explanation for the existence of compensation laws based on the inter-intra molecular potential energy barrier. The apparent multi-compensation order of the chaotic behavior observed for multiple compensations, their sign, and the apparent alternation between them might be modeled by the vertical structuring brought out of equilibrium by special thermomechanical conditions (Rheomolding) inducing large initial values of $\Delta_e(T_p, E)$. See Part I, Chapter 3, Figures 3.8 to 3.10).

There is also another dimension to this book, perhaps well put in the title of Section I.3.1 of Part I: "*Challenging results for the conventional models of polymer physics. Introduction to a new approach to the physics of polymer interactions: the Dual-Phase and Cross-Dual-Phase models*."

This is what I stated at the beginning of Section I.3.1:

> In many ways, the results obtained by TSD or TWD represent a challenge to the classical views on macromolecules. The $T_{g,r}$ peak (Figure 3.5) is in dispute: some scientists claim it is T_{LL}, but we present a different explanation in this text; the compensation of the relaxation modes extracted from the Debye peaks obtained at variable T_p is simulated in Chapter 1 (Figure 1.13), yet its implication on the meaning of compensations must be clarified; the existence of the negative compensations found for $T_p > T_g$ is a novelty without interpretation from the classical views of polymer physics (Part II, Figure 1.25, top, or Part II, Figure 3.61); the existence of the T_{LL} relaxation-transition, which, in the context of TSD/TWD, we derive from relaxation maps in the DG plane (Equation (2.28b)), is still a well-known controversial issue [21, 135]; the network of multi-compensations and super-compensations found for the organization of the enthalpy and entropy in Part II, Chapter 4 (Figures 4.8 to 4.10) represents the greatest challenge to any theory of polymer physics, including our own model: why would all the relaxation modes describing interactive coupling in the amorphous phase resume to a network of positive or negative compensations as sketched in Part II, Figure 4.14?
>
> [...]
>
> In our view, "conformers," the constituents of the macromolecules, gather into statistical systems which go beyond belonging to individual macromolecules. A conformer is shown in Figure 3.1, duplicated from reference [128]. The macromolecules themselves represent a chain of "covalent conformers" put together as an entity. The problem is to determine whether the chain properties, derived from its statistics, control *entirely* the dynamics of the collection of chains making up a polymer. This is what has been assumed by all the other theories, and this is what the Dual-Split Kinetics and the Grain-Field Statistics challenge.

EBSCOhost - printed on 2/13/2023 12:32 AM via . All use subject to https://www.ebsco.com/terms-of-use

In my opinion, *this is a key issue*: the currently established theoretical models of the interactions in polymers are based on "chain dynamics" statistics. In rheology, for instance, the Rouse and reptation models are dominant for $M < M_c$ and $M > M_c$, respectively. The conclusion obtained from the present work, based on the Grain-Field Statistics of the interactions, is that the application of macromolecular (chain) dynamic models could only be justified for conditions of use of the material that position its temperature above the T_{LL} transition ($T > T_{LL}$). The problem is that the existence of T_{LL} is not even recognized by these macromolecular dynamic models. Below T_{LL}, the free energy of the collection of chains assembled as a polymer is not equal to the scaled-up free energy of a macromolecule embedded in a mean field created by the influence of the other macromolecules. Besides, the temperature T_{LL} is itself a function of the dynamics of the experiment and the chain characteristics.

The Dual-Phase model of polymer interactions does not require, in its hypotheses and derivations, a description of the changes which occur to the individual macromolecules. The dynamic statistical systems dealt with in this model, used to determine the free energy and its structure (enthalpy and entropy), are not the macromolecules. However, the fact that macromolecules compose the basic structure *is essential* to understand the basis of our new Dual-Phase statistics and to explain "entanglements," for which the Dual-Phase model provides a completely different interpretation than the ones offered by the conventional macromolecular dynamic models [128].

A "Dual-conformer" is not the same as a "free conformer" (Figure 3.1), defined from the monomer repeat unit involved in the polymerization process. Its interaction to other conformers by covalent bonding modifies the conformational potential energy of a free conformer, and this governs the statistical properties of a "free chain." Here we are still "classical," yet when dealing with a collection of chains put together, our approach differs from the classical one. Conformers belong to two types of sets: they belong to macromolecules, which link them via covalent forces, as we just said, and they belong to the grand ensemble of conformers which are linked by *inter-intra* molecular forces, van der Waals, dipole-dipole, and electrostatic interactions which affect and define the viscous medium. That duality is intrinsic to conformers, which we call the "dual-conformers" to mark this specificity. The potential energy of a dual-conformer is different from the potential energy of a conformer part of a free chain.

To simplify, one could view the difference between our statistical model and the classical model to describe the properties of polymers as follows: according to the classical views, the statistical systems are the macromolecules, i. e., a network of chains; the properties of the chains are disturbed by the presence of other chains and by the external conditions (temperature, stress tensor, electric field, etc.). The classical definition of the statistical system contrasts with our approach whereby the statistical systems are the "*dual-conformers*," not the macromolecules. The interactive coupling between the dual-conformers is defined by a new field of statistics, the Grain-Field Statistics, that explores the correlation between the local conformational property of the dual-conformers and their collective behavior as a dissipative network.

EBSCOhost - printed on 2/13/2023 12:32 AM via . All use subject to https://www.ebsco.com/terms-of-use

The statistics that are used by the classical models and our model to describe the rotational isomeric states (RISs) of the conformers are fundamentally different: the classical molecular dynamic statistics is the Boltzmann statistics, famous for its kinetic formulation of the properties of gases. The dual-split or Dual-Phase statistics, leading to the Grain-Field Statistics, is inspired by the classical Boltzmann concept but departs from it by defining a dissipative term in the equations and assuming that the free energy remains always equal to its minimum value, that of the equilibrium state, even for transient states. The kinetics created by such changes in the fundamental equations result in the formation of free energy structures, which we designate "the elastic dissipative network of dual-conformers."

In our analytical formulation of the dynamics of these "*open dissipative systems of interactions*" generated by our two modifications of the classical formula, we realized that essentially two mechanisms of structuration of the free energy prevail and compete: a "vertical structuring" and a "horizontal structuring," each specifically applying its own version of the basic equations. This distinction increases the complexity of the analytical solution but is, in our opinion, a fundamental aspect of the way interactions work. The vertical structuring refers to a split of the units (collectively interacting in the system) into two compensating sub-systems having each a different statistical partition. The horizontal structuring offers a different split of the collective set, via the generation of N_s identical sub-systems, each with the same statistical partition. Each split mechanism generates a dissipative function. The total dissipative function ought to be minimized (it is 0 at stable equilibrium), a condition that creates their compensation, i. e., whether they work independently, in sequence, or together.

By applying these general principles to polymers, specifically, we can now summarize our model in one sentence:

> We define a polymer as a set of "dual-conformers," i. e., a set of three-bond elements belonging or not to the same macromolecule, submitted to *intra-inter* molecular forces described by an energy potential to which the equations of the dual-split and Grain-Field Statistics theory apply.

If one tests the predictions of the classical approach under conditions that bring its state above T_{LL}, one may conclude that those data validate the classical views since they provide correct answers in the range tested. This is not an easy task, because T_{LL} is rate-dependent, pressure- and shear-dependent, and molecular weight-dependent. Thus, although one will find in the literature convincing experimental evidence of success for the classical models, which is the reason for their acceptance, we claim that these successes are due to the use of conditions that bring the state of the polymer above its T_{LL} transition.

The amount of experimental evidence of failure of the macromolecular dynamic models is growing in many recent publications ([212, 259, 260]), and those experimental facts can no longer be ignored or designated artifacts. The $T_{g,\rho}$, the T_{LL}, and the

EBSCOhost - printed on 2/13/2023 12:32 AM via . All use subject to https://www.ebsco.com/terms-of-use

multi-compensation network described in this book are experimental facts that theories cannot ignore.

Besides, in most experimental set-ups used by the industry, T_{LL} is raised to such high values, due to the high rates and pressures, that the range of validation of the macromolecular dynamics to predict the properties is in default: the use of such classical models in such conditions would provide the wrong answers.

We have advocated elsewhere (Chapter 7 of [128]) to abandon the classical interpretation of polymer physics by single-chain macromolecular dynamics because of its inability to describe the full range of its behavior and other essential properties of polymers such as the dielectric TSD/TWD responses analyzed in this book.

A small number of simulations based on the equations of the dual-split models (horizontal and vertical structuring) are presented in the Appendix of Part I. These simulations lead, by analogy, to the understanding of the coupling between the free volume and the conformational energy characterizing the interactions between the dual-conformers. We symbolize this duality by $[(b/F) \leftrightarrow (c, g, t)]$, where b and F represent two conjugated states of the inter-intra duality and (c, g, t) refers to three conformational states of the dual-conformers (Chapter 1 of [128]).

This local duality, described by the Dual-Split Kinetics (Equations (5) to (7) of the Appendix, for instance) provides a reason for the existence and characteristics of the b grains surrounded by the F conformers, our explanation for the $T_{g,\rho}$ peak observed in TSD (Part II, Chapter 2). In a certain way, the presence of the $T_{g,\rho}$ peak may be considered an indirect validation of the local duality (b/F) in our model.

We present in Chapter 3 and in the Appendix of Part I what we consider the fundamental mechanism for the overall relaxation process in polymers. The phenomena observed in TSD and TWD experiments are the result of the energetic and kinetic nature of the interactions between the conformers. We assume initially that only the equations of the vertical structuring of the free energy of the collective system are at play. This simplification helps understand the physical reality of the compensations between $\mathrm{Ln}(\tau_o)$ and ΔH, the features observed at T_g, the multiple compensations, their sign, and the apparent alternation between them. This represents a coherent set of explanations modeled by a simple mathematic formulation. However, only the Grain-Field Statistical *entire* energetic kinetic approach can address the general solution that determines how the collective dissipative structure has been affected, how many horizontal dynamic systems have been created and modified, and how they have structured themselves by vertical structuring between their b and F state and their (c, g, t) state. As we said, we simplified the solution by assuming that only one dynamic horizontal system existed and remained invariant to let us focus on the vertical structure only. In our simplified approach, the voltage field only modifies the Dual-Phase potential energy Δ_e by an amount equal to the dipolar moment times the voltage field and a temperature term that we made a function of $(T_{LL} - T_p)$ in equation (3.7). Only by simulating the more general solution, letting the voltage field also potentially modify the

EBSCOhost - printed on 2/13/2023 12:32 AM via . All use subject to https://www.ebsco.com/terms-of-use

horizontal structuring, can we be confident that the vertical structuring is dominant, even exclusive.

The fact that the relaxation curves in the normalized ΔG plane (Chapter 2) all converge to the same value $(\Delta G/T_p)_c \sim 66–70$ cal/K/mole for a temperature equal to T_p is probably indicative of the way the voltage field interacts with the dielectric medium. It also reveals that the dielectric medium is the internal viscosity, i. e. is entirely responsible for the relaxation behavior. By probing the dissipative network structure at different T_ps, the voltage field energy modifies the Dual-Phase potential well of the existing dipolar groups, distorting it to store the electrical energy, and this energy is released by thermal stimulus on reheating. The value of $A_c = (\Delta G/T_p)_c = 70$ cal/K/m corresponds to the spinning of the electrons around their orbital, converting the disorder created by the vibration into entropy. Therefore, the primary mechanism of polarization is by energetic kinetic coupling distortion, which is responsible for the $\Delta G_p - T_p$ linear behavior, and not by dipolar orientation, which can only partially occur above T_g.

Beyond T_g, some polarization by orientation occurs for polar materials, which explains the departure from the linear $\Delta G_p - T_p$ behavior in this region. The voltage energy is dissipated between two mechanisms, the distortion of the potential well of conformers and the structuring of the dissipative network to allow rotation of the dipoles in the direction parallel to the field: this is dipolar orientation. The distortion of the free energy at T_p by the voltage field induces a free energy structure at that temperature, different from the equilibrium free energy structure.

Below T_g, even if we had several systems created by horizontal structuring, the systems would all be dependent, and the assumption that the voltage field directly affects the potential well Δ_e is probably a good hypothesis. Above T_g, the modification of the potential well is through the interlock kinetics, and therefore the total electrical energy is not stored in the distortion of the potential well, which becomes a less efficient process (the free energy at T_p remains approximately constant in a certain temperature zone). By comparing the starting free energy, when the dipoles start to relax, and the final free energy, at the end of the Debye relaxation, one can calculate not only the amount of free energy released during depolarization (in addition to the value of the equilibrium free energy for a particular temperature), but also the amount of energy stored by distortion during the polarization stage. This amount depends on the free energy structure, which itself is function of the voltage field energy, in a recursive way. This is, therefore, above T_g, that the activation of the horizontal structuring dynamics would affect the formulation of equation (3.7).

In many ways, our new approach of the interactions in dielectrics challenges the proposed explanations by the scientists who studied thermal-activated depolarization phenomena, an explanation that we even seemingly adhered to by presenting them forward at several places of the book.

For instance, take the statement that “thermal-windowing,” by application of the voltage field and its removal at temperature T_d for a time t_d, permits to “isolate” elementary molecular motions: it is a simplification of language. The complex kinet-

EBSCOhost - printed on 2/13/2023 12:32 AM via . All use subject to https://www.ebsco.com/terms-of-use

ics (see the Appendix) takes its source in the coupling between kinetic and energetic equations and is essentially due to a minimum principle applied at two different levels (horizontal and vertical structuring). The return to equilibrium specifies the changes which occur to the free energy structure and reveals the modification of the potential well Δ_e by the coupling between the voltage field and the temperature, at T_p, T_d and during the ramp-up depolarization stage. By varying T_p, T_d, and t_d we activate or deactivate a part of the cooling (or heating) pattern of the free energy structure (Figure 3.51) and freeze it to lower temperatures. The ramp-up depolarization output, coming right after the partial relaxation stage that brings the system closer and closer to equilibrium, step after step as T_p increases, reveals the fundamental characteristics of the mechanisms of interactive coupling, as modeled by the Dual-Phase and the Grain-Field Statistics.

We conclude that Thermal-Windowing Deconvolution (TWD) is, *de facto*, a method to discover the gears of the vertical and horizontal energetic and kinetics interplays.

Another aspect of our research is presented in this book using interactions in dielectrics as a concrete example: the use of another language to describe interactions. Classical physics formulates interactions by introducing a potential function, V, often expressed in terms of the distance separating the interacting entities; the force of the interaction is the gradient of the potential $F = -\text{Grad}(V)$, using vectors to imply a field of action, not scalars.

We do not specifically deal in this text with the force, covalent or inter-intra molecular, that bonds the conformers together; we assume certain general rules regarding the result of their interactions:

- Locally, the isomeric rotation of the conformers occurs and is governed by their conformational potential energy, as well as their ability to agglomerate as nanometric grains, creating a local inhomogeneity.
- The local density inhomogeneity is "compensated" – this is the way we call this dual aspect of the interactions in the Dual-Phase model – by a collective action of all the interactive conformers working as a dynamic dissipative set. In our statistical model, the dissipative energy is introduced via equations that link the kinetic and the energetic aspect of the conformers statistics variations, and it leads to the definition and the quantification of a new dynamic entity: the dissipative pair (Δ_x, υ_x). This term describes the collective aspect of the duality of the conformers under dynamic conditions ($\Delta_e \neq 0$), whereas (Δ_m, υ_m) represents its local aspect (the local conformational energy properties of the conformers). Δ_x, υ_x define the kinetics of $\text{Ln}(N_b/N_f)$, the dissipative term.
- We find invariably that Δ_x and $\text{Ln}(\upsilon_x)$ compensate when Δ_e varies or Δ_m, υ_m vary. We also find that the two dualities (Δ_m, υ_m) and (Δ_x, υ_x) compensate through the origin when Δ_e varies in a normalized plot of $(\text{Ln}(\upsilon_m) - \text{Ln}(\upsilon_x))$ vs. $(\Delta_m - \Delta_x)$. We call this property of the dissipative Dual-Phase model of the dynamics of the interactions: "a cross-duality."

EBSCOhost - printed on 2/13/2023 12:32 AM via . All use subject to https://www.ebsco.com/terms-of-use

We believe that this duality and cross-duality property of interactions may be applied to many other entities in interactions, not simply conformers.

There is perhaps even another dimension to dissipative energy, duality, and cross-duality. In physics, most of the complex interactive problems involving time we know how to solve are in steady-state and not in transient-state conditions, and this simplifies their mathematical description a great deal: the reason is the separation of the variables. The separation of time from the other variables is, obviously, validated under steady-state conditions, yet the procedure has been generalized to many implicit functions of several variables. In addition, there are instances when time is intrinsically linked to other variables and the separation of the variables to resolve such implicit functions becomes questionable: this is the case for the wave function in quantum mechanics, $Y(r,t) = f(r)g(t)$, when the potential energy is a function of both r and t: $V(r,t)$.

Likewise, we have given the proof elsewhere [138] of the inadequacy of the separation of variables hypothesis in the case of the temperature and molecular weight dependence of the Newtonian viscosity in polymer melts rheology. $h(M,T) = F(M).A(T)$. We showed that the separation of M and T only occurred for specific period doubling values of M ([138]).

The technique of the separation of the variables has, indeed, demonstrated its remarkable utility of simplification over the last 200 years, permitting, as if these variables were independent functions, to easily use the tools of calculus (differentiation or integration) to express their interdependence. Its validity, however, should be carefully verified and their use not systematically generalized.

Let us illustrate this point using the variables studied in this book: the voltage field, E, and the polarizing temperature T_p. A priori, these two variables are independent: one can choose arbitrarily the value of E and T_p. Yet, this is not counting for the interactions induced by the dielectric nature of the material exposed to such a voltage at such a temperature.

In fact, the external field, E_o, triggers the presence of a different field, E, in the material and their ratio is the dielectric constant, $\varepsilon = E_o/E$, expressing the "polarizability," i. e., the tendency of a material to polarize in response to an applied electrical field. The field inside the dielectric, E, is the vector sum, $\mathbf{E} = \mathbf{E}_o + \mathbf{E}_p$, where E_p is generated by the polarization P of the dipoles in the dielectric: $E_p = -P/\varepsilon_o$, where ε_o is the permittivity of the vacuum. The polarization is usually proportional to the macroscopic field: $E_p = -\chi E$, where χ is called the macroscopic susceptibility of the dielectric. The susceptibility, χ, and the polarizability $P = \varepsilon_o(\varepsilon - 1)E_o/\varepsilon$ are equivalent constants to express the polar nature of the chemical structure of the polymer. The Clausius-Mossotti expression of the dielectric constant (equation (3.20) of Part I) correlates the molar mass of the conformer, its density, the total number of activated dipoles, the normalized induced moment, the permanent moment, and the Boltzmann thermal energy. In other words, the dielectric constant, ε, primarily depends on the chemical nature of the conformer (which controls the type and the mag-

EBSCOhost - printed on 2/13/2023 12:32 AM via . All use subject to https://www.ebsco.com/terms-of-use

nitude of the polarizability) but it also varies with the physical state of the polymer, i. e., whether it is a solid, a paste, a liquid, or a liquid crystal, in equilibrium or out of equilibrium, etc., all of which are controlled by the temperature at polarization and by the thermomechanical history of the sample that also determines its non-equilibrium state.

In summary, T_p, E, and ε are interactively coupled in a circular way, and the best way to describe it is with an implicit function of the type $H(\varepsilon, T_p, E) = 0$. This expression would greatly simplify if we could find a simple expression for the temperature dependence of ε. But ε is the sum of various contributions: the electronic permittivity, the atomic permittivity (both quasi-time-independent, i. e., rapidly in steady state), and the dipolar (orientation) permittivity, with its characteristic spectrum of relaxation and its sluggish time dependence, characterized by $\tau(T)$.

But the main purpose of this book is precisely to characterize the temperature dependence of all the relaxation times of the atomic and molecular motions and their interdependence to create the cohesion of the bonds and relate it to the dielectric response as temperature varies. We can, therefore, rewrite the implicit equation by inserting the two constants that define the temperature dependence of $\tau(T) : I(\tau_{oc}, \Delta H_c, T_p, E) = 0$.

The subscript "c" in τ_{oc} and ΔH_c is included to summarize the general result found in this book, c standing for "compensation" (the master compensation result is shown in Figure 3.56).

In the newly written implicit equation, the emphasis has shifted from the expression of ε to describe the behavior of dielectrics, *the classical approach*, to *the compensation approach*, i. e., the description of the interactive couplings between the enthalpy and entropy at different scales. By enthalpy and entropy, we, of course, refer to the physical sense attributed to the slope and intercept in the Arrhenius plane of $\mathrm{Ln}(\tau(T))$ vs. $1/T$, but also to the x- and y-coordinates of compensation plots such as $\mathrm{Ln}(\tau_o)$ vs. ΔH when T_p varies. By "different scales," we symbolize the observed changes of the mechanism of interaction between the voltage field, temperature, and the dielectric material, in a way similar to, but fundamentally different from, the classical school description of the various contributions to the dielectric constants (electronic, atomic, and dipolar). In our Dual-Phase dissipative model of interactive coupling, the normalized variables of the masterplot have two similar terms, $\Delta_m - \Delta_x$ for the x-axis and $\mathrm{Ln}(\upsilon_m) - \mathrm{Ln}(\upsilon_x)$ for the y-axis. But the "m" and "x" terms do not play the same role. Only Δ_x and $\mathrm{Ln}(\upsilon_x)$ vary with Δ_e; Δ_m and $\mathrm{Ln}(\upsilon_m)$ remain constants within the "scales," i. e., within the "ranges of T_p" the way we called ranges 1, 2, and 3 in our discussion of the dielectric interactive coupling in Chapter 3 of Part I. Δ_m, υ_m define the scale and Δ_x, $\mathrm{Ln}(\upsilon_x)$ define the dissipation term of the Dual-Phase dissipative statistics. And, as we have concluded in Part I, Chapter 3, we need both the *dissipative contribution* and the *scale contribution* to complete the masterplot, which goes through the origin at all scales.

EBSCOhost - printed on 2/13/2023 12:32 AM via . All use subject to https://www.ebsco.com/terms-of-use

This is what we wanted to note in this closing chapter of the book: our approach of the interactions tries to find the way to unify the various scales participating in the process of interaction.

It is not surprising, using this new physics language just mentioned, to see that the three scales describing ranges 1, 2, and 3 compensate at T_g (in Figure 3.73). The reason is that the dielectric field defined by the clouds of the electrons in the orbitals, by the geometric disposition of the atoms in a conformer in isomeric conformation rotation, and by the dipolar moment vector submitted to orientation are all interrelated and that they share the same dissipative term, $\mathrm{Ln}(N_b/N_F)$, related to the (b/F) free volume structure, coalescing at T_g, whatever the scale. This collective coalescence of the dissipative term at the T_g phase transition, melting the spatial locality of the b grains, occurs with an increase of the degree of freedom of the statistics dynamics. The last and ultimate increase of the degree of freedom of the Dual-Phase statistics occurs at T_{LL}, where the space-time difference between the b and F conformers collapses, marking the end of the materialization of the Dual-Phase dissipative elastic wave and marking a return to the Boltzmann statistics. The T_g spatial delocalization of the b grains touches all scales related to electrons and their surroundings: this is the reason this is perceived as a super-compensation of ΔH in Figure 3.73.

In the closing sections of Part I (Figures 3.61 to 3.71) we initiate the search for new concepts to build up a ladder of scales. We show that we could unify the types of interactions present in a polymer into a single concept, the compensation of $\mathrm{Ln}(\tau_o)$ vs. ΔH, provided we also divide the temperature range into three ranges, defining three scales of (Δ_m, υ_m) values. The objective of finding the differences between scales 1, 2, and 3 and relating the findings to a unification scheme that would permit to designate T, the temperature, as the fundamental parameter to pass from one scale, say scale 1 identified by $(\Delta_m, \upsilon_m)_1$, to other scales, say scale 2 identified by $(\Delta_m, \upsilon_m)_2$, etc., remains an important (unsolved) objective on its own. We only initiate this research in this book (in Section I.3.4.6.3) presenting preliminary results that clearly raise more questions than answers. We allowed ourselves to be imaginative, however, in the last section of Part I of the book, and introduced the "phantom variable," T_x, in Section I.3.5.4.1, which led to the important discoveries explained in Figures 3.59 and 3.72, and the "conjugated states" across different scales, in Section I.3.5.4.2: $[\Delta H_c = \Delta H(T_p + \delta_{p\tau}),\ \tau_{oc} = \tau_o(T_p + \delta_{pH})]$. The use of the phantom variable also led to the unique discovery of T_{xc} at $\delta_x = 0$ in Figure 3.55 and of the two equations defining the master compensation for the reference grid in equation (3.17).

Conjugated states show surprising properties, as illustrated by the blue triangles in Figures 3.66 to 3.68. Conjugated compensation states at one scale (range 1) can assume real data compensation states of another scale (range 3). Could it be that the temperature drift, $\delta = \delta_{pH} - \delta_{p\tau}$, shown to exist between "conjugated variables," such as those coupled in Figures 3.67, is the key to define the ladder of scales, *completing the unification of the network of the interactions at all scales*?

EBSCOhost - printed on 2/13/2023 12:32 AM via . All use subject to https://www.ebsco.com/terms-of-use

In fact, pursuing our interest in exploring the properties of conjugated variables led not only to the discovery of several other properties of the conjugated states at different scales (Figures 3.69 to 3.71), but also to questioning the role of temperature, T, when coupled to other independent external parameters, in the formulation of the interactions in materials (Section I.3.5.4.3).

Does the imposition of a voltage field on a dielectric material at temperature T_p induce a coupling effect that slightly shifts the temperature scale, as if temperature would have a different scale when acting alone or coupled with a voltage field? This question calls for a possible relativity effect in materials due to the interactions. In a sense, it suggests that it is impossible to measure directly and alone the effect of the voltage field on the dielectric properties of a material, since the measurement is always done at a certain temperature at which the voltage field and temperature couple up to trigger a dissipative response.

The impact of this relativity effect inside materials may be critical as far as our knowledge of reality via measurements is concerned. Our knowledge of reality occurs *through measurements done above the absolute zero temperature* (0 K), so coupling between the absolute temperature T and any other measured parameter must be reflected in the equations describing any of their correlations.

Shall we include the dissipative effect of coupling with temperature in *the definition of the units* that are used as reference values to be able to quantify the other independent variables, such as voltage (in Volts), distances (in meters), time intervals (in seconds), etc., as well as the fields in the physics of interactions (in the latter case by introducing a dissipative term accounting for the coupling between T and the field)?

For instance, should temperature T appear in the description of the potential field function in the Schrödinger equation, $V(r, t, T)$, instead of presently $V(r, t)$, and do we need to add a dissipative term in the equations to solve when the potential includes T?

These are iconoclastic questions, of course, the last question being the most provocative one: it suggests to rescale *the unit* of a physical quantity to account for the dissipative coupling between it and T, implying a radical modification of the equations in physics by incorporating the interaction of absolute temperature and the physical entity in question. To illustrate this simply, the meter, the reference unit for length, would have a different value when (1) distance and voltage are combined in a measurement and when (2) distance and optical measurements are involved. All fundamental "independent" units (time, space, temperature, mass) would need to be defined relative to another, i. e., interactively and coupled, at least in their Planck state.

Finally, the conclusion of this book should end by teasing the reader in trying to know more about the Grain-Field Statistics (Section I.3.5.4.4): what are the two most striking ideas to be remembered of the vertical split structuring defining the Dual-Phase statistics?

EBSCOhost - printed on 2/13/2023 12:32 AM via . All use subject to https://www.ebsco.com/terms-of-use

1. The fact that it defines a dissipative factor from the coupling between energetic and kinetic constraints and that this dissipative factor, $\mathrm{Ln}(N_b/N_F)$, regards the collective response, dynamically represented by Δ_x, υ_x, the quantities that are measured. Our knowledge of the local properties, Δ_m, υ_m, is filtered through the collective response, Δ_x, υ_x, and not the opposite. Should we not reverse our methodology of investigation and focus on determining the fundamental laws of the whole first, since this is what we measure, and learn how to transmit them down to the local scale *rather than doing the opposite*, starting from the local laws (the elementary particles and forces of the standard model, for instance) and constructing the whole (astronomy)?

2. The local will be derived from the whole at phase transitions, where the scales synchronize, i. e., when Δ_e of the collective set collapses ($\Delta_e = 0$ for $\Delta_m = \Delta_x$; $\upsilon_m = \upsilon_x$).

However, I can sense that a teased reader will not be entirely satisfied by the answer above since the real challenge of the Grain-Field Statistics is to find the correct combination of horizontal and vertical splitting to describe interactions, not simply the vertical structuring. This forces me to provide another short preview extracted from another book in preparation with the following chapter title: "The Dynamics of Open-Dissipative Systems of Interactions: the Question of their Finitude and Stability." This chapter, whose title, obviously, resonates with the work of Prigogine in the 1970s [214], although it totally differs from it for its mathematical treatment, should lay down the basic map of what needs to be resolved by the next generation of research scientists interested in these solutions to better understand how the local and the global interactions structure one another to generate transient and steady-state events in time-space, i. e., describe what we call reality (time vs. space, matter vs. vacuum). This would offer new perspectives on the description of the different types of interactions and of their unification as solutions of the network of open dissipative cooperative systems. The first Renaissance in physics, from Newton to Einstein for gravitational interactions to the standard model of interactions to describe the infinitely small, may have exhausted its resources to complete a grand unification. Should the second Renaissance, inspired by Prigogine [214], now take the baton?

This book is the second of a series of six books dedicated to the dissemination of a new understanding of the interactions in polymers using the concepts of "Dual-Phase" and "Cross-Dual-Phase" to describe their rheology [138], their crystallization kinetics [140, 143], and the origin and the stability of their entanglement ability [144]. I have designated this research and the teaching of its principles and objectives under the name "New School Polymer Physics."

In this book, "interactive coupling" is presented as a recursive process modulating the local interactions by the system organized by the collective aspect of those interactions. Thus, in a sense, without the reader even realizing it, because the emphasis was not brought onto that aspect, this work – in Chapter 3 of Part I and its Appendix – may be viewed as a new and original attempt to describe the mathematical correlations between the properties of what interacts and the number of units defining the systems

EBSCOhost - printed on 2/13/2023 12:32 AM via . All use subject to https://www.ebsco.com/terms-of-use

of interactions at play. This is a classical field of physics that will be recognized by those scientists working on chaos, fluctuations, and long-range order generated by local disorder, a field now called “complex systems” although other names were used in the past such as “dissipative systems” by Prigogine.

Arrosa, October 15th, 2021

EBSCOhost - printed on 2/13/2023 12:32 AM via . All use subject to https://www.ebsco.com/terms-of-use

Bibliography

[1] Abdel-Malik, T. G., Abdeen, A. M., Aly, A. A., Phys. Status Solidi A 70, 703 (1982).
[2] Abkowitz, M., Pfister, G., J. Appl. Phys. 46(6), 2560 (1975).
[3] Abkowitz, M., Prest, W. M. Jr., Luca, D. J., Pfister, G., Appl. Phys. Lett. 34(1), 19 (1979).
[4] Alhaj-Mohammed, M. H., Davies, G. R., Jawad, S. A., Ward, I. M., J. Polym. Sci., Part B, Polym. Phys. 26, 1751 (1988).
[5] Aoudi, S., Bemdapis, M., Lacabanne, C., In: Proc. 5th Int. Symp. Electrets, Heidelberg, p. 836, IEEE, NY, (1985).
[6] Aouadi, S., Bendaoud, M., Lacabanne, C., In: Sessler, G. M., Gerhard-Multhaupt, R. (eds.) Proc. 5th Int. Symp. Electrets, p. 836 (1985).
[7] Aouadi, S., Bendaoud, M., Lacabanne, C., TSC Studies of Relaxation Modes in Native and Regenerate Cellulose Below T_g. Influence of Water of Absorption. IEEE Trans. Electr. Insul. E121, 3 (1986).
[8] Aras, L., Vanderschueren, J., Niezette, J., Vanderschueren, R., J. Polym. Sci., Polym. Phys. Ed. 21, 799 (1983).
[9] Barandiaran, J. M., Del Val, J. J., Colmenero, J., Lacabanne, C., Chatain, D., Millan, J., Martinez, G., J. Macromol. Sci., Phys. 822, 645 (1984).
[10] Bayoux, J. P., Pillot, C., Chatain, D., Lacabanne, C., Polymer Preprints, 211, 1 (1983).
[11] Benoit, H., Polymer Preprints, 15(2), 324 (1974).
[12] Bernes, A., A Study of the Metastibility of an Amorphous Polymer (Atactic Polystyrene) in relation to its Thermal History by Dielectric Spectroscopy, Thesis (in French). University Paul Sabatier, Toulouse, France (1985).
[13] Bernes, A., Boyer, R. F., Chatain, D., Lacabanne, C., Ibar, J. P., Thermally Stimulated Current Studies of Transitions in Amorphous Polymers. In: Keinath, S. E., Miller, R. L., Rieke, J. R. (eds.) Order in the Amorphous "State" of Polymers, p. 305. Plenum Press, London (1987).
[14] Bernes, A., Chatain, D., Lacabanne, C., Ibar, J. P., Influence of Rheomolding on the Transitions of Polystyrene. Bull. Am. Phys. Soc. 30(3), 496 (1985).
[15] Bernes, A., Chatain, D., Ibar, J. P., Lacabanne, C., Non-isothermal Polarization Recovery at the Glass Transition. Bull. Am. Phys. Soc. 31(3), 513 (1986).
[16] Bernes, A., Chatain, D., Lacabanne, C., Lorentz, G., Study of the Orientation of the Amorphous Phase in Polyethylene Terephthalate. In: Harrison, I. R. (ed.) Proceedings of the 19th NATAS Conference, Vol. 1, Boston, p. 115 (1990).
[17] Bernes, A., Ibar, J. P., Bettacchioli, A., Chatain, D., Lacabanne, C., Influence of Thermal History on the Relaxation Modes of Polycarbonate. Am. Phys. Soc. 32(3), 423 (1987).
[18] Berticat, P., Bui, A., Hoang, T. G., Chatain, D., Lacabanne, C., Depolarization Thermocurrent and Dielectric Study in Polyethylene. Makromol. Chem. 177, 1583 (1976).
[19] Bettachioli, A., PhD Thesis, Toulouse, France (1987).
[20] Boiteux-Steffan, C., Seytre, G., Vallet, G., Chatain, D., Lacabanne, C., Multiple Transitions in Polyallybenzene. 2 Dielectric Relaxations: Relationship between Structure and Properties. Makromol. Chem. 26, 1448 (1985).
[21] Boyer, R. F., In: Bicerano, J. (ed.) Computational Modeling of Polymers, pp. 1–52. Marcel Dekker, New York (1992).
[22] Boyer, R. F., An apparent double glass transition in semicrystalline polymers. J. Macromol. Sci. B, Phys. 8(3–4), 503–537 (1973).
[23] Bruhat, G., Cours de Physique Generale, Electricite, p. 805. Masson & Cie, 8eme Édition (1967). G. Goudet Ed, Eq. (47).
[24] Bucci, C., Fieschi, R. C., Phys. Rev. Lett. 12, 16 (1964).
[25] Bucci, C., Fieschi, R., Guidi, G., Phys. Rev. 148, 816 (1966).

https://doi.org/10.1515/9783110756746-011

EBSCOhost - printed on 2/13/2023 12:32 AM via . All use subject to https://www.ebsco.com/terms-of-use

[26] Bui, A., Carchano, H., Guastavino, J., Chatain, D., Gautier, P., Lacabanne, C., DTC Study of Very Thin Polystyrene Films at Temperature of about T_g and above. Thin Solid Films 21, 313 (1974).
[27] Carr, S. H., Chapter 5, Thermally Stimulated Discharge Current Analysis of Polymers. In: Electrical Properties of Polymers, p. 215. Academic Press Inc. (1982).
[28] Cazzitti, A., Lacabanne, C., Young, R. A., Hitmi, N., Re-orientable Electric Dipoles and Cooperative Phenomena in Human Tooth Enamel. J. Dent. Res. 64, 283 (1985).
[29] Cebeillac, P., PhD Thesis, Toulouse, France (1987).
[30] Cebeillac, P., Chatain, D., Megret, C., Lacabanne, C., Bernes, A., Dupuis: Int. Symp. on Polymer Materials, San Sebastian. Die Makromol. Chem. (1987).
[31] Cebeillac, P., Fauran-Clavel, M. J., Lacabanne, C., Dupuis, P., Dielectric Spectroscopy for the Characterization of the Microstructure of Latexes. In: ICPADM '88 (1988).
[32] Cebeillac, P., Fauran-Clavel, M. J., Lacabanne, C., Ibar, J. P., Characterization of Latex Copolymers by DSC, DMA and TSC/RMA Spectroscopy. In: Proceedings of ANTEC '89, vol. 35, p. 1855 (1989).
[33] Cebeillac, P., et al., Transitions and Relaxations in Amorphous Polymers. Makromol. Chem., Macromol. Symp. 2021, 335 (1988).
[34] Cebeillac, P., et al., Characterization of Amorphous Copolymers by Dielectric Spectroscopy by TSC/RMA (In French). Revue "Matériaux et Techniques", 45 (1989).
[35] Chafai, A., Chatain, D., Dugas, J., Lacabanne, C., Vayssie, E., Modification of Glass Transition and Liquid-Liquid Transition in PMMA Doped with Fluorescent Dyes. J. Macromol. Sci., Phys. B22(5–6), 633 (1983).
[36] Chatain, D., Gautier, P., Lacabanne, C., Bull. Am. Phys. Soc. 18(3), 462 (1973).
[37] Chatain, D., Gautier, P., Lacabanne, C., DTC Study of Polysulfonamide above the Glass Transition Temperature. Bull. Am. Phys. Soc. 19(3), 265 (1974).
[38] Chatain, D., Gautier, P., Lacabanne, C., DTC Study of Polyglycine. Bull. Am. Phys. Soc. 20(3), 453 (1975).
[39] Chatain, D., Gautier, P., Lacabanne, C., Dispersion et Relaxation Dipolaire à Très Basse Fréquence Dans CaF_2. C.R. Ac. Sci.: Paris 270B, 1694 (1970).
[40] Chatain, D., Gautier, P., Lacabanne, C., Ionic Thermal Current Study of the α' Process in Poly (Hexamethylene Adipamide). J. Polym. Sci., Polym. Phys. Ed. 11, 1631 (1973).
[41] Chatain, D., Gautier, P., Lacabanne, C., Study of the Very Low Frequency Dielectric Behavior of Polyamide 66 by a Non-Contact Method. Phys. Status Solidi A 15, 191 (1973).
[42] Chatain, D., Gautier, P., Lacabanne, C., Transient Method of Measuring Very Low Conductivity Without Contacting Electrodes. Rev. Sci. Instrum. 41(11), 1610 (1970).
[43] Chatain, D., Lacabanne, C., Méthode de mesure de la Conductivité Electrique de Cristaux Isolants Sans Electrode de Contact. C.R. Ac. Sci.: Paris 267B, 723 (1968).
[44] Chatain, D., Lacabanne, C., Maitrot, M., Etude des Relaxations Dans le Polyhexaméthylène Adipamide par la Méthode TCD. Phys. Status Solidi A 13, 303 (1972).
[45] Chatain, D., Lacabanne, C., Maitrot, M., Seytre, G., May, J. F., Depolarization Thermocurrents of Polyglycine I and II. Phys. Status Solidi A 16, 225 (1973).
[46] Chatain, D., Lacabanne, C., Soulier, J. P., Chabert, B., Maitrot, M., Dipolar Relaxation at Low Temperature (LNT) of Polyamides and Polysulfonamides. IUPAC Preprints, 423 (1973).
[47] Chen, R., J. Appl. Phys. 40, 570 (1969).
[48] Chen, R., Kirsh, Y., Analysis of Thermally Stimulated Processes. International Series on the Science of the Solid State, vol. 15. Pergamon Press, Oxford (1981).
[49] Collins, G., Hoescht Celanese, New Jersey, Private Communication.
[50] Crine, J. P., A Thermodynamic Model for the Compensation Law and its Physical Significance for Polymers. J. Macromol. Sci., Phys. B23(2), 201 (1984).
[51] Dandurand, J., Delpech, V., Lebugle, A., Lamure, A., Lacabanne, C., Study of the Mineral-Organic Linkage in an Apatitic Reinforced Bone Cement. J. Biomed. Mater. Res. (1990).

EBSCOhost - printed on 2/13/2023 12:32 AM via . All use subject to https://www.ebsco.com/terms-of-use

[52] Dandurand, J., Lacabanne, C., Moisan, J. Y., Servens, C., In: Das Gupta, D. K., Pattullo, A. W. (eds.) Proceedings of the 6th Int. Symp. on Electrets, ISE 6, p. 241 (1988).
[53] Dandurand, J., Lacabanne, C., Moisan, J. Y., Servens, C., Polarization Phenomena in Resinic Esters of Photothermoplastic Devices for Applications to Holographic Optical Switching In: Staybelite Ester (SE30).
[54] Dawkins, J. V., In: Allport, D. C., Janes, W. H. (eds.) Block Copolymers, p. 363. Halsted Press, John Wiley & Sons, New York (1973).
[55] Dechesne, J. P., Vanderschueren, J., Jaminet, F., J. Pharm. Belg. 39, 341 (1984).
[56] Del Val, J. J., Alegria, A., Colmenero, J., Lacabanne, C., IEEE Trans. Electr. Insul. E121(3), 173 (1986).
[57] Del Val, J. J., Alegria, A., Colmenero, J., Lacabanne, C., Study of the α and β Relaxations in a Commercial Poly(Vinyl Chloride) by Thermally Stimulated Creep and Depolarization Current Techniques. J. Appl. Phys. 59, 3829–3834 (1986).
[58] Deleens, G., Foy, P., Marchal, E., Eur. Polym. J. 13, 343 (1977).
[59] Demont, P., Chatain, D., Lacabanne, C., Glotin, M., Pierson, J. F., Segregation in the Amorphous Phase of PEBA. Bull. Am. Phys. Soc. 31(3), 455 (1986).
[60] Demont, P., Chatain, D., Lacabanne, C., Glotin, M., Pierson, J. F., Fine Structure of the Mechanical Relaxation Modes of Poly(Ether Block Amide). Correlation with Ultimate Properties. Bull. Am. Phys. Soc. 32(3), 837 (1987).
[61] Demont, P., Chatain, D., Lacabanne, C., Glotin, M., Pierson, J. F., Amorphous Phase Segregation in Poly(Ether Block Amide) PEBA. Correlation with Mechanical and Dielectric Properties. In: European Symp. on Polymeric Materials, Lyon (1987). Proceedings GFP/European Polymer Federation, Symp. on Polymeric Materials. GFP, vol. 09, p. 1 (1987).
[62] Demont, P., Chatain, D., Lacabanne, C., Moura, J. L., Ronarc'h, D., Etude des Propriétés Anélastiques des Copolymères Séquencés de Propylène-Ethylène par Fluage Stimulé par la Température. J. Phys., Colloque C9, Suppl. 12(44), 203 (1984).
[63] Demont, P., Chatain, D., Lacabanne, C., Moura, J. L., Ronarc'h, D., Polym. Eng. Sci. 24, 127 (1984).
[64] Demont, P., Chatain, D., Lacabanne, C., Ronarc'h, D., Moura, J. L., Thermally Stimulated Study of Ethylenepropylene Copolymers and Blends. Bull. Am. Phys. Soc. 27(3), 291 (1982).
[65] Demont, P., Fourmaud, L., Chatain, D., Lacabanne, C., In: Craver, C. D., Provder, T. (eds.) Polymer Characterization, Physical Property, Spectroscopic and Chromatographic Methods, Advances in Chemistry, Series 227, Chapter II. American Chemical Society (1990).
[66] Demont, P., Sharif, F., Chatain, D., Lacabanne, C., Glotin, M., Mery, J. M., Phase Segregation in Poly(Ether Block Amide) Copolymers. Bull. Am. Phys. Soc. 30(3), 488 (1985).
[67] Dreyfus, G., Lacabanne, C., Rahal, A., Méthode des Courants Thermostimulés: Théorie et Résultats Expérimentaux. Rev. Gén. Electr. 87(11), 870 (1978).
[68] Dumont, P., Faruque, S. H., Lacabanne, C., Ibar, J. P., A Study of the Structure of Polyether Block Amides (PEBA) Latex by TSC/RMA Spectroscopy. In: Proceedings of the 18th NATAS Conference, p. 840 (1989).
[69] Dussel, G. A., Bube, R. H., Phys. Rev. 155, 764 (1967).
[70] Elhout, J., Chatain, D., Lacabanne, C., Francois, B., Galtier, M., Dielectric and Anelastic Properties of Cis and Trans-Polyacetylene. Am. Phys. Soc. 32(3), 739 (1987).
[71] Elhout, J., Chatain, D., Lacabanne, C., Montaner, A., Galtier, M., Influence of Compression and Rolling on the Oxydation of Polyacetylene. In: Proceedings GFP/European Polymer Federation (1987).
[72] Elsayed, T., Chatain, D., Lacabanne, C., A New Method for the Study of Piezoelectricity in Polymers. Bull. Am. Phys. Soc. 26(3), 428 (1981).
[73] Elsayed, T., Chatain, D., Lacabanne, C., Lemonon, C., Micheron, F., The Morphology Transitions Relationships in PVF_2. IUPAC Preprints 3, 89 (1980).

EBSCOhost - printed on 2/13/2023 12:32 AM via . All use subject to https://www.ebsco.com/terms-of-use

[74] Elsayed, T., Elhout, J., Francois, B., Mathis, C., Chatain, D., Lacabanne, C., Anelastic Properties of Polyacetylene Films. Bull. Am. Phys. Soc. 28(3), 396 (1983).
[75] Elsayed, T., Elhout, J., Nuffer, R., Francois, B., Mathis, C., Chatain, D., Lacabanne, C., Characterization of the Anelastic Properties of Thermal and Chemical Trans Polyacetylene. Bull. Am. Phys. Soc. 30(3), 434 (1985).
[76] Elsayed, T., Elhout, J., Stefenel, M., Chatain, D., Lacabanne, C., Francois, B., Mathis, C., Etude par Fluage Stimulé par la Température de l'Evolution des Propriétés Anélastiqu-es de Films de Polyacétylène en fonction de l'Oxydation. J. Phys., Colloque C9, Suppl. 12(44), 197 (1983).
[77] Faruque, H. S., Thesis, University Paul Sabatier, Toulouse, France (1984).
[78] Faruque, H. S., Lacabanne, C., Indian J. Pure Appl. Phys. 25, 114 (1987).
[79] Faruque, H. S., Lacabanne, C., Phase Segregation of Polyether-Polyamide Copolymer PEBAX by Thermally Stimulated Current Method. Jpn. J. Appl. Phys. 25(3), 473 (1986).
[80] Faruque, H. S., Lacabanne, C., Anelastic and Dielectric Properties of Polyether-Polyamide Copolymer PEBAX Studied by a Thermally Stimulated Depolarisation Current Method. J. Phys. D, Appl. Phys. 25, 114 (1987).
[81] Faruque, H. S., Lacabanne, C., J. Mat. Sci. 22, 675 (1987).
[82] Faruque, H. S., Lacabanne, C., Polymer 27, 527 (1986).
[83] Fauran-Clavel, M. J., Lacabanne, C., Fabre, C., Stefenel, M., Oustrin, J., Lamure, A., Influence du Cadmium sur les Mouvements Moléculaires dans le Collagène natif. In: Harmand, M. F., Ducassou, D. (eds.) Tissus Calcifiés et Biomatériaux. Les Publications de BIOMAT (1988).
[84] Fauran-Clavel, M. J., Lacabanne, C., Fabre, C., Stefenel, M., Oustrin, J., Lamure, A., Influence of Cadnium on the Chain Dynamic of Rat Tail Tendon. Biomaterials (1987).
[85] Ferry, J. D., Viscoelastic Properties of Polymers, p. 316. John Wiley & Sons (1970). Ch. 11, Table 11-II.
[86] Feurer, B., Harel, J. P., Lacabanne, C., Characterization, Using a Non-Contact Dielectric Technique, of a PMMA Surface Modified by Ion Bombardment. Thin Solid Films 100, 249 (1983).
[87] Ficat, J. J., Escourrou, C., Durroux, R., Fauran, M. J., Ficat, P., Lacabanne, C., Micheron, F., Osteogenesis Induced by Bimorph Polyvinylidene Fluoride Films. Ferroelectrics 51(1–2), 121 (1983).
[88] Ficat, J. J., Lacabanne, C., Durroux, R., Ficat, P., Micheron, F., Piezoélectricité et Ostéogénèse. Rev. Chir. Orthop., Suppl. II, 70, 30 (1985).
[89] Ficat, J. J., Thiechart, M., Ficat, P., Lacabanne, C., Bab, I., Micheron, F., Piezoelectric Induction of Bone Formation: Ultrastructural Observations. Ferroelectrics 60, 313 (1985).
[90] Flory, J., Principles of Polymer Chemistry. Cornell University Press, Ithaca and London (1953).
[91] Gibbs, J. H., DiMarzio, E. A., J. Chem. Phys. 28, 373 (1958).
[92] Gorin, S., Monnerie, L., J. Chem. Phys. 67, 869 (1970).
[93] Gourari, A., Bendaoud, M., Lacabanne, C., Boyer, R. F., J. Polym. Sci. 23, 889 (1985).
[94] Goyaud, P., Lacabanne, C., IUPAC Preprints, II D1–18, 1043 (1979).
[95] Goyaud, P., Lacabanne, C., Boyer, R. F., Thermally Stimulated Current (TSC) Study of the T_g and $T_{l,l}$ Transitions in Anionic Polystyrenes, Amorphous Polymers. J. Polym. Sci., Polym. Phys. Ed. 18, 277 (1980).
[96] Goyaud, P., Lacabanne, C., Cotton, J. P., TSC Study of Deuteration Polystyrene. Solid State Commun. 32, 673 (1979).
[97] Goyaud, P., Lacabanne, C., Douillard, A., A Depolarization Thermocurrent Study of Polyethylene. Thin Solid Films 62, 83 (1979).
[98] Gubanski, A., Gubanski, S. M., On The Possibility on the TDS Measuring Technics Application for PET Films Thermal Endurance Estimation. In: Proc. of the 3rd Int. Conf. on Conduction and Breakdown in Solids Dielectrics, p. 259 (1989).

EBSCOhost - printed on 2/13/2023 12:32 AM via . All use subject to https://www.ebsco.com/terms-of-use

[99] Guerdoux, L., Marchal, E., Physical Aging of PMMA and Polycarbonate in the Region of Secondary Relaxation. Polymer 22, 1199 (1981).
[100] Guillaud, G., Fornazero, J., Maitrot, M., Chatain, D., Lacabanne, C., J. Appl. Phys. 48(88), 3428 (1977).
[101] Guillet, J., Seytre, G., Chatain, D., Lacabanne, C., Monpagens, J. C., TSC and Dielectric Study of Multiple Relaxation in Poly L Proline. J. Polym. Sci., Polym. Phys. Ed. 15, 541 (1977).
[102] Guillet, J., Seytre, G., May, J. F., Chatain, D., Lacabanne, C., Low Frequency Dielectric Behavior of Hydrated Poly L Proline II. J. Polym. Sci., Polym. Phys. Ed. 14, 211 (1976).
[103] Harmand, M. F., Lamure, A., Maurel, E., Pieraggi, M.Th., Hitmi, N., Lacabanne, C., Study by Dielectric and Mechanical Spectroscopy of Chain Mobility in Calcified Tissues. Calcif. Tissue Int. 35, A15 (1983).
[104] Hedvig, P., Dielectric Spectroscopy of Polymers. Adam Hilger, Bristol (1977).
[105] Hitmi, N., Chatain, D., Lacabanne, C., Dugas, J., Trombe, J. C., Rey, C., Montel, G., Phys. Status Solidi A 60, 501 (1980).
[106] Hitmi, N., Chatain, D., Lacabanne, C., Dugas, J., Trombe, J. C., Rey, C., Montel, G., Solid State Commun. 33, 1003 (1980).
[107] Hitmi, N., Lacabanne, C., Bonel, G., Roux, P., Young, R. A., J. Phys. Chem. Solids 47(5), 507 (1986).
[108] Hitmi, N., Lacabanne, C., Young, R. A., TSC Study of Electric Dipole Relaxations in Chlorapatite. J. Phys. Chem. Solids 44, 701 (1984).
[109] Hitmi, N., Lacabanne, C., Young, R. A., OH^- Dipole Reorientability in Hydroxyapatites: Effect of Tunnel Size. J. Phys. Chem. Solids 47(6), 533 (1987).
[110] Hitmi, N., Lacabanne, C., Young, R. A., J. Phys. Chem. Solids 47(6), 533 (1986).
[111] Hitmi, N., Lacabanne, C., Young, R. A., J. Phys. Chem. Solids 49(5), 541 (1988).
[112] Hitmi, N., Lamure-Plaino, E., Lamure, A., Lacabanne, C., Re-orientable Electric Dipoles and Cooperative Phenomena in Human Tooth Enamel. Calcif. Tissue Int. 38, 252 (1986).
[113] Hitmi, N., Trombe, J. C., Rey, C., Montel, G., Dugas, J., Chatain, D., Lacabanne, C., Dipolar Movements in Hydroxyapatite. Bull. Am. Phys. Soc. 25(3), 417 (1980).
[114] Hitmi, N., Trombe, J. C., Rey, C., Montel, G., Dugas, J., Lacabanne, C., Chatain, D., TSC Study of Monoclinic Hexagonal Transition in Phosphocalcium Apatites. Bull. Am. Phys. Soc. 26(3), 247 (1981).
[115] Hoffman, J. D., Williams, G., Passaglia, E., J. Polym. Sci., C Polym. Symp. 14, 141 (1965).
[116] Hoffman, J. D., Williams, G., Passaglia, E., Analysis of the α, β and γ Relaxations in Polychlorotrifluoroethylene and Polyethylene: Dielectric and Mechanical Properties. J. Polym. Sci., Part C. 14, 173 (1966).
[117] Ibar, J. P., ACS PMSE Div. Proceedings 61, 767 (1989).
[118] Ibar, J. P., ACS PMSE Div. Proceedings 61, 753 (1989).
[119] Ibar, J. P., ACS PMSE Div. Proceedings 63, 539 (1990). Fall Meeting, Washington D. C. An Analysis of Compensation Phenomena: Description, Critical Review, Alternatives, Interpretation.
[120] Ibar, J. P., J. Non-Cryst. Solids 75, 215 (1985).
[121] Ibar, J. P., Non-Equilibrium Network Deformation. A New Analysis of the Concept of Network. In: IUPAC 28th Macromolecular Symposium Proceedings, p. 854 (1982).
[122] Ibar, J. P., The T_β, T_g and $T_{l,l}$ "Transitions": Are these the Manifestation of a Unique Relaxation Process? In: Keinath, S. E., Miller, R. L., Rieke, J. R. (eds.) Order in the Amorphous "State" of Polymers, p. 371. Plenum Press, New York (1987).
[123] Ibar, J. P., Application of Compensation Phenomena to the Thermal Analysis Characterization of Polymers: Introducing the Degree of Disorder (DOD) Number. Polym. Eng. Sci. 31, 1467 (1991).
[124] Ibar, J. P., Polym.-Plast. Technol. Eng. 17(1), 11 (1981).

EBSCOhost - printed on 2/13/2023 12:32 AM via . All use subject to https://www.ebsco.com/terms-of-use

[125] Ibar, J. P., On the Use of Compensation Law to Describe Cooperative Relaxation Kinetics in Thermally Stimulated Processes: a Review. In: Harrison, I. R. (ed.) Proceedings of the 19th NATAS Conference, Vol. 1, Boston, p. 97 (1990).
[126] Ibar, J. P., Multiple Compensation Phenomena in the Amorphous Phase of Polymers. In: Harrison, I. R. (ed.) Proceedings of the 19th NATAS Conference, Vol. 1, Boston, p. 114 (1990).
[127] Ibar, J. P., Non Linear Kinetics: The Dual Split Kinetic Model. In: Harrison, I. R. (ed.) Proceedings of the 19th NATAS Conference, Vol. 2, Boston, p. 402 (1990).
[128] Ibar, J. P., The Physics of Polymer Interactions. A Novel Approach. Application to Rheology and Processing, Ch. 1. Hanser Publishers, Munich (2019).
[129] Ibar, J. P., On the Use of the Compensation Law to Describe Cooperative Relaxation Kinetics in Thermally Stimulated Processes: a New View. Thermochim. Acta 192, 91 (1991).
[130] Ibar, J. P., Multiple Compensation Phenomena in the Amorphous Phase of Polymers. Thermochim. Acta 192, 265 (1991).
[131] Ibar, J. P., A Dual Split Kinetics Interpretation of Compensation Law at the T_g of Amorphous Polymers. Thermochim. Acta 192, 297 (1991).
[132] Ibar, J. P., Bernes, A., et al., Characterization of Polymers by Thermal Stimulated Current (TSC) and Relaxation Map Analysis Spectroscopy (RMA). In: ANTEC '88, Conference Proceedings, vol. 35, p. 1049 (1988).
[133] Ibar, J. P., et al., Automatic Aging Study of PMMA below T_g Studied with the TSC/RMA Spectrometer. ACS PMSE Proceedings 63, 534 (1990).
[134] Ibar, J. P., Zhang, Z., Li, Z. M., Santamaria, A., Dynamic Rheological Properties of a Polycarbonate Melt Presenting Solid-Like Characteristics and a Departure from Pure Liquid Newtonian Behavior at Long Relaxation Times. J. Macromol. Sci. B, Phys. 54(6), 649–710 (2015).
[135] Ibar, J. P., A Dual-Phase Approach to Reveal the Presence and the Impact of the T_{LL} Transition in Polymer Melts. Part I and Part II. J. Macromol. Sci. B, Phys. 60(10), (2021). Both part I and II in the single issue 10 (112 pages). Part I: pp. 727–791; Part II: pp. 792–838.
[136] Ibar, J. P., 12 Lectures in Polymer Physics Dedicated to Processing, College of Polymer Science and Engineering, Fall 2014, University of Sichuan, Chengdu, China.
[137] Ibar, J. P., The Grain-Field Statistics of the Interactions Applied to Polymers. De Gruyter Publisher, Berlin (2026).
[138] Ibar, J. P., Dual-Phase Rheology of Polymer Melts. De Gruyter Publisher, Berlin (2023).
[139] Ibar, J. P., Do we need a new theory in polymer physics. J. Macromol. Sci., Polym. Rev. 389–458 (1997).
[140] Ibar, J. P., A New Theory for the Properties and the Behavior of Polymeric Materials. M. I. T PhD Thesis (1975), unpublished: https://sites.google.com/a/eknetcampus.com/dual-split-statistics/.
[141] Ibar, J. P., et al., Characterization of Polymers by Thermal Stimulated Current Analysis and Relaxation Map Analysis Spectroscopy. In: Craver, C. D., Provder, T. (eds.) Polymer Characterization: Physical Property, Spectroscopic, and Chromatographic Methods. Advances in Chemistry Series, vol. 227, Chapter 10, p. 167. Washington DC (1990).
[142] Ibar, J. P., et al., A Comparison of TSC/RMA, DSC, DEA and DMA for the Characterization of the Amorphous Phase of Polymers. In: Harrison, I. R. (ed.) Proceedings of the 19th NATAS Conference, Boston, vol. 1, p. 113 (1990).
[143] Ibar, J. P., Dual-Phase Crystallization of Polymer Melts. De Gruyter Publisher, Berlin (2024).
[144] Ibar, J. P., Dual-Phase Polymer Melt Instability. Entanglements. De Gruyter Publisher, Berlin (2025).
[145] Jarrigeon, M., Chabert, B., Nemoz, G., Chatain, D., Lacabanne, C., Multiple Transitions in Polypropylene. Bull. Am. Phys. Soc. 24(3), 286 (1979).

EBSCOhost - printed on 2/13/2023 12:32 AM via . All use subject to https://www.ebsco.com/terms-of-use

[146] Jarrigeon, M., Chabert, B., Chatain, D., Lacabanne, C., Nemoz, G., J. Macromol. Sci. B, Phys. 17(1), 1 (1980).
[147] Kalachandra, University of North Carolina, Private Communication.
[148] Kovacs, A. J., Fortschr. Hochpolym. Sorsch 3, 394–507 (1963).
[149] Kovacs, A. J., In: O'Reilly, J. M., Goldstein, M. (eds.) Annals of the New York Academy of Sciences, vol. 731. New York Academy of Sciences, New York (1981).
[150] Kubon, U., Schilling, R., Wendorff, J. H., Studies on the Influence of Physical Aging Processes on Electret Properties of Amorphous PMMA. Colloid Polym. Sci. 266, 123 (1988).
[151] Lacabanne, C., PhD Thesis, University Paul Sabatier, Toulouse, France (1974).
[152] Lacabanne, C., Etude des Propriétés Mécaniques par Fluage Thermostimulé. Rev. Pratique Contr. Qualit. Industr. 129 (1985).
[153] Lacabanne, C., Bernes, A., APS St Louis Meeting (1989).
[154] Lacabanne, C., Chatain, D., In: Wada, Y., Perlman, M. M., Kokado, H. (eds.) Charge Storage, Charge Transport and Electrostatics with Their Applications. Studies in Electrical and Electronic Engineering, vol. 2, p. 312. Elsevier, Amsterdam (1979).
[155] Lacabanne, C., Chatain, D., Depolarization Thermocurrent of Polyethylene Containing Additives. Makromol. Chem. 179, 2769 (1978).
[156] Lacabanne, C., Chatain, D., Effect of Water on Depolarization Thermocurrents of Poly (L Proline). IUPAC Preprints, III (1975).
[157] Lacabanne, C., Chatain, D., DTC Study of γ Relaxation in Polyethylene Isophtalamide. IUPAC Preprints, IV 2–8, 774 (1974).
[158] Lacabanne, C., Chatain, D., Depolarization Thermocurrents Study of Polymers Above the Glass Transition. J. Phys. Chem. 79, 283 (1975).
[159] Lacabanne, C., Chatain, D., Depolarization Thermocurrents in Amorphous Polymers. J. Polym. Sci., Polym. Phys. Ed. 11, 2315 (1973).
[160] Lacabanne, C., Chatain, D., Phys. Status Solidi A 16, 225 (1973).
[161] Lacabanne, C., Chatain, D., Elsayed, T., Broussoux, D., Micheron, F., Transitions in Poly (Vinylidene Fluoride) by Thermally Stimulated Techniques. Studies of Transitions in PVF_2-Interpretation of TSC Data, Amorphous Regions Free from Constraints, Amorphous Chains under Constraints. Ferroelectrics 30, 307 (1980).
[162] Lacabanne, C., Chatain, D., Elsayed, T., Broussoux, D., Micheron, F., Study by Thermally Stimulated Techniques of Polymeric Materials for Electronic Applications. Organic Coatings and Plastics Chemistry, ACS Preprints, 43, 550 (1980).
[163] Lacabanne, C., Chatain, D., Guillet, J., Seytre, G., May, J. F., J. Polym. Sci., Polym. Phys. Ed. 13, 445 (1975).
[164] Lacabanne, C., Chatain, D., Madru, R., Maitrot, M., Contribution à l'Etude des Propriétés Electriques de la Fluorine. J. Chim. Phys. 4, 597 (1974).
[165] Lacabanne, C., Chatain, D., Monpagens, J. C., A New Temperature Characteristic of Polymers: the Compensation Temperature. Bull. Am. Phys. Soc. 23(3), 272 (1978).
[166] Lacabanne, C., Chatain, D., Monpagens, J. C., Berticat, P., Thermally Stimulated Current and Creep in Polyethylene Terephthalate. J. Appl. Phys. 50(4), 2723 (1979).
[167] Lacabanne, C., Chatain, D., Monpagens, J. C., Hiltner, A., Baer, E., Compensation Temperature in Amorphous Polyolefins. Solid State Commun. 27, 1055 (1978).
[168] Lacabanne, C., Ficat, J. J., Francis, M., Micheron, F., Durroux, R., Ficat, P., In: Anderson, J. M. (ed.) Biomaterials 84 – Transactions, Washington D. C., vol. 7, p. 52 (1984).
[169] Lacabanne, C., Gerard, J., Characteriza-tion of Insulating Composites by Thermally Stimulated Current Spectroscopy (In French) (1989).
[170] Lacabanne, C., Goyaud, P., Boyer, R. F., Thermally Stimulated Current (TSC) Study of the T_g and $T_{l,l}$ Transition in Anionic Polystyrenes. Organic Coatings and Plastics Chemistry, ACS Preprints, 41 (1979).

EBSCOhost - printed on 2/13/2023 12:32 AM via . All use subject to https://www.ebsco.com/terms-of-use

[171] Lacabanne, C., Lamure, A., Hitmi, N., Maurel, E., Pieraggi, M. T., Harmand, M. F., Dielectric and Mechanical Spectroscopy in Collagen and Proteoglycans. In: Anderson, J. M. (ed.) Biomaterials 84-Transactions, Washington D. C., vol. 7, p. 52 (1984).
[172] Lacabanne, C., Monpagens, J. C., Chatain, D., Gauthier, P., Thermally Stimulated Current and Creep in Amorphous Polyethylene Terephthalate. Bull. Am. Phys. Soc. 22(3), 283 (1977).
[173] Lamarre, L., Schreiber, H. P., Wertheimer, M. R., Chatain, D., Lacabanne, C., Study of Multiple Relaxations in Methacrylic Polymers by Thermally Stimulated Current and Creep. In: Proceedings 3rd Int. Symposium IEEE, Boston (1980).
[174] Lamarre, L., Schreiber, H. P., Wertheimer, M. R., Chatain, D., Lacabanne, C., Study of Multiple Relaxations in Methacrylic Polymers by Thermally Stimulated Current and Creep. J. Macromol. Sci., Phys. B18(2), 195 (1980).
[175] Lamure, A., Fauran-Clavel, M. J., Lacabanne, C., Role of Interfaces on a Natural Composite Bioelectret. In: ISE 6, Oxford.
[176] Lamure, A., Fauran-Clavel, M. J., Lacabanne, C., Harmand, M. F., Vignoles, M., Bonel, G., In: Das-Gupta, D. K., Pattulo, A. W. (eds.) Proc. of the Int. Symp. Electrets (ISE 6), p. 462 (1988).
[177] Lamure, A., Fauran-Clavel, M. J., Saadat, A., Lacabanne, C., Dielectric Spectroscopy for the Investigation of Inter and Intramolecular Mobility in Biopolymers. In: ICPADM '88.
[178] Lamure, A., Harmand, M. F., Lacabanne, C., Caractérisation des Mouvements Moléculaires dans le Collagè ne et les Protéoglycannes du Cartilage. In: Harmand, M. F., Ducassou, D. (eds.) Cartilage 85. Les Publications de Biomat. (1986).
[179] Lamure, A., Harmand, M. F., Vignoles, M., Bonel, G., Lacabanne, C., Etude Ex-Vivo des Interfaces Moléculaires dans les Tissus Calcifiés In: Harmand, M. F., Ducassou, D. (eds.) Tissus calcifiés et Biomatériaux. Les Publications de BIOMAT (1988).
[180] Lamure, A., Hitmi, N., Harmand, M. F., Maurel, E., Lacabanne, C., Etude des Mouvements Moléculaires dans le Collagène et les Protéoglycannes par Spectroscopie Diélectrique et Mécanique (France). Bull. Soc. Chim. 4, 532 (1985).
[181] Lamure, A., Hitmi, N., Lacabanne, C., Les entretiens du Carla, V, 99.
[182] Lamure, A., Hitmi, N., Lacabanne, C., Harmand, M. F., Herbage, D., Polarization Phenomena in Collagens from Various Tissues. In: Trans. of the 5th Eur. Conf. on Biomaterials, pp. 738–743 (1985).
[183] Lamure, A., Hitmi, N., Lacabanne, C., Harmand, M. F., Maurel, E., Pieraggi, M. T., Revue ITBM 4(3), 308 (1983).
[184] Lamure, A., Hitmi, N., Maurel, E., Lacabanne, C., Revue ITBM 6, 3 (1985).
[185] Lamure, A., Hitmi, N., Maurel, E., Lacabanne, C., Etude du Vieillissement du Collagène par Spectroscopie Diélectrique Trés Basse Fréquence. Revue ITBM 6(4), 381 (1985).
[186] Lamure, A. G., Lamure, E. M., Young, R. A., Lacabanne, C., Influence of Heat Pretreatment on Human Dental Enamel Dipolar Re-orientations. J. Dent. Res. 65, 734 (1986).
[187] Lamure, A., Martin, M., Harmand, M. F., Lacabanne, C., TSC Study of the Dynamic Behavior of a Bio Composite / Calcified Tissue. In: Harrison, I. R. (ed.) Proceedings of the 19th NATAS Conference, Vol. 1, Boston, p. 116 (1990).
[188] Lamure, A., Maurel, E., Harmand, M. F., Lacabanne, C., Correlation between the Type of Collagen and the Intramolecular Mobility. In: Transactions of the 5th Eur. Conf. on Biomaterials, p. 188 (1985).
[189] Lamure, A., Megret, C., Bauer, M., Lacabanne, C., In: Harmand, M. F., Ducassou, D. (eds.) Tissus Calcifiés et Biomat ériaux. Les Publications de Biomat. (1988).
[190] Lamure, A., Megret, C., Lacabanne, C., L'Analyse Enthalpique Différentielle dans les Laboratoires Pharmaceutiques. In: Les Entretiens du Carla, Actualités en Sc. pharmaceutiques et médicales, Centre de Recherche Pierre Fabre Ed, Castres (1986).
[191] Lamure, A., Plaino-Lamure, E., Lacabanne, C., Hitmi, N., Bonel, G., Young, R. A., Cooperative Dipolar Movements in Synthetic Apatites and Human Tooth Enamel. Adv. Biomaterials 6, 15 (1986).

EBSCOhost - printed on 2/13/2023 12:32 AM via . All use subject to https://www.ebsco.com/terms-of-use

[192] Lamure, A., et al., Study of Molecular Movements in Calcified Tissues by Thermostimulated Techniques. Innov. Tech., Biol. Med. 4, 3 (1983).
[193] Legrand, D. G., J. Appl. Polym. Sci. 13, 2129 (1969).
[194] Levi, D. L., Trans. Faraday Soc. 42A, 152 (1946).
[195] Leyris, J. P., Aicardi, J. P., Soule, S., Rev. Phys. Appl. 18, 147 (1983).
[196] Lilly, A. C., Rosemary, J. R., Henderson, M., Sharp, S., J. Appl. Phys. 41(5), 2001 (1970).
[197] Linkens, A., Vanderschueren, J., J. Appl. Polym. Sci. 22, 3081 (1978).
[198] Loadman, M. J. R., Tinker, A. J., The Application of Swollen-State CW-^{1}H NMR Spectroscopy to the Estimation of the Extent of Crosslinking in Vulcanized Polymer Blends. ACS, Rubber Div., Cincinnati (1988).
[199] Lushchik, C. B., Sov. Phys. JETP 3, 390 (1956).
[200] McCrum, N. G., Polymer 4, 1961 (1982).
[201] McCrum, N. G., On the Physical Significance of Bucci Relaxation Times Obtained from Thermal Sampling. Polymer 23, 1261 (1982).
[202] McCrum, N. G., Read, B. E., Williams, G., Anelastic and Dielectric Effects in Polymeric Solids. J. Wiley & Sons, London (1967).
[203] Min, T. I., Klein, A., El Asser, M. S., J. Polym. Sci., Polym. Chem. Ed. 21, 2045 (1983).
[204] Monpagens, J. C., PhD Thesis, University of Toulouse, France (1977).
[205] Monpagens, J. C., Chatain, D., Lacabanne, C., Gautier, P., A New Method for the Study of Anelastic Effects in Polymeric Solids. Bull. Am. Phys. Soc. 21(3), 415 (1976).
[206] Muller, P., Phys. Status Solidi A 23, 165 (1974).
[207] Neag, C. M., Coatings Characterization By Thermally Stimulated Current (TSC) and Relaxation Map Analysis (RMA). In: Proceedings of the 19th NATAS Conference, vol. 1, p. 104 (1990).
[208] Neki, K., Geil, P. H., J. Macromol. Sci., Phys. B8(1–2), 295 (1973).
[209] Nishinari, K., Chatain, D., Lacabanne, C., Molecular Motions in Solid Pullulan by TSC. Bull. Am. Phys. Soc. 25(3), 280 (1980).
[210] Nishinari, K., Chatain, D., Lacabanne, C., Thermally Stimulated Current of Solid Pullulan. J. Macromol. Sci., Phys. B22(5), 795 (1983).
[211] Nishinari, K., Chatain, D., Lacabanne, C., Thermally Stimulated Current and Creep of Solid Amylose. J. Macromol. Sci., Phys. 22(4), 529 (1983).
[212] Noiret, L., et al., New light on old wisdoms on molten polymers: conformation, slippage and shear-banding in sheared entangled and unentangled melts. Macromol. Rapid Commun. 30, 1709–1714 (2009).
[213] Osawa, S., Imai, N., Kagawa, I., Theory of Strong Poly-electrolyte Solutions. I. Coiled Micro-Ions. J. Polym. Sci. XIII, 93 (1954).
[214] Prigogine, I., Physique, Temps et Devenir. Masson (1980).
[215] Ronarc'h, D., Contribution to the Study of Molecular Motions in the Study of Polyolefins in the Amorphous Regions by TSC. Thesis (in French) (1983).
[216] Saffell, J. R., PhD Thesis, University of Cambridge (1979).
[217] Saffell, J. R., Proceedings of the 17th NATAS Conference, vol. 1, p. 391 (1988).
[218] Sauer, B., Moura Ramos, J. J., Comments on Compensation analysis applied to Thermally Stimulated Current Thermal Sampling. Polymer 38(16), 4065–4069 (1997).
[219] Servet, B., Broussoux, D., Micheron, F., Lacabanne, C., Crystalline Transitions in Poly(Vinylidene Fluoride) from Unoriented γ to Oriented β. Bull. Am. Phys. Soc. 26(3), 433 (1981).
[220] Snuparek, J., Krska, F., J. Appl. Polym. Sci. 20, 1753 (1976).
[221] Soulier, J. P., Chabert, B., Chauchard, J., Chatain, D., Lacabanne, C., Etude par TCD et ATD d'une Transition de Second Ordre dans le Polyethylène 1-3 Benzène Sulfonamide. J. Chim. Phys. 71, 32 (1974).
[222] Squire, W., J. Comput. Phys. 6, 152 (1970).

EBSCOhost - printed on 2/13/2023 12:32 AM via . All use subject to https://www.ebsco.com/terms-of-use

[223] Struik, L. C. E., Physical Aging in Plastics and Other Glassy Materials. Polym. Eng. Sci. 17, 165 (1977).
[224] Tinker, A. J., Crosslink Distribution and Interfacial Adhesion in Vulcanized Blends of NR and NBR. ACS, Rubber Div. 117 (1989).
[225] Tinker, A. J., The Malaysian Rubber Producers' Research Association, Tun Abdul Razak Laboratory, Brickendonbury, Hertford, England, Private Communication.
[226] Uhlmann, D. R., MIT Graduate Research Program (1974).
[227] van Turnhout, J., J. Phys. D, Appl. Phys. 8, L68 (1975).
[228] van Turnhout, J., Thermally Stimulated Discharge of Polymer Electrets. Polym. J. 2(2), 173 (1971).
[229] van Turnhout, J., Klaase, P. T. A., Ong, P. H., Struik, L. C. E., Physical Aging and Electrical Properties of Polymers. J. Electrost. 3, 171 (1977).
[230] van Turnhout, J., van Rheenen, A. H., Thermally stimulated charging and discharging currents in SiO_2. In: Annual Report of the NASA-NRC Conference on "Electrical Insulation and Dielectric Phenomena". National Bureau of Standards, Gaithersburg (1985).
[231] Vanderschueren, J., PhD Thesis, University of Liege, Belgium (1974).
[232] Vanderschueren, J., Analysis of Relaxations in Polymers by Asymmetrical Distribution Functions of Relaxation Times. Appl. Phys. Lett. 25, 5 (1974).
[233] Vanderschueren, J., J. Polym. Sci., Polym. Phys. Ed. 12, 991 (1974).
[234] Vanderschueren, J., Proceedings of NATAS Conference, Boston meeting (1990).
[235] Vanderschueren, J., 1 – Theoretical Expressions of Thermally Stimulated Conductivity. In: Theories of Thermally Stimulated Conductivity and Their Applications to the Study of Non-isothermal Relaxation in Dielectrics. A. I.M, Liège, 2 (1974). (In French).
[236] Vanderschueren, J., 2 – Theoretical Expressions of Non-isothermal Relaxation. In: Theories of Thermally Stimulated Conductivity and Their Applications to the Study of Non-isothermal Relaxation in Dielectrics. A. I.M, Liège, 4 (1974). (In French).
[237] Vanderschueren, J., 3 – Determination of Representative Param-eters of Trapping and Relaxation. In: Theories of Thermally Stimulated Conductivity and Their Applications to the Study of Non-isothermal Relaxation in Dielectrics. A. I.M, Liège, 4 (1975). (In French).
[238] Van Turnhout, J., Thermally Stimulated Discharge of Polymer Electrets. Elsevier, Amsterdam (1975).
[239] Vanderschueren, J., J. Polym. Sci., Polym. Phys. Ed. 15, 873 (1977).
[240] Vanderschueren, J., Aras, L., Boonen, C., Niezette, J., Corapci, M., J. Polym. Sci., Polym. Phys. Ed. 22, 2261 (1984).
[241] Vanderschueren, J., Corapci, M., Niezette, J., Yianakopoulos, G., Conductivity and Thermally Stimulated Processes in Model Ionic Polymers I. Halato Telechelic Polybutadienes. IEEE Trans. Electr. Insul. E1-22(2) (1987).
[242] Vanderschueren, J., Gasiot, J., In: Braunlich (ed.) Thermally Stimulated Relaxation in Solids. Springer-Verlag, Berlin (1979).
[243] Vanderschueren, J., Janssens, A., Ladang, M., Niezette, J., Effect of Tacticity on the Transition Behaviour of Poly(methyl methacrylate)/Poly(vinyl chloride) blends. A Thermally Stimulated Current Study. Polymer 23, 395 (1982).
[244] Vanderschueren, J., Ladang, M., Niezette, J., In: Proc. 5th Int. Symp. Electrets, Heidelberg, p. 477. Avail from IEEE, N.Y. (1985).
[245] Vanderschueren, J., Linkers, A., Am. Chem. Soc. 11(6), 1228 (1978).
[246] Vanderschueren, J., Linkens, A., J. Polym. Sci., Polym. Phys. Ed. 16, 223 (1978).
[247] Vanderschueren, J., Linkens, A., Gasiot, J., Fillard, J. P., Parot, P., J. Appl. Phys. 51(9), 4967 (1980).
[248] Vanderschueren, R., Vanderschueren, J., Hiernaut, J. P., Roch, A., Homerin, P., J. Chem. Solids 46(1), 39 (1985).

EBSCOhost - printed on 2/13/2023 12:32 AM via . All use subject to https://www.ebsco.com/terms-of-use

[249] Vanderschueren, J., Yianakopoulos, G., Niezette, J., Chatry, C., Gasiot, J., Relaxational Behavior of CR-39 Polycarbonate Used as Nuclear Track Detector. J. Appl. Polym. Sci. 44, 1027 (1992).
[250] Vanderschueren, J., et al., Sub-T_g Relaxation in Cold-drawn Polymers-Thermally Stimulated Current Methods. IEEE Trans. Electr. Insul. 24, 3 (1989).
[251] Vanderschueren, J., et al., Influence of Physical Aging Processes on Electrical Properties of Amorphous Polymers. IEEE Trans. Electr. Insul. 25, 4 (1990).
[252] Vanderschueren, J., et al., Simulation of Field-induced Thermally Stimulated Currents in Dielectrics. Application to the Dipolar Case in Polymeric Systems. J. Appl. Phys. (1980).
[253] Vanderschueren, J., et al., Nature of Transient Currents in Polymers. J. Appl. Phys. 49(7) (1978).
[254] Vanderschueren, J., et al., Simulation of Thermally Stimulated Currents in Dielectrics: Effect of Thermal Expansion. J. Appl. Phys. 58(12) (1985).
[255] Vanderschueren, J., et al., Evidence for Clustering in N-Butyl Methacrylate Ionomers as Shown by Thermally Stimulated Currents. J. Polym. Sci., Polym. Phys. Ed. 22 (1984).
[256] Vanderschueren, J., et al., Study of Molecular Relaxations in Aliphatic Polycarbonates by the Method of Thermally Stimulated Currents. J. Macromol. Sci., Phys. B15(3) (1978).
[257] Vanderschueren, J., et al., Water-Dependent Relaxation in Polymers. Study by the Thermally Stimulated Current Method. Macromolecules 11 (1978).
[258] Vanderschueren, J., et al., Thermally Stimulated Depolariza-tion of Phase-Separated Polymer Systems. Macromolecules 13, 973 (1980).
[259] Wang, Z., et al., Fingerprinting Molecular relaxation in Deformed Polymers. Phys. Rev. X (2017). DOI: 10.1103/PhysRevX.7.031003.
[260] Watanabe, H., et al., Rheo-SANS behavior of Entangled Polymer Chains with Local Label under Fast Shear Flow. Activity Report on Neutron Scattering Research: Experimental Reports 14 (2007). Report Number: 146.
[261] Yeh, G. S. Y., Critical Reviews in Macromolecular Science. Baer, Geil, Koenig (eds.) p. 173 (1972).
[262] Yeh, G. S. Y., Geil, H., J. Macromol. Sci., Phys. B1(2), 235 (1967).
[263] Yianakopoulos, G., Vanderschueren, J., Niezette, J., Sub-T_g Relaxation in Cold-drawn Polymers. Thermally-stimulated-current Methods. IEEE Trans. Electr. Insul. 24, 3 (1989).
[264] Yianakopoulos, G., Vanderschueren, J., Niezette, J., Thielen, A., Influence of Physical Aging Processes on Electrical Properties of Amorphous Polymers. IEEE Trans. Electr. Insul. 25(4), 693 (1990).
[265] Zweifel, H., Recent Progress in the Stabilization of Impact Modified PP PolyPro, RETEC (1989).

EBSCOhost - printed on 2/13/2023 12:32 AM via . All use subject to https://www.ebsco.com/terms-of-use

EBSCOhost - printed on 2/13/2023 12:32 AM via . All use subject to https://www.ebsco.com/terms-of-use

Further reading

This is the list of publications sorted by author names who have made important contributions to the subject of dielectrics, motions and relaxations in non-conductive materials.

[1] Adachi, H., Shibata, Y., J. Phys. D, Appl. Phys. 8, 1120 (1975).
[2] Adachi, H., Shibata, Y., Jpn. J. Appl. Phys. 13(9), 1479 (1974).
[3] Agarwal, S. C., Fritzshe, H., Phys. Rev. B 10(10), 4351 (1974).
[4] Akahane, R., Nitta, T., Higuchi, H., Jpn. J. Appl. Phys. 18(9), 1861 (1979).
[5] Akuetey: Thermal Depolarization Measurements on PVK Films. J. Phys. D 22, 174 (1989).
[6] Alexandrowich, P., Karasz, F. E., Macknight, W. J., J. Appl. Phys. 47(10), 4251 (1976).
[7] Algie, J. E., Relaxation Phenomena in Biological Polymers (1980).
[8] Andre, D., Dworkin, A., Figuiere, P., Fuchs, A. H., Szwarc, H., J. Phys. Chem. 46(4), 505 (1985).
[9] Aoki, Y., Brittain, J. O., J. Polym. Sci., Polym. Phys. Ed. 14, 1297 (1976).
[10] Aoki, Y., Brittain, J. O., J. Polym. Sci., Polym. Phys. Ed. 15, 199 (1977).
[11] Apekis, L., Pissis, P., Boudouris, G., Am. Chem. Soc. 4019 (1983).
[12] Asano, Y., Suzuki, T., Jpn. J. Appl. Phys. 11(6), 1139 (1972).
[13] Audren, P., Thesis, Rennes, France (1983).
[14] Baba, A., Ikezaki, K., J. Appl. Phys. 57(2), 359 (1985).
[15] Baccaredda, M., Butta, E., J. Polym. Sci. 44, 421 (1960).
[16] Bakirov, M. Y., Madatov, R. S., Mustafaev, Y. M., Translated from Izv. Akad. Nauk SSSR, Neorg. Mater. 14(10), 1490 (1978).
[17] Banhegyi: AC and DC Dielectric Properties of Some PP/Calcium Carbonate Composites. Polym. Eng. Sci. 30, 374 (1990).
[18] Bayoux, J., Thesis, Grenoble, France (1980).
[19] Berger, L. L., Sauer, B. B., Enhanced Polymer Mobility within Craze Fibrile. Macromolecules 24, 2096 (1991).
[20] Bhatnagar, C. S., Khare, M. L., Mernakshi, G., In: Proc. 5th Int. Symp. Electrets, Heidelberg, p. 952. Avail. from IEEE, N.Y. (1982).
[21] Biros, J., Larina, T., Trekoval, J., Pouchly, J., Colloid Polym. Sci. 260, 27 (1982).
[22] Blaisten-Barojas, E., Mascarenhas, S., J. Chem. Phys. 76(11), 5643 (1982).
[23] Blake, A. E., Charlesby, A., Randle, K. J., J. Polym. Sci., Polym. Phys. Ed. 7, 759 (1974).
[24] Bohm, M., Erb, O., Scharmann, A., Phys. Status Solidi A 41, 535 (1977).
[25] Bohun, A., Pokorny, P., Czechoslov. J. Phys. B29, 473 (1979).
[26] Boon, M. R., Nature 243, 401 (1973).
[27] Brabant, J. C., Pugnet, M., Barbolla, J., Brousseau, M., J. Appl. Phys. 47(11), 4809 (1976).
[28] Brailovskii, E. Y., Marchuk, N. D., Phys. Status Solidi A 58, 41 (1980).
[29] Braunlich, P., Kelly, P., Phys. Rev. B 1(1), 1596 (1970).
[30] Brun, A., Dansas, P., Sixou, P., Solid State Commun. 8, 613 (1970).
[31] Brunskill, I. H., Phys. Status Solidi B 100, K125 (1980).
[32] Bryan, T. F. J., Kydd, R. F., Solid State Commun. 15, 1929 (1974).
[33] Bucci, C., Phys. Rev. 152(2), 833 (1966).
[34] Bucci, C., Phys. Rev. 164(3), 1200 (1967).
[35] Bucci, C., Riva, S. C., J. Phys. Chem. Solids 26, 363 (1965).
[36] Bui, A., Popescu-Stoka, C., Hoang, T. G., Destruel, P., Appl. Phys. Lett. 34(12), 821 (1979).
[37] Bunn, C. W., Proc. R. Soc. A 180, 67, London (1942).
[38] Bunton, L. G., Daly, J. H., Maxwell, I. D., Pethrick, R. A., J. Appl. Polym. Sci. 27, 4283 (1982).
[39] Callens, A., Eersels, L., De Batist, R., J. Mat. Sci. 1375 (1977).
[40] Campos, M., Mergulhao, S., J. Appl. Phys. 51(3), 1619 (1980).

https://doi.org/10.1515/9783110756746-012

EBSCOhost - printed on 2/13/2023 12:32 AM via . All use subject to https://www.ebsco.com/terms-of-use

[41] Cantaloube, B., Dreyfus, G., Lewiner, L., J. Polym. Sci., Polym. Phys. Ed. 17, 95 (1979).
[42] Capelleti, R., De Benedetti, E., Phys. Rev. 165(3), 981 (1968).
[43] Catcjomgs, R. M., J. Appl. Phys. 50(4), 2812 (1979).
[44] Cava, R. J., Fleming, R. M., Rietman, E. A., Dunn, R. G., Schneemeyer, L. F., Phys. Rev. Lett. 53(17), 1677 (1984).
[45] Cavailie, D. Y., Jourdan, C., Zkong, X., Perez, J., Pichot, C., Guillot, J., Polymer 27, 693 (1986).
[46] Chafai, A., Thesis, Toulouse, France (1982).
[47] Chang, T. D., Carr, S. H., Brittain, J. O., Polym. Eng. Sci. 22(18), 1205 (1982).
[48] Changhua, T., Mingzhen, H., Yanguuan, W., J. Appl. Phys. 54(8), 4398 (1983).
[49] Chanussot G., T., Dijon, France (1979).
[50] Chanussot, G., Ann. Phys. 8, 81 (1973–1974).
[51] Chatain, D., PhD Thesis, University Paul Sabatier, Toulouse, France (1974).
[52] Chen, I., J. Appl. Phys. 47(7), 2988 (1976).
[53] Chen, R., J. Mat. Sci. 11, 1521 (1976).
[54] Chowbury, B. B., Am. Lab. 17(1), 49 (1985).
[55] Conner, W. C., J. Catal. 84, 273 (1983).
[56] Corazzari, T., Garofano, T., Il Nuovo Cimento B 33, 719 (1976).
[57] Crine, J. P., Thesis, Montréal (1979).
[58] Crine, J. P., A New Analysis of the Results of Thermally Stimulated Measurements in Polymer. J. Appl. Phys. 66(3) (1989).
[59] Crine, J. P., Analysis of Thermally Stimulated Measurements in Polymers. In: Harrison, I. R. (ed.) Proceedings of the 19th NATAS Conference, Vol. 1, Boston, p. 98 (1990).
[60] Crissman, J. M., Passaglia, E., J. Polym. Sci. C 14, 237 (1966).
[61] Crowley, J. L., Jonath, A. D., Dielectric Relaxation Gradients in an Adhesive Bond. In: Lee, L. H. (ed.) Adhesion and Absorption of Polymers, Part A, p. 165. Plenum Press (1980).
[62] Cruz E., M. A., Palacios A., J., Garcia Rejon, A., Ruiz F., L. M., Rios, G. L., Makromol. Chem. Suppl. 10–11, 87 (1985).
[63] Cusso, F., Jaque, J., J. Phys. C, Solid State Phys. 15, 2875 (1982).
[64] Daniel, J. C., Makromol. Chem. Suppl. 10–11, 359 (1985).
[65] Dansas, P., J. Phys. Chem. Solids 32, 2699 (1971).
[66] Dansas, P., Sixou, P., C.R. Acad. Sci., Paris, B 266, 469 (1968).
[67] Dansas, P., Sixou, P., C.R. Acad. Sci., Paris, B 266, 568 (1968).
[68] Datt, S. D., Singh, R., In: 5th Int. Symp. Electrets, Heidelberg, p. 196. Avail. from IEEE, N.Y. (1985).
[69] Davies, E., Jones Brian, J., Tidy, D., Williams, G., J. Phys. E, Sci. Instrum. 9, 693 (1976).
[70] De Blasi, C., Galassini, S., Manfredotti, C., Micocci, G., Ruggiero, L., Tepore, A., Phys. Status Solidi A 55, 291 (1979).
[71] De Blasi, C., Galossini, S., Manfredotti, C., Micocci, C., Tepore, A., Solid State Commun. 30, 453 (1979).
[72] de Gennes, P. G., Scaling Concept in Polymer Physics, Cornell University, Ithaca and London (1979).
[73] De Murcia, M., Braunlich, P., Egee, M., Mary, G., Solid State Commun. 34, 737 (1980).
[74] De Polignac, A., Jourdain, M., Despujols, J., Interpretation of Experiments on Thermally Stimulated Currents in Silicon Oxide thin films and their Relation to A. C. Conductivity. Thin Solid Films. 71, 201 (1980).
[75] De Polignac, A., Jourdain, M., Despujols, J., Thin Solid Films 71, 201 (1980).
[76] Del Val, J. J., Compensation Laws and β-Relaxation in PVC. Polym. Bull. 17, 489 (1987).
[77] Del Val, J. J., Compensation Laws and Phase Segregation in Polymer Blends. Solid State Commun. 69, 707 (1989).

EBSCOhost - printed on 2/13/2023 12:32 AM via . All use subject to https://www.ebsco.com/terms-of-use

[78] Del Val, J. J., Tacticity and Dielectric Relaxation around the T_g of PVC. A TSDC Study. Makromol. Chem. 190, 893 (1989).
[79] Del Val, J. J., Alegria, A., Colmenero, J., Barandiaran, J. M., Polymer 27, 1771 (1986).
[80] Demont, P., Thesis, University Paul Sabatier, Toulouse, France (1983).
[81] Den Hartog, H. W., Nakata, R., J. Phys. Soc. Jpn. 52(9), 3110 (1983).
[82] Denning, P., Thomas, T., Ibar, J. P., Application of Compensation Phenomena to the Thermal Analysis Characterization of Polymers: Introducing the "Degree of Disorder" (DOD) Number. J. Polym. Sci. B 14, 157 (1991).
[83] Despax, B., Ai, B., Abdulla, M., Nuraux, C., Appl. Lett. 39, 220 (1981).
[84] Destruel, P., Bui, A., Hoang, T. G., J. Polym. Sci., Polym. Phys. Ed. 4(21), 851 (1983).
[85] Diaconnu, I., Dumitrescu, S. V., Polym. Bull. 9, 17 (1983).
[86] Dijon, J., Solid State Commun. 48(1), 79 (1983).
[87] Doi, A., Day, D. E., J. Math. 15, 3047 (1980).
[88] Dworkin, A., Fuchs, A. H., Ghelfenstein, M., Swarc, H., J. Phys. Lett. 43, L21 (1982).
[89] Eby, R. K., J. Chem. Phys. 37, 2785 (1962).
[90] Eda, K., Matsuoka, M., Jpn. J. Appl. Phys. 16, 1 (1977).
[91] Ehrburger, F., Donnet, J. B., Thermally Stimulated Depolarization (TSD) Currents in Absorbed Phases on Silica. J. Appl. Phys. 50(3), 1478 (1979).
[92] El Azab, M. I., Champness, C. H., J. Appl. Phys. 48(6), 295 (1977).
[93] Elhout, J., Thesis, Study of Molecular Motions in Polyacetylene by TSC (In French) (1986).
[94] Elsayed, T., PhD Thesis (in French), University Paul Sabatier, Toulouse, France (1982). Study of Molecular Motions and Transitions Responsible for Piezoelectricity in PVDF, University Paul Sabatier, Toulouse, France (1982).
[95] Exner, O., Collect. Czechoslov. Chem. Commun. 29, 1094 (1964).
[96] Fabre, E., Bhargava, R. N., Appl. Phys. Lett. 24(7), 322 (1974).
[97] Faria, R. M., Guimaraes Neto, J. M., Figueiredo, M. T., Depolarization Current in a Ferroelectric Phase of VDF/TrFE Copolymer. In: Harrison, I. R. (ed.) Proceedings of the 19th NATAS Conference, Boston, vol. 1, p. 125 (1990).
[98] Feigenbaum, M. J., J. Stat. Phys. 19, 25 (1978).
[99] Fields, D. E., Moran, R., Phys. Rev. B 9(4), 1836 (1971).
[100] Fifth International Symposium on Electrets, ISE 5, Heidelberg, Federal Republic of Germany (1985).
[101] Filina, L. I., Ilyashenko, A. G., Vorobev, Yu.V., Karkhanin, Yu. I., Sheinkman, M. K., Phys. Status Solidi A 39, 717 (1977).
[102] Fillard, J. P., Gasiot, J., Manifacier, J. C., Phys. Rev. B 18(8), 4497 (1978).
[103] Fischer, F., Prakash, J., Schober, W., Phys. Status Solidi A 89, K215 (1985).
[104] Fischer, P., Rohl, P., J. Polym. Sci., Polym. Phys. Ed. 14, 531 (1976).
[105] Fleming, R. J., Thermally-Stimulated Conductivity and Luminescence in Organic Polymers. IEEE Trans. Electr. Insul. 24, 3 (1989).
[106] Foldes, E., Pazonyi, T., Hedvig, P., J. Macromol. Sci., Phys. b15(4), 527 (1978).
[107] Fugarassu, E., Martin, G. M., Fabre, E., Appl. Phys. 10, 93 (1976).
[108] Frensch, H., Wendorff, J. H., In: Proc. 5th Int. Symp. Electrets, Heidelberg, p. 132. Avail. from IEEE, N.Y. (1985).
[109] Fuhs, W., Milleville, M., Phys. Status Solidi B 98, K29 (1980).
[110] Fuyuki, N., In: Wada, Y., Perlman, M. M., Kokado, H. (eds.) Charge storage, Charge Transport and Electrostatics with Their Applications. Studies in Electrical and Electronic Engineering, vol. 2, p. 307. Elsevier, Amsterdam (1979).
[111] Fuyuki, S., Hyakutake, N., Hayakawa, S., Jpn. J. Appl. Phys. 17(5), 851 (1978).
[112] Galwey, A. K., J. Catal. 84, 270 (1983).
[113] Gamoudi, Thesis, Dijon I, France (1986).

EBSCOhost - printed on 2/13/2023 12:32 AM via . All use subject to https://www.ebsco.com/terms-of-use

[114] Garofano, T., Corazzari, T., Casalini, G., Il Nuovo Cimento B 38(1), 133 (1977).
[115] Genieyz, M. H., Thesis, University Paul Sabatier, Toulouse, France (1985).
[116] Gerasyuk, A. K., Pisarenko, V. F., Popov, V. V., Phys. Status Solidi B 112, K11 (1982).
[117] Ghosh, A., Jain, K. M., Mallik, B., Misra, T. N., Jpn. J. Appl. Phys. 20, 1059 (1981).
[118] Gil-Zambrano, J. L., Juhasz, C., In: Proc. 5th Int. Symp. Electrets, Heidelberg, p. 235. Avail from IEEE, N.Y. (1985).
[119] Glasstone, S., Laidler, K. J., Eyring, H., The Theory of Rate Processes. McGraw-Hill Book Company, New York (1941).
[120] Gorbachev, V. M., J. Therm. Anal. 21, 129 (1981).
[121] Gourari, A., M. S. Thesis, University of Algeria (1982).
[122] Goyaud, P., M. S. Thesis, University Paul Sabatier, Toulouse, France (1979).
[123] Gross, B., J. Phys. D, Appl. Phys. 8, L127–L128 (1975).
[124] Gubanski, S. M., Gubanski, A., Macalik, B., In: Proc. of the 6th International Symposium on Electrets, (ISE 61: Oxford U. K.), p. 425 (1988).
[125] Guillet, J., Thesis, Lyon, France (1975).
[126] Guillet, J., Makromol. Chem. Suppl. 10–11, 235 (1985).
[127] Guillet, J., Rios-Guerrero, L., Makromol. Chem. 183(8), 1979 (1982).
[128] Guyot, A., G. F. P., 9, Annexe 3 (1980).
[129] Guyot, A., Guillot, J., Pichot, C., Image Chim. 55 (1984).
[130] Hashimoto, S., Sakai, T., Miyata, S., J. Polym. Sci., Polym. Phys. Ed. 16, 1965 (1978).
[131] Hashimoto, T., Shiraki, M., Sakai, T., J. Polym. Sci., Polym. Phys. Ed. 13, 2401 (1975).
[132] Hayashi, S., Tanaka, T., Hirabayashi, S., Shibayama, S., In: Wada, Y., Perlman, M. M., Kokado, H. (eds.) Charge storage, Charge Transport and Electrostatics with Their Applications. Studies in Electrical and Electronic Engineering, vol. 2, p. 277. Elsevier, Amsterdam (1979).
[133] Heitz, R. J., Szwarc, H., Rev. Phys. Appl. 15, 687 (1980).
[134] Hernandez, J. A., Murrieta, H. S., Jaque, F., Rubio, J. O., Solid State Commun. 39, 1061 (1981).
[135] Hickmott, T. W., Phys. Rev. Lett. 32(2), 65 (1974).
[136] Higasi, K., Dielectric Relaxation and Molecular Structure. Monogr. Ser. Res. Inst. Appl, Elec. Hokkaido Univ., Sapporo, Japan (1961).
[137] Hillihouse, R. W. A., Woods, J., Phys. Status Solidi A 67, 119 (1981).
[138] Hino, T., IEEE Trans. Electr. Insul. EI–15(3), 301 (1980).
[139] Hino, T., Jpn. J. Appl. Phys. 11, 1573 (1972).
[140] Hino, T., Jpn. J. Appl. Phys. 46(5), 1956 (1975).
[141] Hino, T., Suzuki, K., Yamashita, K., Jpn. J. Appl. Phys. 12(5), 651 (1973).
[142] Hitmi, N., Thesis in French (1983). Study of Transitions in the Organic and Mineral Component if Calcified Tissues by Dielectric Spectroscopy. by Low Frequency.
[143] Hoffman, J. D., J. Weeks: J. Polym. Sci. 28, 472 (1958).
[144] Hong, J., Brittain, J. O., J. Appl. Polym. Sci. 26, 2459 (1981).
[145] Hong, C. M., Day, D. E., J. Am. Soc. 64(2), 61 (1981).
[146] Hong, C. M., Day, D. E., Thermally Stimulated Polarization Current Technique for Measuring the Electrical Conductivity of Vitreous Solids. J. Appl. Phys. 50(8) (1979).
[147] Hong, C. M., Day, D. E., J. Math. 14, 2493 (1979).
[148] Hoshino, Y., Miyata, H., J. Appl. Phys. 52(10), 6214 (1981).
[149] Hoshino, Y., Tokonaga, Y., J. Appl. Phys. 48(4), 1456 (1977).
[150] Ieda, M., Mizutani, T., Suzuoki, Y., Shimozoto, M., In: Wada, Y., Perlman, M. M., Kokado, H. (eds.) Charge storage, Charge Transport and Electrostatics with Their Applications. Studies in Electrical and Electronic Engineering, vol. 2, p. 322. Elsevier, Amsterdam (1979).
[151] Ikeda, S., Matsuda, K., Jpn. J. Appl. Phys. 50(10), 6475 (1979).
[152] Ikeda, S., Matsuda, K., Jpn. J. Appl. Phys. 19(5), 855 (1980).
[153] Ikeda, S., Matsuda, K., Jpn. J. Appl. Phys. 21(2), 359 (1982).

EBSCOhost - printed on 2/13/2023 12:32 AM via . All use subject to https://www.ebsco.com/terms-of-use

[154] Ikekazi, K., Miki, M., Tamura, J. U., Jpn. J. Appl. Phys. 20(9), 1741 (1981).
[155] International Workshop on "Thermally Stimulated Processes", Montpellier, France (1976).
[156] Isoda, S., Asai, K., Jpn. J. Appl. Phys. 13, 1333 (1974).
[157] Jaffrain, M., Dansas, P., Sixou, P., Extr. J. Chim. Phys. 66(5), 841 (1969).
[158] Jelcic, Z., PE Recycling during Processing. Angew. Makromol. Chem. 176, 65 (1990).
[159] Jeszka, J. K., Ulanski, J., Glowachi, I., Kryszewski, M., Electrostatics 16, 89 (1984).
[160] Jeszka, J., Zielinski, M., Kryszewski, M., Model TSC Calculations for Amorphous Materials. In: Charge Storage, Charge Transport and Electrostatics with Their Applications, p. 287 (1979).
[161] Johnston, G. R., Lyons, L. E., Phys. Status Solidi 37K, 43 (1970).
[162] Jones, A., TSD of Alternate-Layer Langmuir-Blodgett Film Structures. J. Phys. D 21, 95 (1988).
[163] Jonscher, A. K., A New Approach to Thermally Stimulation Depolarization. J. Phys. D, Appl. Phys. 24 (1991).
[164] Jostopoulos, D., Varotsos, P., Mourikis, S., J. Phys. C, Solid State Phys. 13, 3303 (1980).
[165] Kamiya, T., Okuyama, T., Shinohara, I., Takamatsu, T., Fukada, E., Surface Charge Decay and Thermally Stimulated Current in Polymers with Different Molecular Structures. In: Wada, Y., Perlman, M. M., Kokado, H. (eds.) Charge Storage, Charge Transport and Electrostatics with their Applications. Studies in Electrical and Electronic Engineering, vol. 2, p. 342. Elsevier, Amsterdam (1979).
[166] Kao, K. J., Bamji, S. S., Perlman, M. M., J. Appl. Phys. 50(12), 8181 (1979).
[167] Kast, M., et al., Makromol. Chem. Suppl. 10–11, 437 (1985).
[168] Katsube, T., Adachi, Y., Ikoma, T., Solid-State Electron. 19, 11 (1976).
[169] Kawamura, S., Royce, B. S. H., Phys. Status Solidi A 50, 669 (1978).
[170] Keller, J. M., Datt, S. C., In: Proc. 5th Int. Symp. Electrets, Heidelberg, p. 208. Avail from IEEE, N.Y. (1985).
[171] Kemey, G., Mahanii, S. D., Proc. Natl. Acad. Sci. USA 72, 999 (1975).
[172] Kessler, A., Ebert, K., Z. Phys. B34, 1 (1979).
[173] Khanaja, W. A., Walker, S., Adv. Mol. Relax. Inter. Processes 19, 1 (1981).
[174] Kivits, P., J. Phys. C, Solid State Phys. 9, 605 (1976).
[175] Kobayashi, S., Yahagi, K., In: Wada, Y., Perlman, M. M., Kokado, H. (eds.) Charge Storage, Charge Transport and Electrostatics with Their Applications. Studies in Electrical and Electronic Engineering, vol. 2, p. 317. Elsevier, Amsterdam (1979).
[176] Kobayashi, S., Yahagi, K., Jpn. J. Appl. Phys. 16(11), 2053 (1977).
[177] Kobayashi, S., Yahagi, K., Thermally Stimulated Current in Elongated Low Density Polyethylene Film. Interpretation of TSC curves of LDPE. Jpn. J. Appl. Phys. 18(2), 261 (1979).
[178] Köhler, W., Robello, D. R., Dao, B. T., Willand, C. S., Williams, D. J., Second Harmonic Generation and Thermally Stimulated Current Measurements: A Study of Some Novel Polymers for Non-Linear Optics. Chem. Phys. 93(12), 9157 (1990).
[179] Kojima, K., Maeda, A., Takai, Y., Ieda, M., Jpn. J. Appl. Phys. 17(10), 1735 (1978).
[180] Korsunskaya, N. E., Markevich, I. V., Torchinskaya, T. V., Sheinkman, M. K., Phys. Status Solidi A 50, 767 (1978).
[181] Kostopoulos, D., Mourikis, S., Varotsos, P., J. Phys. 42, 1481 (1981).
[182] Kostopoulos, D., Varotsos, Mourikis, S., Measurement of Ionic Thermocurrents in Sodium Iodine. J. Phys. C, Solid State 13, 3003 (1980).
[183] Kotina, I. M., Novikov, S. R., Pirozhkova, T. I., Phys. Status Solidi A 42, 397 (1977).
[184] Kotina, I. M., Novikov, S. R., Pirozhkova, T. I., Phys. Status Solidi A 46, K21 (1978).
[185] Kumins, C. A., Knauss, C. J., Ruch, R. J., McIntyre, F., Structure of Sorbed Polymer Interphases by Thermal Stimulated Spectroscopy. In: International Symposium on Interphase (1993). to be presented.
[186] Kovarskii, A. L., Saprygin, V. N., Polymer 23, 974 (1982).
[187] Kristianpoller, N., Kirsh, Y., J. Phys. C, Solid State Phys. 12, 1073 (1979).

EBSCOhost - printed on 2/13/2023 12:32 AM via . All use subject to https://www.ebsco.com/terms-of-use

[188] Kristianpoller, N., Kirsh, Y., Phys. Status Solidi A 21, 87 (1974).
[189] Krokoszinski, H. J., Barner, K., Freund, F., J. Chem. Phys. 72(4), 2616 (1980).
[190] Krum Von, F., Muller, F. H., Kolloid Z164, 81 (1959).
[191] Kryszewski, M., Zielinski, M., Sapieha, S., Polymer 17, 212 (1976).
[192] Kunze, I., Muller, P., Phys. Status Solidi A 13, 197 (1972).
[193] Kunze, I., Muller, P., Phys. Status Solidi 33, 91 (1969).
[194] Laj, C., Nonmetallic Crystals. Jarnand, S. C., Chadderton, L. T. (eds.): Gordon & Breach, New York, London (1970).
[195] Laj, C., Berge, P., C.R. Acad. Sci. Paris, B 263, 380 (1966).
[196] Laj, C., Berge, P., J. Phys. 28, 821 (1967).
[197] Lambla, M., Schlund, B., Lazarus, E., Pith, T., Makromol. Chem. Suppl. 10–11, 463 (1985).
[198] Lamure, A., Thesis, University Paul Sabatier, Toulouse, France (1983).
[199] Larazidou, M., Phys. Status Solidi A 88, K19 (1985).
[200] Lawson, A. W., J. Chem. Phys. 32, 131 (1960).
[201] Lebotlan, D., Bertrand, T., Mechin, B., Martin, G. J., Nouv. J. Chim. 6, 107 (1982).
[202] Liquori, A. M., J. Polym. Sci., Part C 12, 209 (1966).
[203] Lunn, A. D., The Molecular Basis of Homogeneous Deformation in Glassy Polycarbonate. MIT Thesis (1972).
[204] Lyudskanov, V. G., Vasilev, T. A., Zelenev, Y. V., Polym. Sc. URSS A14(1), 161 (1972).
[205] Mahdavi, S., Alquie, C., Lewiner, J., Favrie, E., Jocteur, R., Measure of the Space Charge in Cables by the Pressure Wage Propagation Method. E6, 269.
[206] Maeda, A., Kojima, K., Takai, Y., Ieda, M., Jpn. J. Appl. Phys. 23(5), L260 (1984).
[207] Maeta, S., Mukai, T., Sakaguchi, K., Jpn. J. Appl. Phys. 16(12), 2287 (1977).
[208] Maeta, S., Sakaguchi, K., Jpn. J. Appl. Phys. 18(10), 1983 (1979).
[209] Maeta, S., Sakaguchi, K., Jpn. J. Appl. Phys. 19(3), 519 (1980).
[210] Maeta, S., Sakaguchi, K., Jpn. J. Appl. Phys. 19(4), 597 (1980).
[211] Manofacier, J. C., Gasiot, J., Parot, P., Fillard, J. P., J. Phys. C, Solid State Phys. 11, 1011 (1978).
[212] Marchal, E., C.R. Acad. Sci. Paris 297(série II), 713 (1983).
[213] Marchal, E., TSDC: a New Analysis and Significance of the Compensation Law. J. Chem. Phys. 96, 4676 (1992).
[214] Marchal, E., TSDC Used in the Study of Chemical Relaxation. Polymer 32, 297 (1991).
[215] Marchal, E., In: Proc. 5th Int. Symp. Electrets, Heidelberg, p. 299. IEEE, N.Y. (1985).
[216] Marchal, E., Benoit, H., Vogel, O., J. Polym. Sci. 16, 949 (1978).
[217] Marchal, E., Monroy-Soto, V. M., Galin, J. C., Heidelberg, p. 247. IEEE, N.Y. (1985).
[218] Mashimo, S., J. Polym. Sci., Polym. Phys. Ed. 19, 213 (1984).
[219] Matsui, M., Murasaki, M., In: Wada, Y., Perlman, M., Kokado, B. (eds.): Charge Storage, Charge Transport and Electrostatics with Their Applications. Studies in Electrical and Electronic Engineering, vol. 2, p. 337. Elsevier, Amsterdam (1979).
[220] Matsuoka, S., In: Proceedings of the 18th NATAS Conference, San Diego, vol. 1, p. 126 (1989).
[221] Matthews, G. E. Jr., Faraday, B. J., Wilsey, N. D., Crawford, J. H. Jr., Phys. Rev. B 23(10), 5011 (1981).
[222] Matthiesen, A., McIntyre, F., Ibar, J. P., Thermal Analysis Spectrometer Characterizes Food Properties. In: Reprint from Food Technology (1991).
[223] Matthiesen, A., McIntyre, F., Ibar, J. P., Saffell, J., Use of Thermal Stimulated Current to Characterize the Amorphous Phase of Polymers. In: American Laboratory (1991).
[224] McCrum, N. G., J. Polym. Sci. 60, 53 (1962).
[225] McCrum, N. G., Polymer 25, 299 (1984).
[226] McCrum, N. G., Pizzoli, M., Chai, C. K., Treurnicht, I., Hutchinson, J. M., Polymer 23, 473 (1982).
[227] McKever, S. W. S., Lilley, E., J. Phys. C, Solid State Phys. 14, 3547 (1981).

EBSCOhost - printed on 2/13/2023 12:32 AM via . All use subject to https://www.ebsco.com/terms-of-use

[228] Medycki, W., Hilczer, B., Kruger, J. K., Marx, A., Polym. Bull. 11, 429 (1984).
[229] Megret, C., Thesis, University Paul Sabatier, Toulouse, France (1988).
[230] Mehendru, P. C., Agrawal, J. P., Jain, K., Thin Solid Films 5(71), L5 (1980).
[231] Mehendru, P. C., Agrawal, J. P., Jain, K., Warrier, A. V. R., Thin Solid Films 78, 251 (1981).
[232] Meuldijk, H., Den Hartog, H. W., Phys. Rev. B 27(10), 6376 (1983).
[233] Meuldijk, H., Den Hartog, H. W., Phys. Rev. B 28(2), 1036 (1983).
[234] Micocci, G., Mongelli, S., Rizzo, A., Tepore, A., Solid State Commun. 53(10), 873 (1985).
[235] Micocci, G., Rizzo, A., Tepore, A., J. Appl. Phys. 54(4), 1924 (1983).
[236] Migahed: TSDC Spectra in Negatively Corona Charged ABS Electrets. Polym. Bull. 23, 61 (1990).
[237] Miller, A. A., Macromolecules 11, 859 (1978).
[238] Miller, A. A., Macromolecules 12, 651 (1979).
[239] Misra, S. C., Pichot, C., El Asser, M. S., Vanderhoff, J. W., J. Polym. Sci., Polym. Chem. Ed. 24, 2383 (1983).
[240] Misra, D. S., Kumar, A., Agarwal, S. C., Philos. Mag. B49(6), L69 (1984).
[241] Misra, D. S., Kumar, A., Agarwal, S. C., Phys. Rev. B 31(2), 1047 (1985).
[242] Miyairi, K., Ieda, M., In: Wada, Y., Perlman, M. M., Kokado, H. (eds.): Charge Storage, Charge Transport and Electrostatics with Their Applications. Studies in Electrical and Electronic Engineering, vol. 2, p. 327. Elsevier, Amsterdam (1979).
[243] Miyairi, K., Yanagisawa, I., Jpn. J. Appl. Phys. 17(3), 593 (1978).
[244] Mizutani, T., Tsukahara, T., Thermally-Stimulated Currents in Oxidized Low-Density Polyethylene. Jpn. J. Appl. Phys. 19, 11 (2095). 1980.
[245] Mizutani, T., Yamada, T., Ieda, M., Thermally Stimulated Currents in Polyvinylidene Fluoride: I. Unstretched α form PVDF. J. Phys. D, Appl. Phys. 14, 1139 (1981).
[246] Moisan, J. Y., Eur. Polym. J. 17, 857 (1981).
[247] Moran, P. R., Fields, D. E., J. Appl. Phys. 45(8), 3266 (1974).
[248] Mucillo, E. N. S., Mucillo, R., Phys. Status Solidi B 122, K127 (1984).
[249] Mucillo, R., Campos, L. L., Phys. Status Solidi A 52, K183 (1979).
[250] Muller, J. C., Stuck, R., Berger, R., Siffert, P., Solid-State Electron. 17, 1293 (1974).
[251] Muller, P., Phys. Status Solidi A 23, 393 (1974).
[252] Muller, P., Phys. Status Solidi A 28, 521 (1975).
[253] Muller, P., Teltow, J., Phys. Status Solidi A 12, 471 (1972).
[254] Namajima, T., Saito, S., J. Polym. Sci. 31, 423 (1958).
[255] Nakamura, S., Sawa, G., Ieda, M., Effect of Electric Field on Thermally Stimulated Current in γ-Irradiated Polyethylene. Interpretation of transitions in LDPE. Jpn. J. Appl. Phys. 18(5), 917 (1979).
[256] Natsui, M., Nagasaka, M., Yamagi, K., Jpn. J. Appl. Phys. 16, 177 (1977).
[257] Nedetzka, T., Reichk, M., Mayer, A., Vogel, H., J. Phys. Chem. 74(13), 2652 (1970).
[258] Nierste, G., Fischer, F., Phys. Status Solidi B 108, 269 (1981).
[259] Niftiev, G. M., Tagiev, B. G., Aslanov, G. K., Phys. Status Solidi A 75, 59 (1983).
[260] Nishitani, T., Yoshino, K., Inuishi, Y., Jpn. J. Appl. Phys. 14(5), 721 (1975).
[261] Noel, S., Laurent, C., Mayoux, C., IEEE Trans. Electr. Insul. EI, 1, 63 (1987).
[262] Nomura, S., Kojima, F., Jpn. J. Appl. Phys. 12(2), 205 (1973).
[263] Nunes de Oliveira, L., Leal Ferreora, G. F., Nuovo Cimento 23B(2), 385 (1974).
[264] Ohara, K., Colloid Polym. Sci. 259, 981 (1981).
[265] Ohara, K., Plast. Ind. News 26(9), 134 (1980).
[266] Ohara, K., Rehage, G., Thermally Stimulated Depolarization Currents of Tactic Polymethyl Methacrylates and Their Mixtures. Colloid Polym. Sci. 3(259), 318 (1981).
[267] Osawa, S., Polyelectrolytes. Marcel Dekker Inc., New York (1971).

EBSCOhost - printed on 2/13/2023 12:32 AM via . All use subject to https://www.ebsco.com/terms-of-use

[268] Pangrle, S., Wu, C. S., Geil, P. H., Low Temperature Relaxation of DGEBA Epoxy Resins: A Thermally Stimulated Discharge Current (TSDC) Study. Polym. Compos. 10, 3 (1989).
[269] Panwar, V. S., Singh, R., Gupta, N. P., Thermally Stimulated Discharge Current Studies in Vinyl Chloride: Vinyl Acetate Copolymers. In: Harrison, I. R. (ed.) Proceedings of the 19th NATAS Conference, Vol. 1, Boston, p. 124 (1990).
[270] Peacock-Lopez, E., Suhl, H., Phys. Rev. B 26, 3774 (1982).
[271] Peralta, L., Thuillier, J. C., Phys. Status Solidi A 22, 473 (1974).
[272] Perlman, M. M., Kav, K. J., Bamji, S. S., J. Appl. Phys. 50(5), 3622 (1979).
[273] Perlman, M. M., Unger, S., J. Appl. Phys. 45(6), 2389 (1974).
[274] Pfister, G., Prest, W. M., Luca, D. J., Abkowitz, M., Appl. Phys. Lett. 27(9), 486 (1975).
[275] Pieper, H., Phys. Status Solidi A 23, K55 (1974).
[276] Patton, T. C. (ed.): Pigment Handbook, 3, Characterization and Physical Relationships John Wiley & Sons, Inc. (1973).
[277] Pilatus, U., Fischer, F., Phys. Status Solidi B 118, 217 (1983).
[278] Pillai, P. K. C., Goel, T. C., Xavier, S. F., Eur. Polym. J. 15, 1149 (1979).
[279] Pillai, P. K. C., Mollah, M., In: Wada, Y., Perlman, M. M., Kokado, H. (eds.) Charge Storage, Charge Transport and Electrostatics with Their Applications. Studies in Electrical and Electronic Engineering, vol. 2, p. 352. Elsevier, Amsterdam (1979).
[280] Pillai, P. K. C., Narula, G. K., Tripathi, A. K., Mendiratta, R. G., Phys. Status Solidi A 67, 649 (1981).
[281] Pillai, P. K. C., Nath, R., Nais, P. K., Phys. Lett. A 58(78), 474 (1976).
[282] Pillai, P. K. C., Rashmi, P. K. C., J. Appl. Phys. 51(6), 3424 (1980).
[283] Pillai, P. K. C., Rashmi, P. K. C., J. Polym. Sci., Polym. Phys. Ed. 17, 1731 (1979).
[284] Pillai, P. K. C., Tripathi, A., Boel, T. C., In: Proc. 5th Int. Symp. Electrets, Heidelberg, Avail from IEEE, N.Y., p. 117 (1985).
[285] Pineri, M., Berticat, P., Marchal, E., J. Polym. Sci., Polym. Phys. Ed. 14, 1325 (1976).
[286] Pinguet, J., Minn, S. S., C.R. Acad. Sci. Paris, B 278, 783 (1974).
[287] Pinguet, J., Minn, S. S., Phys. Status Solidi A 35, 431 (1976).
[288] Pinguet, J., Minn, S. S., Solid State Commun. 19, 451 (1976).
[289] Pissis, P., Anagnostopoulov-Konsta, A., In: Proc. 5th Int. Symp. Electrets, Heidelberg, pp. 842–847. Avail from IEEE, N.Y. (1985).
[290] Pissis, P., Apekis, L., Christodoulides, C., Boudouris, G., Am. Chem. Soc. 4034 (1983).
[291] Plaino-Lamure, E., A Study of Dipolar Re-Orientation in Dental Enamel by Dielectric Spectroscopy. Thesis in French (1983).
[292] Plans, J., Balta Calleja, F. J., Zielinski, M., Kryszews, K. M., Philos. Mag. B48(3), 289 (1983).
[293] Plans, J., Zielinski, M., Kryszenski, M., Phys. Rev. B 23(12), 6557 (1981).
[294] Plans, J., Zielinski, M., Swiderski, T., Kryszenski, M., Ulanski, J., J. Appl. Phys. 53(4), 3103 (1982).
[295] Pochtennyl, A. E., Ratnikov, B., Dokl. Acad. Nauk. USSR 25, 896 (1981).
[296] Prakash, J., A Convenient Method for the Analysis of the Ionic Thermocurrent Data. J. Appl. Phys. 67, 3468 (1990).
[297] Prakash, J., Fischer, F., Phys. Status Solidi A 39, 499 (1977).
[298] Qingquan, L., In: 5th Int. Symp. Electrets, Heidelberg, p. 126. Avail from IEEE, N.Y. (1985).
[299] Rabie, S. A., Phys. Rev. B 14(6), 2569 (1976).
[300] Randak, R., Adamec, V., Plaste und Kautschuk, 19 Jahrgang, Heft 12, 905 (1972).
[301] Reboul, J. P., Toureille, A., J. Polym. Sci., Polym. Phys. Ed. 22, 21 (1984).
[302] Reichle, M., Nedetzka, T., Mayer, A., Vogel, H., J. Phys. Chem. 74(13), 2659 (1970).
[303] Reiss, C., J. Chim. Phys. 63, 1299, 1307, 1319 (1966).
[304] Remhe, R. L., Von Seggern, H., J. Appl. Phys. 54(9), 5262 (1983).
[305] Riehl, B., Physics of Ice. Bullemer, H., Engelhardt (eds.) Plenum Press, New York (1969).

EBSCOhost - printed on 2/13/2023 12:32 AM via . All use subject to https://www.ebsco.com/terms-of-use

[306] Rios-Guerrero, L., Guillot, J., Makromol. Chem. 183(3), 531 (1982).
[307] Roberts, T. R., World Source Corporation, Brochure and Private Communication.
[308] Robertson, R. E., Structure and Mobility in Molecular and Atomic Glasses. O'Reilly, J. M., Goldstein, M. (eds.): Annals of the New York Academy of Sciences, vol. 371. Academy of Sciences, New York (1981).
[309] Ronarc'h, D., Appl. Phys. Lett. 37(8), 707 (1980).
[310] Ronarc'h, D., Audren, P., Haridon, S., Herou, J., J. Appl. Phys. 54(8), 4439 (1983).
[311] Ronarc'h, D., Testard, O., J. Phys. E, Sci. Instrum. 15, 636 (1982).
[312] Rosenberg, B., Bhowmik, B. B., Harder, H. C., Postow, E., J. Chem. Phys. 49, 4108 (1968).
[313] Saadat, A., A Study of the Molecular Mobility of Collagen by TSC, Model for Skin Aging. Thesis in French (1988).
[314] Saffell, J. R., Bernes, A., et al., Proceedings of the 46th ANTEC Conference, p. 1049 (1988).
[315] Saffell, J. R., Matthiesen, A., McIntyre, F., Ibar, J. P., Comparing Thermal Stimulated Current (TSC) with Other Thermal Analytical Methods to Characterize the Amorphous Phase of Polymers. Thermochim. Acta 192, 243 (1991).
[316] Saji, M., Kao, K. C., Jpn. J. Appl. Phys. 15(7), 1393 (1976).
[317] Sakai, K., Adachi, Y., Ikoma, T., Jpn. J. Appl. Phys. 12(11), 1816 (1973).
[318] Sakurai, T., Jpn. J. Appl. Phys. 24(1), 79 (1985).
[319] Samoc, A., Samoc, M., TSC Studies of Charge Storage and Transport in Organic Crystals, a Critical Approach. In: Wada, Y., Perlman, M. M., Kokado, H. (eds.) Charge Storage, Charge Transport and Electrostatics with Their Applications Studies in Electrical and Electronic Engineering, vol. 2, p. 271 (1979).
[320] Samoc, A., Samoc, M., Sworakowski, J., Phys. Status Solidi A 36, 735 (1976).
[321] Samoc, A., Samoc, M., Sworakowski, J., Thomas, J. M., Williams, J. O., Phys. Status Solidi A 37, 271 (1976).
[322] Samoc, A., Samoc, M., Sworakowski, J., Phys. Status Solidi A 39, 337 (1977).
[323] Samoc, M., Samoc, A., Phys. Status Solidi A 51, K195 (1979).
[324] Samoc, M., Samoc, A., Phys. Status Solidi A 57, 667 (1980).
[325] Sano, M., Bull. Chem. Soc. Jpn. 48(1), 343 (1975).
[326] Sasabe, H., J. Polym. Sci., Polym. Phys. Ed. 11, 2418 (1973).
[327] Satoh, S., Igaki, K., Jpn. J. Appl. Phys. 19(35), 485 (1980).
[328] Sauer, B. B., Avakian, P., Cooperative Relaxations in Amorphous Polymers Studied by Thermally Stimulated Currents. Polymer 33, 5128 (1992).
[329] Sauer, B. B., Avakian, P., Cohen, G., Studies of Phase Separated Copolymer Blends Using Thermally Stimulated Currents and Dielectric Spectroscopy. Polymer 33, 2666 (1992).
[330] Sauer, B. B., Avakian, P., Starkweather, H. W. Jr., Hsiao, B. S., Thermally Stimulated Current and Dielectric Studies of Poly(Aryl Ether Ketone Ketone). Macromolecules 23, 5119 (1990).
[331] Sawa, G., Masayuki, M., Chool-Leed, D., Ieda, M., Jpn. J. Appl. Phys. 13(10), 1547 (1974).
[332] Sawa, G., Nakamura, S., Nishio, Y., Ieda, M., Thermally Stimulated Currents from Non-Treated Poly(Ethylene Terephthalate) Films. Jpn. J. Appl. Phys. 17(9), 1507 (1978).
[333] Sawatari, A., In: Wada, Y., Perlman, M., Kokado, H. (eds.): Charge Storage, Charge Transport and Electrostatics with Their Applications. Studies in Electrical and Electronic Engineering, vol. 2, p. 347. Elsevier, Amsterdam (1979).
[334] Scaife, B. K. P., J. Phys. D, Appl. Phys. 7, L171 (1984).
[335] Scaife, B. K. P., J. Phys. D, Appl. Phys. 8, L72 (1975).
[336] Scharager, C., Muller, J. C., Stuck, R., Siffert, P., Phys. Status Solidi A 31, 247 (1975).
[337] Schmieder, Von, K., Wolf, K., Kolloid Z134, 149 (1953).
[338] Schwab, G. M., J. Catal. 84, 1 (1983).
[339] Scott, A. H., Scheiber, D. J., Curtis, A. J., Lauritzen, J. I. Jr., Hoffman, J. D., J. Res. Natl. Bur. Stand. A 66, 269 (1962).

EBSCOhost - printed on 2/13/2023 12:32 AM via . All use subject to https://www.ebsco.com/terms-of-use

[340] Sekiar, S., Tripathi, A. K., Goel, T. C., Pillai, P. K. C., In: Proc. 5th Int. Symp. Electrets, Heidelberg, p. 181. Avail from IEEE, N.Y. (1985).
[341] Sessler, G. M., Study of Carrier Mobilities by a Thermally-Stimulated-Current Technique. J. Electrost. 3, 181 (1977).
[342] Sessler, G. M., West, J. E., Trap-Modulated Mobility of Electrons and Holes in Teflon FEP. J. Appl. Phys. 47(8), 3480 (1976).
[343] Sessler, G. M., West, J. E., Population and Temperature Shift of TSC Peaks of Electron-Beam-Charged Teflon FEP. J. Appl. Phys. 50(5), 3328 (1979).
[344] Sessler, G. M., West, J. E., Phys. Rev. B 10(10), 4488 (1974).
[345] Seytre, G., Thesis, Lyon, France (1973).
[346] Shanfield, Z., IEEE Trans. Nucl. Sci. NS-30(6), 4064 (1983).
[347] Shanfield, Z., Moriwaki, M. M., IEEE Trans. Nucl. Sci. NS-31(6), 1242 (1984).
[348] Sharp, E. J., Garn, L. E., Appl. Phys. Lett. 29(8), 480 (1976).
[349] Shaw, D., Moghaddam, H. R., Phys. Status Solidi A 65, 167 (1981).
[350] Shimizu, H., Nakayama, K., Jpn. J. Appl. Phys. 28, L1616 (1989).
[351] Shindo, K., In: Wada, Y., Perlman, M. M., Kokado, H. (eds.) Charge Storage, Charge Transport and Electrostatics with Their Applications. Studies in Electrical and Electronic Engineering, vol. 2, p. 302. Elsevier, Amsterdam (1979).
[352] Shindo, K., Reports on Progress in Polymer Physics in Japan XXV(II) (1984).
[353] Shrivastava, R. K., Qureschi, M. V., Bhatnagas, C. S., Jpn. J. Appl. Phys. 17(9), 1537 (1978).
[354] Shrivastava, S. K., Ranade, J. D., Shrivastava, A. P., Phys. Lett. A 69(6), 465 (1979).
[355] Shrivastava, S. K., Ranade, J. D., Shrivastava, A. P., Thermally Stimulated Discharge Currents in Polystyrene Films. Thin Solid Films 67, 201 (1980).
[356] Simon: The TSC Technique Applied to Side-Chain Liquid-Crystal Polymers. Polymer 30, 2227 (1989).
[357] Simmons, J. G., Nadkarni, G. S., Phys. Rev. B 6(12), 4815 (1972).
[358] Singh, R., Datt, S. C., In: Proc. 5th Int. Symp. Electrets, Heidelberg, p. 191. IEEE, N.Y., (1985).
[359] Slavinska, D., Nespurek, S., Sorm, M., Polym. Bull. 9, 60 (1983).
[360] Solunov, H. A., Vassilev, T., J. Polym. Sci. 12, 1273 (1974).
[361] Solunov, H. A., Ponevski, CH. S., J. Polym. Sci. 15, 969 (1977).
[362] Sordi, G. M., Watamare, S., Nuovo Cimento 25B(1), 145 (1975).
[363] Stott, J. P., Crawford, J. H. Jr., Phys. Rev. Lett. 26(7), 384 (1971).
[364] Strutt, J. E., Weightman, M. W., Lilley, E., J. Phys. E, Sci. Instrum. 9, 683 (1976).
[365] Stuck, R., Muller, J. C., Ponpon, J. P., Scharager, C., Schwab, C., Siffert, P., J. Appl. Phys. 47(4), 1545 (1976).
[366] Stupp, S. I., Weldert, S. C., Polym. Compos. 7(3), 224 (1984).
[367] Su, W. F. A., Carr, S. H., Brittain, J. O., Thermally Stimulated Discharge Current Studies on Low-Temperature Relaxation in Epoxy Resin. J. Appl. Polym. Sci. 25, 1355 (1980).
[368] Suzuoki, Y., Mizutani, T., Ieda, M., J. Appl. Phys. 15(5), 929 (1976).
[369] Suzuoki, Y., Mizutani, T., Shimozato, M., Sugivra, N., Ieda, M., Jpn. J. Appl. Phys. 19(5), 861 (1980).
[370] Suzuoki, Y., Mizutani, T., Takai, Y., Ieda, M., Jpn. J. Appl. Phys. 16(11), 1929 (1977).
[371] Suzuoki, Y., Yasuda, K., Mizutani, T., Ieda, M., J. Phys. D, Appl. Phys. 10, 1985 (1977).
[372] Suzuoki, Y., Yasuda, K., Mizutani, T., Ieda, M., Jpn. J. Appl. Phys. 17(7), 1215 (1978).
[373] Swiatek, J., Phys. Status Solidi A 52, K69 (1979).
[374] Sworakowski, J., Figueiredo, M. T., Leal Ferreira, G. F., Campos, M., J. Appl. Phys. 54(8), 4523 (1983).
[375] Sworakowski, J., Figueiredo, M. T., Leal Ferreira, G. F., Campos, M., J. Appl. Phys. 56(4), 1149 (1984).
[376] Syamaprasad, U., Vallabhan, C. G., Phys. Rev. B 26(10), 5941 (1982).

EBSCOhost - printed on 2/13/2023 12:32 AM via . All use subject to https://www.ebsco.com/terms-of-use

[377] Syamaprasad, U., Vallabhan, C. G., Solid State Comm., vol. 38, p. 555 (1981).
[378] Takahashi, S., Space Charge in Pb(Zr, Ti)O_3 ceramics. In: Wada, Y., Perlman, M. M., Kokado, H. (eds.) Charge Storage, Charge Transport and Electrostatics with Their Applications. Studies in Electronic and Electrical Engineering, vol. 2, p. 266. Elsevier, Amsterdam (1979).
[379] Takai, Y., Mori, K., Mizutani, T., Ieda, M., Jpn. J. Appl. Phys. 15(12), 2341 (1976).
[380] Takai, Y., Mori, K., Mizutani, T., Ieda, M., Jpn. J. Appl. Phys. 16(11), 1937 (1977).
[381] Takai, Y., Osawa, T., Mizutani, T., Ieda, M., Kojima, K., Jpn. J. Appl. Phys. 15(8), 1597 (1976).
[382] Talwar, I. M., Sinha, H. C., Shri-vastava, A. P., Thin Solid Films 113, 251 (1984).
[383] Tanaka, T., Hayashi, S., Hirabayashi, S., Shibayama, K., J. Appl. Phys. 49, 2490 (1978).
[384] Tanaka, T., Hayaski, S., Shibayama, K., J. Appl. Phys. 48(8), 3478 (1977).
[385] Taylor, P. D., Morgan, D. V., J. Phys. D, Appl. Phys. 10, 73 (1977).
[386] Thurzo, I., Bohun, A., Czechoslov. J. Phys. B25, 1285 (1975).
[387] Thurzo, I., Mariani, E., Barancok, D., Czechoslov. J. Phys. B24, 203 (1974).
[388] Thurzo, I., Mariani, E., Heks, H., Czechoslov. J. Phys. B23, 1241 (1973).
[389] Thurzo, I., Pavlikova, M., Mariani, E., Depolarization Currents Due to Dipole Reorientation, Depolarization Currents due to Ionic Space Charge, Depolarization Currents due to Electronic Charge Carriers. Czechoslov. J. Phys. B25, 1279 (1975).
[390] Tiwari, A. R., Shrivastava, S. K., Saraf, K. K., Shrivastava, A. P., Thin Solid Films 70, 191 (1980).
[391] Topic: Use of Blocked Electrodes in TSDC Measurements. J. Polym. Sci. Phys. 24, 2209 (1986).
[392] Torres, A., Jimenez, J., Carbayo, V., De Saja, J. A., Phys. Status Solidi A 78, 671 (1983).
[393] Tripathi, A., Tripathi, A. K., Pillai, P. K. C., Thermally Stimulated Depolarization of Poly-Vinyl Chloride: Mica Composite Electrets. In: Harrison, I. R. (ed.) Proceedings of the 19th NATAS Conference, vol. 1, Boston, NATAS, p. 117 (1990).
[394] Ulanski, J., Kryssewski, M., In: Martuscelli, E., Palumbo, R., Kryszewski, M. (eds.) Polymer Blends, processing morphology and properties, p. 397. Plenum Press, New York (1980).
[395] Unger, S., Perlman, M. M., Phys. Rev. B 6(10), 3973 (1972).
[396] Varlow, B. R., Thermally stimulated current and morphology in low density PE. In: Fourth Int. Conf. on Dielectric Materials Measurements and Applications (1984).
[397] Vayssie, E., M. S. Thesis, University Paul Sabatier, Toulouse, France (1983).
[398] Vieux-Rochaz, L., Chenevas-Paule, A., J. Non-Cryst. Solids 35, 737 (1980).
[399] Vivadi, Y. A., Khalilov, S. K. H., Barkjolov, B. S., Ragimov, A. V., Thin Solid Films 55, L1 (1978).
[400] Volkenstein, M. V., Dokl. Akad. Nauk USSR 78, 879 (1951).
[401] Bardeleben, H. J., Schwab, C., Scharager, C., Muller, J. C., Siefert, P., Feigelson, R. S., Deep Level Study in $AgGaS_2$ by Thermally Stimulated Current Measurements. Phys. Status Solidi A 58, 143 (1980).
[402] Von Seggern, H., J. Appl. Phys. 50(4), 2817 (1979).
[403] Von Seggern, H., J. Appl. Phys. 52(6), 4081 (1981).
[404] Wagner, J., Mascarenhas, S., Phys. Rev. B 6(12), 4867 (1972).
[405] Wang, D. Y., Nowick, A. S., Phys. Status Solidi A 73, 165 (1982).
[406] Weber, G., Tormala, P., Colloid Polym. Sci. 256, 1137 (1978).
[407] Wilbrand, A., Fischer, F., Phys. Status Solidi B 99, 243 (1980).
[408] Wilbrand, A., Fischer, F., Phys. Status Solidi B 101, 209 (1980).
[409] Williams, A. D., Flory, J., J. Polym. Sci. C16, 2981 (1968).
[410] Williams, G. P., Mullis D, J. R., Phys. Status Solidi A 28, 539 (1975).
[411] Williams, M. L., Landel, R. F., Ferry, J. D., J. Am. Chem. Soc. 77, 3701 (1955).
[412] Wintle: Comment on the Thermodynamic Law. J. Phys. D 21, 1472 (1988).
[413] Wu, C. S., Dispersive Orientational Dipole Relaxation in TSDC. J. Phys. Chem. Solids 51, 349 (1990).
[414] Yamada, T., Mizutani, T., Ieda, M., J. Phys. D, Appl. Phys. 15, 289 (1982).
[415] Yamashita, K., Iwamoto, M., Hino, T., Jpn. J. Appl. Phys. 59(5), 2866 (1978).

EBSCOhost - printed on 2/13/2023 12:32 AM via . All use subject to https://www.ebsco.com/terms-of-use

[416] Yamashita, K., Iwamoto, M., Hino, T., Jpn. J. Appl. Phys. 20(8), 1429 (1981).
[417] Yasuoka, Y., Wada, M., Jpn. J. Appl. Phys. 13(11), 1797 (1974).
[418] Yokota, K., Katayama, S., Yoshikawa, T., Jpn. J. Appl. Phys. 21(3), 456 (1982).
[419] Yoshimo, K., Sakai, T., Yamamoto, Y., Inuishi, Y., Jpn. J. Appl. Phys. 20, 867 (1981).
[420] Zielinski, M., Jeszka, J. K., Kryszewski, M., Phys. Status Solidi A 58, 385 (1980).
[421] Zielinski, M., Kryszewski, M., Theoretical Analysis of the Thermal Sampling Technique for TSD Measurements on Polymers. J. Electrost. 3, 69 (1977).
[422] Zielinski, M., Kryszewski, M., Phys. Status Solidi A 42, 305–314 (1977).
[423] Zielinski, M., Samoc, M., J. Phys. D, Appl. Phys. 10, L105 (1977).
[424] Zielinski, M., Swiderski, T., Kryszewski, M., Polymer 19, 883 (1981).

EBSCOhost - printed on 2/13/2023 12:32 AM via . All use subject to https://www.ebsco.com/terms-of-use

Book acknowledgments

I would like to thank the following collaborators for helping me with the publication of this book:

P. Denning, D. Gardiner, A. Beltzeki, C. Choy, J. Barlow, A. Semenov, C. Lacroix, B. Favis, B. Torok, B. Aral.

A special thank you to Remi Andre of Kep-Technologies Inc. for giving me free and full access to "Fundamentals of Thermal Stimulated Current and Relaxation Map Analysis," by J. P. Ibar, SLP Press, 1993.

https://doi.org/10.1515/9783110756746-013

EBSCOhost - printed on 2/13/2023 12:32 AM via . All use subject to https://www.ebsco.com/terms-of-use

EBSCOhost - printed on 2/13/2023 12:32 AM via . All use subject to https://www.ebsco.com/terms-of-use

Index

100 % HDPE 422
2nd Renaissance, inspired by Prigogine 286
5 % LDPE 95 % HDPE blend 430
Δ_e, a fundamental parameter of the vertical split aspect of the Grain-Field Statistics 233
"Δ_m, υ_m" kinetics 266
Δ_m, υ_m settings 159
Δ_x, Ln(υ_x) are dissipative variables 235
ΔG_p linearly related to T_p 94
ΔG plane 84, 138
ΔH_s grid 215, 237
ΔH_s the shifted value of ΔH 181
ΔH_u the unshifted value of ΔH 181
ΔH grid 241, 246

A.S.S block copolymers 391
ABS 331
accelerated sulfur vulcanization 403
acrylic component 341
acrylic urethane systems-based coatings 344
acrylonitrile–butadiene rubber 375
activation energy 305
activation entropy and enthalpy at T_g 80
aging phenomenon in PMMA by TSD/TWD 469
alloying 391
alloys and blends 391
alternative solution to the separation of variables 216
amorphous component inside the spherulites 137
amorphous lignin 521
amorphous matter is located at the boundary of the rigid spherulites 137
amorphous phase in semi-crystalline polymers 66
amorphous phase in the polyamide 12 119
amorphous phase near T_g 304
amorphous phases in semi-crystalline polymers 101
amorphous state of matter 12
amount of segregation 301
amount of sliding shift 218
annealed Vectra 366, 517
annealing 263, 383
apparent chaos 271
Arrhenius equation 7, 66
Arrhenius lines 9
Arrhenius plane 138
Arrhenius spectral lines 65
Arrhenius system of coordinates 78
Arrhenius transform 66, 101
assign thermal kinetic attributes to the peak shape 110
asymmetry of the ΔH_s and Ln(τ_{os}) grids 237
auto-catalytic effect 266
auto-catalytic process 233
automatic data integration 322

b-grains 145, 483
b-grains and their *F*-conformers surrounding 239
(b/F), the first duality 235
b/F state 150
beverage 340
biaxial orientation 384
biaxially stretched film of PET 324
biphasic structure 393
bipolar FETs 329
birefringence 382
blends of 50:50 PEEK/PEI 470
block copolymers 300
block copolymers of acrylate n-butyl and styrene 300
boiled and unboiled wood samples 521
boiled wood 363
Boltzmann statistics 143
Boltzmann's mean field 147
bonding strength of paints 384
braids 362
Brownian dissipation 147
Bucci–Fieschi–Guidi integral solution 34
Bucci's equation 7
butadiene dipoles 332
"by-product" kinetics (Δ_x, υ_x) 266

(c, g, t), the second duality 235
canned food industry 340
cellulose crystals 521
characteristics of the Debye peaks 174
characteristics of the depolarization peak 56
characteristics of the grid at $\delta_x = 0$ 217
characterization of blends 352
characterization of paints and coatings 11
characterize the amorphous state 65

https://doi.org/10.1515/9783110756746-014

EBSCOhost - printed on 2/13/2023 12:32 AM via . All use subject to https://www.ebsco.com/terms-of-use

characterize the degree of cure 388
Clapeyron's equation 358
classical approach 144
Clausius-Mosotti expression 245
closed thermodynamic system 252
closed-systems statistics 286
coating 340
coatings and adhesives characterization 307
collective behavior 337
collective dissipative network stability 233
combination of horizontal and vertical splitting to describe interactions 286
comparison with AC data 313
compensating modes of structuration 259
compensation 483
compensation in the sub-EE plane 85
compensation laws 148, 186
compensation lines 198
compensation of the Arrhenius lines 233
compensation of the Debye relaxation 11
compensation phenomena 65, 72
compensation phenomenon 320
compensation plots 188
compensation point 9, 65, 148
compensation search 73, 89
compensations of Ln(τ_o) vs. ΔH in ranges 1, 2, 3 241
compensation(s) of the relaxation modes 11
compensations of the slope and intercept of the Arrhenius lines 149
complexity of the cross-compensations 222
compression molding 334, 336
concentration of soluble additives 379
concept of compensation 138
conformational potential energy 143, 243, 542
conformational states 150
conformers 142, 483, 541
confusion between $T_{g,p}$ and T_{LL} 163
conjugated open dissipative systems 259
conjugated states 248
convergence of the normalized ($\Delta G/T_p$) depolarization curves 94
converging Arrhenius lines 72
cooling simulation 255
coordinates of the compensation point 72
corona treatment 324
correctly cured 384
correlation structure across the three ranges 222
coupling between energetic and kinetic constraints 255
coupling between kinetic and energetic equations 243
coupling between relaxation motions 10
coupling of cooperatively interactive dipolar motions 147
coupling of the interactions 141
coupling of the voltage field and the polarization temperature 156
coupling of two types of splitting processes 147
coupling on both sides of T_g 97
critical pigment volume concentration (CPVC) 349
"cross compensation" of the effect of δ_x and T_p 188
cross-compensation between two independent variables 201
Cross-Dual-Phase models of the interactions 11
cross-duality 244
cross-dynamic partition 266
cross-dynamic structure 223
crossing of δ_x and T_p 181
crosslink density 343, 345, 346, 388
crosslinked elastomers 373
crosslinked natural rubber vulcanizates 408
crosslinking 344, 346, 357, 373, 374
crystallizable polymers 485
cure 340
curing of thermosets 381
current measured in the electrometer 330
curve-fitting methods based on peak half-width 42

damping analysis 292
DEA 2, 289
Debye curve-fits 33
Debye relaxation map 153
deconvolute the Dual-Split complexity 163
deconvoluting the Dual-Split complex nature of the interactions 166
deconvolution of thermally windowed peaks 44
decoupling of the relaxation modes 1, 301
define the DOD number 81
degree of cooperativeness between the relaxation modes 7
degree of coupling 138
degree of crosslinking 404
degree of cure with bake time 343

EBSCOhost - printed on 2/13/2023 12:32 AM via . All use subject to https://www.ebsco.com/terms-of-use

degree of disorder 72
degree of disorder (DOD) 7, 72
degree of disorder (DOD) of the phases 391
degree of interpenetration 357
degree of orientation 352
departure from equilibrium 252
depolarization current 3
depolarization current response 162
depolarization of what was polarized 166
depolarization stage 329
depolarization time t_d 56
detecting the melting temperature 311
determination of T_g 80
determination of the compensation point coordinates 321
determination of the DOD 322
dibutylphtalate (DBT) as plasticizer 433
dielectric capacitor 329
dielectric constant, ε 157
dielectric measurement 291
dielectric permittivity 308
difference between $(T_x)_H$ and $T_{x(\tau)}$ 222
different mechanisms of interactions 203
different types of polarization 15
differential microcalorimetry 294
differential scanning calorimeter (DSC) 294
diffusion-controlled migration 420
dipolar orientation polarization 18
Dirac peak 173
discontinuities 271
disentanglement/sustained-orientation 145
dispersed phase 409
dissipative elastic wave 147
dissipative mechanisms of structuration 162
dissipative nature of the collective interactive dynamics 233
dissipative pair (Δ_x, u_x) 243
dissipative parameter, $\mathrm{Ln}(N_b/N_f)$ 259
dissipative structures 12
dissipative term 254
dissipative wave 259
distributed Debye processes 25
distribution of internal stress 325
DMA 1, 289, 351, 366, 372, 392
DOD 381
DOD number 80, 384
drawn polypropylene 127
DSC 1, 289, 373, 391
DTA 2, 295
dual partition 253
dual-conformers 143, 542
Dual-Phase and Cross-Dual-Phase model 141
Dual-Phase and Cross-Dual-Phase model of conformers interactions 233
Dual-Phase and Cross-Dual-Phase of the interactions 63
Dual-Phase and Cross-Dual-Phase physics 220
Dual-Phase and Cross-Dual-Phase theory 495
Dual-Phase and the Cross-Dual-Phase model of polymer interactions 11
Dual-Phase and the Grain-Field Statistics 243
Dual-Phase dissipative elastic wave 246
Dual-Phase dissipative model of conformers interactions 241
Dual-Phase dissipative model of interactive coupling 246
Dual-Phase model 10, 485
Dual-Phase model of the interactions 141
Dual-Phase statistics 143
Dual-Split equations 235
Dual-Split interpretation of the effect of the voltage field 165
Dual-Split Kinetics 142, 253, 255, 541
Dual-Split model explanation 149
Dual-Split statistics 164
Dual-Split (vertical) structuring 162
duality and cross-duality are intrinsically interlocked 235
duality at T_g 83
duality characteristics of the conformers 266
duality of the b/F conformers 146
Dube's formula 109
Dussel–Bube approximation 43, 46, 178
Dussel–Bube equation 179, 190, 234
dynamic free volume 483
dynamic kinetic systems 261
dynamic simulations 251
"dynamics" 252
Dynamics of Open-Dissipative Systems of Interactions 286
dynamics of the collection of chains 142, 541
dynamics open self-dissipative systems 255

EE plot 75
effect of cooling rate on the kinetics rate 260
effect of particle size and concentration 349
effect of phenolic antioxidant on TSD peak 355
effect of polarization time t_p 58

EBSCOhost - printed on 2/13/2023 12:32 AM via . All use subject to https://www.ebsco.com/terms-of-use

effect of temperature of polarization T_p and of the window width 61
effect of the increasing plasticizer content on the TWD parameters 434
effect of the pigment on the surrounding 348
effect of the shifting of the Debye peak 234
effect of the time of depolarization t_d 59
effect of the voltage field 329
effect of the voltage field on the statistics of interactive coupling 149
elastic constants of the materials 305
elastic dissipative network 143
elastic dissipative sweeping motion 239
elastic dissipative wave 239
electrometer 3, 329
electronic entropy 138
elementary modes 5
elementary relaxation curve 66
elementary relaxation modes 297, 327
elementary relaxation time 4
endothermic or exothermic peaks 298
energetic and kinetic nature of the interactions 241
energetic kinetic systems (EKS) 267
entanglement between the cross-compensations 218
entanglement of various cross-compensations 223
entanglements 142
enthalpy 71
enthalpy of activation 7
entropy and enthalpy of activation at T_g 77
entropy of activation 7, 71
epoxy-acrylic component 341
epoxy-based coating 341
epoxy/polyester appliance 389
epoxy/polyester appliance coating 343
EPR 356
equation for the thermally stimulated current 20
equation of the compensation line 321
equation of the Z-line 165
equations of depolarization 23
evidence of failure of the macromolecular dynamic models 144
evolution of units of a population 251
expression of the enthalpy ΔH_p vs. T_p 98
expression of the entropy ΔS_p vs. T_p 94
expression of the free energy ΔG vs. T_p 99
Eyring plane 85
Eyring plot 70
Eyring transform 69, 70, 85

F-conformers 145
F-conformers surrounding the *b*-grains 233
fail/pass test 348
feature of a cross-duality representation 216
fibers 312
fifth-order Runje–Kutta algorithm 255
films 312
Finitude and Stability 286
first Renaissance in physics 286
formulation of the interactions 248
free energy of activation 65
free volume 146
free volume relaxations 337
frequency front factor 265
fundamental constants of the Dual-Split Kinetics model 150
Fundamentals of Thermal Stimulated Current (TSC) 12

general polarization equation 21
geometrical features of the peak 170
glass transition 11
glues 312
“good” and “bad” samples 341
“good” and “bad” seals 358
good paint 348
Grain-Field Statistics 11, 142, 143, 259, 495, 541
Grain-Field Statistics theory of the interactions 165
grand ensemble of conformers 143, 542
gravitational interactions 286
grid of crossed parallel lines 205
grid shift factors 218
grid-shift 235
grid-shifting 167, 205, 214
“grid-shifting” procedure 169

hard domains 409
HDPE 356, 375
heat capacity 297
heating at constant rate 261
homopolymeric phases 391
horizontal and vertical structuring 145
horizontal splitting 267
horizontal splitting kinetics 272
horizontal structuring 143, 162, 543

EBSCOhost - printed on 2/13/2023 12:32 AM via . All use subject to https://www.ebsco.com/terms-of-use

horizontal structuring mode 259
hot melt adhesives 359

identify the state of the additive within the polymer matrix 379
impact of compatibility on long-term stability 357
imposition of non-equilibrium conditions 251
influence of Δ_e on the k_x statistics 150
influence of ΔH and τ_o on a Debye relaxation peak 29
influence of crystallinity on amorphous regions 357
influence of peak shifting on τ_o and ΔH 46
influence of structural parameters 304
influence of the crystalline structure on the amorphous regions 137
influence of the percentage of TiO_2 content on the amorphous state of polystyrene 451
influence of the shifting of Debye peaks 167
influence of the thermal-windowing experimental parameters 56
inside spherulitic structures 66
instantaneous depolarization 311
integration according to a Debye approximation 318
inter-intra molecular forces 143, 542
inter-intra molecular potential energy barrier 485
inter-spherulitic interface 66
interactions between the dual-conformers 251
interactions between the voltage field and temperature 169, 203
interactions between the voltage field and temperature during polarization 233
interactions of the voltage field with the polymer dielectric characteristics 186
interactive coupling 11, 63, 483
interactive coupling between the conformational states and free volume 155
interactive coupling between the conformers 338
interactive coupling between the relaxation modes 148
interactive coupling Dual-Phase model 484
interactive coupling explanation 233
intermolecular coupling 137
internal and thermal stress 381
internal motion 289
interpenetration and segregation of phases 381
interpenetration of the phases 301
intra and *inter*-molecular interactions 266
ionic dipoles 146, 335
Irganox 1076 355, 379
isolate the elementary Debye peaks 165
isomeric rotation of the conformers 243
isothermal depolarization experiments 322
isothermal return to equilibrium 271, 272

kinetic and energetic concerns working in duality 166
kinetic and thermodynamic equations 252
kinetic considerations only 253
kinetic effects 146

Lacabanne's (2/3) rule 35
ladder of scales 247
latex copolymers 391
latexes 312
LDPE 311, 312, 354, 355, 358, 422
level of atactic material 352
lignin 363
linear simplex method 321
liquid crystal polymer 362, 365, 485
$\mathrm{Ln}(\tau_o)$ grid 215, 241, 246
$\mathrm{Ln}(\tau_{os})$ grid 237
$\mathrm{Ln}(k_x)$ vs. $1/T$ 151
local density inhomogeneity 243
local duality 145
local existence of Dual-Phases (the *b* and *F* phases) 338
local microordered structures 485
local ordering 485
low frequency equivalent 146
Lycra® fiber 362

main kinetics 265
manufacturing of diapers tape 359
mastercurve 211
mastercurve compensation 241
"masterplot" of the shifted results 217
mats or fabrics 362
matter vs. vacuum 286
Maxwell–Wagner space charges 360
melamine resin 345
"mesh size" of the cross-network 190
method of "grid-shifting" 203

EBSCOhost - printed on 2/13/2023 12:32 AM via . All use subject to https://www.ebsco.com/terms-of-use

microstructure of blends and block copolymers by TWD spectroscopy 391
migration and plastification 419
migration of impurities 378, 421
migration of soluble additives between polymer phases 379
minimum free energy 252
mobility in the amorphous structure 476
mobility inside the structure 401
model of the interactions in polymers 164
modified Dussel–Bube approach 190
modified Lacabanne's integration technique 318
modulation by the dissipative term 147
modulation by the elastic dissipative network 338
molecular dipole 335
monitoring additive migration between phases or layers 379
monofilaments 362
monophasic 11
monophasic amorphous systems 485
monophasic system 481
MOS operational amplifiers 329
multi-compensation behavior 504
multi-compensation lines 84
multi-compensation network 144
multi-compensations 11, 485
multi-phase system 485
multiple compensation laws 485
multiple compensations 535

natural rubber 350, 373, 375
natural rubber (NR) and styrene–butadiene copolymer (SBR) blends 377
nature of the interactions 203
nature of the interactions in amorphous polymers 203
NBR 376
negative compensation 141, 203, 233, 541
negative compensation law 151
negative peak 331
network modulating collectively the interactions 338
network of chains 143, 542
network of compensations 149, 189
network of multi-compensations and super-compensations 141, 541
network of open dissipative cooperative systems 286
network of positive or negative compensations 141, 541
network of super-compensation lines 266
new kinetic model 255
new non-equilibrium statistics 253
NMR spectroscopy 403
nodular dipoles 373
non-conductive materials 1
normalization of the $\Delta G - T$ curves 92
normalized ΔG plane 138
normalized ΔG relaxation curves 92
normalized compensation in the Arrhenius plane 185
normalized compensation search 157
NR 376
NR/SBR blend 50:50 410
NR/SBR blends of different concentrations 408
number of dipoles 157
number of phases present 305
Nylon 12 351

on-line quality control 347
onset of cold crystallization 476
onset of energetic kinetic coupling 148
open dissipative systems of interactions 143, 543
open system dynamics 254
open-dissipative structures 11
open-dissipative-systems statistics 286
ordered morphological systems 485
orientation 383
oriented PS 384
outputs of TSD and TWD 15
over-cured 384

PA segments in PEBA 532
paints 312, 384
partial isothermal recovery 4
pasty and rubbery materials 312
PE segments in PEBA 532
peak height versus T_p 110
PEBA 2135 529
PEBA 2535 398
PEBA 900 396, 529
PEBA block copolymers 529
PEBAX copolymers 394
PEEK 168

EBSCOhost - printed on 2/13/2023 12:32 AM via . All use subject to https://www.ebsco.com/terms-of-use

pellets 312
PET 324, 332, 360, 361
phantom variable 248
phase separation and immiscibility 433
phosphates 348
physical aging 458
physical meaning of the results of TWD 241
pigments 348, 349
PMMA 66, 70, 73, 80, 81, 217, 332, 351, 433
PMMA 100 % 434
PMMA 70 % (30 % DBP) 437
PMMA 85 % (15 % DBP) 434
polarization by orientation 242
polarization is by energetic kinetic coupling distortion 242
polarization stage 329
polarization temperature 9
polarization time t_p 56
polarization voltage 56
polyacrylate 391
polyamide 12 111, 394
polycarbonate 334, 485, 502
polyester 343, 345, 384
polyether block amide copolymers 403
polyether block amides resins 394
polyethylenes of various densities 354
polymethyl methacrylate (PMMA) 168
polyolefins 351, 357
polypropylene 120, 352, 353, 360
polypropylene homopolymer 352
polystyrene 82, 162, 334, 336, 339, 351, 382, 391, 485, 487
polystyrene (PS) 168
polytetramethylglycol (PTMG) 394
population partition 252
positive and negative compensations 11, 113, 149, 160, 266
positive and negative coupling across the T_g 118
positive compensation 203
positive compensation law 151
post-painting 347
potential energy of a dual-conformer 143, 542
powder coating 340, 389
PP 352, 356
presence of additives 352
presence of heterogeneities in the structure 360
presence of three ranges of T_p values 234
pressure sensitive adhesives (PSAs) 350
pressure-sensitive adhesives (PSA) by TWD 446
Prigogine's work 11
production quality control test 341
properties of Debye peaks 46
properties of the GRID 211
proportionality between Entropy and peak height 108
provocative thoughts 247
PS 384
PTMG 168, 532
PTMG 2000 394
PTMG segment 395
pure PEEK 470

quality assurance 340
quality control applications 312
quality control method 357
quenched PMMA 459
quenching 382

real and imaginary parts of the permittivity ε 18
recovery of equilibrium 251
reference grid 237
regression analysis 321
regression analysis of the "Debye" peaks 138
regression determination of the baseline 320
relativity effect in materials due to the interactions 248
relaxation map 7, 65, 66, 162
relaxation map analysis 66
Relaxation Map Analysis (RMA) 12
relaxation maps in the ΔG plane 141
relaxation maps in the DG plane 541
relaxation *modes* 149
relaxation time 3, 7
residual stresses 381
resins 312
resonance method 289
resonance peak 289
results for annealed and quenched (unannealed) samples 504
results of changing the baseline 319
return to equilibrium 166, 243
return to the Boltzmann statistics 246
return to the equilibrium state 459
return to the undisturbed state 166
reverse our methodology of investigation 249
Rheo-fluidification 145
Rheomolded 334, 339
Rheomolded polystyrene 498

EBSCOhost - printed on 2/13/2023 12:32 AM via . All use subject to https://www.ebsco.com/terms-of-use

Rheomolded PS 81
Rheomolding 145, 334, 337, 489, 536
rubber blends 403
rubber vulcanizate 375

S.A.S block copolymers 391
sample preparation 312
secondary transitions 304
segregation 391
segregation into two phases 376
self-dissipative 253
semi-crystalline polymers 101, 351
separation of the variables 244, 547
shift all the peaks to the T_g temperature 190
shifting Debye peaks to the same temperature 167
shifting effect from the compensation results 54
shifting the peaks at constant δ_x 190
shifting to a given constant free volume state 190
silver lacquer 331
simplex curve-fitting methods 41
simulation of the Debye peaks at T_p 175
single chain macromolecular dynamics 145
single Debye relaxation 25
SLP Press 12
smoothing average technique 318
soft and rubber-likematrix 409
Solomat Instruments 1
solvent-borne system 340
space charges 146, 329, 332, 335, 360, 361, 369
spectrometer 2
spectrum of relaxation lines 65
speed of cooling 382
spontaneous depolarization 324, 458
spontaneous depolarization current (SDC) 324
standard model of interactions 286
statistical copolymer 300
statistical or block copolymers 391
statistical state disturbance 166
statistical system 143, 542
“statistics” 252
structure of compensations and super-compensations 162
structure of the free energy 253
structuring of the free energy into cloning systems 267
structuring of the total population of conformers 265
styrene–butadiene rubber (SBR) 350
sub-ΔH 87
sub-ΔS 87
sub-EE curve 85
sub-EE plane 84, 138
sulphur content 375
super-compensation 160, 189, 530
super-compensation laws 186
super-compensation network 149
super-compensation phenomenon 535
super-compensation point 185, 198
surface conductivity 147
suspension of the specimen 322

T_β 335
T_β and T_{LL} from the variation of the Entropy with T_p 65
T_g, $T_{g,\rho}$ and T_{LL} 335
$T_{g,\rho}$ 144, 164
$T_{g,\rho}$ peak 141, 145, 233, 333–337, 339
$T_{g,r}$ peak 541
$T_g(L)$ and $T_g(U)$ 494
T_{gL} and a T_{gU} 168
$T_g(U)$ glass transition 474
T_{LL} 144, 163, 164, 333, 485
T_{LL} manifestation 233
T_{LL} temperature 168, 495
T_{LL} transition 145, 156, 181
temperature dependence of the shift factor 305
temperature drift between the enthalpic and the entropic term of an interaction 247
temperature gradients 322
temperature of polarization T_p 56
temperature T_{LL} 142
temperature T_x 156
the energetic kinetic dissipative network of conformers (EKNET) 143
the super-compensations 183
the TWD challenge 234
“thermal activated” methods 294
thermal activation alone 163
thermal electret 329
thermal history patterns 489
thermal stimulation 12
Thermal-Stimulated Depolarization peaks 1
Thermal-Stimulated Polarization and Depolarization 19
thermal-stimulated polarization current (TSPC) 371

EBSCOhost - printed on 2/13/2023 12:32 AM via . All use subject to https://www.ebsco.com/terms-of-use

thermal-windowing as a filtering process 165
Thermal-Windowing Deconvolution 1, 4, 166, 297
Thermal-Windowing Deconvolution (TWD) 10, 65
thermal-windowing protocol 153
thermally stimulated current of depolarization 24
thermally stimulated recovery experiment 3
thermokinetic characteristics 327
thermokinetic characteristics of the peak 203
thermokinetic functions 69
thermokinetic parameters 483
thermokinetic relaxation lines 92
thermokinetic variables 65
three mechanisms of interactions 186
time vs. space 286
TiO_2 particles 349
titanium 348
TMA 2
total dissipative function 144, 543
TPOs 356, 357
traditional interpretation 163
traditional interpretations of compensations 163
transitions in polymers by dynamic spectroscopy 304
trapped delocalized charges 324
TSC/RMA 1
TSD 2, 8, 289, 294–296, 300, 305, 309–312, 315–317, 320, 322, 324, 326, 327, 329
TSD and TWD stimulation techniques 251
TSD cell 329
TSD curve for polycarbonate 332
TSD curve for polyethylene terephthalate (PET) 332
TSD depolarization curve 331
TSD spectrum of atactic polypropylene 352
TSD trace of drawn and undrawn polypropylene 353
TSD/TWD 2
TSD/TWD spectrometer 65
TSD/TWD spectroscopy 289
TWD 8, 289, 296–298, 301, 309, 312, 315–317, 320, 322, 327, 392

unannealed Vectra 367, 516
under-cured 342, 384
understanding of the coupling mode 138
undrawn and drawn polypropylene 134
undrawn polypropylene 120

V.O.C. emissions 347
Van der Waals or London forces 348
Vectra 365
Vectra 900 504
Vectra A900 365
vertical and horizontal structuring 165
vertical and horizontal structuring kinetics 150
vertical Dual-Split Kinetic model 265
vertical Dual-Split Kinetics 254
vertical Dual-Split statistics 266, 267
vertical split structuring 249
vertical splitting 253
vertical structuring 143, 536, 543
vertical structuring of the Grain-Field Statistics 235
vibration 489
voltage field stimulation 149
volume around the *F* conformers 146
vulcanizates 403
vulcanization 403
vulcanized blend of NR and NBR 404
vulcanized blends 373

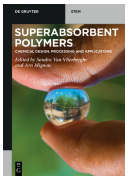
water-borne systems 340
window width $(T_p - T_d)$ 56
windowing polarization techniques 137
wood 363, 521

Z-line 73, 78, 155, 493
Z-lines for the PMMA doped at various content of plasticizer 445
Z-structure 65, 73, 78
zinc oxide 348

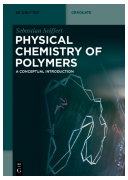
EBSCOhost - printed on 2/13/2023 12:32 AM via . All use subject to https://www.ebsco.com/terms-of-use

EBSCOhost - printed on 2/13/2023 12:32 AM via . All use subject to https://www.ebsco.com/terms-of-use

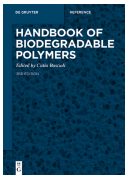
Also of interest



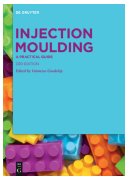
Superabsorbent Polymers.
Chemical Design, Processing and Applications
Sandra Van Vlierberghe and Arn Mignon (Eds.), 2021
ISBN 978-1-5015-1910-9, e-ISBN 978-1-5015-1911-6



Physical Chemistry of Polymers.
A Conceptual Introduction
Sebastian Seiffert, 2020
ISBN 978-3-11-067280-0, e-ISBN 978-3-11-067281-7



Handbook of Biodegradable Polymers
Catia Bastioli (Ed.), 2020
ISBN 978-1-5015-1921-5, e-ISBN 978-1-5015-1196-7



Injection Moulding.
A Practical Guide
Vanessa Goodship (Ed.), 2020
ISBN 978-3-11-065302-1, e-ISBN 978-3-11-065481-3

EBSCOhost - printed on 2/13/2023 12:32 AM via . All use subject to https://www.ebsco.com/terms-of-use

EBSCOhost - printed on 2/13/2023 12:32 AM via . All use subject to https://www.ebsco.com/terms-of-use